Italian Manufacturing Association Conference XVII AITeM

XVII AITeM (Italian Manufacturing Association) Conference
10-12 September 2025,
Politecnico di Bari, Italy



Edited by
Livan Fratini,
Luca Settineri

MRF

Italian Manufacturing Association Conference
XVII AITeM

XVII AITeM (Italian Manufacturing Association) Conference, held at Politecnico di Bari, Italy, from 10 to12 September 2025

Editors
Livan Fratini[1] and Luca Settineri[2]

[1]Dipartimento di Ingegneria, University of Palermo, Palermo, Italy
[2]Dipartimento di Ingegneria Gestionale e della Produzione (DIGEP), Politecnico di Torino, Torino, Italy

Peer review statement

All papers published in this volume of "Materials Research Proceedings" have been peer reviewed. The process of peer review was initiated and overseen by the above proceedings editors. All reviews were conducted by expert referees in accordance to Materials Research Forum LLC high standards.

Copyright © 2025 by authors

Content from this work may be used under the terms of the Creative Commons Attribution 3.0 license. Any further distribution of this work must maintain attribution to the author(s) and the title of the work, journal citation and DOI.

Published under License by **Materials Research Forum LLC**
Millersville, PA 17551, USA

Published as part of the proceedings series
Materials Research Proceedings
Volume 57 (2025)

ISSN 2474-3941 (Print)
ISSN 2474-395X (Online)

ISBN 978-1-64490-372-8 (Print)
ISBN 978-1-64490-373-5 (eBook)

This book contains information obtained from authentic and highly regarded sources. Reasonable efforts have been made to publish reliable data and information, but the author and publisher cannot assume responsibility for the validity of all materials or the consequences of their use. The authors and publishers have attempted to trace the copyright holders of all material reproduced in this publication and apologize to copyright holders if permission to publish in this form has not been obtained. If any copyright material has not been acknowledged please write and let us know so we may rectify in any future reprint.

Distributed worldwide by

Materials Research Forum LLC
105 Springdale Lane
Millersville, PA 17551
USA
https://mrforum.com

Manufactured in the United State of America
10 9 8 7 6 5 4 3 2 1

Table of Contents

Preface
Organizing Committee

Quality engineering and production metrology

Investigation of glass-fiber reinforced polypropylene properties dependence on post-consumer recycled polypropylene content
Anna BORTOLETTO, Matteo MICHELINI, Luca GAZZOLA, Adrian L. KELLY, Ben R. WHITESIDE, Marco SORGATO, Giovanni LUCCHETTA 2

Impact of contour on surface quality, dimensional and geometrical accuracy of Ti48Al2Cr2Nb parts produced with powder bed fusion with electron beam process
Giovanni RIZZA, Manuela GALATI, Paolo MINETOLA, Paolo ANTONIONI, Danilo BRUSON, Giovanni MARCHIANDI, Luca IULIANO 11

A synergistic integration of photogrammetry and Gaussian Splatting for back-in-time quality inspection
Mattia TROMBINI, Domenico A. MAISANO, Fiorenzo FRANCESCHINI 20

Preliminary experimental results on a multidimensional model for cognitive assistance systems in manufacturing
BARTOLOMEI Mirco, BARRAVECCHIA Federico, REA Maria, MASTROGIACOMO Luca, CANNIZZARO Davide, FRANCESCHINI Fiorenzo 29

Detection of sub-superficial defects by infrared thermography in parts made by powder bed fusion with electron beam
Silvio DEFANTI, Simone DE GIORGI, Giovanni RIZZA, Giulia COLOMBINI, Emanuele TOGNOLI, Ahmet Ayberk Gürbüz, Lucia DENTI, Manuela Galati, Luca Iuliano 38

Real-time mental workload assessment with low intrusiveness for assembly processes: Limits and preliminary results
Riccardo GERVASI, Matteo DE MARCHI, Luca MASTROGIACOMO, Dominik T. MATT, Fiorenzo FRANCESCHINI 47

Effect of cast extrusion parameters on the surface properties of films made of polyethylene blends with olefinic ionomers
Annalisa GENOVESI, Alessandra CAGGIANO, Massimiliano BARLETTA 56

Impact of surface determination techniques on dimensional and geometrical metrology using X-ray computed tomography
Federico PIRILLO, Huan SHAO, Stefano PETRÒ, Giovanni MORONI 64

Advanced active thermography for weld joint inspection
Valentino RAZZA, Manuela DE MADDIS, Pasquale RUSSO SPENA, Luca SANTORO 72

Document-type classification errors in bibliometric databases: Insights from the engineering/manufacturing field
Domenico Augusto MAISANO, Lucrezia FERRARA, Fiorenzo FRANCESCHINI 80

Additive manufacturing and reverse engineering

The effect of additive manufacturing-induced anisotropy on tool wear when machining martensitic nitinol
Flavia Tucci, Rachele Bertolini, Andrea Ghiotti, Stefania Bruschi 91

Effect of process parameters on $AlCoCr_2FeMo_{0.5}Ni$ high-entropy alloy coatings produced using laser directed energy deposition
Chiara GIANASSI, Erica LIVERANI, Alessandro ASCARI, Alessandro FORTUNATO 99

Instrumented indentation tests for local temperature-dependent mechanical properties assessment of laser-based powder bed fusion of aluminium alloy
Stefano GUARINO, Gennaro Salvatore PONTICELLI, Alfio SCUDERI, Simone VENETTACCI, Vittorio VILLANI 107

Optimizing 3D printing process parameters for high-performance inflatable soft actuators
RIFINO Rosanna, PRICCI Alessio, PERCOCO Gianluca 116

Understanding powder transport mechanisms in directed energy deposition via design of experiments
Adriano Nicola PILAGATTI, Eleonora ATZENI, Alessandro SALMI, Luca IULIANO 128

Physics-based model for dot geometry prediction in dot-by-dot wire arc additive manufacturing
Niccolò GROSSI, Guido PIERATTINI, Riccardo LILLI, Antonio SCIPPA 136

Design and preliminary testing of innovative tooling system elements obtained by L-PBF process for effective suppression of chatter vibrations
SCALZO Federico, TOTIS Giovanni, VAGLIO Emanuele, ANTONIALLI Armando Ítalo Sette, SORTINO Marco 145

A preliminary study about high-pressure homogenization as a viable alternative to produce powder feedstock for selective laser sintering of biopolymers
Alberto GIUBILINI, Giovanna COLUCCI, Manuela GALATI, Giovanni MARCHIANDI, Massimo MESSORI, Luca IULIANO, Paolo MINETOLA 154

In-situ monitoring of laser powder bed fusion on multi-material substrates for electric mobility
Marco Grasso, Matteo Bugatti, Frank Sarfert, Aitor Echaniz, Bianca Maria Colosimo 164

FFF of PLA reinforced with flax: Effects of the infill strategy on low-velocity impact behavior and the energy consumption
Ersilia COZZOLINO, Ilaria PAPA, Antonello ASTARITA, Valentina LOPRESTO 172

Silicone 3D printing: Experimental validation of a reduced-order numerical model for optimal layer deposition
PRICCI Alessio, PERCOCO Gianluca 180

Optimization of process parameters for fused filament fabrication of ULTEM 1010
VAGLIO Emanuele, BILLÈ Erica, GAMBITTA Alessandro, RONDINELLA Alfredo, TOTIS Giovanni, SCALZO Federico, SORTINO Marco 190

Impact of cell dimensions and beam radius on the bending characteristics of BCC sandwich panels produced via L-PBF of Ti6Al4V
Dina PALMERI, Gaetano POLLARA, Gianluca BUFFA, Livan FRATINI 199

Effect of cyclic loading and thermal stimuli on the shape memory behavior of PLA 3D-printed cellular structures
Desole M.P., Gisario A. 208

From design to reality: Improving multimaterial powder bed fusion laser melting additive manufacturing via in-situ monitoring
Stefania Cacace, Matteo Bugatti, Bianca Maria Colosimo 216

Process capability investigation on the 3D printing technique for hybrid silica-based sands cores
Mukul Ramesh Kumar, Stefania Cacace, Maurizio Chiesa, Daniele Chiesa, Paolo Parenti 225

Preliminary study on evaluation of printing parameters for a MEX repair application
Raniero PIRLO, Marco LAFIRENZA, Maria Grazia GUERRA, Fulvio LAVECCHIA, Luigi Maria GALANTUCCI 234

Experimental characterization of QP1180 steel and its performance in stamping simulation: Comparison with DP1180
Maria Emanuela Palmieri, Matteo Villa, Michele Abruzzo, Giuseppe Macoretta, Stefania Bruschi, Luigi Tricarico 242

Materials processing technology

Textured tools and cryogenic cooling for modifying chip morphology in PEEK machining
Anna Bottin, Rachele Bertolini, Stefania Bruschi 251

Comparison between the mechanical properties and environmental sustainability of basalt and carbon fiber reinforced polymers hoop filament wound components
Iacopo BIANCHI, Massimo DI PIETRO, Archimede FORCELLESE, Francesco GALLIANI, Tommaso MANCIA, Chiara MIGNANELLI, Michela SIMONCINI, Tommaso VERDINI 259

Effect of heat shrinkable tape layer number on mechanical properties and quality of tubular CFRP components obtained by filament winding
Marina ANDREOZZI, Iacopo BIANCHI, Archimede FORCELLESE, Chiara MIGNANELLI, Massimiliano PIERALISI, Michela SIMONCINI, Tommaso VERDINI 268

Comparative study of autoclave thermoforming and hot-press moulding for manufacturing green composite parts
G. Parodo, L. Sorrentino, S. Turchetta 278

Laser texturing of 3D Copper current collector for ultrafast Zinc metal plating
Vincenzina SICILIANI, Nassima YAMINI, Riccardo PELACCIA, Andrea PAOLELLA, Leonardo ORAZI 286

Study of printing parameters on part performance in foamy TPU using material extrusion technology
Francesco de PALMA, Alessandro PELLEGRINI, Roberto SPINA, Fulvio LAVECCHIA 294

Manufacturing processes design, optimization and engineering

Enhancing the robustness of nanostructures through the production of self-protective structures by injection molding of thermoplastic elastomers
Giacomo BARUFFA, Keltoum OUBELLAOUCH, Giulia ZANIBONI, Giovanni LUCCHETTA, Marco SORGATO 303

Physical foaming of 25% post-industrial recycled TPU using the supercritical foaming technology
Francesco MACIARIELLO, Giovanni LUCCHETTA, Marco SORGATO 311

Numerical modeling of high-speed laser cutting of copper current collectors
Samuele Piandoro, Caterina Angeloni, Alessandro Fortunato, Erica Liverani, Alessandro Ascari 319

Friction stir welding of AA6082 and AA5083 T-joints for naval applications: Finite element modeling and experimental analysis of material flow
Guido Di Bella, Mohamed Chairi, Davide Campanella, Riccardo Puleo, Gianluca Buffa 327

Switching supervisory control in fusion laser cutting with vision-based process state detection
CAPRIO Leonardo, GUERRA Sofia, PACHER Matteo, GANDOLFI Davide, SAVARESI Sergio Matteo, TANELLI Mara, PREVITALI Barbara 335

Peripheral coarse grain prediction in extruded AA6082: Combining finite element simulations with neural networks
Marco Negozio, Adrian H.A. Lutey, Antonio Segatori, Riccardo Pelaccia, Sara Di Donato, Barbara Reggiani, Lorenzo Donati 344

Investigating the tube production via friction stir extrusion of aluminum chips
Riccardo PULEO, Muhamad ADNAN, Giuseppe INGARAO, Gianluca BUFFA, Livan FRATINI 352

Identification of tool tip frequency response function through surface location error
Lorenzo MORELLI, Niccolò GROSSI, Antonio Scippa 360

An AI-based approach for flow front monitoring and prediction in liquid composite molding processes based on dielectric and visual data elaboration
Vitantonio ESPERTO, Fausto TUCCI, Felice RUBINO, Pierpaolo CARLONE 369

Modeling of molten pool geometry and remelting layer in the laser ablation of Ti6Al4V alloy
Maria Rosaria SAFFIOTI, Serafino CARUSO, Giovanna ROTELLA, Domenico UMBRELLO 377

Surface Integrity study in cryogenic milling of Ti-6Al-4V titanium alloy
Paolo Albertelli, Michele Monno 385

Resin molds to improve thermal energy consumption in injection molding process
Giulia ZANIBONI, Riccardo PELACCIA, Leonardo ORAZI, Rossella SURACE, Giovanna ROTELLA, Vito BASILE 393

Assembly, disassembly and circular economy

A value-driven approach to printed circuit board inspection: Strategic use of inspection technologies to reduce waste
Stefano PUTTERO, Elisa VERNA, Gianfranco GENTA, Maurizio GALETTO 402

Exploring multi-human multi-robot collaboration in assembly processes: Challenges and opportunities in quality and manufacturing
Matteo CAPPONI, Aurora Sofia DI MATTEO, Luca MASTROGIACOMO 410

Reuse of 316L stainless steel towards zero-waste laser powder bed fusion
Gabriele LOCATELLI, Sara BOCCHI, Mariangela QUARTO, Gianluca D'URSO 418

Welding and wire arc additive manufacturing using FSE solid-state recycled wires: Challenges and future perspectives
Gustavo H.S.F.L. CARVALHO, Gianni CAMPATELLI, Gianluca BUFFA 426

Optimization of manufacturing processes for PS-paper powder compounds in sustainable foodservice plates
Arif Enes KARACA, Alessandra CAGGIANO, Massimiliano BARLETTA 434

Towards the wire-feed friction stir extrusion-based additive manufacturing of aluminum alloys
Kirill KALASHNIKOV, Davide CAMPANELLA, Muhammad ADNAN, Rosa DI LORENZO, Giuseppe INGARAO, Gianluca BUFFA, Livan FRATINI 441

Development of low environmental impact technological solutions based on PLA, PBS, PBAT and Talc blends for multilayer food packaging manufacturing
Marzio MILO DI VILLAGRAZIA, Alessandra CAGGIANO, Annalisa GENOVESI, Massimiliano BARLETTA 449

Reciprocal human–machine learning flow modelling for assisted assembly systems
Yuchen FAN, Alessandro SIMEONE, Dario ANTONELLI 457

Environmental impact assessment of adhesive joints in basalt fibre-reinforced thermoplastic composites using LCA methodology
Luigi BENVENUTO, Chiara MANDOLFINO, Pietro RUSSO, Matteo BENVENUTO, Marco PIZZORNI, Enrico LERTORA 466

A decisional framework for second-life applications of textile waste: A data-driven and generative AI approach
Giovanni DE MARTINO, Rosa LEONE, Marica BUCCI, Michele DASSISTI 475

Thermal and Joule effect debonding techniques: Evaluation of mechanical strength and LCA analysis of bonded joints
Matteo Benvenuto, Enrico Lertora, Marco Pizzorni, Luigi Benvenuto, Alessia Lusiani, Chiara Mandolfino 484

Fostering sustainability-oriented product innovation: A comprehensive framework to support product development for a circular economy
Luigi PANZA, Giulia BRUNO, Paolo CHIABERT 493

Process and system simulation, optimization and digital manufacturing

Implementing Job Sequencing in a CONWIP fully automated assembly line
Arianna ALFIERI, Claudio CASTIGLIONE, Erica PASTORE..... 503

Integrating buffer "stock" and buffer loops in an assembly line with conveyors: An automotive case study
Claudio CASTIGLIONE, Erica PASTORE, Arianna ALFIERI 512

Metaheuristic approaches for solving the scheduling problem in the semiconductor diffusion work area
Roberto Rosario CORSINI, Antonio COSTA, Valeria FICHERA, Giuseppe ORITI, Daniele PAGANO 521

A mathematical modeling approach for job allocation at STMicroelectronics
EL ACHKAR Elias, FRIGERIO Nicla, PAGANO Daniele, MATTA Andrea 530

Digitalization of broaching processes: a scalable approach to industry 4.0 in small and medium enterprises
Michele ABRUZZO, Gino DINI, Gualtiero FANTONI, Luca ROMOLI, Marko VUKOVIC 539

Digital twin solutions for state-aware, dynamic task allocation in flexible cyber-physical production systems
Matteo DE MARCHI, Erwin RAUCH, Dominik T. MATT..... 548

Field-driven design of functionally graded TPMS-based 3D printed sandwich structures: Modeling, printing and testing
Gabriele Marabello, Guido Di Bella 556

Deep learning-based monitoring of laser beam direct energy deposition to detect deviations in process conditions
M. Mazzarisi, M.G. Guerra, A. Angelastro, L.M. Galantucci, S.L. Campanelli 565

Miscellaneous

Nanoscale topographical characterization of permeability-related features in the production of polymeric films for food packaging
Giacomo MACULOTTI, Alberto PIOVANO, Gianfranco GENTA, Maurizio GALETTO..... 575

Design optimization and one-shot 3D printing of a bio-inspired soft robot capable of counter-flexural motion at low actuation pressures
Luca DI LEO, Alessio PRICCI, Andrea GRAVILI, Gianluca PERCOCO 583

Fabrication of shape memory composites for non-explosive release mechanisms in space applications
Denise BELLISARIO, Leandro IORIO, Dounia NOQRA, Giorgio PARTIZII, Alice PROIETTI, Fabrizio QUADRINI, Loredana SANTO 592

Towards efficient defect detection in injection molding with transformer models
Andrea PIERESSA, Marco SORGATO, Giovanni LUCCHETTA..... 600

Supervised autoencoder for fault detection and diagnosis in predictive maintenance of bearing ring grinding machine
Pietro Andrea MICIACCIA, Giovanni PASCOSCHI, Antonio DECATALDO, Domenico MONOPOLI, Concetta SEMERARO, Michele DASSISTI..... 608

An experimental approach exploiting high-voltage fragmentation as a selective comminution technology for the recovery of key metals
Marco DIANI, Shravan TORVI, Marcello COLLEDANI..... 617

Work in progress and laboratories

An automatic system of handling and heating samples during dynamic hot compression tests
G. Soardi, C. Guerra, M. Seiti, A. Abeni, A. Attanasio, E. Ceretti..... 626

A technological analysis and prototype design for efficient and flexible stacking processes
Sen BAI, Nicla FRIGERIO, Daniela FONTANA, Andrea MATTA..... 631

Development of a repair strategy for a thin aerospace component with dot-by-dot deposition approach
Gianni CAMPATELLI, Gustavo H.S.F.L. CARVALHO, Paolo C. PRIARONE..... 639

Manufacturing quotation platform for turned parts: The PLAT4M project
Antonio SCIPPA, Niccolò GROSSI 647

Preliminary numerical and experimental investigation of clamping effects on one-up drilling of stacked aluminium aerospace components
Martina Panico, Massimo Durante, Antonio Langella, Luca Boccarusso 655

Manufacturing of vitrimer matrix composite substrates for cold-spray coatings
Fausto TUCCI, Barbara PALMIERI, Alessia Serena PERNA, Antonio VISCUSI, Alfonso MARTONE, Antonello ASTARITA..... 665

Keyword Index

Preface

This book presents selected peer reviewed papers presented to the XVII AITeM (Italian Manufacturing Association) Conference, held at Politecnico di Bari from 10 to12 September 2025.

AITeM is an officially recognised association dedicated to the academic and industrial world, with a special focus on young researchers. AITeM is a meeting platform for Research and Innovation players – manufacturing companies, universities, other public research institutions, as well as professionals and other experts – to discuss the most urgent issues within our industry. The Association promotes the study, the development of knowledge and the application of manufacturing technologies and systems in all their aspects, including:

- transformation processes of products, from production to assembly, from testing to recycling;
- mechanical and technological characterisation of the transformed materials;
- methodologies and tools for designing transformation systems (instrumental goods), processes, and components;
- programming, management and control of production, assembly, testing, and recycling systems;
- quality management and environmental safeguard management for sustainable development.

AITeM also promotes events and initiatives for disseminating knowledge within the manufacturing sector, either autonomously or in collaboration with national and international partners.

Every two years, AITeM organises a national Conference: the Association's key moment of vitality is a forum to discuss and debate the latest manufacturing topics.

This Conference serves as a meeting place for the scientific community in the field of manufacturing and is open to all researchers working on the themes of manufacturing technologies.

The scientific program of the Conference is divided into different sessions which can guarantee broad participation in the works of the Conference both in the presentation and discussion phases.

The sessions of the XVII AITeM Conference include:

- Quality engineering and production metrology
- Additive Manufacturing and reverse Engineering
- Materials processing technology
- Manufacturing processes design, optimization and engineering
- Assembly, disassembly and Circular Economy
- Process and system simulation, optimization and digital manufacturing
- Miscellaneous
- Work in progress and laboratories

The sessions contain the contributions coming mainly from AITeM members. They are designed to showcase different types of papers: the traditional Scientific sessions contain contributions of

experienced members who want to share the results achieved with colleagues, the Work in Progress and Laboratories session features ongoing activities and laboratories that offer new ideas and propositions for collaboration and explore future research directions.

The selection of papers was made by the Editorial Committee on the basis of peer reviews. More than 150 reviewers were involved. The reviews considered the coherence of the topic covered with the AITeM topics, the novelty with respect to the state of the art, and the overall scientific quality of the work.

Committees

Editorial Committee

Livan Fratini, Università di Palermo - President
Wilma Polini, Università di Cassino
Pierpaolo Carlone, Università di Salerno
Aldo Attanasio, Università di Brescia
Marco Sorgato, Università di Padova
Paolo Parenti, Politecnico di Milano
Flaviana Calignano, Politecnico di Torino
Olivier Terzo, Fondazione Links
Ciro Sinagra, Laminazione Sottile S.p.A.

Organizing Committee

Luigi Maria Galantucci, Politecnico di Bari – Honorary Chairman
Michele Dassisti, Politecnico di Bari - Coordinator
Antonino Squillace, Università di Napoli Federico II – Coordinator of the 2023 AITeM Conference
Fabrizio Memola Capece Minutolo, Università di Napoli Federico II - Board delegate
Members of Dipartimento di Meccanica Matematica e Management – Politecnico di Bari:
Andrea Angelastro, Sabina Luisa Campanelli, Giuseppe Casalino, Nicola Contuzzi, Angela Cusanno, Luigi Ciro Alberto de Filippis, Vito Errico, Maria Grazia Guerra, Pasquale Guglielmi, Fulvio Lavecchia, Marco Mazzarisi, Maria Emanuela Palmieri, Gianfranco Palumbo, Gianluca Percoco, Antonio Piccininni, Donato Sorgente, Roberto Spina, Gianni Stano, Luigi Tricarico

AITeM - Italian Manufacturing Association

Dipartimento di Ingegneria Chimica, dei Materiali e della produzione industriale dell'Università Federico II di Napoli
Piazzale V. Tecchio, 80, 80125 – Napoli, Italy
Phone: +39 3441203243
Email: segreteria@aitem.org
Website: www.aitem.org

Quality engineering and production metrology



Materials Research Proceedings 57 (2025) 2-10 https://doi.org/10.21741/9781644903735-1

Investigation of glass-fiber reinforced polypropylene properties dependence on post-consumer recycled polypropylene content

Anna BORTOLETTO[1,a], Matteo MICHELINI[2,b], Luca GAZZOLA[2,c], Adrian L. KELLY[3,d], Ben R. WHITESIDE[3,e], Marco SORGATO[1,f], Giovanni LUCCHETTA[1,g]

[1]Department of Industrial Engineering, University of Padova, Padova (PD), Italy

[2]R&D Department, Sirmax S.p.A., Cittadella (PD), Italy

[3]IRC in Polymer Science & Technology, University of Bradford, Bradford, Great Britain

[a]anna.bortoletto.4@phd.unipd.it, [b]mmichelini@sirmax.com, [c]lgazzola@sirmax.com, [d]A.L.Kelly@bradford.ac.uk, [e]B.R.Whiteside@bradford.ac.uk, [f]marco.sorgato@unipd.it, [g]giovanni.lucchetta@unipd.it

Keywords: Circular Economy, Sustainability, Fiber-Reinforced Plastic, Post-Consumer Recycling, Polypropylene

Abstract. Polymer composites like glass fiber-reinforced polypropylene (GFRP) are widely used for their strength and lightweight properties, but their limited recyclability has raised significant sustainability challenges. This study explores the potential to improve the sustainability of GFRP composites by adding post-consumer recycled polypropylene (rPP). The impact of rPP and specifically of titanium dioxide (TiO_2), found in rPP as a residue of white inks, is evaluated. Two material sets were analyzed: one with varying rPP percentages and one with different TiO_2 levels intentionally added to virgin PP. Mechanical and rheological properties were evaluated through tensile and impact strength, DSC, TGA, SEM, and fiber length measurements. Results revealed TiO_2 contamination reduces fiber length, contributing to mechanical performance degradation. The findings highlight TiO_2's significant role in recycled GFRP performance and emphasize improving recycling processes to enhance sustainability.

Introduction

Polymer-based composite materials are produced by incorporating a reinforcing phase into a polymer matrix, resulting in a significant enhancement of mechanical properties [1]. These materials are extensively employed across various industrial sectors, particularly in the fabrication of structural components requiring high performance [2]. Among the different types of polymer composites, glass fiber-reinforced polymers (GFRPs) are the most widespread [3], especially in the automotive industry, where they enable substantial weight reduction without compromising mechanical strength [4]. Glass fiber-reinforced polypropylene (GFR-PP), in particular, is valued for its advantageous combination of mechanical strength, low density, corrosion resistance, and cost-effectiveness [5]. Owing to these attributes, the present study focuses on the investigation of this specific material.

A major issue associated with glass fiber composites lies in balancing mechanical performance, production costs, and environmental sustainability. Increasingly stringent regulations and rising consumer awareness regarding sustainability have intensified concerns about the disposal of GFRPs, which are predominantly incinerated or landfilled [6]. A promising approach to reduce dependence on virgin petrochemical-based materials involves the incorporation of recycled polypropylene (rPP) into composite formulations [7]. However, integrating recycled polymers into high-performance applications remains difficult due to potential reductions in mechanical properties and processing limitations.

Content from this work may be used under the terms of the Creative Commons Attribution 3.0 license. Any further distribution of this work must maintain attribution to the author(s) and the title of the work, journal citation and DOI. Published under license by Materials Research Forum LLC.

Different recycling strategies are available for polypropylene-based composites, including mechanical, chemical, and thermal methods, with mechanical recycling being the most widely employed [8]. This process involves grinding and shredding, which often results in fiber degradation and generation of lower-grade recycled materials, typically used as fillers [9]. Research suggests that performance deterioration can be mitigated through strategies such as optimizing fiber content [10], improving fiber-matrix adhesion [11], and applying compatibilization techniques [12]. The mechanical behavior of a composite is generally governed by three primary factors: the properties of the reinforcement, the characteristics of the polymer matrix, and the interaction between these two phases [13]. It is well established that increasing fiber length and content improves tensile and flexural strength, as well as impact resistance, with optimal performance typically achieved in the 40–50 wt% fiber content range [14]. However, recycled polypropylene exhibits reduced mechanical performance due to polymer chain degradation during repeated recycling cycles, and blending rPP with virgin polypropylene may introduce phase incompatibility issues [15].

In light of the increasing emphasis on sustainability in composite material development, there is a clear need for innovative solutions that maintain high performance while minimizing environmental impact. To date, limited research has explored composite formulations that combine virgin and recycled polypropylene matrices with virgin glass fibers. This study aims to evaluate the effects of progressively increasing the proportion of post-consumer recycled (PCR) polypropylene in GFR-PP systems. To this end, composite formulations containing PCR PP concentrations ranging from 0% to 70% were produced and analyzed. The investigation focuses on assessing the properties of the polymer matrix, the characteristics of the reinforcing fibers, and their interfacial interactions to determine their respective contributions to overall mechanical performance. Furthermore, this research introduces a novel aspect by examining the influence of titanium dioxide (TiO_2), a widely used pigment in white inks. Despite undergoing washing steps during recycling, TiO_2 remains in post-consumer recycled polypropylene and may interact with the reinforcing fibers, potentially affecting the mechanical integrity of the resulting composite.

Materials and Methods

The virgin matrix material used in this study is a polypropylene copolymer from Braskem Europe, while the recycled component consists of post-consumer recycled polypropylene provided by Sirmax S.p.A. (Cittadella, Padova, Italy). This recycled polypropylene originates from European urban packaging waste and is processed through a mechanical recycling process. The recycling includes automated plastic identification and separation, followed by grinding, centrifugal and horizontal washing, and drying. Blends of virgin PP with 0%, 5%, 8%, 10%, 30%, 50%, and 70% rPP were prepared. These blends were subsequently reinforced with 30 wt% glass fibers (ThermoFlow®), featuring a diameter of 13 μm and a chopped strand length of 4 mm. This series of formulations is hereafter referred to as “GFRPP + rPP.” In parallel, a second series of compounds was developed to isolate and investigate the effect of TiO_2 on composite performance. These formulations were composed of 100% virgin PP reinforced with glass fibers, to which titanium particles were intentionally added. Several working hypotheses were considered. First, TiO_2, being a very hard particle, could induce mechanical interference with the glass fibers during extrusion and injection molding, resulting in breakage points and microcracks, ultimately leading to fiber shortening. Second, titanium might interfere with fiber-matrix interfacial adhesion. Third, TiO_2 could act as a nucleating agent, negatively affecting the homogeneity of the matrix. This second set of compounds is referred to as “GFRPP + TiO_2” and was specifically developed to address these hypotheses. An overview of the formulations analyzed in this study is provided in Table 1.

Table 1. Compounds manufactured for the two sets of materials, with different contents of recycled polypropylene and titanium dioxide.

GFRPP + rPP		**GFRPP + TiO_2**	
Name of the compound	*Recycled PP content [%]*	*Name of the compound*	*Titanium Dioxide content [%]*
R000/T000	0	R000/T000	0
R001	5	T001	0.1
R002	8	T002	0.2
R003	10	T003	0.3
R004	30	T004	0.5
R005	50	T005	0.7
R006	70	T006	1

Inductively Coupled Plasma Optical Emission Spectroscopy (OCP-OES) was employed to quantify the actual TiO_2 content in the "GFRPP + rPP" formulations. This technique allows the measurement of metallic elements within a material by analyzing the emitted electromagnetic radiation following plasma excitation.

The mechanical properties of the composites were evaluated through standardized testing. Tensile specimens were produced using an electric Fanuc Roboshot injection molding machine (S-2000i100A) and tested on an Instron 5966 machine following ISO 527-2. Impact resistance was assessed using the notched IZOD method, following the ISO 180.

The rheological properties were characterized via differential scanning calorimetry (DSC), thermogravimetric analysis (TGA), and rotational rheometry. Detailed processing conditions are reported in Table 2.

Table 2. Details of the rheological testing that was performed on each of the materials.

DSC		**TGA**		**RHEOMETER**	
Instrument	TA Instrument DSC 2500	*Instrument*	TA Instrument TGA 5500	*Instrument*	Anton Paar Physica MCR 301
Temperature	10 °C/min up to 250 °C, 10 °C/min down to -90 °C, 10 °C/min up to 250 °C	*Temperature*	10 °C/min up to 500 °C	*Temperature*	230 °C
				Sweep	Amplitude: 100 – 0.01 Frequency: 500 - 0.05 rad/s

Fracture surfaces were analyzed to evaluate matrix-fiber adhesion and fiber pull-out phenomena. Both tensile and cryogenically fractured specimens were examined using scanning

electron microscopy (SEM). Cryogenic fractures were obtained by immersing the specimens in liquid nitrogen, followed by manual fracturing. SEM analysis was conducted in high-vacuum mode at an accelerating voltage of 20 kV on gold-coated samples. Elemental composition, with a specific focus on titanium dioxide content and distribution, was determined via energy-dispersive X-ray spectroscopy (EDX).

Fiber length analysis was conducted to investigate potential interactions with titanium dioxide. To isolate the glass fibers, the polymer matrix was removed by pyrolysis: pellets were burned at 400 °C for 4 hours. The recovered fibers were then carefully dispersed onto transparent plastic films using a miniature pump to minimize fiber overlap and ensure uniform distribution. The samples were imaged using an Epson A3 high-resolution scanner in 8-bit greyscale mode at 12800 dpi, with contrast enhanced by placing the films over a black background (Fig. 1a). Image analysis was performed using ImageJ software, and approximately 1000 fibers per material were manually measured to ensure statistical reliability (Fig. 1b).

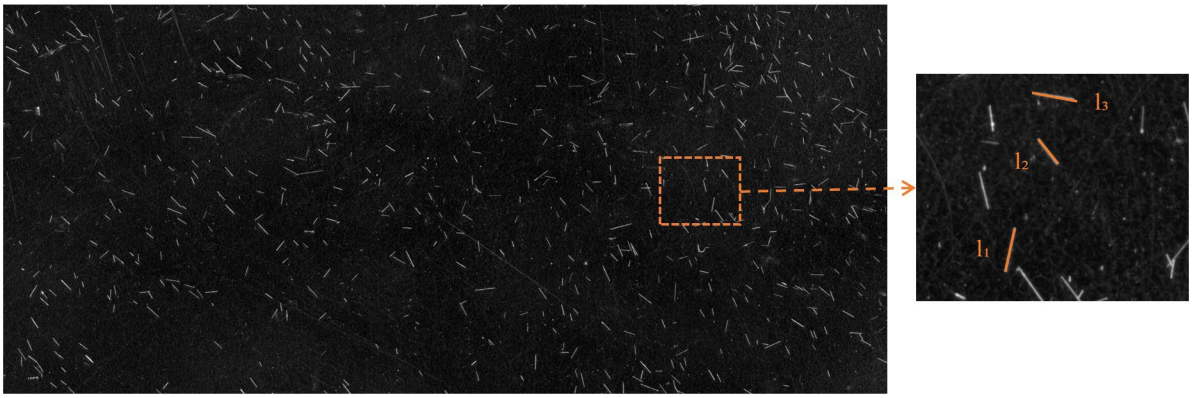


Fig. 1. Example of an image obtained from scanning the fibers (a); example of how the fibers were measured with the "segment" tool of ImageJ.

Results and Discussion

The results of ICP-OES are displayed in Table 3. These data are essential for comparing the "GFRPP+rPP" and "GFRPP+TiO_2" formulations in terms of their TiO_2 content.

Table 3. Results obtained by ICP-OES analysis on GFRPP + rPP set of materials, to measure the actual content of titanium dioxide in the compounds with recycled polypropylene.

GFRPP + rPP

Name of the compound	*Recycled PP content [%]*	*Measured TiO_2 content [%]*
R000/T000	0	0.005
R001	5	0.032
R002	8	0.051
R003	10	0.060
R004	30	0.090
R005	50	0.239
R006	70	0.305

Materials Research Proceedings 57 (2025) 2-10 https://doi.org/10.21741/9781644903735-1

The mechanical characterization results serve as the foundation for the subsequent analyses, offering key insights into how the inclusion of recycled polypropylene affects the overall performance of the composite. The stress-strain curves from the tensile tests are shown in Figure 2, while the corresponding tensile properties, along with the impact strength values, are summarized in Table 3. Among the tensile properties, the tensile modulus remains stable across all formulations, regardless of the rPP or TiO_2 content. Tensile elongation, on the other hand, does not exhibit a clear trend, making it challenging to draw definitive conclusions from the measured values. Tensile strength emerges as the most noteworthy parameter in this context, displaying a similar behavior in both material series. In particular, the addition of small amounts of either rPP or TiO_2 results in an initial drop in tensile strength, followed by a stabilization at higher. Impact strength is particularly affected by the presence of recycled material. In the "GFRPP + rPP" series, impact energy is nearly halved when rPP content increases from 0% to 70%, indicating a significant degradation in strength. While TiO_2 also contributes to a decrease in impact strength, its effect is less severe. This suggests that the reduction in toughness observed with rPP is not solely attributable to the presence of TiO_2. A plausible explanation is the increased heterogeneity introduced by blending two different polymer sources, combined with the presence of contaminants in the recycled fraction. These impurities may act as chemical inclusions, promoting crack initiation and propagation, ultimately compromising the material's resistance to impact.

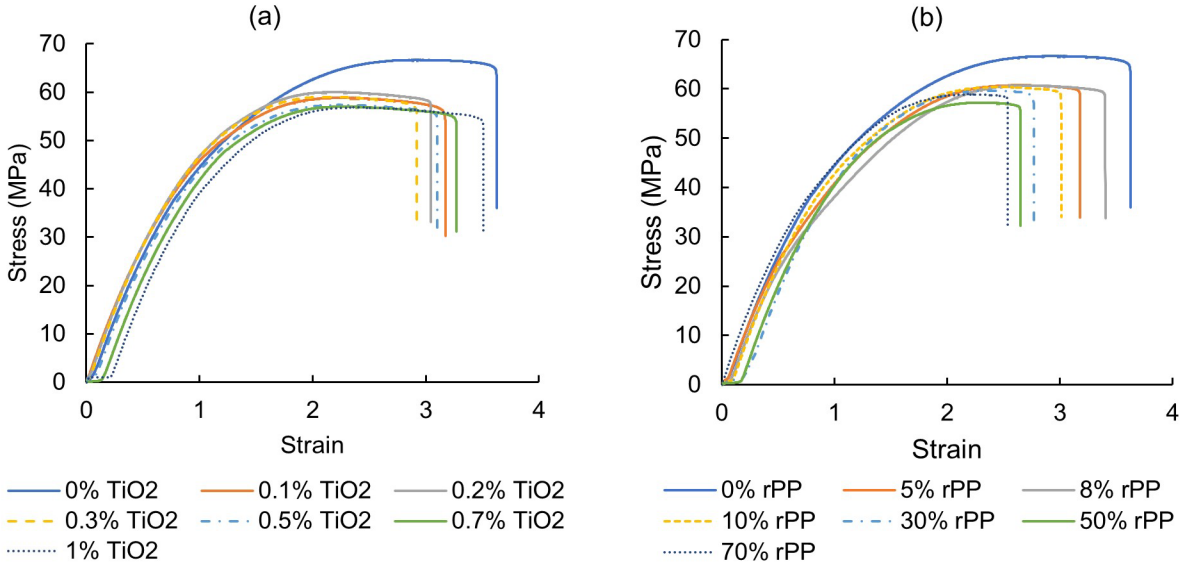


Figure 1. (a) Results of tensile tests for the set "GFRPP+TiO_2"; (b) results of tensile tests for the set "GFRPP+rPP". The curve shown for each compound represents the average of 10 replicates.

Table 4. Results of tensile and impact testing for the two sets of materials.

GFRPP + rPP								
rPP content [%]	*Tensile Modulus [MPa]*	*Std Dev [MPa]*	*Tensile strength [MPa]*	*Std Dev [MPa]*	*Tensile Elongation [%]*	*Std Dev [%]*	*Impact Energy [kJ/m²]*	*Std Dev [kJ/m²]*
0	5817.04	114.79	64.37	0.62	3.43	0.36	15.19	1.58
5	5703.61	152.60	58.58	0.68	3.13	0.41	13.46	2.19
8	5717.67	134.54	58.68	0.92	3.39	0.26	13.07	1.42
10	5871.19	141.01	57.9	0.61	3.01	0.31	13.68	2.60
30	5928.19	189.66	56.99	0.79	2.75	0.23	11.79	2.33
50	5905.58	150.88	55.43	0.87	2.62	0.15	9.71	0.69
70	6239.03	158.70	57.71	0.68	2.48	0.49	8.24	0.19
GFRPP + TiO_2								
TiO_2 content [%]	*Tensile Modulus [MPa]*	*Std Dev [MPa]*	*Tensile strength [MPa]*	*Std Dev [MPa]*	*Tensile Elongation [%]*	*Std Dev [%]*	*Impact Energy [kJ/m²]*	*Std Dev [kJ/m²]*
0	5817.04	114.79	64.37	0.57	3.43	0.36	15.19	1.58
0.1	6104.47	70.87	56.75	1.04	2.98	0.30	12.17	2.49
0.2	6089.77	50.60	56.39	0.89	2.84	0.30	12.35	0.62
0.3	5846.93	153.13	56.03	0.48	2.74	0.38	13.03	3.38
0.5	5576.81	119.93	54.66	0.56	2.87	0.29	12.19	0.28
0.7	5602.26	159.31	54.65	0.87	3.01	0.48	12.07	1.23
1	5687.34	5687.35	53.67	0.77	3.19	0.28	12.39	3.17

Rotational rheometry proved to be of limited effectiveness in detecting differences in material behavior across the various formulations. TGA analysis may suggest the onset of thermal degradation at lower temperatures in materials with high rPP content, potentially due to the presence of contaminants commonly identified in recycled polypropylene, as reported in the literature. However, based on the tests conducted so far, no significant or consistent trend can be confirmed. The observed variations in the curves appear to result mainly from test-to-test fluctuations, rather than from intrinsic differences in material stability. Further investigations are planned to clarify this behavior and to better assess the thermal stability of the recycled compounds. DSC primarily revealed a secondary peak indicative of polyethylene contamination in rPP (Fig. 3b). Due to the similar density characteristics of PE and PP, their separation during recycling is particularly challenging, resulting in residual PE within the final material. Additionally, DSC results addressed the potential influence of TiO_2 on crystallization behavior. An initial hypothesis suggested that TiO_2 might act as a nucleating agent. However, this assumption was not supported by the experimental data, as crystallization enthalpy showed no significant correlation with TiO_2 content.

Materials Research Proceedings 57 (2025) 2-10 https://doi.org/10.21741/9781644903735-1

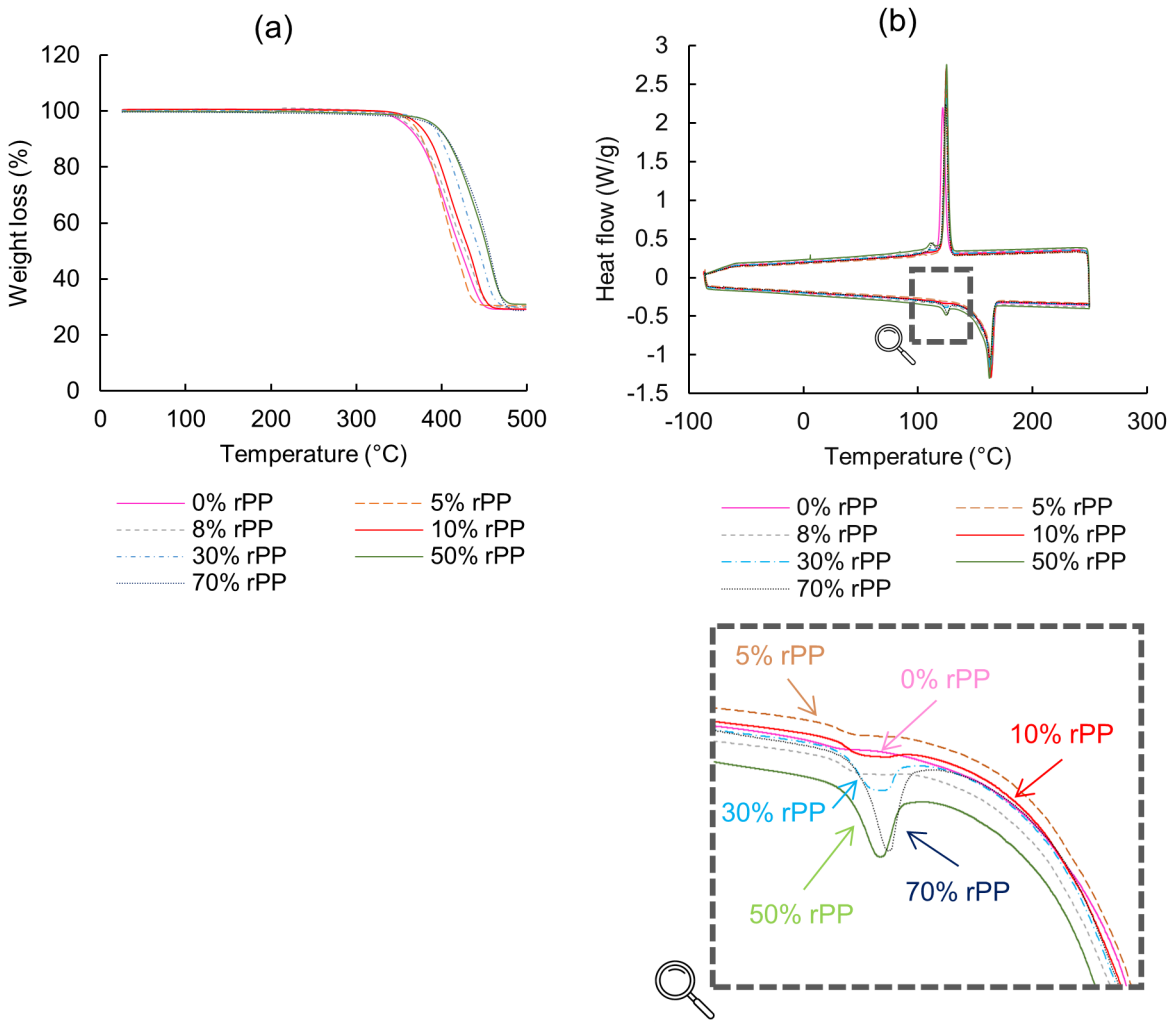


Fig. 2 Significant results from the rheological analysis: TGA results with a focus on the early degradation of high rPP compounds (a); DSC results with a focus on the PE peak (b).

SEM analysis did not reveal any consistent trend in fiber-matrix adhesion as a function of rPP or TiO_2 content, with localized variations in adhesion observed across the surface areas. EDX confirmed the presence of expected elements, including polypropylene components, glass fiber constituents, and titanium (Fig. 4a). Titanium was found to be evenly dispersed within the matrix, with no evidence of aggregation near the fibers or direct involvement in fiber pull-out phenomena. However, isolated TiO_2 conglomerates were occasionally observed, randomly distributed on the surface of various specimens. These could act as chemical inclusions, potentially contributing to the observed drop in impact resistance.

Figure 4b compares the fiber lengths in the "GFRPP + rPP" and "GFRPP + TiO_2" sets, plotted against the titanium content in each formulation. The most significant decrease in fiber length is observed at the initial introduction of TiO_2, specifically between 0% and 0.1–0.2 wt%, where the average fiber length drops by approximately 22%. Beyond this point, increasing the TiO_2 content up to 1 wt% does not lead to a further significant reduction. This suggests that once a critical damage threshold is reached, additional TiO_2 does not cause further substantial fiber breakage. We hypothesize that this may be due to the fibers approaching a minimum length, below which further fragmentation during processing is limited. The proposed mechanism involves a mechanical interaction between TiO_2 particles and glass fibers during extrusion and injection molding. The hardness of TiO_2 may induce microcracks or surface defects, compromising fiber integrity and

Materials Research Proceedings 57 (2025) 2-10 https://doi.org/10.21741/9781644903735-1

promoting initial breakage. Although this phenomenon is not extensively documented in the literature, it is consistent with empirical knowledge from fiber-reinforced materials processing.

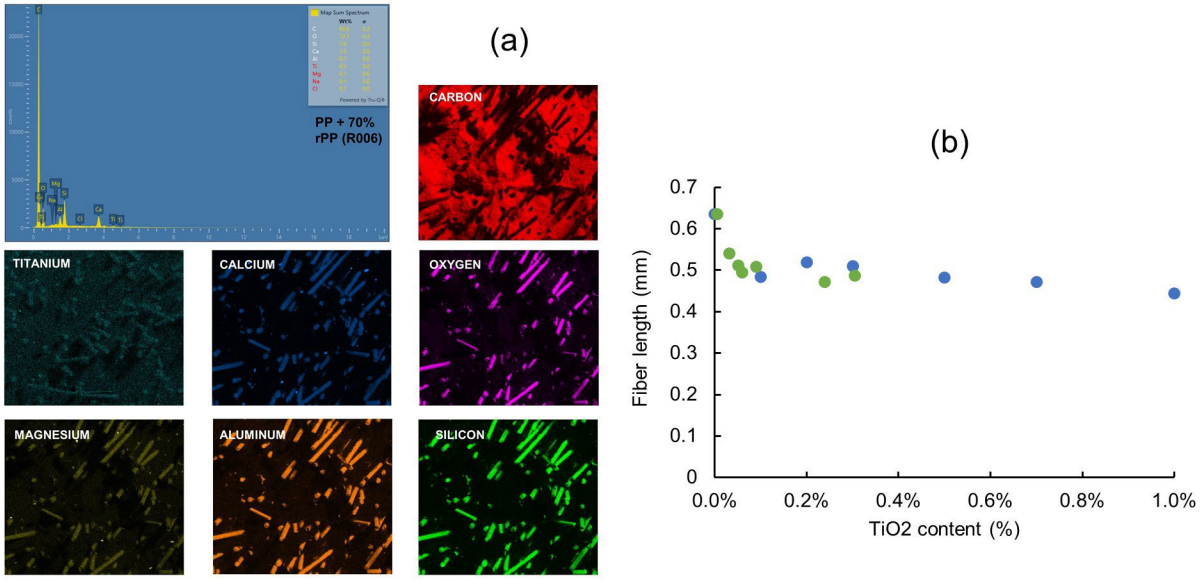


Fig. 3. X-ray energy spectrum and elemental maps as results of an EDX analysis on the compound "GFRPP + 70% rPP" (a); results for fiber length measurements and comparison for the two sets of materials.

Conclusions

This study investigated the properties of glass fiber-reinforced polypropylene composites, focusing on two material sets: virgin polypropylene blended with increasing amounts of recycled polypropylene ("GFRPP + rPP") and virgin polypropylene containing varying concentrations of titanium dioxide ("GFRPP + TiO_2"). Mechanical, rheological, and fracture surface analyses were performed to assess the role of TiO_2 in the performance degradation observed with the incorporation of recycled PP. The findings indicate that tensile strength and notched impact resistance are the properties most affected by the introduction of recycled content. In particular, the reduction in impact resistance cannot be attributed solely to TiO_2; rather, it is also influenced by increased material heterogeneity and the presence of impurities in the rPP, which may act as stress concentrators and promote crack initiation and propagation. While TiO_2 does not appear to alter fiber-matrix adhesion, even low concentrations consistently lead to a significant reduction in fiber length across both material series. This suggests that fiber breakage is primarily induced by TiO_2, likely through a mechanical mechanism rather than a chemical interaction. The presence of hard TiO_2 particles may cause physical damage to glass fibers during processing, particularly in the pelletizing and injection molding stages. These results provide new insights into the challenges associated with recycled composites and offer potential strategies for performance optimization. Specifically, implementing finer extrusion filtration systems or selectively excluding white waste during recycling could help reduce TiO_2 contamination and improve the mechanical properties of GFRPs containing recycled materials.

References

[1] Suschem Materials Working Group, "Polymer Composites Circularity," 2018. Accessed: Aug. 19, 2024. [Online]. Available: http: //www.suschem.org/publications

[2] M. Biron, "Thermoplastic Composites," in *Thermoplastics and Thermoplastic Composites*, Elsevier, 2018, pp. 821–882. doi: 10.1016/B978-0-08-102501-7.00006-0

[3] D. García, I. Vegas, and I. Cacho, "Mechanical recycling of GFRP waste as short-fiber reinforcements in microconcrete," *Constr Build Mater*, vol. 64, pp. 293–300, Aug. 2014. https://doi.org/10.1016/j.conbuildmat.2014.02.068

[4] H. Mohammadi *et al.*, "Lightweight Glass Fiber-Reinforced Polymer Composite for Automotive Bumper Applications: A Review," *Polymers (Basel)*, vol. 15, no. 1, p. 193, Dec. 2022. https://doi.org/10.3390/polym15010193

[5] G. Xian *et al.*, "Design, preparation and mechanical properties of novel glass fiber reinforced polypropylene bending bars," *Constr Build Mater*, vol. 429, p. 136455, May 2024. https://doi.org/10.1016/j.conbuildmat.2024.136455

[6] F. Xie, "Sustainable polymer composites: functionality and applications," *Functional Composite Materials*, vol. 2, no. 1, p. 15, Dec. 2021. https://doi.org/10.1186/s42252-021-00027-z

[7] S. Kolluru, A. Thakur, D. Tamakuwala, V. V. Kumar, S. Ramakrishna, and S. Chandran, "Sustainable recycling of polymers: a comprehensive review," Jul. 01, 2024, *Springer Science and Business Media Deutschland GmbH*. doi: 10.1007/s00289-024-05195-z

[8] D. Borjan, Ž. Knez, and M. Knez, "Recycling of Carbon Fiber-Reinforced Composites—Difficulties and Future Perspectives," *Materials*, vol. 14, no. 15, p. 4191, Jul. 2021. https://doi.org/10.3390/ma14154191

[9] D. P. Gravgaard, M. L. Henriksen, and M. Hinge, "Dissolution recycling for recovery of polypropylene and glass fibres," *J Mater Cycles Waste Manag*, vol. 26, no. 2, pp. 961–969, Mar. 2024. https://doi.org/10.1007/s10163-023-01873-8

[10] S. Lu *et al.*, "Effect of fiber content on mechanical properties of carbon fiber-reinforced polyether-ether-ketone composites prepared using screw extrusion-based online mixing 3D printing," *Addit Manuf*, vol. 80, p. 103976, Jan. 2024. https://doi.org/10.1016/j.addma.2024.103976

[11] L. T. Drzal and M. Madhukar, "Fibre-matrix adhesion and its relationship to composite mechanical properties," *J Mater Sci*, vol. 28, no. 3, pp. 569–610, 1993. https://doi.org/10.1007/BF01151234

[12] Á. Agüero *et al.*, "Evaluation of Different Compatibilization Strategies to Improve the Performance of Injection-Molded Green Composite Pieces Made of Polylactide Reinforced with Short Flaxseed Fibers," *Polymers (Basel)*, vol. 12, no. 4, p. 821, Apr. 2020. https://doi.org/10.3390/polym12040821

[13] C. Cazan, A. Enesca, and L. Andronic, "Synergic Effect of TiO2 Filler on the Mechanical Properties of Polymer Nanocomposites," *Polymers (Basel)*, vol. 13, no. 12, p. 2017, Jun. 2021. https://doi.org/10.3390/polym13122017

[14] J. L. Thomason, "The influence of fibre length and concentration on the properties of glass fibre reinforced polypropylene: 5. Injection moulded long and short fibre PP," *Compos Part A Appl Sci Manuf*, vol. 33, no. 12, pp. 1641–1652, Dec. 2002. https://doi.org/10.1016/S1359-835X(02)00179-3

[15] A. Ladhari, E. Kucukpinar, H. Stoll, and S. Sängerlaub, "Comparison of properties with relevance for the automotive sector in mechanically recycled and virgin polypropylene," *Recycling*, vol. 6, no. 4, Dec. 2021. https://doi.org/10.3390/recycling6040076

Materials Research Proceedings 57 (2025) 11-19 https://doi.org/10.21741/9781644903735-2

Impact of contour on surface quality, dimensional and geometrical accuracy of Ti48Al2Cr2Nb parts produced with powder bed fusion with electron beam process

Giovanni RIZZA[1,a] *, Manuela GALATI[1,b], Paolo MINETOLA[1,c], Paolo ANTONIONI[1,d], Danilo BRUSON[1,e], Giovanni MARCHIANDI[1,f], Luca IULIANO[1,g]

[1]Department of Management and Production Engineering (DIGEP), Integrated Additive Manufacturing Center (IAM@PoliTo), Politecnico di Torino, Corso Duca degli Abruzzi 24, 10129 Torino, Italy

[a]giovanni.rizza@polito.it, [b]manuela.galati@polito.it, [c]paolo.minetola@polito.it, [d]paolo.antonioni@polito.it, [e]danilo.bruson@polito.it, [f]giovanni.marchiandi@polito.it, [g]luca.iuliano@polito.it

Keywords: Additive Manufacturing, Metrology and Tolerancing, Surfaces

Abstract. Powder bed fusion with electron beam (PBF-EB) is an additive manufacturing technique for processing critical materials such as Ti48Al2Cr2Nb. Most of these applications are focused on industrial components that require mirror-like finishing. Therefore, PBF-EB parts are considered only near net shape. The PBF-EB standard procedure involves melting using contours before the inner area. However, because of the need for machining allowance, using contours appears unnecessary, while it may increase the production time significantly. This work highlights the differences between Ti48Al2Cr2Nb parts produced using the standard procedure of PBF-EB and a counterpart produced with a modified single-stage melting. Surface topography, dimensional and geometrical accuracies and mechanical properties are compared. The results show that the parts produced with a single-stage melting are more accurate in dimensions than those produced using a standard strategy, while the production time is over 8% shorter.

Introduction

The building conditions of the powder bed fusion with electron beam (PBF-EB) additive manufacturing process enable the production of materials that are difficult to process using traditional or other additive manufacturing techniques. One such example is the intermetallic γ titanium aluminide alloy [1]. This advantage is guaranteed by the high build process temperature and the vacuum environment in the build chamber [2]. The vacuum level is approximately 10^{-5} mbar, which is sufficient to prevent the backscatter of the electrons by the air molecules and allow the material to be processed without the risk of oxygen or nitrogen pickup [3]. With these processing conditions, γ-TiAl offers remarkable specific properties of strength, Young's modulus and creep resistance, particularly when compared to nickel alloys [2].

During the production of γ-TiAl, particularly the Ti48Al2Cr2Nb (Ti4822), the typical working temperature is between 1050°C and 1100°C [2]. At each layer, this temperature is reached thanks to the preheating step in which the electron beam scans the whole layer repeatedly till the desired temperature is reached. In addition, the vacuum environment , typical of the PBF-EB processes, inhibits the heat dispersion. During the preheating, the powder is partially sintered [4], improving the heat transfer between the melt pool and the surrounding material and in turn reducing the cooling rate of the melt pool [2]. The melting step for Ti4822 processed by PBF-EB consists of melting the section using parallel lines in one single step, identified as hatching. To the best of the authors' knowledge, Ti4822 has never been processed with the PBF-EB using the two-steps standard melting strategy, well established for other materials such as Ti6Al4V [5], [6], or

Content from this work may be used under the terms of the Creative Commons Attribution 3.0 license. Any further distribution of this work must maintain attribution to the author(s) and the title of the work, journal citation and DOI. Published under license by Materials Research Forum LLC.

Ti6Al2Sn4Zr2Mo [7]. In this strategy, melting consists of two melting steps: the contour first and the inner or hatch after [3], [8]. The contour employs a distinctive melting strategy known as the Multibeam™ strategy. During Multibeam™, the PBF-EB machine control rapidly moves the electron beam in different contour locations, simultaneously activating several melt pools [9].

The literature suggests that the use of a contour prior to the hatching of the inner area affects only the surface roughness of the components, which is smaller for components produced using contours [10]. The reason for this difference is connected to the larger amount of energy usually delivered when melting the hatch than that delivered when melting the contour. However, given the requirements typically associated with γ-TiAl components in automotive or aerospace industries, additional machining operations are requested. Despite has already been showed in the literature the part quality issues associated with the PBF-EB production for titanium alloys, such as [11], all of these works are only based on the use of the two-step strategy, and no systematic comparison has been made with the one-step strategy. This paper covers this literature gap, investigating the differences between two-step and one-step strategies. Two artefacts were produced using the standard two-step and the one-step strategy. A comparison of the melting strategies was made considering the topography of the surfaces and the dimensional and geometrical tolerances.

Materials and methods

To investigate the effect of the melting strategy, this work adopts two portions of the benchmark proposed by Minetola et al. [12] and the relative procedure for the measurements developed according to the standard ISO 286:1988 [13] and ISO 286-1:2010 [14]. The benchmark reference part is available as open access here [15]. Fig. 1 shows artefact 1 and artefact 2 adopted in this work.

The overall size of artefact 1 is 110 mm x 25 mm x 33 mm, while artefact 2 has an overall size of 55 mm x 55 mm x 21 mm. Artefacts 1 and 2 include features with sizes that are comprised in the basic size ranges of the ISO 286:1988 [13] and ISO 286-1:2010 [14]: from 1mm to 3 mm, from 3 mm to 6 mm, from 6 mm to 10 mm, from 10 mm to 18 mm, from 18 mm to 30 mm, from 30 mm to 50 mm, from 50 mm to 80 mm and from 80 mm to 120 mm. All these features are built on a supporting plate 5 mm thick. Each set of features is named with an alphabetic index, as shown in Fig. 1 and described below. On one side of artefact 1, there are seven rectangular steps (ST) with dimensions 4 mm x 15 mm. The height of these steps is 1 mm, 3 mm, 6 mm, 10 mm, 15 mm, 21 mm and 28 mm. The central portion of this artefact includes a rectangular block with dimensions 20 mm x 46 mm x 24 mm. This block contains seven rectangular slots (SL) with dimensions 5 mm x 15 mm. The depth of these slots is the same as the steps, except for the slot that is 3 mm deep, which is repeated twice. One side of this central block includes five planes tilted at different angles with respect to the vertical (TP). The first is vertical, the second is tilted at 2 degrees, the third at 4.5 degrees, the fourth at 7 degrees and the fifth at 9 degrees. Artefact 1 also contains seven rectangular blocks (BL) with dimensions of 4 mm x 15 mm separated by a 1 mm gap. The height of these blocks is the same as the steps. Artefact 2 contains two truncated cones with a circular base (TC1), one inside the other. The larger base of the external cone has a diameter of 20 mm, while the smaller base has a diameter of 13.6 mm. The height of this cone is 12 mm. The larger base of the inner cone has a diameter of 10 mm, while the smaller one has a diameter of 6.5 mm. The height of this cone is 10 mm. Artefact 2 also contains a series of coaxial cylinders (CC1). The larger cylinder has a diameter of 24 mm, while the smaller cylinder on top has a diameter of 17 mm. This feature contains two other cylinders with a diameter of 7 mm, the one on top and 5 mm, the one at the bottom. Each cylinder has a height of 8 mm. The last features are two series of quarters of convex and concave spheres (SP1 and SP2). The spheres of SP1 have a diameter of 24 mm, while the spheres of SP2 have a diameter of 16 mm. Artefacts 1 and 2 together allow the evaluation of more than one thousand dimensions in the ISO ranges of 1mm and 120

mm. The disposition of the feature also allows the evaluation with a coordinate measuring machine (CMM) using only one positioning of the sample and a probe of 2 mm in diameter.

The PBF-EB machine, Arcam A2X was adopted to produce artefacts 1 and 2. As mentioned above, the material adopted was the intermetallic Ti48Al2Cr2Nb alloy (Ti4822). The granulometry ranged between 45 μm and 150 μm. According to the literature [16], the layer thickness was selected as equal to 90 μm. Two replicas of artefacts 1 and 2 were produced: one replica for each melt strategy. Table 1 reports the process parameters adopted to melt outer and inner contours with Multibeam^{TM} and hatch for the parts produced with the two-step strategy. The artefacts produced with the one-step strategy were produced using the parameters for the hatch reported in Table 1. No scaling factor was applied to nominal geometries of the samples. The four samples were produced in one build to ensure the same temperature conditions. At the end of the production, the samples were cleaned according to the standard procedure [3], [17] in a powder recovery system in which the breakaway powder was sandblasted using the same powder used in the PBF-EB process. No heat treatments or other post-process operations were performed on the artefacts produced. After extracting the samples from the build chamber of the machine, these were characterised topographically and dimensionally.

To evaluate the differences in the production time between the two melting strategies, two ad-hoc builds were designed in which only one melting strategy at a time was considered. The time for the production was estimated by using the EBM control of the machine. The simulator solely calculates the time required for preheating, the melting of the cross-section and the eventual post-heating/cooling at each layer. the simulator neglects the time for the powder ranking. This is a fixed time which do not depend on the melted material.

Table 2. Process parameters adopted to melt the contour with Multibeam^{TM} and hatch.

	Scan speed [mm/s]	Focus offset [mA]	Beam current [mA]	Number of spots	Number of contours	Contours offset[mm]
Outer contour	440	6	5	40	1	0.25
Inner contour	800	6	10.2	15	2	0.25
	Speed function	Focus offset [mA]	Beam current max [mA]	Reference length [mm]	Reference current [mA]	Line offset [mm]
Hatch	40	15	20	18	7	0.3

The topography was investigated by inspecting peaks and valleys to highlight the differences in the melting strategy adopted. The topography of the samples was obtained through a structured light scanner ATOS compact scan (Carl Zeiss GOM Metrology GmbH, Braunschweig, Germany). The maximum resolution of the scanner is 0.018 mm. The cloud of points was handled using the software GOM inspect 2021 (Carl Zeiss GOM Metrology GmbH, Braunschweig, Germany), with no post-process. The software MountainsLab (Digital Surf, Besançon, France) was adopted to inspect topography characteristics, the average surface roughness (Sa) and the maximum height of surface (Sz). Horizontal surfaces are defined as all the surfaces parallel to the start plate. Vertical surfaces are orthogonal to the start plate and aligned with the build direction.

Materials Research Proceedings 57 (2025) 11-19 https://doi.org/10.21741/9781644903735-2

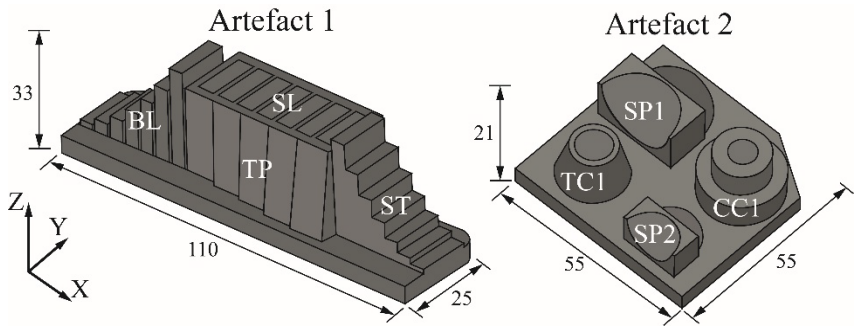


Fig. 1. Artefact 1 and 2 adopted for the topographic, dimensional and geometrical characterisation. Z is aligned to the build direction.

The dimensional accuracy was investigated by a CMM Altera S (LK Metrology Ltd., Derby, England). This machine has an accuracy envelope with an MPEE of 1.8 +L/400. Each artefact was measured three times, and the average measure was adopted for the analysis. The measures taken through the CMM were adopted to evaluate the standard tolerance factor according to the ISO guidelines [13]. The standard tolerance classes, from IT5 to IT18, for measures up to 500 mm, are a function of the standard tolerance factor i described by Eq. 1

$$i=0.45\sqrt[3]{D}+0.001D \quad (1)$$

Where $D=\sqrt{D_1 D_2}$ and D_1 and D_2 are the lower and the upper limits of the basic size range. Table 3 reports the value of the standard tolerance factor i calculated for each size range given by the ISO standard.

Table 3. Standard tolerance factors for each basic size.

Range	Basic size								
Above	D_1 (mm)	1	3	6	10	18	30	50	80
Up to and including	D_2 (mm)	3	6	10	18	30	50	80	120
Standard tolerance factor	i (μm)	0.542	0.733	0.898	1.083	1.307	1.561	1.856	2.173

Table 4 reports the formulas adopted to assign a standard tolerance grade (IT) to a measure. This is assigned to a measure according to the number of times (n) the tolerance factor (i) fits the dimensional deviation of the measure from the nominal measure. The parameter n is evaluated according to Eq. 2.

$$n=1000\ \frac{|D_n-D_m|}{i} \quad (2)$$

Where D_n and D_m represent the nominal and the measured dimension, respectively.

Table 4. Formulas to assign the standard tolerance (IT) grade to a measure, according to his deviation from the nominal.

Basic size		Standard tolerance grades												
		IT 5	IT 6	IT 7	IT 8	IT 9	IT 10	IT 11	IT 12	IT 13	IT 14	IT 15	IT 16	IT 17	IT 18
Above	Up to	Standard tolerance [μm]													
1 mm	500 mm	7i	10i	16i	25i	40i	64i	100i	160i	250i	400i	640i	1000i	1600i	2500i

As an example, to clarify the use of Equation 1 and 2 and tables 3 and 4, assuming a nominal dimension D_n = 40 mm and a measured dimension D_m = 40.250, the standard tolerance factor for this dimension is i = 1.561 (from Table 3 and Equation 1) and the parameter n = 160.15 (Equation 2). With this value of n, the dimension can be classified as an IT13. In order to be classified as IT 12, a measure should have a deviation between 100 i (with n = 100) and 160 i (with n = 160).

Considering all the features of the artefacts, n will have a distribution in each basic ISO range size. In this work, the 95th percentile is assumed as the maximum error when producing a feature in the specific range size of Table 3. The measures taken with CMM were adopted to evaluate the geometric dimensioning and tolerancing (GD&T). In particular, the following factors were investigated: perpendicularity, cylindricity, angle of the planes, flatness of the planes for horizontal (parallel to the start plate), vertical (parallel to the build direction) and tilted with respect to the vertical planes, and parallelism between horizontal and vertical planes.

Results and discussion

Fig. 2 shows artefact 2 after the cleaning operation in the PRS. It also allows a visual comparison among the artefacts produced with the one-step (Figure 2 a)) and the two-step (Figure 2 b))strategy. The time calculated to produce samples with a two-step strategy was 2 hours and 50 minutes, while the time calculated to produce the artefacts with the one-step strategy was 2 hours and 37 minutes. The difference between the two melt strategies was 13 minutes. Therefore, the one-step strategy is approximately 8 % faster than the two-step strategy.

As can be observed in Fig. 2, the surface produced with the one-step strategy shows the presence of the layers, with the stair-stepping effect clearly visible. In the case of the two-step strategy, the stair-stepping and the layers are visible for the highest section of the sphere, where the molten cross-section becomes small.

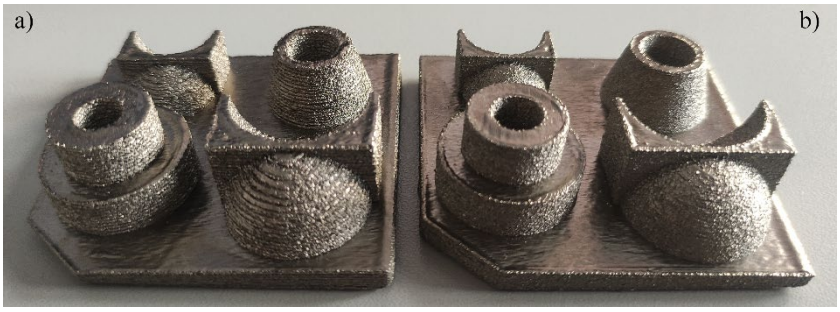


Fig. 2. Artefact 2 produced using the a) one-step and b) the two-step strategy.

Fig. 3 shows the results of the topography analysis on vertical surfaces of artefact 1 produced with the two-step strategy (Fig. 3 a)), and the one-step strategy (Fig. 3b)). As can be observed, the topography is substantially different. The first evidence is that the roughness of the surface is significantly affected by the contour. The surface melted with a two-step strategy is more regular with a less evident staircase effect due to the slicing operation. This evidence is confirmed quantitatively by the areal surface roughness measurements. The surface produced with the two-step strategy is characterised by a Sa = 31.44 μm and an Sz = 331.4 μm. On the other hand, the surface produced with the one-step strategy is characterised by Sa = 54 μm and Sz = 499 μm. The higher values of Sa and Sz for the surfaces produced with the one-step strategy measure the larger number of peaks and valleys. The presence of the peaks on the surface may be due to the fluid dynamics in the melt track. Moreover, the height and depth of these were larger than in the case of surfaces produced with the one-step melting strategy. This is because the presence of the solid contour mitigates the material accumulation at the tail of the melt pool.

Materials Research Proceedings 57 (2025) 11-19 https://doi.org/10.21741/9781644903735-2

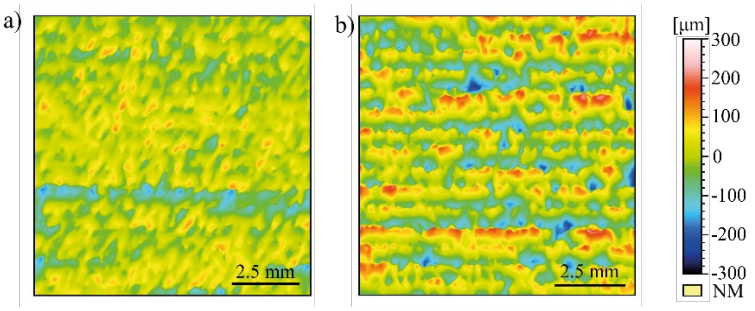


Fig. 3: Topography analysis of the vertical surfaces: a) surface produced with two-step strategy, b) surface produced with one-step strategy.

For the horizontal surfaces, the topography does not show a substantial difference between the two melt strategies, given similar values of average area roughness. For the surface produced using the two-step strategy Sa = 20 µm, while for the surface produced using the one-step strategy Sa = 22 µm.

Regarding the dimensional analysis, Fig. 4 shows the number of tolerance units obtained from the measures of the artefacts for the ISO base ranges considered in this work. The PBF-EB process for Ti4822 with the selected process parameters guarantees IT grades ranging from IT12 to IT16. The larger the feature of the sample, the higher the accuracy of the process (lower IT). For example, for the features comprising 1 mm and 3 mm, the PBF-EB process can guarantee an IT 16, while for larger features with dimensions from 80 mm to 120 mm, the PBF-EB process guarantees an IT 13. These values are comparable to other manufacturing processes, such as casting [18], which are usually compared to the PBF-EB technology. The melt strategies differ from each other only for a few ISO classes. Particularly, the samples produced with the one-step strategy has a higher dimensional accuracy (lower IT) then the samples produced with the two-step strategy for the classes 3mm – 6 mm and 6 mm – 10 mm (two-step process guarantees an IT 16 while, the one-step strategy can guarantee an IT 15), and in the base range 50 mm – 80 mm, for which the two-step strategy guarantees an IT 14, while the one-step strategy guarantees an IT 13.

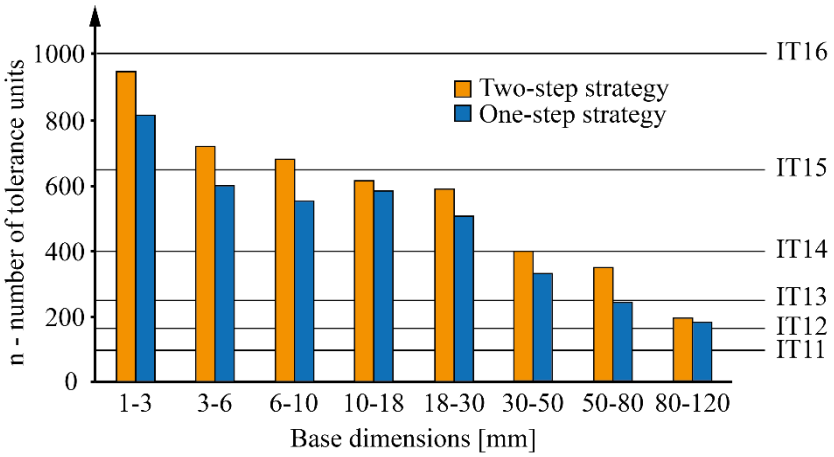


Fig. 4. Number of tolerance units for the artefacts produced using the Two-step strategy and the one-step strategy for each ISO base dimensions.

Fig. 5 shows the geometrical tolerance results for planarity and parallelism in an aggregate form as a box plot. Considering both planarity and parallelism, the melting strategy does not have a statistically relevant effect on the dimensional accuracy since all the boxes overlap. However, the two-step strategy has a beneficial effect on the planarity of the vertical surfaces, which shows a reduced median and interquartile range. The same applies to the parallelism of the vertical surfaces,

where the vertical surfaces produced with a two-step strategy have a smaller median and an interquartile range below that of the vertical surface produced with the one-step strategy. These results agree with the results obtained from the topography analysis of vertical surfaces reported in Section 3.1. The difference in the dimensional accuracy among the melting strategies could be related to the larger peaks and valleys and larger values of surface roughness for vertical surfaces produced with the one-step strategy.

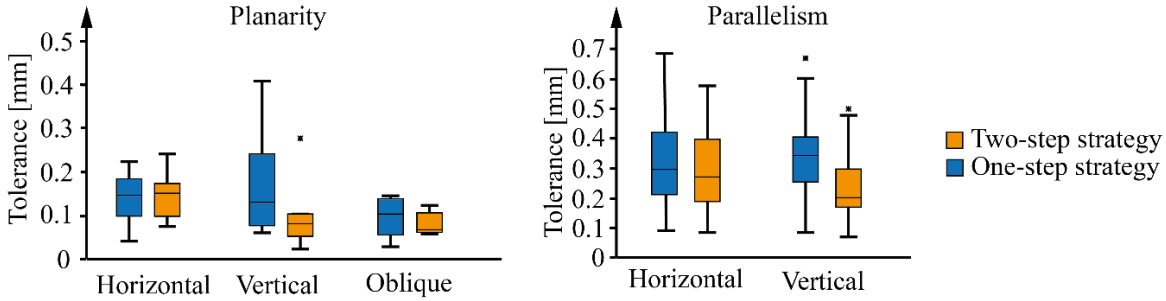


Fig. 5. Geometrical tolerances for planarity and parallelism

Fig. 6 a) summarises the tolerance data for the perpendicularity, coaxiality and cylindricity as box plots for the two melt strategies. The box plot shows that the melting strategy is not statistically relevant to the perpendicularity, coaxiality and cylindricity. Regarding the coaxiality, although the overlapping of the boxes, the median and the interquartile range obtained for the features produced using the two-step strategy are smaller than those produced using the two-step strategy. This means that, on average, the two-step strategy produced better coaxiality of the features. Fig. 6 b) shows the box plots for the tilt angles of the surfaces with respect to the coordinate axes defined in Fig. 1. In this case, for the deviation with respect to the X-axis and the deviation with respect to the Z-axis, the melting strategy is statistically relevant. The two-step strategy produces surfaces tilted with a smaller deviation with respect to the coordinate axes. On the other hand, the melting strategy does not have a statistically relevant effect on the deviation of the tilt angle with respect to the Y-axis. While the interquartile range is comparable for the two-step and the one-step strategy, the median of the two-step strategy is smaller, and the box shows smaller deviation values. However, the interquartile range for surfaces produced with the two-step strategy goes at negative values, while this never happens for surfaces produced with the one-step strategy.

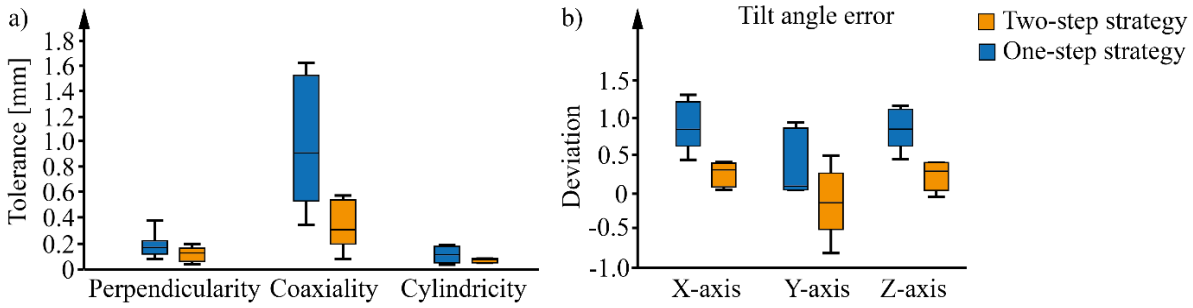


Fig. 6. (a) Tolerance for Perpendicularity, coaxiality and cylindricity and (b) Deviation of the angles with respect to the coordinate axes.

Conclusions

The PBF-EB process enables easier processing of γ-TiAl Ti48Al2Cr2Nb compared to other methods, making it suitable for aerospace, biomedical, and automotive applications. This study examines the impact of one-step and two-step melting strategies on surface topography and dimensional accuracy. The two-step strategy improves surface smoothness and reduces staircasing effects but requires 8% more processing time. Dimensional accuracy analysis shows that PBF-EB

achieves IT12–IT16 grades, with larger features exhibiting higher precision. The one-step strategy ensures a faster production of parts, making it preferable for aerospace and automotive applications that usually require post-processing operations. The two-step strategy, with proper correction, may be suited for biomedical components where as-built roughness is acceptable. Selecting the appropriate melting strategy is crucial for balancing surface quality, dimensional accuracy, and post-processing needs. These results provide guidelines for determining whether PBF-EB alone meets tolerance requirements or if machining is necessary, aiding process optimisation and simulation-based geometric compensation.

References

[1] W. Chen and Z. Li, 11 - Additive manufacturing of titanium aluminides, in Additive Manufacturing for the Aerospace Industry, F. Froes and R. Boyer, Eds., Elsevier, 2019, 235–263. https://doi.org/10.1016/B978-0-12-814062-8.00013-3

[2] R. Wartbichler, H. Clemens, S. Mayer, C. Ghibaudo, G. Rizza, M. Galati, L. Iuliano, et al., On the Formation Mechanism of Banded Microstructures in Electron Beam Melted Ti–48Al–2Cr–2Nb and the Design of Heat Treatments as Remedial Action, Advanced Engineering Materials, 23, (2021), 2101199, https://doi.org/10.1002/adem.202101199

[3] M. Galati, Chapter 8 - Electron beam melting process: a general overview, in Additive Manufacturing, J. Pou, A. Riveiro, and J. P. Davim, Eds., in: Handbooks in Advanced Manufacturing, Elsevier, 2021, 277–301. https://doi.org/10.1016/B978-0-12-818411-0.00014-8

[4] G. Rizza and M. Galati, Powder bed fusion with electron beam: The interplay of sintering, porosity, and coordination number in modelling the powder thermal conductivity through a novel tortuosity formulation, International Journal of Heat and Mass Transfer, 234, (2024), 126055, https://doi.org/10.1016/j.ijheatmasstransfer.2024.126055

[5] P. Wang, W. J. Sin, M. L. S. Nai, and J. Wei, Effects of Processing Parameters on Surface Roughness of Additive Manufactured Ti-6Al-4V via Electron Beam Melting, Materials, 10, (2017), Art. no. 10, https://doi.org/10.3390/ma10101121

[6] M. Galati, G. Rizza, S. Defanti, and L. Denti, Surface roughness prediction model for Electron Beam Melting (EBM) processing Ti6Al4V, Precision Engineering, 69, (2021), 19–28, https://doi.org/10.1016/j.precisioneng.2021.01.002

[7] M. Galati, S. Defanti, A. Saboori, G. Rizza, E. Tognoli, N. Vincenzi, A. Gatto, et al., An investigation on the processing conditions of Ti-6Al-2Sn-4Zr-2Mo by electron beam powder bed fusion: Microstructure, defect distribution, mechanical properties and dimensional accuracy, Additive Manufacturing, 50, (2022), 102564, https://doi.org/10.1016/j.addma.2021.102564

[8] C. Körner, Additive manufacturing of metallic components by selective electron beam melting — a review, International Materials Reviews, 61, (2016), 361–377, https://doi.org/10.1080/09506608.2016.1176289

[9] C. Pirozzi, S. Franchitti, R. Borrelli, G. Diodati, and G. Vattasso, Experimental Study on the Porosity of Electron Beam Melting-Manufactured Ti6Al4V, J. of Materi Eng and Perform, 28, (2019), 2649–2660, https://doi.org/10.1007/s11665-019-04038-7

[10] P. Karimi, C. Schnur, E. Sadeghi, and J. Andersson, Contour design to improve topographical and microstructural characteristics of Alloy 718 manufactured by electron beam-powder bed fusion technique, Additive Manufacturing, 32, (2020), 101014, https://doi.org/10.1016/j.addma.2019.101014

[11] A. L. Cooke and J. A. Soons, Variability in the Geometric Accuracy of Additively Manufactured Test Parts, (2010), Accessed: Oct. 27, 2024. Available: https://hdl.handle.net/2152/88219

[12] P. Minetola, L. Iuliano, and G. Marchiandi, Benchmarking of FDM Machines through Part Quality Using IT Grades, Procedia CIRP, 41, (2016), 1027–1032, https://doi.org/10.1016/j.procir.2015.12.075

[13] ISO 286:1988 ISO system of limits and fits. Part 1 Bases of tolerances deviations and fits, 286–1:1988, (1988).

[14] BS EN ISO 286-1:2010 Geometrical product specifications (GPS). ISO code system for tolerances on linear sizes. Basis of tolerances, deviations and fits, 286–1:2010, (2010). Available: https://bsol.bsigroup.com/Bibliographic/BibliographicInfoData/000000000030288630

[15] Benchmarking of Additive Technologies | 3D CAD Model Library | GrabCAD. Accessed: Feb. 02, 2025. Available: https://grabcad.com/library/benchmarking-of-additive-technologies-1

[16] J. Bieske, M. Franke, M. Schloffer, and C. Körner, Microstructure and properties of TiAl processed via an electron beam powder bed fusion capsule technology, Intermetallics, 126, (2020), 106929, https://doi.org/10.1016/j.intermet.2020.106929

[17] S. Biamino, A. Penna, U. Ackelid, S. Sabbadini, O. Tassa, P. Fino, M. Pavese, et al., Electron beam melting of Ti-48Al-2Cr-2Nb alloy: Microstructure and mechanical properties investigation, Intermetallics, 19, (2011), 776–781, https://doi.org/10.1016/j.intermet.2010.11.017

[18] M. Grazia Violante, L. Iuliano, and P. Minetola, Design and production of fixtures for free-form components using selective laser sintering, Rapid Prototyping Journal, 13, (2007), 30–37, https://doi.org/10.1108/13552540710719190

Materials Research Proceedings 57 (2025) 20-28 https://doi.org/10.21741/9781644903735-3

A synergistic integration of photogrammetry and Gaussian Splatting for back-in-time quality inspection

Mattia TROMBINI[1,a*], Domenico A. MAISANO[1,b*], Fiorenzo FRANCESCHINI[1,c*]

[1]Department of Management and Production Engineering (DIGEP), Politecnico di Torino, 10129 Torino, Italy

[a]mattia.trombini@polito.it, [b]domenico.maisano@polito.it, [c]fiorenzo.franceschini@polito.it

Keywords: Inspection, Quality, Back-in-Time Repeatability

Abstract. Photogrammetry is a well-established technique for 3D inspection of manufactured objects and machinery but its static nature limits re-inspection. If images lead to poor reconstruction, e.g., due to insufficient coverage, the object's original state may become inaccessible, preventing further analysis. This work introduces a synergistic integration of photogrammetry and Gaussian Splatting (GS) to enable *back-in-time* quality inspection. GS creates "frozen" and fully navigable 3D digital scenes, i.e., high-fidelity 3D representations encoded with Gaussians, that preserve the spatial and temporal state of the object at the time of acquisition, allowing the generation of novel synthetic views (i.e., renders) to enrich the original photogrammetric reconstruction. A preliminary case study on the inlet lip skin part of the engine of an aircraft demonstrates how GS renders, when integrated into the photogrammetric workflow, improve the characterisation of surface defects. Results show enhanced defect localisation and a clearer delineation of damage geometry, suggesting that the proposed integration enables effective *back-in-time* inspections.

Introduction

Ensuring the quality and integrity of manufactured goods and industrial machinery requires accurate inspection techniques. Traditional methods often rely on non-destructive testing (NDT) [1], but advances in visual analysis have led to the increasing use of photogrammetry [2]. This technique enables high-fidelity spatial data acquisition, providing a detailed geometric assessment of objects. The integration with unmanned aerial vehicles (UAVs) [3] may further enhance inspection capabilities, facilitating multi-perspective analysis, frequent assessments and reducing health risks for inspectors, particularly in Large-Scale Dimensional Metrology (LSDM) [4,5]. While photogrammetry offers significant advantages, its static nature imposes significant limitations on re-inspection. If the image coverage is inadequate, the reconstruction cannot be subsequently improved by acquiring additional images, since (i) the object may no longer be available for new acquisitions due to service re-entry, even in remote locations, and (ii) external factors such as mechanical vibration or thermal effects may have changed the state of the object in analysis. Even in the absence of significant changes, each subsequent image can show the component in a slightly different state, making direct comparisons between states difficult and limiting the ability to trace the initiation of possible defects. Furthermore, if a defect is discovered in a subsequent inspection, there is no way to retrospectively verify whether it was already present but previously undetected, as past reconstructions are limited by the constraints of the images originally captured. While it is possible to re-examine the object, new viewing perspectives cannot be introduced, and no finer detail can be retrieved beyond the resolution and frame of the original acquisition.

A potential solution to this complex problem can be found in the concept of 3D scene [6], which is a comprehensive, high-fidelity digital representation of an object or environment at a given moment in time. A 3D scene captures not only the geometry of the object, which defines its shape

Content from this work may be used under the terms of the Creative Commons Attribution 3.0 license. Any further distribution of this work must maintain attribution to the author(s) and the title of the work, journal citation and DOI. Published under license by Materials Research Forum LLC.

and structure, but also enhances the realism with additional elements. Specifically, textures are employed to provide surface details such as colours and patterns, lighting is utilised to simulate light sources, thereby creating shadows, highlights and depth, whereas camera perspective is determined to visualise the scene [7]. The high level of realism afforded by a 3D scene facilitates the re-exploration of objects in their original condition, thereby enabling the generation of novel viewpoints and perspectives that would otherwise be inaccessible, facilitating retrospective analysis and permitting detailed inspections beyond the constraints of the initial acquisition.

The emergence of Neural Radiance Field (NeRF) [8] represented a breakthrough, introducing the concepts of sampling and positional encoding to enhance rendering quality. However, despite the notable advancements in rendering quality, the training and rendering times remain extremely high, often exceeding 40 hours using 4-GPU A100 [9]. The recent introduction of 3D Gaussian Splatting (GS) [9] offers a novel approach to efficiently creating a 3D scene, overcoming the limitations of NeRF, with training times reduced to approximately 30 minutes on an A6000 GPU [9]. GS employs a set of Gaussian ellipsoids to model the scene, enabling efficient rendering by rasterising these ellipsoids into images. Further details concerning the technique are discussed in literature [9] and briefly mentioned throughout this paper.

The research question addressed in this study concerns the integration of *back-in-time* visual analysis with high-fidelity 3D scene representation, specifically using Gaussian Splatting, to investigate unexpected defects observed during an inspection. A defect may have either gone completely unnoticed in previous inspections or may have been observed but without a clear definition of its full extent. By revisiting past states, it is possible to more accurately evaluate whether the defect was already present but undetected or insufficiently defined in terms of contour and extent. By employing Gaussian Splatting, this approach seeks to enhance quality in photogrammetric point clouds, exploiting the combination of real images with virtual renders, thus improving reconstruction density and defect detection in terms of quantity, clarity, and dimensional accuracy. It is important to underline that the reconstruction of the 3D scene does not require the acquisition of additional images. Instead, images belonging to a specific past state of the object can be used to generate the scene. The overarching objective of this research is to establish a framework for integrating 3D scene rendering with photogrammetry, ultimately advancing inspection methodologies in manufacturing and industrial settings.

The paper includes an overview of typical defect types in the aerospace sector, followed by a brief explanation of the fundamentals of both photogrammetry and Gaussian Splatting. A case study on the inlet lip skin part of the engine of an aircraft is then presented to demonstrate the proposed synergy and the final section draws some preliminary conclusions.

Taxonomy of defects in manufacturing contexts

In accordance with the aeronautical test case further discussed throughout this paper, the current section aims to provide an overview of typical defects that may affect the operability of objects and that recurrent inspection activities seek to detect. The aeronautical sector is a highly regulated and technologically advanced industry that prioritises safety, efficiency, and durability in aircraft design and maintenance [10]. Aircraft components are subjected to extreme conditions, including high aerodynamic loads, temperature fluctuations, and corrosion-prone environments [11]. Consequently, rigorous inspection and maintenance protocols are implemented to detect and mitigate structural defects before they may escalate into critical failures. These defects include:

- Defects in metallic materials;
- Defects in composite materials;
- Defects in coatings;
- Defects in joints.

The present study focuses on metallic components, particularly defects that arise during in-service conditions, which are characterised by their unpredictability, making it challenging to foresee and diagnose. If undetected, such damage can compromise structural integrity, potentially leading to catastrophic consequences. The categorisation presented in Table 1 is proposed for the establishment of a comprehensive taxonomy of defects and the evaluation of their detectability through photogrammetric inspection. Creep has been excluded from this classification, since elevated temperatures are not typically encountered in standard inspections of aerospace structures, making creep-related deformation not appropriate to the scope of this study [11].

Table 1. *Categorisation of defect types and expected detectability using Machine Vision systems in the aerospace industry [11].*

Type	Description	Classification	Detectable
Fatigue	Degradation and final failure of the materials under cyclic loads, which intensity is always lower than the tensile strength of the material.	Cracks	Partially*
		Surface discoloration / deformation	Yes
		Internal failure	No
Corrosion	Deterioration of the material due to chemical reaction with the environment.	Rust/oxide layer	Yes
		Pitting	Yes
		Subsurface defects	No
Operational overload	Fracture of the component when exceeding the design stress of a material, e.g., damage due to bird strike and landing gear failure after hard landings.	Fracture	Partially*
		Plastic deformation	Partially*
		Internal fracture	No
Wear	Deterioration of the material due to mechanical action that gradually reduces life cycle.	Scratch/grooves	Yes
		Deviation of material thickness	Partially**
Extreme weather conditions	Damage that occurs due to climate conditions, including ice and lightning impacts.	Surface degradation	Yes
		Material discoloration / texture changes	Yes
		Micro-cracking	No
Welding	Defects that may occur in the areas of welded joints.	Porosity/cracks	Partially**
		Misalignment	Yes
		Incomplete fusion	No
		Residual stress	No

*only if on surface
**detectability depends on defect size and on photogrammetric accuracy

Fundamentals of photogrammetry

Photogrammetry involves the use of an array of cameras strategically positioned within a defined measurement area to accurately identify distinct visual features. The photogrammetric process can involve different image capturing modalities, considering (i) multiple cameras able to collect images simultaneously, (ii) a single camera moving around the fixed scene, and (iii) a single fixed camera with a moving object on a rotating turntable [12]. In this study, a camera mounted as a payload on a drone is used and the camera pose network is generated by capturing frames from multiple positions during flight, holding the scene fixed and deploying a moving camera. The captured data is processed by an external Data Processing Unit (DPU), enabling either wireless or cable-based connectivity. As illustrated in Fig. 1, the 3D coordinates of an optical marker, denoted as M_j, are connected to the 2D coordinates of the corresponding image point, $P_{i,j}$, on the projection plane of the i-th camera.

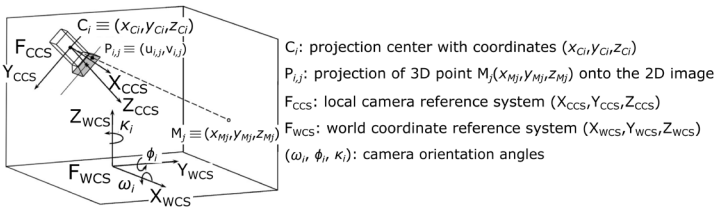


Fig. 1. *Generic setup of a single camera-based localisation in 3D space (adapted from [12]).*

The process is executed through the application of collinearity equations using homogeneous coordinates [2,13], summarised in Eq. (1).

$$\lambda_i \times \begin{bmatrix} u_{i,j} \\ v_{i,j} \\ 1 \end{bmatrix} = \mathbf{K}_i \times \mathbf{W}_i \times \begin{bmatrix} x_{M_j} \\ y_{M_j} \\ z_{M_j} \\ 1 \end{bmatrix} = \begin{bmatrix} u_{f_i} & 0 & u_{0_i} & 0 \\ 0 & v_{f_i} & v_{0_i} & 0 \\ 0 & 0 & 1 & 0 \end{bmatrix} \times \begin{bmatrix} \mathbf{R}_i & -\mathrm{C}_i \\ 0 & 1 \end{bmatrix} \times \begin{bmatrix} x_{M_j} \\ y_{M_j} \\ z_{M_j} \\ 1 \end{bmatrix} \quad (1)$$

where λ_i denotes a non-zero scale factor, and $\mathbf{K}_i$ is the 3x4 intrinsic parameter matrix, composed by u_{0i} and v_{0i} representing the coordinates of the image centre, while u_{fi} and v_{fi} correspond to the focal length components related to the camera. $\mathbf{W}_i$ is the 4x4 matrix representing the external parameters, with $\mathbf{R}_i$ (ω_i, ϕ_i, κ_i) defined as the rotations matrix, defining the relationship between the world coordinate reference system (F_{WCS}) and the local camera coordinate system (F_{CCS}). C_i is the term related to the projection centre in the local camera coordinate system F_{CCS}. Commonly, it is defined $\mathbf{P}_i = \mathbf{K}_i \times \mathbf{W}_i$ as the camera projection matrix. In order to address lens distortions, correction factors are incorporated in the collinearity equation, accounting for radial, tangential, and skew distortions, as detailed in Eq. (2):

$$\lambda_i \times \begin{bmatrix} \tilde{u}_{i,j} \\ \tilde{v}_{i,j} \\ 1 \end{bmatrix} = \lambda_i \times \begin{bmatrix} 1 & 0 & \delta u_{R_{i,j}} + \delta u_{T_{i,j}} + \delta u_{S_{i,j}} \\ 0 & 1 & \delta v_{R_{i,j}} + \delta v_{T_{i,j}} \\ 0 & 0 & 1 \end{bmatrix} \times \begin{bmatrix} u_{i,j} \\ v_{i,j} \\ 1 \end{bmatrix} = \mathbf{P}_i \times \begin{bmatrix} x_{M_j} \\ y_{M_j} \\ z_{M_j} \\ 1 \end{bmatrix} \quad (2)$$

where $\delta u_{Ri,j}$ and $\delta v_{Ri,j}$ account for the radial distortion, $\delta u_{Ti,j}$ and $\delta v_{Ti,j}$ represent the tangential distortion and, eventually, $\delta u_{Si,j}$ is the skewness-related term [12,14]. Photogrammetric reconstruction generates a point cloud as output, consisting of 3D points defined by their coordinates within a spatial reference frame, with each point representing a part of the object's surface [11].

Gaussian Splatting methodology

Gaussian Splatting methodology offers a significant departure from traditional methods like NeRF [9], being a state-of-the-art technique for representing and rendering 3D scenes. This approach prioritises computational efficiency, interpretability, and high-quality visual output, addressing several limitations inherent in NeRF and other neural representations [8]. GS represents a scene as a collection of 3D Gaussian ellipsoids. Each ellipsoid is characterised by the following parameters:

- *Position*: corresponding to its centre point, identifying the spatial location.
- *Covariance matrix:* defining the orientation, size, and shape of the ellipsoid in space.
- *Colour and opacity*: governing the visual appearance and blending behaviour.

GS is a process of rendering that involves the projection of 3D Gaussian ellipsoids onto a 2D image plane to produce a final rendering image. The core of this process is rasterisation, whereby the 3D ellipsoids are directly mapped to 2D pixels on the image plane. Gradient descent techniques play a fundamental role in tuning the abovementioned parameters [9], e.g., position and colour, thereby ensuring an accurate representation of the scene's geometry and appearance.

Materials Research Proceedings 57 (2025) 20-28 https://doi.org/10.21741/9781644903735-3

Instrumentation

In this study, the object of interest is an inlet lip skin part of the engine of an aircraft (see Fig. 2 for reference). The object has an external diameter of approximately 1200 mm and has been transported and installed in a designated location at the Politecnico di Torino, which is suitable for drone operations. The selection of this artefact is driven by the objective of the study, which necessitates the presence of an object of relatively large dimensions, exhibiting a discernible defect. A portion of the surface shows visible damage defined as a bump consistent with the impact caused by the collision with a flock of birds, categorising the defect as an operational overload (bird strike [15]). Images of the component are captured using a Matrice 350RTK drone equipped with a Zenmuse L2 camera and processed by Metashape© [16] for generating photogrammetric reconstructions. Gaussian Splatting is entirely code-based in Python using the PyTorch framework and custom CUDA© for rasterisation, with a completion time of about 35 minutes.

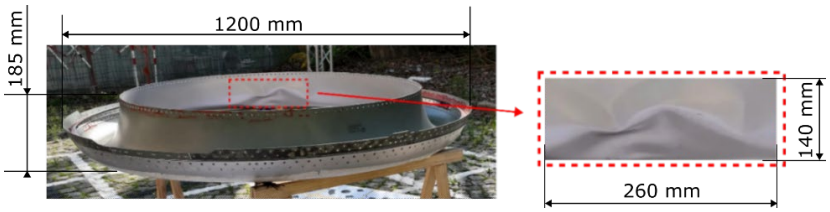


Fig. 2. *(a) Real images of the inlet lip skin part of an engine of an aircraft used as a case study for demonstrating the combination of photogrammetry and Gaussian Splatting, and (b) detail of the bump shape. The image provides also the approximate overall dimensions.*

Preliminary results

In this section, a preliminary case study is analysed in order to facilitate a more comprehensive evaluation of the capabilities of combining photogrammetry and Gaussian Splatting. This combination aims to delineate the discrepancies that may emerge during the inspection of a damaged area when input is augmented with localised renders in the proximity of the defect. The object under consideration is the inlet lip skin in Fig. 2 and two different photogrammetric configurations are analysed:

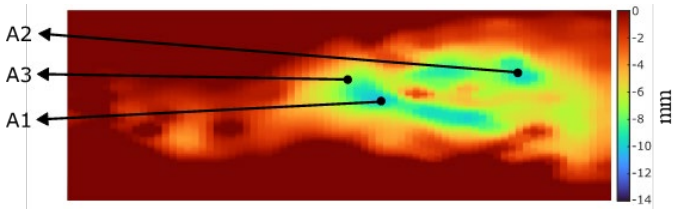
- Case A, consisting of 200 real images;
- Case B, consisting of 200 real images augmented with 30 novel GS renders.

The collection of 200 real images serves as a reference for the Gaussian Splatting pipeline and the generation of the 3D scene. In the generation of case B, 30 additional images, extracted from the 3D GS scene, are obtained from entirely novel viewpoints aiming to enrich the defect visualisation. Consequently, there is no correspondence between reference images and new renders, since the observation angles and location are by definition novel.

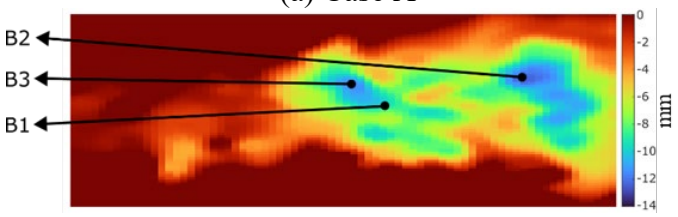
To compute the differences between the clouds, it is fundamental to create a reference surface fitting the internal toroidal surface of the lip. The RANdom SAmple Consensus (RANSAC) [17] fitting toroidal surface is created using the undamaged portion of the surface as a reference, with the point clouds then being overlaid onto the theoretical surface corresponding to this undamaged portion. This approach enables the computation of cloud-to-surface distances, highlighting any differences between the point clouds. As illustrated in Figs. 3a and 3b, each point cloud is projected from 3D onto the 2D image plane where the image of the bump lies. This projection enables the points to be superimposed onto the image, creating a density map where the colour represents the computed distances. The map provides a clear visualisation of variations between the theoretical and observed surfaces. Finally, Table 2 is used to define parameters for comparing the point clouds. The “Average 1” column corresponds to the average distance values when considering the overall extent of the map. The “Average 2” column represents the average distance excluding values close

Materials Research Proceedings 57 (2025) 20-28 https://doi.org/10.21741/9781644903735-3

to 0 mm, since areas where the distance is 0 indicate the absence of defect. This allows a specific comparison of only the regions where the bump is extended. The “Coverage” column assesses the percentage of the surface affected by damage, defined as the ratio between the portion of the surface characterised by a distance from the reference surface lower than 0 mm and the total surface area. In addition, the remaining columns provide a detailed comparison of specific points of interest. For clarity, distances are shown with negative values since the bump in the damaged area brings the object's surface closer to the centre of the fitting toroid than in the undamaged area. “Peak 1” corresponds to the negative peak of distance in case A (labelled as A1 in the figure), and its value in case B is evaluated at the same coordinates (labelled as B1). Similarly, “Peak 2” and “Peak 3” represent the two minima in case B (labelled as B2 and B3, respectively), and their values in case A are evaluated at the same coordinates (labelled as A2 and A3). As illustrated in Fig. 4, in the context of case B, the measurements B1, B2, and B3 are assigned a negative sign, as they denote distances measured inward relative to the mean surface of the toroid, according to the local reference frame. An equivalent consideration applies to case A.



(a) Case A



(b) Case B

Fig. 3. *Projection of point cloud and colour density map based on the distance from best fitting primitive in the damaged area considering (a) case A and (b) case B. Point A1 corresponds to the negative peak of distance in case A, and its counterpart in case B is evaluated at the same coordinates (labelled as B1). B2 and B3 represent two local minima in case B, and their corresponding values in case A are evaluated at the same coordinates (labelled as A2 and A3).*

By observing these results, some preliminary comments can be proposed:

- Case B demonstrates a higher level of damage, as demonstrated in Table 2. Furthermore, “Peak 1” demonstrates consistency across both cases, with a value of -10.05 mm for case A and -10.34 mm for case B. Conversely, case B permits the identification of a greater number of minima, which are less pronounced in case A (see Fig. 3 for reference).
- The cloud in case A is composed of 1994 points, while case B consists of 2071 points. The difference in points is negligible, but the *back-in-time* paradigm is clearly demonstrated. The initial photogrammetric reconstruction, created using 200 real images, provides an approximate geometry of the defect, with its shape and extent significantly underestimated. In contrast, re-examining the object's state at the time of initial acquisition within the 3D scene allows for more precise delineation of the bump geometry in contours and distance peaks from the average reference surface.

Materials Research Proceedings 57 (2025) 20-28 https://doi.org/10.21741/9781644903735-3

Table 2. *Comparison between case A (real images) and case B (real images + GS renders) based on peak distances from the best-fit primitive, along with an evaluation of the damaged area extent.*

	Average 1 / [mm]	Average 2 / [mm]	Coverage / -	Peak 1 / [mm]	Peak 2 / [mm]	Peak 3 / [mm]
Case A	-2.48	-4.23	59%	A1: -10.05	A2: -9.49	A3: -7.03
Case B	-3.46	-5.14	67%	B1: -10.34	B2: -11.83	B3: -11.30

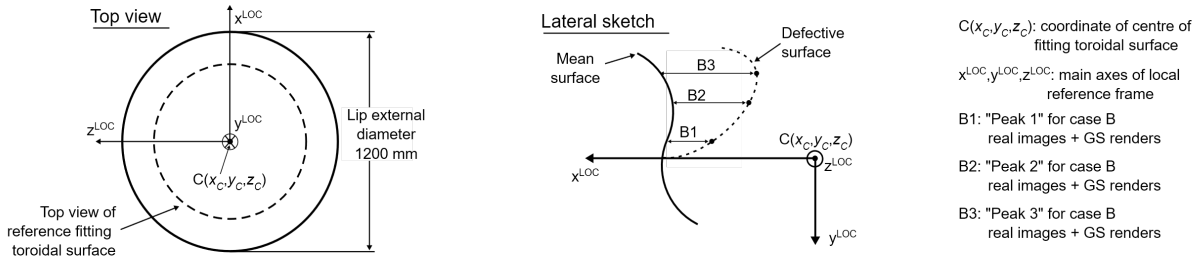


Fig. 4. *Top and sketch view of the inlet lip skin. Definition of the distances B1, B2, B3 relative to the mean surface of the fitting toroid. The measurements are assigned a negative sign as they represent displacements inward with respect to the reference mean surface. The same logic applies to points A1, A2 and A3 (case A), although they are not shown in the figure to avoid overloading the visual representation.*

Conclusions

This work preliminarily explored the integration of photogrammetry and Gaussian Splatting as a novel approach to enhance quality inspection through the novel concept of *back-in-time* analysis. By generating "frozen" and fully navigable 3D scenes from the original image acquisitions, GS enables the extraction of synthetic views (i.e., renders) from previously inaccessible perspectives, without requiring new physical acquisitions. Renders can be introduced into the photogrammetric workflow, along with real images, improving point cloud density and the accuracy of defect characterisation. Once integrated into the photogrammetric pipeline, renders enrich the original acquisitions while preserving the same temporal state, thus enabling retrospective inspection. GS introduces the innovative paradigm of *back-in-time repeatability* into photogrammetry by enabling multiple analyses of the same object state, corresponding to a specific moment in time, regardless of the current condition or availability of the physical asset.

The preliminary case study confirmed the potential of this approach to detect and refine the geometry of surface damage, particularly in areas that were insufficiently covered during initial acquisition. The increased spatial coverage and the ability to revisit the exact temporal state of an object represent a meaningful advancement over conventional inspection techniques.

Beyond the specific application presented, the proposed synergy introduces the concept of *back-in-time repeatability* into the field of 3D reconstruction, expanding photogrammetry from a static imaging tool to a dynamic spatio-temporal framework. This paradigm shift opens novel possibilities in industrial inspection, product traceability, lifecycle monitoring, and digital asset management.

Future research will focus on validating this approach across different defect types (e.g., corrosion, wear), refining integration protocols, and assessing its scalability for real-world industrial environments.

Acknowledgements
This study was carried out within the Space It Up project funded by the Italian Space Agency, ASI, and the Ministry of University and Research, MUR, under contract n. 2024-5-E.0 - CUP n. I53D24000060005.

References

[1] Garnier C, Pastor M-L, Eyma F, Lorrain B (2011) The detection of aeronautical defects in situ on composite structures using Non Destructive Testing. Composite Structures 93(5):1328-1336. https://doi.org/10.1016/j.compstruct.2010.10.017

[2] Mikhail EM, Bethel JS, Mcglone JC (2001) Introduction to Modern Photogrammetry. 1st edn. John Wiley & Sons, New York, USA.

[3] Colomina I, Molina P (2014) Unmanned aerial systems for photogrammetry and remote sensing: A review. ISPRS Journal of Photogrammetry and Remote Sensing 92:79-97. https://doi.org/10.1016/j.isprsjprs.2014.02.013

[4] Franceschini F, Galetto M, Maisano D, Mastrogiacomo L, Pralio B (2011) Distributed Large-Scale Dimensional Metrology: New Insights. 1st edn. Springer London. https://doi.org/10.1007/978-0-85729-543-9_1

[5] Franceschini F, Galetto M, Maisano D, and Mastrogiacomo L (2015) Combining multiple Large Volume Metrology systems: Competitive versus cooperative data fusion. Precision Engineering 43:514-524. https://doi.org/10.1016/j.precisioneng.2015.09.014

[6] Sitzmann V, Zollhöfer M, and Wetzstein G (2019) Scene Representation Networks: Continuous 3D-Structure-Aware Neural Scene Representations. In: 33rd Conference on Neural Information Processing Systems (NeurIPS 2019), pp. 1121 - 1132. Vancouver, Canada.

[7] Alatan AA, Yemez Y, Gudukbay U, Zabulis X, Muller K, Erdem CE, Weigel C, Smolic A (2007) Scene Representation Technologies for 3DTV-A Survey. IEEE Transactions on Circuits and Systems for Video Technology 11:1587-1605. https://doi.org/10.1109/TCSVT.2007.909974

[8] Mildenhall Ben, Srinivasan PP, Tancik M, Barron JT, Ramamoorthi R, Ng R (2021) NeRF: representing scenes as neural radiance fields for view synthesis Commun. ACM 1:99-106. https://doi.org/10.1145/3503250

[9] Kerbl B, Kopanas G, Leimkuehler T, Drettakis G (2023) 3D Gaussian Splatting for Real-Time Radiance Field Rendering. ACM Trans. Graph. 42(4), Article n. 139, pp. 1 - 14. https://doi.org/10.1145/3592433

[10] Brooks CR, Choudhury A (2002) Failure analysis of engineering materials. The McGraw-Hill Education. 1st edn. New York, NY.

[11] Sause MGR, Jasiūnienė E (2022) Structural Health Monitoring Damage Detection Systems for Aerospace. Springer Aerospace Technology. 1st edn. Cham, Switzerland. https://doi.org/10.1007/978-3-030-72192-3_11

[12] Trombini M, Maculotti G, Maisano DA, Pagani A, Franceschini F (2025) Scaling photogrammetry: A comparative evaluation and metrological assessment across small- and meso-scale domains. Precision Engineering 92:124-140. https://doi.org/10.1016/j.precisioneng.2024.12.002

[13] Luhmann T, Robson S, Kyle S, Harley I (2006) Close range photogrammetry. 1st edn. Wiley Whittles Publishing Caithness, UK.

[14] Franceschini F, Galetto M, Genta G (2015) Multivariate control charts for monitoring internal camera parameters in digital photogrammetry for LSDM (Large-Scale Dimensional Metrology) applications. Precision Engineering 42:133-142. https://doi.org/10.1016/j.precisioneng.2015.04.008

[15] Findlay SJ, Harrison ND (2002) Why aircraft fail. Material Today 5(11):18-25. https://doi.org/10.1016/S1369-7021(02)01138-0

[16] Agisoft. Discover intelligent photogrammetry with Metashape. https://www.agisoft.com/ Last accessed 25 April 2025.

[17] Fischler MA, Bolles RC (1981) Random sample consensus: a paradigm for model fitting with applications to image analysis and automated cartography. Commun. ACM 24(6):381-395. https://doi.org/10.1145/358669.358692

Materials Research Proceedings 57 (2025) 29-37 https://doi.org/10.21741/9781644903735-4

Preliminary experimental results on a multidimensional model for cognitive assistance systems in manufacturing

BARTOLOMEI Mirco[1,a], BARRAVECCHIA Federico[1,b], REA Maria[1,c], MASTROGIACOMO Luca[1,d], CANNIZZARO Davide[2,e], FRANCESCHINI Fiorenzo[1,f]

[1]Politecnico di Torino, DIGEP (Department of Management and Production Engineering), Torino, Italy

[2]Leonardo S.p.A., Corso Castelfidardo, 22, 10128, Torino, Italy

[a]mirco.bartolomei@polito.it, [b]federico.barravecchia@polito.it, [c]s298826@studenti.polito.it, [d]luca.mastrogiacomo@polito.it, [e]davide.cannizzaro@leonardo.com, [f]fiorenzo.franceshini@polito.it

Keywords: Human Robot Collaboration, Ergonomics, Quality Engineering

Abstract. Cognitive assistance systems aim to enhance cognitive ergonomics by supporting operators in decision-making and task execution, addressing the high demands imposed by modern manufacturing processes. Existing frameworks for characterising cognitive assistance systems are fragmented, lacking a systematic approach to define and evaluate their constituent features. To address this gap, a multidimensional conceptual model is proposed, encompassing five core dimensions: *cognitive functions, autonomy, adaptivity, interaction modality*, and *portability*. A case study is conducted to preliminarily verify the model's applicability by analyzing how variations in these core dimensions influence cognitive load, number of failures, and cycle time. Overall, the study provides two main contributions: (i) a multidimensional conceptual model to bridge the gap in the characterisation of cognitive assistance systems, and (ii) some preliminary findings from a case study in the context of Human-Robot Collaboration (HRC).

Introduction

Modern manufacturing environments impose high cognitive demands on operators due to task complexity, workflow variability, and precision requirements [1]. When cognitive load—the mental effort required to process task-related information—exceeds manageable levels, it can adversely impact performance, productivity, and operator well-being [2]. To address these challenges, cognitive assistance systems, which integrate real-time data, artificial intelligence, and advanced user interfaces, have emerged as a promising solution. By providing relevant process information, guiding task execution, and correcting operator errors, these systems enhance task performance and reduce the likelihood of operator-induced failures [3].

Cognitive assistance can be delivered through a wide range of technologies and modalities, including augmented reality (AR), virtual reality (VR), conversational agents (e.g., voice assistants or chatbots), wearable devices (e.g., smart glasses or wristbands), and context-aware Internet of Things (IoT) systems [4]. Research highlights a variety of applications for cognitive assistance systems. For instance, Leins et al. [5] illustrate how AR improves manual assembly by overlaying step-by-step instructions to enhance accuracy and efficiency, while Funk et al. [6] proposed a system that provides multimodal feedback mechanisms (e.g., visual, auditory, and haptic signals) to prevent errors during assembly tasks. Despite these advances, the field lacks a comprehensive reference model that defines the core dimensions characterizing cognitive assistance. While numerous studies have identified important properties of these systems, their contributions are often limited to specific, non-overlapping aspects, leaving a lack of integration across frameworks

Content from this work may be used under the terms of the Creative Commons Attribution 3.0 license. Any further distribution of this work must maintain attribution to the author(s) and the title of the work, journal citation and DOI. Published under license by Materials Research Forum LLC.

[7]. This gap hinders the development of effective design strategies and limits the systematic evaluation of cognitive assistance systems. The primary research goal is to establish a structured and generalizable framework for the description and assessment of such systems across diverse technologies and application contexts. To achieve this, a conceptual model is proposed, comprising five core dimensions: *cognitive function, autonomy, adaptivity, interaction modality,* and *portability*. Each dimension is associated with a rating scale to enable consistent evaluation. The model's diagnostic capacity was preliminarily evaluated through a controlled experiment designed to test whether variations in the proposed dimensions correspond to measurable differences in cognitive load and task performance.

The paper is structured as follows. The conceptual model section describes the core dimensions of cognitive assistance. The model application section outlines its use in analyzing four configurations of cognitive assistance systems. The experimental section provides preliminary empirical results through a case study on cognitive load and operational performances. Finally, the discussion and conclusions section highlights the model's implications, practical applications, and potential directions for future research.

Conceptual Model of Cognitive Assistance Systems

To develop a comprehensive model, existing conceptual schemes of cognitive assistance [7–11] were examined, and their constituent dimensions were synthesized and integrated into a unified model. The selected models were identified through a focused literature review conducted using a predefined set of keywords in the Scopus and Web of Science databases, with selection criteria emphasizing conceptual robustness and relevance to cognitive assistance; studies were included based on publication quality, thematic alignment, and methodological clarity. The labels assigned to the model's dimensions serve as reference terms, consolidating the implicit meanings of similar concepts across the different schemes, defined as follows:

- *Cognitive functions:* this dimension captures the specific tasks a system performs to support stages of information processing [7,8].
- *Autonomy:* refers to the system's degree of independence in performing assistance actions. This emphasizes the importance of cognitive systems capable of monitoring task execution, perceiving their environment, and making context-aware decisions [9,10].
- *Adaptivity:* refers to the system's ability to dynamically adjust to changes in task demands or operator states, ensuring effective support even under varying conditions [9,10].
- *Interaction modality:* denotes the modes of communication between the system and its user, particularly through sensory channels such as visual, auditory, or tactile interfaces [9].
- *Portability:* defines the extent to which a device providing cognitive assistance can be moved across different environments. The portability of such devices is recognized as a defining characteristic of cognitive assistance systems, enabling flexibility and broader applicability [11].

In the proposed model (see Figure 1), the five core dimensions are hierarchically organized to reflect their roles within cognitive assistance systems. At the foundation is the *cognitive function* core dimension, defining the system's primary purpose by specifying what it does to assist the operator, focusing on information processing stages. The other four dimensions—*autonomy, adaptivity, interaction modality,* and *portability*—are subordinate, describing how the system delivers its support in every information processing stage addressed.

Materials Research Proceedings 57 (2025) 29-37 https://doi.org/10.21741/9781644903735-4

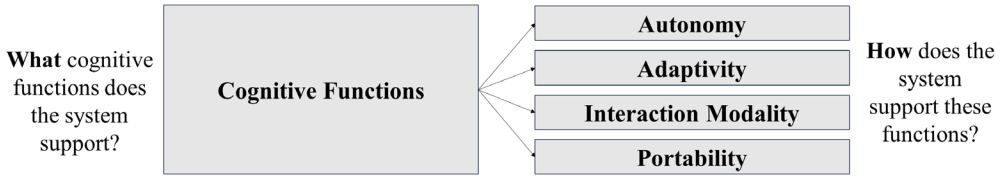


Fig. 1. Conceptual Model of Cognitive Assistance Systems

The Cognitive Functions dimension.

The *cognitive functions* dimension defines what support actions the system provides. Table 1 summarizes the categories of the *cognitive functions* dimension [7,12,13], outlining their descriptions and providing practical examples. For instance, a system that visualizes process parameters and alerts users to deviations performs the functions of *information acquisition* and *information analysis*. In contrast, a system providing step-by-step assembly instructions supports *action selection* and *action implementation*.

By identifying the cognitive functions performed, a critical initial distinction can be drawn between different cognitive assistance systems.

Delivering Cognitive Functions

Analysing a system through the lens of cognitive function enables an initial classification of systems and an assessment of their potential. However, the implementation of cognitive functions can vary significantly, as they can be delivered through different modalities. These approaches can be systematically characterized according to the core dimensions *of autonomy, adaptivity, interaction modality,* and *portability*. To transition from a purely conceptual model to one that facilitates the evaluation and comparison of cognitive assistance systems, the rating scales outlined in Table 2 are proposed. These scales are derived from existing frameworks and adapted to the context of cognitive assistance.

Table 1. Basic categories of Cognitive Functions with descriptions and examples [7,12,13].

Cognitive Functions	Description	Example of Cognitive Assistance
Information Acquisition	Support in perceiving and gathering relevant process data.	A display providing raw process data, e.g. cycle time, machining parameter and process status.
Information Analysis	Assistance in interpreting and processing acquired data to derive meaningful insights	A dashboard displaying trends in system performance for anomaly detection.
Action Selection	Guidance in choosing the most appropriate action based on analyzed information.	A recommendation system suggesting optimal machine settings for energy efficiency.
Action Implementation	Direct aid in executing the selected actions.	Augmented reality overlays showing step-by-step assembly instructions.
Feedback	Support in identifying and correcting errors in task execution.	A visual alert notifying an operator of an error in task execution for immediate correction.

Materials Research Proceedings 57 (2025) 29-37 https://doi.org/10.21741/9781644903735-4

Table 2. Levels and descriptions of autonomy [14], adaptivity [15], interaction modality [16], and portability [11] core dimensions.

Core Dimension	Levels	Description
Autonomy	*L0: Not Performed*	The cognitive assistance system does not perform the cognitive function
	L1: No Autonomy	The system provides information or instructions on demand, but the cognitive function is entirely performed by the human operator.
	L2: Partial Autonomy	The task is performed fully or partially by the system, but either at the operator's request or after receiving the operator's approval.
	L3: High Autonomy	The system independently makes decisions and takes actions, either without informing the user or notifying them only after execution.
Adaptivity	*L0: Not Performed*	The cognitive assistance system does not perform the cognitive function.
	L1: Static	The system provides the same assistance regardless of changing task demands or operator states.
	L2: Reactive	The system adjusts assistance in response to changes in the process or operator state.
	L3: Proactive	The system anticipates changes in the process and the operator state and adapts assistance in advance.
Interaction Modality	*L0: Not Performed*	The cognitive assistance system does not perform the cognitive function
	L1: No Interaction	The system provides assistance without direct user interaction.
	L2: Unimodal	Interaction involves one sensory modality (e.g., visual, auditory, or haptic).
	L3: Multimodal	Interaction engages two or more sensory modalities simultaneously.
Portability	*L0: Not Performed*	The cognitive assistance system does not perform the cognitive function
	L1: Stationary	The device operates in a fixed location and cannot be moved easily.
	L2: Mobile	The device is portable, enabling use in various locations.
	L3: Wearable	The device is attached to the worker during its use.

A Preliminary Experimental Application of the Model

In this section, the proposed model is applied to characterize four representative configurations of cognitive assistance systems used in an assembly process. The experiment aim was to assess the model's ability to distinguish between system setups based on assigned dimension levels, and to examine whether these differences correspond to measurable variations in cognitive load and task performance. Each configuration is defined by two factors: (i) the presence or absence of a UR3e collaborative robot (cobot) (see Figure 2.A), which supports operators in assembly tasks by providing both guidance and physical assistance, and (ii) the type of display used to present assembly instructions, either an assisted reality (aR) device, the RealWear Navigator 520 (see Figure 2.B), or a fixed screen. By combining the two factors, four explicative configurations can be obtained: *Configuration 1* (manual execution with fixed screen), *Configuration 2* (manual execution with aR), *Configuration 3* (collaborative execution with fixed screen), and *Configuration 4* (collaborative execution with aR). The configurations were experimentally evaluated through the assembly of some skateboard variants, with each task involving a different skateboard setup. The components of the assembled skateboard are shown and listed in Figure 3. The four configurations supported the following cognitive functions: *action selection, implementation,* and *feedback*. In *Configuration 1* and *Configuration 2* (manual assembly), cognitive assistance was delivered only via images, videos, and text to guide the assembly process, via either the aR device or the fixed screen, depending on the setup. In *Configuration 3* and *Configuration 4 (*collaborative assembly), the cobot autonomously selected and positioned components based on user input, while still providing assistance on the *feedback* cognitive function via either the aR device or the fixed screen, depending on the setup.

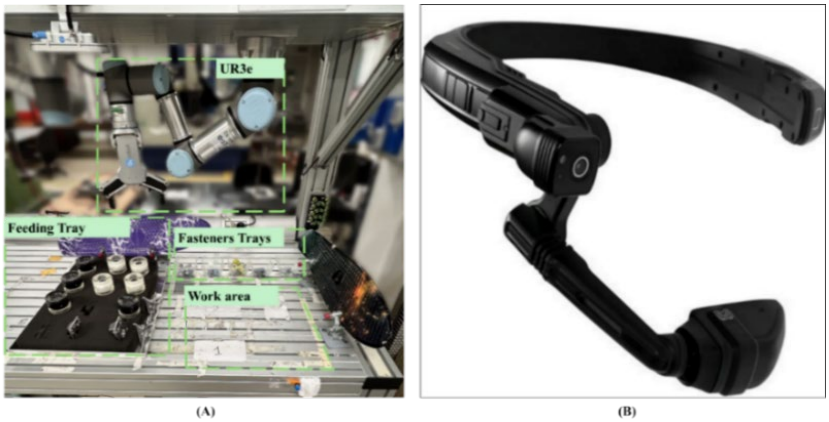
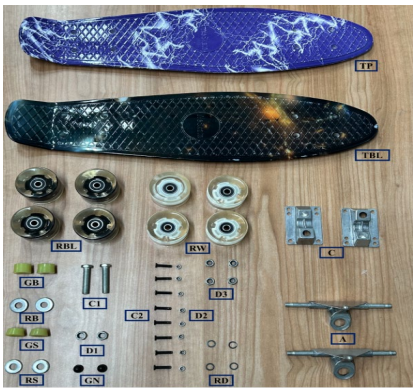


Fig. 2. (A) Overview of the workstation setup; (B) Illustrative picture of the Navigator 520 [17].



Code	Description	Quantity
C	Base plate	2
C1	Kingpin	2
RB	Top cup	2
GB	Bushing	2
RS	Lower cup	2
GS	Cone bushing	2
GN	Pivot bushing	2
A	Hanger	2
D1	Kingpin nut	2
C2	Deck bolt	8
D2	Deck nut	8
RBL	Black wheel	4
RW	White wheel	4
D3	Axle nut	4
TP	Purple skateboard deck	1
TBL	Black skateboard deck	1

Fig. 3. Skateboard components with their corresponding identification codes and descriptions.

The four explicative configurations of cognitive assistance systems were systematically characterised by applying the proposed conceptual model as follows:

- *Configuration 1:* for action selection, action implementation, and feedback, the system provides no autonomy *(L1)* leaving the operator fully responsible for following the instructions and executing the task. Adaptivity is static *(L1)*, offering consistent guidance independent of task or operator status. Interaction is multimodal *(L3)*, as the fixed screen delivers visual instructions and receives input via button presses. Portability is limited since the screen is stationary *(L1)*.
- *Configuration 2:* similarly to *Configuration 1*, for action selection, action implementation, and feedback, system's autonomy is absent *(L1)*, and adaptivity is static *(L1)*, providing uniform support throughout the assembly process. Interaction is multimodal *(L3)*, with the aR system receiving audio input and providing visual information. Portability improves significantly *(L3)* for all the cognitive supported functions performed, as the aR is mounted on the operator's head.
- *Configuration 3:* the robot introduces partial autonomy *(L2)* in action selection and implementation by performing variable tasks independently on operator request. However, despite the visual reference provided by the system, feedback remains fully operator driven *(L1)*. For every supported cognitive function, adaptivity is static (L1), interaction modality remains multimodal *(L3),* and portability is stationary *(L1)*.
- *Configuration 4:* like in *Configuration 3*, robot provides partial autonomy *(L2)* for action selection and implementation. In addition, the aR and the cobot provide multimodal support *(L3)*. Adaptivity remains static *(L1)*, as the system does not adapt to task variations. Portability

Materials Research Proceedings 57 (2025) 29-37 https://doi.org/10.21741/9781644903735-4

is improved *(L3)* for feedback functions, due to the wearable aR device. On the contrary, the robot implementing the action selection and implementation functions is stationary (L1).

Experimental Setup

The experiment evaluated operational performance and cognitive load across the four cognitive assistance system configurations using a within-subject design. Each of the 12 participants, with no prior assembly experience of the selected product (skateboard), completed 4 assembly tasks per configuration. This design minimized the effect of inter-individual variability by allowing each participant to be compared against their own performance across different configurations. In addition, by randomising the sequence of presentation of configurations, the risk of order bias was minimised. Tasks involved identifying, positioning, and fastening components, with varying skateboard base and wheel arrangements in each repetition to prevent reliance on memory. The assembly station setup used for the experiment is shown in Figure 2.A.

Cognitive load was measured using two complementary physiological metrics:

- *Average fixation duration*: ocular activity was recorded via eye tracking device (Tobii Pro-glasses 3). Longer fixations indicates higher cognitive load [18].
- *Skin Conductance Level (SCL):* measured with a wristband wearable device (Empatica E4). Higher SCL are correlated with higher experienced cognitive load [18].

Operational performance was assessed using three metrics:

- *Number of failures*: which combined *product errors* (e.g., incorrect placement or missing components in the final assembly) and *process errors* (e.g., deviations from the prescribed assembly sequence).
- *Cycle time*, the total time taken to complete the assembly process.

Data Processing.

Physiological metrics were standardized using Z-scores to account for inter-individual variability in baseline cognitive load and arousal. The Z-score for each metric was computed using the formula:

$$z_{i,j} = \frac{x_{i,j} - \bar{x}_j}{s_j} \quad (1)$$

where $z_{i,j}$ and $x_{i,j}$ represent the z-score and raw observation for the i-th metric (i.e., average fixation duration and SCL) of participant j, respectively, $\bar{x}_j$ is the mean value for participant j, and s_j is the standard deviation for participant j. Standardizing the data ensured that differences between configurations were not influenced by individual physiological variations. To account for repeated measures nested within participants, a Linear Mixed-effects Model (LMM) was employed. LMM accounts for within-participant variability by modelling repeated measures, controls for between-participant differences as a random effect, and handles task replications across system configurations. The model accounts for the effects of screen type (fixed screen vs aR), execution modality (collaborative or manual), and their interaction, while incorporating a random effect to adjust for individual variability across participants.

Subsequently, ANOVA was conducted to evaluate the statistical significance of the fixed effects. Finally, post-hoc pairwise comparison of Estimated Marginal Means (EMMs) were conducted to enable direct comparisons between the four configurations [19].

Results

Post-hoc pairwise comparisons of average fixation duration, SCL, task failures, and cycle time revealed key differences between the cognitive assistance systems on cognitive load and cycle times.

As shown in Figure 4.A, ocular activity indicated variations in cognitive load across the configurations. Fixation duration, positively correlated with cognitive load, was significantly

shorter in *Configuration 4* compared to *Configuration 1* (p=0.008) and *Configuration 2* (p=0.042). This reduction suggests that the combination of robotic autonomy and the portability provided by the aR device in *Configuration 4* distributed the cognitive effort for feedback and guidance more effectively.

Electrodermal activity, measured through *SCL*, provided further evidence of reduced cognitive load in the configuration combining greater autonomy and portability (see Figure 4.B). *SCL* was significantly lower in *Configuration 4* compared to *Configuration 1* (p=0.015), *Configuration 2* (p=0.020) and *Configuration 3* (p<0.001), indicating that the combined effect of robotic support and wearable aR technology helped alleviate cognitive load.

Considering the performance metrics, cycle time exhibited a trend opposite to that of cognitive load. As shown in Figure 4.C, *Configuration 1*—characterized by manual operations and a fixed screen—had significantly shorter cycle times compared to *Configuration 2* (p=0.01691), *Configuration 3* (p=0.0138), and *Configuration 4* (p=0.006). These results indicate that, in this particular scenario, the configuration without the robot and aR was the most efficient. No statistically significant differences were observed in terms of failures rates.

These preliminary results indicate that cognitive assistance systems with higher portability and autonomy, such as *Configuration 4*, reduce cognitive demands. However, these benefits come at the cost of efficiency, as reflected by longer cycle times.

Discussions and conclusions

This work presents a multidimensional conceptual model for characterizing cognitive assistance systems and some preliminary results of its application.

The model integrates key attributes of cognitive assistance into a comprehensive framework, defining five core dimensions: *cognitive function, autonomy, adaptivity, interaction modality,* and *portability*. The hierarchical organization of these dimensions highlights their interplay, with *cognitive function* defining the system's purpose and the other subordinate core dimensions specifying the mechanisms of their implementation.

The experimental results show that the model proves effective in distinguishing cognitive assistance systems based on their characteristics and their impact on cognitive load and task performance. The preliminary results suggested that, in the specific scenario examined, wearable-assisted reality systems and robotic assistance may be effective in reducing cognitive load, highlighting the model's potential to address the design of cognitive assistance systems.

Despite its strengths, the proposed model has some limitations. It assumes an independent structure among core dimensions. As a consequence, potential interdependencies remain underexplored, warranting further investigation. Finally, while evaluation scales are suggested for each core dimension, their practical implementation and standardization across different systems are yet to be validated. These limitations appear as valuable opportunities for future research to enhance the proposed model. Efforts should focus on refining the model, verifying its applicability across diverse contexts, and possibly broadening the range of rating metrics to achieve a more comprehensive understanding of cognitive assistance systems. Finally, the model could be useful as a reference framework for developing a taxonomy of cognitive assistance systems and creating practical tools to support their design.

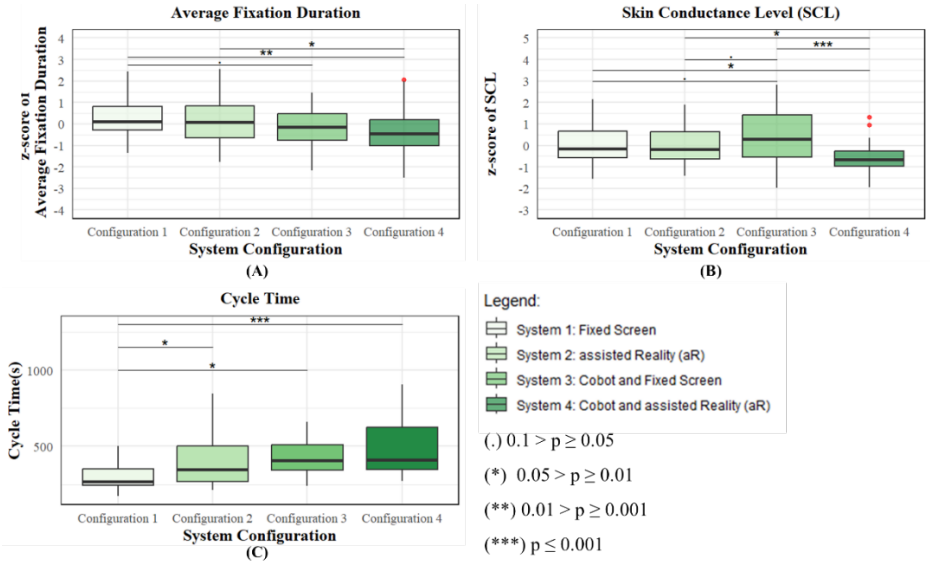


Fig. 4. Cognitive load and cycle time across four system configurations. (A) Boxplots of the distributions of z-scores of Average Fixation Duration. (B) Boxplots of the distributions of z-scores of SCL. (C) Boxplots of the distributions of Cycle Times.

Acknowledgments

This publication is part of the project PNRR-NGEU which has received funding from the MUR – DM 352/2022. This study was carried out within the Space It Up project funded by the Italian Space Agency, ASI, and the Ministry of University and Research, MUR, under contract n. 2024-5-E.0 - CUP n. I53D24000060005. This study was carried out within the "Empathically enhanced robot for the collaboration with HUmans in MANufacturing (E.HU.MAN)" project – funded by the Ministero dell'Università e della Ricerca – within the PRIN 2022 program (D.D.104 02/02/2022).

References

[1] Barravecchia F, Bartolomei M, Mastrogiacomo L, Franceschini F. Redefining Human-Robot Symbiosis: a bio-inspired approach to collaborative assembly. International Journal of Advanced Manufacturing Technology 2023;128:2043-2058. https://doi.org/10.1007/s00170-023-11920-1

[2] Bartolomei M, Barravecchia F, Mastrogiacomo L, Gatta DM, Franceschini F. Streamlining Assembly Instruction Design (S-AID): A comprehensive systematic framework. Computers in Industry 2025;165:104232. https://doi.org/10.1016/j.compind.2024.104232

[3] Eversberg L, Ebrahimi P, Pape M, Lambrecht J. A cognitive assistance system with augmented reality for manual repair tasks with high variability based on the digital twin. Manufacturing Letters 2022;34:49-52. https://doi.org/10.1016/j.mfglet.2022.09.003

[4] Mark BG, Rauch E, Matt DT. Worker assistance systems in manufacturing: A review of the state of the art and future directions. Journal of Manufacturing Systems 2021;59:228-250. https://doi.org/10.1016/j.jmsy.2021.02.017

[5] Leins N, Gonnermann-Müller J, Teichmann M. Comparing head-mounted and handheld augmented reality for guided assembly. Journal on Multimodal User Interfaces 2024;18:313-328. https://doi.org/10.1007/s12193-024-00440-1

[6] Funk M, Heusler J, Akcay E, Weiland K, Schmidt A. Haptic, Auditory, or Visual? Towards Optimal Error Feedback at Manual Assembly Workplaces. Proceedings of the 9th ACM International Conference on PErvasive Technologies Related to Assistive Environments, New York, NY, USA; 2016. https://doi.org/10.1145/2910674.2910683

[7] Cai H, Lin Y. Coordinating Cognitive Assistance With Cognitive Engagement Control Approaches in Human-Machine Collaboration. IEEE Transactions on Systems, Man, and Cybernetics - Part A: Systems and Humans 2012;42:286-294. https://doi.org/10.1109/TSMCA.2011.2169953

[8] Stoessel Christian and Wiesbeck M and SS and ZMF and SA. Towards Optimal Worker Assistance: Investigating Cognitive Processes in Manual Assembly. Manufacturing Systems and Technologies for the New Frontier, 2008, p. 245-250. https://doi.org/10.1007/978-1-84800-267-8_50

[9] Preum SM, Munir S, Ma M, Yasar MS, Stone DJ, Williams R, et al. A Review of Cognitive Assistants for Healthcare: Trends, Prospects, and Future Directions. ACM Computer Surveis 2021;53:130. https://doi.org/10.1145/3419368

[10] Angulo C, Chacón A, Ponsa P. Towards a cognitive assistant supporting human operators in the Artificial Intelligence of Things. Internet of Things 2023;21:100673. https://doi.org/10.1016/j.iot.2022.100673

[11] Sochor R, Kraus L, Merkel L, Braunreuther S, Reinhart G. Approach to increase worker acceptance of cognitive assistance systems in manual assembly. Procedia CIRP, vol. 81, 2019, p. 926 - 931. https://doi.org/10.1016/j.procir.2019.03.229

[12] Parasuraman R, Sheridan TB, Wickens CD. A model for types and levels of human interaction with automation. IEEE Transactions on Systems, Man, and Cybernetics Part A:Systems and Humans 2000;30. https://doi.org/10.1109/3468.844354

[13] Wickens CD, Carswell CM. INFORMATION PROCESSING. HANDBOOK OF HUMAN FACTORS AND ERGONOMICS, John Wiley & Sons, Ltd; 2021, p. 114-158. https://doi.org/10.1002/9781119636113.ch5

[14] O'Neill T, McNeese N, Barron A, Schelble B. Human-Autonomy Teaming: A Review and Analysis of the Empirical Literature. Human Factors 2022;64:904-938. https://doi.org/10.1177/0018720820960865

[15] Bernabei M, Costantino F. Adaptive automation: Status of research and future challenges. Robotics and Computer-Integrated Manufacturing 2024;88:102724. https://doi.org/10.1016/j.rcim.2024.102724

[16] van Erp JBF, Toet A, Janssen JB. Uni-, bi- and tri-modal warning signals: Effects of temporal parameters and sensory modality on perceived urgency. Safety Science 2015;72:1-8. https://doi.org/10.1016/j.ssci.2014.07.022

[17] RealWear: Navigator520 device, https://www.realwear.com/devices/navigator-520.

[18] Capponi M, Gervasi R, Mastrogiacomo L, Franceschini F. Assembly complexity and physiological response in human-robot collaboration: Insights from a preliminary experimental analysis. Robotics and Computer-Integrated Manufacturing 2024;89:102789 https://doi.org/10.1016/j.rcim.2024.102789

[19] Kutner MH, Nachtsheim CJ, Neter J. Applied Linear Statistical Models. 5th ed. New York: 2005.

Materials Research Proceedings 57 (2025) 38-46 https://doi.org/10.21741/9781644903735-5

Detection of sub-superficial defects by infrared thermography in parts made by powder bed fusion with electron beam

Silvio DEFANTI[1,a *], Simone DE GIORGI[2,b], Giovanni RIZZA[2,c], Giulia COLOMBINI[1,d], Emanuele TOGNOLI[1,e], Ahmet Ayberk Gürbüz[3,f], Lucia DENTI[1,g], Manuela Galati[2,h] and Luca Iuliano[2,i]

[1]Department of Engineering 'Enzo Ferrari', University of Modena and Reggio Emilia, Via Vivarelli 10, 41125 Modena, Italy

[2]Department of Management and Production Engineering, Politecnico di Torino, Corso Duca degli Abruzzi 24, 10129 Torino, Italy

[3]Izmir Institute of Technology, Gülbahçe Kampüsü 35430 Urla İzmir, Turkey

[a]silvio.defanti@unimore.it, [b]simone.degiorgi@polito.it, [c]giovanni.rizza@polito.it, [d]giulia.colombini@unimore.it, [e]emanuele.tognoli@unimore.it, [f]ayberkgurbuz96@gmail.com, [g]lucia.denti@unimore.it, [h]manuela.galati@polito.it, [i]luca.iuliano@polito.it

Keywords: Powder Bed Fusion, Thermography, Inspection

Abstract. This study explores infrared thermography as a cost-effective alternative to computed tomography for detecting subsurface defects in parts produced by powder bed fusion with an electron beam (PBF-EB). Ti6Al4V specimens were produced with designed defects that mimic subsurface pores or discontinuities whose size and depth are typical of PBF-EB. Computed tomography (CT-scan) was used to collect information on the defect dimensions and coordinates accurately. The same samples were therefore analysed using Joule heating infrared thermography, applying electric current while an infrared camera recorded the temperature development on the surface of the sample. The joint analysis of CT scan and thermography data provided a comprehensive study on the limits of the inspection technologies, PBF-EB process, and measuring system in terms of defect size, depth, and the size-to-depth ratio. The results showed that the surface characteristics of the PBF-EB are critical for thermography.

Introduction

Additive manufacturing (AM), in particular powder bed fusion with electron beam (PBF-EB), has gained significant traction in various industries including aerospace, automotive and medical sectors, owing to its ability to efficiently produce complex metallic components for high-end applications. However, as AM becomes more widespread, the challenge of ensuring part qualification is also growing, particularly in applications where safety and reliability are critical.

Defects in AM parts originate from various sources and can significantly affect the morphology, size and geometry of the defect. These factors contribute to the varying degrees of detectability for such defects [1,2]. Common issues include porosity that may contain unmelted powder or trapped gases [3,4] and can range from small, spherical configurations to irregular shapes [5,6]. Gas-induced porosity includes trapped inert gas (spherical, 10-80 μm) and gas inclusions such as hydrogen pores (spherical, 5-20 μm) [7,8]. Process-induced porosity is caused by excess energy (keyhole porosity) or insufficient energy (lack of fusion). Keyhole porosity, where deep vapor cavities form in the melt pool, leads to spherical pores with a diameter of about 100 μm after collapse [9,10]. Lack of fusion consists of large and irregular cavity formations between neighbouring melt lines or layers (lengths of 400 μm to 600 μm and heights of 140 to 240 μm) [3,6,10,11,12]. Spatter particles can contribute to these voids by absorbing the energy destined for the powder bed. Balling defects, which occur when molten material separates into spherical shapes

Content from this work may be used under the terms of the Creative Commons Attribution 3.0 license. Any further distribution of this work must maintain attribution to the author(s) and the title of the work, journal citation and DOI. Published under license by Materials Research Forum LLC.

Materials Research Proceedings 57 (2025) 38-46 https://doi.org/10.21741/9781644903735-5

due to improper process settings, also contribute to the overall porosity(in the size range of 150 μm to 250 μm) [13]. Foreign debris inclusions and delamination due to insufficient interlayer adhesion further complicate defect profiles, together with cracks due to solidification stresses (150-200 μm long, 60-70 μm wide) [8,14].

To address these challenges, ex-situ IRT emerges as a promising inspection technique for detecting subsurface defects of AM components. This is particularly true for active methods that rely on an external excitation source to thermally stimulate the inspected part [15,16]. The effectiveness of IRT is closely linked to the excitation method used, as the different techniques have different advantages and limitations depending on the specific applications of non-destructive testing. In particular, current-excited thermography is characterised by a favourable signal-to-noise ratio and the ability to identify subsurface defects. However, it often requires a careful contact setup and is limited to electrically conductive materials.

Given the critical focus on qualification of PBF-EB produced metal parts, detailed assessment of defects and overall quality is paramount to meet stringent performance standards. IRT provides a fast, non-contact solution for defect detection and offers advantages such as ease of use and early identification of defective components [17,18,19]. Despite its demonstrated potential, the method faces significant challenges, including susceptibility to noise and limited ability to detect smaller or deeper defects. Recent studies have explored advanced post-processing algorithms and machine learning to improve the sensitivity of thermographic techniques, particularly in the detection of calibrated porosity defects. While larger defects can often be easily identified, reliable detection of smaller anomalies still requires advanced algorithms to reach limits of 127 μm in diameter and depth [20]. Spherical defects with a diameter to depth ratio greater than 3 were reliably detected, with improved probabilities using thermal signal reconstruction techniques. Convective stimulated thermography detected open defects up to 300 μm in size in an Inconel 718 sample, but was ineffective for smaller defects [21]. The ASTM report found that optical flash thermography and convective step heating detected open surface defects, with convective heating identifying defects down to 0.2 mm in size, although both methods had problems with deep-seated defects [1].

The current landscape of IRT applications related to AM remains limited, since there is a lack of standardised testing protocols and comprehensive benchmarking with established methods such as CT. This research aims to pave the way for a robust testing protocol dedicated to the detection of defects in PBF-EB components, utilising active thermography with Joule excitation. By conducting preliminary tests and using CT data as a reference, the work proposes a standardised methodology for defect detection and contributes to the overall qualification process for additive manufacturing.

Materials and methods

Samples with intentional defects were designed using Solidworks 2023 CAD software (Dassault Systemes) with a square constant cross-section of 10 mm x 10 mm and a gripping area to facilitate connection to the power supply. This preliminary study is part of a broader investigation that considers many types of defects that mimic those typical of PBF-EB. In this first step, the development of a method for non-destructive testing by thermography is proposed. For this purpose, samples with cylindrical defects open at one end and characterised by a diameter (hereafter size) between 0.5 and 1 mm and a depth below the continuous surface, under which they are located, between 0.25 and 2 mm are used. Fig. 1 shows four defects in the same sample with different diameters and at different depths under the same surface, called hereafter “target surface”, misaligned with each other to minimise current flow disruption. These defects are larger than those typically formed during PBF-EB, so they should be easier to detect with the chosen method, also as a result of at least partial emptying of the unconsolidated powder. More challenging defects will be considered at a later stage, when the test protocol will be more consolidated.

Materials Research Proceedings 57 (2025) 38-46 https://doi.org/10.21741/9781644903735-5

Joule excitation leads to localised heating of the defect, which is greater the larger the defect is. Thermographic observation of the target surface shows a thermal inhomogeneity that is all the more pronounced the higher the temperature reached by the defect and the shallower the defect. Consequently, the ratio of size-to-depth is a decisive factor for detectability. It is consistently stated in the literature that one of the limiting factors for the effectiveness of thermographic detection is the finish of the surfaces being analysed [20], and in PBF-EB the surface morphology is highly dependent on the relative orientation of the surface under consideration in the build chamber [2]. Therefore, different samples were built with defects below four target surface types: Upskin, Side, Downskin built on loose powder and Downskin built directly on the build platform and subsequently detached from it.

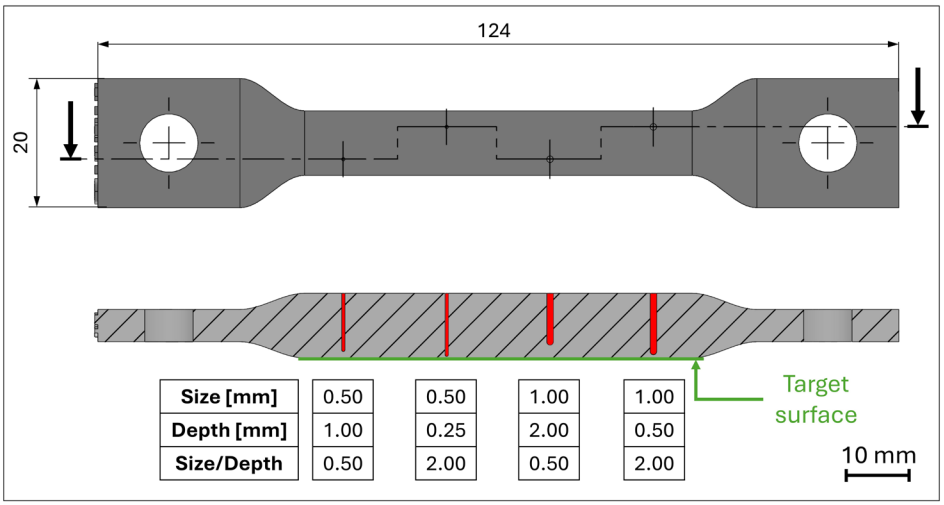


Fig. 1: Geometry of the samples showing the placement of the defects, their size, and depth below the target surface.

Samples were produced with an Arcam A2X PBF-EB system using standard Ti6Al4V powder with a size distribution ranging between 50 and 150 µm. Before the melting phase, each layer was preheated at 700 °C. The layer thickness was set equal to 0.050 mm. Details regarding the other process parameters are given in Table 1 [22]

Table 1: standard process parameters for Ti6Al4V

	Scan speed [mm/s]	Focus Offset [mA]	Beam current [mA]	Number of contours	Line offset [mm]
Contour (MultiBeam mode)	850	5	6	3	0.25
Hatching	1754	25	12	-	0.2

The surface topology of the samples was recorded using a Nikon LV 150 optical microscope (Nikon, Tokyo, Japan) equipped with a Confovis system. Specifically, an area of 4.5 x 2.5 mm^2 was scanned on the four types of surfaces. A 100x objective and a layer discretization of 0.50 µm were used.

The samples were CT scanned with a GE Phoenix V|tome|x S 240 with a voxel size of 20 µm to confirm the presence of the seeded defects and their detectability by tomography.

Materials Research Proceedings 57 (2025) 38-46 https://doi.org/10.21741/9781644903735-5

The thermography tests were performed with the following devices:

- Power supply: Xingtongli GKDM24-1000CVC, supplying DC current with a maximum voltage of 24 V and a maximum current of 1000 A.
- IR camera: Teledyne FLIR A700, placed at a distance of 40 mm from the target surface and equipped with a 2x macro lens that allows focussing on an area of 25.5 x 19.1 mm^2 with a sensor resolution of 640x480 pixels, resulting in a spatial resolution of 40 μm/pixel. The acquisition rate is 30 Hz.

Preliminary tests have shown that it is necessary to paint the target surface with a black, matt colour to avoid the effect of reflections. The sample to be analysed is placed on a fixed base in a partially enclosed chamber to limit interference from ambient light. The camera is positioned and focussed on the surface of the sample, then the recording begins and the current is applied for a few seconds. Before each test, it was checked that the temperature difference between the sample and the environment was less than 0.5°C. Each sample was tested 6 times, the repetitions of the experiments were randomized.

The recorded IR videos were post-processed with Matlab using the "FLIR Science File SDK for MatLab" to extract and process the individual IR frames as matrices. The first step in processing the data was to identify the captured image that had the highest defect contrast compared to the rest of the sample. For this purpose, the signal-to-noise ratio (SNR) was calculated as in [23,24]:

$$SNR = \frac{|\overline{T_d} - \overline{T_{nd}}|}{\sigma_{nd}} \quad (1)$$

Where:
$\overline{T_d}$ = average level of the signal in the defect region of interest (ROI), i.e. a rectangle closely enclosing the defect (Fig. 2)
$\overline{T_{nd}}$ = average level of the signal in the reference ROI, a hollow rectangular region (hatched in Fig. 2) obtained by offsetting the defect ROI.
σ_{nd} = standard deviation of the signal in the reference ROI
The defect is thus theoretically detectable if SNR > 1. In the initial development of the methodology, defect detection was based on the manual positioning of the reference ROI in an area adjacent to the defect. This approach was later replaced by the current automated solution, based on the self-referencing method proposed by Usamentiaga et al. [24], which ensures a more reliable adaptation to the defect shape while eliminating the risk of arbitrarily selecting a non-representative region.

Various approaches were tested to automatically determine the size of the defect from the thermographic images. These included: i) fitting a Gaussian curve to the temperature profile crossing the defect and evaluating the start and end of the peak or full width at half maximum; ii) mathematically analysing the temperature profile across the defect or its derivative.

Materials Research Proceedings 57 (2025) 38-46 https://doi.org/10.21741/9781644903735-5

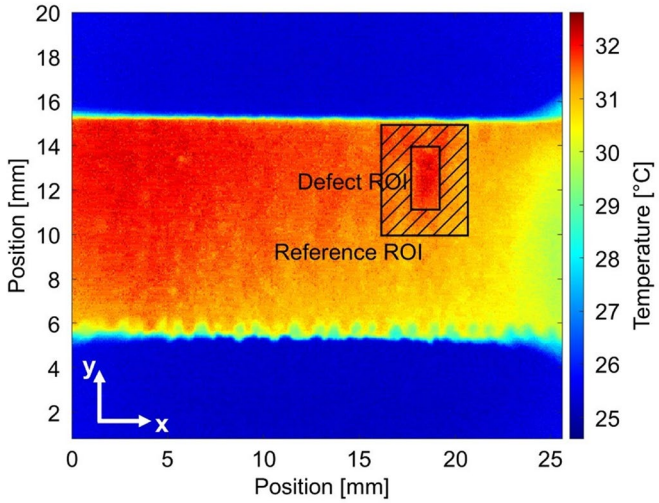


Fig. 2: Representation of the ROIs for SNR calculation.

Results and Discussion

The results of the confocal measurements on the target surfaces are shown in Fig. 3 together with the 3D average areal surface roughness S_a. The upskin has the most even surface while the roughness of the downskin varies depending on the costruction on the build platform or the loose powder. The side surfaces have the highest roughness of 38.4 µm. These variations significantly impact defect detectability, assessed using the SNR methodology. This effect is clearly illustrated in Fig. 4, where the same defect is analyzed on both the downskin and upskin surfaces. The results differ considerably, with an SNR of 2.36 in one case, while in the other it is close to the minimum detection threshold of 1, demonstrating a clear decline in detection efficiency as surface roughness increases.

Detection is also strongly influenced by the size and depth of the defects. Table 2 shows the nominal values and the corresponding SNR calculations for the individual artefacts produced. Smaller defects and greater depths reduce detectability, which often leads to non-detection and thus illustrates the limitations of this inspection technology. Defects at a depth of 2 mm mostly remain undetected, even at larger sizes, while a 0.5 mm defect is only detected at a shallow depth of 0.25 mm. All defects were successfully detected with tomography instead.

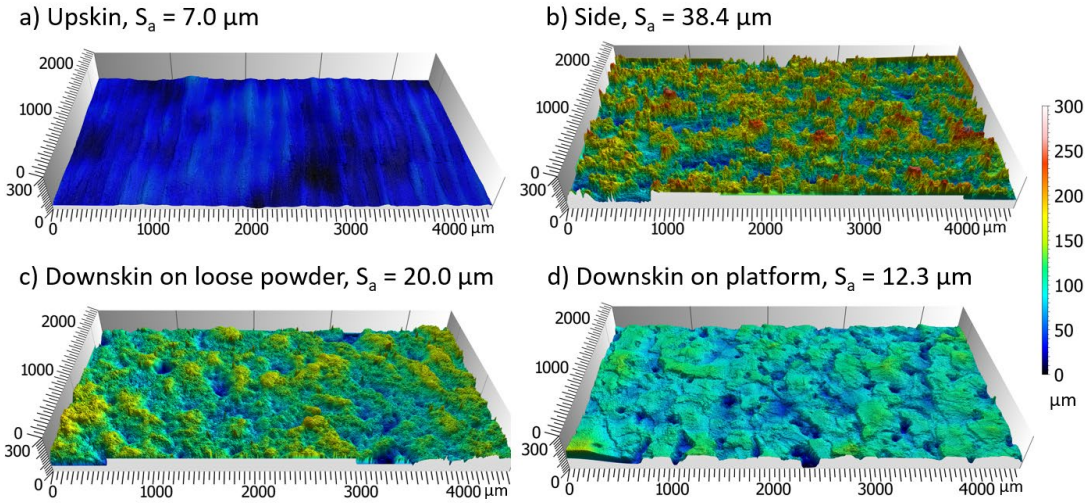


Fig. 3: Confocal maps of the target surfaces.

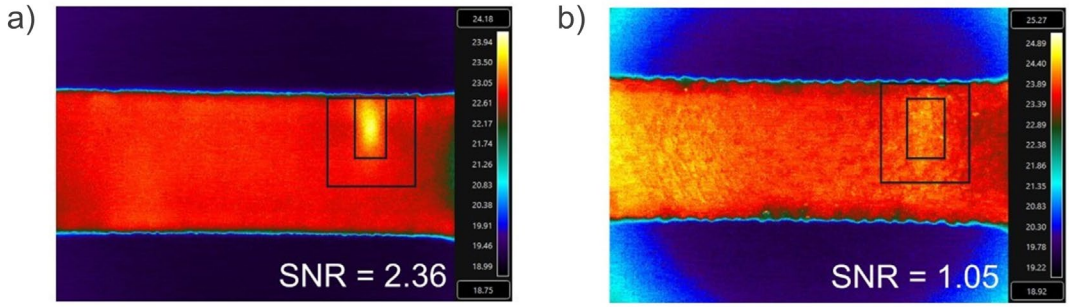


Fig. 4: Results of the SNR calculation for the defect with 1 mm diameter and 0.5 mm depth in the case of downskin (a) and upskin (b) target surface.

The thermographic images were also processed to determine the defect size. Robust results were obtained using the following method:

- An additional Measurement ROI was determined, i.e. a rectangle with a large base crossing the defect in the direction of current flow (x) and a height smaller than the hot area in the y-direction (Fig. 5a).
- A temperature profile was calculated by averaging the temperature values along the y-direction for each x-position (Fig. 5b).
- The experimental data were fitted with a three-term Gaussian function and the first derivative of the Gaussian profile was calculated (Fig. 5c).
- The defect size was determined as the x-distance between the maximum and minimum positions (Fig. 5d).

Table 2: Results of the thermographic analysis.

Target surface	Nominal		Thermography				Target surface	Nominal		Thermography			
	Size [mm]	Depth [mm]	SNR		Size [mm]			Size [mm]	Depth [mm]	SNR		Size [mm]	
			Avg.	S.D.	Avg.	S.D.				Avg.	S.D.	Avg.	S.D.
Up	0.5	1.00	0.43	0.05	-	-	Down	0.5	1	0.63	0.10	1.26	0.27
	0.5	0.25	1.90	0.38	0.86	0.07		0.5	0.25	1.03	0.10	1.26	0.16
	1	2	0.20	0.09	-	-		1	2	0.39	0.05	-	-
	1	0.5	2.36	0.20	1.02	0.05		1	0.5	1.05	0.05	1.46	0.39
Side	0.5	1	0.27	0.06	-	-	Down-platform	0.5	1	1.26	0.25	0.77	0.10
	0.5	0.25	0.59	0.15	-	-		0.5	0.25	1.52	0.27	0.88	0.10
	1	2	0.38	0.07	-	-		1	2	1.13	0.14	1.66	0.06
	1	0.5	1.74	0.08	1.28	0.05		1	0.5	2.89	0.42	0.99	0.09

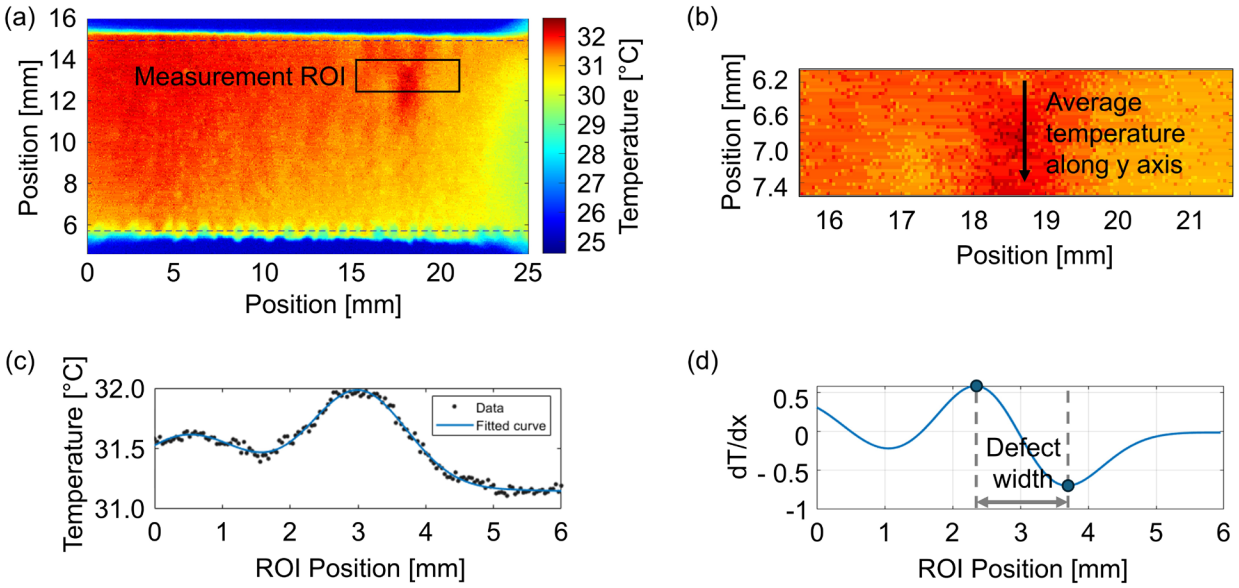


Fig. 5: Defect measurement procedure: a) identification of the measurement ROI, b) magnification of the measurement ROI, c) temperature vs. position plot with the fitted Gaussian curve, d) indication of the defect width in the first derivative curve.

Conclusions

This study aims to define a robust methodology for the application of active IRT with Joule excitation for defect detection in PBF-EB components. Open cylindrical defects of different sizes (0.5–1 mm) and depths (0.25–2 mm) were intentionally introduced into the fabricated samples, which were used as test artefacts for the development of an NDT procedure. Key achievements include an automated and reliable method for SNR calculation and Gaussian-based automatic defect sizing, as well as the identification of a robust test setup. In particular, the experimental measurements have shown that detectability is critically affected by the morphology of the target surface, leading to a reduction in detection efficiency for rougher surfaces, and by the dimensional characteristics of the defects analysed, with defects at a depth of 2 mm not being detected even at larger sizes, and a 0.5 mm diameter defect being detected at a shallow depth of only 0.25 mm. IRT is thus confirmed as a valuable technique for rapid non-destructive evaluation, and this study represents the first step in the evaluation of this method compared to accurate and time-consuming alternatives such as tomography.

References

[1] ASTM International and ISO/ASTMTR52905, *Additive Manufacturing of Metals—Nondestructive Testing and Evaluation—Defect Detection in Parts*. ASTM International100 Barr Harbor Drive, PO Box C700, West Conshohocken, PA 19428-2959, 2023. https://doi.org/10.1520/ISO/ASTMTR52905-EB

[2] M. Galati, “Electron beam melting process,” in *Additive Manufacturing*, Elsevier, 2021, pp. 277–301. https://doi.org/10.1016/B978-0-12-818411-0.00014-8

[3] ASTM International and E3166-20, “Standard Guide for Nondestructive Examination of Metal Additively Manufactured Aerospace Parts After Build,” Feb. 01, 2020, *ASTM International, West Conshohocken, PA*. https://doi.org/10.1520/E3166-20

[4] Y. Zhu, Z. Wu, W. D. Hartley, J. M. Sietins, C. B. Williams, and H. Z. Yu, “Unraveling pore evolution in post-processing of binder jetting materials: X-ray computed tomography,

computer vision, and machine learning," *Addit Manuf*, vol. 34, p. 101183, Aug. 2020. https://doi.org/10.1016/j.addma.2020.101183

[5] Y. Gui, K. Aoyagi, and A. Chiba, "Development of macro-defect-free PBF-EB-processed Ti–6Al–4V alloys with superior plasticity using PREP-synthesized powder and machine learning-assisted process optimization," *Materials Science and Engineering: A*, vol. 864, p. 144595, Feb. 2023. https://doi.org/10.1016/j.msea.2023.144595

[6] Z. Snow, A. R. Nassar, and E. W. Reutzel, "Invited Review Article: Review of the formation and impact of flaws in powder bed fusion additive manufacturing," *Addit Manuf*, vol. 36, p. 101457, Dec. 2020. https://doi.org/10.1016/j.addma.2020.101457

[7] T. Liu, S. Guessasma, J. Zhu, W. Zhang, H. Nouri, and S. Belhabib, "Microstructural defects induced by stereolithography and related compressive behaviour of polymers," *J Mater Process Technol*, vol. 251, pp. 37–46, Jan. 2018. https://doi.org/10.1016/j.jmatprotec.2017.08.014

[8] P. Charalampous, I. Kostavelis, and D. Tzovaras, "Non-destructive quality control methods in additive manufacturing: a survey," *Rapid Prototyp J*, vol. 26, no. 4, pp. 777–790, Mar. 2020. https://doi.org/10.1108/RPJ-08-2019-0224

[9] X. Yang, Y. Li, and B. Li, "Formation mechanisms of lack of fusion and keyhole-induced pore defects in laser powder bed fusion process: A numerical study," *International Journal of Thermal Sciences*, vol. 188, p. 108221, Jun. 2023. https://doi.org/10.1016/j.ijthermalsci.2023.108221

[10] C. Du *et al.*, "Pore defects in Laser Powder Bed Fusion: Formation mechanism, control method, and perspectives," *J Alloys Compd*, vol. 944, p. 169215, May 2023. https://doi.org/10.1016/j.jallcom.2023.169215

[11] M. S. Palm, B. Diepold, S. Neumeier, H. W. Hoeppel, M. Goeken, and M. F. Zaeh, "Detection and effects of lack of fusion defects in Hastelloy X manufactured by laser powder bed fusion," *Mater Des*, vol. 230, p. 111941, Jun. 2023. https://doi.org/10.1016/j.matdes.2023.111941

[12] R. Zhao, A. Shmatok, R. Fischer, and B. C. Prorok, "Investigation of Causal Relationships between Printing Parameters, Pore Properties and Porosity in Laser Powder Bed Fusion," *Metals (Basel)*, vol. 13, no. 2, p. 330, Feb. 2023. https://doi.org/10.3390/met13020330

[13] W. Wang *et al.*, "Processing defect, microstructure evolution and mechanical properties of laser powder bed fusion Al-12Si alloys," *Journal of Materials Research and Technology*, vol. 26, pp. 681–696, Sep. 2023. https://doi.org/10.1016/j.jmrt.2023.07.231

[14] N. Kouraytem *et al.*, "Solidification crack propagation and morphology dependence on processing parameters in AA6061 from ultra-high-speed x-ray visualization," *Addit Manuf*, vol. 42, p. 101959, Jun. 2021. https://doi.org/10.1016/j.addma.2021.101959

[15] R. Yang and Y. He, "Optically and non-optically excited thermography for composites: A review," *Infrared Phys Technol*, vol. 75, pp. 26–50, Mar. 2016. https://doi.org/10.1016/j.infrared.2015.12.026

[16] B. Wiecek, "Review on thermal image processing for passive and active thermography," in *2005 IEEE Engineering in Medicine and Biology 27th Annual Conference*, IEEE, 2005, pp. 686–689. doi: 10.1109/IEMBS.2005.1616506

[17] C. Meola, S. Boccardi, and G. M. Carlomagno, *Infrared Thermography in the Evaluation of Aerospace Composite Materials*. Elsevier, 2015

[18] A. Heifetz, X. Zhang, J. Saniie, and W. Cleary, “Detection of Defects in Additively Manufactured Metallic Materials with Machine Learning of Pulsed Thermography Images,” Argonne, IL (United States), Sep. 2020. doi: 10.2172/1673390

[19] N. Montinaro, D. Cerniglia, and G. Pitarresi, “Defect detection in additively manufactured titanium prosthesis by flying laser scanning thermography,” *Procedia Structural Integrity*, vol. 12, pp. 165–172, 2018. https://doi.org/10.1016/j.prostr.2018.11.098

[20] E. D’Accardi, S. Altenburg, C. Maierhofer, D. Palumbo, and U. Galietti, “Detection of Typical Metal Additive Manufacturing Defects by the Application of Thermographic Techniques,” in *The 15th International Workshop on Advanced Infrared Technology and Applications*, Basel Switzerland: MDPI, Sep. 2019, p. 24. doi: 10.3390/proceedings2019027024

[21] C. G. Kolb *et al.*, “An investigation on the suitability of modern nondestructive testing methods for the inspection of specimens manufactured by laser powder bed fusion,” *SN Appl Sci*, vol. 3, no. 7, p. 713, Jul. 2021. https://doi.org/10.1007/s42452-021-04685-3

[22] M. Galati and S. Defanti, “Additive Manufacturing of Locally Weakened Parts to Obtain a Designed Fracture,” *Metals and Materials International*, vol. 30, no. 2, 2024. https://doi.org/10.1007/s12540-023-01506-7

[23] F. J. Madruga, C. Ibarra-Castanedo, O. M. Conde, J. M. López-Higuera, and X. Maldague, “Infrared thermography processing based on higher-order statistics,” *NDT & E International*, vol. 43, no. 8, pp. 661–666, Nov. 2010. https://doi.org/10.1016/j.ndteint.2010.07.002

[24] R. Usamentiaga, C. Ibarra-Castanedo, and X. Maldague, “More than Fifty Shades of Grey: Quantitative Characterization of Defects and Interpretation Using SNR and CNR,” *J Nondestr Eval*, vol. 37, no. 2, p. 25, Jun. 2018. https://doi.org/10.1007/s10921-018-0479-z

Materials Research Proceedings 57 (2025) 47-55 https://doi.org/10.21741/9781644903735-6

Real-time mental workload assessment with low intrusiveness for assembly processes: Limits and preliminary results

Riccardo GERVASI[1,a *], Matteo DE MARCHI[2,b], Luca MASTROGIACOMO[1,c], Dominik T. MATT[2,d] and Fiorenzo FRANCESCHINI[1,e]

[1]Department of Management and Production Engineering, Politecnico di Torino, Turin, Italy

[2]Faculty of Science and Technology, Free University of Bozen-Bolzano, Bolzano, Italy

[a]riccardo.gervasi@polito.it, [b]Matteo.DeMarchi@unibz.it, [c]luca.mastrogiacomo@polito.it, [d]Dominik.Matt@unibz.it, [e]fiorenzo.franceschini@polito.it

Keywords: Human Aspects, Monitoring, Quality Engineering

Abstract. The real-time assessment of mental workload emerges as crucial in Industry 5.0 for optimizing human performance and wellbeing when interacting with complex systems. However, balancing diagnosticity and sensitivity with low intrusiveness in such assessments remains challenging. According to ISO 10075, mental workload is a broad concept encompassing several observable phenomena (e.g., monotony and mental fatigue), each requiring special attention. This paper explores current techniques for real-time assessment of mental workload in manufacturing and presents preliminary results from a case study in an assembly line. The case study integrates physiological metrics (i.e., heart rate variability, electrodermal activity, and eye-tracking) collected by non-invasive biosensors with task performance metrics to highlight benefits and limitations of a low intrusive real-time assessment setup. The need to use more metrics to reliably identify the operator's psychophysical state is also highlighted.

Introduction

The transition to Industry 5.0 aims to achieve a human-centric approach in industrial systems by encouraging seamless interaction between humans and complex technological systems, such as collaborative robots. Cognitive ergonomics plays a key role in this paradigm, addressing how mental processes affect the interaction between operators and autonomous systems and trying to adapt the work environment to the cognitive abilities and needs of the human operators involved [1]. There are some pioneering works in the literature that present real-time assessment frameworks and setups [2], however they often require the adoption of biosensors that can be invasive and limiting for an operator in a manufacturing context, especially in assembly processes. The objectives of this paper can be summarized by the following research questions: (i) *How intrusive are current methodologies for real-time monitoring of mental workload in a manufacturing context?* (ii) *What limitations may arise by using a nonintrusive setup?*

To address these questions, an overview of current methods related to real-time assessment of mental workload will be presented, highlighting intrusiveness and diagnosticity. A preliminary case study of an assembly process will also be presented, in which noninvasive methodologies for studying the mental processes involved are implemented to explore advantages and limitations of a noninvasive setup.

Cognitive ergonomics and real-time evaluation methods

Cognitive ergonomics deals with the interaction between a human being and the elements of a system by studying the mental processes involved (e.g., perception, attention, memory, reasoning, and emotion), with the ultimate goal of designing systems in line with users' cognitive abilities and mental representation. A topic closely involved in cognitive ergonomics is the evaluation of aspects related to mental workload, which is a domain that analyzes the mental-level effects of

Content from this work may be used under the terms of the Creative Commons Attribution 3.0 license. Any further distribution of this work must maintain attribution to the author(s) and the title of the work, journal citation and DOI. Published under license by Materials Research Forum LLC.

Materials Research Proceedings 57 (2025) 47-55 https://doi.org/10.21741/9781644903735-6

external factors (e.g., environment, task) on human beings [3]. In the context of cognitive ergonomics, it therefore becomes crucial to identify and mitigate the negative effects related to mental workload. The following subsections will describe the negated effects related to mental workload according to ISO 10075 [4], as well as methodologies for evaluating these effects in real time showing potentials, limitations and tradeoffs in terms of invasiveness.

Negative effects related to mental workload

According to ISO 10075 [4], mental workload refers to a domain which encompasses concepts and constructs related to the relationship between external factors (i.e., stressors) and the resulting mental processes for exposure to them, modulated by an individual's internal characteristics (e.g., age, gender, skills, attitudes, health).

The work environment is composed of various stressors that together constitute a certain “load”, called *mental stress*, that mentally affects an individual [4]. Some examples of stressors are task requirements (e.g., task content, duration), physical conditions (e.g., noise, climatic conditions), social and organizational factors (e.g., conflicts, group factors), and societal factors external to the organization (e.g., cultural standards, economic situation).

The exposure to *mental stress* induces mental processes that can lead to facilitating/positive effects or impairing/negative effects. The immediate impact within an individual resulting from *mental stress* is called *mental strain* and it is moderated by the individual’s characteristics and actual conditions [4]. Depending on the duration and frequency of exposure to a given mental stress, short- and long-term effects may occur. Short-term effects (both positive and negative) are characterized by being transient, in that they can be eliminated by a change of task or by rest. Table 1 presents an overview of the short-term effects outlined in ISO 10075. Repeated exposure to certain conditions can lead to effects (both positive and negative) that persist for long periods or are chronic [4]. For example, burnout is a long-term negative effect that can be achieved after repeated exposure over time to conditions that lead to short-term negative effects such as mental satiation. On the other hand, skill development is a positive long-term effect that is achievable with prolonged and repeated exposures to certain conditions. Consequently, to create a healthy work environment from the perspective of cognitive ergonomics, it is first necessary to identify the presence of short-term negative effects in order to mitigate or eliminate their causes.

Real-time evaluation methods

In the context of cognitive ergonomics, there are several techniques for assessing mental workload-related effects which can be divided into mainly three categories: self-reporting methods, performance measures, and psychophysiological measures [5]. The term “real-time” refers to the process of collecting, processing, and interpreting data at short intervals — typically within seconds or minutes — so that a system can detect changes immediately as they happen. Real-time monitoring of mental strain can enable dynamic adaptation, allowing timely corrective interventions (e.g., rest breaks, task changes) or proactive management through support systems such as cobots. In a real-time setting, the intrusiveness (i.e., the extent to which it interferes with the performance of the primary task and the operator comfort) of an assessment method plays a key role in collecting information in a naturalistic manner in a dynamic context (e.g., assembly processes).

Self-reporting methods rely on subjective evaluations, mostly though questionnaires, providing direct insight into an individual’s perceived workload. Example of widely used self-reporting methods are the NASA-TLX and SWAT [5]. Although these methods allow operator perceptions to be collected, these methods are often not suitable for real-time monitoring, as they usually require the operator to interrupt the process.

Performance measures are objective indicators that monitor performance aspects in a given task and are used to indirectly assess mental workload [5]. Examples of commonly used performance measures are task completion time, cycle time, error rate, reaction time, and accuracy. The extremely low intrusiveness of these methods makes them suitable for real-time monitoring, however, performance-only measures are often not very sensitive to changes in mental strain and in identifying affective states.

Table 1. Short-term effects according to ISO 10075 [4].

Type of effect	***Consequence of mental strain***	***Description***
Felicitating/ Positive effect	*Warming-up effect*	Phenomenon characterized by a decrease in the effort needed to perform an activity shortly after it begins, compared to the effort initially required.
	Activation	Internal state that leads to increased mental and physical activity. Varying levels of activation can occur based on the duration and intensity of mental strain, with an optimal range where activation levels yield the highest functional efficiency.
	Learning	Process driven by experiences that results in enduring changes in an individual's behavior, plans and attitudes.
Impairing/ Negative effect	*Mental fatigue*	Internal state characterized by a temporary reduction in mental and physical functional efficiency (e.g., feelings of tiredness and/or increased likelihood of errors). It can be eliminated through rest.
	Monotony	Gradually developing state of reduced activation, typically associated with drowsiness and diminished performance, responsiveness, and adaptability. It commonly arises during repetitive, prolonged, and uniform tasks. Although not immediately, recovery from this state occurs after changes in the task or environment.
	Reduced vigilance	State characterized by decreased activation and diminished detection performance during monitoring or inspection tasks that involve limited variety. Recovery from this state occurs after changes in the task or environment.
	Mental satiation	State of nervously unsettled, strongly emotional rejection of a repetitive task or situation in which the experience is of "marking time" or "not getting anywhere". It is often associated with unchanged or increased activation and adverse emotion or mood (feelings of tiredness and/or decreased performance, and a tendency to withdraw).
	Stress response	State within an individual characterized by increased mental (concerning both cognitive and emotional components) and/or physical activation resulting from the negative interpretation of *mental stress* (e.g., perceived as threat or hindrance to one's goals or values).

Psychophysiological measures are particularly well-suited for real-time evaluation settings and provide objective insights into mental workload by monitoring an individual's psychophysiological signals and responses linked to mental strain [6]. Electroencephalography (EEG) and functional Near Infrared Spectroscopy (fNIRS) monitor brain activity, allowing for accurate detection of activations of different brain areas associated with different functions (e.g., motor area, emotional area, cognitive area) [7,8]. Although EEG provides extensive information about mental processes, it is very sensitive to artifacts commonly found in a manufacturing context [5]. In addition, EEG often requires head-mounted electrodes that can be intrusive to the operator and cause discomfort. Electrocardiography (ECG) and photoplethysmography (PPG) are two techniques for monitoring hearth activity, which is influenced by the autonomic nervous system and, consequently, by an individual's physical and mental process [9]. One heart parameter often observed is heart rate variability (HRV), which represents the variability present in the time intervals between systolic peaks (i.e., NN-intervals). The lower the HRV, the lower the individual's ability to adapt to imposed physical or mental stresses, translating into greater strain. Two

commonly used measures of HRV are the standard deviation of NN-intervals (SDNN) and root mean square of the successive differences of NN-intervals (RMSSD) [5]. Acquiring information about the heart's activity can be noninvasive, as there are specific wearable biosensors in the form of bracelets, smartwatches, and chest bands that do not hinder an operator's activity. Electrodermal activity (EDA) monitors changes in skin conductance due to the sweat gland activity, which is directly influenced by the sympathetic nervous system arousal [9]. Consequently, through EDA, physical and mental activations can be accurately monitored. EDA can be decomposed into two components: skin conductance response (SCR) and skin conductance level (SCL). SCR consists of rapid fluctuations in skin conductance that usually occur in response to emotional or arousing stimuli (i.e., phasic activity). SCL, on the other hand, consists of slower fluctuations that reflect the continuous activity of the sympathetic nervous system (i.e., tonic activity). Facial expressions analysis can also provide useful clues on the operator state and can be performed non-invasively though external cameras [10]. Eye tracking is a useful method for gathering information on visual attention and its related mental strain, relying on the analysis of fixations, saccades, and pupillary dilation [11]. Eye tracking can be performed noninvasively, either through special external cameras or wearable glasses.

Preliminary case study

To investigate the potential and limitations of a noninvasive setup for real-time assessment of cognitive ergonomics, a preliminary case study will be presented and analyzed.

A 100-minute repetitive assembly process of a diaphragm water pump (Figure 1) was recreated at the Mind4Lab laboratories of the Politecnico di Torino. This process was intended to elicit mental states of monotony, mental satiation and mental fatigue in the operator. The assembly process can be decomposed in the following steps:

1) *Assembly of the pump head*. Flange F1 is inserted inside flange F2, and diaphragm D1 is attached to flange F1 with three screws (V2). Next, the component CV is inserted with the diaphragm D1 into the slots provided, and finally the cover (C) is placed on the flange F2, securing it with three screws (V2).
2) *Joining with the engine block*. The rubber support (RF) is attached to the engine block (EB) with the two screws (V1). The previous assembly related to the pump head is taken and fitted to EB, finally securing it with three screws (V3).
3) *Finalization of the pump*. The diaphragm D2 is inserted into the cover housing (C) and then the pressure switch (PS) is fixed with two screws (V4). Assembly is completed by fitting the filter (FIL) and the two adapters (AF1 and AF2).

During the assembly process, the operator wore two noninvasive biosensors: a pair of Tobii Pro Glasses 3 eye-tracking glasses and the Empatica E4 wristband (Figure 2). These biosensors were used to obtain information on fixations, pupil dilation, EDA and HRV. The assembly cycle time of each assembled product was tracked as a performance indicator. The assembly cycle time of each assembled product was also tracked. Unstructured feedback from the operator was collected every 20 minutes by asking what sensations he or she was experiencing. This information was used to verify the onset of the expected mental states in the operator and a match in the observed patterns in the evolution of psychophysiological and performance indicators.

Preliminary results

This section will present, as an example, the results of one participant (25-year-old male) drawn from a group of participants who had no previous experience in assembling the case study product. After explaining the structure of the study, how to assemble the pump and mounted the biosensors on the participant, the 100-minute assembly process began. Table 2 shows the unstructured feedback collected at various points in the process every 20 minutes without interrupting the process. EDA was decomposed using the MATLAB tool Ledalab [12], while eye-tracking

Materials Research Proceedings 57 (2025) 47-55 https://doi.org/10.21741/9781644903735-6

indicators were extracted through the software Tobii Pro Lab. As HRV indicator, RMSSD was obtained from the NN-intervals extracted by the Empatica E4 internal algorithm.

Table 2. Unstructured feedback of the participant collected during the assembly process.

20th minute	***40th minute***	***60th minute***	***80th minute***	***100th minute***	***Overall feedback***
"Fine, all smooth"	"Bored"	"Tired, alienated, bored, slow on some activities, faster on others"	"Somewhat stressed, more distracted, mentally tired, monotonous activity"	"Increasingly stressed"	"Tedious and boring experience, I feel tired and less responsive."

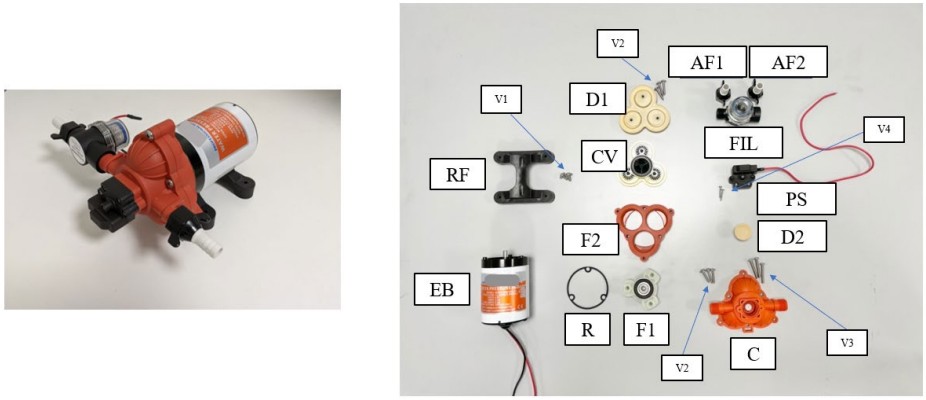


Figure 1. The diaphragm water pump and its components.



Figure 2. The implemented noninvasive biosensors: Tobii Pro Glasses 3 and Empatica E4 wristband.

Figure 3 shows the evolution of the psychophysiological indicators and performance in terms of assembly cycle time. Psychophysiological indicators were calculated every 30 seconds considering a time window of 240 seconds, to ensure sufficient data for each type of signal and reduce noisy fluctuations. It can be observed that:

- By the 20th minute, the SCL and SCR were quite stable with low values, which can be associated with a calm state, in line with the participant's feedback. The number of fixations at the beginning increased and then decreased, which can be associated with an initial activation due to a learning process. This effect can also be seen in pupillary dilation, which starting from high values, a decrease is observed gradually, showing a decrease in mental strain. Regarding HRV, from the RMMSD a slight gradual increase is observed associated

with a gradual relaxation. The effect of warming-up and learning is also visible in performance, with a consistent decrease in assembly cycle time.

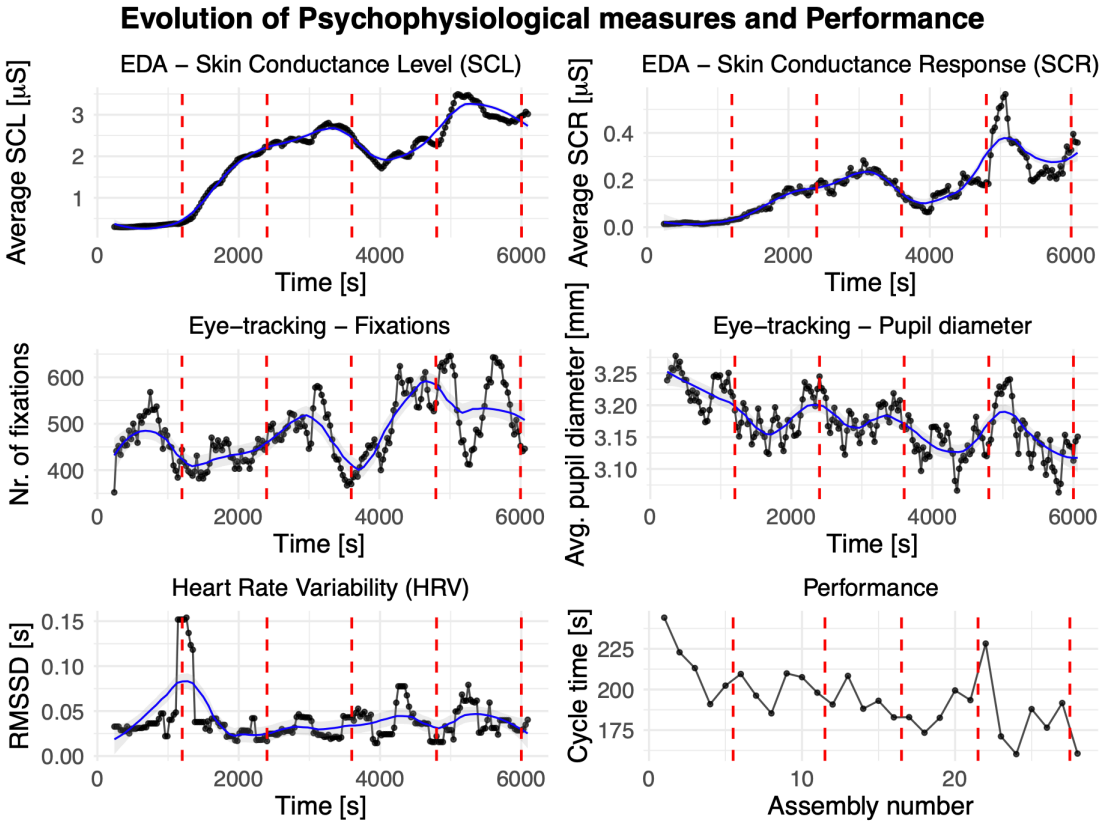


Figure 3. Evolution of psychophysiological indicators and performance for the selected participant. The dashed red lines represent the moments when unstructured feedback was asked to the participant.

- By the 40th minute, perceived boredom seems to be reflected in more unstable signals (i.e., number of fixations and pupil diameter). SCL and SCR increase stably, while RMSSD decreases slightly, suggesting increased activation attributable to physical activity. Assembly cycle times fluctuate slightly but still remain lower at the beginning of the process.
- By the 60th minute, SCL and SCR still increase, indicating increased physiological activation probably due to physical exertion, and then begin to decrease slightly. Pupillary diameter continues to fluctuate, while the number of fixations at first increases and then decreases significantly, indicating a reduction in attention. RMSSD remains fairly stable, while assembly cycle times tend to decrease slightly. The observed patterns are partially matched by feelings of fatigue, alienation and boredom attributable to mental satiation.
- By the 80th minute, the participant feels somewhat stressed, more distracted, mentally tired, symptoms of mental satiation. SCL and SCR grow slightly, presenting fluctuations. As the number of fixations increases, pupillary diameter decreases slightly and has several fluctuations, attributable to more distraction seeking stimuli. RMSSD also exhibits more fluctuations and there is a decrease in performance with an increase in assembly cycle time. These increased fluctuating activations and decreased performance are in line with the mental satiation state.
- By the 100th minute, the participant feels more stressed, indicating mental fatigue. This state is reflected in an increase in SCL and SCR with noticeable fluctuations in the latter.

More fluctuations continue to be evident in the RMSSD. Notable fluctuations are also evident in the number of fixations, while instead the pupillary diameter increases rapidly initially and then slowly decreases. There is also a worsening of performance, especially in the 22nd assembly, where due to an error the assembly cycle time increased and resulted in particularly observable activations in the SCR, pupillary diameter and number of fixations.

Table 3 provides a summary of the observed signal patterns associated with the different mental strain effects present in the exploratory case study. In addition, a comparison of the observed patterns with the expected qualitative patterns based on expert evaluation and literature is reported, showing a fair correspondence [11,13,14]. Only a discrepancy can be observed for the monotony state in SCL and SCR, which were observed to be increasing mainly due to physical activation, but the observation of fluctuations in eye-tracking metrics and performance were helpful in identifying the phenomenon. In addition, it emerges how the use of multiple signals becomes necessary to ensure the reliability of identification of the operator's psychophysical state, since individual signals can also be influenced by other factors.

Table 3. Summary of observed signal patterns associated with the different mental strain effects present in the preliminary case study. Expected patterns based on experts and literature are reported in brackets.

Legend: ↗ Increasing; ↘ Decreasing; → Stationary; ↝ Fluctuating.

Mental strain effect	***EDA***		***Eye-tracking***		***HRV***	***Performance***
	SCL	***SCR***	***Nr. of fixations***	***Avg. pupil diameter***	***RMSSD***	***Cycle time***
Activation	↗ (↗)	↗ (↗)	↗ (↗)	↗ (↗)	↘ (↘)	↘ (↘)
Learning	→ (↘)	→ (↘)	↘ (↘)	↘ (↘)	↗ (↗)	↘ (↘)
Mental fatigue	↝ / ↗ (↝)	↝ / ↗ (↝)	↝ (↝)	↘ (↘)	↝ (↘)	↝ (↝ /↗)
Monotony	↗ (↝ / ↘)	↗ (↝ / ↘)	↝ (↝ / ↘)	↝ (↝ / ↘)	↝ (↗)	↝ (↝ /↗)
Mental satiation	↗ (↗)	↗ (↗)	↗ (↗)	↝ (↝)	↝ (↘)	↝ (↝ /↗)

Discussion and Conclusions

Monitoring cognitive and mental aspects in real-time in dynamic environments, such as manufacturing, requires the use of non-invasive and unobstructive methodologies, so that information about the operator can be obtained in the most naturalistic manner possible without introducing discomfort. Among the various methodologies, psychophysiological signals offer an interesting opportunity to monitor in real-time the mental and emotional processes involved in a work environment. Different signals offer different perspectives on the nature of physiological activations, providing a broad overview of a person's psychophysical state. However, there is often a trade-off between invasiveness and diagnosticity.

The example case study implemented a noninvasive setup consisting of two wearable biosensors in the form of commonly used accessories: a bracelet and a pair of glasses. Preliminary results showed the importance of considering more than one psychophysiological signal to fully understand the operator's psychophysical state. EDA provided information on activations of both a physical and mental nature, while eye-tracking metrics allowed better identification of moments of learning, relaxation, and distraction. The combination of these two methods, together with performance monitoring, allowed different mental states (e.g., learning, activation, monotony,

mental satiation, and mental fatigue) to be distinguished, finding evidence in participants' unstructured feedback. HRV, particularly RMSSD, was not useful in distinguishing the various mental states. However, the main general limitation that emerged is the not immediate understanding of the valence of the operator's affective state. Valence allows one to distinguish between positive (e.g., relaxation or engagement) and negative (e.g., boredom or nervousness) affective states and interpret the origin of psychophysiological activations. In the case study, valence information was inferred by jointly analyzing the context, time spent in the process, performance, and patterns of psychophysiological signals. The results presented should be treated in exploratory terms, as generalization of the observations that emerged will be possible following larger experimental campaigns. However, these initial results help to formulate an initial hypothesis on signal patterns that might be observed in a systematic study. In addition, it should be noted that different subjects may have different initial signal baselines that should be considered when analyzing data across multiple subjects. Future work will focus on comparing the current setup with more comprehensive and invasive setups (e.g., with EEG) to check whether significant differences in information emerge for assessing operator state in an assembly process. In addition, a systematic experimental campaign will be carried out on a large sample of subjects, supported by a quantitative analysis to better explore the consistency of signal patterns.

Acknowledgements
This study was carried out within the “Empathically enhanced robot for the collaboration with HUmans in MANufacturing (E.HU.MAN)” project – funded by the Ministero dell’Università e della Ricerca – within the PRIN 2022 program (D.D.104 02/02/2022). This manuscript reflects only the authors’ views and opinions, and the Ministry cannot be considered responsible for them.

References

[1] A. Ricci, V. Ronca, R. Capotorto, A. Giorgi, A. Vozzi, D. Germano, G. Borghini, G. Di Flumeri, F. Babiloni, P. Aricò, Understanding the Unexplored: A Review on the Gap in Human Factors Characterization for Industry 5.0, Appl. Sci. 15 (2025) 1822. https://doi.org/10.3390/app15041822

[2] M. Lagomarsino, M. Lorenzini, E. De Momi, A. Ajoudani, An Online Framework for Cognitive Load Assessment in Industrial Tasks, Robot. Comput.-Integr. Manuf. 78 (2022) 102380. https://doi.org/10.1016/j.rcim.2022.102380

[3] M. Capponi, R. Gervasi, L. Mastrogiacomo, F. Franceschini, Assembly complexity and physiological response in human-robot collaboration: Insights from a preliminary experimental analysis, Robot. Comput.-Integr. Manuf. 89 (2024) 102789. https://doi.org/10.1016/j.rcim.2024.102789

[4] ISO 10075-1:2017, Ergonomic principles related to mental workload - Part 1: General issues and concepts, terms and definitions, International Organization for Standardization, Geneva, CH, 2017.

[5] D. Tao, H. Tan, H. Wang, X. Zhang, X. Qu, T. Zhang, A Systematic Review of Physiological Measures of Mental Workload, Int. J. Environ. Res. Public. Health 16 (2019) 2716. https://doi.org/10.3390/ijerph16152716

[6] A.K. Raj, M.J. Doyle, J.D. Cameron, Psychophysiology and Performance: Considerations for Human-Centered Design, in: Handb. Hum.-Mach. Interact., CRC Press, 2011.

[7] S. Midha, H.A. Maior, M.L. Wilson, S. Sharples, Measuring Mental Workload Variations in Office Work Tasks using fNIRS, Int. J. Hum.-Comput. Stud. 147 (2021) 102580. https://doi.org/10.1016/j.ijhcs.2020.102580

[8] S. Ma, X. Yan, J. Billington, N. Merat, G. Markkula, Cognitive load during driving: EEG microstate metrics are sensitive to task difficulty and predict safety outcomes, Accid. Anal. Prev. 207 (2024) 107769. https://doi.org/10.1016/j.aap.2024.107769

[9] R.L. Charles, J. Nixon, Measuring mental workload using physiological measures: A systematic review, Appl. Ergon. 74 (2019) 221–232. https://doi.org/10.1016/j.apergo.2018.08.028

[10] S. Luo, C. Zhang, W. Zhu, H. Chen, J. Yuan, Q. Li, T. Wang, C. Jiang, Noncontact perception for assessing pilot mental workload during the approach and landing under various weather conditions, Signal Image Video Process. 19 (2024) 98. https://doi.org/10.1007/s11760-024-03619-x

[11] R. Gervasi, M. Capponi, L. Mastrogiacomo, F. Franceschini, Eye-tracking support for analyzing human factors in human-robot collaboration during repetitive long-duration assembly processes, Prod. Eng. 19 (2025) 47–64. https://doi.org/10.1007/s11740-024-01294-y

[12] Ledalab, (n.d.). http://www.ledalab.de/ (accessed June 23, 2021).

[13] S.D. Kreibig, Autonomic nervous system activity in emotion: A review, Biol. Psychol. 84 (2010) 394–421. https://doi.org/10.1016/j.biopsycho.2010.03.010

[14] S. Delliaux, A. Delaforge, J.-C. Deharo, G. Chaumet, Mental Workload Alters Heart Rate Variability, Lowering Non-linear Dynamics, Front. Physiol. 10 (2019). https://doi.org/10.3389/fphys.2019.00565

Materials Research Proceedings 57 (2025) 56-63 https://doi.org/10.21741/9781644903735-7

Effect of cast extrusion parameters on the surface properties of films made of polyethylene blends with olefinic ionomers

Annalisa GENOVESI[1,a*], Alessandra CAGGIANO[1,b] and Massimiliano BARLETTA[1,c]

[1]Department of Industrial, Electronics, and Mechanical Engineering, University of Roma Tre, Via della Vasca Navale 79, 00146 Rome (RM), Italy

[a]annalisa.genovesi@uniroma3.it, [b]alessandra.caggiano@uniroma3.it, [c]massimiliano.barletta@uniroma3.it

Keywords: Plastic & Composite Material Processes, Extrusion, Polymers

Abstract. In critical applications where long-term toughness and ductility are required in the manufactured products, such as pipes for drinking water distribution, polyethylene is the optimal material choice. Pipes for hot water transportation are usually multilayered and polyurethane foam is used to provide thermal insulation. Polyurethane and polyethylene have a high difference in polarity determining a poor interfacial adhesion. To increase the polarity of the compound, blends of polyethylene and a zinc ionomer were produced via twin screw extrusion. The pellets were then used to fabricate films via cast extrusion. The surface properties of the films were modified by varying the drawing roll speed. As the drawing speed of the film increases, an intensified presence of the polar groups on the film surface was observed via FTIR analysis. The mechanical and thermal properties of the produced films and of the compounds were evaluated to ensure the applicability for extrusion pipe manufacturing.

Introduction

Polyethylene (PE) is currently the material of choice in the natural gas distribution industry and is widely used in critical applications requiring long-term toughness and ductility, such as drinking water distribution, industrial and mining pipelines, and force mains. Among the properties of PE, its smooth and non-stick surface, invulnerability to biological attack and to electrochemical based corrosion processes are the most appealing for these kinds of applications [1].

Different grades of polyethylene resins, such as PE63, PE80 and PE100, are used for plastic pipe production. Among these, PE100 exhibits the best properties and performance, especially in terms of long term creep resistance [2]. Pipes for hot water transportation are usually multilayered and include a polyurethane foam to provide the required thermal insulation. Polyurethane and polyethylene have a strong difference in polarity, since polyurethane is polar whereas polyethylene is non-polar, resulting in poor interfacial adhesion between the two materials [3].

In order to allow the assembly of multilayer pipes, corona discharge treatment is used on polyethylene to increase the surface wettability [4]. The corona discharge treatment increases the polar component of the surface energy and the concentration of hydro-peroxides which, however, are subjected to aging and tend to decrease over time [5].

In recent years, ionomer-based copolymers of ethylene and methacrylic acid have been used as polar compatibilizers for polyolefins, as they increase the matrix polarity [6,7]. Ethylene with monomers containing acid groups neutralized with metal cations are marketed by DuPont under the trademark Surlyn™. Zinc ions (Zn^{2+}) and sodium ions (Na^{+}) are the most common neutralizing cations [8]. Sodium ionomers were successfully used as compatibilizers for Polyethylene Terephthalate (PET)/ Linear Low Density Polyethylene (LLDPE) [9]. The beneficial effect is related to the strong bonding formed at the interface between the polar polymer and the ionomer [10]. When used as polar compatibilizers in High Density Polyethylene (HDPE) and Polyurethane

Content from this work may be used under the terms of the Creative Commons Attribution 3.0 license. Any further distribution of this work must maintain attribution to the author(s) and the title of the work, journal citation and DOI. Published under license by Materials Research Forum LLC.

(PU) blends, Zinc Ionomers are more effective compared to Sodium Ionomers. Papadopoulou and Kalfoglou [11] observed a higher elongation at break and energy to tensile failure in blends compatibilized with Zn ionomers compared to Na ionomers. The best compatibilization effect was observed by first diluting the ionomer in the PE [11]. Ali et al. produced a PE/ionomer blend with the purpose of introducing polar groups on the surface of blown extruded films. The take-up ratio (TUR) adopted during blown extrusion has a deep influence on the surface properties and turns the film from being hydrophobic to hydrophilic [12].

The scope of the present study is to evaluate the possibility of including charges on the surface of a PE100/ionomer cast extruded film by varying the processing parameters. A Zinc ionomer was chosen, as it showed an increased compatibilizing effect when combined with HDPE [11]. Three different blends were produced via extrusion compounding and films were produced via cast extrusion. Cast extrusion allows to process thicker films compared to other technologies (e.g. blown extrusion), thus working with conditions closer to the ones of pipe profile extrusion. During cast extrusion, the draw ratio was progressively increased. The introduction of charges on the surface can improve the compatibility of PE100 with a polyurethane foam in view of allowing the assembly of multilayer pipes without the need of performing a corona treatment.

Materials and methods

Materials. The employed PE100 grade is ELTEX Superstress TUB121N9000 produced by Ineos (Ineos, London, UK). Surlyn 9020, a zinc-neutralized acid acrylate terpolymer, was purchased from Safic Alcan Italia s.p.a. (Safic Alcan Italia s.p.a., Novate Milanese (MI), Italy). ADK Stab 611 is a primary – secondary antioxidant marketed by Adeka Corporation (Adeka Corporation, Tokyo, Japan). Ethylene bis stearamide (EBS), an organic wax, was utilized in order to reduce stickiness and improve processability. The studied blends are presented in Table 1.

Table 1. Composition of the blends

	Eltex	**ElZn10**	**ElZn20**	**ElZn30**
	wt%	wt%	wt%	wt%
ELTEX® SuperstressTM TUB121N9000	100	88.8	78.8	68.8
Surlyn 9020		10	20	30
ADK Stab 611		0.2	0.2	0.2
EBS		1	1	1
tot	100	100	100	100

Compounding and Cast Extrusion. The blends of PE100 and Surlyn 9020 were prepared via co-rotating screw extrusion using a Leistritz ZSE MAXX 27 I Extrusion line (Leistritz, Nuremberg, Germany). The screws have a diameter of 27 mm and a length to diameter ratio (L/D) of 40. The high length allows to obtain a homogeneous mixing. The extrusion system allows to control ten temperature zones independently. The pellets were cut via a strand pelletizer system equipped with a double water tub. The compounding parameters are presented in Table 2. The produced pellets were dried for 3h at 70°C before further processing. The films were produced via cast extrusion using an Eurexma MiniCast 20 extruder (Eurotech Extrusion Machinery srl, Tradate (VA), Italy). The system is equipped with a single screw having a diameter of 20 mm and a length to diameter ratio of 25. The die is 200 mm long and presents two water-cooled calendering rolls with a diameter of 150 mm. It is possible to control four temperature zones of the extruder and three temperature zones of the extrusion die independently. The process parameters are presented in Table 3. For each material, three different film samples were produced by varying the ratio between the drawing roll speed and the calender speed. In detail, samples A were produced by imposing a drawing roll to calender speed ratio of 4/3, samples B with a ratio of 4.5/3 and samples C with a ratio of 5/3. Details about the adopted speeds are presented in Table 3. The bulk samples were produced via

Materials Research Proceedings 57 (2025) 56-63 https://doi.org/10.21741/9781644903735-7

injection molding on a Ripi 60 Injection Molding Unit (Ripi, Bologna, Italy). The screw diameter is 18 mm and the length to diameter ratio is 18. The system allows to control four temperature zones independently. The temperature profile was maintained between 200 and 230°C.

The production process of the blends is presented in Figure 1. The chosen PE100 grade and the ionomer have a similar processing window, therefore it was possible to identify an optimum temperature profile which allowed smooth production without degradation. Lower temperatures led to an unstable process, as the strands tended to break and it was necessary to draw them slowly through the cooling tubs. As the percentage of ionomer of the blend increases, a better flowability was observed at the exit of the die, due to the reduced viscosity of Surlyn 9020 compared to PE100. The production process of the film is presented in Figure 2. Pure PE100 was used to get the process up to speed. An increasing temperature profile was used in order to allow progressive melting and plasticization of the material. The maximum temperature (235°C) was set in the external region of the extrusion head, in order to obtain a uniform flow through the die. For each compound, three different film samples were produced by increasing the speed of the drawing roll from 4.0 m/min to 4.5 m/min and 5.0 m/min, as indicated in Table 3. At higher drawing speed, some defects related to the elastic return of the polymer appeared on the surface of the film (Figure 2b and Figure 2c).

Table 2. Compounding parameters

Extrusion temperature profile									
Temp.1	*Temp.2*	*Temp.3*	*Temp.4*	*Temp.5*	*Temp.6*	*Temp.7*	*Temp.8*	*Temp.9*	*Temp.10*
190 °C	200 °C	205 °C	210 °C	210 °C	220 °C	220 °C	215 °C	210 °C	200 °C
Screw speed							280 rpm		

Table 3. Minicast processing parameters

Cast Extrusion Temperature profile						
Temp.1	*Temp.2*	*Temp.3*	*Temp.4*	*Head right*	*Head center*	*Head left*
220 °C	225 °C	235 °C	230 °C	235 °C	230 °C	235 °C
Extruder	**Calender 1**	**Calender 2**	**Drawing**	*Sample A*	*Sample B*	*Sample C*
95 rpm	3.0 m/min	3.0 m/min		4.0 m/min	4.5 m/min	5.0 m/min

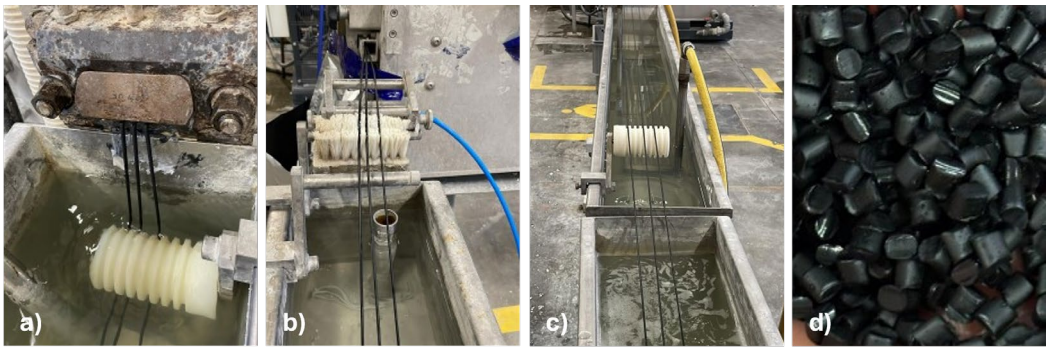


Figure 1. *Twin screw extrusion of the compounds: a) Strands at exit of the extrusion die; b) Strands entering the rotary pelletizer; c) Cooling tubs; d) Produced pellets.*

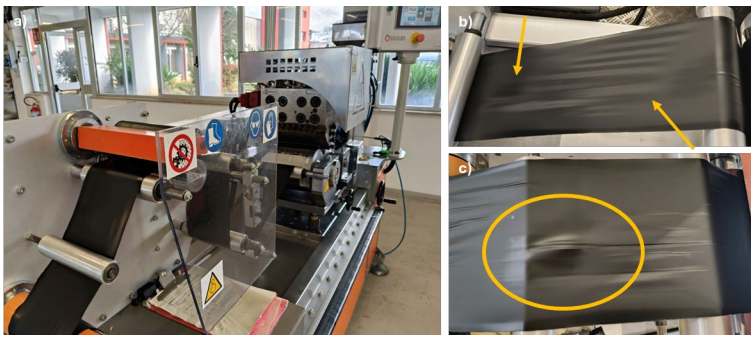


Figure 2. *Production of the films: a) lab-scale cast extruder; b) Defects related to the elastic recovery of the film after the calender; c) Defects related to the elastic recovery of the film before winding.*

Characterization

Mechanical characterization. The mechanical properties of cast films were evaluated by means of a Shimadzu AGS-X tester (Shimadzu Corporation, Tokyo, Japan) according to ISO 527. The samples were cut in Machine Direction and the initial distance between the grips was set at 50 mm. The testing speed was set at 200 mm/min.

Fourier Transform Infrared (FTIR) Spectroscopy. Fourier Transform Infrared Spectroscopy (FTIR) was used for surface analysis of the produced samples [13]. The infrared absorption spectra were obtained using a Jasco FT/IR-6600 FT-IR Spectrometer (Jasco Europe s.r.l., Cremella (LC), Italy) in attenuated total reflectance mode (ATR). The analysis was conducted on the cast-extruded films of the produced compound. The spectra were acquired between 600 and 4000 cm^{-1} with a resolution of 0.4 cm^{-1} and 128 scanning times. The FTIR spectrum of the ionomer was obtained by scanning a pellet. For each compound containing ionomer, the ratios between the intensity of peaks at 1585 cm^{-1}, 1698 cm^{-1} and 1735 cm^{-1} and the peak at 718 cm^{-1} were evaluated.

Rheological Characterization. The rheological properties were evaluated by measuring the Melt Flow Rate (MFR), by means of a capillary rheometer and a torque rheometer. The MFR was measured using a AMSE MFI-1221 XNR-400 B apparatus (AMSE S.r.l., Turin, Italy) according to ISO 1133 [14]. The MFR was measured at 200°C, 220°C and 240°C under a load of 2.16 kg.

Results and discussion

Mechanical properties. The stress-strain curves of the injection-molded samples are presented in Figure 3a and the results are reported in Table 4. The set cross-head speed was 200 mm/min. PE100 (i.e. Eltex) presents a high rigidity, with an elastic modulus of over 420 MPa, an elongation at break lower than 30% and high yielding stress and maximum stress. As the percentage of the ionomer increases, a more ductile behavior can be observed. The elongation at break increases, going from around 30% of ElZn10 to over 200% of ElZn30 whereas the elastic modulus, the maximum stress and the yielding stress decrease. One of the most important properties of PE100 is its resistance to rapid crack propagation (RCP), which can be evaluated by means of the yielding stress obtained in tensile tests at high cross-head speed [15]. The introduction of 10% of Surlyn leads to an increase in the mean value of yielding stress, suggesting an improvement of RCP resistance. On the other hand, a further increase worsens the RCP resistance of the compounds.

The stress-strain curves obtained from the characterization of the cast extruded films are presented in Figure 3 and the results are reported in Table 4. All the films exhibited a very ductile behavior and a yielding strain below 10%. The films displayed higher yield strength compared to the one measured in dog bone specimens. A higher yielding strength is related to a higher crystallinity [16], which can be related to the increasing drawing during cast extrusion. As the drawing ratio increases, the properties of ElZn10 undergo a sharp worsening compared to the ones of pure PE100, particularly in terms of elongation at break and maximum stress. In ElZn10B and

Materials Research Proceedings 57 (2025) 56-63 https://doi.org/10.21741/9781644903735-7

ElZn10C, the extent of the decrease of stress after yield is less severe, with larger yielding zones. The sharp drop of the stress after yielding is often observed in polyolefins with a row-nucleating microstructure [17] and can be achieved through a stretching process of the melt during cast extrusion [18]. A definite trend cannot be observed for all the films because of the elastic recovery of polyethylene during cast extrusion.

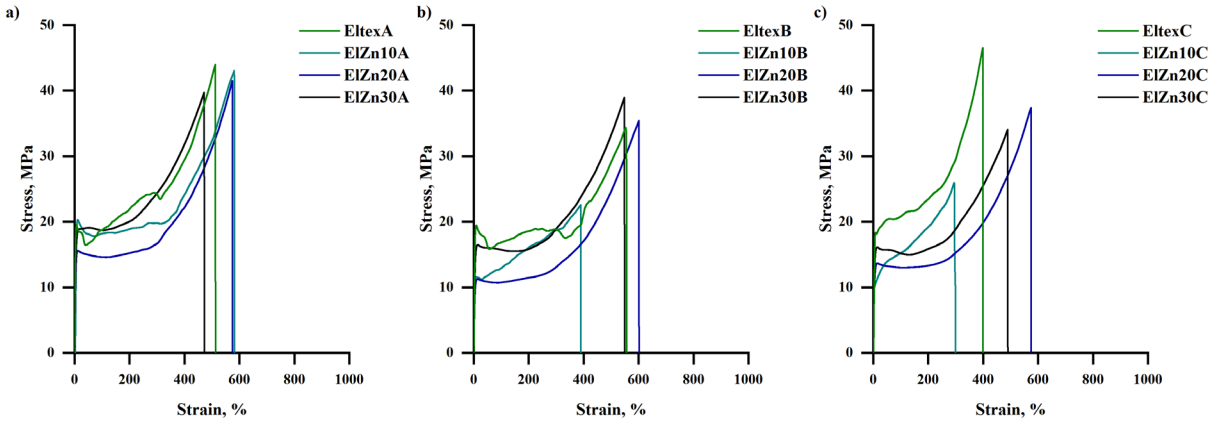


Figure 3. *Tensile test results: a) Samples A; b) Samples B; c) Samples C.*

Table 4. Results of the tensile test of the cast films tested in Machine Direction (MD)

	Max Stres [MPa]	Max Strain [%]	Elastic Modulus [MPa]	Yielding Stress [MPa]
EltexA	36.3 ± 5.4	534 ± 23	575 ± 40	17.3 ± 2.2
EltexB	33.0 ± 1.7	572 ± 13	581 ± 60	16.8 ± 1.4
EltexC	44.6 ± 4.8	429 ± 84	644 ± 236	21.9 ± 7.6
ElZn10A	35.9 ± 4.9	523 ± 41	557 ± 37	17.9 ± 1.3
ElZn10B	20.4 ± 4.5	402 ± 34	326 ± 111	9.6 ± 1.9
ElZn10C	27.3 ± 5.7	297 ± 3	419 ± 34	20.1 ± 7.4
ElZn20A	42.0 ± 3.7	520 ± 47	380 ± 20	14.7 ± 0.6
ElZn20B	31.4 ± 2.3	556 ± 25	284 ± 37	10.3 ± 0.3
ElZn20C	38.5 ± 2.2	588 ± 30	296 ± 15	12.0 ± 0.4
ElZn30A	39.9 ± 2.1	521 ± 61	392 ± 26	15.0 ± 1.0
ElZn30B	37.8 ± 3.8	502 ± 106	356 ± 11	14.3 ± 0.6
ElZn30C	33.2 ± 3.0	497 ± 71	318 ± 46	12.6 ± 1.6

FTIR Spectroscopy. The Fourier Transform Infrared Analysis was performed on the produced cast film in order to analyze the composition of the surface [13]. The FTIR spectra of the defined samples are provided in Figure 4a. All the spectra present two absorption peaks at 2914 cm^{-1} and 2847 cm^{-1} which can be attributed to C-H asymmetric and symmetric stretching vibration of CH_2 respectively. The spectra present a small peak at 1462 cm^{-1} which can be related to the C-H deformation vibrations of the $–(CH_2)_n-$ segments. The peak at 718 cm^{-1} is related to the C-C rocking vibrations of the $–(CH_2)_n-$ segments [19] and can be used as reference signal in characterizing polyethylene [20].

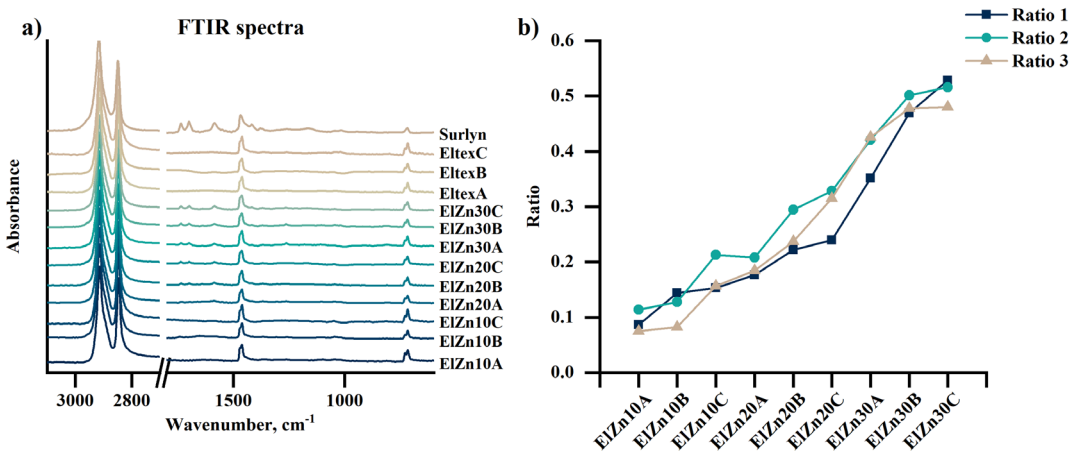


Figure 4. *FTIR Analysis; a) Stacked spectra; b) Ratio of the intensity of the peaks related to the presence of ionomer.*

The peaks at 1585 cm^{-1}, 1698 cm^{-1} and 1735 cm^{-1} can be attributed to the presence of the Zinc Ionomer and to the formation of different types of structures associated with the carboxylic acid groups and their salts [21]. These bands are particularly intense in the spectrum of Surlyn and cannot be identified in the spectra of EltexA, EltexB and EltexC. In order to evaluate the presence of the ions on the film surface in relation to the draw ratio adopted during the production of the film, the ratios between the intensity of the signals at 1585 cm^{-1}, 1698 cm^{-1} and 1735 cm^{-1} and the intensity of the 718 cm^{-1} peak were evaluated. These ratios are indicated as “Ratio 1”, “Ratio 2” and “Ratio 3”, respectively, and they are presented in Figure 4b. It can be observed that for each compound, all the ratios increase with the increasing drawing adopted during cast extrusion, suggesting that the ionomer charges appear on the surface of the film. The effect is more evident as the percentage of ionomer in the blend increases. The result appears of extreme interest in a potential industrialization of the process, as it is possible to limit the presence of the expensive ionomer in the blend and still obtain good performances just by increasing the drawing ratio.

Table 5. Melt Flow Rate (MFR) values

MFR (g / 10 min)				
	Eltex	**ElZn10**	**ElZn20**	**ElZn30**
200°C - 2.160 kg	< 0.01	< 0.01	0.68 ± 0.02	1.16 ± 0.02
220°C - 2.160 kg	< 0.01	0.71 ± 0.06	0.85 ± 0.03	1.95 ± 0.04
240°C - 2.160 kg	< 0.01	1.08 ± 0.07	1.41 ± 0.04	2.87 ± 0.12

Rheological characterization. PE100 grades possess high molecular weight, as confirmed by the low Melt Flow Rate (MFR) values, which are presented in Table 5 [22]. The high viscosity also guarantees excellent tensile and melt strength, abrasion resistance and stiffness [1]. As reported in the technical data sheet, Surlyn 9020 possesses a higher MFR compared to the selected PE100 grade, therefore its introduction in the blends causes a decrease of the melt viscosity. The same trend was observed by Hashemi Motlagh et al. when LLDPE/HDPE masterbatches were introduced in a PE100 compounds [22]. Under the selected testing conditions, Eltex boasts an extremely low viscosity which is scarcely altered by the temperature increase. The MFR of the compounds containing ionomer increases with both the increasing percentage of Surlyn 9020 and with the increasing testing temperature. In general, for plastic pipe extrusion a MFR below 2 g/10 min at the processing temperature is required [23], therefore all the compounds are suitable for plastic pipe production.

Conclusions

The possibility of tailoring the surface properties of a PE100 grade – ionomer blend by properly varying the processing parameters to improve the multilayer pipe production process was assessed.

To ease the assembly of the PE100 layers with a polyurethane foam insulating layer, compounds of PE100 and a zinc olefinic ionomer (Surlyn 9020) were produced via twin screw extrusion. Different draw ratios were adopted during the production of cast films to assess the effect of processing parameters on the surface properties. From the experimental analysis and the characterization tests, the following results were obtained:

- The FTIR analysis confirmed that by increasing the draw ratio it is possible to increase the presence of the ions on the film surface, as the peak ratios increased by ~ 400%.
- The introduction of Surlyn 9020 does not significantly alter the ductility of the cast extruded films but leads to a decrease in the elastic modulus by ~ 40%.
- The experimental tests showed that the mechanical properties and the rheological properties of the compounds are altered by the introduction of the ionomer. In particular, the introduction of the ionomer leads to a decrease of the viscosity. However, considering all the above mentioned properties, the requirements for pipe production are met when Surlyn 9020 is kept below 20%wt, so that the MFR < 2 g/10 min.

References

[1] Plastic Pipe Institute, Irving. The Plastic Pipe Institute: Handbook of polyethylene pipe. 2008.

[2] Pircheraghi G, Sarafpour A, Rashedi R, Afzali K, Adibfar M. Correlation between rheological and mechanical properties of black PE100 compounds – Effect of carbon black masterbatch. Express Polymer Letters 2017;11:622–34. https://doi.org/10.3144/expresspolymlett.2017.60

[3] Yuan H, Hu P. Study of a compatibilized ultra-high-molecular-weight polyethylene and polyurethane blend. Journal of Applied Polymer Science 2001;81:3290–5. https://doi.org/10.1002/app.1785

[4] Lee JH, Kim HG, Khang GS, Lee HB, Jhon MS. Characterization of wettability gradient surfaces prepared by corona discharge treatment. Journal of Colloid and Interface Science 1992;151:563–70. https://doi.org/10.1016/0021-9797(92)90504-F

[5] Novák I, Pollák V, Chodák I. Study of Surface Properties of Polyolefins Modified by Corona Discharge Plasma. Plasma Processes and Polymers 2006;3:355–64. https://doi.org/10.1002/ppap.200500163

[6] Santamaría P, Eguiazábal JI, Nazábal J. Structure and properties of polyethylene ionomer based nanocomposites. Journal of Applied Polymer Science 2010;116:2374–83. https://doi.org/10.1002/app.31771

[7] Bragaglia M, McNally T, Lamastra FR, Cherubini V, Nanni F. Compatibilization of an immiscible blend of EPDM and POM with an Ionomer. Journal of Applied Polymer Science 2021;138:50423. https://doi.org/10.1002/app.50423

[8] Sánchez-Valdes S, López-Quintanilla ML, Ramírez-Vargas E, Medellín-Rodríguez FJ, Gutierrez-Rodriguez JM. Effect of Ionomeric Compatibilizer on Clay Dispersion in Polyethylene/Clay Nanocomposites. Macromolecular Materials and Engineering 2006;291:128–36. https://doi.org/10.1002/mame.200500330

[9] Kalfoglou NK, Skafidas DS, Sotiropoulou DD. Compatibilization of blends of poly(ethylene terephthalate) and linear low density polyethylene with the ionomer of poly(ethylene-*co*-methacrylic acid). Polymer 1994;35:3624–30. https://doi.org/10.1016/0032-3861(94)90538-X

[10] Jia T, Wang R, Zhang M, Ren C, Yang Y, Wang J, et al. A Short Review on Polyethylene-based Ionomers: Synthesis, Structure, and Applications. Chem Bio Eng 2025;2:156–70. https://doi.org/10.1021/cbe.4c00138

[11] Papadopoulou CP, Kalfoglou NK. Polyurethane/HDPE blends: 2. Compatibilization with an olefinic ionomer. Polymer 1999;40:905–11. https://doi.org/10.1016/S0032-3861(98)00323-1

[12] Ali S, Ji Y, Zhang Q, Zhao H, Chen W, Wang D, et al. Preparation of Polyethylene and Ethylene/Methacrylic Acid Copolymer Blend Films with Tunable Surface Properties through Manipulating Processing Parameters during Film Blowing. Polymers 2019;11:1565. https://doi.org/10.3390/polym11101565

[13] Planinšek O, Planinšek D, Zega A, Breznik M, Srčič S. Surface analysis of powder binary mixtures with ATR FTIR spectroscopy. International Journal of Pharmaceutics 2006;319:13–9. https://doi.org/10.1016/j.ijpharm.2006.03.048

[14] ISO 1133-1:2011(en), Plastics — Determination of the melt mass-flow rate (MFR) and melt volume-flow rate (MVR) of thermoplastics — Part 1: Standard method n.d. https://www.iso.org/obp/ui/#iso:std:iso:1133:-1:ed-1:v1:en (accessed February 14, 2025).

[15] Wu T, Yu L, Cao Y, Yang F, Xiang M. Effect of molecular weight distribution on rheological, crystallization and mechanical properties of polyethylene-100 pipe resins. J Polym Res 2013;20:271. https://doi.org/10.1007/s10965-013-0271-9

[16] Humbert S, Lame O, Vigier G. Polyethylene yielding behaviour: What is behind the correlation between yield stress and crystallinity? Polymer 2009;50:3755–61. https://doi.org/10.1016/j.polymer.2009.05.017

[17] Gururajan G, Froude V, Riutta S, Thomas A, Gao I, Samuels SL, et al. Effect of poly(ethylene methyl acrylate) copolymer on thermal, morphological, and mechanical properties of polypropylene copolymer blown films. Journal of Applied Polymer Science 2008;107:2500–8. https://doi.org/10.1002/app.27275

[18] Xu RJ, Chen XD, Cai Q, Chen CB, Lin YF, Lei CH, et al. In situ study of the annealing process of a polyethylene cast film with a row-nucleated crystalline structure by SAXS. RSC Adv 2015;5:27722–34. https://doi.org/10.1039/C5RA00659G

[19] De Geyter N, Morent R, Leys C. Surface characterization of plasma-modified polyethylene by contact angle experiments and ATR-FTIR spectroscopy. Surface and Interface Analysis 2008;40:608–11. https://doi.org/10.1002/sia.2611

[20] Jahani Y, Valavi A, Ziaee F. Reactive melt modification of polyethylene by ethyl acrylate/acrylic acid copolymers: rheology, morphology and thermal behavior. Iran Polym J 2015;24:449–58. https://doi.org/10.1007/s13726-015-0336-1

[21] Painter PC, Brozoski BA, Coleman MM. FTIR studies of calcium and sodium ionomers derived from an ethylene–methacrylic acid copolymer. Journal of Polymer Science: Polymer Physics Edition 1982;20:1069–80. https://doi.org/10.1002/pol.1982.180200614

[22] Hashemi Motlagh G, Ebrahimi F, Azizi M, Elhamnia M. Effects of HDPE and LLDPE as masterbatch base on the properties of PE100. J Polym Res 2024;31:202. https://doi.org/10.1007/s10965-024-04051-y

[23] Qenos | Polyethylene | Technical Guides n.d. https://qenos.com/internet/home.nsf/web/PolyethyleneTechGuides (accessed February 6, 2025).

Materials Research Proceedings 57 (2025) 64-71 https://doi.org/10.21741/9781644903735-8

Impact of surface determination techniques on dimensional and geometrical metrology using X-ray computed tomography

Federico PIRILLO[1,a *], Huan SHAO[1,b], Stefano PETRÒ[1,c] and Giovanni MORONI[1,d]

[1]Department of Mechanical Engineering, Politecnico di Milano, Milano, Italy

[a]federico.pirillo@polimi.it, [b]huan.shao@polimi.it, [c]stefano.petro@polimi.it, [d]giovanni.moroni@polimi.it

Keywords: Radiography and Tomography, Image Processing, Coordinate Metrology

Abstract. X-ray Computed Tomography enables non-destructive dimensional and geometrical measurements of both external and internal features, including those that are difficult or impossible to access with contact probes or optical systems. However, the accuracy of XCT-based measurements is influenced by several factors, one of which is surface determination, which defines the surface points of the object within the tomographic data. This work aims to investigate the impact of different surface determination techniques on the evaluation of dimensional and geometrical measurands, with the goal of understanding their influence on measurement results and contributing to improved traceability in XCT-based metrology.

Introduction

X-ray Computed Tomography (XCT), unlike traditional tactile and optical systems, provides a full volumetric representation, but its accuracy depends on several factors, including scan conditions, reconstruction algorithms, and surface determination techniques (SDTs) [1].

Surface determination is a critical step in XCT metrology, as it defines the object's boundaries and directly affects measurement precision. It typically involves segmentation, where material and background are classified based on grayscale values, followed by surface extraction, which refines boundary points to create a detailed point cloud. Different SDTs can influence the accuracy of dimensional and geometric measurements, yet their impact has not been fully explored.

Recent studies have explored the use of machine learning techniques and neural networks for segmentation in XCT [2], typically for defect detection. However, to simplify the analysis or due to processing and training limitations, many learning-based methods are still applied in 2D or 2.5D, analysing individual slices or local sections of the volume. This dimensional reduction can lead to a loss of spatial information that a full 3D analysis would be better able to capture.

This study compares three SDTs from the literature with a widely used commercial method from Volume Graphics Studio (VGS) [3]. Their performance is evaluated by analysing diameter and cylindricity errors, using Coordinate Measuring Machine (CMM) data as a reference. The goal is to better understand how SDTs affect XCT measurements and contribute to improving accuracy and consistency in industrial applications such as aerospace, automotive, and additive manufacturing.

Methods

Four SDT methods have been considered in this work, which have been summarized in Table 1.

Content from this work may be used under the terms of the Creative Commons Attribution 3.0 license. Any further distribution of this work must maintain attribution to the author(s) and the title of the work, journal citation and DOI. Published under license by Materials Research Forum LLC.

Materials Research Proceedings 57 (2025) 64-71 https://doi.org/10.21741/9781644903735-8

Table 1: List of methods used presented with the segmentation and the subsequent subvoxeling applied

N.	*Name*	*Segmentation*	*Surface extraction*
1	Canny_Tay	Canny	Taylor expansion
2	Otsu_mc	Otsu	Marching cubes
3	MCW_gc	Marker-controlled watershed	Gravity center
4	VGS	ISO50	Steinbeiss

"Canny_Tay" [4] is an SDT method that applies the Canny edge detection algorithm for segmentation, followed by a subvoxeling step using Taylor series expansion. The Canny algorithm [5] first identifies boundary voxels, which will be used as a reference points during the following surface extraction step. For each point, a third order Taylor expansion is applied to approximate the gray value function, allowing the calculation of the displacement needed to refine the surface position along the gradient direction.

"Otsu_mc" is based on the Otsu [6] segmentation algorithm, a global thresholding technique. This method outputs a threshold value that represents the gray level estimating the surface position, making it particularly suitable to be combined with the Marching Cubes [7] surface extraction approach. This combination enables the definition of surface points at the isovalue determined by Otsu's threshold. One of its main advantages is that it does not require any parameter tuning.

"MCW_gc" is an SDT introduced by Yang et al. [8, 9]. It primarily relies on Marker Controlled Watershed (MCW) for segmentation, while the surface refinement follows a subvoxeling approach proposed by Yagüe-Fabra et al. [10]. The goal of this method is to minimize measurement errors caused by manually defined parameters, ensuring a more automated process.

"VGS" refers to the SDTs implemented in the commercial software VGStudioMax (version 3.4.2). When inspecting single-material objects, this method employs a similar concept of Steinbeiss algorithm [11] and requires defining different parameters. In this study, we used the "Advanced (classic)" approach, enabling the "Iterative surface determination" option and setting the "Search distance" parameter to 8 voxels. The selection of these parameters was guided by a preliminary analysis of the possible combinations.

Validation

For validation we used the Zeiss Cube, a machined aluminium part provided by Zeiss to compare different coordinate measuring systems. This cube features several internal and external geometries. In this work, we focused on three features: three internal cylindrical holes of different diameters and depths. A visual representation of the location of these three features is given in Fig. 1. Each hole was evaluated based on its diameter (as a size feature) and cylindricity (as a form feature). These values were calibrated using a ZEISS Prismo VAST HTG coordinate measuring machine and shown in Table 2. All measurements were performed at a temperature of 20 ±0.5 °C and the thermal expansion was compensated.

Materials Research Proceedings 57 (2025) 64-71 https://doi.org/10.21741/9781644903735-8

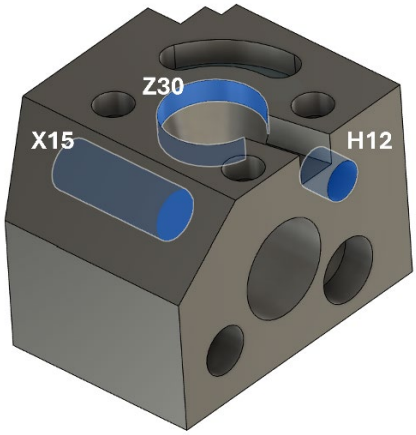


Figure 1: Zeiss Cube with the three measurands considered for the analysis

Table 2: CMM Calibrated Values

Geometric Feature	Nominal Value [mm]	Calibrated Value [mm]	Extended Uncertainty [µm]	Coverage Factor
Diameter Z 30	30	29.9539	0.4	2
Diameter X 15	15	14.9981	0.4	2
Diameter H 12	12	11.975	2	2
Cylindricity Z 30	0	0.0079	0.4	2
Cylindricity X 15	0	0.0136	0.5	2
Cylindricity H 12	0	0.0051	0.3	2

To assess experimental variability, three XCT scans were performed using a Phoenix V|tome|x M300 scanner (Waygate Technologies) under identical conditions. The scanner was operated at 250 kV and 210 µA, corresponding to an effective power of 52.5 kW. A 1 mm thick copper filter was employed. Furthermore, the sample was oriented approximately 45° relative to the scanner's rotation axis. Each scan included 2016 projections, with four images averaged per projection angle at an exposure time of 100 ms. The first image was discarded, and the remaining three were averaged to generate the final projection. As a result of the setup of the part and the positioning of the rotating table, a voxel size equal to 64 µm was achieved.

The image reconstruction process was handled by the proprietary Phoenix software, which includes image filtering, geometric correction, and beam hardening correction. After reconstruction, the voxel data was aligned with a nominal model to facilitate partitioning the final point cloud. Specifically, for the considered cylindrical features, surface points were extracted keeping a 1 mm safety distance from the bases of each cylinder.

About geometric fitting, diameter measurements were determined using the least squares method, while peak-to-valley cylindricity deviation was estimated applying the Chebyshev (min-max) fitting approach, as indicated in ISO 1101 standard [12].

To assess SDT performance, we compared XCT-based measurements with calibrated values from the CMM. The measurement error was defined as the difference between these two values. An error closer to zero indicated better accuracy.

Results

We applied Analysis of Variance (ANOVA) to determine whether the factors had statistically significant effects and the results for diameter and cylindricity errors are shown in Table 3 and Table 5, respectively. To carry out the analysis, we took into account the factors related to Measurand, Method, and their interaction. Preliminarily, a qualitative analysis has been performed

Materials Research Proceedings 57 (2025) 64-71 https://doi.org/10.21741/9781644903735-8

on the results and presented in Fig. 2 and Fig. 4, which display the main effects plots of diameter and cylindricity errors relative to the calibrated values. Additionally, interaction plots in Fig. 3 and Fig. 5 further illustrate the relationship between the factors. Since these plots show how much the average measurement error deviates from the calibrated value, values closer to zero (either positive or negative) indicate XCT measurements are similar to the reference measurements of the CMM.

Starting from the diameter measurement error, the main effects plot suggests that all methods produced comparable results, while the specific measurand analysed had a slightly greater impact. Particularly for what concerned the Z30 hole, which displayed a seemingly relevant difference in the measurement error compared to the other two features. There could be different reasons for this behaviour. It could be attributed to the different orientation of this hole compared to the other two and its small height.

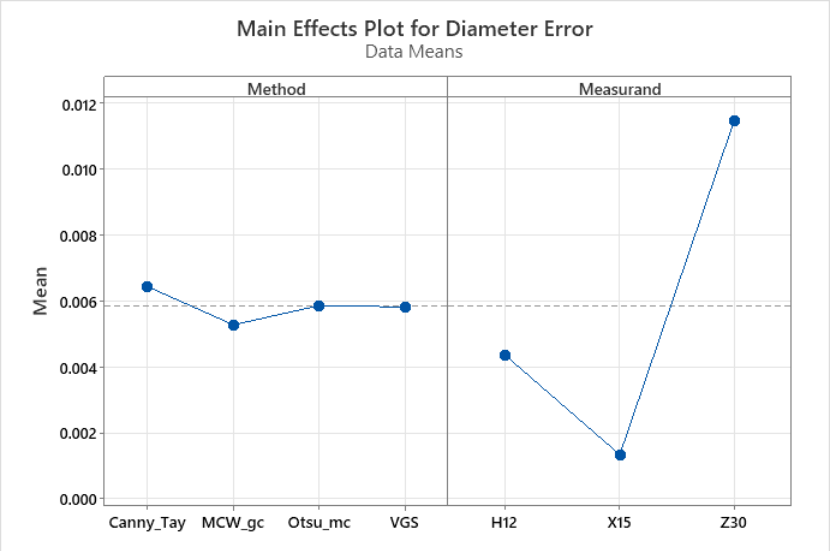


Figure 2: Main Effect Plot for Diameter Error [mm]

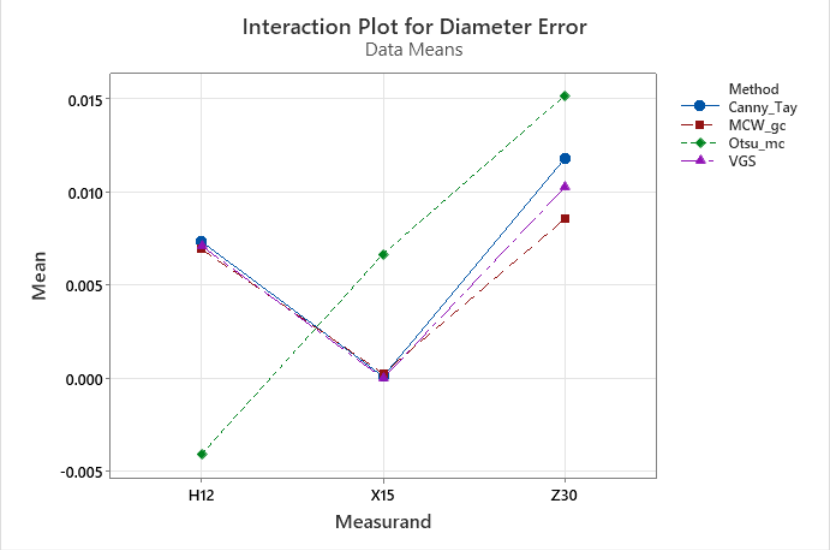


Figure 3: Interaction Plot for Diameter Error [mm]

Materials Research Proceedings 57 (2025) 64-71 https://doi.org/10.21741/9781644903735-8

Table 3: Analysis of Variance for the Diameter Error

Source	DF	Adj SS	Adj MS	F-Value	P-Value
Method	3	0.000006	0.000002	0.71	0.558
Measurand	2	0.000584	0.000292	100.29	0.000
Method*Measurand	6	0.000417	0.000070	23.91	0.000
Error	23	0.000067	0.000003		
Total	34	0.001125			

The fitted model for the ANOVA achieved an adjusted R-squared of 91.2%, which is acceptable. The assumptions of normality and equal variance have been verified.

ANOVA also indicated that the Method factor was not significant. As a confirmation, Post-ANOVA has been performed through a Tukey test (Table 4), to statistically compare the SDTs. As ANOVA had already suggested, the test found no significant differences between the methods, grouping them together. The diameter measurement errors remained close to zero, with deviations between 5.3 and 6.4 μm. This consistency is likely due to the high number of sampled points used in the least squares fitting process.

The Measurand factor is significant, and more interestingly, the interaction between Measurand and Method is also significant. This result is further illustrated in the interaction plot. From the plot, it can be observed that for the measurand Z30, the behaviour is consistent across the four methods. However, for the measurands H12 and X15, Otsu_mc shows an anomalous behaviour, where the diameter has been more underestimated for H12 and more overestimated for X15 compared to the other three methods.

Table 4: Tukey comparison of the methods with 95% Confidence Interval for Diameter Error

Method	N	Mean [mm]	Grouping
Canny_Tay	9	0.0064283	A
Otsu_mc	8	0.0059441	A
VGS	9	0.0058091	A
MCW_gc	9	0.0052656	A

For cylindricity errors, the results showed greater variation among methods compared to diameter measurements. As shown in the corresponding main effect plot (Figure 4), the choice of SDT had a clear impact on the result, with "Canny_Tay" performing better than the others. Also the measurands had a great impact on the final result, particularly in relation to the X15 hole.

The fitted model for the ANOVA achieved an adjusted R-squared of 95.92% and the assumptions of normality and equal variance have been verified. The analysis quantitatively confirmed the preliminary analysis discussed earlier. The Method factor was found to be significant, requiring a post-ANOVA analysis to compare the performance of different methods.

The Tukey test (Table 6) identified two distinct groups. Group B included only the "Canny_Tay" method, which had an average cylindricity error of 56.5 μm. Group A included the other three methods, with errors ranging from 97.8 to 112.1 μm. Within the limits of this analysis, 'Canny_Tay' showed higher accuracy for this type of form measurement compared to the other tested methods.

In this case as well, both the Measurand factor and the interaction between Method and Measurand are found to be significant. The interaction plot reveals an interaction due to two slightly different behaviours: one shared by Otsu_mc and VGS, and the other shared by Canny_Tay and MCW_gc.

Materials Research Proceedings 57 (2025) 64-71 https://doi.org/10.21741/9781644903735-8

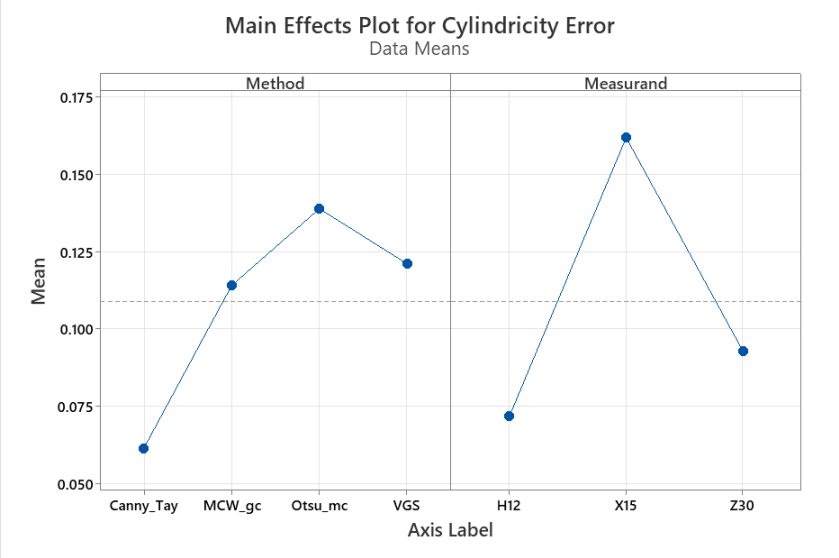


Figure 4: Main Effect Plot for Cylindricity Error [mm]

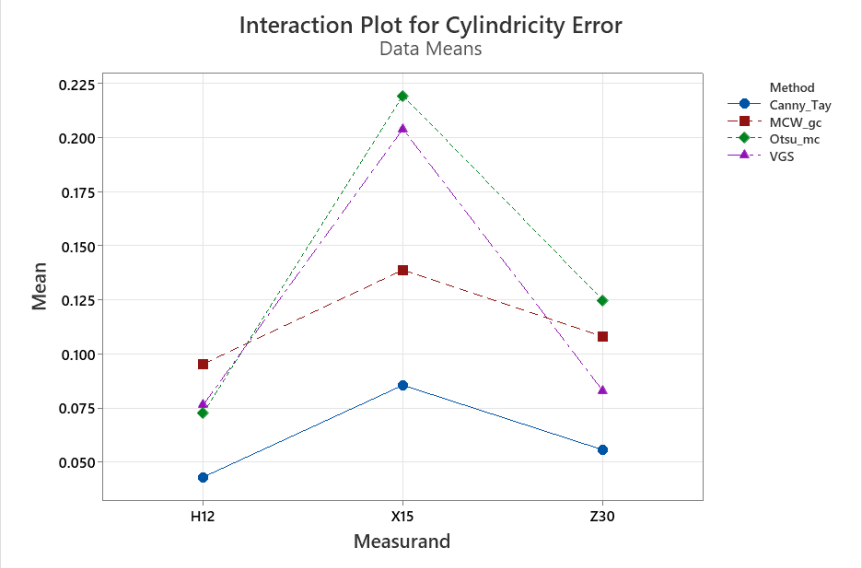


Figure 5: Interaction Plot for Cylindricity Error [mm]

Table 5: Analysis of Variance for the Cylindricity Error

Source	DF	Adj SS	Adj MS	F-Value	P-Value
Method	3	474.81	158.271	142.77	0.000
Measurand	2	378.76	189.380	170.83	0.000
Method*Measurand	6	70.48	11.746	10.60	0.000
Error	24	26.61	1.109		
Total	35	950.66			

Table 6: Tukey comparison of the methods with 95% Confidence Interval for Cylindricity Error

Method	N	Mean [mm]	Grouping	
Otsu_mc	9	0.112	A	
MCW_gc	9	0.111	A	
VGS	9	0.098	A	
Canny_Tay	9	0.057		B

Conclusions

This study provided a preliminary comparison between three SDTs from the literature and a widely used commercial method by analysing diameter and cylindricity errors using CMM reference data across three geometries. For diameter measurements, the results were generally comparable, with ANOVA indicating no significant differences among the methods. In contrast, the cylindricity error analysis suggested some variation between the methods, with the "Canny_Tay" approach yielding lower errors compared to the others. However, these findings should be considered indicative rather than definitive. To confirm this trend, future studies should incorporate a broader range of form and orientation measurands for further comparative analysis. Moreover, extending the evaluation to a wider set of parts, materials, and XCT acquisition conditions would help assess the robustness of each SDT and support more general conclusions applicable to different industrial scenarios.

References

[1] Kruth J. P., Bartscher M., Carmignato S., Schmitt R., De Chiffre L., Weckenmann A. Computed tomography for dimensional metrology. CIRP Annals 60, 821-842 (2011). https://doi.org/10.1016/j.cirp.2011.05.006

[2] Bellens, S., Guerrero, P., Vandewalle, P., & Dewulf, W. (2024). Machine learning in industrial X-ray computed tomography-a review. CIRP Journal of Manufacturing Science and Technology, 51, 324-341. https://doi.org/10.1016/j.cirpj.2024.05.004

[3] Volume Graphics VGSTUDIO MAX. https://www.volumegraphics.com/en/products/vgsm.html.

[4] Pirillo, F., Shao, H., Petrò, S., Moroni G. A Surface Determination Technique for Dimensional and Geometrical Analysis in Industrial X-ray Computed Tomography. Nanomanuf Metrol 7, 20 (2024). https://doi.org/10.1007/s41871-024-00239-4

[5] Canny J. (1986) A computational approach to edge detection, IEEE Transactions on pattern analysis and machine intelligence, 6, 679-698 https://doi.org/10.1109/TPAMI.1986.4767851

[6] Otsu N. (1975) A threshold selection method from gray-level histograms. Automatica, 11(285-296), 23-27

[7] Lorensen W.E., Cline H.E. (1998) Marching cubes: A high resolution 3D surface construction algorithm, In Seminal graphics: pioneering efforts that shaped the field, 347-353 https://doi.org/10.1145/280811.281026

[8] Yang X., Sun W., Giusca C.L. (2022) An automated surface determination approach for computed tomography, NDT & E International, 131:102697 https://doi.org/10.1016/j.ndteint.2022.102697

[9] Yang X., Sun W., Giusca C. L. Surface determination algorithm for accurate XCT bidirectional length measurements. Precision Engineering 85, 40-47 (2024). https://doi.org/10.1016/j.precisioneng.2023.09.003

[10] Yagüe-Fabra J.A., Ontiveros S., Jiménez R., Chitchian S., Tosello G., Carmignato S. (2013) A 3D edge detection technique for surface extraction in computed tomography for dimensional metrology applications, CIRP Annals, 62(1), 531-534 https://doi.org/10.1016/j.cirp.2013.03.016

[11] Steinbeiß H.P. (2005) Dimensionelles messen mit mikro-computertomographie, Hieronymus Buchreproduktions GmbH, Munche, ISBN 3-89791-349-6

[12] ISO 1101:2017 Geometrical product specifications (GPS). Geometrical tolerancing. Tolerances of form, orientation, location and runout.

Materials Research Proceedings 57 (2025) 72-79 https://doi.org/10.21741/9781644903735-9

Advanced active thermography for weld joint inspection

Valentino RAZZA[1,3,a *], Manuela DE MADDIS[1,3,b], Pasquale RUSSO SPENA[1,3,c] and Luca SANTORO[2,3,d]

[1]Dipartimento di Ingegneria Gestionale e della Produzione, Politecnico di Torino, Corso Duca degli Abruzzi 24, Torino, Italy

[2]Dipartimento di Ingegneria Meccanica e Aerospaziale, Politecnico di Torino, Corso Duca degli Abruzzi 24, Torino, Italy

[3]J-Tech@PoliTO - Advanced Joining Technologies Laboratory, Politecnico di Torino, Corso Duca degli Abruzzi 24, Torino, Italy

[a]valentino.razza@polito.it, [b]manuela.demaddis@polito.it, [c]pasquale.russospena@polito.it, [d]luca.santoro@polito.it

Keywords: Resistance Welding, Quality Control, Thermography

Abstract. Ensuring the integrity and mechanical performance of critical components is essential in many industrial applications. Widely used inspection methods have several limitations: destructive testing is accurate but involves sample destruction and time-consuming procedures, ultrasonic testing is slow and requires contact and skilled operators, and radiographic testing is expensive and demands stringent safety measures. This work presents an innovative non-destructive inspection method based on active infrared thermography. Modulated heat sources locally heat the specimen while advanced algorithms process the resulting thermal images to generate high-contrast maps for rapid defect detection and material characterization. Its cost-effectiveness and ease of integration into in-line production processes make it highly suitable for automotive, aerospace, and high-precision manufacturing applications.

Introduction

Evaluating weld quality is crucial in manufacturing, as it directly affects the structural integrity and performance of welded components. Conventional inspection methods, such as destructive testing, provide accurate results but lead to significant material waste and require considerable downtime. Nondestructive techniques, such as ultrasonic and radiographic testing, while valuable, are often limited by slow processing speeds, the need for physical contact, complex safety requirements, and the reliance on highly skilled operators [1, 2, 3, 4].

Active thermography has emerged as a powerful alternative in non-destructive testing (NDT). In this technique, an external heat source (e.g., a laser) is used to stimulate the specimen, and an infrared (IR) camera captures the transient thermal response [5, 6, 7, 8, 9]. When combined with a lock-in approach – where the heat source is modulated at a fixed frequency – the method can isolate thermal wave components that are highly sensitive to local variations in thickness, thermal diffusivity, and subsurface defects [10, 11, 12].

In our work, we develop a comprehensive framework for active thermographic inspection that integrates:

- An analytical model of thermal diffusion in a homogeneous slab under laser excitation,
- A gradient-based image processing method to enhance both phase and amplitude contrast in thermal images, and
- An AI-based (transfer learning) model to quantitatively predict microstructural dimensions.

Content from this work may be used under the terms of the Creative Commons Attribution 3.0 license. Any further distribution of this work must maintain attribution to the author(s) and the title of the work, journal citation and DOI. Published under license by Materials Research Forum LLC.

Materials Research Proceedings 57 (2025) 72-79 https://doi.org/10.21741/9781644903735-9

This framework not only produces high-contrast thermal maps for rapid defect detection but also provides quantitative insights into the internal structure of inspected components. Its simplicity, cost-effectiveness, and compatibility with in-line production environments make it an attractive solution for a wide range of industrial applications.

It is worth noting that the present work is still at a feasibility stage, aiming to assess the potential and applicability of the proposed approach. A comprehensive quantitative comparison with existing methodologies, as well as validation on industrial applications, will be addressed in future developments.

Overview on Active Thermography and Frequency Based Approach

Active thermography relies on externally heating the sample and capturing its thermal response over time. In lock-in thermography, the heat source is modulated periodically. For example, when a laser with power $\boldsymbol{P_0}$, having spot radius $\boldsymbol{a}$ and a Gaussian profile defined as a function of the distance $\boldsymbol{r}$ from the spot center excites a slab of thickness $\boldsymbol{\ell}$, the absorbed power is defined as

$$\boldsymbol{P(r) = \eta \frac{P_0}{\pi\, a^2} \exp\left(-\frac{2r^2}{a^2}\right)} \tag{1}$$

where $\boldsymbol{\eta}$ is the power fraction absorbed. The phase delay of the thermal wave at the rear surface is a function of both the material's thermal diffusivity $\boldsymbol{D_s}$ and the modulation frequency $\boldsymbol{f_\ell}$. Under periodic excitation, the phase delay $\boldsymbol{\phi}$ decreases linearly with the distance from the center of the laser spot at a rate of $\boldsymbol{-\ell/\lambda}$, where the thermal diffusion length $\boldsymbol{\lambda}$ is given by

$$\boldsymbol{\lambda = \sqrt{\frac{2D_s}{\omega}}, \quad \omega = 2\pi\, f_\ell.} \tag{2}$$

This relationship shows that even small changes in thickness or thermal diffusivity (due to defects and impurities) can result in measurable phase differences [13].

Lock-in thermography effectively suppresses noise and isolates the oscillatory component, making it suitable for detecting defects in composite materials, metal welds, and other essential structures [10, 11, 12].

The Proposed Methodology: Gradient Method

In our approach, the active thermography experiment generates a series of thermal images $\boldsymbol{T_k^{(r,c)}}$ where $\boldsymbol{k = 0, \dots, N-1}$ denotes the time index and $\boldsymbol{(r, c)}$ represents the pixel coordinates. For each pixel, the temperature signal is analyzed using the Discrete Fourier Transform (DFT)

$$\boldsymbol{\widetilde{T}_n = \sum_{k=0}^{N-1} T_k e^{\frac{i2\pi nk}{N}}, \qquad n = 0, \dots, N-1.} \tag{3}$$

We extract the Fourier coefficient corresponding to the laser modulation frequency, given $\boldsymbol{n_\ell = \lceil (N\, f_\ell)/f_r \rceil}$, and compute its phase as

$$\boldsymbol{\angle \widetilde{T}_{n_\ell} = \operatorname{atan2}\left(\mathrm{I}\{\widetilde{T}_{n_\ell}\}, \Re\{\widetilde{T}_{n_\ell}\}\right).} \tag{4}$$

Due to system delays, an offset $\boldsymbol{\phi_0}$ is present, so the effective phase is

$$\boldsymbol{\phi = \angle \widetilde{T}_{n_\ell} - \phi_0.} \tag{4}$$

Since the ideal theoretical model for a homogeneous slab would yield a smooth phase delay, any local deviations in $\boldsymbol{\phi}$ are indicative of defects or changes in material properties.

Materials Research Proceedings 57 (2025) 72-79 https://doi.org/10.21741/9781644903735-9

An example of such an application can be found in the classification of resistance spot welding (RSW) joints.

In fact, the internal uniformity of the weld spot can be evaluated through statistical indices computed on the phase map (see, e.g., [14]). For instance, we can compute the variance of the phase delay as an internal uniformity index. Moreover, the size of the joint can be estimated from the area in the frame that shows larger heat transfer from the magnitude of $\widetilde{\boldsymbol{T}}_{\mathbf{n}_\ell}$. The contour plot depicted in Figure 1 shows the correlation between the nugget area and phase variance $\boldsymbol{v}$ to the ultimate tensile strength (UTS), highlighting that welds with higher mechanical strength correspond to points with larger nugget areas and lower phase variance. The tests have been performed in different welding conditions:

1. conditions that lead to "bad" spot welds due to a low current value, and thus the presence of an undersized nugget;
2. condition leading to "good" spot welds obtained with the optimized process parameters;
3. condition leading to "bad" spot welds due to high current and the presence of spatter.

To provide information to a non-expert user about the material internal defect, we compute the spatial gradient of the phase map, i.e.,

$$\boldsymbol{\nabla\phi}(\mathbf{x},\mathbf{y}) = \frac{\boldsymbol{\partial\phi}}{\boldsymbol{\partial x}}\hat{\boldsymbol{\imath}} + \frac{\boldsymbol{\partial\phi}}{\boldsymbol{\partial y}}\hat{\boldsymbol{\jmath}}, \tag{5}$$

with the gradient magnitude given by

$$|\boldsymbol{\nabla\phi}(\mathbf{x},\mathbf{y})| = \sqrt{\left(\frac{\boldsymbol{\partial\phi}}{\boldsymbol{\partial x}}\right)^{\mathbf{2}} + \left(\frac{\boldsymbol{\partial\phi}}{\boldsymbol{\partial y}}\right)^{\mathbf{2}}}. \tag{6}$$

Furthermore, to better accentuate radially oriented features (i.e., the weld nugget edges), we compute the vector from each pixel $(\boldsymbol{x},\boldsymbol{y})$ to the weld center $(\boldsymbol{x_c},\boldsymbol{y_c})$

$$\vec{\boldsymbol{c}}\,(\boldsymbol{x},\boldsymbol{y}) = (\boldsymbol{x}-\boldsymbol{x_c})\hat{\boldsymbol{\imath}} + (\boldsymbol{y}-\boldsymbol{y_c})\hat{\boldsymbol{\jmath}}, \tag{7}$$

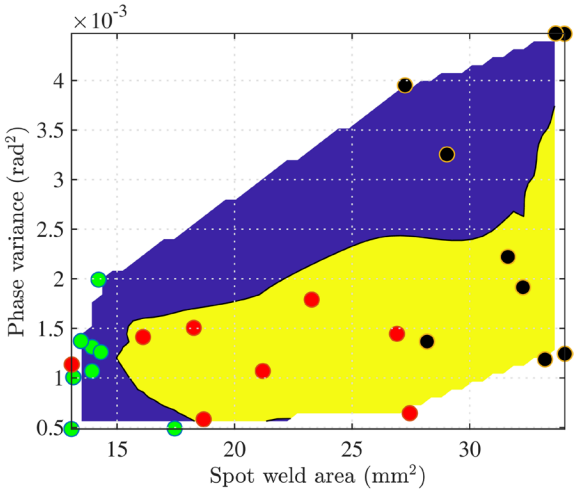


Figure 1: Contour plot relating the thermographic features (nugget area and phase variance) to the ultimate tensile strength (UTS) of the weld. The blue region highlights areas associated with poor-quality welds, defined as those with UTS below 80% of the maximum strength, while the yellow region corresponds to high-quality welds. Dot markers indicate experimentally tested data points from specimen sets 1 (green), 2 (red), and 3 (black)

Materials Research Proceedings 57 (2025) 72-79 https://doi.org/10.21741/9781644903735-9

and define the adjusted gradient magnitude by projecting $\nabla\boldsymbol{\phi}(\mathbf{x},\mathbf{y})$ onto $\vec{\boldsymbol{c}}\,(\boldsymbol{x},\boldsymbol{y})$

$$|\nabla\boldsymbol{\phi}(\mathbf{x},\mathbf{y})|_{\boldsymbol{adj}} = \nabla\boldsymbol{\phi}(\mathbf{x},\mathbf{y})\,\cos\boldsymbol{\theta}(\boldsymbol{x},\boldsymbol{y}), \tag{8}$$

where

$$\cos\boldsymbol{\theta}(\boldsymbol{x},\boldsymbol{y}) = \frac{\nabla\boldsymbol{\phi}(\mathbf{x},\mathbf{y})\cdot\vec{\boldsymbol{c}}\,(\boldsymbol{x},\boldsymbol{y})}{|\nabla\boldsymbol{\phi}(\mathbf{x},\mathbf{y})||\vec{\boldsymbol{c}}\,(\boldsymbol{x},\boldsymbol{y})|}. \tag{9}$$

The gradient-based processing dramatically improves the visualization of the weld features, and it can also be applied to $\left|\widetilde{\boldsymbol{T}}_{\mathbf{n}_\ell}\right|$. Figure 2 shows an example of the magnitude gradient map $\left|\nabla\left|\widetilde{\boldsymbol{T}}_{\mathbf{n}_\ell}\right|\right|$.

A 3D printed PLA plate was used as the test sample, with controlled defects generated in the form of the letters of the "JTech" logo, each embedded in a 1 × 1 cm region at a depth of 0.5 mm. Darker regions indicate higher gradient magnitudes, corresponding to the edges of internal defects. The interested reader finds further details in [15].

Nugget Size Analysis in RSW: Experimental and AI-Assisted Results

The method was used to predict the nugget and corona bond size in resistance spot welding, which is crucial for the quality assurance of the welds.

Notice how the gradient map provides enhanced contrast at the nugget boundary, improving the visualization of the nugget button size (see Figure 3) [16, 17].

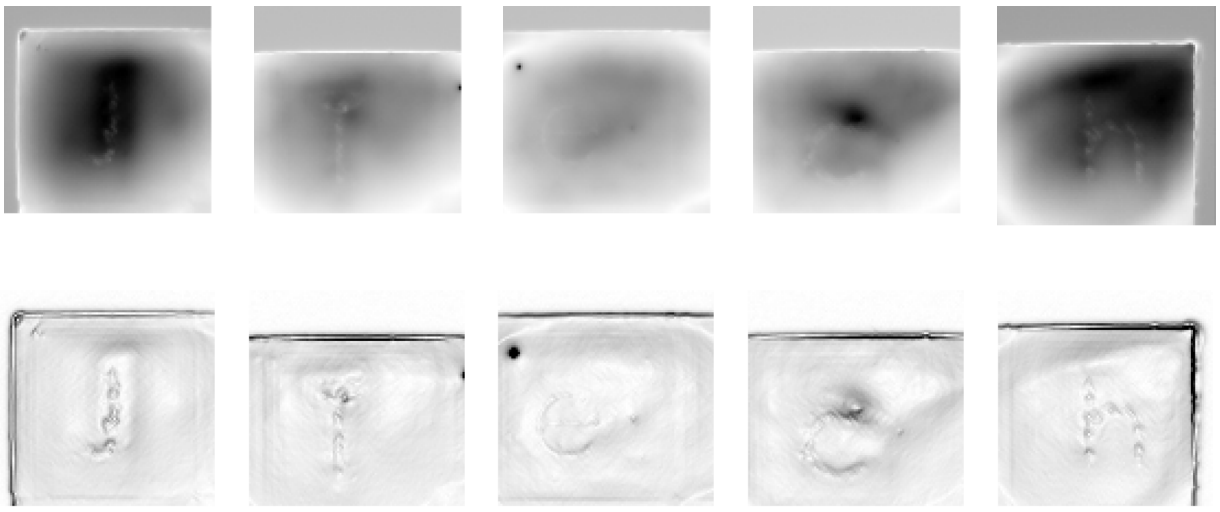
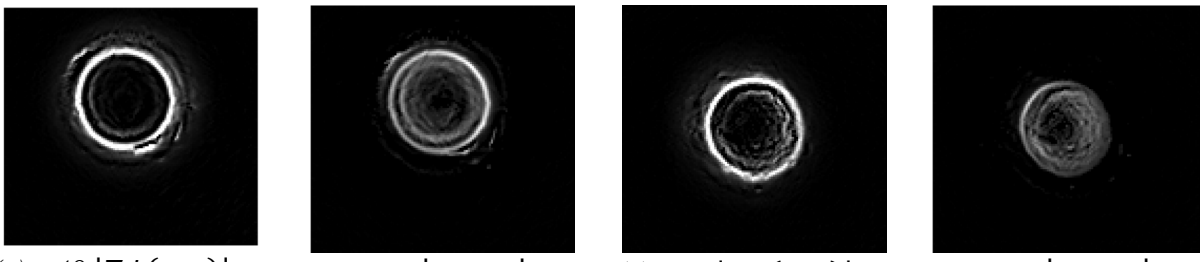


Figure 2: "Jtech" test plate. On the top row, the amplitude map $\left|\widetilde{\boldsymbol{T}}_{\boldsymbol{n}_\ell}\right|$. On the bottom, the amplitude gradient map $\left|\nabla\left|\widetilde{\boldsymbol{T}}_{\boldsymbol{n}_\ell}\right|\right|$.

Materials Research Proceedings 57 (2025) 72-79 https://doi.org/10.21741/9781644903735-9



(a) - 48 $|\nabla\phi(x,y)|_{adj}$ (b) - 48 $\left|\nabla|\tilde{\mathbf{T}}_{\mathbf{n}_\ell}|\right|_{adj}$ (c) - 52 $|\nabla\phi(x,y)|_{adj}$ (d) - 48 $\left|\nabla|\tilde{\mathbf{T}}_{\mathbf{n}_\ell}|\right|_{adj}$

Figure 3: Comparison of adjusted maps for different nugget sizes

A convolutional neural network (CNN) further exploits the gradient-based images. Our approach uses a transfer learning model based on the InceptionV3 architecture. The process is as follows

1. *Preprocessing:* The gradient maps from phase and amplitude channels are normalized and converted into three-channel images.
2. *Feature Extraction*: The pre-trained InceptionV3 model acts as a feature extractor.
3. *Regression*: Custom dense layers (with ReLU activation) are appended, and the final output layer (with linear activation) produces a regression estimate of the nugget diameter $\tilde{\boldsymbol{L}}$.

Figure 4 shows the overall CNN architecture used in our study. The network is trained with labeled weld data, and its predictions are compared with metallurgical measurements (see, e.g., [18]). A linear regression model is then used to relate the estimated nugget diameter $\tilde{L}$ to the measured value L as

$$\boldsymbol{L = m\,\tilde{L} + q}, \tag{10}$$

where the regression coefficients m and q are determined via least-squares fitting.

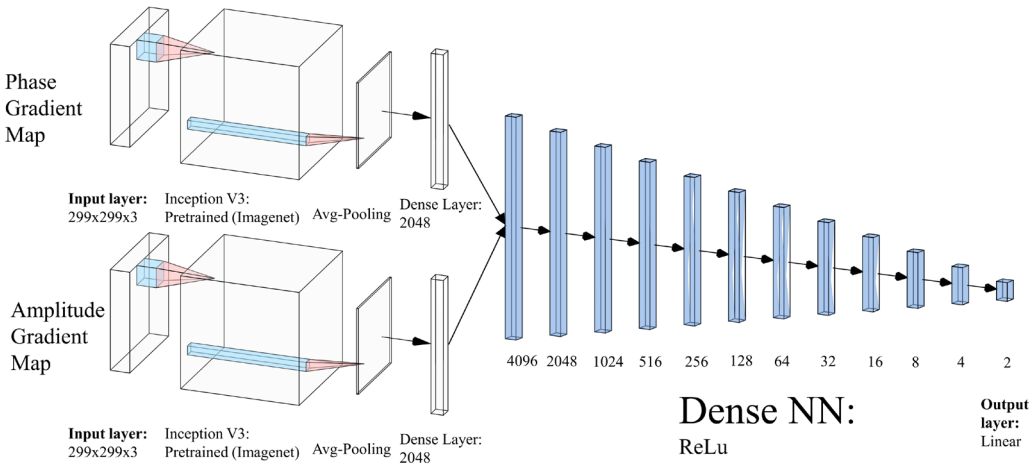


Figure 4: Overview of the CNN architecture based on InceptionV3 used for nugget diameter estimation.

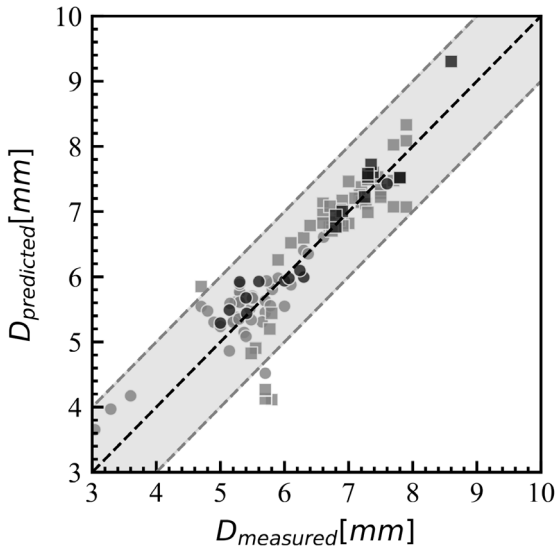


Figure 5: Correlation between AI-predicted nugget diameters $\tilde{\boldsymbol{L}}$ and metallurgical measurements $\boldsymbol{L}$. Gray dots and squares represent nugget and corona bond data from the training set, respectively; black markers correspond to the validation set.

Training a convolutional neural network (CNN) requires a large amount of data that cannot be easily generated from experimental welding tests. It is worth noting that, within the signal processing community, the problem of training reliable CNNs to retrieve info from 2D convolution is a standard procedure in image processing. Thus, we exploit a pre-trained general-purpose image parser neural network, whose output is parsed by a tailored dense neural network (DNN), which provides the nugget and corona bond sizes.

Our experiments yield a Pearson correlation coefficient of 0.94 between the predicted and measured values. Figure 5 shows the correlation between the CNN-predicted nugget sizes and the metallurgical measurements.

Conclusions

In this work, we present a comprehensive methodology for non-destructive evaluation of weld joints using active thermography, combined with gradient-based image processing and artificial intelligence. By employing lock-in thermography, the phase delay, which is highly sensitive to weld thickness and thermal diffusivity, is accurately measured. Subsequent computation of spatial gradients enhances the imaging of weld nugget boundaries and defects. Finally, a CNN leveraging transfer learning from InceptionV3 can predict weld geometrical dimensions with strong correlation to metallurgical measurements.

This integrated approach offers significant promise for automated in-line quality control, reducing the need for destructive testing and enabling more effective process monitoring. Future work will focus on refining the excitation frequency and expanding the dataset to facilitate further validation and improvement of the AI model.

References

[1] T. F. Dahmene, S. Yaacoubi, E. M. Mahjoub, A. E. Bouzenad, P. Rabaey, M. Masmoudi, P. Nennig, T. Dupuy, Y. Benlatreche and A. Taram, "On the nondestructive testing and monitoring of cracks in resistance spot welds: recent gained experience," Welding in the World, vol. 66, no. 4, pp. 629-641, 2022. https://doi.org/10.1007/s40194-022-01249-w

[2] Ó. Martín, M. Pereda, J. I. Santos and J. M. Galán, "Assessment of resistance spot welding quality based on ultrasonic testing and tree-based techniques," Journal of Materials Processing Technology, vol. 214, no. 11, pp. 2478-2487, 2014. https://doi.org/10.1016/j.jmatprotec.2014.05.021

[3] K. Zhou and P. Yao, "Overview of recent advances of process analysis and quality control in resistance spot welding," Mechanical Systems and Signal Processing, vol. 124, pp. 170-198, 2019. https://doi.org/10.1016/j.ymssp.2019.01.041

[4] E. Misokefalou, M. Papoutsidakis and G. Priniotakis, "NON-DESTRUCTIVE TESTING FOR QUALITY CONTROL IN AUTOMOTIVE INDUSTRY," International Journal of Engineering Applied Sciences and Technology, vol. 7, no. 1, pp. 349-355, 2022. https://doi.org/10.33564/IJEAST.2022.v07i01.054

[5] L. Cantini, M. Cucchi, G. Fava and C. Poggi, "Fourier analysis applied to Infrared Thermography of Fiber Composites used for the Strengthening of Structural Elements," in 11th International Conference on Quantitative InfraRed Thermography, 2022.

[6] J. Song, B. Gao, W. L. Woo and G. Y. Tian, "Ensemble tensor decomposition for infrared thermography cracks detection system," Infrared Physics & Technology, vol. 105, p. 103203, 2020. https://doi.org/10.1016/j.infrared.2020.103203

[7] N. Rajic, "Principal component thermography for flaw contrast enhancement and flaw depth characterisation in composite structures," Composite Structures, vol. 58, no. 4, pp. 521-528, 2002. https://doi.org/10.1016/S0263-8223(02)00161-7

[8] K.-L. Huang, S. Sfarra, C.-M. Wen, Y. Yao and C. Zhao, "Exploratory factor analysis for defect identification with active thermography," Measurement Science and Technology, vol. 32, no. 11, p. 114010, 2021. https://doi.org/10.1088/1361-6501/ac17f9

[9] C. Maierhofer, M. Röllig, H. Steinfurth, M. Ziegler, M. Kreutzbruck, C. Scheuerlein and S. Heck, "Non-destructive testing of Cu solder connections using active thermography," NDT & E International, vol. 52, pp. 103-111, 2012. https://doi.org/10.1016/j.ndteint.2012.07.010

[10] K. Strzałkowski, M. Streza, D. Dadarlat and A. Marasek, "Thermal characterization of II-VI binary crystals by photopyroelectric calorimetry and infrared lock-in thermography," Journal of Thermal Analysis and Calorimetry, vol. 119, no. 1, pp. 319-327, 2015. https://doi.org/10.1007/s10973-014-4137-0

[11] A. Mendioroz, R. Fuente-Dacal, E. Apiñaniz and A. Salazar, "Thermal diffusivity measurements of thin plates and filaments using lock-in thermography," Review of Scientific Instruments, vol. 80, no. 7, p. 074904, 2009. https://doi.org/10.1063/1.3176467

[12] A. Philipp, N. W. Pech-May, B. A. F. Kopera, A. M. Lechner, S. Rosenfeldt and M. Retsch, "Direct Measurement of the In-Plane Thermal Diffusivity of Semitransparent Thin Films by Lock-In Thermography: An Extension of the Slopes Method," Analytical Chemistry, vol. 91, no. 13, pp. 8476-8483, 2019. https://doi.org/10.1021/acs.analchem.9b01583

[13] H. Kato, T. Baba and M. Okaji, "Anisotropic thermal-diffusivity measurements by a new laser-spot-heating technique," Measurement Science and Technology, vol. 12, no. 12, p. 2074, 2001. https://doi.org/10.1088/0957-0233/12/12/307

[14] L. Santoro, V. Razza and M. De Maddis, "Frequency-based analysis of active laser thermography for spot weld quality assessment," International Journal of Advanced Manufacturing Technology, 2023. https://doi.org/10.1007/s00170-023-12845-5

[15] V. Razza, L. Santoro and M. De Maddis, "Gradient-based image generation for thermographic material inspection," Applied Thermal Engineering, vol. 268, p. 125900, 2025. https://doi.org/10.1016/j.applthermaleng.2025.125900

[16] Á. Cifuentes, A. Mendioroz and A. Salazar, "Simultaneous measurements of the thermal diffusivity and conductivity of thermal insulators using lock-in infrared thermography," International Journal of Thermal Sciences, vol. 121, pp. 305-312, 2017. https://doi.org/10.1016/j.ijthermalsci.2017.07.023

[17] L. Santoro, R. Sesana, R. Molica Nardo and F. Curà, "Infrared in-line monitoring of flaws in steel welded joints: a preliminary approach with SMAW and GMAW processes," International Journal of Advanced Manufacturing Technology, 2023. https://doi.org/10.1007/s00170-023-12044-2

[18] L. Santoro, V. Razza and M. De Maddis, "Nugget and corona bond size measurement through active thermography and transfer learning model," International Journal of Advanced Manufacturing Technology, vol. 133, no. 11, pp. 5883-5896, 2024. https://doi.org/10.1007/s00170-024-14096-4

Materials Research Proceedings 57 (2025) 80-89 https://doi.org/10.21741/9781644903735-10

Document-type classification errors in bibliometric databases: Insights from the engineering/manufacturing field

Domenico Augusto MAISANO[1,a *], Lucrezia FERRARA[1,b] and Fiorenzo FRANCESCHINI[1,c]

[1] Politecnico di Torino, Department of Management and Production Engineering (DIGEP), Corso Duca degli Abruzzi 24, 10129, Torino (Italy)

[a] domenico.maisano@polito.it, [b] lucrezia.ferrara@polito.it, [c] fiorenzo.franceschini.polito.it

Keywords: Document-Type Classification, Quality, Performance Indicators

Abstract. Document types (DTs) – e.g., *research articles, reviews, conference proceedings, letters*, etc. – are not only used to classify scientific publications, but also to routinely guide inclusion-exclusion decisions in bibliometric assessments, often without adequate consideration of the quality of underlying content. This study examines DT-classification errors in Scopus and Web of Science (WoS), focusing on engineering/manufacturing publications. These errors – which may directly affect publication/citation counts, citation-impact indicators, and consequently academic evaluations and careers – are analyzed in a *corpus* of about 10,000 documents, using a recent semi-automated method. The results indicate that these errors, while occurring in several percentage points, are far from negligible. Furthermore, statistical analyses reveal systematic differences among publishers (e.g., Springer, Elsevier, Taylor & Francis, etc.), with some contributing more to errors, probably due to editorial styles or inconsistent metadata. This study provides insights for researchers, evaluators and database managers, highlighting the need for publisher-specific guidelines to enhance classification accuracy and reduce errors.

1. Introduction

Document types serve as classification labels for scientific documents (e.g., *research articles, reviews, conference proceedings*) and facilitate targeted bibliographic searches. These classifications, assigned by authors, editorial committees, publishers, or bibliometric databases, are not always consistent, leading to discrepancies in document categorization [1,2]. This study examines DT classifications within Scopus and WoS, two leading bibliometric databases widely utilized for research retrieval and evaluation [3]. DT-classification errors in these databases can have significant implications in academic assessments, including research evaluations for individual scholars, research groups, and institutions [4]. Prior studies indicate that such errors, while occurring at relatively low rates, are non-negligible and may lead to document misclassification, affecting research assessments and academic decisions [5,6].

Maisano et al. [7] recently introduced a semi-automated methodology for detecting DT-classification errors by analyzing discrepancies between Scopus and WoS. This approach, which combines automated identification with manual verification, enables large-scale analysis while minimizing the labour-intensive nature of prior studies. Building on this work, the present study focuses on publications from Politecnico di Torino (PoliTO) and addresses three key questions:

***RQ1**: What is the incidence of DT-classification errors in engineering/manufacturing publications?*

***RQ2**: Do publishers systematically influence DT-classification errors?*

***RQ3**: Are error distributions consistent across Scopus and WoS?*

To investigate these questions, a structured methodological framework is adopted, comprising document and publisher identification, data consolidation (i.e., grouping sub-publishers into

Content from this work may be used under the terms of the Creative Commons Attribution 3.0 license. Any further distribution of this work must maintain attribution to the author(s) and the title of the work, journal citation and DOI. Published under license by Materials Research Forum LLC.

macro-publishers or publishing groups to avoid excessive fragmentation in the analysis), the detection of DT-classification errors, statistical analysis, and comparative assessment of DT-classification discrepancies across databases. The remainder of this article is organized as follows: Sect. 2 outlines the methodological framework, Sect. 3 presents the empirical findings, and Sect. 4 the conclusions, practical implications, limitations, and directions for future research.

2. Methodology

This section details the methodological framework adopted in the study, which is structured into two key phases: (a) data collection and identification of DT-classification errors in Scopus and WoS and (b) publisher identification and aggregation into macro-publishers, along with computation of relevant statistics.

2.1 Data collection and analysis of DT-classification errors

Building on previous research [7], this study analyzes a dataset of 10,834 scientific documents authored by PoliTO faculty members from 2019 to 2023. The dataset, indexed in both Scopus and WoS and identified through DOI codes, ensures a consistent and comparable document pool within the field of engineering/manufacturing, a discipline characterized by relatively homogeneous publishing practices [8]. To detect DT-classification errors, a semi-automated methodology [7] was adopted. The initial phase identified 10,471 concordant documents, (i.e., classified identically in both databases), and 363 discordant documents which exhibit classification discrepancies (Table 1). The manual analysis of all 363 discordant documents confirmed a substantial number of classification errors.

Table 1 *– Concordance matrix for the corpus of interest of 10,834 documents. While the elements in the diagonal (in round brackets) denote DT classifications that are concordant between competing databases, those off-diagonal denote potential DT-classification errors. Documents corresponding to the latter elements were manually analysed.*

DT classifications →		by Scopus									
↓		*Article*	*Conf. paper*	*Review*	*Editorial*	*Book chapter*	*Erratum*	*Note*	*Letter*	*Short Survey*	**Row total**
by WoS	*Article*	(8,378)	29	100	3	3	–	10	6	2	**8,531**
	Proceedings Paper	15	(1,463)	–	1	55	–	–	–	–	**1,534**
	Review	70	–	(413)	–	–	–	–	–	3	**486**
	Editorial Material	20	4	17	(162)	–	1	14	–	3	**221**
	Correction	1	–	–	–	–	(48)	–	–	–	**49**
	Letter	2	–	–	–	–	–	–	(7)	–	**9**
	Retraction	–	–	–	–	–	2	–	–	–	**2**
	Meeting Abstract	–	1	–	–	–	–	–	–	–	**1**
	Book Review	1	–	–	–	–	–	–	–	–	**1**
	Column total	**8,487**	**1,497**	**530**	**166**	**58**	**51**	**24**	**13**	**8**	**10,834**

Tables 2 and 3 present error matrices for Scopus and WoS, where rows indicate the "true" DTs (determined through manual validation), and columns reflect the DTs assigned by each database. Diagonal elements denote correct classifications, while off-diagonal entries indicate misclassifications. Common errors include the misclassification of *research articles* as *reviews* or *conference papers* and *vice versa*. The overall error rate (ε), calculated as:

$$\varepsilon = \frac{\sum_{\forall(i,j) \mid i \neq j} x_{(i,j)}}{\sum_{\forall(i,j)} x_{(i,j)}}, \quad (1)$$

where $x_{(i,j)}$ represents the number of documents reported in the i-th row and j-th column of the error table, for the database of interest. The ε values resulting from the analysis are shown in the lower right vertex of the error tables (i.e., 2.1% for Scopus and 1.3% for WoS) in Tables 2 and 3, consistent with prior studies [6,7,9]. These findings confirm that while both databases exhibit classification inconsistencies, the overall error rate remains within a few percentage points.

Table 2 *– Error table for Scopus, with error rate (ε, cf. Eq. 1) highlighted in bold. The diagonal elements indicating correctly classified documents are marked with round brackets.*

		DT classification by Scopus									
		Article	*Conf. Paper*	*Review*	*Editorial*	*Book chapter*	*Erratum*	*Note*	*Letter*	*Short Survey*	Row total
"True" DT classifications	*Article*	(8,400)	23	28	-	3	-	2	-	1	8,457
	Conf. Paper	15	(1,473)	-	1	51	-	-	-	-	1,540
	Review	50	-	(483)	-	-	-	-	-	1	534
	Editorial	14	1	14	(164)	-	-	3	-	3	199
	Erratum	1	-	-	-	-	(49)	-	-	-	50
	Note	5	-	2	1	-	-	(19)	-	1	28
	Letter	1	-	-	-	-	-	-	(13)	-	14
	Book Chapter	-	-	-	-	(4)	-	-	-	-	4
	Other	1	-	3	-	-	-	-	-	-	4
	Short Survey	-	-	-	-	-	-	-	-	(2)	2
	Retracted	-	-	-	-	-	2	-	-	-	2
	Column total	8,487	1,497	530	166	58	51	24	13	8	10,834
											$\varepsilon \cong 2.1\%$

Table 3 *– Error table for WoS, with error rate (ε, cf. Eq. 1) highlighted in bold. The diagonal elements indicating correctly classified documents are marked with round brackets.*

		DT classification WoS									
		Article	*Proc. Paper*	*Review*	*Editorial Material*	*Correction*	*Letter*	*Retraction*	*Book Review*	*Meeting Abstract*	Row total
"True" DT classifications	*Article*	(8,441)	-	17	1	-	1	-	-	-	8,460
	Proc. Paper	6	(1530)	-	3	-	-	-	-	1	1,540
	Review	63	-	(467)	2	-	-	-	-	-	532
	Editorial Material	3	-	-	(198)	-	-	-	-	-	201
	Correction	-	-	-	1	(49)	-	-	-	-	50
	Other	8	-	2	15	-	-	-	-	-	25
	Letter	6	-	-	-	-	(8)	-	-	-	14
	Book Chapter	-	4	-	-	-	-	-	-	-	4
	News Item	3	-	-	-	-	-	-	-	-	3
	Retraction	-	-	-	-	-	-	(2)	-	-	2
	Book Review	1	-	-	-	-	-	-	(1)	-	2
	Biographical-Item	-	-	-	1	-	-	-	-	-	1
	Column total	8,531	1,534	486	221	49	9	2	1	1	10,834
											$\varepsilon \cong 1.3\%$

2.2 Identification and rationalization of publishers

This phase of the analysis examines publishers as the entities responsible for the editorial management of scientific documents, a role distinct from the scientific content itself, which is typically overseen by expert committees and peer reviewers [8]. Publisher information for each document was extracted using the "Publisher" field in Scopus and WoS.

The initial analysis revealed significant fragmentation, with a total of 333 distinct publishers identified across the dataset. This fragmentation arises not only from the existence of genuinely independent publishers but also from the structural complexity of major publishing groups. Large publishers frequently operate under multiple "sub-brands", which bibliometric databases may report inconsistently. For instance, Elsevier is variously listed as "Elsevier GmbH," "Elsevier USA," "Elsevier Masson s.r.l.," and "Elsevier B.V.," among others. Similarly, naming inconsistencies exist within other major publishers, such as variations in the representation of John Wiley & Sons (e.g., "John Wiley and Sons Inc.", "John Wiley and Sons Ltd.").

To address these inconsistencies, a data cleaning and aggregation process was undertaken, consolidating sub-publishers into broader macro-publishers. The rationale for this approach is that macro-publishers impose standardized editorial policies, work practices, and metadata conventions, ensuring a degree of consistency across their sub-brands. Additionally, aggregating sub-publishers reduces dataset fragmentation, increasing the statistical robustness of subsequent analyses [10]. The manual aggregation process relied on online sources detailing publisher affiliations with broader editorial groups, which was one of the most laborious aspects of the entire analysis. Following this rationalization, 218 macro-publishers were identified. To enhance

statistical reliability, only macro-publishers with at least 300 documents were considered in further analyses, resulting in a subset of 7 macro-publishers, with the remaining entities grouped under the category "Other". For simplicity, the term "publishers" will henceforth refer to these 7 macro-publishers. The cumulative chart in Fig. 1 reveals that the top 7 publishers listed account for approximately 80% of the total documents included in the analysis (i.e., $\frac{Documents\ of\ the\ major\ 7\ macro-publishers}{Total\ corpus\ of\ documents} = \frac{8,629}{10,834} \approx 80\%$) and 79% of the identified discordant documents (i.e., $\frac{Discordant\ documents\ of\ the\ major\ 7\ macro-publishers}{Discordant\ documents\ in\ the\ total\ corpus} = \frac{286}{363} \approx 79\%$). This finding reinforces the rationale for excluding macro-publishers with fewer documents from the analysis, grouping them into the "Other" category.

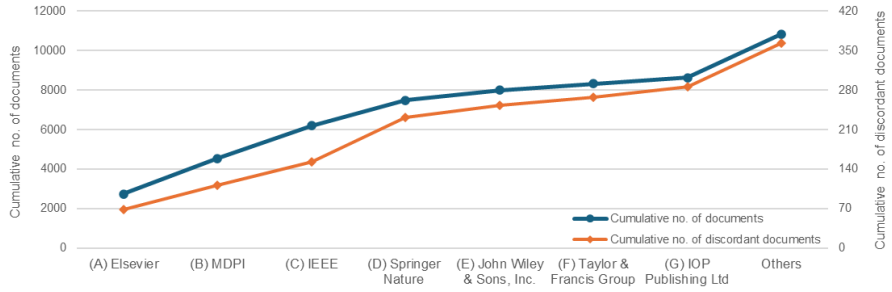


Figure 1 *– Cumulative diagram of the total number of documents considered in the analysis (left-hand scale) and the total number of discordant documents (right-hand scale). The macro-publishers on the x-axis are listed in descending order based on the total number of documents included in the analysis (cf. Table 4).*

3. Results

This section examines the results of the analysis of the decomposition of error tables related to the documents of specific publishers for each database. Analyses are supported by various statistical tests.

The error statistics for documents associated with a given p-th publisher can be modelled as a binomially distributed variable, characterized by the following mean (μ) and variance (σ^2):

$$E_p \sim Bin[\mu = d_p \cdot \varepsilon_p, \sigma^2 = d_p \cdot \varepsilon_p \cdot (1 - \varepsilon_p)], \tag{2}$$

where d_p represents the total number of documents included in the analysis and ε_p is the error rate from the perspective of the p-th publisher.

When the condition $d_p \cdot \varepsilon_p \geq 5$ is satisfied, e_p can be approximated by a normal distribution with the same mean and variance as above[1]:

$$E_p \sim N\left[\mu = d_p \cdot \varepsilon_p, \sigma^2 = d_p \cdot \varepsilon_p \cdot (1 - \varepsilon_p)\right]. \tag{3}$$

Based on this approximation, a symmetric 95% confidence interval (CI) around the estimated error rate $\hat{\varepsilon}_p$ can be defined as follows:

$$\hat{\varepsilon}_p \pm z_{1-\frac{\alpha}{2}} \cdot \sqrt{\frac{\hat{\varepsilon}_p \cdot (1-\hat{\varepsilon}_p)}{d_p}}, \tag{4}$$

where:

α is the type-I error (e.g., α=5% for a 95% CI);

[1] This condition is generally met when considering relatively large sets of misclassified documents (e_p). However, even when it is not strictly met, Eq. 4 still provides a practical and reasonable estimate of the confidence interval in Eq. 4 [10].

$z_{1-\frac{\alpha}{2}}$ is the unit normal deviate corresponding to a cumulative probability $1-\frac{\alpha}{2}$. E.g., for a symmetrical 95% CI, α = 5%, hence $z_{0.975} \approx 1.96$.

This approach ensures robust estimates of the ε_p values and their relevant CIs, enabling a statistically rigorous comparison of error rates among publishers. For instance, based on Table 4, it can be observed that – with respect to Scopus – the $\hat{\varepsilon}_p$ value for documents published by "Springer Nature" is significantly higher than those for "Elsevier", "MDPI" and "IEEE". The difference is further evidenced by the non-overlapping 95% CIs around the same $\hat{\varepsilon}_p$ values (see graphical representation via the boxplot in Fig. 2). Such non-overlap suggests that the "true" error rates for these publishers are statistically distinct, implying systematic differences in how documents from different publishers are classified.

Table 4 *– Summary of the publisher-specific analysis for the Scopus database (on the left) and WoS database (on the right). For each p-th publisher (listed in the table rows), the following values are reported: the total number of analyzed documents (d_p), the number of observed document-type classification errors (e_p), the corresponding (estimated) error rate ($\hat{\varepsilon}_p = \frac{e_p}{d_p}$), the 95% CI around $\hat{\varepsilon}_p$ (see Eq. 4), and the deviation (dev_p) associated with the χ^2 test, which accounts for differences among publishers (see Eqs. 7 and 8). The bottom row reports the overall values for the entire document corpus.*

		Scopus					WoS				
				95% CI					95% CI		
Publisher	d_p	e_p	$\hat{\varepsilon}_p$	Lower limit	Upper limit	dev_p	e_p	$\hat{\varepsilon}_p$	Lower limit	Upper limit	dev_p
(A) Elsevier	2,735	37	0.014	0.009	0.018	7.195	32	0.012	0.008	0.016	0.231
(B) MDPI	1,812	22	0.012	0.007	0.017	6.714	21	0.012	0.007	0.017	0.188
(C) IEEE	1,648	29	0.018	0.011	0.024	0.886	15	0.009	0.005	0.014	1.710
(D) Springer Nature	1,290	59	0.046	0.034	0.057	37.817	19	0.015	0.008	0.021	0.401
(E) John Wiley & Sons, Inc.	515	18	0.035	0.019	0.051	4.817	5	0.010	0.001	0.018	0.371
(F) Taylor & Francis Group	321	8	0.025	0.008	0.042	0.241	8	0.025	0.008	0.042	3.741
(G) IOP Publishing Ltd	308	11	0.036	0.015	0.056	3.203	8	0.026	0.008	0.044	4.236
Overall	**8,629**	**184**	**0.021**			**60.873**	**108**	**0.013**			**10.879**

The chi-squared (χ^2) test confirms these considerations, evaluating whether the observed error rates differ significantly across publishers. For each *p*-th publisher, the deviation (dev_p, representing the standardized residuals of the χ^2 test) is calculated as follows [10]:

$$dev_p = \frac{(O_p - E_p)^2}{E_p}, \tag{5}$$

where $O_p = e_p = \varepsilon_p \cdot d_p$ is the *observed* number of errors and $E_p = \varepsilon \cdot d_p$ is the *expected* number of errors under the null hypothesis (H_0) of equal error rates across publishers.
The deviation relative to the *p*-th publisher therefore becomes:

$$dev_p = \frac{(\varepsilon_p \cdot d_p - \varepsilon \cdot d_p)^2}{\varepsilon \cdot d_p} = \frac{(\varepsilon_p - \varepsilon)^2}{\varepsilon} \cdot d_p. \tag{6}$$

The test statistic χ^2 is then computed as:

$$\chi^2 = \sum_{\forall p} dev_p = \sum_{\forall p} \frac{(\varepsilon_p - \varepsilon)^2}{\varepsilon} \cdot d_p, \tag{7}$$

which is compared against the critical value $\chi^2_{\alpha,\, DoF}$ for the chosen significance level (e.g., α = 5%)

Materials Research Proceedings 57 (2025) 80-89 https://doi.org/10.21741/9781644903735-10

and *degrees of freedom*, determined as:

$$DoF = (rows - 1) \cdot (colums - 1), \tag{8}$$

as a function of the number of rows and columns of the contingency table containing the data of interest. In this case, *rows* = 2 (distinguishing between correctly classified and misclassified documents), while *columns* is equal to the number of publishers, determining $DoF = (2 - 1)\cdot(7 - 1) = 6$. The comparison between the calculated χ^2 value and the critical one leads to two possible outcomes:

$$\begin{gathered}\chi^2 > \chi^2_{\alpha,DoF} \text{ (or } p < \alpha\text{): Reject the null hypothesis (H}_0\text{);} \\ \chi^2 \leq \chi^2_{\alpha,DoF} \text{ (or } p \geq \alpha\text{): Do not reject H}_0\text{,}\end{gathered} \tag{9}$$

where H_0 is that there are no significant differences between publishers in terms of DT-classification error rates. In the specific case under analysis, the result for Scopus is:

$$\chi^2 = 60.873 > \chi^2_{\alpha,\,DoF} = 12.592 \;\; \left(p = 3 \times 10^{-11} < \alpha = 0.05\right), \tag{10}$$

which leads to rejecting H_0. From the dev_p values (cf. Table 4 on the left) it becomes evident that certain publishers deviate more significantly than others. For instance, “Springer Nature”, “IOP Publishing Ltd” and “John Wiley & Sons, Inc.” have significantly higher ε_p values, while “Elsevier”, “MDPI” and “IEEE” exhibit significantly lower values compared to the rest.

In WoS (cf. Table 4 on the right), the χ^2 test does not indicate significant differences among publishers:

$$\chi^2 = 10.879 \leq \chi^2_{\alpha,\,DoF} = 12.592 \;\; (p = 0.09 \geq \alpha = 0.05), \tag{11}$$

which leads to failing to reject H_0, meaning that there is no strong statistical evidence of significant differences in DT-classification error rates among publishers. This result appears to be further supported by the diagram in Fig. 2 on the right, which shows that the CIs around the ε_p values for different publishers in WoS tend to overlap, albeit slightly.

Table 5 includes an additional test on pairwise differences in error rates. Specifically, for each pair of publishers (e.g., considering two generic publishers *A* and *B*), the null hypothesis (H_0) assumes that the two error rates (ε_p) are equal, while the alternative hypothesis (H_1) assumes they differ. The test statistic *z* is defined as follows:

$$z = \frac{\varepsilon_A - \varepsilon_B}{\sqrt{\varepsilon_{pool}\cdot(1-\varepsilon_{pool})\cdot\left(\frac{1}{d_A}+\frac{1}{d_B}\right)}}, \tag{12}$$

where:

ε_A and ε_B are the observed error rates for the two publishers, calculated as: $\varepsilon_A = \frac{e_A}{d_A}$, $\varepsilon_B = \frac{e_B}{d_B}$;

d_A and d_B are the numbers of documents analyzed for each publisher;

ε_{pool} is the pooled error rate, computed as: $\varepsilon_{pool} = \frac{e_A + e_B}{d_A + d_B}$.

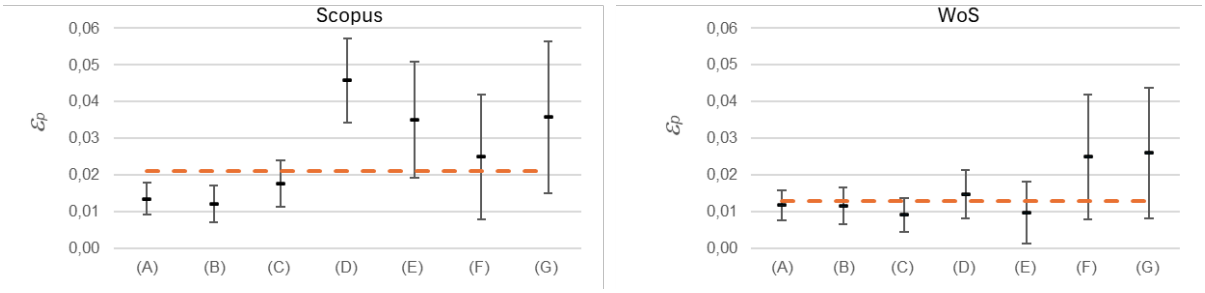


Figure 2 *– ε_p values and corresponding 95% CIs for Scopus (on the left) and WoS (on the right). The numerical values are provided in Table 4. The horizontal dashed line represents the overall error rate (ε) of the referenced database. On the x-axis the related publisher listed in descending order based on the total number of documents included in the analysis (cf. Fig. 1 and Table 4).*

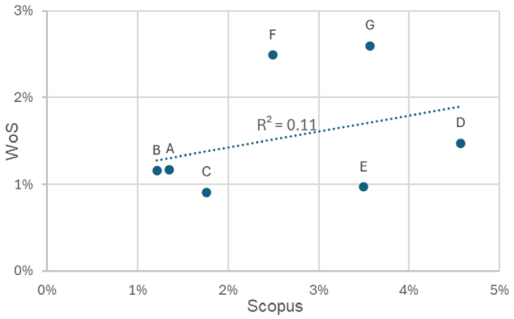
Table 5 *– Contingency table of z-values for pairwise comparisons of error rates. Values where* $|z| > 1.96$ *are highlighted in bold.*

		(A) Elsevier	(B) MDPI	(C) IEEE	(D) Springer Nature	(E) John Wiley & Sons, Inc.	(F) Taylor & Francis Group	(G) IOP Publishing Ltd
Scopus	(A) Elsevier	0.00	0.40	-1.07	**-6.25**	**-3.46**	-1.60	**-2.96**
	(B) MDPI	-0.40	0.00	-1.33	**-5.78**	**-3.51**	-1.79	**-3.09**
	(C) IEEE	1.07	1.33	0.00	**-4.44**	**-2.36**	-0.88	**-2.06**
	(D) Springer Nature	**6.25**	**5.78**	**4.44**	0.00	1.02	1.67	0.77
	(E) John Wiley & Sons, Inc.	**3.46**	**3.51**	**2.36**	-1.02	0.00	0.81	-0.06
	(F) Taylor & Francis Group	1.60	1.79	0.88	-1.67	-0.81	0.00	-0.79
	(G) IOP Publishing Ltd	**2.96**	**3.09**	**2.06**	-0.77	0.06	0.79	0.00
WoS	(A) Elsevier	0.00	0.03	0.81	-0.80	0.39	**-1.97**	**-2.09**
	(B) MDPI	-0.03	0.00	0.72	-0.76	0.36	-1.90	**-2.01**
	(C) IEEE	-0.81	-0.72	0.00	-1.42	-0.13	**-2.41**	**-2.52**
	(D) Springer Nature	0.80	0.76	1.42	0.00	0.84	-1.27	-1.38
	(E) John Wiley & Sons, Inc.	-0.39	-0.36	0.13	-0.84	0.00	-1.73	-1.81
	(F) Taylor & Francis Group	**1.97**	1.90	**2.41**	1.27	1.73	0.00	-0.08
	(G) IOP Publishing Ltd	**2.09**	**2.01**	**2.52**	1.38	1.81	0.08	0.00

In practice, after computing the *z*-statistic (Eq. 12), it is compared with the critical value $z_{1-\frac{\alpha}{2}} \approx 1.96$ for $a = 5\%$. If $|z| > 1.96$, the null hypothesis is rejected, indicating that the two error rates (ε_A and ε_B) are statistically different [10]. The procedure is then repeated for all $\binom{7}{2} = 21$ possible pairwise comparisons. With regard to Scopus, three pairwise comparisons (bolded) show statistically significant differences, confirming the findings of the previous statistical tests. The pairwise comparisons revealing the largest differences involve publishers "Springer Nature", "John Wiley & Sons, Inc." and "IOP Publishing Ltd". With regard to WoS, it is observed that "Taylor and Francis Group" and "IOP Publishing Ltd" exhibit statistically significant differences compared with the other publishers, as they tend to have higher ε_p values (cf. boxplots in Fig. 2). The results from each database's perspective can be summarized into the map in Fig. 3, which plots the ε_p values for Scopus on the *x*-axis and those for WoS on the *y*-axis, for each of the 7 (macro-)publishers. Notably, there appears to be no significant correlation between the publishers that are most "critical" for one database (in terms of ε_p values) and those that are most critical for the other, as indicated by the relatively low $R^2 = 0.11$. This finding suggests that the two databases may differ in their familiarity with handling DTs for specific publishers. The causes of this apparent independence will be investigated in future studies, including: (a) the two databases may adopt different DT classification rules, which could align closely with the editorial standards of specific publishers, leading to varying error patterns and (b) some publishers may have a closer relationship with a given database (e.g., Elsevier and the Scopus database are part of the same organization

Materials Research Proceedings 57 (2025) 80-89 https://doi.org/10.21741/9781644903735-10

(RELX Group), which could reduce the likelihood of classification errors or facilitate their prompt correction when they occur) [11].



Publisher		Scopus	WoS
(A)	Elsevier	1.4%	1.2%
(B)	MDPI	1.2%	1.2%
(C)	IEEE	1.8%	0.9%
(D)	Springer Nature	4.6%	1.5%
(E)	John Wiley & Sons, Inc.	3.5%	1.0%
(F)	Taylor & Francis Group	2.5%	2.5%
(G)	IOP Publishing Ltd	3.6%	2.6%

Figure 3 – *Map comparing the* $\boldsymbol{\varepsilon_p}$ *results for the two databases: Scopus (x-axis) and WoS (y-axis).*

4. Concluding remarks

This research yielded several findings of interest for academic researchers in the field of engineering/manufacturing. Firstly, while DT-classification errors can be considered relatively rare events, their occurrence is nonetheless significant in both Scopus (error rate ~2.1%) and WoS (error rate ~1.3%) (cf. ***RQ1***). In addition to influencing various types of academic assessments—such as evaluations of individual researchers for career advancement, rankings of groups of researchers for funding calls, etc.—these errors could lead to more specific effects in the engineering/manufacturing sector. For instance, they could cause the distortion of metrics related to technology transfer and industrial innovation of research groups/institutions.

A deeper analysis from the publishers' perspective revealed statistically significant differences in their propensity to incur DT-classification errors. Specifically, Scopus appears to struggle more with publishers "Springer Nature", "IOP Publishing Ltd" and "John Wiley & Sons, Inc.", with relevant ε_p values of ~4.6%, ~3.6% and ~3.5% respectively, whereas WoS shows higher error rates with publishers "IOP Publishing Ltd" and "Taylor & Francis Group", with relevant ε_p values of ~2.6% and ~2.5% respectively (cf. ***RQ2***). The reasons behind these discrepancies remain to be thoroughly investigated, but they could include various factors (cf. ***RQ3***). Possible causes include differences in editorial conventions, alignment with database classification rules, and the diversity of DTs within publishers' portfolios (i.e., larger publishers span a broader range of disciplines—even within the same field—and manage extensive portfolios of journals and books; this increased diversity of DTs may lead to a higher likelihood of DT-classification errors). Mergers and acquisitions (M&A), where smaller publishers are absorbed by larger groups, may also influence DT-classification consistency, as editorial standards can either remain unchanged or be adapted to align with the acquiring publisher's guidelines.

From a practical standpoint, this work aims to raise awareness of the possibility of DT-classification errors and the fact that, depending on the database in use, documents from certain publishers may be at a higher risk of misclassification. In general, although Scopus and WoS do not seem to routinely conduct periodic reviews of the accuracy of indexed data, such as by cross-referencing results with those of competing databases, they do appear to be relatively responsive in addressing reported errors through designated channels [12].

This study has some limitations, primarily its focus on engineering/manufacturing, which may restrict the generalizability of the findings to other disciplines [13,14]. Additionally, some documents were excluded, such as those without DOI codes or those assigned multiple DT-classifications in WoS. Future research will seek to expand the sample to a broader range of

scientific fields and further investigate the underlying causes of publisher-specific classification discrepancies.

Acknowledgements
This study was carried out within the MICS (Made in Italy – Circular and Sustainable) Extended Partnership and was partially funded by the European Union Next-GenerationEU (PIANO NAZIONALE DI RIPRESA E RESILIENZA (PNRR) – MISSIONE 4 COMPONENTE 2, INVESTIMENTO 1.3 – D.D. 1551.11-10-2022, PE00000004). This manuscript reflects only the authors' views and opinions, neither the European Union nor the European Commission can be considered responsible for them.

References

[1] Harzing, A. W. (2013). Document categories in the ISI Web of Knowledge: Misunderstanding the social sciences?. Scientometrics, 94(1), 23-34. https://doi.org/10.1007/s11192-012-0738-1

[2] Donner, P. (2017). Document type assignment accuracy in the journal citation index data of Web of Science. Scientometrics, 113(1), 219-236. https://doi.org/10.1007/s11192-017-2483-y

[3] Franceschini, F., Maisano, D., Mastrogiacomo, L. (2015). Influence of omitted citations on the bibliometric statistics of the major Manufacturing journals. Scientometrics, 103(3), 1083-1122. https://doi.org/10.1007/s11192-015-1583-9

[4] García-Pérez M.A. (2010) Web of Science, PsycINFO, and Google Scholar: A case study for the computation of h indices in psychology. Journal of the American society for information science and technology, 61/10: 2070-85. https://doi.org/10.1002/asi.21372

[5] Sigogneau, A. (2000). An analysis of document types published in journals related to physics: Proceeding papers recorded in the Science Citation Index database. Scientometrics, 47(3), 589-604. https://doi.org/10.1023/A:1005628218890

[6] Mokhnacheva, Y. V. (2023). Document Types Indexed in WoS and Scopus: Similarities, Differences, and Their Significance in the Analysis of Publication Activity. Scientific and Technical Information Processing, 50(1), 40-46. https://doi.org/10.3103/S0147688223010033

[7] Maisano, D.A., Mastrogiacomo, L., Ferrara L., and Franceschini F. (2025) A large-scale semi-automated approach for assessing document-type classification errors in bibliometric databases. Scientometrics, 130, 1901-1938. https://doi.org/10.1007/s11192-025-05244-y

[8] Franceschini, F., Maisano, D. (2014). Sub-field normalization of the IEEE scientific journals based on their connection with Technical Societies. Journal of Informetrics, 8(3), 508-533. https://doi.org/10.1016/j.joi.2014.04.005

[9] Haupka, N., Culbert, J. H., Schniedermann, A., Jahn, N., Mayr, P. (2024). Analysis of the Publication and Document Types in OpenAlex, Web of Science, Scopus, PubMed and Semantic Scholar. arXiv preprint arXiv:2406.15154.

[10] Ross, S.M. (2017). Introductory statistics. Academic Press (Elsevier), London. https://doi.org/10.1016/B978-0-12-804317-2.00031-X

[11] Franceschini, F., Maisano, D., Mastrogiacomo, L. (2016). Empirical analysis and classification of database errors in Scopus and Web of Science. Journal of informetrics, 10(4), 933-953. https://doi.org/10.1016/j.joi.2016.07.003

[12] Franceschini, F., Maisano, D., & Mastrogiacomo, L. (2016). Do Scopus and WoS correct "old" omitted citations? Scientometrics, 107, 321-335. https://doi.org/10.1007/s11192-016-1867-8

[13] Franceschini, F., & Maisano, D. (2011). Bibliometric positioning of scientific manufacturing journals: A comparative analysis. Scientometrics, 86(2), 463-485. https://doi.org/10.1007/s11192-010-0301-x

[14] Franceschini, F., Maisano, D., Turina, E. (2012). European research in the field of production technology and manufacturing systems: an exploratory analysis through publications and patents. The International Journal of Advanced Manufacturing Technology, 62(1-4), 329-350. https://doi.org/10.1007/s00170-011-3791-7

Additive manufacturing and reverse engineering



Materials Research Proceedings 57 (2025) 91-98 https://doi.org/10.21741/9781644903735-11

The effect of additive manufacturing-induced anisotropy on tool wear when machining martensitic nitinol

Flavia Tucci[1,a,*], Rachele Bertolini[1,b], Andrea Ghiotti[1,c], Stefania Bruschi[1,d]

[1]Department of Industrial Engineering, University of Padova, via Venezia 1, 35131 Padova, Italy

[a]flavia.tucci@unipd.it, [b]rachele.bertolini@unipd.it, [c]andrea.ghiotti@unipd.it, [d]stefania.bruschi@unipd.it

Keywords: Powder Bed Fusion, Nitinol, Turning

Abstract. Machining Nitinol (NiTi), one of the most exploited shape memory alloys in biomedical and aerospace fields, is challenging, with rapid cutting tool wear being a significant issue. This study evaluates how the anisotropy of martensitic NiTi, induced by laser powder bed fusion (LPBF), affects tool wear. NiTi samples were printed in two orientations, 0° and 90°, corresponding to vertical and horizontal directions relative to the building one. The printed samples were machined on a CNC lathe and flank wear was measured via SEM analysis. LPBF induced an anisotropic microstructure with different grain sizes, phase distributions, and mechanical properties, which, in turn, affected the material response to cutting. Tool wear analysis showed how the printing orientation influenced the interaction between the workpiece and tool, with the 0° samples causing higher tool wear than the 90°. This behavior was ascribed to the different morphology of the microstructure in the turned sections and a higher amount of austenitic phase characterizing the 0° samples than the 90° ones.

Introduction

Shape memory alloys (SMAs), such as Nitinol, have reached significant importance in many engineering applications in recent years. They have two unique thermomechanical properties: the so-called shape memory effect (SME), which is the ability to store a macroscopic geometrical configuration and completely recover it following heat-imparted deformation, and superelasticity (SE), which is the capability to undergo larger deformations than traditional metal alloys, that are restored once the load is removed without plastic deformation [1]. Both properties are attributed to the austenitic-martensitic phase transformation, which can either be triggered by stress or temperature changes. Depending on the different imposed thermomechanical stress conditions, SMAs exhibit two different crystallographic phases called the austenitic (or parent) phase and the martensitic phase [2]. However, the actual chemical composition of the alloy determines which phase is stable at room temperature. When the nickel content is relatively high (Ni-rich alloys), the material is austenitic at room temperature and is superelastic. Conversely, with decreasing nickel content (towards equiatomic or slightly richer in Ti composition), the martensitic start temperature (Ms) is considerably above room temperature, thereby ensuring the stability of the martensitic phase at room temperature. Hence, the alloy cannot exhibit SE at room temperature but can exhibit the SME at high temperatures once it is heated above the martensitic-to-austenitic transformation temperature [3]. In recent years, additive manufacturing (AM) has been increasingly adopted for producing NiTi parts, replacing traditional casting and powder metallurgy techniques [4]. AM allows the production of a wider variety of geometric shapes and significantly reduces material waste, in contrast with subtractive manufacturing methods. Among the different AM techniques, laser powder bed fusion (LPBF) is the most commonly employed, as it enables high precision and detailed control of process parameters [5]. However, in most cases, as-built parts require further processing to achieve their final shape, with machining being one of the most common finishing methods. NiTi machinability is quite challenging because of its previously

Content from this work may be used under the terms of the Creative Commons Attribution 3.0 license. Any further distribution of this work must maintain attribution to the author(s) and the title of the work, journal citation and DOI. Published under license by Materials Research Forum LLC.

Materials Research Proceedings 57 (2025) 91-98 https://doi.org/10.21741/9781644903735-11

mentioned unique functional properties (e.g., SE and SME), high deformation resistance, toughness, low thermal conductivity, and pronounced strain hardening [6]. One of the most relevant indicators of the NiTi poor machinability is the high tool wear that develops during the cutting process. The combination of high mechanical strength, toughness, and strain hardening increases friction and heat generation at the tool-workpiece interface, accelerating the tool degradation. In addition, the generation of build-up edge (BUE) due to the NiTi tendency to adhere to the cutting tool affects its wear. The type of wear is also strongly influenced by the tool material, which directly impacts the machining performance. These difficulties in machining are further exacerbated by the microstructural anisotropy introduced by the AM process, as it can cause fluctuations in cutting forces, ultimately affecting tool wear and overall machining performance [7]. Anisotropy refers to the variation in the material mechanical or physical properties depending on the direction along which they are evaluated. The primary axis of the printed part doesn't always correspond to the axis perpendicular to the building platform, giving rise to the concept of 'building orientation'. This orientation affects the extent of overlap of successive printing layers, influencing the thermal gradient and, thus, the material microstructure. The columnar grains always tend to grow in the direction of heat dissipation, which typically coincides with the building direction (BD) itself [8]. Prior studies investigated the AM-induced anisotropy of as-built austenitic NiTi parts and its effect on the material mechanical properties. On the other hand, very few studies present a comprehensive analysis of the anisotropy of as-built martensitic NiTi. For instance, the superelastic behavior of as-built austenitic LPBF NiTi specimens was analyzed in [9], examining how the building orientation influenced the critical stress and strain recovery. The former, defined as the stress at which a 0.2% deviation from the initial linear elastic behavior occurs in a tensile test, was found to be 31% lower in specimens with their axis parallel to the BD compared to those with their axis perpendicular. Moreover, specimens with their axis perpendicular to the BD exhibited a 0.5% residual strain, whereas those with their axis parallel displayed complete strain recovery. These findings suggest that in the case of a part that demands a maximum strain recovery in a certain direction, it is advisable to print it with the loading axis parallel to the building direction, whereas if the part may allow small amounts of plastic deformation, then horizontal orientation is also a viable option. One recent work [3] on martensitic NiTi demonstrated that the physical and mechanical property variations are smaller in vertically (V-built) compared to horizontally (H-built) built samples. However, fluctuations in H-built samples were found to be strongly correlated with the LPBF parameters, suggesting that this orientation offers greater control over material properties and shape memory functionality. In addition, the study illustrated to what extent the applied strain influences the SME, which, in turn, affects the amount of unrecovered residual strain. The reported characteristics of LPBF austenitic and martensitic NiTi are typically examined in their as-built condition. On the contrary, few studies have explored the impact of AM-induced anisotropy on the alloy's machinability. In this context, the present work aims to investigate how microstructural variations induced by building orientation influence the behavior of martensitic LPBF NiTi, both in its as-built state and after machining, the latter with a particular focus on tool wear and machined surface quality, quantified in terms of surface roughness.

Materials and methods

NiTi gas-atomized powders were supplied from Eckart™, with a chemical composition of 50.1 at% Ni and 49.9 at% Ti that makes the material martensitic at room temperature. The powders had spherical shape and size range of 15-45 μm. Cylinders of 16 mm diameter and 40 mm height were printed vertically and horizontally - namely 0° and 90° orientations - with respect to the building direction (BD) (see Fig. 1a) using a MYSINT100 SISMA™ LPBF machine, operating in an argon atmosphere. To minimize the deformation and detachment of the cylinders from the platform, 5 mm high supports were printed. The chosen scanning strategy followed the island pattern with a

Materials Research Proceedings 57 (2025) 91-98 https://doi.org/10.21741/9781644903735-11

laser power of 70 W, scanning speed of 1100 mm/s, hatching distance of 0.06 mm, and layer thickness of 0.025 mm. These process parameters were previously optimized to obtain fully dense parts [10]. No post-AM heat treatment was performed, as, unlike in the case of austenitic NiTi, it would not have significantly altered the relevant functional properties, such as the shape memory effect (SME). Three cylinders were printed and further processed for each orientation for the sake of repeatability. Small pieces were metallographically prepared from the LPBF cylinders for microstructural characterization before and after machining. First, the cylinders were sectioned using a QATM™ Brillant 210A compact automatic precision cutting machine able to minimize thermal effects that can unevenly modify the martensitic NiTi behavior. For 0° and 90° cylinders, cutting processing was performed both perpendicularly and parallel to the BD (see Fig. 1a). Subsequently, the cut pieces were cold embedded in epoxy resin, sanded with silicon carbide abrasive papers to 4000 grit, and polished with a suspension of colloidal silica (SiO_2) mixed with hydrogen peroxide. A chemical color etching was performed to reveal the microstructure, which allowed for the differentiation of grains with different crystallographic orientations through color variations resulting from varying levels of oxidation and light interference. The chemical solution used for the color etching consisted of 3 mL of HCl, 5 g of $K_2S_2O_5$, 0.4 g of NH_4HF_2, and 24 mL of H_2O, with an optimal exposure time of 40 seconds. These features are visible only under a polarized light microscope. A Leica™ DMR optical microscope, equipped with a Zeiss™ AxioCam ERc5s camera, was used for imaging. The average grain size was calculated using a Matlab™ code, which implements the intercept method from micrographs [11]; these measurements were specifically taken from the highlighted section of both 0° and 90° samples shown in Fig. 1. Thermal characterization was executed using differential scanning calorimetry (DSC) on a Q200™ DSC to determine the NiTi main transformation temperatures such as martensite start M_s, martensite finish M_f, austenite start A_s, and austenite finish A_f. In addition, enthalpy (ΔH) values were obtained, which indicate the thermal energy uptake or release taking place across these phase transitions of martensite and austenite. The DSC was performed according to the ASTM standard F2004-17 [12], which establishes the method for determining the transformation temperatures of nickel-titanium alloys by thermal analysis. Hardness measurements were performed using an iMicro Nanoindenter™ (Nanomechanics, Inc.) equipped with a Berkovich pyramid tip. Hardness values in Vickers (HV) were obtained through the conversion algorithms implemented in the InView™ Review Data software. To assess the effect of anisotropy on LPBF NiTi machinability, all cylinders were longitudinally turned on a Mori Seiki™ CNC lathe using VCEX 110301L F-1125 inserts. This type of tool is suitable for machining ISO S-class materials, which include nickel and titanium alloys. These are materials that harden during machining, generating significant heat, and tend to adhere to the tool, thus generating the built-up edge (BUE) adhesion wear phenomenon. A conventional continuous-flow lubrication was employed. The chosen cutting parameters, optimized by the authors in a previous study [13], were cutting speed (V_c) of 50 m/min, cutting depth (a_p) of 0.35 mm, and feed rate (f) of 0.05 mm/rev. A Kistler™ Type 9129AA dynamometer was mounted on the lathe to measure the cutting force (F_c), the radial force (F_r), and the feed force (F_t) with a fixed sampling rate of 2500 Hz (see the scheme in Fig. 1b). For each test condition, a fresh tool was used to properly assess the tool life and compare it across different building orientations. Tool wear characterization was carried out by examining the progressive flank wear of the tool using SEM inspection with the Backscattered Electron Detector (BSED). Surface roughness was assessed using a Sensofar Metrology™ S Neox 3D optical profiler, which features a Nikon™ 20x confocal objective. The scans obtained were then processed with the Sensofar Metrology™ SensoSCAN software. The arithmetic mean roughness (Ra) was chosen as the primary parameter, providing a quantitative measure of the overall surface texture. Measurements were conducted according to ISO 16,610-61:2015 [14], utilizing a 2.5 μm S-filter and a 250 μm L-filter.

Materials Research Proceedings 57 (2025) 91-98 https://doi.org/10.21741/9781644903735-11

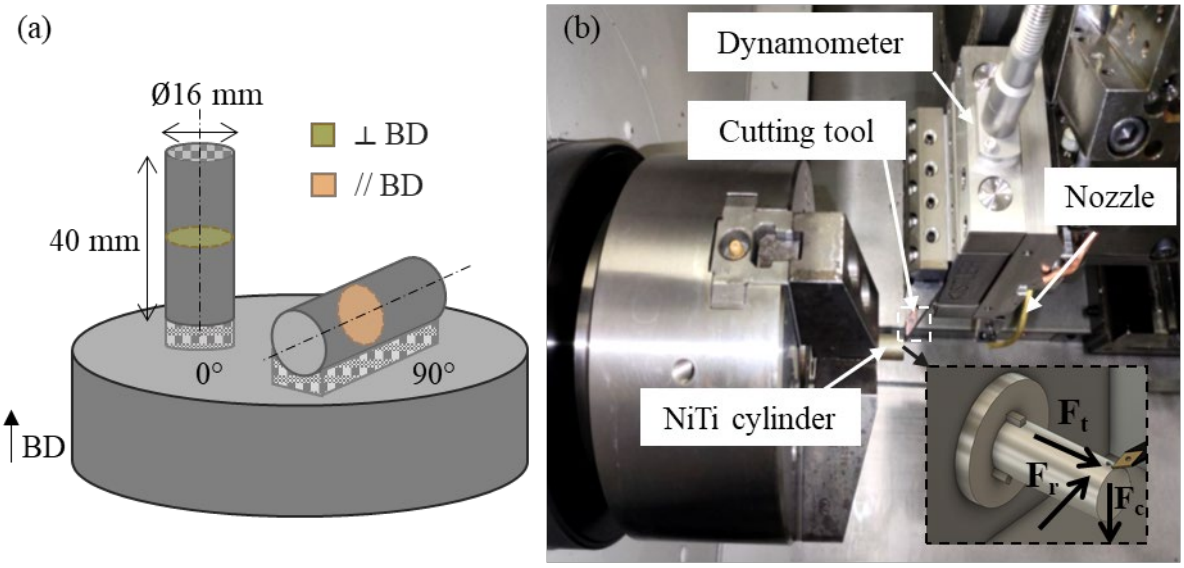
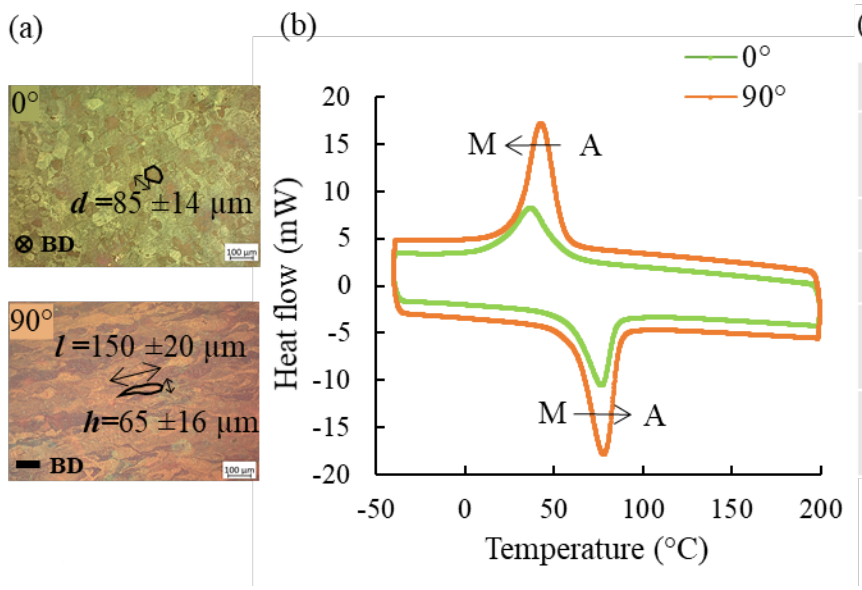


Figure 1. LPBF NiTi cylinders configurations and sections interested in the cutting process(a); experimental turning setup with a close-up of the cutting force scheme (b).

Results and discussion

Microstructural examination revealed that both samples printed with 0° and 90° orientations exhibit a dual microstructure, with columnar grains in the section parallel to the BD and equiaxed grains in the section transverse to the BD. This is an intrinsic characteristic of the LPBF process due to the directional heat flow during solidification. In the samples at 0°, the section along the BD shows an equiaxed microstructure with an average grain size of 85 ± 14 μm, while the section along the BD shows columnar grains with an orientation along the BD typical of layer-by-layer solidification. As expected, in the 90° samples, the section perpendicular to the BD shows an equiaxed microstructure, but the section parallel to the BD shows elongated columnar grains with an average length of 150 ± 20 μm and an average height of 65 ± 16 μm (see Fig. 2a). For the purpose of this study, the cross-section involved in the machining differs depending on the building orientation of the sample (see Fig. 1a). The machined surface of the 0° samples corresponds to the section perpendicular to the BD with equiaxed microstructure. Instead, the machined surface of the 90° samples corresponds to the section parallel to the BD, where elongated columnar grains are present. This distinction will help to understand the role played by the microstructure on machining behavior and tool wear in each of these building orientations. The analysis of the transformation temperatures in the 0° and 90° samples shows differences caused by the microstructure generated by the printing direction. The 0° samples showed a slight increase in the austenite-martensite transformation start temperature, M_s, and an increase in the transformation end temperature, M_f, which means that the transformation from austenite to martensite occurred more progressively. For the reverse transformation, the 90° samples showed a higher martensite-austenite transformation start temperature, A_s, but the transformation end temperature A_f was similar for both sample configurations. The DSC study also showed a difference in the transformation enthalpies - corresponding to the area under the endothermic ($\Delta H_{M\rightarrow A}$) and exothermic ($\Delta H_{A\rightarrow M}$) peaks - with increased values for the 90° samples compared to the 0° ones. This suggests that the austenite-to-martensite transformation in the 90° samples involves and releases more energy than in the 0° samples. In addition, the 0° samples exhibit lower M_f, reflecting a higher fraction of austenite at room temperature.

Materials Research Proceedings 57 (2025) 91-98 https://doi.org/10.21741/9781644903735-11



(c)

	0°	90°
M_s [°C]	57.12	55.70
M_f [°C]	17.05	24.38
A_s [°C]	58.99	60.43
A_f [°C]	87.40	87.0
$\Delta H_{M\rightarrow A}$ [J/g]	25.04	27.29
$\Delta H_{A\rightarrow M}$ [J/g]	26.92	29.13

Figure 2. Microstructure (a), DSC curves (b), transformation temperatures and enthalpies from the DSC curves (c) of the as-built 0° and 90° samples in the sections of interest in the cutting process.

Furthermore, nanoindentation measurements performed on the section perpendicular to the building direction revealed average hardness values of 494 ± 33 HV for the 0° samples and 412 ± 30 HV for the 90° ones, both in the as-built state. The building orientation had a significant impact on the cutting tool wear (Fig. 3a) and cutting forces registered during turning (Fig. 4a). Tool wear occurred through various mechanisms, namely adhesion, BUE, and notch wear (Fig. 3b). According to ISO3685 [15], the primary wear mechanism observed, which is **notch wear**, was analyzed. This type of **wear** is particularly common in **Ni-based alloys – also called V-shaped notch –** and typically occurs in regions located at a distance **at least equal to the depth of cut** from the tool tip (i.e., 'N' zone), resulting from a combination of abrasive, adhesive, and oxidative wear mechanisms. This is consistent with previous studies, as the one in [16], where tool abrasion and adhesion, especially in the 'N' zone, were generally ascribed to the NiTi high hardness and low thermal conductivity. Despite a broadly similar average trend in the early wear stages, there was a notable increase in notch wear when machining 0° samples, with a rapid rise in the wear width (VB_N) after about 1.5 min of machining, compared to 90° samples (see Fig. 3a). This behavior can be related to the equiaxed grain structure of the section interested to the turning process in the 0° samples: the cutting tool encounters more grain boundaries, which offer more resistance to cutting compared to the section of the 90° samples. The latter offers indeed a columnar microstructure to the cutting tool action, characterized by a reduced density of grain boundaries and, therefore, less resistance. The data presented in Fig. 3a correspond to the mean values obtained from three replicates for each test condition. Error bars represent the standard deviation. It showed little variability, confirming the consistency and robustness of the experimental procedure. Notch wear shows a non-linear trend with alternating increases and decreases due to the interplay between abrasive and adhesive mechanisms and the intermittent formation of protective layers that temporarily slow the wear. In addition, as can be seen in Fig. 3b, the 90° samples are less prone to provoke adhesion on the tool. In summary, the reduced tool wear seen in the 90° samples indicates that this configuration is more advantageous for cutting, leading to prolonged tool life. The higher hardness of the 0° samples supports this assumption. Besides a different morphology of the microstructure interested by the cutting action, the 90°

Materials Research Proceedings 57 (2025) 91-98 https://doi.org/10.21741/9781644903735-11

samples show a more energy-absorbing phase transformation (see Fig. 2b-c), which implies the existence of a higher volume fraction of martensite at room temperature, compared to the 0° samples. This can further explain the higher machinability of the 90° samples, being martensite softer and, therefore, easier to machine. The values of the average cutting forces registered during turning are in agreement with the tool wear evolution for the two samples' configurations: at an early stage of cutting, the values are quite close, but when the turning inserts of the 0° samples reached the end of life, the average cutting force increased to 171 N, while, when turning the 90° samples, the cutting force was significantly lower, namely 110 N (see comparison in Fig. 4a). The higher forces requested for cutting the 0° samples reflect the higher resistance to material removal, already underlined to explain the observed tool wear. The average roughness Ra of the 90° samples turned at the tool end-of-life was lower than that of the 0° samples (see Fig. 4b). The superior surface quality of the 90° samples can be attributed to their columnar microstructure, which facilitates the cutting process and minimizes surface irregularities (the latter evident from the surface topographies shown in Fig. 4b). Additionally, the lower adhesion observed in the tools cutting the 90° samples further contributed to the improved surface finish. In terms of surface quality, the results suggest that the 90° orientation results in a better part finish, reducing the need for post-process surface improvement machining.

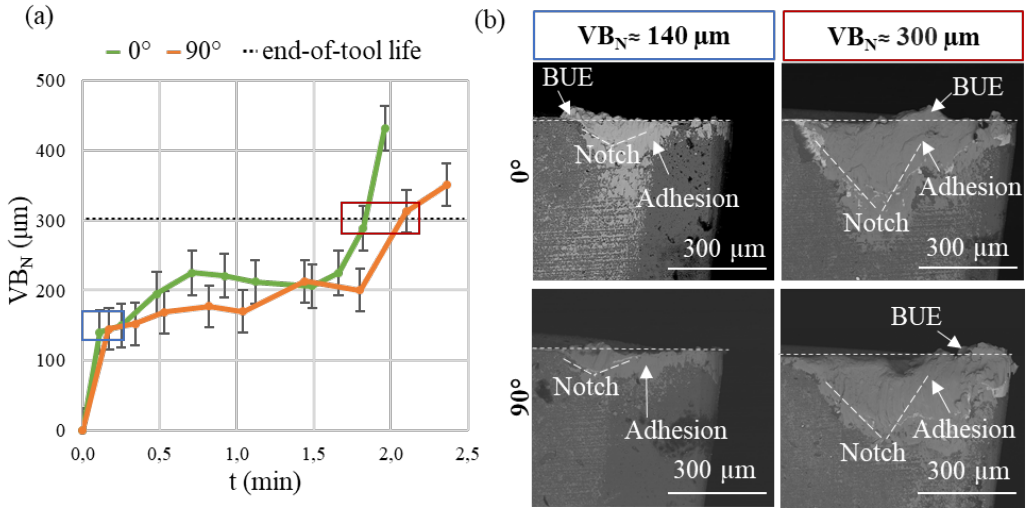


Figure 3. Notch wear width vs. machining time, the error bars indicate the standard deviation (a); SEM images of the tool wear at early stage and end-of-life (b) when cutting the 0° and 90° samples.

Materials Research Proceedings 57 (2025) 91-98 https://doi.org/10.21741/9781644903735-11

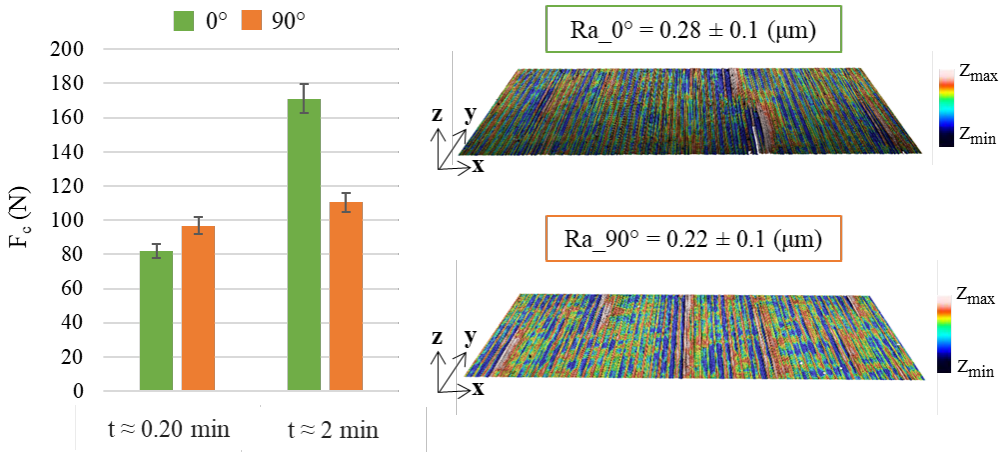


Figure 4. Average cutting forces at early stage of tool wear (t ≈ 0.20 min) and end-of-life (t ≈ 2 min) (a), surface topographies of the 0° and 90° samples turned at the tool end-of-life with Ra values (± standard deviation) (b).

Conclusions

Microstructural anisotropy induced by LPBF in martensitic Nitinol significantly influences tool wear. Higher tool wear and reduced machined surface finish were evidenced when turning samples oriented at 0° with respect to the building direction compared to samples oriented at 90°. This was attributed to the equiaxed microstructure characterizing the section interested in the cutting in the 0° samples, which has a higher density of grain boundaries, and the greater presence of the austenitic phase, as evidenced by microstructural observations and DSC analysis conducted before machining, These findings underscore the importance of the building orientation in Nitinol printing, particularly in relation to machining performance, including tool life, cutting forces, and overall part quality. The 90° orientation, which has the section interested in cutting along the building direction, is seen to be more advantageous in terms of machinability. It is worth noting that, in standard production environments, a tool life of two minutes, as obtained in this study, would generally be considered unacceptable unless justified by unique process requirements or material constraints. Anyway, for actual industrial applications, optimization of cutting parameters, tool material or coatings would be required to achieve a more cost-effective tool life.

References

[1] E. Patoor, D. C. Lagoudas, P. B. Entchev, L. C. Brinson, and X. Gao, “Shape memory alloys, Part I: General properties and modeling of single crystals,” Mechanics of Materials, 2006, vol. 38, no. 5-6, pp. 391–429. https://doi.org/10.1016/j.mechmat.2005.05.027

[2] J. Van Humbeeck, “Shape memory alloys: a material and a technology,” Advanced Engineering Materials, 2001, vol. 3, no. 11, pp. 837–850. https://doi.org/10.1002/1527-2648(200111)3:11%3C837::AID-ADEM837%3E3.0.CO;2-0

[3] J. C. Chekotu, G. Degli-Alessandrini, M. Z. Mughal, S. Chatterjee, R. Goodall, D. Kinahan, and D. Brabazon, “Control of mechanical and shape memory characteristics in martensitic NiTi by setting L-PBF parameters and build orientation,” Journal of Materials Research and Technology, 2023, vol. 25, pp. 6407–6431. https://doi.org/10.1016/j.jmrt.2023.07.092

[4] M. Elahinia, N. S. Moghaddam, M. T. Andani, A. Amerinatanzi, B. A. Bimber, and R. F. Hamilton, “Fabrication of NiTi through additive manufacturing: A review,” Progress in Materials Science, 2016, vol. 83, pp. 630–663. https://doi.org/10.1016/j.pmatsci.2016.08.001

[5] M. H. Elahinia, M. Hashemi, M. Tabesh, and S. B. Bhaduri, “Manufacturing and processing of NiTi implants: A review,” Progress in Materials Science, 2012, vol. 57, no. 5, pp. 911–946. https://doi.org/10.1016/j.pmatsci.2011.11.001

[6] R. Bertolini, S. Bruschi, A. Ghiotti, E. Savio, L. Ceseracciu, and I. S. Jawahir, “Surface integrity and superelastic response of additively manufactured Nitinol after heat treatment and finish machining,” CIRP Annals, 2023, vol. 72, no. 1, pp. 501–504. https://doi.org/10.1016/j.cirp.2023.04.025

[7] P. Guo, B. Zou, C. Huang, and H. Gao, “Study on microstructure, mechanical properties and machinability of efficiently additive manufactured AISI 316L stainless steel by high-power direct laser deposition,” Journal of Materials Processing Technology, 2017, vol. 240, pp. 12–220. https://doi.org/10.1016/j.jmatprotec.2016.09.005

[8] M. Nematollahi, S. E. Saghaian, K. Safaei, P. Bayati, P. Bassani, C. Biffi, and M. Elahinia, “Building orientation-structure-property in laser powder bed fusion of NiTi shape memory alloy,” Journal of Alloys and Compounds, 2021, vol. 873, p. 159791. https://doi.org/10.1016/j.jallcom.2021.159791

[9] G. Carlucci, L. Patriarca, A. G. Demir, J. N. Lemke, A. Coda, B. Previtali, and R. Casati, “Building orientation and heat treatments effect on the pseudoelastic properties of NiTi produced by LPBF,” Shape Memory and Superelasticity, 2022, vol. 8, no. 3, pp. 235–247. https://doi.org/10.1007/s40830-022-00391-0.

[10] S. Khademzadeh, F. Zanini, J. Rocco, K. Brunelli, P. F. Bariani, and S. Carmignato, “Quality enhancement of microstructure and surface topography of NiTi parts produced by laser powder bed fusion,” CIRP Journal of Manufacturing Science and Technology, 2020, vol. 31, pp. 575–582. https://doi.org/10.1016/j.cirpj.2020.08.009

[11] ASTM E112-13, “Standard Test Methods for Determining Average Grain Size,” ASTM International, 2013.

[12] ASTM F2004-17, “Standard Test Method for Transformation Temperature of Nickel-Titanium Alloys by Thermal Analysis,” ASTM International, 2017.

[13] R. Bertolini, F. Tucci, A. Ghiotti, I. S. Jawahir, and S. Bruschi, “Analysis of Tool Wear and Surface Integrity in Turning Wrought and Additively Manufactured $Ni_{50.8}Ti_{49.2}$ Shape Memory Alloys,” Wear, 2025, p. 205890, https://doi.org/10.1016/j.wear.2025.205890

[14] ISO 16610-61:2015, “Geometrical Product Specifications (GPS) – Filtration Part 61: Linear areal filters – Gaussian filters,” International Organization for Standardization, 2015.

[15] ISO 3685:1993(E), “International Standard, Tool testing with single point turning tools,” International Organization for Standardization, 1993.

[16] Y. Kaynak, H. E. Karaca, R. D. Noebe, and I. S. Jawahir, “Tool-wear analysis in cryogenic machining of NiTi shape memory alloys: A comparison of tool-wear performance with dry and MQL machining,” Wear, vol. 306, no. 1–2, pp. 51–63, 2013. https://doi.org/10.1016/j.wear.2013.05.011

Materials Research Proceedings 57 (2025) 99-106 https://doi.org/10.21741/9781644903735-12

Effect of process parameters on $AlCoCr_2FeMo_{0.5}Ni$ high-entropy alloy coatings produced using laser directed energy deposition

Chiara GIANASSI[1,a *], Erica LIVERANI[1,b], Alessandro ASCARI[1,c] and Alessandro FORTUNATO[1,d]

[1]Department of Industrial Engineering (DIN), Viale del Risorgimento 2, Alma Mater Studiorum – University of Bologna, Bologna, Italy

[a]chiara.gianassi2@unibo.it, [b]erica.liverani2@unibo.it, [c]a.ascari@unibo.it, [d]alessandro.fortunato@unibo.it

Keywords: Additive Manufacturing, Direct Energy Deposition (DED), Laser Processes, High-Entropy Alloys, Coating, Aeronautical & Aerospace

Abstract. In the aerospace sector, High-Entropy Alloys (HEAs) are emerging as promising alternatives to nickel superalloys for turbine components due to their exceptional thermal stability, fatigue strength, and corrosion resistance. HEAs, composed of five or more elements in near-equal proportions, typically form stable crystal structures. Additive manufacturing, notably Laser Directed Energy Deposition (L-DED), addresses the limitations of conventional fabrication methods. In this study, L-DED was used to print the $AlCoCr_2FeMo_{0.5}Ni$ HEA to produce defect-free deposits with strong substrate adhesion. Single-track and multi-track tests assessed the impact of laser power, scanning speed, and powder feed rate on defects, with optimal conditions identified through optical microscopy. SEM analysis provided insights into the microstructure and composition, while 3D mapping characterized the surface morphology and roughness. The results demonstrate the potential of L-DED for advanced HEA manufacturing.

Introduction

The aerospace industry is at the forefront of engineering innovation, requiring components capable of withstanding extreme operating conditions such as elevated temperatures and intense mechanical stresses. Turbine engine design has continually evolved to enhance power, fuel efficiency, and safety, demanding higher compression ratios and turbine inlet temperatures. As a result, materials engineering plays a crucial role in the development of high-performance turbines. Nickel-based superalloys, renowned for their strength and creep resistance, are the current material of choice for turbine engines [1]. However, their high density (approximately 9 $g \cdot cm^{-3}$) and reliance on critical raw materials have spurred interest in alternative solutions, including the evaluation of innovative materials such as High Entropy Alloys (HEAs). HEAs are a class of materials distinguished by their unique composition, typically consisting of five or more principal elements in equiatomic or near-equiatomic proportions (5–35%). Their high configurational entropy, combined with sluggish diffusion, lattice distortion, and the cocktail effect, imparts them unique mechanical and physical properties, including exceptional tensile strength, hardness and thermal stability [2]. While conventional fabrication methods like casting and sintering are commonly used for HEAs, these approaches limit design flexibility and control over features such as porosity and microstructure. Additive manufacturing (AM) techniques, particularly Directed Energy Deposition (DED), allow to overcome these limitations, enabling greater control over process and shorter production cycles. Among HEAs, AlCoCrFeNi alloys have emerged as promising candidates for aerospace applications due to their high strength, hardness, and oxidation resistance. Previous studies have explored their microstructure, phase composition, and mechanical properties [3, 4]. Moreover, researchers have investigated the effects of varying alloying elements [5], discovering that aluminum content significantly influences the formation of

Content from this work may be used under the terms of the Creative Commons Attribution 3.0 license. Any further distribution of this work must maintain attribution to the author(s) and the title of the work, journal citation and DOI. Published under license by Materials Research Forum LLC.

Materials Research Proceedings 57 (2025) 99-106 https://doi.org/10.21741/9781644903735-12

BCC structures [5] [6], and that the addition of molybdenum promotes the formation of high-hardness sigma-phase intermetallics [7]. Despite substantial progress, much of the existing research has focused on microstructural analysis and small-scale samples, with limited attention to the optimization of process parameters or large-scale depositions. This study aims to address these gaps by utilizing a pre-mixed $AlCoCr_2FeMo_{0.5}Ni$ alloy powder produced through gas atomization to ensure uniform chemical composition. Samples of progressively larger sizes were deposited using a single-track to multi-track approach in an effort to optimize the key process parameters, i.e. laser power, scan speed, and powder flow rate. The correlations between these parameters and the final properties of the samples were analysed, with a particular focus on microstructure, deposition defects and surface morphology.

Materials and Methods

The experimental campaign focused on the printing of $AlCoCr_2FeMo_{0.5}Ni$ High Entropy Alloy powder supplied by Heeger Materials Inc (CO, US). The powder had a particle size range of 45 – 106 μm, suitable for Directed Energy Deposition process. SS 316L austenitic stainless steel plate with a thickness of 10 mm was chosen as the substrate material. This choice aimed to minimize intergranular corrosion, prevent surface hardening – thanks to the low carbon content (< 0.03%) – and enhance oxidation resistance [6]. The chemical compositions of both the powder and substrate are reported in Table 1.

Table 1. Chemical compositions of the high-entropy alloy powder and substrate materials

[wt %]	***Al***	***Co***	***Fe***	***Cr***	***Mo***	***Ni***	***Mn***	***C***	***Si***	***N***
$AlCoCr_2FeMo_{0.5}Ni$	7.89	17.60	15.44	29.06	13.42	16.57	-	0.01	-	0.01
AISI 316L	-	-	bal.	18.58	0.44	8.40	1.69	0.02	0.44	0.11

The DED system used for the specimen production features a 6-axis ABB IRB 4600 robot, a GTV PS2/2 powder delivery system and a six-outlets GTV PN6625 nozzle with a standoff distance of 25 mm and a powder-jet focus of 2 mm. The heat source consists of a Laserline LDF-4500-60 diode laser with a maximum output power of 4.5 kW, equipped with OTS-5 focusing optics, resulting in a spot diameter of 2.2 mm on the print surface. Argon was used as both the carrier and shielding gas, with flow rates of 8 and 20 lpm, respectively. The experiment was organized into four progressively complex steps, with a decreasing number of samples per phase: (1) single-track depositions; (2) multi-track depositions with 8 adjacent tracks in a single-layer (2a) and double-layer (2b) configuration, and (3) multi-layer depositions with 8 layers using a scanning strategy that combines a contour path with a zig-zag infill pattern rotated by 90° at each layer. Single-track specimens were printed varying the main process parameters: laser power, scan speed, and powder flow rate. The laser source employed in the experimental campaign operates within a power range of 600 to 4500 W. To ensure comprehensive investigation, six power levels were selected to cover the entire range available, with a maximum limit of 3800 W imposed for safety considerations. Based on the chosen power values, the scanning speeds and powder feed rates were determined to achieve specific energy levels comparable to those reported in similar studies on AlCoCrFeNi alloys [3], [8], [9]. Table 3 summarizes the values considered in the study for each parameter. Specific energy (E) was calculated as:

$$E = \frac{P}{v \cdot D}$$

where P is the laser power, v is the scan speed, and D is the laser spot diameter.

Materials Research Proceedings 57 (2025) 99-106 https://doi.org/10.21741/9781644903735-12

Table 2. List of the experimental steps and deposition geometry

PHASE	DESCRIPTION	N. SPECIMENS	N. ADJACENT TRACKS	N. LAYERS
1	Single track	36	1	1
2A	Multi-track, 1 layer	12	8	1
2B	Multi-track, 2 layers	6	8	2
3	Multi-layer	2	25	8

Table 3. Laser power (P_L1 to P_L6), scan velocity (v_L1 to v_L3) and powder flow rate (g_L1 to g_L2) levels considered for single-track experiments

	L1	L2	L3	L4	L5	L6
POWER, *P* [W]	800	1400	2000	2600	3200	3800
SCAN VELOCITY, *V*	600	1020	1440			
POWDER FLOW RATE, *G*	10	17				

In order to determine the optimal process parameters for phases 2 and 3, a microstructural analysis of all the single tracks deposited in phase 1 was conducted by cutting cross-section from the center of the deposition, polishing and etching. The relative density was evaluated using a Zeiss AXIO Observer A1m optical microscope, while the microstructure was analyzed with a Tescan Mira3 SEM-FEG microscope. For the density evaluation, ImageJ software was used to calculate the porosity in the cross-section of each specimen. The relative density was then determined as (*100 – porosity*%), representing the percentage of the material's theoretical density achieved. Additionally, six 25 x 25 mm^2 single-layer specimens were fabricated to study the effects of laser power and scan speed on the deposition morphology, using the process parameters listed in the Results and Discussion section (Table 4). For each specimen, the surface profile of a 6.5 x 6.5 mm^2 area in the middle of the deposition was captured using a Keyence VHX-7000 digital optical microscope with 100x lens to generate 3D morphological maps. The surface maximum height (S_z) was calculated as the sum of the highest peak and the deepest valley within the area of interest, while the surface average roughness (S_a) represents the mean of the absolute height values at all points in the same area.

Results and Discussion

Process parameters optimization. In the single-track depositions, two criteria were established to define acceptable results: (i) absence of cracks or detachment and (ii) a relative density exceeding 99%. Visual inspection of the micrographs was used to verify the compliance with these requirements. The findings show that specimens fabricated with an energy density below 65 $J \cdot mm^{-2}$ are prone to cracking (Fig. 1). Among the crack-free depositions, samples produced at a scan speed of 600 $mm \cdot min^{-1}$ exhibited lower and more variable results compared to those produced at higher speeds. Tests conducted at 1020 and 1440 $mm \cdot min^{-1}$ achieved densities above 99.5%; consequently, the scan speed of 600 $mm \cdot min^{-1}$ was excluded from further testing. Summarizing the results of single-track experiments, requirements (a) and (b) were satisfied for scanning velocities v greater than 600 $mm \cdot min^{-1}$ and energy densities E greater than 65 $J \cdot mm^{-2}$. The final operating window was determined by solving this system of inequalities using the parameters listed in Table 3:

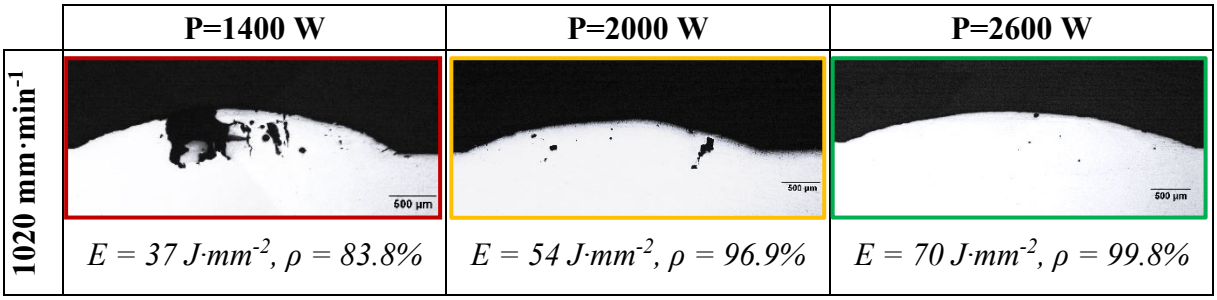
- For v = 1020 $mm \cdot min^{-1}$ it is required that P>2431 W. The power values that meet this condition are 2600, 3200 and 3800 W

Materials Research Proceedings 57 (2025) 99-106 https://doi.org/10.21741/9781644903735-12

- For v = 1440 mm·min^{-1} it is required that P>3432 W. Therefore, the only acceptable power value is 3800 W.

For both scanning speeds, the investigation in the following steps included also a power level slightly below the minimum acceptable threshold. This choice was based on the reasoning that a larger sample size, due to its longer interaction time, receives a higher total energy input, which could enable lower power levels to still achieve high densities.

Figure 1. Examples of single-track micrographs and their dependence on process parameters



For multi-track tests in single-layer configuration (step 2a), the combinations of laser power and scan speed resulted from the previous analysis and summarized in Table 4 were deposited at both 10 and 17 g·min^{-1}.

Table 4. Combinations of process parameters used for multitrack tests

Specimen	***Power,*** *P [W]*	***Scan velocity,*** *v [mm·min^{-1}]*	***Specimen***	***Power,*** *P [W]*	***Scan velocity,*** *v [mm·min^{-1}]*
1	2000	1020	4	3800	1020
2	2600	1020	5	3200	1440
3	3200	1020	6	3800	1440

Cracks were observed in all tests conducted at 17 g·min^{-1}. Consequently, a powder flow rate of 10 g·min^{-1} was selected and all the combinations in Table 4 were tested with two overlapping layers. Conditions 2 and 6 produced depositions with low porosity and no cracks (Fig. 2a, 2b). As a result, these parameters combinations were used for eight-layers multi-track tests, which similarly achieved high quality depositions with densities greater than 99% (Fig. 2c,2d).

The presence of cracks may be associated with adhesion issues between the deposited material and the substrate. Although not observed in single-track tests, this defect could have been exacerbated by the repeated thermal cycles during multi-track tests. Furthermore, as shown in the phase diagram of the alloy under study (Fig. 2e), intermetallic compounds can form in addition to BCC phases. Specifically, the sigma phase is a hard and brittle intermetallic compound whose formation is facilitated by the presence of molybdenum [7]. The phase diagram indicates that the sigma phase occupies a broad region and forms over a wide temperature range, making it highly likely to form and contribute to crack formation within the material.

Materials Research Proceedings 57 (2025) 99-106 https://doi.org/10.21741/9781644903735-12

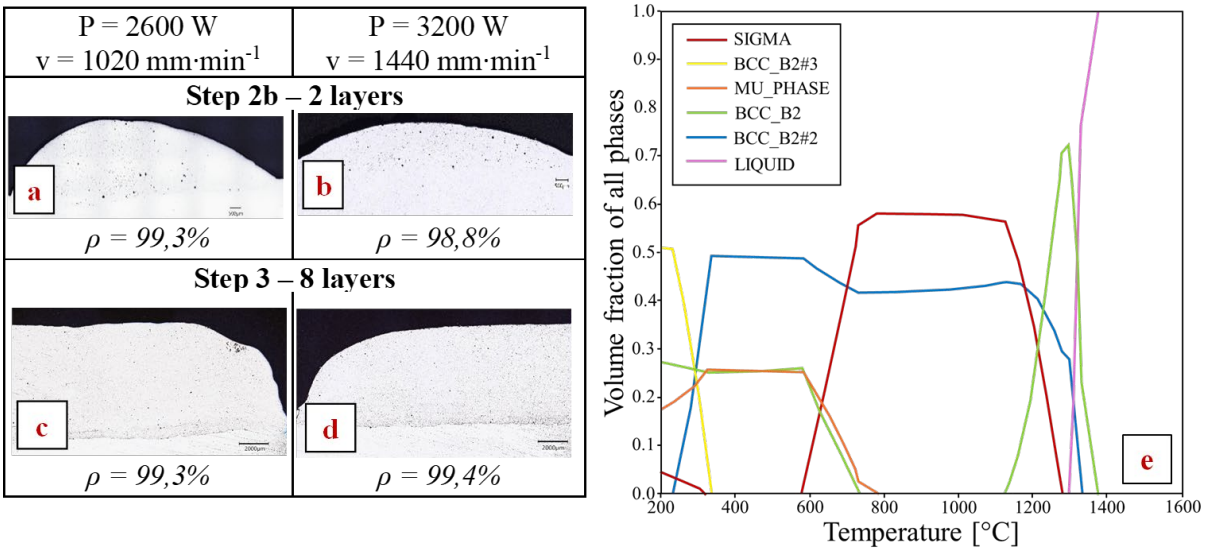


Figure 2. Photos of multitrack (a,b) and multilayer (c,d) tests with the optimal parameters; (e) phase diagram of $AlCoCr_2FeMo_{0.5}Ni$ alloy

Microstructural analysis. The microstructural study was performed comparing the results obtained both with optical and scanning electron microscopy, identifying four distinct regions within the deposition sections, consistent with observations by Sui et al. [3]: the interface, the planar grain zone, the transition zone, and the equiaxed grain zone.

The interface between the base material and the HEA deposition is characterized by a distinct change in microstructure. As shown in Fig. 3a, the lower section presents the austenitic grains of AISI 316L, while columnar HEA grains appear above the interface. Fig. 3b reveals a flake structure at the interface, with higher Fe and lower Al, Cr content, suggesting Fe diffusion from the substrate and possible segregation.

Above the dilution zone, elongated planar grains dominate the microstructure. Columnar grains grow in length when increasing the distance from the interface, influenced by the small grain size of the substrate and rapid cooling near the base. At higher deposition heights, slower cooling allows grain growth along the direction of heat flow, perpendicular to the interface. EDS results (Fig. 3c) show a higher concentration of Al and Fe within the crystals, while Cr and Mo tend to segregate at the grain boundaries. The presence of a Cr and Mo-rich phase is consistent with findings by Zhuang et al. [7].

Further from the interface, a transition from columnar to equiaxed grains occurs, visible under OM (Fig. 3d). The equiaxed grains nucleate in the liquid region ahead of the columnar grains, as described by Kurz et al. [10]. These differences in growth mechanisms result in varied morphologies: equiaxed grains form dendritic structures, while planar grains can exhibit cellular, planar, or dendritic patterns depending on local cooling conditions. A mixed microstructure is shown in Fig. 3e.

At greater deposition heights, grains fully transition to an equiaxed structure without a preferential orientation. At high-magnification, grain boundaries and fine dendritic structures are clearly distinguishable (Fig. 3f).

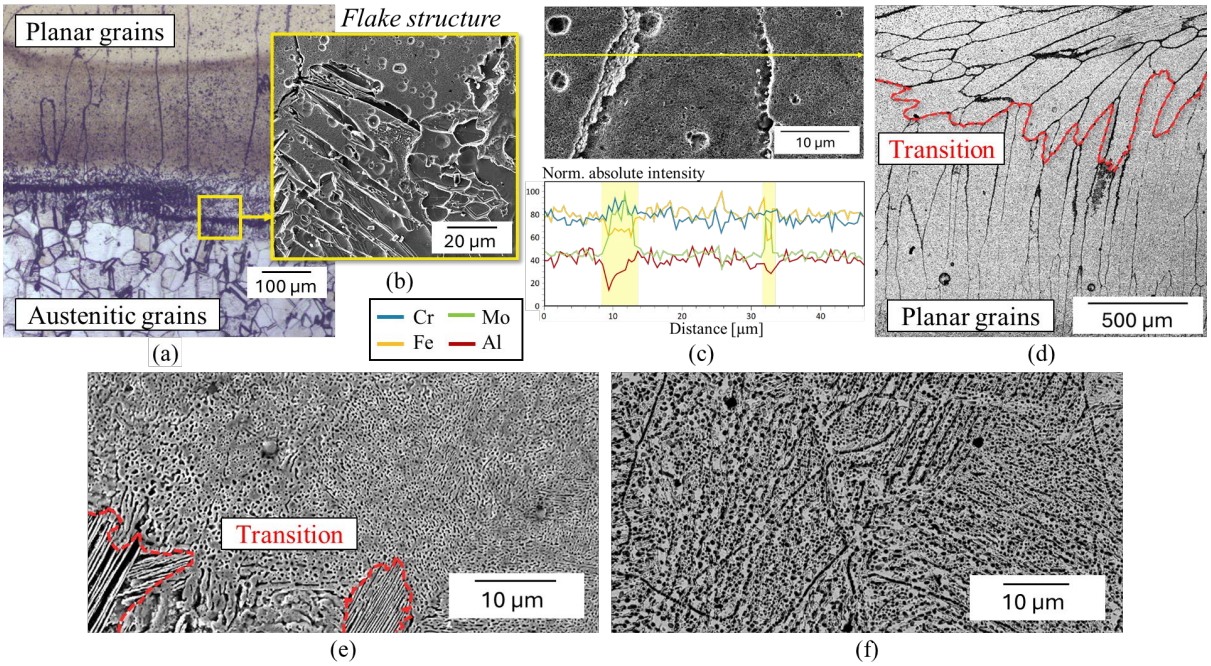


Figure 3. SEM and OM images of the interface (a,b), planar grain (c,d), transition (e,f) and equiaxed grain (g,h) zone

Morphological tests. Table 5 reports the average areal roughness (S_a and S_z) values for the morphological samples. Tests M1 and M3, conducted at a laser power of 800 W and scanning speeds of 600 and 1440 mm/min respectively, exhibited significantly higher roughness and spherical clusters on the surface (Fig. 4). This phenomenon occurs when material fails to solidify into continuous layers and, according to Liu et al. [11], it is linked to low energy input. In test M1, some of these clusters reached up to 1 mm in size, while in test M3, the surface particles were smaller and closer in size to the original powder. The formation of spherical clusters is attributed to the Plateau-Rayleigh instability: the molten pool elongates and fragments into islands at high scanning speeds to maintain uniform capillary pressure [12].

Table 5. Process parameters and average areal roughness values of morphological samples

#	P [W]	V [MM·MIN⁻	G [G·MIN^{-1}]	SA [µM]	Sz [µM]
M1	800	600	10	114	1013
M2	3800	600	10	33	302
M3	800	1440	10	45	467
M4	3800	1440	10	25	261
M5	2600	1020	10	20	283
M6	3200	1440	10	26	254

In contrast, tests M2 and M4, performed at 3800 W with the same scanning speeds (600 and 1440 mm·min^{-1} respectively), showed no spherical clusters but exhibited material accumulations (Fig. 4). This phenomenon, known as “humping”, is likely caused by hydrodynamic instability and occurs when the liquid material moves slower than the shielding gas. As stated by DebRoy et al. [12], humping appears to be more relevant at high scanning speeds and energy densities.

Finally, tests M5 and M6, produced using intermediate energy density values and the optimal process parameters, showed minimal spherical clusters and reduced humping defects. Test M5, conducted at 2600 W, had fewer humping defects compared to those performed at higher power

Materials Research Proceedings 57 (2025) 99-106 https://doi.org/10.21741/9781644903735-12

levels (3200 W and 3800 W). These results suggest that intermediate power and speed parameters effectively minimize morphological defects, leading to improved surface roughness. To achieve a more detailed analysis, the surface of the M5 sample underwent EDS examination to assess the distribution of alloying elements. The compositional map (Fig. 5) revealed a tendency to form two distinct types of clusters: one consisting solely of aluminum, which appears reflective in SEM images and is also visible to the naked eye, and another composed of the remaining alloying elements, which appears white and opaque. The differing behavior of aluminum compared to the other elements could be attributed to its lower melting point, potentially leading to localized vaporization in some areas.

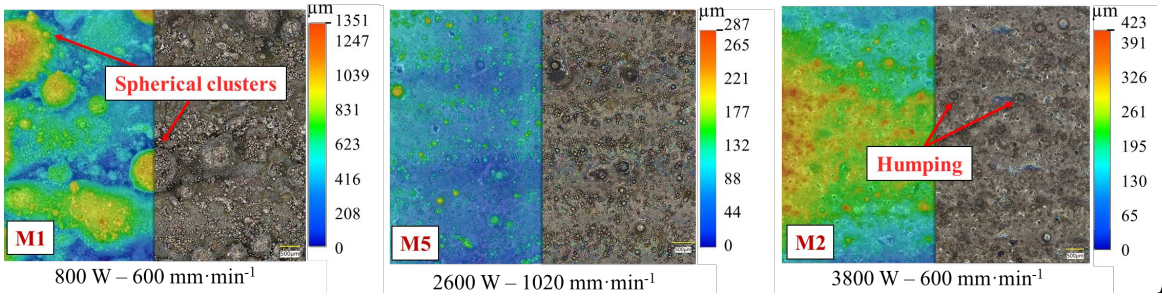


Figure 4. Examples of morphological maps for spherical clusters, humping and intermediate case

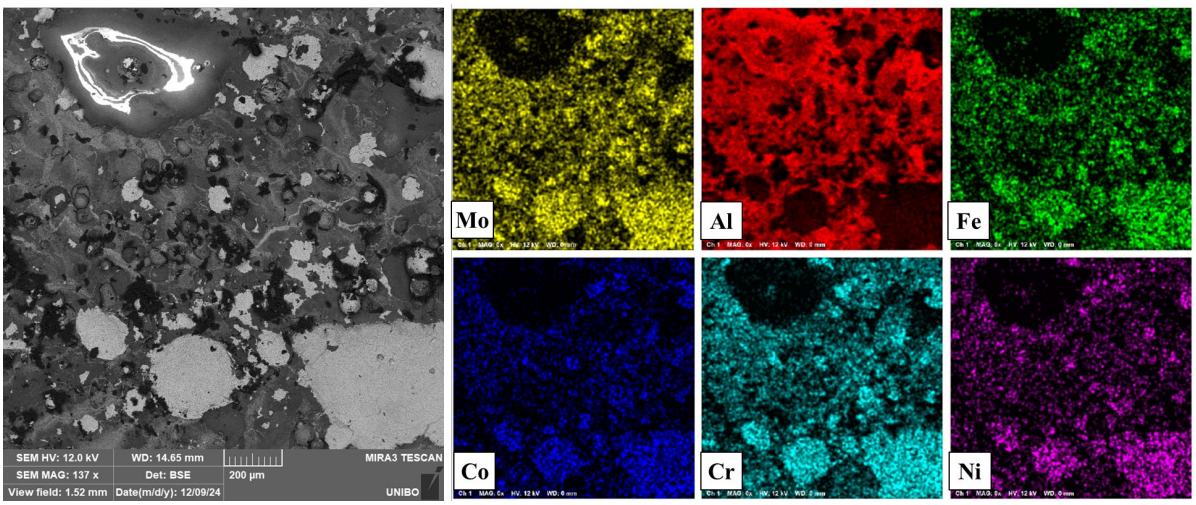


Figure 5. Compositional maps of the surface of M5 sample

Conclusions

This study demonstrated the feasibility of producing AlCoCr2FeMo0.5Ni high-entropy alloy coatings using Laser Directed Energy Deposition technology. The investigation of process parameters revealed that optimal combination of laser power, scanning speed, and powder flow rate are crucial for achieving high quality depositions with minimal defects and relative densities exceeding 99%. Specifically, intermediate energy density values minimized morphological issues such as spherical clusters and humping defects, leading to improved surface roughness.

The microstructural analysis identified four zones in the deposition with distinct microstructure, reflecting the influence of thermal and mechanical processing conditions. These findings highlight the potential of L-DED for tailoring HEA microstructures for aerospace applications. Future work should focus on further optimizing energy input to enhance the mechanical performance of HEA components.

References

[1] A. Morad e Y. Shash, «NICKEL BASE SUPERALLOYS USED FOR AERO ENGINE TURBINE BLADES», *The International Conference on Applied Mechanics and Mechanical Engineering*, vol. 16, fasc. 16, pp. 1–22, mag. 2014. https://doi.org/10.21608/amme.2014.35549

[2] M. Tokarewicz e M. Grądzka-Dahlke, «Review of Recent Research on AlCoCrFeNi High-Entropy Alloy», *Metals*, vol. 11, fasc. 8, Art. fasc. 8, ago. 2021. https://doi.org/sui

[3] Q. Sui *et al.*, «The microstructure and mechanical properties of the additive manufactured AlCoCrFeNi high entropy alloy», *Materials Science and Engineering: A*, vol. 833, p. 142507, gen. 2022. https://doi.org/10.1016/j.msea.2021.142507

[4] Z. Liang, Y. Zhang, Y. Liu, Z. Zhu, e H. Zhang, «Microstructure and properties of AlCoCrFeNi2.1 eutectic high-entropy alloy formed by laser melting deposition (LMD)», *Materials Letters*, vol. 317, p. 132092, giu. 2022. https://doi.org/10.1016/j.matlet.2022.132092

[5] S. Arun, N. Radhika, e B. Saleh, «Effect of Additional Alloying Elements on Microstructure and Properties of AlCoCrFeNi High Entropy Alloy System: A Comprehensive Review», *Met. Mater. Int.*, vol. 31, fasc. 2, pp. 285–324, feb. 2025. https://doi.org/10.1007/s12540-024-01752-3

[6] Q. Chao, T. Guo, T. Jarvis, X. Wu, P. Hodgson, e D. Fabijanic, «Direct laser deposition cladding of Al CoCrFeNi high entropy alloys on a high-temperature stainless steel», *Surface and Coatings Technology*, vol. 332, pp. 440–451, dic. 2017. https://doi.org/10.1016/j.surfcoat.2017.09.072

[7] Y. X. Zhuang, X. L. Zhang, e X. Y. Gu, «Effect of molybdenum on phases, microstructure and mechanical properties of Al0.5CoCrFeMo Ni high entropy alloys», *Journal of Alloys and Compounds*, vol. 743, pp. 514–522, apr. 2018. https://doi.org/10.1016/j.jallcom.2018.02.003

[8] Q. Sui *et al.*, «Strength-ductility balance of AlCoCrFeNi2.1 eutectic high-entropy alloy via additive manufacturing», *Journal of Materials Research and Technology*, vol. 30, pp. 1992–2003, mag. 2024. https://doi.org/10.1016/j.jmrt.2024.03.207

[9] J. An, Y. Zhou, M. Yan, Z. Liu, e Q. Zhu, «Effect of Heat Treatment on Microstructure and Mechanical Properties of Direct Energy Deposited AlCoCrFeNi2.1», *J Therm Spray Tech*, vol. 31, fasc. 5, pp. 1634–1648, giu. 2022. https://doi.org/10.1007/s11666-022-01390-4

[10] W. Kurz, C. Bezençon, e M. Gäumann, «Columnar to equiaxed transition in solidification processing», *Science and Technology of Advanced Materials*, vol. 2, fasc. 1, pp. 185–191, gen. 2001. https://doi.org/10.1016/S1468-6996(01)00047-X

[11] M. Liu, A. Kumar, S. Bukkapatnam, e M. Kuttolamadom, «A Review of the Anomalies in Directed Energy Deposition (DED) Processes & Potential Solutions - Part Quality & Defects», *Procedia Manufacturing*, vol. 53, pp. 507–518, 2021. https://doi.org/10.1016/j.promfg.2021.06.093

[12] T. DebRoy *et al.*, «Additive manufacturing of metallic components – Process, structure and properties», *Progress in Materials Science*, vol. 92, pp. 112–224, mar. 2018. https://doi.org/10.1016/j.pmatsci.2017.10.001

Materials Research Proceedings 57 (2025) 107-115 https://doi.org/10.21741/9781644903735-13

Instrumented indentation tests for local temperature-dependent mechanical properties assessment of laser-based powder bed fusion of aluminium alloy

Stefano GUARINO[1,a], Gennaro Salvatore PONTICELLI[1,b], Alfio SCUDERI[1,c], Simone VENETTACCI[1,d], Vittorio VILLANI[1,e *]

[1]Department of Engineering, University Niccolò Cusano, Via Don Carlo Gnocchi 3, 00166, Rome, Italy

[a]stefano.guarino@unicusano.it, [b]gennaro.ponticelli@unicusano.it, [c]alfio.scuderi@unicusano.it, [d]simone.venettacci@unicusano.it, [e]vittorio.villani@unicusano.it

Keywords: Powder Bed Fusion, Mechanical Testing, Aluminium Alloys

Abstract. Laser-based powder bed fusion of metals has grown rapidly due to high product customization and streamlined processing, though limited data and reproducibility still hinder its industrial adoption. In this study, instrumented indentation tests were performed with the aim of evaluating local and global mechanical properties of laser-based powder bed fused aluminium alloy from room temperature up to 300°C, while simultaneously demonstrating the potential of the proposed procedure for their determination. Comparing the results to conventional die-casted samples, it emerges that at room temperature the yield strength of additively manufactured specimens is better than the traditional ones, at the expense of stiffness. Indentation tests show a local and temperature dependence of mechanical properties along the building direction, in favour of the bottom part for yield strength and of the upper part for rigidity, but which tends to homogenize with temperature.

Introduction

Laser-based powder bed fusion of metals (PBF-LB/M) is an additive manufacturing (AM) technique that uses the energy transferred by means of a laser beam in an inert chamber to selectively melt the particles of a powder bed, to fabricate layer-by-layer the desired part in metallic material [1, 2]. In addition to high construction accuracy and mechanical properties of the so-produced components [3], the PBF-LB/M technique allows to overcome the limitations of traditional technologies, ensuring wide flexibility in terms of choice of materials, as well as high levels of customization and geometry complexity of the finished objects [4]. In addition, this technology has proven to be optimal for rapid prototyping or small series production, and more sustainable, due to the possibility of reducing scrap, time and cost in production [5].

One of the most widely used materials in PBF-LB/M is the $AlSi_{10}Mg$ aluminium alloy, due to its excellent mechanical, physical, and thermal properties [6]. The high property-to-weight ratio makes this alloy very attractive for multiple industries, such as automotive and aerospace [7]. However, the use of PBF-LB/M technology in these sectors is still limited due to uncertainty about the quality and mechanical properties of the produced components [8], as anisotropy of the material [9], high surface roughness and the presence of defects, such as internal porosity [10]. Moreover, very few studies have evaluated the mechanical properties at high temperatures so far [11]. This highlights the need for further studies and investigations, locally and globally, essential to ensure the reliability, repeatability and performance of manufactured components [12].

FIMEC (Flat-top cylinder Indenter for Mechanical Characterization) is a testing methodology that allows non-destructive evaluation of local mechanical properties [13], mainly yield stress and modulus of elasticity [14, 15]. Moreover, FIMEC tests are not affected by surface roughness [8],

Content from this work may be used under the terms of the Creative Commons Attribution 3.0 license. Any further distribution of this work must maintain attribution to the author(s) and the title of the work, journal citation and DOI. Published under license by Materials Research Forum LLC.

Materials Research Proceedings 57 (2025) 107-115 https://doi.org/10.21741/9781644903735-13

the equipment can be easily implemented allowing for a wide versatility in characterizing a broad range of materials for many industrial applications [16]. Several literature studies have already confirmed the effectiveness of FIMEC tests for traditionally manufactured specimens, made of steel and other metal alloys, investigated from ambient temperature up to 500°C [17], or at cryogenic temperatures of -100°C [18]. Some recent literature studies have used such tests for the first time to evaluate the local mechanical properties of specimens fabricated through AM, e.g., selective laser sintering [19] or PBF-LB/M [8], but at ambient temperature only. While, to date, to the best of the author's knowledge, no literature work has investigated the possibility of using such instrumented indentation tests to verify the local and global effect of temperature on the mechanical performance of additively produced samples.

The present work aims to fill such gap providing insights about the local and global mechanical properties of $AlSi_{10}Mg$ aluminium alloy PBF-LB/M-ed specimens under different temperature conditions.

Materials and Methods

Metallic samples made of $AlSi_{10}Mg$ (m4p Materials Solutions GmbH) were fabricated by using the PBF-LB/M machine SLM 280HL (SLM Solutions GmbH). The starting material is supplied as powder with a median particle size of 37 μm, whose main characteristics are listed in Table 1.

Table 1 – Main characteristics of the starting material as declared by the supplier.

Chemical composition [wt%]				**Melting point [°C]**
Al	78.38	*Si*	18.93	570
Mg	1.36	*C*	0.94	**Relative density [g/cm^3]**
O	0.39			2.63

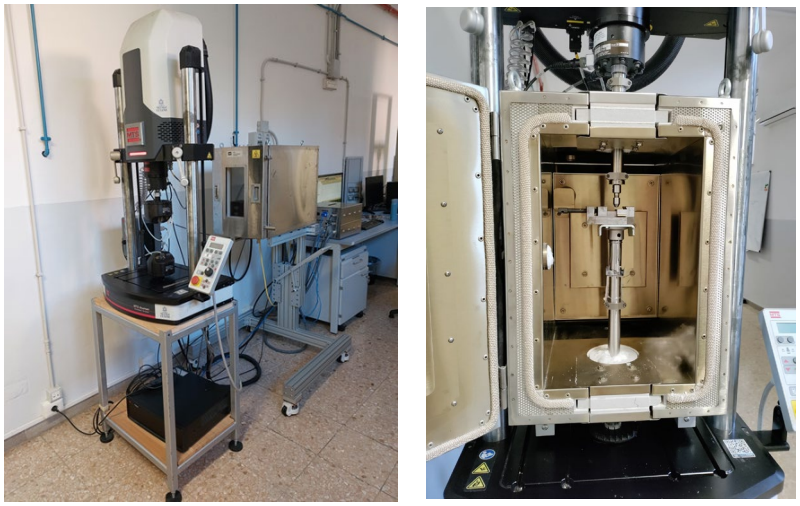
Sample fabrication

The samples, with the shape of parallelepiped 45x20x10 mm^3 in size, were produced by using the optimal parameters suggested by the machine manufacturer to obtain the highest density of approximately 99.95%, i.e., laser power 350 W, layer thickness 30 μm, laser scanning speed 1650 mm/s, and hatch distance 100 μm. All parts were manufactured using the Meander Hatching Pattern, with a 67° rotation applied after each layer, as the default strategy for the SLM 280 HL machine. Additionally, a block-type support structure featuring square perforated pegs that provide a total contact area equal to 50% of the sample's projected surface was employed. To mitigate possible defects and reduce residual stresses [20], the samples are post-processed with a heating treatment for 60 minutes at 600°C.

Indentation test

Instrumented indentation tests were carried out to investigate the local temperature-dependent mechanical properties of the PBF-LB/M-ed samples. The setup, shown in Fig. 1, consists of a cylindrical indenter of sintered tungsten carbide (1 mm in diameter and 1.5 mm in axial length) [21], anchored to the MTS Acumen 3 electrodynamic testing machine, to which the environmental chamber MTS 651 (that controls the temperature) is connected.

Materials Research Proceedings 57 (2025) 107-115 https://doi.org/10.21741/9781644903735-13

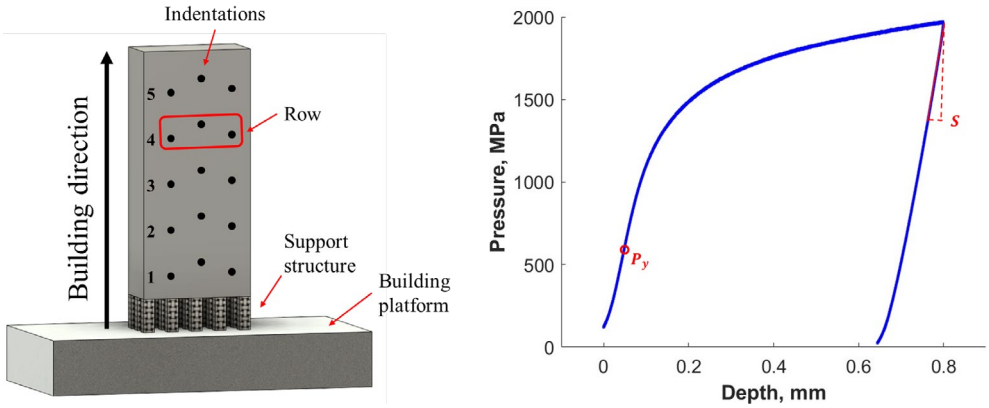


(a) (b)

Fig. 1 – Experimental setup: (a) MTS Acumen 3 + MTS 651 Chamber; (b) FIMEC indenter.

This method allows to perform several tests on the same sample leaving a very small mark on the surface, which allows the technique to be considered non-destructive [22]. Therefore, experimental tests were carried out at four temperatures (i.e., 23°C, 100°C, 200°C, 300°C) on five positions (i.e., along the building direction for local characterization, see Fig. 2a) onto three different samples (i.e., replications), for a total of 60 indentations. It is worth noting that although there should be no significative influence due to the permanence at high temperatures on the mechanical properties [23, 24], each sample was maintained in the climate chamber for the sole duration of the test, e.g., up to maximum 30 minutes for the tests carried put at 300°C.

The experimental campaign was designed according to the Design of Experiments methodology [25]. It is worth noting that the indentations, highlighted as black dots in Fig. 2a, were randomized on the sample surface to maximize the number of tests, i.e., 15, to satisfy the requirement of 5 mm spacing between indentations and edges of the samples to avoid any border effect [16]. The randomization provided the position of three indentations at different temperatures for each of the five rows. Both sides of the samples were used to complete the experiments.



(a) (b)

Fig. 2 – (a) Sample geometry and indentations randomization; (b) typical FIMEC curve and parameters identification.

The procedure, according to ASTM E2546 standard, allows the recording of applied force vs. penetration depth (i.e., up to 0.8 mm and back to the starting position) at a constant speed (i.e., 0.01 mm/min), for varying temperatures. These data were adopted to draw the FIMEC curve as

Materials Research Proceedings 57 (2025) 107-115 https://doi.org/10.21741/9781644903735-13

pressure vs. depth diagram, being the pressure defined as the ratio between force and indenter section. The mechanical properties determined from the FIMEC curves were yield stress ($\sigma_{y,F}$) and elastic modulus (E_F), as schematized in Fig. 2b and described by Eq. 1 to Eq. 3 [17, 21]:

$$\sigma_{y,F} \cong \frac{P_y}{3}, \quad (1)$$

$$S = 2E_a\sqrt{\frac{A}{\pi}}, \quad (2)$$

$$\frac{1}{E_a} = \frac{1-\nu_F^2}{E_F} + \frac{1-\nu_i^2}{E_i}, \quad (3)$$

where P_y is the inflection point of the loading phase, E_a is the apparent elastic modulus calculated through the slope S of the unloading part of the curve and the indentation section A, considered to be equal to that of the indenter (thus $S = E_a$), E_i = 668.35 GPa is the elastic modulus of the indenter, ν_i = 0.24 its Poisson ratio [26], and ν_F = 0.36 is an average Poisson ratio for PBF-LB/M-ed $AlSi_{10}Mg$ [27, 28].

Lastly, the outcomes were compared with conventional tensile tests of both PBF-LB/M-ed and die-casted samples carried out in a previous work [8].

Results and Discussion

Temperature-controlled instrumented indentation tests were carried out to characterize the mechanical properties of laser powder bed fused aluminium samples at a local level by varying temperature and position of indentation. This latter aspect is of crucial importance when dealing with layer-by-layer manufacturing processes, as PBF-LB/M, to verify any induced anisotropic effect [4], which cannot be determined by traditional tensile testing methods. The same can be said for the dependence of the mechanical properties from temperature, especially the elastic modulus, since an accurate evaluation can be very challenging [23].

To ensure proper initial contact and minimize the roughness effect, quantified around 15.83 ±0.87 μm as average surface area roughness (i.e., Sa, according to ISO 25178), a 100 N pre-load was applied. Standard preloads are generally lower for indented metal samples (e.g., from 5 N to 50 N [29]), but research proves that a higher preload can help assure initial non-linearity and reduce potential problems related to absence of perfect parallelism in the sample geometry [30], that are typical of PBF-LB/M printed specimens [9]. Experimental results show a clear correlation of the mechanical properties with the temperature variation, as proved in the following.

Fig. 3 shows a representative curve of each FIMEC test obtained for the four experimental scenarios here investigated, i.e., 23°C, 100°C, 200°C and 300°C. As can be seen, the initial slope of the loading phase is very similar for each condition up to around 300 N, while the inflection point varies, decreasing with temperature, therefore resulting in a reduced yield strength. This finding can be due to the decrease in cohesion between the particles or the softening of the material, while at higher temperature, the material shows a greater capacity for deformation, with a transition from a brittle to a more ductile behaviour.

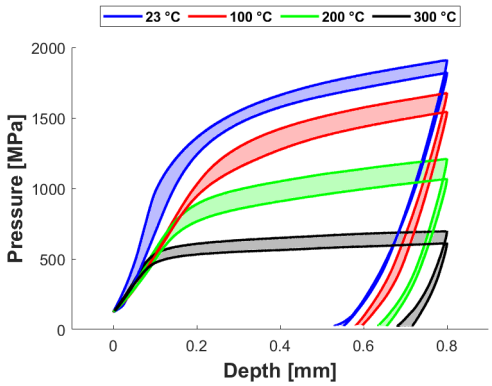


Fig. 3 – FIMEC curves for varying temperature.

Fig. 4a presents the comparison of the elastic modulus of the samples. The DC specimens offer the higher value due to the absence of porosities and other structural defects that are present in the PBF-LB/M samples [8, 31]. The slight difference at 23°C of the two PBF-LB/M samples is related to the different geometry of the specimens and strain speed variation, i.e., FIMEC is 100 times slower than traditional test [32]. Fig. 4b illustrates the results of the yield strength. At room temperature, PBF-LB/M samples, due to the finer grains [33] and finer Si phase distribution [34], present a higher value than the DC one. The higher testing speed of the tensile test led to higher yield value, as expected. Temperature increase facilitates the dislocation mobility, reducing the yield strength. It is interesting to note a significant linear decrease in both the elastic modulus and yield stress with temperature, from 31.7 ±2.2 GPa and 220.7 ±11.8 MPa at 23°C down to 21.9 ±1.69 GPa and 104.1 ±12.1 MPa at 300°C, with a R^2 around 1.

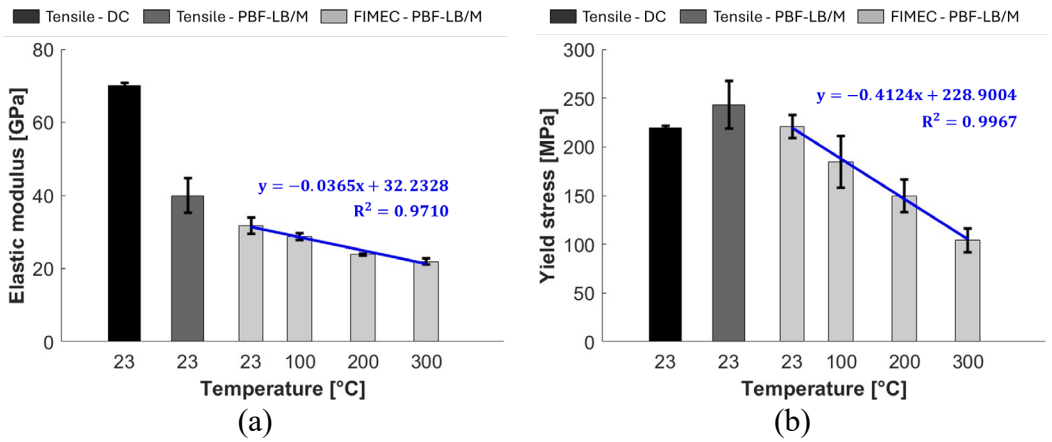


Fig. 4 – Global temperature effect on FIMEC results compared to traditional die-casted samples (DC): (a) elastic modulus and (b) yield stress. The bars represent the standard deviation.

The building direction effect on the PBF-LB/M sample properties is shown in Fig. 5. During production, the volume close to the building platform (i.e., Row 1) remains at a higher temperature for longer, inducing a more marked stress-relief effect, that results in a reduced elastic modulus [35], if compared to the upper layers (i.e., Rows 4 and 5). While the opposite occurs for the yield strength, which decreases moving the indentation site to the top portion of the samples. This is probably due to microporosity, segregation, and microstructure, but the effect of the cooling rate on grain size can be considered the main influencing factor [36]. However, this effect appears to be mitigated with temperature increase, which acts with a homogenizing effect on the material properties, also supported by the flattening of the standard deviation, represented as error bars in Fig. 5. Although there is a greater gap between the average values as the test zone changes, the

Materials Research Proceedings 57 (2025) 107-115 https://doi.org/10.21741/9781644903735-13

overlap of the standard deviations may suggest that their difference is not statistically significant even at low temperatures, for elastic modulus. But formal statistical tests, e.g., the ANOVA test, should be conducted for verification. As temperature increases, the distance from the building platform seems to become less impactful, for both properties, with closer average experimental values and much less variability. This could allow the PBF-LB/M-ed samples testing on a single location, or at few of them, above a certain temperature to have a global characterization, which can be useful for industrial verification applications. Moreover, while PBF-LB/M process may induce layer anisotropy due to the production process [37], as depicted in Fig. 5, an unexpected trend for the yield stress at Row 2 and Row 4 can be observed, which are characterized by a lower yield stress if compared to the other rows. This could be attributed to some variations experienced during the fabrication process, since all the test samples were manufactured during the same production batch.

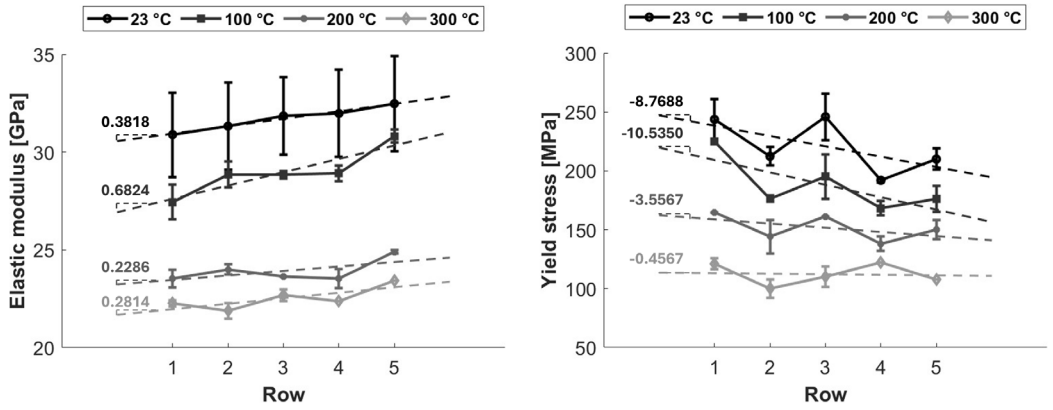


Fig. 5 – Local temperature effect on FIMEC results: (a) elastic modulus and (b) yield stress. The numbers represent the slope of the fitting line.

The alternative method here presented for the estimation of the elastic modulus and yield strength of PBF-LB/M-ed samples made of AlSi10Mg proves to overcome the main limitations of traditional tests while also providing local property characterization for varying temperatures as additional information, thanks to its greater sensitivity, due to both the shape of the indenter and the testing procedure itself [38].

Conclusions

This work present novel testing results that extend the feasibility and operational possibilities of metal components fabricated with additive manufacturing, providing both scientific and industrial communities useful data to evaluate the performance of produced parts.

Instrumented indentation tests (FIMEC) allowed an accurate and non-invasive characterization of PBF-LB/M samples under varying temperature conditions, i.e., from room temperature at 23°C up to 300°C, on different sites to evaluate any effect due to the layer-by-layer nature of the process, providing both global and local information about mechanical performance in terms of elastic modulus and yield strength.

Globally, the temperature increase reduces the elastic modulus from 31.7 ±2.2 GPa at 23°C down to 21.9 ±1.69 GPa at 300°C, and the yield stress from 220.7 ±11.8 MPa to 104.1 ±12.1 MPa. Locally, the elastic modulus increases moving the indentation site from the bottom to the top part of the sample, while the yield strength decreases. This can be due to the longer residence time of the bottom layers at high temperatures during the manufacturing process, which contribute to modify the microstructure and therefore the resulting properties. However, at higher temperature,

such effect appears to be less evident, thus allowing local properties to be considered as representative of global characteristics.

Ease of implementation and reliability of the results confirm that FIMEC can be effectively implemented in process-control scenarios, providing non-invasive insights for temperature-critical components. Further works may investigate different indentation speeds to define a constitutive law for the material, also including cryogenic conditions.

References

[1] Yadroitsev I, Du Plessis A, Yadroitsava I (2021) Basics of laser powder bed fusion. Fundamentals of Laser Powder Bed Fusion of Metals 15–38. https://doi.org/10.1016/B978-0-12-824090-8.00024-X

[2] Kumar S (2014) Selective Laser Sintering/Melting. Comprehensive Materials Processing: Thirteen Volume Set 10:93–134. https://doi.org/10.1016/B978-0-08-096532-1.01003-7

[3] Yasa E (2021) Selective laser melting: principles and surface quality. Addit Manuf 77–120. https://doi.org/10.1016/B978-0-12-818411-0.00017-3

[4] Venettacci S, Ponticelli GS, Guarino D, Guarino S (2022) Tribological properties of Laser Powder Bed Fused AlSi10Mg : Experimental study and statistical analysis. J Manuf Process 84:1103–1121. https://doi.org/10.1016/j.jmapro.2022.10.065

[5] Mehrpouya M, Vosooghnia A, Dehghanghadikolaei A, Fotovvati B (2021) The benefits of additive manufacturing for sustainable design and production. Sustainable Manufacturing 29–59. https://doi.org/10.1016/B978-0-12-818115-7.00009-2

[6] Leary M, Maconachie T, Sarker A, et al (2019) Mechanical and thermal characterisation of AlSi10Mg SLM block support structures. Mater Des 183:108138. https://doi.org/10.1016/J.MATDES.2019.108138

[7] Blakey-Milner B, Gradl P, Snedden G, et al (2021) Metal additive manufacturing in aerospace: A review. Mater Des 209:110008. https://doi.org/10.1016/J.MATDES.2021.110008

[8] Villani V, Ponticelli GS, Venettacci S, Guarino S (2024) Assessment of Local Mechanical Properties of Laser Powder Bed Fused Aluminium Alloy By Non-Destructive Testing Based on Fimec Indentation. Acta Polytech CTU Proc 48:52–55. https://doi.org/10.14311/APP.2024.48.0052

[9] Guarino D, Venettacci S, Villani V, et al (2024) Tribo-Technological Features of Laser Powder Bed Fusion Process: Scratch and Wear Resistance of Alsi10Mg Aluminium Alloy. Acta Polytech CTU Proc 48:34–40. https://doi.org/10.14311/APP.2024.48.0034

[10] Du Plessis A (2021) Porosity in laser powder bed fusion. Fundamentals of Laser Powder Bed Fusion of Metals 155–178. https://doi.org/10.1016/B978-0-12-824090-8.00007-X

[11] Michi RA, Plotkowski A, Shyam A, et al (2022) Towards high-temperature applications of aluminium alloys enabled by additive manufacturing. International Materials Reviews 67:298–345. https://doi.org/10.1080/09506608.2021.1951580/ASSET/IMAGES/LARGE/10.1080_09506608.2021.1951580-FIG5.JPEG

[12] Xiao X (2024) Sustainability in Laser Powder Bed Fusion (LPBF). Encyclopedia of Sustainable Technologies 572–585. https://doi.org/10.1016/B978-0-323-90386-8.00125-X

[13] Genna S, Trovalusci F, Tagliaferri V (2017) Indentation test to study the moisture absorption effect on CFRP composite. Compos B Eng 124:1–8. https://doi.org/10.1016/J.COMPOSITESB.2017.05.053

[14] Di Siena M, Genna S, Moretti P, et al (2023) Study of the laser-material interaction for innovative hybrid structures: Thermo-mechanical characterization of polyethylene-based polymers. Polym Test 120:107947. https://doi.org/10.1016/J.POLYMERTESTING.2023.107947

[15] Ciambella L, Montanari R (2014) New Algorithm to Determine the Yield Stress from FIMEC Test. Materials Science Forum 783–786:2272–2277. https://doi.org/10.4028/www.scientific.net/MSF.783-786.2272

[16] Montanari R, Varone A (2021) Flat-Top Cylinder Indenter for Mechanical Characterization: A Report of Industrial Applications. Materials 14:. https://doi.org/10.3390/ma14071742

[17] Montanari R, Filacchioni G, Iacovone B, et al (2007) High temperature indentation tests on fusion reactor candidate materials. Journal of Nuclear Materials 367-370 A:648–652. https://doi.org/10.1016/j.jnucmat.2007.03.099

[18] Donato A, Gondi P, Montanari R, et al (1998) A remotely operated FIMEC apparatus for the mechanical characterization of neutron irradiated materials. Journal of Nuclear Materials 258–263:446–451. https://doi.org/10.1016/S0022-3115(98)00428-0

[19] Villani V, Ponticelli GS, Venettacci S, Guarino S (2024) Effect of water absorption on the properties of selective laser-sintered PA12 specimens. Progress in Additive Manufacturing. https://doi.org/10.1007/s40964-024-00826-3

[20] Aboulkhair NT, Simonelli M, Parry L, et al (2019) 3D printing of Aluminium alloys: Additive Manufacturing of Aluminium alloys using selective laser melting. Prog Mater Sci 106:100578. https://doi.org/10.1016/J.PMATSCI.2019.100578

[21] Riccardi B, Montanari R (2004) Indentation of metals by a flat-ended cylindrical punch. Materials Science and Engineering: A 381:281–291. https://doi.org/10.1016/j.msea.2004.04.041

[22] Gondi P, Donato A, Montanari R, Sili A (1996) A miniaturized test method for the mechanical characterization of structural materials for fusion reactors. Journal of Nuclear Materials 233–237:1557–1560. https://doi.org/10.1016/S0022-3115(96)00315-7

[23] Uzan NE, Shneck R, Yeheskel O, Frage N (2018) High-temperature mechanical properties of AlSi10Mg specimens fabricated by additive manufacturing using selective laser melting technologies (AM-SLM). Addit Manuf 24:257–263. https://doi.org/10.1016/J.ADDMA.2018.09.033

[24] Michi RA, Plotkowski A, Shyam A, et al (2022) Towards high-temperature applications of aluminium alloys enabled by additive manufacturing. International Materials Reviews 67:298–345. https://doi.org/10.1080/09506608.2021.1951580

[25] Montgomery DC (1991) Design and Analysis of Experiments. John Wiley, Chichester

[26] Oliver WC, Pharr GM (2004) Measurement of hardness and elastic modulus by instrumented indentation: Advances in understanding and refinements to methodology. J Mater Res 19:3–20. https://doi.org/10.1557/JMR.2004.19.1.3/METRICS

[27] Sert E, Schuch E, Öchsner A, et al (2019) Tensile strength performance with determination of the Poisson‘s ratio of additively manufactured AlSi10Mg samples. Materwiss Werksttech 50:539–545. https://doi.org/10.1002/mawe.201800233

[28] Chmelko V, Šulko M, Škriniarová J, et al (2023) Strength and Cyclic Properties of Additive vs. Conventionally Produced Material AlSi10Mg. Materials 2023, Vol 16, Page 2598 16:2598. https://doi.org/10.3390/MA16072598

[29] Boschetto A, Quadrini F, Squeo EA (2011) Extracting local mechanical properties of steel bars by means of instrumented flat indentation. Measurement 44:129–138. https://doi.org/10.1016/J.MEASUREMENT.2010.09.038

[30] Barletta M, Puopolo M, Trovalusci F, Vesco S (2017) High-Density Polyethylene/SrAl2O4:Eu2+, Dy3+ Photoluminescent Pigments: Material Design, Melt Processing, and Characterization. Polym Plast Technol Eng 56:400–410. https://doi.org/10.1080/03602559.2016.1227840

[31] Haselhuhn AS, Buhr MW, Wijnen B, et al (2016) Structure-property relationships of common aluminum weld alloys utilized as feedstock for GMAW-based 3-D metal printing. Materials Science and Engineering: A 673:511–523. https://doi.org/10.1016/J.MSEA.2016.07.099

[32] Hart EW (1967) Theory of the tensile test. Acta Metallurgica 15:351–355. https://doi.org/10.1016/0001-6160(67)90211-8

[33] Cordero ZC, Knight BE, Schuh CA (2016) Six decades of the Hall–Petch effect – a survey of grain-size strengthening studies on pure metals. International Materials Reviews 61:495–512

[34] Kempen K, Thijs L, Van Humbeeck J, Kruth JP (2012) Mechanical Properties of AlSi10Mg Produced by Selective Laser Melting. Phys Procedia 39:439–446. https://doi.org/10.1016/J.PHPRO.2012.10.059

[35] Mfusi BJ, Mathe NR, Tshabalala LC, Popoola PAI (2019) The Effect of Stress Relief on the Mechanical and Fatigue Properties of Additively Manufactured AlSi10Mg Parts. Metals 2019, Vol 9, Page 1216 9:1216. https://doi.org/10.3390/MET9111216

[36] Casamichele L, Quadrini F, Tagliaferri V (2007) Non-destructive evaluation of local mechanical properties of Al die cast large components by means of FIMEC indentation test. Measurement 40:892–897. https://doi.org/10.1016/j.measurement.2006.11.012

[37] Zhu X, Ma Y, Wu H, et al (2024) In-situ tensile testing of fracture and strain in a selective laser melted AlSi10Mg alloy. Heliyon 10:e34137. https://doi.org/10.1016/J.HELIYON.2024.E34137

[38] Maculotti G, Genta G, Lorusso M, Galetto M (2019) Assessment of Heat Treatment Effect on AlSi10Mg by Selective Laser Melting through Indentation Testing. Key Eng Mater 813:171–177. https://doi.org/10.4028/WWW.SCIENTIFIC.NET/KEM.813.171

Materials Research Proceedings 57 (2025) 116-127 https://doi.org/10.21741/9781644903735-14

Optimizing 3D printing process parameters for high-performance inflatable soft actuators

RIFINO Rosanna[1,2,3,a*], PRICCI Alessio[1,2,3,b], PERCOCO Gianluca[1,2,3,c]

[1]Department of Mechanics, Mathematics and Management, Polytechnic of Bari, Via Orabona 4, 70125, Bari, Italy

[2]Interdisciplinary Additive Manufacturing (IAM) Lab, TTEC Taranto Polytechnic, Polytechnic University of Bari, Viale del Turismo 8, 74123, Taranto, Italy

[3]Sustainable Materials for Additive Manufacturing for Soft Robotics (SMAM 4 SoRo), Polytechnic University of Bari, Via Orabona 4, 70125, Bari, Italy

[a]r.rifino1@phd.poliba.it, [b]alessio.pricci@poliba.it, [c]gianluca.percoco@poliba.it

Keywords: Material Extrusion, Tensile Strength, Polymers

Abstract. Inflatable actuators have shown great potential in soft robotics; however, the usage of 3D printing technologies is still at its infancy phase. This paper focuses on the usage of Material Extrusion (MEX) to advance the fabrication of soft inflatable actuators and enhance performance. Two different designs were studied and the softest thermoplastic elastomer available on the market was used. Printing parameters (i.e., infill direction, ironing and extrusion temperature) were investigated to maximize the elongation and improve the intra-layer adhesion which is crucial to achieve air-tightness. A design of experiments approach was used to analyze the effect of each process parameter on mechanical properties. Additionally, hyperplastic simulations were performed and benchmarked with experimental results. The relationship process parameters-mechanical properties- performance is evaluated, laying the foundation for a broader usage of MEX for the fabrication of soft inflatable actuators.

Introduction

Soft robotics is a disruptive technology which is gradually transforming fields from medicine to industrial automation, offering superior compliance, adaptability, and safe human-robot interaction [1], [2]. Among its applications, soft pneumatic actuators (SPAs) stand out for their high power-to-weight ratio and ability to achieve extremely complex motions [3], [4]. SPAs operate by pressurizing internal chambers to achieve bending, twisting, and elongation movements [5], [6]. As a matter of fact, the internal geometry (and pattern) of the chambers is key to achieve motions. Motions can be programmed through design resulting in the unique possibility to employ such a class of actuators for a myriad of tasks.

Advancements in additive manufacturing (AM), especially material extrusion (MEX), have revolutionized SPAs fabrication, enabling the fabrication of intricate geometries and multi-material structures with embedded functionalities (such as embedded sensors and variable stiffness areas) [7], [8]. Alongside with such features, several researchers have been conducted to enhance mechanical properties of 3D printed parts, which is translated into an improvement of inter (and intra)-layer adhesion, resulting in a reduction of voids and improvement of elongation and air-tightness of SPAs actuators [9]. Beyond experimental works, also simulations including surrogate models of the 3D printed process and parts, have been widely investigated: such approach also can be translated to 3D printed SPAs, in order to extend their operability [10].

SPA design is application-driven [11] the geometry and shape of the internal chambers and the overall structures depends on the final application: a rigid bottom layer alongside with soft rectangular shaped chambers are used to maximize bending, [12, 13] while bellow-like chambers

Content from this work may be used under the terms of the Creative Commons Attribution 3.0 license. Any further distribution of this work must maintain attribution to the author(s) and the title of the work, journal citation and DOI. Published under license by Materials Research Forum LLC.

Materials Research Proceedings 57 (2025) 116-127 https://doi.org/10.21741/9781644903735-14

have been proven to improve elongation [14] [15], [16]. Geometry, material and fabrication technologies are crucial for optimizing SPAs performance [17], [18].

While most studies have been focusing on improving the performance of 3D printed bending-based SPAs often used to fabricate grippers, [19] the present study aims at investigating the relationship between process parameters, and design optimization for elongation-based SPAs fabricated through MEX. This class of elongation-based SPAs, still underexploited, has been proven to be extremely efficient for the fabrication of soft robotic arms with multiple degree of freedom, capable of complex motions within the 3D space. The authors were motivated by a preliminary study, which showed all the benefit achieved by elongation-based SPAs fabricated through inexpensive MEX technology against traditional manufacturing methods [9]. In this study, the authors used the softest thermoplastic material available on the market (Chinchilla, elongation at break 600%) and studied the relationship between some key 3D printing parameters (infill orientation, ironing, and printing temperature) and mechanical properties of the 3D printed structure. The aim of this investigation is the improvement of layer-by-layer adhesion to create airtight SPAs reflected in the airtightness, and extended lifespan of this kind of actuators. Moreover, two main actuator geometries, (traditional AM I-Support and proposed U-shaped bellow) have been extensively studied through finite element hyperelastic (FE) simulations and experimentally validated, in order to find the optimal design parameters and geometry capable of maximizing elongation under the same pressure input. The outcome of this work is a specific simulation-driven geometry, with tailored design parameters and fabrication strategy which maximize elongation in SPAs actuators. This work aims at elevating the role of MEX for the fabrication of high-performance elongation-based SPAs, with optimized process, and design parameters for the fabrication of actuators which could be potentially used to create inexpensive soft robotic systems laying the foundation for a broader utilization of this kind of actuation technology [20], [21].

Materials and methods

Additive manufacturing and DoE for maximizing UTS.

A filament-based MEX (JG Maker – Artist D Pro, China) was used to 3D print the SPAs with Chinchilla (Ninjatek, USA), a soft thermoplastic elastomer filament. This material was chosen for its commercial availability and suitability as one of the softest materials extrudable via MEX. Key properties of Chinchilla are listed in **Tab. 1**.

A good intralayer adhesion is paramount when fabricating SPAs, since it allows to:

i) avoid breakage of the structure when pressurized,
ii) maximize the elongation when actuated, and
iii) enable a higher-pressure actuation.

The impact of process parameters on Chinchilla's mechanical properties was studied, focusing on maximizing Ultimate Tensile Strength (UTS), which correlates with stronger adhesion and reduced breakage occurrence. A full factorial plan (2^3) was conducted to analyze the relationship between process parameters and material properties. For every process parameter, two levels with three replications each have been investigated, i.e. level -1 (low level) and level +1 (high level). In this way both i) the effect of each factor on UTS, and ii) the interaction of all factors were studied.

The three key process parameters of this investigation are:

- Infill Direction: Orientation of infill deposition. Level -1: 0° (vertical, orthogonal to tensile load); Level +1: 90° (horizontal, parallel to tensile load).
- Ironing: Heated nozzle remelts the top layer to improve surface quality. Level -1: OFF; Level +1: ON (zig-zag pattern, 0.35 mm spacing, 0.5 mm inset, 10% flow).

Materials Research Proceedings 57 (2025) 116-127 https://doi.org/10.21741/9781644903735-14

- Extrusion temperature: MEX temperature. Level -1: 225 °C (minimum recommended); Level +1: 235 °C (maximum recommended).

An overview of the Design of Experiments (DoE) was given in **Tab. 2**, while the main fixed processing process parameters are reported in **Tab. 3**.

Table 1. Mechanical proprieties of Chinchilla.

Material feature	Attribute/ Value
Type	TPE
Hardness	75 Shore A
Elongation at break	600%
Tensile strength at break	22 Mpa

Table 2. DoE levels and factors.

Factor					
Extrusion temperature		**Infill direction**		**Ironing**	
Levels		**Levels**		**Levels**	
-1	1	-1	1	-1	1
225°C	235°C	0°	90°	OFF	ON

Table 3. 3D printing process parameters.

Printing parameter	Value	Printing parameter	Value
Layer height	0.2 mm	**Flow**	120%
Layer width	0.35 mm	**Printing speed**	10 mm/s
Infill density	100%	**Infill pattern**	Lines

Mechanical testing.

Once the DoE was performed, mechanical tensile tests were conducted on Chinchilla samples, following the ASTM D412 – Standard Test Methods for Vulcanized Rubber and Thermoplastic Elastomers. Type C of the standard was chosen for dogbones dimensions, and three samples were fabricated and tested for all the combinations of parameters. The shape and dimensions of the dogbones are represented in **Fig. 1**. The aim of the mechanical tests was to find the best combination of parameters to have the maximum elongation at break and the best intra-layer adhesion to ensure air-tightness.

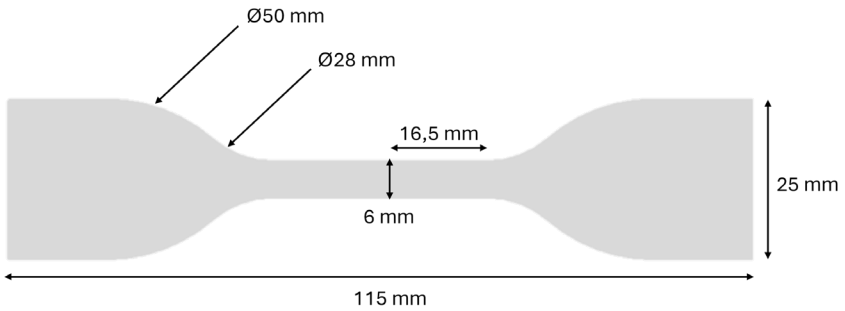


Figure 1. Dogbones dimensions for mechanical test.

Materials Research Proceedings 57 (2025) 116-127 https://doi.org/10.21741/9781644903735-14

Geometry of the soft actuator.

According to Gorissen [22] there are different classifications of SPAs based on their overall deformation. Among those, two geometries have been selected, numerically simulated and experimentally produced to reach the maximum elongation under the same input pressure (i.e., 2 bar):

- The AM I-Support [9], and
- The most used geometry in literature, i.e. the U-shaped bellow [10],[15],[23].

Both actuators consist of four parameterized chambers (see **Fig. 2 a) b)**), characterized by fixed and variables geometrical parameters (**Tab. 4**). AM I- Support has three variable design parameters: d_i, l_c and S_M, listed in **Tab. 5** and U-shaped bellow has two variable design parameters: R and S_M in **Tab. 6**. The external geometry can thus vary from an ellipse ($S_m < S_M$) to a circle ($S_m = S_M$), **Fig. 2 c)**. In both geometries, the chambers have been designed and manufactured to avoid non-removable support structures inside and outside the chambers.

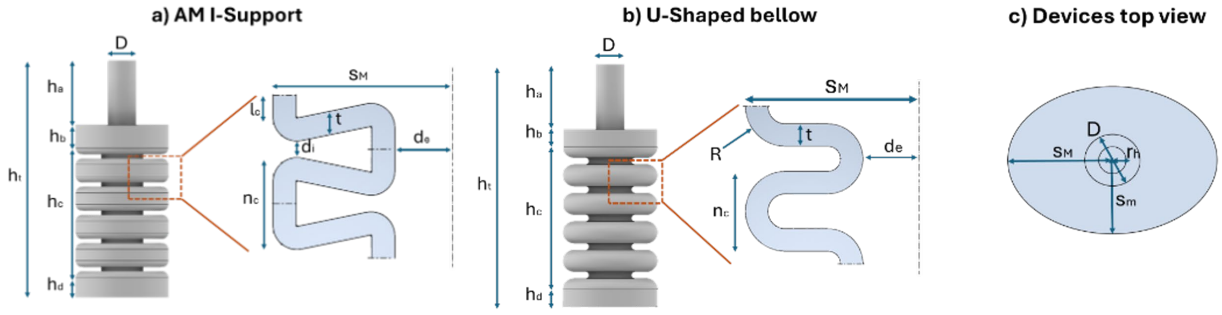


Figure 2. Design parameters of a) AM I-Support; b) U-shaped bellow; c) AM I-Support and U-shaped bellow top view.

Table 4. Fixed SPAs geometrical parameters.

Parameter name	Symbol	Value	Parameter name	Symbol	Value
Distance from central axis	d_e	3.50 mm	External length	h_b, h_d	4.00 mm
Chambers Length	h_c	32.87 mm	Hole radius	r_h	3.00 mm
Semi- minor axis ellipses	S_m	10.86 mm	Actuators Total Length	h_t	55.87 mm
Thickness	t	1.40 mm	Number of chambers	n_c	4
Inlet diameter	D	6.50 mm	Inlet length	h_a	15.00 mm

Table 5. AM I-Support variables parameters.

Parameter name	Symbol	Lower Limit	Upper Limit
Inter-chamber distance	d_i	0.40 mm	1.00 mm
Chamber length	$2\ l_c$	0.80 mm	1.35 mm
Major semi-axis ellipses	S_M	10.50 mm	10.86 mm

Table 6. U-shaped bellow variables parameters.

Parameter name	Symbol	Lower Limit	Upper Limit
Outer Radius	R	1.60 mm	3.20 mm
Major semi-axis ellipses	S_M	10.50 mm	10.86 mm

Materials Research Proceedings 57 (2025) 116-127 https://doi.org/10.21741/9781644903735-14

Finite element simulation.

The design optimization of the variable design parameters of the SPA chambers was performed with numerical simulations. In particular, the finite element software COMSOL Multiphysics v.6.2 (Static Structural module) was chosen.

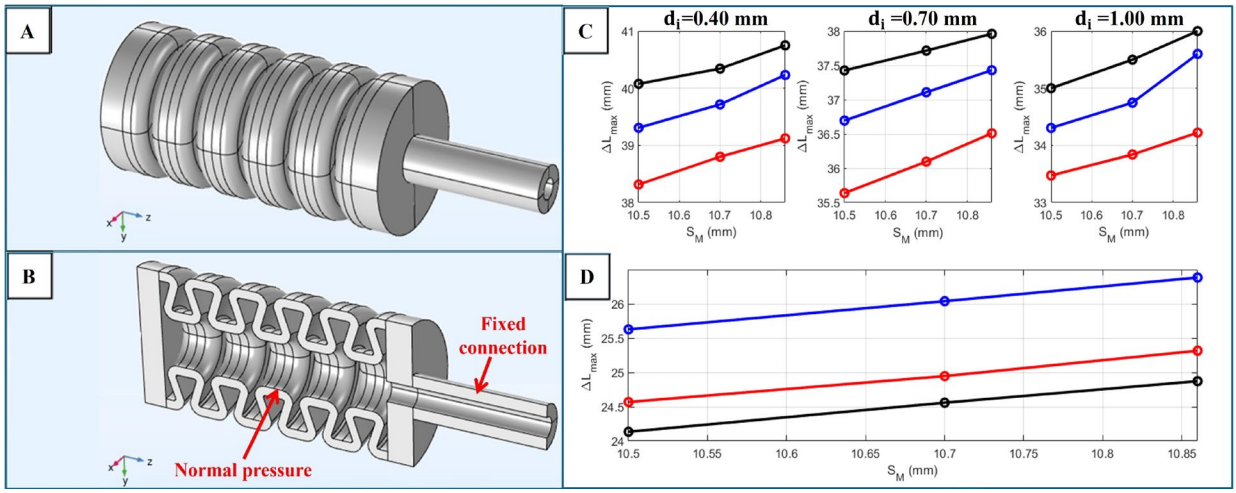


Figure 3. a) Three-dimensional geometrical domain; b) cross-sectional view and boundary conditions; c) parametric optimization of the AM-I Support design; red: $2l_c$=0.8 mm, blue: $2l_c$=1.07 mm; black: $2l_c$=1.35 mm; d) parametric optimization of the U-shaped design: red: R=1.6 mm; blue: R=2.4 mm; black: R=3.2 mm.

An unstructured mesh was chosen to study the deformation of the SPAs (**Fig. 3**), under the following set of boundary conditions (see **Fig. 3 b)**):

- Fixed connection: a fixed constraint boundary condition was set on the pin outer surface, replicating the connection to the pneumatic actuation system, and
- Normal pressure: a given absolute pressure is imposed on the internal surfaces.

Quadratic shape functions were found to be sufficient to describe the large deformations undergone by the SPAs both under elastic and hyperelastic modeling.

The optimization variable was the maximum axial deformation ΔL_{max} The geometrical parameters varied, along with their respective variation intervals, were presented in **Tab. 5** and in **Tab.6**, and for each combination the maximum axial deformation ΔL_{max} . calculated via FEM was registered.

Results

DoE for UTS maximization.

The DoE is aimed at identifying process parameters that maximize UTS, to allow maximum elongation for the actuator. UTS of 3D-printed dogbones was measured using an INSTRON tensile testing machine.

Extrusion temperature, infill line direction and ironing produce a remarkable effect on the maximization of the UTS, as shown in **Tab. 7.**

Materials Research Proceedings 57 (2025) 116-127 https://doi.org/10.21741/9781644903735-14

Table 7 - Mechanical values for the different tensile tests, varying the three process parameters.

Temperature	Lines	Ironing	UTS [Mpa]	Elongation [%]	E [Mpa]
-1	-1	-1	7.24	615.37	6.80
1	-1	-1	6.64	569.47	6.75
-1	1	-1	4.62	237.60	7.83
1	1	-1	4.63	228.87	7.50
-1	-1	1	7.46	575.88	7.37
1	-1	1	7.56	545.13	7.11
-1	1	1	6.21	423.74	7.25
1	1	1	5.40	346.07	6.69
-1	-1	-1	7.14	584.33	7.13
1	-1	-1	6.64	569.47	6.75
-1	1	-1	4.71	240.85	7.84
1	1	-1	4.66	234.17	7.91
-1	-1	1	7.24	599.87	7.36
1	-1	1	7.22	582.55	7.37
-1	1	1	5.65	369.71	7.15
1	1	1	5.15	347.39	6.17
-1	-1	-1	6.79	556.47	6.79
1	-1	-1	6.51	530.72	7.04
-1	1	-1	4.65	241.94	7.77
1	1	-1	4.24	227.82	7.13
-1	-1	1	6.92	561.44	7.15
1	-1	1	7.08	634.00	7.18
-1	1	1	5.96	400.00	7.13
1	1	1	5.26	357.70	8.75

Each mechanical property value represents the average of three samples produced and tested for each set of process parameters. In particular:

- Changing values of temperature and ironing from the low level (-1) to the high level (+1) resulted in an increase of UTS. On the other hand, moving from the high level (+1) to the low level (-1) of line direction increases UTS.
- The lines direction parameter produces the highest effect (at 0°), followed by the ironing (ON) and printing temperature (235°C).

Details of the results discussed above appear in **Fig. 4**. In the Pareto chart of **Fig. 4 a),** factor B (lines direction) has the most significant effect on the UTS. The main effects plot (**Fig 4. b)**) displays the impact of each parameter on UTS: line direction strongly influence the response, while ironing and temperature have a smaller effect. Cube plot (**Fig 4. c)**) illustrates the interaction between factors. The highest tensile stress (7.29 MPa, green circle) occurs at high temperature, ironing ON, and infill lines at 0°, while the lowest tensile stress (4.51 MPa, red circle) is at high temperature, lines at 90°, and ironing OFF.

Materials Research Proceedings 57 (2025) 116-127 https://doi.org/10.21741/9781644903735-14

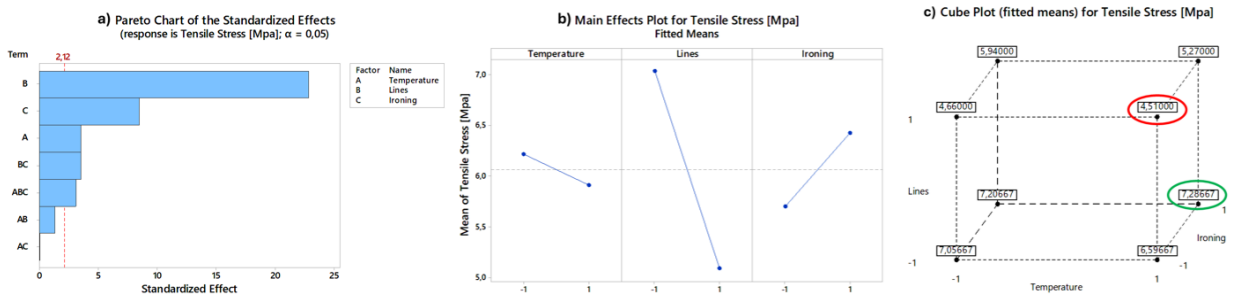


Figure 4. DoE results: a) standardized effect of the factors, b) main effect of the three process parameters studied, c) cube plot.

Mesh independence study.

Prior to analyzing the geometrical design points, a mesh-independence study was performed; the goal is to find the minimum number of finite elements beyond which there is no increase in numerical results accuracy. The number of finite elements was gradually increased, leading to finer computational grids; for each computational domain, ΔL_{max} was registered.
The mesh-independence study was performed on a trial bellow-type chamber geometry with: S_M=10.86 mm, l_c=1.6 mm and d_i=0.3 mm.

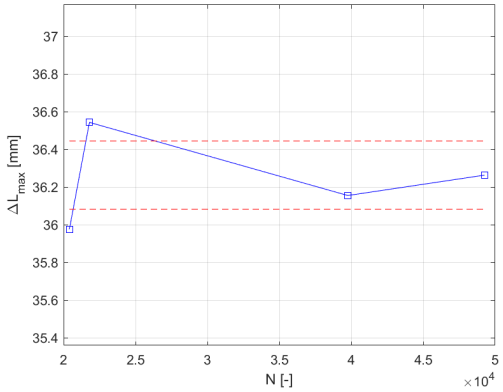


Figure 5. Maximum elongation for the trial bellow-type device at increasing number of finite elements; in red: ±0.5% of the maximum elongation found with the finest mesh.

From **Fig. 5** the optimal mesh was found to be the one with 39759 elements; a further inflation in the number of finite elements does not lead to higher accuracy, while requiring higher computational costs.

Hyperelastic simulations.
Both elastic and hyperelastic simulations based on the optimal results coming from mechanical test have been made. The Young modulus has been estimated with respect to the mean stress-strain curve (straight dashed blue line in **Fig. 6**), resulting in being 8.61 MPa.

Materials Research Proceedings 57 (2025) 116-127 https://doi.org/10.21741/9781644903735-14

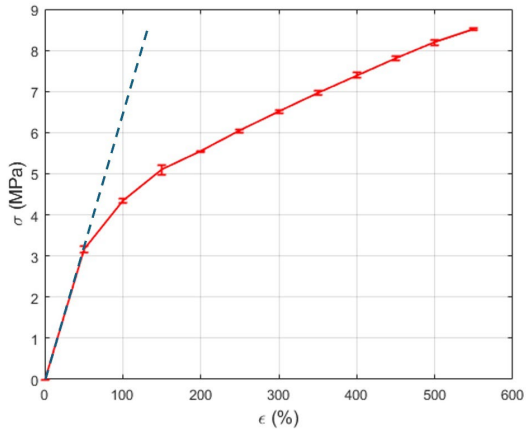


Figure 6. Mean stress-strain curve with error bars; σ: stress; ϵ: strain.

In addition, hyperelastic regression based on the abovementioned tensile stress results was performed. The results of the lest square fit regression for different hyperelastic materials were reported in **Tab. 8**.

Table 8. Least square fit regression for different hyperelastic constitutive models.

Model	Residue	Model	Residue
Mooney-Rivlin – 2 parameters	5.88e-3	Yeoh – Second order	9.16
Mooney-Rivlin – 3 parameters	4.96e-3	Yeoh – Third order	44.24
Mooney-Rivlin – 5 parameters	1.14e-3	Ogden – First order	15.69
Neo – Hookean	26.20	Ogden – Second order	1.42
Yeoh – First order	12.40	Ogden – Third order	0.17

The 5-parameters Mooney-Rivlin model provided the best results and was used for hyperelastic simulations on the complete geometrical dataset. The constitutive model equation is:

$$W = C_{10}(I_1 - 3) + C_{01}(I_2 - 3) + C_{20}(I_1 - 3)^2 + C_{02}(I_2 - 3)^2 + C_{11}(I_1 - 3)(I_2 - 3) \quad (1)$$

Here W is the strain energy density function, while I_i is the i-th strain tensor invariant. The fitted material constants are: C_{01} = 1.3436 MPa, C_{02} = − 0.11666 MPa, C_{10} = 0.66856 MPa, C_{11} = 0.022977 MPa and C_{20} = − 0.0028594 MPa.

The best and worst design for each SPA design and under the assumption of elastic modeling have been reported in the following **Tab. 9**.

Table 9. Best and worst designs for pneumatic chambers under elastic modeling.

U-shaped bellow				AM I-Support			
Parameters (best device)	$\Delta L_{max}^{(FEM)}$	Parameters (worst device)	$\Delta L_{max}^{(FEM)}$	Parameters (best device)	$\Delta L_{max}^{(FEM)}$	Parameters (worst device)	$\Delta L_{max}^{(FEM)}$
S_M=10.86 mm R=2.50 mm	85.18 mm	S_M=10.52 mm R=1.60 mm	73.0 mm	S_M=10.86 mm l_c=1.35 mm d_i=1 mm	125.47 mm	S_M=10.50 mm l_c=0.8 mm d_i=0.4 mm	105.0 mm

The results under the assumption of hyperelastic modeling are summarized in **Tab. 10**.

Materials Research Proceedings 57 (2025) 116-127 https://doi.org/10.21741/9781644903735-14

Table 10. Best and worst designs for pneumatic chambers under hyperelastic modeling.

U-shaped bellow				AM I-Support			
Parameters (best device)	$\Delta L_{max}^{(FEM)}$	Parameters (worst device)	$\Delta L_{max}^{(FEM)}$	Parameters (best device)	$\Delta L_{max}^{(FEM)}$	Parameters (worst device)	$\Delta L_{max}^{(FEM)}$
S_M=10.86 mm R=2.50 mm	26.44 mm	S_M=10.50 mm R=1.80 mm	24.14 mm	S_M=10.86 mm l_c=1.35 mm d_i=0.4 mm	40.75 mm	S_M=10.50 mm l_c=0.8 mm d_i=1 mm	33.43 mm

The following considerations can be made:

- The U-shaped bellow-type chamber always performs worse than AM I-Support one.
- Choosing a circular pneunet cross-section always gives the maximum displacement while the opposite is true for the elliptical one (i.e., S_M equal to 10.50 mm).
- Elastic modeling always overestimates the maximum pneunet elongation.
- The best and worst designs vary when considering hyperelasticity.
- The maximum displacement for AM I-Support geometry under hyperelastic modeling can be achieved with S_M=10.86 mm (i.e., circular device front section), d_i=0.4 mm and l_c=1.35 mm (see **Fig. 3 c)**).
- The maximum displacement for U-shaped bellow actuator under hyperelastic modeling can be achieved with S_M=10.86 mm and R=2.50 mm (see **Fig. 3 d)**).

Elongation experiment.

The AM I-Support (**Fig. 7 c)**) and U-shaped bellow (**Fig. 7 a)**) were tested under 2 bar pressure to evaluate elongation and mechanical response. The AM I-Support in its best configuration (S_M=10.86 mm, l_c=1.35 mm, d_i=0.40 mm) achieved 77% elongation, reaching a total length of 92.90 mm (**Fig. 7 b)**), matching simulation predictions. The U-shaped bellow in its best configuration (S_M=10.86 mm, R=2.50 mm) achieved 50% elongation, with a total length of 79.40 mm (**Fig. 7 d)**), also aligning with simulations. As listed in **Tab. 11** the relative error between hyperelastic simulation and experimental results is low, ranging between 3.66% and 4.44%.

It should be said that actuators fabricated through traditional manufacturing methods (i.e., molding) are generally characterized by higher elongation values, as the materials (i.e., silicone) composing the actuators result more flexible than TPU processed via MEX. [24] On the other hand, despite having better performance they require multi-assembly steps, as well as manual labor lacking in automation: for this reason advancing MEX for the fabrication of soft actuators is key. The hyperelastic simulations, using the 5-parameter Mooney-Rivlin model, accurately predicted the material's mechanical behavior, showing strong correlation with experimental results. This validated both the geometries' performance and the reliability of the hyperelastic model in predicting SPA response under actuation.

Materials Research Proceedings 57 (2025) 116-127 https://doi.org/10.21741/9781644903735-14

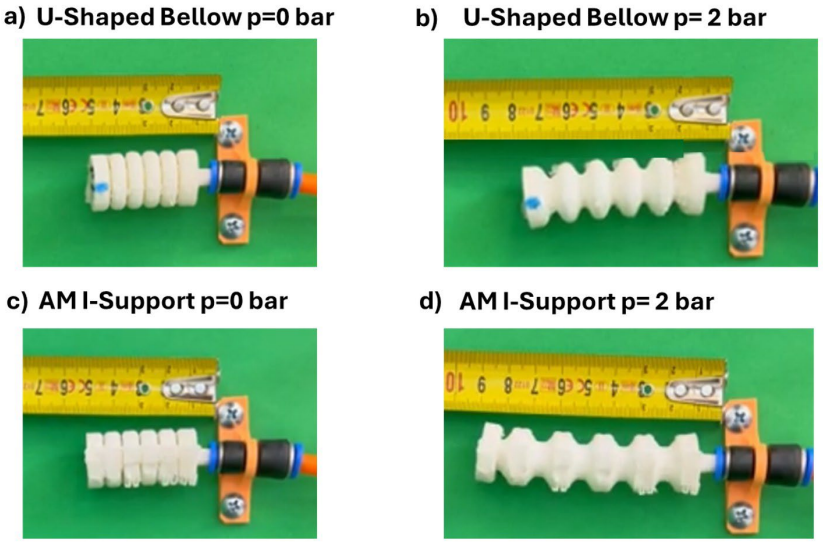


Figure 7. a) U-shaped bellow best configuration at p=0 bar, rest b) U-shaped bellow best configuration elongation at p=2 bar, c) AM I-Support best configuration at p=0, rest d) AM I-Support best configuration elongation at p=2 bar.

Table 11 - Relative error (%) between simulation and experimental results at p=2 bar.

Experimental results			Elastic modeling				Hyperelastic modeling			
Device	**ΔL_{max} [mm]**	**Total Length [mm]**	**Device**	**ΔL_{max} [mm]**	**Total Length [mm]**	**Relative error %**	**Device**	**ΔL_{max} [mm]**	**Total Length [mm]**	**Relative error %**
U-shaped bellow	23.53	79.40	U-shaped bellow	85.18	141.05	77.64	U-shaped bellow	26.44	82.31	3.66
U-shaped bellow	21.13	77.00	U-shaped bellow	73.00	128.87	67.36	U-shaped bellow	24.14	80.01	3.91
AM I-Support	37.03	92.90	AM I-Support	125.47	181.34	95.20	AM I-Support	40.75	96.62	4.00
AM I-Support	29.63	85.50	AM I-Support	105.00	160.87	88.15	AM I-Support	33.43	89.3	4.44

Conclusions and further work

In this paper, the inexpensive MEX has been used for the fabrication of an underexploited class of soft actuators, i.e. elongation-based SPA, which has great potential for the creation of multiple-degree of freedom soft robotic arms.

A framework based on the process-parameters, design-parameters relationship is proposed and experimentally validated to fabricate high-performance, airtight actuators. The whole approach is hyperelastic simulation-driven: as a matter of fact, two different geometries have been designed, numerically simulated and experimentally tested. Different process parameters (i.e., infill orientation, ironing and printing temperature) have been studied and optimized. In particular, the best process parameters resulted to be: lines direction at 0°, ironing “on”, and printing temperature at 225°C. Experimental results demonstrate that the AM I-Support SPA design reached an elongation of 77%, while the U-shaped bellow was limited to 50% when pressurized at 2 bar. A

good agreement with hyperplastic simulations has been found under all experimental conditions and SPA designs.

In further works, artificial intelligence will be used to further study the relationship between actuator performance and other design/process parameters.

References

[1] El-Atab N, Mishra RB, Al-Modaf F, et al (2020) Soft Actuators for Soft Robotic Applications: A Review. Advanced Intelligent Systems 2:. https://doi.org/10.1002/aisy.202000128

[2] Xavier MS, Tawk CD, Zolfagharian A, et al (2022) Soft Pneumatic Actuators: A Review of Design, Fabrication, Modeling, Sensing, Control and Applications. IEEE Access 10:59442–59485

[3] Yap HK, Ng HY, Yeow CH (2016) High-Force Soft Printable Pneumatics for Soft Robotic Applications. Soft Robot 3:144–158. https://doi.org/10.1089/soro.2016.0030

[4] Su H, Hou X, Zhang X, et al (2022) Pneumatic Soft Robots: Challenges and Benefits. Actuators 11

[5] Zhang YF, Ng CJX, Chen Z, et al (2019) Miniature Pneumatic Actuators for Soft Robots by High-Resolution Multimaterial 3D Printing. Adv Mater Technol 4:. https://doi.org/10.1002/admt.201900427

[6] Lalegani Dezaki M, Sales R, Zolfagharian A, et al (2023) Soft pneumatic actuators with integrated resistive sensors enabled by multi-material 3D printing. International Journal of Advanced Manufacturing Technology 128:4207–4221. https://doi.org/10.1007/s00170-023-12181-8

[7] Stavropoulos P, Foteinopoulos P (2018) Modelling of additive manufacturing processes: A review and classification. Manuf Rev (Les Ulis) 5:. https://doi.org/10.1051/mfreview/2017014

[8.Gul JZ, Sajid M, Rehman MM, et al (2018) 3D printing for soft robotics–a review. Sci Technol Adv Mater 19:243–262. https://doi.org/10.1080/14686996.2018.1431862

[9] Arleo L, Stano G, Percoco G, Cianchetti M (2021) I-support soft arm for assistance tasks: a new manufacturing approach based on 3D printing and characterization. Progress in Additive Manufacturing 6:243–256. https://doi.org/10.1007/s40964-020-00158-y

[10] Yao Y, Chen Y, He L, Maiolino P (2023) Design Optimization for Bellow Soft Pneumatic Actuators in Shape-Matching. In: 2023 IEEE International Conference on Soft Robotics, RoboSoft 2023. Institute of Electrical and Electronics Engineers Inc.

[11] Tawk C, Alici G (2022) 5 - 4D-printed pneumatic soft actuators modeling, fabrication, and control. In: Bodaghi M, Zolfagharian A (eds) Smart Materials in Additive Manufacturing. Elsevier, pp 103–140

[12] Stano G, Arleo L, Percoco G (2020) Additive manufacturing for soft robotics: Design and fabrication of airtight, monolithic bending PneuNets with embedded air connectors. Micromachines (Basel) 11:. https://doi.org/10.3390/MI11050485

[13] Zolfagharian A, Mahmud MAP, Gharaie S, et al (2020) 3D/4D-printed bending-type soft pneumatic actuators: fabrication, modelling, and control. Virtual Phys Prototyp 15:373–402. https://doi.org/10.1080/17452759.2020.1795209

[14] Zlatintsi A, Dometios AC, Kardaris N, et al (2020) I-Support: A robotic platform of an assistive bathing robot for the elderly population. Rob Auton Syst 126:103451. https://doi.org/https://doi.org/10.1016/j.robot.2020.103451

[15] Saleh MA, Soliman MA, Mousa MA, et al (2020) Design and implementation of variable inclined air pillow soft pneumatic actuator suitable for bioimpedance applications. Sens Actuators A Phys 314:. https://doi.org/10.1016/j.sna.2020.112272

[16] Gariya N, Kumar P, Prasad B, Singh T (2023) Soft pneumatic actuator with an embedded flexible polymeric piezoelectric membrane for sensing bending deformation. Mater Today Commun 35:. https://doi.org/10.1016/j.mtcomm.2023.105910

[17] Coyle S, Majidi C, LeDuc P, Hsia KJ (2018) Bio-inspired soft robotics: Material selection, actuation, and design. Extreme Mech Lett 22:51–59. https://doi.org/https://doi.org/10.1016/j.eml.2018.05.003

[18] Kim K, Park J, Suh J, et al (2017) 3D printing of multiaxial force sensors using carbon nanotube (CNT)/thermoplastic polyurethane (TPU) filaments. Sens Actuators A Phys 263:493–500. https://doi.org/https://doi.org/10.1016/j.sna.2017.07.020

[19] Song Z, Wang Z, Liu B, et al (2025) A soft gripper based on PneuNets structure with stiffness-variable-enhanced load capacity for object grasping. Sens Actuators A Phys 383:116253. https://doi.org/https://doi.org/10.1016/j.sna.2025.116253

[20] Manti M, Cacucciolo V, Cianchetti M (2016) Stiffening in Soft Robotics: A Review of the State of the Art. IEEE Robot Autom Mag 23:93–106. https://doi.org/10.1109/MRA.2016.2582718

[21] Ansari Y, Manti M, Falotico E, et al (2017) Towards the development of a soft manipulator as an assistive robot for personal care of elderly people. Int J Adv Robot Syst 14:1–17. https://doi.org/10.1177/1729881416687132

[22] Gorissen B, Leuven KU, De Volder M, et al (2017) Elastic Inflatable Actuators for Soft Robotic Applications. https://doi.org/10.17863/CAM.9606

[23] Yao Y, He L, Maiolino P (2023) SPADA: A Toolbox of Designing Soft Pneumatic Actuators for Shape Matching based on Surrogate Modeling

[24] Pagliarani N, Arleo L, Albini S, Cianchetti M (2023) Variable Stiffness Technologies for Soft Robotics: A Comparative Approach for the STIFF-FLOP Manipulator. Actuators 12:. https://doi.org/10.3390/act12030096

Materials Research Proceedings 57 (2025) 128-135 https://doi.org/10.21741/9781644903735-15

Understanding powder transport mechanisms in directed energy deposition via design of experiments

Adriano Nicola PILAGATTI[1,a *], Eleonora ATZENI[1,b], Alessandro SALMI[1,c] and Luca IULIANO[1,d]

[1]Department of Management and Production Engineering (DIGEP), Politecnico di Torino, Corso Duca degli Abruzzi 24, 10129 Torino, Italy

[a]adriano.pilagatti@polito.it, [b]eleonora.atzeni@polito.it, [c]alessandro.salmi@polito.it, [d]luca.iuliano@polito.it

Keywords: Additive Manufacturing; Laser Processes; Design of Experiment; Manufacturing Systems

Abstract. Laser beam powder metal directed energy deposition (DED-LB/Powder) is a metal additive manufacturing (AM) technique that can build, repair, and remanufacture metal components. The objective of this study is to investigate the behaviour of the powder supply system, based on a rotating disk powder metering and pneumatic conveying. The powder mass flow rate was related to different levels of carrier gas flow rate and perforated disc rotation. A sensor acquisition system was designed to measure and acquire the boundary conditions (BCs) exterior to the powder feeder system, in order to identify possible external noise. Based on the data analysis, it was possible to identify different feeding conditions as the input parameters were varied and how the responses were affected by them.

Introduction

Directed Energy Deposition (DED) is an additive manufacturing (AM) category that uses focused thermal energy to fuse feedstock material as it is deposited along a programmed path. Depending on the energy source employed, DED can be distinguished into laser-based (LB), electric arc (Arc), and electron beam (EB) processes. The feedstock material can be supplied as either a continuous wire or a powder stream. When a laser beam is used as the thermal source for fusing powdered material, the process is specifically referred to as DED-LB/Powder, in accordance with ISO/ASTM 52900:2021(E) [1].

A key aspect in determining the impact of DED-LB/Powder processes on part quality is the correct tuning of the powder mass flow rate ($\dot{m}_{\mathrm{powder}}$). Precise control of $\dot{m}_{\mathrm{powder}}$ is essential for maintaining process stability, achieving uniform material deposition, and optimizing mechanical properties [2]. The structured powder handling mechanism used by the DED-LB/Powder systems basically consists of three interrelated phases: powder metering, powder conveyance, and powder delivery. The first phase is the metering, either in mass or volume, of the amount of powder to be fed into the melt pool from the reservoir. Powder metering can be achieved by a number of methods including aspirating/dispensing, screw/auger, feeder wheel, and electrostatic. In the second phase the powder is conveyed from the metering device to the nozzle. This is usually accomplished by an inert carrier gas flow. Other conveyance methods include mechanical conveyance, as well as vibration-assisted and gravity-driven conveyance. The third phase, accomplished via a powder delivery nozzle, converges the powder stream into a single focal spot. The pipe system connecting the feeding system to the deposition head [2-5] and the nozzle configuration define the transport mechanism. Despite the clear distinction made here between powder metering, conveyance, and delivery, it should be emphasised that these phases are frequently interconnected. Collectively, these phases determine the efficiency and reliability of the powder deposition process [6].

Content from this work may be used under the terms of the Creative Commons Attribution 3.0 license. Any further distribution of this work must maintain attribution to the author(s) and the title of the work, journal citation and DOI. Published under license by Materials Research Forum LLC.

Materials Research Proceedings 57 (2025) 128-135 https://doi.org/10.21741/9781644903735-15

The effectiveness of powder transport and deposition is influenced by the interplay between powder feeding parameters. Understanding these interactions is essential for improving process stability and optimizing deposition efficiency. Several research studies have optimized feeding parameters in the literature. Among them, Oh *et al.* [7], explored gas flow rate between 4 L min^{-1} and 6 L min^{-1} for AISI 316L and reported that increasing the carrier gas flow rate reduces the powder flow rate, thereby lowering the height of the deposited material. However, excessive powder flow can exceed the desired dimensions, highlighting the need for optimization alongside other process parameters. Regarding powder transport studies, Iams *et al.* [8] examined how variations in particle size affect $\dot{m}_{powder}$ in DED processes. Their findings demonstrated that even a slight increase in particle size results in higher flow resistance. This increase in resistance, attributable to larger and heavier particles, leads to a corresponding decrease in the powder velocity. Simoneau *et al.* [9] emphasized that a defined powder flow rate (2.1 g min^{-1},) and a controlled particle size distribution contribute to improved powder fluidity within the DED feeding system. This suggests that powder flow rate is a key factor influencing process consistency and reproducibility of mechanical properties. Whiting *et al.* [10] used an Optomec powder feeder to monitor the metallic powder mass flow in a DED process with an acoustic emission sensor. They calibrated the system for flow levels ranging from 4 rpm to 8 rpm using AISI 316L powder and established a correlation between the acoustic signal and the actual mass flow rate. This innovative method accurately detects minor flow fluctuations and, with the integration of waveguides, enables more precise and reliable in situ process control, enhancing overall system performance.

The present study aims to characterize the powder mass flow rate, $\dot{m}_{powder,}$ in a DED-LB/Powder system by evaluating the effects of powder feeding parameters. Boundary conditions are monitored as covariates to identify potential noise. To achieve this, the study employs analysis of covariance (ANCOVA) within the framework of the design of experiments (DoE) methodology. The objective is to improve predictive accuracy and enhance process stability by examining the interactions among these factors. The response surface methodology (RSM) approach is used to develop a response surface model. This model enables the identification of both stable combinations of parameters and the onset of undesired effects such as fluctuations in powder flow, which are correlated with the powder feeding mechanisms.

Material and Methods

The experimental setup consisted of a Laserdyne 430 DED system (Prima Additive, Italy) and an Optomec CS 150 powder feeder (Albuquerque, NM, USA), depicted in Fig. 1. The gravity-type powder feeder employs a perforated disk metering system, rotating around a horizontal axis, to regulate powder flow through an orifice on a coupled fixed disk. Pressurised gas is employed to enable suction and conveyance of powders.

Disk rotation speed (ω) and carrier gas flow rate ($\dot{V}_{cg}$) serve as the primary control factors for the powder mass flow rate. The powder feeder is connected to the deposition head by a flexible polymer pipeline with an internal diameter of 6.35 mm and a total length of 2.4 m. The powder feeder has upper limits of 24 rpm for ω and 10 L min^{-1} for $\dot{V}_{cg}$. The deposition head features four distinct nozzles with a nominal diameter of 1 mm each. These nozzles converge the powder stream at an 8 mm standoff distance, ensuring optimal delivery and uniform distribution of the powder material.

Feedstock Material. The feedstock material is gas-atomized MetcoAdd AISI 316L stainless steel powder (Oerlikon, Switzerland) with a particle size distribution ranging from 45 µm to 106 µm (D10 = 54 µm, D50 = 79 µm, D90 = 110 µm), a powder density of 7.896(0.005) g cm^3, and a Carr's compressibility index of 8.3 %, confirming excellent powder flow characteristics [11].

Materials Research Proceedings 57 (2025) 128-135 https://doi.org/10.21741/9781644903735-15



Fig. 1: Optomec CS 150 powder feeder system metering chamber.

Boundary Conditions Monitoring System. Uncontrollable factors, namely chamber temperature (T) and absolute humidity (Ha), were measured as BCs to assess, if present, their impact on $\dot{m}_{powder}$. A custom ESP32-based monitoring system was developed to track BCs. The system employs a Bosch BME280 sensor housed in an IP55-protected enclosure within the build chamber, ensuring exposure only to the measurement environment. Data were recorded at 100 Hz and processed using a simple moving average filter to eliminate transient fluctuations.

Experimental Design. Argon was used as carrier gas. A design comprising four levels for $\dot{V}_{Ar}$, and six levels for ω, equally spaced, was employed to investigate the effects of varying factors on the resulting $\dot{m}_{powder}$ at the nozzles. Based on knowledge from previous experiments, ω varied from 2 rpm to 22 rpm, avoiding the upper limit of 24 rpm due to frequent mechanical issues. A range for $\dot{V}_{Ar}$, from 2 L min^{-1} to 8 L min^{-1}, was explored, with the objective of expanding the typical range reported in the literature. A two-step approach was used to determine the sample size [12]. First, a priori calculations were conducted using G*Power 3.1.9.4, a software tool developed by the Heinrich Heine University of Düsseldorf (Düsseldorf, Germany), resulting in a minimum sample size of 69 [13]. To ensure adequate statistical power and simplify design replications, a sample size of 72 was selected corresponding to a factorial design with 6 levels of ω and 4 levels of $\dot{V}_{Ar}$, and 3 replications (as depicted in Fig. 2). A post hoc type II error analysis confirmed that the selected sample size was sufficient, achieving 99 % power for $\dot{V}_{Ar}$, 97 % for ω and 68 % for the interaction term (Table 1). These results validate the robustness of the experimental design and its ability to detect significant effects.

Table 1: Post hoc computed type II error for the experiment conducted with 72 trials.

Factor	*df*	Critical *F*	Power [%]
$\dot{V}_{Ar}$	3	2.8	99
ω	5	2.4	97
$\omega \cdot \dot{V}_{Ar}$	15	1.9	68

Materials Research Proceedings 57 (2025) 128-135 https://doi.org/10.21741/9781644903735-15

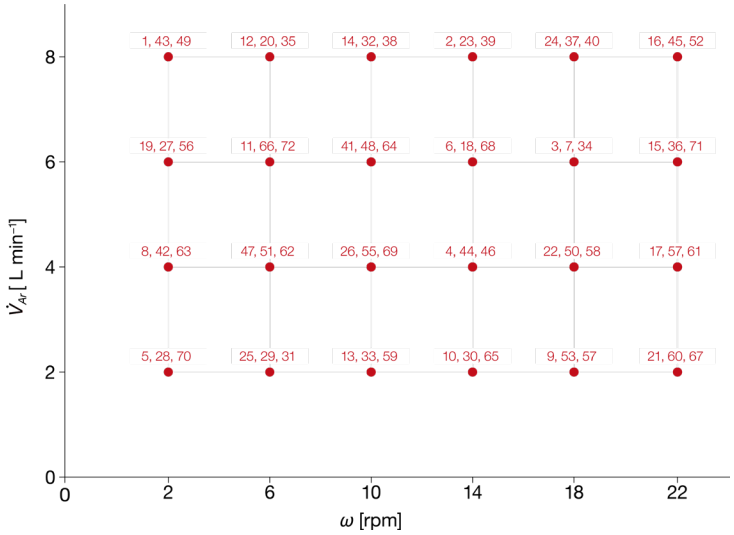


Fig. 2: General Full Factorial design with levels and run orders.

Powder Flow Rate Measurement. The $\dot{m}_{powder}$ was measured using a dual-bottle collection method designed to differentiate between transient and steady-state powder flow (see Fig. 3). The first bottle (with the blue funnel) collected the powder flow during the transient phases (30 s), corresponding to the activation and deactivation of the powder stream. The second bottle (with the black funnel) exclusively captured powder during the steady-state phase (120 s), ensuring a more accurate measurement of the delivered powder in stable condition. The entire procedure was programmed using G-code. Following each trial, the powder from the steady-state bottle was weighed using a high-precision ANJ-NM/ABS -N balance by KERN (Gottlieb, Germany). Finally, the $\dot{m}_{powder}$ was determined as the ratio of the collected mass to the flow time. After measurement, the powder from both bottles was carefully removed, sieved, and recycled. The bottles were then repositioned on the machine table to ensure consistency across measurements.



Fig. 3: Experiment setup for powder mass flow rate.

Materials Research Proceedings 57 (2025) 128-135 https://doi.org/10.21741/9781644903735-15

Table 2. Analysis of covariance (R^2(adj)=99 %).

Source	*df*	Contribution [%]	Adj *SS*	Adj *MS*	*F*	*p*-value [%]
Model	25	99.37	3153.64	126.145	291.78	<0.1
Covariates	2	5.93	0.76	0.379	0.88	42.3
***T* [°C]**	1	2.66	0.45	0.455	1.05	31.0
***H*$_a$ [g m^{-3}]**	1	4.54	0.53	0.532	1.23	27.3
Linear	8	79.97	2504.51	313.063	724.13	<0.1
***ω* [rpm]**	5	47.45	981.03	196.205	453.83	<0.1
$\dot{V}_{Ar}$[L min^{-1}]	3	32.52	865.53	288.508	667.34	<0.1
2-Way Interactions						
ω·$\dot{V}_{Ar}$ [rpm L min^{-1}]	15	13.47	427.41	28.494	65.91	<0.1
Error	46	0.63	19.89	0.432		
Total	71	100				

Results and discussion

Attention was given to avoiding systematic errors throughout the experiment. Thus, the experimental campaign was conducted on a single day by a single operator. To minimize errors due to the gas flow regulation system, the $\dot{V}_{Ar}$ was initially maximized and then cautiously reduced to the correct rate during the transient phase of each test. All trials were carried out with the same argon upstream flow rate (10 L min^{-1}) of the feeder system. The test order was randomized.

During the experiments covariate ranges were detected, which were between 25.2 °C and 29.5 °C for the temperature and 10.3 g m^{-3} and 12.4 g m^{-3} for absolute humidity. The analysis is conducted using MINITAB® 20.1.3 software (Gaithersburg, MD, USA). Data results are evaluated by ANCOVA (see Table 2) to identify if noise factors are active in the process, and neither covariate appears to influence $\dot{m}_{powder}$. Consequently, covariates are not taken into consideration for the next steps of the work. However, covariate acquisition could be helpful over the long term, and data are stored for future studies. The outliers analysis reveals issues with the 14 rpm (ω) level and low $\dot{V}_{Ar}$ values (2 L min^{-1} and 4 L min^{-1}); specifically, these issues are observed in the trials with Run Order 30 and 65 (14 rpm and 2 L min^{-1}) and Run Order 4 (14 rpm and 4 L min^{-1}). Data analysis reveals that linear terms contribute most to total Adj *SS*, with a greater contribution for the ω. Furthermore, the main effects and the interaction are significant for the significance level chosen, as confirmed by their *p*-value.

The R^2(adj) of 99 % indicates that the resulting model properly explains the variability of the data. Fig. 4(a) displays the plot of the main effects. As expected, as the ω factor increases, the response $\dot{m}_{powder}$ mean increases too. This is attributable to the greater quantity of powder entering the flow in a given time, consequent to an increase in disk rotation speed. However, at speeds exceeding 18 rpm, a decline in the $\dot{m}_{powder}$ mean response was observed. Conversely, the $\dot{V}_{Ar}$ factor demonstrated a counterintuitive tendency, in fact as the $\dot{V}_{Ar}$ increases, the $\dot{m}_{powder}$ decreases.

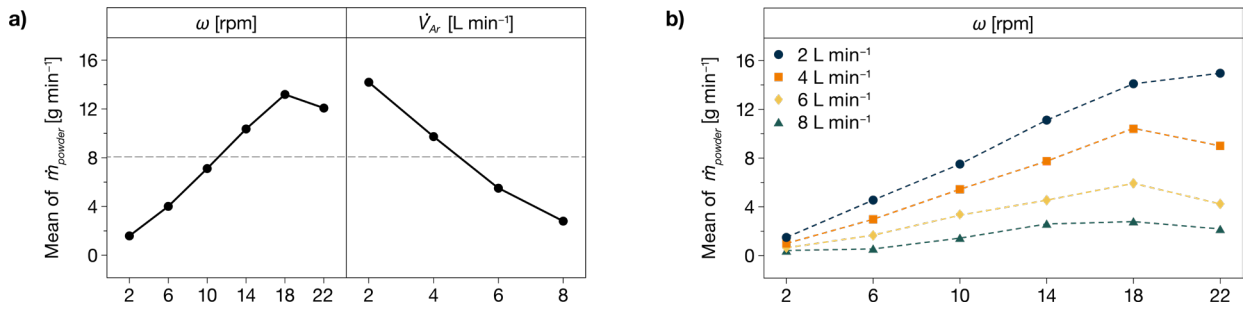


Fig. 4: (a) Main Effects plot and (b) Interaction plot for $\dot{m}_{powder}$ [g min^{-1}].

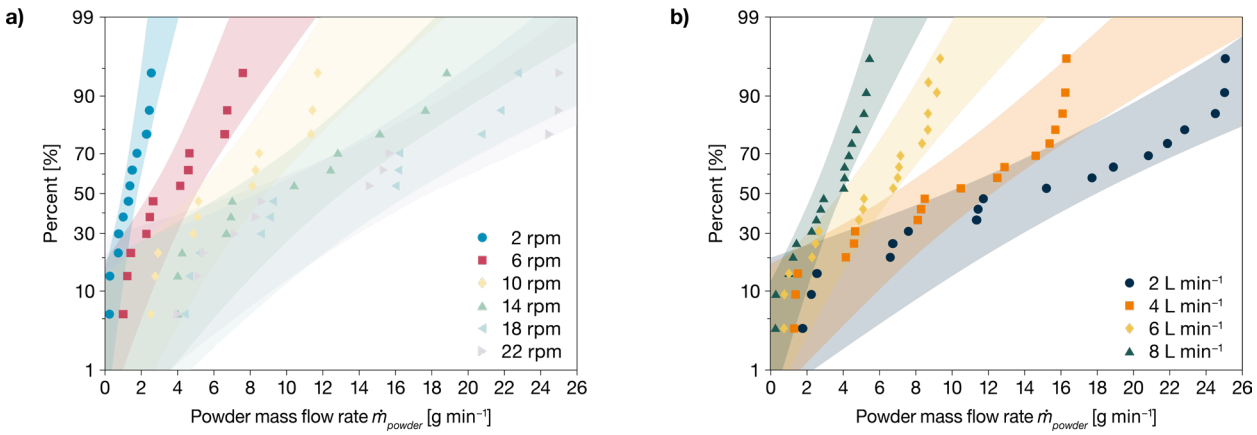


Fig. 5: Factorial main effect probability plot, Johnson's method, (a) versus ω and (b) versus $\dot{V}_{Ar}$ with the corresponding 95 % confidence intervals bands.

The interaction plot in Fig. 4(b) details that this trend is consistently observed across all levels of the ω factor, although it becomes more pronounced as both ω and $\dot{V}_{\mathrm{Ar}}$ increase. Furthermore, it is evident that the as $\dot{V}_{\mathrm{Ar}}$ increases, the inversion of the $\dot{m}_{powder}$ mean trend occurs at a lower ω. The normal probability plot (NPP) using Johnson's method (Fig. 5) highlights differences in means and variability across factor levels. However, despite absolute changes in standard deviation, the coefficient of variation remains stable, indicating that variability is primarily driven by factor levels rather than internal system inconsistencies. This suggests that at high ω and $\dot{V}_{\mathrm{Ar}}$ levels, powder feeding may reach an operating limit.

The observed trends are attributable to the mechanisms involved in the feeding system and especially to the pressure losses in the conveyance system. At the suction point, a pressure drop occurs since the powder particles are accelerated by the conveying gas, which overcomes their inertia. The presence of powder particles and frictional forces within the piping system leads to an additional pressure drop, with the magnitude of these drops increasing with the amount of powder entering the flow. Analogously, an increase in $\dot{V}_{\mathrm{Ar}}$ leads to an increase in gas velocity and, consequently, a higher pressure drop due to friction at pipe walls. Furthermore, an increase in powder mixture in the conveyance system, or a higher gas velocity, generates turbulence in the flow, causing more particles to collide with the walls, be retarded, and be accelerated again, thus leading to flow fluctuations and further consequences in pressure loss. Consequently, the pressure drop from the inlet and outlet of the system is significantly influenced by the parameters of the feeding process. The reduction in pressure leads to a substantial decrease in $\dot{m}_{powder}$ as a critical point is attained.

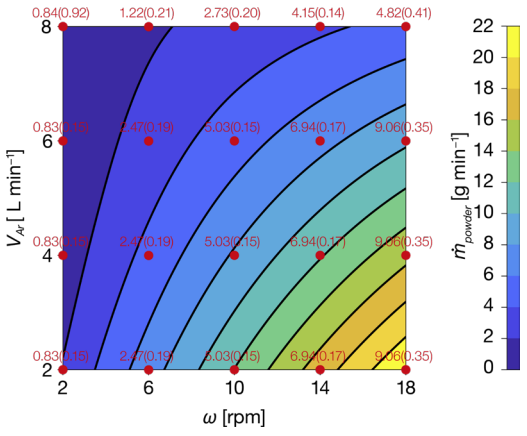


Fig. 6: $\dot{m}_{powder}$ [g min^{-1}] contour plot with the mean(deviation) response.

The regression model for the response surface is developed using stepwise methodology, incorporating linear, quadratic, and interaction terms while excluding uninformative data at $\omega = 22$ rpm. A non-hierarchical approach with a 10 % significance level for entry and removal ensures a conservative model. After four iterations, the model achieves $S = 0.7$, R^2(adj) = 98.7 %, and R^2(pred) = 98.5 %, indicating strong predictive accuracy. Residual analysis confirms normality through the NPP and Anderson-Darling test, with residuals forming a horizontal band around zero, showing no discernible patterns. The final response surface equation (Eq 1) is obtained, with the corresponding plotted response surface shown in Fig. 6, as follows:

$$\dot{m}_{\text{powder}}\ [\text{g min}^{-1}] = 6.574 + 5.911\ \omega - 4.676\ \dot{V}_{\text{Ar}} + 0.794\ \dot{V}_{\text{Ar}}{}^{2} - 3.977\ \omega\ \dot{V}_{\text{Ar}} \quad (1)$$

Although the quadratic term is included in the model, it is found to be less significant, as the non-linearity of the response is better captured by the two-way interaction term.

Conclusions

This study investigated the powder mass flow rate ($\dot{m}_{powder}$) of AISI 316L powder in a horizontal disc-based feeder system, employing a General Full Factorial DoE while accounting for potential noise factors. The objective was to characterize powder transport mechanisms and determine their dependence on disk rotation speed (ω) and carrier gas flow rate ($\dot{V}_{\text{Ar}}$), considering boundary conditions (BCs) as covariates. The findings indicate the presence of specific operational ranges that constrain the effective performance of the system. Especially, rotational speed exceeding 18 rpm adversely affected the efficiency of powder conveyance due to an increase in inertia and friction effects. Furthermore, at high $\dot{V}_{\text{Ar}}$ turbulence is generated into the system, amplifying the inertia effect and causing an additional pressure drop, which negatively affects the powder feeding. Findings suggest that $\dot{V}_{\text{Ar}}$ should be set up at the lowest possible level to ensure the lift force on the powder in the carrier gas is maintained, as well as to shield the melt pool if the same gas is utilised for both purposes. Future studies should refine the $\dot{V}_{\text{cg}}$ range, increase replications, and explore alternative DoE designs to enhance the robustness of the response model and reduce standard error in regression coefficients.

Acknowledgement

This study was carried out within the MICS (Made in Italy – Circular and Sustainable) Extended Partnership and received funding from the European Union Next-GenerationEU (PIANO NAZIONALE DI RIPRESA E RESILIENZA (PNRR) – MISSIONE 4 COMPONENTE 2, INVESTIMENTO 1.3 – D.D. 1551.11-10-2022, PE00000004). This manuscript reflects only the authors' views and opinions, neither the European Union nor the European Commission can be considered responsible for them. This work has been supported by the Interdepartmental Centre for Integrated Additive Manufacturing (IAM@PoliTo) at the Politecnico di Torino, Torino, Italy.

References

[1] ISO/ASTM 52900:2021(E), Additive Manufacturing - General Principles - Fundamentals and vocabulary, American Society for Testing and Materials (ASTM) International, West Conshohocken (USA), 2021.

[2] A.J. Pinkerton, Advances in the modeling of laser direct metal deposition, J. Laser Appl. 27, S15001 (2015) 1-7. https://doi.org/10.2351/1.4815992

[3] M. Ansari, A. Mohamadizadeh, Y. Huang, V. Paserin, E. Toyserkani, Laser directed energy deposition of water-atomized iron powder: Process optimization and microstructure of single-tracks, Opt. Laser Technol. 112 (2019) 485-93. https://doi.org/10.1016/j.optlastec.2018.11.054

[4] M.A. Jackson, A. Kim, J.A. Manders, D.J. Thoma, F.E. Pfefferkorn, Production of mechanically-generated 316L stainless steel feedstock and its performance in directed energy deposition processing as compared to gas-atomized powder, CIRP J. Manuf. Sci. Technol. 31 (2020) 233-43. https://doi.org/10.1016/j.cirpj.2020.05.014

[5] A.B. Spierings, M. Voegtlin, T. Bauer, K. Wegener, Powder flowability characterisation methodology for powder-bed-based metal additive manufacturing, Prog. Addit. Manuf. 1 (2016) 9-20. https://doi.org/10.1007/s40964-015-0001-4

[6] A. Singh, S. Kapil, M. Das, A comprehensive review of the methods and mechanisms for powder feedstock handling in directed energy deposition, Addit. Manuf. 35 (2020) 101388. https://doi.org/10.1016/j.addma.2020.101388

[7] W.J. Oh, W.J. Lee, M.S. Kim, J.B. Jeon, D.S. Shim, Repairing additive-manufactured 316L stainless steel using direct energy deposition, Opt. Laser Technol. 117 (2019) 6-17. https://doi.org/10.1016/j.optlastec.2019.04.012

[8] A.D. Iams, M.Z. Gao, A. Shetty, T.A. Palmer, Influence of particle size on powder rheology and effects on mass flow during directed energy deposition additive manufacturing, Powder Technology. 396 (2022) 316-26. https://doi.org/https://doi.org/10.1016/j.powtec.2021.10.059

[9] L. Simoneau, A. Bois-Brochu, C. Blais, Tensile Properties of Built and Rebuilt/Repaired Specimens of 316L Stainless Steel Using Directed Energy Deposition, J. Mater. Eng. Perform. 29 (2020) 6139-46. https://doi.org/10.1007/s11665-020-05087-z

[10] J. Whiting, A. Springer, F. Sciammarella, Real-time acoustic emission monitoring of powder mass flow rate for directed energy deposition, Addit. Manuf. 23 (2018) 312-8. https://doi.org/https://doi.org/10.1016/j.addma.2018.08.015

[11] A. Aversa, G. Marchese, E. Bassini, Directed energy deposition of aisi 316l stainless steel powder: Effect of process parameters, Metals. 11 (2021) https://doi.org/10.3390/met11060932

[12] P. Mathews, Sample size calculations: Practical methods for engineers and scientists, first ed., Fairport Harbor, Ohio, 2010.

[13] F. Faul, E. Erdfelder, A.G. Lang, A. Buchner, G*Power 3: A flexible statistical power analysis program for the social, behavioral, and biomedical sciences, Behav. Res. Methods. 39 (2007) 175-91. https://doi.org/10.3758/BF03193146

Materials Research Proceedings 57 (2025) 136-144 https://doi.org/10.21741/9781644903735-16

Physics-based model for dot geometry prediction in dot-by-dot wire arc additive manufacturing

Niccolò GROSSI[1,a *], Guido PIERATTINI[1,b], Riccardo LILLI[1,c] and Antonio SCIPPA[1,d]

[1]University of Florence, Department of Industrial Engineering, Via Santa Marta, 3, Firenze, 50139, Italy

[a]niccolo.grossi@unifi.it, [b]guido.pierattini@edu.unifi.it, [c]riccardo.lilli@unifi.it, [d]antonio.scippa@unifi.it

Keywords: Wire Arc Additive Manufacturing (WAAM), Geometric Modelling, Predictive Model

Abstract. Dot-by-dot is an emerging Wire and Arc Additive Manufacturing (WAAM) technology, allowing for the precise deposition of tiny spheres of molten material, to form slender bars that could be used to manufacture complex lattice structures. Dots' geometry plays a key role in determining both the welding torch optimal toolpath and the mechanical properties of the final product. In this paper an analytical physics-based geometrical model is presented, capable of predicting the geometric characteristics of dot-by-dot additively manufactured bars from the properties of the feedstock material, the welding process parameters and interpass temperature. The proposed model is based on heat transfer and mass conservation and can be applied to different scenarios and materials, being more general with respect to experimental-regressive approaches. A preliminary experimental validation on ER70S-6 steel bars was performed on different case studies, showing fair accuracy in predicting bars diameter and height.

Introduction

Wire and arc additive manufacturing (WAAM) is a Directed Energy Deposition 3D printing technological process, traditionally consisting in the deposition of layers of molten material on top of each other using a metal wire and a welding source. As a result, WAAM technologies allow for the creation of metallic components with complex curvilinear geometries, with minimal waste production. Moreover, by offering a higher deposition rate compared to other metal AM techniques, WAAM processes feature a generally greater level of cost effectiveness [1]. Dot-by-dot is a recently developed deposition strategy for the manufacturing of components using WAAM technological process, allowing for the creation of complex-shape lattice structure objects [2]. As opposed to the continuous deposition of layers, typical of traditional WAAM, dot-by-dot WAAM features the discrete, intermittent deposition of spheres of molten material (dots), stacked on top of each other, forming the struts of a lattice structure. The mechanical properties of dot-by-dot printed bars make them suitable for custom-made structural and civil applications for example as substructures and independent structural components [3] but also as vertical steel reinforcement in reinforced concrete constructions [4]. Wire-structures have also shown to be suitable in a large number of fields ranging from the design of intricate items [5] to the manufacturing of lightweight structural components for aircraft and buildings [6].

The dots' geometry plays a key role in determining both the welding torch's optimal tool-path strategies and the mechanical properties of the finite objects. As such, its determination is of utmost importance for the future development of the dot-by-dot printing strategy. Predicting bars' geometry proves particularly complex given its dependence from boundary conditions such as wire feedstock's material properties, welding process parameters and interpass temperatures. Thus, it is necessary to develop adequate geometrical models, which will be the objective of this contribution.

Content from this work may be used under the terms of the Creative Commons Attribution 3.0 license. Any further distribution of this work must maintain attribution to the author(s) and the title of the work, journal citation and DOI. Published under license by Materials Research Forum LLC.

Materials Research Proceedings 57 (2025) 136-144 https://doi.org/10.21741/9781644903735-16

The scientific literature shows that the vast majority of existing geometrical models for dot-by-dot were developed on the basis of regression-based experimental solutions at the expense of generality [7–9], given that such solutions apply with accuracy mainly to the specific set of parameters used in each case study. This circumstance owes to the novelty of the process and a lack of in-depth studies, which would allow the development of a physics-based approach with the advantage of being more general and applicable to different scenarios, materials and deposition modes (e.g., CMT, pulsed).

For traditional WAAM, a limited number of analytical, physics-based geometrical models were developed based in particular on physical principles such as thermo-capillarity [10] and adding gravity [11,12]; no such type of model has been developed for dot-by-dot deposition.

This work presents the development of an analytical physics-based model for dot-by-dot WAAM geometry, presenting important advantages over experimental regressive models, such as to be easily extrapolated and extended to different materials and outside the range of tested parameters.

Proposed model

The dot-by-dot process is a variation of Wire and Arc Additive Manufacturing (WAAM) used for manufacturing complex metallic structures (e.g., lattice). This method adds material through successive metal dots additions rather than continuous bead deposition. The process for a single point deposition involves these steps: i) positioning of the welding torch, ii) pre-gas started, iii) arc process begins melting the wire and remelting the substrate, iv) the post-gas protects the weld as it solidifies, v) an idle time allows the deposited droplet to cool down. The developed model aims at predicting the dot geometry deposited using such a process, considering the deposition on a bar using the welding nozzle axis parallel to the bar axis. Fig. 1a shows a scheme of the manufacturing process.

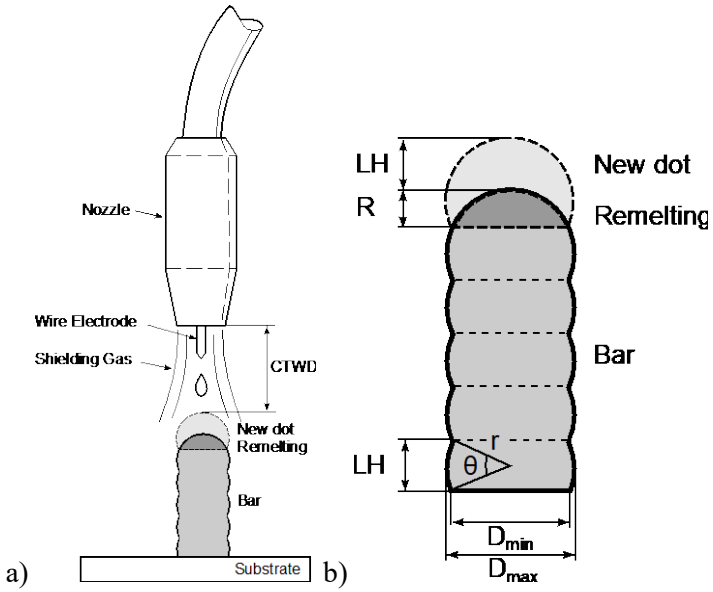


Fig. 1 Dot-by-dot WAAM process a) schematic representation b) geometric description used

Geometry description. In this work, for strut geometry a spherical deposit hypothesis was made, as in Ref. [10], resulting in the cross section shown in Fig. 1b. The fundamental parameters necessary to determine the dots' geometry are then merely layer angle θ and layer radius r, as the other parameters; namely, layer height LH, remelting R, maximum bar diameter D_{max} and minimum bar diameter D_{min}, can be derived from them with simple equations:

Materials Research Proceedings 57 (2025) 136-144 https://doi.org/10.21741/9781644903735-16

$$\mathbf{LH} = \mathbf{2r} \cdot \mathbf{sin}\frac{\boldsymbol{\theta}}{\mathbf{2}} \tag{1}$$

$$\mathbf{R} = \mathbf{r} \cdot \left(\mathbf{1} - \mathbf{sin}\frac{\boldsymbol{\theta}}{\mathbf{2}}\right) \tag{2}$$

$$\mathbf{D_{max}} = \mathbf{2r} \tag{3}$$

$$\mathbf{D_{min}} = \mathbf{2r} \cdot \mathbf{cos}\frac{\boldsymbol{\theta}}{\mathbf{2}} \tag{4}$$

Geometry predictive model. The proposed analytical model is based on the model developed for traditional WAAM by Haghighi et al. [11], which was modified and expanded to fit the characteristics of the dot-by-dot process. Since two variables need to be defined (i.e., θ and r), two equations are required, resorting in particular to conservation laws of energy and mass. First, the power supply required for melting the wire Q_w in the w-DED process is [7]:

$$\boldsymbol{Q_w} = \frac{\boldsymbol{\pi}}{\mathbf{4}} \boldsymbol{D_w^2} \cdot \boldsymbol{WFS} \cdot \boldsymbol{\rho_0} \cdot \boldsymbol{H_0} \cdot \frac{\mathbf{1}}{\boldsymbol{\eta_w}} \tag{5}$$

Where D_w is the wire diameter, WFS is the wire feed speed, ρ_0 is the density of the material at room temperature T_0 and H_0 is the enthalpy difference of the material between melting temperature and room temperature, i.e. $H_0 = H(T_m) - H(T_0) = C_p (T_m - T_0)$. η_w is wire melting efficiency, which is the ratio of the power consumed for melting the wire to the power absorbed by the wire, as there is a small amount of power, usually less than 11 % ($\eta_w > 89\%$), that is lost to the environment. It was set equal to 0.93 as in other works [7]. Subsequently, the penetration power Q_p, which is defined as the remaining power after the supplied power for melting wire Q_w is subtracted from the total transferred power Q_t can be expressed as:

$$\boldsymbol{Q_p} = \boldsymbol{Q_t} - \boldsymbol{Q_w} = \frac{\boldsymbol{V_p}}{\boldsymbol{t_{dep}}} \cdot \boldsymbol{\rho_m} \cdot \boldsymbol{H_i} \cdot \frac{\mathbf{1}}{\boldsymbol{\eta_p}} \tag{6}$$

where V_p is the penetration volume, corresponding in Fig. 1 to the spherical cap of height R, t_{dep} is the deposition time, ρ_m is the density of the material at melting temperature and H_i is the enthalpy difference of the material between melting temperature and interpass temperature T_i, i.e. $H_i = H(T_m) - H(T_i) = C_p (T_m - T_0)$. Finally, η_p is penetration melting efficiency, i.e. a parameter defined as the ratio of power used to create a molten pool to the power delivered to and absorbed by the workpiece [7]. We propose the following analytical expression for determining penetration efficiency, $\eta_p = V_p/V_t$. I.e. η_p is defined as the ratio of penetration volume V_p to the total dot volume V_t. Therefore, conservation of energy can be expressed as follows:

$$\boldsymbol{Q_t} = \boldsymbol{WFS} \cdot \frac{\boldsymbol{\pi}}{\mathbf{4}} \boldsymbol{D_w^2} \cdot \boldsymbol{\rho_0} \cdot \boldsymbol{C_p} (\boldsymbol{T_m} - \boldsymbol{T_0}) \frac{\mathbf{1}}{\boldsymbol{\eta_w}} + \frac{\boldsymbol{V_p}}{\boldsymbol{t_{dep}}} \cdot \boldsymbol{\rho_m} \cdot \boldsymbol{C_p} (\boldsymbol{T_m} - \boldsymbol{T_i}) \frac{\boldsymbol{V_t}}{\boldsymbol{V_p}} \tag{7}$$

Conservation of mass takes the following form, equating the volume of wire consumed and the volume of deposited material per layer, in the unit of time:

Materials Research Proceedings 57 (2025) 136-144 https://doi.org/10.21741/9781644903735-16

$$\boldsymbol{WFS \cdot A_w = \frac{V_l}{t_{dep}} \Rightarrow V_l = WFS \cdot A_w \cdot t_{dep} = WFS \cdot \frac{\pi}{4} D_w^2 \cdot t_{dep}} \quad (8)$$

Where A_w is the wire's cross section area, D_w the wire's dimeter and V_l the deposited layer volume, corresponding in Fig. 1 to the volume of height LH. We operate the following substitutions:

Spherical cap volume:

$$\mathbf{V_p = \pi r^3 \cdot \left[\left(1 - \sin\frac{\theta}{2}\right)^2 - \frac{1}{3}\left(1 - \sin\frac{\theta}{2}\right)^3 \right]} \quad (9)$$

Total volume:

$$\mathbf{V_t = \frac{4}{3} \pi r^3} \quad (10)$$

Layer volume:

$$\mathbf{V_l = \pi r^3 \cdot \left[\frac{4}{3} - 2\left(1 - \sin\frac{\theta}{2}\right)^2 + \frac{2}{3}\left(1 - \sin\frac{\theta}{2}\right)^3 \right]} \quad (11)$$

Considering that:

$$\mathbf{\frac{V_p}{t_{dep}} = \frac{V_l}{t_{dep}} \cdot \frac{V_p}{V_l}} \quad (12)$$

Rearranging Eq. 8:

$$\mathbf{\frac{V_l}{t_{dep}} = WFS \cdot \frac{\pi}{4} D_w^2} \quad (13)$$

Equation 6 becomes:

$$\begin{aligned} \mathbf{Q_p} &= \mathbf{WFS \cdot \frac{\pi}{4} D_w^2 \cdot \frac{V_p}{V_l} \cdot \rho_m \cdot C_p (T_m - T_i) \cdot \frac{V_t}{V_p}} \\ &= \mathbf{WFS \cdot \frac{\pi}{4} D_w^2 \cdot \frac{\rho_m \cdot C_p (T_m - T_i) \cdot \frac{4}{3}}{\frac{4}{3} - 2\left(1 - \sin\frac{\theta}{2}\right)^2 + \frac{2}{3}\left(1 - \sin\frac{\theta}{2}\right)^3}} \end{aligned} \quad (14)$$

Hence, conservation of energy (Eq. 7) becomes:

$$\mathbf{Q_t = WFS \cdot \frac{\pi}{4} D_w^2} \quad (15)$$

Materials Research Proceedings 57 (2025) 136-144 https://doi.org/10.21741/9781644903735-16

$$\cdot \left[\frac{\rho_0 \cdot C_p\,(T_m - T_0)}{\eta_w} + \frac{\rho_m \cdot C_p\,(T_m - T_i) \cdot \frac{4}{3}}{\frac{4}{3} - 2\left(1 - \sin\left(\frac{\theta}{2}\right)\right)^2 + \frac{2}{3}\left(1 - \sin\left(\frac{\theta}{2}\right)\right)^3} \right]$$

While, considering (Eq. 11), conservation of mass (Eq. 8) becomes:

$$V_l = \pi r^3 \cdot \left[\frac{4}{3} - 2\left(1 - \sin\frac{\theta}{2}\right)^2 + \frac{2}{3}\left(1 - \sin\frac{\theta}{2}\right)^3 \right] = WFS \cdot \frac{\pi}{4} D_w^2 \cdot t_{dep}$$

$$\Rightarrow r = \sqrt[3]{\frac{WFS \cdot \frac{\pi}{4} D_w^2 \cdot t_{dep}}{\pi \cdot \left[\frac{4}{3} - 2\left(1 - \sin\frac{\theta}{2}\right)^2 + \frac{2}{3}\left(1 - \sin\frac{\theta}{2}\right)^3 \right]}} \quad (16)$$

Once material properties, interpass temperature and process parameters are known, layer angle θ can be computed through Eq. 15; and then used to obtain layer radius r through Eq. 16.

Experimental validation

For the validation a total of 39 tests were performed, each test consisting of three printed straight steel bars, formed by the deposition of 20 dots, using the torch axis parallel to the bar axis. Samples of dot-by-dot printed specimens are shown in Fig. 2 (a).

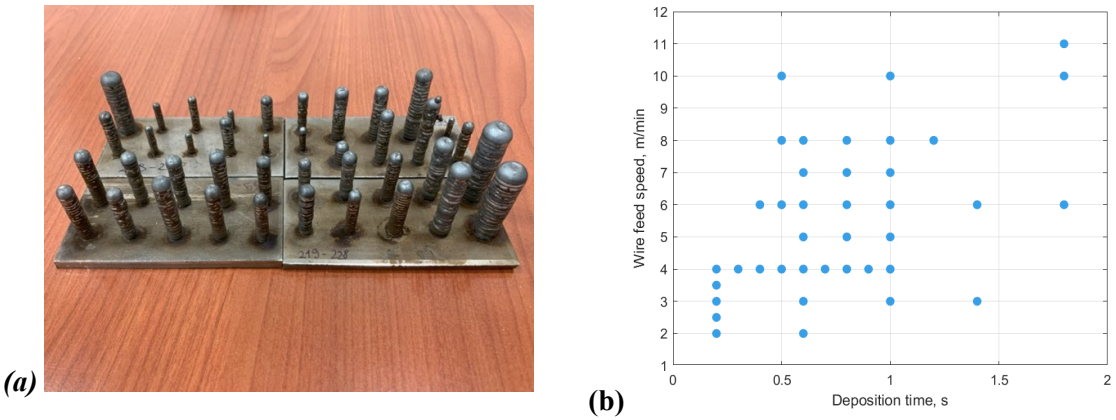


Fig. 2 (a) Samples of dot-by-dot printed bars, (b) Validation tests overview.

The experimental setup was as follows: the welding source was a Fronius TPS 320i welding machine, performing a cold metal transfer CMT-MAG welding process for which a spot-welding operating mode was selected, in order to control deposition time through the welding source. Both the substrate plate and wire were made of mild steels; in particular, substrate was made of S235JR, while for the wire feedstock ER70S-6 was used.

Wire diameter was 1 mm. The shielding gas mixture was composed of 82% Ar and 18% CO2, with a 15 l/min flow rate. Gap-bridging welding characteristic was used, specifically designed for cold deposition as required by the process and the specific filler metal. The power source was connected to a 5-axes DMU75 milling machine, which could move the welding torch along three dimensions, allowing it, e.g., to raise vertically as the bar grew while maintaining a constant Contact Tip to Work Distance (CTWD), or to shift when a new bar was to be printed. For each test a different combination of welding parameters was selected. The commanded parameters, i.e. deposition time, wire feed speed, were chosen to guarantee the feasibility and regularity of the bars

Materials Research Proceedings 57 (2025) 136-144 https://doi.org/10.21741/9781644903735-16

in accordance with what was found by Abe, Sasahara et al. [2]. In Fig. 2 (b) the 39 validation tests are visualized in terms of deposition time and wire feed speed. Idle time was selected to achieve an adequate cooling of the bars and avoid the collapse of the structure; hence higher idle times are used with increasing WFS and deposition time. Finally, CTWD was set equal to 10 mm for every test.

The welding source log file allowed for the collection of the effective parameters for each deposited dot. Using the results of each bar's log, average wire feed speed, deposition time and power were computed for each test. A mean constant value for interpass temperature was assumed equal to 100 °C as a first guess value based on Ref. [11]. This is a strong assumption, used for this first preliminary validation. In general, interpass temperature is varying during the deposition and it is expected to be different across the different tests. Temperature dependent material properties were set according to a database created using JMatPro [13] for the specific wire material. Since the interpass temperature and the melting temperature are the constant for all tests, the same material properties are used. The proposed analytical geometrical model was then applied to each test's set of parameters, resulting in the estimation of average dot radius r and layer angle θ, which were used to compute average bar diameter d and total bar height H_{tot}, through the following equations:

$$\mathbf{d = D_{max} = 2r} \tag{17}$$

$$\mathbf{H_{tot} = (n_{dot} - 1) \cdot LH + R = (20 - 1) \cdot 2r \cdot \sin\frac{\theta}{2} + r \cdot \left(1 - \sin\frac{\theta}{2}\right)} \tag{18}$$

The predicted values were then compared to the measured ones, and relative percentage errors for diameter and total height were calculated. The results of the validation are shown in Fig. 3.

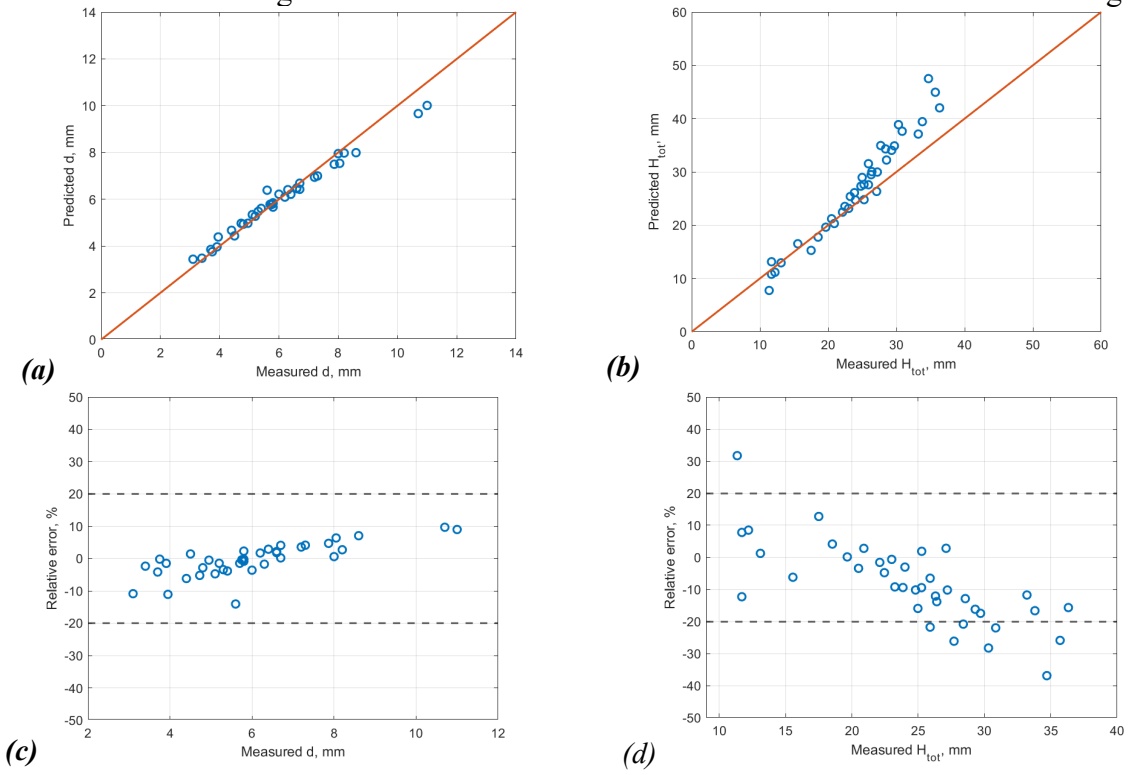


Fig. 3 (a) Predicted diameter vs. Measured diameter, (b) Predicted total height vs. Measured total height, (c) Relative percentage error on diameter, (d) Relative percentage error on total height.

Materials Research Proceedings 57 (2025) 136-144 https://doi.org/10.21741/9781644903735-16

Discussion

The results of this preliminary validation appear satisfactory both for diameter and total height, considering that significant simplifying assumptions were made regarding material properties, process parameters and interpass temperature. In particular for the interpass temperature a first guess value was used (100° C) just to start testing the model, however using constant idle time an increase in interpass temperature between dots is expected during deposition [14]. In addition, the proposed approach was applied to very different case studies both in terms of process parameters and geometry results, a variation of interpass temperature and hence material properties is predictable. Particularly an increase of interpass temperature with the increase of deposition volume (i.e., diameter of the bar) is expected. This aspect should be further investigated by measuring the actual interpass temperature.

Predictions on mean bar diameter appear particularly accurate, while predictions on total height present higher discrepancies. This is probably due to that errors in the geometrical model have stronger impact on layer height than diameter, since LH depends on the product of both r and sin(theta/2) (Eq. 1). In both cases percentage error mostly maintains itself within the 20% range, with a few outliers. As expected, the worst results are observed for higher values of both diameter and total height, where deposition volume increases, hence potentially leading to higher interpass temperature.

In conclusion, the results of the preliminary validation tests are promising and confirm that the analytical model developed is adequate at predicting the geometry of steel bars printed with the novel dot-by-dot WAAM printing strategy.

For the future development of the models for dot-by-dot, more accurate measurements of the bars' geometry will be required (e.g. with the aid of 3D scans or pictures analysis) and more rigorous in-depth analysis of influential parameters such as material thermal properties and interpass temperatures should be carried out.

Conclusions

The following conclusions are drawn:

- A geometrical analytical model was developed for the novel dot-by-dot WAAM printing strategy, as predicting the bars' geometry is a fundamental step for the further development of the process (e.g., toolpath generation).
- The results of the validation tests show that the model is able to predict the bars' geometry with good accuracy; with values for percentage error on bar mean diameter and total height within the 20% range, in the vast majority of cases.
- More accurate information on interpass temperatures will be necessary for better evaluation and future development the geometrical analytical model.
- Physics-based analytical models, as the one developed in this work, are preferable over numerical models as they can be more easily extrapolated and applied to different materials and parameters. Validation of the proposed model to a different material forms part of the future works.

Funding: Part of the research activities were conducted within the CIRCULAR WELD PRIN 2022PNRR project funded by the European Union - Next Generation EU, Mission 4 Component 1 CUP B53D23027320001.

References

[1] C.R. Cunningham, S. Wikshåland, F. Xu, N. Kemakolam, A. Shokrani, V. Dhokia, S.T. Newman, Cost Modelling and Sensitivity Analysis of Wire and Arc Additive Manufacturing, Procedia Manuf 11 (2017) 650–657. https://doi.org/10.1016/J.PROMFG.2017.07.163

[2] T. Abe, H. Sasahara, Layer geometry control for the fabrication of lattice structures by wire and arc additive manufacturing, Addit Manuf 28 (2019) 639–648. https://doi.org/10.1016/j.addma.2019.06.010

[3] J. Müller, M. Grabowski, C. Müller, J. Hensel, J. Unglaub, K. Thiele, H. Kloft, K. Dilger, Design and Parameter Identification of Wire and Arc Additively Manufactured (WAAM) Steel Bars for Use in Construction, Metals 2019, Vol. 9, Page 725 9 (2019) 725. https://doi.org/10.3390/MET9070725

[4] V. Mechtcherine, J. Grafe, V.N. Nerella, E. Spaniol, M. Hertel, U. Füssel, 3D-printed steel reinforcement for digital concrete construction – Manufacture, mechanical properties and bond behaviour, Constr Build Mater 179 (2018) 125–137. https://doi.org/10.1016/J.CONBUILDMAT.2018.05.202

[5] N. Grossi, F. Lazzeri, G. Venturini, Deposition Strategies for Bar Intersections Using Dot-by-Dot Wire and Arc Additive Manufacturing, J. Manuf. Mater. Process 9 (2025) 77. https://doi.org/10.3390/jmmp9030077

[6] Z. Yu, L. Yuan, F. He, D. Ding, J. Polden, Z. Pan, The Strategy for Fabricating Wire-Structure Parts Using Robotic Skeleton Arc Additive Manufacturing, 9th IEEE International Conference on Cyber Technology in Automation, Control and Intelligent Systems, CYBER 2019 (2019) 119–124. https://doi.org/10.1109/CYBER46603.2019.9066636

[7] Z. Yu, Z. Pan, D. Ding, J. Polden, F. He, L. Yuan, H. Li, A practical fabrication strategy for wire arc additive manufacturing of metallic parts with wire structures, International Journal of Advanced Manufacturing Technology 115 (2021) 3197–3212. https://doi.org/10.1007/s00170-021-07375-x

[8] V.A. Silvestru, I. Ariza, J. Vienne, L. Michel, A.M. Aguilar Sanchez, U. Angst, R. Rust, F. Gramazio, M. Kohler, A. Taras, Performance under tensile loading of point-by-point wire and arc additively manufactured steel bars for structural components, Mater Des 205 (2021). https://doi.org/10.1016/j.matdes.2021.109740

[9] M. Karmuhilan, A.K. Sood, Intelligent process model for bead geometry prediction in WAAM, Mater Today Proc 5 (2018) 24005–24013. https://doi.org/https://doi.org/10.1016/j.matpr.2018.10.193

[10] S. Ríos, P.A. Colegrove, F. Martina, S.W. Williams, Analytical process model for wire + arc additive manufacturing, Addit Manuf 21 (2018) 651–657. https://doi.org/10.1016/j.addma.2018.04.003

[11] A. M. Haghighi, J. Ding, Y. Sun, C. Wang, S. Williams, Thermo-capillary-gravity bidirectional modelling for evaluation and design of wire-based directed energy deposition additive manufacturing, J Manuf Process 107 (2023) 320–332. https://doi.org/10.1016/j.jmapro.2023.09.069

[12] M.S. Mohebbi, M. Kühl, V. Ploshikhin, A thermo-capillary-gravity model for geometrical analysis of single-bead wire and arc additive manufacturing (WAAM) Deposition efficiency, The International Journal of Advanced Manufacturing Technology 109 (2020) 877–891. https://doi.org/10.1007/s00170-020-05647-6

[13] N. Saunders, U.K.Z. Guo, X. Li, A.P. Miodownik, J.-Ph. Schillé, Using JMatPro to model materials properties and behavior, JOM 55 (2003) 60–65. https://doi.org/10.1007/s11837-003-0013-2

[14] F. Montevecchi, G. Venturini, N. Grossi, A. Scippa, G. Campatelli, Idle time selection for wire-arc additive manufacturing: A finite element-based technique, Addit Manuf 21 (2018). https://doi.org/10.1016/j.addma.2018.01.007

Materials Research Proceedings 57 (2025) 145-153 https://doi.org/10.21741/9781644903735-17

Design and preliminary testing of innovative tooling system elements obtained by L-PBF process for effective suppression of chatter vibrations

SCALZO Federico[1,a *], TOTIS Giovanni[1,b], VAGLIO Emanuele[1,c], ANTONIALLI Armando Ítalo Sette[2,d] and SORTINO Marco[1,e]

[1]Polytechnic Department of Engineering and Architecture, via delle Scienze, 206 Udine Italy

[2]Departamento de Engenharia Mecânica, Universidade Federal de São Carlos, Rod. Washington Luís, km 235, São Carlos, Brasil

[a]federico.scalzo@uniud.it, [b]giovanni.totis@uniud.it, [c]emanuele.vaglio@uniud.it, [d]antonialli@ufscar.br, [e]marco.sortino@uniud.it

Keywords: Powder Bed Fusion, Vibration, Chatter

Abstract. Undesired vibrations in milling processes negatively affect dimensional accuracy, tool life, surface quality, and the overall productivity. Passive approaches to suppress chatter are highly valued due to their simplicity and ease of implementation. In this study, cylindrical tooling systems with various internal structures — including lattice, auxetic, and Tuned Mass Damper (TMD) — were designed and manufactured using the Laser Powder Bed Fusion technology. Experimental modal analysis was conducted on each tooling system to assess their potential for enhanced attenuation of chatter vibrations. The TMD and unmelt powder filler configurations exhibited superior damping performance, demonstrating significant potential for real-world industrial applications.

Introduction

Milling operations are often affected by undesirable vibrations, which can lead to reduced surface quality, increased tool wear, and unstable cutting conditions [1]. Instability in milling can arise due to a combination of factors, particularly when machining difficult-to-cut materials [2]. The use of slender tools exacerbates the instability as they are more prone to bending and dynamic deflection under high cutting forces [3]. The combination of sub-optimal cutting conditions results in unstable cutting process, increased chatter, and a reduction in tool life, necessitating the use of effective damping techniques to ensure process stability.

Chatter control methods are generally classified as passive or active. Passive damping techniques are the preferred ones, since they ensure multiple advantages: compactness, ease of implementation and efficiency [4]. The most common passive techniques used to suppress chatter vibrations are those based on the energy dissipation effect and those exploiting tuned mass dampers [5].

The energy dissipation effect can be implemented exploiting multiple strategies. With friction damping, vibratory energy is dissipated through the interaction between tool elements [6]. In impact damping, the energy dissipation is attained utilizing free masses that move inside the tool structure [7]. Friction and impact damping can be combined to enhance damping efficiency [8]. Particle dampers are a specific type of impact dampers. They are composed by small spherical elements placed inside the body of the tool. Collisions and friction between the particles offer an effective vibration reduction solution [9]. Another approach to dissipate vibratory energy involves the use of high internal damping materials, such as foams, rubbers, plastics, shape memory alloys, and composite materials [10–12]. High-damping boring bars for internal turning were investigated

Content from this work may be used under the terms of the Creative Commons Attribution 3.0 license. Any further distribution of this work must maintain attribution to the author(s) and the title of the work, journal citation and DOI. Published under license by Materials Research Forum LLC.

Materials Research Proceedings 57 (2025) 145-153 https://doi.org/10.21741/9781644903735-17

by Sortino et al. [13], while Totis [14] provided a performance comparison between conventional and high-damping toolholders in milling.

The second technique is based on Tuned Mass Dampers (TMDs). Matching the spindle-holder-tool (SHT) system natural frequency with the TMD one it is possible to dampen the SHT critical mode. Various studies have optimized TMD designs by embedding them in cutting tools or modifying system parameters [15,16]. However, TMDs require space, limiting their application to large diameter and overhang length tools. Moreover, TMDs embedded in cutting tools are typically assembled from multiple small components, such as gaskets, rubber rings, and masses.

Development and testing of monolithic or fully integrated high damping designs are still under investigation. Additive Manufacturing (AM) could offer innovative, integrated solutions to overcome these limitations. For example, Sortino et al. and Scalzo et al. demonstrated the superior damping properties of 3D printed lattice structures made of aluminum and stainless steel compared to solid materials [17,18]. In a subsequent study, the same authors found that lattice structures combined with unmelt powder could be effectively used for passive chatter suppression [19]. The study on high-damping 3D printed milling tools was further explored by Yang et al. [20], confirming their potential for applications where vibration energy reduction is crucial.

Several studies have investigated chatter control methods based on energy dissipation and TMDs. However, the combined use of both strategies, exploiting AM for the creation of a compact integrated solution, remains largely unexplored. To address this gap, this paper presents a study that examines the dynamic behavior of various types of extensor elements for milling cutters produced by Laser Powder Bed Fusion (LPBF), evaluating their damping performance based on the chosen vibrational energy dissipation strategy. Specifically, the proposed designs incorporate lattice structures and TMD, with and without metallic powder filling, enabling an experimental comparison of different strategy combinations for vibrational energy reduction.

Specimens' design and numerical simulation

As previously mentioned, slender tools are more prone to bending and dynamic deflection under high cutting forces, increasing the likelihood of chatter [3]. Therefore, developing new solutions to enhance the stability of the cutting process under these critical conditions remains an ongoing challenge.

The design phase of the extensor elements was initiated based on a potential industrial application requiring a tool with high aspect ratio (see Fig. 1). Specifically, the extensor elements were designed to be coupled with a Sandvik Coromant square shoulder milling cutter (R390-16T08-11L) featuring an external diameter of D = 16 mm. The total overhang of the entire tooling system relative to the collet chuck was set at L = 136 mm, resulting in a length-to-diameter ratio of L/D = 8.5. This ratio is characteristic of high-damping commercial tooling systems made from cemented carbide or incorporating an internal TMD.

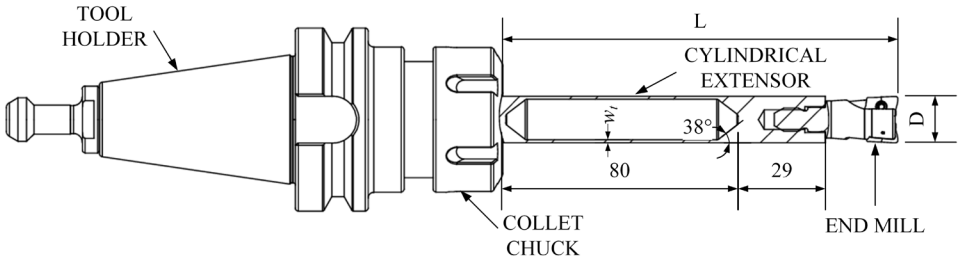


Figure 1 Assembled milling tool (mm).

Materials Research Proceedings 57 (2025) 145-153 https://doi.org/10.21741/9781644903735-17

Each extensor featured an inner cavity with an axial length of 80 mm and a cylindrical wall thickness (w_t) equal to 1 mm or 2 mm. Both ends of the cavity were tapered at a 38° angle to accommodate the manufacturing constraints of LPBF for overhanging surfaces. This design choice allowed the specimens to be produced without internal supports, as their removal would be unfeasible. Additionally, a 1 mm material allowance was included for machining, to ensure proper balancing and achieve the final shape with high geometric accuracy and surface quality.

The experimental investigation was designed using a full factorial design of experiments with two factors. The first factor was the cylindrical wall thickness (w_t=1 mm and w_t=2 mm), and the second one was the type of inner structure integrated into the void section of the specimens (void, unmelt powder, lattice+pow., auxetic+pow. and TMD).

Two replicates of each configuration were 3D printed, for a total of twenty specimens. All configurations, except the void one, had their internal core filled with unmelt powder, which itself contributes to vibrational energy dissipation [19].

The first configuration was designed on the basis of the findings of previous research [18] and a face-centered cubic cell with Z struts (FBCCZ) lattice structure topology was selected. Cross-sectional views of the specimen filled with this lattice structure are shown in Fig. 2A. The second configuration featured an auxetic re-entrant hexagon structure [21], selected taking inspiration by the promising results achieved by Kim et al. [22] with auxetic lattices. The unit cell size and strut thickness were chosen to ensure that the static compliance of the auxetic specimen remained comparable to that of the FBCCZ one. The final infill pattern is illustrated in Fig. 2B. A completely void configuration served as the main reference for the final comparison (Fig. 2C). The fourth type of specimen was identical to the void one but the inner cavity was filled with unmelt powder, enabling the distinction of vibrational energy dissipation caused by the particle damping effect from other energy dissipation mechanisms.

The first four configurations leveraged the energy dissipation effect to reduce vibrational energy. The fifth type of extensor utilized both the particle damping provided by the unfused metal powder filling and an integrated TMD within the cylindrical stem (see Fig. 2D).

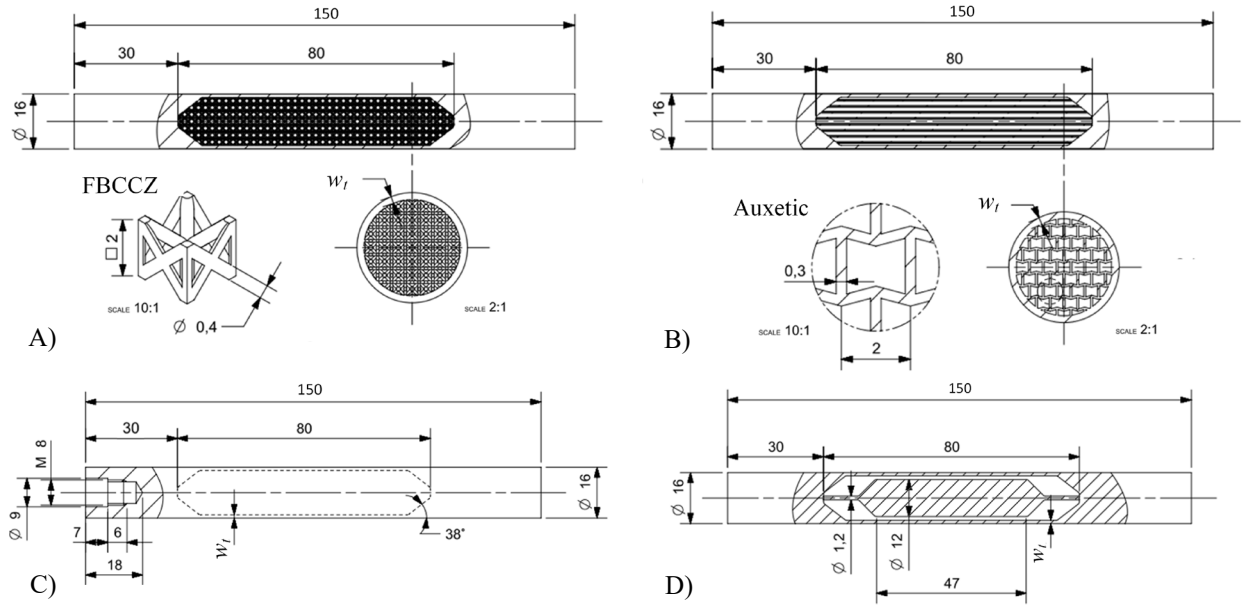


Figure 2 Section view of the specimens under investigation (mm).

It is worth noting that this solution is innovative because it consists of a single component, printed in one piece via LPBF, requires no assembly, and combines multiple strategies for

Materials Research Proceedings 57 (2025) 145-153 https://doi.org/10.21741/9781644903735-17

absorbing vibrational energy. The geometry of the mass and links of the TMD were optimized to align and attenuate the primary resonance of the tooling system by means of analytical calculations implemented in MATLAB.

The mechanical behavior of each configuration was assessed through Finite Element Analysis (FEA) conducted using SolidWorks Simulation. The primary design constraint was to limit the static compliance variations across the configurations. To estimate the static compliance, a force of 1 N was applied to the tip of each specimen. Subsequently, the first natural frequencies and mode shapes were determined through modal analysis.

High-damping elements manufacturing

The 3D geometrical representation of each of the ten different cylindrical extensors was created using SolidWorks. The build process preparation, including positioning and slicing of STL files, was carried out using Materialise Magics. The samples were vertically oriented to leverage the self-supporting features of the FBCCZ and auxetic topologies, eliminating the need for support structures.

Two replicates of each specimen were then manufactured using a Concept Laser M2 Cusing LPBF 3D printing machine. The manufacturing process was conducted in an argon inert atmosphere to minimize oxidation. The material selected was an AISI 316L stainless steel due to its excellent strength, corrosion resistance, and manufacturability. Each cylindrical extensor was produced from gas-atomized metal powders with particle sizes ranging between 10 and 45 μm. The main process parameters were set as follows: laser power 180W, laser diameter 120 μm, scan speed 600 mm/s, layer thickness 25 μm and overlap 30%.

To reduce the influence of thermally induced stresses, the specimens were subjected to an annealing heat treatment at the end of the AM process.

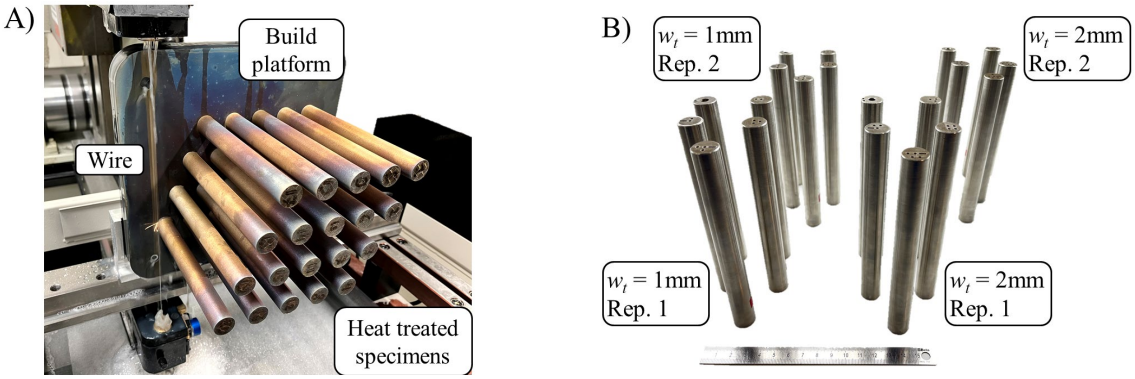


Figure 3 As-built heat threated A) and machined specimens B).

The heat treatment involved heating the specimens to 550 °C, maintaining this temperature for 6 hours, and then cooling them to room temperature. Afterwards, the as-built specimens were detached from the build platform using an ECUT32D wire electrical discharge machining (WEDM) equipment, as shown in Fig. 3A. Therefore, all the test samples underwent turning, utilizing the radial and axial allowance material to obtain balanced cylindrical extensors with the final geometry specified in Fig. 2. The specimens ready for testing are shown in Fig. 3B.

Experimental modal analysis

To assess the dynamic behavior of each cylindrical extensor, Experimental Modal Analysis (EMA) was performed by exciting the structure with a measured force. Each specimen was clamped in an ISO-BT40 tool holder equipped with an ER32 collet chuck. The tool holder was then mounted on the main spindle of a HAAS VF-2TR CNC milling machine. A Sandvik Coromant R390-16T08-11L square shoulder milling cutter was coupled with each cylindrical shank to examine the

Materials Research Proceedings 57 (2025) 145-153 https://doi.org/10.21741/9781644903735-17

behavior of the actual assembly ready for machining. The overhang of the assembled tool relative to the collet chuck was set to 136 mm, achieving an L/D ratio of 8.5. The impulsive force was applied at the extremity of the cylindrical extensor using a Dytran 5800B4 impact hammer (sensitivity 2.41 mV/N), coupled with a Kistler signal conditioning unit. To assess the influence of stiffness variation in the milling machine structure on the dynamic behavior of each extensor, measurements were repeated by applying an impulsive force along the X and Y axes of the machine (see Fig. 4). Additionally, the tests were repeated after rotating the spindle by 90 degrees to account for potential variations caused by manufacturing defects or the anisotropy of the metamaterials used as fillers. The resulting displacement was measured using two Micro-Epsilon ES1 inductive probes (range ±0.5 mm) connected to two NCDT3010-M eddy current controller. Data acquisition was performed using a National Instruments NI-9215 DAQ device with a sampling rate of 25 kHz. Data processing was carried out in the MATLAB environment.

A simple model based on a single harmonic oscillator was sufficient to characterize the damping properties of the different specimens.

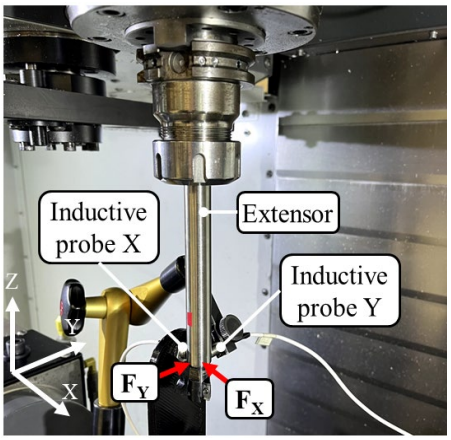


Figure 4 Dynamic behavior assessment – Experimental Modal Analysis.

Results and discussion

The dynamic behavior of each configuration was calculated through Experimental Modal Analysis (EMA). To assess the damping performance of the investigated configurations, the damping ratio trend was analyzed. The analysis of variance (ANOVA) indicated that the configuration type and wall thickness had a statistically significant influence on the damping ratio (p-value < 0.05). In contrast, the force application direction, spindle angular position, and 3D printing process repeatability were not statistically significant. Based on these findings, the results are presented by grouping them according to the factors that have a significant effect. The estimated dynamic compliances of the specimens with minimum wall thicknesses (w_t) of 2 mm and 1 mm are shown in Fig. 5A and 5B, respectively.

The effect of different vibration energy dissipation mechanisms was evaluated by calculating the modal parameters, and measurement adequacy was confirmed by observing the coherence function plot.

Comparing the results in terms of static compliance obtained from EMA with those estimated preliminarily through simulations, FEA predictions were found to be quite accurate. Error never exceeded 14%. On the other hand, resonance frequency estimations accuracy was affected by the fact that spindle-tool holder assembly was neglected. As expected, the static compliance of specimens with w_t=2 mm was lower compared to those with w_t=1 mm, consequently resonance peaks occurred at higher frequencies for the thicker specimens. The void specimens exhibited the highest energy peak at the lowest frequency.

Materials Research Proceedings 57 (2025) 145-153 https://doi.org/10.21741/9781644903735-17

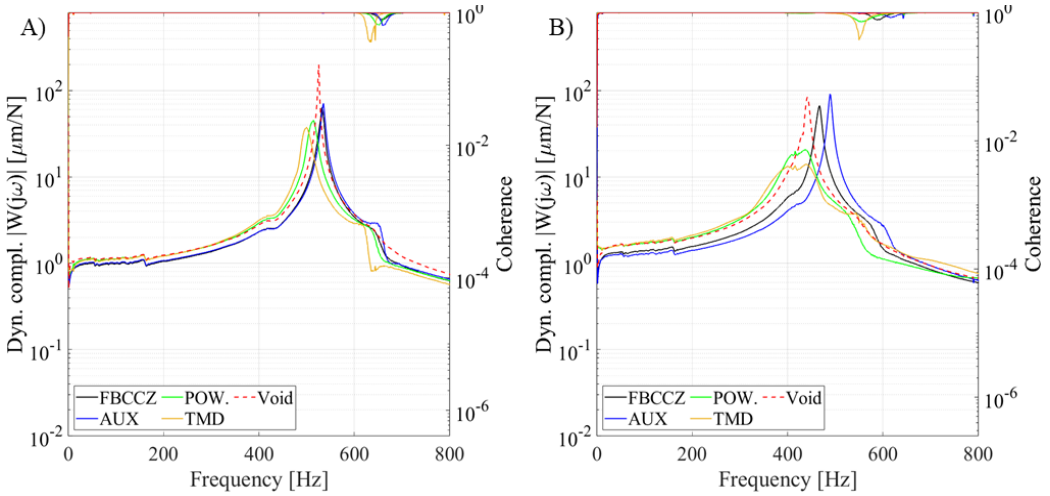


Figure 5 Dynamic compliance of cylindrical extensors for w_t = 2mm A) and w_t = 1mm B).

Lattice (FBCCZ) and auxetic (AUX) configurations showed similar dynamic compliance amplitudes at the resonance peak for w_t=2 mm. For w_t=1 mm the FRF amplitude of FBCCZ specimens was lower compared to AUX ones, suggesting that in this specific case the auxetic behavior had no beneficial effect on vibration energy dissipation. Peaks for the powder-only (POW) and TMD configurations were significantly lower for w_t=1 mm, with the FRF signal spread over a wider frequency range, an effect that was less pronounced for a w_t=2 mm. This indicates that the influence of inner structures on dynamic behavior was more significant for thinner specimens. The main modal parameters for each configuration are summarized in the statistical boxplots of Fig. 6. Specifically, static compliance (G), main resonance frequency (f_n), amplitude of the frequency response at the resonance frequency ($|W_n|$), and damping ratio (ξ) were reported to compare the dynamic performance of the specimens.

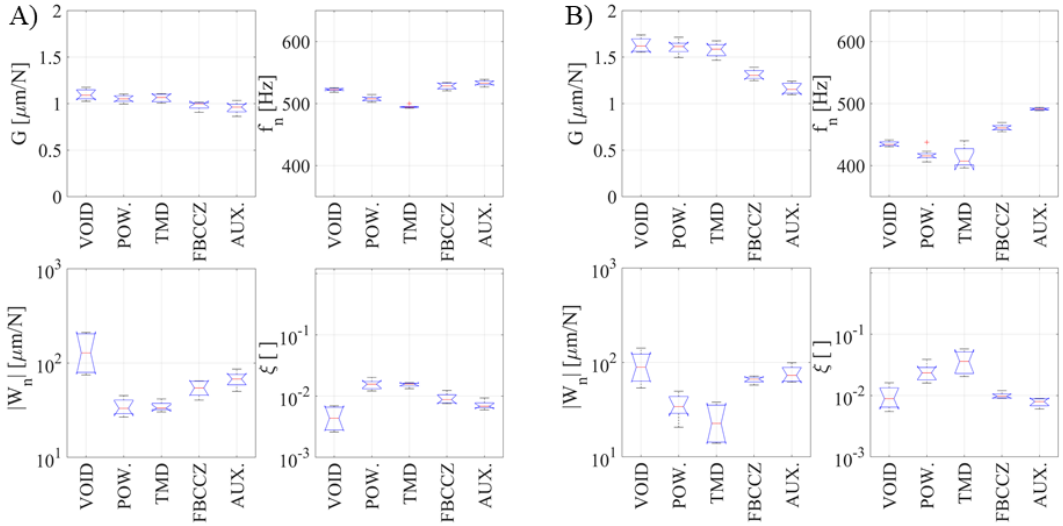


Figure 6 Modal parameters boxplots of cylindrical extensors for w_t = 2mm A) and w_t = 1mm B).

As expected, the static compliance (G) of the void, only powder and TMD configurations was almost identical, due to the absence of variations between the elements contributing to the stiffness of each extensor. FBCCZ and auxetic specimens were stiffer due to the contribution of the metamaterial infill. AUX specimens exhibited greater stiffness compared to FBCCZ ones when w_t

is thinner. This confirms that the influence of the metamaterial on the dynamic behavior of the cylindrical extensor depends on w_t.

The resonance frequency (f_n) of the different configurations was influenced by both the static compliance and powder infill. Even with similar static compliances, the resonance frequency of specimens with only powder infill and TMD was lower than that of void specimens, primarily due to the increase in mass caused by the powder.

The resonance frequency of the auxetic configuration with w_t=1 mm was slightly higher than that of the FBCCZ configuration, confirming that the influence of inner metamaterials is more pronounced at lower wall thicknesses.

The amplitudes of the frequency responses at the resonance frequency ($|W_n|$) varied significantly among the extensor elements. Unmelt powder and TMD configurations displayed low amplitude values, while the lattice and auxetic configurations were only slightly lower than the void configuration for w_t=2 mm.

Therefore, the damping ratio (ξ) of configurations containing either unmelt powder or TMD was significantly higher, indicating a good vibration energy dissipation performance. FBCCZ specimens performed better with respect to the void configuration when w_t=2 mm. This outcome could not be confirmed for w_t=1 mm. No significant difference was observed between the auxetic and void configurations in terms of damping performance.

Conclusions

Chatter vibrations remain a significant challenge during machining operations, especially when slender tools are involved. To address this issue, the industry commonly adopts solutions such as special tools made of cemented carbides or embedded Tuned Mass Dampers (TMDs), as they are both effective and commercially available. However, these solutions tend to be relatively expensive and difficult to manufacture. Monolithic or fully integrated tools are still under investigation and market-ready solutions are still lacking, leaving a gap for innovative, cost-effective devices for passive chatter suppression.

To address this gap, this study explores the design and production of enhanced vibration energy dissipation cylindrical extensors, leveraging the design flexibility offered by Laser Powder Bed Fusion (LPBF) technology. The damping performance of these tools was evaluated through experimental modal analysis (EMA) to assess their potential for passive chatter suppression in milling applications.

Five configurations were designed and tested. The first two incorporated lattice and auxetic structures, which are engineered materials known for their potential enhanced vibration damping properties. The next two configurations utilized unmelt metallic powder filler, which has previously demonstrated effectiveness in reducing chatter vibrations, and an optimized Tuned Mass Damper (TMD) embedded within the cylindrical extensor. For comparison, a reference hollow specimen was also produced. The wall thickness of the inner cavity of the extensors varied on two levels (w_t=1 mm and w_t=2 mm). Two replicates of each specimen were 3D-printed, annealed and machined, obtaining a total of twenty cylindrical extensors.

Configurations featuring unmelt powder or TMD were the best in terms of damping ratio, demonstrating their potential for vibration energy absorption. The lattice structure provided an improved damping performance over the void specimen considering a w_t=2 mm. Nevertheless, no significant improvement was observed with w_t=1 mm, comparing lattice or auxetic specimens with the reference one.

In conclusion, the configurations with unmelt powder and TMD demonstrated potential for enhancing the damping properties of tooling elements for passive chatter suppression. It would be of further interest to validate the proposed tooling systems by performing chatter tests. By so doing, it will be possible to determine their effective stability against undesired chatter vibrations. The

final comparison between the tested tooling systems should prove the superior performance of the tooling system endowed with an inner tuned mass damper.

Acknowledgements
This study was carried out within the Interconnected Nord-Est Innovation Ecosystem (iNEST) and received funding from the European Union Next-GenerationEU (PIANO NAZIONALE DI RIPRESA E RESILIENZA (PNRR) – MISSIONE 4 COMPONENTE 2, INVESTIMENTO 1.5 – D.D. 1058 23/06/2022, ECS00000043). This manuscript reflects only the authors' views and opinions, neither the European Union nor the European Commission can be considered responsible for them.

References

[1] Yue C, GAO H, LIU X, LIANG SY, WANG L. A review of chatter vibration research in milling. Chinese Journal of Aeronautics 2019;32:215–42. https://doi.org/10.1016/J.CJA.2018.11.007

[2] Kishawy HA, Hosseini A. Machining Difficult-to-Cut Materials 2019. https://doi.org/10.1007/978-3-319-95966-5

[3] Wang M, Qin P, Zan T, Gao X, Han B, Zhang Y. Improving optimal chatter control of slender cutting tool through more accurate tuned mass damper modeling. J Sound Vib 2021;513:116393. https://doi.org/10.1016/J.JSV.2021.116393

[4] Zhu L, Liu C. Recent progress of chatter prediction, detection and suppression in milling. Mech Syst Signal Process 2020;143:106840. https://doi.org/10.1016/J.YMSSP.2020.106840.

[5] Yang Y, Yang Y, Liu H-C, Wan M, Zhang W-H. A new cutting tool filled with metallic lattice and design method for vibration suppression in milling. Mech Syst Signal Process 2024;212:111310. https://doi.org/10.1016/j.ymssp.2024.111310

[6] Madoliat R, Hayati S, Ghalebahman AG. Investigation of chatter suppression in slender endmill via a frictional damper. Scientia Iranica 2011;18:1069–77. https://doi.org/10.1016/J.SCIENT.2011.08.008

[7] Galarza FAM, de Albuquerque MV, Antonialli AÍS, Pederiva R, Diniz AE. Design and experimental evaluation of an impact damper to be used in a slender end mill tool in the machining of hardened steel. International Journal of Advanced Manufacturing Technology 2020;106:2553–67. https://doi.org/10.1007/S00170-019-04786-9/

[8] Saciotto VR, Diniz AE. An experimental evaluation of particle impact dampers applied on the tool for milling of hardened steel complex surface. International Journal of Advanced Manufacturing Technology 2022;119:7579–97. https://doi.org/10.1007/S00170-022-08782-4/

[9] Chockalingam S, Natarajan U, George Cyril A. Damping investigation in boring bar using hybrid copper-zinc particles 2015;23:2128–34. https://doi.org/10.1177/1077546315610946

[10] Möhring HC. Composites in Production Machines. Procedia CIRP 2017;66:2–9. https://doi.org/10.1016/J.PROCIR.2017.04.013

[11] Munoa J, Beudaert X, Dombovari Z, Altintas Y, Budak E, Brecher C, et al. Chatter suppression techniques in metal cutting. CIRP Annals 2016;65:785–808. https://doi.org/10.1016/J.CIRP.2016.06.004

[12] LI Z, SONG Q, JIN P, LIU Z, WANG B, MA H. Chatter suppression techniques in milling processes: A state of the art review. Chinese Journal of Aeronautics 2024;37:1–23. https://doi.org/10.1016/J.CJA.2023.10.001

[13] Sortino M, Totis G, Prosperi F. Modeling the dynamic properties of conventional and high-damping boring bars. Mech Syst Signal Process 2013;34:340–52. https://doi.org/10.1016/J.YMSSP.2012.05.016

[14] Totis G. RCPM—A new method for robust chatter prediction in milling. Int J Mach Tools Manuf 2009;49:273–84. https://doi.org/10.1016/J.IJMACHTOOLS.2008.10.008

[15] Hintze W, Hinrichs M, Rosenthal O, Schleinkofer U, Venturini R. Model based design of tuned mass dampers for boring bars of small diameter. Procedia CIRP 2023;117:193–8. https://doi.org/10.1016/J.PROCIR.2023.03.034

[16] van Zyl D, Altintas Y, Ostling D. Parametric design of boring bars with adaptive tuned mass dampers. CIRP J Manuf Sci Technol 2022;38:491–9. https://doi.org/10.1016/J.CIRPJ.2022.06.003

[17] Sortino M, Totis G, Scalzo F, Vaglio E. Preliminary Investigation of Static and Dynamic Properties of SLM Lattice Structures for Robotic Applications. Mechanisms and Machine Science, vol. 66, Springer Netherlands; 2019, p. 260–7. https://doi.org/10.1007/978-3-030-00365-4_31

[18] Scalzo F, Totis G, Vaglio E, Sortino M. Experimental study on the high-damping properties of metallic lattice structures obtained from SLM. Precis Eng 2021;71:63–77. https://doi.org/10.1016/j.precisioneng.2021.02.010

[19] Scalzo F, Totis G, Vaglio E, Sortino M. Passive Chatter Suppression of Thin-Walled Parts by Means of High-Damping Lattice Structures Obtained from Selective Laser Melting. Journal of Manufacturing and Materials Processing 2020;4:117. https://doi.org/10.3390/jmmp4040117

[20] Yang Y, Liu HL, Yuan JW, Kong WL, Wan M, Zhang WH. Development of an anti-vibration cutting tool combining the lattice structures infill with damping particles. Mech Syst Signal Process 2025;228:112425. https://doi.org/10.1016/J.YMSSP.2025.112425

[21] Yin H, Zhang W, Zhu L, Meng F, Liu J, Wen G. Review on lattice structures for energy absorption properties. Compos Struct 2023;304:116397. https://doi.org/10.1016/j.compstruct.2022.116397

[22] Kim J, Hegde H, Kim H, Lee C. Spindle vibration mitigation utilizing additively manufactured auxetic materials. J Manuf Process 2022;73:633–41. https://doi.org/10.1016/j.jmapro.2021.11.051

Materials Research Proceedings 57 (2025) 154-163 https://doi.org/10.21741/9781644903735-18

A preliminary study about high-pressure homogenization as a viable alternative to produce powder feedstock for selective laser sintering of biopolymers

Alberto GIUBILINI[1,2,a *], Giovanna COLUCCI[3,b], Manuela GALATI[1,2,c], Giovanni MARCHIANDI[1,2,d], Massimo MESSORI[3,e], Luca IULIANO[1,2,f] and Paolo MINETOLA[1,2,g]

[1]Department of Management and Production Engineering (DIGEP), Politecnico di Torino, Corso Duca degli Abruzzi 24, 10129 Torino, Italy

[2]Integrated Additive Manufacturing Centre (IAM@PoliTO), Politecnico di Torino, Corso Duca degli Abruzzi 24, 10129 Torino, Italy

[3]Department of Applied Science and Technology (DISAT), Politecnico di Torino, Corso Duca degli Abruzzi 24, 10129 Torino, Italy

[a]alberto.giubilini@polito.it, [b]giovanna.colucci@polito.it, [c]manuela.galati@polito.it, [d]giovanni.marchinadi@polito.it, [e]massimo.messori@polito.it, [f]luca.iuliano@polito.it, [g]paolo.minetola@polito.it

Keywords: Powder Bed Fusion, Polymers, Sustainable Development

Abstract. Selective laser sintering is an established technique for producing complex plastic components, yet its broader adoption is limited by the scarcity of commercially viable materials. This study evaluates high-pressure homogenization, a fully mechanical process, for producing micronized biopolymer particles as a sustainable feedstock for selective laser sintering. The biopolymer powder was characterized in terms of morphology and flowability, followed by processability validation on a selective laser sintering machine using both simple and more complex geometries. The resulting 3D printed components were assessed for dimensional accuracy and subjected to dynamic mechanical characterization. By offering an industrially scalable method for biopolymer powder production, high-pressure homogenization expands material options for selective laser sintering, advancing sustainable additive manufacturing.

Introduction

Additive manufacturing (AM) of polymers has become essential for producing advanced plastic components in industries such as automotive, electronics, biomedical, and aerospace. Among AM techniques, material extrusion and vat photopolymerization are widely used due to their accessibility. However, material extrusion often results in coarse resolutions [1], while vat photopolymerization relies on thermoset resins that are difficult to recycle [2]. In contrast, Selective Laser Sintering (SLS) is a versatile and well-established AM method that enables the fabrication of complex, high-quality parts without support structures. Despite these advantages, one of the factors limiting the widespread adoption of SLS is the restricted commercial availability of polymer powders, which are predominantly synthetic materials such as polyamides [3].

The reliance on fossil-derived polymers raises environmental concerns, driving interest in biodegradable and bio-based alternatives that align with sustainability goals. Biopolymers have gained significant attention as eco-friendly materials in AM, with the polyhydroxyalkanoates (PHAs) standing out due to their tunable properties, cytocompatibility, and biodegradability under various environmental conditions [4]. Among PHAs, poly(3-hydroxybutyrate-*co*-3-hydroxyhexanoate) (PHBH) has emerged as a valuable candidate, offering a balance of mechanical strength and flexibility comparable to conventional plastics like polypropylene [5]. Derived from

Content from this work may be used under the terms of the Creative Commons Attribution 3.0 license. Any further distribution of this work must maintain attribution to the author(s) and the title of the work, journal citation and DOI. Published under license by Materials Research Forum LLC.

Materials Research Proceedings 57 (2025) 154-163 https://doi.org/10.21741/9781644903735-18

bacterial fermentation of renewable feedstocks, PHBH might represent a sustainable alternative to petroleum-based polymers also for AM applications. Previous research on PHA powders for SLS has primarily focused on biomedical applications [6]. For instance, studies have demonstrated the feasibility of fabricating scaffolds for tissue engineering and assessing cell viability on SLS 3D printed structures [7,8]. However, a major limitation of existing approaches is the production method for biopolymer powders. Most studies have relied on solvent-induced phase separation, where a polymer solution is precipitated in an aqueous medium [9,10]. While this technique allows for controlled particle morphology and thermal stability, it suffers from low production yield and environmental drawbacks due to the extensive use of organic solvents. These challenges hinder the scalability and broader adoption of biopolymers in SLS.

To overcome these limitations, this study explores high-pressure homogenization (HPH) as a novel, solvent-free method for producing PHBH powder suitable for SLS. HPH is a purely mechanical process that enables efficient micronization of polymer particles, ensuring fine and uniform size distribution critical for successful SLS. The resulting powder was characterized in terms of morphology and flowability, two critical factors influencing powder bed homogeneity and processability in SLS. Additionally, 3D printed parts were examined for their dynamic mechanical properties and dimensional accuracy to assess the feasibility of PHBH powder obtained by HPH for SLS applications. By establishing a scalable, sustainable route for biopolymer powder production, this work expands the material options for SLS, with potential applicability to other biopolymers. Ultimately, this research contributes to bridging the gap between biopolymer development and practical implementation in AM, advancing the transition toward more sustainable manufacturing practices.

Materials and Methods

Materials and equipment

Poly(3-hydroxybutyrate-*co*-3-hydroxyhexanoate) (PHBH) pellets were purchased from MAIP Group (MAIP S.r.l., Settimo Torinese, Italy). Poly(vinyl alcohol) (PVA) 8-88 and silica oxide were obtained from Merck (Merck KGaA, Darmstadt, Germany). Glycerol EP 99% was supplied by ACEF (ACEF SpA, Fiorenzuola d'Arda, Italy). All materials were used as received, without further purification. For preliminary cryo-grinding, an A10 basic mill (IKA, Staufen, Germany) was used. HPH was then performed using a Panther NS3006L homogenizer (GEA Mechanical Equipment, Parma, Italy), equipped with a single-stage system, a pump for abrasive and viscous products, and a heat exchanger.

PHBH powder preparation

The production process of PHBH powder consists of four main steps: cryo-grinding, suspension preparation, high-pressure homogenization, and final washing and drying. PHBH pellets were first cryo-ground using liquid nitrogen and sieved through a 1 mm mesh. The resulting powder was then dispersed at 1 wt.% in a medium composed of 50 wt.% glycerol and 50 wt.% aqueous PVA solution (5 wt.%). The suspension underwent high shear mixing at 3000 rpm before being processed via HPH, which included two initial passes at 300 bar, followed by 18 passes at 1000 bar. Sample coding was designated as NH for non-homogenized PHBH, while PHBH_H refers to the homogenized powders. After homogenization, the powder was filtered, washed with distilled water, and oven-dried at 50 °C overnight before being sieved through a 100 μm mesh. To improve flowability in SLS, the PHBH_H powder was blended with 0.25 wt.% silica oxide for 30 min, a method previously reported to enhance the processability of laboratory-produced polymer powders [11].

PHBH powder characterization

The morphology of the PHBH powder was examined using a Phenom™ XL G2 Desktop scanning electron microscope (SEM) (Thermo Fisher Scientific, Waltham, MA, USA) operated at an

Materials Research Proceedings 57 (2025) 154-163 https://doi.org/10.21741/9781644903735-18

accelerating voltage of 20 kV. Prior to imaging, the powder was sputter-coated with gold for 180 s at a pressure of 10^{-3} mbar and a current of 10 mA (Complete Sputter Coating System, West Chester, PA, USA).

Particle size distribution (PSD) was analyzed using a Mastersizer 3000 laser granulometer (Malvern Panalytical, Malvern, UK), which utilizes laser diffraction to measure particle sizes in water-suspended samples. Data processing was performed using the Fraunhofer model, and the span was calculated based on particle size percentiles D_{10}, D_{50}, and D_{90}, representing the sizes below which 10%, 50%, and 90% of the total particle volume falls, respectively, following Eq. 1:

$$Span = \frac{D_{90} - D_{10}}{D_{50}} \tag{1}$$

Flowability was assessed by determining the compressibility index (C) and the Hausner ratio (HR). The parameters C and HR were measured using a simplified version of the ASTM D7481 standard with a 25 mL graduated cylinder, following Equations (2), (3), and (4), where ρ_{bulk} and ρ_{tap} denote the apparent and tapped densities of the PHBH powder, respectively.

$$C = \frac{\rho_{tap} - \rho_{bulk}}{\rho_{tap}} \times 100 \tag{2}$$

$$HR = \frac{\rho_{tap}}{\rho_{bulk}} \tag{3}$$

Selective Laser Sintering

Two different geometries were 3D printed using the same PHBH powder. First, bar-shaped samples (35 mm×10 mm×1 mm) were fabricated for thermomechanical analysis. Next, a small boat model was used as a reference part to evaluate the dimensional accuracy of SLS with PHBH powder feedstock. The boat has overall dimensions of 40 mm x 16 mm x 5.5 mm and features classical geometric elements that facilitate dimensional inspection. Figure 1 presents the CAD of the model boat.

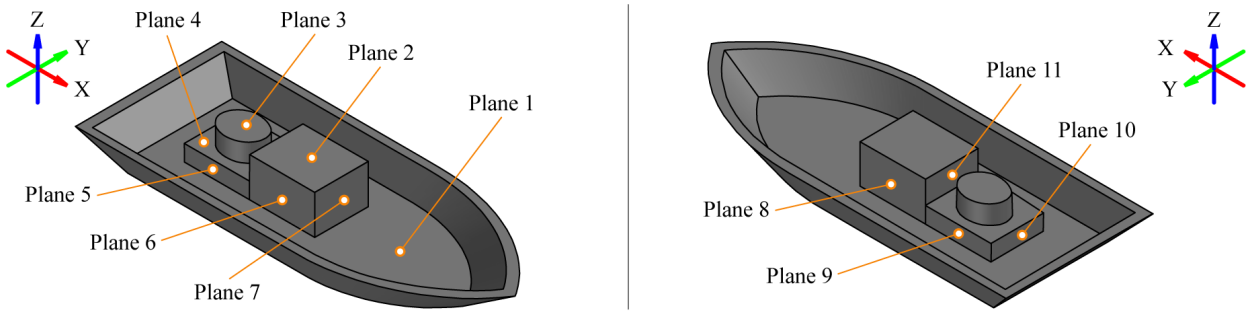


Figure 1: Isometric view of the reference model with indication of the planes used for dimensional inspection

Above the flat deck, two adjacent square blocks of different heights are positioned. These blocks own a base measuring 5.82 mm x 7.12 mm. The higher block has a height of 4.25 mm, while the smaller one is 1.75 mm high. Additionally, an elliptical block, standing 2 mm high, is placed on top of the smaller square block. The Cartesian reference frame is centered in the middle of the boat, with the Z-axis origin at the base of the hull, the positive Y-axis pointing port, and the

Materials Research Proceedings 57 (2025) 154-163 https://doi.org/10.21741/9781644903735-18

positive X-axis aligned with the bow. The following planes are considered to measure the heights and sizes of the different geometric features:

- Plane 1: Deck level at Z = 1.25 mm
- Plane 2: Top face of the larger square block at Z = 5.50 mm
- Plane 3: Top face of the elliptical block at Z = 5.00 mm
- Plane 4: Top face of the smaller square block at Z = 3.00 mm
- Plane 5: Right face (starboard) of the smaller square block at Y = −2.91 mm
- Plane 6: Right face (starboard) of the larger square block at Y = −2.91 mm
- Plane 7: Front face (bow) of the larger square block at X = 1.00 mm
- Plane 8: Left face (port) of the larger square block at Y = 2.91 mm
- Plane 9: Left face (port) of the smaller square block at Y = 2.91 mm
- Plane 10: Back face (stern) of the smaller square block at X = −13.24 mm
- Plane 11: Back face (stern) of the larger square block at X = −6.12 mm

All components were fabricated using a SnowWhite2 SLS machine (Sharebot S.r.l., Nibionno, Italy) equipped with a CO_2 laser operating at a wavelength of 10.6 μm. The biopolymer powder was evenly distributed in an air environment using a blade recoater. After reaching the target build chamber temperature, a 300 s waiting period was applied to ensure uniform heating of the powder bed. The key processing parameters are summarized in Table 1.

Table 1: Selective laser sintering process parameters

Process parameters	
Laser power [W]	3.5
Scan speed [mm/s]	2400
Border scan speed [mm/s]	3300
Layer height [μm]	100
Environmental temperature [°C]	90
Number of warming layers	50-150

3D printed components characterization

Dynamic mechanical analysis (DMA) was performed using an MCR 702e Multidrive Device (Anton Paar, Graz, Austria), applying a uniaxial sinusoidal stress with an amplitude of 1 N and a frequency of 1 Hz. A micro-CT scanner (X-CT) (Phoenix v|tome|x S240, GE Baker Hughes-Waygate Technologies, Wunstorf, Germany) was used to examine the 3D printed specimens, with the scanning parameters shown in Table 2. X-ray images were reconstructed into 3D models using datos|reconstruction software, and visualization and analysis were performed with VG Studio Max (version 3.4, Volume Graphics, Heidelberg, Germany). For dimensional analysis, surface determination was first carried out using the Advanced (classic) approach. This process involved contour identification from the histogram with an automatic material definition at an isovalue threshold of 50%.

Table 2: X-CT scanning parameters

Scanning parameters	
Voxel size [μm]	49.2
Voltage [kV]	210
Current [μA]	130
Timing [ms]	100
Number of images	1500

Materials Research Proceedings 57 (2025) 154-163 https://doi.org/10.21741/9781644903735-18

The Atos Compact Scan structured-light 3D scanner (Carl Zeiss AG, Oberkochen, Germany) was used for the scanning process. It is certified under the VDI/VDE 2637 standard for metrological performance. This device features two lateral CCD cameras for stereoscopic imaging and triangulation, along with a central projector for structured light projection. It has a 2-megapixel resolution, allowing it to capture around 2 million points per scan with 0.075 mm spacing and an accuracy of 0.02 mm. Belonging to safety class 2 (eye-safe), the scanner operates independently of ambient lighting. It utilizes a blue LED light source, which enhances stability by reducing performance fluctuations caused by heat buildup or changes in lighting conditions.

Results and Discussions

SEM analysis (Figure 2a, 2b) highlights the impact of homogenization on PHBH powders, showing a reduction in particle size due to compression, cavitation, shear forces, and impact over the homogenizing ring [12]. The powders exhibit an irregular morphology, likely due to plastic deformation at elevated processing temperatures (up to 70 °C) and high pressures.

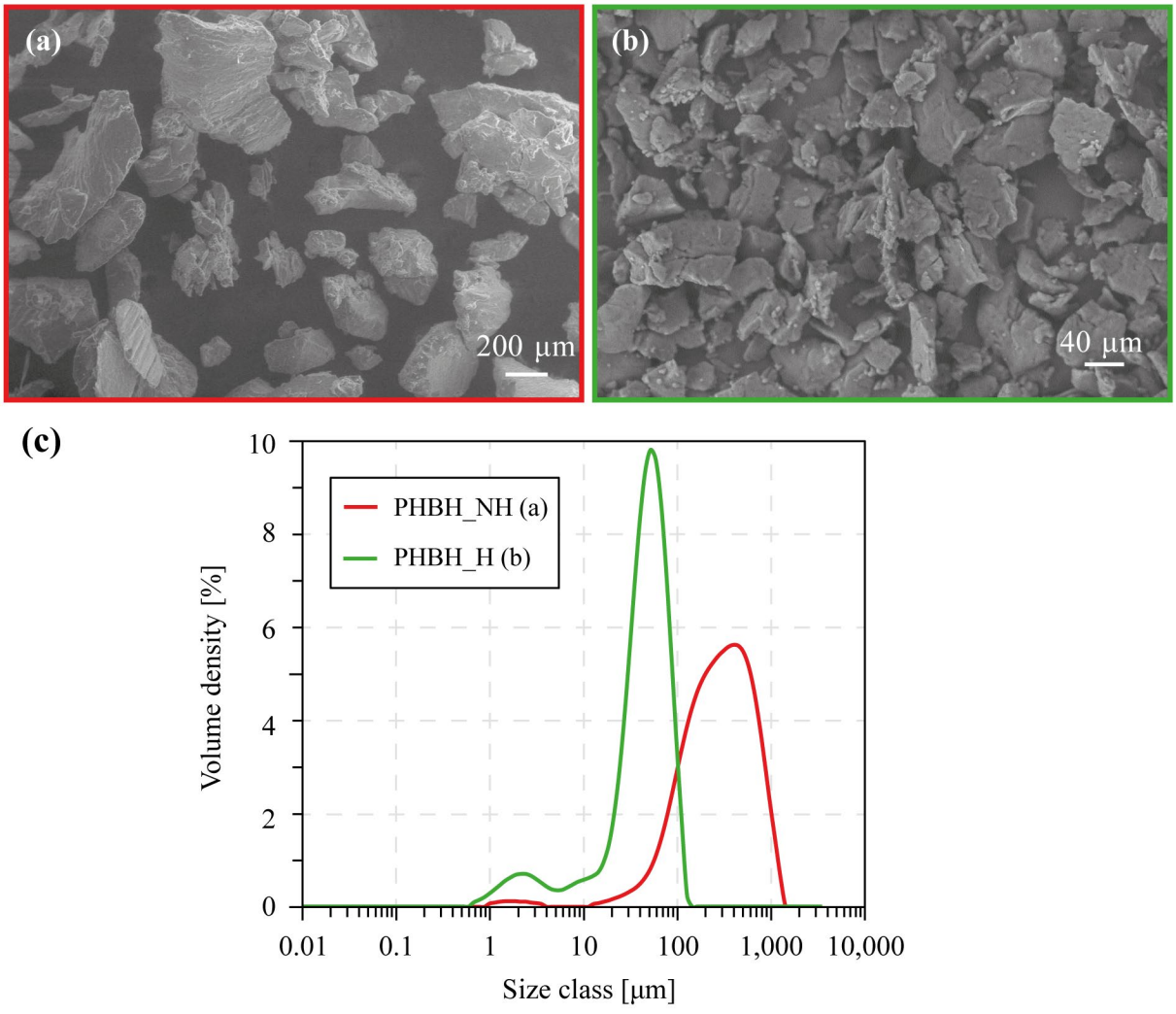


Figure 2: Morphology analysis. SEM micrographs: PHBH_NH (a) and PHBH_H (b). Particle size granulometric curves: PHBH_NH (c) and PHBH_H (d)

Granulometric analysis (Figure 2c) confirms size distributions of D_{10}, D_{50}, and D_{90} at 105 µm, 313 µm, and 727 µm for PHBH_NH, and 11 µm, 49 µm, and 88 µm for PHBH_H. Both samples display a single-peaked distribution, with homogenization narrowing the peak and reducing span values from 2 to 1.6, indicating improved powder spreading [13].

Powder packing and flowability, crucial for SLS processing, were assessed via Hall flow and tap density tests, yielding a C value of 25.3%±0.1% and HR of 1.34±0.01. According to Carr's classification, PHBH_H exhibits "passable flowability" [14]. Morphological analysis supports this suboptimal flowability; however, past studies have shown that polymer-based composites with irregular morphologies can still be successfully processed via SLS [15,16]. Therefore, despite non-ideal flow properties, this preliminary characterization suggests PHBH powder from HPH is suitable for SLS applications.

The viscoelastic properties of 3D printed specimen were analyzed via DMA to assess their thermomechanical behavior. Figure 3 shows the extensional storage modulus and tan delta as functions of temperature. The glass transition temperature, determined from the tan delta peak, is 6 °C. The extensional storage modulus in the rigid plateau region is approximately 2.23 GPa, highlighting the potential of PHBH_H powder for SLS processing and its suitability for semi-structural applications, such as in the biomedical field [17].

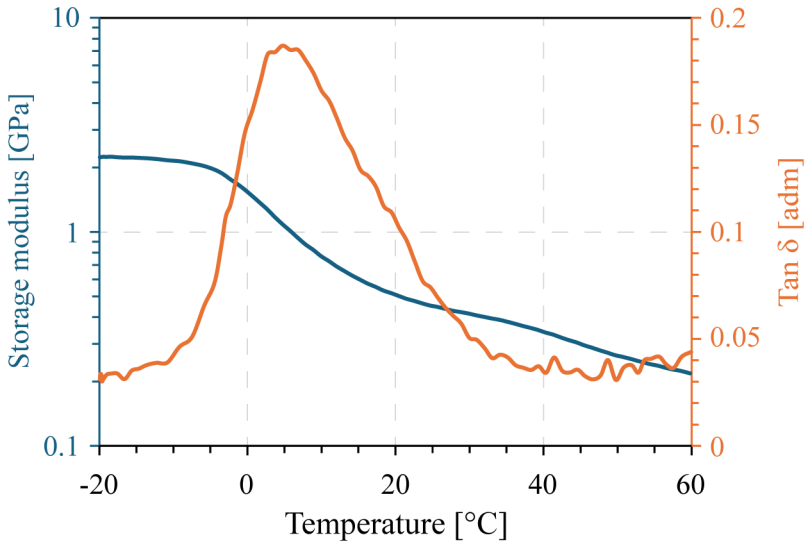


Figure 3: DMA curves of 3D printed specimen of PHBH_H obtained by SLS

To assess the 3D printability of PHBH_H powder using SLS, one replica of the boat model (Figure 1) was fabricated. Figure 4 shows the 3D printed replica (Fig. 4a) with a zoom-in of a central detail from the top view (Fig. 4b).

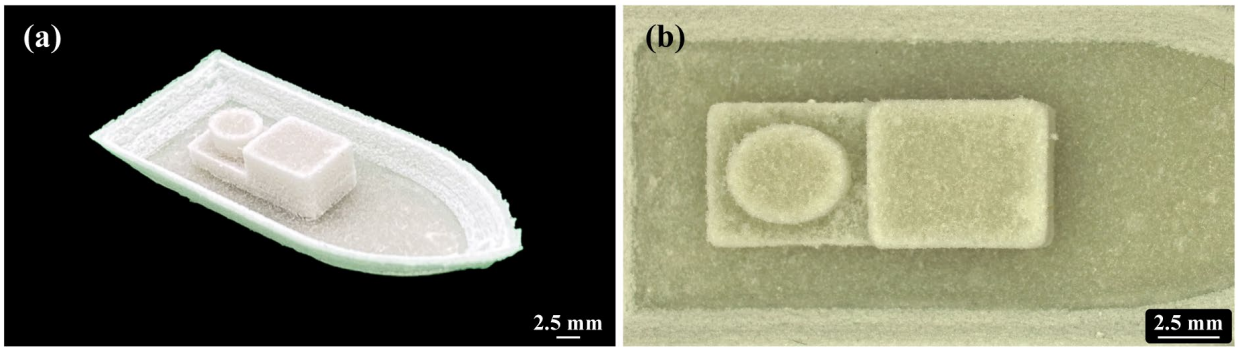


Figure 4: 3D printed boat using PHBH_H powder: (a) SLS replica; (b) optical microscope image of a detail of the SLS replica

The dimensional accuracy of the SLS replica was evaluated using GOM Inspect software by comparison of the actual scan data to the nominal CAD model. Figure 5 presents the colored map of nominal-to-actual deviations. Structured light optical scanning showed an average deviation of

Materials Research Proceedings 57 (2025) 154-163 https://doi.org/10.21741/9781644903735-18

0.28±0.28 mm (Fig. 5a), while X-CT scan measurements yielded a mean deviation of 0.11±0.28 mm (Fig. 5b). These results indicate good reproducibility of complex small geometries, though the deviation map highlights areas for optimization.

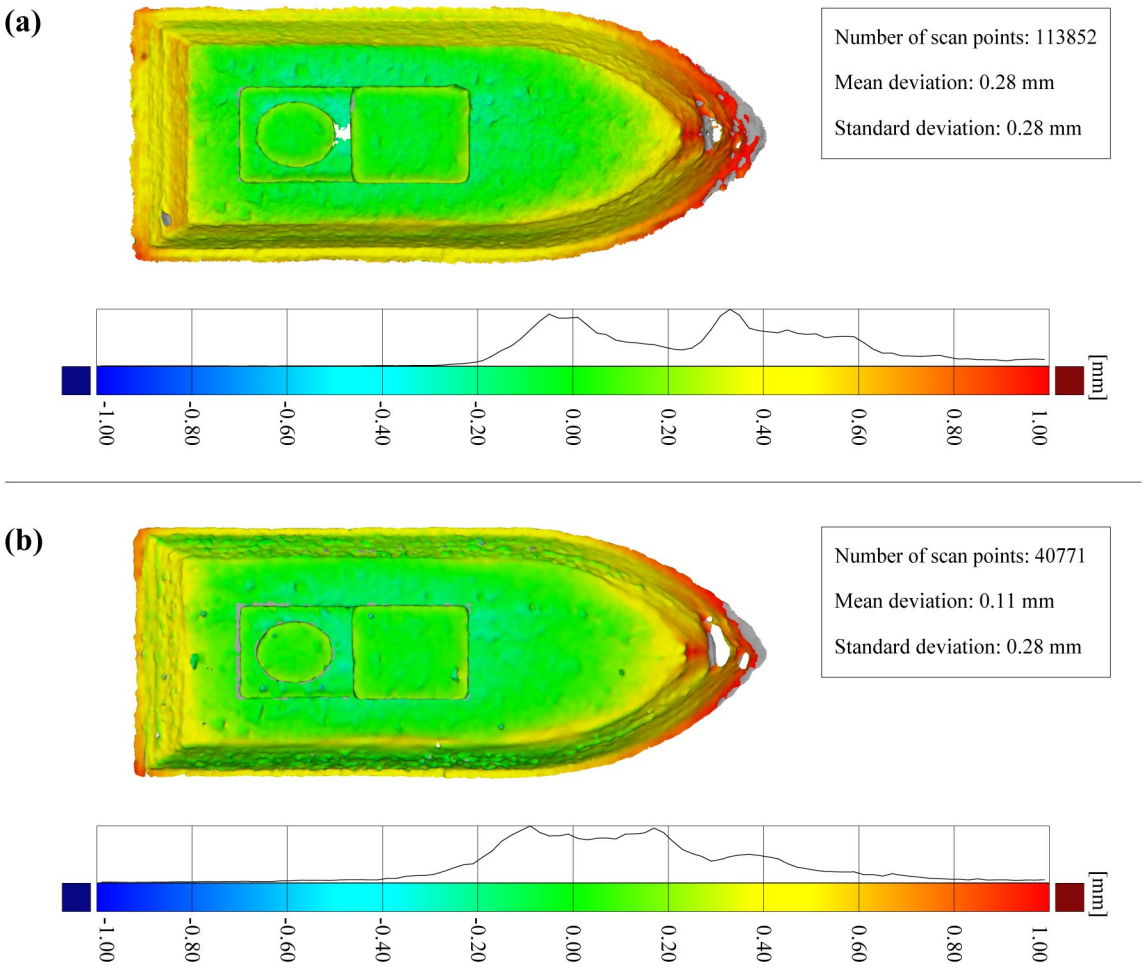


Figure 5: Deviation analysis for the SLS replica from optical scan data (a) and X-CT data (b).

As a bio-based polymer, PHBH undergoes thermal shrinkage upon cooling, contributing to negative dimensional deviations. Moreover, the spatial positioning of parts in the build chamber also affects heat dissipation and powder fusion, leading to anisotropic shrinkage. The highest deviations were observed at the bow and in tilted lateral zones, likely due to the difficulty of forming inclined thin walls, which are prone to material instability and distortions [18].

Table 3 summarizes key dimensional evaluations, referencing the planes in Figure 1, which play a crucial role in assessing dimensional accuracy. A comparison between X-CT and optical scanning reveals measurement discrepancies. While both methods provided consistent data for some features, such as the Z-height at Plane 1, larger discrepancies appeared in others, such as Plane 3, where X-CT recorded 5.26 mm and optical scanning measured 5.20 mm, deviating from the nominal 5.00 mm. Similarly, along the Y-axis, deviations were found between Plane 6 and Plane 8, with X-CT measuring 5.65 mm and optical scanning 6.02 mm. These differences may result from resolution limitations, surface reflectivity, or occlusions during optical scanning, as previously reported in studies evaluating the accuracy of 3D scanning techniques for polymer-based materials [19].

Table 3: Dimensional analysis of the boat model with optical scanner and X-CT

Dimensional evaluations (all values are in mm)	Nominal value	Actual values	
		X-CT	Scanner
Z-height Plane 1	1.25	1.06	1.06
Z-height Plane 2	5.50	5.50	5.48
Z-height Plane 3	5.00	5.26	5.20
Z-height Plane 4	3.00	2.69	2.69
Distance Plane 5 - Plane 9 along Y-axis	5.82	5.77	6.01
Distance Plane 6 - Plane 8 along Y-axis	5.82	5.65	6.02
Distance Plane 7 - Plane 10 along X-axis	14.24	14.03	14.31
Distance Plane 10 - Plane 11 along X-axis	7.08	7.15	7.37

To improve dimensional accuracy, further optimization is needed. Optimization strategies may include refining processing parameters like laser power, hatch spacing, and scan strategies to enhance feature fidelity. Thermal compensation models could minimize shrinkage effects, while post-processing techniques such as surface treatments or annealing may help reduce warping. These findings suggest PHBH has strong potential for sustainable SLS applications, warranting further research to enhance precision and reproducibility. Understanding the interplay between processing conditions and material behavior will be key to advancing PHBH for industrial additive manufacturing.

Conclusions

This study demonstrated the feasibility of HPH as a scalable and sustainable method for producing biopolymer powders for SLS, providing an efficient alternative to previously explored techniques. The HPH process successfully micronized PHBH, achieving a median particle size of 49 μm. Despite their irregular morphology, flowability tests confirmed the powders' suitability for SLS processing. The powders enabled the fabrication of both simple and complex geometries. For dynamic mechanical property testing, the 3D printed samples exhibited a maximum storage modulus of 2.23 GPa. Additionally, a more intricate geometry, such as the boat model, was successfully produced with good dimensional accuracy. Optical scanning analysis of the 3D printed part revealed an average deviation of 0.28 mm from the nominal CAD surface, suggesting the reliability of the powder for SLS applications. This work contributes to bridging the gap between laboratory-scale powder development and industrial production. Future research should focus on optimizing powder morphology and flowability, refining SLS process parameters, and enhancing HPH productivity to further improve its competitiveness. By utilizing a purely mechanical approach, this study underscores the potential of HPH produced biopolymer powders for sustainable AM, paving the way for greener applications.

References

[1] G. D. Goh, Y. L. Yap, H. K. J. Tan, S. L. Sing, G. L. Goh, W. Y. Yeong, Process–Structure–Properties in Polymer Additive Manufacturing via Material Extrusion: A Review, Crit Rev Solid State 45 (2020) 113-133. https://doi.org/10.1080/10408436.2018.1549977

[2] A. Davoudinejad, Vat photopolymerization methods in additive manufacturing, in: J. Pou, A. Riveiro, J. P. Davim (Eds.), Additive Manufacturing, Elsevier, 2021, pp. 159–181. https://doi.org/10.1016/B978-0-12-818411-0.00007-0

[3] P. C. Gomes, O. G. Piñeiro, A. C. Alves, O. S. Carneiro, On the Reuse of SLS Polyamide 12 Powder, Materials 15 (2022) 5486. https://doi.org/10.3390/ma15165486

[4] S. Bano, A. A. Aslam, A. Khan, A. Shabbir, F. Qayyum, N. Wahab, A. Jabar, I. Ul Islam, S. L. Ng, A mini-review on polyhydroxyalkanoates: Synthesis, extraction, characterization, and applications, Process Biochem 146 (2024) 250-261. https://doi.org/10.1016/j.procbio.2024.07.033

[5] K. Eraslan, C. Aversa, M. Nofar, M. Barletta, A. Gisario, R. Salehiyan, Y. A. Goksu, Poly(3-hydroxybutyrate-co-3-hydroxyhexanoate) (PHBH): Synthesis, properties, and applications - A review, Eur Polym J 167 (2022) 111044. https://doi.org/10.1016/j.eurpolymj.2022.111044

[6] V. Volpini, A. Giubilini, L. Corsi, A. Nobili, F. Bondioli, Characterization of biocompatible scaffolds manufactured by fused filament fabrication of poly(3-hydroxybutyrate-co-3-hydroxyhexanoate), R. Soc. Open Sci. 9 (2022) 211485. https://doi.org/10.1098/rsos.211485

[7] B. Duan, M. Wang, W. Y. Zhou, W. L. Cheung, Z. Y. Li, W. W. Lu, Three-dimensional nanocomposite scaffolds fabricated via selective laser sintering for bone tissue engineering, Acta Biomater 6 (2010) 4495-4505. https://doi.org/10.1016/j.actbio.2010.06.024

[8] B. Duan, W. L. Cheung, M. Wang, Optimized fabrication of Ca–P/PHBV nanocomposite scaffolds via selective laser sintering for bone tissue engineering, Biofabrication 3 (2011) 015001. https://doi.org/10.1088/1758-5082/3/1/015001

[9] B. Duan, M. Wang, Customized Ca–P/PHBV nanocomposite scaffolds for bone tissue engineering: design, fabrication, surface modification and sustained release of growth factor, J R Soc Interface 7 (2010) S615. https://doi.org/10.1098/rsif.2010.0127.focus

[10] A. Giubilini, G. Colucci, G. De Trane, F. Lupone, C. Badini, P. Minetola, F. Bondioli, M. Messori, Novel 3D printable bio-based and biodegradable poly(3-hydroxybutyrate-co-3-hydroxyhexanoate) microspheres for selective laser sintering applications, Mater Today Sustain 22 (2023) 100379. https://doi.org/10.1016/j.mtsust.2023.100379

[11] K. T. Kunnath, S. Tripathi, S. S. Kim, L. Chen, K. Zheng, R. N. Davé, Selection of Silica Type and Amount for Flowability Enhancements via Dry Coating: Contact Mechanics Based Predictive Approach, Pharm Res 40 (2023) 2917-2933. https://doi.org/10.1007/s11095-023-03561-6

[12] R. Levy, Z. Okun, A. Shpigelman, High-Pressure Homogenization: Principles and Applications Beyond Microbial Inactivation, Food Eng Rev 13 (2021) 490-508. https://doi.org/10.1007/s12393-020-09239-8

[13] M. Schmid, A. Amado, K. Wegener, Polymer powders for selective laser sintering (SLS), AIP Conf Proc 1664 (2015) 160009. https://doi.org/10.1063/1.4918516

[14] A. T. Sutton, C. S. Kriewall, M. C. Leu, J. W. Newkirk, Powder characterisation techniques and effects of powder characteristics on part properties in powder-bed fusion processes, Virtual Phys Prototyp 12 (2017) 3-29. https://doi.org/10.1080/17452759.2016.1250605

[15] F. Lupone, E. Padovano, V. G. Lambertini, R. Sampieri, F. Casamento, S. Zecchi, C. Badini, Selective Laser Sintering versus Multi Jet Fusion: A Comprehensive Comparison Study Based on the Properties of Glass Beads-Reinforced Polyamide 12, Adv Eng Mater 26 (2024) 2301345. https://doi.org/10.1002/adem.202301345

[16] R. Ajdary, N. Kretzschmar, H. Baniasadi, J. Trifol, J. V Seppälä, J. Partanen, O. J. Rojas, Selective Laser Sintering of Lignin-Based Composites, ACS Sustain Chem Eng 9 (2021) 2727-2735. https://doi.org/10.1021/acssuschemeng.0c07996

[17] J. Ivorra-Martinez, L. Quiles-Carrillo, T. Boronat, S. Torres-Giner, J. A. Covas, Assessment of the Mechanical and Thermal Properties of Injection-Molded Poly(3-hydroxybutyrate-co-3-

hydroxyhexanoate)/Hydroxyapatite Nanoparticles Parts for Use in Bone Tissue Engineering, Polymers 12 (2020) 1389. https://doi.org/10.3390/polym12061389

[18] H. Z. Shen, N. A. Muhayudin, K. S. Basaruddin, S. F. K. M. Khan, L. Tajul, T. D. Hoang, Benchmarking artifact of selective laser sintering (SLS) components fabricated with exible and rigid polymers, Eng. Res. Express 7 (2025) 015409. https://doi.org/10.1088/2631-8695/ada48c

[19] M. Kritikos, J. Urminsky, I. Buransky, Comparison of Optical Scanner and Computed Tomography Scan Accuracy, Lect Notes Mech. Eng (2022) 521-530. https://doi.org/10.1007/978-3-030-90421-0_44

Materials Research Proceedings 57 (2025) 164-171 https://doi.org/10.21741/9781644903735-19

In-situ monitoring of laser powder bed fusion on multi-material substrates for electric mobility

Marco Grasso[1], Matteo Bugatti[1], Frank Sarfert[2], Aitor Echaniz[2], Bianca Maria Colosimo[1]

[1]Politecnico di Milano, Dipartimento di Meccanica, Via La Masa 1, 20156 Milano, Italy

[2]Robert Bosch GmbH, Renningen, 70465 Stuttgart, Germany

Keywords: Additive Manufacturing, Electric Mobility, In-Situ Monitoring

Abstract. The growth of electromobility has driven the demand for advanced power electronics. Meeting the increasing functional requirements necessitates innovative manufacturing solutions. A promising approach involves combining traditional processes with additive manufacturing technologies. This paper focuses on a novel approach, which involves laser powder bed fusion (LPBF) to fabricate high-performance cooling structures directly on a Direct Bonded Copper (DBC) substrate made of a ceramic core sandwiched between two copper layers. This innovative method allows enhancing the cooling performance, but it introduces challenges, including residual stresses, substrate warpage, and ceramic layer cracking. To address these issues, this work presents a novel in-situ monitoring approach for LPBF of pure copper on multi-material substrates. By leveraging multi-sensor data fusion with efficient in-line processing, the proposed approach allows a fast detection of anomalies and defects.

Introduction

The transition to electromobility is driving a demand for more efficient, lightweight, and thermally optimized components, challenging conventional manufacturing techniques. Additive manufacturing (AM) has emerged among enabling technologies in this sector, offering unprecedented design freedom, material efficiency, and the ability to integrate complex functionalities directly into components [1 - 3]. Beyond weight reduction, AM facilitates the production of topology-optimized structures, embedded cooling channels, and multifunctional materials tailored for power electronics, battery systems, and electric drivetrains. Moreover, its potential for decentralized and on-demand production reduces supply chain dependencies and enhances design iterations for next-generation electric vehicles.

In this study, we address the use of AM for the series production of enhanced power electronics [4 – 6]. We introduce a new solution that consists of manufacturing high-performance cooling structures for power electronics directly fabricated on a Direct Bonded Copper (DBC) substrate using laser powder bed fusion (LPBF). The substrate consists of a thin ceramic layer (Al_2O_3) sandwiched between two copper sheets. Producing parts on substrates implies two major challenges. One regards possible positioning errors of the substrates in the baseplate, which may lead to an undesired variability in cooling structure position on the substrate, from one part to another. Another challenge regards the significant temperature gradients involved in the LPBF process and the mismatch in thermal expansion coefficients between copper and Al_2O_3. Because of them, residual stresses can develop, leading to substrate warpage and cracks in the ceramic layer.

This study presents a multi-sensor approach leveraging in-situ data to address two key challenges in LPBF: accurate substrate positioning and early crack detection. A high-resolution imaging system, mounted on the recoating arm, captures the precise position and orientation of

Content from this work may be used under the terms of the Creative Commons Attribution 3.0 license. Any further distribution of this work must maintain attribution to the author(s) and the title of the work, journal citation and DOI. Published under license by Materials Research Forum LLC.

Materials Research Proceedings 57 (2025) 164-171 https://doi.org/10.21741/9781644903735-19

substrates within the build area. Additionally, a structure-borne acoustic sensor beneath the substrates enables real-time detection of cracking events.

While in-situ powder bed imaging is well-established for detecting recoating defects and monitoring layer geometry or surface topography [7–8], this work introduces a novel application: adapting the job file before processing, based on measured substrate alignment. Manufacturing parts on multi-layer substrates, rather than directly on the baseplate, increases the risk of positioning errors, compromising dimensional accuracy and functional performance. Tight tolerances require high-resolution imaging; here, we employ a contact image sensor (CIS) mounted on the recoater blade, offering 21 µm/pixel resolution without the need for perspective correction [9]. In-situ acoustic monitoring for crack detection has been studied using deep learning [10–12], but prior work has not addressed cracks originating in multi-layer or multi-material substrates, such as ceramic layers in LPBF. These scenarios require sensitive acoustic coupling and the ability to detect low-severity events. Given the scarcity of real crack data, we adopt a multivariate statistical approach and evaluate its performance by inducing cracks during the process.

The proposed solutions aim to support the reliable LPBF manufacturing of cooling structures for advanced power electronics in electromobility applications.

Case Study

Two distinct experimentations have been carried out, one devoted to testing and demonstrating the suitability of the blade-mounted CIS system [9] for fine positioning assessment of multi-layer substrates, and one devoted to evaluating the effectiveness of the proposed in-situ crack detection approach.

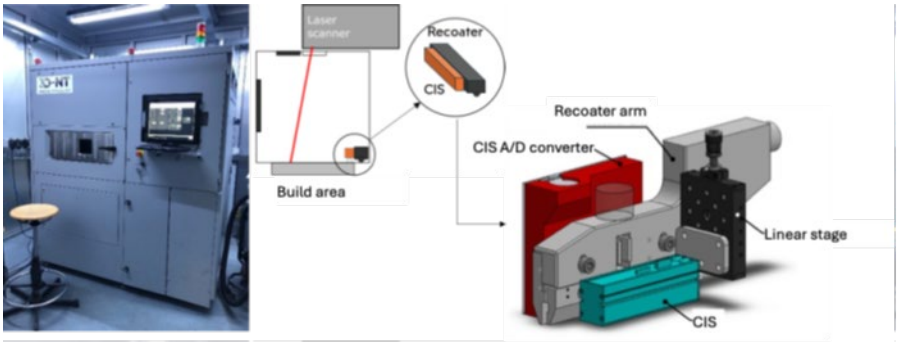


Fig. 1 – LPBF system used for the first experimentation and blade-mounted CIS setup [9]

The CIS was manufactured by WHEC, and it is composed by the sensor itself and an A/D converter and it offers a high optical resolution of 21 µm/px (1200 dpi). Such industrial optical scanner eliminates the typical sources of image distortion in traditional off-axis imaging systems. The industrial scanner integrates two internal RGB LED arrays that illuminate the scene co-axially. An incremental linear encoder Elgo GSI2 was used in this work, having a resolution of 1 µm. Full details and specifications can be found in [9].

The multi-material substrate consists of a thin ceramic layer sandwiched between two copper sheets, with typical thicknesses of 300 µm copper, 630 µm aluminum-oxide, and 300 µm copper. A custom aluminium baseplate with a diameter of 150 mm was produced, involving four pockets where four substrates of size 42 x 40.8 mm could be placed. The CIS images of the working area with the four embedded substrates were captured after blade alignment and before powder spreading.

Since the 3DNT (3D New Technologies) used for these tests is still not equipped with an integrated structure-borne acoustic emission (AE) sensor, the second experimentation was performed on a prototype LPBF machine developed by Robert Bosch GmbH and available in their

Materials Research Proceedings 57 (2025) 164-171 https://doi.org/10.21741/9781644903735-19

facilities. The prototype machine features a 100 x 100 x 70 mm build volume. It is equipped with a 1 kW IPG (IRE-Polus Group) laser operating at 1070 nm with a laser spot diameter of 60 µm.

The AE sensor was mounted underneath the baseplate, in a custom pocket directly milled on the bottom side of the baseplate to minimize the distance between the sensor and the substrates. Acoustic coupling was ensured by a cap plate and contact grease. AEs were acquired in the range up to 1 MHz by means of a Kistler 8152C0 structure-borne AE sensor. The experiment involved the production of one single square-based prismatic specimen per substrate. Multiple specimens were printed by varying the base area and the height of the specimen, as both the exposed area on top of the substrate and the heat accumulation across the build direction could be drivers of thermal stress development and consequent cracking events.

Table 1 summarizes the salient specifications of the sensors. LPBF process parameters cannot be disclosed, but they allow a density >99.5%.

Table 1 –AE sensor specification for the crack detection experimentation

AE sensor specifications	Sampling frequency	Frequency range $\pm 10\ dB$	Sensitivity
	1 MHz	50 – 400 kHz	57 dBref 1V/(m/s)

After the LPBF process, the specimen where embedded, cut, etched and visually analysed using an optical microscope. Two types of cracks can be observed: small vertical cracks originating at the Cu/Al_2O_3 interface on the copper sheet opposite the built component, and large horizontal cracks forming at the Cu/Al_2O_3 interface on the copper sheet supporting the built component. These cracks typically extend across the entire width of the structure.

Table 2 shows whether cracks and which type of crack were observed for each tested specimen.

Specimen	Base area	Height	Vertical cracks	Horizontal cracks
1	3 x 3 mm	0.12 mm	No	No
2	3 x 3 mm	0.24 mm	No	No
3	3 x 3 mm	0.36 mm	No	No
4	3 x 3 mm	0.6 mm	Yes	Yes
5	3 x 3 mm	0.84 mm	Yes	No
6	6 x 6 mm	0.72 mm	Yes	Yes
7	6 x 6 mm	0.84 mm	Yes	Yes

Fig. 2 shows an example of vertical and horizontal cracks in one substrate where a specimen having a base area of 6 x 6 mm was manufactured.

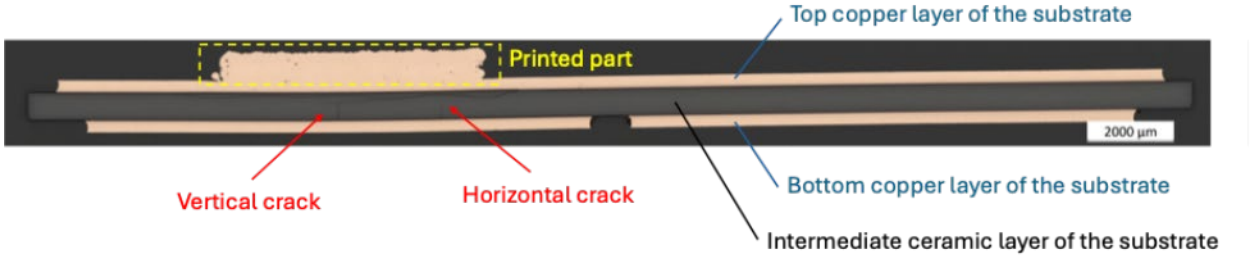


Fig. 2 – Example of vertical and horizontal cracks in a ceramic layer of the power electronics substrates

Methodology

A scheme of the overall methodology is shown in Fig. 3.

The fine positioning approach and the crack detection method are briefly described in the two following subsections.

Materials Research Proceedings 57 (2025) 164-171 https://doi.org/10.21741/9781644903735-19

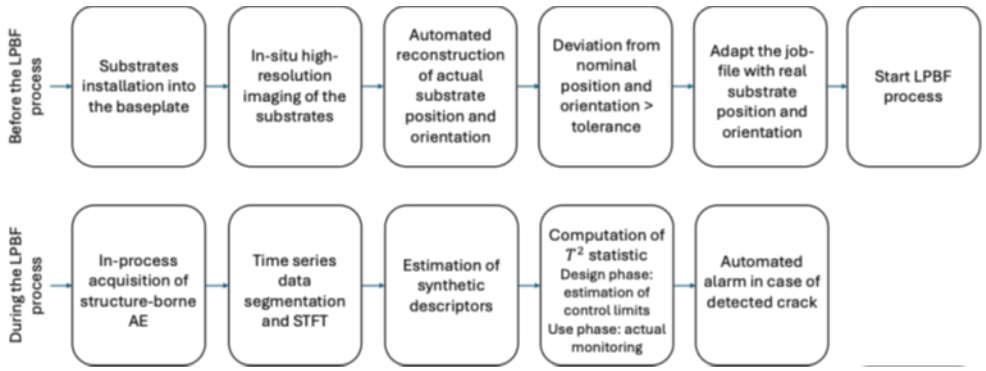


Fig. 3 – Scheme of the method

Fine positioning

The proposed methodology involves a sequence of steps. First, the baseplate with embedded substrates is mounted in the build volume and aligned to the recoater. Then, the high-resolution image of the substrates is captured before any powder is spread over the surface. The image is then processed to reconstruct the coordinates of each j-th substrate center of mass, namely $(x_{0,j}, y_{0,j})$, and its orientation with respect to the x-axis, namely $\gamma_{0,j}$.

To this aim, an image segmentation approach is proposed, which consists of the steps schematically illustrated in Fig. 4

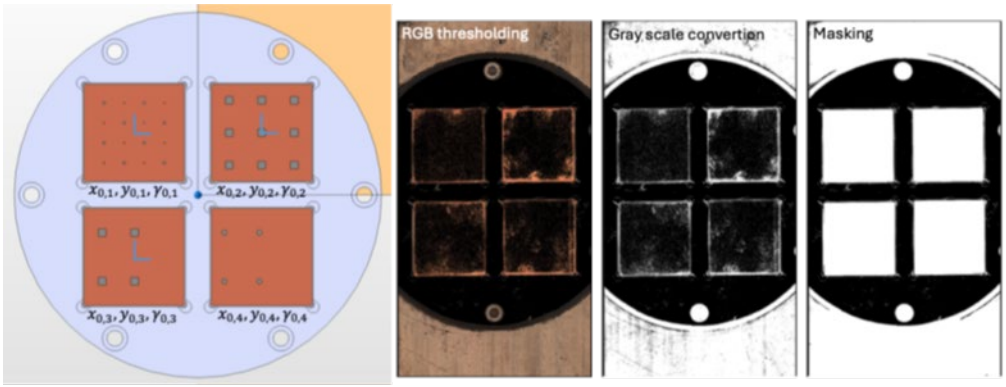


Fig. 4 – Example of build-job view of the baseplate with 4 substrates (left) and schematic illustration of the salient steps of the proposed approach (right)

An RGB (red greed blue) segmentation is applied to isolate the contours of copper layer of each substrate from the surrounding material. The resulting segmentation is then converted into gray scale and binarized. A masking approach that fills the region of interest (ROI) of the substrates is then applied, leading to one connected component for each substrate. A bounding rectangle with the nominal aspect ratio of the substrate is then fit to each connected component, and the coordinates of its four corners are extracted.

The center of mass $(x_{0,j}, y_{0,j})$ of the four corners is then computed and used as in-situ reconstructed position of the j-th substrate. Similarly, the $\gamma_{0,j}$ angle is computed as the average inclination of lines passing through the four corners.

The in-situ estimated coordinates of each substrate are referred with respect to a fixed reference, e.g., the center of the baseplate, as it is the common origin of the reference systems used in job-file preparation software tools. The center of the baseplate can be marked by the LPBF laser itself before CIS image acquisition.

Materials Research Proceedings 57 (2025) 164-171 https://doi.org/10.21741/9781644903735-19

If the deviation from the nominal position and nominal orientation of each substrate is larger than a given tolerance, t, the job-file is corrected accordingly, such that parts are printed considering the real position and orientation of each substrate, rather than the nominal one. If the deviation is lower than the given tolerance, no further correction is needed.

The tolerance t depends on the specific application. In this specific case study, a tolerance $t = 0.1$ mm has been considered. This implies the need to detect possible deviations with an accuracy that is about one order of magnitude lower than t. The analysis performed in this study was specifically aimed at quantifying such accuracy.

As ground truth, a manual annotation of original images was performed. For each substrate, the coordinates of the four corners were annotated and used to compute the ground truth position of the center of mass and the ground truth orientation.

Crack detection in the ceramic layer

AE signals were acquired continuously throughout the process, capturing time series data with four phases per layer: (1) z-axis movement, (2) powder recoating, (3) melting, and (4) idle time. Analysis focused on phases where the substrate experienced external loading (phases 1–3 combined), as all cracks occurred during these steps. Idle state signals were excluded for brevity.

Signals were preprocessed using a 5th-order Butterworth band-pass filter (65–400 kHz), selected for its balance between noise reduction and sensitivity to high-frequency elastic wave propagation. A sliding window segmented the filtered signals, enabling feature extraction in both time and frequency domains. Key features included RMS, peak-to-peak amplitude, kurtosis, skewness, and maximum spectral energy density. Short-time Fourier transform (STFT) was applied within each window to estimate spectral energy and capture time-frequency crack signatures.

While deep learning approaches have been used for crack detection in AM [8–10], their reliance on extensive labeled data limits practical application. Instead, a statistical process monitoring method was adopted. A multivariate Hotelling's T^2 control chart combined all features, accounting for their correlations. Kernel density estimation (KDE) modeled the empirical distribution of T^2 statistics, with the control limit set at the 99.73rd percentile ($\alpha = 0.0027$). Control charts were designed using data from three crack-free samples. Remaining data were used to evaluate the crack detection system.

Results

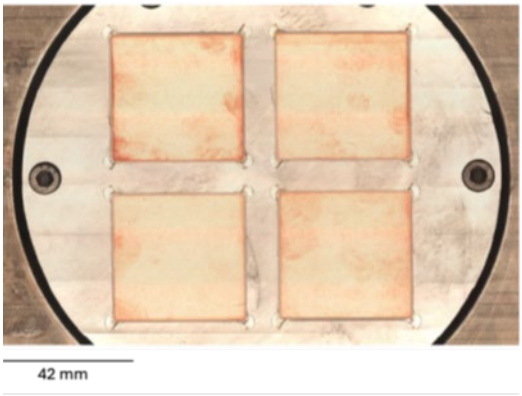
Fig. 5 (left) shows a sample image of the baseplate with four embedded substrates acquired with the blade-mounted CIS. The table on the right-hand side of Fig. 5 summarizes the estimated errors for the substrate position and orientation. Mean errors and the standard deviation of errors were estimated by means of 4 random replicates.

The results shown in Fig. 5 show that the average error in detecting the actual substrate position ranges between 0.01 and 0.03 mm, which is expected to be sufficient to detect positioning errors above the tolerance $t = 0.1$ mm. The orientation error ranges between 0.02° and 0.12°, which confirms the high in-situ reconstruction accuracy.

The results of the proposed approach for in-situ detection of cracks originate in the ceramic layer of the substrate are summarized here below.

Fig. 6 shows the result of the T^2 control chart, where the vertical lines separate data from different specimens. Every point in the control chart correspond to the statistic computed in a sliding window of duration 0.1 s.

Materials Research Proceedings 57 (2025) 164-171 https://doi.org/10.21741/9781644903735-19



Substrate	Center positing error (mm)		Orientation error (°)
	X	Y	
Top-left	0.011 (0.013)	0.005 (0.013)	0.09 (0.049)
Top-right	0.022 (0.015)	0.009 (0.011)	0.1 (0.036)
Bottom-left	0.010 (0.017)	0.028 (0.014)	0.02 (0.024)
Bottom-right	0.014 (0.010)	0.017 (0.021)	0.12 (0.066)

Fig. 5 – Example of baseplate CIS image (left) and estimated accuracy of in-situ reconstruction of substrate positioning

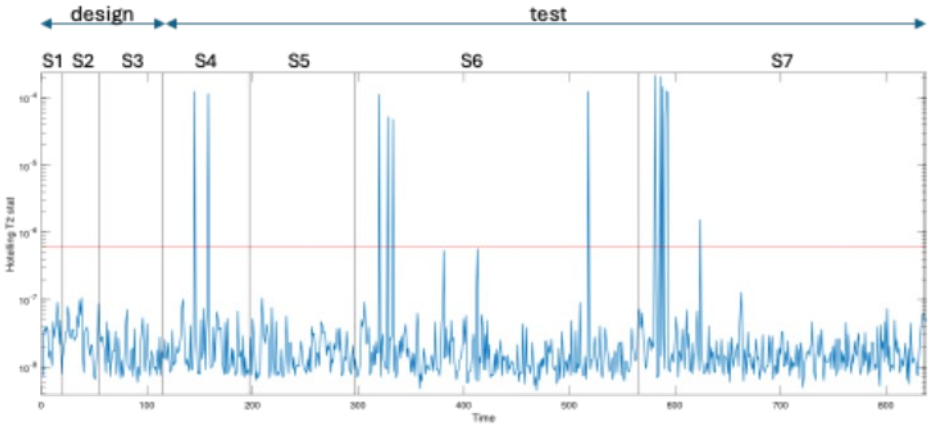


Fig. 6 – Control chart for in-situ crack detection (vertical bars separate data corresponding to different specimens, labelled as S1, …, S7)

Fig. 6 shows that different alarms are signalled for specimens 4, 6 and 7, where both vertical and horizontal cracks where observed. No alarms are signalled during the design phase, which involved only substrates without cracks. However, no alarm was signalled also during the production of specimen 5, where only a tiny vertical crack was observed. This may indicate that the energy release in the presence of such tiny crack was not captured by the sensor, or the selected synthetic features are not sensitive enough for such low intensity events.

It is also interesting to note that multiple alarms were observed in a row, when cracks originate in the substrate, which is compliant with the nature of damages observed via destructive testing, where multiple cracks are present in the same ceramic layer.

Fig. 7 shows two examples of STFT time-frequency patterns of detected cracks, respectively one crack detected during the production of a 3 x 3 mm specimen and a crack detected during the production of a 6 x 6 mm one.

Fig. 7 shows that signalled alarms correspond to events that are highly localized in time while affecting the whole frequency spectrum up to highest frequencies. This is a typical signature of crack events, which further confirms the effectiveness of the in-situ crack detection.

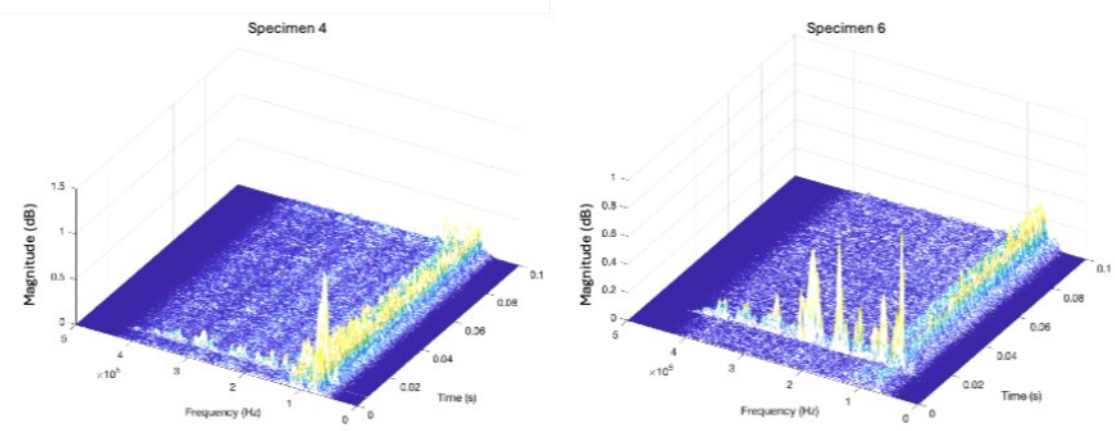


Fig. 7 – Examples of crack events in the STFT time-frequency domain

Conclusions

AM has the potential to unlock new opportunities in the series production of electronic components for the electromobility sectors. In this study, we investigated a new solution that involves the use of LPBF to produce high-performance cooling structures for power electronics on DBC multi-layer and multi-material substrates. In-situ sensing and monitoring represents a key capability to enable the production of defect-free and high-quality components. The proposed methods are aimed to verify the proper positioning of the substrates within the build area and to detect, in-line and in-situ, the onset of cracks in the ceramic layer of the substrate during the LPBF process. Results highlight the suitability and effectiveness of the proposed methods, but there are also open issues to face, which motivate further research efforts. The entity of cracks may vary depending on the type of crack (vertical or horizontal) and depending on the exposed area during the process. Detecting smaller cracks is necessary but still challenging. New solutions are under investigation, both in terms of AE sensing and AE signal processing and monitoring. Moreover, other anomalies and defects may arise because of various nuisance factors, possibly related to heat accumulations, spatter contamination and geometrical deviations along the layerwise production of cooling structures. Because of this, additional and complementary methods are under investigation, to broaden the range of detectable anomalies, towards a first-time-right AM capacity. Additional experiments are ongoing to determine whether the time-frequency signature varies from vertical to horizontal conditions. To this aim, controlled experiments where different types of cracks are artificially induced are foreseen.

Acknowledgements

The research activity has been carried out in the framework of the GlobalAM project, funded by the European Commission within the HORIZON-CL4-2023-TWIN-TRANSITION-01 program (Grant agreement ID: 101138289).

References

[1] Mahr, A., Schütt, T., Rosnitschek, T., Tremmel, S., & Döpper, F. (2024). Evaluation of Powder-and Extrusion-Based Metal Additive Manufacturing Processes for the Sustainable Fabrication of Spare Parts in Electromobility. Sustainability, 16(8), 3425. https://doi.org/10.3390/su16083425

[2] Charles, A., Hofer, A., Elkaseer, A., & Scholz, S. G. (2021, September). Additive manufacturing in the automotive industry and the potential for driving the green and electric transition. In Proceedings of the International Conference on Sustainable Design and

Manufacturing (pp. 339-346). Singapore: Springer Singapore. https://doi.org/10.1007/978-981-16-6128-0_32

[3] Schuhmann, D., Rockinger, C., Merkel, M., & Harrison, D. K. (2022). A study on additive manufacturing for electromobility. World Electric Vehicle Journal, 13(8), 154. https://doi.org/10.3390/wevj13080154

[4] Zhang, Z., & Yuan, X. (2021). Applications and future of automated and additive manufacturing for power electronics components and converters. IEEE Journal of Emerging and Selected Topics in Power Electronics, 10(4), 4509-4525. https://doi.org/10.1109/JESTPE.2021.3135285

[5] Lopera, L., Rodriguez, R., Yakout, M., Elbestawi, M., & Emadi, A. (2021). Current and potential applications of additive manufacturing for power electronics. IEEE Open Journal of Power Electronics, 2, 33-42. https://doi.org/10.1109/OJPEL.2021.3052541

[6] Szabó, L. (2022, January). Additive manufacturing of cooling systems used in power electronics. A brief survey. In 2022 29th International workshop on electric drives: advances in power electronics for electric drives (IWED) (pp. 1-8). IEEE. https://doi.org/10.1109/IWED54598.2022.9722580

[7] Grasso, M., Remani, A., Dickins, A., Colosimo, B. M., & Leach, R. K. (2021). In-situ measurement and monitoring methods for metal powder bed fusion: an updated review. Measurement Science and Technology, 32(11), 112001. https://doi.org/10.1088/1361-6501/ac0b6b

[8] McCann, R., Obeidi, M. A., Hughes, C., McCarthy, É., Egan, D. S., Vijayaraghavan, R. K., ... & Brabazon, D. (2021). In-situ sensing, process monitoring and machine control in Laser Powder Bed Fusion: A review. Additive Manufacturing, 45, 102058. https://doi.org/10.1016/j.addma.2021.102058

[9] Bugatti, M., Grasso, M., & Colosimo, B. M. (2023). Unlocking New In-Situ Defect Detection Capabilities in Additive Manufacturing with Machine Learning and a Recoater-Based Imaging Architecture. In Selected Topics in Manufacturing: Emerging Trends from the Perspective of AITeM's Young Researchers (pp. 89-102). Cham: Springer Nature Switzerland. https://doi.org/10.1007/978-3-031-41163-2_6

[10] Kononenko, D. Y., Nikonova, V., Seleznev, M., van den Brink, J., & Chernyavsky, D. (2023). An in situ crack detection approach in additive manufacturing based on acoustic emission and machine learning. Additive manufacturing letters, 5, 100130. https://doi.org/10.1016/j.addlet.2023.100130

[11] Seleznev, M., Gustmann, T., Friebel, J. M., Peuker, U. A., Kühn, U., Hufenbach, J. K., ... & Weidner, A. (2022). In situ detection of cracks during laser powder bed fusion using acoustic emission monitoring. Additive Manufacturing Letters, 3, 100099. https://doi.org/10.1016/j.addlet.2022.100099

[12] Ito, K., Kusano, M., Demura, M., & Watanabe, M. (2021). Detection and location of microdefects during selective laser melting by wireless acoustic emission measurement. Additive Manufacturing, 40, 101915. https://doi.org/10.1016/j.addma.2021.101915

[13] Montgomery, D. C. (2020). Introduction to statistical quality control. John wiley & sons.

Materials Research Proceedings 57 (2025) 172-179 https://doi.org/10.21741/9781644903735-20

FFF of PLA reinforced with flax: Effects of the infill strategy on low-velocity impact behavior and the energy consumption

Ersilia COZZOLINO[1,a *], Ilaria PAPA[1,b], Antonello ASTARITA[1,c], Valentina LOPRESTO[1,d]

[1]Department of Chemical, Materials and Industrial Production Engineering, University of Naples "Federico II", P.le Tecchio 80, 80125 Naples, Italy

[a]ersilia.cozzolino@unina.it, [b]ilaria.papa@unina.it, [c]antonello.astarita@unina.it, [d]valentina.lopresto@unina.it

Keywords: Natural Fiber Composites, Additive Manufacturing, Low Velocity Impact Test, Energy Consumption

Abstract. In recent decades, demand for sustainable materials and processes has been triggered globally, thus motivating researchers towards biocomposites. Also, Additive Manufacturing (AM) plays a crucial role in advancing sustainability because it enables efficient use of resources, energy and materials. Fused Filament Fabrication (FFF) is among the most popular AM processes that use continuous thermoplastic material filament. Among all the process parameters of the FFF process, the infill pattern is crucial for the mechanical characteristics of the printed parts. In this scenario, Natural Fiber Composites (NFC) are growing their interest but despite their potentialities, still limitations exist in their mechanical properties. Low velocity Impact (LVI) test of NCFs printed by FFF has not deeply investigated. This work aims to fill this gap of knowledge. In particular, the effect of the pattern infill on the low velocity impact of FFFed PLA reinforced with flax has been investigated. Energy consumption has also been monitored during printing to release guidelines on mechanical behavior from an energy-saving perspective.

1. Introduction

Composite materials are widely used for a wide range of applications, including biomedical, aerospace, and structural due to their excellent mechanical properties as well as wear and fatigue resistance. Despite these advantages, impact damage can have catastrophic effects, compromising the integrity of the structures [3].

It is well known that Additive Manufacturing (AM) offers numerous advantages in terms of both geometrical flexibility and sustainability. In particular, Fused Filament Fabrication (FFF) is among the most popular AM processes which use a continuous filament of a thermoplastic material. Among all the process parameters of the FFF process, infill density and pattern are crucial for the mechanical characteristics of the printed parts [4].

The infill density is the amount of material used to fill the layer's inner area. It is typically fed in the form of percentages. The infill pattern rules the motion of the nozzle or platform along the XY direction in filling the area of the layer. It controls the build time, the amount of raw material needed to print the volume unit and the mechanical characteristics of the FFF parts [5].

Infill density and pattern strongly affect strength-to-weight. In general, it is demonstrated that a higher infill density offers more bonding between layers as well as more resistance to deformation due to a smaller air gap. The literature demonstrates that flexural and tensile strength decrease with the increase in feed rate [6]. A higher thickness leads to higher strength due to the interfacial bonding [5]. In fact, better adhesion between the adjacent raster results in higher impact resistance. Moreover, an increase in the infill density is typically associated with better physical behavior due to the inter-layer bonding between two consecutive layers. Moreover, it is said that the triangular

Content from this work may be used under the terms of the Creative Commons Attribution 3.0 license. Any further distribution of this work must maintain attribution to the author(s) and the title of the work, journal citation and DOI. Published under license by Materials Research Forum LLC.

Materials Research Proceedings 57 (2025) 172-179 https://doi.org/10.21741/9781644903735-20

infill pattern mechanically performs better than other patterns. This is because it has more contact points per unit area.

The growing awareness of the need for sustainable and bio-based materials has increased interest in Natural Fiber Composites (NFC). Despite their potential, still, challenges and limitations exist in their regard [1].

Low-velocity impact (LVI) tests are used in the automotive industry to evaluate the crashworthiness of vehicles and their components [2]. LVI is not widely investigated for FFF NFCs. This work aims to fill this gap of knowledge. In this study, the effect of the pattern infill on the low-velocity impact of FFFed PLA reinforced with flax has been investigated. Energy consumption has also been monitored during printing to release guidelines on mechanical behavior from an energy-saving perspective.

2. Materials and Methods

2.1 Experimental setup

This work investigates the low-velocity impact behavior of PLA reinforced with flax printed by FFF. In particular, it investigates the effect of different infill strategies and printing density on both the low-velocity impact and the energy consumption needed for printing. Nanovia PLA Lin, made of PLA reinforced with flax, is the filament used to perform the FFF process. In Table 1 the mechanical and thermal properties of the material used are reported.

Table 1. Nanovia PLA Lin properties

Mechanical features		**Thermal features**	
Density	1 g/cm^3	Glass transition temperature, T_g	54°C
Tensile Modulus	3400 MPa	Temperature of deflection under load (DTUL)	50°C
Flexural Modulus	2300 MPa	Flammability class	HB UL 94 @ 1.6 mm
Elongation at break	2%		

Flashforge Creator 4S is a 3D printer used to perform the FFF process. All the specimens were modelled by Solidworks software, sliced by Flash Print software, and then printed by selecting the same FFF process conditions, illustrated in Table 2. These choices have been made according to the Original Equipment Manufacturer (OEM) datasheet recommendations.

The solid strategy with an infill density of 100% represents the chosen reference to compare other possible, and eventually more sustainable, strategies and infill. It consists of a linear configuration with a degree deposition ±45°. In this perspective, an infill of 80% was fixed for all the strategies, as indicated in Table 3. Fig. 1 is a schematic representation of the infill strategies adopted in comparison with the solid one: a) straight, b) gyroid, c) triangular, d) hexagonal.

Table 2. Process parameters adopted to print the samples by FFF

Nozzle diameter	0.6 mm
Layer height	0.2 mm
Plate temperature	50 °C
Nozzle temperature	200 °C
Scan speed	80 mm/s

Materials Research Proceedings 57 (2025) 172-179 https://doi.org/10.21741/9781644903735-20

Table 3. Infill strategies and densities investigated in this work

Strategy	Solid	Solid	Straight	Gyroid	Triangular	Hexagonal
Infill density (%)	100	80	80	80	80	80
Starting raster angle (°)	45	45	45	-	45	-

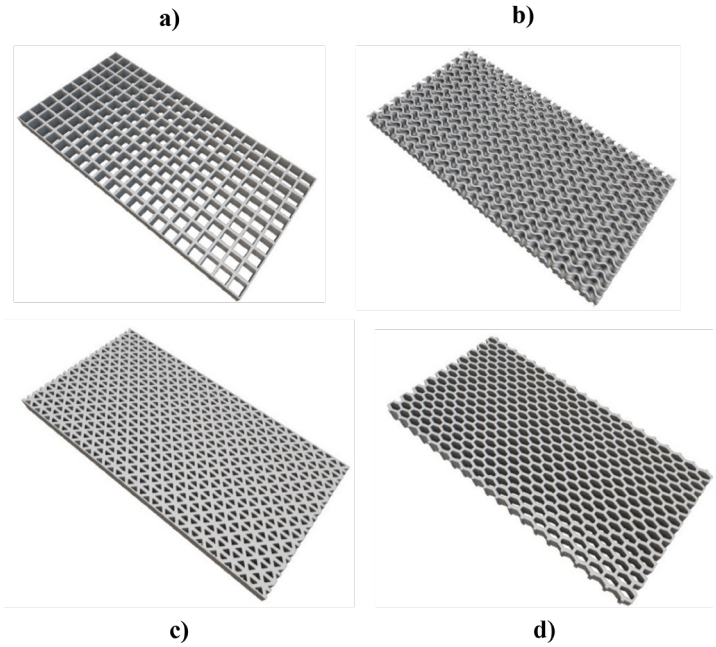


Figure 1. Schematic representation of the infill strategies adopted in comparison with the solid one: a) straight, b) gyroid, c) triangular, d) hexagonal

2.2 Low Velocity Impact test

Low-velocity impact (LVI) tests were carried out by CEAST FRACTOVIS drop test machine. This machine allows adjustment of the impactor mass system and the drop height. The machine is equipped with a braking system to avoid multiple impacts. To perform high-energy values tests, a springs system can be activated for increasing the system energy capacity. The impactor, equipped with threaded connection, allows interchangeable tups to adapt to different applications. The tup used for the low-velocity impact test campaign is hemispherical (as per ISO 6630) with a diameter equal to 19.8 mm. The tests were conducted using an impact mass, kept constant, of 5.3 kg. The specimens (80x80x2 mm^3) were supported by a cylindrical support with an internal diameter of 40mm and an external diameter of 76 mm. For each condition, three samples were tested.

2.3 Energy consumption

Energy consumption was measured during the printing of all the samples by using the Chauvin Arnoux C.A. 8331 power device. It is a high-quality analyser with a colour and battery graphic display built-in rechargeable, that is equipped with four tension cables, four crocodile clips and three current sensors MiniFLEX MA193-350. The electrical connection of each machine determined the number of tension cables and current sensors to be adopted to measure energy consumption. In particular, the 3d printer adopted in these experimental activities has a monophase with a neutral connection, so two tension cables and one current sensor were used to measure the energy consumption. A sample period of 1 second was fixed to perform the measurements.

Materials Research Proceedings 57 (2025) 172-179 https://doi.org/10.21741/9781644903735-20

The mass of each sample was measured three times by using a Gibertini ETERNITY 200 CAL balance, having an accuracy of ± 0.05 mg. These measurements have allowed calculating the specific energy consumption (SEC), which is highly used in the literature as a key sustainable performance indicator [7].

In the FFF process, SEC represents the total energy consumption for printing the mass unit, m, and is expressed as follows [8], [9], [10]:

$$SEC = \frac{E_{tot}}{m} \quad (1)$$

Where the total energy consumption is given by:

$$E_{tot} = E_{setup} + E_{printing} \quad (2)$$

Where E_{setup} is the energy consumption spent to perform all the pre-printing stages, such as the movement of the axes, the reaching of the desired bed and nozzle temperatures, while $E_{printing}$ is the energy spent to actually print the samples.

3. Results and Discussion

3.1 Low velocity impact results

This section examines the impact characteristics, including peak force, penetration limit, residual velocity, penetration acceleration, penetration energy, and material stiffness. The peak force refers to the highest force applied to the material during the LVI test, determined from the collected data and the force-displacement/time curve. The purpose of the LVI test was to identify the velocity at which the impactor begins to penetrate the material (puncture test). After penetration, the impactor may still retain some velocity, referred to as residual velocity. The difference between the initial velocity and the residual velocity defines the material's penetration limit. The magnitude of penetration acceleration/deceleration or the rate at which these values change provides insight into the material's strength and impact attenuation capability. Penetration energy is calculated as the difference between the impactor's initial and residual energy before and after the impact. A higher penetration energy indicates greater energy absorption capacity, indicating increased material toughness. Finally, the maximum displacement of the impactor occurs when the force either drops to zero or gradually decreases. In this study, the variable parameter used is the infill pattern. In Fig. 2 all the load displacement curves at penetration for all the infill patterns selected are reported. The performance of each sample (or each infill pattern) depends on the number of contact points/number of layers where the two layers on the surface intersect at one point. The number of contacts per unit area in each sample defines the resistance of the printed specimen against the external load. In fact, as visible in Fig. 3 for the strategy solid 100 and solid 80 where only the density changes, Solid 100 reaches an impact strength, F_{max} , with higher respect the Solid 80. However, the last maintains a maximum load for a higher displacement, d, interval denoting a higher propensity to deform and a different mode of energy absorption. The same occurs for the Straight, Triangular and Hexagonal strategies, where the maximum load reached, Fmax, is lower with respect to the solid strategies, but it is maintained for a long time and it results in very useful in particular application fields. The same behaviour can be discussed regarding the penetration energy, U_p, necessary to completely penetrate the samples. No differences are recorded for Solid 100 and Solid 80 where an U_p value of 5J is recorded. This combination of similar penetration energy and energy transfer is an important characteristic of some engineering applications. Further, absorbing energy capacity with porosity is necessary in the same application where the stress-shielding effect can be removed [11], [12]. For the other pattern, an Up=3.5 J is detected, resulting

Materials Research Proceedings 57 (2025) 172-179 https://doi.org/10.21741/9781644903735-20

in lower respect for the solid configuration. All the results discussed before are confirmed in Fig. 3 a) and b).

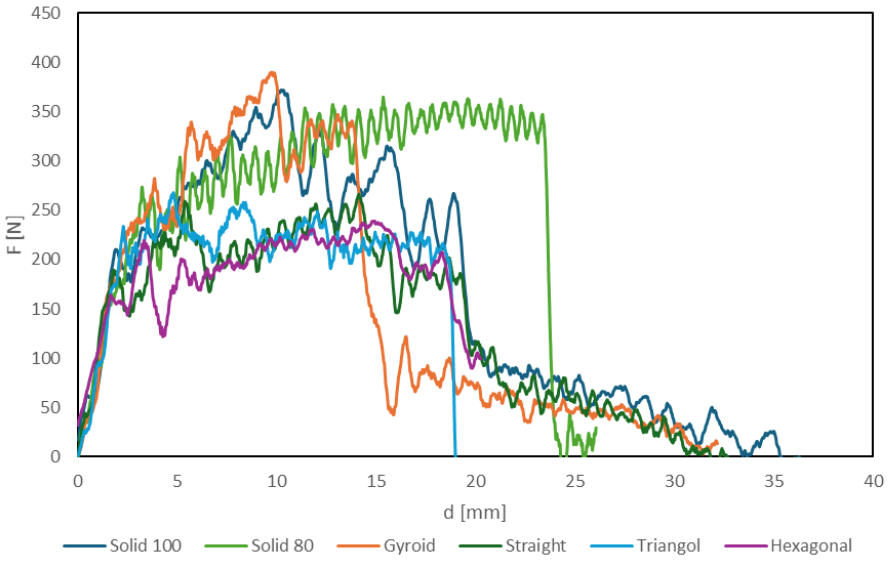


Figure 2. Load displacement curves comparison

The velocity response of the impacted specimen and the energy response as a function of time obtained during the impact tests are shown in Fig. 3 a) and b), respectively. The observed penetration limit (the difference between the impact velocity and the residual one recorded at the end of the test) was completely different. Higher is the difference between the two Solid patterns. The higher penetration limit value for Solid 100 infill patterns was attributed to more contact points/sheared points per unit area. This meant that it has more resistance against the impactor (penetration); consequently, it can absorb more energy, leading to a high value of toughness and stiffness. As it is possible to observe in Fig. 3 a), the response in terms of the velocity of the other infill strategies turns out to be a compromise between the two limiting cases, denoting a good compromise in terms of energy absorption also from the point of view of the material development. The latter can be evaluated as the slope of the v-t. The infill pattern also has a significant effect on the penetrating deceleration. For instance, the calculated penetrating deceleration of the impactor at the time of Solid 100 was around 2.3±0.4 times more compared to the Gyroid, Hexagonal, Straight and Triangular strategies.

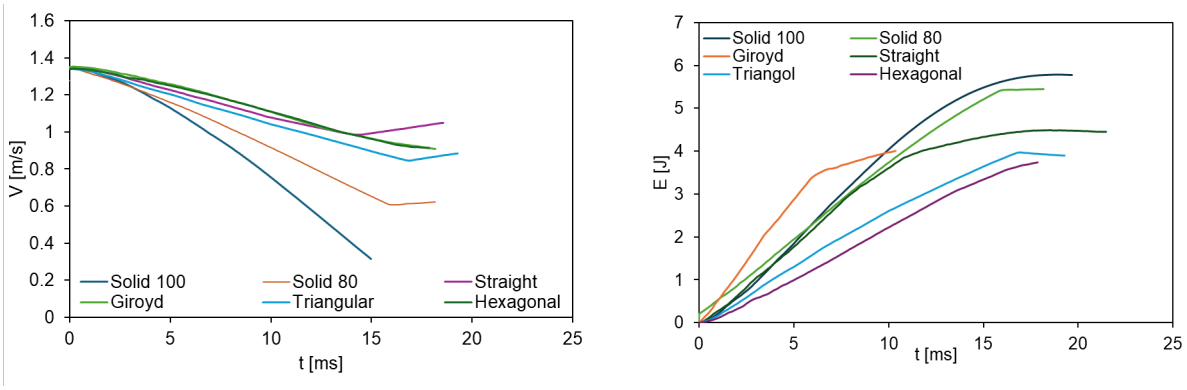


Figure 3. a) Impact Velocity, V, and b) Impact Energy, E, vs time for all tested infill patterns

Materials Research Proceedings 57 (2025) 172-179 https://doi.org/10.21741/9781644903735-20

These results were confirmed by E-t response (Fig. 3 b)) which confirmed that the infill patterns and density have a significant effect on the penetration energy, and it was attributed to the arrangement of layers like stacking of pattern structure and non-uniform porosity.

3.2 Energy consumption results

Before the LVI test, the mass of all the specimens have been measured as previously described. Table 3 contains all the results. The difference between the mass estimated by the slicing software and the real mass of the specimen is around 7-9%. This means that actually there is an amount of voids/air gaps which need to be considered in the design of FFF parts.

Energy consumption has been measured as described in section 2.3. Total energy consumption has been considered as the sum of the energy consumption needed for setup and that one required for actually printing the sample to be tested by LVI test.

It can be observed that the energy consumption for setup was the same, and this result is justified by the fact that the same temperature, for the nozzle and the bed, has been selected to be reached for all the infill strategies. Instead, a different energy consumption has been required to print the object having the same geometry and volume – that of the standardised LVI specimen.

In particular, Fig. 4 a) shows that Solid 100 infill required the greatest amount of energy. This result is justified by the higher duration of the printing, as visible in Table 4. Also, comparing Solid 100 and Solid 80, it can be seen that a reduction of 20% in the density results in a reduction of around 7.52% in total energy consumption, E_{tot}, even if all the other process conditions have been the same. This means that the density strongly impacts the total energy consumption. Among all the strategies investigated at the same infill density (80%), Solid 80 required the minimum amount of energy consumption, while straight the highest one, even if the printing duration was lower. This result can be justified considering that the average power over the whole period of printing has been slightly higher due to the strategy adopted, which probably required more movements of the nozzle to accomplish the desired geometry. SEC, calculated as the ratio between the total energy consumption and the real mass of the specimen, showed a similar trend over the infill strategy adopted except the Solid 100, which showed the minimum SEC. These results are justified by the real mass of the samples. Solid strategy results in the higher mass, while hexagonal and gyroid lead to the minimum ones, agreeing with the literature [13].

Table 4. Main outputs of the energy consumption analysis

Infill strategy	**Estimated mass (g)**	**Real mass (g)**	**Mass percentage reduction %**	**Printing duration (h:m:s)**	E_{setup} **(kJ)**	$E_{printing}$ **(kJ)**	E_{tot} **(kJ)**	SEC **(kJ/g)**
Solid 100	23.88	22.20	7.03	01:01:27	64.84	792.00	856.84	38.60
Solid 80	20.71	19.20	7.30	00:59:03	64.84	727.60	792.44	41.27
Hexagonal	15.88	14.70	7.43	00:59:03	64.84	742.30	807.14	47.09
Gyroid	16.18	14.67	9.33	00:58:41	64.84	756.40	821.24	55.98
Triangular	20.13	18.62	7.50	00:58:03	64.84	748.80	813.64	43.70
Straight	18.65	17.14	8.09	00:57:54	64.84	770.80	835.64	56.85

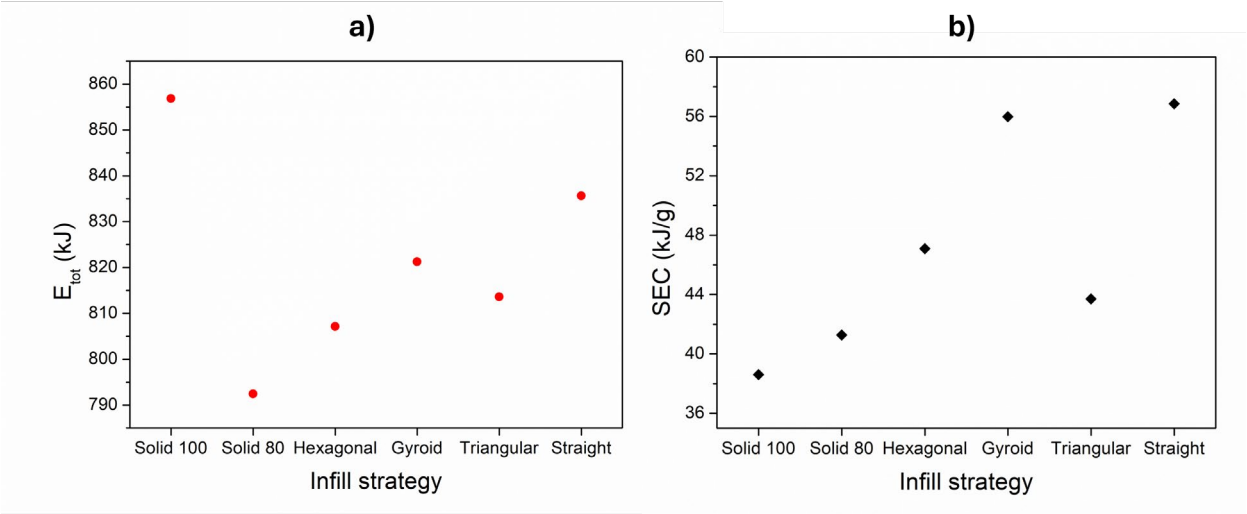


Figure 4. a) Total energy consumption and b) Specific Energy consumption for all the investigated infill strategies

4. Conclusions

In this work, the effect of pattern infill on the LVI of FFFed PLA reinforced with flax has been investigated. Mass, printing time and energy consumption have also been monitored. The main conclusions that can be enucleated are the following:

- Solid 100 reaches an impact strength with higher respect the Solid 80. However, the last maintains a maximum load for a higher displacement interval denoting a higher propensity to deform and a different mode of energy absorption. The same occurs for the Straight, Triangular and Hexagonal strategies.
- The infill pattern also has a significant effect on the penetrating deceleration. For instance, the calculated penetrating deceleration of the impactor at the time of Solid 100 was around 2.4 times more compared to the Gyroid, Hexagonal, Straight and Triangular strategies.
- Solid 100 infill required the greatest amount of energy consumption to be printed. Also, comparing Solid 100 and Solid 80, a reduction of 20% in the density results in a reduction of around 7.52% in total energy consumption even if all the other process conditions have been the same.
- Among all the strategies investigated at the same infill density (80%), Solid 80 required the minimum amount of energy consumption, while straight the highest one, even if the printing duration was lower.

References

[1] F. Khan *et al.*, "Advances of composite materials in automobile applications – A review," *Journal of Engineering Research*, Feb. 2024. https://doi.org/10.1016/J.JER.2024.02.017

[2] Y. Wang, Y. Zhou, L. Lin, J. Corker, and M. Fan, "Overview of 3D additive manufacturing (AM) and corresponding AM composites," *Compos Part A Appl Sci Manuf*, vol. 139, p. 106114, Dec. 2020. https://doi.org/10.1016/J.COMPOSITESA.2020.106114

[3] M. Qamar Tanveer, G. Mishra, S. Mishra, and R. Sharma, "Effect of infill pattern and infill density on mechanical behaviour of FDM 3D printed Parts- a current review," *Mater Today Proc*, vol. 62, pp. 100–108, Jan. 2022. https://doi.org/10.1016/J.MATPR.2022.02.310

[4] M. M. Hanon, J. Dobos, and L. Zsidai, "The influence of 3D printing process parameters on the mechanical performance of PLA polymer and its correlation with hardness," *Procedia Manuf*, vol. 54, pp. 244–249, Jan. 2021. https://doi.org/10.1016/J.PROMFG.2021.07.038

[5] J. Zhou *et al.*, "Bio-based and bio-degradable nanofiber materials: A sustainable platform for energy, environmental, and biomedical applications," *Chemical Engineering Journal*, vol. 491, p. 152105, Jul. 2024. https://doi.org/10.1016/J.CEJ.2024.152105

[6] B. Aloyaydi, S. Sivasankaran, and A. Mustafa, "Investigation of infill-patterns on mechanical response of 3D printed poly-lactic-acid," *Polym Test*, vol. 87, p. 106557, Jul. 2020. https://doi.org/10.1016/J.POLYMERTESTING.2020.106557

[7] E. Cozzolino, V. Lopresto, D. Borrelli, and A. Caraviello, "An integrated approach to investigate the energy consumption for manufacturing and surface finishing 3D printed Inconel 718 parts," *J Manuf Process*, vol. 79, no. February, pp. 193–205, 2022. https://doi.org/10.1016/j.jmapro.2022.04.045

[8] E. Cozzolino, F. Napolitano, I. Papa, A. Squillace, and A. Astarita, "Influence of the Heated-Bed Material on PLA Mechanical Properties and Energy Consumption in the FDM Process," *Arab J Sci Eng*, 2024. https://doi.org/10.1007/s13369-024-09170-8

[9] F. Napolitano, E. Cozzolino, I. Papa, A. Astarita, and A. Squillace, "Experimental integrated approach for mechanical characteristic optimization of FDM-printed PLA in an energy-saving perspective," *The International Journal of Advanced Manufacturing Technology*, pp. 3551–3565, 2022. https://doi.org/10.1007/s00170-022-09535-z

[10] E. Cozzolino, F. Napolitano, A. Astarita, V. Lopresto, I. Papa, and A. Squillace, *Sustainability of Fused Deposition Modeling: The Role of the Plate Material*. Springer International Publishing, 2023. https://doi.org/10.1007/978-3-031-28547-9_12

[11] A. S. Alaboodi and S. Sivasankaran, "Experimental design and investigation on the mechanical behavior of novel 3D printed biocompatibility polycarbonate scaffolds for medical applications," *J Manuf Process*, vol. 35, pp. 479–491, Oct. 2018. https://doi.org/10.1016/J.JMAPRO.2018.08.035

[12] S. Wu, X. Liu, K. W. K. Yeung, C. Liu, and X. Yang, "Biomimetic porous scaffolds for bone tissue engineering," *Materials Science and Engineering: R: Reports*, vol. 80, no. 1, pp. 1–36, Jun. 2014. https://doi.org/10.1016/J.MSER.2014.04.001

[13] A. P. Agrawal, V. Kumar, J. Kumar, P. Paramasivam, S. Dhanasekaran, and L. Prasad, "An investigation of combined effect of infill pattern, density, and layer thickness on mechanical properties of 3D printed ABS by fused filament fabrication," *Heliyon*, vol. 9, no. 6, p. e16531, Jun. 2023. https://doi.org/10.1016/J.HELIYON.2023.E16531

Materials Research Proceedings 57 (2025) 180-189 https://doi.org/10.21741/9781644903735-21

Silicone 3D printing: Experimental validation of a reduced-order numerical model for optimal layer deposition

PRICCI Alessio[1,2,3,a], PERCOCO Gianluca[1,2,3,b]

[1]Department of Mechanics, Mathematics and Management, Polytechnic of Bari, Via Orabona 4, 70125, Bari, Italy

[2]Interdisciplinary Additive Manufacturing (IAM) Lab, TTEC Taranto Polytechnic, Polytechnic University of Bari, Viale del Turismo 8, 74123, Taranto, Italy

[3]Sustainable Materials for Additive Manufacturing for Soft Robotics (SMAM 4 SoRo), Polytechnic University of Bari, Via Orabona 4, 70125, Bari, Italy

[a]alessio.pricci@poliba.it, [b]gianluca.percoco@poliba.it

Keywords: Material Extrusion, Virtual Modeling, Silicone 3D Printing

Abstract. Silicone 3D printing holds a significant potential in soft robotics, stretchable electronics, and custom medical devices. However, challenges such as inconsistent material deposition continue to limit printing precision. This study presents a reduced-order numerical model integrating material rheology, process parameters and nozzle geometry to optimize silicone extrusion. A support vector regression algorithm fine-tunes printing parameters to generate an inlet pressure profile that minimizes over- and under-extrusion and ensures precise layer contouring. Full three-dimensional simulations of non-Newtonian silicone deposition coupled with experimental validation confirm the model's accuracy in 3D printing a 90-degree rounded corner shape. The proposed approach yields more stable printing paths and reduces layer width variability to 4.21%, compared to 15.02% obtained with constant inlet pressure. Finally, the proposed model is applied to fabricate wavy and multi-strand paths, demonstrating enhanced accuracy and consistency.

Introduction

Silicones are a versatile class of synthetic polymers that have garnered significant attention in recent years thanks to their unique combination of properties, such as exceptional flexibility [1], enhanced electrical properties [2] and biocompatibility [3].

Traditional methods for silicone fabrication, such as molding and soft lithography, are limited in their ability to create increasingly complex structures. However, the advent of additive manufacturing techniques has expanded the design freedom for silicone-based materials.

Silicone 3D printing utilizes variants of direct ink writing (DIW). These can be classified on the basis of the actuation mechanism as i) flow-controlled [4] and ii) pressure-controlled systems [5].

In recent years, 3D printing has also been extensively studied through numerical models. Computational fluid dynamics (CFD) simulations have been employed to investigate both single and multi-layer deposition [6], [7], [8], highlighting the impact of non-Newtonian features on the final strand geometry [9].

More recently, three-dimensional CFD models have been applied to study silicone 3D printing to enhance layer contouring precision [10]. However, CFD simulations are computationally intensive, limiting their applicability to the study of a limited number of processing conditions.

In this context, reduced-order semi-analytical models are gaining increasing attention. The fluid flow of one-component moisture-cured silicone through tapered needles was analyzed in [5], using a pressure-based DIW dispensing system to extrude silicone under free-air conditions.

Content from this work may be used under the terms of the Creative Commons Attribution 3.0 license. Any further distribution of this work must maintain attribution to the author(s) and the title of the work, journal citation and DOI. Published under license by Materials Research Forum LLC.

Materials Research Proceedings 57 (2025) 180-189 https://doi.org/10.21741/9781644903735-21

Similarly, a reduced-order CFD model was proposed in [11] to study the deposition of polysiloxane on a substrate. This model resulted in accurate silicone/air surface tracking.

In [12] a correlation between material rheology and the printing operating window was established to prevent both silicone over- and under-extrusion.

Several studies have demonstrated the feasibility of modeling the fluid flow through tapered wedges by solving the Navier-Stokes equations in cylindrical coordinates [13], [14]. These models typically apply to specific fluid rheologies, such as Newtonian, Casson, and power-law fluids.

A semi-analytical method for modeling the extrusion of non-Newtonian fluids through DIW needles was initially proposed in [15] and experimentally validated in [16].

However, there remains a gap in correlating rheology and processing parameters in real-world silicone extrusion scenarios. The final properties of the printed part are influenced by the microstructure and material rheology in the uncured state. Thus, linking the fluid dynamics within the DIW tapered needle to optimized toolpath planning is crucial to avoid over- and under-extrusion, which can significantly impact part functionality.

In this work, a fast-converging reduced-order semi-analytical model is integrated with a machine learning algorithm to find the optimal inlet pressure profile for pressure-driven silicone DIW.

The remainder of the paper is organized as follows: first, the silicone preparation and extrusion setup are introduced; next, the reduced-order semi-analytical model and its integration with the machine learning algorithm is discussed. Next, silicone rheological characterization is presented. The model is applied to 3D print 90-degree silicone corner, sinusoidal shapes, and multi-strand paths, such as the Italian peninsula. Finally, conclusions and directions for future work are drawn.

Materials and methods

Silicone preparation and extrusion setup.

A two-part platinum cure silicone (Ecoflex 00-10) was purchased by Ferba s.r.l., serving as target material for the reduced-order model validation. This material was chosen because of its exceptional elongation (up to 1260% when thinner is added, [1]).

Silicone preparation consisted in mixing silicone part A and B in 1:1 volume ratio. Then, the mixture was stirred and degassed using a single-stage BACOENG 3CFM (85 mL/min) for around 15 minutes, to completely remove air bubbles trapped during mixing.

A BioX Gen3 bioprinter was used for experimental validation of the proposed model. This pressure-based DIW system is equipped with up to three extrusion heads, each capable of delivering pressures up to 200 kPa. Additionally, the BioX Gen3 provides high precision, with specified XY and Z resolutions of approximately 1 μm.

Reduced-order numerical model.

The reduced-order model is based on the solution of Navier-Stokes equations in spherical coordinates, to predict the fluid flow of a non-Newtonian fluid inside a DIW tapered needle [15].

Approximating the needle geometry as a spherical sector – commonly referred to as the Jeffery–Hamel approximation – is effective at low taper angles, which are typical in DIW. In this context, the fluid flow within the needle can be modeled as a flow directed towards the center of a spherical sector. Consequently, it is particularly convenient to choose spherical coordinates $(r;\ \theta;\ \varphi)$, where r is defined as positive when pointing outward from the center of the idealized sphere. The remaining are polar and azimuthal coordinates, respectively.

The following assumptions are made:

Fluid flow is stationary, incompressible and isothermal.

- Inertial and body forces are negligible.
- No-slip boundary condition is applied to the needle internal walls.
- Azimuthal symmetry ($\partial(.)/\partial\varphi = 0$) holds because of the absence of swirl motions.

Materials Research Proceedings 57 (2025) 180-189 https://doi.org/10.21741/9781644903735-21

- Purely radial flow, i.e., $v_r = v_r(r;\theta)$.
- The effect of crosslinking on material rheology has been neglected.

Due to the last two boundary conditions, the mass conservation equation in spherical coordinates takes the form:

$$\frac{\partial(r\, v_r)}{\partial r} = 0 \tag{1}$$

After integration with respect to r, mass conservation becomes:

$$v_r = f(\theta)/r \tag{2}$$

Here, ρ represents the fluid density, $f(\theta)$ is the integration function, which depends only on polar coordinate due to the assumption of azimuthal symmetry, and r denotes the radial coordinate. As demonstrated in [15], the momentum equations along r and θ can be expressed as:

$$\frac{\partial p}{\partial r} = \frac{1}{r^2}\frac{\partial(r^2\tau_{rr})}{\partial r} + \frac{1}{r\sin\theta}\frac{\partial(\tau_{r\theta}\sin\theta)}{\partial\theta} + \frac{1}{r\sin\theta}\frac{\partial\tau_{r\varphi}}{\partial\varphi} - \frac{\tau_{\theta\theta}+\tau_{\varphi\varphi}}{r} \tag{3}$$

$$\frac{1}{r}\frac{\partial p}{\partial\theta} = \frac{1}{r^2}\frac{\partial(r^2\tau_{r\theta})}{\partial r} + \frac{1}{r\sin\theta}\frac{\partial(\tau_{\theta\theta}\sin\theta)}{\partial\theta} + \frac{1}{r\sin\theta}\frac{\partial\tau_{\theta\varphi}}{\partial\varphi} + \frac{\tau_{r\theta}}{r} - \frac{\cot\theta}{r}\tau_{\varphi\varphi} \tag{4}$$

By deriving Eq. (3) with respect to θ variable and by first multiplying both members of Eq. (4) by r and then deriving it with respect to r itself, Eqs. (3) and (4) can be combined to obtain a single momentum equation.

It is particularly interesting the reduction of the former system of partial differential equations to a third-order ordinary differential equation (ODE) where the only unknown is $f(\theta)$. This ODE can be solved by applying proper boundary conditions on $f(\theta)$:

$$\begin{cases} f(0) = f_{max} \\ f(\alpha) = 0 \\ f'(0) = 0 \end{cases} \tag{5}$$

These boundary conditions are motivated by the linear relationship between $f(\theta)$ and v_r (see Eq. (2)). The first represents the maximum of $f(\theta)$, which is reached on the symmetry axis, the second is the wall no-slip condition and the third is the maximum in $f(\theta)$ profile, which is reached on the symmetry axis, where the maximum of fluid velocity is located.

The boundary value problem is solved iteratively using a MATLAB routine. Flow rate is evaluated at each iteration after v_r profile reconstruction:

$$Q = 2\pi\int_0^{\alpha} r^2 v_r(r\,;\theta)\sin\theta\, d\theta \tag{6}$$

Convergence is reached when the absolute relative error between real and estimated flow rate goes below 1%. Finally, the pressure profile is reconstructed by solving the abovementioned Navier-Stokes equations with the correct v_r profile.

The proposed reduced-order model exploits the geometrical and flow symmetry around needle axis to dramatically reduce the computational time. In addition, it is applicable practically to all non-Newtonian fluids since Eqs. (3) and (4) are independent of effective fluid rheology; shear stress tensor components are specified according to the exact silicone rheological data:

$$\bar{\bar{\tau}} = 2\eta(\dot{\gamma})\bar{\bar{D}} \tag{7}$$

Materials Research Proceedings 57 (2025) 180-189 https://doi.org/10.21741/9781644903735-21

Here $\bar{\bar{\tau}}$ and $\bar{\bar{D}}$ are the stress and strain rate tensors, respectively. The relationship between dynamic viscosity η and shear rate $\dot{\gamma}$ is characterized experimentally by means of rheological testing.

Coupling the optimized machine learning algorithm.
The fast-converging nature of the semi-analytical reduced-order model allows calculating a wide range of processing conditions, which is important for proper training of the support vector regression (SVR) algorithm.

Different FINGERINSPIRE needle sizes, ranging from 14G to 30G, and flow rates corresponding to pressure drops ranging from 1 to 200 kPa were tested. In addition, ten values of both printing speed and layer thickness, ranging from 1 mm/s to 25 mm/s, and from $\phi/4$ to ϕ, respectively, were considered for the SVR training.

Layer width (LW) was calculated by applying mass conservation along printing direction:

$$LW = \frac{\dot{m}}{\rho V_p h} \quad (8)$$

Here $\dot{m}$ is mass flow rate, ρ fluid density, V_p printhead speed and h layer thickness.

Since this equation does not consider over or under-extrusion, proper control over these conditions was needed; in particular, conditions in which the layer width was lower than the nozzle diameter or higher than 1.25 ϕ were excluded from the final dataset employed in SVR training and test.

Once the set of processing parameters ensuring the desired layer properties was established, the machine learning algorithm could be trained. The SVR was optimized by performing a grid-search for the best values of hyperparameters; the box constraint (C), epsilon (ε) and kernel scale (KS) were varied according to **Table 1**.

Table 1. *Grid-search parameters for the optimization of the SVR.*

SVR parameter	Discrete search interval
C	{0.1, 1, 10}
ε	{0.01, 0.1, 1}
KS	{0.1, 1, 10}

In addition, a 5-fold cross-validation was applied and the mean squared error (MSE) of training data with respect to the reduced-order model data was chosen as the reference metric.

Results and discussion

Rheological characterization.
Silicone samples (10 mL each) were prepared and tested using an Anton Paar 702e rheometer to determine i) the influence of viscoelasticity on flow properties and ii) the relationship between dynamic viscosity and shear rate.

An oscillatory sweep over 0 – 100 rad/s was initially performed, finding storage (G') and loss (G'') moduli (see **Fig. 1**).

Materials Research Proceedings 57 (2025) 180-189 https://doi.org/10.21741/9781644903735-21

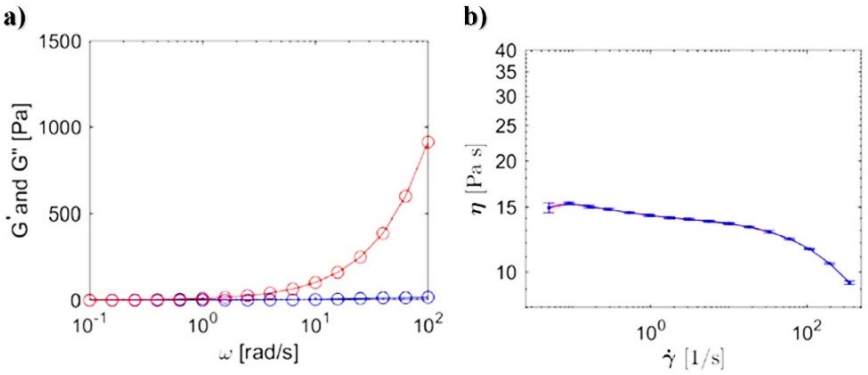


Fig. 1. *a) Oscillatory sweep test and b) standard viscosity test for Ecoflex 00-10.*

The oscillatory sweep test revealed that G" remained consistently higher than G' over the full sweep range. For that reason, the elastic behavior of the investigated material was neglected and the assumption to deal with the modeling of a purely viscous non-Newtonian fluid proved to be valid.

For the standard viscosity test four replications were provided, and shear rate was varied over 0 – 350 1/s, finding a distinct shear-thinning behavior was found.

Viscosity data at different shear rates were used in conjunction with the reduced-order model to study the fluid flow in the tapered needle in all successive applications.

Application to smoothed corner and wavy paths.

Silicone 3D printing of a 90-degree rounded corner was investigated. The nozzle being used is a FINGERINSPIRE tapered plastic needle with a 20G size (i.e., internal diameter ϕ = 0.81 mm).

Initially, the x- and y- velocities were specified as input vectors, and the overall printing speed (V_P) was evaluated at each time step, as it is required as input along with nozzle diameter and layer thickness for the SVR algorithm.

The grid-search optimization over the discrete hyperparameters values listed in **Table 1** showed that the MSE is minimized with the following hyperparameters: C=10, ε=0.10, KS=1. Additionally, the relative error on the entire training dataset was calculated (see **Fig. 2**).

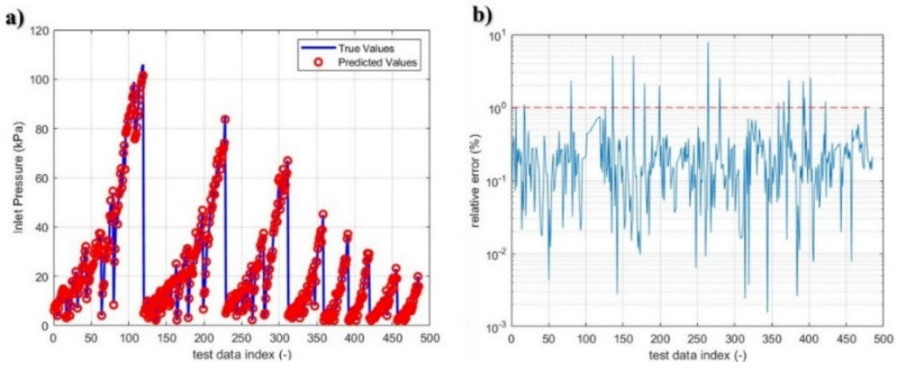


Fig. 2. *a) True vs predicted inlet pressure values for the complete training dataset and b) relative error on inlet pressure values for the complete dataset used for training.*

The relative error between the true and SVR-predicted inlet pressures consistently remained below 1% (indicated by the red dotted line in **Fig. 2**), with only a few localized deviations. Hyperparameter optimization was performed over the discrete intervals listed in **Table 1**, resulting in a locally optimal SVR. Although the global optimum may lie between these discrete values, the grid search approach was considered sufficient for this study, as only 2.94% of the predictions (14 out of 475) exhibited a relative error greater than 1%.

Materials Research Proceedings 57 (2025) 180-189 https://doi.org/10.21741/9781644903735-21

Next, the inlet pressure to be supplied by the bioprinter internal compressor at each time step is calculated (see **Fig.3**).

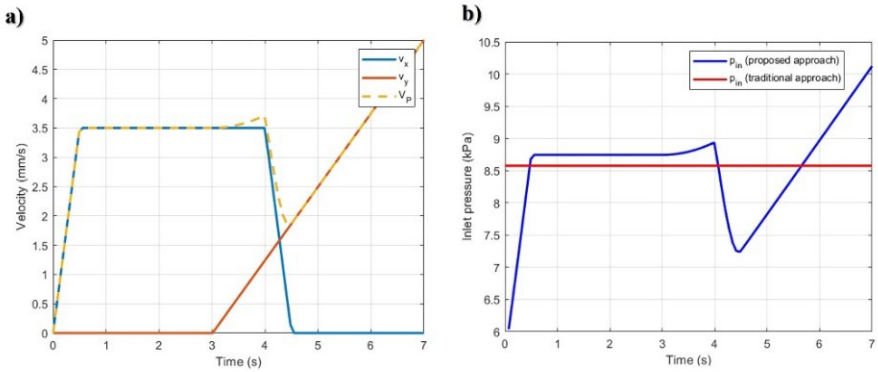


Fig. 3. *a) Velocity and b) pressure profiles for 90-degree corner deposition.*

Initially, a velocity ramp was applied in the x-direction, with no motion along the y-axis. During this phase, the pressure increases to approximately 9 kPa. After the ramps conclude, the printhead moves at a constant speed along the x-direction, leading to pressure stabilization. At around 4 seconds, a rounded corner develops due to a combination of deceleration along the x-axis and simultaneous acceleration along the y-axis. Notably, in the proposed adaptive approach, the inlet pressure profile continues to track the V_p profile. In contrast, the traditional approach refers to the application of a constant inlet pressure, set to the mean pressure predicted by the SVR.

Both experiments and numerical simulations were performed to investigate the advantage of the proposed (adaptive) approach over the traditional one (three replications each, see **Fig. 4**).

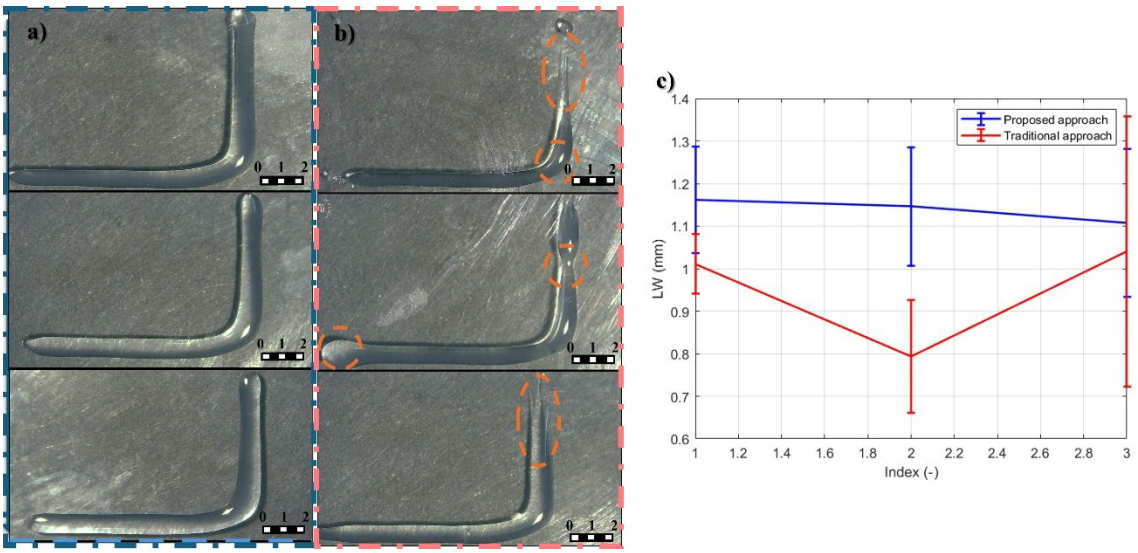


Fig. 4. *a) Proposed adaptive approach, b) traditional approach and c) their quantitative comparison for 90-degree rounded corner deposition. All dimensions are in mm.*

Fig. 4 c shows significant variability in the final printed strand width when using constant inlet pressure. This effect is especially pronounced during motion along y-direction, where distinct under-extrusion zones and flow breakage are observed. The underlying cause is that the constant inlet pressure is consistently lower than the one required to maintain a uniform strand width during y-direction acceleration, which is accurately captured by the proposed adaptive approach (see **Fig. 4 a**).

Materials Research Proceedings 57 (2025) 180-189 https://doi.org/10.21741/9781644903735-21

In contrast, testing the GCode generated by the reduced-order informed SVR algorithm results in i) smoother corner shapes, free from under- or over-extrusion zones, and ii) improved layer width consistency even during printhead accelerations and decelerations.

The training time needed for the SVR in this specific case is less than a minute. To further validate these results, a full three-dimensional CFD simulation was carried out using Flow-3D 2024-R1, which is based on the one-phase volume-of-fluid method.

The nozzle geometry was imported as an .stl file, and motion laws along both x- and y-directions and inlet pressure were implemented using i) the traditional approach and ii) the proposed adaptive approach (**Fig. 5**).

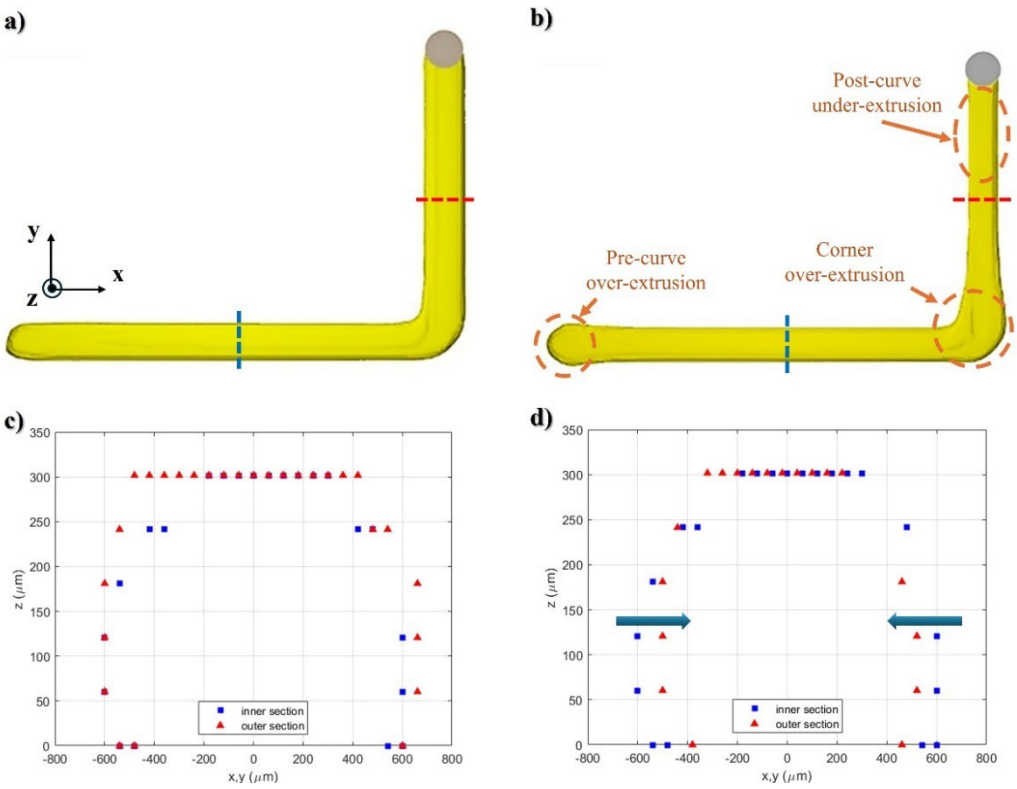


Fig. 5. *Fully three-dimensional numerical simulation of silicone corner deposition using a) proposed and b) traditional approach, and comparison of inner and outer cross-sectional shape between c) proposed and d) traditional approach.*

The traditional approach fails in extruding a smooth 90-degree corner, with evident over-extrusion near the strand turn. Moreover, under-extrusion manifests in the final motion steps along y-direction, similarly to the situation observed in experiments.

These findings are physically consistent with **Fig.3 b**, where the constant inlet pressure (traditional approach) is higher and lower with respect to the value calculated by the adaptive method near the turn and in the final part of y-motion, respectively.

On the other hand, the proposed adaptive approach produces a deposited strand whose shape is consistent along printhead motion direction, without over- or under-extrusion zones (see **Fig. 5 c** and **d**). In particular, the maximum layer width is 1.21 mm and 1.02 mm at inner (middle of x-path) and outer (middle of y-path) sections, respectively, when choosing the traditional approach, showing a variation of 15.02%. On the other hand, the proposed approach leads to maximum layer width of 1.21 mm and 1.26 mm at the same abovementioned positions, showing only a 4.21% error (error reduction in layer width prediction: 10.81%).

Materials Research Proceedings 57 (2025) 180-189 https://doi.org/10.21741/9781644903735-21

Similarly, the possibility to produce wavy patterns has been tested; a sinusoidal motion law along x- and y-direction has been prescribed and both traditional and proposed adaptive approaches have been tested with three replications each (see **Fig. 6**).

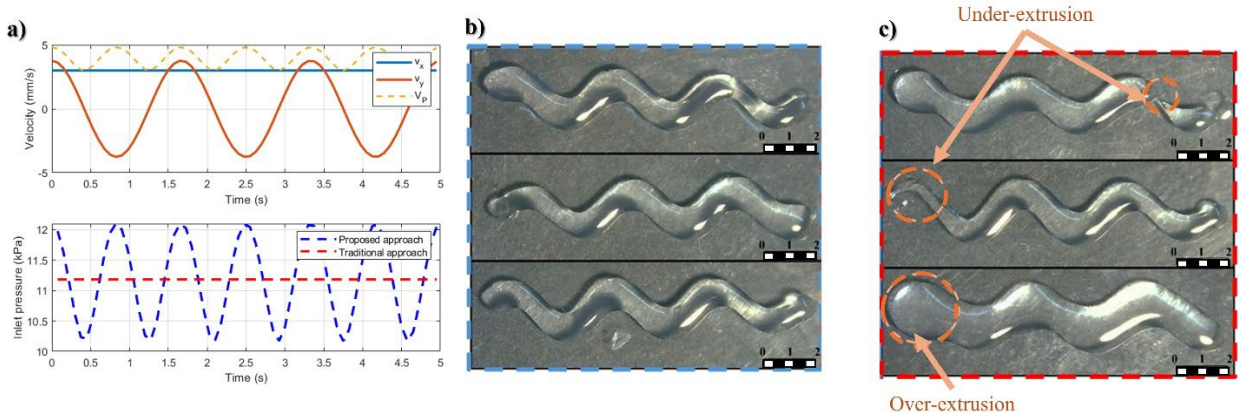


Fig. 6. *A) Sinusoidal silicone motion laws, pressures and deposition status with a) the proposed adaptive approach and b) the traditional approach. All dimensions are in mm.*

The proposed approach performs way better than the traditional one because of wavy strand consistency along replications. Similarly to the investigated 90-degree rounded corner path, the traditional method shows fluid breakage, under-deposition and over-deposition.

Application to multi-strand printing paths.
To further validate the application of the proposed adaptive approach in silicone DIW of more challenging shapes, the Italian peninsula was 3D printed with both methods (see **Fig. 7**). In this case, a 25G tapered needle was used (internal diameter: $\phi = 0.45$ mm).

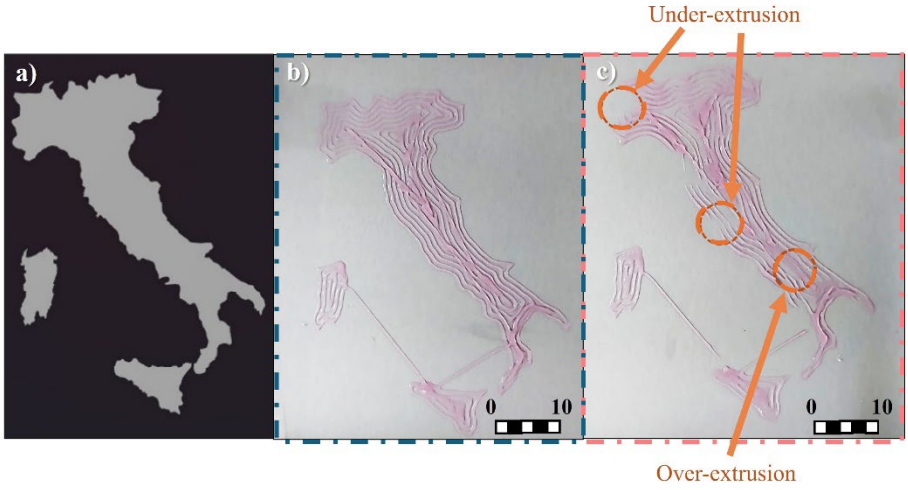


Fig. 7. *a) CAD model of the Italian peninsula; b) proposed adaptive approach; c) traditional approach. All dimensions are in mm.*

Despite the exterior shape is well-predicted by both approaches, the proposed one gives improved layer smoothing, geometrical consistency and control during infill deposition.

In addition, the pressure-based DIW silicone extrusion system performs similarly to the custom-made extrusion system proposed in [4], where Italian peninsula was 3D printed leveraging electromagnetic force; for such a system, this shape cannot be produced with base Ecoflex 00-10

(i.e., without adding ferromagnetic powder), while the machine-learning enhanced pressure-based extrusion system provides full control over layer deposition.

Conclusions and further work

This study introduces a reduced-order numerical model integrated with an optimized machine learning algorithm to enhance silicone 3D printing. The proposed approach combines silicone rheology, process parameters and nozzle geometry to generate an adaptive inlet pressure profile that strictly follows the accelerations and decelerations occurring during manufacturing. In comparison to the traditional constant-pressure DIW, the proposed approach demonstrated significant improvements in different printing scenarios.

The reduced-order model, coupled with the SVR, is highly efficient, training in less than a minute, while full three-dimensional CFD models require over an hour. This reduction in computational time makes the proposed adaptive approach highly practical for real-time applications. The machine learning-enhanced approach resulted in smoother corner shapes and improved layer width consistency. This was particularly evident when compared to the traditional method, where inconsistent deposition was observed both experimentally and numerically. Similar conclusions were drawn with respect to wavy motions of the printhead.

When applied to 3D printing multiple strand paths, such as the Italian peninsula, the proposed method demonstrated better layer smoothing and geometrical consistency during infill deposition.

In conclusion, the integration of a reduced-order numerical model with SVR offers a powerful solution for optimizing silicone 3D printing. The proposed approach significantly improves deposition consistency, geometrical accuracy, and material performance, making it a promising technique for the fabrication of intricate silicone-based structures. Three-dimensional numerical simulations revealed that the layer width variation in 3D printing rounded corner shapes reduces from 15.02% to 4.21%, when choosing the proposed adaptive approach. The higher variation found by applying the traditional approach is due to its intrinsic impossibility to follow the continuous accelerations and decelerations of 3D printing process. Further work will consider integrating cure kinetics inside the adaptive model to produce multi-layered silicone structures. In addition, viscoelasticity and cross-linking effects on material rheology will be included in the reduced-order model, widening its application to other DIW materials. Finally, the potential of this model in tailoring 4D printing structure functionalities will be explored.

References

[1] A. Hamidi and Y. Tadesse, “3D printing of very soft elastomer and sacrificial carbohydrate glass/elastomer structures for robotic applications,” Mater Des, vol. 187, p. 108324, Feb. 2020. https://doi.org/10.1016/j.matdes.2019.108324

[2] S. Shang, L. Gan, M. C. Yuen, S. Jiang, and N. Mei Luo, “Carbon nanotubes based high temperature vulcanized silicone rubber nanocomposite with excellent elasticity and electrical properties,” Compos Part A Appl Sci Manuf, vol. 66, pp. 135–141, Nov. 2014. https://doi.org/10.1016/j.compositesa.2014.07.014

[3] M. Carrabba et al., “Design, fabrication and perivascular implantation of bioactive scaffolds engineered with human adventitial progenitor cells for stimulation of arteriogenesis in peripheral ischemia,” Biofabrication, vol. 8, no. 1, p. 015020, Mar. 2016. https://doi.org/10.1088/1758-5090/8/1/015020

[4] G. Stano, A. Pricci, A. Pavone, and G. Percoco, “Electromagnetic assistance enables 3D printing of silicone-based thin-walled bioinspired soft robots,” Addit Manuf, vol. 81, p. 104028, Feb. 2024. https://doi.org/10.1016/j.addma.2024.104028

[5] Y. Jin, J. Plott, and A. J. Shih, “Extrusion-Based Additive Manufacturing of the Moisture-Cured Silicone Elastomer,” in International Solid Freeform Fabrication Symposium, 2015.

[6] R. Comminal, M. P. Serdeczny, D. B. Pedersen, and J. Spangenberg, “Numerical modeling of the strand deposition flow in extrusion-based additive manufacturing,” Addit Manuf, vol. 20, pp. 68–76, Mar. 2018. https://doi.org/10.1016/j.addma.2017.12.013

[7] S. Jafarzadeh, R. Comminal, M. P. Serdeczny, M. Bayat, C. R. H. Bahl, and J. Spangenberg, “Geometric characterization of orthogonally printed layers in material extrusion additive manufacturing: numerical modeling and experiments,” Progress in Additive Manufacturing, vol. 8, no. 6, pp. 1619–1630, Dec. 2023. https://doi.org/10.1007/s40964-023-00426-7

[8] A. Pricci and G. Percoco, “Towards a digital twin of extrusion-based additive manufacturing: an experimentally validated numerical model of ironing process,” Progress in Additive Manufacturing, Feb. 2025. https://doi.org/10.1007/s40964-025-00988-8

[9] R. Comminal et al., “Modelling of material deposition in big area additive manufacturing and 3D concrete printing,” in Joint Special Interest Group meeting between euspen and ASPE, 2019. [Online]. Available: www.euspen.eu

[10] Y. Tu et al., “Numerical Prediction and Experimental Validation of Deposited Filaments in Direct Ink Writing: Deposition Status and Profile Dimension,” Polymers (Basel), vol. 17, no. 5, p. 573, Feb. 2025. https://doi.org/10.3390/polym17050573

[11] F. Liravi, R. Darleux, and E. Toyserkani, “Additive manufacturing of 3D structures with non-Newtonian highly viscous fluids: Finite element modeling and experimental validation,” Addit Manuf, vol. 13, pp. 113–123, Jan. 2017. https://doi.org/10.1016/j.addma.2016.10.008

[12] Y. Tu, A. Hassan, A. Siadat, and G. Yang, “Analytical modeling of deposited filaments for high viscosity material-based piston-driven direct ink writing,” The International Journal of Advanced Manufacturing Technology, vol. 123, no. 9–10, pp. 3387–3398, Dec. 2022. https://doi.org/10.1007/s00170-022-10511-w

[13] S. I. Voropayev, S. A. Smirnov, and F. Y. Testik, “On the case when steady converging/diverging flow of a non-Newtonian fluid in a round cone permits an exact solution,” Mech Res Commun, vol. 31, no. 4, pp. 477–482, Jul. 2004. https://doi.org/10.1016/j.mechrescom.2003.11.014

[14] J. Nagler, “Jeffery-Hamel flow of non-Newtonian fluid with nonlinear viscosity and wall friction,” Appl Math Mech, vol. 38, no. 6, pp. 815–830, Jun. 2017. https://doi.org/10.1007/s10483-017-2206-8

[15] A. Pricci, M. D. de Tullio, and G. Percoco, “Semi-analytical models for non-Newtonian fluids in tapered and cylindrical ducts, applied to the extrusion-based additive manufacturing,” Mater Des, vol. 223, p. 111168, Nov. 2022. https://doi.org/10.1016/j.matdes.2022.111168

[16] A. Pricci, S. M. Al Islam Ovy, G. Stano, G. Percoco, and Y. Tadesse, “Semi-analytical and numerical models to predict the extrusion force for silicone additive manufacturing, as a function of the process parameters,” Additive Manufacturing Letters, vol. 6, p. 100147, Jul. 2023. https://doi.org/10.1016/j.addlet.2023.100147

Materials Research Proceedings 57 (2025) 190-198 https://doi.org/10.21741/9781644903735-22

Optimization of process parameters for fused filament fabrication of ULTEM 1010

VAGLIO Emanuele[1,a *], BILLÈ Erica[1,b], GAMBITTA Alessandro[2,c], RONDINELLA Alfredo[1,d], TOTIS Giovanni[1,e], SCALZO Federico[1,f], SORTINO Marco[1,g]

[1]Polytechnic Department of Engineering and Architecture, University of Udine, Via delle Scienze 206, 33100 Udine, Italy

[2]Elettra-Sincrotrone Trieste, Area Science Park, 34149 Basovizza, Trieste, Italy

[a]emanuele.vaglio@uniud.it, [b]erica.bille@uniud.it, [c]alessandro.gambitta@elettra.eu, [d]alfredo.rondinella@uniud.it, [e]giovanni.totis@uniud.it, [f]federico.scalzo@uniud.it, [g]marco.sortino@uniud.it

Keywords: Additive Manufacturing, Material Extrusion, ULTEM 1010

Abstract. Fused Filament Fabrication is an Additive Manufacturing process increasingly used to manufacture advanced products from engineering polymers. ULTEM 1010 is particularly well-suited for this purpose due to its exceptional physical and chemical properties, which support high-performance applications across the aerospace, medical, automotive, food, and mechanical industries. However, its adoption remains limited and less common than that of other polyetherimides due to insufficient knowledge of the process. In this study, the effects of extrusion temperature, nozzle speed and layer thickness on the surface and material properties of products were systematically investigated through Scanning Electron Microscopy, X-ray microtomography, tensile tests, indentation tests, and Fourier Transform Infrared Spectroscopy. Synchrotron radiation was employed to further characterize the structure of selected samples at an unexplored scale, while Ultra-High Vacuum testing was conducted to validate the process for special applications across aerospace engineering, nuclear fusion, laser technology, electronics, and high-energy physics. The results provide new insights to optimize the process for advanced engineering applications.

Introduction

Polyetherimide (PEI) is a high-performing thermoplastic polymer known for its exceptional combination of mechanical strength, stiffness, heat and flame resistance, low smoke emission, broad chemical resistance, good electrical properties and transparency [1]. ULTEM 1010 is a high-purity grade of PEI, recognized for its superior physical, chemical, and biocompatibility properties. However, its high purity also results in reduced flowability and moldability, which complicates processing [2].

Pure PEI can generally be processed by injection molding, extrusion, and thermoforming [3]. However, these processes are typically used in mass production due to the high costs of equipment and setup, which often limit the design flexibility required for advanced products. To address this limitation, there is growing interest in the possibility of processing ULTEM 1010 through additive manufacturing.

Several authors have investigated the processability of blended PEI by Fused Filament Fabrication (FFF), primarily focusing on ULTEM 9085 (PEI/Polycarbonate) [4]. Conversely, the literature on processing of ULTEM 1010 is limited, likely due to the processing challenges. Ding et al. [5] showed that increasing nozzle temperature improves both density and flexural strength, while tensile strength exhibits a non-monotonic trend, and elongation at break remains stable. The

Content from this work may be used under the terms of the Creative Commons Attribution 3.0 license. Any further distribution of this work must maintain attribution to the author(s) and the title of the work, journal citation and DOI. Published under license by Materials Research Forum LLC.

Materials Research Proceedings 57 (2025) 190-198 https://doi.org/10.21741/9781644903735-22

maximum density achieved was ρ_r=89.9%, while the maximum tensile strength $\sigma_r \approx 78$ MPa was obtained at both the highest and lowest densities. The material fracture was found to be predominantly brittle. Ouassil et al. [6] found that nozzle speed is the most significant parameter affecting tensile properties, while nozzle temperature primarily influences density and Young's modulus. The maximum density achieved was ρ_r=95.67%, while the maximum tensile strength σ_r=102.24 MPa was obtained with a different set of process parameters. Thermal treatments were found to have minimal impact due to the amorphous nature of PEI. However, Yilmaz et al. [7] demonstrated the effectiveness of annealing in enhancing the material structure and interfacial bonding, while Han et al. [8] further highlighted the potential to improve tensile strength by promoting interlayer adhesion through in-process laser pre-heating. This approach also led to a significant improvement in the material's isotropy. Taylor et al. found that also the raster angle significantly affects fracture toughness [9], as well as flexural modulus and strength [10], while Pandelidi et al. [11] showed that the air gap influences tensile strength and Young's modulus, the build direction affects Young's modulus and tensile strain at break, and the highest tensile strength σ_r=94 MPa can be achieved with a raster angle of ±45°.

Based on the literature review, it is clear that the knowledge regarding the processing of ULTEM 1010 by FFF is still fragmented, incomplete, and often contradictory. This work aims to bridge the existing gaps through a systematic investigation on the effects of the nozzle temperature T_n, nozzle speed v_{nb}, and layer thickness t_l on the properties of parts produced from ULTEM 1010 by FFF, and to identify the optimal process conditions for both conventional and advanced applications.

Materials and methods

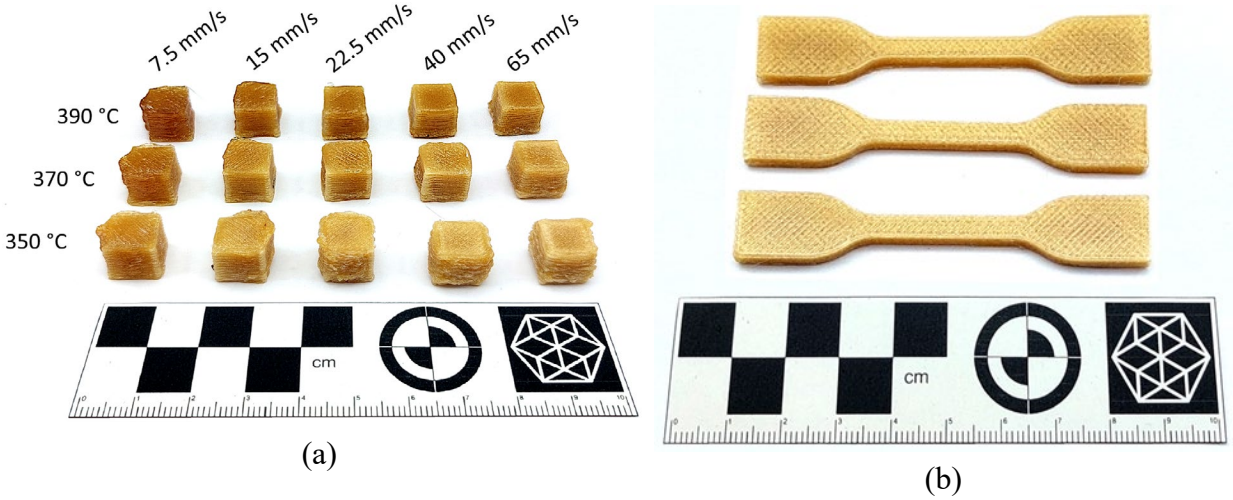
The samples used in this study were fabricated using an INTAMSYS FUNMAT HT system and a 1.75 mm diameter ULTEM 1010 filament supplied by the same manufacturer.

In detail, 30 cubic samples 10x10x10 mm in size were produced one at a time according to a full factorial Design of Experiments that included three levels of nozzle temperature, five levels of nozzle speed, and two levels of layer thickness, as detailed in Table 1. The simple geometry of the samples was selected to facilitate a more generalized investigation, focusing on the core aspects of the process by minimizing uncontrolled factors, while the small size ensured that the results accurately reflect the most critical condition, namely, the production of small, detailed features. On the other hand, T_n and v_{nb} levels were established to cover the process window recommended by the filament supplier, together with an extended range aimed at capturing the complete spectrum of process-related phenomena, while the non-uniform spacing of nozzle speed levels was chosen to more thoroughly explore the process window with the highest expected potential.

Table 1: Process parameters employed for producing the samples.

	Manufacturer recommended	Investigated
Nozzle temperature T_n	340 – 360 °C	350, 370, 390 °C
Nozzle speed v_{nb}	10 – 30 mm/s	7.5, 15, 22.5, 40, 65 mm/s
Layer thickness t_l	–	0.1, 0.2 mm
Nozzle diameter d_n	–	0.4 mm
Building plate temperature T_{bp}	130 – 160 °C	130 °C
Building chamber temperature T_{bc}	–	90 °C

Materials Research Proceedings 57 (2025) 190-198 https://doi.org/10.21741/9781644903735-22



(a) (b)

Fig. 1: Representative image of (a) the cubic samples manufactured at t_l=0.1 mm and (b) the set of tensile samples manufactured at T_n=370 °C, v_{nb}=40 mm/s and t_l=0.1 mm.

To fabricate the samples, a single outer perimeter was deposited first, followed by filling the core volume with bidirectional and alternated beads at a ±45° raster angle. The contour and core volumes overlapped each other by 0.2 mm and were scanned at the same nozzle speed, in accordance with the Design of Experiments.

In addition to the cubic samples, 30 tensile specimens conforming to ISO 527-2/5A were produced according to a reduced experimental design, including the 8 extreme parameter configurations and two central points corresponding to T_n=370 °C, v_{nb}=40 mm/s and t_l=0.1 mm, 0.2 mm, which allowed for the evaluation of trend continuity and potential curvature in the responses. Three replicates were individually produced for each configuration, following the same procedures described above. The cubic samples produced at t_l=0.1 mm and the set of tensile samples produced at T_n=370 °C, v_{nb}=40 mm/s and t_l=0.1 mm are shown as representative examples in Figure 1.

The obtained specimens were then subjected to an extended series of tests, some of which encompassed all the experimental conditions, thereby facilitating the evaluation of interaction effects, while others were necessarily limited to the sub-design carefully conceived to combine scientific rigor and efficiency, or to specific conditions of particular relevance.

The top surfaces of the cubic samples were then examined using a Zeiss Evo 40 Scanning Electron Microscope to characterize the surface morphology under different process conditions.

A subset of samples corresponding to the parameter configurations adopted for producing the tensile samples was also examined using X-ray μCT at the TomoLab station of the Elettra Sincrotrone Trieste to investigate internal porosity. To this aim, the voltage of the X-ray tube was set to 50 kVp, and a 0.5 mm thick aluminum filter was placed between the source and the samples. The system resolution was 11 μm. The internal porosity of the most and least dense samples was then further examined at a higher resolution of 1.31 μm using the SYRMEP Synchrotron X-ray μCT at the same research facility.

Subsequently, the cubic samples were sectioned and polished to obtain flat surfaces. Five hardness measurements were then taken for each sample according to the EN ISO 2039-1 standard using a DuraJet G5 tester equipped with a 5 mm spherical indenter and an applied load of 358 N. The subset of samples subjected to X-ray μCT with t_l = 0.1 mm was also analysed using a Thermo Fisher Scientific Nicolet iSTM 50 FT-IR spectrometer, performing 32 scans for each measurement.

At the same time, tensile tests were performed on the dedicated samples using a Shimadzu

Materials Research Proceedings 57 (2025) 190-198 https://doi.org/10.21741/9781644903735-22

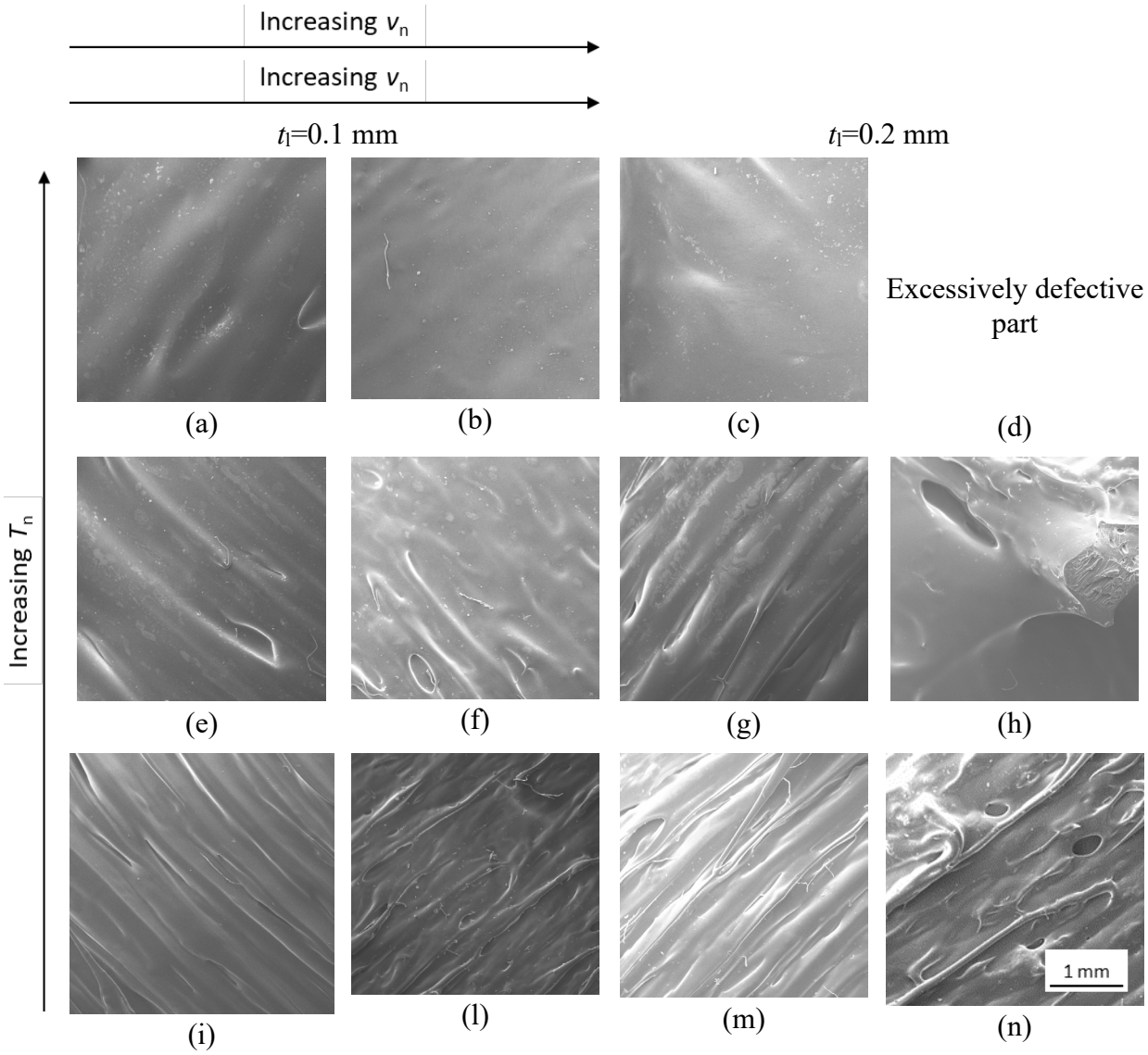


Fig. 2: SEM view of the horizontal surfaces of the samples produced at (a) T_n=390 °C, v_{nb}=7.5 mm/s and t_l=0.1 mm, (b) T_n=390 °C, v_{nb}=65 mm/s and t_l=0.1 mm, (c) T_n=390 °C, v_{nb}=7.5 mm/s and t_l=0.2 mm, (d) T_n=390 °C, v_{nb}=65 mm/s and t_l=0.2 mm, (e) T_n=370 °C, v_{nb}=7.5 mm/s and t_l=0.1 mm, (f) T_n=370 °C, v_{nb}=65 mm/s and t_l=0.1 mm, (g) T_n=370 °C, v_{nb}=7.5 mm/s and t_l=0.2 mm, (h) T_n=370 °C, v_{nb}=65 mm/s and t_l=0.2 mm, (i) T_n=350 °C, v_{nb}=7.5 mm/s and t_l=0.1 mm, (l) T_n=350 °C, v_{nb}=65 mm/s and t_l=0.1 mm, (m) T_n=350 °C, v_{nb}=7.5 mm/s and t_l=0.2 mm, (n) T_n=350 °C, v_{nb}=65 mm/s and t_l=0.2 mm.

AGX-V2 machine equipped with a 5 kN load cell. To this aim, the strain rate was initially set to 1 mm/min for measuring the Young's modulus (E), and then increased to 5 mm/min.

Finally, the most promising sample underwent Residual Gas Analysis (RGA) using a HAL 201 RC mass spectrometer, both before and after a bake-out at 100 °C for 48 hours.

Results and discussion

Most of the cubic samples produced showed significant shape defects compared to typical FFF products, highlighting the challenges of processing ULTEM 1010 with this technology. Specifically, the samples produced with any combination of T_n=390 °C - 370 °C, v_{nb}=65 mm/s - 40 mm/s and t_l=0.2 mm were deemed unsuitable for practical applications, while the others exhibited less severe defects. Notably, tensile samples produced under the same conditions showed

Materials Research Proceedings 57 (2025) 190-198 https://doi.org/10.21741/9781644903735-22

no visible defects, further emphasizing the significance of sample geometry in the experimental results.

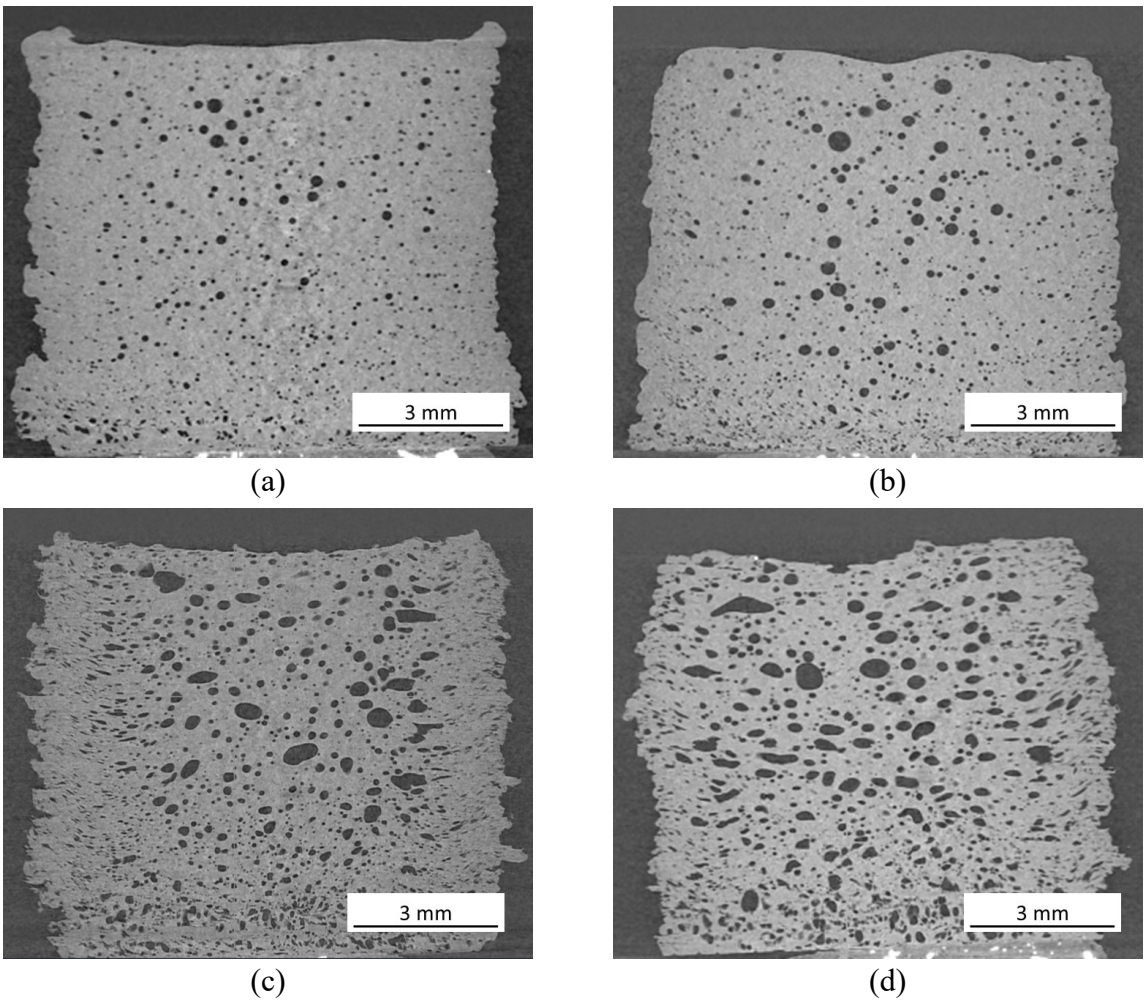


Fig. 3: X-ray μCT of the samples produced at (a) T_n=390 °C, v_{nb}=15 mm/s and t_l=0.1 mm, (b) T_n=390 °C, v_{nb}=15 mm/s and t_l=0.2 mm, (c) T_n=350 °C, v_{nb}=65 mm/s and t_l=0.1 mm, (d) T_n=350 °C, v_{nb}=65 mm/s and t_l=0.2 mm.

Surface morphology. SEM inspections revealed a noticeable deterioration in surface quality with decreasing T_n and increasing v_{nb} and t_l, highlighting the formation of burrs, likely due to the over-fluidization of the extruded material, which is then spread by the nozzle (Fig. 2). However, it is clear from the results that T_n plays a dominant role in creating a smooth substrate for the layer-by-layer deposition of material.

Density. The X-ray μCT analysis revealed the presence of various types of pores in the material. Under high T_n conditions (Fig. 3 (a) and (b)), predominantly spherical voids typically associated with gas entrapment were observed. In contrast, under low T_n conditions (Fig. 3 (c) and (d)), both irregular voids typically associated with under-extrusion and spherical voids were identified. Under-extrusion pores appeared to be mainly concentrated near the edges, possibly due to more efficient cooling of the material, and are relatively uniform in size. In contrast, the gas pores were primarily concentrated in the core volume, likely due to heat accumulation, and span a wide dimensional spectrum, ranging from the nanoscale to several tenths of a millimeter. The complex pore structures found in the material are shown in greater detail in Fig. 4.

Materials Research Proceedings 57 (2025) 190-198 https://doi.org/10.21741/9781644903735-22

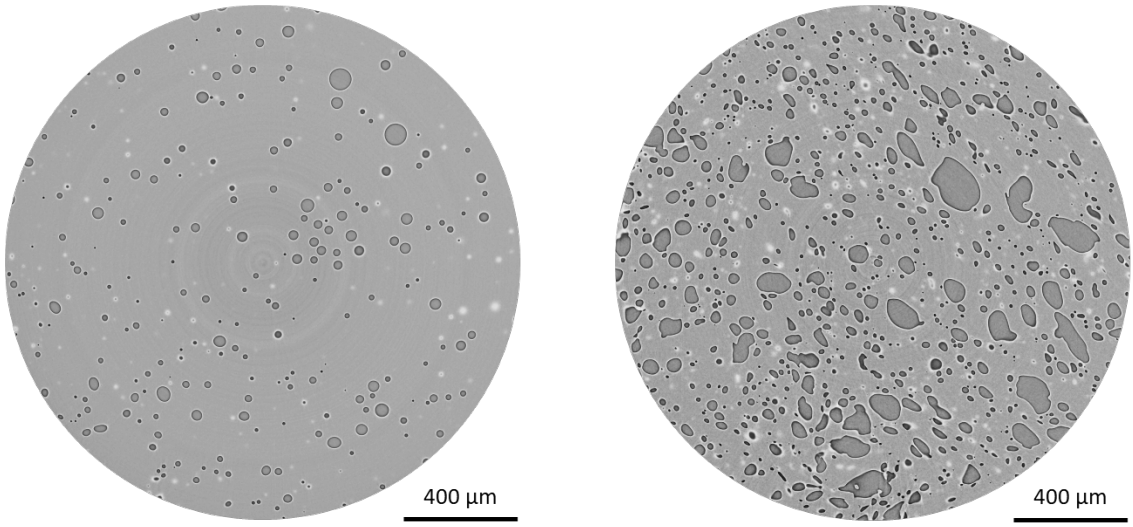


Fig. 4: Synchrotron X-ray µCT of the samples produced at (a) T_n=390 °C, v_{nb}=15 mm/s and t_l=0.1 mm and (b) T_n=350 °C, v_{nb}=65 mm/s and t_l=0.2 mm.

Overall, the material density increases with increasing T_n and decreases with increasing v_{nb} and t_l, although all samples exhibited significant porosity. The highest density to ρ_r=94.74 % was achieved at T_n=390 °C, v_{nb}=15 mm/s and t_l=0.1 mm (Fig. 3 (a)). While this value is relatively low compared to typical FFF process standards, it remains comparable to or exceeds current industrial and scientific benchmarks [5][6]. At T_n=390 °C, v_{nb}=65 mm/s and t_l=0.1, the density decreased only slightly to ρ_r=89.01 %, while the corresponding process parameters results in significantly higher productivity, which may be more relevant for specific applications.

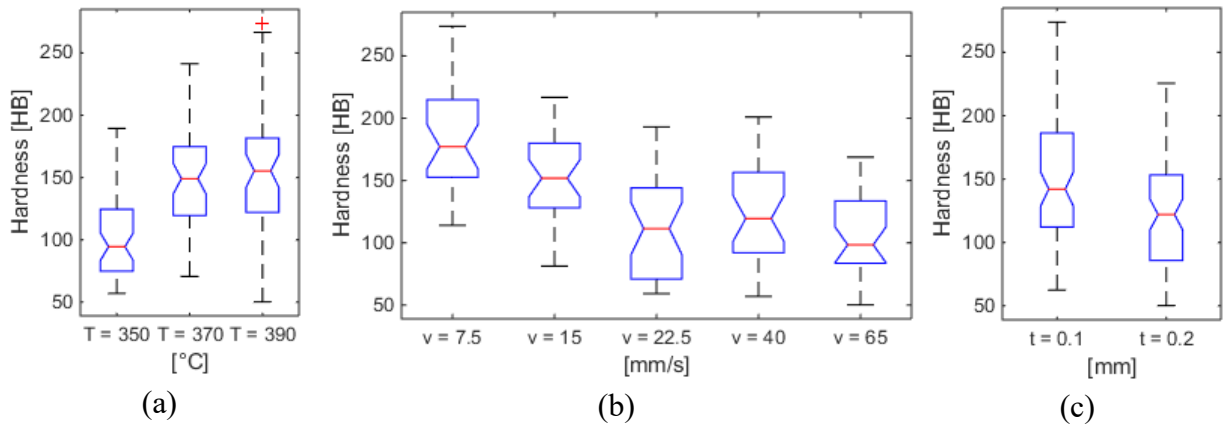


Fig. 5: Effect of the process parameters on the material hardness. On each box, the red line denotes the median, and the edges correspond to the 1st and 3rd quartiles. The whiskers extend to the most extreme data points within 1.5 times the interquartile range, while outliers are plotted as '+' symbols. The notches reflect the variability of the medians, with non-overlapping notches suggesting a significant difference between medians at the 5% significance level.

Mechanical properties. Fig. 5 shows the effect of process parameters on the material hardness. A positive effect is observed with increasing T_n and decreasing v_{nb} and t_l. The analysis of variance demonstrated the statistical significance of all the examined factors (p-value < 0.0001), and also revealed a significant interaction between T_n and v_{nb}. The Correlation analysis highlighted instead a direct relationship between hardness measurements and porosity measurements.

Materials Research Proceedings 57 (2025) 190-198 https://doi.org/10.21741/9781644903735-22

The tensile test results for the samples from the reduced experimental design are presented in Table 2, alongside the corresponding hardness data. The statistical analysis indicated an unclear effect of T_n on Young's modulus (E), a negative effect of increasing T_n and t_l on Ultimate Tensile Strength (UTS), and a negative effect of increasing T_n on elongation at fracture (A). Interestingly, when tensile properties were compared with density, an unexpected negative correlation was observed. This behavior is likely attributable to the effect of the specimen geometry, as the tensile samples appeared visibly more conformal and flawless compared to the cuboids, presumably due to a more effective extrusion and cooling cycle resulting from the increased surface area of the layers. At the same time, it is plausible that the thermal cycle resulting from the different parameter combinations may have induced distinct structural characteristics in the material, thereby influencing its specific mechanical strength. This is further supported by the negative correlation observed between tensile properties and hardness, with harder samples exhibiting more brittle behavior characterized by lower UTS and A, as well as by the weak positive correlation observed between UTS and A, with more ductile samples showing slightly higher strength.

Table 2: Hardness and tensile properties for the samples from the reduced experimental design expressed as the mean value and (standard deviation).

T_n [°C]	v_{nb} [mm/s]	t_l [mm]	HB [MPa]	UTS [MPa]	E [MPa]	Max. elong. [%]	ρ_r [%]
390	65	0.2	111 (48)	49 (1)	1414 (86)	7.6 (0.1)	–
390	65	0.1	138 (29)	53 (4)	1433 (142)	7.0 (0.9)	89.01
390	15	0.2	147 (25)	51 (1)	1423 (73)	7.0 (0.1)	91.52
390	15	0.1	167 (33)	51 (8)	1334 (297)	6.9 (0.6)	94.74
370	40	0.2	125 (24)	56 (1)	1696 (68)	6.1 (0.2)	83.25
370	40	0.1	129 (17)	61 (4)	1545 (236)	6.4 (0.4)	86.33
350	65	0.2	84 (7)	66 (3)	1560 (51)	7.7 (0.3)	76.90
350	65	0.1	95 (12)	72 (3)	1601 (120)	7.6 (0.5)	81.33
350	15	0.2	92 (8)	62 (1)	1481 (295)	7.6 (0.2)	80.14
350	15	0.1	140 (14)	73 (5)	1451 (121)	8.1 (0.9)	85.12

Chemical properties. The functional groups distinguished in the samples by FT-IR spectroscopy were consistent with the investigated material. Notably, no significant differences were observed among the samples, indicating that the heating, extrusion, and cooling processes do not influence the chemical structure of the material.

Optimal process parameters. Based on the obtained results, it was determined that the optimal process parameters are not straightforward. The highest mechanical strength was achieved with low nozzle temperature, nozzle speed, and layer thickness. However, these samples also exhibited significant porosity and morphological defects. The best combination of surface morphology, density, and hardness was achieved at T_n =390 °C, v_{nb}=15 mm/s and t_l=0.1 mm, which also yielded aesthetically satisfactory results in cuboid production.

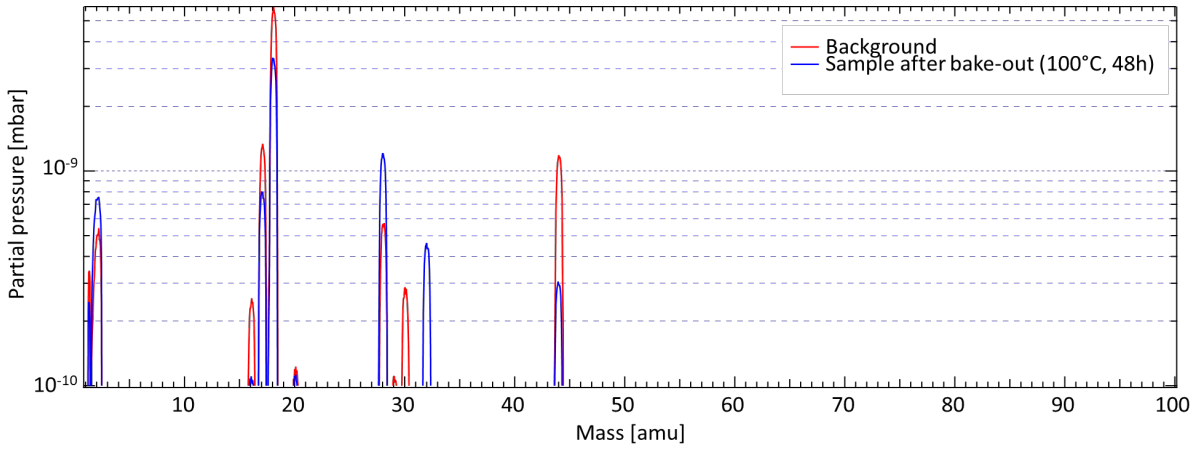


Fig. 6: Residual Gas Analysis under Ultra-High Vacuum condition of the samples produced at T_n =390 °C, v_{nb}=15 mm/s and t_l=0.1 mm.

For advanced applications where ULTEM 1010 may be particularly useful, achieving a high degree of inertness is crucial, which is typically associated with higher density levels. As a result, the combination that produced the highest density was selected for Residual Gas Analysis.

Ultra-High Vacuum behavior. The Residual Gas Analysis performed on the optimal sample (Fig. 6) at a base pressure of 9.4×10^{-8} mbar after 5 days of pumping without bake-out showed no significant deviations from the background mass spectrum. At a base pressure of 5.7×10^{-9} mbar after bake-out at 100°C for 48 hours, the presence of H_2 (2 amu), CO/N_2O (28 amu) and O_2 (32 amu) was instead detected. However, the detected species contributed less than 10% to the total pressure. Consequently, highly dense ULTEM 1010 processed by FFF can be effectively adopted for UHV applications.

Summary

This study investigated the effects of nozzle temperature (T_n), nozzle speed (v_{nb}) and layer thickness (t_l) on the properties of ULTEM 1010 processed via Fused Filament Fabrication to determine optimal process parameters. The results demonstrated that surface morphology, material density, and hardness can be generally improved by increasing T_n and decreasing v_{nb} e t_l. However, an opposite trend was observed for the tensile properties, which may be attributed to the combined effects of the sample geometry and the thermal cycles induced by the process parameters. Overall, the attained density was lower than conventional process standards, but it was comparable to or even exceeded current industrial and scientific benchmarks. The highly dense ULTEM 1010 was proved to be suitable for Ultra High Vacuum applications, while higher v_{nb} may be adopted for consumer applications, where a slight reduction in density can be accepted in exchange for a significant increase in production throughput. Future work will focus on further investigating the anomalous correlations between density and mechanical strength, taking into account the impact of sample geometry on the analysis.

Acknowledgements

The authors are grateful to Dr. D. Dreossi for conducting the µCT analysis, to Dr. L. Novinec for performing the UVH tests, and to Dr. M. Billè for his support with image acquisition and reconstruction at the SYRMEP beamline. Elettra-Sincrotrone Trieste and the Laboratory for Advanced Mechatronics - LAMA FVG - of the University of Udine are also gratefully acknowledged for providing the equipment used for the experimental work and for the technical support. Emanuele Vaglio is grateful for funding under the REACT EU Italian PON 2014–2020 Program – Action IV.4 – Innovation (DM 1062, 10/08/2021).

References

[1] G.H. Melton, E.N. Peters, R.K. Arisman, Engineering thermoplastics, in M. Kutz (Ed.), Applied plastics engineering handbook, William Andrew Publishing, 2011, pp. 7-21. https://doi.org/10.1016/B978-1-4377-3514-7.10002-9

[2] J. Ramiro, J.I. Eguiazabal, and J. Nazabal, Synergistic mechanical behaviour and improved processability of poly (ether imide) by blending with poly (trimethylene terephthalate), Polym. Adv. Technol. 14 (2003) 129-136. https://doi.org/10.1002/pat.340

[3] V.R. Sastri, Plastics in medical devices: properties, requirements, and applications, second ed., William Andrew Publishing, 2014. https://doi.org/10.1016/C2012-0-05946-7

[4] D.P. Simunec, J. Jacob, A.E. Kandjani, A. Trinchi and A. Sola, Facilitating the additive manufacture of high-performance polymers through polymer blending: A review, Eur. Polym. J. 201 (2023) 112553. https://doi.org/10.1016/j.eurpolymj.2023.112553

[5] S. Ding, B. Zou, P. Wang and H. Ding, Effects of nozzle temperature and building orientation on mechanical properties and microstructure of PEEK and PEI printed by 3D-FDM, Polym. Test. 78 (2019) 105948. https://doi.org/10.1016/j.polymertesting.2019.105948

[6] S.E. Ouassil, A. El Magri, H.R. Vanaei and S. Vaudreuil, Investigating the effect of printing conditions and annealing on the porosity and tensile behavior of 3D-printed polyetherimide material in Z-direction, J. Appl. Polym. Sci. 140 (2023) e53353. https://doi.org/10.1002/app.53353

[7] M. Yilmaz, N.F. Yilmaz and M.F. Kalkan, Rheology, crystallinity, and mechanical investigation of interlayer adhesion strength by thermal annealing of polyetherimide (PEI/ULTEM 1010) parts produced by 3D printing, J. Mater. Eng. Perform. 31 (2022) 9900-9909. https://doi.org/10.1007/s11665-022-07049-z

[8] P Han, A. Tofangchi, A. Deshpande, S. Zhang and K. Hsu, An approach to improve interface healing in FFF-3D printed Ultem 1010 using laser pre-deposition heating, Procedia Manuf. 34 (2019) 672-677. https://doi.org/10.1016/j.promfg.2019.06.195

[9] G. Taylor, S. Anandan, D. Murphy, M. Leu and K. Chandrashekhara, Fracture toughness of additively manufactured ULTEM 1010, Virtual Phys. Prototyp. 14 (2019) 277-283.

[10] G. Taylor, X. Wang, L. Mason, M.C. Leu, K. Chandrashekhara, T. Schniepp and R. Jones, Flexural behavior of additively manufactured Ultem 1010: experiment and simulation, Rapid Prototyp. J. 24 (2018) 1003-1011. https://doi.org/10.1108/RPJ-02-2018-0037

[11] Pandelidi, Chrysoula, Tobias Maconachie, Stuart Bateman, Ingomar Kelbassa, Sebastian Piegert, Martin Leary, and Milan Brandt. "Parametric study on tensile and flexural properties of ULTEM 1010 specimens fabricated via FDM." Rapid prototyping journal 27, no. 2 (2021): 429-451.

Materials Research Proceedings 57 (2025) 199-207 https://doi.org/10.21741/9781644903735-23

Impact of cell dimensions and beam radius on the bending characteristics of BCC sandwich panels produced via L-PBF of Ti6Al4V

Dina PALMERI[1,a *], Gaetano POLLARA[1,b], Gianluca BUFFA[1,c] and Livan FRATINI[1,d]

[1]Università Degli studi di Palermo, Dipartimento di Ingegneria, Viale delle Scienze, 90128 Palermo, Italia

[a]dina.palmeri@unipa.it, [b]gaetano.pollara@unipa.it, [c]gianluca.buffa@unipa.it, [d]livan.fratini@unipa.it

Keywords: Laser Powder Bed Fusion, Ti6Al4V, BCC Sandwich Panels, Three-Point Bending Tests

Abstract. Ti-6Al-4V lattice structures created through Laser Powder Bed Fusion L-PBF find extensive use in sandwich panels for applications that demand both high strength and lightweight characteristics, particularly in aerospace and biomedical fields. L-PBF technology provides significant design flexibility, enabling the fabrication of complex geometry and modification of lattice mechanical properties to meet specific requirements. Understanding the correlation among unit cell type, relative density, unit cell arrangement, and mechanical properties is essential for the design of effective lattice structures. The aim of the study was to examine how the panel's behaviour varied with changes in the two body centered cubic (BCC) cell parameters cell size and beam radius. The samples produced were evaluated mechanically through the carrying out of three-point bending tests. Simulations of the additive process were conducted to emphasize the existence of residual stresses, connecting with the findings from previous tests.

Introduction

Additive manufacturing (AM) has grown in popularity in recent years because to its ability to produce highly customizable parts, lightweight structures, and multifunctional components [1, 2]. This is especially true in the aerospace sector, where lightweight constructions result in reduced buy-to-fly ratios and cost savings during the product's useful life [3]. In this case, a metal lattice structure can be beneficial in reducing the weight of the component while retaining high strength [4]. Lattice structures are formed by the repeating of a basic cell, which can be strut-based or mathematically structured to achieve zero-mean curvature at all points on the surface (triply periodic minimum surface, or TPMS) [5]. In the first scenario, the unit cell is basically defined by two geometrical properties: cell size and beam radius, which determine the mechanical response of the lattice [6, 7]. Recently, BCC lattice structures have been investigated for metal lattice sandwich panels (MLSPs) with anti-icing or energy absorption applications [8, 9]. Ti-6Al-4V can be used to print MLSPs, especially in aerospace applications where good mechanical properties and corrosion resistance are requested. Since a high resolution is needed to print small features, such as the struts within the unit cell, laser powder bed fusion (LPBF) is the most suitable among AM technologies for metals [10].

Few studies can be found in the literature on MLSPs made of a lattice core and a solid skin. Acanfora et al. [9] analyzed the influences of different BCC cell configurations on the shock-absorbing capacity of hybrid sandwich panels made of an additive-manufactured metal lattice core and composite skins. The impact response of these panels has been investigated through FEM analysis and validated with some literature studies. The results confirm the reduction of the mass

Content from this work may be used under the terms of the Creative Commons Attribution 3.0 license. Any further distribution of this work must maintain attribution to the author(s) and the title of the work, journal citation and DOI. Published under license by Materials Research Forum LLC.

and the increase in the shock-absorbing capacity by using a lattice core with respect to the reference literature test case. FEM analysis was carried out also by Wey et al. [11] to assess the blast response of Ti-6Al-4V Auxetic honeycomb sandwich panels manufactured with LPBF. They demonstrate that AM sandwich panels can be used for modern protective structures for enhanced blast resistance. Li et al. [12] investigated multi-layer lattice panels' compressive modulus and crushing strength with body-centered cubic with vertical strut (BCCZ) cells. AlSi10Mg panels fabricated via LPBF were subjected to compressive tests. FEM analysis was used to predict the compressive response of multi-layer lattice panels. The results show that the lattice panels' layer and cell number strongly affect the entire structure's mechanical response. Kang et al. [13] proposed a multi-lattice design for stainless steel 630 panels using both BCC and octet-truss lattice structures. The topology optimization was performed to obtain the minimum relative density. Three-point bending tests were used to validate the proposed method and to compare the new design with the traditional uniform lattice structures. The new design leads to an increase in the panel's stiffness and a different deformation mode. The compression failure of AlSi10Mg trabecular structures has been analyzed by Ferro et al. [14]. Two different structures, BCC and BCCZ, were printed by LPBF and tested. The effect of cell shape, strut, and cell dimension was studied to establish the best design for the final application. From this study, the most influential factors are the cell shape and cell dimension.

The literature review shows a lack of studies on the mechanical behavior of Ti-6Al-4V lattice sandwich panels, especially on their flexural strength, by changing the geometrical cell characteristics. This paper analyzes the effect of unit cell size and beam radius on the flexural response of Ti-6Al-4V MLSPs through three-point bending tests.

Materials and Methods

The objective of the study was to analyze the behavior of the MLSPs, built with L-PBF technology, by modifying two cell parameters: cell size and beam radius. Specifically, two distinct values were selected for the two parameters, while maintaining the sample dimensions (see Fig. 1a). After establishing the dimensions of the samples, the subsequent values for cell size and beam radius were selected:

Cell size: 2 mm - 3 mm;

Beam Radius: 0.25 mm - 0.35 mm.

Based on the aforementioned geometric characteristics, the characterized samples have been designated as C2 - R0.25, C2 - R0.35, C3 - R0.25, and C3 - R0.35. Depending on the selected geometric parameters, each panel was also characterized by the V_f (Volume fraction) parameter, which indicates the ratio between the volume of the panel and the volume of the sample considered as full. This metric indicates the extent of weight reduction provided by the examined lattice configuration. The samples were fabricated by means of L-PBF technique with Ti-6Al-4V grade 23 alloy, which has minimal interstitial components including oxygen and iron, resulting in favorable ductility and strength characteristics. The longitudinal orientation of the samples was selected to align with the z-building direction to reduce panel distortions. A gas-atomized spherical powder was utilized for the studies. The particle size exhibits a Gaussian distribution, with d10 and d90 values of 20µm and 63µm, respectively. The employed process parameters are those recommended by SLM Solutions for Ti-6Al-4V powder. Laser power is set at P=350 W, scanning speed at v=1400 mm/s, layer thickness at t=30 µm, and hatch distance at h=120 µm. The diameter of the laser beam focus was established at 100 µm. The employed scan strategy combines hatching and contour, with the scanning direction rotated by 15° on the plane for each layer. The Build Plate temperature is maintained at 200 °C to reduce thermal gradients.

The mechanical behavior of MLSP was evaluated using three-point bending tests. Samples were manufactured in accordance with the ASTM E290 standard, with dimensions of 80 mm in length (L), 13 mm in height (H), and 12 mm in width (W), with the lattice core region (refer to

Materials Research Proceedings 57 (2025) 199-207 https://doi.org/10.21741/9781644903735-23

Fig. 1) possessing a cross-sectional area of 12 mm x 12 mm. Three-point bending tests were conducted using a Galdabini Quasar 600 universal testing machine at a constant velocity of 0.5 mm/min.

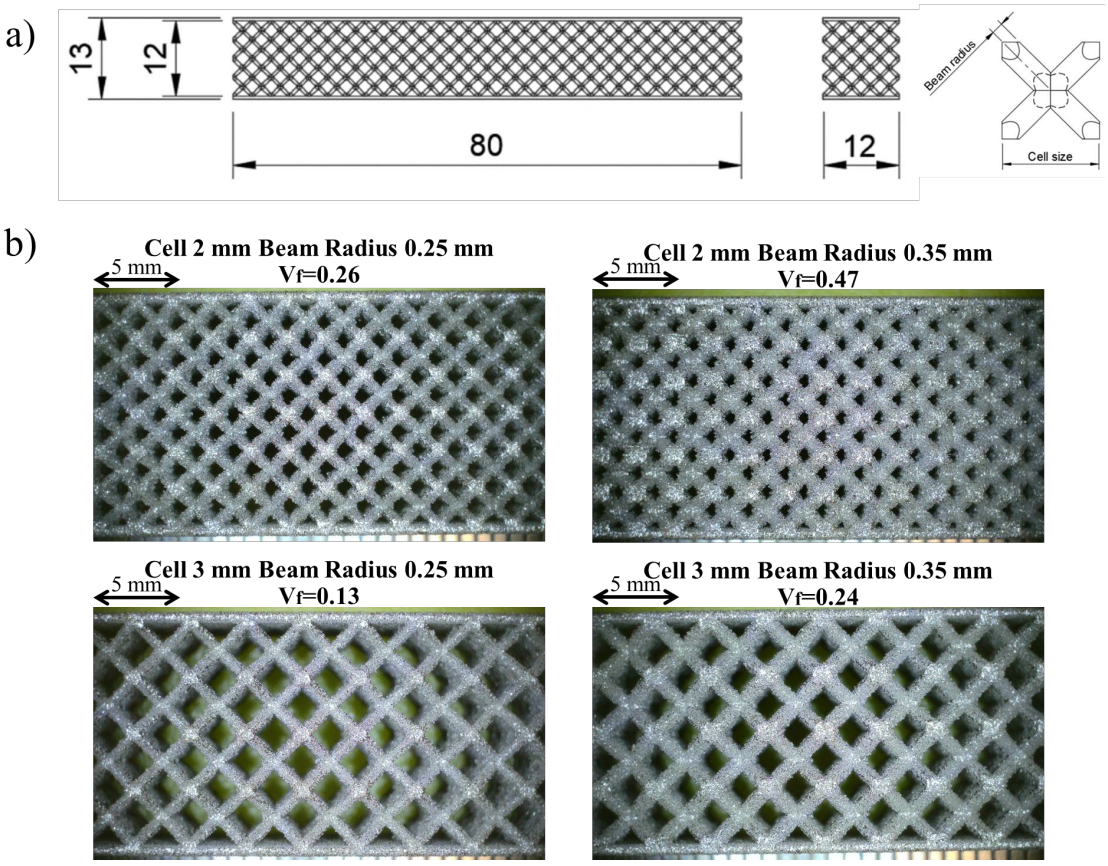


Figure 1. a) Samples dimensions for three-point bending test in accordance with the ASTM E290 standard, length L=80 mm, height H=13 mm, and width W=12 mm, b) Printed lattice samples with varying geometric characteristics.

In addition to the mechanical assessments of the samples through the use of three-point bending tests, the additive process was simulated in order to discover any significant dimensional mismatches that existed between the geometry that was planned and the geometry that was ultimately obtained. Through the use of simulations, it was possible to determine the distribution of residual stresses that were generated throughout the additive process. These findings were then correlated with the strength that was found in the individual samples. Numerical simulations were conducted with Netfabb Simulation (Autodesk) to study distortions and residual stress distributions along the building direction (z) during the L-PBF process of Ti-6Al-4V on the MLSPs. Correlation analyses were performed between the results of additive simulations and the outcomes of experimental tests, specifically focusing on the lattice region of the sandwich panels.

To carry out the numerical simulation, it is essential to create a parameter file (PRM) containing the mesoscale information required for the part-scale simulation. The PRM file must specify what is being used 3D printing machine, material characteristics, and scanning procedure. Consequently, a calibration step for the model is unneeded [15].

Results and Discussions

The results of the three-point bending tests allowed the characterization of the strength of the MLSPs. The acquired data concerned the load and stroke of the punch, from which all the useful

Materials Research Proceedings 57 (2025) 199-207 https://doi.org/10.21741/9781644903735-23

data and graphs for comparing the panels characterized by different geometric parameters were then obtained. Furthermore, the test was enhanced with the acquisition of images to analyze the deformation of the sample and, where possible, the progression of the crack (phenomena that vary significantly among the different types of samples).

In the following Fig.2, the results of the mechanical characterization tests of the sandwich panels with BCC lattice core structure are reported. As can be observed from Fig. 2 and the photo acquisitions shown in Fig. 3 for the C2 specimens, both in the case of R0.25 and in the case of R0.35, after a slight deflection, there is a brittle fracture with an unstable crack propagation, which opens in mode I, that is, by tension. For the C3 specimens, a completely different behavior is observed. The panel initially behaves as if it were subjected to compression, as the load is transferred to the core with a punch penetration; thereafter, it also breaks with a mode I crack. This behavior occurs for a beam radius of 0.25, while for R0.35, a behavior similar to that previously described for the C2 panels is restored.

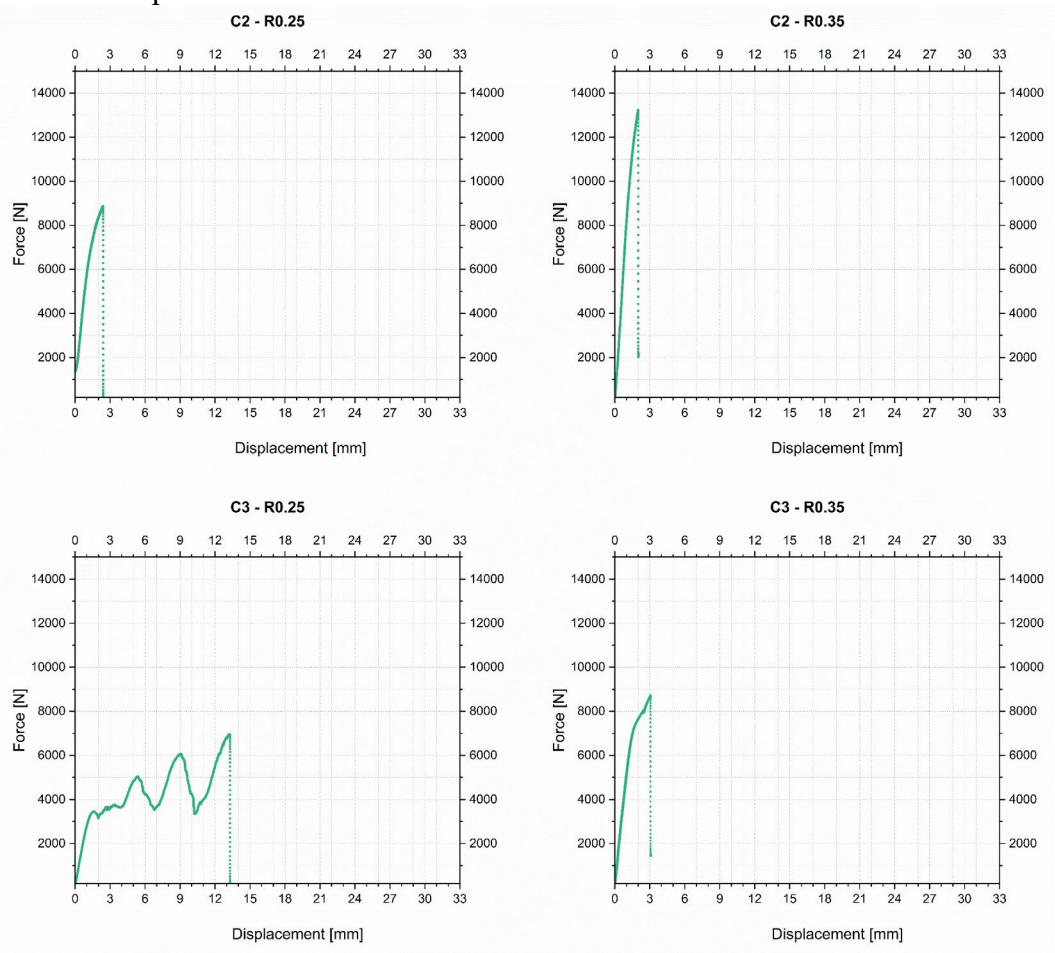


Figure 2. Three point bending test results: maximum load to failure [N] and punch displacement [mm].

Materials Research Proceedings 57 (2025) 199-207 https://doi.org/10.21741/9781644903735-23

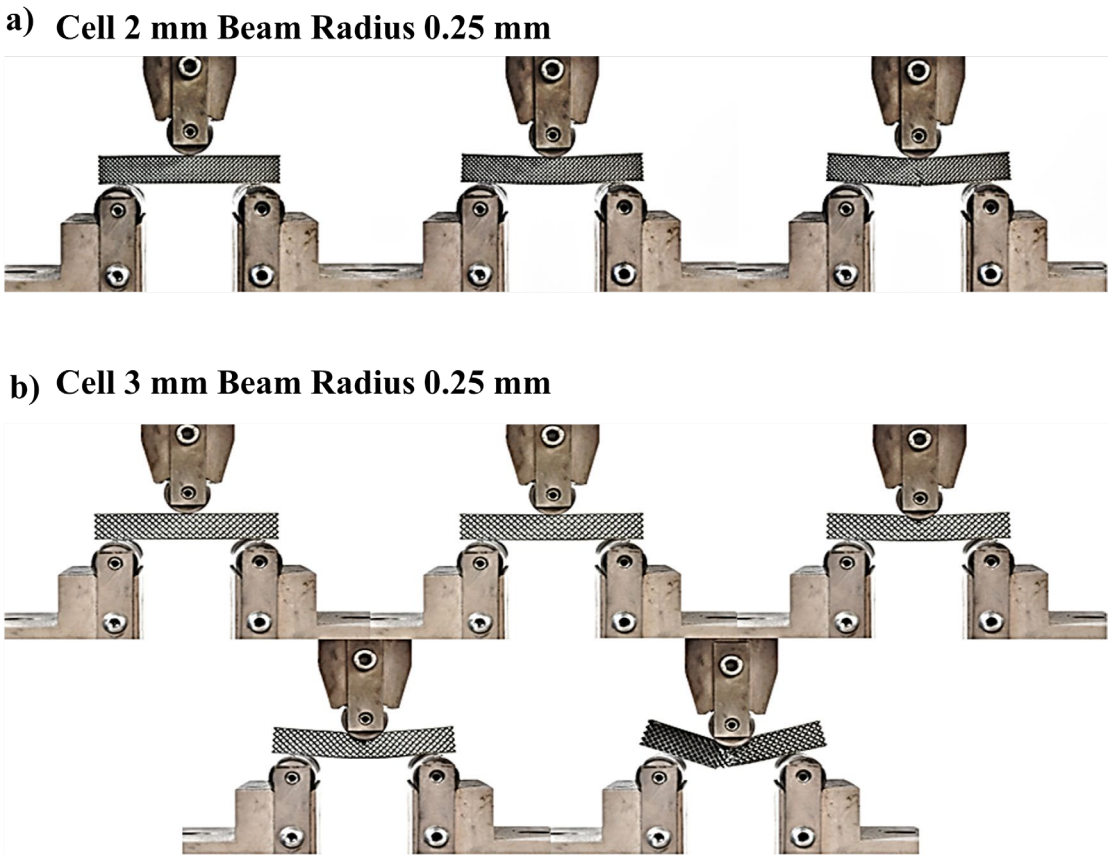


Figure 3. Photographic acquisitions during the three-point bending test. a) panels with cell size equal to 2 mm and beam radius 0.25 mm b) panel with cell size 3 mm and beam radius 0.25 mm.

The results indicated that as cell size increases and V_f decreases, it is feasible, in certain instances, to preserve the strength of a panel with a smaller cell size, thereby enhancing ductility and achieving a lightweight effect on the sandwich panel. This condition was observed for moderate reductions in V_f. For V_f values significantly lower than those held by the C2-R0.25 and C2-R0.35 panels, the MLSPs experience a considerable reduction in resistance.

The numerical simulations of additive manufacturing, the results of which are presented in Fig. 4 and Fig. 5 as the size of the unit cell changes, have emphasized that the additive process does not cause major variations between the design geometry and the geometry actually produced.

A higher variation is found in the panels characterized by the 2 mm cell, notably in the first printed layers. Such deviation affects a slightly larger area of the sample in the case where the beam radius is greater while keeping the cell size constant. The residual stresses linked to the additive process in the z-direction indicate that an increase in beam radius for a cell size of 2 mm results in a substantial rise in compressive forces in the longitudinal mid-section of the samples. This stress distribution enhances the strength as indicated in Fig. 2. For an elementary cell with a higher dimension (C3 mm), an increase in beam radius consistently results in increased residual compressive stresses within the longitudinal section of the panel along the z-axis. This impact is, however, less strong than in the previous scenario.

Materials Research Proceedings 57 (2025) 199-207 https://doi.org/10.21741/9781644903735-23

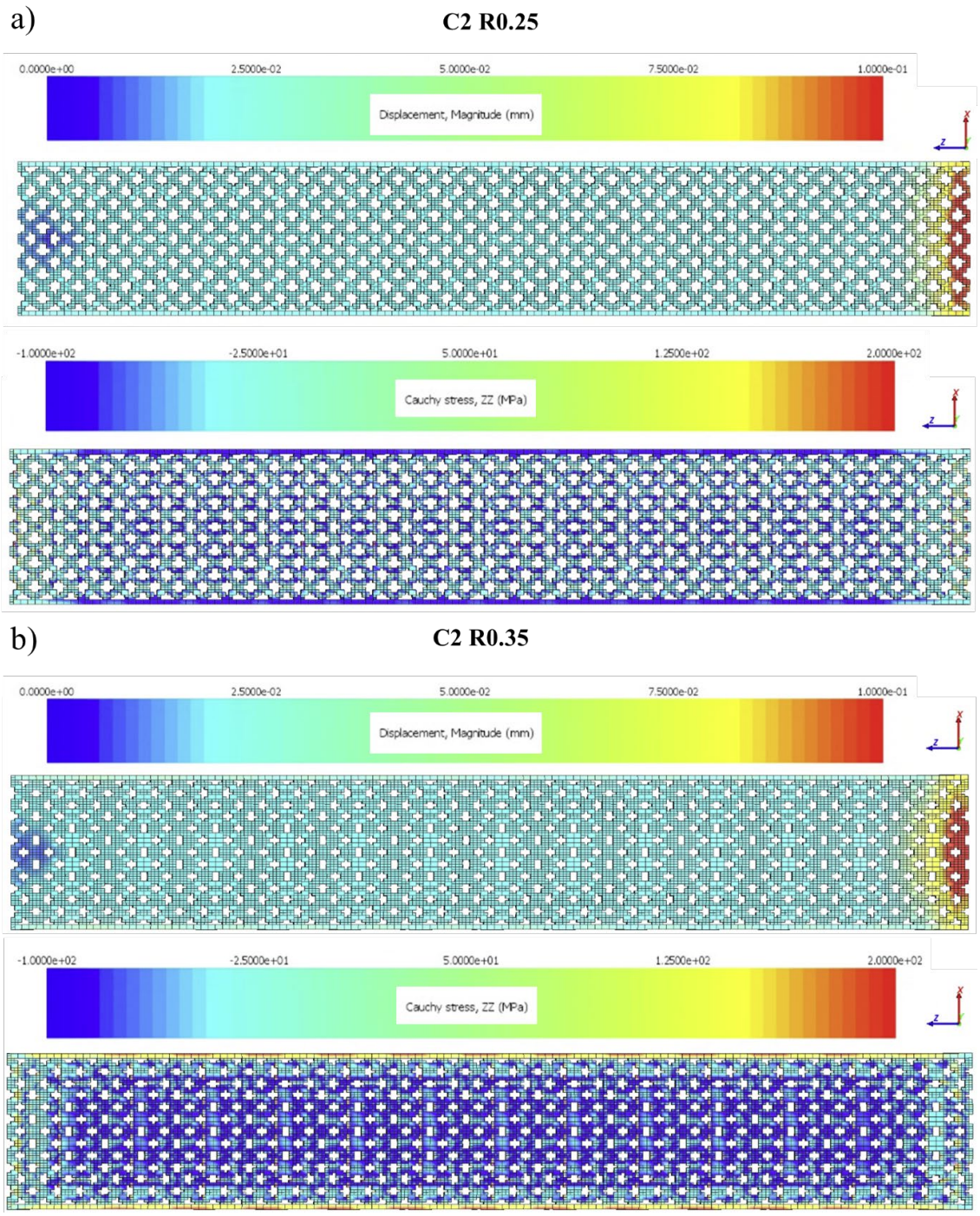


Figure 4. Numerical simulation of L-PBF process results. a) displacement and residual stress along the z direction for the panel C2 – R0.25, b) displacement and residual stress along the z direction for the panel C2 – R0.35.

Materials Research Proceedings 57 (2025) 199-207 https://doi.org/10.21741/9781644903735-23

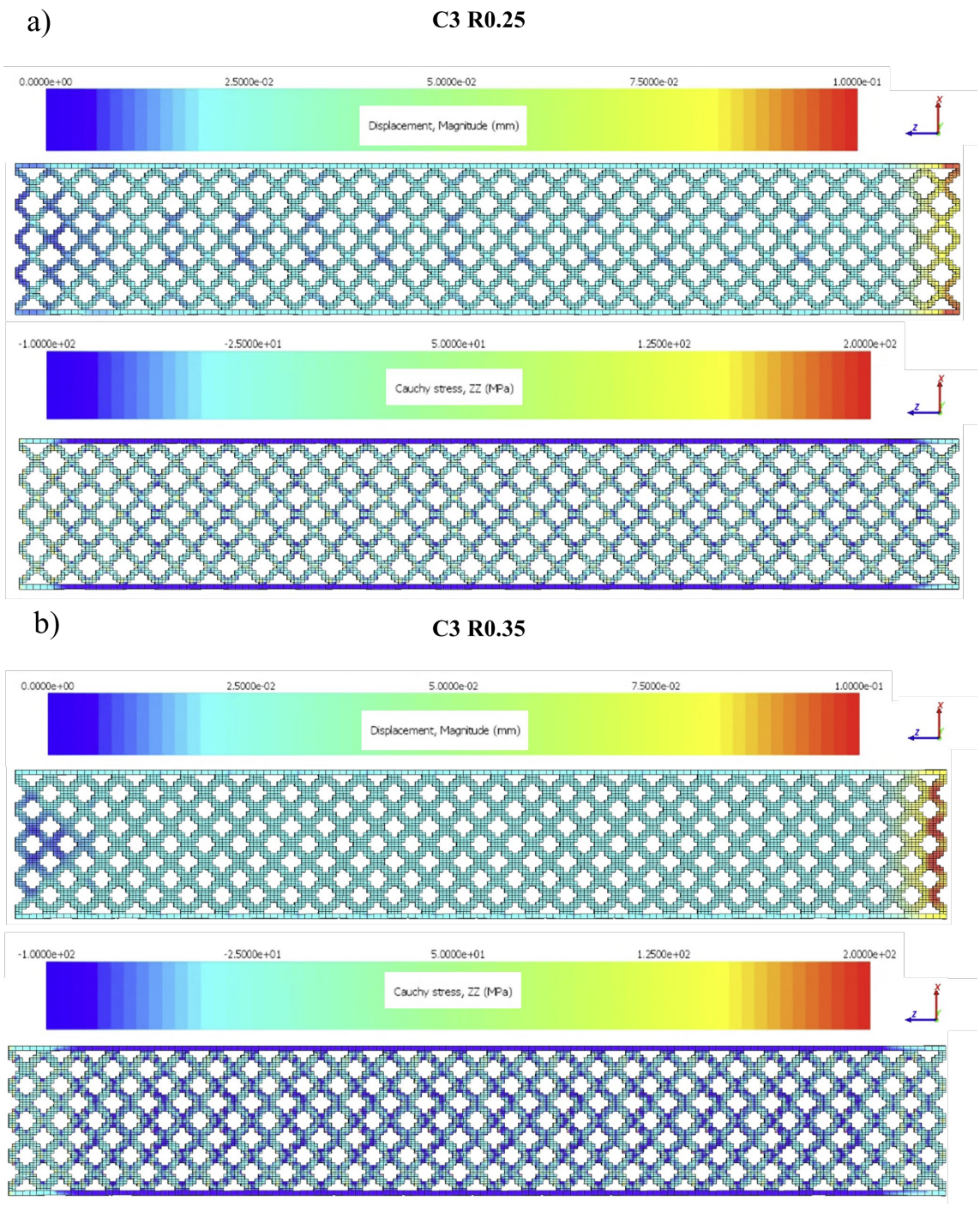


Figure 5. Numerical simulation of L-PBF process results. a) displacement and residual stress along the z direction for the panel C3 – R0.25, b) displacement and residual stress along the z direction for the panel C3 – R0.35.

The growth of beam radius in the 3 mm cell results in a longitudinal distribution of residual stresses similar to the C2 – R0.25 scenario. This situation results in a bending resistance for the C3 – R0.35 sample comparable to that of the C2 – R0.25 example, but with an enhancement in ductility due to the decrease in the V_f parameter.

Conclusions

In this paper, the mechanical properties of BCC MLSPs produced by L-PBF technology at the varying of two body centered cubic cell parameters as the cell size and the beam radius are investigated. Three-point bending tests and a numerical model of the process allowed the prediction of the residual stresses and distortions in the BCC MLSPs and the mechanical characterization of the panels as the geometry of the lattice core varies.

Based on the main findings, it can be concluded that:

- For the C2 specimens, after a small deflection, there is a brittle fracture with an unstable crack propagation, which opens in mode I, that is, by tension. This occurs in both the case of R0.25 and the case of R0.35, respectively. The behavior of the C3 specimens is shown to be entirely different from what was seen. As the load is carried to the core by a punch penetration, the panel first exhibits the behavior of a panel that has been exposed to compression. Subsequently, the panel likewise fractures with a mode I crack. The behavior described here takes place when the beam radius is 0.25, however when the radius is 0.35, a behavior that is comparable to the one that was described before for the C2 panels is restored.
- As the cell size grows and the value of V_f decreases, the findings suggested that it is possible, in some circumstances, to maintain the strength of a panel with a smaller cell size. This would result in an increase in ductility and the achievement of a lightweight effect on the sandwich panel.
- The numerical simulations of additive manufacturing show that the design geometry and the geometry produced are not significantly different.
- Continuously increasing beam radius increases residual compressive stresses in the longitudinal panel section along the z-axis. This effect decreases with cell size increasing.

References

[1] Guo N, Leu MC (2013) Additive manufacturing: Technology, applications and research needs. Frontiers of Mechanical Engineering 8:215–243. https://doi.org/10.1007/s11465-013-0248-8

[2] Herzog D, Seyda V, Wycisk E, Emmelmann C (2016) Additive manufacturing of metals. Acta Mater 117:371–392. https://doi.org/10.1016/j.actamat.2016.07.019

[3] Blakey-Milner B, Gradl P, Snedden G, et al (2021) Metal additive manufacturing in aerospace: A review. Mater Des 209:. https://doi.org/10.1016/j.matdes.2021.110008

[4] Soro N, Saintier N, Merzeau J, et al (2021) Quasi-static and fatigue properties of graded Ti–6Al–4V lattices produced by Laser Powder Bed Fusion (LPBF). Addit Manuf 37:101653. https://doi.org/10.1016/j.addma.2020.101653

[5] AlMahri S, Santiago R, Lee D-W, et al (2021) Evaluation of the dynamic response of triply periodic minimal surfaces subjected to high strain-rate compression. Addit Manuf 46:102220. https://doi.org/10.1016/j.addma.2021.102220

[6] Riva L, Ginestra PS, Ceretti E (2021) Mechanical characterization and properties of laser-based powder bed–fused lattice structures: a review. The International Journal of Advanced Manufacturing Technology 113:649–671

[7] Chen L-Y, Liang S-X, Liu Y, Zhang L-C (2021) Additive manufacturing of metallic lattice structures: Unconstrained design, accurate fabrication, fascinated performances, and challenges. Materials Science and Engineering: R: Reports 146:100648. https://doi.org/10.1016/j.mser.2021.100648

[8] Bici M, Brischetto S, Campana F, et al (2018) Development of a multifunctional panel for aerospace use through SLM additive manufacturing. Procedia CIRP 67:215–220. https://doi.org/10.1016/j.procir.2017.12.202

[9] Acanfora V, Saputo S, Russo A, Riccio A (2021) A feasibility study on additive manufactured hybrid metal/composite shock absorbers. Compos Struct 268:113958. https://doi.org/10.1016/j.compstruct.2021.113958

[10] Liu S, Shin YC (2019) Additive manufacturing of Ti6Al4V alloy: A review. Mater Des 164:. https://doi.org/10.1016/j.matdes.2018.107552

[11] Wei Y, Zhang C, Yuan Y, et al (2023) Blast response of additive manufactured Ti–6Al–4V sandwich panels. Int J Impact Eng 176:104553. https://doi.org/10.1016/j.ijimpeng.2023.104553

[12] Li C, Lei H, Liu Y, et al (2018) Crushing behavior of multi-layer metal lattice panel fabricated by selective laser melting. Int J Mech Sci 145:389–399. https://doi.org/10.1016/j.ijmecsci.2018.07.029

[13] Kang D, Park S, Son Y, et al (2019) Multi-lattice inner structures for high-strength and light-weight in metal selective laser melting process. Mater Des 175:107786. https://doi.org/10.1016/j.matdes.2019.107786

[14] Ferro CG, Varetti S, Maggiore P, et al (2020) Design and characterization of trabecular structures for an anti-icing sandwich panel produced by additive manufacturing. Journal of Sandwich Structures & Materials 22:1111–1131. https://doi.org/10.1177/1099636218780513

[15] Peter N, Pitts Z, Thompson S, Saharan A. Benchmarking build simulation software for laser powder bed fusion of metals. Addit Manuf 2020;36:101531. https://doi.org/10.1016/j.addma.2020.101531

Materials Research Proceedings 57 (2025) 208-215 https://doi.org/10.21741/9781644903735-24

Effect of cyclic loading and thermal stimuli on the shape memory behavior of PLA 3D-printed cellular structures

Desole M.P.[1,a*], Gisario A.[1,b]

[1]Sapienza Università di Roma, Dipartimento di Ingegneria Meccanica e Aerospaziale, Via Eudossiana 18, 001884 Roma, Italy

Keywords: Additive Manufacturing, Shape Memory Polymers, Energy Absorption

Abstract. This study investigates the shape memory behaviour of PLA 3D printed cellular structures subjected to bending cycles. The focus is on their ability to recover the original shape following the application of a thermal stimulus. Both water and hot air were tested as activation media, with the structures subjected to three alternating cycles of stress and recovery to evaluate their performance. Two structural designs were considered: a topology with negative stiffness, modified to enhance performance and a structure inspired by the spring-loaded crossbow. The latter proved to be more effective, standing out for its mechanical strength and energy absorption capacity. The type of thermal stimulus significantly influences the recovery of the original shape. Specifically, the use of hot air enables localized recovery of the structure, reducing damage to the geometry as a result of cyclic stresses and increasing the energy absorption properties of the structure.

Introduction

Shape memory polymers (SMPs) are smart materials capable of recovering their original configuration after undergoing permanent deformation, triggered by an external stimulus such as a temperature change. [1,2]. This is known as the shape memory effect (SME) [3]. The integration between SMP and additive manufacturing (AM) also known as 3D printing, has shown significant potential in the realization of complex structures, which would be complicated to achieve through traditional production processes [4]. Traditionally, this technology has been associated with static processes, where the shape and function of objects remain constant over time [5]. The introduction of "4D printing," which incorporates time as a variable in the process [6], marks a significant paradigm shift in the production of complex lattice structures. Polylactic acid (PLA) is a commonly used SMP in 4D printing, enabling the creation of environmentally friendly artifacts [7]. Lattice structures are often studied [8,9] both in mechanical terms [10] and as energy absorbers [11]. Research on these structures frequently focuses on compression [12,13] and impact loads [14,15], whereas studies on bending behavior are more limited. Generally, these structures are analyzed in terms of flexural stiffness [16] and energy absorption capacity [17], but without investigating cyclic loading. The only study that examines three-point cyclic bending stress [18], does not delve into energy absorption capacity. Moreover, no comparisons between thermal stimuli have been conducted, nor has the influence of the type of thermal stimulus on energy absorption and shape recovery been analyzed. The most commonly used thermal stimulus is immersion in hot water [19,20]; however, one of the main issues associated with this method is the hydrostatic force exerted on the geometry during immersion [21]. Additionally, heating is not applied in a localized manner but affects the entire structure instead of focusing solely on the deformed area. To address these challenges, a possible solution is the application of a thermal stimulus using hot air, which allows for more targeted heating control while reducing unwanted effects related to hydrostatic force. The aim of this study is to analyze the behavior of two types of cellular structures made of PLA, fabricated using the Fusion Deposition Modeling technology, subjected to cyclic bending

Content from this work may be used under the terms of the Creative Commons Attribution 3.0 license. Any further distribution of this work must maintain attribution to the author(s) and the title of the work, journal citation and DOI. Published under license by Materials Research Forum LLC.

Materials Research Proceedings 57 (2025) 208-215 https://doi.org/10.21741/9781644903735-24

loads while investigating shape recovery under two different thermal stimuli: water and hot air. The analyzed geometries are classified into two main categories: one characterized by negative stiffness and the other inspired by a leaf spring. The structures undergo three loading cycles, during which elastic recovery and shape restoration are observed. This analysis enables their characterization from both a mechanical standpoint and in terms of energy absorption capacity. The best-performing structure is then tested with a different thermal stimulus, transitioning from water to hot air. Applying hot air to the deformed area allows for localized restoration, reducing geometric damage caused by cyclic loading and improving the structure's energy absorption properties.

Material and method

Material and geometry design

The analyzed structures were fabricated using non-technical PLA filament produced by Ultimaker (Utrecht, Netherlands), with a diameter of 2.85 ± 0.10 mm. This material is frequently used in 4D printing as a shape memory material [22]. The geometries include a negative-stiffness type, inspired by an existing design in the literature [23] and a leaf spring-based design. In the first case, the structure incorporates an ellipsoidal element with its major axis parallel to the specimen length, replacing the traditional vertical rigid element. This modification aims to extend the elastic phase of the structure and reduce force concentration along the cell edges. The second geometry is inspired by the leaf spring, a well-known configuration for its high mechanical resistance and energy absorption capacity [24]. Figure 1 shows the CAD models of the examined structures, designed using Autodesk Inventor 2024. The dimensions were defined following ISO 178:2019 standards. To facilitate the inclusion of hydrophilic support material in Butene Diol Vinyl Alcohol Copolymer (BVOH) and prevent direct contact between the heated bed and the printed pattern, a 1 mm-thick step was added. The densities of the NS_Spring and Leaf_Spring structures are 27% and 30%, respectively.

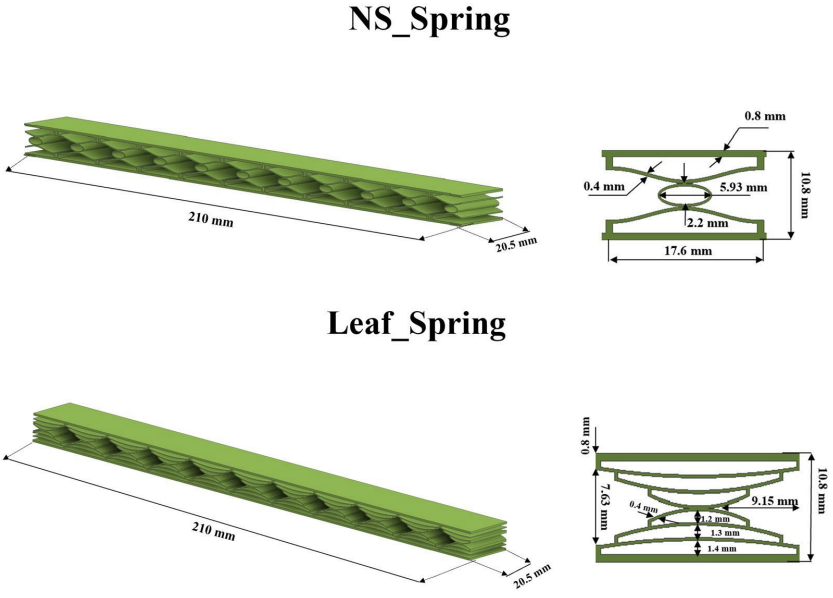


Figure 1. CAD model of the NS_Spring (a) and Leaf_Spring (b) structures.

Manufacturing process

The samples were produced using FDM technology with an Ultimaker S5 3D printer. The "Ultimaker Care" software was used to set the printing parameters. The printing temperature was set to 200°C for PLA and 210°C for BVOH, in accordance with the materials' technical specifications. To ensure good mechanical strength, the infill density was set to 100%. The printing speed was maintained at 60 mm/s, a value that provides a good balance between part quality and

production time [25]. The layer thickness was set to 0.2 mm, a choice that allows for an optimal balance between detail resolution and printing speed.

Bending Test

The machine used for the three-point bending tests is the Shimadzu "Autograph AGS-X series", equipped with a 5 kN load cell and a maximum guaranteed error of 1%. The bending tests were conducted according to the ISO 178:2019 standard, designed to analyze the three-point flexural strength of plastic materials. This standard defines the support span and provides a range of values for the central punch descent speed, which should be selected based on the test conditions. The tests were performed with a speed of 2 mm/min and a displacement of 16 mm, while the support span was set to 60 mm.

Springback and shape recovery

The elastic recovery was measured in terms of variation in the structure's rotation angle and reduction in mid-span height compared to the nominal structure height of 10.8 mm. These measurements were taken using a digital protractor and a vernier caliper, respectively, and were recorded over 35 minutes with a 5-minute interval. The recovery process was conducted for comparison purposes using both hot water and hot air. For hot water, the specimens were immersed at 55°C for 90 seconds, a temperature below the material's glass transition temperature (≈58°C [25]). This temperature proved sufficient due to the slenderness of the geometries. Shape recovery using hot air was performed with a STEINEL 2520E hot air gun [26]. The gun was set to 60°C, with an airflow rate of 50%. To ensure uniform heat application, the device was securely mounted on a support, maintaining a constant 60 mm distance between the nozzle and the structure. For recovery monitoring, a tracking software was used, with two markers placed on the beam-like structure: one at the center to track height variations and one at the extremity to measure the rotation angle.

Cyclical stress and energy absorption

Three cycles of bending, elastic recovery, and shape recovery were performed for each structure, totaling three cycles per structure. In the case of the NS_Spring, permanent fractures occurred during the fourth cycle, making further testing impossible. Consequently, only the first three cycles were considered for both configurations. For the calculation of the absorption energy, reference was made to the Specific Energy Absorption (SEA), which represents the ratio of absorbed energy, considered as the underlying area of the bending curve and the mass of the structure [27].

Results and discussion

Compression test - 3 Cycles

Figure 2 presents the Force-Displacement curves for three cycles, respectively, for the NS_Spring and Leaf_Spring structures. In the case of NS_Spring, the structure exhibits maximum loads of approximately 50 N in the first cycle, with lower values in the subsequent cycles. Despite the geometrical modifications, which extended the elastic phase and reduced stress concentration compared to the reference structure in the literature [18], its mechanical resistance remains limited. By the third cycle, a decline in resistance is observed due to damage at the layer-to-sinusoid connection, leading to a 35% load drop. Conversely, the Leaf_Spring structure demonstrates a higher maximum load than NS_Spring across all three cycles, consistently exceeding 150 N. Its plastic yielding is more controlled, with limited structural damage, primarily due to its higher density.

Materials Research Proceedings 57 (2025) 208-215 https://doi.org/10.21741/9781644903735-24

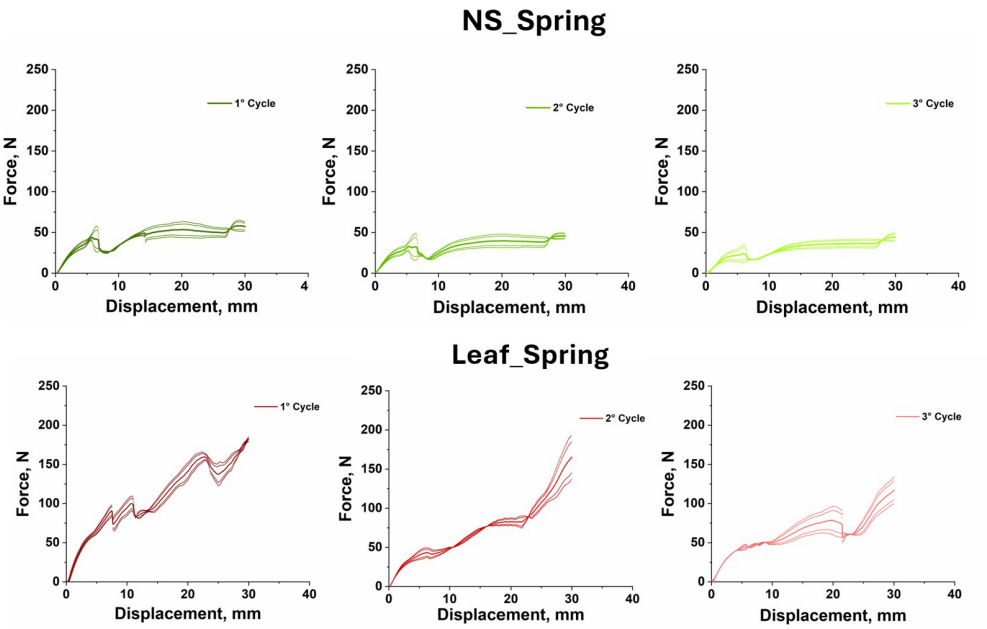


Figure 2. Curve Force-Displacement 3 Cycles

Springback - 3 Cycles

Figure 3 illustrates the average trend of elastic recovery for the analyzed geometries, expressed in terms of rotation angle and mid-span height. For the NS_Spring, the angle recovery is nearly complete across all three loading cycles, with a final value of approximately 3°. In terms of height, the final value reaches around 8 mm, showing a progressive increase from the first to the third cycle. Conversely, the Leaf Spring structure exhibits less effective elastic recovery. The final angle in the first cycle is 17°, increasing progressively up to 28° in the third cycle. A similar trend is observed for height, with final values ranging between 6 and 7 mm from the first to the third cycle.

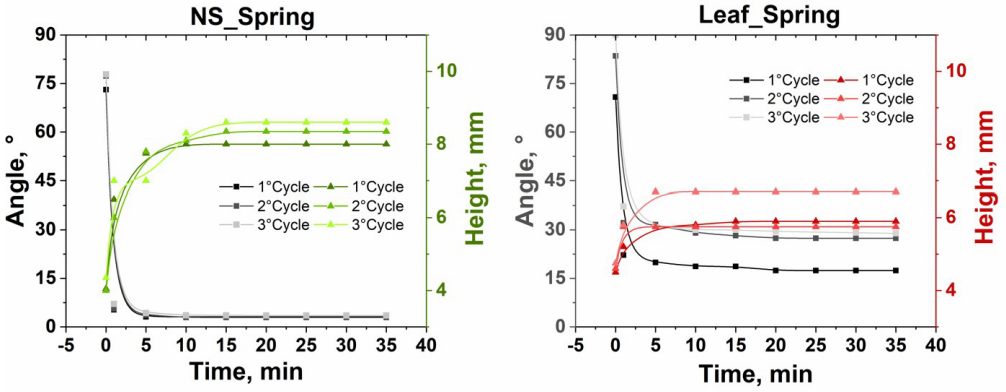


Figure 3. Springback 3 Cycles

Shape recovery - 3 Cycles

Figure 4 illustrates the average shape recovery of the analyzed geometries, expressed in terms of rotation angle and mid-span height. The results confirm the observations from the elastic recovery analysis, highlighting consistency in the deformation recovery data. The NS_Spring exhibits complete angle recovery, demonstrating excellent repeatability of the phenomenon. In terms of height, the recovery is nearly total, reaching values of approximately 10 mm. Contrary to [23], this study shows that targeted geometric changes improve angular recovery even in the presence of repeated cycles. Conversely, the Leaf Spring structure shows greater difficulty in angle recovery, achieving only 2.5° in the third cycle, likely due to the effect of hydrostatic force and the density

Materials Research Proceedings 57 (2025) 208-215 https://doi.org/10.21741/9781644903735-24

of the structure. However, height recovery proves to be more effective, with final values exceeding 8 mm across all three cycles.

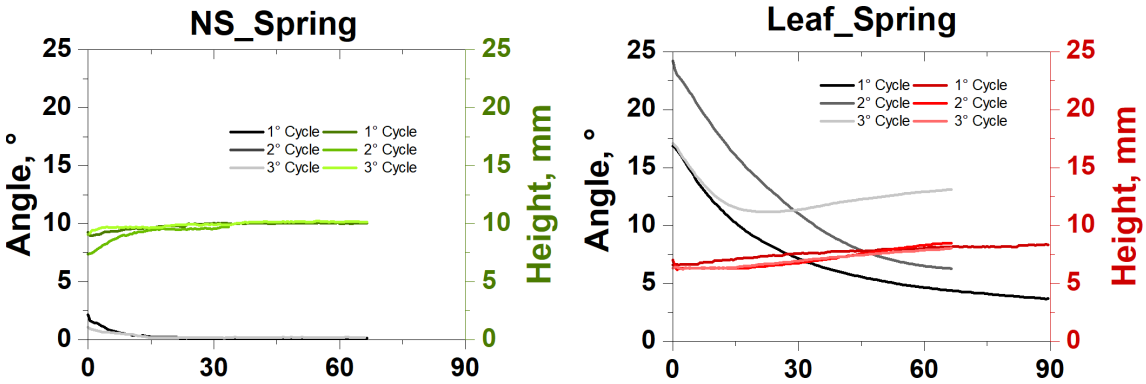


Figure 4. Angle and height recovery 3 Cicli

Specifically, the NS_Spring demonstrates a highly effective angle recovery, although the height restoration in the third cycle appears to be limited.

Conversely, the Leaf Spring exhibits an almost constant height recovery across all cycles but struggles more with angle recovery.

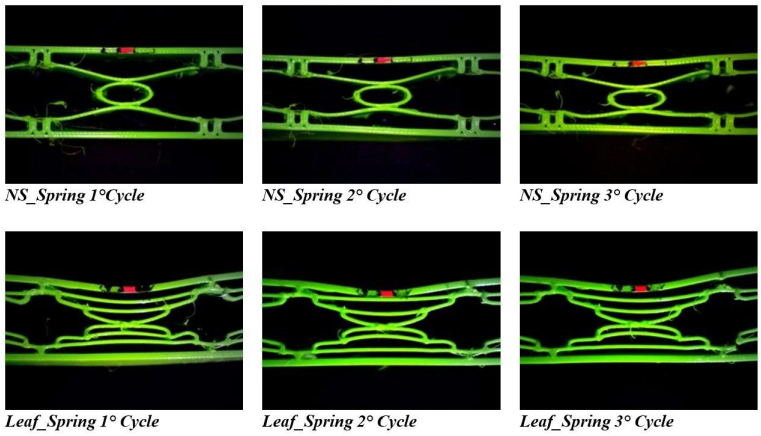


Figure 5. Visual analysis of the structures after three cycles

Energy Absorption – shape recovery hot air

The energy absorption was measured using the specific energy absorption (SEA) parameter [28], which represents the ratio between the energy absorbed during the bending test and the mass of the structure. Figure 6 presents the average energy absorption values, showing that the Leaf_Spring structure exhibits a higher energy absorption capacity, with values ranging from 194 mJ/g in the first cycle to 112.3 mJ/g in the third cycle. In contrast, the NS_Spring structure demonstrates lower energy absorption compared to the Leaf_Spring. However, it shows a moderate energy reduction of approximately 32%, due to its more limited plastic deformation. In contrast to previous studies focusing on compression tests [10,12,16], the results show that the Leaf_Spring structure, thanks to its symmetrical and flexible geometry, is suitable for repeated cycles without obvious damage up to the third cycle. The energy absorbed remains above 100 mJ/g, making it suitable for cyclic applications such as reusable packaging or active devices.

Materials Research Proceedings 57 (2025) 208-215 https://doi.org/10.21741/9781644903735-24

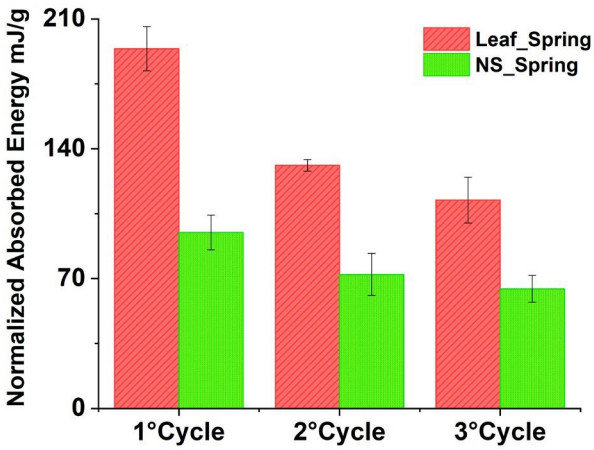


Figure 6. Energy Absorption with Recovery Using Hot Water

Leaf_Spring Energy Absorption – Comparison in shape recovery water/hot air

Figure 7 shows the methodology used for stress cycles (a), the comparison of absorption energy between water and hot air (b) and a visual analysis of the structure at the end of the third cycle, with recovery by water and hot air. Three stress cycles were usually performed, followed by elastic return and shape recovery, with a warm air recovery following the same principle as hot water. For all three cycles of stress, elastic return and shape recovery, an increase in the absorption energy is observed if the recovery is performed with hot air, with variations of 11% in the first and second cycle and 9% in the third cycle. This behaviour can be explained by the increased mechanical strength of the structure, resulting from a localized rather than global shape recovery.

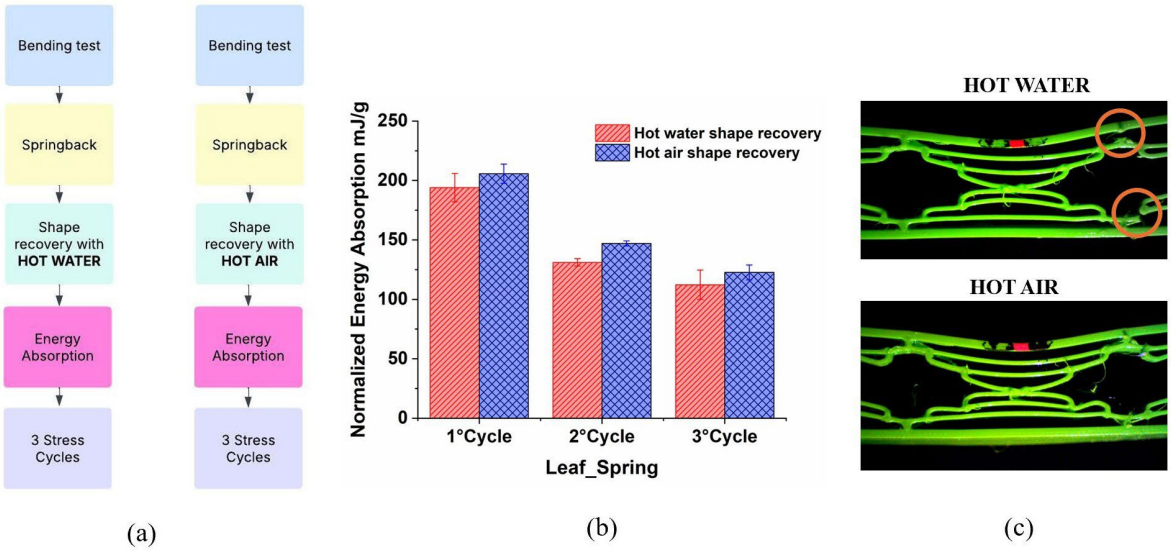


Figure 7. Energy Absorption with Recovery Using Hot Air

Conclusions

The present study analyzed the bending behavior of two cellular structures made of PLA, with different densities, optimized through targeted modifications to improve mechanical resistance and energy absorption capacity. The structures underwent three loading cycles, including bending, elastic recovery, and shape recovery using hot water, to evaluate their mechanical resistance and energy absorption. From the analysis, the NS_Spring, characterized by lower density, exhibited lower mechanical resistance but demonstrated more effective elastic recovery and better shape recovery. In contrast, the Leaf_Spring, inspired by the leaf spring, showed higher mechanical

resistance and better energy absorption. As a result, the Leaf_Spring structure was subjected to three additional loading cycles with shape recovery using hot air, to assess the effect of different thermal stimuli. The hot air stimulus induced localized recovery, unlike hot water, which acts more uniformly. This approach enhanced the structure's performance, increasing energy absorption by approximately 10% on average, while also eliminating the hydrostatic force issue typically associated with hot water recovery.

References

[1] B. Ch. Kholkhoev *et al.*, «4D-printing of mechanically durable high-temperature shape memory polymer with good irradiation resistance», *Applied Materials Today*, vol. 36, p. 102022, feb. 2024. https://doi.org/10.1016/j.apmt.2023.102022
[2] G. Dixit e P. M. Pandey, «Experimental investigations of temperature-sensitive shape memory polymer composites for 4D printing», *Journal of Thermoplastic Composite Materials*, vol. 38, fasc. 2, pp. 537–563, feb. 2025. https://doi.org/10.1177/08927057241254322
[3] W. Xu, Z. Ping, X. Gong, F. Xie, Y. Liu, e J. Leng, «Self-Healing Polymers Coupling Shape Memory Effect», *Langmuir*, vol. 40, fasc. 31, pp. 15957–15968, ago. 2024. https://doi.org/10.1021/acs.langmuir.4c01369
[4] J. Ukwaththa, S. Herath, e D. P. P. Meddage, «A review of machine learning (ML) and explainable artificial intelligence (XAI) methods in additive manufacturing (3D Printing)», *Materials Today Communications*, vol. 41, p. 110294, dic. 2024. https://doi.org/10.1016/j.mtcomm.2024.110294
[5] G. Ehrmann e A. Ehrmann, «3D printing of shape memory polymers», *Journal of Applied Polymer Science*, vol. 138, fasc. 34, p. 50847, 2021
[6] A. Sadraei e S. M. Naghib, «4D printing of physical stimuli-responsive hydrogels for localized drug delivery and tissue engineering», *Polymer Reviews*, vol. 65, fasc. 1, pp. 104–168, 2025.
[7] E. Rezvani Ghomi *et al.*, «The life cycle assessment for polylactic acid (PLA) to make it a low- carbon material», *Polymers*, vol. 13, fasc. 11, p. 1854, 2021.
[8] J. Wu, W. Wang, e X. Gao, «Design and optimization of conforming lattice structures», *IEEE transactions on visualization and computer graphics*, vol. 27, fasc. 1, pp. 43–56, 2019.
[9] W. Tao e M. C. Leu, «Design of lattice structure for additive manufacturing», presentato al 2016 International Symposium on Flexible Automation (ISFA), IEEE, 2016, pp. 325–332.
[10]M. Munford, U. Hossain, S. Ghouse, e J. R. T. Jeffers, «Prediction of anisotropic mechanical properties for lattice structures», *Additive Manufacturing*, vol. 32, p. 101041, mar. 2020. https://doi.org/10.1016/j.addma.2020.101041
[11]H. Yin, W. Zhang, L. Zhu, F. Meng, J. Liu, e G. Wen, «Review on lattice structures for energy absorption properties», *Composite Structures*, vol. 304, p. 116397, gen. 2023. https://doi.org/10.1016/j.compstruct.2022.116397
[12]P. Xu *et al.*, «Compression behavior of 4D printed metamaterials with various Poisson's ratios», *International Journal of Mechanical Sciences*, vol. 264, p. 108819, feb. 2024. https://doi.org/10.1016/j.ijmecsci.2023.108819
[13]Y. Chen, L. Ye, Y. X. Zhang, e K. Fu, «Compression behaviours of 3D-printed CF/PA metamaterials: Experiment and modelling», *International Journal of Mechanical Sciences*, vol. 206, p. 106634, set. 2021. https://doi.org/10.1016/j.ijmecsci.2021.106634
[14]K. K. Dudek, W. Wolak, R. Gatt, e J. N. Grima, «Impact resistance of composite magnetic metamaterials», *Scientific Reports*, vol. 9, fasc. 1, p. 3963, mar. 2019. https://doi.org/10.1038/s41598-019- 40610-w

[15]L. Meng *et al.*, «Impact resisting mechanism of tension–torsion coupling metamaterials», *International Journal of Mechanical Sciences*, vol. 272, p. 109100, giu. 2024. https://doi.org/10.1016/j.ijmecsci.2024.109100
[16]N. Korshunova *et al.*, «Bending behavior of octet-truss lattice structures: Modelling options, numerical characterization and experimental validation», *Materials & Design*, vol. 205, p. 109693, lug. 2021. https://doi.org/10.1016/j.matdes.2021.109693
[17]H. Jiang, H. Ziegler, Z. Zhang, S. Atre, e Y. Chen, «Bending behavior of 3D printed mechanically robust tubular lattice metamaterials», *Additive Manufacturing*, vol. 50, p. 102565, feb. 2022. https://doi.org/10.1016/j.addma.2021.102565
[18]D. Koske e A. Ehrmann, «Infill designs for 3D-printed shape-memory objects», *Technologies*, vol. 9, fasc. 2, p. 29, 2021.
[19]B. B. Samal, A. Jena, S. K. Varshney, e C. S. Kumar, «FDM 4D printing: A low-cost approach of shape programming and assessing the shape memory properties using angle measurement methods in hot water actuation testing apparatus», *Materials Today: Proceedings*, vol. 101, pp. 7–14, gen. 2024. https://doi.org/10.1016/j.matpr.2023.02.038
[20]J. Wu *et al.*, «Multi-shape active composites by 3D printing of digital shape memory polymers», *Scientific Reports*, vol. 6, fasc. 1, p. 24224, apr. 2016. https://doi.org/10.1038/srep24224.
[21]A. Gisario, M. P. Desole, M. Mehrpouya, e M. Barletta, «Energy absorbing 4D printed meta-sandwich structures: load cycles and shape recovery», *The International Journal of Advanced Manufacturing Technology*, vol. 127, fasc. 3, pp. 1779–1795, 2023.
[22]Y. Wang *et al.*, «Photoresponsive triple shape memory polymers with a self-healing function based on poly (lactic acid)/polycaprolactone blends», *Polymer Testing*, vol. 120, p. 107966, mar. 2023. https://doi.org/10.1016/j.polymertesting.2023.107966
[23]D. Koske e A. Ehrmann, «Advanced infill designs for 3d printed shape-memory components», *Micromachines*, vol. 12, fasc. 10, p. 1225, 2021.
[24]J. Jancirani e H. Assarudeen, «A review on structural analysis and experimental investigation of fiber reinforced composite leaf spring», *Journal of Reinforced Plastics and Composites*, vol. 34, fasc. 2, pp. 95–100, gen. 2015. https://doi.org/10.1177/0731684414564477
[25]Q. Zhao, H. J. Qi, e T. Xie, «Recent progress in shape memory polymer: New behavior, enabling materials, and mechanistic understanding», *Progress in Polymer Science*, vol. 49–50, pp. 79–120, ott. 2015. https://doi.org/10.1016/j.progpolymsci.2015.04.001
[26]Y. Wu, Y. Han, Z. Wei, Y. Xie, J. Yin, e J. Qian, «4D Printing of Chiral Mechanical Metamaterials with Modular Programmability using Shape Memory Polymer», *Advanced Functional Materials*, vol. 33, fasc. 52, p. 2306442, 2023. https://doi.org/10.1002/adfm.202306442
[27]A. Rajput, M. R. Sunny, e A. Sarkar, «Optimization of honeycomb parameters of sandwich composites for energy and specific energy absorption using particle swarm optimization», *Marine Structures*, vol. 92, p. 103498, nov. 2023. https://doi.org/10.1016/j.marstruc.2023.103498
[28]Y. Ji, Z. Gao, W. Chen, H. Huang, M. Li, e X. Li, «Study on the deformation mode and energy absorption characteristics of a corner-enhanced biomimetic spider web hierarchical structure», *Thin- Walled Structures*, vol. 199, p. 111810, giu. 2024. https://doi.org/10.1016/j.tws.2024.111810

Materials Research Proceedings 57 (2025) 216-224 https://doi.org/10.21741/9781644903735-25

From design to reality: Improving multimaterial powder bed fusion laser melting additive manufacturing via in-situ monitoring

Stefania Cacace[1], Matteo Bugatti[1], Bianca Maria Colosimo[1]

[1]Dipartimento Di Meccanica, Politecnico di Milano, Via La Masa 1, 20156, Milano, Italy

Keywords: Additive Manufacturing, Manufacturing Materials, Monitoring

Abstract. Multimaterial additive manufacturing enables the fabrication of components that integrate materials with distinct properties, unlocking unprecedented opportunities for the optimization of functionally integrated mechanical parts. Combined with the design flexibility of additive manufacturing, this capability allows for the creation of innovative solutions tailored to specific performance requirements. A novel platform for multimaterial Powder Bed Fusion – Laser Melting (PBF-LM) has been recently presented with the aim of depositing up to three materials on the same layer to achieve multimaterial products. Despite its unprecedented potential, multimaterial LPBF brings several challenges to achieve high-quality components without flaws or defects. This study leverages real-time process monitoring to aid process parameter optimization for multimaterial LPBF, with a special focus on combining steel and copper alloys for space and energy applications.

1. Introduction

The advancement of multi-material additive manufacturing has opened new possibilities for fabricating high-performance components by combining materials with complementary properties in a single build [1]. Multi-material components, such as bimetallic structures and functionally graded materials (FGMs), enable the optimization of mechanical, thermal, and electrical properties at specific locations, addressing limitations of individual materials while enhancing overall functionality [2].

Among the various additive manufacturing (AM) technologies, Powder Bed Fusion - Laser Melting (PBF-LM) has emerged as a promising approach for producing multi-material structures with complex geometries that are challenging or impossible to achieve using conventional methods like casting [3], welding [4], and powder metallurgy [5].

These traditional manufacturing techniques for multi-material components are constrained by geometric limitations and require extensive post-processing [6]. In contrast, PBF-LM provides design freedom, allowing for intricate and optimized multi-material structures with minimal material waste [7].

This capability is particularly advantageous in aerospace applications, where weight reduction and thermal management are critical. For instance, high-performance heat exchangers can benefit from the integration of materials like CuCrZr, which offers excellent thermal conductivity, with high-strength alloys such as Inconel 718 (IN718), commonly used for its oxidation and fatigue resistance [8].

Despite its potential, multi-material PBF-LM presents several challenges, particularly in managing the interface between dissimilar materials. The significant differences in thermophysical properties between metals such as IN718 and CuCrZr lead to issues like differential thermal expansion, residual stresses, and the formation of brittle intermetallic phases, all of which can result in cracking at the interface [2]. Additionally, the PBF-LM process is prone to typical defects such as porosity, warping, and lack of fusion, which can further compromise mechanical performance.

Content from this work may be used under the terms of the Creative Commons Attribution 3.0 license. Any further distribution of this work must maintain attribution to the author(s) and the title of the work, journal citation and DOI. Published under license by Materials Research Forum LLC.

Materials Research Proceedings 57 (2025) 216-224 https://doi.org/10.21741/9781644903735-25

One major limitation of multi-material PBF-LM is powder cross-contamination, which can alter the chemical composition of the interface and deteriorate part quality. Studies [9] [10] have highlighted the need for effective powder separation strategies to mitigate cross-contamination and enable economically viable multi-material fabrication. Another key challenge is the optimization of process parameters [11] [12], particularly at the interface, to ensure defect-free bonding and robust mechanical properties.

Given the complexity of multi-material PBF-LM, real-time monitoring techniques have been explored to improve process control and defect detection [13] [14] [15] [16]. Optical and thermal monitoring systems have been employed to track layer-wise variations in melt pool dynamics, powder distribution, and defect formation. In-situ monitoring provides valuable data that can be leveraged for adaptive process optimization, enabling faster calibration of laser parameters and enhancing the reproducibility of high-quality multi-material builds.

This work focuses on the fabrication of IN718-CuCrZr multi-metallic structures using PBF-LM, with a specific emphasis on understanding how different scanning strategies influence thermal profiles measured through in-situ pyrometry. By analyzing the thermal data acquired during the process, we aim to assess the impact of scanning strategies on heat distribution and stability at the material interface. This investigation will provide insights into optimizing processing conditions to enhance interfacial bonding and overall build quality. The findings contribute to the broader effort of refining multi-material PBF-LM for high-performance applications.

2. Materials and methods

2.1 Multi-material deposition system

To implement a multi-material PBF-LM process, an Aconity MIDI+ machine is used with an integrated Aerosint deposition system. The

Table 1. Aconity MIDI+ machine specifications.

Parameter	**Value**
Laser emission wavelength [nm]	1070
Maximum power [W]	400
Laser spot size [μm]	80
Build volume	Ø 100 mm x H 250 mm

The Aerosint commercial Selective Powder Deposition (SPD) system can simultaneously deposit up to three powders on a single layer. The operation of the recoating system is schematized in Figure 1.

The powder is stored in hoppers located above the drums, with each drum dedicated to a specific material. Each hopper holds 1L of powder. A thin layer of powder is deposited onto the drums, which are covered by a fine mesh. The powder remains on the drum surface due to a slight under-pressure, controlled by a process parameter called suction pressure. Localized deposition of powder onto the platform is achieved by ejecting inert gas through the mesh, regulated by the ejection pressure parameter.

The required ejection and suction pressures vary depending on the density of each material. These parameters must be carefully adjusted to prevent the powder from either falling uncontrollably from the drums or remaining adhered to them. The height of the deposited powder layer is set by adjusting the scraping blade to the desired value. The recoater enables the deposition of three-material patterns with an in-plane resolution of 300 × 300 μm [17]. For the present experiment, only two materials were used.

Materials Research Proceedings 57 (2025) 216-224 https://doi.org/10.21741/9781644903735-25

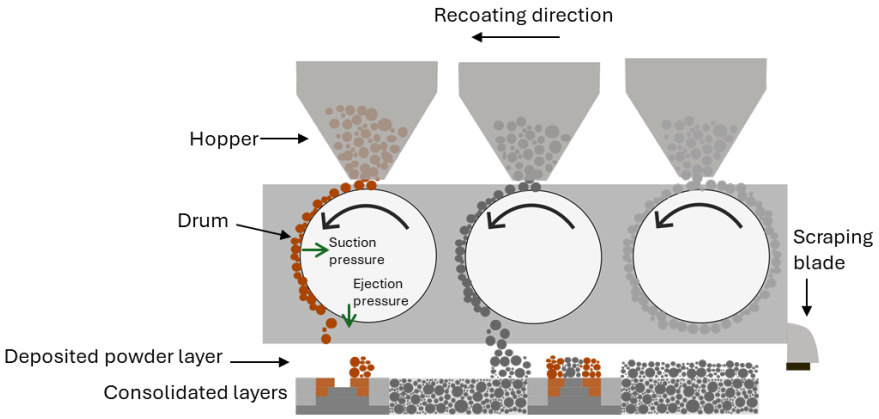


Figure 1. Schematization of Aerosint Selective Powder Deposition system.

2.2 Powders

The starting raw materials are spherical Inconel 718 powders from Mimete Srl (Italy) and CuCrZr alloy from m4p material solutions GmbH (Austria).

The CuCrZr powder was sieved using a mesh size of 32 µm, to obtain a particle size distribution coherent with the suggestion of Aerosint and allow a better recoating quality during the process. The IN718 powder was used as received with a PSD between 18 – 48 µm. The PSD of the CuCrZr powder after sieving is 16-34 µm. The PSD was measured using Morphologi G4 automatic microscope.

2.3 Design of the experiment

One of the main challenges in multi-material additive manufacturing is optimizing the interface surface. This paper investigates the influence of the scan strategy, designing four different scanning patterns to assess their effect on interface surface quality.

The specimens are thin walls measuring 3 mm in width, 20 mm in length and 5 mm in height, each consisting of two materials, CuCrZr and IN718, with each material occupying a width of 1.5 mm.

IN718 and CuCrZr have different optimal process parameters; therefore, to enhance their compatibility, a compromise must be found between the volumetric energy density (VED) used when processing the interface (Table 2). However, to process both materials simultaneously, the hatch distance and layer thickness must be set to the same values. In this study, these parameters were fixed at 0.1 mm and 0.04 mm, respectively. The layer thickness value is the one suggested by Aeronsit for multi-material deposition.

Table 2. Optimal VED for IN718 and CuCrZn when processed individually.

	IN718	**CuCrZr**
Optimal VED [J/mm^3]	107	286
Power [W]	150	400
Scan speed [mm/s]	350	
Hatch distance [mm]	0.1	
Layer thickness [mm]	0.04	

Materials Research Proceedings 57 (2025) 216-224 https://doi.org/10.21741/9781644903735-25

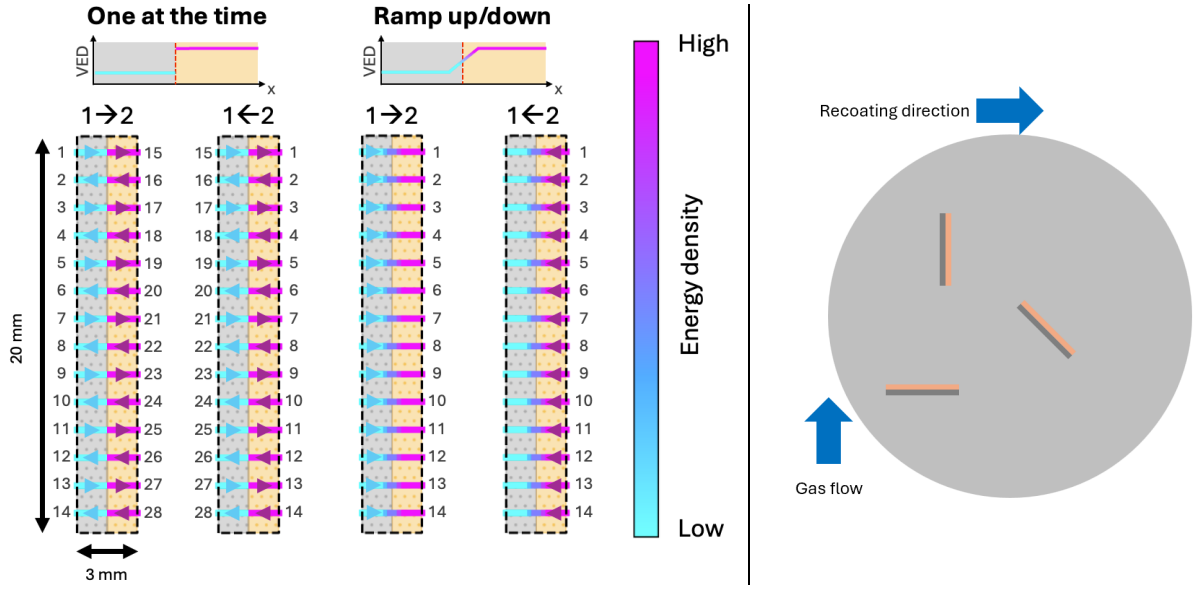


Figure 2. Left: Four scanning strategies involved in the experiment. Grey colour indicates IN718 and yellow indicates CuCrZr alloy. The scan lines colours refer to the VED (blue lower VED and purple higher VED) with the scan order and track direction. Right: position of the specimens.

The four scan strategies are indicated here:

1. *One at the time*:
   a) In the first pattern, IN718 is scanned first using its optimal VED then CuCrZn is processed at the optimal VED.
   b) In the second pattern, CuCrZn is processed at its optimal VED and then IN718 is processed at the optimal VED
2. *Ramp up/down*:
   a) Here the laser power is adjusted in four steps along the scan lines, increasing from low VED to high VED as the laser moves from IN718 to CuCrZn.
   b) The same strategy was tested in the opposite direction, where the laser power decreases to transition from high VED (CuCrZn) to low VED (IN718).

The optimal VEDs are the ones indicated in Table 2. The “one at the time” scanning strategies are commonly used in multi-material PBF-LM systems; however, they exhibit certain drawbacks. Specifically, heat is not distributed homogeneously between the two materials, which may lead to thermal stress, cracks and deformations in the parts.

The “ramp up/down” scanning strategy is an innovative solution enabled by the control system of the Aconity MIDI+. We designed this strategy to (i) increase productivity and (ii) improve the interface surface quality.All hatches are kept perpendicular to the interface between the two materials.

To investigate the potential influence of position relative to gas flow and deposition patterns, the specimens are placed on the building platform at different angles. The building platform consists of an AISI 316L plate with a diameter of 100 mm.

2.4 Monitoring setup

The on-axis dual pyrometer installed on the Aconity MIDI+ was employed for monitoring each of the four scanning strategies. The main acquisition parameters and specifications are reported in Table 3.

Materials Research Proceedings 57 (2025) 216-224 https://doi.org/10.21741/9781644903735-25

Table 3. On-axis Dual Pyrometer

Sensor type	2 x fiber coupled pyrometers
Spectral range	Pyrometer 1: 1,45 - 1,7 µm
	Pyrometer 2: 2,00 - 2,2 µm
Measuring range	500 - 2500 °C
Frame rate	100 kHz

Assuming the emissivity of the two materials do not change widely in the spectral ranges of the two pyrometers, the dual pyrometer setup allows to measure the temperature in the ≈ 400 x 400 µm region around the laser through the following equation:

$$T = \left(\frac{1}{\lambda_2} - \frac{1}{\lambda_1}\right) \frac{h \cdot c}{k \ln\left(\frac{\lambda_1^5}{\lambda_2^5}\right)}$$

Where λ_1 and λ_2 are the wavelengths of the two pyrometers, h is the Planck's constant, k is the Boltzmann constant, and c is the speed of light.

3. Results and discussion

The raw sensor readings from the pyrometer were processed to calculate the temperatures. The thermal maps acquired during the print for each of the four scan strategies are shown in Figure 3. From a first visual inspection, it appears that each of the four scan strategies exhibit their own thermal signature, with distinctive characteristics. As expected, the one-at-the-time scanning strategies (Figure 3a-b) show a clear separation between the two materials. The temperature difference reflects the difference in melting temperatures between the two materials. However, the large temperature difference might create undesired thermal stresses and gaps in a critical region such as the interface between the two materials [18]. Interestingly, the scan order between the materials seems to influence the temperature distribution. The temperature difference between In718 and CuCrZr seems less prominent when the In718 layer is printed first. Printing the In718 layer first may bring some heat to the CuCrZr substrate, hence leading to a higher average temperature. On the other hand, when CuCrZr is printed first heat will tend to dissipate quicker, resulting in a "cooler" temperature reading.

The ramp up/down scanning strategies (Figure 3c-d) shows a completely different thermal map from the previous. The introduction of a common hatching pattern with continuous tracks across the interface region results in a more homogeneous heat distribution across the layer. CuCrZr section still tends to show lower temperature values, but temperature differences gradually fade at the interface. Similarly to the "one-at-the-time" scanning strategies, also in this case the order of material seems to affect the heat distribution. When the laser track starts from In718 and the energy density ramps up as it transitions into the CuCrZr region, temperature is on average higher than when the laser starts from CuCrZr and moves into the In718 region.

Materials Research Proceedings 57 (2025) 216-224 https://doi.org/10.21741/9781644903735-25

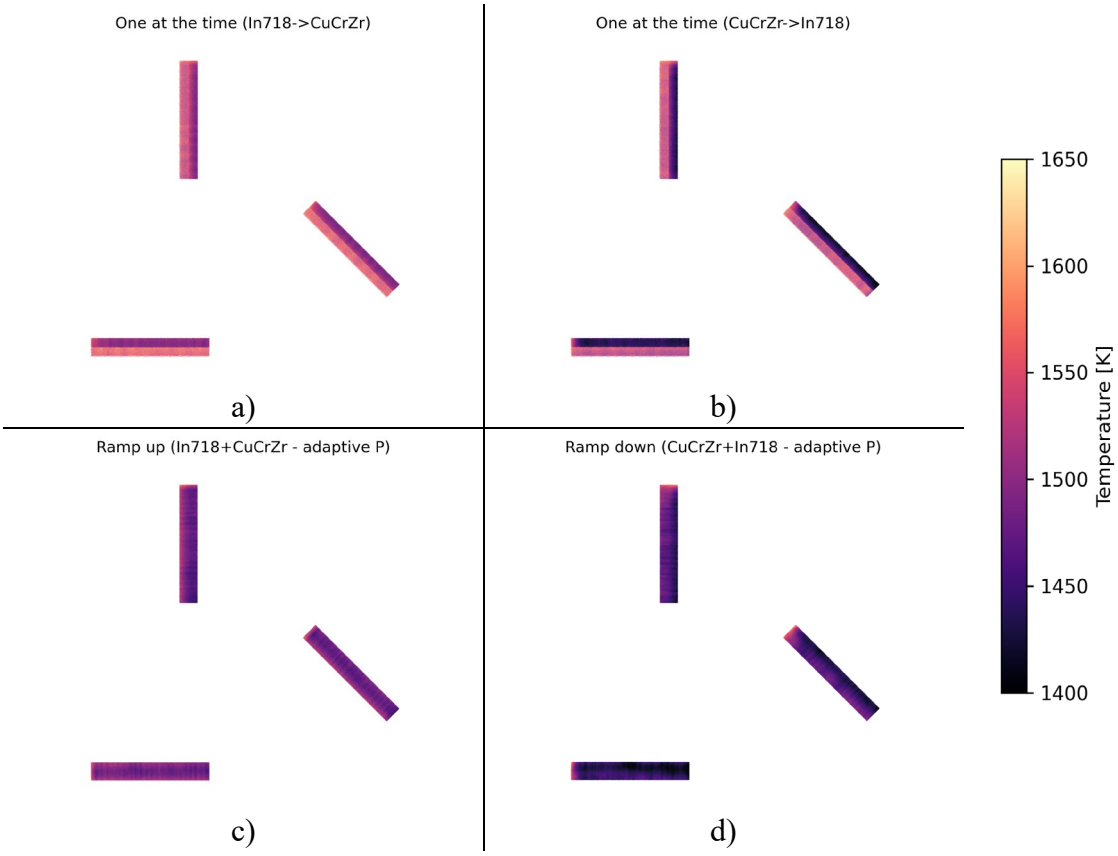


Figure 3. Temperature maps for all the investigated printing strategies.

Since sample orientation does not seem to influence the temperature reading, the temperature profiles of all the tracks as they scan across the thin wall samples were extracted and plotted for each condition after applying a moving average with window size equal to 5. The general trends observed in the thermal maps are confirmed by the temperature profiles shown in Figure 4. Ramp up/down strategies offer a significantly smoother transition from one material to the other at the interface. It is also interesting to notice that, despite the same moving average operation, different strategies seem to show higher/lower noise levels.

Materials Research Proceedings 57 (2025) 216-224 https://doi.org/10.21741/9781644903735-25

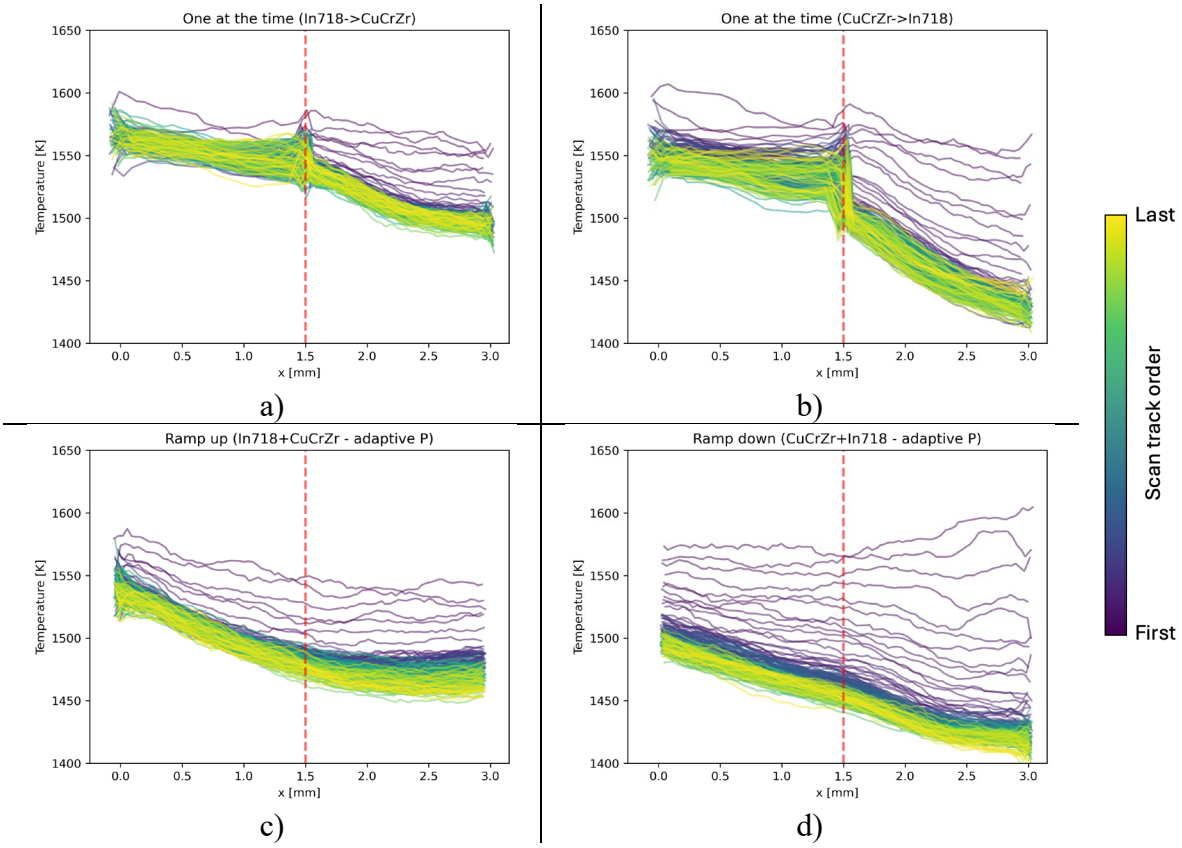


Figure 4. Temperature profiles of the individual tracks across the thickness of the sample. Dark lines indicate first scanned tracks; yellow lines indicate last scanned tracks. The red dashed line marks the position of the interface between In718 (left) and CuCrZr (right).

All scan strategies exhibit a clearly transient behavior. The first few tracks of each scan strategy (Figure 4, darker lines) show a higher average temperature compared with the rest of the tracks. This transient effect is more evident in correspondence of the CuCrZr section, where the temperature delta between the first track and the steady-state condition is the largest.

The plots in Figure 4 show that this behavior can involve up to 10-15 of the first hatches, which correspond to roughly 1-1.5mm in length. Although this behavior is present also in standard “one at the time” scanning strategies, where materials are printed independently, the effect of this transitory state on the quality of the print should be carefully assessed.

4. Conclusions

Multimaterial 3D printing offers unprecedented possibilities for optimization and functional integration of mechanical components. However, issues such as porosity, cracking, element segregation are common at the interface of different materials. In-situ monitoring can offer a fresh new look to the problems that typically affect the quality of multimaterial print.

The dual pyrometer monitoring data demonstrates how big an impact scan strategy can make to the thermal signature of the part. While printing one material at the time is the most common way of printing multiple materials, pyrometer data shows that this strategy creates a large temperature discontinuity in the layer. On the other hand, the proposed ramp up/down strategy, which prints the two materials at the same time in a single track by dynamically adjusting the line energy density across the interface, results in smoother temperature transition at the interface. This preliminary work demonstrates the ability to control multimaterial print temperature gradients with advanced scanning strategies.

Future work will focus on characterizing the quality of the samples printed with advanced scan strategies, while studying other strategies with in-situ monitoring to model and improve the quality of multimaterial prints.

Declarations Funding
The research was supported by MICS (Made in Italy – Circular and Sustainable) Extended Partnership and received funding from the European Union Next-GenerationEU (PIANO NAZIONALE DI RIPRESA E RESILIENZA (PNRR) – MISSIONE 4 COMPONENTE 2, INVESTIMENTO 1.3 – D.D. 1551.11-10-2022, PE00000004).

Competing interest
The authors declare that they have no known competing financial interests or personal relationships that could have appeared to influence the work reported in this paper.

References

[1] A. Kavousi Sisi, D. Ozherelkov, S. Chernyshikhin, I. Pelevin, N. Kharitonova, and A. Gromov, "Functionally graded multi-materials by laser powder bed fusion: a review on experimental studies," *Prog. Addit. Manuf.*, Aug. 2024. https://doi.org/10.1007/s40964-024-00739-1

[2] D. Wang *et al.*, "Recent progress on additive manufacturing of multi-material structures with laser powder bed fusion," *Virtual Phys. Prototyp.*, vol. 17, no. 2, pp. 329–365, Apr. 2022. https://doi.org/10.1080/17452759.2022.2028343

[3] C. Locke *et al.*, "Compound Casting of Aluminum with Sheet Steel in 3D Sand Casting Using an Inductive Heating System," *Metals*, vol. 13, no. 2, Art. no. 2, Feb. 2023. https://doi.org/10.3390/met13020354

[4] D. Wallerstein *et al.*, "Recent Developments in Laser Welding of Aluminum Alloys to Steel," *Metals*, vol. 11, no. 4, p. 622, Apr. 2021. https://doi.org/10.3390/met11040622

[5] M. Hamamcı, F. Nair, and A. A. Cerit, "Microstructural and mechanical characterization of functionally graded Fe/Fe2B (Fe/B4C) materials fabricated by in-situ powder metallurgy method," *Ceram. Int.*, vol. 49, no. 11, pp. 18786–18799, Jun. 2023. https://doi.org/10.1016/j.ceramint.2023.02.259

[6] C. Wei and L. Li, "Recent progress and scientific challenges in multi-material additive manufacturing via laser-based powder bed fusion," *Virtual Phys. Prototyp.*, vol. 16, no. 3, pp. 347–371, May 2021. https://doi.org/10.1080/17452759.2021.1928520

[7] A. Bandyopadhyay and B. Heer, "Additive manufacturing of multi-material structures," *Mater. Sci. Eng. R Rep.*, vol. 129, pp. 1–16, Jul. 2018. https://doi.org/10.1016/j.mser.2018.04.001

[8] L. Zhang, P. Dong, Y. Zeng, H. Yao, and J. Chen, "Additive manufacturing of Inconel 718/CuCrZr multi-metallic materials fabricated by laser powder bed fusion," *Addit. Manuf.*, vol. 92, p. 104377, Jul. 2024. https://doi.org/10.1016/j.addma.2024.104377

[9] M. Montazeri, R. Yavari, P. Rao, and P. Boulware, "In-Process Monitoring of Material Cross-Contamination Defects in Laser Powder Bed Fusion," *J. Manuf. Sci. Eng.*, vol. 140, no. 11, p. 111001, Nov. 2018. https://doi.org/10.1115/1.4040543

[10] M. Schneck, M. Horn, M. Schmitt, C. Seidel, G. Schlick, and G. Reinhart, "Review on additive hybrid- and multi-material-manufacturing of metals by powder bed fusion: state of

technology and development potential," *Prog. Addit. Manuf.*, vol. 6, no. 4, pp. 881–894, Dec. 2021. https://doi.org/10.1007/s40964-021-00205-2

[11] K. Chen *et al.*, "Selective laser melting 316L/CuSn10 multi-materials: Processing optimization, interfacial characterization and mechanical property," *J. Mater. Process. Technol.*, vol. 283, p. 116701, Sep. 2020. https://doi.org/10.1016/j.jmatprotec.2020.116701

[12] C. Wei *et al.*, "Cu10Sn to Ti6Al4V bonding mechanisms in laser-based powder bed fusion multiple material additive manufacturing with different build strategies," *Addit. Manuf.*, vol. 51, p. 102588, Mar. 2022. https://doi.org/10.1016/j.addma.2021.102588

[13] P. Posa, V. Errico, A. Angelastro, and S. L. Campanelli, "Interfacial analysis by optical monitoring of layer level multi-material parts fabricated via Powder Bed Fusion–Laser Beam," *Procedia CIRP*, vol. 124, pp. 172–176, 2024. https://doi.org/10.1016/j.procir.2024.08.093

[14] V. Errico, P. Posa, A. Fusco, A. Angelastro, and S. Luisa Campanelli, "Intralayer multi-material structure stainless-steel/nickel-superalloy fabricated via laser-powder bed fusion process," *Manuf. Lett.*, vol. 35, pp. 11–15, Jan. 2023. https://doi.org/10.1016/j.mfglet.2022.11.004

[15] I. Meyer, M. Oel, T. Ehlers, and R. Lachmayer, "Additive manufacturing of multi-material parts – Design guidelines for manufacturing of 316L/CuCrZr in laser powder bed fusion," *Heliyon*, vol. 9, no. 8, p. e18301, Aug. 2023. https://doi.org/10.1016/j.heliyon.2023.e18301

[16] A. Pfaff, S. Schäffer, M. Jäcklein, and F. Balle, "Measuring the Cooling Behavior of Melt Pools in L-PBF by Pyrometry," *Materials*, vol. 16, no. 10, p. 3647, May 2023. https://doi.org/10.3390/ma16103647

[17] "User Manual - Schaeffler Aerosint," Apr. 2024.

[18] T. Schroeder *et al.*, "Transition zone parameter development in multi-material powder bed fusion: a general approach," *Prog. Addit. Manuf.*, vol. 9, no. 3, pp. 613–624, Jun. 2024. https://doi.org/10.1007/s40964-024-00663-4

Materials Research Proceedings 57 (2025) 225-233 https://doi.org/10.21741/9781644903735-26

Process capability investigation on the 3D printing technique for hybrid silica-based sands cores

Mukul Ramesh Kumar[1,a] *, Stefania Cacace[1,b] *, Maurizio Chiesa[2,c] *, Daniele Chiesa[2,d] *, Paolo Parenti[1,e] *

[1]Dipartimento di Meccanica, Politecnico di Milano, Via La Masa 1, 20156 (Milano), Italy

[2]Fonder Shell S.r.l., Via Del Santuario 54 – Fraz. Strà Alta Val Tidone, 29031 (Piacenza), Italy

[a]mukul.ramesh@polimi.it, [b]stefania.cacace@polimi.it, [c]mauriziochiesa@fondershell.it, [d]danielechiesa@fondershell.it, [e]paolo.parenti@polimi.it

Keywords: Binder Jetting (BJ), Additive Manufacturing, Casting Sand, Density

Abstract. Sand Binder Jetting is one of the most important innovations that foundry field experienced in recent years. One of the main challenges of Binder Jetting consists in the handling of the large machine volumes and in the consequent tendency to show building box inhomogeneity, in terms of performance and quality of the printed pieces. This paper presents a process capability study of an industrial sand printer, used in the field of cores for the cast iron foundry of hydraulic valves, with a focus on the part dimensional accuracy and mechanical resistance (bending strength). Printing orientation of the parts, as well as their positioning inside the building box, are considered as factors of the investigations. Results show that the printing direction is the most impactful parameters, whereas the Z oriented parts show less dimensional accuracy and the weakest mechanical resistance. XY location in the layer is also seen to vary the parts resistance, more than the parts accuracy. Part density varies by about 20% while their bending resistance of about 30% in the building box. Expressions of an existing correlation between parts resistance and part density are observed, but these are not strong enough to justify all of the observed results.

1. Introduction

With the advancement of Industry 4.0 and hybrid manufacturing the integration of additive manufacturing (AM) into casting processes has gained momentum. Foundries can now overcome traditional limitations in the sand moulds and cores production, by producing highly intricate components directly from digital models through Binder Jetting (BJ) technique [1]. This process enables the rapid production of high-quality, complex sand molds and sand cores tailored for improved casting outcomes [2]. Compared to conventional sand mold fabrication, BJ molds can achieve weight reductions of up to 33% [1] and contribute to sustainable production by cutting resin consumption by approximately 50% [3],[4]. Along with the above benefits, BJ printing presents challenges. The reduction in resin content comes with a trade-off, leading to reduced core strength compared to standard manufacturing techniques, such as blown method. This makes resin selection a crucial factor in determining both structural integrity and thermal resistance [3],[5],[6],[7]. On the other side, mechanical consistency and dimensional precision, particularly when large build boxes are employed to meet high production demands, are additional aspects that requires attention. In this process, binder droplets infiltrate compacted sand layers primarily through capillary action [8], yet variations in sand compaction can lead to inconsistencies in local binder saturation and adsorption, ultimately affecting the uniformity of BJ sand parts [9],[10]. Furthermore, large build boxes introduce additional variability in printed core properties, complicating efforts to systematically evaluate machine performance across different regions of the build chamber. Beyond these aspects, numerous process parameters, including sand type, particle distribution, recoating velocity, layer thickness, activator concentration, and binder

Content from this work may be used under the terms of the Creative Commons Attribution 3.0 license. Any further distribution of this work must maintain attribution to the author(s) and the title of the work, journal citation and DOI. Published under license by Materials Research Forum LLC.

Materials Research Proceedings 57 (2025) 225-233 https://doi.org/10.21741/9781644903735-26

saturation, can further contribute to variations in thermo-mechanical behaviour of the sand cores [2],[3],[11].

Therefore, assessing the dimensional accuracy and mechanical reliability of BJ printed cores, a thorough assessment of machine performance and process stability is essential [3].

This study focuses on evaluating the homogeneity of an industrial BJ printer's build box by analysing the dimensional consistency of printed cores, as well as their density and mechanical behaviour under bending loads. The paper is organized as follows: Section 2 introduces the Binder Jetting industrial system used for the experimentation and the build box homogeneity characterization approach. Section 3 presents the experimental assessment of mechanical strength and dimensional uniformity through homogeneity analysis. Section 4 summarizes key findings and provides recommendations for future research.

2. Material and Methods

2.1 Sand Binder Jetting Machine

ExOne S-Max Pro 3D system was used to print the tested specimens, **Figure 1**. The printer has a building box of 1260 Liters (1.8 m x 1 m x 0.7 m). As the main objective of this work is to study the effect of different setup configurations on the homogeneity of sand cores properties, the printing parameters of the BJ process were kept constant (basing on previously performed printing tests). In particular, the adopted layer thickness was 0.28 mm, the X-resolution was 0.14 mm, the Y-resolution was 0.10 mm, the deposition speed was 155 mm/s. The sand adopted is a mixture of Silica and synthetic ceramic sand. The binder used is a Furan-based resin, commonly employed in 3D sand printing for foundry applications. The percentage of binder used are 1.8%vol, while catalyst is added in 0.1%vol.

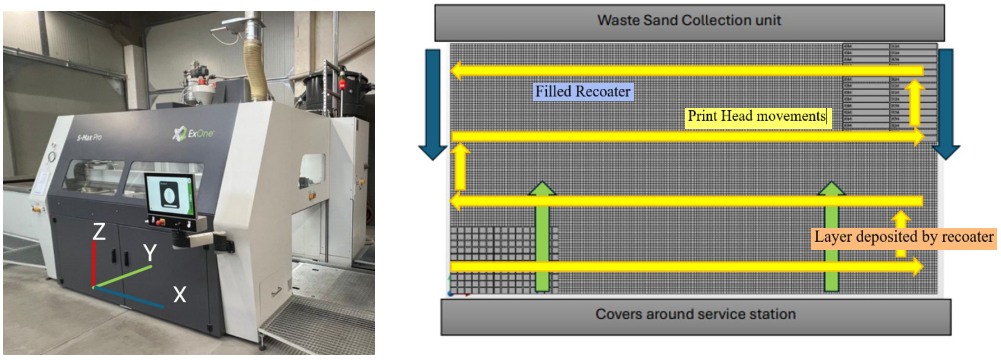


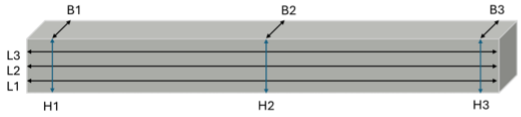
Figure 1 *Binder Jetting printer and top view of its building box (in the XY plane)*

2.2 Experiments description:

2.2.1 Specimens geometry

The printed specimens are rectangular prisms with a square cross-section and nominal dimensions of 172 mm × 22.4 mm × 22.4 mm according to guidelines of the American Foundry Society (AFS) for the bending strength characterization. The specimens were stored 24 hours after printing and then depowered. The dimensional analyses of the parts were conducted between 24h-36h after the printing of the specimens and were executed following the scheme illustrated in **Figure** 2 by adopting multiple vernier caliper measurements. For each specimen, three measurements were taken for each dimension (L, W, B). The mean values of these three measurements per direction were analyzed. Parts were then weighed once with aid of digital balance.

Materials Research Proceedings 57 (2025) 225-233 https://doi.org/10.21741/9781644903735-26



	Specimens printed along X machine	Specimens printed along Z machine
L	X	Z (layering)
B	Y (recoater direction)	Y (recoater direction)
H	Z (layering)	X

Figure 2 *Dimensional Measurements and relation with recoater and printed layer directions.*

2.2.2. Experimental Design

The experiments are designed to establish the homogeneity of the printed specimens in terms of dimensions, density and bending strength. The following factors are considered:

- Part orientation with respect to the printing direction ("Direction") inside the building box
- The vertical distance Z from the platform ("Z position")
- The position inside each layer on the platform XY ("Location")

The levels for each of the varied factors are indicated in **Table 1**.

Table 1 *Factors and levels for the homogeneity experiment*

Factor	Number of levels	Levels
Direction	2 levels	X, Z
Z position	3 levels	Bottom, Middle, Top
Location	5 levels	L1, L2, L3, L4, L5

For each combination of Direction, Z position and Location 5 specimen replicates were printed, therefore the total number of experiments was equal to 150 specimens: 2 Directions x 3 Height x 5 Locations x 5 replicates. All specimens were printed in the same printing job.

2.3 Mechanical Characterization

The Transverse Rupture Strength (TRS) was used as mechanical characterization method to quantify the performances of the cores in different configurations of the building volume. Tests were performed on a Benet Lab equipment at ambient conditions (24°C) by using a three-point bending method after 24h/36h from the printing (to lock the known effect of self-curing time of the cores [12],[13]). The maximum bending force, tackled by the parts, is transformed into TRS value, by considering the resistant cross section. The TRS is estimated with the following formula: $TRS=3LF/2bd^2$ (eq.1) where F is the measured force, L the distance between supports (150 mm), and b and d are the parts' cross-section dimensions.

3 Results

3.1 Dimensional Analysis

In almost all cases, the actual specimen sizes exceed the nominal values of about 0.8-1.2% per direction. **Figure 3** presents boxplots illustrating the deviation of the average dimensions from the nominal values for different Z-positions and orientations. The only undersized dimensions were found on the specimens printed in X and Z direction for the BOTTOM Z-position level, for the breadth and the length direction, respectively. The parts printed in Z direction generally present higher sizing errors than those printed along X direction (except for the Z oriented parts in the MIDDLE Z-position level). This anisotropic behavior confirms what previous works have noticed for sand BJ parts [14],[15]. The error in the length of the Z oriented specimens drops from the TOP

Materials Research Proceedings 57 (2025) 225-233 https://doi.org/10.21741/9781644903735-26

to the BOTTOM Z-position level, where it is almost negligible. The absolute values found are in the same range of previous literature. At the same time, the other dimensions of the Z oriented parts seem not to vary with the Z-position level in the building box. Conversely, the X specimens tend to show variable breadth with the printing level, whereas at the TOP Z-position level the parts seem larger in breadth. Overall, the average parts' height remains almost stable across different Z-positions (but with an overall oversizing error of about 0.8%). To conclude, the average error in Specimen Height is quantified as +0.2 mm, and +0.18 mm, for the X and Z oriented parts respectively. The average error in Specimen Breadth is quantified as +0.06 mm, and +0.23 mm, for the X and Z oriented parts respectively. The average error in Specimen Length is quantified as +0.19 mm, and +0.92 mm, for the X and Z oriented parts respectively.

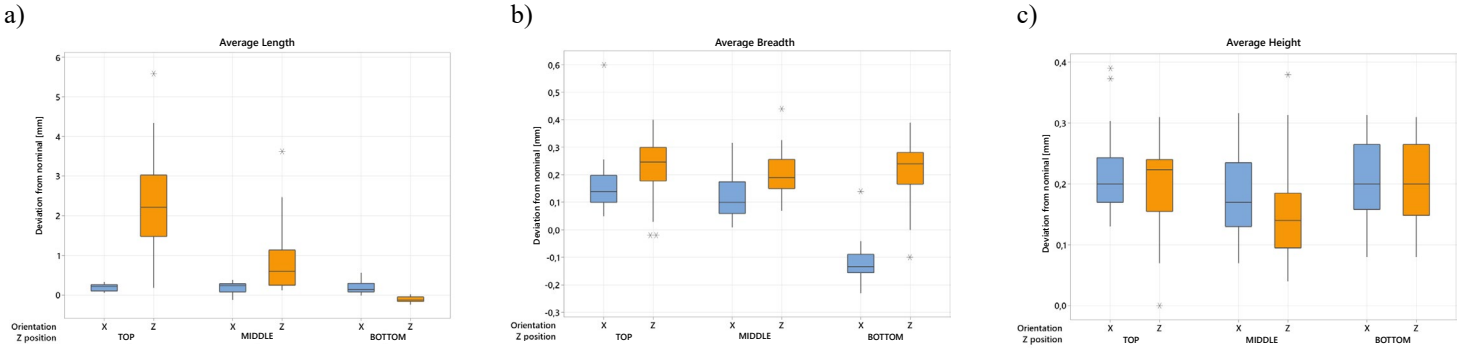


Figure 3. *Box plot of the dimensional deviation from the nominal value for a) length, b) breadth and c) height.*

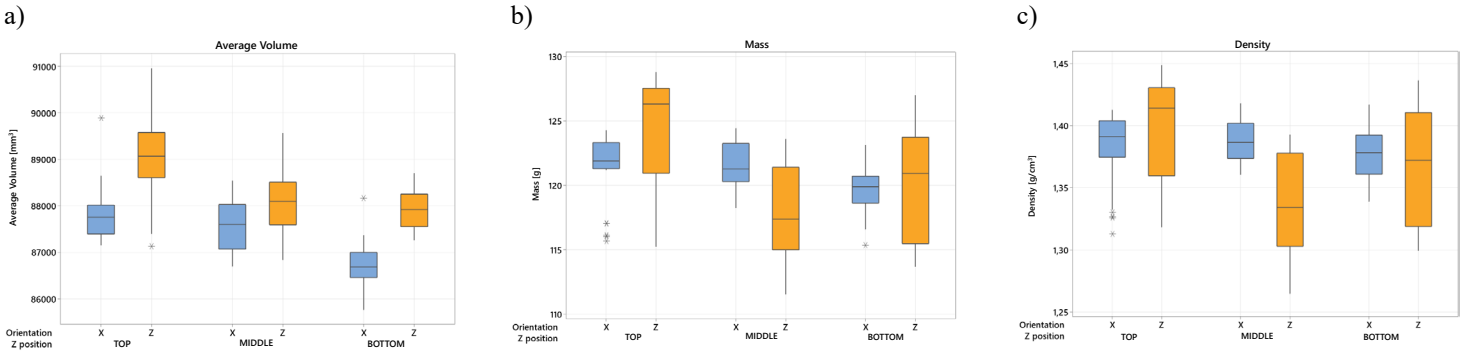


Figure 4 *Box plot of the dimensional deviation from the nominal value for a) Density, b) Average Volume and c) Mass*

Figure 4 shows the Volume, Mass and Density boxplots. It can be observed that the volume of the parts is on average bigger than the nominal of about 1.9% and that the Z-position strongly affects the response (lower volume errors are observed in the BOTTOM plane. Mass property for the parts, is varying in a less clear manner. The mass of the parts printed in Z orientation show much larger variability (about 6.5% in average) than those printed in X direction (in average 2%). This suggests the sequence of layering effect is very much governing the binder adsorption and the sand agglomeration. Parts' densities are affected consequently: larger variability in Z oriented parts is observed with a clear contribution of the Z-position factor.

A statistical analysis was conducted to assess the effects of the varied factors. Since the three dimensions are uncorrelated, three separate linear regression models were estimated. The boxplots indicate that Z-position has a strong influence on the variability of the average length response. Consequently, a weighted model was applied to this response. The weights were computed as the inverse of the estimated variance for each Z-position level, following the equation $\boldsymbol{w_i} = \frac{\mathbf{1}}{\hat{\sigma}_{h_i}}$, eq.2,

where $\hat{\sigma}_{h_i}$ represents the estimated residual variance for each of the three levels (i) of the Z-position factor. The model for height exhibited poor fit (adjusted R^2 around 10%) and was therefore excluded from the summary. In fact, Height dimension remains largely unchanged across different conditions and therefore the average height value can be adequately described by its mean value. Several key findings can be derived from the statistical analysis, summarized in **Table 2.**

- The *py* position has a significant influence, particularly on the Length response.
- The Orientation factor is highly influential for both Length and Breadth responses.

A highly significant interaction is observed between Z-position and Orientation.

Breadth	**Term**	**Estimate**	**Std. Error**	**t-value**	**p-value**	
	(Intercept)	23	0.064211	351,381	< 2e-16	***
	px	-0.003500	0.008706	-0.402	0.68827	
	py	-0.015722	0.008706	-1,806	0.07305	
	py^2	0.029222	0.019467	1,501	0.13554	
	Height	0.037467	0.067435	0.556	0.57936	
	DirectionZ	-0.113422	0.041204	-2,753	0.00668	**
	Height*Direction_Z	0.137133	0.019074	7,190	3.4e-11	***
	$Height^2$	-0.043967	0.016518	-2,662	0.00867	**
Length	**Term**	**Estimate**	**Std. Error**	**t-value**	**p-value**	
	(Intercept)	172.4793	0.481592	358,144	< 2e-16	***
	px	0.009921	0.020196	0.491	0.62401	
	py	0.062740	0.020196	3,107	0.00229	**
	py^2	0.150664	0.045160	3,336	0.00108	**
	Height	-0.427558	0.442730	-0.966	0.33582	
	DirectionZ	2,928,218	0.295401	9,913	< 2e-16	***
	Height_Direction_Z	-1,078,817	0.101174	-10,663	< 2e-16	***
	$Height^2$	0.098100	0.097792	1,003	0.31750	

Table 2 *ANOVA results for the average breadth and length (*** significant factor with p-value < 10-4, ** factor significant with a p-value < 0.01 and * factor significant with a p-value < 0.05. R^2adj = 60.1% for the Breadth. R^2adj = 66.48% for the Length.*

3.2 TRS Homogeneity

In terms of TRS values, the obtained values range from about 50 to 350 N/cm^2. The maximum values measured are in line with previous literature adopting the same printing equipment and binder type, but different sand type

A correlation analysis between the density of the specimens and the resulting TRS value was conducted, **Figure 5**. Five specimens were identified as outliers, due to their significantly lower-than-expected TRS values (these specimens exhibited printing defects). The correlation seems weak, with an R^2 of 29.3%. This indicates that specimen density alone is insufficient to fully describe the overall mechanical behavior of the specimens.

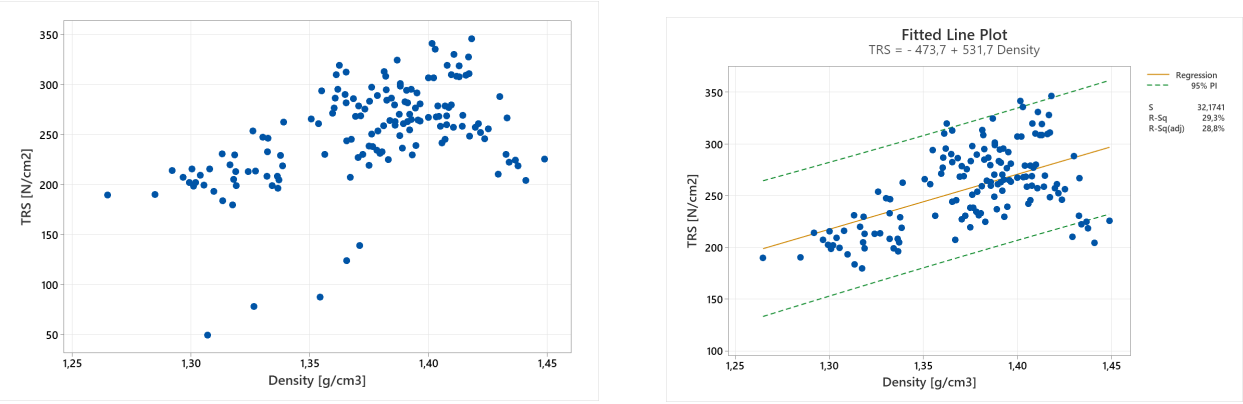
The effects of Location, Z-position, and Orientation on TRS performance were then analyzed. Given the weak correlation between density and TRS, a multivariate regression model was employed to enhance predictive capability by incorporating this relationship. The ANOVA results are presented in **Table 3**.

The low correlation between TRS and density leads to distinct significance structures for each response. For TRS, the most significant effects are attributed to the position on the XY plane (py^2), Orientation, and the interaction between Z-position and Orientation. In contrast, for Density, nearly all factors are significant, with Orientation being the least influential.

To visualize the variation of TRS and Density within the build volume, prediction maps were generated based on the estimated equations. The prediction map for TRS (**Figure 6**) confirms a strong influence of the XY position, as expected. It also highlights that the worst conditions occur at the Top position when specimens are oriented in the Z direction. Conversely, for specimens oriented along the X-axis, the Z-position has a smaller effect. This explains why the interaction

Materials Research Proceedings 57 (2025) 225-233 https://doi.org/10.21741/9781644903735-26

between Z-position and Orientation is significant for TRS: the impact of Z-position depends on how specimens are oriented during the printing.



(A) *(B)*

Figure 5 *Correlation between density and TRS. a) Plot with all of the specimens, b) Correlation analysis, after removing outliers.*

TRS	**Term**	**Estimate**	**Std. Error**	**t-value**	**p-value**	
	(Intercept)	264,689	15,742	16,814	< 2e-16	***
	px	3,608	2,177	1,657	0.09985	
	py	-5,175	2,177	-2,377	0.01886	*
	py^2	19,756	4,774	4,138	6.08e-05	***
	Height	-2,275	16,613	-0.137	0.89130	
	DirectionZ	-30,261	10,358	-2,921	0.00408	**
	Height*Direction_Z	-13,115	4,783	-2,742	0.00692	**
	$Height^2$	1,938	4,071	0.476	0.63488	
Density	**Term**	**Estimate**	**Std. Error**	**t-value**	**p-value**	
	(Intercept)	1,400,275	0.015806	88,590	< 2e-16	***
	px	-0.012209	0.002186	-5,584	1.22e-07	***
	py	-0.010783	0.002186	-4,932	2.32e-06	***
	py^2	0.059017	0.004793	12,312	< 2e-16	***
	Height	-0.075364	0.016681	-4,518	1.34e-05	***
	DirectionZ	0.005305	0.010401	0.510	0.611	
	Height*Direction_Z	-0.010467	0.004802	-2,180	0.031	*
	$Height^2$	0.018428	0.004088	4,508	1.39e-05	***

Table 3 *. ANOVA results for the TRS and density. (*** significant factor with p-value < 10-4, ** factor significant with a p-value < 0.01 and * factor significant with a p-value < 0.05). R^2adj = 62.76 for the TRS. R^2adj = 63.76% for the Density.*

For part density, **Figure 7**, Orientation does not appear to have a significant effect, as the maps remain similar for X and Y orientations at the same Z-position and XY location. However, Z-position is clearly a highly significant factor, with specimen density decreasing as the distance from the platform increases. For both TRS and Density, the py^2 factor is significant, as evident in the influence of the L5 position, which consistently yields different results compared to the corners of the build volume (positions L1, L2, L3, and L4). Consequently, mechanical properties are different at platform edges compared to the center position. These findings indicate that part position within the build volume and orientation can significantly impact the quality of cores produced using the BJ system.

There is a high complexity of the physical phenomena involved in sand BJ printing and many reasons could justify the observed behaviors. Clearly, the bed packing density is a leading factor

Materials Research Proceedings 57 (2025) 225-233 https://doi.org/10.21741/9781644903735-26

that affects the binder adsorption and therefore the binder distribution. A more densely packed sand bed and more resin content in the parts result in higher TRS values, primarily because of increased interlocking among the sand particles within a given area and more resin necking among sand particles, respectively. Loss of Ignition (LOI) testing have been preliminary conducted on few of the tested samples, giving values ranging from 1.85%. This preliminary finding, which agrees with the theoretical binder content adopted, seems to suggest that there were no sensible variations in the actual binder content of the printed parts, excluding the binder content variations from the leading mechanisms, that could have generated anisotropies among the parts. However, further experiments must be carried out to confirm this point. Surely, the adopted hybrid sand, which is composed of two sand types, with different shapes and flowability, is another important factor that can introduce a relevant variability in the powder bed density. This could be the results of powder spreading behavior of the sand mixture (with maybe some powder segregation) and further investigations are required to confirm the importance of this aspect. The much lower values in the TRS and density values, as well as in the geometrical and dimensional accuracy, noticed in the Z-oriented parts is something that requires particular attention in the tested BJ system, which confirms part orientation is a strong factor for the quality of the printing.

All in all, further analyses are required to determine whether the observed anisotropies inside the powder bed also affect other core properties, with respect to studied ones.

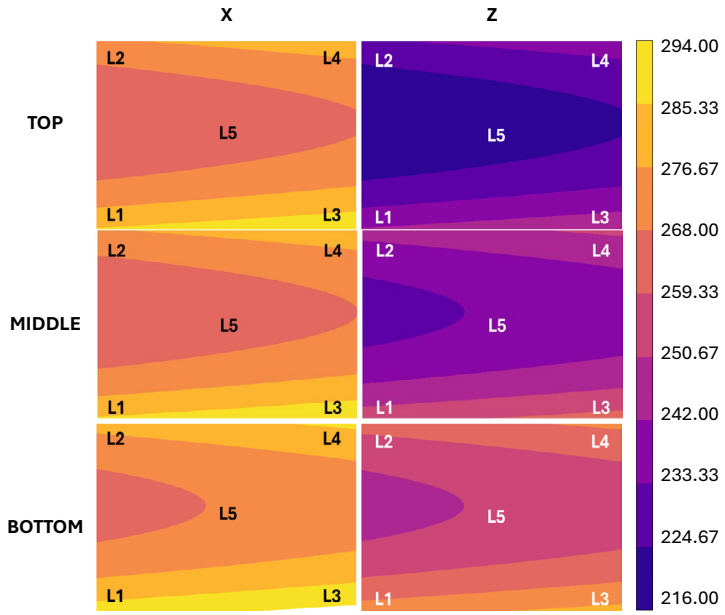


Figure 6 *Prediction map for TRS (N/cm^2) based on the multivariate regression model estimated.*

Materials Research Proceedings 57 (2025) 225-233 https://doi.org/10.21741/9781644903735-26

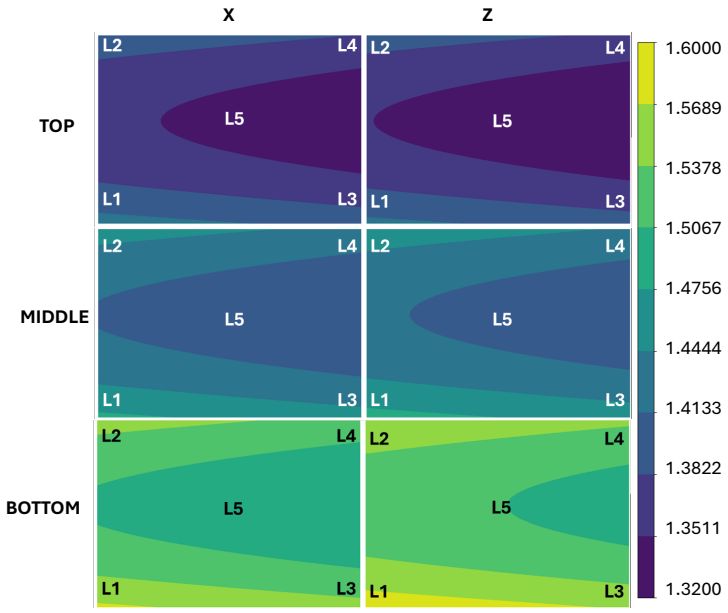


Figure 7 *Prediction map for density (g/cm^3), based on the multivariate regression model estimated.*

5. Conclusions

The analysis confirms that dimensional accuracy and mechanical strength of the horizontally and vertically printed specimens are notably different. This makes the selection of the molds/core orientation in the building box of the BJ machine critical and suggests that this aspect must undergo detailed optimization. With respect to the very few previous literature works that attempt to map the volumetric behavior of the BJ printer, such as [14],[15], this works provide a detailed statistical characterization which improves the robustness of the findings and that can be straightly used to develop advanced compensation algorithms, basing on the predicted map.

The sand BJ process appeared sensitive also to the position on the building box (both XY and Z). Quadratic effects were found on the XY positions, whose causes could be likely attributed to the spreading inhomogeneities caused by the blade recoater mechanism.

The observed variability of the part strength could not be entirely explained by taking into account the variations of the average part density. This suggests that the mechanical response observed could have been led by contributes of local defects inside the printed cores, as a result of the BJ process, or to additional inhomogeneities caused by unstudied factors, such as binder adsorption and distribution or temperature evolution inside the bed. Future dedicated experimental campaigns are needed to further investigate these aspects.

More generally, the applied statistical methodology enables the systematic mapping of all these effects, enabling the possibility of verifying the effect of many other factors - such as sand characteristics or printing parameters - on many other responses (such as cast quality). This can be useful not only for implementing larger process optimization schemes, but also for running condition maintenance routines on the system.

References

[1] Shepler J, Chapman S. ExOne - A Case Study in Optimizing Casting Design Using 3 D Printing. 2017.

[2] Low ZX, Chua YT, Ray BM, Mattia D, Metcalfe IS, Patterson DA. Perspective on 3D printing of separation membranes and comparison to related unconventional fabrication techniques. J Memb Sci 2017; 523:596–613. https://doi.org/10.1016/j.memsci.2016.10.006

[3] Saptarshee Mitra. Experimental and numerical characterization of functional properties of sand moulds produced by additive manufacturing (3D printing by jet binding) in a fast foundry. Ecole nationale supérieure d'arts et métiers- ENSAM, 2019. English. NNT :2019ENAM0043 tel-02466819v2. https://pastel.hal.science/tel-02466819v2

[4] Khandelwal H, Ravi B. Effect of Binder Composition on the Shrinkage of Chemically Bonded Sand Cores. Mater Manufacturing Process 2015; 30:1465–70. https://doi.org/10.1080/10426914.2014.994779.

[5] A. Bobrowski et al., "3D Printed (Binder Jetting) Furan Molding and Core Sands—Thermal Deformation, Mechanical and Technological Properties," Materials, vol. 16, no. 9, p. 3339, Apr. 2023. https://doi.org/10.3390/ma16093339

[6] M. Łągiewka, "Determination of Thermophysical Properties for Selected Molding Sands," Acta Phys. Pol. A, vol. 136, no. 6, pp. 992–995, Dec. 2019. https://doi.org/10.12693/APhysPolA.136.992

[7] J. T. H. Pearce, N. Valun-araya, O. Chantrarasukkasem, and S. Nusen, "Case Studies Experience in Using 3D Sand Printing to Produce Molds for New and Replacement Cast Components," Int. J. Met., Aug. 2024. https://doi.org/10.1007/s40962-024-01426-1

[8] C. Hartmann, J. Silberhorn, P. Erhard, and D. Günther, "On the mechanism of binder migration in furan binder jetting of sand molds and cores," Addit. Manuf., vol. 83, p. 104073, Mar. 2024, https://doi.org/10.1016/j.addma.2024.104073

[9] T. Sivarupan et al., "A review on the progress and challenges of binder jet 3D printing of sand moulds for advanced casting," Addit. Manuf., vol. 40, p. 101889, Apr. 2021, https://doi.org/10.1016/j.addma.2021.101889

[10] H. Miyanaji, S. Zhang, and L. Yang, "A new physics-based model for equilibrium saturation determination in binder jetting additive manufacturing process," Int. J. Mach. Tools Manuf., vol. 124, pp. 1–11, Jan. 2018. https://doi.org/10.1016/j.ijmachtools.2017.09.001

[11] N. Bryant, T. Frush, J. Thiel, E. MacDonald, and J. Walker, "Influence of Machine Parameters on the Physical Characteristics of 3D-Printed Sand Molds for Metal Casting," Int. J. Met., vol. 15, no. 2, pp.361–372, Apr. 2021. https://doi.org/10.1007/s40962-020-00486-3

[12] Saptarshee Mitra & Antonio Rodríguez de Castro & Mohamed El Mansori, The effect of ageing process on three-point bending strength and permeability of 3D printed sand molds, The International Journal of Advanced Manufacturing Technology (2018) 97:1241–1251, https://doi.org/10.1007/s00170-018-2024-8

[13] Anwar N, Major-Gabryś K, Jalava K, Orkas J (2024) Effect of Additives on Heat Hardened Inorganic Solid Foundry Binder. Int J Met 10: https://doi.org/10.1007/s40962-024-01277-w

[14] Shi De-quan, Hou Yin-yu, Gao Gui-li (2023) Effect of printing parameters on properties of 3D printing sand samples. China Foundry 20:553–562. https://doi.org/10.1007/s41230-023-3002-9

[15] Sivarupan T, El Mansori M, Coniglio N, Dargusch M (2020) Effect of process parameters on flexure strength and gas permeability of 3D printed sand molds. J Manuf Process 54:420–437. https://doi.org/10.1016/j.jmapro.2020.02.043

[16] Gao G (2021) Investigation of selected parameters effect on 3D printed sand mold properties through Taguchi method. 3:627–635. https://doi.org/10.1108/RPJ-11-2019-0294

Materials Research Proceedings 57 (2025) 234-241 https://doi.org/10.21741/9781644903735-27

Preliminary study on evaluation of printing parameters for a MEX repair application

Raniero PIRLO[1,a *], Marco LAFIRENZA[1,b *], Maria Grazia GUERRA[1,c], Fulvio LAVECCHIA[1,d], Luigi Maria GALANTUCCI[1,e]

[1]Department of Mechanics, Mathematics and Management of Politecnico Di Bari, Via Orabona 4, 70125 Bari, Italy

[a]r.pirlo@phd.poliba.it, [b]marco.lafirenza@poliba.it, [c]mariagrazia.guerra@poliba.it, [d]fulvio.lavecchia@poliba.it, [e]luigimaria.galantucci@poliba.it

Keywords: Repair, Hybrid Manufacturing, Reverse Engineering

Abstract. Hybrid manufacturing, combining Additive Manufacturing (AM) and Subtractive Manufacturing (SM), represents a promising approach for the repair and upgrade of existing components produced via AM. In this context, repair applications with Material Extrusion (MEX) processes remain largely unexplored. The present work provides a preliminary study on the use of Fused Filament Fabrication (FFF) with a consumer-grade 3D printer as repairing tools for damaged or incomplete parts. While complete reprinting of a component is often considered the most straightforward option, repair can offer significant advantages in terms of material savings, time efficiency, and reduced energy consumption. Additionally, the process enables the integration of new geometries or functionalities, extending the original use of the component. This study sets the basis for MEX repair application by analyzing the printing parameters that have more influence on the repair process in terms of geometric deviation. Results show that the MEX-based repair process is highly dependent on printing temperature and material flow rate.

Introduction

Additive Manufacturing (AM) gained its popularity thanks to the possibility to produce complex parts, which were almost impossible to produce with conventional chip removal technologies [1].

The increasing usage of these technologies is creating new important applications in industrial sectors, which differs from the simple object production. For instance, a new interesting approach enabled by AM is the possibility to repair manufacts to restore their initial conditions after they have reached their end of life [2]. So far, many repair applications have been proposed mainly using metal laser-based AM technologies, such as Laser-Powder Bed Fusion (L-PBF), Laser-Direct Energy Deposition (L-DED) and cold spray as highlighted in [3,4]. This can be justified because of the relevant industrial application in which these technologies are exploited, such as aerospace, automotive and biomedical sectors.

According to the authors knowledge, despite the wide interest in repairing applications based on metal AM technologies, MEX-based repair application remains largely unexplored. Lately, many important applications in different industry fields have been found based on high value-added PLA-based composites and nanocomposites parts. A hybrid MEX process would guarantee better surface quality, consequently increasing the degree of interaction between fillers and matrix (PLA). This would exponentially improve the quality of the filament itself compared with the simple PLA filament [5].

An example of repair for this technology has been reported in a recent study, where FFF was employed to repair PLA specimens using tough PLA as the filler material. This study emphasized the importance of optimizing key parameters, such as infill pattern, infill percentage, and raster angle, to achieve optimal mechanical performance and efficiency in the repair process [6].

Content from this work may be used under the terms of the Creative Commons Attribution 3.0 license. Any further distribution of this work must maintain attribution to the author(s) and the title of the work, journal citation and DOI. Published under license by Materials Research Forum LLC.

Materials Research Proceedings 57 (2025) 234-241 https://doi.org/10.21741/9781644903735-27

A repair process involving additive manufacturing technologies and traditional chip removal technologies that has garnered significant attention in the literature involves the removal of the defect through CNC, modelling of the seat for the filler material and subsequent filling of the removed volume. Each step is interspersed with inspection using techniques such as laser scanning (LiDAR, triangulation, time-of-flight), optical interferometry, and photogrammetry [7]. This is of particular pertinence for multi-step Hybrid Additive Manufacturing (HAM) processes that require iterated workpiece positioning.

This work proposes a preliminary study on the printing parameters influence in a MEX repair application. The widespread adoption of MEX technology is gaining more and more attention also because of the increasing materials that can be processed. In this regard, it is important to highlight that also metals filaments can be extruded to produce metal components, along with ceramics and copper. Due to the lack of knowledge of repairing solutions related to MEX, this work sets the basis for further repair applications. As starting approach, it is important to understand how the main printing parameters influence the repair process. For this reason, the parameters under evaluation will be the printing temperature, the flow rate and the influence of the fan on the overall geometric deviation of the repaired part compared with the nominal one. In section 2 the material and method paragraph will be discussed, by explaining the printing set-up, the artefacts used and the design of experiment. After that the results will be discussed in section 3, showing the influence of each of the considered printing parameters on the final quality of the repaired part. Finally, in section 4, the conclusion will be presented.

Material and Method

This section will describe the individual machines that participated in the investigation and their use in the printing and monitoring setup developed, and for the collection of other process quality data.

Instruments and Setup. The setup and procedure for monitoring the material deposition inside the slot is similar to that presented in [8], with the only difference being the 3D printer. The printer used for producing the specimens of this work has been a Prusa MK4 with a custom profile for polylactic acid (PLA). The Prusa MK4 is a highly accurate and repeatable printer, with a declared positional error of ±0.1 mm on the X/Y axes and 0.05 mm (50 μm) on the Z axis, while ensuring repeatability of ±0.02 mm on X/Y and ±0.01 mm on Z. This ensured that the outputs were not significantly influenced by the system, given their size. To facilitate monitoring process, it was decided to print the artifacts with a white PLA. The artifact was processed in Prusa Slicer v.2.7.

The filling phase was followed by the dimensional analysis of the specimens in the proximity of the filled slot to observe the amount of material surfacing. The Zeiss GOM ATOS Q is an advanced blue light 3D scanner designed for precise industrial measurements. It utilizes structured light technology to capture high-resolution 3D data with exceptional detail. The system projects a structured pattern onto the surface and analyzes deformation to generate accurate point clouds. The instrument was equipped with the 100mm lens, that guarantees high precision and fine detail on small to medium-sized parts. ATOS Q offers accuracy of up to 0.005mm (VDI 2634), making it ideal for quality control. The acquisition of the specimens took place after each print has been removed from the printing bed. The measurements were obtained with Zeiss Optical Inspect 2023.

Artifact and Strategy description. The investigation outlined in this study involved the fabrication of polymer 3D-printed (MEX) artifacts that incorporated a tapered slot in their center. The design of these artifacts was chosen to emulate the post-removal scenario of a defect Fig. 1a. The draft angle (50°) and slot depth (1mm) were determined based on the tapered surface and the exposed length of the nozzle. The dimensions of both the artifact and the feature are provided in the Fig. 1b.

Materials Research Proceedings 57 (2025) 234-241 https://doi.org/10.21741/9781644903735-27

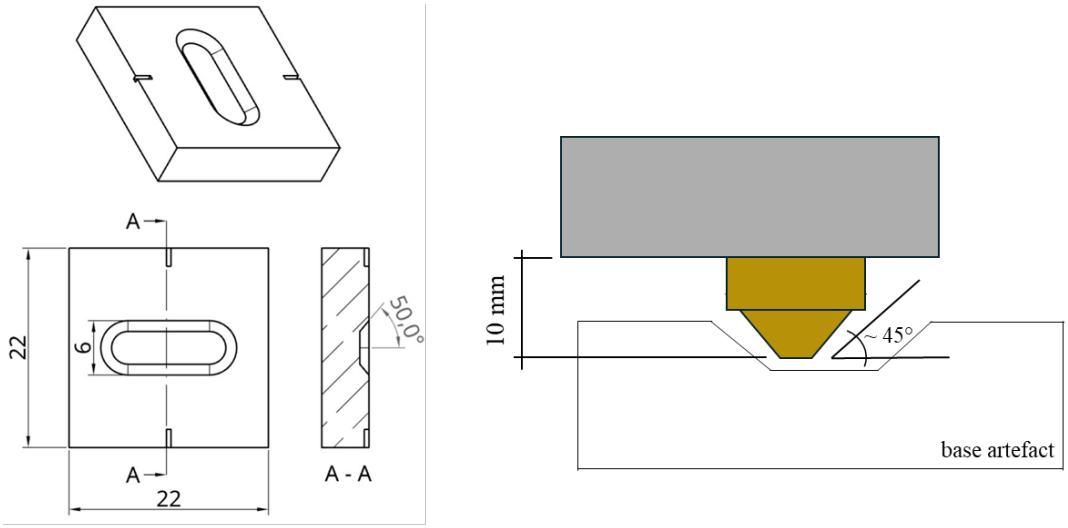


Fig. 1: a) Artifact design; b) engagement between the base artifact and the nozzle.

In the context of additive technologies, such as DED and Wire Arc Additive Manufacturing (WAAM), it is common practice to ensure optimal adhesion of the filler material to the part being repaired and to minimize the risk of voids by adjusting the taper angle of the slot walls. This process is further facilitated by the action of gravity. The specimens production consisted of three phases: the printing of the base artifact, 90 seconds of waiting time and the slot filling. The base artifact was made with a layer height of 0.2mm so that it would also match the layer height chosen for fill volume. In future developments, a different layer height could be included among other factors. The other parameters are not of interest in the discussion. The waiting time was provided to allow the system to switch to the same plate temperature and speed conditions for all tests.

Specifically, the plate was switched from 50° to 35°C so as not to thermally stress the base artefact, and the nozzle was switched to 150°C and then reheated to the temperatures predicted by the factor. The process of filling was characterized by an alternating sequence of actions, whereby the nozzle was immersed in the slot and the newly deposited layer inside it was subjected to monitoring. Each layer scan took approximately 10 seconds.

Regarding the print profile of the filling volume, the slot depth of 1mm was filled with a 0.2mm layer height volume resulting in a total of 5 layers of new deposited material. The perimeter walls were of critical importance to the scope of the work, given that they were in contact with the internal surfaces of the component to be repaired. Two walls were chosen as the optimum compromise between the amount of material required to effectively bond the base polymer and the filler polymer. The infill was configured to 100% (lines pattern). The line width of 0.44 mm was set for a 100% flow rate. The five filling layers so deposited were classified with the letter L. The L0 resulted in the preliminary state of the empty slot surface (Fig. 2b).

Materials Research Proceedings 57 (2025) 234-241 https://doi.org/10.21741/9781644903735-27

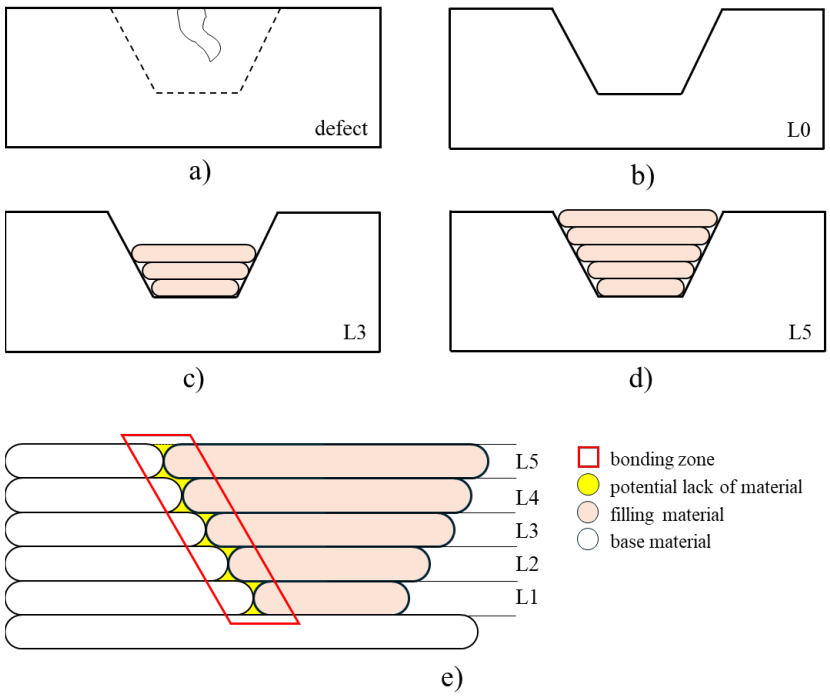


Fig. 2: Repair phases on the artifact, section view. a) The defect is localized and removed; b) the artifact is scanned and ready to be filled. From "a" to "b" takes place by mechanical chip removal. In this work, it was simulated to start from this step, making the slot already in the printed model; c) 3rd filling layer; d) 5th filling layer; e) Potential adhesion of the inner surface of slot to the filling volume.

The dimensional study of the artifacts was achieved by the structured light scanner ATOS Q at the end of each print. In particular, the analysis consisted in the alignment of each repaired specimens point cloud (artifacts with filled slot) with the point cloud of a reference block (housing no slot), printed with the same printing profile and dimension of the base artifact. In Fig. 3 is shown the process of measurement after the alignment phase.

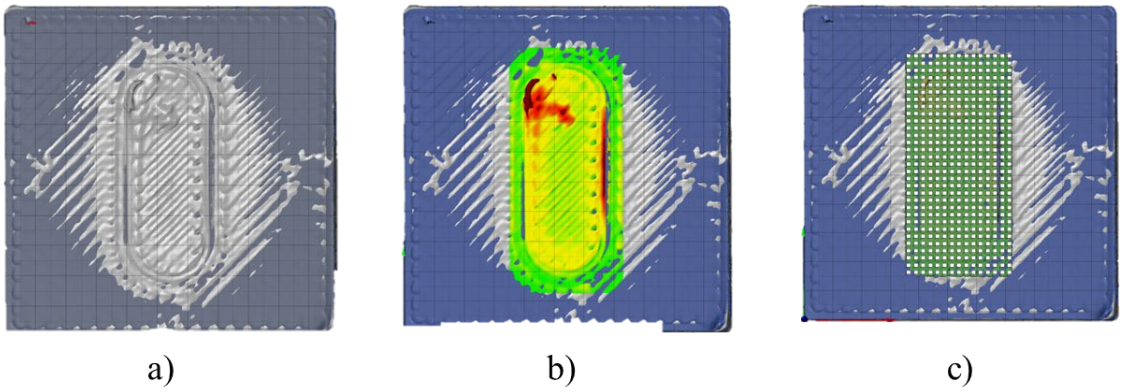


Fig. 3: Data gathering steps on Zeiss Optical Inspect. a) Alignment between the top surfaces of the reference specimen scan and the experiment; b) color map identifying deviations from the reference surface; c) surface sampling and Avg_devZ derivation.

The mean deviation from the reference surface resulted in the first output (Avg_devZ) which will be discussed further on in this work.

Materials Research Proceedings 57 (2025) 234-241 https://doi.org/10.21741/9781644903735-27

Design of Experiments (DoE). The experimental plan involved an investigation of various printing parameters on the quality and effectiveness of the repair. The experimental design chosen was an asymmetrical full factorial design that required the production of 18 experiments (3x3x2) and three iterations for a total of 54 experiments. These were based on three key factors chosen for the study:

- Nozzle Temperature. Higher temperatures promote material melting and interdiffusion of polymer chains, improving the adhesion strength of the repaired joint and reducing brittleness. However, lower temperatures offer advantages such as greater control over deposit size, reduced thermal degradation of the polymer, and minimization of surface artifacts such as excessive stringing or smearing. Furthermore, during the printing process, the nozzle remains in proximity to the slot walls, causing them to be partially activated and thus promoting adhesion of the newly deposited material. This factor has been studied at 190°C, 205°C, 220°C.
- The flow rate is a critical factor, controlling the extruded material, thereby influencing the density of the deposited layer and the quality of the repair. A higher flow rate ensures a firmer fill of the repaired area but can lead to excessive extrusion and geometric imperfections. Conversely, a lower flow rate can minimize excess material and improve the geometric accuracy of the repair. The levels chosen for the investigation were 90%, 100, and 110% (Fig. 4).
- The cooling fan (on/off) determined the cooling rate of the material, thereby influencing critical processes such as crystallization, thermal contraction, and residual stress formation. Disabling the fan has been known to promote better interlayer diffusion, thus improving adhesion and reducing stress accumulation. However, it should be noted that slower cooling can lead to greater dimensional instability, especially in overhanging or unsupported sections. Conversely, rapid cooling can minimize warping and shrinkage, thereby preserving the dimensional accuracy of the repair. However, it may also increase the risk of delamination due to insufficient bonding time. The “on” state resulted in the 80% of the maximum fan speed (rpm). Air was released onto the artifact via a shaped duct.

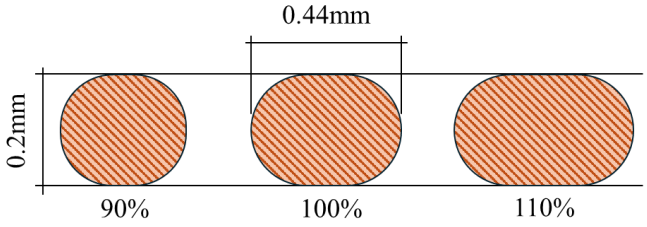


Fig. 4: Line width variation according to a flow rate increment.

To decrease the effects of systematic errors, the principle of randomness was respected by generating the specimens in a random order within each iteration.

Results and Discussion

Each of the 54 scans produced two outputs from the sampling points taken on the compared surfaces (Fig. 3c). The first was “Avg_devZ”, mean deviation of all the points from the reference plane. The second was “Avg_std” which consisted of the standard deviation within the same measuring point.

Materials Research Proceedings 57 (2025) 234-241 https://doi.org/10.21741/9781644903735-27

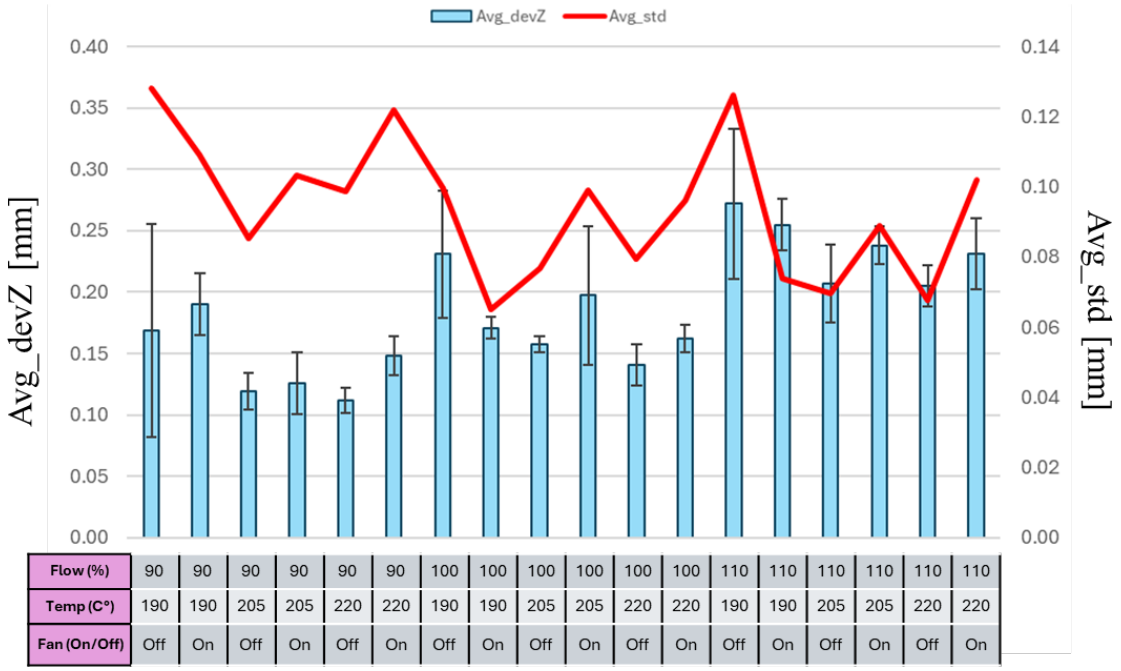


Fig. 5: Barplots with error bars of the experimental plan.

The graph in Fig. 5 shows the average values of the parameter Avg_devZ (light blue bars) calculated over the three iterations, along with their average standard deviations (represented by error bars). The red line represents the standard deviation calculated from the Avg_devZ averages across the three iterations. The variability indicated by the red line is generally higher and more fluctuating compared to the average deviations shown by the blue bars, suggesting that the overall consistency between iterations is relatively low.

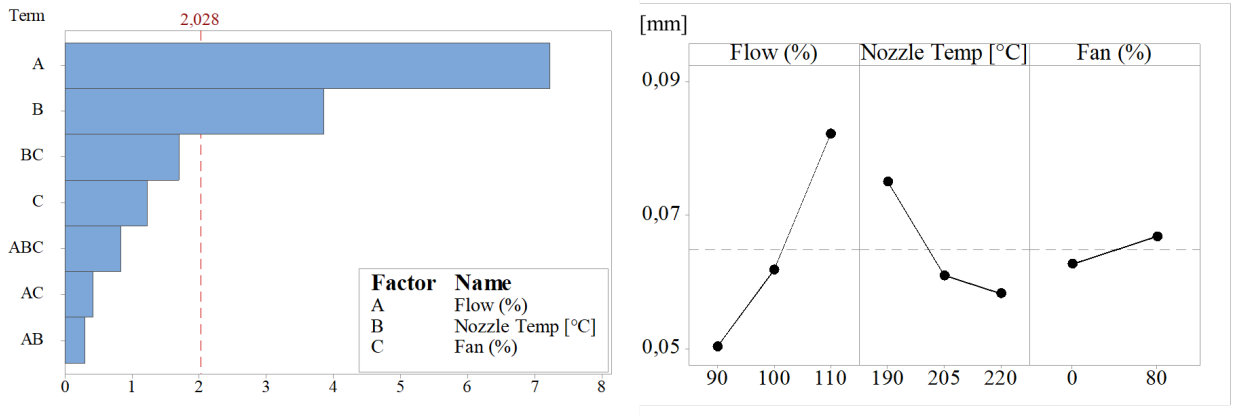


Fig. 6: Pareto chart and Main Effect plot.

According to the Pareto in Fig. 6 (confidence interval set to 95%), both the Flow and the Nozzle Temperature are influent for the increase in material emerging from the slot, exceeding the threshold value. Whether the fan is on or off, however, it does not seem to make any noticeable change to the surface. No combination of factors is influential either. The evidence in the Pareto chart is confirmed by the Main Effect Plot whereby, while the growth of the flow and temperature factors leads to an increase and decrease in Avg_devZ respectively, the fan factor is represented by an almost flat curve.

Materials Research Proceedings 57 (2025) 234-241 https://doi.org/10.21741/9781644903735-27

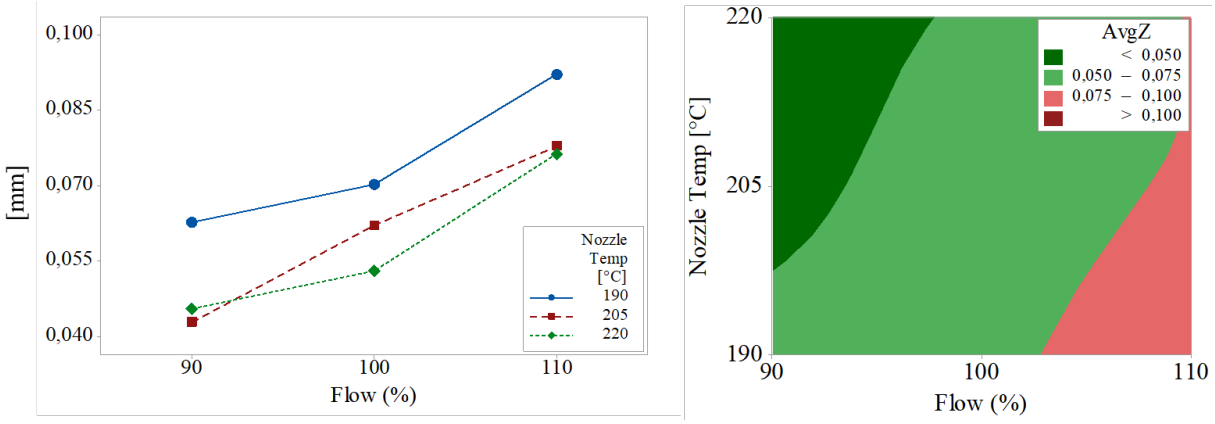


Fig. 7: Interaction plot and Contour plot between Flow (%) and Nozzle Temperature (°C).

As can be seen in Fig. 7, the interaction plot shows that an increase in flow results in an increase in material on the surface. However, this tendency is less noticeable at higher extrusion temperatures. This suggests that, at higher temperatures, the polymer can more easily settle on the walls of the host artefact, resulting in a denser volume and stronger bonds with the base material.

Conclusions and Future Development

This work evaluated the possibility of using MEX technology in a repair process chain involving polymeric (PLA) components to be filled with the same material. According to the investigation strategy adopted, material Flow and Nozzle Temperature showed a decisive influence on the amount of the material emerging from the slot (Avg_devZ). It has been noted that the least amount of emerging material is recorded with a combination of lower flow and higher temperature. The underlying causes of this phenomenon remain to be fully elucidated.

Thus, the preliminary results obtained showed the need for further evaluation parameters, and the investigation will shift to finding data more in line with the quality of the bonding between the component walls and the deposit, highlighting critical issues regarding the filling volume and density. In this regard, it would be advisable to employ in-process monitoring and destructive inspection techniques to correctly set the most appropriate printing parameters.

Although conducted on a consumer-grade system, the approach shows potential scalability toward industrial applications, paving the way for sustainable and cost-effective repair strategies. Future work will include aspects related to the actual localized hybrid repair or upgrade of polymeric components. Even though the defect has been simulated, future experiments could use CNC systems to investigate the effect of lower roughness on the inner surfaces of the slots.

Reference

[1] T. Peng, Y. Zhu, M. Leu, and D. Bourell, “Additive manufacturing-enabled design, manufacturing, and lifecycle performance,” Dec. 01, 2020, *Elsevier B.V.* https://doi.org/10.1016/j.addma.2020.101646

[2] L. Portolés, O. Jordá, L. Jordá, A. Uriondo, M. Esperon-Miguez, and S. Perinpanayagam, “A qualification procedure to manufacture and repair aerospace parts with electron beam melting,” *J Manuf Syst*, vol. 41, pp. 65–75, Oct. 2016. https://doi.org/10.1016/j.jmsy.2016.07.002

[3] Rahito, D. A. Wahab, and A. H. Azman, “Additive manufacturing for repair and restoration in remanufacturing: An overview from object design and systems perspectives,” Nov. 01, 2019, *MDPI AG*. https://doi.org/10.3390/pr7110802

[4] J. M. Flynn, A. Shokrani, S. T. Newman, and V. Dhokia, “Hybrid additive and subtractive machine tools - Research and industrial developments,” Feb. 01, 2016, *Elsevier Ltd*. https://doi.org/10.1016/j.ijmachtools.2015.11.007

[5] M. Petousis, K. Ninikas, N. Vidakis, N. Mountakis, and J. D. Kechagias, “Multifunctional PLA/CNTs nanocomposites hybrid 3D printing integrating material extrusion and CO2 laser cutting,” *J Manuf Process*, vol. 86, pp. 237–252, Jan. 2023. https://doi.org/10.1016/j.jmapro.2022.12.060

[6] C. Chadha, K. James, I. M. Jasiuk, and A. E. Patterson, “Extending the Operating Life of Thermoplastic Components via On-Demand Patching and Repair Using Fused Filament Fabrication,” *Journal of Manufacturing and Materials Processing*, vol. 6, no. 5, Oct. 2022. https://doi.org/10.3390/jmmp6050103

[7] R. Pirlo, M. G. Guerra, F. Lavecchia, and L. M. Galantucci, “Evaluation of a photogrammetry-based scanner for measuring small-sized features in an additive manufacturing repair process chain,” *The International Journal of Advanced Manufacturing Technology*, vol. 136, no. 11–12, pp. 5581–5598, Feb. 2025. https://doi.org/10.1007/s00170-025-15153-2

[8] M. Lafirenza, M. G. Guerra, and F. Lavecchia, “A layerwise monitoring methodology based on blue laser line profilometer for Material Extrusion processes,” *The International Journal of Advanced Manufacturing Technology*, vol. 127, no. 11–12, pp. 5421–5436, Aug. 2023. https://doi.org/10.1007/s00170-023-11864-6

Materials Research Proceedings 57 (2025) 242-249 https://doi.org/10.21741/9781644903735-28

Experimental characterization of QP1180 steel and its performance in stamping simulation: Comparison with DP1180

Maria Emanuela Palmieri[1,*], Matteo Villa[1], Michele Abruzzo[2], Giuseppe Macoretta[2], Stefania Bruschi[3] and Luigi Tricarico[1]

[1]Department of Mechanical, Mathematic and Management, Polytechnic of Bari, Bari, 70125, Italy

[2]Department of Civil and Industrial Engineering, University of Pisa, Pisa, Italy

[3]Deptartment of Industrial Engineering, University of Padova, Padova, Italy

[*]mariaemanuela.palmieri@poliba.it

Keywords: Stamping, High Strength Steel, Deformation-Induced Martensitic Transformation

Abstract. The increasing demand for lighter vehicles and improved safety has driven the adoption of Advanced High-Strength Steels (AHSS). Among these, third-generation Quenching and Partitioning (QP) steels stand out for their exceptional combination of ultra-high strength and ductility, attributed to the TRansformation-Induced Plasticity (TRIP) effect, making them highly suitable for automotive applications. This study focuses on the characterization of QP1180 steel using tensile tests, complemented by Digital Image Correlation (DIC) to analyze mechanical behavior in different rolling directions (0°, 90°, 45°). The data obtained were then integrated into Finite Element (FE) software to simulate the stamping process of a B-Pillar. The simulation results were compared with those obtained from simulating the stamping process of a first-generation steel, DP1180, with a similar tensile strength. Finally, fractographic and microstructural analyses were performed to deepen the understanding of the steel's fracture mechanisms.

Introduction

The automotive industry today is increasingly focused on refining materials to improve vehicle performance, especially in terms of reducing weight, saving energy, and enhancing corrosion resistance. In this context, Advanced High-Strength Steels (AHSS) have become crucial [1-2]. Among them, Dual-Phase (DP) steel, part of the first generation of AHSS, is extensively used due to its combination of high work-hardening, high strength, and good ductility [1, 3]. Its microstructure, which consists of a softer ferrite phase combined with a harder martensite phase through intercritical annealing, results in a material with strength ranging from 500 to 1000 MPa and strain from 5% to 20% [4-7].

Recently, there has been growing interest in third-generation AHSS, such as Quenching and Partitioning (QP) steels, which offer mechanical strength between 600 and 1200 MPa and significantly greater plastic strain at fracture (15% to 30%) compared to DP steels. This enhanced deformability derives from multiphase hardening coupled with Transformation-Induced Plasticity (TRIP), due to the presence of metastable Retained Austenite (RA) [8–10]. QP steels are typically produced by austenitizing above the Ac_3 temperature, followed by rapid cooling between the martensite start (M_s) and finish (M_f) temperatures, and then a partitioning treatment to promote C diffusion from martensite to austenite [11]. This process results in a triphasic microstructure of C-rich martensite, C-poor tempered martensite (essentially ferrite), and RA, leveraging DIMT to improve toughness. Understanding and controlling this transformation is essential for optimizing performance and predicting material behavior. While AHSS properties are typically assessed through quasi-static uniaxial tensile tests at room temperature, it is evident that DIMT is also

Content from this work may be used under the terms of the Creative Commons Attribution 3.0 license. Any further distribution of this work must maintain attribution to the author(s) and the title of the work, journal citation and DOI. Published under license by Materials Research Forum LLC.

Materials Research Proceedings 57 (2025) 242-249 https://doi.org/10.21741/9781644903735-28

influenced by strain rate, temperature evolution during testing, and RA grain orientation—which is affected by sheet orientation (i.e., rolling vs test direction) [12-13]. These factors can be leveraged to control the martensitic transformation in QP steels during stamping processes. Understanding these influences will enable process optimization, fine-tuning forming responses and tailoring the stamped components' properties. This study will focus on investigating the mechanical properties of QP1180 steel in relation to sheet orientation. By analyzing fracture surfaces and the microstructure of broken specimens, we aim to establish a correlation between sheet orientation and fracture mechanisms. Furthermore, since accurately predicting the plastic behavior of textured sheet metals is crucial for reliable numerical analysis of sheet deformation, the mechanical characterization data will be integrated into a Finite Element (FE) simulation software to model the stamping process of an automotive structural component—the B-Pillar. Finally, QP1180 will be compared to the first-generation DP1180 steel to assess mechanical performance, formability, and determine which material can be used to produce the highest-quality component at the end of the stamping process. The novelty of this study lies in its comprehensive mechanical and numerical investigation of the underexplored QP1180 steel, moving beyond prior research that mainly addresses microstructural evolution or basic tensile behavior. By integrating mechanical characterization with realistic forming simulations of an automotive component, this work provides original data on the material's anisotropic response and delivers valuable insights to support its industrial application.

Materials and Method

In this study, QP1180 steel—a third-generation AHSS of interest for automotive stamping of structural components—was analyzed. Commercial 1.2 mm thick QP1180 sheets were supplied by Centro Ricerche FIAT (CRF) – Stellantis in the quenched and partitioned condition with zinc coated surfaces.

The first phase involved mechanical characterization at room temperature through uniaxial tensile tests on specimens oriented at various angles relative to the Rolling Direction (RD) to understand the material's anisotropic behavior. The experimental data (flow curve, Young's modulus, and anisotropy coefficients) were used for the numerical simulation of an automotive B-Pillar stamping process (Fig. 1 (a)).

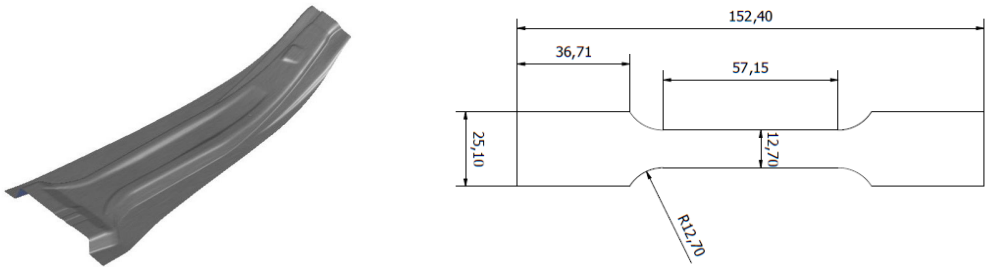


Fig. 1: Geometry of B-Pillar (a) and specimen for tensile testing with dimensions in mm (b)

The tensile tests were performed using an Instron 4485 universal testing machine, electronically controlled by the Zwick-Roell software, with a crosshead speed set to 1 mm/min. Strain measurements were conducted using the digital image correlation system (DIC - Aramis, provided by GOM), enabling a detailed analysis of the strain field. Specifically, the strain along the loading direction ($\varepsilon_{(0°/90°/45°),L}$) was determined using a video extensometer with a gauge length of 30 mm, while the strain along the transverse direction ($\varepsilon_{(0°/90°/45°),w}$) was measured with a video extensometer with a 9 mm gauge length. The anisotropy coefficients were calculated according to Eq. 1.

Materials Research Proceedings 57 (2025) 242-249 https://doi.org/10.21741/9781644903735-28

$$r_{0°/90°/45°} = \frac{\varepsilon_{(0°/90°/45°),w}}{-(\varepsilon_{(0°/90°/45°),L}+\varepsilon_{(0°/90°/45°),w})} \quad (1)$$

While this method does not fully comply with ISO 10113 standard, recent studies [14] support the use of DIC for preliminary anisotropy evaluation.

Fig. 1 (b) shows the geometry of the tensile test specimens; three specimens per direction were tested to ensure reliable results.

Metallographic investigations were performed on samples taken both parallel and perpendicular to the sheet plane, with the latter showing a surface orthogonal to the RD. Samples were ground with 1200 SiC paper, polished with diamond suspension, and etched with Nital.

Fractographic analyses examined the fracture surfaces to assess the influence of orientation relative to the RD. Scanning electron microscopy was carried out using a FEI QUANTA 450 ESEM-FEG at CISUP, University of Pisa.

The stamping process was simulated with AutoForm®R10. The blank was defined at 1.2 mm thickness (matching the test specimens), and the tooling geometries were modeled as shown in Fig. 2 (a). A forming speed of 295 mm/s was used with uniform lubrication (1 g/m²). Frictional behavior was modeled using a variable friction law generated in TriboForm®, based on lubrication quantity and contact conditions, with an average friction coefficient of 0.099. The punch and die were considered rigid tools, while the blank holder was controlled using a force-based approach, with a value set at 1000 kN, determined through preliminary simulations aimed at optimizing component quality by minimizing wrinkling and preventing splits.

To evaluate the effect of mechanical properties, the simulation was repeated using DP1180 steel, with material data from Baosteel (no experimental tests were performed). For an accurate numerical simulation of the stamping process and a reliable assessment of the final component's quality, it is essential to integrate the Formability Limit Curve (FLC) into the FE software. Although future studies are planned to derive it for QP1180 steel, this work has opted to use the curve provided by Baosteel. Fig. 2 (b) presents the forming limit curves for both QP1180 and DP1180 steels.

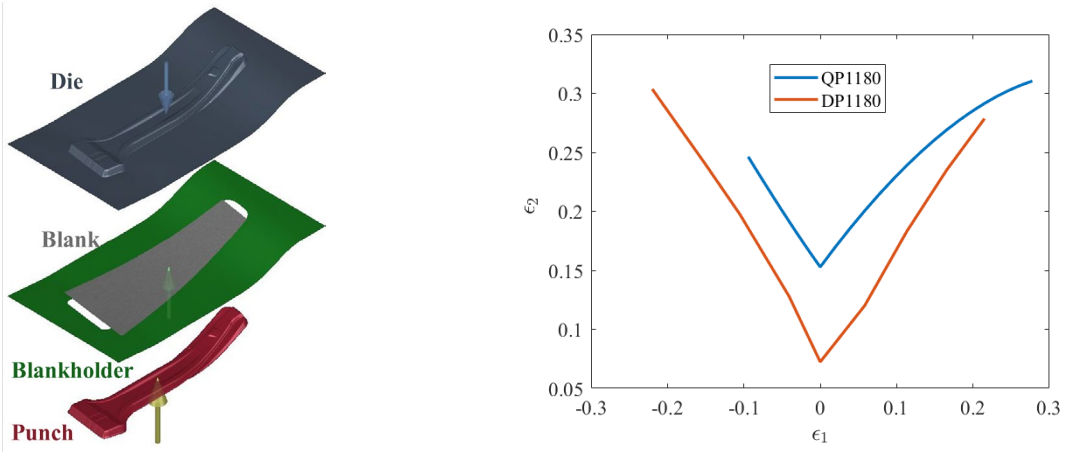


Fig. 2: Tool geometry (a) and formability limit curves for QP1180 steel and DP1180 steel provided by Baosteel (b)

As detailed in the results, differences in the mechanical properties of the two materials affect process performance, enhancing the understanding of high-strength steels in industrial applications.

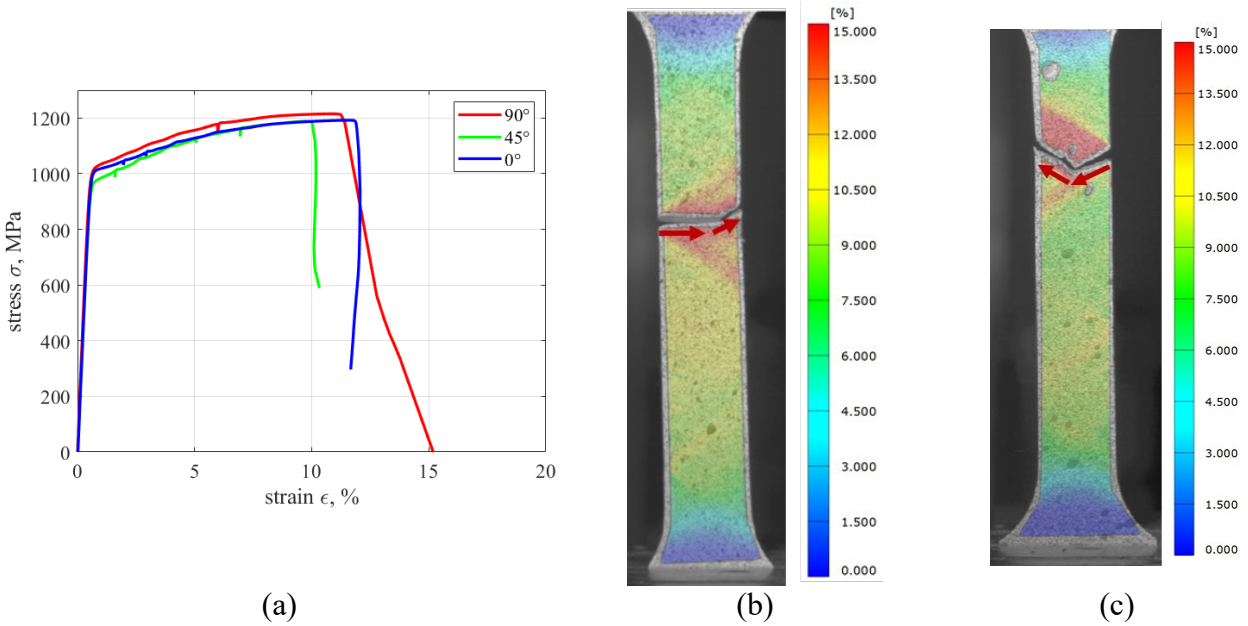
Materials Research Proceedings 57 (2025) 242-249 https://doi.org/10.21741/9781644903735-28

Tensile testing results

The tensile test results, shown as engineering stress-strain curves in Fig. 3a, are compared for the three RDs. The average curve from three tests is presented for each specimen orientation relative to the sheet RD.

The comparison reveals minimal anisotropic strength under uniaxial tension. Specimens cut at 90° to the RD show the highest strength, while those at 45° exhibit the lowest strength and elongation at fracture. These findings align with the literature [15].

Thanks to the use of the DIC technique, it was possible to perform a detailed analysis of the fracture mode and the strain distribution occurring during the tensile test. This methodology allowed for precise information on the localization of strains in the sample and their evolution up to the moment of fracture.



(a) (b) (c)

Fig. 3: (a) Average engineering stress-strain curves for different specimen orientations and DIC strain maps at fracture for specimens cut along the RD (b) and at 45° (c)

Figures 3b and 3c compares strain maps at fracture onset for two specimen types: one cut along the RD (Fig. 3 (b)) and another at a 45° angle (Fig. 3 (c)). Specimens cut at 90° to the RD showed a fracture mode similar to those cut along the RD, indicating comparable mechanical behavior.

The fracture initiation and propagation mechanisms, highlighted by arrows in the figures, show that in RD-oriented specimens, cracks start at the edge, propagate transversely, then deviate at an angle, leading to complete failure. In specimens cut at 45° to the RD, cracks initiate at the edge, propagate at an inclined angle, and form a V-shaped fracture upon reaching the center.

Table 1: Anisotropy values and yield stress ratios for definition of yield surface according to BBC 2005 model.

r_0	0.681
r_{45}	0.776
r_{90}	0.701
σ_0/σ_0	1
σ_{45}/σ_0	0.972
σ_{90}/σ_0	1.019

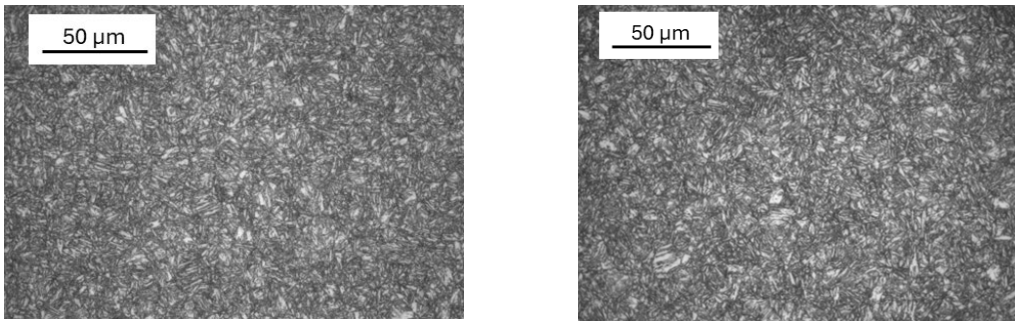
The elastic modulus was determined to be 200 ± 2.1 GPa. The true flow curve was derived from the engineering stress-strain curves and input into FE software. To define the yield surface, the

Materials Research Proceedings 57 (2025) 242-249 https://doi.org/10.21741/9781644903735-28

BBC 2005 model [16] was used, with input parameters including the anisotropy coefficients (r_0, r_{45}, r_{90}) and yield stress ratios, as shown in Table 1.

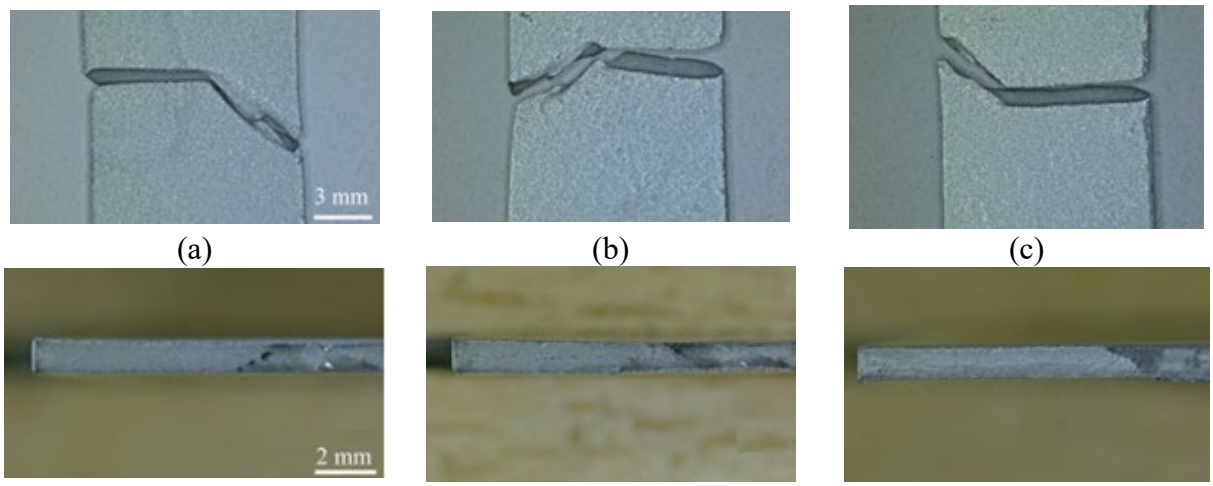
Fractographic and microstructural observations

The as-received material's microstructure consists of a fine martensitic matrix with ferritic islands and occasional RA regions, as shown in Fig. 4. The RD did not affect the microstructure, as the final QP heat treatment produced an isotropic martensitic matrix. This microstructure aligns with recent literature on the as-received material [17].



(a) (b)

Fig. 4: Microstructure of as-received material, samples extracted in direction (a) perpendicular and (b) parallel to the sheet plane.



(a) (b) (c)

(d) (e) (f)

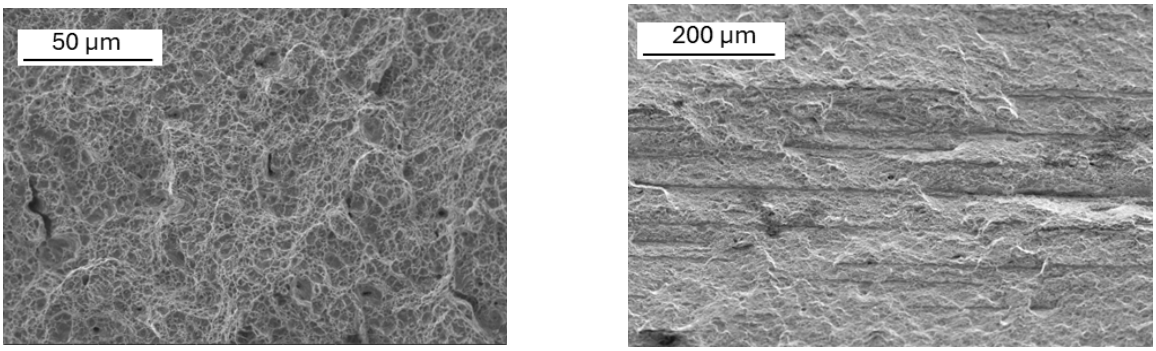
Fig. 5: Fracture surfaces of the tensile specimens observed via stereomicroscope. Specimens extracted at 0°(a) (d), 45°(b) (e), and 90° (c) (f) to the sheet RD

The fracture surface of the tensile specimens featured a wide region of ductile fracture, irrespectively on the angle between the specimen longitudinal axis and the sheet RD. As previously observed from DIC monitoring, the fracture surface presented a wide portion orthogonal to the loading direction and an small region angled at about 45° in proximity to the specimen edges for both the 0° and 90° specimens, Fig. 5. The specimen extracted at 45° to the RD, presented instead two angled surfaces. No macroscopic defects were observed for all the specimens.

As shown in Fig. 6, SEM investigations confirmed the ductile nature of the fracture surface, characterized by the presence of dimples having a dimension consistent with the elongation at fracture in line with the results of the tensile tests. For the samples extracted at 45° and 90° to the sheet RD, the SEM investigation revealed the presence of elongated segregation bands in the middle of the sheet thickness. Those bands, which were not evident from metallographic

Materials Research Proceedings 57 (2025) 242-249 https://doi.org/10.21741/9781644903735-28

investigations, could be produced by the combined effect of the structure produced by the sheet rolling and the TRIP effect occurring during the tensile test.



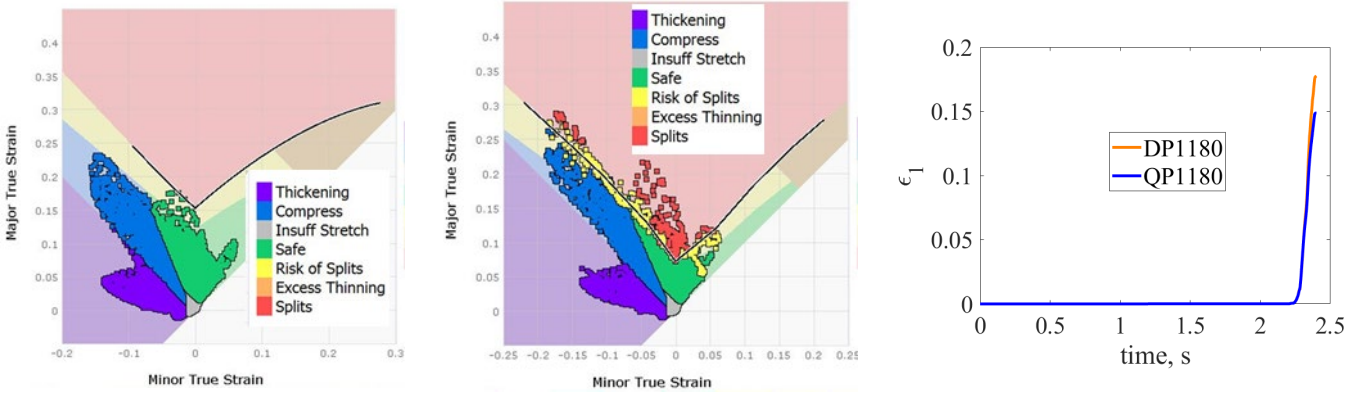
(a) (b)

Fig. 6: Fracture surfaces observed via SEM. Ductile fracture dimples observed for all the specimens(a), segregation bands from a specimen at 90° to the sheet RD (b).

Although not directly used in the FE model, fractographic and microstructural analyses support the modeling assumptions by confirming the ductile fracture behavior and the absence of critical defects, in line with the FLC-based approach.

FE results

The numerical simulation of the B-Pillar stamping process assessed the deformational behavior of DP1180 and QP1180 under identical conditions, using the Forming Limit Diagram (FLD) to evaluate failure susceptibility. The results revealed distinct formability responses. The QP1180 component showed favorable behavior, with principal stresses staying below the forming limit curve in all areas (Fig. 7 (a)), reflecting its superior mechanical properties, higher ductility, and better plastic deformation absorption. In contrast, the DP1180 component showed criticalities, with stresses exceeding the forming limit curve in areas of high deformation, such as curvature radii and stretching zones, leading to fractures (Fig. 7 (b)).The difference in material response is due to their distinct microstructures. QP1180, with its multiphase microstructure and metastable RA, offers superior strength and ductility compared to the older DP1180, a dual-phase steel with a ferrite-martensite structure that provides high strength but lower ductility and plastic deformation capacity.



(a) (b) (c)

Fig. 7: Formability results for (a) QP1180 (b) DP1180; and (c) comparison of the major strain over time at the critical point of the component for the two steels.

To complement the FLD-based evaluation and enable a more objective comparison, the major strain was mapped on the stamped components for both steels. The strain maps reveal that DP1180

exhibits higher major strain in critical areas (curvature and flange), indicating a greater ability to undergo plastic deformation before localization. In contrast, QP1180 shows lower major strain values overall, despite its superior mechanical strength, suggesting more localized deformation due to its higher yield strength and rigid martensitic matrix. This may delay necking in moderate strain zones but increase the risk of sudden failure if strain localization occurs. Figure 7c shows the time evolution of major strain in a critical area for both steels. This behavior also affects thickness reduction: DP1180 shows more pronounced, evenly distributed thinning, while QP1180 exhibits less thinning but more localized reductions in critical areas.

Conclusions

The mechanical behavior and formability of QP1180 steel were studied through experiments and simulations, compared to DP1180 steel. Key findings include:

- Tensile tests showed slight anisotropy in QP1180, with the highest strength in specimens cut at 90° to the RD and the lowest at 45°. The QP heat treatment results in an isotropic martensitic matrix.
- DIC analysis allowed for detailed observation of strain distribution and localization. Moreover, the image sequence acquired by the DIC system enabled the identification of fracture propagation patterns. Specimens at 0° and 90° showed a combination of transverse and oblique crack paths, while 45° specimens exhibited a characteristic V-shaped fracture. SEM analysis confirmed the ductile nature of the failure.
- Numerical simulation of the B-Pillar stamping process showed QP1180's superior formability due to its multiphase microstructure and metastable RA, which enhance ductility and plastic deformation.

These findings demonstrate the potential of QP1180 for high-strength, ductile automotive structural components.

Acknowledgments

Financed by the European Union - NextGenerationEU (National Sustainable Mobility Center CN00000023, Italian Ministry of University and Research Decree n. 1033 - 17/06/2022, Spoke 11 - Innovative Materials & Lightweighting). The authors are also grateful to AutoForm Engineering GmbH for the support in FE model and MANAGE 5.0 project (F/310302/01-05/X56) for its contribution to the research activities.

References

[1] J. Huang, S. Li, H. Zhong, S. Xiao, D. Li, Microstructure, mechanical properties, and corrosion behavior of laser-welded dissimilar joints between DP980 and QP980 steel, Steel Res. Int. 93 (2022) 2100541. https://doi.org/10.1002/srin.202100541

[2] D.K. Matlock, S. Kang, E. De Moor, J.G. Speer, Applications of rapid thermal processing to advanced high strength sheet steel developments, Mater. Charact. 166 (2020) 110397. https://doi.org/10.1016/j.matchar.2020.110397

[3] F. Badkoobeh, A. Nouri, H. Hassannejad, H. Mostaan, Microstructure and mechanical properties of resistance spot welded dual-phase steels with various silicon contents, Mater. Sci. Eng. A 790 (2020) 139703. https://doi.org/10.1016/j.msea.2020.139703

[4] D.K. Kim, H.J. Kim, S. Gong, S.E. Shin, S.J. Lee, A comparative study on the wear behavior of dual phase (DP) steel and quenching and partitioning (QP) steel, Tribol. Int. 194 (2024) 109445. https://doi.org/10.1016/j.triboint.2024.109445

[5] D.K. Kim, H.J. Kim, S. Gong, S.E. Shin, S.J. Lee, A comparative study on the wear behavior of dual phase (DP) steel and quenching and partitioning (QP) steel, Tribol. Int. 194 (2024) 109445. https://doi.org/10.1016/j.triboint.2024.109445

[6] R. Kuziak, R. Kawalla, S. Waengler, Advanced high strength steels for automotive industry, Arch. Civ. Mech. Eng. 8 (2008) 103-117. https://doi.org/10.1016/S1644-9665(12)60197-6

[7] O. Kwon, K.Y. Lee, G.S. Kim, K.G. Chin, New trends in advanced high strength steel developments for automotive application, Mater. Sci. Forum 638 (2010) 136-141. https://doi.org/10.4028/www.scientific.net/MSF.638-642.136

[8] H. Jirková, L. Kučerová, B. Mašek, Effect of quenching and partitioning temperatures in the QP process on the properties of AHSS with various amounts of manganese and silicon, Mater. Sci. Forum 706 (2012) 2734-2739. https://doi.org/10.4028/www.scientific.net/MSF.706-709.2734

[9] Q. Liu, Q. Zhou, J. Venezuela, M. Zhang, A. Atrens, Hydrogen concentration in dual-phase (DP) and quenched and partitioned (Q&P) advanced high-strength steels (AHSS) under simulated service conditions compared with cathodic charging conditions, Adv. Eng. Mater. 18 (2016) 1588-1599. https://doi.org/10.1002/adem.201600217

[10] H.L. Yi, L. Sun, X.C. Xiong, Challenges in the formability of the next generation of automotive steel sheets, Mater. Sci. Technol. 34 (2018) 1112-1117. https://doi.org/10.1080/02670836.2018.1424383

[11] H.J. Kim, M.G. Lee, Analysis of hydrogen trapping behaviour in plastically deformed quenching and partitioning steel in relation to microstructure evolution by phase transformation, J. Alloys Compd. 904 (2022) 164018. https://doi.org/10.1016/j.jallcom.2022.164018

[12] J. Hu, G. Thomas, Evolving the “Banana Chart”: Temperature and strain rate effects on tensile properties of new-generation advanced high-strength steels, JOM 73 (2021) 3204-3213. https://doi.org/10.1007/s11837-021-04900-x

[13] C.B. Finfrock, Temperature and strain rate dependence of the martensitic transformation and mechanical properties in advanced high strength steels, Ph.D. dissertation, Colorado School of Mines, 2022. 10.3389/fmats.2020.615361

[14] E. Seidi, S.F. Miller, F. Kaviari, L. Huang, T.B. Stoughton, Novel method to assess anisotropy in formability using DIC, Int. J. Mech. Sci. 285 (2025) https://doi.org/10.1016/j.ijmecsci.2024.109782

[15] C. Zhang, Y. Wang, Z. Chen, N. Yang, Y. Lou, T. Clausmeyer, Q. Zhang, Characterization of plasticity and fracture of a QP1180 steel sheet, Procedia Manuf. 50 (2020) 529–534. https://doi.org/10.1016/j.promfg.2020.08.095

[16] D. Banabic, Sheet Metal Forming Processes: Constitutive Modelling and Numerical Simulation, Springer Science & Business Media, 2010.

[17] W. Li, W. Wu, Q. Zhou, W. Li, J. Li, Analysis of hydrogen-induced delayed cracking and hydrogen trapping behavior in plastically deformed quenching and partitioning steel, Corros. Sci. 223 (2023) 111437. https://doi.org/10.1016/j.corsci.2023.111437.

Materials processing technology



Materials Research Proceedings 57 (2025) 251-258 https://doi.org/10.21741/9781644903735-29

Textured tools and cryogenic cooling for modifying chip morphology in PEEK machining

Anna Bottin[1,a*], Rachele Bertolini[1,b], Stefania Bruschi[1,c]

[1]Università degli Studi di Padova, Dipartimento di Ingegneria Industriale, via Venezia 1, Padova, 35131, Italy

[a]anna.bottin.1@phd.unipd.it, [b]rachele.bertolini@unipd.it, [c]stefania.bruschi.unipd.it

Keywords: Textured Tools, Cryogenic, Turning

Abstract. PEEK is a high-performance polymer widely used for biomedical applications, but its machinability remains a critical issue. Traditional coolants are unsuitable for biomedical use, and dry machining produces long, entangled chips that hinder surface quality. Cryogenic machining has been recently introduced for PEEK chip breaking. Textured tools can be exploited to modify the chip formation further. In this context, the study examines the effects of tool rake face texturing on chip formation in cryogenic and dry cutting conditions. Turning trials were conducted with plain and laser-textured tools with grooves of different geometry at varying depths of cut. The results indicate that cryogenic cooling promotes chip breakage, with textured tools enhancing the fragmentation process. A correlation was observed between groove design and chip morphology, highlighting the potential of these solutions to improve machining efficiency.

Introduction

PEEK (Polyether-ether-ketone) is being used in biomedical applications thanks to its unique characteristics: compared to metals, which can produce hypersensitivity reactions, it has a greater lightness, high resistance to degradation (chemical stability), and biocompatibility. It also possesses excellent mechanical properties and an elastic modulus very close to that of human bones [1]. PEEK implants require high-dimensional precision, controlled roughness, and consistent surface properties to ensure proper biological response and wear resistance [2]. The machining of polymer materials is increasingly adopted in biomedical applications to achieve high precision and customization. However, polymer machining presents challenges, as performance depends on the material's chemical and thermo-physical properties [3]. Furthermore, using traditional coolants is unsuitable for biomedical applications, nevertheless, dry machining usually generates long, entangled chips that may damage the surface quality. In order to promote chip fragmentations, new approaches such as cryogenic cooling and innovative tools can be applied.

Cryogenic cooling has been shown to enhance surface integrity and chip breakage in polymer machining. The study [4] investigates the grinding process of PEEK under various cutting conditions, focusing on surface roughness, forces, and chip morphology. The findings indicate that cryogenic cooling significantly improves surface quality, reduces grinding forces, and minimizes chip adhesion. The application of LN_2 facilitates chip breakage, transitioning the chip from continuous to discontinuous, thereby contributing to a more efficient machining process. PEEK turning with cryogenic internal injection cooling was studied to understand low-temperature material behavior [5]. The research indicates that cryogenic cooling suppresses the thermal deformation of the polymer, promoting a brittle fracture. Due to the reduced plastic behavior of PEEK and the jet impact effect of LN_2, chip breakage was achieved.

The application of innovative cutting tools, such as textured tools, in the same way as cryogenic cooling, has the potential to enhance chip fragmentation. While studies on polymer machining with textured tools are limited, research on metal machining provides useful insights. The review in [6] investigates advancements in textured cutting tools, reporting their influence on chip

Content from this work may be used under the terms of the Creative Commons Attribution 3.0 license. Any further distribution of this work must maintain attribution to the author(s) and the title of the work, journal citation and DOI. Published under license by Materials Research Forum LLC.

Materials Research Proceedings 57 (2025) 251-258 https://doi.org/10.21741/9781644903735-29

formation and tool-chip interaction. Specific surface textures, such as grooves and dimples, can facilitate the chip flow, reducing tool-chip interface friction and favoring chip breakability. The study in [7] investigated the impact of textured tools on machining performance in various applications. The findings indicate that introducing textured tools represents an advancement in metal cutting. The textures demonstrate the capability to effectively regulate the direction of chip flow, improving the machinability of difficult-to-cut materials.

This study aims to understand the role of textures in tools used in dry and cryogenic machining of PEEK at different depths of cut. New insights into the chip formation mechanisms arising when adopting such a cutting approach are given, proving that it can represent a suitable way to enhance efficiency when turning PEEK.

Materials and methods

Material. The biomedical-grade PEEK (TECAPEEK™) was supplied as cylindrical bars 42 mm in diameter and 1000 mm in length in the annealed state, which was achieved by heating the material at 221 °C for four hours to reduce residual stresses and stabilize the polymer structure. The PEEK thermal properties were characterized using a DSC™200 system, where samples were heated at a controlled rate of 10 °C/min from 40 °C to 360 °C. This analysis identified a glass transition temperature (T_g) of 154 °C, a melting temperature (T_m) of 344 °C, and a degree of crystallinity of 28%. The crystallinity was calculated by comparing the melt enthalpy of the sample with that of fully crystalline PEEK.

Tool texturing and characterization. For cutting experiments, Tungaloy VNMA 160402-330.5 TH10 uncoated inserts with a 0° rake angle were used. Laser texturing of the rake face was performed using a Trumpf™ TruMark 5050 nanosecond pulsed laser system, operating at 50 W average power, 1,000 pulse frequency kHz, and a beam spot size of 50 µm. The grooves were created with a scanning speed of 100 mm/s and a pulse duration of 250 ns, requiring eight passes to achieve a depth of 40 µm. Two groove orientations were studied: 90° (perpendicular to the cutting edge) and 0° (parallel to the cutting edge) (see Fig. 1a and 1b). The two configurations were chosen to enhance chip breakage: perpendicular to facilitate chip removal by guiding the chip in the rake face and parallel to increase resistance to chip flow [8].

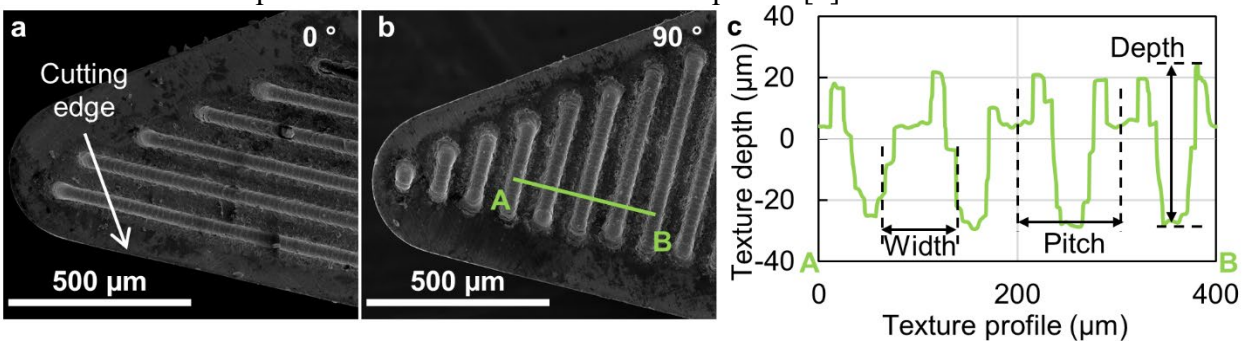


Figure 1. Laser-textured cutting tools (a) 0° texture, (b) 90° texture; (c) texture profile in the correspondence of the green line of Fig. 1b.

The texture quality was assessed using a Sensofar™ S Neox 3D optical profilometer and a Keyence™ optical microscope. The measurements evaluated the pitch between two consequent grooves (100 µm), the distance from the cutting edge (100 µm), and the width (50 µm) and depth of the texture (40 µm), as can be seen in Fig. 1c. The measured values aligned with the nominal ones, with the maximum deviation below 20%.

Turning trials. Machining trials were conducted on a Mori Seiki™ NL 1500 CNC lathe (Fig. 2). Initially, the PEEK bars were rough-machined under dry conditions to a diameter of 40 mm. Two cooling conditions were tested: dry machining, with no coolant applied, and cryogenic

Materials Research Proceedings 57 (2025) 251-258 https://doi.org/10.21741/9781644903735-29

machining, where liquid nitrogen (LN_2) was delivered via 15 bar pressurized dewar through two copper nozzles with 1 mm internal diameter targeting the rake and flank faces of the insert (Fig. 2a). The PEEK bars were finished at a cutting speed (V_c) of 200 m/min, feed rate (f) of 0.1 mm/rev, and cutting length (L) of 5 mm. The depth of cut (a_p) was varied at 0.15, 0.25 and 0.5 mm. This selection of parameters was based on prior studies to minimize surface roughness [9]. The turning trials were repeated three times for each machining parameter and cooling condition.

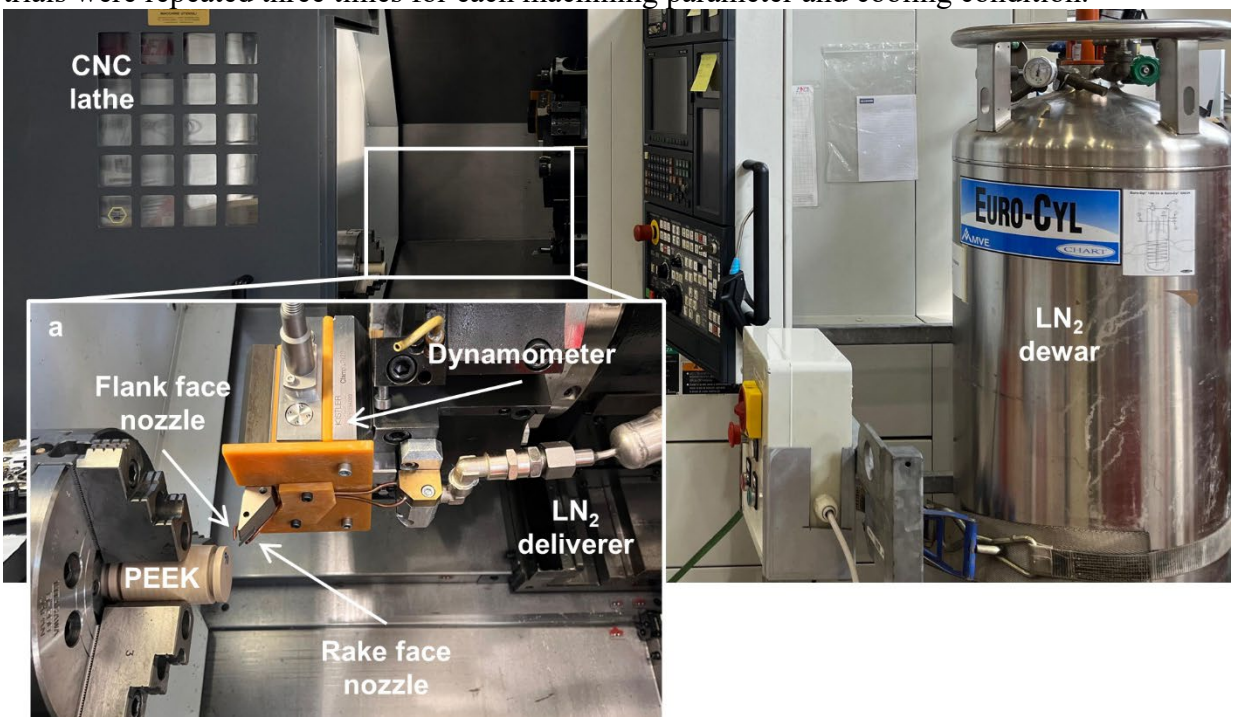


Figure 2. Turning set-up with (a) close-up of the cutting zone with the cryogenic cooling apparatus.

The cutting forces were recorded using a Kistler™ 9129AA piezoelectric dynamometer. The signals for the cutting force (F_c), radial force (F_r), and thrust force (F_t) were acquired using the Dynoware™ software at a sampling rate of 2500 Hz. The force data were filtered at 12 Hz to remove noise and to calculate the mean values. A glass fiber-reinforced thermoset polymer was used as thermal insulation to protect the dynamometer during cryogenic cooling.

Post-machining characterization. Chips were collected after each turning trial and observed under the optical microscope. The analysis focused on the chip geometry (width and length of discontinuous chips) and overall morphology. Additionally, the chips were gold-coated with a sputter coater Denton Vacuum™ Desk V and examined using a FEI™ QUANTA 450 scanning electron microscope (SEM).

After machining, the cylinders were cut and analyzed to assess the role of cryogenic cooling and textured tools on the machined surface quality. The arithmetic mean height (Sa), the reduced valley depth (Svk), the reduced peak height (Spk), and the core roughness depth (Sk) were analyzed. As highlighted in [10], controlling these parameters is crucial for biomedical applications, where surface texture affects wear resistance and lubrication, thereby enhancing the long-term performance of joint implants. The measurements adhered to ISO 25178-2:2021 standards, with a 2.5 µm S-filter and a 0.25 mm L-filter.

Results and discussion

Fig. 3 shows the PEEK bar at the end of the cutting operation, clearly displaying two distinct chip morphologies under dry and cryogenic machining conditions. Regardless of the tool texture, dry

Materials Research Proceedings 57 (2025) 251-258 https://doi.org/10.21741/9781644903735-29

machining produced a continuous chip (Fig. 3a), while cryogenic machining led to chip fragmentation (Fig. 3b). These results are consistent with previous findings [4-5]. The continuous chips became tangled around the freshly machined bar, creating a challenge for productivity and requiring machining downtime for their removal. In addition, increasing a_p resulted in more pronounced chip curling. While no macroscopic differences in the length of the dry chips were visible at a specific depth of cut, the length of the cryogenically fragmented chips was measured to understand the impact of the texture. The values in Table 1 show that, with the plain tool under cryogenic conditions, the longest chips were produced at a_p = 0.15 mm, while the shortest were produced at a_p = 0.25 mm. Regardless of the depth of cut, the 90° texture resulted in shorter chips, with a reduction of approximately 75% for each depth of cut. In contrast, the most significant reduction for the 0° texture was 68% at a_p = 0.15 mm.

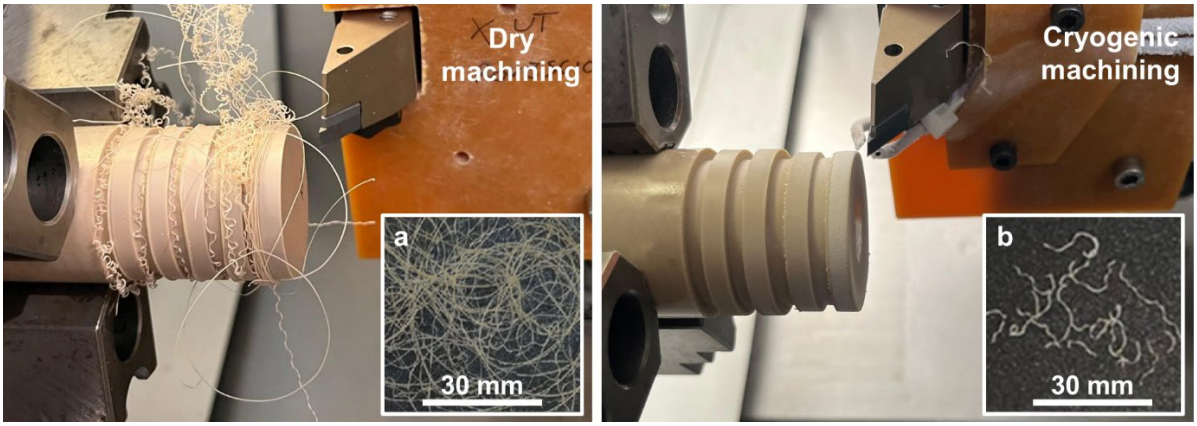


Figure 3. Cutting zone at the end of the turning operations conducted at a_p = 0.25 mm. Photos of the chips under dry (a) and cryogenic cooling (b).

The chip width also exhibited significant variations (Table 1). As expected, increasing the depth of cut led to wider chips; however, cryogenic cooling consistently produced narrower chips compared to dry cutting conditions. Additionally, textured tools reduced the chip width compared to the plain tool. The significant influence of the texture was evident at a 0.5 mm depth of cut, where the 90° texture reduced the chip width by 32% under cryogenic conditions. With the 0° texture, the reduction was 12%. The reduction in the width favored a greater curvature of the chip [11]. This, in turn, enhanced chip breakage thanks to the texture's presence.

Table 1. Chip length and width under different machining conditions.

a_p [mm]	Cooling	Chip length [mm]			Chip width [µm]		
		No texture	0°	90°	No texture	0°	90°
0.15	Dry	\	\	\	322 ± 5	318 ± 3	284 ± 5
	Cryo	73.7 ± 18.6	23.2 ± 8.0	18.1 ± 5.7	316 ± 14	289 ± 13	232 ± 8
0.25	Dry	\	\	\	447 ± 4	381 ± 4	352 ± 4
	Cryo	27.3 ± 12.1	12.4 ± 2.9	6.7 ± 5.2	399 ± 7	370 ± 9	326 ± 12
0.5	Dry	\	\	\	689 ± 1	621 ± 5	542 ± 1
	Cryo	36.8 ± 11.4	13.4 ± 4.3	7.0 ± 4.2	608 ± 3	533 ± 6	415 ± 10

To gain a deeper understanding of chip formation, chips were analyzed microscopically using SEM, as shown in Fig. 4. Dry-cut chips exhibited smoother surfaces and lower material deformation compared to those formed under cryogenic conditions. Regardless of the cooling

Materials Research Proceedings 57 (2025) 251-258 https://doi.org/10.21741/9781644903735-29

method, textured tools increased deformation, as evidenced by the presence of serrations (S) and serrated teeth (ST). Between the 0° and 90° textures, the latter left more pronounced texture marks (TM) on the chips, especially at the highest depth of cut. In this case, shear bands (SB) were more distinct, indicating greater chip curvature under both cooling conditions. The 0° texture produced less deformed chips, consistent with the observed reduction in chip length under cryogenic cooling.

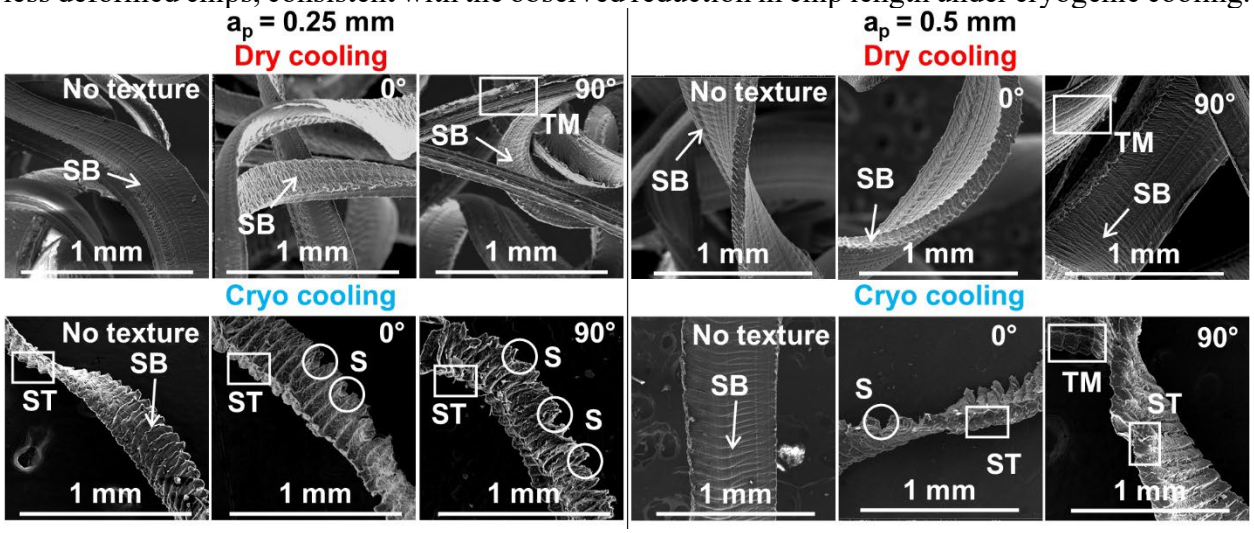


Figure 4. Chip morphology at a_p = 0.25 mm and 0.5 mm.

Table 2 presents the surface parameters for a depth of cut of 0.25 mm, selected as a representative case. The Sa values deteriorate only when using the textured tool in the 0° configuration, while they remain unchanged in the 0° configuration compared to the values obtained with untextured tools. The formation of rougher surfaces in the 90° orientation can be attributed to the imprinting of the tool pattern onto the machined surface, as confirmed by deformation observed on the chip surface.

Textured tools contribute to an increase in Svk compared to the untextured condition, indicating enhanced lubricant retention capacity. Additionally, Sk values were reduced for both 0° and 90° textures relative to the untextured configuration, indicating a decrease in core roughness depth. Conversely, Spk was generally higher for textured tools, particularly in the 0° orientation under dry conditions, suggesting an increased risk of initial wear due to more pronounced surface peaks. Notably, the increase in Spk was less significant under cryogenic cooling than under dry conditions.

Table 2. Sa, Sk, Svk, and Spk values of machined parts with a_p = 0.25 mm.

Cooling	Texture	Sa [µm]	Sk [µm]	Svk [µm]	Spk [µm]
Dry	No Texture	0.73 ± 0.09	2.36 ± 0.05	0.61 ± 0.08	0.86 ± 0.08
Cryo		1.04 ± 0.07	2.76 ± 0.07	1.00 ± 0.10	1.65 ± 0.11
Dry	0°	0.94 ± 0.03	1.57 ± 0.02	0.70 ± 0.04	1.94 ± 0.03
Cryo		1.15 ± 0.02	2.58 ± 0.03	1.11 ± 0.03	1.86 ± 0.04
Dry	90°	0.74 ± 0.04	1.98 ± 0.02	1.21 ± 0.05	1.30 ± 0.01
Cryo		0.92 ± 0.01	2.67 ± 0.01	1.40 ± 0.01	1.75 ± 0.05

Materials Research Proceedings 57 (2025) 251-258 https://doi.org/10.21741/9781644903735-29

Despite the variation in the surface parameters, textured tools consistently led to lower standard deviations, which agrees with previous research [12, 13]. This suggests that while textured tools do not directly reduce the surface roughness, they contribute to achieving more uniform surface finishes compared to plain tools.

Fig. 5a presents an example of the evolution of the cutting forces over time, while Fig. 5b shows the average cutting force values under varying cutting parameters. It is worth noting that only the average cutting force results are reported since a consistent trend was achieved also for the F_r and F_t. Fig. 5b indicates that, for each depth of cut, forces were higher under cryogenic cooling, with an average increase of approximately 40% over dry cutting. Additionally, the cutting force increased with the depth of cut, which can be attributed to the greater material removal over time. The increase was about 70% from a_p = 0.15 mm to a_p =0.25 mm and over 200% from a_p = 0.15 mm to a_p =0.5 mm.

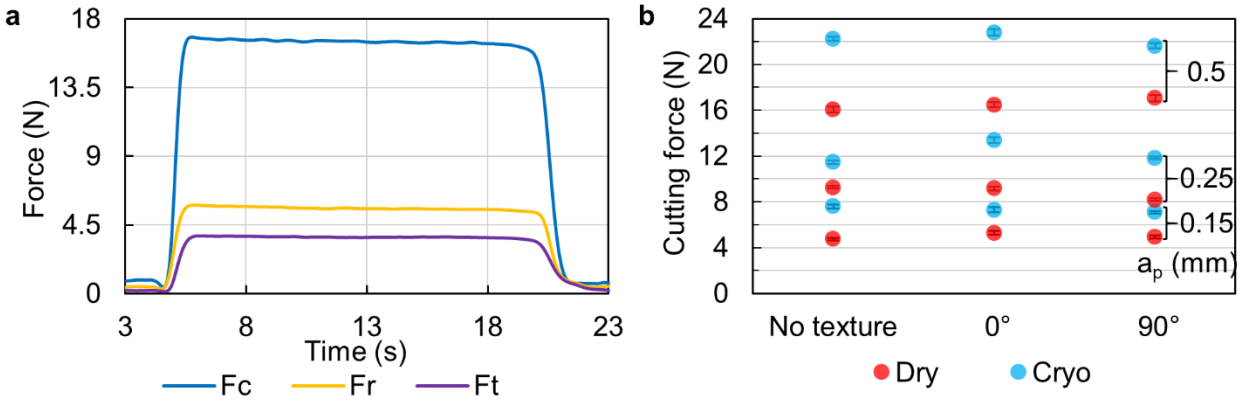


Figure 5. (a) Forces vs. time at a_p= 0.5 mm for 0° textured tool under dry conditions and (b) mean cutting force at varying cutting parameters.

Under the same cutting conditions, tool texture did not significantly affect cutting forces, as: (i) no clear trend can be identified from the data in Fig. 5b, and (ii) differences compared to the plain tool did not exceed 10%. This suggests that the textures did not alter the primary cutting mechanism but primarily influenced chip breakage, guiding the chip after its formation [14].

The modification of chip morphology was not solely attributed to cryogenic machining; textured tools also promoted the fragmentation process. Different texture designs produced varying results, making the selection of the appropriate texture configuration crucial for optimizing chip control and machining efficiency. The 90° texture directed material flow along the tool surface in the texture's direction, increasing chip deformation and consequently reducing the chip length and width. The 0° texture had a similar effect, though less pronounced.

Conclusions

In this study, PEEK samples were turned under dry and cryogenic cooling using tools with different textures (plain, 0°, and 90°) while varying the depth of cut (0.15 mm, 0.25 mm, and 0.5 mm). Cutting forces were measured, and the chips and machined surfaces were analyzed.

The main conclusions drawn from the results are as follows:

- Cryogenic machining effectively produced fragmented chips, while textured tools further enhanced chip breakage. The 90° texture had the greatest impact on reducing the chip length and width, improving chip flow control compared to the 0° texture.
- Textured tools affected surface finish by increasing Spk values, indicating rougher surfaces and a higher risk of initial wear, while also improving Svk and reducing Sk values, implying better lubricant retention. Cryogenic cooling mitigated the increase in

Spk compared to dry conditions. Despite changes in surface parameters, textured tools consistently resulted in lower standard deviations, indicating more uniform surface finishes compared to untextured tools.

- Cutting forces increased with the depth of cut and under cryogenic conditions. However, no significant influence of tool texture on cutting forces was observed, suggesting that texturing primarily affects chip breaking rather than the cutting mechanism itself.
- The depth of cut influenced the chip morphology and dimensions. Greater depths resulted in more pronounced curling under dry conditions and increased breakage under cryogenic cooling.

These results highlight the potential of combining cryogenic cooling with textured tools to optimize PEEK machining, to possibly achieve effective chip breakage even in dry machining conditions.

References

[1] S.M. Kurtz, J.N. Devine, PEEK biomaterials in trauma, orthopedic, and spinal implants, Biomaterials, 28(32), 2007, pp. 4845-4869. https://doi.org/10.1016/j.biomaterials.2007.07.013

[2] V. Shivam, S. Nitin, K. Saurabh, S. Sumit, Developments of PEEK (Polyetheretherketone) as a biomedical material: A focused review, European Polymer Journal, 147, 2021, https://doi.org/10.1016/j.eurpolymj.2021.110295

[3] R. Bertolini, A. Ghiotti, S. Bruschi, Machinability of Polyamide 6 under Cryogenic Cooling Conditions, Procedia Manufacturing, 48, 2020, pp. 419-427. https://doi.org/10.1016/j.promfg.2020.05.064

[4] H. Adibi, A. Zarandi, O. Hatami, Application of a Cryogenic Cooling System on the Grinding Operation of Polyether Ether Ketone Biomaterial (PEEK), Arabian Journal for Science and Engineering, 2022. 10.1007/s13369-022-07497-8

[5] K. Liu, J. Zhang, J. Li, R. Bao, Y. Zuo, H. Liu, Experiment study of surface formation mechanism during cryogenic turning of PEEK, Journal of Manufacturing Processes, 104, 2023. pp. 322-333. 10.1016/j.jmapro.2023.09.024

[6] T. Özel, D. Biermann, T. Enomoto, P. Mativenga, Structured and textured cutting tool surfaces for machining applications, CIRP Annals, 70, 2021. https://doi.org/10.1016/j.cirp.2021.05.006

[7] R. Ranjan, S. Hiremath, Role of textured tool in improving machining performance: A review, Journal of Manufacturing Processes, 43, 2019, pp. 47-73. https://doi.org/10.1016/j.jmapro.2019.04.011

[8] P. Fernández-Lucio, I. Villarón-Osorno, O.P. Neto, E. Ukar, L.L. de Lacalle, A.G. del Val, Effects of laser-textured on rake face in turning PCD tools for Ti6Al4V, Journal of Materials Research and Technology, 15(1), 2021, pp. 177-188. https://doi.org/10.1016/j.jmrt.2021.08.004

[9] R. Bertolini, S. Bruschi, A. Ghiotti, Enhanced surface integrity of a biomedical grade polyetheretherketone through cryogenic machining, Procedia CIRP, 102, 2021, pp. 488-493. https://doi.org/10.1016/j.procir.2021.09.083

[10] S. Bruschi, R. Bertolini, F. Medeossi, A. Ghiotti, E. Savio, R. Shivpuri, Case study: The application of machining-conditioning to improve the wear resistance of Ti6Al4V surfaces for human hip implants, Wear, 394–395, 2018, pp. 134-142, https://doi.org/10.1016/j.wear.2017.10.013

[11] H. Bharath, K. Venkatesan, Investigation of machinability characteristics of Inconel 713C using new novel honeycomb and broken-parallel texture cutting inserts with graphene-based solid lubricants, Journal of Manufacturing Processes, 109, 2024, pp. 643-668. https://doi.org/10.1016/j.jmapro.2023.11.048

[12] J. Xie, M.J. Luo, J.L. He, X.R. Liu, T.W. Tan, Micro-grinding of Micro-groove Array on Tool Rake Surface for Dry Cutting of Titanium Alloy, International Journal of Precision Engineering and Manufacturing, 13, 2012. pp.1845-1852. https://doi.org/10.1007/s12541-012-0242-9

[13] Y. Xing, J. Deng, J. Zhao, G. Zhang, K. Zhang, Cutting performance and wear mechanism of nanoscale and microscale textured Al2O3/TiC ceramic tools in dry cutting of hardened steel, International Journal of Refractory Metals and Hard Materials, 43, 2014, pp. 46–58. https://doi.org/10.1016/j.ijrmhm.2013.10.019

[14] M. Bertolete, P. Barbosa, A. Machado, R. Samad, N. Vieira, R. Vilar, W. de Rossi, Effects of texturing the rake surfaces of cemented tungsten carbide tools by ultrashort laser pulses in machining of martensitic stainless steel, The International Journal of Advanced Manufacturing Technology, 98, 2018, pp. 1-12. https://doi.org/10.1007/s00170-018-2407-x

Materials Research Proceedings 57 (2025) 259-267 https://doi.org/10.21741/9781644903735-30

Comparison between the mechanical properties and environmental sustainability of basalt and carbon fiber reinforced polymers hoop filament wound components

Iacopo BIANCHI[1,a *], Massimo DI PIETRO[1,2,b], Archimede FORCELLESE[1,c], Francesco GALLIANI[2,d], Tommaso MANCIA[3,e], Chiara MIGNANELLI[1,f *], Michela SIMONCINI[1,g], Tommaso VERDINI[1,h]

[1]Università Politecnica delle Marche, Dipartimento di Ingegneria Industriale e Scienze Matematiche, Via Brecce Bianche 12, 60131, Ancona, Italy

[2]COMEC INNOVATIVE S.R.L., Via Papa Leone XIII 40, 66100 Chieti, Italy

[3]Università eCampus, Dipartimento di Scienze Teoriche e Applicate, Via Isimbardi 10, 22060 Novedrate (CO), Italy

[a]i.bianchi@staff.univpm.it, [b]m.dipietro@pm.univpm.it, [c]a.forcellese@staff.univpm.it, [d]galliani.francesco@comec.it, [e]tommaso.mancia@uniecampus.it, [f]c.mignanelli@pm.univpm.it, [g]m.simoncini@staff.univpm.it, [h]t.verdini@pm.univpm.it

Keywords: Filament Winding, Mechanical Testing, Sustainability

Abstract. Filament Winding (FW) is one of the most effective composites manufacturing processes used to produce structural axisymmetric components in fiber reinforced polymers (FRPs), such as pipes, tubular parts and vessels. Among FRPs, basalt fibers (BFs) reinforced composites are gaining an increasing interest in many industrial fields, such as aerospace, automotive and nautical ones, since BFs are natural fibers characterized by good mechanical properties, thermal and chemical stability, as well as reduced costs, compared to synthetic carbon fibers (CFs). In this context, the present research aims at evaluating and comparing the mechanical properties, in terms of hoop tensile strength and compressive strength, of Basalt Fiber Reinforced Polymer (BFRP) and Carbon Fiber Reinforced Polymer (CFRP) tubular components obtained by FW process. Furthermore, a Life Cycle Assessment analysis was performed to evaluate the environmental impacts associated to the different composite materials. The comparison between the impacts obtained using BFRCs and CFRPs has highlighted the ecological benefits of BFRPs.

Introduction

In the last decades, Fiber Reinforced Polymers composites have been widely used in many different applications in several engineering industries due to their physical, chemical and mechanical properties combined with their low weights [1]. Specifically, Carbon Fibers are the most used fibers to reinforce polymeric matrixes, in order to achieve lightweight structures characterized by high performances [2]. Unfortunately, the CF production involves relevant CO_2 emissions and energy intensive phases, resulting in CFRP parts characterized by both elevated costs and high carbon footprint [2]. Consequently, the study of natural fibers, as a sustainable alternative to reinforce composite materials, is gaining an increasing interest in many industrial fields [3,4]. In this context, basalt fibers have emerged as one of the most promising alternatives due to their good mechanical properties, high resistance to corrosion, low thermal conductivity, chemical inertness, and low environmental impacts [5,6].

Many industries, in particular aerospace and automotive ones, require tubular reinforced composite components. In scientific literature, many researchers have focused on the evaluation of mechanical performances of FRP tubular structures manufactured by Filament Winding [7], a process based on the winding of fiber reinforced polymer tows or tapes on a rotating mandrel [8].

Content from this work may be used under the terms of the Creative Commons Attribution 3.0 license. Any further distribution of this work must maintain attribution to the author(s) and the title of the work, journal citation and DOI. Published under license by Materials Research Forum LLC.

Lapena et al. and Kessler et al. [9–11] evaluated the tensile strength, elastic modulus and thermal properties of Glass Fiber (GFRPs), Basalt Fiber (BFRPs), and Carbon Fiber Reinforced Polymers (CFRPs) wound components using unidirectional flat specimens realized by winding the composite material on a planar mandrel. Lapena et al. [12] and Amula et al. [7] compared the mechanical properties of BFRPs and GFRPs rings realized with different winding angles in terms of hoop tensile strength (HTS), by means of split-ring tests performed according to ASTM D2290. Özbek et al. [13] investigated the radial and axial compressive properties of BFRP samples realized using polar and helicoidal windings. Unfortunately, no scientific papers that provide a comprehensive comparison of the hoop tensile strength and axial compressive strength of BFRP and CFRP filament wound tubular components are available.

In this framework, the present investigation aims at evaluating and comparing the mechanical properties, in terms of hoop tensile strength and axial compression strength, of BFRP and CFRP tubular components obtained by FW process. Furthermore, a comparative analysis of the environmental impacts of reinforced composite wound components was performed by means of the Life Cycle Assessment (LCA) methodology to identify the most environmentally sustainable alternative.

Materials and Methods

Materials

Composite tubular specimens were manufactured using both basalt fiber and carbon fiber towpregs. Unidirectional fiber tows were impregnated with an epoxy resin using an automated process [14]. A Huntsman International LLC epoxy resin, characterized by a gel temperature (T_{gel}) of 90°C and a glass transition temperature (T_g) of 120°C, was used. To prevent degradation of the resin or premature curing, the towpregs spools were stored in an industrial refrigerator at -18°C.

The Basaltex 1200 was used as reinforcement of basalt tows used in the present research consider were characterized by a width equal to 6 mm. The BF towpreg resulted in a resin weight fraction (w_m%) equal to 28.2%. As far as the carbon fiber towpregs are concerned, TRH 50 Mitsubishi 30K CF filaments, with a width equal to 10 mm, were used. The CF towpreg resulted in a resin weight fraction equal to 28.2%. By assuming zero voids content of the towpregs, the fiber content for both CFRP and BFRP is equal to 71.8%.

Manufacturing process and mechanical characterization

Composite tubular specimens were manufactured using a laboratory-scale filament winding machine (X-Winder, 4X-23). The machine has four controlled axis and four stepper motors that allow the rotation of the mandrel, the translation of the deposition head along the longitudinal section of the mandrel (w-axis) and towards it (z-axis) and the rotation of the deposition head.

The towpreg spools were removed from the refrigerator 12 hours before the winding process to reach room temperature and obtain an optimal resin tack. Hence, different tubular specimens were produced to evaluate and compare the mechanical properties of the two investigated materials. In all cases, hoop winding was used, and three layers were deposited for each specimen. A winding angle equal to 88° was imposed to allow a correct tow deposition, without having excessive overlap during the winding process. A FALC muffle furnace (FM 8.2 Lt) was used to cure the tubular components. In line with the resin producer recommendations, the parts were cured at 120°C for 2 h and at 150°C for 2 hours before air cooling.

In order to characterize the mechanical behaviour of the wound components in BFRP and CFRP composite materials, ring tensile test (Figure 1a) and axial compression test (Figure 1b) were carried out. For the ring tensile test, specimens were prepared and tested according to ASTM D2290 [15]. The initial tubular components were transversally cut and then drilled so that ring specimens had a width of 25 mm, with a notch radius of 5 mm. Five specimens for each material

Materials Research Proceedings 57 (2025) 259-267 https://doi.org/10.21741/9781644903735-30

were realized and tested. A dedicated split-disk fixture, consisting of two semicircular supports, was used for the test in the MTS 810 universal testing machine. A crosshead speed equal to 0.1 mm/s was set for the test, within the range defined by the ASTM D2290 standard.

For the axial compression test, two tubular specimens were cut at both extremities to remove irregular thickness of the turning zones obtained during the winding process. According to the ASTM D695 standard, tubular specimens were 70 mm in the inner diameter and 150 mm in height [16]. The axial compression tests were performed using the MTS 810 universal testing machine equipped with compression plates. Load vs displacement curves were obtained as well as the compressive stress on the parts.

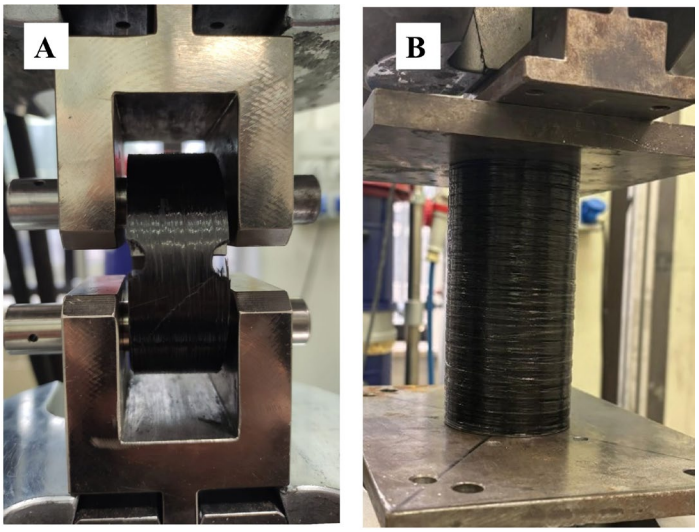


Figure 1 (a) Ring tensile test and (b) axial compression test.

Life Cycle Assessment analysis

The mechanical characterization tests were paired with a sustainability analysis to determine if the basalt fiber based composite material can provide environmental impacts reduction with respect to the synthetic alternative of CFs. To this purpose, the standardized methodology of Life Cycle Assessment, defined by the ISO 14040-14044 standard, was employed. The four iterative phases described in the standard, i.e. 1) Goal and Scope definition, 2) Life Cycle Inventory, 3) Life Cycle Impact Assessment, and 4) Results and discussion, were performed.

The Functional Unit (FU) was defined as the production of composite tubular components characterized by an inner diameter equal to 70 mm, a length equal to 150 mm and a laminate stacking sequence as that used for the mechanical characterization (i.e. 3 layers with 88° orientation); in these conditions, a composite tubular component, with thickness equal to about 2.5 mm, results. Data related to the fiber and matrix volume fraction for the composite materials were the same reported in the previous sections.

Two scenarios were hence included in the analysis to represent the production of basalt fiber (Scenario 1) and carbon fiber (Scenario 2) reinforced composite tubular parts. In order to focus on the material production and manufacturing stages, a cradle to gate approach was adopted; impacts related to materials extraction (carbon and basalt fibers, epoxy resin, consumable materials) and preparation, transport and all the manufacturing phases (including prepreg production, filament winding and parts curing) were included within the system boundaries. The service life was not included within the system boundaries as it would be strongly influenced by the specific use of the component (e.g. in automotive or building sectors) and the analysis would have lost general value.

For the Life Cycle Inventory (LCI) phase, direct measurements and secondary data from literature analyses and commercial database (Ecoinvent) were used.

Materials Research Proceedings 57 (2025) 259-267 https://doi.org/10.21741/9781644903735-30

The weight of the tubular component was directly measured and, considering the fiber and matrix fractions in the two scenarios, constituents' consumption was calculated. Whenever possible, raw materials production was modelled using the Ecoinvent database (e.g. in the case of aluminium, epoxy resin…). Carbon fibers were modelled according to literature [2]; similarly, basalt fibers were modelled according to Fort et al. [17]. The prepregging phase was modelled according to literature [14]. Refrigerated storage was also considered for the prepreg. Transport distances were estimated considering the material suppliers geographical location and the production plant in center Italy. The energy consumption of the filament winding was directly measured via a power meter. Curing energy and consumable material use were estimated according to literature analysis [18]. Ecoinvent was employed to model electric energy consumption (low voltage, Italian energy mix) and transport impacts (i.e. considering road and water routes).

The two scenarios were modelled in SimaPro and LCIA results were obtained. Impacts were evaluated in terms of Global Warming Potential (GWP, IPCC methodology); GWP quantifies the possible effects of the FU on global warming, and it is expressed in kg of CO_2 eq. This impact category was selected among the most significant and used ones for composite parts LCA analyses.

Results and discussions

Mechanical characterization results

Figure 2 shows typical specific load vs. displacement curves obtained by ring tensile tests of BFRP and CFRP samples. Irrespective of the material investigated, the specific load increases with displacement until reaching a peak value at which the ring specimen fracture occurs. However, the curves of BFRP and CFRP composite materials are characterized by different slopes: specifically, for a given displacement, the specific load of CFRP is always higher than that of BFRP composite. Furthermore, the maximum specific load value reached by the CFRP specimens, equal to about 7 kN/g, is more than three times higher than the one obtained by the BFRP ring specimens (about 2 kN/g). This result can be attributed to the higher ultimate tensile strength of CFs with respect to the one of BFs. Since the load is applied along the direction in which the fibers are oriented (hoop winding), the fibers are responsible for the mechanical response of the specimens. However, it is interesting to observe that BFRP specimens reach the fracture at a displacement of 3.5 mm, which is higher than the one reached by CFRP specimens, equal to 2.1 mm. Table 1 summarizes the mean values of weight, thickness obtained by the specimens' measurements, maximum load, specific maximum load, HTS and specific HTS resulted by the performed test.

The comparison between CFRPs and BFRPs in terms of HTS and specific HTS, calculated according to ASTM D2290 standard, shows that the CFRP specimens are characterized by higher HTS and specific HTS values than those obtained by BFRP ones, even though BFRPs fail after higher displacements than those applied to CFRPs.

Table 1 Mean geometric values of ring specimens and typical mechanical properties obtained by ring tensile tests.

	Weight [g]	Thickness [mm]	Max Load [kN]	Specific Max Load [kN/g]	HTS [MPa]	Specific HTS [MPa/g]
BFRP	29.07±4.86%	2.73±2.45%	64.74±4.08%	2.23±3.37%	720.98±4.16%	24.80±3.58%
CFRP	7.02±2.03%	1.10±4.09%	50.66±4.42%	7.22±3.71%	1358.17±4.4%	194.54±3.89%

Materials Research Proceedings 57 (2025) 259-267 https://doi.org/10.21741/9781644903735-30

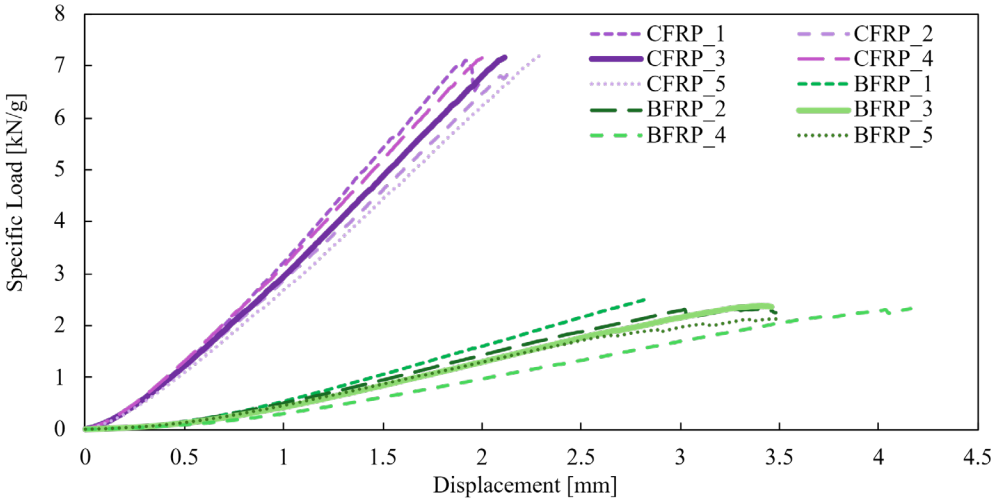


Figure 2 Typical specific load versus displacement curves of BFRP and CFRP ring specimens subjected to ring tensile tests.

To investigate the compressive behavior of BFRP and CFRP composites, axial compressive tests were performed according to ASTM D695 standard [16]. Figure 3 shows typical compressive strength vs. strain curves obtained by axial compressive tests of BFRPs and CFRPs. It can be observed that the BFRP tubular components are characterized by a different compressive behavior as compared to the CFRP ones. Specifically, the compressive strength exhibited by BFRP increases with strain until a peak value equal to about 78 MPa; then, the compressive strength vs. strain curve shows a sawtooth pattern with a gradual and slow reduction in strength until failure. The BFRP material exhibits such behavior up to a mean strain value of 6%. On the contrary, the compressive strength of CFRP specimens rises with strain until the similar peak value reached by the BFRP, at which the fracture clearly occurs, then a decrease in the compressive strength can be observed. Such result can be attributed to the different failure mechanisms of the tubular samples related to the different reinforcements used. According to Abolfazli et al. [19], the tubular component in CFRP is characterized by a fiber resin interface cracking (Figure 4a). The compressive force applied to the tubular composite part can cause the separation between fibers and resin, leading to the formation of cracks and overall failure. On the other hand, the tubular component in BFRP exhibits the end crushing, that is a type of failure mechanism where the material is crushed at the end of the structure (Figure 4b).

The similar compressive strength reached by the two materials at the first peak value of the curves can be attributed to the failure of the matrix since the direction of the applied load during tests is almost perpendicular to the fiber orientation in the hoop configuration investigated in the present study.

Table 2 summarizes both the mean values of weight and thickness obtained by the specimens' measurements, and the maximum load and maximum compressive strength obtained by the performed axial compressive tests, for both materials investigated.

Table 2 Mean geometric values of tubular specimens and typical mechanical properties obtained by axial compressive tests

	Weight [g]	Thickness [mm]	Max Load [kN]	Max Compressive strength [MPa]
BFRP	150±3.78%	2.4±4.25%	42.75±3.87%	78.34±4.09%
CFRP	130±3.23%	2.625±3.56%	44.61±4.02%	74.52±4.17%

Materials Research Proceedings 57 (2025) 259-267 https://doi.org/10.21741/9781644903735-30

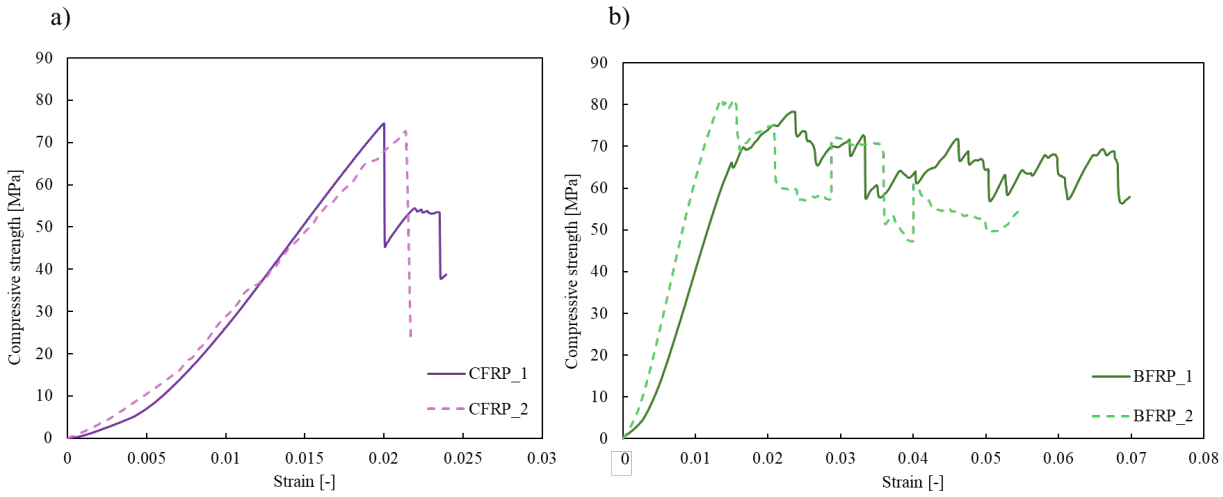


Figure 3 Typical compressive strength-strain curves obtained by (a) CFRP, and (b) BFRP specimens subjected to axial compressive tests.

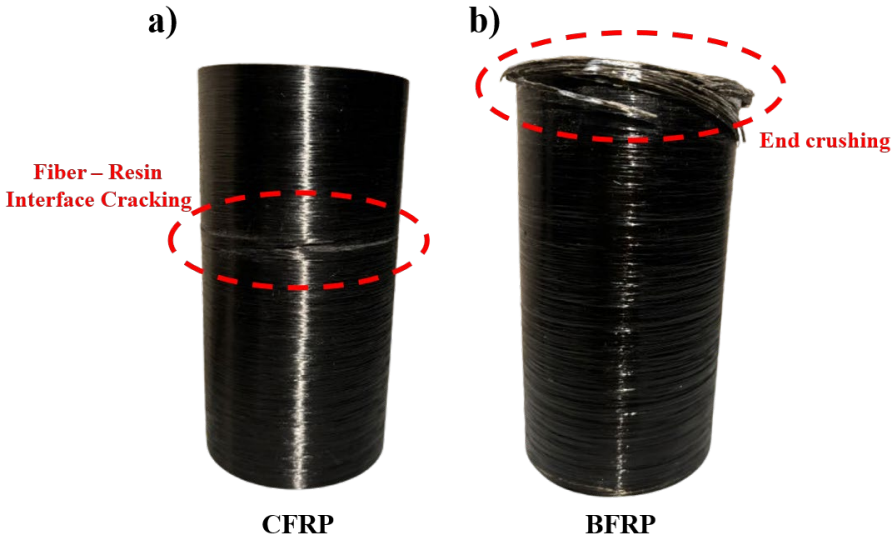


Figure 4 Fractured tubular components in (a) CFRP and (b) BFRP composite after axial compressive tests.

Life Cycle Assessment results

Figure 5 shows the results of the LCA analysis in terms of Global Warming Potential for the two considered scenarios. The Basalt Fiber composite (Scenario 1) resulted the most sustainable alternative with total footprint equal to 1.60 kg CO_2 eq whilst the Carbon Fiber one (Scenario 2) has an associated impact equal to 3.56 kg CO_2 eq.

Indeed, the main advantage associated with Scenario 1 is related to the low unitary carbon footprint of BFs with respect to the CFs (i.e. 0.4 kg CO_2 per kg vs. 39.9 kg CO_2 per kg). The production of carbon fibers represents the higher contributor in Scenario 2, accounting for about 67% of total manufacturing impact; on the contrary, the production of basalt fibers has almost a negligible impact; hence, despite the higher density of basalt fibers (and overall weight of the tubular components), they represent a sustainable alternative to synthetic materials.

Materials Research Proceedings 57 (2025) 259-267 https://doi.org/10.21741/9781644903735-30

In both scenarios, the preimpregnation and filament winding phases have almost negligible impacts; this result further highlights that FW can represent a low emissions and automated production process for composites. On the other hand, the curing phase, that is the same in both scenarios as it is basically not affected by the fiber reinforcement used, is associated with relevant impacts, both for the energy requirements and the consumable materials (i.e. these phases combined account for more than 80% of Scenario 1 impacts). It follows that improvement solutions are required.

In the present analysis, the functional unit was defined only considering the geometry of the components as similar compressive behavior was assumed. Different results could be obtained as different properties are selected as benchmark for the definition of the FU; for instance, as tensile strength or modulus are considered, CFs could provide strong benefits in terms of weight reduction. These assessments will be further explored and developed in future studies.

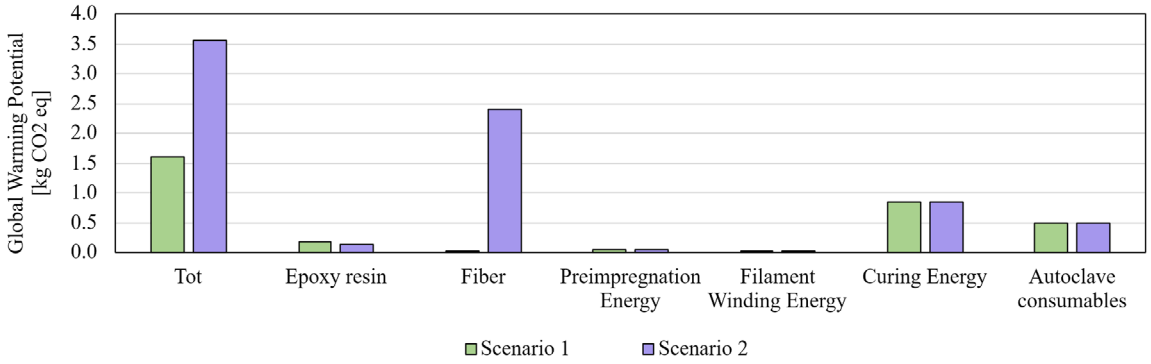


Figure 5 LCA results in terms of GWP for the two considered scenarios.

Conclusions

The present study aimed at evaluating the differences between the mechanical properties of CFRP and BFRP tubular specimens obtained by FW process, in terms of hoop tensile strength and axial compressive strength. In addition, the environmental impacts of both materials were evaluated by means of LCA methodology. The main results can be summarized as follows:

- Irrespective of the material investigated, the specific load measured by means of ring tensile tests on specimens increases with displacement until reaching a peak value at which the fracture of the specimen occurs.
- The maximum specific load, as well as the maximum specific HTS value, reached by the CFRP specimens (respectively 7.22 kN/g and 194.54 MPa/g) are relevantly higher than those obtained by BFRP specimens (respectively 2.23 kN/g 24.80 MPa/g).
- The compressive behaviour of the tubular components can be attributed to the different failure mechanisms related to the different reinforcements used. In particular, the tubular component in CFRP is characterized by a fiber resin interface cracking whilst the part in BFRP exhibits an end crushing mechanism.
- A negligible discrepancy in the maximum axial compressive strength obtained by CFRP and BFRP specimens can be observed due to the failure of the matrix since the direction of the applied load during tests is almost perpendicular to the fiber orientation in the hoop configuration investigated in the present study.
- The environmental impacts related to the production of a BFRP tubular component are significantly lower (1.60 kg CO_2 eq) than those of CFRP one (3.56 kg CO_2 eq). The main difference is due to the impacts related to the fibers: the unitary carbon footprint of CF is relevantly higher than the one of BF.

Future works will concern the study of other mechanical properties of both BFRP and CFRP, such as the radial compressive strength. In addition, the effect of different winding angles and FW parameters on mechanical behaviour and environmental impact will be investigated to optimize the performances of the BFRP components produced using FW process.

References

[1] Z.A. OĞUZ, Ö. ÖZBEK, A. ERKLİĞ, Ö.Y. BOZKURT, Hydrothermal aging effect on crushing characteristics of intraply hybrid composite pipes, Eng Struct 297 (2023) 117011. https://doi.org/10.1016/J.ENGSTRUCT.2023.117011

[2] A. Forcellese, M. Marconi, M. Simoncini, A. Vita, Life cycle impact assessment of different manufacturing technologies for automotive CFRP components, J Clean Prod 271 (2020). https://doi.org/10.1016/J.JCLEPRO.2020.122677

[3] Ö. Özbek, Z.A. Oğuz, Ö.Y. Bozkurt, A. Erkliğ, Crashworthiness characteristics of hydrothermally aged intraply glass/basalt composite pipes, Marine Structures 97 (2024) 103656. https://doi.org/10.1016/j.marstruc.2024.103656

[4] H. Sun, D. Xiang, Z. Liu, L. Liu, E. Harkin-Jones, M. Wang, W. Tan, P. Luo, J. Zhang, B. Wang, Y. Liu, Y. Wu, Failure analysis of glass fiber and basalt fiber reinforced polymer composites under an extreme environment with high-temperature, high-pressure and H2S/CO2 exposure, Polym Compos 45 (2024) 10124–10136. https://doi.org/10.1002/pc.28462

[5] V. Dhand, G. Mittal, K.Y. Rhee, S.J. Park, D. Hui, A short review on basalt fiber reinforced polymer composites, Compos B Eng 73 (2015) 166–180. https://doi.org/10.1016/J.COMPOSITESB.2014.12.011

[6] V. Lopresto, C. Leone, I. De Iorio, Mechanical characterisation of basalt fibre reinforced plastic, Compos B Eng 42 (2011) 717–723. https://doi.org/10.1016/J.COMPOSITESB.2011.01.030

[7] T.A.D.M.S. Almula, I.H. Amori, M.Y. Yahya, A. Ayob, An experimentally and numerically comparison between e-glass/epoxy and basalt/epoxy pipes pressurized internally, Solid State Phenomena 305 (2020) 49–56. https://doi.org/10.4028/www.scientific.net/SSP.305.49

[8] I. Bianchi, A. Forcellese, T. Mancia, C. Mignanelli, M. Simoncini, T. Verdini, Effect of Heat-Shrinkable Tape Application on the Mechanical Performance of CFRP Components Obtained by a Filament Winding Process, Journal of Composites Science 2024, Vol. 8, Page 535 8 (2024) 535. https://doi.org/10.3390/JCS8120535

[9] M.H. Lapena, G. Marinucci, O. De Carvalho, Mechanical characterization of unidirectional basalt fiber epoxy composite, 16th European Conference on Composite Materials, ECCM 2014 (n.d.) Seville.

[10] E. Kessler, R. Gadow, P. Weichand, Investigation of mechanical properties of filament wound unidirectional basalt fiber reinforced polymers for automotive and pressure vessel application, ICCM International Conferences on Composite Materials 2015 (2015) 2015.

[11] E. Kessler, R. Gadow, J. Straub, Basalt, glass and carbon fibers and their fiber reinforced polymer composites under thermal and mechanical load, AIMS Mater Sci 3 (2016) 1561–1576. https://doi.org/10.3934/matersci.2016.4.1561

[12] M.H. Lapena, G. Marinucci, Mechanical characterization basalt and glass fiber epoxy composites by the ring-type test specimens, ECCM 2016 - Proceeding of the 17th European Conference on Composite Materials (n.d.) Munich.

[13] Özbek, Y. Bozkurt, A. Erkliğ, Effect of Basalt Intraply Fiber Hybridization on the Compression Behavior of Filament Wound Composite Pipes, International Polymer Processing 36 (2021) 193–204. https://doi.org/10.1515/IPP-2020-4005/MACHINEREADABLECITATION/RIS.

[14] L. Postacchini, M. Simoncini, A. Forcellese, M. Bevilacqua, F.E. Ciarapica, G. Andreassi, A.C. Russo, Environmental assessment of an automated impregnation process of carbon fiber tows, in: Procedia CIRP, 2020: pp. 445–450. https://doi.org/10.1016/j.procir.2020.05.077

[15] Test Method for Apparent Hoop Tensile Strength of Plastic or Reinforced Plastic Pipe, (2019). https://doi.org/10.1520/D2290-19A

[16] Test Method for Compressive Properties of Rigid Plastics, (2023). https://doi.org/10.1520/D0695-23.

[17] J. Fořt, J. Kočí, R. Černý, Environmental Efficiency Aspects of Basalt Fibers Reinforcement in Concrete Mixtures, Energies 2021, Vol. 14, Page 7736 14 (2021) 7736. https://doi.org/10.3390/EN14227736

[18] B. Iacopo, M. Chiara, S. Michela, V. Tommaso, Life cycle analyses of a composite towbar realized via filament winding and comparison with traditional metallic alternatives, Sustainable Materials and Technologies (2024) e00980. https://doi.org/10.1016/J.SUSMAT.2024.E00980

[19] M. Abolfazli, M. Bazli, A. Rajabipour, M. Heitzmann, H. Pourasiabi, H. Wang, M. Arashpour, Residual compressive strength of filament wound hybrid glass/carbon fibre reinforced polymer tubes after exposure to elevated temperature, Compos Struct 316 (2023) 117050. https://doi.org/10.1016/J.COMPSTRUCT.2023.117050

Materials Research Proceedings 57 (2025) 268-277 https://doi.org/10.21741/9781644903735-31

Effect of heat shrinkable tape layer number on mechanical properties and quality of tubular CFRP components obtained by filament winding

Marina ANDREOZZI[1,a], Iacopo BIANCHI[1,b], Archimede FORCELLESE[1,c], Chiara MIGNANELLI[1,d], Massimiliano PIERALISI[1,e], Michela SIMONCINI[1,f], Tommaso VERDINI[1,g] *

[1]Università Politecnica delle Marche, Dipartimento di Ingegneria Industriale e Scienze Matematiche, Via Brecce Bianche 12, 60131, Ancona, Italy

[a]m.andreozzi@staff.univpm.it, [b]i.bianchi@staff.univpm.it, [c]a.forcellese@staff.univpm.it, [d]c.mignanelli@pm.univpm.it, [e]m.pieralisi@staff.univpm.it, [f]m.simoncini@staff.univpm.it, [g]t.verdini@pm.univpm.it

Keywords: Filament Winding, Mechanical Testing, Radiography & Tomography

Abstract. The most common manufacturing process for tubular Carbon Fiber Reinforced Polymer (CFRP) components is Filament Winding (FW), that requires a subsequent curing process to obtain the final parts. The most widely used curing process is the autoclave one, that involves high environmental and economic impacts. Then, other curing solutions must be investigated to find a valuable sustainable alternative. In this context, the present work aims at studying the effect of the number of heat shrinkable tape (HT) layers applied on the wound CFRP components before the oven curing process, on the mechanical properties, thickness uniformity and void content of the tubular parts. To this purpose, ring tensile tests and tomography analysis were performed on ring specimens cut from tubular parts realized by FW, using different HT layers. It was demonstrated that the increase in HT layers allows an improvement both of mechanical properties and thickness uniformity, and a reduction in void content.

Introduction

In recent decades, the manufacturing industry has increasingly focused on developing materials that combine high mechanical performance and light weight in order to optimize energy efficiency and overall system performance [1], [2], [3]. Among these materials, carbon fiber-reinforced polymers (CFRPs) represent a class of composite materials highly valued in advanced technological areas such as the aerospace industry, the automotive sector, and the production of sports equipment [4], [5]. CFRPs feature a structure that achieves an excellent strength-to-weight ratio; they are characterized by high stiffness, tensile strength, light weight and durability, offering reliable and versatile solutions for applications requiring maximum engineering performance [6].

Among the many manufacturing processes, Filament Winding (FW) is one of the most popular technologies for the production of tubular CFRP components, as it enables high precision in fiber placement and good process repeatability [7], [8]. FW involves the controlled winding of resin-impregnated filaments around a rotating mandrel, following specific angles and patterns to optimize the mechanical properties of the final component. This technique is particularly advantageous for the fabrication of cylindrical or spherical structures, such as pressure vessels, drive shafts, and high-performance pipelines [9], [10].

A fundamental aspect of the FW process is the curing of the polymer matrix, which is essential to achieve the desired mechanical properties and reduce internal defects, ensuring the quality of the composite component. There are different methods of polymerization, of which autoclave curing is among the most widely used as it allows uniform pressure to be applied to the entire

Content from this work may be used under the terms of the Creative Commons Attribution 3.0 license. Any further distribution of this work must maintain attribution to the author(s) and the title of the work, journal citation and DOI. Published under license by Materials Research Forum LLC.

Materials Research Proceedings 57 (2025) 268-277 https://doi.org/10.21741/9781644903735-31

surface of the component, promoting the removal of trapped air and reducing the formation of defects [11], [12]. However, the autoclave process requires significant energy consumption, making the search for alternative solutions sustainable and efficient [13], [14].

In this context, oven curing represents a valid alternative due to its greater operational simplicity and lower costs [15]. Nevertheless, the absence of applied pressure during the curing process can lead to thickness non-uniformity, internal defects, and a reduction in mechanical performance [16]. Additionally, temperature variations, combined with the lack of precise pressure control, can cause defects such as residual voids, micro-cracks, and non-uniformity in resin distribution.

To overcome these challenges, the use of heat shrinkable tape, applied to the components prior to curing, is proving to be promising strategy. HT is a tape designed to be applied around composite components, which contracts when exposed to heat, exerting uniform pressure on the surface of the part. This effect, during the curing phase, can apply consistent pressure to the component, optimizing resin distribution, reducing voids, and improving both mechanical properties and surface quality [17].

The present study aims to analysing the effect of the number of layers of HT applied to tubular CFRP components made by FW. Specifically, it aims to evaluate how the variation of this parameter affects the mechanical properties, thickness uniformity and void content. To this end, ring tensile tests and tomographic analysis were conducted on ring specimens made from tubes cured in an oven with different configurations of HT.

The results of this research will provide a more in-depth understanding of the consolidation dynamics of composite materials in absence of autoclaving and provide practical guidance for improving the quality of the final product through more efficient and environmentally friendly manufacturing techniques.

Materials and Methods

In order to investigate the effect of the HT on the mechanical properties and the void content, a tubular component with a circular section was taken into account, since the pressure during shrinkage is constant for axisymmetric geometry. A filament winding process was used to realize composite tubular components. The composite material was a towpreg characterised by carbon fiber filaments embedded in an epoxy resin matrix. The reinforcement consists of T700 30K carbon fibers with a diameter of 7 μm. The matrix is an epoxy resin (Huntsman International LLC) with a gelation temperature (Tgel) of 90°C and a glass transition temperature (Tg) of 120°C. The towpreg is characterized by a total width and thickness respectively equal to 8mm and 0.2mm, and a weight fraction of CFs and epoxy resin, of 60% and 40%.

The mechanical properties of the composite were calculated from the constituent data sheets using mixture rule [18]. Calculation of the transverse modulus of a unidirectional composite material and of the modulus of an aggregate. Table 1 summarises both the mechanical properties of the constituent materials and composite material.

Table 1: Mechanical properties of CFs, epoxy resin from data sheet, and CFRP calculated by using the mixture rule

	Carbon fiber	**Epoxy resin**	**Composite material**
Elastic modulus (E)	230 GPa	3.5 GPa	75 GPa
Ultimate Tensile Strength (UTS)	4900 MPa	73 MPa	2900 MPa
Density (ρ)	1.8 g/cm^3	1.1 g/cm^3	1.52 g/cm^3

The heat shrink tape used was produced by DIATEX SAS (Saint-Genis-Laval, France). This tape is applied externally to the CFRP tubular component immediately after the filament winding

Materials Research Proceedings 57 (2025) 268-277 https://doi.org/10.21741/9781644903735-31

process. When heated, the tape shrinks, exerting a compressive force on the underlying material, thereby enhancing its compactness. In particular, the shrinkage begins at 100°C, with a shrinkage of 11% at 150°C, and 15% at 200°C, as reported in the technical datasheet. A key advantage of this tape is its lack of adhesive, which facilitates easy removal after the polymerization process, preventing residues or surface damage.

The filament winding process was performed using the X-Winder machine to manufacture the CFRP tubular components. This automated winding system features four degrees of freedom, each controlled by a dedicated axis. The X-axis translates the cross carriage, controlling its distance from the rotating mandrel. The Z-axis provides linear translation of the carriage along the mandrel's longitudinal axis. The W-axis controls the azimuthal rotation of the mandrel. The U-axis controls the rotation of the fiber deposition head. The coordinated motion of these axes enables the precise winding of the mandrel. The X-axis is crucial for dome formation. The Z and U axes control the fiber placement on the cylinder portion. The W-axis is used to rotate the mandrel. The final fiber angle is a function of both the translational velocity of the deposition head and the rotational speed of the mandrel.

The effect of the layer number of the heat shrinkable tape on both the mechanical properties, void volume fractions, and the void volume was investigated. To this purpose, the composite tubular components were realized by winding three layers of CFRP with a theoretical winding angle of 88°, but different HT layers were used, as summarized in Table 2. The carriage and mandrel maximum speeds were imposed equal to 101.60 mm/s and 3.14 rad/s, respectively.

Table 2: Condition evaluated in this study

Condition	**Composite Layers**	**HT layers**	**n. of specimens**
0 HT Layers	3	0	5
1 HT Layers	3	1	5
2 HT Layers	3	2	5
3 HT Layers	3	3	5

After the winding process, the tubular components were removed from the winding machine and placed in a FALC muffle furnace. This furnace allows a maximum temperature of 1200°C, for the curing process, to be reached. According to the physical properties of the epoxy resin, the thermal curing process consists of two distinct stages. The primary cure is conducted at 120°C for a duration of 2 hours. To ensure complete polymerization and optimal material properties, a secondary post-cure stage is required. This involves maintaining the chamber temperature at 150°C for an additional 2 hours. The part is then allowed to cool to room temperature via natural convection (air cooling).

Then, ring specimens were obtained from the CFRP tubular components by means of drilling and cutting operation, according to ASTM D2290 standard (Procedure A). The split-disk test is a standard method for characterizing the circumferential tensile behaviour of filament-wound composites. The mechanical properties of the ring tensile specimens were evaluated by means of the split-disk test carried out on a servo-hydraulic testing machine (MTS 810®) equipped with a 250 kN load cell. During tests, the crosshead speed was kept constant at 0.1 mm/s. The experimental results were plotted as applied load versus displacement curves from which the hoop tensile strength was evaluated by using Equation 1:

$$\sigma_{HTS} = \frac{P}{2 \cdot A_{min}} \quad (1)$$

in which P [kN] is the maximum load during the tensile test and A_{min} [mm^2] is the minimum area between the two reduced sections.

Materials Research Proceedings 57 (2025) 268-277 https://doi.org/10.21741/9781644903735-31

Finally, the X-ray Computed Tomography (X-CT) scan was performed using a Zeiss METROTOM 1500 CT to evaluate the void volume fraction (VVF) and Void Volume (VV). The system was equipped with an X-ray tube with a minimum focal spot of 7 μm, a maximum accelerating voltage of 199 kV and a maximum current leakage of 1000 μA. The source-detector distance was maintained at 1500 mm with a maximum measuring range of 350 mm x 300 mm and a detector resolution of 2048 x 2048 pixels. The voxel size of the X-CT is 50.7 μm. The scanning was carried out after the machining necessary to produce the ring specimen. In particular, the void analyses were performed on the central ring of the tubular component, as this is the area where the machine works at full capacity, so the ring quality should be higher with respect to the other zone.

The tubular components produced both with and without the HT are shown in Figure 1.

(a) Without HT (b) With HT



Figure 1: Tubular parts and ring specimens obtained (a) without and (b) with HT.

Results and Discussion

In order to evaluate the effect of the heat-shrinkable tape application on the mechanical properties of CFRP wound parts, ring specimens, obtained from tubular components, were tested using ring tensile tests. Figure 1 shows the typical hoop tensile stress versus displacement curves of CFRP ring specimens subjected to the split ring tests. Irrespective of the number of HT layers, it can be observed that the HTS rises with increasing displacement up to a peak value corresponding to the ring fracture. The HT tape application involves an increase in the hoop tensile strength as compared to the condition without the HT tape. Furthermore, it can be observed that the HTS values increase as the number of HT tape layers applied increases, even though such effect tends to decrease with increasing the HT layers. As a matter of fact, the application of a HT layer (condition 1 HT Layer of Table 3) leads to the obtaining of an increase in HTS value of about 38.7% as compared to the condition without the tape; as the number of HT layers increases, the HTS increases by 53.4% (condition 1 HT layer) and 64.9% (condition 2 HT layers), respectively, compared to the condition 0 HT layer. The hoop tensile strength values obtained at different HT layers are summarized in Table 3. Since the weights of the specimens are different between the different analyzed conditions, the specific HTS was evaluated (Table 3).

Materials Research Proceedings 57 (2025) 268-277 https://doi.org/10.21741/9781644903735-31

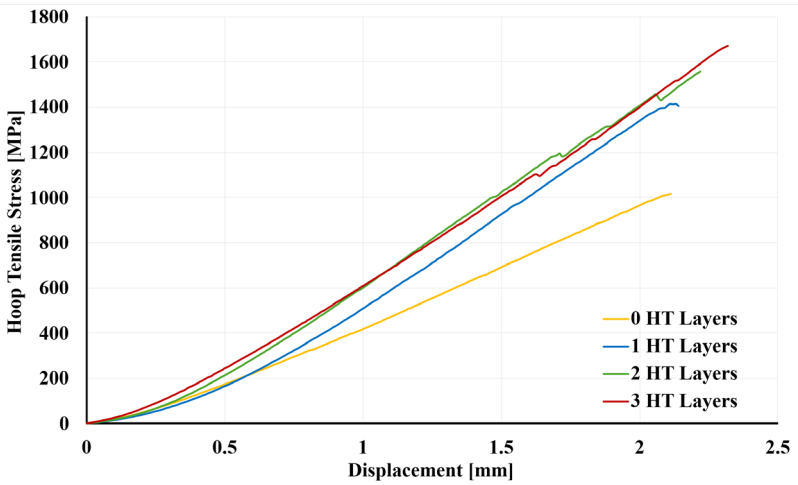


Figure 2: Effect of the number of HT layers on the typical hoop tensile stress - displacement curves obtained from CFRP ring specimens

Table 3: Average HTS, thickness, weight, specific HTS and the respectively percentual standard deviation obtained

	HTS [MPa]	Thickness [mm]	Weight [g]	Specific HTS [MPa/g]	Load [kN]
0 HT Layer	1014.77 ± 4.1%	1.49 ± 7.7%	12.79 ± 3.8%	79.33 ± 5.9%	52.92 ± 3.9%
1 HT Layer	1407.36 ± 2.3%	1.33 ± 3.6%	11.16 ± 2.9%	126.11 ± 2.95%	61.11 ± 2.4%
2 HT Layers	1556.39 ± 2.2 %	1.32 ± 3.3%	10.74 ± 2.4%	144.92 ± 2.8%	65.55 ± 1.9%
3 HT Layers	1672.95 ± 1.9%	1.20 ± 3.4%	10.40 ± 2.7%	160.86 ±2.7%	66.65 ± 2.1%

The improvement in mechanical properties of the CFRP ring specimens given by the application of HT layers can be also observed by the Figure 2 in which the specific HTS values as a function of the number of HT layers is shown. The specific HTS increases as the number of HT layers increases, with a non-linear trend. To evaluate the benefit related to the application of HT tape, a linear trend between two consequent conditions (i.e. 0 - 1 HT Layers; 1 - 2 HT Layers; 2 - 3 HT Layers) was considered. In particular, the ratios $\frac{\Delta y}{\Delta x}$ reported in the figure correspond to the slopes of the different segments of the curve, representing the rate of increase of specific HTS for each additional layer. Specifically, the slope of the linear trend represents the increment of the specific HTS between the conditions considered. The application of heat-shrink tape improves the specific HTS, but with a decreasing marginal benefit as the number of layers increases. The addition of a layer has the greatest impact on HTS ($\frac{\Delta y}{\Delta x} = 46.77$), suggesting that the application of pressure during curing significantly reduces structural defects (such as voids or poor resin impregnation). Applying two layers instead of one, a reduced improvement can be obtained ($\frac{\Delta y}{\Delta x} = 18.81$), indicating that beyond a certain level of compression, the benefit stabilizes. This can be also highlighted with the addition of three HT layers ($\frac{\Delta y}{\Delta x} = 15.94$).

Materials Research Proceedings 57 (2025) 268-277 https://doi.org/10.21741/9781644903735-31

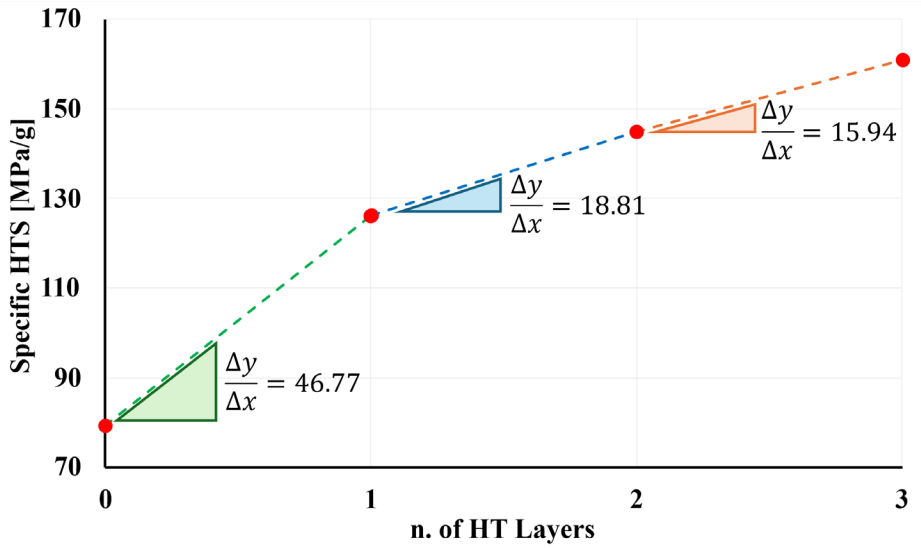


Figure 3: Influence of the number of HT tape layers on the specific HTS

The increase in the hoop tensile strength with HT layers can be attributed to the reduction in the ring thickness, due to the compressive force applied to the tape on the tubular component during the curing phase. Furthermore, the reduction in thickness leads to a decrease in the void content in the tubular component. To this purpose, Figure 3 shows the results obtained from the X-CT for each condition investigated, in order to quantify the Volume Void Fraction, and to highlight the void distribution in ring specimens. The analysis of void distribution in the ring specimens reveals a clear alignment of voids along the direction of fiber deposition. This pattern suggests a strong correlation between the manufacturing process and void formation, indicating that voids are inherently linked to the material deposition technique. The specimen characterized by the highest void content is the one manufactured without heat-shrink tape (0 HT layer). As a matter of fact, it exhibits larger and more irregularly distributed voids, with a void volume fraction of about 3.1%. When HT tape is applied (1 HT layer), the void fraction decreases significantly, resulting in smaller and more evenly distributed voids. However, beyond the first layer of HT tape, the reduction in voids becomes marginal, suggesting that additional layers do not substantially enhance the compaction. In fact, the void volume fractions are about 0.61%, 0.58%, and 0.53% for the condition with 1, 2, or 3 HT layers, respectively. The observed reduction in thickness is directly related to the decrease in void content. The external pressure exerted by the HT tape during the curing process enhances material compaction, leading to a more structurally sound component with few internal voids. This improvement in compaction results in better mechanical properties and overall material quality.

Materials Research Proceedings 57 (2025) 268-277 https://doi.org/10.21741/9781644903735-31

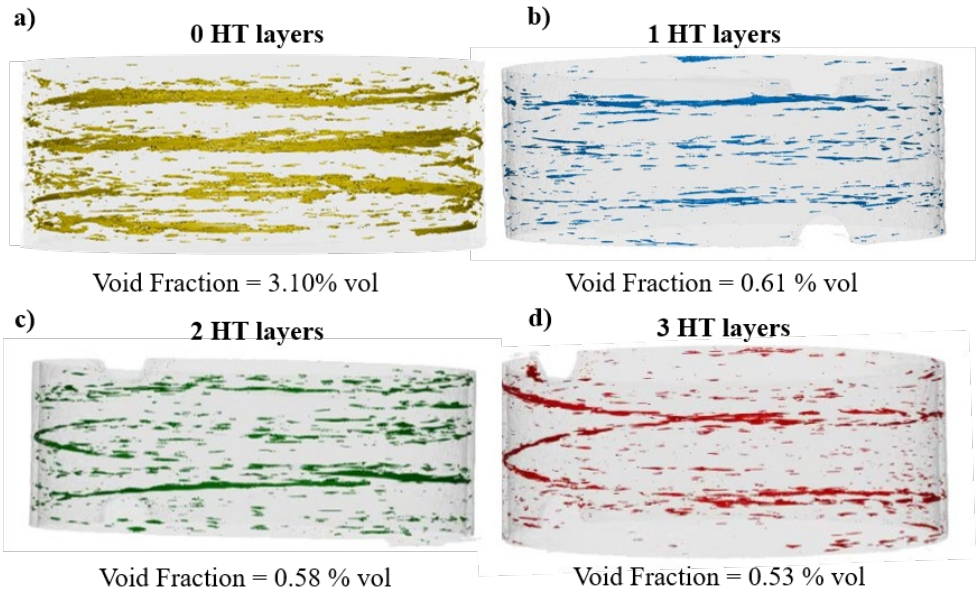


Figure 4: Effect of the number of HT layers on the void fraction: (a) without HT, (b) 1 HT layer, (c) 2 HT layers, and (d) 3 HT layers.

In Figure 4 the void volume dimensions are shown, as a function of the number of HT layers applied. The sample without HT tape (0 HT layer) is characterized by the highest void volume (i.e. 230.23 mm³). The widespread presence of large voids (red areas) indicates a lack of external pressure during polymerization, which prevented the escape of trapped air and led to the formation of macroscopic defects. The application of a single layer of HT tape (1 HT layer) significantly reduces the total void volume to 43.52 mm³, with a predominance of small voids (green/yellow areas). This result demonstrates that the compression exerted by the tape facilitates the elimination of trapped air, significantly improving the compaction of the composite materials. By applying two layers of HT tape (condition 2 HT layers), the total void volume is slightly reduced to 43.27 mm³. However, the change compared to the sample with only one layer is minimal, suggesting that the effect of compression reaches a limit beyond which further increments do not provide significant benefits. The application of the third layer (3 HT layers) leads to a marginal reduction in the total void volume, which stands at 37.39 mm³. The difference compared to previous samples is negligible, confirming that the effectiveness of the compression gradually decreases with increasing layers. The reduction in total void volume has a direct impact on the structural quality of the composite material, as the presence of internal defects compromises mechanical properties. The application of the first layer of HT tape is the most effective in reducing internal porosity, with a decrease in the total void volume of approximately 81% compared to the sample without HT tape. From the first to the second layer, and from the second to the third layer, a reduction of 0.25% VVF and 0.12% VVF, respectively, can be obtained. These results indicate that the effect of the compression exerted by the heat shrink tape reaches a plateau beyond which further increments are no longer effective. Residual voids are mainly concentrated along the fiber direction of the composite material, suggesting that the initial deposition process significantly influences the formation of porosity and must be optimized to obtain structurally superior components. The smaller voids in volume, on the other hand, are related to the impregnation phase for each condition.

Materials Research Proceedings 57 (2025) 268-277 https://doi.org/10.21741/9781644903735-31

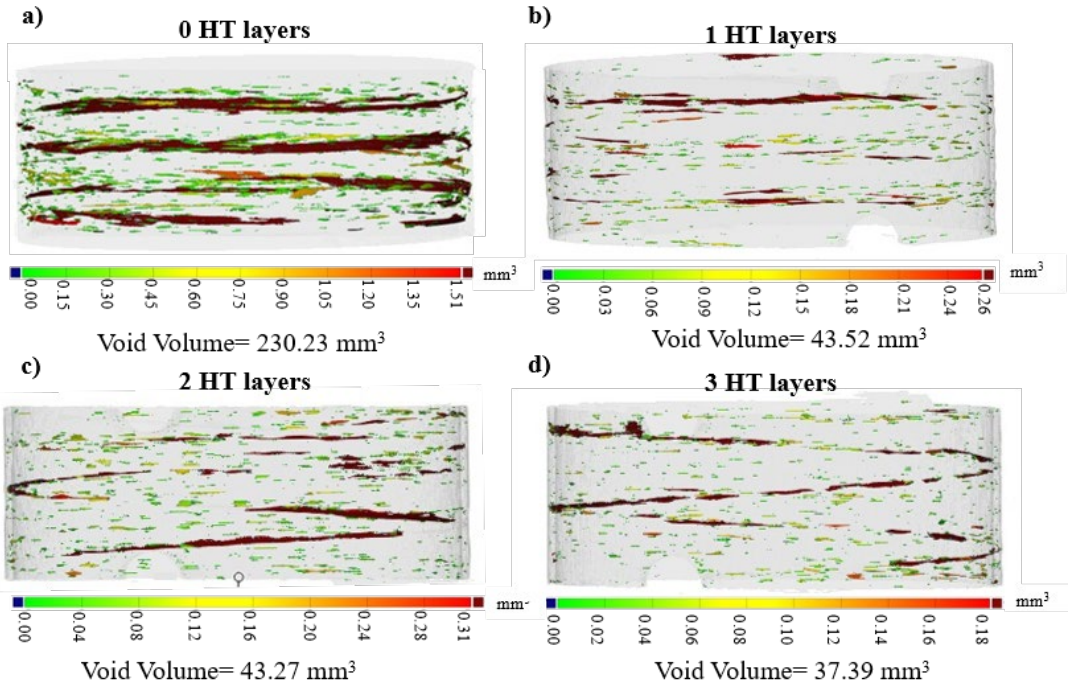


Figure 5: Effect of the number of HT layers on the void volume: (a) without HT, (b) 1 HT layer, (c) 2 HT layers, and (d) 3 HT layers.

Conclusions

The present study investigated the effect of the heat-shrinkable tape application and of the number of HT layers on the mechanical properties, void content, and structural quality of carbon fiber-reinforced polymer tubular components manufactured via filament winding and cured in an oven. The main outcomes can be summarized as follows:

- The HTS and specific HTS increase with increasing the number of HT layers applied before curing phase. Specifically, the HTS improves of about 47 MPa by applying 1 HT layer of about 19 MPa by adding a second HT layer, and of about 16 MPa by applying the third HT layer.
- The HTS and specific HTS tend to decrease with increasing the number of HT layers, with a nonlinear trend in which the first layer provides the highest improvement (equal to 46.77 MPa).
- The increase in the hoop tensile strength with HT layers can be attributed to the reduction in the ring thickness, due to the compressive force applied to the HT on the tubular component during the curing phase.
- The improvement in compaction results in better mechanical properties and overall material quality.
- The voids are typically aligned along the direction of fiber deposition, indicating a strong correlation between manufacturing processes and void formation.
- The application of the HT tape leads to a decrease in the void volume fraction from 3.1%, in the condition without HT, to 0.53% in the condition with 3 HT layers.
- Additional layers of HT result in marginal reductions both in mechanical properties and void fraction, this indicates that the effectiveness of HT tape compression reaches a plateau beyond one layer.

Further studies are recommended to explore the effect of HT tape in tubular component with a greater thickness with respect to the tubular components investigated in this study, the effect of

the use of the breather and peel ply, and the use of expandable mandrels in these curing processes with HT tape.

References

[1] J. Bai, "Fiber-reinforced polymer types and properties," *Advanced Fibre-Reinforced Polymer (FRP) Composites for Structural Applications*, pp. 93–99, Jan. 2023. https://doi.org/10.1016/B978-0-12-820346-0.00014-9

[2] F. Khan *et al.*, "Advances of composite materials in automobile applications – A review," *Journal of Engineering Research*, Feb. 2024. https://doi.org/10.1016/J.JER.2024.02.017

[3] B. Castanie, "Review of Composite Structures in Aeronautic Applications Part 1 Year of Conclusion: 2023 Master Course in Advanced Structural Analysis and Design using Composite Materials THE ENTIRE REPRODUCTION OF THIS THESIS IS AUTHORIZED ONLY FOR," 2023.

[4] B. Dhiman, V. Guleria, and P. Sharma, "Applications and Future Trends of Carbon Fiber Reinforced Polymer Composites: A Review," *International Research Journal of Engineering and Technology*, 2020, Accessed: Feb. 06, 2025. [Online]. Available: www.irjet.net

[5] J. Zhang, G. Lin, U. Vaidya, and H. Wang, "Past, present and future prospective of global carbon fibre composite developments and applications," *Compos B Eng*, vol. 250, p. 110463, Feb. 2023. https://doi.org/10.1016/J.COMPOSITESB.2022.110463

[6] "A Review Paper on Properties of Carbon Fiber Reinforced Polymers", Accessed: Feb. 06, 2025. [Online]. Available: www.ijirst.org

[7] M. Munro, "Review of manufacturing of fiber composite components by filament winding," *Polym Compos*, vol. 9, no. 5, pp. 352–359, Oct. 1988. https://doi.org/10.1002/PC.750090508

[8] M. Azeem *et al.*, "Application of Filament Winding Technology in Composite Pressure Vessels and Challenges: A Review," *J Energy Storage*, vol. 49, p. 103468, May 2022. https://doi.org/10.1016/J.EST.2021.103468

[9] S. Carosella, S. Hügle, F. Helber, and P. Middendorf, "A short review on recent advances in automated fiber placement and filament winding technologies," *Compos B Eng*, vol. 287, p. 111843, Dec. 2024. https://doi.org/10.1016/J.COMPOSITESB.2024.111843

[10] S. Alimirzaei, M. Ahmadi Najafabadi, and A. Nikbakht, "Investigation of Mechanical Properties and Failure Behavior of CFRP Filament-Wound Composites Using an Acoustic Emission-Based Methodology and Numerical Simulation," *Fibers and Polymers*, vol. 24, no. 2, pp. 693–707, Feb. 2023. https://doi.org/10.1007/S12221-023-00050-W

[11] H. Stadler, P. Kiss, W. Stadlbauer, B. Plank, and C. Burgstaller, "Influence of consolidating process on the properties of composites from thermosetting carbon fiber reinforced tapes," *Polym Compos*, vol. 43, no. 7, pp. 4268–4279, Jul. 2022. https://doi.org/10.1002/PC.26687

[12] D. H. Lee, S. K. Kim, W. Il Lee, S. K. Ha, and S. W. Tsai, "Smart cure of thick composite filament wound structures to minimize the development of residual stresses," *Compos Part A Appl Sci Manuf*, vol. 37, no. 4, pp. 530–537, Apr. 2006. https://doi.org/10.1016/J.COMPOSITESA.2005.05.017

[13] S. Rao, S. V. Revgade, N. M. Manjunath, and M. R. Prakash, "Microwave Assisted Curing of CFRP Composite Laminates for Aerospace Applications," *Springer Proceedings in Materials*, vol. 39, pp. 131–138, 2024. https://doi.org/10.1007/978-981-99-8807-5_11

[14] H. Bao, P. Marguerès, P. Olivier, H. Bao, P. Marguerès, and P. Olivier, "An innovative and low-cost system for in situ and real-time cure monitoring using electrical impedancemetry for thermoset and CFRP laminate," *MeScT*, vol. 35, no. 3, p. 035603, Mar. 2024. https://doi.org/10.1088/1361-6501/AD14DF

[15] S. Muhammad Shafiq Irfan, "Operating cost reduction of filament wound glass reinforced epoxy pipes by optimization of the oven curing time /," 2018, Accessed: Feb. 17, 2025. [Online]. Available: http://digitalarchive.uet.edu.pk/handle/123456789/1233

[16] Y. Ma, J. Wang, Y. Chen, L. Ju, S. Li, and Y. Zhao, "Effect of no-pressure curing temperature on bending property of 2D-T700/E44 composite," *Emerging Materials Research*, vol. 9, no. 3, pp. 695–704, Sep. 2020. https://doi.org/10.1680/JEMMR.19.00171

[17] I. Bianchi, A. Forcellese, T. Mancia, C. Mignanelli, M. Simoncini, and T. Verdini, "Effect of Heat-Shrinkable Tape Application on the Mechanical Performance of CFRP Components Obtained by a Filament Winding Process," *Journal of Composites Science 2024, Vol. 8, Page 535*, vol. 8, no. 12, p. 535, Dec. 2024. https://doi.org/10.3390/JCS8120535

[18] E. Jacquet, F. Trivaudey, and D. Varchon, "Calculation of the transverse modulus of a unidirectional composite material and of the modulus of an aggregate. Application of the rule of mixtures," *Compos Sci Technol*, vol. 60, no. 3, pp. 345–350, Feb. 2000. https://doi.org/10.1016/S0266-3538(99)00128-1

Materials Research Proceedings 57 (2025) 278-285 https://doi.org/10.21741/9781644903735-32

Comparative study of autoclave thermoforming and hot-press moulding for manufacturing green composite parts

G. Parodo[1], L. Sorrentino[2], S. Turchetta[2]

[1]Department of Engineering and Sciences, Faculty of Technological and Innovation Sciences, Universitas Mercatorum, Piazza Mattei 10, Rome, 00186, Italy

[2]Department of Civil and Mechanical Engineering, University of Cassino and Southern Lazio, via G. di Biasio, 43, Cassino (FR),03043, Italy

Keywords: Composites, Press Moulding, Thermoforming, Thermoplastics, Eco-Design

Abstract. The demand for sustainable and efficient manufacturing of lightweight polymer composite parts is driving the adoption of thermoplastic-based composites reinforced with natural fibres. This study explores two distinct manufacturing processes (autoclave thermoforming and hot-press moulding) to produce green composites from flax fibre woven fabric and polypropylene prepregs. The thermoforming process in autoclave offers precise pressure and temperature control, ensuring high-quality consolidation and fibre impregnation. Conversely, hot-press moulding allows for faster cycle times and increased production efficiency due to its direct compression approach. A comparative analysis of the two methods highlights differences in fibre-matrix adhesion, mechanical properties, and process repeatability. The results demonstrate that while both methods achieve high-performance eco-friendly composites, the choice of process can be optimized based on production rate and sustainability goals.

Introduction

The increasing demand for sustainable materials in the manufacturing sector has driven significant research interest in natural fibre-reinforced polymer composites [1]. Among these, flax fibre-reinforced polypropylene (PP) composites have emerged as promising candidates due to their advantageous mechanical properties, low environmental impact, and recyclability [2,3]. These materials are particularly suitable for applications in the automotive, aerospace, and consumer goods industries, where lightweight structures and eco-friendly solutions are becoming increasingly critical. However, the processing of such composites remains a key challenge, as it must balance the need for high mechanical performance with energy-efficient and cost-effective manufacturing techniques [2]. Autoclave thermoforming has long been considered the gold standard for processing high-performance composite materials, particularly in industries where structural integrity and defect minimization are critical. The ability to apply uniform pressure and precisely control temperature profiles makes this process particularly attractive, especially for aerospace and aeronautic sectors. The combination of vacuum assistance and pressurization ensures optimal consolidation, reducing void content and enhancing fibre-matrix adhesion—key factors in determining the mechanical performance and long-term durability of the final part [4]. In fact, one of the primary advantages of autoclave processing is the superior quality of the manufactured components. The high-pressure environment effectively compacts the laminate, minimizing internal defects and ensuring excellent interlaminar bonding. This is particularly beneficial for thermoplastic matrices, where achieving uniform impregnation of the fibre reinforcement can be challenging due to the inherently higher viscosity compared to thermosetting resins. Additionally, the controlled heating and cooling rates help to mitigate residual stresses, which can otherwise lead to warpage or premature failure in service [5,6]. Despite these advantages, autoclave processing is not without its limitations. The most significant drawback is the high energy consumption, as the process requires sustained heating and pressurization over

Content from this work may be used under the terms of the Creative Commons Attribution 3.0 license. Any further distribution of this work must maintain attribution to the author(s) and the title of the work, journal citation and DOI. Published under license by Materials Research Forum LLC.

Materials Research Proceedings 57 (2025) 278-285 https://doi.org/10.21741/9781644903735-32

extended cycle times [7]. This not only increases operational costs but also raises concerns regarding its environmental footprint, an aspect particularly relevant when dealing with "green" composite materials. Furthermore, the necessity of vacuum bagging materials and auxiliary consumables, such as release films and breather layers, contributes to material waste, reducing the overall sustainability of the process. From a production standpoint, autoclave processing is inherently less suited to high-throughput manufacturing. The long cycle times and batch-processing nature limit its scalability, making it less competitive for industries that require cost-effective, mass production solutions [8]. While the process remains indispensable for aerospace applications, where performance requirements justify the investment, its practicality for broader applications (such as automotive or consumer goods) remains debatable, particularly in comparison to alternative techniques like hot-press moulding. Hot-press moulding has gained significant attention as an alternative to autoclave processing for the manufacturing of thermoplastic composites, particularly in applications where cost efficiency and high-throughput production are paramount [9]. Unlike autoclave thermoforming, which relies on a controlled pressurized environment to consolidate laminates, hot-press moulding applies direct mechanical pressure between heated platens, enabling rapid material consolidation and shorter cycle times. This characteristic makes it an attractive option for industries aiming to integrate bio-based composites, such as flax/PP laminates, into mainstream production while maintaining an economically viable and scalable process [10].

One of the main advantages of hot-press moulding is its efficiency in terms of both time and energy consumption. The direct transfer of heat from the press platens to the laminate significantly accelerates the heating and cooling phases, reducing overall cycle times compared to the extended dwell times required in an autoclave. Moreover, the absence of a vacuum bagging system simplifies the setup, minimizing the use of consumables and thereby reducing material waste. These factors contribute to a more sustainable and cost-effective manufacturing approach, aligning with the growing demand for greener production technologies [11].

However, hot-press moulding is not without its challenges. The primary concern is the non-uniform pressure distribution across the laminate, which can lead to localized defects such as incomplete fibre impregnation, void formation, or thickness variations. Unlike an autoclave, which applies pressure uniformly around the entire part, a hot press relies on direct contact with heated platens, which may result in uneven consolidation, particularly for large or complex geometries [12]. Additionally, temperature gradients within the laminate can affect the crystallization behaviour of the thermoplastic matrix, potentially leading to internal stresses or suboptimal mechanical performance. During consolidation, matrix material undergoes squeeze flow, which is influenced by fibre orientation and processing conditions. Kobler et al [13] have shown that in high-pressure processes, such as hot-press moulding, the matrix flow can be significantly altered, affecting fibre distribution and interlaminar properties. This phenomenon is particularly relevant when comparing autoclave processing and hot-press moulding, where different pressure levels may lead to distinct adhesion mechanisms and interlaminar shear strength (ILSS) values.

This study aims to investigate the processing–property relationships in flax fibre-reinforced polypropylene (PP/flax) laminates manufactured using two distinct forming techniques: autoclave thermoforming and hot-press moulding. While these processes are often considered alternatives, their different operating conditions (particularly in terms of pressure application, temperature control, and cooling rate) suggest that they may serve complementary roles in defining the mechanical performance of the final composite.

The research specifically focuses on evaluating how processing parameters, particularly temperature and pressure, affect interlaminar shear strength (ILSS). Given that previous studies [14] have shown an increasing trend in performance with temperature in autoclave processing - until reaching the inherent limitations of this technique in terms of temperature and pressure- this

Materials Research Proceedings 57 (2025) 278-285 https://doi.org/10.21741/9781644903735-32

work extends the analysis to a processing window that can only be explored via hot-press moulding, which allows for higher pressure and temperature levels. With thermoplastic-based materials, this technique significantly reduces cycle time, enabling faster consolidation and higher production rates compared to autoclave processing, thus enhancing manufacturing efficiency.

The objective is not only to compare the two technologies but to define their respective advantages and limitations, providing insight into how they can be leveraged for different applications in sustainable composite manufacturing.

Materials and Methods

For this study, a twill 2×2 woven flax fibre-reinforced polypropylene (PP) prepreg, commercially known as Amplitex 5040 and manufactured by Bcomp, was used. This prepreg is supplied in rolls with a nominal thickness of 0.8 mm and an areal density of 300 g/m2.

In a previous work [14], the processing window of the material was defined through DSC and TGA analyses, while inter-ply adhesion was evaluated using ILSS tests for the autoclave process. The results showed a continuous increase in performance, with the main limitation being the maximum temperature tolerable by the auxiliary materials used in the process, such as the vacuum bag, breather, and sealant, which are typically suitable for 120–180°C. The present study aims to investigate the continuation of this trend within a processing window beyond these conventional temperature constraints, which cannot be explored in the autoclave using standard auxiliary materials but is accessible through hot-press moulding. For this purpose, a Fontijne Labtop laboratory press with a 150 kN capacity and 200 × 200 mm heated plates was used for manufacturing the laminates. Forming cycle consisted in an heating ramp of 4°C/min until target temperature, while the cooling rate was equal to -60°C/min. For each laminate, 8 layers of prepreg were used. For completeness, the experimental plan is reported in Table 1.

The morphological characterization of the PP/flax laminates was conducted using both optical and scanning electron microscopy (SEM) to investigate laminate surfaces and fracture mechanisms. In particular, optical microscopy was employed to examine the surface morphology of the laminates, focusing on fibre distribution and potential defects induced during the hot-pressing process. Observations were performed using an optical microscope in reflected light mode. For a more detailed analysis of the fracture behaviour, scanning electron microscopy (SEM) was used to investigate the failure mechanisms at the microstructural level. Fractured specimens were sectioned and mounted on aluminium stubs using conductive carbon tape. SEM imaging was performed with an accelerating voltage of 10 kV and working distances between 1 and 1.5 mm.

Moreover, Fourier Transform Infrared Spectroscopy (FT-IR) analysis was performed using the Attenuated Total Reflectance (ATR) technique to investigate possible surface chemical modifications induced by the hot press forming process respect to autoclave process. The spectra were acquired in the range of 4000–400 cm^{-1}, with a resolution of 4 cm^{-1} and an average of 8 scans per measurement to enhance the signal-to-noise ratio. Once upon the laminates were manufactured, they were cut to produce ILSS specimens with dimension of 40 x 12 mm, while the thickness depends on the process parameters and vary in a range of 4.8-5.4 mm. ILSS test were conducted according to ASTM D2344, using an INSTRON 34TM30 universal testing machine with a crosshead speed of 1mm/min. For each process condition, three replicates were made.

Materials Research Proceedings 57 (2025) 278-285 https://doi.org/10.21741/9781644903735-32

Table 1. Experimental plan developed in this work.

Laminate identification number	Forming temperature [°C]	Forming pressure [bar]
1	160	4
2	160	6
3	170	4
4	170	6
5	180	4
6	180	6
7	180	10
8	180	20
9	180	30
10	200	10
11	200	20
12	200	30
13	220	10
14	220	20
15	220	30

Results and Discussions

The analysis of ILSS test results (Figure 1) clearly highlights the effectiveness of the hot platen press compared to the autoclave in forming PP/flax laminates. The ILSS values obtained using the press are generally consistent, suggesting that the high pressure applied during the process promotes good interlaminar adhesion while significantly reducing cycle times. Specifically, while an autoclave cycle lasts approximately 4.5 hours, the press cycles require only about 30 minutes for laminate production, allowing a decrease of the production time higher than 80%. Additionally, in an industrial setting, the use of preheated platens (with a temperature range of approximately 80-100°C for polypropylene) could further optimize cycle times, potentially reducing forming time by an additional 30-40% and increasing overall productivity. This approach is particularly advantageous in continuous processing, where maintaining elevated temperatures between cycles improves thermal efficiency and reduces heating times. Moreover, data analysis reveals that in the autoclave process, interlaminar strength remains very low up to 170°C, with a noticeable increase only occurring from 180°C onwards at pressures of at least 6 bar. This behaviour suggests that merely increasing the temperature is insufficient to ensure effective fusion of the thermoplastic matrix. In fact, without adequate pressure, fibre wettability and ply coalescence are likely to remain incomplete. Conversely, in the case of the hot platen press, ILSS values comparable to or even superior to the best results obtained in the autoclave are already achieved at 180°C and 10 bar.

As pressure increases, a progressive improvement in interlaminar strength is observed, reaching its peak for 180°C and 20 bar with ILSS values approaching 21 MPa. This finding confirms that high pressure plays a crucial role in enhancing laminate quality, facilitating consolidation, and minimizing interlaminar defects such as voids or poor fibre impregnation.

However, the behaviour of press-formed laminates beyond 200°C suggests the onset of detrimental phenomena affecting the composite structure. At 220°C, a significant drop in ILSS is observed, with values decreasing even as pressure increases. This trend could be attributed to multiple factors: thermal degradation of the flax fibres, thermal degradation of the matrix, or a combination of both.

The FT-IR spectra obtained for samples processed using the same forming method were highly similar, regardless of the specific process parameters applied. This indicates that variations in temperature and pressure within the investigated range did not induce significant chemical

Materials Research Proceedings 57 (2025) 278-285 https://doi.org/10.21741/9781644903735-32

modifications at the surface level. However, when comparing the spectra of laminates formed by hot pressing with those processed in an autoclave under equivalent conditions, noticeable differences were observed, as shown in Figure 2. These differences are likely attributed to the distinct processing environments: in the hot press, the laminate is in direct contact with air, whereas in the autoclave, the process is conducted under vacuum. This discrepancy could influence surface oxidation, volatile compound retention, or matrix-fibre interactions, leading to detectable chemical variations.

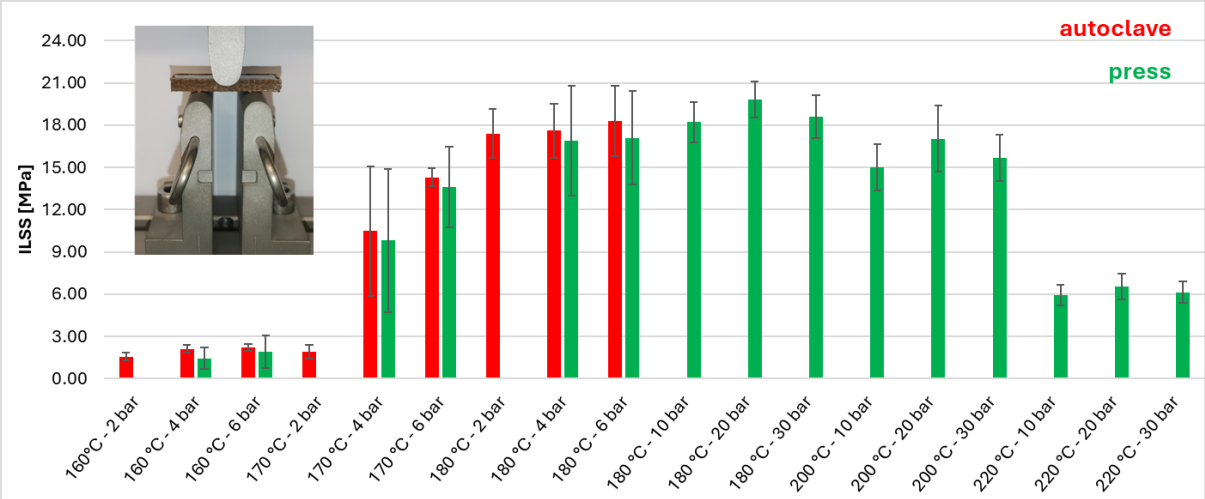


Figure 1. Experimental results for ILSS tests

The surfaces of the manufactured laminates were examined using optical microscopy. Representative images are provided in Figure 3. Here, the surface finish appears superior in laminates produced with the press compared to the tool-side surface of autoclave-processed laminates. Nevertheless, a noticeable colour changes in the flax fibres formed at 220°C is observed, suggesting potential thermal degradation. To assess the potential degradation of the reinforcement, SEM analyses were performed on the fracture surfaces. The obtained images (Figures 4 and 5) provide valuable insights into the effects of the forming temperature on the failure mechanisms of PP/flax laminates. In Figure 4, corresponding to a laminate formed at 180°C, the flax fibre reinforcement exhibits a pronounced tendency for fibre pull-out and fibrillation, indicating suboptimal adhesion between the fibres and the polymer matrix. This suggests that at this temperature, the matrix has not yet fully optimized its wetting and bonding with the reinforcement, leading to a failure mode dominated by fibre debonding and delamination.

Conversely, Figure 5, corresponding to the laminate formed at 220°C, reveals a different failure morphology. The reinforcement demonstrates improved adhesion with the matrix, as evidenced by a reduced occurrence of fibre pull-out. However, this enhanced bonding is overshadowed by the detrimental effect of elevated temperature on the mechanical performance of the reinforcement.

The fracture surface exhibits a more brittle failure behaviour, characterized by clean fibre breakage and sharp fracture edges. Additionally, intralaminar fractures within the reinforcement are observed, suggesting that while higher temperatures promote better matrix-fibre interaction, they also induce thermal degradation of the flax fibres, compromising their structural integrity and reducing their ability to withstand mechanical stresses. These results are in accordance with the scientific literature, where thermal degradation of flax fibres was highlighted for temperature higher than 190 °C [15,16]. This result indicates that achieving the right balance between fibre-matrix adhesion and thermal degradation is crucial for optimizing the mechanical performance of PP/flax laminates. While higher temperatures improve adhesion, they also accelerate the degradation of natural fibres, ultimately compromising structural integrity.

Materials Research Proceedings 57 (2025) 278-285 https://doi.org/10.21741/9781644903735-32

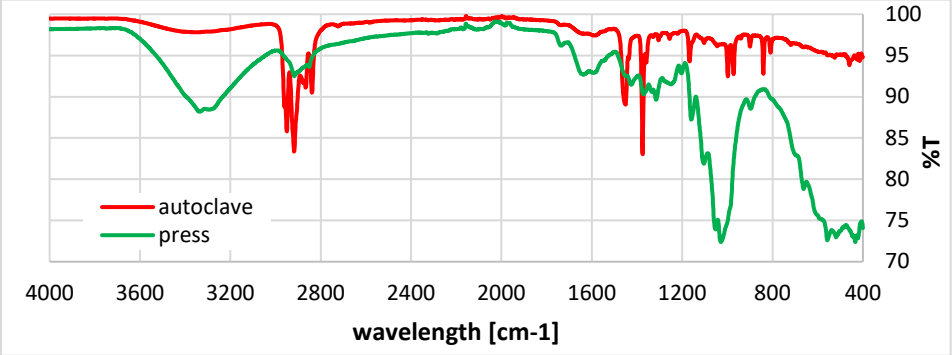


Figure 2. FT-IR spectra for laminates formed at 180°C and 6 bar.

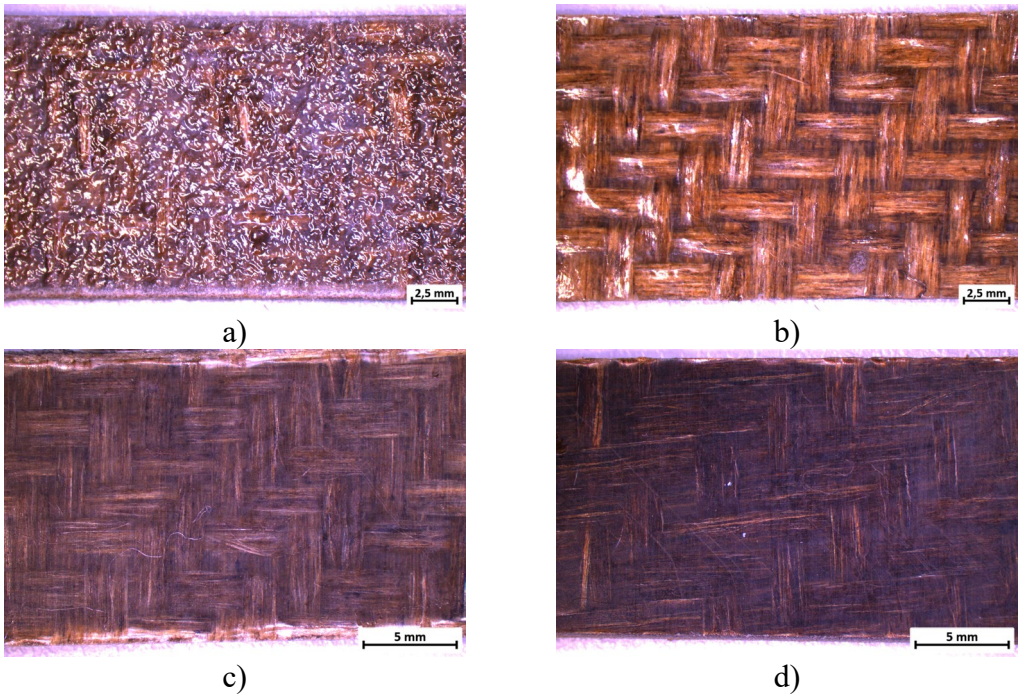
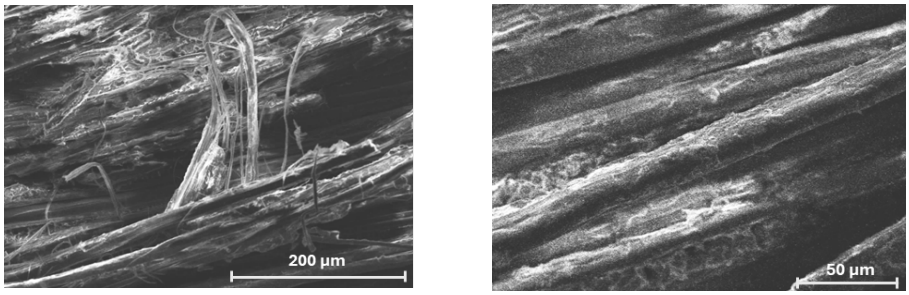


Figure 3. Optical observation of formed laminates: a) autoclave 180°C – 4 bar, bag side; b) autoclave 180°C – 4 bar, tool side; c) hot press, 200°C – 20 bar; d) hot press, 220 °C – 20 bar

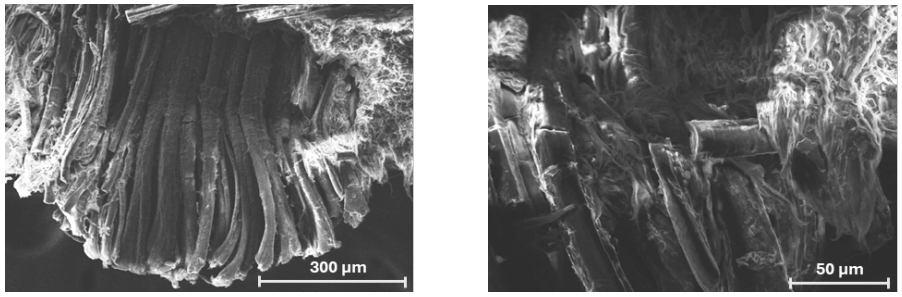
However, the findings suggest that this trade-off can be effectively managed by adjusting the applied pressure, which plays a key role in enhancing fibre impregnation and promoting a more uniform consolidation of the laminate. In this regard, the hot platen press emerges as the more suitable manufacturing process for PP/flax panels compared to the autoclave. Its ability to apply significantly higher pressures allows for improved interlaminar bonding at lower temperatures, thereby minimizing fibre degradation while maintaining excellent mechanical properties. Additionally, the press eliminates the need for auxiliary consumables, making it not only more efficient but also more cost-effective and environmentally sustainable. Although a direct measurement of energy consumption was not conducted in this study, a qualitative comparison suggests that hot-press moulding exhibits inherently lower energy demand per laminate. This advantage arises from several factors, including the absence of vacuum bagging, shorter heating and cooling cycles, and the elimination of auxiliary consumables such as release films and breather fabrics. However, a precise quantification of energy savings would require equipment of comparable scale and architecture, as well as real-time monitoring of power input throughout the process.

Materials Research Proceedings 57 (2025) 278-285 https://doi.org/10.21741/9781644903735-32



a) b)

Figure 4. SEM image of specimens formed at 180°C: a) flax fibres pull-out; b) particular of the fibres.



a) b)

Figure 5. SEM image of specimens formed at 220°C: a) fractured fibres; b) particular of the fibres.

Conclusions

This work highlights the influence of processing conditions on the mechanical performance of PP/flax laminates, comparing hot-press moulding with autoclave thermoforming. The results demonstrate that the hot-press process enables a substantial reduction in cycle time (from approximately 4.5 hours to 30 minutes) while achieving ILSS values up to 21 MPa, comparable to or exceeding those obtained in autoclave. The use of higher forming pressures (≥10 bar) proved critical in enhancing fibre impregnation and reducing interlaminar defects, especially at 180°C. Conversely, forming at 220°C resulted in a marked drop in ILSS, attributed to thermal degradation of the flax fibres, as confirmed by SEM analysis. In addition to performance, the hot-press process offers benefits in terms of sustainability and scalability, eliminating the need for auxiliary consumables and enabling faster, more efficient processing. Although increasing temperature improves fibre–matrix adhesion, careful control is required to avoid compromising fibre integrity. Future investigations could explore the use of surface treatments or thermal stabilizers to mitigate flax fibre degradation at elevated temperatures, as well as the integration of in situ monitoring techniques to optimize temperature and pressure control during moulding, thereby enhancing process reliability and industrial scalability.

References

[1] S.D.S. Kopparthy, A.N. Netravali, Review: Green composites for structural applications, Compos. Part C Open Access. 6 (2021) 100169. https://doi.org/10.1016/j.jcomc.2021.100169

[2] G. Parodo, L. Sorrentino, S. Turchetta, G. Moffa, Manufacturing of Sustainable Composite Materials: The Challenge of Flax Fiber and Polypropylene, Materials (Basel). 17 (2024) 4768. https://doi.org/10.3390/ma17194768

[3] O. El Hawary, L. Boccarusso, M.P. Ansell, M. Durante, F. Pinto, An Overview of Natural Fiber Composites for Marine Applications, J. Mar. Sci. Eng. 11 (2023) 1076. https://doi.org/10.3390/jmse11051076

[4] E. Pourahmadi, F. Shadmehri, R. Ganesan, Interlaminar shear strength of Carbon/PEEK thermoplastic composite laminate: Effects of in-situ consolidation by automated fiber placement and autoclave re-consolidation, Compos. Part B Eng. 269 (2024) 111104. https://doi.org/10.1016/j.compositesb.2023.111104

[5] C. Bellini, L. Sorrentino, Analysis of cure induced deformation of CFRP U-shaped laminates, Compos. Struct. 197 (2018) 1–9. https://doi.org/10.1016/j.compstruct.2018.05.038

[6] Y. Li, A. Yang, Y. Liu, Y. Gao, J. Zhou, Y. Dong, S. Zhu, Analysis of warping defect formation mechanisms in hot molding of CF/PEEK thin-wall structures and their influence on mechanical properties, Thin-Walled Struct. 207 (2025) 112740. https://doi.org/10.1016/j.tws.2024.112740

[7] C.J. Ogugua, S. V. Anton, A.P. Tripathi, M.D. Larrabeiti, S.O. van Hees, J. Sinke, C.A. Dransfeld, Energy analysis of autoclave CFRP manufacturing using thermodynamics based models, Compos. Part A Appl. Sci. Manuf. 166 (2023) 107365. https://doi.org/10.1016/j.compositesa.2022.107365

[8] O.A. Ekuase, N. Anjum, V.O. Eze, O.I. Okoli, A Review on the Out-of-Autoclave Process for Composite Manufacturing, J. Compos. Sci. 6 (2022). https://doi.org/10.3390/jcs6060172

[9] D. Tatsuno, T. Yoneyama, K. Kawamoto, M. Okamoto, Hot press forming of thermoplastic CFRP sheets, Procedia Manuf. 15 (2018) 1730–1737. https://doi.org/10.1016/j.promfg.2018.07.254

[10] K.R. Ramakrishnan, N. Le Moigne, O. De Almeida, A. Regazzi, S. Corn, Optimized manufacturing of thermoplastic biocomposites by fast induction-heated compression moulding: Influence of processing parameters on microstructure development and mechanical behaviour, Compos. Part A Appl. Sci. Manuf. 124 (2019) 105493. https://doi.org/10.1016/j.compositesa.2019.105493

[11] J. Bachmann, C. Hidalgo, S. Bricout, Environmental analysis of innovative sustainable composites with potential use in aviation sector—A life cycle assessment review, Sci. China Technol. Sci. 60 (2017) 1301–1317. https://doi.org/10.1007/s11431-016-9094-y

[12] M. Mehdikhani, L. Gorbatikh, I. Verpoest, S. V. Lomov, Voids in fiber-reinforced polymer composites: A review on their formation, characteristics, and effects on mechanical performance, J. Compos. Mater. 53 (2019) 1579–1669. https://doi.org/10.1177/0021998318772152

[13] E. Kobler, J. Birtha, C. Marschik, K. Straka, G. Steinbichler, S. Schlecht, Modeling the anisotropic squeeze flow during hot press consolidation of thermoplastic unidirectional fiber-reinforced tapes, J. Thermoplast. Compos. Mater. 37 (2024) 2775–2801. https://doi.org/10.1177/08927057231214458

[14] G. Parodo, L. Sorrentino, S. Turchetta, Study of autoclave process to manufacture thermoplastic composites constituted by PP/flax fibers, in: Mater. Res. Proc., 2023: pp. 385–392. https://doi.org/10.21741/9781644902714-46

[15] J. George, E.T.J. Klompen, T. Peijs, Thermal degradation of green and upgraded flax fibres, Adv. Compos. Lett. 10 (2001) 81–88. https://doi.org/10.1177/096369350101000205.

[16] J. Gassan, A.K. Bledzki, Thermal degradation of flax and jute fibers, J. Appl. Polym. Sci. 82 (2001) 1417–1422. https://doi.org/10.1002/app.1979

Materials Research Proceedings 57 (2025) 286-293 https://doi.org/10.21741/9781644903735-33

Laser texturing of 3D Copper current collector for ultrafast Zinc metal plating

Vincenzina SICILIANI[1,a *], Nassima YAMINI[2,b], Riccardo PELACCIA[1,c], Andrea PAOLELLA[2,d], and Leonardo ORAZI[1,3,e]

[1]DISMI – University of Modena and Reggio Emilia, via Amendola 2, 42122 Reggio Emilia, Italy

[2]DSCG – University of Modena and Reggio Emilia, Via Campi 103, 41125 Modena, Italy

[3]EN&TECH – University of Modena and Reggio Emilia, Piazzale Europa 1, 42124 Reggio Emilia, Italy

[a]vincenzina.siciliani@unimore.it, [b]nassima.yamini@unimore.it, [c]riccardo.pelaccia@unimore.it, [d]andrea.paolella@unimore.it, [e]leonardo.orazi@unimore.it

Keywords: Laser Processes, Texture, Anode-Free Batteries

Abstract. Anode-free metal batteries with increased energy density hold promise for next-generation energy storage systems. However, the development of unwanted metal dendrites limits their practical application as electrodes. Zinc-ion batteries are promising since zinc is low-cost and allows the use of non-flammable aqueous electrolytes. 3D electrodes can reduce the current density per unit area and thus the dendrite formation. Quick laser texturing can selectively enhance zincphilicity within the grooves on Cu current collectors, increasing the charging rate. In this study, laser textures with different depths are performed on 100 μm Cu sheets electrode. Then, zinc metal is electrolytically deposited on the substrates and characterized by morphological and chemical (SEM/EDS) analysis. The half-cells with these collectors are tested in their functionality using a potentiostat. The textured current collectors will be evaluated as electrodes in Zn-ion batteries to achieve high charging rates.

Introduction

Zinc has emerged as a promising material in the field of energy storage, particularly for use in rechargeable batteries such as zinc-ion and zinc-air batteries. Its abundant availability, low cost, and high energy density make it an attractive alternative to other metal-based systems. The use of aqueous electrolytes [1] makes Zn-ion batteries safer than Li-ion batteries, which require flammable liquid electrolytes (e.g., 1M LiPF6 in Ethylene Carbonate/Diethylene Carbonate) [2].

The operating voltage of Zn-ion batteries is lower than that of Li-ion batteries, specifically 2V for Zn-ion vs 4V for Li-ion. However, the performance of zinc-based batteries heavily relies on the efficiency of the Current Collectors (CCs), which play a critical role in facilitating electron flow between the electrodes and external circuits. The selection of appropriate current collectors is crucial for enhancing the overall performance, stability, and lifespan of these systems. Metallic zinc can plate onto copper, forming dendrites, especially at high current densities. Therefore, this reduces the specific power attainable.

To overcome this limit, 3D electrodes are designed in order to limit the formation of dendrites. These three-dimensional structures can be obtained with several methods [3]. Among these, the use of laser treatment to modify current collectors represents an innovation in the field of energy storage.

Laser-based processes are largely studied as promising technologies for producing battery materials, cells, and packs. Laser welding is nowadays a reliable joining process for elements, cells, and batteries [4] while advances in laser cutting, especially using ultrafast laser sources are opening perspectives to substitute mechanical cutting [5]. Focusing on electrode production, laser

Content from this work may be used under the terms of the Creative Commons Attribution 3.0 license. Any further distribution of this work must maintain attribution to the author(s) and the title of the work, journal citation and DOI. Published under license by Materials Research Forum LLC.

Materials Research Proceedings 57 (2025) 286-293 https://doi.org/10.21741/9781644903735-33

drying is an alternative method compared to hot air blowing for efficient and homogeneous removal of solvent from the slurry deposited on the current collectors [6].

The laser can moreover be a valuable tool for structuring the electrodes to increase and homogenize the diffusivity of charges, reduce overpotentials, favor ion migration, and increase the performance of thick electrodes, guaranteeing high capacity coupled with high current density. Direct structuring was first implemented through laser drilling of micro-holes [7] and by grooving [8] the material electrodes with appropriate designs. The use of ultrashort pulses can strongly increase the aspect ratio of the holes and reduce the size of the Heat Affected Zone (HAZ), limiting the alteration of the chemical composition in the surrounding material. The coupling of low energy per pulse and high repetition rate demonstrated the achieving of good results in a relatively short processing time [9]. Laser surface structuring can be of great benefit when applied to the metallic current collectors, usually thin foils of Cu for the negative anode, and Al for the positive cathode. The laser beam can easily operate at the micrometric scale patterning features with dimensions that are comparable to the thickness of modern CCs, as thin as 10 μm In [10] a dense matrix of craters obtained by ns processing was employed to increase the adhesion of the active material layer on both Cu and Al foils, the process effectiveness was evaluated by peel-off test according to ASTM D 3167 and correlated with the laser fluence. Similar Al foils are then used to prepare Lithium Iron Phosphate half-cell electrodes that demonstrated a long-life capacity 86% higher with respect to cells based on commercial Al CC foil [11].

The bonding strength and the electrochemical contact between the CCs and the electrode material can be improved by ultrafast processing. Femtosecond pulses naturally induce hierarchical micro and nano-textures on the metallic foils increasing roughness and decreasing the wettability. Authors in [12] created a cross-hatched grid increasing the electrochemical performances, in particular, the long-life durability of both the half-cell electrodes based on Al cathode and Cu anode cells and the full batteries, compared to the counterparts assembled with commercial CCs.

Similar results are obtained in [13], by laser structuring CCs with a picosecond laser to generate a linear pattern. The linear pattern approach could in principle be more easily scaled up for mass production, authors moreover suggest that linear pattern can increase the recyclability of the materials thanks to the preferential orientation of the delamination cracks.

The peculiar characteristics of ultrashort pulses grant the possibility to operate exploiting different mechanisms: the generation of sub-micron Laser Induced Periodic Surface Structures (LIPSS), and the use of special optics to split the beam and produce Direct Laser Interference Patterns (DLIP) that, with enough available power can strongly increase the throughput of the texturing step. Both approaches were applied in [14] to process Silicon Carbide CC for next-generation Li-ion battery. DLIP appeared to appreciably increase the cycling stability of the electrodes, while LIPSS texturing appears marginally effective.

The objective of this work is to evaluate laser 3D structuring of current collectors for the reduction of local current density to minimize dendrite formation. The final aim is the future development of anode-less Zn-ion batteries.

Materials and Methods

Substrate preparation

The substrate material is a commercial 100 μm copper coil, generally used for electrodes. From this, samples in 60x40 mm^2 dimensions were obtained, and they were treated for 30 minutes in a 0.1 M $(NaPO_3)_6$ solution at 50 °C to remove any surface impurities and oxides.

They were then sonicated for 5 minutes, rinsed with water and acetone, and stored in acetone during the experimental campaign.

Materials Research Proceedings 57 (2025) 286-293 https://doi.org/10.21741/9781644903735-33

Cu Laser texturing

The experimental laser set up includes an ultrashort-pulsed Ekspla Atlantic 50 laser source with a pulse duration of about 10 ps, equipped with three different wavelengths. To exploit the maximum power of the laser on copper, a wavelength of 1064 nm was employed. In addition, a Raylase Superscan V galvanometric scanning head precisely controls and directs the laser on the target and an F-theta lens provides a focused beam with a waist diameter at $1/e^2$ intensity of about 10 µm..

The 3D texturing chosen to ensure uniform deposition of zinc on copper is based on equispaced parallel lines with a pitch of 30 µm, to have about the same width of treated and untreated area, with three different depths: 5 µm (hereafter referred to as "5LT"), 10 µm ("10LT"), and 15 µm ("15LT"). The base material ("As is") shows the rolling direction signs.

The final laser parameters to ensure the design depths and good processing quality were: 500 kHz of repetition rate, 30 µm line spacing, 1000 mm/s of scan speed, 4-10-15 passes, 6 W of power, corresponding at 12 µJ energy per pulse and 15.3 J/cm^2 of fluence, see Table 1.

***Table 1**. Laser parameters employed in copper foils processing.*

	Fill spacing [µm]	Mark speed [mm/s]	Repetition Rate [kHz]	Passes	Power [W]	Energy per pulse [µJ]	Fluence [J/cm^2]
5 LT	**30**	**1000**	**500**	**4**	**6.0**	**12.0**	**15.3**
10 LT	**30**	**1000**	**500**	**10**	**6.0**	**12.0**	**15.3**
15 LT	**30**	**1000**	**500**	**15**	**6.0**	**12.0**	**15.3**

Zn metal electroplating

The zinc plating process was carried out using an electrochemical cell that was based on a glass container holding 40 mL of 0.5 M aqueous solution of $ZnSO_4$•7 H2O of electrolyte, see Fig. 1. The working electrode was connected to the copper sheet (10 × 20 mm^2), the counter electrode was connected to graphite (10 × 20 mm^2), and an Ag/AgCl electrode was used as the reference electrode. The immersed surface area of the copper (a) and graphite sheets (b) in the electrolyte solution (c) was consistently maintained at approximately 1 cm^2.

By using a Potentiostat Biologic VMP, two types of studies have been conducted: a first test lasting 10 minutes with an applied current of 20 mA/cm^2. and a second test lasting 20 minutes with an applied current of 10 mA/cm^2 between the graphite and copper electrodes.

Copper samples with deposited zinc were stored in Argon atmosphere before subsequent analysis.

Materials Research Proceedings 57 (2025) 286-293 https://doi.org/10.21741/9781644903735-33

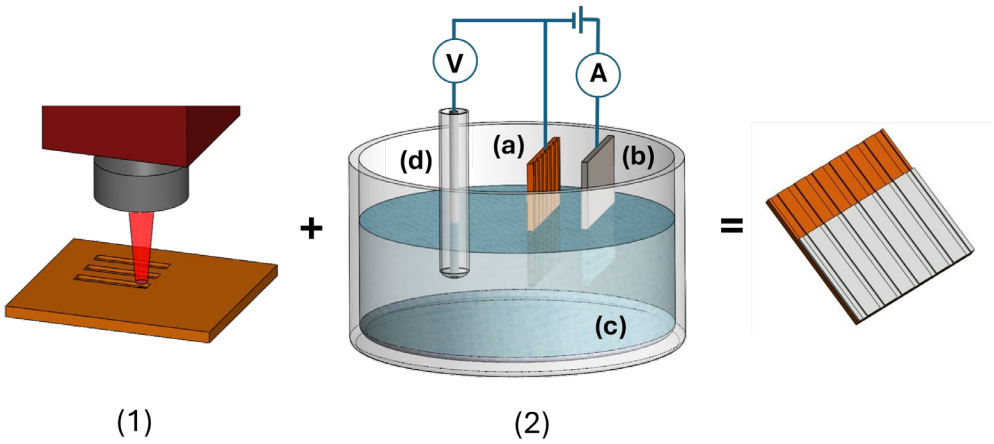


Fig. 1. *Scheme of fabricating samples: (1) Cu sheet laser processing, (2) electrochemical zinc deposition where (a) copper working electrode, (b) graphite counter electrode, (c) solution with electrolyte, (d) Ag/AgCl reference electrode.*

Morphological and chemical characterization

Firstly, an optical microscope was used to assess the depth of laser treatment by focusing on the lower surface of the treated region and on the upper surface of the untreated material and measuring the height difference.

Then, the specimen surface morphology was examined at various magnifications using a scanning electron microscope, the Nova NanoSEM 450 (Fei Company), and the surface composition was examined using EDS analysis (X-EDS Oxford INCA-350).

Point spectra were obtained every 30 seconds, and elemental maps were acquired after 6 minutes for untreated and laser-treated samples. The percentage of zinc, copper, and oxygen was evaluated quantitatively.

Results and Discussion

The processing time with the chosen parameters for patterning a 10 x 20 mm^2 5LT, 10LT, and 15LT area on the copper foils is 40 seconds, 1:40 minutes, and 2:30 minutes respectively.

The morphology of the untreated and 5LT laser-treated material without any deposition can be seen in the SEM images of Fig. 2 (a) and (b) respectively. Untreated foils show the striations caused by the rolling process while the grooves obtained by laser processing are quite regular with a depth of 5, 10, and 15 µm, a width of about 12 µm, and a taper angle of the vertical wall of about 20 degrees. The bottom of the processed grooves is filled with LIPPS with a pitch slightly less than 1 µm. The direction of the grooves is perpendicular to the rolling direction, while the orientation of the polarization plane was chosen parallel to the direction of the grooves, so the LIPSS are oriented perpendicular to the grooves with the final aim of generating a more pronounced hierarchical structure.

The other two images, Fig. 2 c) and d) show examples of the surface state after deposition at the very high current of 20 mA/cm^2 per 10 minutes. It is seen that the untreated foils in Fig. 2 (c) are very uneven, large portions of the material surface present free oxidation, which looks darker, the oxidation is caused by the dendritic aspect of the deposited zinc with a large surface exposed to the electrolyte. Zinc deposition on the patterned foils looks like in Fig. 2 (d), the linear grooves allow zinc to follow the morphology of the substrate and distribute uniformly over the surface, so the patterning promotes orderly zinc growth, preventing zinc oxidation.

Materials Research Proceedings 57 (2025) 286-293 https://doi.org/10.21741/9781644903735-33

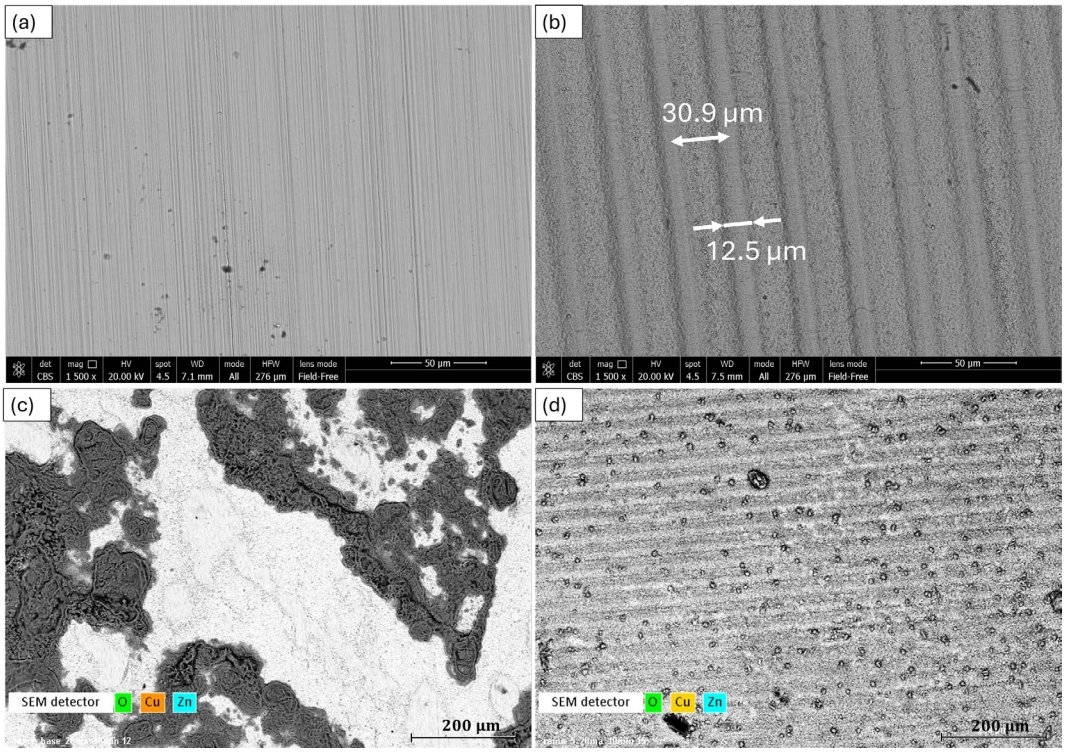


***Fig. 2**. SEM morphology of the (a) untreated and the (b) 5 µm groove laser treated material (LT5) without any zinc deposition; (c) untreated material and (d) LT5 with zinc deposition at 20mA for 10 minutes.*

Fig. 3 shows the voltage profile of the different samples of the copper foils during zinc electrodeposition. The two graphs illustrate the potential behavior during zinc electrodeposition on copper at current densities of 10mA/cm^2 and 20 mA/cm^2. In the first case, the potential is more negative for the "10LT" substrate compared to "5LT" and the "As is" indicating higher deposition overpotential on the substrate with a more complex microstructure. A similar trend in the potential hierarchy is observed in the second case, with more negative values across all curves compared to the 10 mA/cm^2 condition. The differences between the substrates become more pronounced, suggesting that microstructure significantly affects the deposition kinetics at higher current densities.

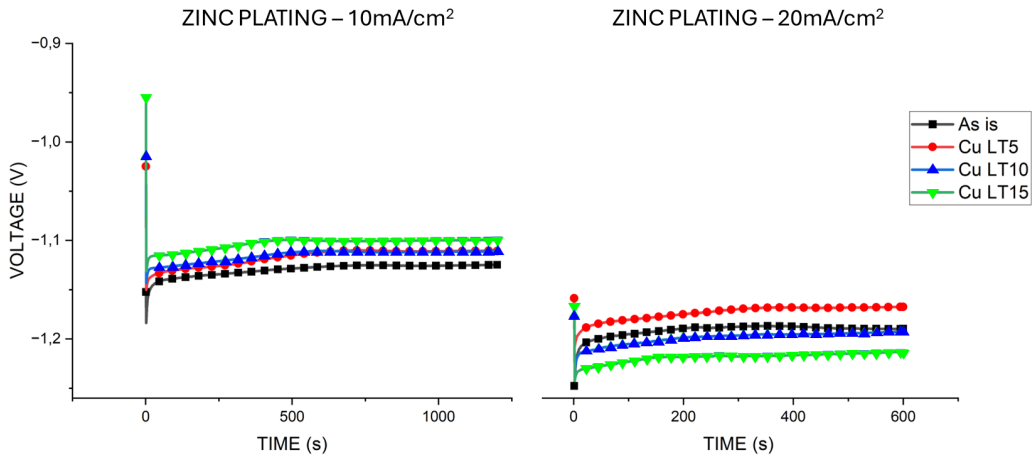


***Fig. 3.** Voltage profiles of Zinc deposition at 10 and 20 mA/cm^2.*

Materials Research Proceedings 57 (2025) 286-293 https://doi.org/10.21741/9781644903735-33

Following zinc deposition, the samples are evaluated by X-EDS for a semi-quantitative comparison of the elemental balance and the uniformity of zinc on the surface.

The results of the quantitative mass percentages of oxygen, copper, and zinc are shown in the histograms in Fig. 4 for the untreated and laser treated materials. The histograms were obtained investigating areas of 0.75 mm^2, and the error bars represent 1σ error.

Regardless of the deposition strategy, laser treatment mostly increases the percentage of local zinc deposited. By depositing at a higher current, on average, an increase in the presence of oxygen is observed as expected. With a high charging current, the effectiveness of the laser patterning is obtained with the 10 µm deep grooves.

X-EDS map results for bare Cu foils and 10LT at 20 mA/cm^2 are presented in Fig. 5a) and b) respectively. In the images, Zn is highlighted in light blue on the right part of the images and Cu in orange on the left one.

It is evident from the results that laser structuring in Fig. 5b makes Zn deposition more homogeneous. Several large areas of exposed Cu are found in the bare copper, Fig. 5a) where Zn is missing altogether.

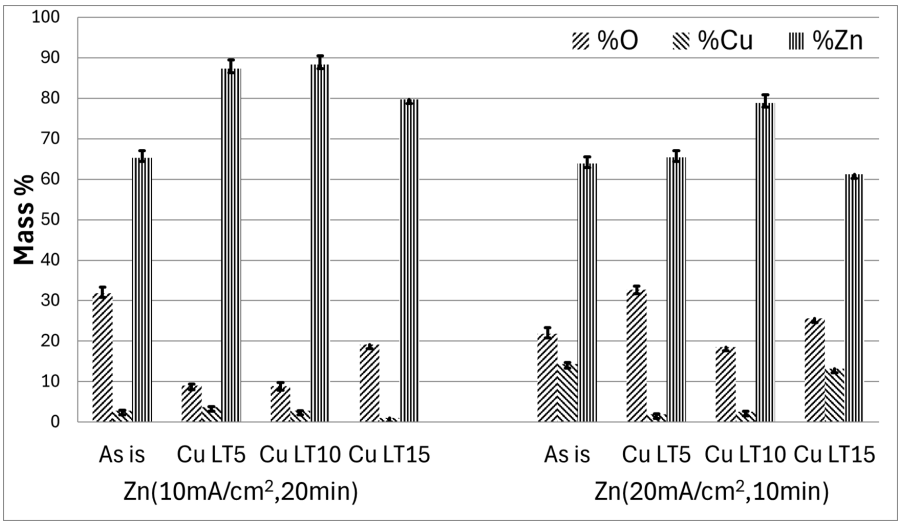


Fig. 4. *Quantitative mass percentages of Oxygen, Copper and Zinc, for the untreated material (As is), and laser treated material (CuLT5, CuLT10 and CuLT15) after the two different zinc deposition strategies. The bar error is calculated at 1σ.*

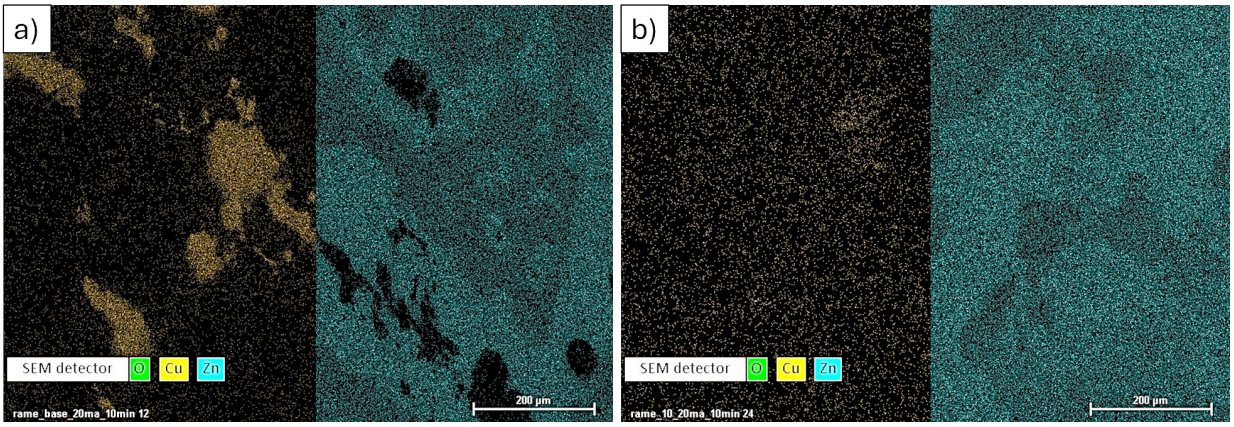


Fig. 5*. X-EDS map results for As is Cu (a) and 10LT (b) after zinc deposition at 20 mA for 10 minutes: copper is in orange on the left, zinc is in light blue on the right.*

Conclusions

In the field of energy storage, zinc has shown great promise, especially for usage in rechargeable batteries like zinc-ion and zinc-air batteries. It is a desirable substitute for other metal-based systems due to its high energy density, affordability, and wide availability.

However, to increase the overall performance, stability, and longevity of these systems, the right current collectors must be used. Particularly, metallic zinc can generate dendrites by depositing on copper. In this context, laser-structured 3D current collectors can be used for high current densities.

A regular parallel-line texture with 30 μm pitch was tested in this study, in three versions at different depths, 5, 10, and 15 μm. Zinc was electrolytically deposited on the textured copper according to two different deposition strategies, one at 10 mA/cm^2 for 20 minutes and the other at 20 mA/cm^2 for 10 minutes.

From the morphological analyses highlighting the percentage mass elemental components, it is found that the structuring makes the zinc deposition on the copper much more uniform. On the untreated copper, there are whole areas where zinc is missing.

Quantitative analysis shows that the percentage of zinc on treated copper increases regardless of the deposition strategy and with little influence on the depth of treatment between 5 and 10 μm with a saturation effect for more aggressive patterning 15 μm in depth. This demonstrates the validity of the proposed solution.

Further analysis should test the electrode in a high-current density battery. Our results have significant potential implications: using a 3D structure, we demonstrated the possibility of depositing Zn at high current densities more homogeneously compared to a 2D current collector. The currents used in this work (20 mA/cm²) are much higher than those typically reported in the literature for Zn-ion batteries (4-5 mA/cm²) and Li-ion batteries (1-2 mA/cm²). This study lays the groundwork for future applications such as Li-ion and Na-ion batteries.

References

[1] X. Zeng, J. Hao, Z. Wang, J. Mao, Z. Guo, Recent progress and perspectives on aqueous Zn-based rechargeable batteries with mild aqueous electrolytes, Energy Storage Materials 20 (2019) 410–437. https://doi.org/10.1016/j.ensm.2019.04.022

[2] D. Aurbach, Y. Talyosef, B. Markovsky, E. Markevich, E. Zinigrad, L. Asraf, J.S. Gnanaraj, H.-J. Kim, Design of electrolyte solutions for Li and Li-ion batteries: a review, Electrochimica Acta 50 (2004) 247–254. https://doi.org/10.1016/j.electacta.2004.01.090

[3] H. Sun, J. Zhu, D. Baumann, L. Peng, Y. Xu, I. Shakir, Y. Huang, X. Duan, Hierarchical 3D electrodes for electrochemical energy storage, Nat Rev Mater 4 (2019) 45–60. https://doi.org/10.1038/s41578-018-0069-9

[4] M. Kim, H. Bang, S. Hyun, S. Yi, C. Kim, Review on Ultrasonic and Laser Welding Technologies of Multi-Layer Thin Foils for the Lithium-Ion Pouch Cell Manufacturing, J Weld Join 41 (2023) 462–474. https://doi.org/10.5781/JWJ.2023.41.6.6

[5] E. Audouard, M. Fleureau, D. Pallarès, J.-M. Romano, F. Mermet, Characterization of batteries materials ablation by femtosecond pulses, Procedia CIRP 124 (2024) 57–60. https://doi.org/10.1016/j.procir.2024.08.070

[6] D. Neb, S. Kim, H. Clever, B. Dorn, A. Kampker, Current advances on laser drying of electrodes for lithium-ion battery cells, Procedia CIRP 107 (2022) 1577–1587. https://doi.org/10.1016/j.procir.2022.05.194

[7] T. Tsuda, N. Ando, S. Nakamura, Y. Ishihara, N. Hayashi, N. Soma, T. Gunji, T. Tanabe, T. Ohsaka, F. Matsumoto, Improvement of high-rate discharging performance of LiFePO4 cathodes

by forming micrometer-sized through-holed electrode structures with a pico-second pulsed laser, Electrochimica Acta 296 (2019) 27–38. https://doi.org/10.1016/j.electacta.2018.11.014

[8] L. Hille, M.P. Noecker, B. Ko, J. Kriegler, J. Keilhofer, S. Stock, M.F. Zaeh, Integration of laser structuring into the electrode manufacturing process chain for lithium-ion batteries, Journal of Power Sources 556 (2023) 232478. https://doi.org/10.1016/j.jpowsour.2022.232478

[9] A. Sikora, L. Gemini, M. Faucon, G. Mincuzzi, Benefits of Femtosecond Laser 40 MHz Burst Mode for Li-Ion Battery Electrode Structuring, Materials 17 (2024) 881. https://doi.org/10.3390/ma17040881

[10] L. Romoli, A.H.A. Lutey, G. Lazzini, Laser texturing of Li-ion battery electrode current collectors for improved active layer interface adhesion, CIRP Annals 71 (2022) 481–484. https://doi.org/10.1016/j.cirp.2022.04.034

[11] E. Ravesio, A.H.A. Lutey, D. Versaci, L. Romoli, S. Bodoardo, Nanosecond pulsed laser texturing of Li-ion battery electrode current collectors: Electrochemical characterisation of cathode half-cells, Sustainable Materials and Technologies 38 (2023) e00751. https://doi.org/10.1016/j.susmat.2023.e00751

[12] Y. Wang, Z. Zhao, J. Zhong, T. Wang, L. Wang, H. Xu, J. Cao, J. Li, G. Zhang, H. Fei, J. Zhu, Hierarchically Micro/Nanostructured Current Collectors Induced by Ultrafast Femtosecond Laser Strategy for High-Performance Lithium-ion Batteries, Energy & Environ Materials 5 (2022) 969–976. https://doi.org/10.1002/eem2.12223

[13] P. Tallone, S. Spriano, D. Versaci, S. Ferraris, A. Tori, S. Bodoardo, Picosecond laser texturing of Al current collector to improve cycling performances and simplify recycling of Lithium-ion batteries, Surfaces and Interfaces 51 (2024) 104659. https://doi.org/10.1016/j.surfin.2024.104659

[14] E. Ravesio, G. Montinaro, G. Mincuzzi, M. Negozio, D. Versaci, V. Gartiser, A.H.A. Lutey, F. Bella, S. Bodoardo, Ultrashort pulsed laser texturing of current collector for Si/C Li-ion anodes: Characterization of electrochemical performance and evolution of interface morphology, Journal of Energy Storage 109 (2025) 115226. https://doi.org/10.1016/j.est.2024.115226

Materials Research Proceedings 57 (2025) 294-301 https://doi.org/10.21741/9781644903735-34

Study of printing parameters on part performance in foamy TPU using material extrusion technology

Francesco de PALMA[1,a *], Alessandro PELLEGRINI[1,b], Roberto SPINA[1,c], Fulvio LAVECCHIA[1,d]

[1]Department of Mechanics, Mathematics and Management, Politecnico di Bari, Via Orabona, 4, 70125 Bari, Italy

[a]f.depalma2@phd.poliba.it, [b]alessandro.pellegrini@poliba.it, [c]roberto.spina@poliba.it, [d]fulvio.lavecchia@poliba.it

Keywords: Material Extrusion, Polymers and Compression Test

Abstract: Recent advances in Additive Manufacturing, particularly Material Extrusion (MEX), expand foam thermoplastic polyurethane's use in medical and fashion applications. Studies and applications, still in the early stages, require further development. This work investigates how the properties of Foam TPU change with print parameters such as Extrusion Temperature (ET) and Flow Rate (FR). Cylindrical compression test specimens were printed using MEX technology by varying three levels of each process parameter. After, compressive strength, density and aesthetic aspect were analyzed. The result showed that increasing ET and FR, the specimens density increased while compression strength decreased. Using low values of ET and FR, the aesthetic aspect improved, with a reduction of superficial mistakes and flaws.

Introduction

Many companies approach Additive Manufacturing (AM), producing whole products or parts of complex assemblies in biomedical [1][2], sport [3][4][5], fashion[6][7][8] fields.

One of the main advantages of the AM is the possibility to have compatibility with several materials such as polymers, metals and ceramics. Polymers cover a large part of the material portfolio of AM technologies, particularly the Material Extrusion [9]. Elastomers are polymers characterized by flexible properties and the capability to deform and regain their shape when a force is applied to them (elasticity). Thermoplastic Polyurethane (TPU) belongs to this class of polymers. Thanks to their softness and more durable interlayer adhesion, TPU based filaments are the main processed elastomers through MEX [10].

TPU is very interesting to use, operating also with foam form. This material is employed in specific areas such as biological scaffolds, adsorption carriers, and sensing materials. TPU is manufactured using various methods: injection molding, casting and extrusion, producing objects with different densities and layer thicknesses, working better in compression [11][12][13]. Various studies have been done in recent years. Iacop MC et al. [14][15] investigated the compression behavior of 3D printed specimens in TPU foam, varying several printing parameters and infill strategy. The research results revealed that the most influential factor was the temperature, followed by infill density and pattern type. Lin X. et al. [16] explains a correct strategy to produce a high-quality object in TPU foam without compromising the final mechanical properties producing several specimens with different velocities and feeding ratios and evaluating in terms of tensile and tear strength that it shows an improvement of behavior compared to injection molding production. The research of Wang X. et al. [17] on the addition of nano clay in a TPU foam structure reported that the dispersed nano clay in the cell walls effectively reinforced the foams while retarded the permanent deformation. Ramirez B. et al. [18] showed the mechanical behavior and the difference between polyurea and TPU foam. Both materials have similar attitudes tensile strength and resilience while polyurea has increased properties in elongation and tear

Content from this work may be used under the terms of the Creative Commons Attribution 3.0 license. Any further distribution of this work must maintain attribution to the author(s) and the title of the work, journal citation and DOI. Published under license by Materials Research Forum LLC.

Materials Research Proceedings 57 (2025) 294-301 https://doi.org/10.21741/9781644903735-34

strength and decrease in compression set values compared to TPU foam. All these studies are very recent because this material is relatively new, and research is still in progress. TPU foam is a variant of typical TPU, obtaining from a virgin material in which a blowing agent like butene (C_4H_8), azodicarbonamide ($C_2H_4O_2N_4$), sodium bicarbonate ($NaHCO_3$) or carbon dioxide (CO_2) can act to form bubbles. Spina [19] showed different techniques, conventional foam injection-molding process equipped with mold opening and gas counter-pressure techniques, special mold technology to produce components with locally graded foam structures and locally different densities, compression molding process to vary density and cellular structure independently and foaming process of recycled polymers. In [20] are explained other techniques based on injection molding, use with nitrogen (N_2) as the main blowing agent or as co-blowing agent with CO_2. The results showed that physical blowing agents yielded softer foams. In contrast, CO_2 and nitrogen N_2 as co-blowing agents helped manufacture foams with lower bulk densities, better microstructures, and lower hysteresis loss ratios. One of the limits of the chemical-blowing is an earlier degradation onset temperature. A foam TPU is characterized by porous structure with open and closed cells, creating a lighter structure and saving material Fig. 1A). The main difference with an unfoamed TPU Fig. 1B) is the high content of bubbles due to the chemical agent's effect. As a result, cushioning performance and porosity improve insulating ability to heat, sound, electricity and electromagnetic waves [12].

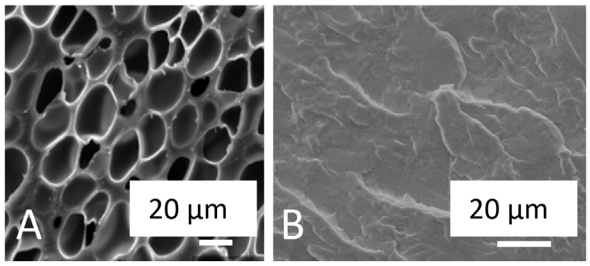


Fig. 1 A) Foam TPU [21] - B) TPU [22]

In the present work, a TPU filament including a chemical blowing agent was 3D printed using MEX technology. The aim of the work was to investigate the effects of printing parameters on the dimensional and mechanical characteristics of parts produced by MEX technology. The effects on part density, dimensional accuracy, and compressive behavior were investigated varying Extrusion Temperature (ET) and Flow Rate (FR). The analysis was been supported by a Design of Experiment (DoE) approach.

Materials and Methods

In this study has been used a TPU filament with a 2,2,4-trimetilpentane blowing agent with a 0.3-1.5% in volume. The used material is "Filaflex Foamy filament" (Recreus Industries S.L., Elda, Spain). The properties provided by the supplier show a density of 1.05 g/cm^3 and ShoreA Hardness (H) of 78. After printing, these values change because hardness and density decreased with a reduction of the flow rate [23]. For example, material datasheet shows that with a Flow rate of 70%, it is possible obtain a Shore A hardness equal to 51, and density of 0.71 g/cm^3. Raise 3D Pro3 (CostaMesa, CA, USA) was used to print specimens. According to the UNI EN ISO 7743:2017 standard [24], cylindrical shape specimens with height (h) of 25 mm and diameter (d) of 17.8 mm were printed using a 0.8 mm nozzle diameter. The relevant printing parameters were: layer height of 0.6 mm, number of top, bottom and side walls equal to 1, printing speed of 15 mm/s, raster angle of ±45° and infill density equal to 100% (fully solid). ET and FR were varied according to a 3^2 full factorial design reported in Table 1, with 3 replications.

Table 1 3^2 Full factorial design

Parameter	Levels		
Extrusion temperature (°C)	240	250	260
Flow rate (%)	70	80	90

Before printing, the filament was dried for 6 hours at 45°C to remove moisture, with a vacuum oven (Vismara Scientific Equipment, Italy) according with Recreus guidelines.

After printing, the height and diameter of the specimens were measured using a digital caliper with a resolution of 0.01mm. Digital microscope, Hirox RH-2000 (Hirox Co., Ltd, Japan) equipped with MXB-5040RZ body and AD-5040LOWS optical lens (10x magnification). The specimen inspection was used for aesthetical analysis with the aim to detect printing mistakes and flaws.

Density was measured through Archimedean's method, using distilled water at 24°C (ρ=0.9973 g/cm^3), applying the conventional method for floating solids. Received values were used to define the relative density as the ratio between the obtained value and the filament density equal to 1.05 g/cm^3. After this step the specimens were dried with the same procedure previously reported.

The last test performed was the compression test. Specimens were conditioned according to the UNI ISO 471 "Rubber-Temperatures, humidity and times for conditioning and testing" [25]. The test was carried out using a tensile test machine ETM503 (Shenzhen Wance Testing Machine Co., Ltd.), equipped with a 5 kN load cell. The standard UNI ISO 7743 method C, used for the test, indicated that the specimens were positioned between the two plates of the machine without lubricants or sandpaper at interface. Four compression cycles were executed without relaxation between the load\unload runs. The test parameters were a plate movement with strain from 0% to 25% of the pre-testing test piece height, a preload of 2 N, and the crosshead speed of 10 mm/min. Fig. 2 shows how the compression test was realized. The output of the compression test was the Maximum Stress (MSS) and specific compressive cycle stress (σ_{spec}), all computed at the latest compressive cycle.

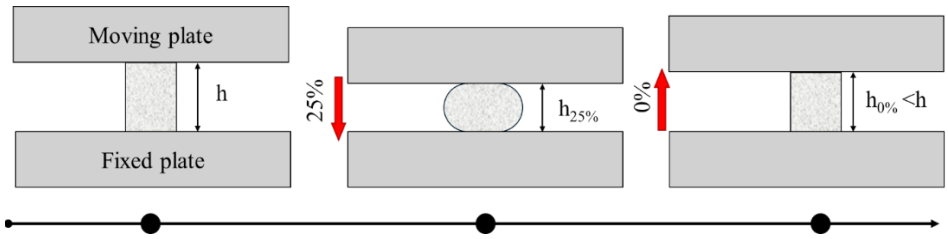


Fig. 2 Schematic representation of compression test.

Results and Discussion

Measurement of printed specimens: In Fig. 3 *the average of the height and diameter of printed specimens before compression test was reported.* No significant differences can be observed regarding the several investigated process parameters configurations. However, for the higher values of ET and FR, the average height and diameter exceeded about 5% of the nominal values. The x-axis in Fig. 3 shows the pairs of FR – ET investigated in the current work.

Materials Research Proceedings 57 (2025) 294-301 https://doi.org/10.21741/9781644903735-34

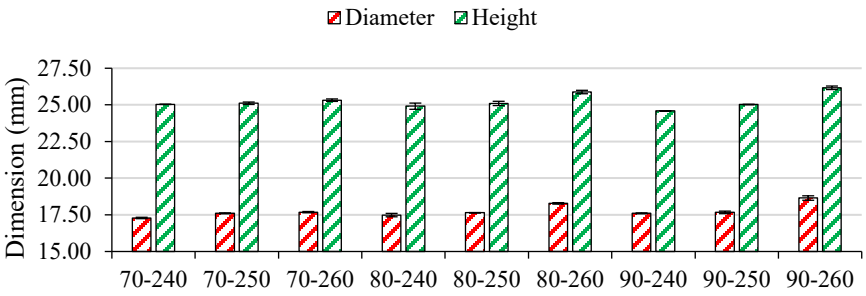


Fig. 3 Average value of height and diameter for all configurations investigated (FR-ET).

Aesthetic aspect: Fig. 4 shows the benchmarks made with the different combinations of printing parameters. The result shows that increasing the FR, with a fixed value of ET at 240°C and 250°C (A and B), the aesthetic aspect gets worse because holes appear, gaps, non-flat surfaces, etc. The situation changes at ET to 260°C (Fig. 4), as with an FR of 70% or 80%, gaps and no-flat surfaces appear in the top layer, and it is possible to locate the tip roads. However, an increasing of FR up to 90% provided improvements in the aspect quality of the specimens and although it is easy to distinguish tip roads, holes or gaps are not present.

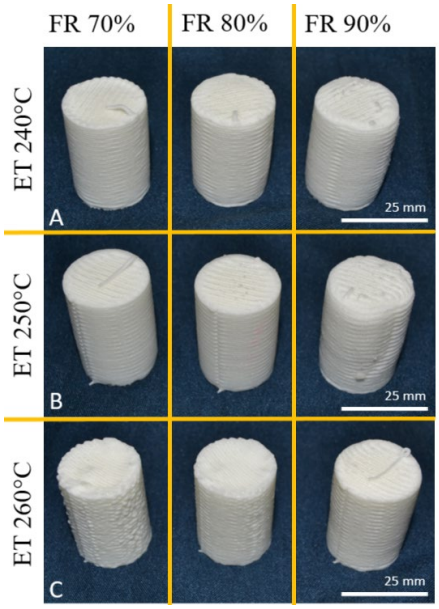


Fig. 4 Benchmarks of specimens

Archimedes test – density: The results of the density were reported in Table 2**.**

Table 2 Overview of the density results from Archimedean's method.

DENSITY (g/cm³)			
	Extrusion temperature (°C)		
Flow rate (%)	240	250	260
70	0.75±0.02	0.81±0.01	0.84±0.01
80	0.81±0.01	0.89±0.05	0.91±0.01
90	0.83±0.03	0.86±0.02	0.93±0.05

Materials Research Proceedings 57 (2025) 294-301 https://doi.org/10.21741/9781644903735-34

The results confirmed that by increasing the flow rate, the density of specimens increased from a minimum of 0.75±0.02 g/cm^3 to a maximum of 0.93±0.05 g/cm^3 (Fig. 5A). Furthermore, it was observed that by keeping the flow rate constant and increasing the extrusion temperature, the density increased. Hence, to better understand the effects of the extrusion temperature and flow rate on the density, the data were analyzed using an Analysis of Variance (ANOVA) approach with a confidence level of 95% (α=0.05). The results of the statistical analysis confirmed a strong influence of the two single parameters on the density as reported in Fig. 5B with an R-sq coefficient of 67.02%. On the other hand, the interaction between them has no reported significative influence on the parameter investigated.

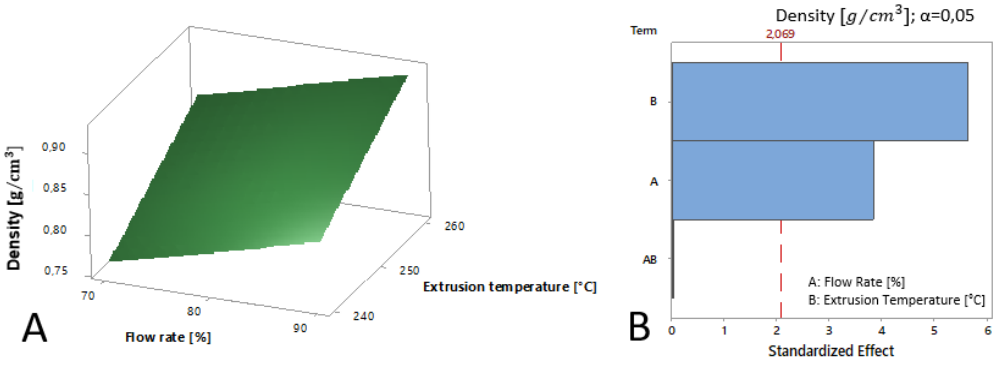


Fig. 5 Density results on A) Surface plot – B) Pareto Chart

Compression test: The results of the compression test values are shown in Table 3. As mentioned in the Material as Methods section, the last cycle was considered in the study.

Table 3 Results of the compression test.

AVG. MAX. STRESS 4th CYCLE [MPa]			
	Extrusion temperature (°C)		
Flow rate (%)	240	250	260
70	1.19 ± 0.02	0.99 ± 0.04	1.04 ± 0.11
80	1.76 ± 0.03	1.39 ± 0.06	1.40 ± 0.25
90	2.26 ± 0.11	1.74 ± 0.05	1.67 ± 0.12

The lowest values were obtained when a flow rate of 70% was adopted, with a minimum MSS of 0.99 MPa for the configuration 70-250. Instead, the maximum value of MSS was achieved for the 90-240 configuration equal to 2.26 MPa Fig. 6. The global trend of the MSS with respect to all levels were reported in the surface plot in Fig. 7B). It was possible to highlight how the main relevant effects were reported for a variation of the flow rate. Furthermore, in an opposite way to the density, keeping the flow rate constant, increasing the extrusion temperature, the strength of the part decreased. The ANOVA method was adopted to study the influence of extrusion temperature and flow rate on the maximum compressive stress. From the ANOVA, the model showed an R-sq coefficient equal to 92.23%. Furthermore, as reported in the Pareto Chart Fig. 7A), the single factors and their interactions had a significant influence on maximum stress. Studying the MSS 4th cycle and how it changes with ET and FR, it is possible to show that the highest value is at 240°C and 90%, while the lowest is just over 250°C and 70%**.** It is essential to underline that by increasing the ET and fixing FR**,** the MSS 4th cycle first increases, but then, over 250°C, it decreases. Fig. 6 and Fig. 7B) show the trend.

Materials Research Proceedings 57 (2025) 294-301 https://doi.org/10.21741/9781644903735-34

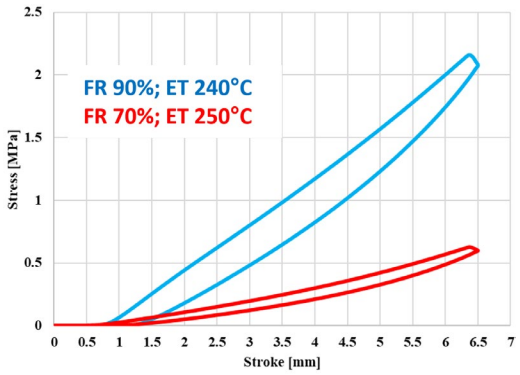


Fig. 6 Max. Stress 4th cycle – Representation of 4th curve, in blue best behaviour, in red worst behaviour

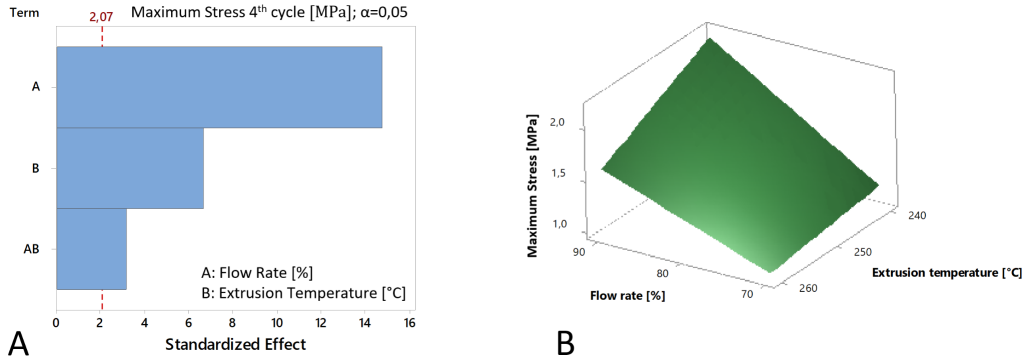


Fig. 7 Maximum Stress 4th cycle on A) Pareto Chart - B) Surface Plot

Fig. 8 shows the Maximum Specific Stress 4th cycle [MPa/g] that it is obtained from the ANOVA study of Density and Maximum Stress 4th cycle. In this graph the minimum value is always with an ET of 260°C and a FR of 70% while the maximum on 240°C – 90%.

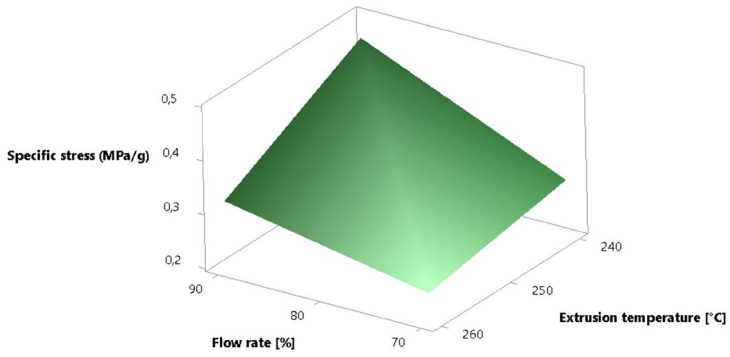


Fig. 8 Surface plot of Maximum Specific Stress 4th cycle

Conclusion

Highest compressive properties were obtained printing the specimen with a FR of 90% and a TE equal to 240°C. However, this specimen showed several flaws with a not perfect aesthetic aspects and an average density value. In contrast, specimens produced using 70% FR showed the lower values of mechanical proprieties. A general trend is that when the FR increases, the mechanical

behavior improves. Considering the results obtained, the adoption of an extrusion temperature of 240-250°C and a flow rate of 80% provided the best aesthetic, dimensional and mechanical performances. This first work offers new research perspectives directed to evaluate the impact of a lower extrusion temperature (<240°C) and the influence of environmental factors on the part properties.

Acknowledgements
A special thank you is given to Crea3D for the support of material and knowledge.

References

[1] M. Davia-Aracil, J.J. Hinojo-Pérez, A. Jimeno-Morenilla, H. Mora-Mora, 3D printing of functional anatomical insoles, Comput Ind 95 (2018) 38–53. https://doi.org/10.1016/j.compind.2017.12.001

[2] A.C.M. Oliveira, E. Bernalte, R.D. Crapnell, M.J. Whittingham, R.A.A. Muñoz, C.E. Banks, Advances in additive manufacturing for flexible sensors: bespoke conductive TPU for multianalyte detection in biomedical applications, Appl Mater Today 42 (2025). https://doi.org/10.1016/j.apmt.2025.102597

[3] Beiderbeck Daniel, Kruger Harry, Minshall Tim, The Future of Additive Manufacturing in Sports, in: S.L. Schmidt (Ed.), 21st Century Sports, 1st ed., 2020: pp. 111–132.

[4] C.M. Llanos, D. Saakes, M. Mehrpouya, Additive manufacturing of adaptive architected structures for enhanced protective equipment, European Journal of Mechanics, A/Solids 112 (2025). https://doi.org/10.1016/j.euromechsol.2025.105649

[5] Vinay Deep Punetha, Akhila Raman, Saritha Appukuttan, 15 - Additive manufacturing of functional polymers and nanocomposites for sport goods applications, 2025.

[6] P. Yap, W.Y. Yeong, Additive manufacture of fashion and jewellery products: a mini review: This paper provides an insight into the future of 3D printing industries for fashion and jewellery products, Virtual Phys Prototyp 9 (2014) 195–201.

[7] S.H. Khajavi, Additive manufacturing in the clothing industry: Towards sustainable new business models, Applied Sciences (Switzerland) 11 (2021). https://doi.org/10.3390/app11198994

[8] Sun, L. (2022). 3D Printing and Additive Manufacturing in Fashion. In: Lee, YA. (eds) Leading Edge Technologies in Fashion Innovation. Palgrave Studies in Practice: Global Fashion Brand Management. Palgrave Macmillan, Cham. https://doi.org/10.1007/978-3-030-91135-5_4

[9] P. Wang, B. Zou, S. Ding, C. Huang, Z. Shi, Y. Ma, P. Yao, Preparation of short CF/GF reinforced PEEK composite filaments and their comprehensive properties evaluation for FDM-3D printing, Compos B Eng 198 (2020). https://doi.org/10.1016/j.compositesb.2020.108175

[10] L. Rodríguez-Parada, S. De La Rosa, P.F. Mayuet, Influence of 3D-printed TPU properties for the design of elastic products, Polymers (Basel) 13 (2021). https://doi.org/10.3390/polym13152519

[11] H.A. Kharbas, J.D. McNulty, T. Ellingham, C. Thompson, M. Manitiu, G. Scholz, L.S. Turng, Comparative study of chemical and physical foaming methods for injection-molded thermoplastic polyurethane, Journal of Cellular Plastics 53 (2017) 373–388. https://doi.org/10.1177/0021955X16652107

[12] Zhao Jinchuan, Wang Guilong, Zhang Aimin, Zhao Guoqun, Park Chul B., Nanocellular TPU composite foams achieved by stretch-assisted microcellular foaming with low-pressure gaseous CO2 as blowing agent, Journal of CO2 Utilization 53 (2021).

[13] E.J. Shin, Y.S. Jung, H.Y. Choi, S. Lee, Synthesis and fabrication of biobased thermoplastic polyurethane filament for FDM 3D printing, J Appl Polym Sci 139 (2022). https://doi.org/10.1002/app.52959

[14] M.C. Iacob, D. Popescu, C. Stochioiu, F. Baciu, A. Hadar, Compressive behavior of thermoplastic polyurethane with an active agent foaming for 3D-printed customized comfort insoles, Polym Test 137 (2024). https://doi.org/10.1016/j.polymertesting.2024.108517

[15] M.C. Iacob, D. Popescu, F. Baciu, Effect of Process Parameters on the Hardness of 3D-printed Thermoplastic Polyurethane that Includes Foaming Agent, Materiale Plast 60 (2023) 144–154. https://doi.org/10.37358/Mat.Plast.1964

[16] X. Lin, J. Gao, J. Wang, R. Wang, M. Gong, L. Zhang, Y. Lu, D. Wang, L. Zhang, Desktop printing of 3D thermoplastic polyurethane parts with enhanced mechanical performance using filaments with varying stiffness, Addit Manuf 47 (2021). https://doi.org/10.1016/j.addma.2021.102267

[17] X.C. Wang, Q.S. Zhu, B. Bin Dong, H.H. Wu, C.T. Liu, C.Y. Shen, L.S. Turng, T. Geng, The effects of nanoclay and deformation conditions on the inelastic behavior of thermoplastic polyurethane foams, Polym Test 79 (2019). https://doi.org/10.1016/j.polymertesting.2019.106043

[18] B.J. Ramirez, V. Gupta, High polyurea vs tpu foam, Int J Mech Sci 150 (2019) 29–34.

[19] R. Spina, Technological characterization of PE/EVA blends for foam injection molding, Mater Des 84 (2015) 64–71.

[20] C. Ge, S. Wang, W. Zheng, W. Zhai, Preparation of microcellular thermoplastic polyurethane (TPU) foam and its tensile property, Polym Eng Sci 58 (2018) E158–E166. https://doi.org/10.1002/pen.24813

[21] S. Wang, H. Feng, J. Hong, G. Wang, Enhanced foaming ability of thermoplastic polyurethane by crystallization during mold-opening foam injection molding with supercritical N2 as blowing agents, Journal of Materials Research and Technology 22 (2023) 2489–2501.

[22] A. Huang, X. Peng, L.-S. Turng, FOTO TPU In-situ fibrillated polytetrafluoroethylene (PTFE) in thermoplastic, Polymer (Guildf) 134 (2017) 263–274.

[23] Recreus, FILAFLEX FOAMY TECHNICAL DATA SHEET TDS 2025, (n.d.). https://drive.google.com/drive/folders/1jGRJ_JDQWngTsKU96shCkoZUh-BFmGrR (accessed May 9, 2025).

[24] ISO 7743, Rubber, vulcanized or thermoplastic — Determination of compression stress strain properties, (2011).

[25] UNI ISO 471, Rubber-Temperatures, humidities and times for conditioning and testing Caoutchouc-Temperatures, humidites et durees pour Ie conditionnemen t et I ’essai, 1995.

Manufacturing processes design, optimization and engineering



Materials Research Proceedings 57 (2025) 303-310 https://doi.org/10.21741/9781644903735-35

Enhancing the robustness of nanostructures through the production of self-protective structures by injection molding of thermoplastic elastomers

Giacomo BARUFFA[1,a *], Keltoum OUBELLAOUCH[2], Giulia ZANIBONI[2], Giovanni LUCCHETTA[1] and Marco SORGATO[3,b]

[1]Department of Industrial Engineering, University of Padova, via Venezia 1, Padova, 35131, Italy

[2]Department of Sciences and Methods for Engineering, University of Modena and Reggio Emilia, via Amendola, 42122 Reggio Emilia, Italy

[3]EN&TECH, University of Modena and Reggio Emilia, Italy

[a]giacomo.baruffa@studenti.unipd.it, [b]marco.sorgato@unipd.it

Keywords: Thermoplastics, Micro Injection, Surface Functionalization

Abstract. Nanostructures are often proposed for anti-counterfeiting and decoration, yet their practical use is frequently limited by poor durability under mechanical stress and high production costs. To enhance the robustness of nanopatterns (specifically LIPSS), this study proposes a combined approach using sacrificial microstructures and elastomeric materials. The designed textures were fabricated through micro-injection molding (μ-IM) of thermoplastic elastomers (TPEs), a process suited for mass production. The process parameters were optimized to better understand the behavior of TPEs in μ-IM, with particular focus on replication fidelity and uniformity. Finally, the durability of the LIPSS was evaluated through abrasion tests. The results showed that melt temperature, mold temperature, and injection speed are the most influential process parameters. The integration of protective micropatterns and the use of TPE led to an increase in the durability of LIPSS of 37% and 18%, respectively.

Introduction

Nanostructures, particularly periodic ones like Laser-Induced Periodic Surface Structures (LIPSS), have attracted significant attention for their ability to generate structural color, with applications in decorative design and anti-counterfeiting [1]. However, their inherent fragility makes them susceptible to mechanical stress, limiting their practical use in real-world applications. A potential solution to enhance their durability is integrating nanofeatures with larger-scale elements, creating a hierarchical structure that can withstand greater mechanical loads while maintaining functionality through the nanofeatures, thus forming self-protecting surfaces [2]. A notable example is provided by Wang et al., who developed a robust superhydrophobic surface by combining a microstructure of interconnected microcavities with a nanocoating. This hierarchical structure retained its wettability properties after various durability tests [3]. Similarly, W. Luo et al. designed a hierarchical texture with a triangular micropattern to protect nanoparticles. The surface maintained its superhydrophobic functionality even after sandpaper abrasion [4]. Conversely, Xu et al. developed an anti-reflective surface with superhydrophobic properties through laser doping and plasma etching. A microscale grid protected the antireflection cones, and the resulting pattern maintained its functionality even after 150 cycles of severe abrasion [5].

Although resilient, self-protective features are still susceptible to degradation. Under cyclic loading, even reinforcement features can fail over time, resulting in damage to the nanofeatures [2]. A potential solution is using elastomeric materials, which can restore their original shape once the load is removed. As a result, textures deform under mechanical stress but return to their original

Content from this work may be used under the terms of the Creative Commons Attribution 3.0 license. Any further distribution of this work must maintain attribution to the author(s) and the title of the work, journal citation and DOI. Published under license by Materials Research Forum LLC.

Materials Research Proceedings 57 (2025) 303-310 https://doi.org/10.21741/9781644903735-35

configuration when the load is relieved, thereby restoring surface functionality [6]. This concept was demonstrated by Su et al., who fabricated a superhydrophobic surface using an elastomeric polyurethane (PU). Tests confirmed that the PU surface was more durable than rigid materials [6]. Yamauchi et al. developed a superhydrophobic surface by blending tetrapod-shaped ZnO with poly(dimethylsiloxane) (PDMS), which preserved its functionality even after an abrasion test [7]. Similarly, Hoshian et al. manufactured a durable superhydrophobic PDMS-TiO_2 surface with high resistance to abrasion and human touch, thanks to the elasticity of PDMS [8].

Most studies on nanostructure durability focus on features that alter surface wettability, often involving expensive production processes unsuitable for large-scale production. In contrast, micro-injection molding (µ-IM) offers an efficient solution for mass-producing polymer-based components with micro- and nanoscale features. Moreover, self-recovering functionality can be combined with µ-IM using thermoplastic elastomers (TPEs), which offer the processability of thermoplastics united with the elasticity of vulcanized rubber. Despite their potential, few studies exist on the µ-IM of TPEs. Baruffi et al. studied µ-IM process parameters on a TPE micro-ring [9], Vega et al. investigated the replication capability of various TPEs on cylindrical features [10], Birkar et al. assessed the effect of TPE hardness and molding conditions on replication fidelity [11, 12], and Stormonth-Darling et al. examined µ-IM for nanogroove production in TPE [13].

This study evaluates the feasibility of fabricating self-protective structures in TPE, imparting self-recovery properties to the texture. Therefore, a durable diffraction grating capable of generating structural color was developed for potential anti-counterfeiting and decorative applications. To achieve this, the µ-IM process was combined with laser machining techniques for mold fabrication. The influence of processing parameters on the replication fidelity of two TPEs was systematically assessed during the study. Finally, the durability of the surfaces was tested through wear tests designed to mimic human touch. The findings aim to enhance the understanding of TPE behavior in µ-IM, addressing current research gaps and expanding the application of nanostructured surfaces toward practical, scalable solutions.

Materials and Methods

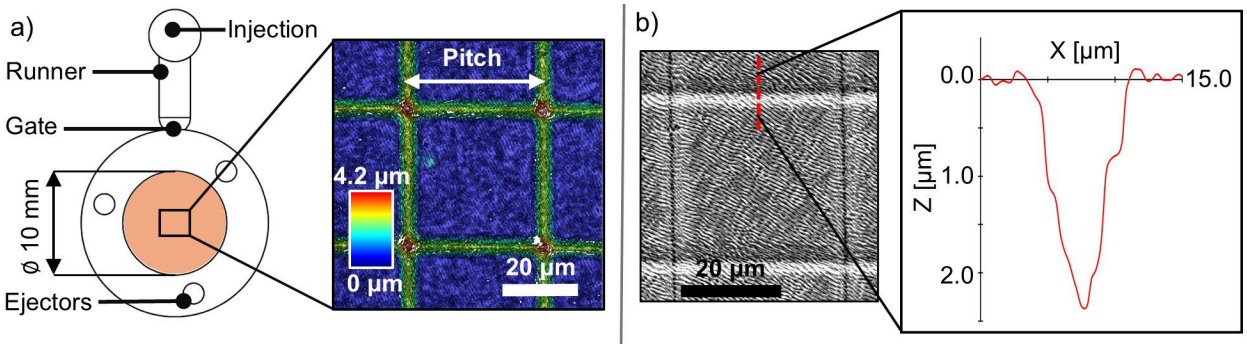


Figure 1: Representation of the molded component: (a) Schematization of a polymer sample and micrograph of the texture; (b) profile of the microstructure fabricated on the inserts.

Texture Design and Inserts Manufacturing. During the insert design process, the geometry of the micro- and nanostructures was defined separately. For the microstructure optimization (micro-armor or microgrid), continuous raised features were arranged to form closed pockets. These pockets followed a square pattern, with the pitch optimized to balance available space for nanostructures and the deformation of the abrasive medium, assessed using the simply supported beam model. Two inserts with different microstructure pitches (40 µm and 250 µm) were fabricated, along with an unprotected (UP) insert (Fig. 1a). The microfeatures had a triangular cross-section with a height of 2.5 µm and a width of 10 µm (Fig. 1b). Between the micro-armor walls, LIPSS with a periodicity of approximately 900 nm and an average height of 300 nm were fabricated. These structures were oriented at a 45° angle relative to the microstructures (Fig. 1a).

Materials Research Proceedings 57 (2025) 303-310 https://doi.org/10.21741/9781644903735-35

The mold inserts are 10 mm in diameter, cylindrical, and made from 16MnCr5 steel. After polishing to a surface roughness (Sa) of 0.03 µm, they are processed with an EKSPLA Atlantic 50 picosecond laser system at 532 nm and 1064 nm wavelengths. The microstructure was created using the 532 nm wavelength with 75 mW power, 1200 mm/s scan speed, 400 kHz frequency, and 80 passes, achieving the required groove depth and excellent surface quality with minimal thermal impact. LIPSS were then generated using the 1064 nm wavelength at 0.69 W power, 1500 mm/s scan speed, and 333 kHz frequency.

Micro Injection Molding. The inserts were replicated using a micro-injection molding machine (Micropower 15, Wittmann-Battenfeld). The material used was styrene-ethylene-butylene-styrene (SEBS). Given the impact of TPE hardness on replication quality, two SEBS materials with Shore A hardness values of 50 and 80 were selected for this study [10, 11].

A two-phase optimization was conducted to identify process parameters that optimize replication quality and evaluate their impact on part quality. In the first phase (screening phase), a two-level fractional factorial Design of Experiments (DOE) with resolution IV was used to identify the process parameters that statistically impact replication quality. In the second phase, the effects of the previously identified parameters were further investigated using a three-level Full Factorial DOE (Optimization DOE). During the first phase, seven factors were considered: mold temperature (T_{mold}), melt temperature (T_{melt}), injection speed (V_{inj}), switch-over point (so), holding pressure (P_{hold}), cooling time (t_{cool}), and material hardness (Shore A). Both DOEs were carried out using the insert with a microgrid pitch of 250 µm. The process parameters optimizing the replication of the first insert were reused to replicate the remaining two textures.

For each experimental point, five repetitions were performed. Each parameter set's first 10 molding cycles were discarded to ensure process stability.

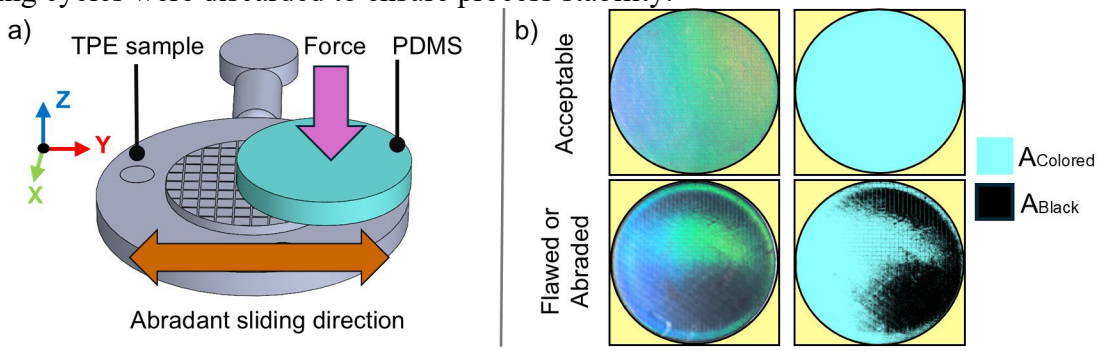


Figure 2: Abrasion test of TPE samples: a) Schematic representation of the loading conditions; b) Illustration of the functionality assessment method.

Abrasion Test. The durability of the samples fabricated via µ-IM was evaluated through abrasion tests simulating the effect of human touch on the surface texture. The tests were conducted using a tribometer (MFT-5000, Rtec-Instruments), where a PDMS disc was slid over the textured surfaces (Fig. 2a). The cylindrical PDMS disc, with a diameter of 10 mm, was prepared with a base-to-catalyst ratio of 10:1, yielding an elastic modulus of 14 MPa.

The test procedure involved aligning the PDMS disc with the center of the sample and applying a vertical force of 5 N. A sinusoidal motion was applied to the sample along the y-axis, with an amplitude of 10 mm and a velocity of 25 mm/s. Wear tests were conducted on each sample for 5, 10, 15, and 30-minute durations, each repeated five times for statistical reliability.

Geometrical and Functional Characterization of The Texture. The inserts and molded samples were characterized using an optical microscope (VHX-S770E/S750E, Keyence) and a confocal profilometer (Plu Neox, Sensofar, SP) equipped with a 100x objective. The inserts were marked with an inverted L-shaped reference (0.25 mm x 0.5 mm) near the gate to ensure repeatability.

Materials Research Proceedings 57 (2025) 303-310 https://doi.org/10.21741/9781644903735-35

Initially, optical microscopy was used to verify the presence of defects on inserts and samples. Subsequently, the confocal profilometer was employed for quantitative analysis of replication quality. Scans (1.10 mm x 0.20 mm) were acquired 7.5 mm from the pin gate.

The height of the microfeatures on the TPE components (h_{sample}) and the depth on the inserts (d_{mold}) were measured at six different points in each scan. Then, the replication quality at the microscale was evaluated using the Q_{micro} parameter, defined as in eq.1. On the other hand, the replication quality at the nanoscale is assessed using the roughness parameters Spk (reduced peak height) and Svk (reduced valley height), measured according to the ISO 25178-3 standard. Sampling of the roughness parameters was repeated three times for each scan. By comparing the roughness values of the inserts and samples, the quality parameters for the positive features (Q_p) and negative nanofeatures (Q_v) of the polymer parts are defined as in eq. 2 and eq. 3.

$$Q_{micro} = \frac{h_{sample}}{d_{mold}} \quad (1) \qquad Q_p = \frac{Spk_{sample}}{Svk_{mold}} \quad (2) \qquad Q_v = \frac{Svk_{sample}}{Spk_{mold}} \quad (3)$$

The optical microscope was also employed to evaluate the functionality of the nanofeatures (structural coloration) in the components made from TPE. For this purpose, the microscope was used with a 20x magnification to capture the entire textured area. Images of all the specimens, both worn and unworn, were captured under the same lighting conditions (partial ring illumination).

Due to the stresses applied during the wear tests, areas without structural coloration appeared on the samples (A_{Black}). The size of these areas was assessed through a threshold analysis: starting from the microscope images, a height map was generated. By applying two threshold levels, it was possible to determine the size of the area where, despite the abrasion, the surface functionality remained intact ($A_{Colored}$), which is expressed as a percentage of the total textured area (Fig. 2b).

Results and Discussion

Inserts Design and Manufacture. The insert design was split into two phases: developing the protective microstructure and designing the nanostructure. This approach enabled separate optimization of functionality and durability [3]. A continuous grid was chosen as the reinforcing microstructure due to its greater robustness than discrete support features. In microstructure design, it's crucial to balance the space between the reinforcing grid and nanofeatures. Higher grid density improves durability but may reduce functionality by limiting nanofeature availability. Therefore, the relationship between the available area for nanofeatures, the shape, and the pitch of the reinforcing grid was investigated (Fig. 3a). The analysis revealed that square and hexagonal patterns offer a larger area for nanostructures at a given pitch. However, the square pattern was preferred over the hexagonal one due to its higher mechanical strength [5].

To prevent the formation of defects (melt pools) that could compromise the functionality of the surface, microfractures with a cross-section equal to the laser spot size were selected [5].

The pitch of the microfeatures on the inserts was determined by evaluating the deformation of the abrasive medium (PDMS) relative to microfeature spacing (Fig. 3 b). The data show that the PDMS bend exceeds the feature height only when the reinforcement pitch exceeds 220 μm. If this happens, the abrasive medium contacts the nanofeatures directly, accelerating functionality loss.

LIPSS were implemented at a 45° angle to achieve structural coloration and to minimize the reinforcing grid's influence on the resulting color. The dimensions of the microfeatures and the roughness parameters of the fabricated inserts are summarized in Tab. 1.

Materials Research Proceedings 57 (2025) 303-310 https://doi.org/10.21741/9781644903735-35

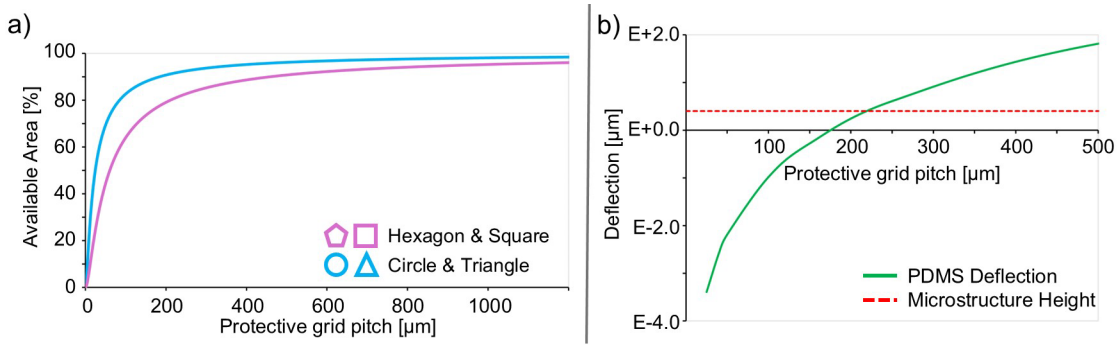


Figure 3: Texture design: a) area available for nanofeatures, b) abradant (PDMS) deformation.

Micro Injection Molding. Once the inserts were manufactured, the effect of µ-IM process parameters on the replication fidelity was investigated.

Through the screening phase, mold temperature, melt temperature, injection speed, and material hardness were identified as statistically significant factors affecting feature replication. Among these, both temperatures had a positive effect on replication quality. The effect of injection speed is particularly interesting: lower speeds enhanced texture replication [13]. This occurs because higher injection speeds increase shear stress on the polymer, causing greater elongation and alignment of macromolecules. During cooling, the macromolecules in the soft phase relax and contract (especially when highly stretched), ultimately reducing replication accuracy [11, 12]. Material hardness further influenced replication outcomes. The SEBS with Shore A 50 exhibited replication indices for peaks and valleys frequently exceeding 100%, unlike the Shore A 80 material. Values above 100% are attributed to mold adhesion (leading to feature elongation) and superficial defects (leading to increased roughness) caused by polymer relaxation [11, 13]. This suggests that softer SEBS, with a higher proportion of soft phase, is more prone to relaxation and adhesion phenomena. Furthermore, preliminary wear tests showed that the harder SEBS ensured higher robustness, leading to the selection of TPS with Shore A 80 for the next DOE phase.

Contrary to expectations, packing pressure did not show statistically significant effects. This is likely due to the low aspect ratio of the features (0.25), which requires minimal pressure for proper filling. Additionally, the relaxation of TPE during cooling may overshadow the influence of holding pressure. Similar observations can be made regarding the switchover point.

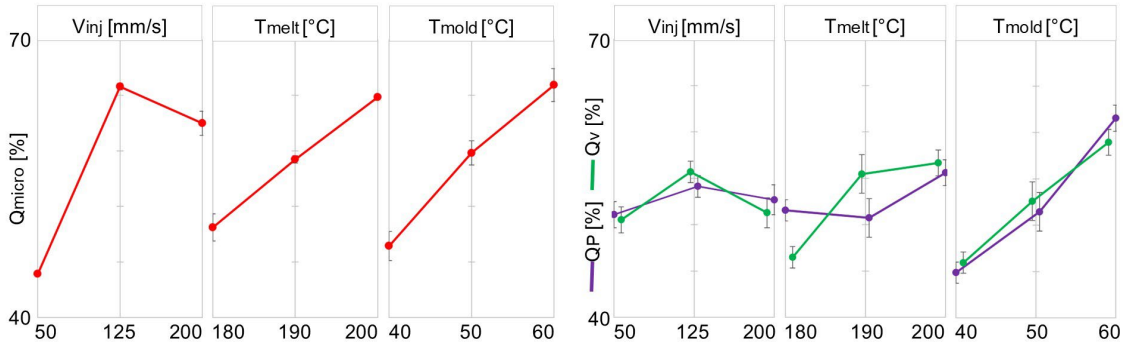


Figure 4: Optimization DOE: effect of process parameters on quality parameters.

Fig. 4 shows the main effects plots for the quality parameters from the Full Factorial DOE, including error bands for each point to highlight the influence of process parameters while accounting for variability. Consistent with previous observations, it is evident that an increase in mold temperature enhances feature replication at both the micro and nanoscale. A similar trend is observed with the increasing melt temperature. Higher mold temperatures improved replication by delaying material solidification during filling [9]. Similarly, melt temperature significantly affected feature replication, with higher melt temperatures resulting in longer cooling times and

Materials Research Proceedings 57 (2025) 303-310 https://doi.org/10.21741/9781644903735-35

reduced viscosity, both of which enhanced replication fidelity [10]. Particularly noteworthy is the effect of injection speed on replication quality. The injection speed exhibits a nonlinear influence on feature replication at both the micro- and nanoscales. Specifically, there is an optimal speed at which feature replication is maximized. Initially, replication quality improves with increasing injection speed due to reduced melt viscosity and a thinner skin layer. However, at higher speeds, excessive macromolecular alignment and elevated residual stresses in the component lead to increased material relaxation and a decline in feature replication accuracy [9].

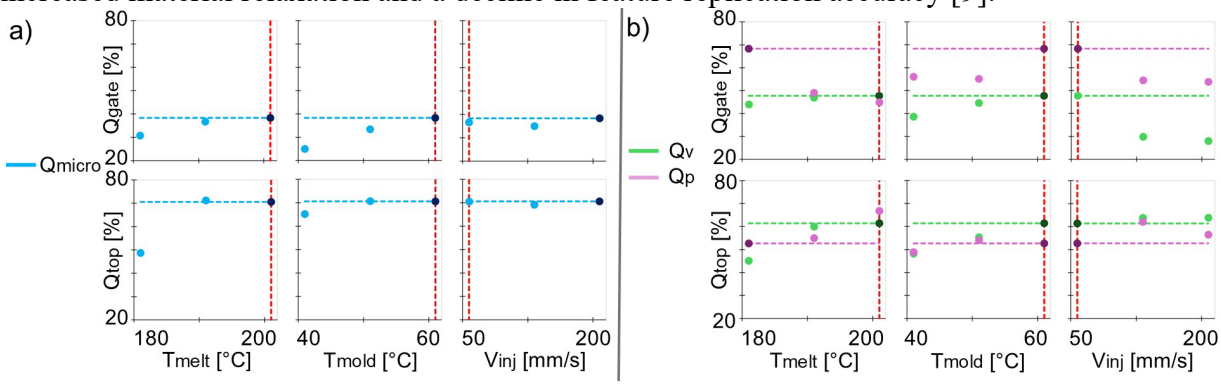


Figure 5: Optimization of replication uniformity: (a) microscale and (b) nanoscale.

During screening, structural color was seen in most molded samples, though its homogeneity was inconsistent (Fig. 2b). Therefore, in the Optimization DOE, two scans per sample were collected: at 2.5 mm and 7.5 mm from the gate. A multivariable optimization was performed to simultaneously maximize replication in areas near (Q_{gate}) and far from the gate (Q_{top}).

Figure 5 shows the optimization results (horizontal lines) and the selected process parameters (vertical lines). The optimization suggests high injection speeds for Q_{micro} but lower speeds for nanofeature replication (Q_v and Q_p). Since functionality depends on nanofeatures, LIPSS replication was prioritized, and samples were produced at 50 mm/s. Simultaneous replication near and far from the gate requires lower injection rates than previously observed (Fig. 4) due to high shear rates near the injection point, which promote greater material relaxation.

The optimization process suggests high melt temperature values for all parameters, except for Q_p. However, it was determined that this apparent inconsistency arises from the development of surface defects at lower temperatures in the region near the pin gate, due to material relaxation, which affects surface roughness [13]. Therefore, a high melt temperature of 200°C was selected. Additionally, it was noted that increasing the mold temperature consistently improves texture replication. Consequently, a high mold temperature of 90°C was chosen. Finally, unlike rigid thermoplastics, the μ-IM of TPEs exhibits maximized replication farther from the gate, emphasizing the critical role of the relaxation phenomenon in these materials.

Table 1: Results of the characterization of the inserts and samples used in the abrasion tests.

	Inserts				Samples		
P [μm]	250	40	UP	P [μm]	250	40	UP
d [μm]	2.0±0.1	2.1±0.1	/	Q_{micro}[%]	96.5±4.0	95.7±2.9	/
Spk [nm]	50.7±0.2	46.8±1.5	44.1±0.8	Q_p [%]	104.7±5.6	130.7±8.0	147.9±1.8
Svk [nm]	46.1±0.4	39.61±0.5	37.7±0.7	Q_v [%]	79.4±2.5	77.4±2.7	82.21±1.5

The selected parameters were used to produce samples for abrasion tests. The result of the characterization of samples is reported Tab. 1. The data reveal that variations in microgrid density had no significant impact on microscale replication. However, UP and 40 μm pitch samples

exhibited nanoscale quality parameters exceeding 100% (particularly for Q_p), likely due to excessive material adhesion to the mold, which can be attributed to the high mold temperature.

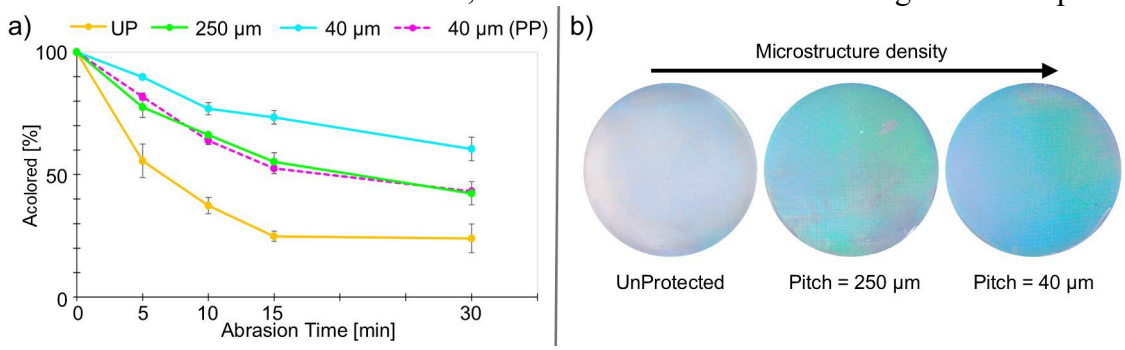


Figure 6: (a) Evolution of functionality over time under wear conditions; (b) examples of samples worn for 5 minutes with different reinforcement grid densities.

Functionality Durability. The samples produced via µ-IM underwent abrasion tests to evaluate the evolution of their functionality (structural color) over time under wear conditions. When subjected to periodic mechanical stresses, the LIPSS on the surface are progressively removed. Furthermore, surface defects may form, reducing the periodicity of the LIPSS. This degradation leads to areas where the structural color appears less intense or is entirely absent. As exposure time increases, the area without structural color gradually expands due to the progression of these phenomena.

In Fig. 6a, it is evident that the presence of the reinforcement grid slows down the loss of functionality. After 30 minutes of abrasion (circa 2200 wear cycles), the UP, 250 µm, and 40 µm inserts retain functional areas corresponding to 23%, 42%, and 60% of the total surface area, respectively. This improvement is due to several factors. Firstly, the reinforcement microstructure (even with limited density) reduces the contact pressure between the abrasive and the LIPSS, lowering stresses on the nanofeatures. Secondly, high-density reinforcement grids delay (as long as they remain intact) the contact between the LIPSS and the abrasive, postponing wear. Finally, microgrids help to limit the movement of detached surface fragments, preventing accelerated degradation of the nanostructures. Fig. 6b shows that the UP insert loses its functionality after just 5 minutes, with the remaining structural color having very low intensity. These results highlight the effectiveness of self-protective surfaces in improving the durability of nanometric textures.

Finally, Fig. 6a compares two microgrid samples with a 40 µm pitch made from SEBS and Polypropylene (PP). After 30 minutes of abrasion, the SEBS sample retained an 18% larger functional area than the PP sample. This significant improvement is due to the high elongation at break of the TPE used. During abrasion tests, the material experiences normal (pressure) and tangential (friction) stresses, stressing the texture. The elastomer features stretch and returns to their initial position once the load is removed. This behavior is not seen with PP [6, 8], where features tend to break or deform permanently under repeated stress due to the material's lower elongation at break and higher stiffness. The results confirm that self-recovering surfaces enhance the durability of nanofeatures by using temporary deformation as a protective mechanism.

Conclusions

This study explored the design, fabrication, and durability of nanostructured surfaces produced via µ-IM of TPE. A diffraction grating was fabricated using LIPSS, and its durability was enhanced by combining self-protective and self-recovering surface features. The protective microstructures were designed to balance the LIPSS spacing with the deformation behavior of the abrasive. Laser machining was employed to produce µ-IM inserts. Process optimization for µ-IM showed the key role of T_{mold}, T_{melt}, and V_{inj} in ensuring high-quality replication. Experimental results indicated that the microstructured design enhanced the durability of nanofeatures by 37%, whereas the elasticity of TPE contributed an additional 18% improvement when compared to rigid PP. The results

demonstrate the potential of self-protective and self-recovering surfaces to improve the durability of nanostructures, particularly for anti-counterfeiting and decorative applications, thereby bringing these nanostructures closer to practical, real-world implementation.

References

[1] Florian C, Kirner S V, Krüger J, et al. Surface functionalization by laser-induced periodic surface structures. J Laser Appl; 32. https://doi.org/10.2351/7.0000103

[2] Chen F, Wang Y, Tian Y, et al. Robust and durable liquid-repellent surfaces. Chem Soc Rev 2022; 51: 8476–8583. https://doi.org/10.1039/D0CS01033B

[3] Wang D, Sun Q, Hokkanen MJ, et al. Design of robust superhydrophobic surfaces. Nature 2020; 582: 55–59. https://doi.org/10.1038/s41586-020-2331-8

[4] Luo W, Xu J, Li G, et al. Fabrication of robust, anti-reflective, transparent superhydrophobic coatings with a micropatterned multilayer structure. Langmuir 2022; 38: 7129–7136. https://doi.org/10.1021/acs.langmuir.2c00264

[5] Xu K, Hu J, Wang M, et al. Armored nanocones engraved by selective laser doping enhanced plasma etching for robust supertransmissivity. ACS Appl Mater Interfaces 2022; 14: 47237–47245. https://doi.org/10.1021/acsami.2c13033

[6] C. Su, Y. Xu, F. Gong, F. Wang, and C. Li, “The abrasion resistance of a superhydrophobic surface comprised of polyurethane elastomer,” Soft Matter, vol. 6, no. 24, pp. 6068–6071, 2010. https://doi.org/10.1039/c0sm00804d

[7] Yamauchi Y, Tenjimbayashi M, Samitsu S, et al. Durable and flexible superhydrophobic materials: abrasion/scratching/slicing/droplet impacting/bending/twisting-tolerant composite with porcupinefish-like structure. ACS Appl Mater Interfaces 2019; 11: 32381–32389. https://doi.org/10.1021/acsami.9b09524

[8] Hoshian S, Jokinen V, Franssila S. Robust hybrid elastomer/metal-oxide superhydrophobic surfaces. Soft Matter 2016; 12: 6526–6535. https://doi.org/10.1039/c6sm01095d

[9] Baruffi F, Calaon M, Tosello G. Effects of micro-injection moulding process parameters on accuracy and precision of thermoplastic elastomer micro rings. Precis Eng 2018; 51: 353–361. https://doi.org/10.1016/j.precisioneng.2017.09.006

[10] Vega MDJ, Mead J, Barry C. Injection molding microstructured substrates from rubber-containing polymers. In: AIP Conference Proceedings. AIP Publishing, 2016. https://doi.org/10.1063/1.4965463

[11] Birkar S, Mendible G, Park J, et al. Effect of feature spacing when injection molding parts with microstructured surfaces. Polym Eng Sci 2016; 56: 1330–1338. https://doi.org/10.5254/rct.14.86924

[12] Birkar S, Mead J, Barry C. Injection molding of thermoplastic elastomers for microstructured substrates. Rubber Chemistry and Technology 2014; 87: 629–646. https://doi.org/10.5254/rct.14.86924

[13] Stormonth-Darling JM, Saeed A, Reynolds PM, et al. Injection Molding Micro-and Nanostructures in Thermoplastic Elastomers. Macromol Mater Eng 2016; 301: 964–971. https://doi.org/10.1002/mame.201600011

Materials Research Proceedings 57 (2025) 311-318 https://doi.org/10.21741/9781644903735-36

Physical foaming of 25% post-industrial recycled TPU using the supercritical foaming technology

Francesco MACIARIELLO[1,a *], Giovanni LUCCHETTA[2,b] and Marco SORGATO[3,c]

[1]Department of Industrial Engineering, University of Padova, via Venezia 1, 35131 Padova, Italy

[a]francesco.maciariello@phd.unipd.it, [b]giovanni.lucchetta@unipd.it, [c]marco.sorgato@unipd.it

Keywords: Sustainability, Thermoplastics, Foaming

Abstract. The production of recyclable TPU foams has seen rising interest due to the requirement for a green alternative to chemical foams. While extensive research has been conducted on batch foaming and microcellular injection molding of TPU, the processing of recycled TPU (rTPU) remains largely unexplored. This paper investigated the foaming process of 25% post-industrial recycled TPU using the microcellular method and nitrogen as the physical blowing agent. Rectangular specimens with a thickness of 14 mm and a density of 0.22 g/cm^3 were molded. Gas counterpressure was utilized to favor the uniform foaming of the component. Average cell size and cell number analyses were performed, demonstrating that in the core region of the specimen, the recycled TPU foams exhibited similar properties as the foams manufactured using virgin material. In the skin region, rTPU samples showed an improved morphology when compared to the non-recycled foams. The processing temperature of rTPU proved to have a great impact on the properties of the material, with lower temperatures being favorable to avoid excessive degradation.

Introduction

It is estimated that 22 billion pairs of shoes are landfilled each year [1], pushing the footwear industry to search for more sustainable alternatives to traditional manufacturing technologies [2]. Foamed TPU components have recently entered the footwear market as a possible recyclable alternative to the commonly used polyurethane (PU) and ethylene-vinyl acetate (EVA) foams.

Microcellular injection molding using supercritical fluids (SCFs) is often the preferred manufacturing method for the production of highly expanded TPU foams. This technology is free from impurities and hazardous chemical residues that are associated with the use of traditional chemical blowing agents [3], producing a finer and more uniform cell structure, and offering a higher productivity if compared to the batch foaming process [4]. Other technologies such as gas counterpressure (GCP) [5] and precision mold opening [6, 7], are often coupled to the microcellular foaming process to improve cell morphology and the mechanical properties of the product. Additives, such as talc powder, have been successfully employed to favor heterogeneous nucleation in N_2 foamed parts, increasing cell number density and reducing the average bubble size [8].

Given the current push in manufacturing recyclable TPU foams, it is expected that future trends will focus on the actual recycling of these materials. Although the manufacturing of TPU foams has been extensively studied, no research has been conducted on their recycling and reprocessing. In addition to the technical difficulties associated with the physical foaming technology, mechanical recycling of TPU poses other complications due to the material's propensity to degradation at processing temperatures.

TPUs are block copolymers containing hard segments (HS), and soft segments (SS) that are incompatible at room temperature [9]. The soft segments contribute to the elastic properties of the polymer, while the hard segments can crystalize and cross-link, increasing the stiffness and strength of the material [10, 11]. Since HSs are the first to degrade during the extrusion process [12], and hard segment content was shown to affect the foam morphology in expanded TPU [13],

Content from this work may be used under the terms of the Creative Commons Attribution 3.0 license. Any further distribution of this work must maintain attribution to the author(s) and the title of the work, journal citation and DOI. Published under license by Materials Research Forum LLC.

Materials Research Proceedings 57 (2025) 311-318 https://doi.org/10.21741/9781644903735-36

it is expected that the recycling process will have a significant effect on the cell structure of rTPU foams.

This study aims to investigate the processability of 25% post-industrial recycled TPU for the production of lightweight flexible foams. The cellular structure of expanded samples obtained through microcellular injection molding of both virgin and recycled TPU will be analyzed. Close attention will be placed on the degradation behavior of the polymer as a consequence of the various processing steps.

Experimental

Injection molding equipment. All samples were manufactured on a custom non-commercial microcellular injection molding machine. The plasticizing unit was equipped with a high-pressure gas dosing system used to inject high-pressure nitrogen into the molten polymer. Once injected, the supercritical fluid was completely dissolved into the resin and formed with it a uniform mixture. A schematic representation of the microcellular foaming process is shown in Fig. 1, the most significant process parameters adopted in this study are listed in Table 1

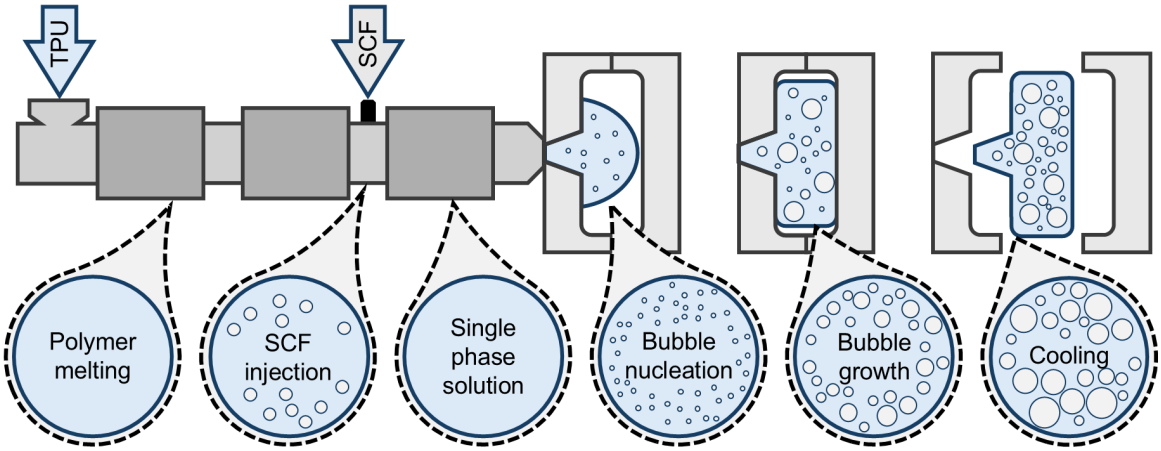


Figure 1: Microcellular injection molding foaming process.

The mold was equipped with a gas counterpressure system that allowed the pressurization of the cavity from the end opposite the injection location. GCP was performed using high-pressure dry air at 10 bar. The mold temperature was regulated via an external water-cooling system.

The molded samples consisted of square tablets with an overall size of 265 mm × 100 mm × 14 mm, as represented in Fig. 2a. The polymer was injected through a conical sprue having a diameter of 13.4 mm at its largest section. A region with reduced thickness was located at the far end of the cavity to serve as a vent (see Fig. 2a), letting gas through but stopping the flow of the polymer.

Table 1: Injection molding parameters common to all samples.

Parameter	Value
Foam density [g/cm^3]	0.22
Shot size [cm^3]	70
Nitrogen quantity [g]	0.5
Gas counterpressure [bar]	10
Mold temperature [°C]	30

Materials Research Proceedings 57 (2025) 311-318 https://doi.org/10.21741/9781644903735-36

Molded materials. The polymer used in this study was 1185A10 U SCF TPU provided by BASF, Germany. The material was dried for three hours at 90°C before the injection molding tests to remove any residual moisture. During production start-up, many samples foamed from the virgin TPU were collected to be recycled. This post-industrial waste was milled into small pieces with dimensions less than 10 mm across. A dry mix was prepared containing 25% recycled material and 75% virgin 1185A TPU, as this was the maximum amount of rTPU that could be included without incurring in severe process instability. A higher rTPU content led to issues in the gas dosing phase and promoted polymer-gas separation in the injection unit. Prior to the injection molding experiments, the mix was dried at 90°C for three hours. The rTPU blend was processed at two different temperatures to investigate the effect of this parameter on cell morphology. To ensure proper mixing of the polymer–gas solution, the melt temperature used in the microcellular injection molding process was set higher than the conventional processing temperature for TPU. After the first processing step, the TPU polymer chains are expected to undergo degradation and chain scission, resulting in reduced molecular weight and lower viscosity. Therefore, a second, lower melt temperature was used when processing the rTPU blend to minimize further degradation while still allowing effective polymer-gas mixing due to the decreased viscosity. The processing temperatures used in the experimental study are reported in Table 2. The virgin TPU foamed samples are labeled *V*, while the ones manufactured in recycled TPU are labeled *R1* and *R2* for the low and high temperature groups, respectively.

Table 2: Melt temperature in the three experimental groups: foamed virgin material (V); recycled material group 1 (R1); recycled material group 2 (R2).

Sample name	*V*	*R1*	*R2*
Melt temperature [°C]	225	215	225

Cell morphology analysis. Three foamed components were selected from each group (*V*, *R1*, *R2*) to be characterized. From each of these specimens, four different samples were cut with a sharp razor blade, as shown in Fig. 2a. All samples were sputter-coated with a thin layer of gold-palladium alloy and scanned using a Fei Quanta 450 scanning electron microscope (SEM). Of each scanned sample, two distinct zones with an area of 5.96 mm × 5.02 mm were studied, one near the outer skin of the part and one at the core, as shown in Fig. 2b. The two different zones were selected to study the different morphology of the cell structure in the skin and core layers.

The average diameter of the bubbles and their number density were evaluated via image analysis in MATLAB R2024a using an adaptive thresholding method.

Materials Research Proceedings 57 (2025) 311-318 https://doi.org/10.21741/9781644903735-36

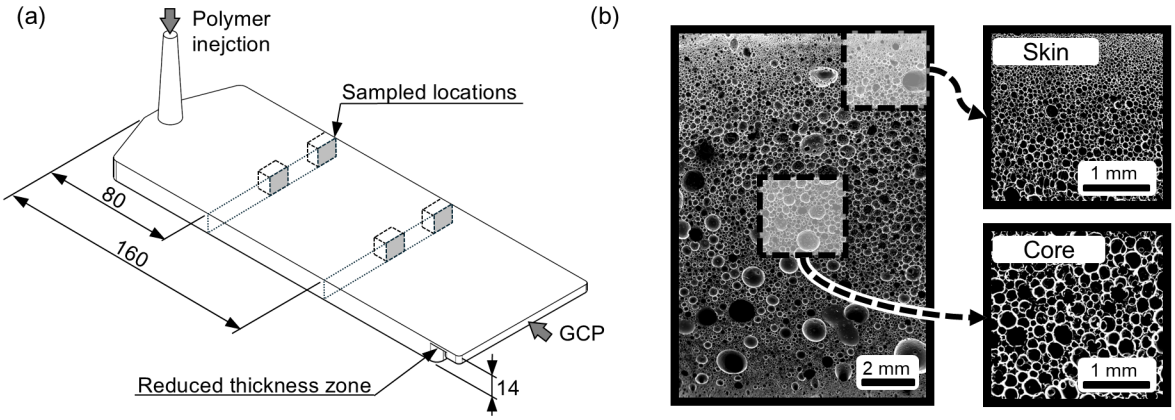


Figure 2: Design of the mold cavity and location of the samples (a); location of the skin and core regions utilized in the image analysis (b).

Thermal analysis. Differential scanning calorimetry (DSC) was employed to assess the degree of degradation endured by the polymer in the foaming process. Samples from the three foamed groups were tested on a TA Instruments Q200 DSC analysis machine, along with a sample of the unprocessed virgin material. All samples weighed 10-15 mg. The DSC procedure comprised a first heating cycle to 220°C followed by cooling to -50°C and a second heating cycle to 260°C. Between each cycle, an isothermal phase lasting 5 minutes was employed to equilibrate the temperature in the samples. All cycles were performed with a heating/cooling rate of 10°C/min. Variations in crystallization temperature and enthalpy were used to evaluate the degradation of the material and the variation in HSs crystallinity [13].

Results and discussion

Fig. 3 shows the foam morphology obtained by processing the virgin and recycled TPU. While a similar cell structure was observed in the core region of all the samples, a much finer foam was obtained in the skin region of the *R1* and *R2* samples compared to the *V* samples. The image analysis results shown in Fig. 4 (a-b) confirm this observation.

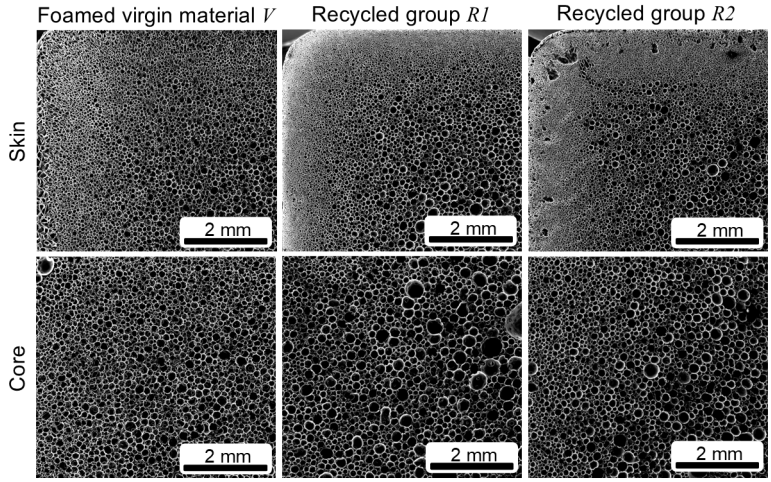


Figure 3: SEM micrographs of the samples in the skin and core regions.

The difference between the virgin and recycled expanded TPU was negligible in the core region, with an average cell diameter of 190 μm and an average number of bubbles of 1365 across all specimens. In the skin region, the cell number increased from 4780 in the *V* specimens to 7300 in the *R1* specimens, consisting in a 52.7% improvement. The average cell diameter was reduced

Materials Research Proceedings 57 (2025) 311-318 https://doi.org/10.21741/9781644903735-36

from 89.8 µm in the *V* specimens to 69.4 µm in the *R1* specimens, a reduction of 22.8 %. No statistically significant difference was observed between the two recycled material groups, *R1* and *R2*.

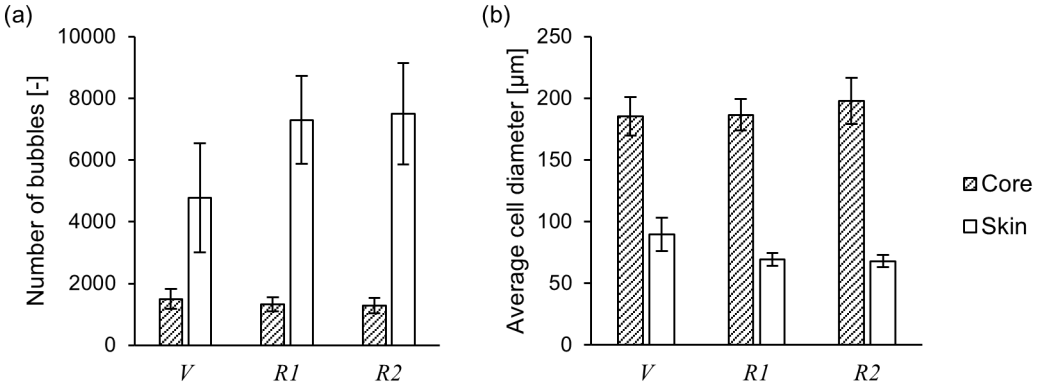


Figure 4: Number of bubbles (a) and average cell diameter (b) in the three tested groups: virgin foamed material (V); rTPU processed at low temperature (R1); rTPU processed at high temperature (R2).

The different cell structure of the rTPU blend is attributed to the variation in the HSs' length distribution in the recycled material fraction. As a result of high shear and thermal stress during the SCF foaming process, the hard segments in the TPU are degraded and shortened in length. The higher mobility of the shorter hard segments in rTPU facilitates the reorientation of the molecules in crystalline structures during the cooling process [14]. The formation of HS crystals increases the melt strength of the polymer and creates several sites for heterogeneous nucleation to occur. In the skin region, the rapid cooling of the polymer caused a higher number of HS crystals to form in the rTPU blend, producing a fine cell structure that was rapidly stabilized by the increased melt strength of the resin. In the core region, the prolonged stay at high temperatures, favored by the insulation properties of the foamed skin region, caused the coalescence and growth of bubbles that assumed a similar morphology in both the virgin and recycled foamed blends.

TPU degradation. The DSC analysis confirmed that the hard segments underwent degradation during the first foaming process. Fig. 6 (a-d) displays the results of the DSC analysis of the virgin unprocessed material, and all the foamed samples. The unprocessed material showed a narrow crystallization peak starting at 101°C, with a crystallization enthalpy of 12.23 J/g. After the first processing step (Fig. 6b), the crystallization peak was widened and HS crystals started to form at a higher temperature of 154°C, with a crystallization enthalpy of 15.45 J/g. The higher crystallization enthalpy in the foamed virgin material suggests the formation of a more crystalline structure thanks to the shortened length and higher mobility of the HSs. The increased crystallinity and higher crystallization temperature resulting from the first SCF foaming step are the reason for the finer cell structure in the skin layer in the rTPU samples.

The reprocessing of 25% recycled TPU induced further degradation in the hard segments. Since the expanded material in the mix needed to be compressed by the plasticizing screw before it could be melted, the addition of rTPU to the polymer blend led to an increase in residency time. After reprocessing, the average length of the HSs was reduced as witnessed by the higher crystallization onset temperature of the recycled samples *R1* and *R2*. The crystallization of the hard segments started at 160°C in the *R1* foams and 157°C in the *R2* foams. While the crystallization onset temperature is similar between the three foamed materials, the size distribution of the HSs in rTPU samples was clearly affected by the processing temperature. The samples processed at lower temperature showed a narrower crystallization peak, indicating a less broad HSs size distribution.

Materials Research Proceedings 57 (2025) 311-318 https://doi.org/10.21741/9781644903735-36

This result suggests a higher degree of degradation in the HSs due to the increased shear stress at lower temperatures. The *R1* group foams also showed a lower crystallization enthalpy of 10.55 J/g, indicating a lower crystallinity compared to the *V* and *R2* groups. The crystallization enthalpy of the *R2* group foams was 14.33 J/g, a similar value compared to the foams in the *V* group.

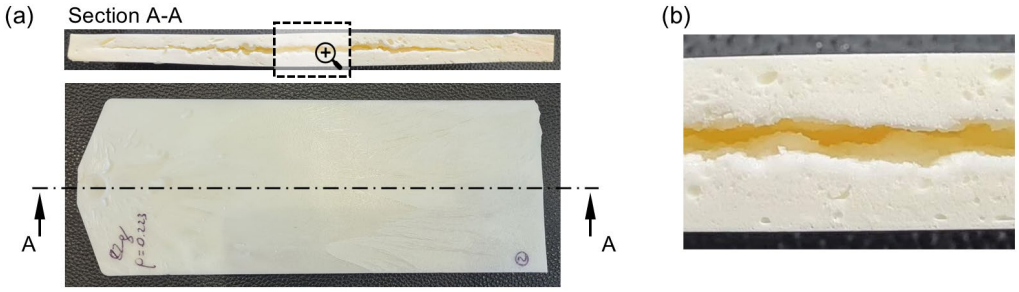


Figure 5: Section view of the R2 group specimen showing the crack defect (a); closeup view of the defect (b).

Although these results suggest a higher degree of degradation in the HSs of rTPU foams processed at lower temperature (group *R1*), the samples foamed at a higher temperature were characterized by the presence of a large crack running across the core region of the entire sample (see Fig. 5a-b). This defect is an indication of poor mechanical performance of the foamed material and is probably due to the increased degradation of the soft segments at higher temperatures. Although a finer cell structure has been associated with better mechanical performance [6], it is expected that the degradation induced by the recycling step will hinder the ability of the recycled material to sustain high loads and deformations, especially in the rTPU foams processed at high temperature.

Some of the complications due to the increased residency time of the rTPU blend could be mitigated by preprocessing the recycled material to obtain pellets similar in size and density to the virgin material prior to the dry mixing step. This would eliminate the need for the plasticizing screw to compress the foamed material prior to melting and would drastically reduce the residency time.

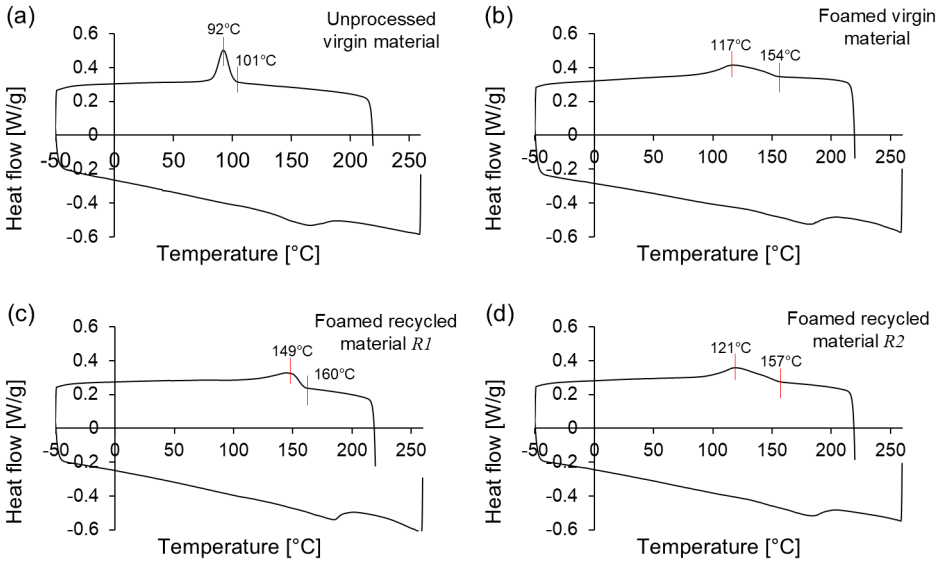


Figure 5: DSC analysis results for the virgin unprocessed material (a); foamed virgin TPU, group V (b); foamed rTPU at low temperature, group R1 (c); foamed rTPU at high temperature, group R2 (d).

Conclusions

This study investigates the effects of post-industrial recycling on the cell morphology and thermal properties of microcellular injection molded components. The cell morphology and crystallization behavior of 25% recycled TPU foams was examined and compared to the virgin foamed samples. The key findings can be summarized as follows:

- In the core region of the specimens, the foam structure was similar in both virgin and recycled foams.
- After the first processing cycle, the thermal degradation of the hard segments increased the crystallization onset temperature and crystallinity of the material, leading to a finer cell structure in the skin layer of the rTPU samples.
- The recycling process induced further degradation in the polymer, with lower processing temperatures being most detrimental to the integrity of the hard segments.
- A higher processing temperature reduced the shear stress in the material, reducing the degradation of the HSs, although the foamed parts showed worse structural integrity probably due to the increased degradation of the soft segments at higher temperatures.

These findings suggest that TPU foams obtained via physical foaming methods can be successfully recycled and reprocessed to obtain a similar cell morphology as the foams manufactured with virgin material. The degradation of the hard segments may have an adverse effect on the mechanical properties of the rTPU foams. Consequently, mechanical evaluations such as cyclic compression, compression set, and abrasion resistance tests should be conducted to assess the material's suitability for use in commercial footwear applications.

References

[1] D. I. Alves, Ó. Carvalho, N. A. Fernandes, L. T. Cosentino, A. C. Paula Junior, R. Fangueiro, D. P. Ferreira, Upcycling of industrial footwear waste into nonwoven fibrous structures with thermal and acoustic insulation properties, J. Environ. Manag. 363 (2024), 121363. https://doi.org/10.1016/j.jenvman.2024.121363

[2] M. L. Van Rensburg, S. L. Nkomo, N. M. Mkhize, Life cycle and End-of-Life management options in the footwear industry: A review, Waste Manag Res 38 (2020) 599–613. https://doi.org/10.1177/0734242X20908938

[3] W. Zhai, J. Jiang, C. B. Park, A review on physical foaming of thermoplastic and vulcanized elastomers, Polym. Rev. 62 (2022) 95–141. https://doi.org/10.1080/15583724.2021.1897996

[4] E. Di Maio, E. Kiran, Foaming of polymers with supercritical fluids and perspectives on the current knowledge gaps and challenges, J. Supercrit. Fluids 134 (2018) 157–166. https://doi.org/10.1016/j.supflu.2017.11.013

[5] S.-C. Chen, K.-H. Lee, C.-W. Chang, T.-J. Hsu, C.-T. Feng, Using Gas Counter Pressure and Combined Technologies for Microcellular Injection Molding of Thermoplastic Polyurethane to Achieve High Foaming Qualities and Weight Reduction, Polymers 14 (2022) 2017. https://doi.org/10.3390/polym14102017

[6] G. Wang, G. Zhao, G. Dong, Y. Mu, C. B. Park, G. Wang, Lightweight, super-elastic, and thermal-sound insulation bio-based PEBA foams fabricated by high-pressure foam injection molding with mold-opening, Eur. Polym. J. 103 (2018) 68–79. https://doi.org/10.1016/j.eurpolymj.2018.04.002

[7] H.-P. Heim, M. Tromm, General aspects of foam injection molding using local precision mold opening technology, Polymer 56 (2015) 111–118. https://doi.org/10.1016/j.polymer.2014.10.070

[8] J. W. S. Lee, C. B. Park, Use of Nitrogen as a Blowing Agent for the Production of Fine-Celled High-Density Polyethylene Foams, Macromol. Mater. Eng. 291 (2006) 1233–1244. https://doi.org/10.1002/mame.200600203

[9] X. Sun, H. Kharbas, L. Turng, Fabrication of highly expanded thermoplastic polyurethane foams using microcellular injection molding and gas-laden pellets, Polym. Eng. Sci. 55 (2015) 2643–2652. https://doi.org/10.1002/pen.24157

[10] A. Voda, K. Beck, T. Schauber, M. Adler, T. Dabisch, M. Bescher, M. Viol, D. E. Demco, B. Blümich, Investigation of soft segments of thermoplastic polyurethane by NMR, differential scanning calorimetry and rebound resilience, Polym. Test. 25 (2006) 203–213. https://doi.org/10.1016/j.polymertesting.2005.10.007

[11] J. Jiang, M. Zhou, Y. Li, B. Chen, F. Tian, W. Zhai, Cell structure and hardness evolutions of TPU foamed sheets with high hardness via a temperature rising foaming process, J. Supercrit. Fluids 188 (2022) 105654. https://doi.org/10.1016/j.supflu.2022.105654

[12] B. Wölfel, A. Seefried, V. Allen, J. Kaschta, C. Holmes, D. Schubert, Recycling and Reprocessing of Thermoplastic Polyurethane Materials towards Nonwoven Processing, Polymers 12 (2020) 1917. https://doi.org/10.3390/polym12091917

[13] M. Nofar, E. Büşra Küçük, B. Batı, Effect of hard segment content on the microcellular foaming behavior of TPU using supercritical CO2, J. Supercrit. Fluids 153 (2019) 104590. https://doi.org/10.1016/j.supflu.2019.104590

[14] S.-K. Yeh, R. Rangappa, T.-H. Hsu, S. Utomo, Effect of extrusion on the foaming behavior of thermoplastic polyurethane with different hard segments, J. Polym. Res. 28 (2021) 244. https://doi.org/10.1007/s10965-021-02604-z

Materials Research Proceedings 57 (2025) 319-326 https://doi.org/10.21741/9781644903735-37

Numerical modeling of high-speed laser cutting of copper current collectors

Samuele Piandoro[1,a *], Caterina Angeloni[1,b], Alessandro Fortunato[1,c], Erica Liverani[1,d], Alessandro Ascari[1,e]

[1]Department of Industrial Engineering (DIN), Alma Mater Studiorum University of Bologna, Viale Risorgimento 2, 40136 Bologna, Italy

[a]samuele.piandoro2@unibo.it, [b]caterina.angeloni2@unibo.it, [c]alessandro.fortunato@unibo.it, [d]erica.liverani2@unibo.it, [e]a.ascari@unibo.it

Keywords: Laser Cutting, Copper, Multi-Physics Simulation, Process Optimization

Abstract. The increasing demand for lithium-ion batteries requires precise, efficient cutting of copper current collectors. Laser cutting offers advantages over mechanical methods in terms of speed, precision, and flexibility. This study uses validated multi-physics simulations to model the interaction between a single-mode continuous laser and 8 μm copper foils, analyzing how power, speed (up to 25 m/s), and foil thickness affect cut quality. Four outcomes were identified: no cut, dross, spatter, and clean cuts. Process maps for 8 μm and 16 μm foils were derived, offering insights for optimizing battery manufacturing.

Introduction

To meet the increasing demands for productivity and quality in lithium-ion battery production and assembly, optimizing the manufacturing process is essential. Among the various steps, trimming the current collectors (thin conductive metal foils) is one of the most delicate. Laser beam cutting is a state-of-the-art technique due to its ability to provide higher processing speed and quality compared to traditional methods [1], [2]. However, as a thermal process, it is inherently associated with defects in the edge profile, such as spatter, dross, and uneven kerf, which can negatively impact battery performance.

Dross formation is particularly undesirable, as detached particles can mix with the electrode slurry, creating preferential pathways for metallic deposition. Over multiple charge/discharge cycles, this may lead to dendrite growth, which can pierce the separator and cause short circuits, ultimately resulting in premature battery failure or even explosions.[3], [4].

Spatter occurs when the local momentum of the molten material exceeds a threshold, represented by the dimensionless Weber number ($We >> 2$) [5], [6]. The primary force driving this process is the recoil pressure caused by the almost instant vaporization of the material.

Although ultra-short, pulsed beams (e.g., picosecond and femtosecond lasers) have been extensively studied with good results [7], [8], their high cost and low productivity make them unattractive from an industrial perspective. In a previous study [9], the authors compared the cutting quality between a continuous source and a commercial nanosecond pulsed source, showing that the single-mode continuous source yields higher quality.

Numerous models [10], [11], [12] have been developed to simulate the laser cutting process of thick sheets; however, while they are valuable for understanding certain melt flow dynamics, they fall short in addressing the unique challenges of processing thin foils such as current collectors. Only a few have been applied to current collectors and micrometer-thick electrodes. In this context, Lee et al. [13] is, to the author's knowledge, the only existing application of a 3D consistent numerical model [14] for the laser cutting of current collectors and electrodes. However, his study was limited to relatively low power and speed, reaching a maximum of 300 W and 5 m/s.

Content from this work may be used under the terms of the Creative Commons Attribution 3.0 license. Any further distribution of this work must maintain attribution to the author(s) and the title of the work, journal citation and DOI. Published under license by Materials Research Forum LLC.

Materials Research Proceedings 57 (2025) 319-326 https://doi.org/10.21741/9781644903735-37

In this research, we developed a CFD framework for simulations of laser-material interactions using the well-known volume of fluid (VOF) method to predict defects occurring during the laser cutting of pure copper current collectors. The model was tuned and validated against experimental results and subsequently used to analyze and compare outcomes at different process parameters and foil thicknesses. As a result, a power-speed graph was generated for 8 µm and 16 µm foil thicknesses.

Materials and methods

Experimental procedure

The laser system employed was a continuous wave nLight 1200 W single-mode, equipped with a 14 µm optical fiber and scanning head with a 340 mm f-theta lens (the actual setup is shown in Fig. 1A). The spot size was measured as 65 µm with an $M^2 \leq 1.1$. Current collectors of pure copper 8 µm thick were cut from rolls and kept in a clamping system to maintain the foils stretched out in the focal plane. Linear and parallel cuts 20 mm long were performed with 5 mm distances between adjacent cuts (Fig. 1B). The parameters measured for defect analysis and quality assessment are shown in Fig.1C, four parameters were evaluated: i) dross thickness (front m_1 and back m_2), ii) remelted area, iii) spatter max distance, and iv) kerf width.

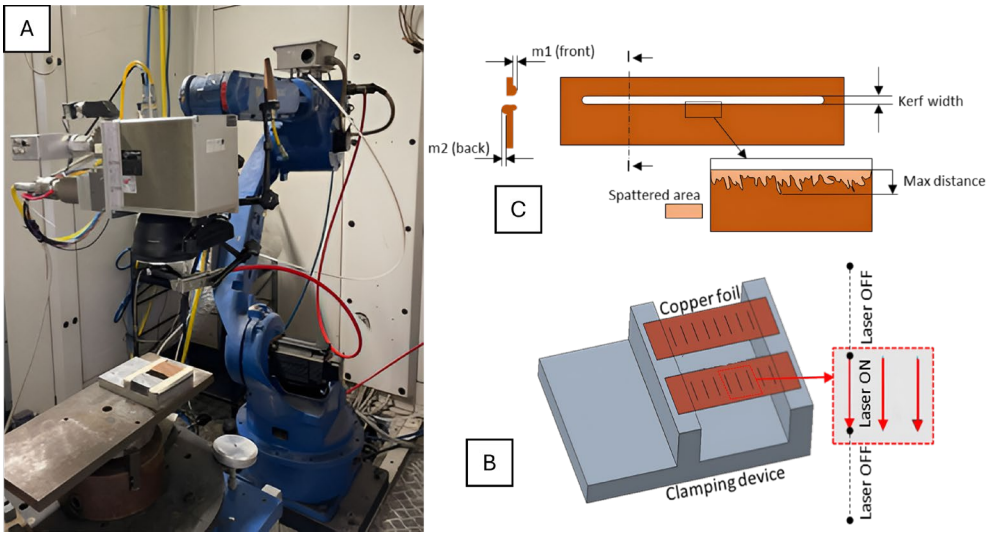


Figure 1: Experimental setup (A), cutting geometry (B), and parameters evaluated (C).

The operative range investigated was selected based on the previous study [1] and constrained by the limitations of the experimental setup. The power and velocity ranges were set to [200–1000] W and [2–25] m/s, respectively. Five representative cases were then selected for the calibration (three cases) and validation (two cases) of the numerical model. Each case exhibits distinct outcomes in terms of cut quality and defect formation: case A: bubble-shaped recast, case B: good cut, case C: spatter, case D: wide kerf with burn, and case E: no cut. These cases correspond to the extreme values of the operative window — i.e., minimum and maximum values of power and velocity — except for the 'no cut' condition, where the first velocity value leading to a failed cut was identified and used. This selection was intended to ensure the model's robustness across a wide range of operative conditions. The corresponding process parameters and experimental outcomes for each case are summarized in Table 1, where the irradiance (I) and fluence (F) were calculated as follows:

Materials Research Proceedings 57 (2025) 319-326 https://doi.org/10.21741/9781644903735-37

$$I = \frac{P}{A_{spot}}\left[\frac{W}{cm^2}\right] \qquad F = I \cdot \tau = I \cdot \frac{d_{spot}}{v}\left[\frac{J}{cm^2}\right] \tag{1}$$

Where τ is the interaction time calculated from the spot diameter and the laser velocity.

Table 1: Process parameters employed for laser cutting tests.

	P [W]	Laser speed [m/s]	I [MW/cm^2]	F [J/cm^2]	Model	Defect
A	200	2	6.0	195.9	Tuning	Bubble Recast
B	600	10	18.1	117.5	Tuning	Good Cut
C	1000	25	30.1	78.4	Tuning	Spatter
D	1000	2	30.1	979.4	Validation	Burn
E	200	5	6.0	78.4	Validation	No Cut

Optical microscopy (OM, Nikon Optiphot-100) and SEM-FEG microscopy (SEM, Tescan Mira3 with a Schottky emitter) were used to evaluate the cutting quality. OM was initially used to provide a preliminary assessment of cut quality. Hence, high-quality images for spatter quantification and kerf measurements were carried out with SEM on the same surfaces.

To quantify the remelted area, the experimental images were processed with Trainable Weka Segmentation, a Fiji plugin [2]. The Fast Random Forest machine learning algorithm was applied as the classifier to be trained on one SEM image given as input. Three classes were therefore selected for input labelling: kerf, surface and remelted area. Once the model was confirmed to make accurate predictions, the area with an 80-100% probability of belonging to the spatter class was measured.

The spatter maximum distance was defined as the greatest distance measured from the cut edge to the furthest melted metal finger lying on the copper foil. Data was collected through SEM image analysis, with three SEM images acquired from the front and three from the back of the cut. For each image analyzed, three measurements were taken, and the maximum value, along with the standard deviation of these measurements, was calculated.

The same images were used for average kerf width comparisons, both on the top and back of the surface, and the mean value was calculated considering five measurements for each picture.

After non-destructive cut analysis, the current collectors were sectioned and embedded in resins for dross height measurements (m_1 and m_2 in Fig. 1C). By polishing the samples, it was possible to evaluate the mean dross thickness in the middle section of the cut (20 measurements were taken for each cut condition).

Numerical Model

The laser cutting process was simulated using the commercial CFD software FLOW-3D (v12.0 Update 3) with the laser module FLOW-3D WELD (release 7 Update 3). FLOW-3D employs the finite volume method and implements an advanced Volume of Fluid (VoF) algorithm to track phase boundaries. This model defines a scalar function F_i representing the fraction of phase i within a computational cell. The sum of all phase fractions in each cell must equal one; therefore, by considering only the metal and the surrounding air as distinct phases, we obtain:

$$\begin{cases} F = 0 & metal \\ 0 < F < 1 & interface \\ F = 1 & air \end{cases} \tag{2}$$

Materials Research Proceedings 57 (2025) 319-326 https://doi.org/10.21741/9781644903735-37

The conservation of F is governed by the following equation:

$$\frac{\partial F}{\partial t} + u\frac{\partial F}{\partial x} + v\frac{\partial F}{\partial y} + w\frac{\partial F}{\partial z} = 0 \quad (3)$$

Where u, v, and w are the velocity components of the flow field.

The simulation incorporates the main physical phenomena governing laser cutting, including viscous laminar flow, energy conservation with phase change, volumetric thermal expansion, temperature-dependent surface tension with Marangoni forces, multiple laser reflections with temperature-dependent absorption, and evaporation-driven recoil pressure.

Recoil pressure is the key driver of material ejection in laser cutting, it arises from the rapid vaporization of the molten material, generating a force that pushes the liquid metal away from the laser focus. This force modeled empirically based on the Clausius-Clapeyron relation and follows the equation:

$$P_{recoil} = C_1 exp C_2 \left(1 - \frac{T_v}{T}\right) \quad (4)$$

C_1 and C_2 are parameters that must be tuned through experimental results, while T_v refers to the saturated curve provided by the Clausius-Clapeyron equation. The influence of the plasma plume, which affects laser absorption and energy distribution, is indirectly incorporated through a temperature-dependent absorption coefficient, following approaches previously validated in the literature [11]. The laser beam is modeled as multiple rays propagating along the z-axis, interacting with the material based on the temperature-dependent absorption coefficient. Absorbed energy induces heating, melting, and evaporation, whereas reflected rays, guided by the local surface normal, redistribute energy through multiple reflections, shaping the keyhole and influencing cutting quality. Material properties for pure copper, including thermal conductivity, density, specific heat, surface tension, and viscosity, were sourced from the literature [12]. These properties were integrated as temperature-dependent functions to ensure an accurate representation of material behavior under laser irradiation. To keep the text concise, only the main models are mentioned without detailing all equations and numerical implementation. However, the implementation follows similar studies where FLOW-3D was utilized for laser welding simulations; readers can refer to [11] and [13].

By considering the process symmetrical to the laser direction (x-axis), only half of the domain can be discretized, which reduces the total number of cells and computational cost. A staggered Cartesian grid composed of two nested regions was created (Figure 2): a main region measuring 0.1 mm x 0.15 mm x 0.1 mm with a 1.5 μm cell size, and a thermal diffusion region that is 0.1 mm larger in the x and y dimensions with a cell size five times larger. The main region captures the laser-current interaction and, therefore, requires a finer mesh, while the thermal diffusion region only accounts for heat transfer. A constant atmospheric pressure (101325 Pa) was applied to both the top and bottom surfaces and fixed walls on the remaining sides, but the symmetric plane.

Materials Research Proceedings 57 (2025) 319-326 https://doi.org/10.21741/9781644903735-37

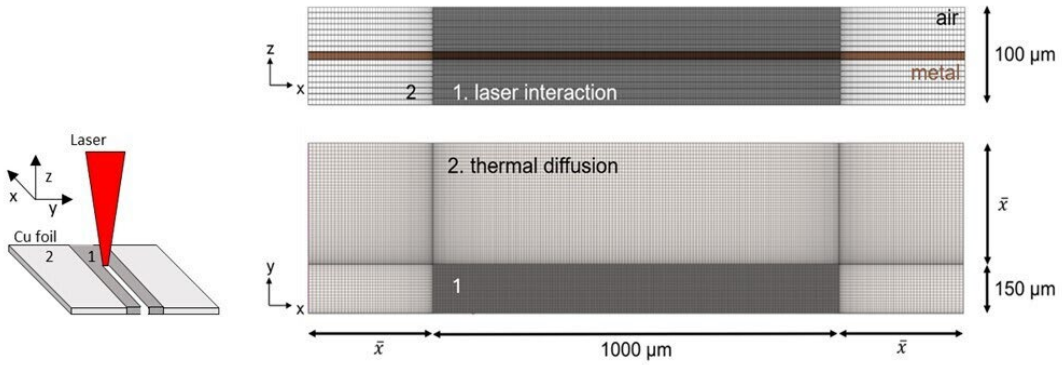


Figure 2: Computational Domain

Cut conditions

The developed framework simulated laser cutting of pure copper current collectors across all the entire range of process parameters shown as black dots in Fig. 3. The tuning conditions, detailed in Table 1, are represented by red dots, while blue squares indicate the validation cases.

The same process parameters were selected to evaluate the effect of cutting as the current collector thickness increases from 8 to 16 µm.

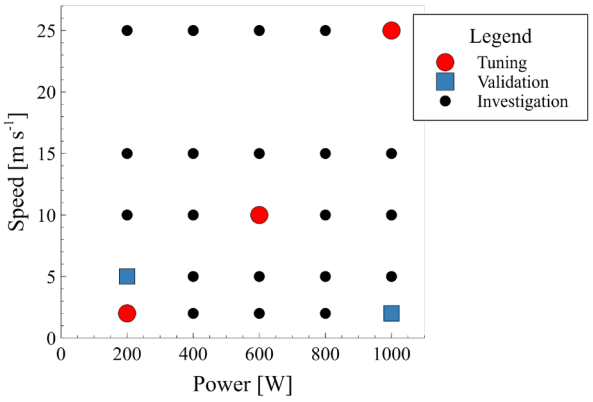


Figure 3: Simulated cut conditions

Results and discussion

The experimental cuts exhibit distinct defect patterns, as shown in Figure 4. SEM images reveal bubble-shaped recast and an uneven kerf width in cut A, resulting from low speed and power, which promote melting over vaporization. In contrast, cut C shows spatter formation, as high speed and power enhance the ejection of metal droplets. Cut B demonstrates good quality, with dross limited to the back surface, as seen in the optical microscope image. Among the validation conditions, cut E fails to reach the melting and vaporization temperatures and is therefore not included in Figure 4 below, Cut D represents an intermediate case, displaying dross on both surfaces, a nearly constant kerf width, and no spatter.

Materials Research Proceedings 57 (2025) 319-326 https://doi.org/10.21741/9781644903735-37

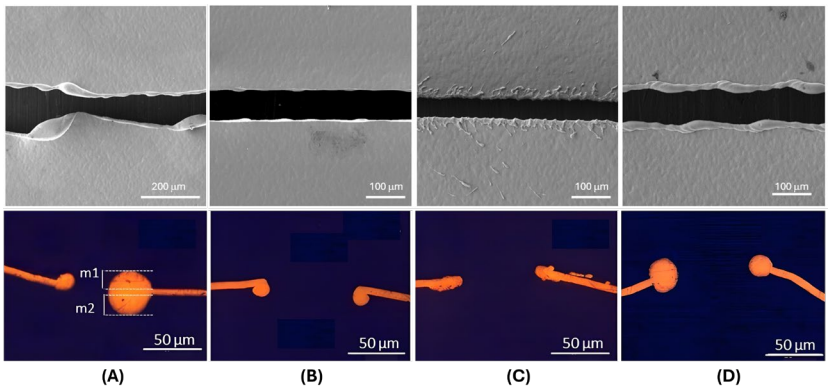


Figure 4: SEM images of front surface (first row) and optical images of edge profile (second row) for tuning and validation cuts

Model tuning and validation

Given the wide range of power and speed investigated—and consequently, the significant variation in fluence and irradiance—a single set of parameters C_1 and C_2 for the recoil pressure (equation 4) did not yield accurate results across the entire process window. Therefore, C1 was tuned with a power trend against the fluence and C2 with a linear trend against the irradiance. The following equations were found:

$$C_1 = 14.4E^7 \cdot F^{-1.18} \quad (5)$$

$$C_2 = 0.358 \cdot I + 0.068 \quad (6)$$

The quantitative evaluation of the data matching between the model and experiments can be seen in Figure 5, with the mean value and the standard deviation obtained through the 160 total measurements as specified in the Materials and Methods section.

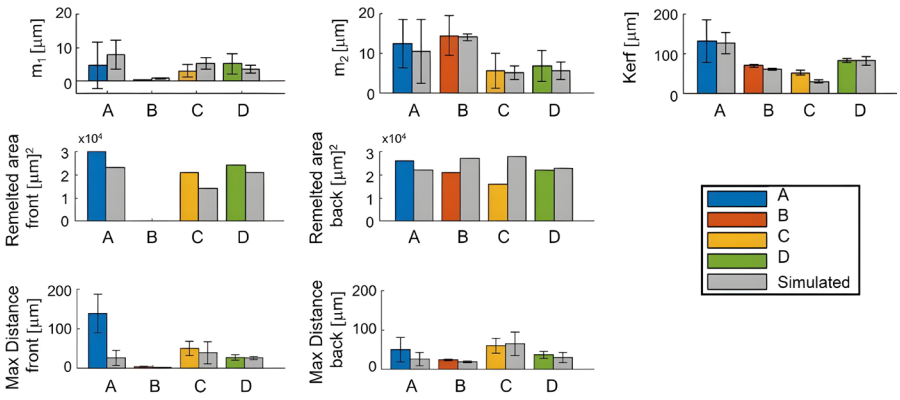


Figure 5: Comparison between simulated and experimental cut by kerf, dross measurements, and spatter area and distance

Overall, the model demonstrates good agreement with the experimental results across all metrics and test cases, as shown in Fig. 5. The simulated values generally follow the same trend as the experimental data, with differences that fall within the standard deviation of the measurements. The only noticeable discrepancy concerns the "Max Distance front" in case A, where the model underestimates the experimentally observed values. This deviation is attributed to the limited mesh resolution and computational domain size, which were optimized to capture the phenomena occurring near the laser–material interaction zone, while high-velocity spatters may exit the domain before being tracked.

Materials Research Proceedings 57 (2025) 319-326 https://doi.org/10.21741/9781644903735-37

Cutting quality prediction

Once the robustness of the model in accurately predicting the laser-current collector interaction was established, the influence of power, speed, and foil thickness on defect formation was investigated. The cutting quality was divided into five different conditions: No cut, Recast, Dross, Good, and Spatter. Figure 6 shows the results for both foil thicknesses in the total parameters window.

For the 8 µm case, the figure shows both the SEM and simulation results, while for the 16 µm only simulations were performed as no foil with this value of thickness was available.

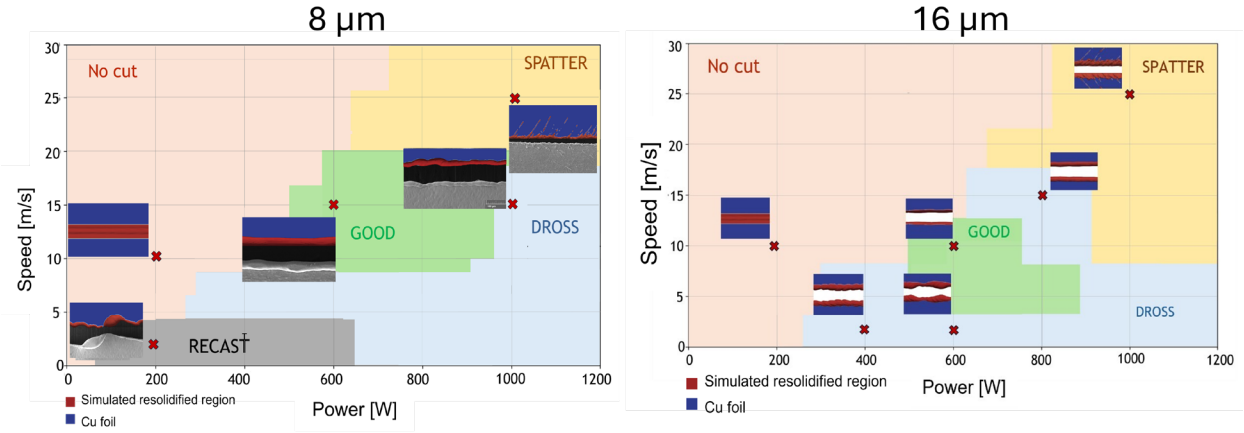


Figure 6: Cut quality prediction for 8 and 16 µm

The analysis of the kerf width, dross formation, and spatter behavior across different process parameters reveals clear trends in cut quality. At lower power and speed levels, the formation of recast material is prevalent due to the instability of the molten region, leading to high kerf variability and significant standard deviations in m_1 and m_2. As power increases, the transition from recast to dross-dominated regions occurs, with dross height exceeding critical thresholds relative to foil thickness. At higher speeds, particularly above 19 m/s, spatter formation becomes evident, mainly at the back of the cut, as the melt ejection becomes irregular. Increasing power beyond 1000 W further exacerbates droplet ejection at the front, confirming a shift in defect behavior.

The definition of the good cut region highlights the importance of both kerf stability and minimal dross accumulation. In this optimal range, front dross is nearly absent, kerf width remains uniform, and molten material is confined close to the cutting edge. However, a further increase in power, even within this stable region, can negatively impact edge quality, leading to the onset of dross formation.

It is important to highlight that the model was calibrated using a specific laser source and copper foil, and its predictive capabilities are currently limited to the tested operating conditions. The empirical coefficients adopted in the CFD formulation were fitted using experimental data representative of distinct cutting regimes; however, these values may not generalize to significantly different materials or beam configurations. A broader generalization would require additional parameters that explicitly account for material and source variability.

The effect of foil thickness was also examined by doubling the thickness from 8 µm to 16 µm. The results indicate a shift in the process window, with a general increase in dross formation and a reduction in the range of process parameters that yield a good cut. The higher thermal mass of the thicker foil affects heat dissipation, requiring an adjustment of power and speed combinations to maintain an optimal cut. While good cut conditions are still achievable, the increased tendency for spatter and dross at higher powers and speeds suggests a narrower operating range for achieving high-quality cuts in thicker foils.

Conclusion

In this study, the developed CFD model successfully predicted the behavior of CW laser cutting of thin copper foils used as current collectors in lithium-ion battery electrodes. After tuning and validating the model with experimental results, it was possible to investigate the influence of laser power, speed, and foil thickness on cut quality, including kerf dimensions, dross formation, and spatter behavior. The threshold laser parameters for achieving high-quality cuts were identified, as well as the conditions leading to defect formation. Experimental results revealed the presence of spatter, dross, and recast material, which the model accurately captured, confirming its reliability in predicting defect-prone regions. By analyzing the interplay of process parameters, this study identified key physical mechanisms responsible for defect formation and provided predictive equations for determining process windows that minimize unwanted effects. The findings offer a valuable reference for optimizing laser cutting conditions, ensuring quality even when input parameters such as material properties, spot size, or thickness vary. This approach reduces the need for extensive experimental testing, offering a more efficient path to process optimization.

References

[1] C. Angeloni, E. Liverani, A. Ascari, A. Fortunato, J. Mater. Process. Technol. 324 (2024) 118266. https://doi.org/10.1016/j.jmatprotec.2023.118266

[2] J. Schindelin, I. Arganda-Carreras, E. Frise, V. Kaynig, M. Longair, T. Pietzsch, S. Preibisch, C. Rueden, S. Saalfeld, B. Schmid, J.-Y. Tinevez, D.J. White, V. Hartenstein, K. Eliceiri, P. Tomancak, A. Cardona, (2012).

[3] M. Luetke, V. Franke, A. Techel, T. Himmer, U. Klotzbach, A. Wetzig, E. Beyer, Phys. Procedia 12 (2011) 286-291. https://doi.org/10.1016/j.phpro.2011.03.135

[4] W. Schulz, V. Kostrykin, M. Nießen, J. Michel, D. Petring, E.W. Kreutz, R. Poprawe, J. Phys. Appl. Phys. 32 (1999) 1219-1228. https://doi.org/10.1088/0022-3727/32/11/307

[5] W. Pfleging, Nanophotonics 7 (2018) 549-573. https://doi.org/10.1515/nanoph-2017-0044

[6] M.J. Assael, A.E. Kalyva, K.D. Antoniadis, R. Michael Banish, I. Egry, J. Wu, E. Kaschnitz, W.A. Wakeham, J. Phys. Chem. Ref. Data 39 (2010) 033105. https://doi.org/10.1063/1.3467496

[7] X. Zhu, D.M. Villeneuve, A.Y. Naumov, S. Nikumb, P.B. Corkum, Appl. Surf. Sci. 152 (1999) 138-148. https://doi.org/10.1016/S0169-4332(99)00331-1

[8] C. Hartmann, J. Laser MicroNanoengineering 8 (2013) 266-270. https://doi.org/10.2961/jlmn.2013.03.0013

[9] J. Grabow, J. Klink, R. Benger, I. Hauer, H.-P. Beck, Batteries 9 (2022) 9. https://doi.org/10.3390/batteries9010009

[10] Y. Yuan, H. Wang, X. Han, Y. Pan, Y. Sun, X. Kong, L. Lu, M. Ouyang, Appl. Energy 361 (2024) 122968. https://doi.org/10.1016/j.apenergy.2024.122968

[11] G. Chianese, S. Jabar, P. Franciosa, D. Ceglarek, S. Patalano, Procedia CIRP 111 (2022) 484-489. https://doi.org/10.1016/j.procir.2022.08.075

[12] S.P. Lin, R.D. Reitz, Annu. Rev. Fluid Mech. 30 (1998) 85-105. https://doi.org/10.1146/annurev.fluid.30.1.85

[13] W. Huang, H. Wang, T. Rinker, W. Tan, Mater. Des. 195 (2020) 109056. https://doi.org/10.1016/j.matdes.2020.109056

Materials Research Proceedings 57 (2025) 327-334 https://doi.org/10.21741/9781644903735-38

Friction stir welding of AA6082 and AA5083 T-joints for naval applications: Finite element modeling and experimental analysis of material flow

Guido Di Bella[1,a], Mohamed Chairi[1,b*], Davide Campanella[2,c], Riccardo Puleo[2,d], Gianluca Buffa[2,e]

[1]Department of Engineering, University of Messina, Contrada di Dio 1, 98166, Messina, Italy

[2]Department of Engineering, University of Palermo, Viale delle Scienze, 90128, Palermo, Italy

[a]guido.dibella@unime.it, [b]mohamed.chairi@unime.it, [c]davide.campanella@unipa.it, [d]ricchardo.puleo01@unipa.it, [e]gianluca.buffa@unipa.it

Keywords: Friction Stir Welding, Tensile Strength, Aluminum Alloys

Abstract. This study investigates the influence of rotational speed on material flow during friction stir welding (FSW) of dissimilar aluminum T-joints made of AA6082 and AA5083 alloys for naval applications. A finite element (FE) model was used to simulate the thermomechanical behavior and visualize the material flow during the welding process. Simulations were carried out at two rotational speeds, 500 rpm and 900 rpm, to evaluate their effects on heat distribution, strain rate and deformation patterns. The numerical results show that higher speeds improve plasticization and material mixing but also increase the risk of defect formation due to excessive heat input. The simulation outcomes are confirmed by the experimental observations made in the previous study, particularly with regards to the formation of heat-affected zones (HAZ) associated with the microhardness variations.

Introduction

In modern manufacturing, assembly systems play a critical role in joining materials to create strong, durable structures. Among the various joining techniques, including in naval applications, welding stands out as fundamental method for connecting materials. One such advanced welding process is friction stir welding (FSW), a solid-state joining technique that has drawn a lot of attention because it can join aluminum and other non-ferrous metals with excellent quality, little distortion, and no filler materials, is one example of an advanced welding process [1,2]. Essential parameters for friction stir welding (FSW) are tool rotation speed, welding speed, axial force, tilt angle and tool geometry. Higher rotational speeds increase heat input, improving material mixing but potentially causing excessive intermetallic compounds. Welding speed affects the thermal cycle and defect formation, while axial force ensures material consolidation and minimizes defects. The tilt angle enhances material mixing, and tool geometry influences material flow and heat generation, with specific designs optimized for different materials [1,3,4].

A T-joint is a common type of joint in welding, particularly in the transportation industry, where one piece (called the stringer) is welded perpendicularly to another piece (referred to the skin) to for a “T” shape [5]. These two metallic parts can be joined from similar materials, or dissimilar materials. In the latter case, the welding process is often complicated by differing physical properties such as melting points, thermal conductivities and mechanical properties [6,7]. However, for the process of creating a T-joint involves control of several parameters, including the tool’s rotation and feed rate. These parameters must be adjusted differently compared to butt joints to ensure effective material flow and bonding, as T-joint configuration requires a forging action to create fillets at the joints corners [8]. In [9], found that the feed rate significantly affects the temperature distribution during welding process. Lower feed rate results in higher heat input,

Content from this work may be used under the terms of the Creative Commons Attribution 3.0 license. Any further distribution of this work must maintain attribution to the author(s) and the title of the work, journal citation and DOI. Published under license by Materials Research Forum LLC.

Materials Research Proceedings 57 (2025) 327-334 https://doi.org/10.21741/9781644903735-38

which can led to increased temperatures in the weld zone while increasing feed rate reduces the heat input, which in turn lowers the temperature-time gradient. This reduction cand lead to lower residual stresses in the joint. Variations in feed rate can also lead to different types of surface defects. As an example, at lower feed rates (e.g. 20 mm/min), the weld can be more prone to defects such as large voids, while higher feed rates (e.g. 80 mm/min) can lead to tears. In [10], higher rotational speeds generally improve mechanical properties by enhancing heat generation, material plasticization, and joint strength. The study evaluated three rotational speeds—1000 rpm, 1400 rpm, and 1800 rpm—revealing that higher speeds promote finer grain microstructures and stronger welds, particularly when coupled with an optimal penetration depth (7 mm) with an optimal tensile strength of 175.2 MPa reported at 1800 rpm.

Material flow in FSW is a critical factor in final quality as it affects mixing, heat distribution and material deformation during the process. Understanding how the materials move and interact in the weld allows you to predict potential defects and optimize processing parameters. Finite element modeling (FEM) is a robust approach for simulating material flow dynamics and evaluating the effects of different welding conditions on the final weld quality. However, there are few works that use numerical models, such as [11], that carried out a numerical approach to predict flow-induced defects and to optimize the tool geometry and welding for T-joints. In [12], the author performed a fully coupled thermomechanical FEM analysis of friction stir welding (FSW) for AA6061-T6 T-joints using an Arbitrary Lagrangian-Eulerian (ALE) formulation. The simulation captured temperature distributions, stress and strain evolution, and tool reaction forces during welding phases.

Moreover, Harikrishna et al. [13] investigated the FSW of a T-joint between AA6156 aluminum alloy and Titanium Grade 2 using both numerical simulations and experimental validation. Their FEM model predicted the distribution of key parameters such as temperature, material flow velocity, and stress during welding, helping to correlate thermal history with joint quality. In another study [14], DEFORM-3D was used to simulate the FSW of AA6082-T6 at a rotational speed of 800 rpm. A viscoplastic material model incorporating strain, strain rate, and temperature dependency was adopted. The results showed that increasing temperature led to a reduction in flow stress, facilitating plastic deformation and improving weldability, Sarfaraz Z et al. in [15], developed a coupled thermomechanical model to analyze FSW of dissimilar aluminum alloys, specifically AA5086-O (retreating side) and AA2024-T3 (advancing side). The thermal model computed the transient temperature fields, which were then used as input for the mechanical model to evaluate residual stress distribution. Their findings indicated that the tool rotational speed significantly influenced thermal profiles and residual stress magnitude, with higher temperatures and lower residual stresses observed at higher speeds, particularly on the retreating side.

Despite the advances in FEM and material flow studies, there is still a gap in understanding how different rotational speeds affect material flow in T-joint FSW welding, especially for dissimilar aluminum alloys. This study aims to fill this gap by developing a finite element model to simulate material flow in FSW welding of T-joints made of AA6682 and AA5083. The model examines the effect of rotational speed on material flow in terms of its impact on mechanical performance in our earlier study in [16].

Materials and Method

Experimental method

Two aluminum alloys were used for the experimental T-impact friction stir welding process (FSW): AA6082 for the skin and AA5083 for the stringer, both with a thickness of 6 mm. Welding was carried out using a 3-axis ESAB LEGIOTM 3ST FSW machine from OEMER Motori Elettrici located Rescaldina, Italy. A double-shoulder tool made of H13 tool steel was used to allow effective heat generation, enabling optimum welding at the joints between the skin and stringer

Materials Research Proceedings 57 (2025) 327-334 https://doi.org/10.21741/9781644903735-38

and resulting in well-formed joints. The mechanical properties of the two alloys are listed in Table 1. Further details on the FSW process can be found in [16].

In the current study, two rotation speeds, 500 rpm and 900 rpm, were selected to evaluate their influence on the material flow during the welding process. The welding speed was set to a constant 100 mm/min.

Table 1. Mechanical properties of the alloys used for skin and stringer [16].

	AA6082	**AA5083**
Tensile strength [MPa]	310	275
Yield strength [MPa]	260	125
Elongation [%]	10	15
Brinell hardness	94	75

Numerical method

A finite element analysis of T-joint friction stir welding was carried out using DEFORM 3D software in the context of thermomechanical coupled simulation with a Lagrangian formulation. The model consists of two main components: a rotating tool and a single T-block, as shown in **Fig 1.a**. The tool was modelled as a rigid body with 25,000 elements, while the two sheets were represented as a single T-block using a viscoplastic material model characterized by strain, strain rate, and temperature dependent flow stress ($\sigma = f(\varepsilon, \dot{\varepsilon}, T)$)., with the horizontal sheet being AA6082 and the vertical sheet AA5083. The T-block was meshed with 38,000 elements, with a mesh size of 2 mm in the region under the tool.

This T-block configuration was selected to ensure stability by minimizing the issues caused by the interaction between two deformable bodies, preventing unrealistic deformation in the simulation.

Numerical simulation was tuned with the experimental tests by matching the experimental temperature recording with the numerical one. This phase is crucial for evaluating the correct frictional contact and heat transfer coefficient. Specifically, temperature data were collected at the centre of the A6082 sheet, near the path where the shoulder path (see **Fig 1.b**).

Boundary conditions.

The bottom surface of the T-block was fixed in all directions to prevent any movement of the rigid body. The tool was set in a rotational motion, with the angular speed set according to the selected rotational speed (500 rpm or 900 rpm). The heat generated by the tool was transferred to the T-block along the interface between the tool and the workpiece. A convective heat transfer coefficient of 11 J/mm °C was used to model the heat transfer to the environment. Frictional contact between the tool and the T-block was assumed to have a coefficient of friction of 0.3. This value was chosen based on experimental observations and was used to accurately model the material flow during the welding process.

Materials Research Proceedings 57 (2025) 327-334 https://doi.org/10.21741/9781644903735-38

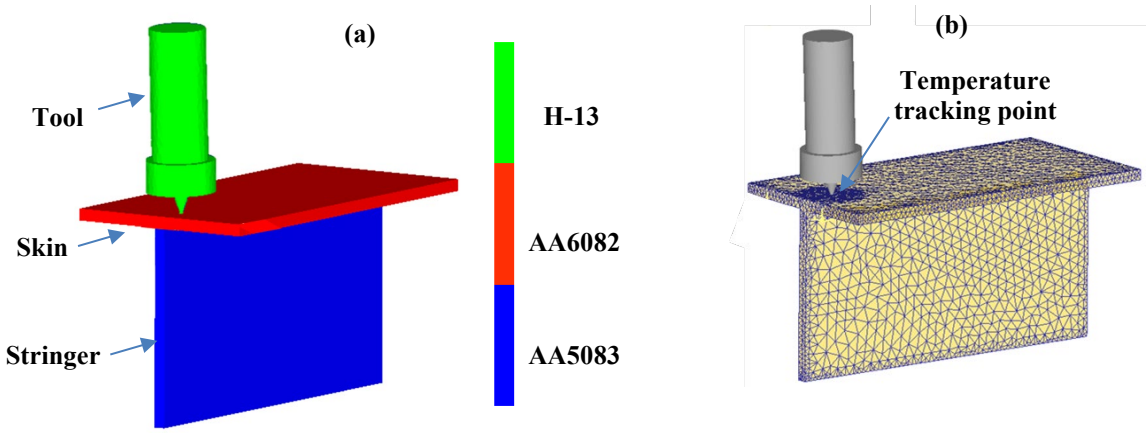


Fig 1. FSW numerical model a) material assignment b) meshing

Results and Discussion

The temperature evolution at the tracking point is presented in **Fig 2** comparing numerical predictions with experimental measurements. In the experimental setup, temperature was measured using an infrared (IR) pyrometer positioned to monitor the surface temperature near the tool-workpiece surface.

The numerical model demonstrates good agreement with the experimental data, particularly in capturing the heating trend and peak temperature. Minor deviations, especially between 110–140 seconds, may be attributed to local surface emissivity variations or transient thermal effects.

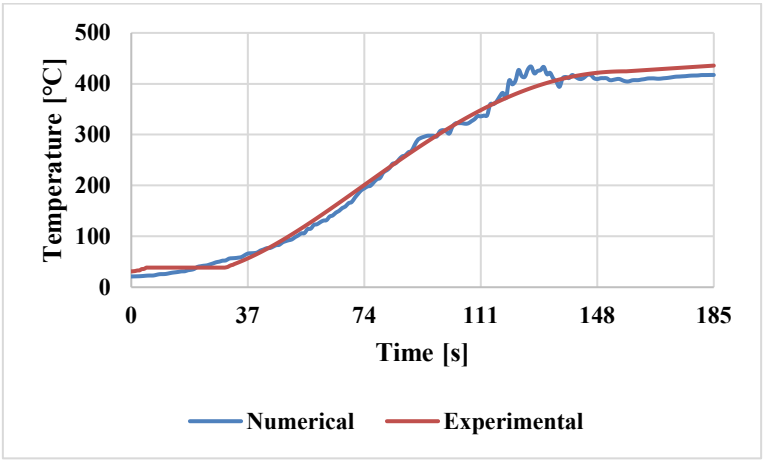


Fig 2. Temperature recording of tracking point.

The strain, stress and temperature were measured along the weld length to evaluate the influence of process parameters on joint quality in friction stir welding. Their distributions under different rotational speeds are presented in **Fig 3** and **4**, highlighting the effects of flow and high heat input conditions.

Materials Research Proceedings 57 (2025) 327-334 https://doi.org/10.21741/9781644903735-38

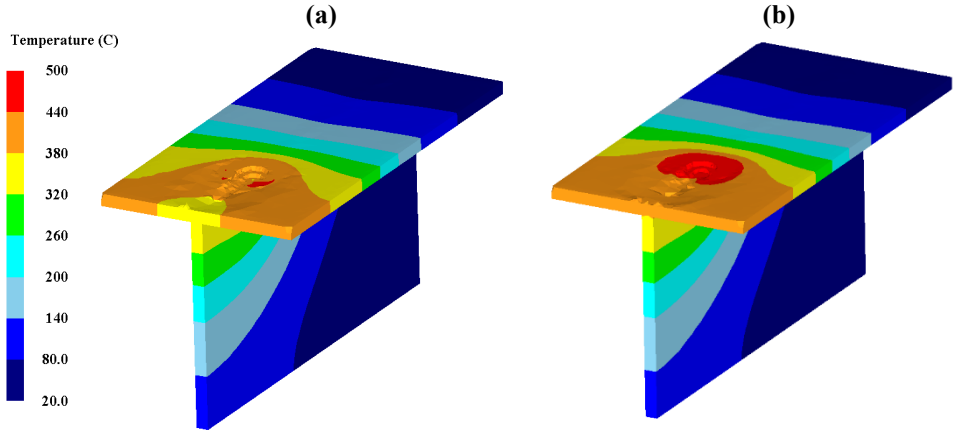


Fig 3. Friction stir welding temperature plotting for the case a) 500 rpm – 100 mm/min and b) 900 rpm – 100 mm/min

At a speed of 500 rpm, the heat-affected zone (HAZ) is less extensive, with maximum temperatures reaching around 320-380 °C. The lower rotational speed generates less frictional heat, leading to more uniform, but lower thermal distribution. While this helps reduce the risk of overheating and thermal degradation, the limited heat may result in insufficient plasticization, especially at the edges, potentially weakening the joint in those areas.

In contrast, at 900 rpm, the maximum temperature reaches higher values (above 440-500 °C) in the central zone, with a more pronounced and concentrated heat distribution. The increased rotational speed promotes stronger plasticization and improved flow. However, this higher het input increases the risk of thermal degradation and the buildup of residual stresses, which may compromise weld integrity.

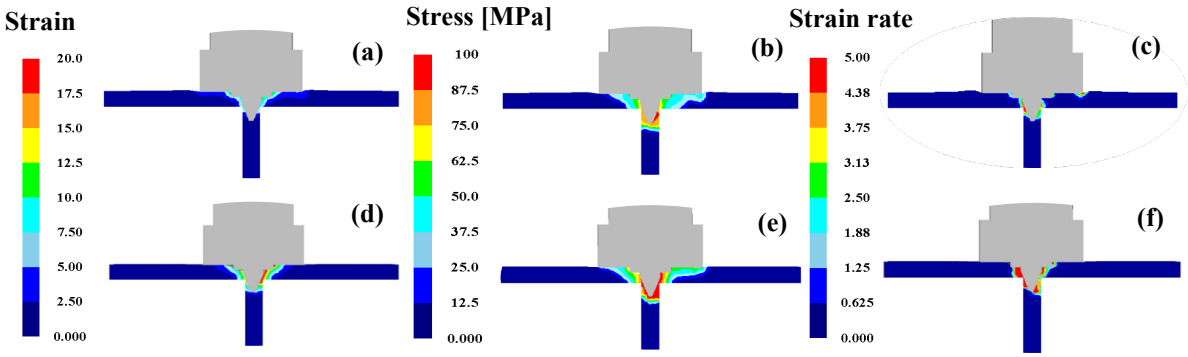


Fig 4. Friction stir welding strain, stress and strain rate plotting for the case a,b,c) 500 rpm – 100 mm/min and d,e,f) 900 rpm – 100 mm/min

Looking at the strain results in **Fig 4**, it can be seen that the deformation is higher at 900 rpm than at 500 rpm. This effect can be attributed to the higher speed, which generates more heat, making the material more plastic and easier to deform. The strain distribution appears to be greater near the bolt, indicating a more uniform deformation process. As for the stress, in both cases the maximum values are concentrated in the contact zone of the pin. However, at 500 rpm, the stress is more concentrated in the stirring zone of the pin than at 900 rpm. This indicates that the lower speed leads to lower friction and a more moderate heat transfer, resulting in a more balanced process. As shown in panels (c) and (f), the strain rate is significantly higher at 900 rpm. The larger color scale reflects a faster deformation rate, which facilitates stirring of the material at more

Materials Research Proceedings 57 (2025) 327-334 https://doi.org/10.21741/9781644903735-38

aggressive parameters. However, this fast deformation rate could lead to surface defects, a phenomenon that was also observed in the tests.

Fig 5 also shows the deformations along the longitudinal beam in detail. At a speed of 500 rpm, the strain is limited to a relatively small area near the tool. The strain values are lower, with a maximum elongation of around 15. If the speed is set to 900 rpm, however, the strain distribution becomes more extensive and reaches higher values, with the strain zone spreading further under the horizontal sheet. The maximum strain is then around 20.

Higher speeds lead to higher strain values, which indicates that the material has become more plastic due to the increased heat input. The larger and more uniform strain distribution indicates that the material is undergoing more deformation, which promotes better material flow and allows for a more effective joint, especially in areas that are difficult to weld. However, this more aggressive deformation could also increase the likelihood of defects such as excessive material flow, which could affect weld quality. In contrast to the 500 rpm sample, the material under the horizontal plate deforms in a more limited way, which can lead to a less effective bond in the edge areas of the weld.

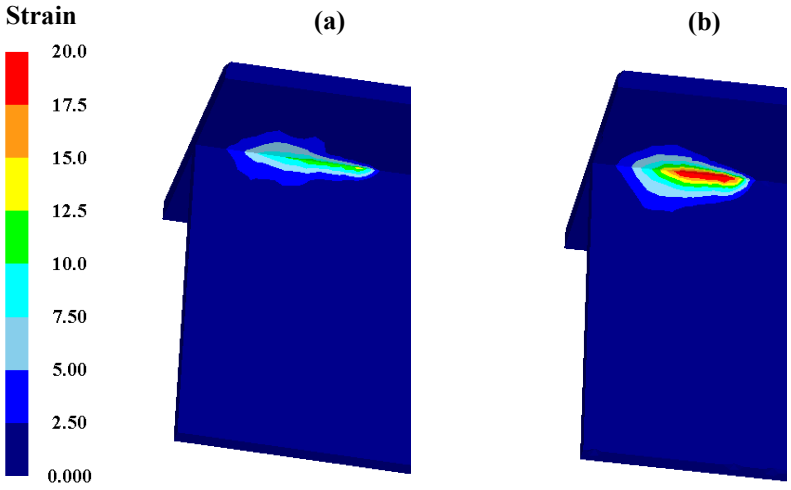


Fig 5. Strain evaluation under the horizontal sheet: a) 500 rpm and b) 900 rpm

In our study [16], the experimental findings align well with the results obtained from the Finite Element Method (FEM) analysis presented in this study, particularly regarding the influence of rotational speed on heat generation, material flow, and microhardness distribution. In Fig 6, microhardness variations across the different FSW zones (SZ, TMAZ, HAZ, and BM). At 500 rpm, the FEM analysis shows a less extensive (wider) HAZ heat-affected zone (HAZ) and lower strain values, which corresponds to the experimental observation of more controlled material flow and fewer defects. The relatively uniform microhardness profile observed in the tests, with values between 75 HV and 90 HV, is confirmed by the FEM results, which indicate uniform heat input and plasticization throughout the joint. In contrast, the FEM simulation at 900 rpm predicts a wider HAZ and higher strain values, which is consistent with experimental results of increased defect formation, such as wormholes, due to excessive heat and turbulent material flow. In addition, the variations in microhardness (65 HV to 95 HV) observed at 900 rpm in the experiments are reflected in the FEM results, which show more pronounced temperature and strain variations, highlighting the direct correlation between speed, heat input, material deformation and microstructure.

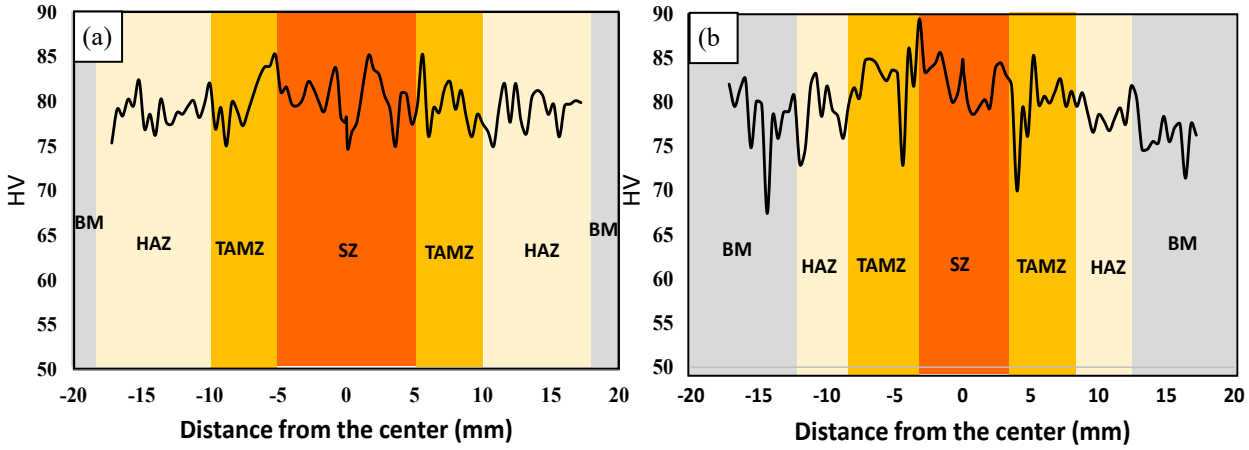


Fig 6. Microhardness profiles with FSW zones at (a) 500 rpm and (b) 900 rpm [SZ: stir zone; TAMZ: Thermo-mechanically affected zone; HAZ: heat affected zone; BM: Base material]. (Reworked and adapted from [16]).

Summary

In this study, the material flow during friction stir welding (FSW) of T-joints made of AA6082 and AA5083 was investigated using both experimental and finite element modeling (FEM) techniques. The results show that the rotation speed has a significant effect on material flow, heat distribution and joint quality. At 500 rpm, the heat-affected zone (HAZ) is smaller, which leads to greater local deformation. In contrast, at 900 rpm, plasticization is enhanced by a higher heat input, which leads to better material mixing, but also entails a higher risk of thermal degradation and defect formation. The experimental and FEM results agreed and confirmed that higher speeds improve material flow and bonding, especially in the central and peripheral areas of the weld. This study provides important insights for the optimization of FSW parameters and ensures high quality joints for marine applications by balancing heat input, material flow and defect avoidance.

References

[1] Di Bella G, Favaloro F, Borsellino C. Effect of Process Parameters on Friction Stir Welded Joints between Dissimilar Aluminum Alloys: A Review. Metals 2023, Vol 13, Page 1176 2023;13:1176. https://doi.org/10.3390/MET13071176

[2] Meschut G, Merklein M, Brosius A, Drummer D, Fratini L, Füssel U, et al. Review on mechanical joining by plastic deformation. Journal of Advanced Joining Processes 2022;5:100113. https://doi.org/10.1016/J.JAJP.2022.100113

[3] Zens A, Zaeh MF, Marstatt R, Haider F. Friction stir welding of dissimilar metal jointsRührreibschweißen von Metall-Mischverbindungen. Materwiss Werksttech 2019;50:949–57. https://doi.org/10.1002/MAWE.201900023

[4] Kilic S, Ozturk F, Demirdogen MF. A comprehensive literature review on friction stir welding: Process parameters, joint integrity, and mechanical properties. Journal of Engineering Research 2023. https://doi.org/10.1016/J.JER.2023.09.005

[5] Fratini L, Micari F, Squillace A, Giorleo G. Experimental Characterization of FSW T-Joints of Light Alloys. Key Eng Mater 2007;344:751–8. https://doi.org/10.4028/WWW.SCIENTIFIC.NET/KEM.344.751

[6] Majeed T, Wahid MA, Alam MN, Mehta Y, Siddiquee AN. Friction stir welding: A sustainable manufacturing process. Mater Today Proc 2021;46:6558–63. https://doi.org/10.1016/J.MATPR.2021.04.025

[7] Mansoor B, Dorbane A, Ayoub G, Imad A. Friction Stir Welding of AZ31B Magnesium Alloy with 6061-T6 Aluminum Alloy: Influence of Processing Parameters on Microstructure and Mechanical Properties. Friction Stir Welding and Processing VIII 2015:259–66. https://doi.org/10.1007/978-3-319-48173-9_28

[8] Buffa G, Fratini L, Ruisi V. Friction Stir Welding of tailored joints for industrial applications. International Journal of Material Forming 2009;2:311–4. https://doi.org/10.1007/S12289-009-0579-5/METRICS

[9] Campanella D, Buffa G, Lamia D, Fratini L. Residual stress and material flow prediction in Friction Stir Welding of Gr2 Titanium T-joints. Manuf Lett 2022;33:249–58. https://doi.org/10.1016/J.MFGLET.2022.07.032

[10] Sabry I, Singh VP, Alkhedher M, El-Zathry NE, Mourad AHI, Naseri M. Effect of rotational speed and penetration depth on Al-Mg-Si welded T-joints through underwater and conventional friction stir welding. Journal of Advanced Joining Processes 2024;9:100207. https://doi.org/10.1016/J.JAJP.2024.100207

[11] Fratini L, Buffa G, Micari F, Shivpuri R. On the material flow in FSW of T-joints: Influence of geometrical and tecnological parameters. International Journal of Advanced Manufacturing Technology 2009;44:570–8. https://doi.org/10.1007/S00170-008-1836-3/METRICS

[12] Salloomi KN. Fully coupled thermomechanical simulation of friction stir welding of aluminum 6061-T6 alloy T-joint. J Manuf Process 2019;45:746–54. https://doi.org/10.1016/J.JMAPRO.2019.06.030

[13] Rana H, Buffa G, Micari F, Fratini L. Numerical Investigation on Dissimilar Titanium-Aluminum T-joints Produced by Friction Stir Welding: Process Mechanics and Material Flow. Lecture Notes in Mechanical Engineering 2024:157–68. https://doi.org/10.1007/978-3-031-41341-4_17

[14] Sibalic N, Vukcevic M. Numerical Simulation for FSW Process at Welding Aluminium Alloy AA6082-T6. Metals 2019, Vol 9, Page 747 2019;9:747. https://doi.org/10.3390/MET9070747

[15] Sarfaraz Z, Awan YR, Saeed HA, Khan R, Wieczorowski M, Din NA. Residual Stress in Friction Stir Welding of Dissimilar Aluminum Alloys: A Parametric Study. Materials 2025, Vol 18, Page 316 2025;18:316. https://doi.org/10.3390/MA18020316

[16] Di Bella G, Borsellino C, Chairi M, Campanella D, Buffa G. Effect of Rotational Speed on Mechanical Properties of AA5083/AA6082 Friction Stir Welded T-Joints for Naval Applications. Metals 2024, Vol 14, Page 1410 2024;14:1410. https://doi.org/10.3390/MET14121410

Materials Research Proceedings 57 (2025) 335-343 https://doi.org/10.21741/9781644903735-39

Switching supervisory control in fusion laser cutting with vision-based process state detection

CAPRIO Leonardo[1,a *], GUERRA Sofia[1,2], PACHER Matteo[3], GANDOLFI Davide[3], SAVARESI Sergio Matteo[2], TANELLI Mara[2], PREVITALI Barbara[1]

[1]Department of Mechanical Engineering, Politecnico di Milano, Via La Masa 1, 20156 Milano (MI), Italy

[2]Department of Electronics, Information and Bioengineering, Politecnico di Milano, via G. Ponzio 34/5, 20133 Milano (MI), Italy

[3]Adige S.p.A., BLM GROUP, Via per Barco 11, 38056 Levico Terme (TN), Italy

[a]leonardo.caprio@polimi.it

Keywords: Laser Cutting, Machine Learning, Process Control

Abstract. Future unmanned laser cutting machines will require the capability to automatically detect and adapt to process states avoiding critical defects. In the fusion laser cutting of metals with low thickness (1-3 mm) the process can rapidly evolve from successful separation to plasma-dominated or loss of cut due to uncontrolled factors. Thus industrial systems set the cut velocity conservatively to ensure separation while avoiding low quality or incomplete cuts. This work proposes a novel switching supervisory control architecture to increase process productivity by regulating the velocity in real-time accordingly to the detected condition. A coaxial camera-based vision system was employed to develop a classification framework capable of a low latency process state identification during the cutting of 2 mm thick mild steel. The control logic allowed high quality cutting of 2 mm thick mild steel with a productivity increase of 10-33% hence validating the architecture for autonomous machines.

Introduction

Laser cutting is the most widely adopted laser-based process in the industrial sector. Throughout the years there has been a constant strive to employ the latest technological innovations, aiming to improve process productivity whilst maintaining a high quality cut profile. High-power laser sources exceeding 50–100 kW [1] along with advanced beam-shaping techniques [2] have emerged as some of the most significant innovations. However, the greatest appeal is provided by Machine Learning (ML) techniques that exploit the elevated data streams provided by latest generation sensorized machines and may enable fully autonomous and intelligent systems capable of improving process efficiency and facing shortages of skilled labor. Literature shows that these approaches may be exploited to identify optimal processing conditions[3] whilst advanced analysis of sensor data can provide relevant information in real-time to avoid defects. Photodiodes may be exploited to correlate data to quality metrics of the cut edge [4,5] and effectively determine plasma-dominated cutting conditions[6]. Alternatively, image processing approaches combined with ML algorithms can be exploited to detect cut interruptions [7]. Given the potential of such techniques, our research group at the Politecnico di Milano has been developing coaxial vision-based approaches that exploit ML algorithms to correlate images to quality metrics, enabling control of the laser cutting process. Real-time dross estimation [8] supports a velocity-based controller architecture to obtain high quality cuts whilst maximizing productivity [9]. In the case of reactive fusion cutting, profile roughness may be employed as the estimated metric for process control [10]. While these solutions hold great promise for future unmanned autonomous cutting systems, further

Content from this work may be used under the terms of the Creative Commons Attribution 3.0 license. Any further distribution of this work must maintain attribution to the author(s) and the title of the work, journal citation and DOI. Published under license by Materials Research Forum LLC.

Materials Research Proceedings 57 (2025) 335-343 https://doi.org/10.21741/9781644903735-39

advancements are needed beyond cut quality evaluation to ensure stable processing conditions. During fusion cutting, if the value of the cutting velocity is increased with respect to the reference set value, dross formation gradually increases (Figure 1 a)). While in industrial systems the velocity is set conservatively such defect is typically kept under control by the architecture previously presented. However, if the velocity is further increased or other external factors reduce the specific energy delivered to the material, a plasma-dominated cutting front may evolve (Figure 1 b)) leading to highly damaged part quality. Eventually, incomplete separation can occur corresponding to a loss of cut (LOC) condition (Figure 1c)). Both these conditions are considered unacceptable from a qualitative perspective and must be avoided. Moreover, these effects may occur independently of the cutting speed due to external influences that may impinge during the cutting process (i.e. thermal variations due to complex geometries, local changes in material thickness, deterioration of consumables). Therefore, developing the next generation of autonomous cutting machines requires a robust, self-regulating system that leverages a novel control architecture, ensuring real-time process state detection and adaptive velocity adjustment.

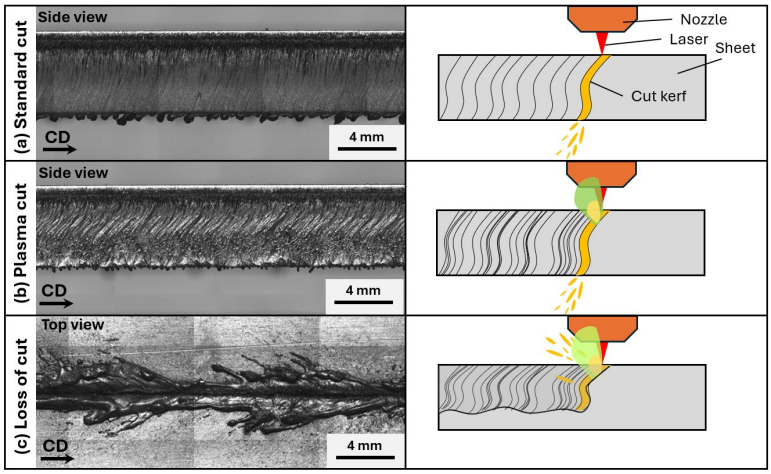


Figure 1. Representative images and schematic of process states during fusion cutting of AISI304 with 5 mm thickness a) successful cut, b) plasma dominated cut and c) loss of cut

The cutting of low thickness metal sheets (i.e in the range of 1-3 mm) are a promising situation to develop this novel approach given that when they are processed with kW levels of power, dross formation does not occur. Rather the process state directly switches from a standard condition to a plasma-dominated cut and eventually loss of cut. Hence, the previously developed controller that regulates speed accordingly to the dross estimate may not be employed [9]. Rather, a novel switching supervisory control logic may be implemented. Hence, in the present research this control technique was employed, always exploiting the data stream of information provided by the coaxial monitoring system. Vision-based techniques coupled to a supervised classification algorithms allowed to detect the process state in real-time. Finally, the novel control architecture was benchmarked during the fusion cutting of 2 mm thick mild steel.

Materials & method

Laser cutting system and monitoring equipment

An industrial laser cutting system was employed to perform the experiments (LC5, BLM, Levico Terme, Italy). The system is equipped with a 6 kW fiber laser source (YLS-6000-CUT, IPG Photonics, USA) emitting at 1070 nm. The beam is transported via an optical fiber (d_{f0}=100 µm) and focalized to a beam waist diameter of 207 µm by means of a collimation and focalization lens. The system specifications are reported in Table 1.

Materials Research Proceedings 57 (2025) 335-343 https://doi.org/10.21741/9781644903735-39

Table 1. Main specifications of the laser cutting system and monitoring equipment

Laser cutting system		**Monitoring equipment**	
Parameter	**Value**	**Parameter**	**Value**
Power, P	6 kW	Acquisition frequency, f_{acq}	750 Hz
Emission wavelength, λ_{laser}	1070 nm	Wavelength band, λ_{obs}	700 -1000 nm
Fiber diameter, d_{f0}	100 µm	Spatial Resolution, SR	6 µm/pixel
Beam waist diameter, $d0$	207 µm	Field of view, FOV	320x320 pixels

To extract process relevant information, a coaxial melt pool monitoring system was and deployed onto the industrial cutting system by exploiting a dichroic mirror reflective to the laser radiation and transmissive to the light in the near-infrared regime. The process emission light is then filtered in the 700-1000 nm wavelength band and focalized onto a CMOS camera (xiQ MQ013MG-ON, Ximea, Münster, Germany). A reduced region of interest (ROI) of the sensor is maintained active yielding a field of view of 320x320 pixels with a spatial resolution of 6 µm/pixel, allowing the maximization of the acquisition frame rate to 750 Hz thus enabling real-time control applications. The laser cutting system together with the optical monitoring scheme are shown in Figure 2 whilst the parameters are reported in Table 1.

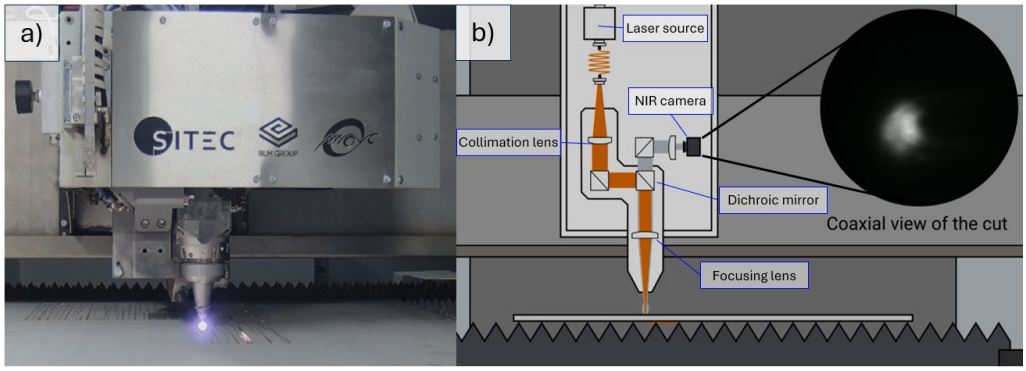


Figure 2. Laser cutting system a) during cutting and b) scheme of the main components

In order to provide physically relevant indicators of the process state for the training of the ML algorithm, the acquired frames were processed as follows: a circular ROI was imposed allowing to extract only relevant information regarding the cut kerf rather than internal reflections in the cutting head. The same frame was hard thresholded at different levels to obtain binary images of the melt from which geometrical features were extracted (such as width, area, length). For greater details regarding the image processing pipeline the reader is referred to previous publications and Figure 3 [8].

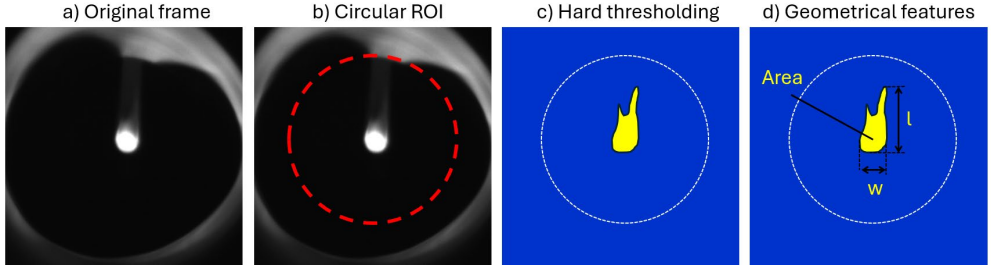


Figure 3 Image analysis pipeline a) original frame b) circular region of interest c) hard thresholding of the grayscale image and d) geometrical feature extraction

Materials Research Proceedings 57 (2025) 335-343 https://doi.org/10.21741/9781644903735-39

Experimental design & machine learning method for defect identification

An experimental campaign was designed to determine the transition between the different process states that might occur during the fusion laser cutting of low thickness metallic sheets. The selected material was 2 mm thick mild steel S235 (taken as representative of carbon steels typically processed via fusion cutting in both tubular and sheet formats). The material was cut via fusion cutting with high pressure (p=15 bar) N_2 assist gas delivered through a single chamber nozzle with 2 mm diameter. The laser power was set to the maximum level P= 6 kW (thus corresponding to the highest productivity condition). The focal position was kept at Δf= -2 mm whilst the stand-off distance corresponded to 0.7 mm. The variable factors corresponded to different levels of cutting speed (v= 13; 17; 21; 25; 29 m/min) along a linear trajectory 400 mm and different cutting directions (θ= 0°; 90°; 180° and 270°). The cutting velocity was chosen as a variable to induce the process states whilst different directions were required to develop a robust algorithm as discussed by Guerra *et al.*[11]. Fixed and variable factors are reported in Table 2.

Table 2. Fixed and variable factors of the experimental design to train the ML algorithm

Fixed factors		**Variable factors**	
Material	S235	Speed, v (m/min)	13; 17; 21; 25; 29
Thickness, t	2 mm	Direction, θ (°)	0; 90; 180; 270
Assist gas	N_2		
Laser power, P	6 kW		
Focal position, Δf	-2 mm		
Pressure, p	15 bar		
Stand-off distance, SOD	0.7 mm		
Nozzle diameter, d_{noz}	2 mm		

The scope of the experiments was to train a supervised classification machine learning algorithm capable of detecting the process state in real-time. The cut samples were labelled after observing the process (expert observation) and qualitatively assessing the cut profile with an optical microscope (QVC-1, Mitutoyo, Kanagawa, Japan). Clearly, loss of cut conditions could be determined by the fact that the cut was incomplete, whilst plasma-dominated cut exhibited high luminosity emission during the cut and a worse edge quality when observing samples. Such labels were then associated to the data extracted from the image processing pipeline. A random forest classifier algorithm was selected which enabled real-time processing for the successive implementation in the controller architecture while yielding elevated accuracy. Other algorithms were tested but such analysis is not reported in the present work for brevity. The experimental design yielded in total 37885 datapoints, divided in 70% training with 10 fold cross-validation and a 30% testing set. The algorithm performance was evaluated based on the accuracy (Eq. 1) of the model, computed by means of the confusion matrix for both training and testing phase assessing the number of True Positives (TP), True Negatives (TN), False Positives (FP) and False Negatives (FN).

$$Accuracy = \frac{TP+TN}{Total\ samples} \quad (1)$$

Switching supervisory control architecture

The switching supervisory controller designed for the present application represents a simple architecture often employed for categorical conditions. As schematized in Figure 4, the coaxial monitoring system acquires images of the cutting process in real-time. These images are then analyzed allowing the real-time process state identification according to the selected classification algorithm. The output provided by the classification algorithm ($\hat{y}$) is then provided to the supervisor which performs the logical decision on the action that the speed controller must

Materials Research Proceedings 57 (2025) 335-343 https://doi.org/10.21741/9781644903735-39

conduct. In the present case, if the process state is detected in either LOC or plasma-dominated cut then the speed controller provides a constant decrement of 0.1% of the current set value. On the other hand, if the classifier detects a standard processing condition it increases the cutting speed always by 0.1%. The real-time monitoring of the process state according to such logic thus attempts at maintaining the process under stable standard condition whilst maximizing the productivity. The controller is activated only once the cut speed achieves 90% of the initial set velocity (i.e. the system is not active during transitory phases).

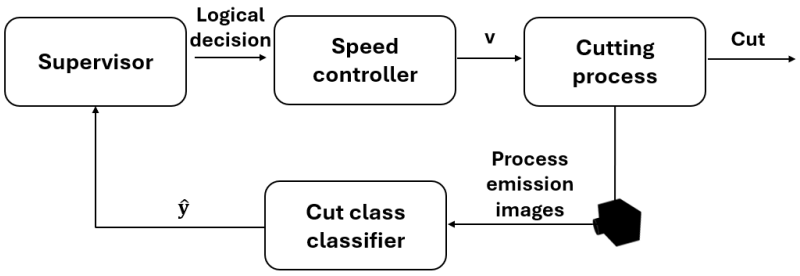


Figure 4. Schematic representation of the switching supervisory control architecture

Experimental design for controller architecture testing

Three final experiments were designed to test the controller architecture in different conditions that might occur during the cutting of metallic sheets (reported in Table 3). The fixed factors corresponded to the same of the previous experimental design whilst the varied condition corresponded to the initial set velocity v_i which was regulated by the controller. Run 1 considers the case in which a conservative value of cutting velocity is chosen corresponding to the current reference value for 2 mm thick mild steel (i.e. v_{ref}=v_i=15 m/min). Hence, the controller must be able to increase the cut speed whilst avoiding plasma formation. Run 2 and Run 3 on the other hand start from unacceptable cut conditions (respectively a plasma-dominated cut and a LOC situation). Hence, the controller must activate itself to decrease the cutting velocity and regain standard processing conditions. For Run 1 and Run 2 the cutting geometry corresponded to a rectangle 400x10 mm whilst for Run 3 a linear trajectory of 400 mm was maintained given that with loss of cut it is not be possible to remove samples from the sheet.

Table 3. Experimental runs to test the controller architecture

Run	Starting condition	Target class	Cut geometry
1	Standard cut (v_i=15 m/min)	Standard cut at v_{max}	Rectangle 400 mm x10 mm
2	Plasma cut (v_i=24 m/min)	Standard cut at v_{max}	Rectangle 400 mm x10 mm
3	Loss of cut (v_i=29 m/min)	Standard cut at v_{max}	Linear 400 mm

Results

Process state mapping

Figure 5 shows the cut profile of the samples as a function of the variable factors of the experimental campaign to build the supervised machine learning algorithm. It is clearly possible to observe that non-significant differences in terms of cut quality may be detected as a function of the cutting direction. On the other hand, as the cut speed increases the profile quality is modified. Cuts performed at v=13 and 17 m/min exhibit the typical regular profile of standard cutting process, whilst cuts done at v=21 and 25 m/min show a turbulent ejection of the melt on the lower side of the edge typical of plasma-dominated cutting states. Finally, cuts performed at 29 m/min were not successfully completed resulting in LOC conditions (for such reason only top view acquisitions are reported).

Materials Research Proceedings 57 (2025) 335-343 https://doi.org/10.21741/9781644903735-39

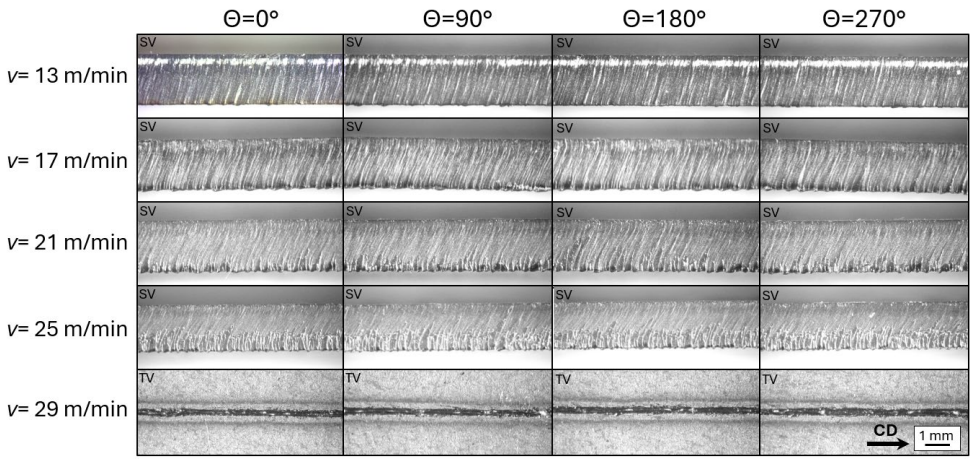


Figure 5 Top view (TV) or side view (SV) of the cut profile as a function of cut speed v and direction θ. CD indicates the cutting direction.

The categorical evaluation conducted qualitatively was also confirmed by visual observations during the cutting process (plasma-dominated cuts are characterized by a green light emission). Hence, the process map shown in Figure 6 a) was designed and employed as label for the dataset required for the successive training of the machine learning classification algorithm. Figure 6 b) also reports representative frames from the acquisitions in different cutting conditions. It is clearly possible to observe a correlation between the frame intensity and the loss of cut condition (saturated images of the cut kerf can be easily distinguished). On the other hand, from a qualitative perspective it is more complicated to distinguish between the plasma-dominated and standard cutting conditions.

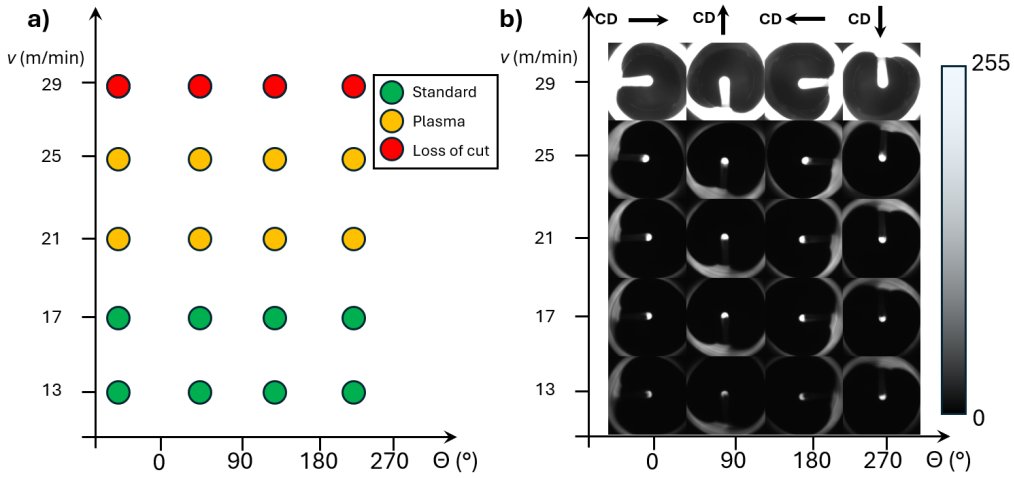


Figure 6. a) categorical evaluation of the process state and b) process emission images acquired

Supervised classification

The results of the supervised classification algorithm are shown in the confusion matrixes of Figure 7 (a) for the training phase and b) for the testing phase. It is clearly possible to observe that in both cases an elevated level of accuracy corresponding to 98.7% can be achieved. The only confounding effect that may be observed (in terms of false positives and negatives) is between plasma-dominated cut and standard cutting condition whilst the loss-of-cut condition (the most critical situation) is always correctly identified. Once the algorithm was trained it could run below the cycle time available for real-time control ($t_{algorithm}$= 700 µs < t_{cycle}=1/f_{acq}=1333 µs).

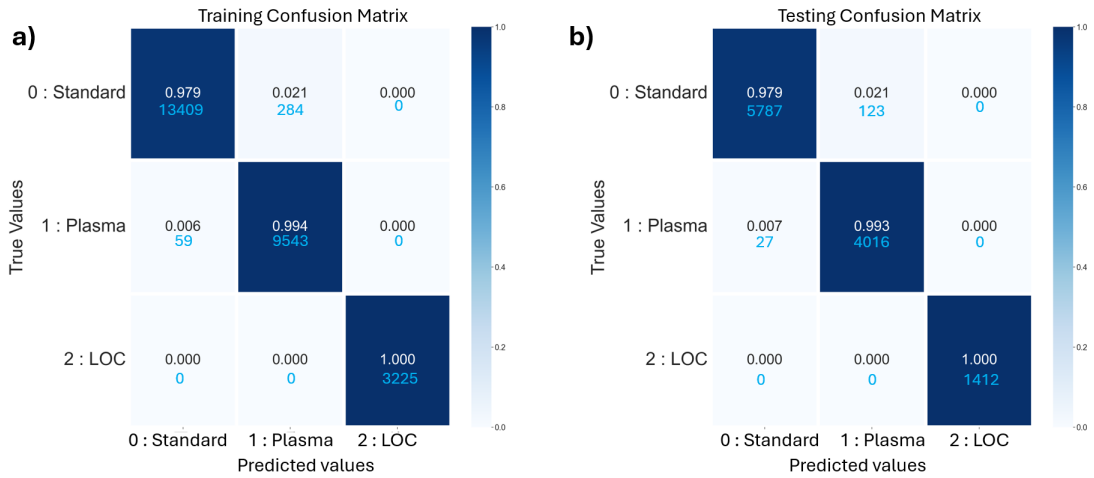


Figure 7. Confusion matrix of a) the training phase of the algorithm and b) testing

Switching supervisory control for stable cutting process

To validate the developed approach, real-time control experiments were performed. Results are reported in Figure 8 for the different conditions tested. In all cases, it is possible to observe that, accordingly to the process state condition detected by the ML algorithm, the controller automatically regulates the cut speed. In Figure 8 a) the controller starts from the reference level of cutting speed employed industrially (v_{ref}=v_i=15 m/min) and gradually increases the velocity up to about 20 m/min. Just before the end of the cut an incipient plasma formation condition is detected. As previously mentioned, when the cutting speed is below 90% of the initial set velocity, the control action is deactivated (as visible in Figure 8 a) by the interruption of trend in increasing the speed which corresponds to the end of the first side of the rectangle.

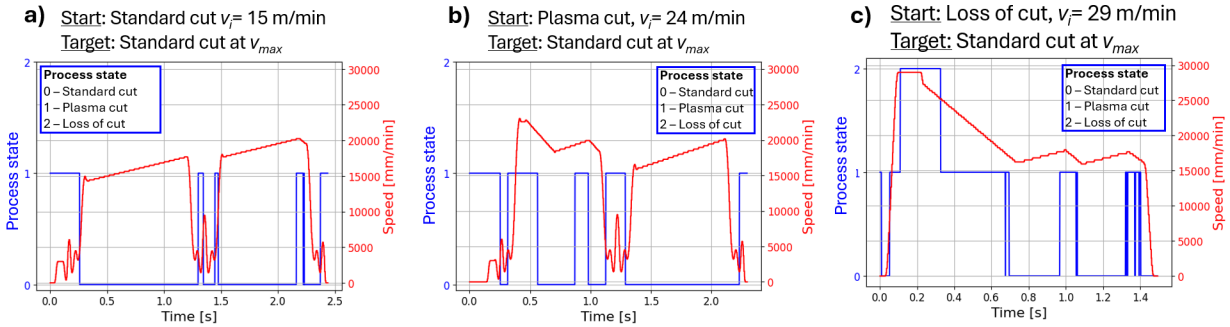


Figure 8. Real-time control experiments performed in different starting conditions a) standard cut v_i=15 m/min b) plasma cut v_i= 24 m/min and c) loss of cut v_i=29 m/min.

When the process begins in a plasma dominated state (Figure 8 b)) the controller is capable of reducing the cutting speed and once again operate in a more productive condition with respect to the reference condition (v=18-20 m/min). Finally, in the case the system detects a loss of cut condition (as imposed at the beginning in Figure 8 c)), the controller is capable of regulating the cut velocity transitioning through the plasma-dominated state finally achieving a velocity in a range between 16.5-18 m/min. Hence, the productivity increase with respect to reference velocity v_{ref}=15 m/min ranges between v_{max}=16.5-20 m/min, enabling an increase between 10 to 33%. Although the system can successfully regulate the cut velocity, it still possesses a significant oscillatory behaviour which could be reduced by the use of more complex controller architectures (currently under study for future developments). On the other hand, the devised solution provides a ruggedized approach capable of providing benefits in an industrial scenario through the deployment of advanced sensing and data analysis techniques enabling an unmanned process.

Conclusion

This research demonstrates a novel control architecture enabling productivity increase in laser cutting whilst avoiding unacceptable defects towards the development of unmanned autonomous laser cutting systems. The main outcomes can be summarized as follows:

- Process state is affected by the cutting velocity, where excessive velocities yield plasma-dominated or loss of cut conditions.
- Exploiting process images a supervised ML classifier can be implemented for real-time detection and classification of the state with overall accuracy above 98%.
- A switching supervisory control architecture can be deployed to perform real-time control of the cutting process, enabling the system to regulate the cut condition effectively thus ensuring the avoidance of critical defects (such as loss of cut) whilst guaranteeing an increase in productivity (10-33% at regime).

Future developments will aim at generalizing the ML algorithm for process state detection to different materials and thicknesses and benchmark the system over representative geometries.

Acknowledgements

The authors would like to thank the Ministry of University and Research (MUR) for supporting the research activities via the National Plan for Recovery and Resilience (PNRR).

References

[1] Y. Kawahito, H. Wang, S. Katayama, D. Sumimori, Ultra high power (100 kW) fiber laser welding of steel, Opt Lett 43 (2018) 4667–4670.

[2] M. Kardan, N. Levichev, S. Castagne, J.R. Duflou, Cutting thick aluminum plates using laser fusion cutting enhanced by dynamic beam shaping, J Laser Appl 35 (2023). https://doi.org/10.2351/7.0001095.

[3] H.-T. Nguyen, C.-K. Lin, P.-C. Tung, V.-C. Nguyen, J.-R. Ho, Manufacturing motor core lamination from thin non-oriented silicon steel sheet direct by pulsed laser cutting using multi-quality optimized process parameters, The International Journal of Advanced Manufacturing Technology (2024). https://doi.org/10.1007/s00170-024-13661-1.

[4] M. Schleier, B. Adelmann, B. Neumeier, R. Hellmann, Burr formation detector for fiber laser cutting based on a photodiode sensor system, Opt Laser Technol 96 (2017) 13–17. https://doi.org/10.1016/j.optlastec.2017.04.027.

[5] N. Levichev, G.C. Rodrigues, J.R. Duflou, Real-time monitoring of fiber laser cutting of thick plates by means of photodiodes, Procedia CIRP 94 (2020) 499–504. https://doi.org/10.1016/j.procir.2020.09.171.

[6] B. Adelmann, M. Schleier, B. Neumeier, R. Hellmann, Photodiode-based cutting interruption sensor for near-infrared lasers, Appl Opt 55 (2016) 1772. https://doi.org/10.1364/ao.55.001772.

[7] B. Adelmann, M. Schleier, R. Hellmann, Laser cut interruption detection from small images by using convolutional neural network, Sensors (Switzerland) 21 (2021) 1–13. https://doi.org/10.3390/s21020655.

[8] M. Pacher, L. Franceschetti, S.C. Strada, M. Tanelli, S.M. Savaresi, B. Previtali, Real-time continuous estimation of dross attachment in the laser cutting process based on process emission images, J Laser Appl 32 (2020) 042016. https://doi.org/10.2351/7.0000145.

[9] M. Pacher, S. Strada, M. Tanelli, B. Previtali, S.M. Savaresi, Real-time velocity regulation for productivity optimization in laser cutting, in: IFAC-PapersOnLine, Elsevier B.V., 2021: pp. 1230–1235. https://doi.org/10.1016/j.ifacol.2021.08.146.

[10] M. Pacher, L. Caprio, G. Delama, D. Gandolfi, S.M. Savaresi, B. Previtali, M. Tanelli, Real-time roughness estimation in laser oxidation cutting via coaxial process vision, in: WLT (Ed.), Lasers in Manufacturing Conference2023, WLT, 2023.

[11] S. Guerra, L. Vazzola, L. Caprio, M. Pacher, D. Gandolfi, M. Tanelli, S.M. Savaresi, B. Previtali, Velocity-based closed-loop control in fusion laser cutting for multi-directional and curved geometries, J Laser Appl 37 (2025). https://doi.org/10.2351/7.0001617.

Materials Research Proceedings 57 (2025) 344-351 https://doi.org/10.21741/9781644903735-40

Peripheral coarse grain prediction in extruded AA6082: Combining finite element simulations with neural networks

Marco Negozio[1,a *], Adrian H.A. Lutey[1,b], Antonio Segatori[2,c], Riccardo Pelaccia[3,d], Sara Di Donato[4,e], Barbara Reggiani[3,5f] and Lorenzo Donati[4,g]

[1]University of Parma - DISTI Department for Industrial Systems and Technologies, Parco Area delle Scienze, 181/A, 43124 Parma, Italy

[2]Hydro, Innovation and Technology, Myrkärrsvägen 1, 612 31 Finspång, Sweden

[3]University of Modena and Reggio Emilia - DISMI Department of Sciences and Methods for Engineering, Via Amendola 2, 42122, Reggio Emilia, Italy

[4]University of Bologna - DIN Department of Industrial Engineering, Viale Risorgimento 2, 40136, Bologna, Italy

[5]University of Modena and Reggio Emilia - InterMech - MO.RE, Piazzale Europa 1, Reggio Emilia 42124, Italy

[a]marco.negozio@unipr.it, [b]adrian.lutey@unipr.it, [c]antonio.segatori@hydro.com, [d]riccardo.pelaccia@unimore.it, [e]sara.didonato2@unibo.it, [f]barbara.reggiani@unimore.it, [g]l.donati@unibo.it

Keywords: Aluminum Alloy Extrusion, Finite Element Simulation, Artificial Neural Network, Peripheral Coarse Grain, Microstructure Prediction

Abstract. Peripheral Coarse Grain (PCG) is a critical defect that affects the mechanical and crash performance of extruded AA6XXX aluminum profiles, particularly in automotive applications. Traditional methods to address this issue rely on extensive experimental campaigns, which are resource-intensive and often lead to conservative process parameters, reducing production efficiency. This study develops and validates a predictive model for PCG formation, combining finite element method (FEM) simulations and machine learning (ML) techniques. Data from FEM simulations and experiments were used to train and test a model employing artificial neural networks (ANNs) for PCG prediction. The proposed approach enables accurate PCG forecasting, providing a robust tool for optimizing process parameters, reducing reliance on empirical methods and advancing smart manufacturing solutions.

Introduction

The extrusion of AA6XXX aluminum alloys plays a crucial role in manufacturing lightweight structural components, particularly for the automotive industry, where mechanical strength and crash resistance are critical factors influencing structural integrity [1,2]. However, one of the most persistent challenges in this process is the formation of Peripheral Coarse Grain (PCG), which can significantly degrade mechanical properties and energy absorption performance [3–5]. The mechanisms behind PCG formation are complex, as they depend on a combination of process parameters, such as billet temperature, extrusion speed and die geometry, as well as metallurgical factors like chemical composition of the billet material, dispersoid distribution and recrystallization kinetics [6].

Previous studies have explored various strategies to mitigate PCG, primarily relying on experimental investigations that require significant time and resources [7]. Computational approaches, particularly those based on Finite Element Method (FEM) simulations, have been employed to analyze the thermomechanical conditions leading to PCG formation [8,9]. However, despite their potential, these models often struggle to provide accurate predictions across different

Content from this work may be used under the terms of the Creative Commons Attribution 3.0 license. Any further distribution of this work must maintain attribution to the author(s) and the title of the work, journal citation and DOI. Published under license by Materials Research Forum LLC.

Materials Research Proceedings 57 (2025) 344-351 https://doi.org/10.21741/9781644903735-40

extrusion conditions. Recent advancements in machine learning (ML) have demonstrated promising results in improving the accuracy of predictions in the field of materials processing, particularly through the use of artificial neural networks (ANNs) that can be applied to large datasets, identifying complex relationships between variables [10,11].

In this work, three different extruded profiles in AA6082 alloy were analyzed experimentally, with microstructural observations carried out to measure PCG thickness in various positions within each profile. Data obtained from these experiments were then employed to train an ANN based on input data obtained via FEM simulations performed with commercial software package QForm Extrusion UK to predict the occurrence of PCG during the extrusion process.

The study aims to develop a framework for robust predictive modeling of PCG formation by integrating FEM simulations and ML techniques. The approach involves training ANNs using both numerical and experimental data to enhance predictive accuracy under diverse process conditions. By merging physics-based modeling and data-driven methodologies, this study provides an advanced tool for optimizing extrusion parameters, reducing dependency on iterative experimental methodologies and contributing to the development of intelligent manufacturing processes. The implementation of this predictive framework is expected to help industries improve the quality and efficiency of extruded aluminum components while minimizing risks associated with PCG formation.

Experimental Analysis

To validate the ANN developed for predicting microstructural evolution during extrusion, a hollow profile was produced using AA6082 alloy (Figure 1c). The extrusion process was conducted under five different sets of process parameters, with billet preheating temperatures of 450°C and 500°C. At 450°C, the ram speed was set to 5 mm/s and 15 mm/s, while at 500°C, tests were performed at 5 mm/s, 10 mm/s and 15 mm/s. The alloy chemical composition, homogenization parameters and press parameters including billet/tool dimensions and temperature distribution are reported in Table 1. Extrusion experiments were conducted in a strictly monitored environment to ensure correct acquisition of the extrusion load and profile exit temperature for validation of the FEM simulation. For ANN training, experimental data from two previously extruded profiles in the same alloy [8] were used (Figure 1a and 1b). The profile reported in this study served as an independent dataset to validate ANN prediction of the peripheral coarse grain defect.

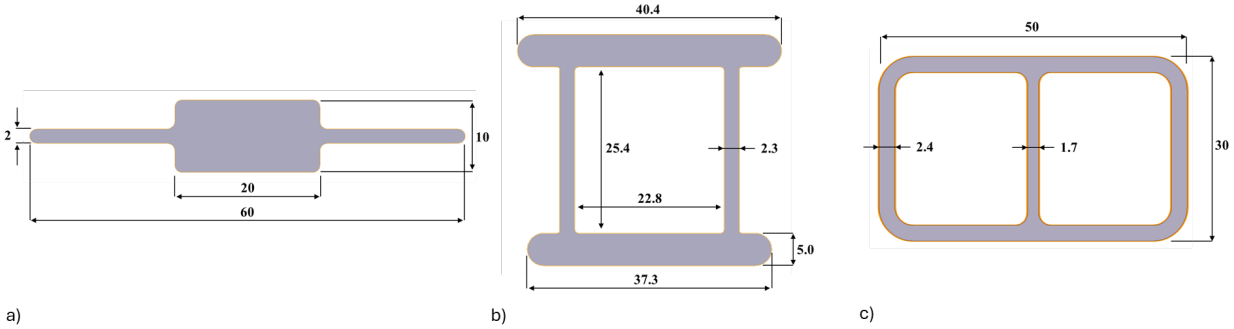


Figure 1: Geometry of a) Profile a; b) Profile b; c) Profile c.

Materials Research Proceedings 57 (2025) 344-351 https://doi.org/10.21741/9781644903735-40

Table 1: Process parameters employed for experiments.

Process parameters	Profile *a*	Profile *b*	Profile *c*
Press capacity [MN]	10	10	10
Aluminum alloy	AA6082	AA6082	AA6082
Extrusion ratio	18.2	31.5	21.9
Container temperature [°C]	410	410	410
Billet temperature [°C]	350 / 450 / 500	500	450 / 500
Die temperature [°C]	480	480	480
Billet length [mm]	400	350	400
Billet diameter [mm]	100	100	100
Billet Rest length [mm]	15	15	15
Billet Homogenization	565°C - 2h	565°C - 2h	565°C - 2h
Container diameter [mm]	107	107	107
Ram speed [mm/s]	2 / 5 / 10	2 / 5 / 10 / 15 / 20	5 / 10 / 15
Ram acceleration time [s]	5	5	5

Microstructural characterization was performed in the middle section of each extruded profile, where steady-state conditions were expected to be achieved in terms of temperature and velocity. Electrolytic etching (40 V dc, 4 min, 15 mL HBF_4 reagent, 750 mL H_2O), followed by image acquisition using the optical microscope Zeiss Axio Observer 3 was carried out to collect PCG data. The resulting micrographs were analyzed using ImageJ software to measure grain size and distribution. This analysis allowed direct comparison between predicted and experimentally observed microstructural features, providing insight into the model's accuracy and reliability.

Numerical Simulation

The extrusion process was simulated using QForm Extrusion UK. Within the software, a viscoplastic material model was employed to govern the process, meaning that material behavior was defined directly by a constitutive equation linking flow stress to strain, strain rate and temperature. Each individual extrusion experiment employing unique process parameters was investigated through a dedicated simulation. The Qshape tool within QForm was used to automatically generate and optimize the mesh for the tool components. Although standard mesh settings are generally recommended to balance precision and computational cost, simulations were performed with the finest available refinement to capture detailed process phenomena.

Material properties for AA6082 aluminum alloy employed in simulations are provided in [1]. The Hensel-Spittel law was employed to describe the flow behavior of AA6082. In this model, the flow stress, $\bar{\sigma}$, is expressed as a function of strain, $\bar{\varepsilon}$, strain rate, $\dot{\bar{\varepsilon}}$, and temperature T:

$$\bar{\sigma} = A \cdot e^{m_1 T} \cdot \bar{\varepsilon}^{-m_2} \cdot \dot{\bar{\varepsilon}}^{-m_3} \cdot e^{\frac{m_4}{\bar{\varepsilon}}} \cdot (1+\bar{\varepsilon})^{m_5 T} \cdot e^{m_7 \bar{\varepsilon}} \cdot \dot{\bar{\varepsilon}}^{m_8 T} \cdot T^{m_9} \quad (1)$$

For AA6082, parameter A is 280 MPa, while m_1 and m_5, which account for temperature effects, are –0.00461 K^{-1} and 0.00036 K^{-1}, respectively. Constants m_2, m_3, and m_4 are –0.16636, 0.12 and –0.02056, whereas m_7, m_8 and m_9 are all equal to zero [8].

Friction between the workpiece and tools was set based on optimized default values within Qform. Specifically, sticking conditions were applied at the billet interfaces with the container, ram and die, while the bearings were modeled using the Levanov friction model with m = 0.3 and n = 1.25.

Materials Research Proceedings 57 (2025) 344-351 https://doi.org/10.21741/9781644903735-40

Finally, to validate the simulation results, the predicted extrusion load and exit temperature of the profile were compared with experimental measurements. The exit temperature was recorded using a pyrometer aimed at the top-center of the investigated profiles. Discrepancies in both load and temperature predictions remained below 5%, underscoring the reliability of the simulation.

In accordance with the Negozio-Donati framework [12,13], parameters obtained directly from the FEM simulation were utilized to determine the maximum strain rate, $\dot{\varepsilon}_{max}$, Zener-Hollomon parameter, Z, subgrain size, δ, internal dislocation density, ρ_i, misorientation angle, Θ, stored energy, Pd, and percentage dynamic recrystallization, X_{DRX}. The approach for calculating the maximum strain rate was based on the procedure detailed in [13], which involves examining strain rate values at each time step throughout the deformation sequence from the initial billet to the final profile and determining the peak value. All remaining parameters were subsequently derived following the methodology described in [13], as outlined below.

$$\frac{1}{\delta} = C\,(lnZ)^n \tag{2}$$

$$Z = \dot{\varepsilon}_{max}\, exp\left(\frac{Q}{RT}\right) \tag{3}$$

$$\rho_i = \left(C_1 * Z^{C_2}\right) * (1 - e^{C_3 * \varepsilon}) \tag{4}$$

$$\Theta = (C_4 * Z^{C_5}) * (1 - e^{C_6 * \varepsilon}) \tag{5}$$

$$\mathrm{Pd} = \frac{Gb^2}{10}\left[\rho_i(1\text{-}\ln(10b\rho_i^{0,5})) + \frac{2\theta}{b\delta} * \left(1 + \ln\left(\frac{\theta c}{\theta}\right)\right)\right] \tag{6}$$

$$X_{DRX} = 1 - \exp\left[-\beta\left(\frac{\varepsilon - \varepsilon_c}{\varepsilon_s}\right)^m\right] \tag{7}$$

where T is the exit temperature, $C = 3.36\times10^{-9}$ m^{-1} and $n = 5.577$ are constants, Q is the activation energy of AA6082 (182000 J/mol·K), R is the universal gas constant (8.341 J/mol), G is the material shear modulus (2.05×10^{10} Pa), b is the Burgers vector (2.86×10^{-10} m) and Θc the misorientation angle limit (15°). For evaluation of the internal dislocation density, ρ_i, and misorientation angle, Θ, six material constants were determined from experimental data via regression (C_1= 328157965, C_2= 0.27, C_3= -5, C_4= 0.85, C_5= 0.05, C_6= -2.5). Finally, for calculation of X_{DRX}, ε_c is critical strain for DRX, ε_s is the saturated strain and β = 1.823 and m = 1.109 are material constants.

Figure 2 displays an example of FEM outcomes for extrusion of the Profile *c* with a billet temperature of 500 °C and ram speed of 15 mm/s. These results exhibit a generally symmetrical distribution for all investigated parameters across the two adjacent cavities. In particular, contour plots indicate that higher values tend to concentrate near the inner edges of cavities and along boundary regions, suggesting localized intensification of both stress and material flow. The temperature field appears relatively uniform, while plastic strain concentrates along the inner edges and corners where geometric discontinuities typically intensify stress. Stress-related fields exhibit pronounced peaks at corners, indicative of stress concentration that is typical in geometries with sharp transitions. The velocity exhibits a fairly balanced exit speed (velocity deviation < 5%) with negligible accelerated flow near the mid-plane between the cavities, gradually decreasing toward the outer edge. The percentage dynamic recrystallization (X_{DRX}) follows a similar pattern to plastic

Materials Research Proceedings 57 (2025) 344-351 https://doi.org/10.21741/9781644903735-40

strain, with relatively uniform regions in the bulk of the material and more pronounced gradients in proximity to the internal and external boundaries.

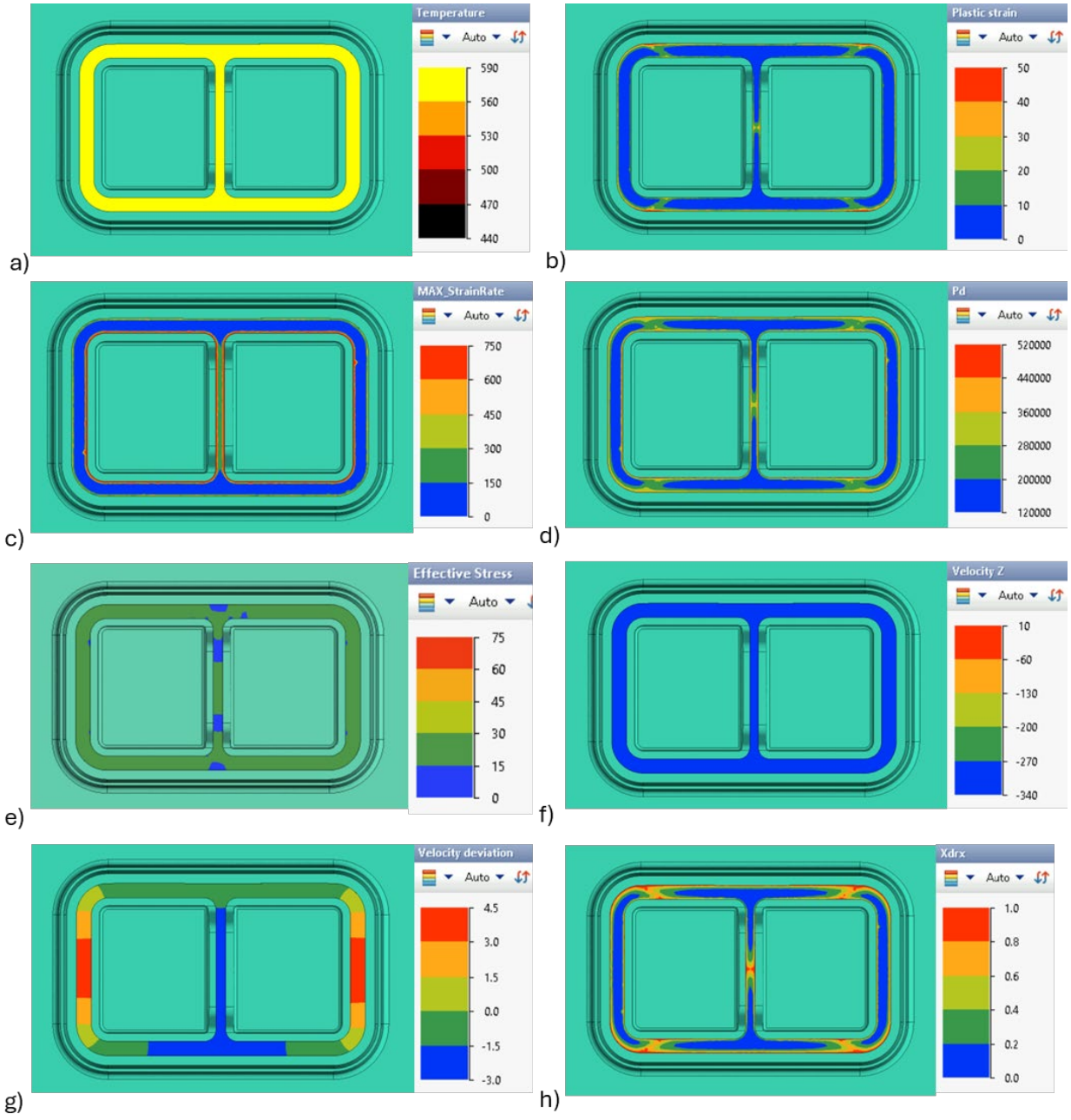


Figure 2: FEM outcomes for Profile c with a billet temperature of 500°C and ram speed of 15 mm/s: a) profile exit temperature, b) plastic strain, c) maximum strain rate, d) stored energy, e) effective stress, f) profile exit velocity, g) velocity deviation and h) $\boldsymbol{X_{DRX}}$.

ANN prediction model for PCG formation

A fully connected artificial neural network (ANN) for classification was trained for predicting PCG formation using simulation and experiment data from extrusion of Profiles *a* and *b* (Figure 1) in a previous study [8]. Training was performed with the *fitcnet* function in MATLAB employing the Broyden-Fletcher-Goldfarb-Shanno quasi-Newton algorithm (LBFGS) to minimize cross-entropy loss. Input parameters were considered as the exit temperature, strain, maximum strain rate, stored energy, percentage dynamic recrystallization, effective stress, velocity and

Materials Research Proceedings 57 (2025) 344-351 https://doi.org/10.21741/9781644903735-40

velocity deviation. The output parameter was considered as classification of PCG formation ('yes') or not ('no'). For training, labelled PCG data for Profiles *a* and *b* were employed as output data. Outcomes of hyperparameter optimization indicated that lowest cross-entropy loss was achieved with a single hidden layer with 22 neurons and a ReLU activation function. This configuration was employed for the final ANN employed to predict PCG formation in Profile *c*.

Results and Discussion

Figure 3 presents the microstructures of Profile *c* extruded with different process parameters. The outcomes are consistent with those reported in [8]. In particular, PCG formation is localized in regions where both the strain and maximum strain rate are highest, exhibiting notable correlation with the strain rate. For instance, when comparing microstructures obtained at the same extrusion speed but at different temperatures (e.g., Figure 3a and 3c, or Figure 3b and 3e), similar PCG thicknesses are observed. Moreover, analysis of Figure 3d and 3e reveals that increasing the ram speed from 10 mm/s to 15 mm/s does not significantly alter the PCG thickness, whereas a change is evident when increasing the speed from 5 mm/s to 10 mm/s (see Figure 3c and 3d). These results align with previous findings by the authors [6–8,14], where a proportional relationship between the ram speed and PCG thickness was identified up to a critical ram velocity. Beyond this threshold, the thickness remains essentially constant, likely due to the fact that the ram speed is not the sole factor governing PCG formation; temperature, plastic strain and consequently X_{DRX} must also exceed certain threshold levels.

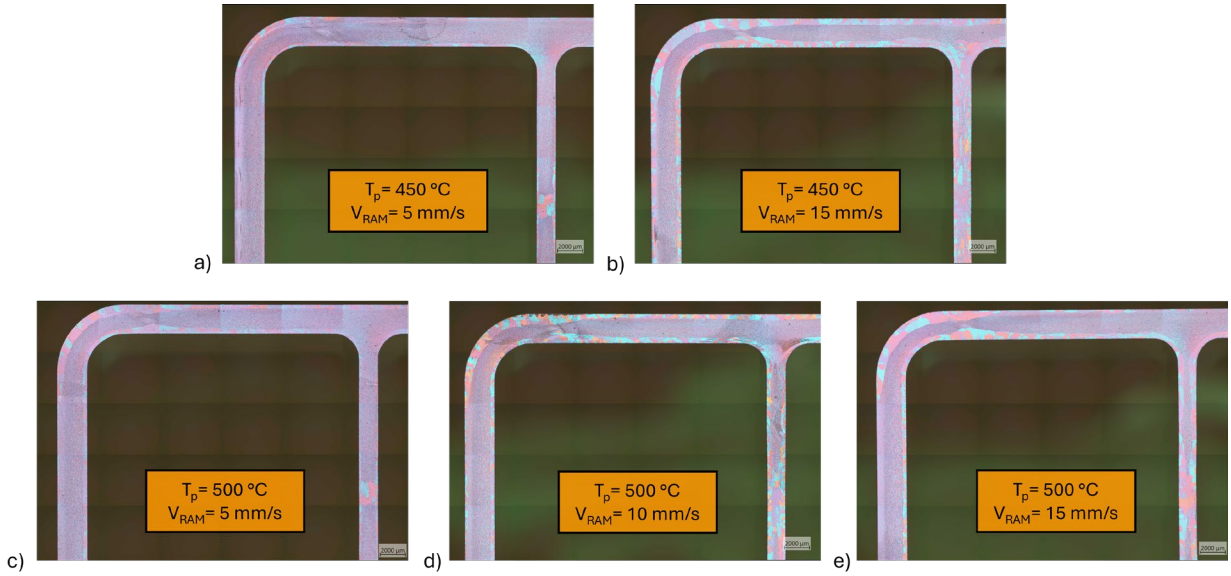


Figure 3: Cross-section images of extruded Profile c under different process conditions: a) T = 450 °C, V_{ram} = 5 mm/s; b) T = 450 °C, V_{ram} = 15 mm/s; c) T = 500 °C, V_{ram} = 5 mm/s; d) T = 500 °C, V_{ram} = 10 mm/s; e) T = 500 °C, V_{ram} = 15 mm/s.

Figure 4 presents maps of ANN predictions of PCG formation under the same conditions as in Figure 3. Marked alignment between predicted and experimental outcomes is evident both in terms of PCG extension and location. Figure 4a and 4b present extruded profiles obtained at a billet temperature of 450 °C, whereas Figure 4c, 4d and 4e correspond to a billet temperature of 500 °C. ANN predictions effectively capture the overall trend of experimental PCG formation, which increases proportionally to extrusion speed. However, some discrepancies can be observed at 15 mm/s, where predicted PCG formation at 450 °C is more extensive than in micrographs, despite similarities in PCG zones in both cases. Nonetheless, these differences do not compromise the overall accuracy of the prediction, especially considering that the analyzed scenario represents a

Materials Research Proceedings 57 (2025) 344-351 https://doi.org/10.21741/9781644903735-40

test case, thereby underscoring the value of the combined FEM and ANN approach. Further developments are warranted to generate a balanced training dataset comprising extruded profiles with varying dimensions produced under different process parameters. The implications of these outcomes in an industrial production setting are significant, with ANN prediction of PCG formation paving the way for rapid process optimization with next-generation digital tools.

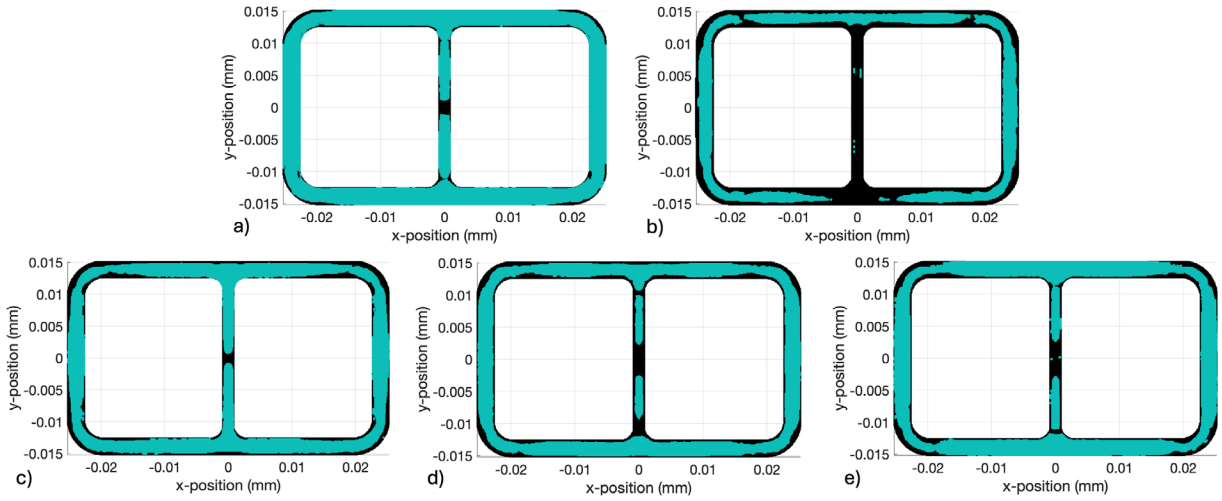


Figure 4: PCG prediction maps of extruded Profile c under different processing conditions: a) T = 450 °C, V_{ram} = 5 mm/s; b) T = 450 °C, V_{ram} = 15 mm/s; c) T = 500 °C, V_{ram} = 5 mm/s; d) T = 500 °C, V_{ram} = 10 mm/s; e) T = 500 °C, V_{ram} = 15 mm/s. PCG formation shown in black.

Conclusion

The present study has demonstrated integration of FEM simulations with ANNs to predict PCG formation in extruded profiles. The developed ANN was trained on both simulation and experimental data from two different AA6082 extruded profiles (Profiles *a* and *b*), utilizing eight input parameters including exit temperature, strain, maximum strain rate, stored energy, percentage dynamic recrystallization, effective stress, velocity and velocity deviation to classify PCG formation.

Experimental analysis of Profile *c*, extruded at billet temperatures of 450 °C and 500 °C and ram speeds of 5, 10 and 15 mm/s, confirmed that PCG formation was localized in regions of high strain and strain rate. Quantitatively, a proportional increase in PCG thickness with ram speed was observed up to a critical threshold, beyond which additional speed increases (e.g., from 10 mm/s to 15 mm/s) produced minimal changes in thickness. While the overall trends of predictions obtained with the trained ANN closely matched experimental observations, a slight discrepancy was noted at a billet temperature of 450 °C and ram speed of 15 mm/s, where the model indicated a higher extent of PCG formation compared to that observed in micrographs. Despite this minor deviation, the ANN prediction remained robust, particularly considering that the analyzed scenario served as a test case. These outcomes validate the effectiveness of the combined FEM and ANN approach for predicting microstructural phenomena, highlighting its potential for rapid process optimization. Future work will focus on generating a balanced training dataset, including extruded profiles of varying dimensions and processing parameters, to further enhance model accuracy and industrial applicability.

References

[1] Negozio M, Pelaccia R, Donati L, Reggiani B. Numerical investigation of the surface recrystallization during the extrusion of a AA6082 aluminum alloy under different process

conditions. Int J Adv Manuf Technol 2023;129:1585–99. https://doi.org/10.1007/s00170-023-12397-8

[2] Donati L, Reggiani B, Pelaccia R, Negozio M, Di Donato S. Advancements in extrusion and drawing: a review of the contributes by the ESAFORM community. Int J Mater Form 2022;15:41. https://doi.org/10.1007/s12289-022-01664-w

[3] Li Z, Qin J, Zhang H, Wang X, Zhang B, Nagaumi H. Improved Distribution and Uniformity of α-Al(Mn,Cr)Si Dispersoids in Al-Mg-Si-Cu-Mn (6xxx) Alloys by Two-Step Homogenization. Metall Mater Trans A 2021;52:3204–20. https://doi.org/10.1007/s11661-021-06243-3

[4] Qian X, Parson N, Chen X-G. Effects of Mn addition and related Mn-containing dispersoids on the hot deformation behavior of 6082 aluminum alloys. Mater Sci Eng A 2019;764:138253. https://doi.org/10.1016/j.msea.2019.138253

[5] Negozio M. Experimental analysis and modeling of the recrystallization behaviour of a AA6060 extruded profile, 2023, p. 477–86. https://doi.org/10.21741/9781644902479-52

[6] Eivani AR, Zhou J. Application of physical and numerical simulations for interpretation of peripheral coarse grain structure during hot extrusion of AA7020 aluminum alloy. J Alloys Compd 2017;725:41–53. https://doi.org/10.1016/j.jallcom.2017.06.297

[7] Eivani AR, Zhou J, Duszczyk J. Mechanism of the formation of peripheral coarse grain structure in hot extrusion of Al-4.5Zn-1Mg. Philos Mag 2016;96:1188–96. https://doi.org/10.1080/14786435.2016.1157637

[8] Negozio M, Segatori A, Pelaccia R, Reggiani B, Donati L. Experimental investigation and numerical prediction of the peripheral coarse grain (PCG) evolution during the extrusion of different AA6082 aluminum alloy profiles. Mater Charact 2024;209:113723. https://doi.org/10.1016/j.matchar.2024.113723

[9] Eivani AR, Jafarian HR, Zhou J. Simulation of peripheral coarse grain structure during hot extrusion of AA7020 aluminum alloy. J Manuf Process 2020;57:881–92. https://doi.org/10.1016/j.jmapro.2020.07.011

[10] Negozio M, Ferraro V, Donati L, Lutey AHA. Predicting grain size in extruded AA6063 profiles: A unified approach based on finite element analysis and machine learning. Int J Adv Manuf Technol 2024;133:4543–60. https://doi.org/10.1007/s00170-024-14021-9

[11] Shang H, Wu P, Lou Y, Wang J, Chen Q. Machine learning-based modeling of the coupling effect of strain rate and temperature on strain hardening for 5182-O aluminum alloy. J Mater Process Technol 2022;302:117501. https://doi.org/10.1016/j.jmatprotec.2022.117501

[12] Negozio M, Pelaccia R, Donati L, Reggiani B. Simulation of the microstructure evolution during the extrusion of two industrial-scale AA6063 profiles. J Manuf Process 2023;99:501–12. https://doi.org/10.1016/j.jmapro.2023.05.075

[13] Negozio M, Segatori A, Pelaccia R, Reggiani B, Donato SD, Donati L. Modeling of recrystallization behaviour of AA6xxx aluminum alloy during extrusion process. Trans Nonferrous Met Soc China 2024;34:3170–84. https://doi.org/10.1016/S1003-6326(24)66600-8

[14] Negozio M, Di Donato S, Pelaccia R, Lutey AH, Carosi D, Reggiani B, et al. Impact of die design and bearing geometry on grain size and PCG formation during extrusion of AA6082 aluminum alloy. J Mater Sci Technol 2025;230:80–92. https://doi.org/10.1016/j.jmst.2025.01.017

Materials Research Proceedings 57 (2025) 352-359 https://doi.org/10.21741/9781644903735-41

Investigating the tube production via friction stir extrusion of aluminum chips

Riccardo PULEO[1,a*], Muhamad ADNAN[1,b], Giuseppe INGARAO[1,c], Gianluca BUFFA[1,d], Livan FRATINI[1,e]

[1]Department of Engineering, University of Palermo, Viale delle Scienze, Palermo, 90128, Italy

[a]riccardo.puleo01@unipa.it, [b]muhammad.adnan06@unipa.it, [c]giuseppe.ingarao@unipa.it, [d]gianluca.buffa@unipa.it, [e]livan.fratini@unipa.it

Keywords: Aluminium Alloys, Manufacturing Materials, Sustainability, FSE

Abstract. Friction stir extrusion (FSE) is one of the friction stir based techniques commonly adopted among the solid state recycling (SSR) category. In the last decade this process was widely explored as one of the most straightforward applications for wire or rod production from recycling metal scraps. Nowadays, the friction stir extrusion techniques have also been investigated as a possible alternative for tube production. In this research, this friction-based process was explored aiming to obtain a consolidated tube by directly processing machining chips. Generally, the FSE setup involves a die, where the metal scraps are collected, and a tool with a designed hole for backward extrusion, but for the case of tube production the setup changes, and the clearance between die and tool becomes the extrusion channel. This process was investigated by varying the vertical load and the rotational speed of the tool, which were directly linked to the pressure and heat generation, respectively. Three parameter combinations were selected, namely cold, warm, and hot conditions. Moreover, a numerical simulation campaign was developed to give an insight into the process' dynamics and material flow characteristics.

Introduction

Primary aluminium production is the most energy demanding production process among the five key materials which have the highest greenhouse gas (GHG) emissions released by industry worldwide every year [1]. The implementation of circular economy strategies has been one of the most important approaches for reducing the primary production and decoupling the resource depletion from the economic growth [2]. Among the circular economy strategies, material recycling resulted to have a great applicability for aluminium scraps. Aluminium scraps were commonly recycled through conventional methods, e.g. remelting and recasting, which are characterized by high energy demand and material losses due to the oxidation of the light fragments floating on the melting bath. In the last decade, researchers have addressed these drawbacks by switching their focus to the solid-state recycling (SSR) techniques, where the metal scraps are processed and turned into consolidated products without reaching the melting condition; the working temperature is always below the melting point, therefore the melting phase is skipped. Among the SSR techniques, the most applied for recycling purposes are the equal channel angular pressing (ECAP), where metal chips are converted into consolidated extruded products having round or hollow profile [3], [4], friction-induced recycling processes (FIRP) which were born to rework solid wires but are also used for recycling metal scraps [5]. Moreover, a more static process is the spark plasma sintering (SPS) proposed by Paraskevas et. al [6]. Among the friction stir based technologies, it is worth mentioning the friction stir consolidation (FSC) [7], [8], [9] which directly turns recycling chips into consolidated billets, and friction stir extrusion [10], [11], [12] commonly used for turning recycling chips into wires and rods. Recently, the friction stir extrusion process was also explored for tube production, in this respect Asadi et al. [13] investigated the impact of

Content from this work may be used under the terms of the Creative Commons Attribution 3.0 license. Any further distribution of this work must maintain attribution to the author(s) and the title of the work, journal citation and DOI. Published under license by Materials Research Forum LLC.

Materials Research Proceedings 57 (2025) 352-359 https://doi.org/10.21741/9781644903735-41

the tool taper angle for tube manufacturing by FSE, Zhang et al. [14] studied the effect of the oxide fragments on tube's mechanical and microstructure properties. Lastly, Behnagh et al. [15] investigated the production of seamless tube via friction stir consolidation of aluminium machining chips. In most of the research, the recycling chips are first homogenized or consolidated and then turned into a tube, for this reason this paper aims to study the feasibility of the friction stir extrusion technique to turn chips into consolidated tube, by skipping a homogenizing/consolidation step. Specifically, three combinations of process parameters have been selected to point out the effect of three different thermal conditions, and a numerical campaign was performed to investigate the material flow and the evolution of the field variables during the process.

Material and methods

A fixed mass of 40 g aluminium chips, obtained from a milling process of a AA2024-O round bar characterized by a Vicker hardness 61.5, was cleaned in acetone, dried and collected into a die with 25 mm inner diameter. The process was carried out by using two different tools: one 24.9 mm diameter, for the compaction phase (Fig. 1a), the second one was designed to provide a clearance of 1.5 mm with the die, for the tube production phase (Fig. 1b). The die chamber was not big enough to host the entire mass of chips, therefore two compaction phases were needed. After two pre-compactions at 35 kN, the chips were friction stir extruded into tubes 1.5 mm thickness. The tubes were produced by exploring three process parameters combination 1000 rpm – 15kN, 1500 rpm – 15kN and 2000 rpm – 15kN, from now on referred to as "cold", "warm" and "hot" conditions, respectively (table 1). The obtained specimens were mounted, polished and etched using the Keller's reagent (2 ml HF, 3 ml HCl, 5 ml HNO_3, and 190 ml H_2O) and a microstructure analysis was performed by using the GX51 Olympus optical microscope for the grain size evaluation.

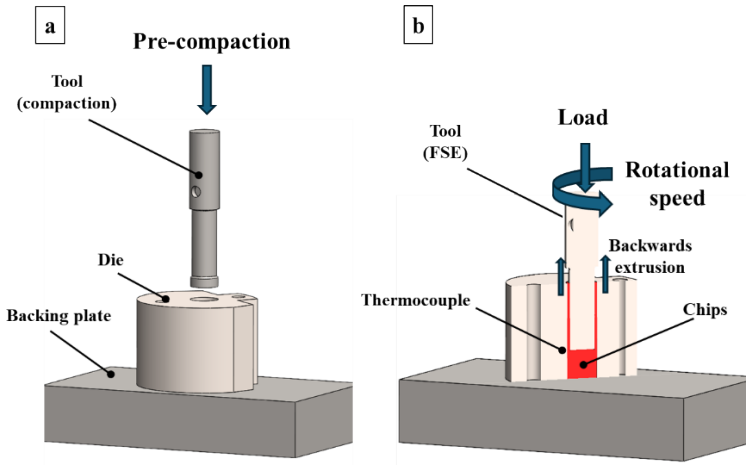


Fig. 1. *a) pre-compaction setup and b) friction stir extrusion setup.*

Table 1. *Parameter combinations for friction stir extrusion of tubes.*

Rotational speed [rpm]	Force [kN]	Condition
1000	15	cold
1500	15	warm
2000	15	hot

The same process parameters were used for the numerical simulation of the process. A numerical model was created on SFTC DEFORM environment (Fig. 2a). In this approach the

Materials Research Proceedings 57 (2025) 352-359 https://doi.org/10.21741/9781644903735-41

recycling chips were considered as porous billet having an initial relative density of 0.7 and a mesh window of 30000 elements. Moreover, a refined mesh window was placed along the tool-material contact to improve the quality of the results near the more stressed part. The other components were modelled as rigid bodies with a mesh size of 60000, 60000 and 30000 elements for the tool, die and backing plate, respectively. The Shear factor was set to 0.2 and the heat transfer coefficient equal to 11, 45, 45 J/mm/K, for the billet-tool, die-billet and backing plate-billet contacts. These values were obtained after a tuning of the experimental temperature recorded using a thermocouple placed at 1/3 of the die height and distanced by 1 mm from the internal wall (Fig. 2b).

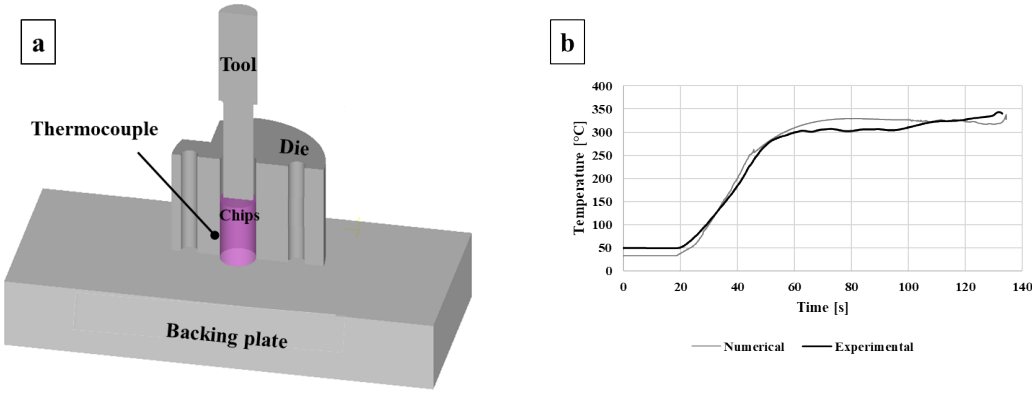


Fig. 2. *a) numerical setup of the friction stir extrusion of tube and b) temperature tuning for the case 1500 rpm – 15 kN.*

The material flow was also explored using numerical simulations, from the beginning of the process to 50 seconds of tube production.

Results and discussion

The tubes produced by FSE are presented in figure 3, where the main macroscopical differences are depicted. Comparing figure 3a and 3c, it is possible to see that the effect of the temperature on the material has an important impact. For the 1000 rpm (Fig. 3a), the temperature (Fig. 4) reached during the process was not high enough to provide the correct softening of the material, moreover the chips are still visible at the bottom and top portion of the tube. On the other hand, the temperature of the case study 2000 rpm was too high resulting in an extreme softening exhibiting hot cracks phenomena (Fig. 3c). The "warm" condition has the most uniform tube surface (Fig. 3b).

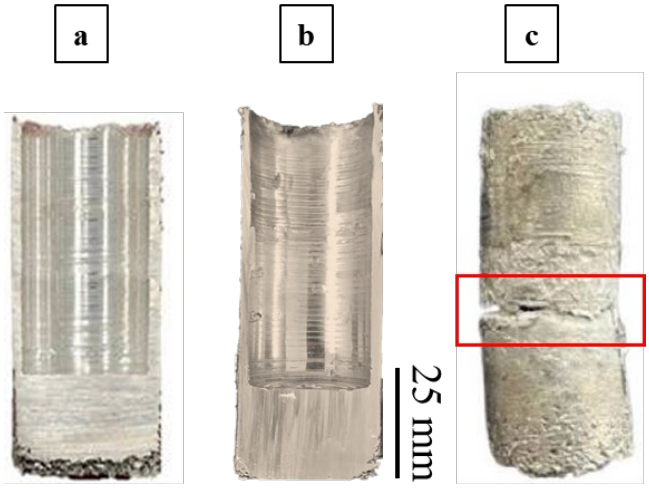


Fig. 3. *Tube produced at a) 1000 rpm – 15 kN, b) 1500 rpm – 15 kN, and c) 2000 rpm – 15 kN.*

Materials Research Proceedings 57 (2025) 352-359 https://doi.org/10.21741/9781644903735-41

The experimental temperature and displacement recordings are plotted and compared in figure 4a and 4b. Although the thermocouple was not directly in contact with the material, it was positioned close to the zone where the highest temperature was predicted by the numerical simulation (Fig. 7). In figure 4a, the 2000 rpm case study showed the highest temperature peak, and obviously the process lasted less time than the other tests (Fig. 4b). It is clear that lower temperatures result in longer process time due to the low extrusion rate.

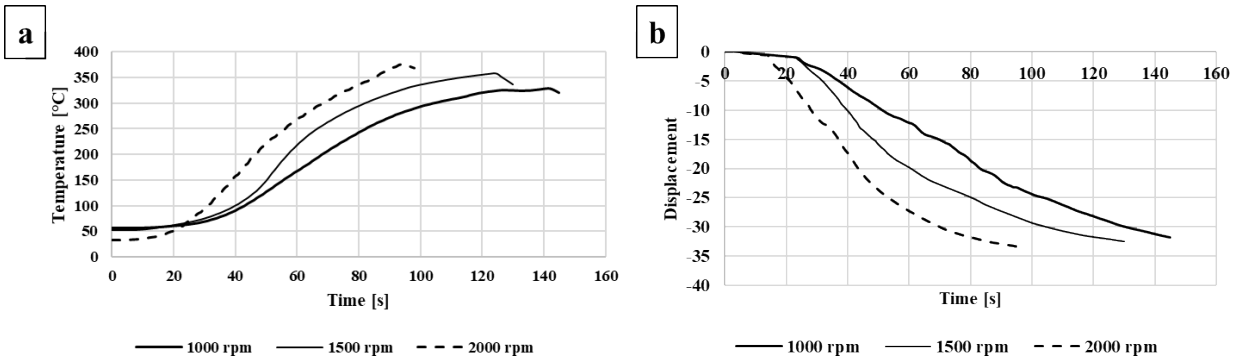


Fig. 4. *a) Temperature and b) displacement comparison for all three case study.*

Concerning the tube's quality, the grain size values were investigated in three loci along the ring section of the tube. Specifically, two observation loci were considered close to the internal and external surface, while the third one at the middle of the ring thickness (Fig. 5a). From this analysis, it resulted that in terms of average grain size the 1000 rpm had the lowest value compared to 1500 and 2000 rpm. It can be assumed that at the same vertical load, lower rotational speed leads to lower heat generation which slows down the process (long process time), but as the temperature was not high enough the grain growth was limited. It is worth remarking that in all three cases the hardness values exhibited an increment of approximately 200-250 % with respect to the base material (Fig. 5e).

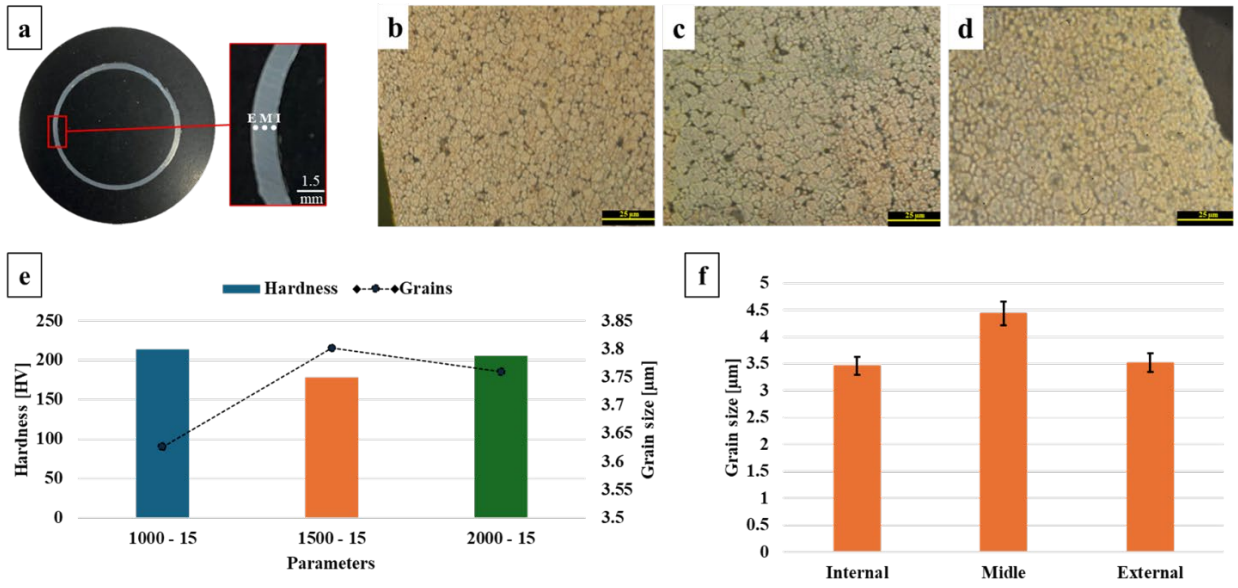


Fig. 5. *a) Loci position for the b) external (E), c) middle (M) and d) internal (I) grain size analysis. e) average grain size and hardness distribution and f) Internal, middle and external grain size 1500 rpm – 15 kN.*

Materials Research Proceedings 57 (2025) 352-359 https://doi.org/10.21741/9781644903735-41

Looking at the single value of the grain size at the internal, middle and external loci, different grain's dimension has been observed (Fig. 5f). Specifically, the grain size at the middle (Fig. 5c) of the ring surface results to be the largest compared with the internal (Fig. 5d) and external one (Fig. 5b) and, this phenomenon can be explained looking at figures 6 and 7. Due to the high rotational speed, the tool-tube contact is characterized by a high level of strain which generates a higher surface roughness than the external surface, where the material undergoes lower frictional effects. Additionally, a variable grain size along the radial direction was already observed in literature [16] for the friction stir extrusion of wires, and it was mainly related to the strain level which the wire was subject to. A material flow analysis (Fig. 6) was also performed by implementing the flownet method (feature of Deform 3D); this method allows to create a grid of squares (100x50) on the porous-billet's cross-section for studying the distortion of this surface during the process. In this figure, the initial state (Fig. 6a) was compared to 50 seconds of process (Fig. 6b) and, it is clear that, because of tool's friction at the bottom of the tool, the material is subjected to a uniform circular stirring effect, whilst on the side of the tool the material has a high non- uniform flow. This effect in the side part is more emphasized near the bottom part of the tool as the material is progressively extruded.

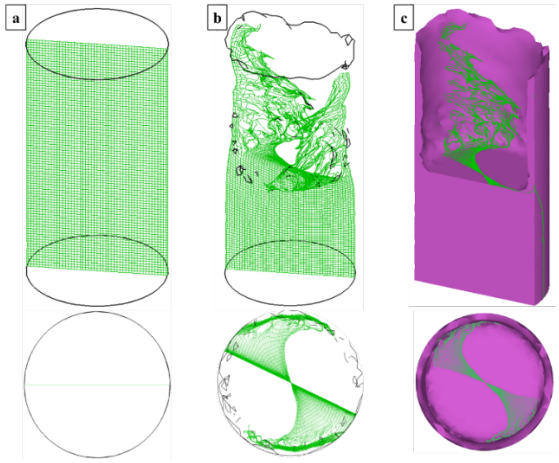


Fig. 6. *Flownet plot of the material flow during tube production at a) initial state (0 seconds), b) 50 seconds, and c) flownet plot on tube surface at 50 seconds.*

It can be assumed that the same phenomenon happens during the tube production process. The tool's stirring effect generates a high level of strain on the internal surface which, combined with the high temperature condition (Fig. 7), leads to the grain's recrystallization. Despite the strain level in the external surface of the tube are less than the internal one, as it is visible in figure 3, the external surface is affected by a low level of roughness which results in an inhibiting of the grain growth, therefore the grain size close to the external surface are as small as the internal one (Fig. 5f).

Materials Research Proceedings 57 (2025) 352-359 https://doi.org/10.21741/9781644903735-41

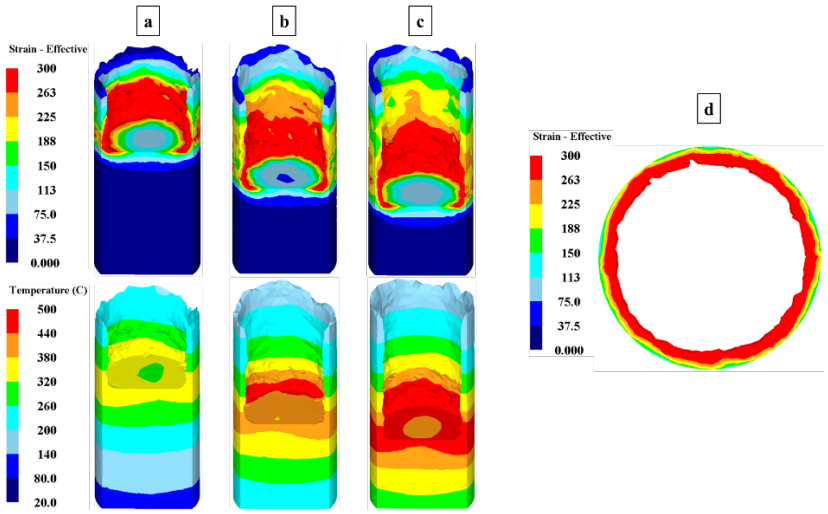


Fig. 7. *Effective strain and temperature plot for a) 1000 rpm, b) 1500 rpm and c) 2000 rpm, at 50 seconds of process, d) ring cross section of the tube for the strain evaluation along the radial direction.*

Conclusions

The friction stir extrusion process was successfully performed for obtaining tube from recycling aluminium chips. Three tests were conducted by varying the rotational speed at the same vertical load to test the feasibility of the process at different heat inputs. The conclusions drawn are the following:

- Tube production is possible starting directly from chips instead of using bulk material or homogenized chips-billet.
- The parameters combination 1000 rpm - 15 kN and 2000 rpm – 15 kN showed small grain size and high hardness, compared to the 1500 rpm – 15 kN. The average hardness measured was 180 - 200 HV which is around 200 % of the base material one (61.5 HV).
- The grain size is small in the surfaces close to the tool and die contact, while it is big at the middle of the tube's ring cross section.
- The temperature and strain are crucial to obtain a good tube. If it is too high, the tube may be soft enough to break but on the other hand, if it is too low, the tube may have low bonding occurrence.
- The flow analysis showed a homogeneous flow right below the tool while an inhomogeneous flow characterized the material along the side of the tool. Moreover, the biggest concentrations of strain are close to the bottom part of the tool where the extrusion starts.

Acknowledgements

Part of this study was funded by Italian MUR funds through European Union-NEXT Generation EU scheme; title of the project: "Finalizing processes for multi-material based Functionally Graded billets and wires obtained through solid state recycling operations of aluminum alloy chips - FULL RECYCLE", PRIN 2022.

Part of this study was also carried out within the activity of project using Italian MUR funds: "Aluminum Low Impact Circular Economy (ALICE)", funded by the European Union - Next Generation EU, Mission 4 Component 1, Project: P2022WN727, CUP: B53D23027340001 PRIN 2022-PNRR.

References

[1] G. Oberhausen, Y. Zhu, and D. R. Cooper, "Reducing the environmental impacts of aluminum extrusion," *Resour Conserv Recycl*, vol. 179, Apr. 2022. https://doi.org/10.1016/j.resconrec.2021.106120

[2] T. Tolio *et al.*, "Design, management and control of demanufacturing and remanufacturing systems," *CIRP Ann Manuf Technol*, vol. 66, no. 2, pp. 585–609, 2017. https://doi.org/10.1016/j.cirp.2017.05.001

[3] B. S. Taysom *et al.*, "Shear assisted processing and extrusion of enhanced strength aluminum alloy tubing," *Int J Mach Tools Manuf*, vol. 169, Oct. 2021. https://doi.org/10.1016/j.ijmachtools.2021.103798

[4] S. Whalen *et al.*, "Porthole die extrusion of aluminum 6063 industrial scrap by shear assisted processing and extrusion," *Manuf Lett*, vol. 36, pp. 52–56, Jul. 2023. https://doi.org/10.1016/j.mfglet.2023.01.005

[5] T. Borgert, D. Milaege, S. Schweizer, W. Homberg, M. Schaper, and T. Tröster, "Potentials of a friction-induced recycling process to improve resource and energy efficiency in manufacturing technology," *International Journal of Material Forming*, vol. 16, no. 6, Nov. 2023. https://doi.org/10.1007/s12289-023-01785-w

[6] D. Paraskevas, S. Dadbakhsh, J. Vleugels, K. Vanmeensel, W. Dewulf, and J. R. Duflou, "Solid state recycling of pure Mg and AZ31 Mg machining chips via spark plasma sintering," *Mater Des*, vol. 109, pp. 520–529, Nov. 2016. https://doi.org/10.1016/j.matdes.2016.07.082

[7] A. Latif, G. Ingarao, M. Gucciardi, and L. Fratini, "A novel approach to enhance mechanical properties during recycling of aluminum alloy scrap through friction stir consolidation," *International Journal of Advanced Manufacturing Technology*, vol. 119, no. 3–4, pp. 1989–2005, Mar. 2022. https://doi.org/10.1007/s00170-021-08346-y

[8] R. Puleo, A. Latif, G. Ingarao, and L. Fratini, "A generalized parametric model for the bonding occurrence prediction in friction stir consolidation of aluminum alloys chips," *J Manuf Process*, vol. 131, pp. 604–618, Dec. 2024. https://doi.org/10.1016/j.jmapro.2024.09.049

[9] S. Kefyalew Abebe, D. K. Sinha, H. Beri Tufa, and G. A. Mengesha, "Physical and mechanical behavior of aluminum-magnesium alloy matrix hybrid composite fabricated through friction stir consolidation process," *Advances in Mechanical Engineering*, vol. 15, no. 6, Jun. 2023. https://doi.org/10.1177/16878132231180013

[10] K. TAHMASBI, M. MAHMOODI, and H. TAVAKOLI, "Corrosion resistance of aluminum alloy AA7022 wire fabricated by friction stir extrusion," *Transactions of Nonferrous Metals Society of China (English Edition)*, vol. 29, no. 8, pp. 1601–1609, Aug. 2019. https://doi.org/10.1016/S1003-6326(19)65067-3

[11] G. Buffa, D. Campanella, F. Micari, and L. Fratini, "Design and development of a new machine tool for continuous friction stir extrusion," *CIRP J Manuf Sci Technol*, vol. 41, pp. 391–400, Apr. 2023. https://doi.org/10.1016/j.cirpj.2023.01.004

[12] G. Ingarao, D. Baffari, E. Bracquene, L. Fratini, and J. Duflou, "Energy demand reduction of aluminum alloys recycling through friction stir extrusion processes implementation," in *Procedia Manufacturing*, Elsevier B.V., 2019, pp. 632–638. doi: 10.1016/j.promfg.2019.04.079

[13] P. Asadi, M. Akbari, T. Sadowski, Y. D. Asl, N. Choupani, and F. Bedir, "Examining the

impact of tool taper angle in Al-Si tube manufacturing by friction stir extrusion," *J Manuf Process*, vol. 131, pp. 532–544, Dec. 2024. https://doi.org/10.1016/j.jmapro.2024.09.047

[14] Z. Zhang *et al.*, "Effects of Oxide Fragments on Microstructure and Mechanical Properties of AA6061 Aluminum Alloy Tube Fabricated by Thermomechanical Consolidation of Machining Chips," *Materials*, vol. 16, no. 4, Feb. 2023. https://doi.org/10.3390/ma16041384

[15] R. A. Behnagh, F. Fathi, M. Yeganeh, M. Paydar, M. A. Mohammad, and Y. Liao, "Production of seamless tube from aluminum machining chips via double-step friction stir consolidation," *International Journal of Advanced Manufacturing Technology*, vol. 104, no. 9–12, pp. 4769–4777, Oct. 2019. https://doi.org/10.1007/s00170-019-04326-5

[16] D. Baffari, G. Buffa, and L. Fratini, "A numerical model for Wire integrity prediction in Friction Stir Extrusion of magnesium alloys," *J Mater Process Technol*, vol. 247, pp. 1– 10, Sep. 2017. https://doi.org/10.1016/j.jmatprotec.2017.04.007

Materials Research Proceedings 57 (2025) 360-368 https://doi.org/10.21741/9781644903735-42

Identification of tool tip frequency response function through surface location error

Lorenzo MORELLI[1,a *], Niccolò GROSSI[1,b], Antonio Scippa[1,c]

[1]Department of Industrial Engineering, University of Firenze, Via di Santa Marta 3, Firenze 50139, Italy

[a]lorenzo.morelli@unifi.it, [b]niccolo.grossi@unifi.it, [c]antonio.scippa@unifi.it

Keywords: Milling, Vibration, Geometrical Tolerances

Abstract. In machining, tool vibrations are one of the main causes of process inaccuracies and poor finishing. To tackle these phenomena, the identification of the tool tip frequency response function (FRF) is essential, since it allows to determine the most suitable cutting conditions for an accurate and stable cut. Nonetheless, the identification of the tool tip FRF is usually achieved through experimental modal methods whose set up and testing phases require specific expertise as well as sensors and devices to be mounted on the machine tool. This paper investigates a methodology to identify tool tip FRF starting from the surface location error (SLE) without the need of additional equipment for the machine tool. The method exploits on-machine sensors (i.e., measuring probe), and it identifies tool tip FRF using a frequency domain cutting force model and the SLEs measured in different cutting tests. The method was experimentally tested to verify its effectiveness and limitations.

Introduction

The accuracy and surface finishing are essential features for the functioning of mechanical components in their application. These features are usually obtained with machining processes which realize the desired shape through cutting tools. Nonetheless, due to the tool flexibility, in certain conditions vibrations may compromise the cutting process leading to poor finishing and inaccuracies [1]. To deal with vibrations, several approaches are found in literature from predictive methods [2], which evaluate the impact of vibrations before the cutting process, to damping systems [3] which reduce vibrations on their occurrence during the cutting process. The effectiveness and reliability of these methods strongly depend on the tool Frequency Response Function (FRF), also known as tool "receptance". Indeed, the tool receptance is an essential input of any methods dealing with vibration in machining since it describes the tool response in terms of flexibility to an applied load as a function of the frequency [4]. Nonetheless, the estimation of the tool FRF is tricky from an experimental point of view due to the limitations and uncertainties of the available measuring techniques. Generally, tool FRF is measured through Experimental Modal Analysis (EMA) which includes a device to excite the tool and sensor to measure the tool response. In this context, impact hammer testing adopts an instrumented hammer to excite the tool and an accelerometer to measure the tool response; this method is widely used for its simplicity, yet poor measurement repeatability, which is related to the expertise of the operator, limits the reliability of this method. Indeed, this method applies to the tool mounted on the machine tool in its idle condition with limited accessibility. Furthermore, this limitation does not allow to include operational aspects, such as spindle speed, which may influence the tool behaviour [5]. To fill this gap, alternative methods to identify tool FRF under operational condition have been investigated. Focusing on milling processes, Wiederkehr et al. [6] presented a method to evaluate tool FRF in micro-milling based on shooting microspheres during its rotation. Similarly, Bachrathy et al. [7] presented an online measurement method with a ball shooter to evaluate workpiece FRF in thin wall milling. On the other hand, Takàcs et al. [8] measured the tool FRF using a ball shooter and

Content from this work may be used under the terms of the Creative Commons Attribution 3.0 license. Any further distribution of this work must maintain attribution to the author(s) and the title of the work, journal citation and DOI. Published under license by Materials Research Forum LLC.

Materials Research Proceedings 57 (2025) 360-368 https://doi.org/10.21741/9781644903735-42

a contactless photonic beam reduction sensor. Yamato et al. [9] developed a non-contact electromagnetic loading system to measure the FRF of the spindle system through a dummy tool. Instead, Zaghbani et al. [10] used Operational Modal Analysis (OMA) techniques to estimate tool FRF using only accelerometers signals acquired during actual cutting tests. In this case the tool FRF accounts for the actual operational conditions, yet no information was available regarding the excitation used to measure the tool FRF limiting its application in defining tool FRF parameters. To overcome this limit, Aguirre et al. [11] used the cutting force harmonics as excitation to estimate fixture FRF with a dynamometric tool holder. Overall methods to identify tool FRF in milling rely on additional sensors to be added to the machine tool, and depending on the accuracy and reliability required for the application these methods become costly and time consuming. Nonetheless, Budak et al [12] presented an analytical inverse approach to identify some of the parameters (i.e., damping ratios) defining the tool FRF directly from chatter tests without the need of additional sensors. The method considers the operating conditions and identifies the FRF parameters, yet it is limited to simple cases due to the limitations of the analytical model adopted as reference. In this regard, this paper investigates an inverse analytical method to estimate tool FRF using only a measuring probe, which is usually present on modern machine tool. In detail, the proposed method is dedicated to peripheral milling which presents a particular feature. Indeed, in peripheral milling surface error is not constant but present a particular shape along the tool axis [13]. This error, known as Surface Location Error (SLE), changes with the cutting conditions, and it can be predicted using the analytical method proposed by Schmitz et al. [14]. The main idea of the proposed method is to use SLE measured in cutting tests to obtain the tool FRF through a frequency domain cutting force model. The proposed method has been experimentally validated to test its effectiveness. The applicability of this method is limited to peripheral milling and simple cases where the mathematical model is valid, yet the simplicity of the approach along with the absence of additional sensors are advantages which make the proposed method a valid alternative.

Proposed approach

The proposed approach aims at evaluating the tool FRF from measured surface errors in peripheral milling. First, an overview of the process and surface error, also known as Surace Location Error (SLE) is shown in Fig. 1a where x is the feed direction, y is the cross-feed direction and z is the tool axis direction. In detail, in peripheral milling SLEs are caused by the tool flexibility in the cross-feed direction, and they present a particular shape along the axial depth of cut a_p (Fig. 1b). This shape is due to the tool helix angle (α_{el}) which allows the machined surface to be generated gradually and not instantly. Furthermore, this shape is not constant, but it changes according to the tool geometry, cutting parameters and cutting strategy (i.e., down-milling or up-milling) [13]. The time interval t_s in which the machined surface is created is expressed according to the following equations:

$$t_s = [\frac{\phi_{out}}{2\pi n}, \frac{\phi_{out}+\alpha_{sw}}{2\pi n}] \quad \text{down-milling;} \; t_s = [\frac{\phi_{in}}{2\pi n}, \frac{\phi_{in}+\alpha_{sw}}{2\pi n}] \quad \text{up-milling;} \tag{1}$$

$$\alpha_{sw} = k_b a_p; \; k_b = 2\tan(\alpha_{el})/D \tag{2}$$

where ϕ_{out} and ϕ_{in} are the tool exit and entry angles respectively, α_{sw} is the axial engagement, n is the spindle speed expressed in rpm, k_b is the lag introduced by the helix angle, and D is the tool diameter.

Materials Research Proceedings 57 (2025) 360-368 https://doi.org/10.21741/9781644903735-42

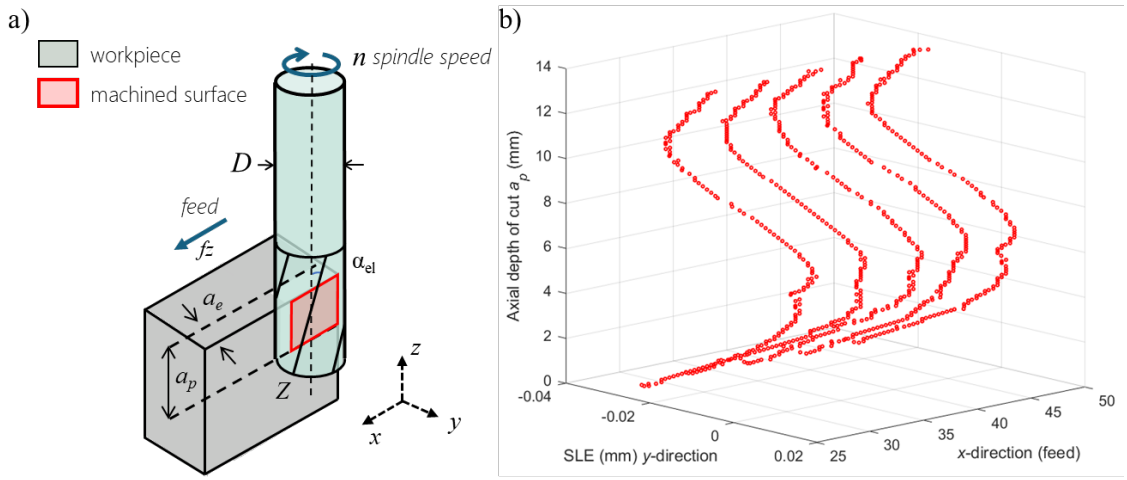


Fig. 1 a) Peripheral milling process b) Surface Location Error in peripheral milling

Considering these aspects related to the surface generation, the tool FRF, which this work is focused on, is the direct tooltip FRF in the cross-feed direction, and it is referred to as $G_{yy}(\omega)$ where ω indicates the frequency variable in the frequency domain. In literature SLEs are predicted with the analytical method by Schmitz et al. [14] which estimates SLE starting from the following equation in the frequency domain:

$$Y(\omega) = G_{yy}(\omega) * F_y(\omega); \tag{3}$$

where $Y(\omega)$ is the tooltip displacement in the frequency domain, while $F_y(\omega)$ is the cutting force spectrum in the cross-feed direction; From the inverse Fourier transform of $Y(\omega)$ the tooltip displacement in the time domain $y(t)$ is found, and SLE is obtained by evaluating $y(t)$ at the instants in which the machined surface is created (Eq.1):

$$SLE = y(t_s); \tag{4}$$

Using the analytical method by Schmitz et al. [14] as reference an inverse analytical method was developed. In detail, the proposed approach requires the cutting parameters (i.e., axial depth of cut a_p, radial depth of cut a_e and feed per tooth f_z), the cutting force coefficients (i.e., k_{cs} and k_{ns}), the number of harmonics (v), the tool geometry (i.e., tool diameter D, helix angle α_{el}, number of teeth Z), and the measured SLEs obtained from different cutting tests. These elements are combined in three steps: cutting force prediction in the frequency domain, SLE measurement and analytical inversion. The core idea of the proposed approach is to exploit the fact that SLE changes with spindle speed n. Indeed, given the same cutting parameters, the cutting force F_y stays the same, yet with different spindle speeds n different parts of $G_{yy}(\omega)$ are excited leading to different tool vibrations and different SLEs. However, it must be noted that the tool vibration causing SLE may alter the actual tool/workpiece engagement conditions with an impact on the cutting forces; The proposed approach simplifies this aspect considering that the engagement conditions do not change despite the different vibrations so that the cutting force stays the same at every spindle speed. With this simplification, for each spindle speed considered, depending on the number of harmonics (v) considered in the prediction of $F_y(\omega)$, v points of $G_{yy}(\omega)$ are obtained. Indeed, each force harmonic excite the tooltip FRF at the tooth passing frequency f_τ and its multiples according to the following equation:

$$f_k = kf_\tau \,, k = 1, 2, .., v \,;\; f_\tau = \frac{1}{\tau} \,;\; \tau = \frac{60}{nZ}; \tag{5}$$

Materials Research Proceedings 57 (2025) 360-368 https://doi.org/10.21741/9781644903735-42

where f_k represents the frequencies exciting $G_{yy}(\omega)$ according to the cutting force F_y. In this regard it must be highlighted that the tool is assumed to be a constant pitch tool with no runout. Clearly, for a detailed reconstruction of G_{yy}, it is essential to perform several cutting tests adopting the same cutting parameters with different spindle speeds. A scheme of the proposed method is shown in Fig. 2. where the inputs required are listed.

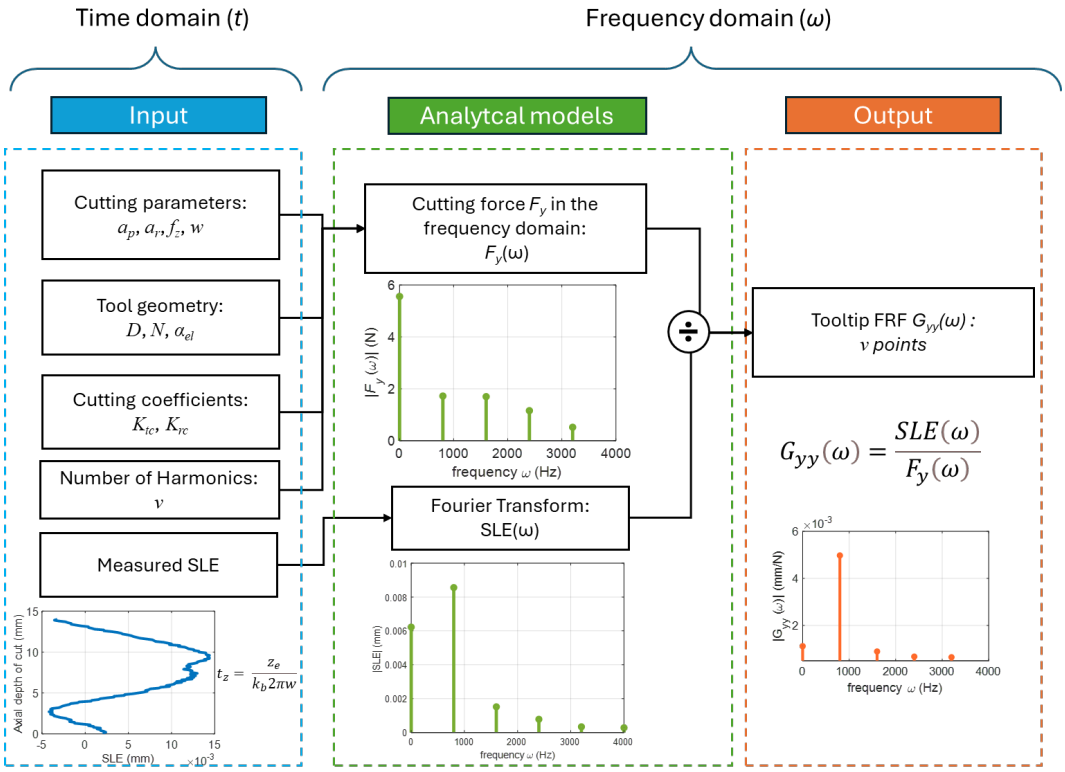


Fig. 2: Scheme of the proposed approach

The proposed approach relies on two elements: the cutting force model in the frequency domain for F_y and the measured SLEs.

Regarding the cutting force F_y the analytical model proposed by Morelli et al. [2] was considered for the proposed approach. The cutting model is based on an ideal endmill with constant pitch and no runout, and it is composed of a unique analytical expression for F_y:

$$F_y(\phi) = a_0^* \cdot Za_p + \sum_{q=1}^{Z} \sum_{m=1}^{v} \left(\left(\left(\frac{a_m^*}{mk_b} sin\, mk_b a_p + \frac{b_m^*}{mk_b} cos\, mk_b a_p - \frac{b_m^*}{mk_b} \right) cos\, m\phi_q + \left(-\frac{a_m^*}{mk_b} cos\, mk_b a_p + \frac{a_m^*}{mk_b} + \frac{b_m^*}{mk_b} sin\, mk_b a_p \right) sin\, m\phi_q \right) \right), \quad (6)$$

$$\phi_j = nt + \left(\frac{2\pi}{Z} \right) (q-1) \;\; q = 1,2,\dots,Z, \quad (7)$$

where t is the time variable, m is the index identifying the m-th harmonic considered for the frequency domain representation of F_y and a_0^*, a_m^* and b_m^* are the Fourier series coefficients which are related to the cutting coefficients (i.e., k_{cs} and k_{ns}), the radial depth of cut (a_e) and the feed per tooth (f_z). For the full expression of the Fourier series see the appendix at the end of the paper.

Instead, regarding the measured SLEs, to analyse SLE in the frequency domain, first the surface errors must be moved from the spatial domain to the time domain, so each point along the axial depth of cut a_p is moved to the time domain with the following equation:

Materials Research Proceedings 57 (2025) 360-368 https://doi.org/10.21741/9781644903735-42

$$t_z = \frac{z_e}{k_b 2\pi n}; \quad (8)$$

where z_e represent the generic SLE point along a_p, and t_z is the instant at which the z_e point was created during the cut. Moreover, to compare the two spectra $F_y(\omega)$ and SLE(ω) is it essential that they present the same components in terms of frequencies, therefore the period in which SLE is created (i.e. Eq.1) should be equal or higher than the tooth passing period. From an analytical point of view this aspect leads to a limit condition for the axial depth of cut a_p to be used in the cutting tests:

$$a_p > a_p^*; \; a_p^* = \frac{2\pi}{Zk_b}, \quad (9)$$

Where a_p^* is the lower limit value for the axial depth of cut corresponding to the tooth passing period. In this regard, it must be noted that if the cutting test are performed with a_p equal to a_p^* would cause the method to fail because in such conditions the cut is more continuous due to the fact that the angular position in which a tooth exit the cut correspond to the angular position in which the following tooth enters the cut creating a continuity in the cutting process. In such conditions the frequency content of $F_y(\omega)$ is dominated by the mean component and the harmonics at different frequencies f_k would be negligible therefore no points of the tool FRF would be found. Despite this, Eq. 9 is interesting since it relates the cutting parameters with the tool geometry showing whether the tool geometry and the necessary cutting parameters for the proposed approach are suitable one with each other. Indeed, this aspect also represents a significant limit of the proposed approach which is not appliable to any endmill but only to those who fit the condition expressed in Eq.9.

Experimental validation

The proposed approach has been experimentally validated to test its effectiveness; Peripheral milling cutting tests with different spindle speeds were performed (Fig. 3a) on a DMG MORI DMU 75 machine-tool already equipped with an on-board measuring probe RENISHAW OMP 60 which was used to measure the machined surface in every test (Fig. 3b).

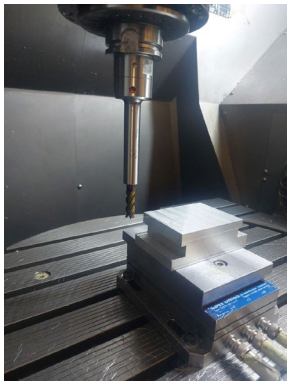
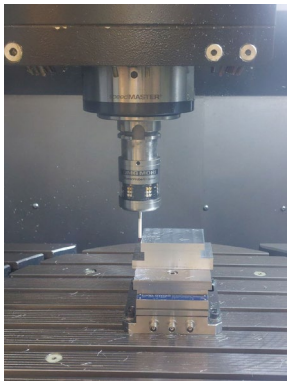
a)  b) 

Fig. 3: Experimental Setup a) Cutting test b) SLE measurement

Six cutting tests were performed on an Aluminium 6082 workpiece with an endmill GARANT 202512 12M whose geometrical features along with the fixed cutting parameters adopted are summarised in Table 1. For the cutting force in the frequency domain four harmonics were considered (i.e., v=4) with a k_{cs} of 609,84 MPa and k_{ns} of 162,40 MPa.

Materials Research Proceedings 57 (2025) 360-368 https://doi.org/10.21741/9781644903735-42

Table 1 : Endmill geometry and fixed cutting parameters

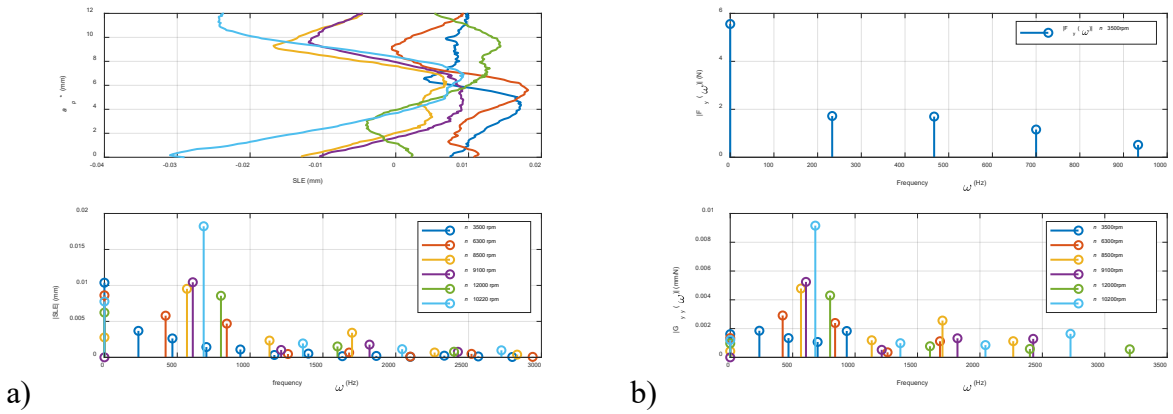
Tool	D (mm)	α_{el}(deg)	Z	Strategy	a_p (mm)	a_p^*(mm)	a_e (mm)	f_z (mm)
202512	12	38	4	up-milling	14	12.06	0.8	0.1°

The different spindle speeds and the exciting frequencies adopted for the validation are summarised in Table 2.

Table 2: Spindle speed and exciting frequencies

Test	n (rpm)	f_1 (Hz)	f_2 (Hz)	f_3 (Hz)	f_4 (Hz)
1	3500	233	466	700	933
2	6300	420	840	1260	1680
3	8500	566	1133	1700	2266
4	9100	606	1213	1820	2426
5	12000	800	1600	2400	3200
6	10200	681	1363	2044	2725

Experimental SLEs were measured in five sets along the feed direction each one with an axial spacing of 0.1mm to ensure a high resolution along the axial depth of cut as well as a high frequency resolution in the SLEs analysis. The results obtained are shown in Fig. 4. In this regard, Fig. 4a show the measured SLE within the range of interest for the proposed method (i.e. from 0 to a_p^*) in both spatial domain and frequency domain. In detail, given the same cutting parameters SLEs changes with spindle speed showing harmonics that becomes higher in amplitude as they get close to the resonance of the tooltip FRF. However, a discrepancy between the measured SLES could be seen at zero frequency where the mean value changes with different tests. This discrepancy is probably related to some inaccuracies in the reference surface occurred between one test and the other. The $F_y(\omega)$ spectrum obtained from the cutting model adopted is reported in Fig. 4b, and, given the same depths of cut and feed per tooth, it is the same for every spindle speed considered



a) b)

Fig. 4: Experimental Results a) measured SLEs b) $F_y(\omega)$ spectrum and experimental $G_{yy}(\omega)$ points

Nonetheless the evolution of the $G_{yy}(\omega)$ points obtained is in line with the evolution of tooltip FRF with a resonance around 700 Hz. To better analyse the results obtained, the experimental $G_{yy}(\omega)$ points were reordered and compared with the tooltip FRF $G_{yy}(\omega)$ obtained from an Impact Hammer testing.

Materials Research Proceedings 57 (2025) 360-368 https://doi.org/10.21741/9781644903735-42

a) b)

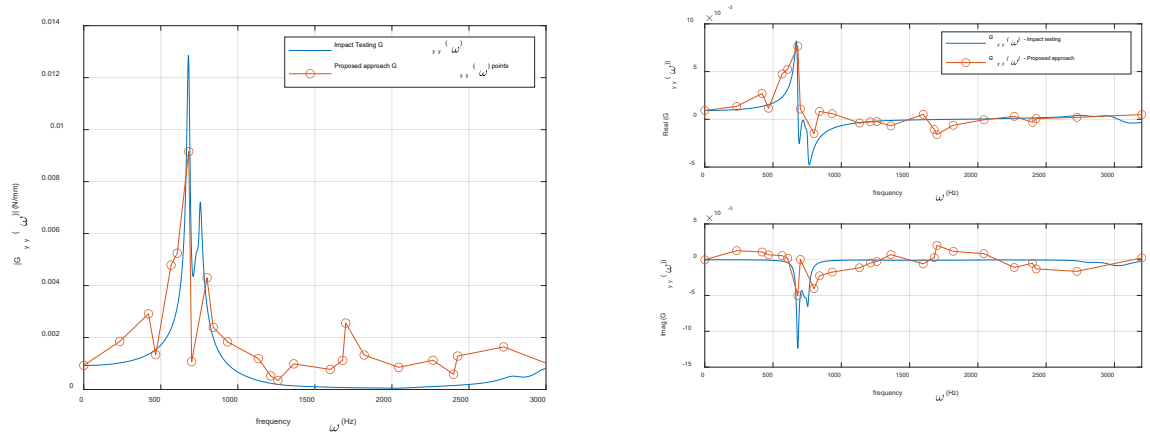


Fig. 5: Comparison between Proposed approach and Impact testing a) $G_{yy}(\omega)$ Amplitude b) real and imaginary $G_{yy}(\omega)$ parts

In Fig. 5a the comparison in terms of amplitude between the $G_{yy}(\omega)$ obtained from Impact testing and the sequence of experimental $G_{yy}(\omega)$ points is shown. Despite the limited number of points available the proposed approach manages to reproduce a satisfying FRF compared to the ones obtained from an impact testing. In detail, the $G_{yy}(\omega)$ at zero frequency (i.e., static stiffness k) was obtained as the mean of all the six values available at zero frequency obtaining a static stiffness of 9.27e-04 mm/N in line with 9.24e-04 mm/N found in the Impact testing. Furthermore, the two FRFs were compared in terms of Root Mean Square Deviation (RMSD) obtaining a 0.0015 mm/N value which is acceptable considering the reduced number of points available. As a further comparison the real and imaginary parts of the experimental $G_{yy}(\omega)$ points were compared with their counterparts obtained from the Impact Hammer testing (Fig. 5b). In this case, for the resonance (i.e., natural frequency) a value of 741Hz was found from the evolution of the real part of the sequence of experimental $G_{yy}(\omega)$ points compared to 681 Hz found from impact testing. Moreover, despite the few points available, the proposed approach manages to give a good representation of the evolution of both real and imaginary parts despite higher RMSD values (i.e., 0.0016 mm/N for the real part and 0.0021 mm/N for the imaginary part) allowing the identification of both static stiffness and natural frequency, yet the minimum of the imaginary part of $G_{yy}(\omega)$ was not accurately evaluated in the proposed approach. This discrepancy is probably related the variation in the tool/workpiece engagement caused by the high vibration. Overall, the first results for the are promising and they show that the proposed approach could be a worthy alternative for the tool tip FRF evaluation considering its simplicity and the advantages of exploiting sensors already available on the machine tool.

Conclusions

In this paper the idea for an inverse analytical model to evaluate the tool tip Frequency Response Function (FRF) in peripheral milling from Surface location Errors (SLEs) measured in different cutting tests was investigated. The findings of this work are summarised as follows:

- The proposed method is based on the inversion of a simple analytical method which estimates SLE from the spectrum of the cutting force in the cross-feed direction F_y and the direct tool tip FRF in the same direction.
- The proposed method does not require any additional sensors to be mounted on the machine tool, but only the measuring probe which most machine tools are already equipped with.

- The first results provided a satisfactory evaluation of the tool tip FRF in terms of static stiffness with a relative error close to zero and natural frequency with a relative error of 9%, yet the peak value of the FRF was not correctly evaluated.
- The simplicity of the analytical model adopted introduces constraints on the propose in terms of the cutting parameters to adopt for the cutting tests and suitable tool geometry. Furthermore, conditions of high forced vibration limit the effectiveness of the analytical model.

Overall, the proposed approach looks promising, yet more cutting tests should be performed and organized to solidify the method. Furthermore, the analytical model should be improved to better evaluate the conditions of high forced vibrations.

References

[1] Mann, B.P., Edes, B.T., Easley, S.J., Young, K.A., Ma, K., Chatter vibration and surface location error prediction for helical end mills, Int J Mach Tools Manuf. 48, 350-361 (2008). https://doi.org/10.1016/j.ijmachtools.2007.10.003

[2] Morelli, L., Grossi, N., Campatelli, G., Scippa, A., Surface location error prediction in 2.5-axis peripheral milling considering tool dynamic stiffness variation, Precis Eng. 76, 95-109 (2022). https://doi.org/10.1016/j.precisioneng.2022.03.008

[3] Munoa, J., Beudaert, X., Dombovari, Z., Altintas, Y., Budak, E., Brecher, C., Stepan, G., Chatter suppression techniques in metal cutting, CIRP Annals. 65, 785-808 (2016). https://doi.org/10.1016/j.cirp.2016.06.004

[4] Schmitz, T., Betters, E., Budak, E., Yüksel, E., Park, S., Altintas, Y., Review and status of tool tip frequency response function prediction using receptance coupling, Precis Eng. 79, 60-77 (2023). https://doi.org/10.1016/j.precisioneng.2022.09.008

[5] Iglesias, A., Taner Tunç, L., Özsahin, O., Franco, O., Munoa, J., Budak, E., Alternative experimental methods for machine tool dynamics identification: A review, Mech Syst Signal Process. 170, 108837 (2022). https://doi.org/10.1016/j.ymssp.2022.108837

[6] Wiederkehr, P., Wilck, I., Siebrecht, T., Determination of the dynamic behaviour of micro-milling tools at higher spindle speeds using ball-shooting tests for the application in process simulations, CIRP Annals. 69, 97-100 (2020). https://doi.org/10.1016/j.cirp.2020.04.036

[7] Bachrathy, D., Kiss, A.K., Kossa, A., Berezvai, S., Hajdu, D., Stepan, G., In-Process Monitoring of Changing Dynamics of a Thin-Walled Component During Milling Operation by Ball Shooter Excitation, Journal of Manufacturing and Materials Processing 2020, Vol. 4, Page 78. 4, 78 (2020). https://doi.org/10.3390/jmmp4030078

[8] Takács, D., Wohlfart, R., Miklós, Á., Krajnyák, G., Tóth, A., Stépán, G., Ball shooting tests for identification of modal parameter variation in rotating main spindles, Procedia CIRP. 77, 481-484 (2018). https://doi.org/10.1016/j.procir.2018.08.260

[9] Yamato, S., Yokohara, K., Nara, Y., Matsubara, A., Static and Dynamic Measurements of Spindle System During Rotation by Noncontact Electromagnetic Loading System, Int. J. Autom. Technol. 19, 24-40 (2025). https://doi.org/10.20965/ijat.2025.p0024

[10] Zaghbani, I., Songmene, V., Estimation of machine-tool dynamic parameters during machining operation through operational modal analysis, Int J Mach Tools Manuf. 49, 947-957 (2009). https://doi.org/10.1016/j.ijmachtools.2009.06.010

[11] Aguirre, G., Iglesias, A., Munoa, J., Astarloa, A., Aguirre, G., Iglesias, A., Muñoa, J., Astarloa, A., Ciurana, J., Real milling force based dynamic parameter extraction method, Proceedings of ISMA. (2014).

[12] Tunc, L.T., Budak, E., Identification and modeling of process damping in milling, J Manuf Sci Eng. 135, (2013). https://doi.org/10.1115/1.4023708

[13] Morelli, L., Grossi, N., Scippa, A., Campatelli, G., Extended classification of surface errors shapes in peripheral end-milling operations, J Manuf Process. 71, 604-624 (2021). https://doi.org/10.1016/j.jmapro.2021.09.054

[14] Schmitz, T.L., Mann, B.P., Closed-form solutions for surface location error in milling, Int J Mach Tools Manuf. 46, 1369-1377 (2006). https://doi.org/10.1016/j.ijmachtools.2005.10.007

Appendix

Cutting force in cross-feed direction (y)

$$a_{y0}^{*} = -\frac{1}{2\pi}\left[k_{cs}f_z\left(-\frac{x}{2}+\frac{1}{4}\sin(2x)\right)-k_{ns}f_z\left(\frac{1}{4}\cos(2x)\right)\right]_{\phi_{in}}^{\phi_{out}}, \tag{10}$$

$$a_{y1}^{*} = -\frac{1}{\pi}\left[k_{cs}f_z\left(-\frac{1}{4}\sin(x)+\frac{1}{12}\sin(3x)\right)+k_{ns}f_z\left(-\frac{1}{4}\cos(x)-\frac{1}{12}\cos(3x)\right)\right]_{\phi_{in}}^{\phi_{out}} \tag{11}$$

$$a_{y2}^{*} = -\frac{1}{\pi}\left[k_{cs}f_z\left(\frac{1}{4}x-\frac{1}{4}\sin(2x)+\frac{1}{16}\sin(4x)\right)-k_{ns}f_z\left(\frac{1}{16}\cos(4x)\right)\right]_{\phi_{in}}^{\phi_{out}}, \tag{12}$$

$$a_{yj}^{*} = -\frac{1}{\pi}\left[k_{cs}f_z\left(-\frac{1}{2j}\sin(jx)+\frac{1}{4(j-2)}\sin\big((j-2)x\big)+\frac{1}{4(j+2)}\sin\big((j+2)x\big)\right)+k_{ns}f_z\left(\frac{1}{4(j-2)}\cos\big((j-2)x\big)-\frac{1}{4(j+2)}\cos\big((j+2)x\big)\right)\right]_{\phi_{in}}^{\phi_{out}} \tag{13}$$

$$b_{y1}^{*} = -\frac{1}{\pi}\left[k_{cs}f_z\left(\frac{3}{4}\cos(x)-\frac{1}{12}\cos(3x)\right)+k_{ns}f_z\left(\frac{1}{4}\sin(x)-\frac{1}{12}\sin(3x)\right)\right]_{\phi_{in}}^{\phi_{out}}, \tag{14}$$

$$b_{y2}^{*} = -\frac{1}{\pi}\left[k_{cs}f_z\left(\frac{1}{4}\cos(2x)-\frac{1}{16}\cos(4x)\right)+k_{ns}f_z\left(\frac{1}{4}x-\frac{1}{16}\sin(4x)\right)\right]_{\phi_{in}}^{\phi_{out}}, \tag{15}$$

$$b_{yj}^{*} = -\frac{1}{\pi}\left[k_{cs}f_z\left(\frac{1}{2j}\cos(jx)-\frac{1}{4(j-2)}\cos\big((j-2)x\big)-\frac{1}{4(j+2)}\cos\big((j+2)x\big)\right)+k_{ns}f_z\left(\frac{1}{4(j-2)}\sin\big((j-2)x\big)-\frac{1}{4(j+2)}\sin\big((j+2)x\big)\right)\right]_{\phi_{in}}^{\phi_{out}} \tag{16}$$

Materials Research Proceedings 57 (2025) 369-376 https://doi.org/10.21741/9781644903735-43

An AI-based approach for flow front monitoring and prediction in liquid composite molding processes based on dielectric and visual data elaboration

Vitantonio ESPERTO[1,a], Fausto TUCCI[1,b], Felice RUBINO[1,c*] and Pierpaolo CARLONE[1,d]

[1]Department of Industrial Engineering, University of Salerno, Via Giovanni Paolo II, 132 84084 Fisciano (SA), Italy

[a]vesperto@unisa.it, [b]ftucci@unisa.it, [c]frubino@unisa.it, [d]pcarlone@unisa.it

Keywords: Neural Network, Machine Learning, Composites, Image Processing, In-Process Measurement, Predictive Model, Vacuum-Bag Molding

Abstract. Liquid composite molding processes involve the impregnation and saturation of a dry preform by a liquid reactive resin, driven by pressure gradients. The correct advance of the resin flow front during the infusion is crucial to achieve defect-free composite products. In the present work, monitoring architecture based on real-time acquisition of data provided by dielectric and visual sensors has been developed. A machine learning approach, based on the You Only Look Once (YOLO) algorithm, has been integrated with the visual monitoring system to detect and dynamically track the resin flow front, deriving relevant process parameters in real-time. The data obtained highlights the effectiveness of the combined monitoring strategy and proposes a sensing tool for the further study of impregnation and saturation phenomena in liquid composite processing.

Introduction

In recent years, significant improvements have been made in the field of liquid composite molding (LCM) processes to produce fiber reinforced polymeric composite parts, motivated by the constant growth in the composite market, which forecasted an increase from 105,74 billion dollars in 2024 to 116,25 billion in 2025 [1] and by ever-increasing attention paid by academy and industry to the sustainability in the composite production and usage. Recent investigations have indeed shown that raw materials and manufacturing of composites have a higher footprint along the life cycle of composite parts. Lunetto et al found that the energy consumption of constituent materials, fibers and matrices, and composite manufacturing technologies (the so-called embodied energies) represent the highest contributions to the overall environmental impact [2]. Similarly, De Sio et al. conducted the LCA analysis on composite battery enclosures to be used in electrical vehicles manufactured by pultrusion, observing that the highest contribution to the environmental impact is represented by the extraction of raw material [3]. In this scenario, reducing production waste in the composite manufacturing industry due to non-compliance or defects is pivotal. In the framework of the LCM process, great importance is played by the detection of the resin flow front to evaluate the infusion stage and control the occurrence of process anomalies, like race tracking, which can cause the formation of dry spot or void defects. Several strategies have been proposed in recent years to enhance and, at the same time, monitor the resin flow based on conventional sensing systems and artificial neural network (ANN)-based approaches. The authors, in their previous works, combined microwave technology for the resin preheating and dielectric analysis to monitor the resin advance, obtaining a reduction in preform impregnation time together with a minimization in void content [4], [5]. Capturing the position of the flow front and the velocity during the infusion is a crucial issue in evaluating the generation of possible voids. Gonzalez et al

Content from this work may be used under the terms of the Creative Commons Attribution 3.0 license. Any further distribution of this work must maintain attribution to the author(s) and the title of the work, journal citation and DOI. Published under license by Materials Research Forum LLC.

Materials Research Proceedings 57 (2025) 369-376 https://doi.org/10.21741/9781644903735-43

in [6] developed a system based on a convolutional neural network to detect the occurrence of manufacturing disturbances. Race tracking channel defects and position has been investigated by Agogué in [7] and Fernàndez in [8]. Other authors focused on the study of the capillary number as parameters, which permits to discriminate between the formation of micro- and macro-voids [9–11].

In the present work, Seeman's Composite Resin Infusion Molding Process (SCRIMP) has been used to manufacture composite components in a laboratory-scale setup. The addition of the distribution medium on the fiber stack used to accelerate the impregnation stage and reduce the overall manufacturing time, leads on the other hand to the formation of two resin flow fronts, one through the distribution medium and one through the dry preform, which further complicates the process monitoring. An integrated system, consisting of a machine learning approach based on the YOLO algorithm coupled with visual and dielectric sensors, was proposed to detect both resin flow fronts. The aim was the detection of the resin flow front by using a machine learning system integrated with flexible dielectric sensors.

Materials and Methods

Tests are conducted with SCRIMP process setup, by using glass fiber HexForce twill 2/2 and epoxy resin SX10 EVO. The dry preform is composed of 8 sheets, 240 x 300 mm^2. The overall procedure is detailed in [5]. The laboratory scale setup is depicted in Fig.1, which reports a scheme of the setup (left picture) and a photo of the vacuum bag equipped with the dielectric sensors (right picture). The resin flows from the vessel (1) to the vacuum pump, through the dry preform (2). The sensing system consisted of a camera (3), with a resolution of 1920 x 1080 pixels, and four dielectric sensors are applied, 20x20 mm^2 (S1, S2, S3, S4) connected to an Arduino board and a laptop (4), which acquire and process the data detected by both systems. A black mask is applied on each sensor (as depicted in the right image in Fig.1) and covers the wires to uniform the appearance of the sensors and make their recognition easier by the machine learning algorithm. The mask is slightly larger than the sensor.

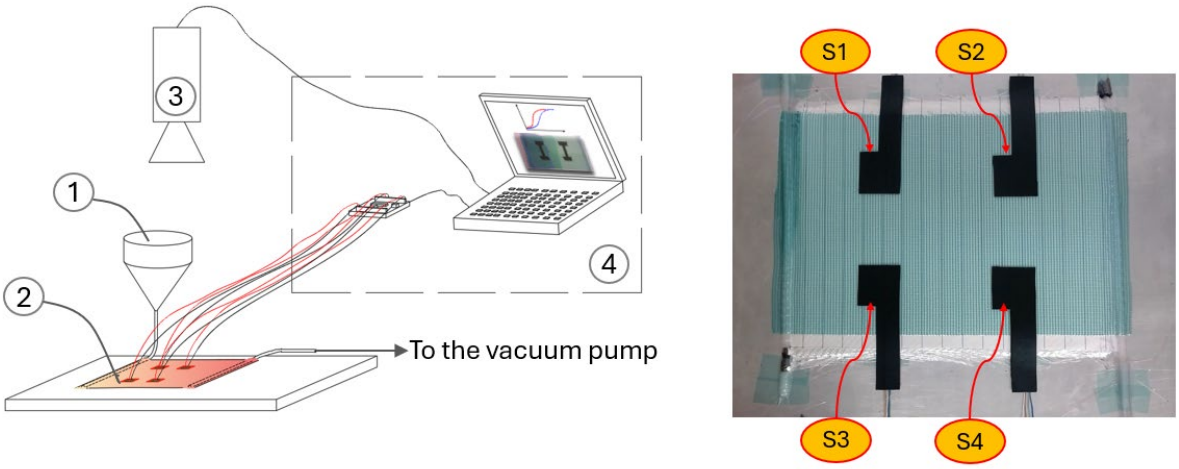


Fig. 1- Laboratory setup scheme.

To detect the resin flow front, a neural network based on the YOLO algorithm was trained. A data set was constructed, as depicted in Fig.2, from the data acquired by a camera. Data segmentation and labeling were necessary to track the flow front, and a data augmentation strategy was adopted to increase the training set by creating modified copies of existing data.

Materials Research Proceedings 57 (2025) 369-376 https://doi.org/10.21741/9781644903735-43

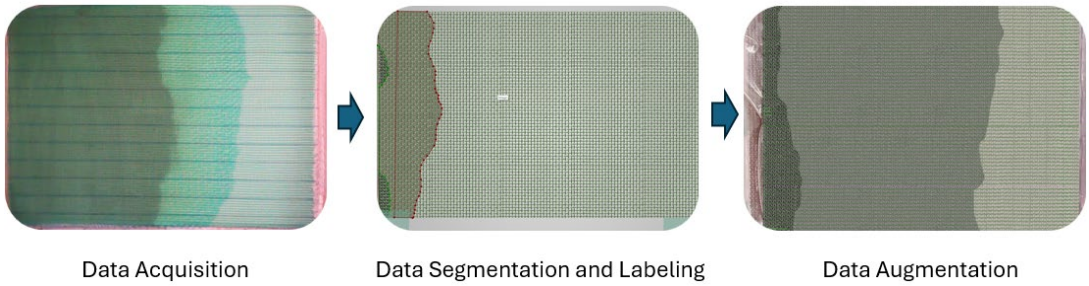


Fig. 2- Dataset construction stages.

Starting from the images acquired, a convolutional neural network (CNN) has been trained to detect the bounding boxes depicted in the left picture of Fig.3. Then, the data set segmentation (right picture of Fig.3) leads to the real flow front contour.

The training process of the YOLO model uses a pre-trained segmentation model (on a standard database of images provided by Google and similar) specifically designed to recognize the contour/segment of the selected objects. A hybrid training was conducted, that is, it trains both to detect bounding boxes and segments, in particular:

a. The bounding boxes provide a precise localization of the object within the image making the entire training and detection process simpler and faster, lightening the computational burden.
b. The segmentation provides at pixel level a precise delimitation of the shape of the object.

Polygons are created around the objects to be detected by manually selecting the needed points (see Figure 3). The number of points is chosen by the user based on the complexity of the curve to describe the flow front. The file created is converted into binary masks (white = object, black = background) which are used to train CNN networks for semantic segmentation.

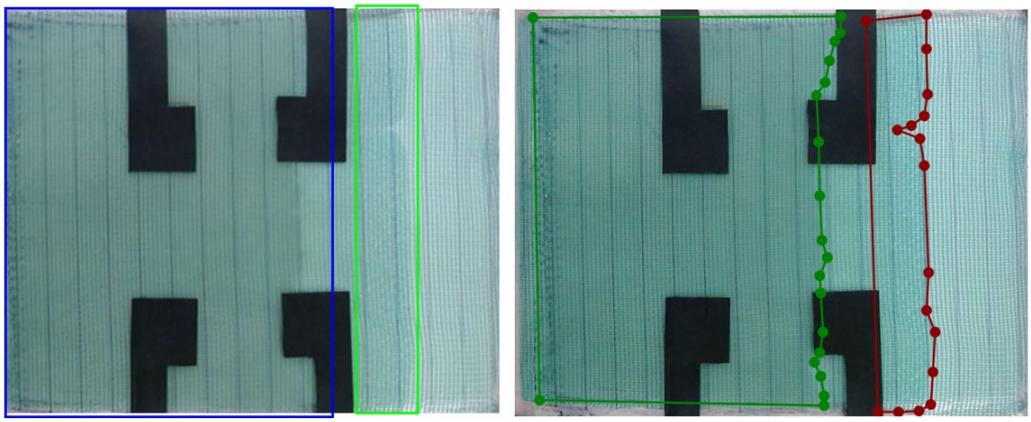


Fig.3 - From bounding box to segmentation.

Data augmentation is a fundamental step to generalize the model so that it can detect the flow front even in contexts never seen before. Data augmentation has been implemented using a Python library (Albumination) dedicated to the computer vision field, as shown in Fig.4. For data augmentation 'n' images of the dataset are used (where n is determined by the size of the batch chosen for training, in the present case it was 16) for 'y' cycles (where y would be the number of cycles for which the data augmentation occurs, in the present case it was 10). The images are taken randomly and altered using these parameters whose values are chosen randomly within the previously defined thresholds:

- translate: 0.1 (translates the image by a max of 10% on x,y)

Materials Research Proceedings 57 (2025) 369-376 https://doi.org/10.21741/9781644903735-43

- scale: 0.2 (scales the image by a maximum of 20%)
- shear: 0.2 (crops the image by a max of 20%)
- perspective: 0.1 (changes the perspective by a maximum of 10%)
- flipud: 0.7 (flips the image vertically with a probability of 70%)
- mosaic: 0.3 (creates a mosaic texture of the image with a probability of 30%)
- mixup: 0.2 (interpolates 2 images to create a new one with a probability of 20%)
- label_smoothing: 0.05 (it defines how much the segment is “smoothed” in front of jagged parts that should be curved, with a limit of 5%)
- nbs: 16 (batch size, number of images analyzed per cycle)
- hsv_h: 0.015 (increase of color tint value by 1.5%)
- hsv_s: 0.7 (change of saturation by 70%)

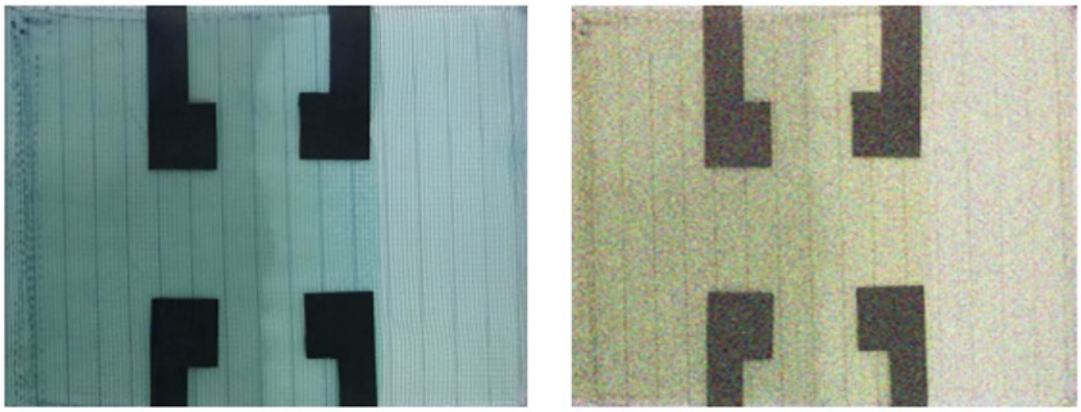


Fig.4 – Data augmentation example.

The system based on Yolo can detect a resin flow front each 0.122 [s]. The inference time (i.e., 0.122 s) is determined during the training of the model as a function of several parameters: (i) model complexity, (ii) training level (the more robust the model, the easier it recognizes objects and the shorter the inference time), (iii) hardware used. This time can therefore be reduced based on the desired stability of the model, the similarity of the target image or frame with the image of the dataset used for training, the performance of the hardware, and the number of parameters to calculate. The images used to train the model without obstacles were: 126 for training, 8 for testing, and 5 for validation. For the augmentation, a batch size of 16 for 10 cycles (160 images) was used. The number of images is far below the recommended dataset, which should be 1000-2000 images, and may pose reasonable doubts about the reliability of the system. However, the similarity between the experiments and the dataset in terms of backgrounds and colors as well as the use of a guided segmentation allowed to greatly accelerate the learning of the model allowing to obtain good results even with a reduced dataset.

Once properly defined all the necessary configurations, Yolo system was able to recognize the two resin flow fronts along the distribution medium and through the dry preform, hereinafter labelled as ‘resin flow front 1’ and ‘resin flow front 2’, respectively. The results reported in Fig.5 are related to the first dataset used to train the machine learning system to detect the two resin flow fronts without dielectric sensors, which will represent obstacles for the visual acquisition system.

Materials Research Proceedings 57 (2025) 369-376 https://doi.org/10.21741/9781644903735-43

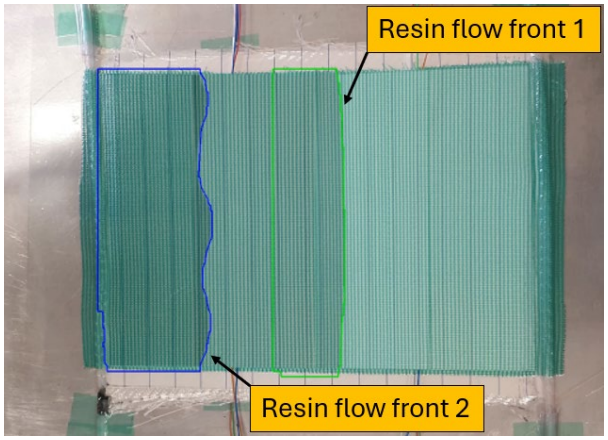


Fig. 5- Resin flow front detection without obstacles.

To allow the system to detect the two resin flow fronts in the case of visual obstacles placed on the vacuum bag, which mimicked the presence of the dielectric sensors, a second dataset was constructed to train the neural network. Fig.6 shows the results of the training of four datasets consisting of different numbers of images. The dataset with 120 images (Fig.6a) was not able to detect any flow front. When the number of images was increased to 200 images the system detected a wrong resin flow front, pointed by the black arrow in Fig.6b. With a dataset size of 350 images the system could recognize only the first flow front (Fig.6c); only by using a dataset with 500 images, the system was able to properly track both resin flow fronts (Fig.6d).

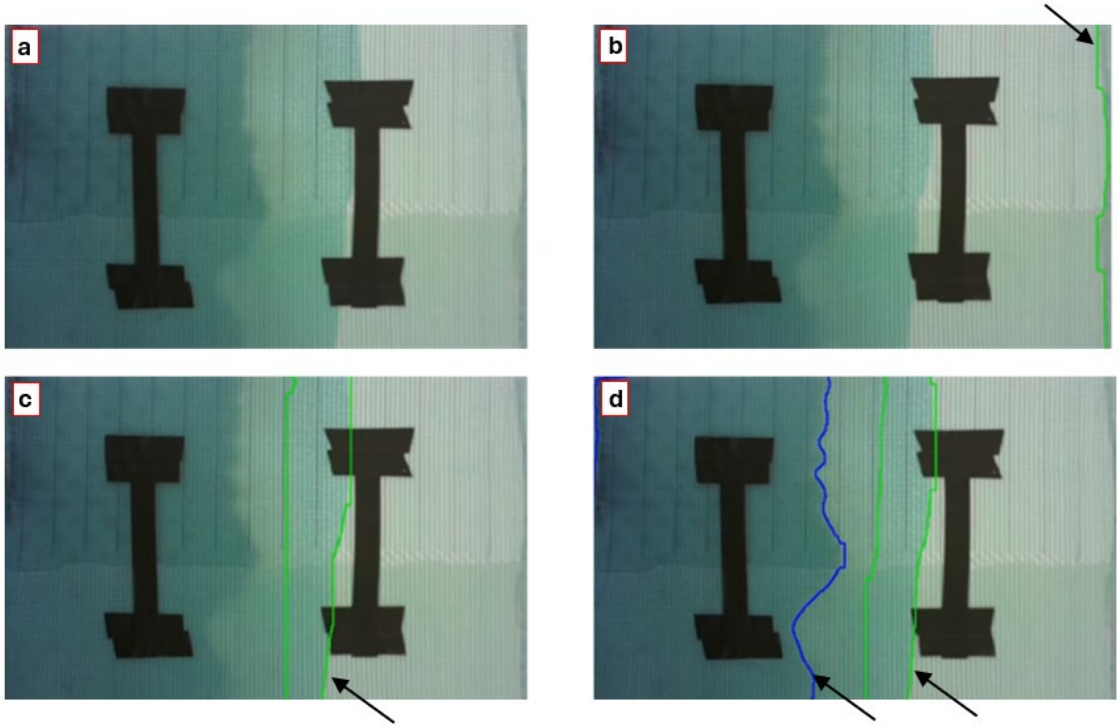


Fig. 6- Resin flow front detection by using neural network trained with different dataset size: a) dataset size of 120 images, b) dataset size of 200 images, c) dataset size of 350 images, d) dataset size of 500 images.

Materials Research Proceedings 57 (2025) 369-376 https://doi.org/10.21741/9781644903735-43

Results and Discussions

In this section, the results of impregnation tests are reported. Fig.7 shows the graph of capacity vs time from the signal acquired by sensor S2 together with the resin flow front detection obtained by the neural network. Considering the similarity in the shape of the signals, the curves from the other sensors were omitted. Four representative timesteps of the impregnation were reported in the sub-pictures (a, b, c, and d) which depict the resin flow fronts detected by the neural network.

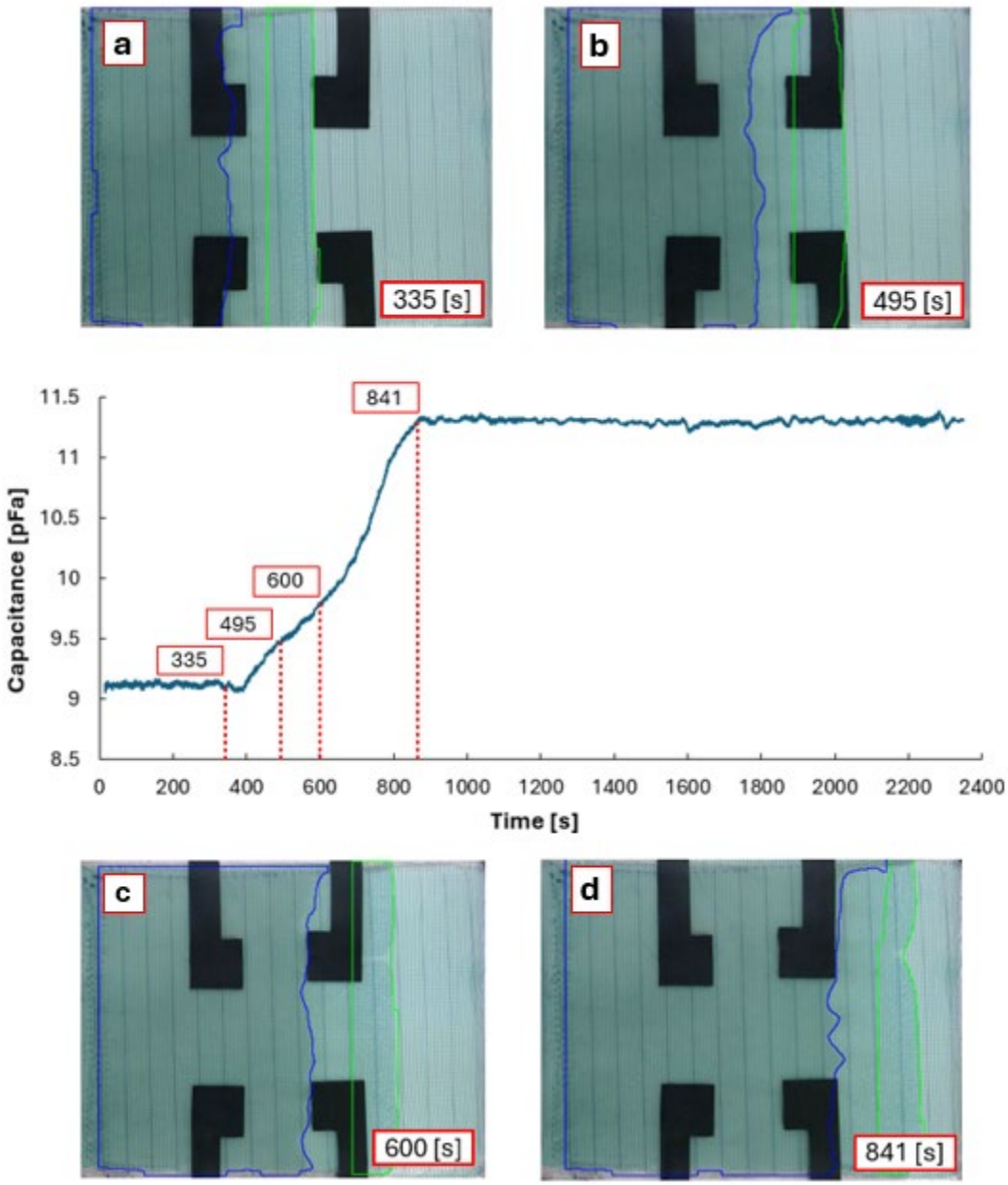


Fig. 7- Resin flow front position on sensor S2.

At 335 s, the resin flow front 1 reached the edge of the mask corresponding to the location of sensor S2, slightly before the start of the sensor ramp since, as mentioned, the black mask covering the sensor is larger than the sensing area. At 495 s, the flow front 1 completely passed the sensor S2 and covered the sensing area. It corresponds to a local reduction in the curve slope indicating the occurrence of slower variations in capacitance. The capacitance started to increase again at a high rate when the second flow front 2 reached the sensing area (Fig.7c) after approximately 600 s and reached a plateau after 841 s indicating that the sensing area was completely covered by the

second flow front. Of course, the capacitance curve is smooth and the arrival of the two flow fronts occurred seamlessly, since a transition zone was established between the two flow fronts [12].
Fig. 8 reports the instantaneous average flow front position of front 1 (orange curve) and front 2 (blue curve). As expected, the flow front 1 reached the vent in high advance with respect to the flow front 2 due to the higher permeability of the distribution medium and the curve well matches the closed solution of Darcy's equation for 1-D flow [4]. The average profile of the flow front 2 is less smooth than that of the flow front 1 due to the irregular shape of the front induced by local differences in the permeability within the preform (as observed in Fig.7). It is relevant to note that after a short transitory the distance between the two flow fronts stabilized and remained constant during the entire impregnation [12].

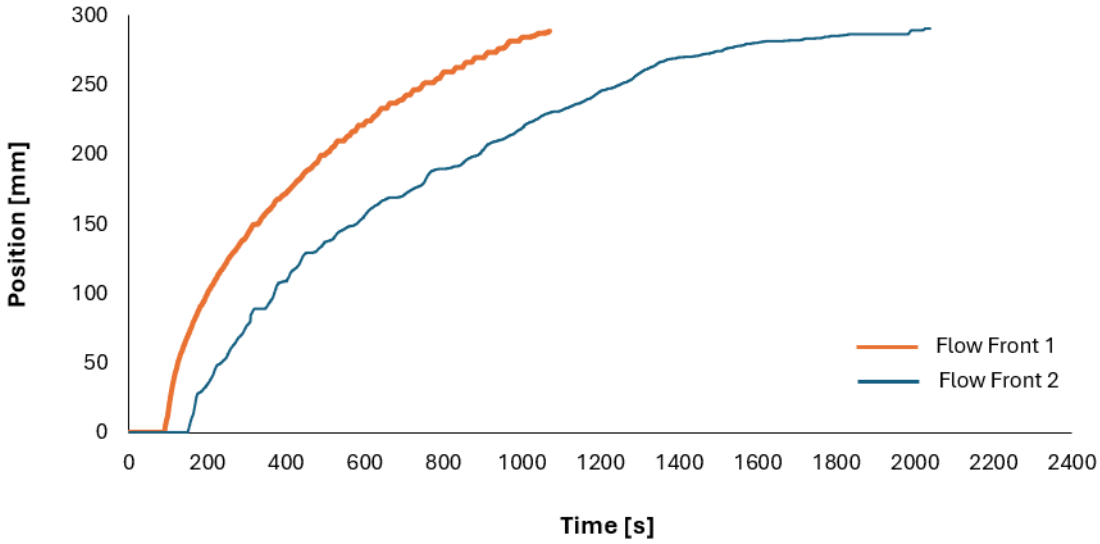


Fig. 8- Resin flow front position estimated by YOLO.

Conclusions

A neural network system based on the YOLO algorithm has been successfully implemented. The NN methods was able to track the resin flow front consistently in with the dielectric sensors signal. In addition, the YOLO algorithm was able to distinguish both the resin flow front through the distribution medium and the one through the dry preform. Further development of the proposed methods may involve the use of higher number of classes in the neural network training datasets in order to detect defects, such as race tracking and fingering, which may occur during the resin infusion and implement corrective actions.

Acknowledge

Funding: This research was funded by the project 'National Centre for Sustainable Mobility' (cod. CN00000023—CUP D43C22001190001)—National Recovery and Resilience Plan PNRR—Italian Ministry of University and Research.

References

[1] Informatio on https://www.thebusinessresearchcompany.com/report/composites-global-market-report, (February 2025).

[2] V. Lunetto, M. Galati, L. Settineri, L. Iuliano, Sustainability in the manufacturing of composite materials: A literature review and directions for future research, J Manuf Process 85 (2023) 858–874. https://doi.org/10.1016/J.JMAPRO.2022.12.020

[3] P. De Sio, M. Gaito, V. Esperto, E. Cozzolino, A. Astarita, F. Tucci, Life Cycle Assessment of a Composite Prototype Battery Enclosure for Electric Vehicles, Sustainability (Switzerland) 17 (2025). https://doi.org/10.3390/su17041579

[4] F. Rubino, F. Tucci, V. Esperto, P. Carlone, Filling Time Reduction in Liquid Composite Molding Processes, Journal of Composites Science 6 (2022). https://doi.org/10.3390/jcs6080222

[5] V. Esperto, C. Gallo, S. Lomov, J. Soete, P. Carlone, System Integration for Advanced Manufacturing of Composites by Microwave Preheated Resin Infusion: An Experimental Study, J Mater Eng Perform (2024). https://doi.org/10.1007/s11665-024-10397-7

[6] C. González, J. Fernández-León, A machine learning model to detect flow disturbances during manufacturing of composites by liquid moulding, Journal of Composites Science 4 (2020). https://doi.org/10.3390/jcs4020071

[7] R. Agogué, M. Shakoor, P. Beauchêne, C.H. Park, Analysis and Minimization of Race Tracking in the Resin-Transfer-Molding Process by Monte Carlo Simulation, Materials 16 (2023). https://doi.org/10.3390/ma16124438

[8] J. Fernández-León, K. Keramati, D. Garoz, L. Baumela, C. Miguel, C. González, A Machine Learning Strategy for Race-Tracking Detection During Manufacturing of Composites by Liquid Moulding, Integr Mater Manuf Innov 11 (2022) 296–311. https://doi.org/10.1007/s40192-022-00263-6

[9] B. Neitzel, F. Puch, Optical Detection of Void Formation Mechanisms during Impregnation of Composites by UV-Reactive Resin Systems, Journal of Composites Science 6 (2022). https://doi.org/10.3390/jcs6110351

[10] B. Neitzel, F. Puch, Application of capacitive sensors and controlled injection pressure to minimize void formation in resin transfer molding, Polym Compos 44 (2023) 1658–1671. https://doi.org/10.1002/pc.27195

[11] P. He, W. Zhao, B. Yang, J. Wang, A. Ni, S. Li, Void content reduction of composites with sensor-aided injection strategy in liquid composite molding process, Mater Res Express 8 (2021). https://doi.org/10.1088/2053-1591/ac1532

[12] F. Rubino, P. Carlone, A semi-analytical model to predict infusion time and reinforcement thickness in VARTM and SCRIMP processes, Polymers (Basel) 11 (2019). https://doi.org/10.3390/polym11010020

Materials Research Proceedings 57 (2025) 377-384 https://doi.org/10.21741/9781644903735-44

Modeling of molten pool geometry and remelting layer in the laser ablation of Ti6Al4V alloy

Maria Rosaria SAFFIOTI[1,a *], Serafino CARUSO[1,b *], Giovanna ROTELLA[2,c] and Domenico UMBRELLO[1,d]

[1]Department of Mechanical, Energy and Management Engineering, University of Calabria, Rende, CS 87036, Italy

[2]Department of Engineering, University LUM Giuseppe Degennaro, Casamassima, BA 70010, Italy

[a]mariarosaria.saffioti@unical.it, [b]serafino.caruso@unical.it, [c]rotella@lum.it, [d]domenico.umbrello@unical.it

Keywords: Laser Processes, Surface, Industrial Sector

Abstract. The present study investigates a finite element model to simulate the thermal effects of high-energy-density surface treatments, such as laser surface treatment, on Ti6Al4V titanium alloy. Using a 3D conical Gaussian heat source, the model allows to predict molten pool geometry and remelting layers due to phase transformations. Validation with experimental laser treatment data confirms the model's accuracy in capturing temperature-dependent welding characteristics. The research makes it possible to deepen the understanding of thermal behavior and phase evolution in Ti6Al4V, highlighting the critical role of process optimization in achieving desired microstructure and mechanical properties.

Introduction

Laser surface treatment is a precise technique which allows for the introduction of localized microstructural and geometric changes, particularly beneficial for enhancing Ti6Al4V alloy surface properties, such as wear and fatigue resistance [1–3]. Numerous studies have explored the influence of laser texturing on corrosion resistance and durability [4–6]; however, the complex thermal effects generated during rapid heating and cooling cycles pose significant modeling challenges, especially due to the resulting residual stresses [7]. Finite Element Modeling (FEM) has proven effective for simulating such thermo-mechanical behavior, enabling detailed predictions of temperature distribution, deformation and surface changes in both machining and laser processing contexts [8–11]. Accurate thermal modeling is highly influenced by appropriate heat source representation, as shown by Unnia et al. [12], while empirical models, like those developed by Li et al. [13], help relate processing parameters to peak temperatures and microstructural changes. Experimental validation remains vital for ensuring model reliability, as demonstrated by Zahi et al. [14] in their study on heat-affected zone thickness in laser-assisted machining. These works underscore the importance of integrating experimental data with computational models to gain a comprehensive understanding of the key phenomena driving the process. This study aims to make a significant contribution to the existing knowledge by performing a comprehensive comparative analysis, both numerical and experimental, of the evolution of laser track geometry during the laser surface treatment of Ti6Al4V alloys. Specifically, the aim is to introduce a novel methodology for heat source modeling, based on process temperature, thereby demonstrating the potential of a temperature-driven approach as an effective alternative to conventional geometric-based definitions of heat flux and thermal efficiency.

Content from this work may be used under the terms of the Creative Commons Attribution 3.0 license. Any further distribution of this work must maintain attribution to the author(s) and the title of the work, journal citation and DOI. Published under license by Materials Research Forum LLC.

Materials Research Proceedings 57 (2025) 377-384 https://doi.org/10.21741/9781644903735-44

Materials and methods

The material used in this study is Ti6Al4V titanium alloy, characterized by a microstructure consisting of α-phase and intergranular β-phase and a chemical composition as shown in Table 1. Laser irradiation was performed using an air-cooled ytterbium fiber laser system (Lasit Compact Mark G8) with a maximum average power of 100 W and a wavelength of 1064 nm. The laser beam was focused onto the surface using an F-theta lens (f = 160 mm). The pulse duration was set to 250 ns and the focal spot diameter was approximately 55 μm. During the experimental campaign, the following processing parameters were kept constant: pulse frequency (f) at 1 MHz and average power (P) at 80 W. The laser scanning speed (V) was varied at two levels: 30 mm/s and 45 mm/s. The process parameters were selected through preliminary experimental trials aimed at ensuring that the surface temperature exceeded the β-transus of Ti6Al4V, while maintaining oxide formation within acceptable limits.

Table 1 – Material chemical composition [%]

Ti	Al	V	O	Fe	N	C	H	Y	Each	Total
Bal	6.31	4.25	0.17	0.13	0.021	0.014	0.001	<0.001	0.10	<0.4

For each test three replications were performed (whit a total of six experiments) to ensure the robustness of the obtained data and the reliability of the developed FE numerical model. During laser texturing the thermal history was recorded by a FLIR A655sc Infra-Red Camera (IRC), allowing to measure the temperature profiles on the heat treated surface. The material emissivity was determined by calibrating infrared camera measurements against thermocouple readings on a sample heated in controlled temperature increments, yielding a consistent emissivity value of 0.36. A range of 100-650 °C was set to analyze the thermal cooling phase of the process due to its longer duration. The temperature was measured along the entire treated line and it was used to calibrate, by an iterative trial and error procedure, both the temperature and the convection coefficient of the heat exchange windows adopted in SFTC DEFORM-3DTM for modeling the laser heat source. After surface treatment, three samples were cut for each experimental test for a total of 18 samples. The transverse sections were embedded in a black bakelite mounting resin and polished for optical microscope analysis to measure molten pool width, penetration depth and remelting layer of laser treatment. Fig. 1 presents the macrograph obtained from the optical microscope (OM) and the geometrical parameters adopted to characterize the cross-section of the laser process.

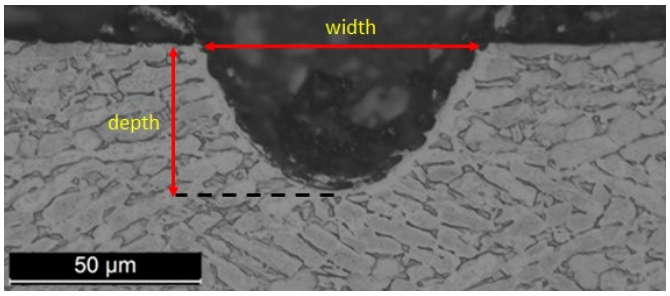


Figure 1 – Optical microscopy image of the transverse section of the laser-treated surface (scanning speed = 45 mm/sec)

Numerical procedure.

The process simulation was conducted using SFTC DEFORM-3D™ with the heat transfer mode activated. The workpiece, with dimensions of 2 mm thickness, 5 mm width and 5 mm length, was modeled as a plastic body and discretized into 389,000 iso-parametric tetrahedral elements (Fig. 2). For the thermal boundary conditions, it was assumed that the entire workpiece was in contact with the surrounding air, thus facilitating heat exchange with the environment. A free-air

Materials Research Proceedings 57 (2025) 377-384 https://doi.org/10.21741/9781644903735-44

convection coefficient of 20 W/(m²K) was applied, which is within the typical range of 5 to 25 W/(m²K) as reported in [15].

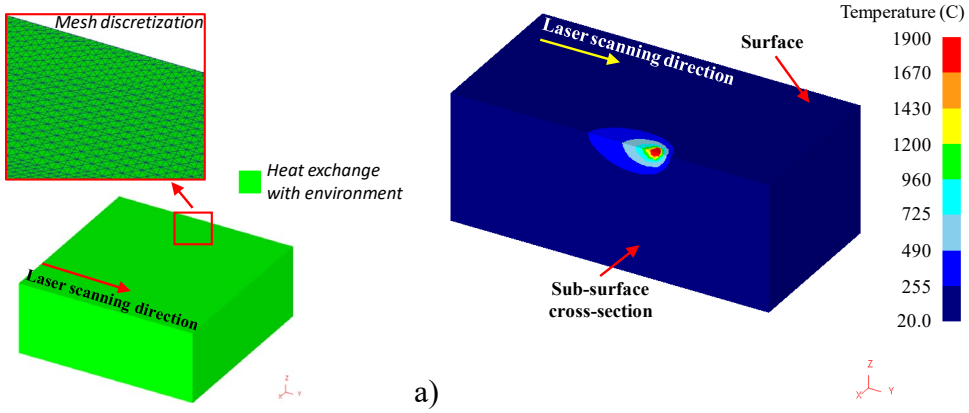


Figure 2 – Finite element a) modeling of thermal boundary conditions and b) workpiece sliding view (section along x axis) showing the heat source movement across the surface and subsurface

To represent the laser surface treatment, a three-dimensional conical Gaussian heat source model was employed. In this model, r_e and r_i correspond to the upper and lower radii, respectively, while z_e and z_i denote the cone's height (Fig. 3a). The heat source model was integrated into the software by defining a series of concentric 3D heat exchange windows that replicate the conical shape (Fig. 3b). To accurately simulate the laser thermal behaviour, each of these windows requires the specification of both temperature and convection coefficient values. Based on the experimental setup, two distinct movement speeds 30 and 45 mm/sec were applied to the heat exchange windows. All heat source parameters, as well as the thermal parameters (temperature and convection coefficients) of the heat exchange windows, were determined by considering the experimental macrographs and the thermal gradient.

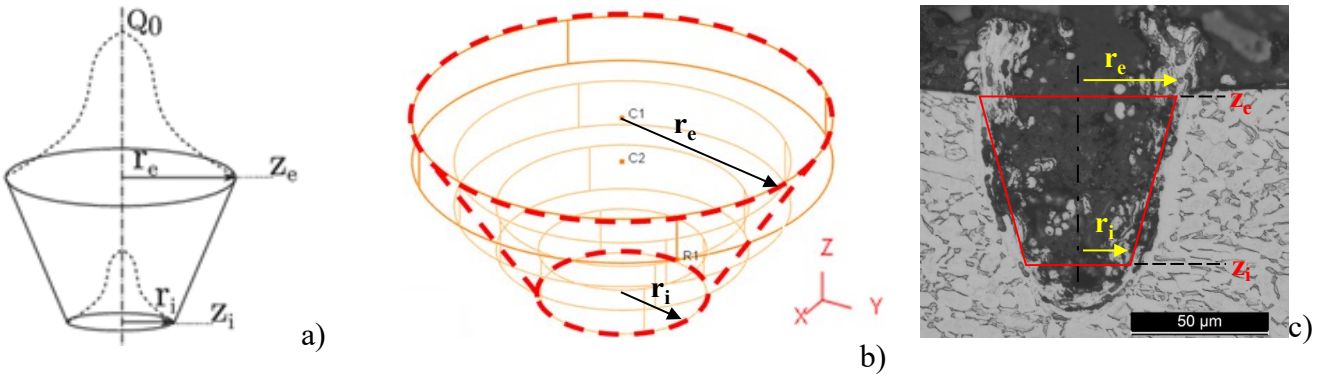


Figure 3 – a) Gaussian heat source model, b) DEFORM heat exchange windows and c) OM macrograph for heat source model parameters (scanning speed = 30 mm/sec)

In particular, the geometrical parameters defining the conical shape were extracted from the macrographs (Fig. 3c). The temperature and convection coefficients associated with the heat exchange windows were calibrated using an iterative trial-and-error approach [16]. In this process, numerical simulation results were systematically compared with experimental data, including molten pool width, penetration depth, remelting zone (Ti-oxide region) induced by laser treatment and the overall temperature distribution. Calibration was performed using a single reference case with a laser scanning speed of 30 mm/s. This process yielded calibrated values of 10,000 °C for temperature and 300 N/s/mm/°C for the convection coefficient, enabling the identification of the optimal trade-off in terms of the absolute error across all investigated outputs (Fig. 4).

Materials Research Proceedings 57 (2025) 377-384 https://doi.org/10.21741/9781644903735-44

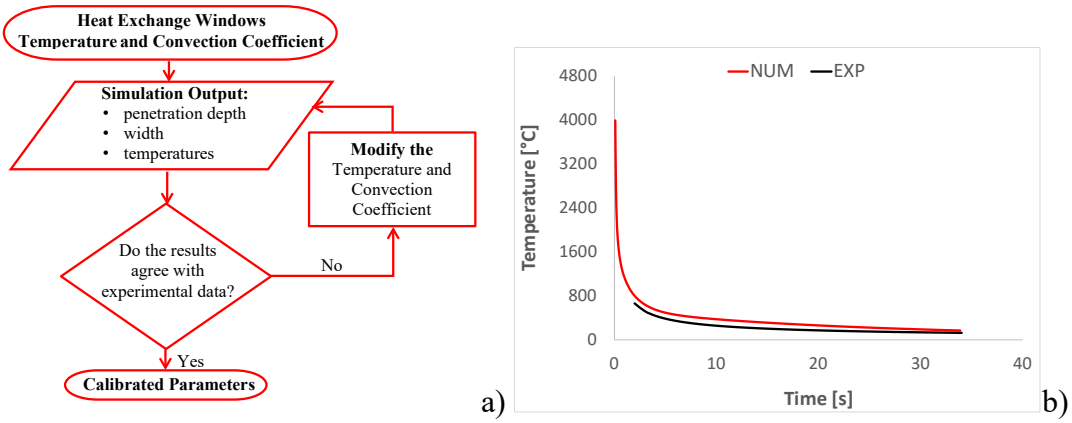


Figure 4 – a) Iterative trial and error calibration procedure for the thermal coefficients of the heat exchange window and b) numerical and experimental comparison of the temperature cooling rate (scanning speed = 30 mm/sec)

Results

The numerical procedure was validated by comparing experimental results with predicted data under varying laser scanning speeds at 30 and 45 mm/sec. Fig. 5 shows a comparison between the simulated molten pool width and penetration depth of the laser and the corresponding experimental results obtained from metallographic analysis, showing good agreement.

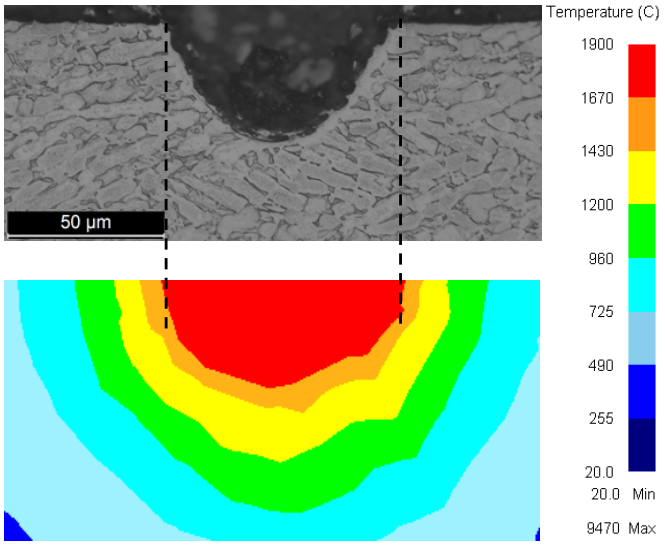


Figure 5 – Numerical laser surface heat treatment prediction and validation (scanning speed = 45 mm/sec)

As outlined in [17], the temperature distribution predicted by the numerical model at the edge of the molten pool illustrates how the selected process parameters facilitate the ablation of the material surface and the remelting, leading also to the formation of a liquid molten pool that solidifies rapidly (at a cooling rate exceeding 400°C/sec). This rapid cooling process effectively suppresses grain growth, prompting a shift in the microstructure that promotes martensite formation. The remelted layer, with its martensitic microstructure, exhibits refined grains, resulting in improved microhardness, Young's modulus and wear resistance, which are characteristic of the martensitic phase [18].

Materials Research Proceedings 57 (2025) 377-384 https://doi.org/10.21741/9781644903735-44

Fig. 6 presents the stable and uniform numerical results, offering detailed insights into the simulated thermal field. The data reveals a decrease in the thermally affected zone as the scanning speed increases from 30 to 45 mm/sec, which accentuates the "comet tail" profile. This observation is consistent with the findings in [19], where laser power, spot size and scanning speed are used to define the laser energy line (Eq. 1).

$$E_{line} = \frac{P_{laser}}{V_s \cdot A} \left[\frac{J}{m^3}\right] \quad (1)$$

In this equation, P_{laser} represents the laser power, V_s denotes the scanning speed and A refers to the laser spot size. This parameter is crucial for assessing laser material removal mechanisms. In this study, where only the scanning speed was varied, being the laser energy line an inverse function of scanning speed, it was highlighted that increasing the scanning speed results in a decrease in E_{line} (Tab. 2). Such reduction corresponds to a lower energy input per unit volume, which in turn sharpens the localization of the thermal gradient around the laser spot, thereby enhancing the visibility of the "comet tail" profile.

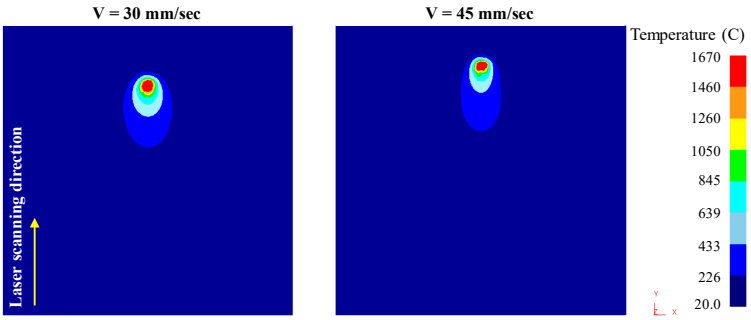


Figure 6 – FE thermal gradient prediction

This observation aligns with the results presented in Fig. 7, where the comparison between numerical and experimental data shows that an increase in scanning speed leads to a reduction in the laser energy line, resulting in decreased width and penetration depth. Notably, a relative error of less than 10% was observed for both the width and penetration depth. The minor discrepancy between the numerical and experimental outcomes can be attributed to several factors: (i) the trial-and-error approach used to define the heat source constants, (ii) the mathematical modeling of the heat source (iii) the discretization of the material.

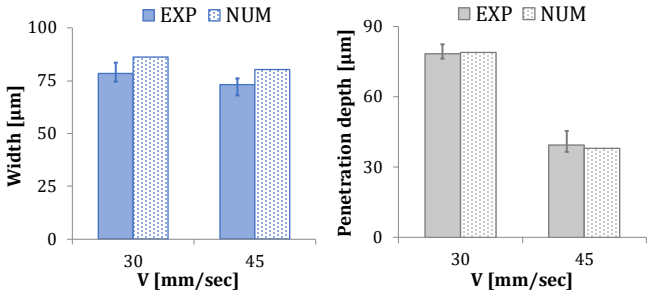


Figure 7 – Numerical and experimental molten pool geometry comparison

Furthermore, the ratio of penetration depth to molten pool width (Table 2) serves as a critical indicator for assessing process quality. The slight variation in molten pool width with changes in scanning speed causes this ratio to be predominantly governed by the penetration depth.

Materials Research Proceedings 57 (2025) 377-384 https://doi.org/10.21741/9781644903735-44

Table 2 – Experimental laser energy and molten pool geometry

Scanning speed (mm/sec)	**30**	**45**
Energy line (J/m^3)	1.12 x 10^{12}	7.48 x 10^{11}
Depth/Width	1.02	0.54

A comprehensive analysis of both experimental and numerical data reveals that increasing the laser scanning speed from 30 to 45 mm/sec reduces the laser energy line, which in turn lowers laser effectiveness in material removal and causes a significant decrease in penetration depth. Finally, Fig. 8 presents a comparison between the predicted laser track and the experimental results, demonstrating a strong agreement in shape and confirming the accuracy of the model in simulating the laser effect.

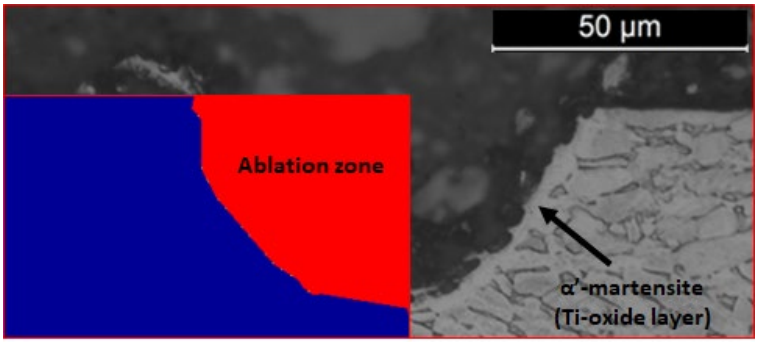


Figure 8 – FE molten pool geometry prediction (scanning speed = 45 mm/sec)

The proposed tool demonstrates outstanding effectiveness in predicting temperature distribution, molten pool geometry and assessing the impact of laser heat treatment as a function of scanning speed. This approach significantly reduces the need for labor-intensive experimental trial-and-error procedures, while also enabling efficient control of the laser as a material modification tool, allowing for precise management of both molten pool width and penetration depth.

Summary

This study presents a comprehensive investigation of the laser surface treatment of Ti6Al4V alloy, integrating both experimental and numerical approaches. The key findings are as follows:

- Experimental analysis and finite element modeling (FEM) underscore the critical role of precisely controlled laser parameters in shaping molten pool geometry and influencing thermal effects during treatment.
- Increasing the scanning speed from 30 to 45 mm/s led to a reduction in both molten pool width and penetration depth, due to the corresponding decrease in line energy.
- FEM simulations provided valuable insights into temperature distribution and molten pool geometry, essential for evaluating the effectiveness and quality of the laser material removal process.
- A high level of accuracy was achieved, with relative errors below 10% when comparing numerical predictions with experimental results, confirming the reliability of the FEM model.
- The study highlighted the importance of the ratio between penetration depth and molten pool width as a key indicator of process quality.
- The developed numerical tool proved highly effective in predicting laser treatment outcomes, significantly reducing the need for costly and time-consuming trial-and-error experimentation.

- The proposed numerical strategy demonstrated the effectiveness of a process-temperature-driven approach for heat source modeling, offering a robust alternative to conventional geometry-based definitions of heat flux and laser thermal efficiency. This method allows for the integration of various heat source geometries, thereby enhancing the versatility and precision of the model.
- The modeling framework supports efficient management of laser parameters, enabling precise control over molten pool dimensions, crucial for optimizing material properties and improving overall treatment performance.

References

[1] E. Akman, A. Demir, T. Canel, T. Sınmazcelik, Laser welding of Ti6Al4V titanium alloys, J. Mater. Process. Technol. 209 (2009) 3705–3713. https://doi.org/10.1016/j.jmatprotec.2008.08.026

[2] S. Caruso, D. Umbrello, J.C. Outeiro, L. Filice, F. Micari, An experimental investigation of residual stresses in hard machining of AISI 52100 steel, Proc. Eng. 19 (2011) 67-72. https://doi.org/10.1016/j.proeng.2011.11.081

[3] G. Rotella, F. Cosco, M.R. Saffioti, D. Umbrello, Evaluation of fretting corrosion fatigue in burnishing of Ti6Al4V component for artificial hip joint, CIRP Annals 72 (2023) 509-512. https://doi.org/10.1016/j.cirp.2023.04.010

[4] M. Conradi, A. Kocijan, D. Klobcar, M. Godec, Influence of laser texturing on microstructure, surface and corrosion properties of Ti-6Al-4V, Metals 10 (2020) 1504. https://doi.org/10.3390/met10111504

[5] G. Rotella, C. Morano, M.R. Saffioti, D. Umbrello, Surface functionalization of titanium screws for orthopaedic implant applications, CIRP Annals 73 (2024) 453-456. https://doi.org/10.1016/j.cirp.2024.04.095

[6] A. Woźniak, O. Bialas, M. Adamiak1, B. Hadzima, J. Szewczenko, The influence of laser texturing on the tribological behavior of titanium alloy Ti6Al4V in medical applications, Arch. Civ. Mech. Eng. 24 (2024) 146. https://doi.org/10.1007/s43452-024-00960-3

[7] B. Li, J. Du, Y. Sun, S. Zhang, Q. Zhang, On the importance of heat source model determination for numerical modeling of selective laser melting of IN625, Optic. Laser Technol. 158 (2023) 108806. https://doi.org/10.1016/j.optlastec.2022.108806

[8] Y. Wang, S. Xiu, G. Yang, S. Zhou, C. Sun, B. Li, D. An, S. Zhang, S. Xiu, Effect of laser remelting on microstructure and mechanical properties of Ti–6Al–4V alloy prepared by inside-beam powder feeding, Mat. Sci. Eng. A 861 (2022) 144266. https://doi.org/10.1016/j.msea.2022.144266

[9] A. Del Prete, L. Filice, D. Umbrello, Numerical simulation of machining nickel-based alloys, Proc. CIRP, 8 (2013) 540-545. https://doi.org/10.1016/j.procir.2013.06.147

[10] M.R. Saffioti, G. Rotella, D. Umbrello, Superfinishing processes applied on the biomedical implants surface to improve their performance, Mater. Res. Proc. 28 (2023) 1341-1346. https://doi.org/10.21741/9781644902479-145

[11] G. Rotella, M. Sanguedolce, M.R. Saffioti, L. Filice, F. Testa, Strategies for shaping of different ceramic foams, Procedia Manuf. 47 (2020) 493-497. https://doi.org/10.1016/j.promfg.2020.04.345

[12] A.K. Unnia, M. Vasudevana, Determination of heat source model for simulating full penetration laser welding of 316 LN stainless steel by computational fluid dynamics, Mater. Today Proc. 45 (2021) 4465–4471. https://doi.org/10.1016/j.matpr.2020.12.842

[13] F.S. Li, L.H. Wu, H.B. Zhao, P. Xue, D.R. Ni, D.R. Xiao, Z.Y. Ma, Realizing deep penetration and superior mechanical properties in a titanium alloy thick plate joint via vacuum laser beam welding, J. Mater. Res. Technol. 26 (2023) 2254-2264. https://doi.org/10.1016/j.jmrt.2023.08.059

[14] C. Zhai, J. Xu, Y. Li, Y. Hou, S. Yuan, X. Wang, Q. Liu, Study on surface heat-affected zone and surface quality of Ti-6Al-4V alloy by laser-assisted micro-cutting, J. Adv. Manuf. Technol. 109 (2020) 2337–2352. https://doi.org/10.1007/s00170-020-05794-w

[15] D. Umbrello, S. Caruso, S. Imbrogno, Finite element modelling of microstructural changes in dry and cryogenic machining AISI 52100 steel, Mater. Sci. Technol. 32 (2016) 1062-1070. https://doi.org/10.1080/02670836.2015.1104

[16] D. Umbrello, L. Filice, S. Rizzuti, F. Micari, On the Evaluation of the Global Heat Transfer Coefficient in Cutting, Int. J. Mac. Tools. Manuf. 47 (2007) 1738-1743. https://doi.org/10.1016/j.ijmachtools.2006.12.002

[17] K. Bartsch, D. Herzog, B. Bossen, C. Emmelmann, Material modeling of Ti6Al4V alloy processed by laser powder bed fusion for application in macro-scale process simulation. Mater. Sci. Eng. A, 814 (2021) 141237. https://doi.org/10.1016/j.msea.2021.141237

[18] M. Kumagai, M.E. Curd, H. Soyama, T. Ungar, G. Ribarik, P.J. Withers, Depth-profiling of residual stress and microstructure for austenitic stainless steel surface treated by cavitation, shot and laser peening, Mater. Sci. Eng. A, 813 (2021) 141037. https://doi.org/10.1016/j.msea.2021.141037

[19] D. Lee, S. Pyo, Experimental investigation of multi-mode fiber laser cutting of cement mortar, Materials 11 (2018) 278. https://doi.org/10.3390/ma11020278

Materials Research Proceedings 57 (2025) 385-392 https://doi.org/10.21741/9781644903735-45

Surface Integrity study in cryogenic milling of Ti-6Al-4V titanium alloy

Paolo Albertelli[1,2,a *] and Michele Monno[1,2,b]

[1]Mechanical Engineering Department, Politecnico di Milano, via la Masa 1, 20156 Milan, Italy

[2]Consorzio MUSP via Callegari 29122 Piacenza Italy

[a]paolo.albertelli@polimi.it, [b]monno.michele@polimi.it

Keywords: Cryogenic Milling, Surface Integrity, Residual Stresses, Modelling

Abstract. Titanium alloys, such as Ti-6Al-4V, are widely used in aerospace and biomedical fields due to their superior properties, but machining these materials remains a significant challenge. This study investigates the effects of cryogenic machining on the surface integrity of Ti-6Al-4V. Experimental milling tests were conducted under varying cutting conditions of feed and cutting velocities, focusing mainly on residual stresses. It was found that residual stresses are affected mostly by the feed per tooth. A preliminary Finite Element Model was developed and validated, across different cutting conditions, to predict residual stresses in cryogenic machining, incorporating both mechanical and thermal aspects. Maximum error of 9% was observed on the residual stress estimation, both considering the residual stresses on the surface and the maximum compressive values. Higher errors were found regarding the estimation of the depth of the maximum compressive stresses.

Introduction

Titanium alloys are interesting metals for their performance and capabilities in different fields, like aerospace and biomedical, however they are hard to cut materials, and their processing is a challenge. Cryogenic may represent an alternative to conventional cutting strategies, so its potential benefits (friction reduction, temperature reduction, better surface finishing and compressive residual stresses) should be explored to understand its real advantages [1], [2]. The generation of compressive residual stress is a crucial aspect in machining because it can bring a lot of benefits to the final component, such as an enhanced resistance to crack initiation under fatigue loading. Cryogenic machining is a new-born technology the possibility of using Finite Element FE Analysis can be very helpful in understanding the origins of the residuals stresses. Although several works on this topic were found (e.g. [1]), the novelty of this research is linked to the simulation of a high-feed tool milling operations with a through nozzle cryogenic system.

Materials and methods

In the following subsection, an overview of the experimental activities and the details of the developed model are provided.

Experimental set-up

The machining test were performed on a Mandelli M5 horizontal spindle milling machine. The machine is equipped with a hydrostatic spindle (maximum available torque of 130Nm, cutting power of 65kW and with a maximum rotational speed of 8000rpm). Moreover, the machining center was equipped with a custom-made cryogenic setup that allowed to deliver the cryogenic coolant respectively through the machine head and the inner tool nozzles. The setup is presented and described in Fig. 1 a). The workpiece Fig. 1 b) was machined using a high feed mill (JX06R203SA20S) produced by Mitsubishi with a diameter of 20 mm and three teeth Z=3. Mitsubishi JOMT06T216ZZER-JL MP9140 inserts were used for the experimental campaign. The measurement of residual stress was done using the X-ray diffraction XRD technique with the AST

Content from this work may be used under the terms of the Creative Commons Attribution 3.0 license. Any further distribution of this work must maintain attribution to the author(s) and the title of the work, journal citation and DOI. Published under license by Materials Research Forum LLC.

Materials Research Proceedings 57 (2025) 385-392 https://doi.org/10.21741/9781644903735-45

X-Stress 3000 machine equipped with XTronic software for processing the measurements, Fig. 1 c). The analyses were performed on the cross section of the workpiece, Fig. 1 c). Residual stresses were evaluating according to the depth from the machined surface. The stress on the surface $\sigma_{surface}$, the maximum compressive stress σ_{peak} and its location (peak depth) underneath the machine surface were evaluated.

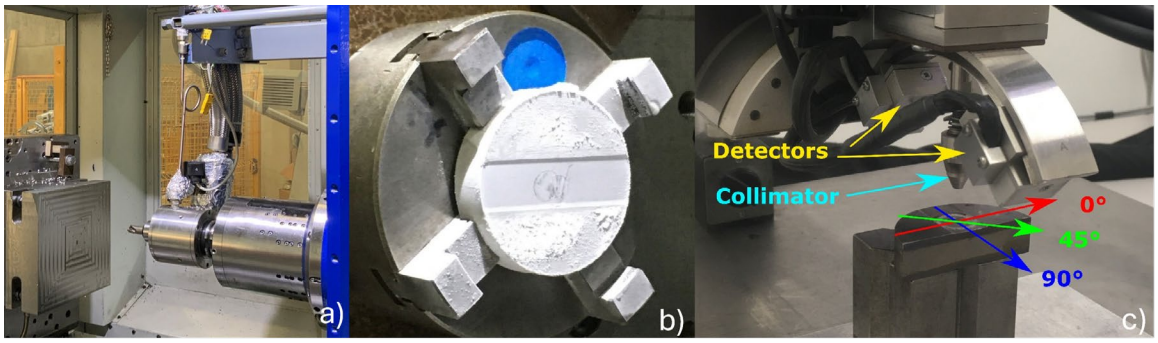


Fig. 1: a) Cryogenic experimental set-up b) processed workpiece c) Detail of directions for XRD measurements

Experiments were conducted in different cutting conditions to analyze the effects two parameters. A 2^2 factorial approach was adopted. The feed per tooth f_z and the cutting velocity v_c were the considered factors, Table 1. In this study one single repetition for each test condition was carried out. Although it could seem limiting, other research works used the same approach, [2].

Table 1: Experimented cutting conditions

	$v_c[m/min]$	$f_z[mm/tooth]$	condition
C1	75	0.7	cryogenic
C2	50	0.85	cryogenic
C3	100	0.55	cryogenic
C6	100	0.85	cryogenic
C8	50	0.55	cryogenic

Model Development

The setup of the simulation was crucial to understand the effect of the cryogenic cooling on the machining of the piece. The simulation was arranged in several steps, each of them representing a specific condition of the cutting operation. First, the material removal performed by the insert is simulated, then the following material cooling phase was considered, including the return to equilibrium with the environment was taken into consideration. The proposed approach is in accordance with what adopted by Liu et al. [3]. Liquid nitrogen is delivered by the tool in front of the insert. However, the interaction between the coolant and the workpiece continues also after the cut when the mill keeps rotating and feeding, and the other inserts pass on the machined region. A series of steps with the alternation between cooling in air and in liquid nitrogen, till a final cooling in air brings the component to ambient condition can be considered. The delivery of the coolant is simulated as a box placed in front of the insert, the red and green ones in Fig. 2. The picture shows a schematic representation of the simulation principle. As every new insert approaches the studied area (orange rectangle), the cryogenic box moves in the feed direction.

Materials Research Proceedings 57 (2025) 385-392 https://doi.org/10.21741/9781644903735-45

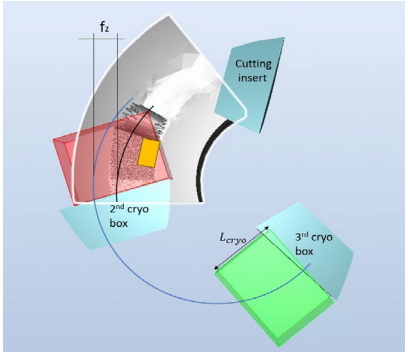


Fig. 2: Cryogenic Model set-up: considered phases

The feed per tooth parameter affects the number of times the liquid nitrogen interacts with the machined area. The size of the box affects the area that is cooled at every passage of the insert and even the amount of time a point on the machined surface is cooled by LN_2. While height and width are defined as the front edge of the insert, the length L_{cryo} (Fig. 2) of this box is more difficult to be set (Tamasebhi [4]). When the cryogenic window passes on the workpiece, the material exchanges heat with the evaporated nitrogen that surrounds the tool. If the length is set too high, the time period of cryogenic cooling is over-estimated and the temperature on the surface decreases more than the real conditions, vice-versa the temperature does not decrease enough. The geometries of the tool and workpiece were generated on a CAD software (Inventor) and then imported in FORGE. Here, the trajectory of the insert is set depending on the combination of feed and cutting velocity. The adopted formulation for describing the material behavior (flow stress $\bar{\sigma}$) as function of the main involved quantities $\bar{\sigma} = f(\epsilon, \dot{\epsilon}, T)$, ϵ strain, $\dot{\epsilon}$ strain rate and temperature is provided by Johnson-Cook, Eq. 2.

$$\bar{\sigma} = [A + B \cdot \epsilon^n] \cdot \left[1 + C \cdot ln\frac{\dot{\epsilon}}{\dot{\epsilon_0}}\right] \cdot [1 - (T^*)^m] \quad (2)$$

Where T^* is the homologous temperature $T^* = (T - T_r)/(T_m - T_r)$. T_r is the reference temperature for the fitted coefficients, and T_m is the melting temperature of the material. This model allows to account for the strain hardening, the effect of strain rate and the temperature softening, all relevant in machining operations. The adopted experimental coefficients were taken from Lee-Lin [5]: A= 782.7 MPa; B = 498.4 MPa; C = 0.028; n = 1.0; m = 1 ×10−5.

To assure a correct simulation of the chip morphology, the material model was paired with a Damage model, the Latham-Cockcroft one, Eq. 3 (Albertelli et al. [2]). D is the threshold value that is used for eliminating the damaged elements during the simulations, σ_I is the highest principal component of the stress tensor, and ϵ_f is the limit fracture strain, i.e. the effective strain value where the damage function (Eq. 3) reaches the limit value D

$$D = \int_0^{\epsilon_f} \sigma_I \, d\epsilon \quad (3)$$

In this research a D=400MPa was set, (Albertelli et al. [2]). After setting the characteristics of the material, the interactions between the parts and with the environment should be accounted. Between the insert and the workpiece, a stick-slip friction model (Coulomb-Tresca) was adopted with the coefficients set to μ = 0.2 and m_f=0.25 to describe the presence of the cryogenic flow in a proper way, (Albertelli et al. [2]). Also, it is important to characterize the thermal problem for both the machining and cooling part of the simulation. First, the heat exchange between the tool and the workpiece was accounted by setting the conductance at the tool-workpiece interface to 10 kW/m^2. Then, the tool effusivity is computed as $e = 111\, kW\sqrt{s}/\left(K\sqrt{m}\right)$. Then, the heat transfer coefficients (HTC) between the material and the environment are set. When the cryogenic window

Materials Research Proceedings 57 (2025) 385-392 https://doi.org/10.21741/9781644903735-45

passes on the workpiece, the material exchanges heat with the evaporated nitrogen that surrounds the tool. For this purpose, the ambient temperature is reduced to −150 ◦C. For evaporated nitrogen the HTC is set to 1500 $W/(m^2\ K)$. However, close to the tool, where the coolant is delivered, there is a high probability of finding liquid nitrogen. In this region, the temperature of −195 ◦C was set. In this area, the heat exchange is faster, and a dedicated HTC was defined for this condition. For liquid nitrogen, the HTC is a function of the temperature of the workpiece's surface, Pusavec et al. [5].

Results and Discussion

The results of this experimental campaign are collected Fig. 3. This comparison is helpful to understand the effect of the cutting parameters on the residual stresses a). In Fig. 3 b) the estimated quantities reported in Table 2 were put into evidence.

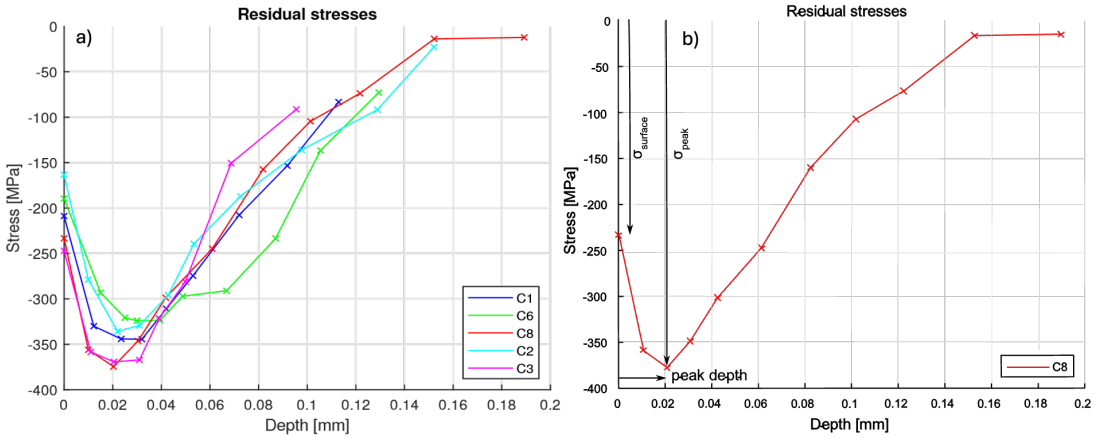


Fig. 3: Measured Residual Stresses – different cutting conditions - cryogenic a), b) analysed quantities

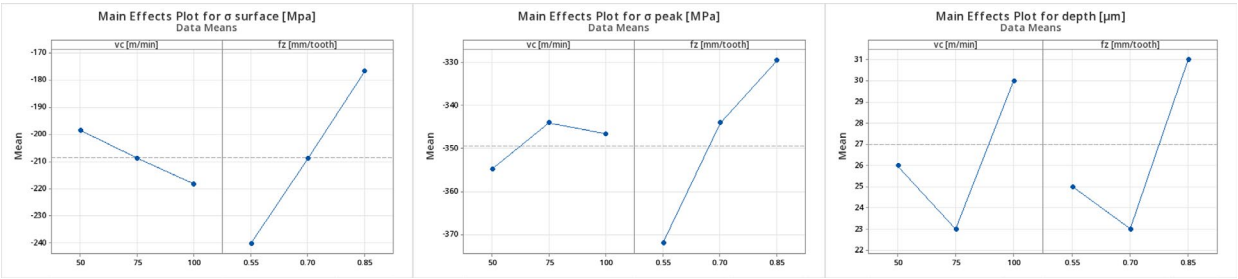


Fig. 4: Mean effect plots (experimental data) on the main quantities reported in Fig. 3.

Overall, the following observation can be carried out:

- The cutting velocity v_c influences the depth of material affected by the process and in which residual stresses are significant. Higher cutting velocity is associated to a deeper portion of material interested by the phenomenon.
- The feed per tooth f_z influences the peak of stresses (σ_{peak}) below the surface. Lower is f_z, higher is the peak value of the compressive residual stress.

However, between the two, the effect of the feed is more important and visible from the experimental data (main effect plot in Fig. 4), while the cutting velocity v_c is more marginal and not so relevant. The most important conclusion is that both the peak value σ_{peak} and the surface value of residual stress $\sigma_{surface}$ get more compressive with lower values of the feed. A challenge of this research is to try to understand and to predict this phenomenology using a model. In Fig. 5, the results of the simulations runs in the same cutting conditions that were tested in the experiments

Materials Research Proceedings 57 (2025) 385-392 https://doi.org/10.21741/9781644903735-45

are presented. By comparing Fig. 3 and Fig. 5, the effect of f_z is visible also considering the simulated results. It can be noticed that the increase of f_z (from 0.55mm/tooth to 0.85mm/tooth considering the min and max conditions) reduces both the peak and surface values of stress. Instead, the effect of the cutting velocity is not well represented, and the results have a worse agreement to the experimental data when comparing the profiles after the compressive peak in the material. In all the simulated cases, residual stresses approach zero faster than the real case after the peak. After having discussed the results of the simulations and resumed the comparison between the experimental and numerical results (Table 2), the objective of the discussion is to understand the phenomenology that drives the generation of residual stresses during the cutting. The numerical-experimental errors are rather limited. Maximum error of 9% was observed on the residual stress estimation, both considering the residual stresses on the surface and the maximum compressive values. From the phenomenological perspective, the temperature evolution resulting from the succession of machining and cooling is analyzed in Fig. 6 b), for the cutting condition C1. After the initial temperature decreases due to the cryogenic flow present in front of the insert, the temperature reaches a peak while the insert is cutting the material. Later, the workpiece goes through an alternate cooling in contact with air and cryogenic coolant, which is due to the passage of the successive inserts of the mill on the surface. Starting from the stress evolution during the cut, Fig. 6 a) is a screen capture of the FE model while the insert is in the material. Five zones are highlighted in the picture.

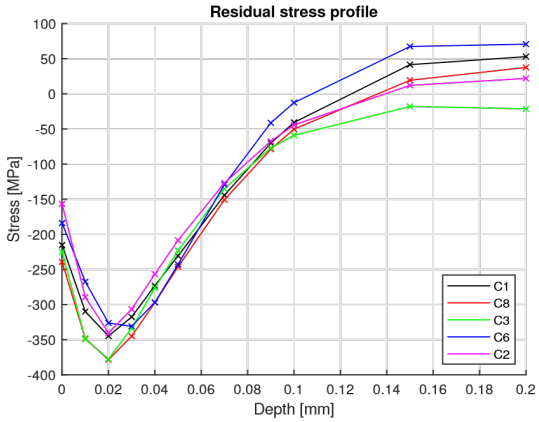


Fig. 5: Simulated Residual Stresses – different cutting conditions – cryogenic

The primary deformation zone is where the strain hardening of the material takes place, with the formation of the chip. Here, the largest strain rate and compressive stress are registered. The secondary deformation zone is where the contact between the tool and the chip occurs, here the largest temperature is found due to friction. Both these zones are the major heat sources in the process. Then, other three zones are found in the material.

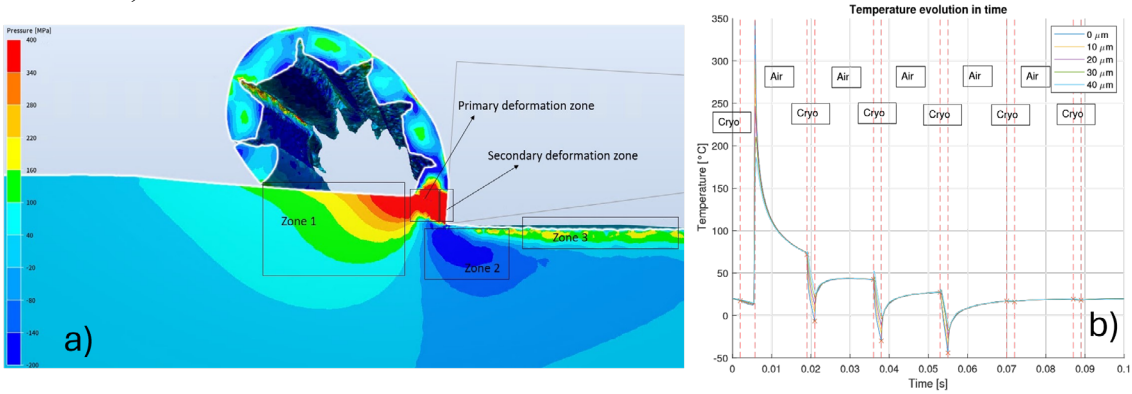


Fig. 6: a) Hydrostatic stress distribution b) temperature evolution in time – cutting condition C1

Materials Research Proceedings 57 (2025) 385-392 https://doi.org/10.21741/9781644903735-45

The first (zone 1) is ahead of the cutting tool, where there is an area with large compressive stresses directly induced by the cutting forces (red color). Then the second zone (zone 2) is along the shear plane, but in the opposite direction. While the stress in this plane is compressive where there is chip generation, in the opposite direction, so towards the core of the workpiece, the stress generated by the shear movement of the workpiece is tensile (blue color).

Table 2: comparison between simulated and experimental data for the tested conditions

	$\sigma_{surface}$ $[MPa]$	σ_{peak} $[MPa]$	Peak depth $[\mu m]$	Err. $\sigma_{surface}$[%]	Err. σ_{peak}[%]	Err. depth [%]
C1 (exp)	-208.7	-344	23	-3.2	-0.2	-30.4
C1 (sim)	-215.3	-344.7	30			
C2 (exp)	-163.7	-335.2	22	4.3	-1.6	9.1
C2 (sim)	-156.7	-340.4	20			
C3 (exp)	-247.0	-369.3	20	9.0	-2.2	0.0
C3 (sim)	-224.8	-377.4	20			
C6 (exp)	-189.6	-323.9	40	3.0	-2.2	25.0
C6 (sim)	-183.9	-330.9	30			
C8 (exp)	-233.3	-374.5	30	-2.6	-1.0	0.0
C8 (sim)	-239.4	-378.3	30			

This may be explained by equilibrium reasons, the compressive area in the secondary deformation zone is balanced by a tensile region in zone 2. Then, away behind the insert (zone 3), the mechanical action is not directly affecting the workpiece, but the thermal loads start to be more important. Here, the largest compressive stress is found not on the surface but below it. In this phase, cooling takes place in air, since it is assumed that the cryogenic flow is placed only in front of the insert. In Fig. 7 a), the residual stress distribution for cutting condition C1 found at the end of the simulation is compared to the stress profile at the end of the first air cooling after the cut. While at the end of the simulation the estimated residual stress agrees with the experimental data, the distribution is quite different at the end of the first air cooling. The trend of the profile is the same, but the values of the peak (σ_{peak}) and on the surface ($\sigma_{surface}$) are lower. It can be derived that the presence of the cryogenic coolant impacts the residual stress formation also during the subsequent cooling phases.

The first two cooling steps right after the cutting operation (the first in air and the second with the cryogenic flow) bring down the temperature of the workpiece. Liquid nitrogen gives a fast cooling in a short time, resulting in the formation of a temperature gradient between the surface and the sub-surface. Indeed, Fig. 7 b) shows the temperature difference along the depth of the workpiece after the cryogenic cooling. The lower temperature (T_{cryo0} = -6.5 ◦C) is found on the surface, while higher values are seen below it, like at 40 μm where T_{cryo5} = 29 ◦C.

Materials Research Proceedings 57 (2025) 385-392 https://doi.org/10.21741/9781644903735-45

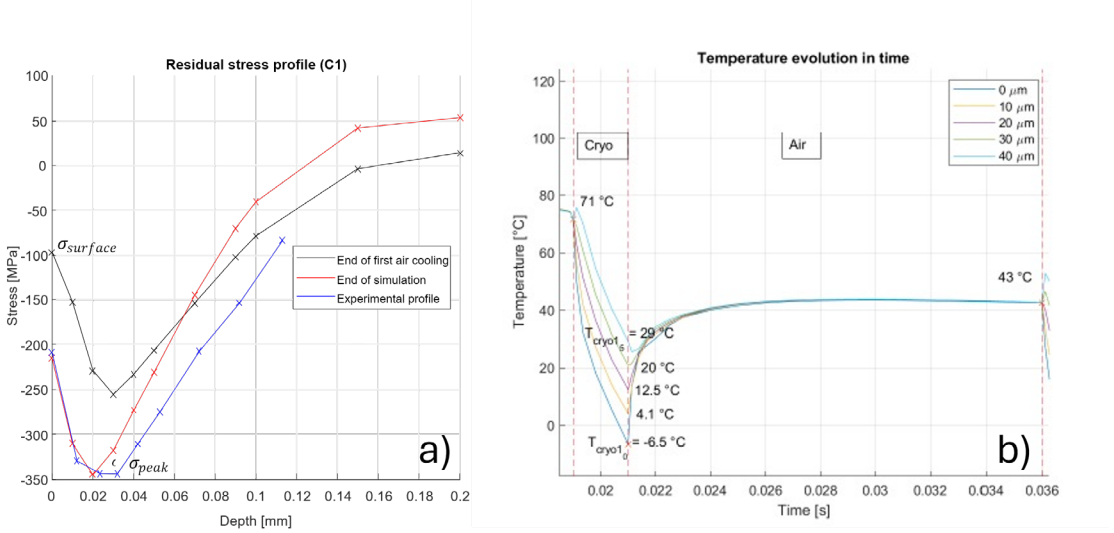


Fig. 7: a) evolution of the residual stresses after subsequent cooling steps – b) temperature evolution

Later on, the surface is exposed again to air, and since the surface temperature is lower than ambient one, there is an increase of temperature in the workpiece and the temperature gradient between the surface and the sub-surface progressively vanishes. This represents a sort of cooling and heating cycle, which is repeated each time the coolant interacts with the surface after the cut, which depends on the feed per tooth. There are four cycles for the conditions C8 and C3 (feed f_z = 0.55 mm/tooth), while there are three for conditions C2, C6 (feed f_z = 0.85 mm/tooth) and C1 (feed f_z = 0.7 mm/tooth). This is because the cutter moves on, meaning a given point on the machined surface is no longer exposed to the liquid nitrogen flux after a certain number of spindle revolutions. Temperature is decreasing, the material contracts. Since in this area, which was called zone 3, a plane stress state is present, the workpiece can be seen as a series of layers piled one over the other. Each of these layers will contract in a different way, according to its temperature reduction. The largest contraction takes place on the surface (greater cooling action) and this is associated to the formation of tensile residual stresses since the sub-surface layers act as a constrain to the upper ones. Thermal residual stresses form since each layer would like to contract freely but is stopped from the other ones. The opposite phenomenon takes place in the air-cooling phase. The material, which is contracted, is now heated in a slow process till it all reaches the same temperature, without a gradient. The material, with the formation of compressive residual stresses on the surface of the workpiece. The opposite happens in the core of the material, where, due to equilibrium, tensile stresses are instead accumulated. The overall effect is the superposition to the initial stress distribution of an amount of compressive stress which depends on the considered depth. The largest contribution is on the surface, where the largest temperature gradient is located deeper in the workpiece, after about 100 μm, tensile stresses are added because of equilibrium.

Results and Discussion

In this work a FE modelling for predicting residual stresses in cryogenic milling was developed and tested in several cutting conditions.

It was found that:

- Liquid nitrogen influences the generation of residual stress during both the cutting and the cooling phases.
- It was experimentally observed that feed per tooth is the most relevant factor affecting the $\sigma_{surface}$, σ_{peak} and the peak depth.

- A FE model was developed for predicting the residuals stresses. The model developed in this work fits best for the lowest cutting velocity and feed (C8) and worst for the highest (C6). The main discrepancies between simulations and experiments were in predicting the compressive peak depth and subsequent stress profile, with simulations reaching tensile stresses faster. The model well reproduces the effect of the feed per tooth.
- From the phenomenological perspective, the low temperature of the cryogenic flow (-195°C) and the high heat transfer coefficient, which promote rapid heat removal from the cutting zone, lowers the maximum temperature in the workpiece, a beneficial aspect for residual stress formation. During post-cutting cooling, the heat accumulated in the workpiece dissipates through contact with the environment or the coolant flow, inducing tensile stresses due to the contraction of the surface layers, while the core acts as a constraint.

References

[1] ISS Jawahir, H. Attia, D Biermann, J. Duflou, F. Klocke, D. Meyer, STT Newman, F. Pusavec , M. Putz, J. Rech, V. Schulze, D. Umbrello. Cryogenic manufacturing processes. CIRP Ann Manuf Technol (2016) 65:713–36. https://doi.org/10.1016/j.cirp.2016.06.007

[2] S. Isakson, M. I. Sadik, A. Malakizadi, and P. Krajnik. Effect of cryogenic cooling and tool wear on surface integrity of turned Ti-6Al-4V (2018). https://doi.org/10.1016/j.procir.2018.05.061

[2] P. Albertelli, M. Strano, M. Monno, Simulation of the effects of cryogenic liquid nitrogen jets in Ti6Al4V milling. Journal of Manufacturing Processes (2023) 85: 323-244. https://doi.org/10.1016/j.jmapro.2022.11.053

[3] H. Liu, C. Wang, Z. Liu, K. Liu, S. Jiang, Y. Wang, Numerical prediction of machininginduced surface residual stress for tc4 cryogenic turning. The International Journal of Advanced Manufacturing Technology (2021) 114:131 144

[4] E. Tahmasebi, P. Albertelli, T. Lucchini, M. Monno, V. Mussi, CFD and experimental analysis of the coolant flow in cryogenic milling. Int J Mach Tools Manuf (2019) 140:20–33. https://doi.org/10.1016/J.IJMACHTOOLS.2019.02.003

[5] W.S. Lee, C. F. Lin, Hightemperature deformation behaviour of ti6al4v alloy evaluated by high strain-rate compression tests. Journal of Materials Processing Technology (1998), 75(1-3):127 136.

[6] F. Pusavec, T. Lu, C. Courbon, J. Rech, U. Aljancic, J. Kopac, and IS Jawahir, Analysis of the influence of nitrogen phase and surface heat transfer coeffcient on cryogenic machining performance. Journal of materials processing technology (2016) 233:19 28.

Materials Research Proceedings 57 (2025) 393-400 https://doi.org/10.21741/9781644903735-46

Resin molds to improve thermal energy consumption in injection molding process

Giulia ZANIBONI[1,a *], Riccardo PELACCIA[2,b], Leonardo ORAZI[1,2,c], Rossella SURACE[3,d], Giovanna ROTELLA[4,e], Vito BASILE[3,f]

[1]EN&TECH, University of Modena and Reggio Emilia, Piazzale Europa 1, 42124 Reggio Emilia, Italy

[2]DISMI, University of Modena and Reggio Emilia, Via Amendola 2, 42122, Reggio Emilia, Italy

[3]CNR-STIIMA, National Research Council, Via P. Lembo 38 F, 70124 Bari, Italy

[4]Department of Engineering, University LUM Giuseppe Degennaro, Casamassima, 70010 Bari Italy

[a]giulia.zaniboni@unimore.it, [b]riccardo.pelaccia@unimore.it, [c]leonardo.orazi@unimore.it, [d]rossella.surace@stiima.cnr.it, [e]rotella@lum.it, [f]vito.basile@stiima.cnr.it

Keywords: Injection Molding, Mold, Energy Efficiency

Abstract. The injection molding process is one of the most widely used in industry to produce plastic parts. To optimize overall energy consumption, controlling thermal energy is a key factor. This can be achieved through smart modifications to the mold design. In this study, two molds made from different materials are compared, focusing on thermal analysis using numerical models. Examined materials for the mold base parts are mold steel and High Temp Resin (Formlabs), while an insert made in steel is used for both cases. The aim is to optimize the thermal energy management inside the mold. The software used is COMSOL Multiphysics for thermal characterization to evaluate thermal behaviour within the mold. Numerical models are calibrated by experimental testing. The results demonstrated that the resin's capacity to retain heat within the steel insert is superior, requiring less thermal energy to maintain the desired temperature and for thermal transients.

Introduction

Injection molding is the most widely used process for high-volume plastic product manufacturing due to its versatility in accommodating various materials and product geometries [1]. Considering all process phases, thermal energy plays a critical role, directly influencing efficiency, product quality, and cost-effectiveness. A global assessment of energy consumption in injection molding reveals that total cycle time is the primary factor affecting overall energy use, with cooling time representing the most significant component [2,3]. Therefore, reducing cooling time leads to a reduction of cycle time and energy consumption. Although the highest power peaks occur during the filling stage, extended cooling times can make cooling phase a significant energy consumer [4]. It becomes central to manage cooling phase in proper mode to reduce energy consumption. A key strategy to this purpose is to optimize the thermal energy distribution within the mold.

Mold design has to take into account this aspect considering geometry, material and channel layout. Traditionally, cooling channels are created by drilling several straight holes within the mold core and cavity. This approach results in variable distances between the cooling channels and mold cavity, leading to non-uniform heat extraction from the cooler.

To address this limitation, it is possible to apply localized cooling by using mold inserts with conformal cooling lines, made using additive manufacturing technologies [5,6]. These technologies are economically sustainable when used in a "hybrid construction" approach,

Content from this work may be used under the terms of the Creative Commons Attribution 3.0 license. Any further distribution of this work must maintain attribution to the author(s) and the title of the work, journal citation and DOI. Published under license by Materials Research Forum LLC.

Materials Research Proceedings 57 (2025) 393-400 https://doi.org/10.21741/9781644903735-46

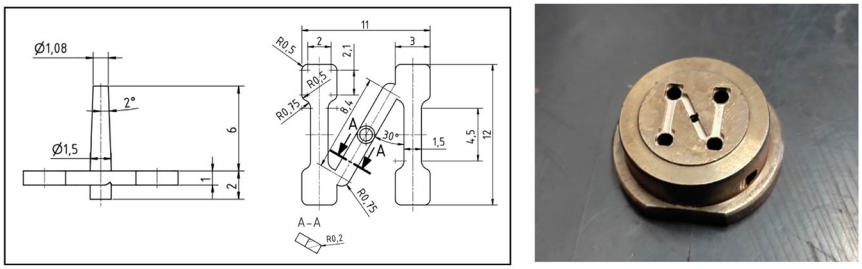
combining conventionally pre-manufactured base workpieces, as a build platform, with additively generated functional geometries of minimized volume [7,8].

Alongside cooling system design, the thermal conductivity of the mold is one of the primary factors influencing the thermal energy behavior. Typically, high-strength steels are used for mold and mold insert fabrication. With the advent of additive manufacturing (AM), different scenarios are now available [9-11]. Among these, the state-of-the-art presents several studies of soft mold inserts (or plates) with cavities made of polymers or composites via AM technologies, but maintaining a conventional steel mold base to guarantee the required mechanical stiffness and strength [11–14]. Leveraging previous results, in this work the research approach is inverted. Assuming the limitations of polymers and composites for mold inserts with cavities, it is possible to conceive a new structure of mold with steel mold inserts and polymeric/composite mold base components (i.e., support plates). These hybrid molds limit the possible drawbacks of thermal and mechanical weaknesses, by exploiting, instead, advantages from the material properties of polymers and composites (i.e., lightweight and thermal insulation). This is an original approach since no previous works were found in the literature. Maintaining a steel mold core with the cavity made by AM technologies allows us to achieve the advantages of conformal cooling and reduced cycle times without limitations compared to conventional steel molds. At the same time, polymeric/composite mold base components change the thermal behavior of the mold and the process, since they do not participate in thermal conduction and heat transfer. Finally, the use of polymer and composite for mold components allows to design of lightweight molds with additional advantages in terms of mechanical energy committed for mold motion (close/open) during the production and in the turnover phases. This approach enables the conception of a more sustainable injection molding process.

In this context, this study aims to test a new mold design by using unconventional materials to optimize thermal energy commitment. The experimental campaign was conducted with a micro-injection molding press by designing and testing hybrid molds consisting of polymeric bases and steel inserts. The comparison with the conventional fully steel system allowed us to preliminary indagate the heat transfer regimes, the thermal transients' evolution as well as the benefits in the use of proposed hybrid solution. For transient numerical analysis, the simulation software COMSOL Multiphysics has been used to model the heat exchanges during the entire injection molding process and then evaluate thermal behaviour inside the mold. COMSOL software is based on finite element method (FEM), used often as a tool to analyze complex multi-physics processes [15,16]. Experimental-numerical comparison was performed to calibrate the numerical model and ensure the numerical approach's goodness as a powerful tool to optimize and reduce the design phase of the mold systems and the entire process.

Experimental procedure

The aim of the experimental activity is to acquire thermal transient data on the molds (traditional and innovative), such as mold temperature variations during the injection molding cycles, from transient to steady state regime. The tested specimen was a mini dog bone tensile sample with a part thickness of 1 mm, length of 12 mm, and width of 1.5 mm in the narrow region and 3 mm in the larger one (Figure 1) [17]. The overall molded mass is about 78mg, comprehensive of sprue, cold runner channels and cavities.



(a) (b)

Figure 1 Specimen design (a) [17] and mold insert, ejection side (b)

Each mold side (injection and ejection) is composed of a mold plate and a mold insert. Mold inserts were fabricated in X33CrS16 steel (Werkstoff nr.1.2085) with traditional cutting (milling and grinding) technologies. By maintaining the same steel inserts, traditional steel mold (TM) and hybrid steel - resin mold (HM) were tested (Figure 2). In TM, mold plates were realized as mold inserts, (i.e., same material and manufacturing technologies). In HM, mold plates were fabricated of photopolymer (Formlabs High-Temp V02) specifically engineered for high-temperature applications via Stereolithography (SLA). The polymer mold plates were designed with a bulk structure in close proximity to bushes and columns required for guiding and alignment of the mold parts and a hexagonal lattice structure in low-stress regions. A Formlabs Form3 machine was used for the mold plates fabrication, by setting the following process parameters: layer thickness of 25µm, part orientation flat on the build platform (XY plane) on base and supports, support density of 1, support attach size of 0.6mm, base thickness of 2mm, part distance from the base of 5mm. Part post-processing consisted of three phases: 1) washing in high purity (99%) isopropyl alcohol (IPA) for 20 minutes; 2) UV-curing in a Formlabs Cure machine for 120 minutes at 80°C; 3) Annealing for 180 minutes at 160°C. Postprocessing operations 2 and 3 allow to achieve an increase in the mechanical properties of the part. Particularly, the annealing allows for reaching a heat deflection temperature of 238°C (HDT at 0.45 MPa, ASTM D648-16), which is a relevant parameter to guarantee the required mechanical performance (stiffness and stability) at the temperatures of injection molding.

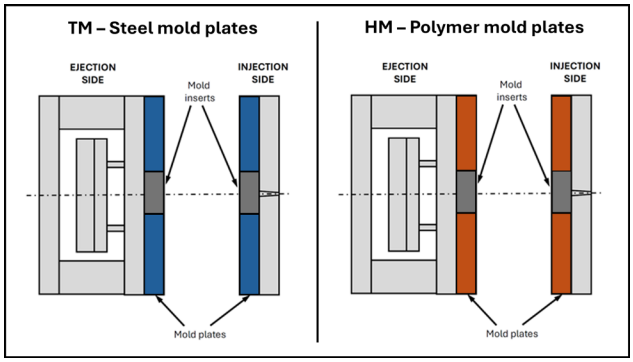


Figure 2 Schematic section of two setups: TM with steel mold plates; HM with polymer mold plates.

Molds are mounted on the injection molding machine Formica Plast 1K by DesmaTec, available in the CNR-STIIMA Lab (maximum injected volume 150 mm^3, maximum injection pressure 300 MPa and maximum injection rate 3.5 cm^3/s).

The polymer used for injection was Polyoxymethylene (POM, Ultraform N2320 003, BASF Engineering Plastics), due to his diffusion for mechanical parts manufacturing, without using coolant during the cooling stage, to analyse the mold's thermal transitory and demonstrate the

Materials Research Proceedings 57 (2025) 393-400 https://doi.org/10.21741/9781644903735-46

feasibility of polymer molds to store the heat committed during the process. Indeed, in the context of sustainable injection molding process, this heat energy can be subsequently extracted with efficient cooling systems of the mold core, thus without heat dispersion into the environment. Process conditions are reported in Table 1.

Table 1 Process parameters settings.

Symbol	Description	Units	Value
T_m	Melt Temperature	°C	230
T_{mo}	Mold Temperature (ambient)	°C	18
V_{inj}	Injection speed	mm/s	150
t_f	Filling Time	s	0.4
t_h	Holding time	s	4
P_h	Holding Pressure	bar	500
S	Piston stroke	mm	10
t_c	Average total cycle time (without coolant)	s	12

The machine has been equipped with sensors to acquire temperature information. The system was designed to acquire the values from two K-types thermocouples every 400ms, thus with a sampling frequency of 2.5 Hz. This enabled a temperature acquisition inside the molding cycle. In detail, thermocouples named T1 and T2 were placed into the holes made in the movable and fixed insert, respectively, which were close to the mold cavity. Data were acquired for 134 cycle, starting from cold mold at room temperature up to the steady-state temperature. This survey permitted to acquire data during heating process of molds for each setup.

Numerical Modeling

The experimental data were used to calibrate the boundary conditions applied in the process simulations for both TM and HM. Consistent with the experimental configuration all process parameters, excluding the mold material properties, were identical for both TM and HM. Numerical simulations were conducted using COMSOL Multiphysics 6.1. To reduce computational time, the 3D model of mold block used for the simulation was simplified compared to the original one. In detail, the injection and the extractor units were modeled as plates, to consider the heat exchanges with the injector and the extractor systems. The complete simulation model, as implemented in COMSOL Multiphysics, is illustrated in Figure 3.

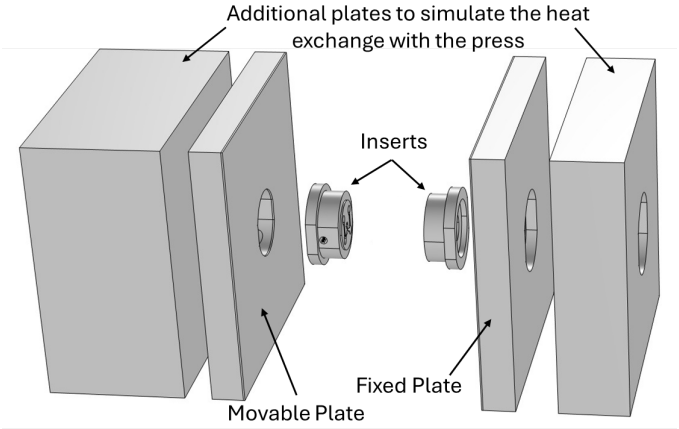


Figure 3 Model used in COMSOL Multiphysics

After importing modified 3D model inside the software all the boundaries were set as shown in Figure 4, considering the injection process dynamics.

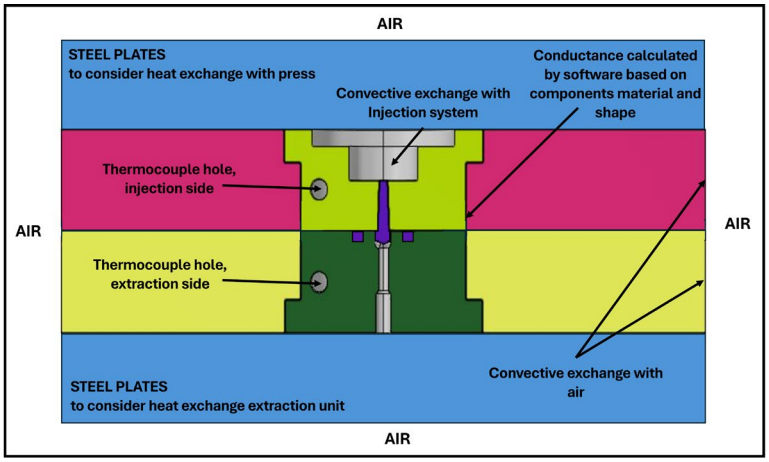


Figure 4 Boundaries setted in COMSOL Multiphysics

Since the model was focused on predicting the thermal field during the process, to strongly reduce the computational time, the fluid dynamic of the injection was simplified with a variable heat source, which increased the POM temperature within the cavity during the filling stage. In addition to heat exchange with air, two boundary conditions were calibrated: the heat exchange with the injector and the heat exchange with the extractors. In this way, the numerical prediction can be accurate at reduced computational time, by avoiding modeling the press in all its complexity. Injection molding process time parameters, such as holding time, filling time, and cooling time (without coolant), were managed within COMSOL by events interface module to replicate the actual experimental process evolution. Three-dimensional mesh consisting of 406.670 tetrahedral elements (maximum element size of 1 mm for cavities and insert, 5 mm for other components), ensuring accurate representation of the geometry. Process parameters used are reported in Table 2, while Table 3 reports material properties taken from material datasheets.

Table 2 Process parameters and boundary conditions set within the numerical model.

Process parameters	**Units**	**Value**
Melt temperature	°C	230
Filling time	s	0.4
Holding time	s	4
Cooling time (no coolant)	s	4
Mold open/close time	s	3.6
Initial molds temperature	°C	18
Air (ambient) temperature	°C	18
Injector temperature	°C	200
HTC with air	$W/(m^2 * K)$	15
HTC with injector	$W/(m^2 * K)$	500 (filling+holding), 150 (cooling)
HTC with extractors	$W/(m^2 * K)$	Linear decrease from 500 to 100 in 500s

Table 3 Material properties implemented within the numerical model

Material properties	**Units**	**POM**	**X33CrS16 Stainless steel**	**High-Temp resin V02**
Density	g/cm^3	1.4	7.8	1.3
Thermal conductivity	W/(m*K)	0.14	17	0.31
Heat capacity at constant pressure	J/(kg*K)	f(T), 2137 at 230°	460	2900

Materials Research Proceedings 57 (2025) 393-400 https://doi.org/10.21741/9781644903735-46

Results and Discussion

Data acquired during the experimental campaign were compared to results from numerical simulation. As a remarkable result, the hybrid system was not damaged during the whole campaign of 134 cycles, confirming its reliability in terms of mechanical resistance. The numerical-experimental comparison has been made based on thermocouples within the inserts, considering an overall molding time of 1600s, as reported in Figure 5.

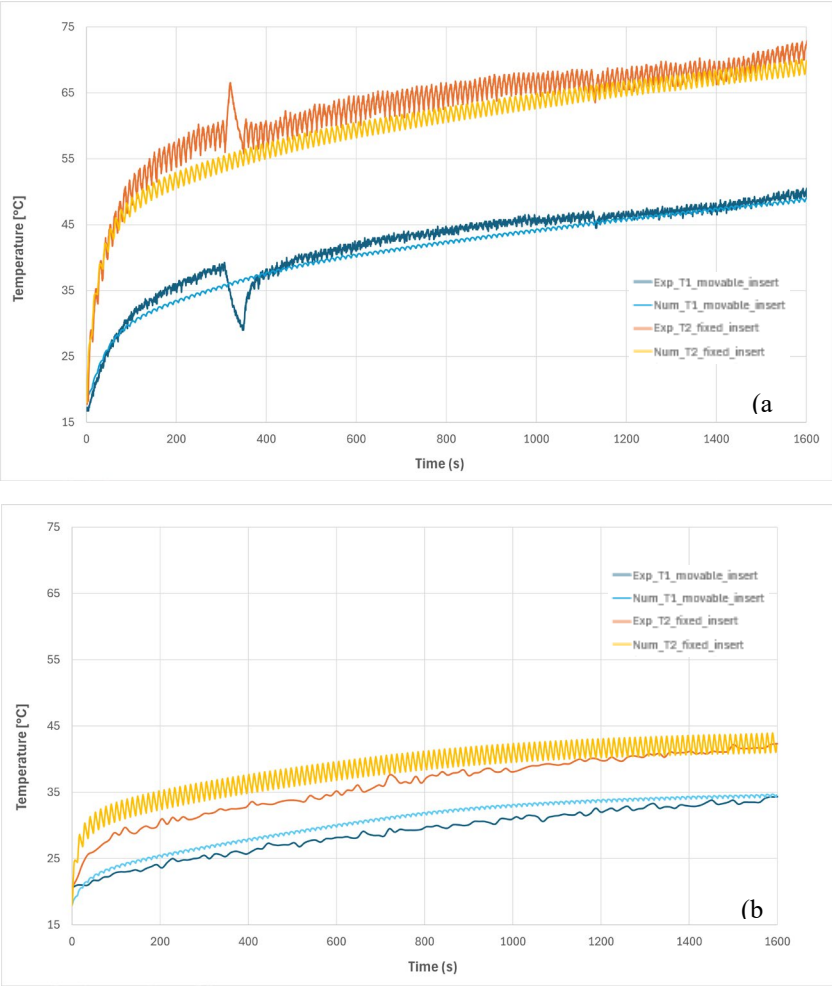


Figure 5 Experimental-numerical comparison of temperature transients acquired by the thermocouples located within the mold inserts, (a) HM, polymer mold plates (b) TM, steel mold plates

It is worth noting that the temperature spike with the subsequent stabilizing transient that occurred on the HM about at time t=300s was due to a part ejection failure, which required the operator's intervention to manually remove the part from the mold cavity. This perturbation was not simulated with the numerical model. The ripple of measurements is due to actual temperature oscillations during the mold opening/closing phases, when the molded part is ejected. Indeed, data temperatures are acquired with a sampling frequency of 2.5 Hz (i.e., one measure every 0.4s), while the part ejection phase requires 3.6 seconds. Therefore, the data acquisition system is capable of acquiring the cooling transients during the opening/closing phase.

Despite the model simplification, the calibration of the simulations was good, thus demonstrating the potentiality of numerical tools in terms of thermal field prediction. At steady-state condition the numerical-experimental error is under 1% for steel plates and under 4,5% for

resin plates. This error can be reduced performing a thermal characterization of used resin, to refine model calibration. The graphs reported above evidence how in both setup the injection side is typically warmer than the ejection side. Moreover, the thermal transient phase of the mold core on the hybrid innovative solution was much faster than the traditional steel mold. This is due to the lower conductive mass and to thermal insulation of the hybrid mold.

Comparing the internal temperatures HM always presented higher values, with an average difference on injection side of 30°C respect TM. The temperature difference between the injection and ejection sides was about 20°C in the HM and about 5°C in the traditional one. HM acted, indeed, as insulating support for the steel insert, resulting in higher core temperatures and thermal sensitivity but lower thermal energy dispersion. The thermal transient of internal components of the TM was characterized by a fast exponential rise followed by a quasi-linear trend, while in the HM, only the linear trend was present. The slopes of the linear trend were almost equal (i.e., about 2-3°C/200s). In continuous long-term molding, the regime temperatures tend to stabilize at higher temperatures in HM due to its low thermal inertia.

Summary

This work indagated an innovative mold design for injection molding process to optimize thermal energy consumption. The designed mold was composed by a steel insert with conformal cooling channel and a base plate realized with high temperature resin. This hybrid mold has been tasted on a micro-injection machine, without cooling activation. The same tests were done using a classical steel plate in substitution of the polymeric one, to compare behaviours.

The experimental results evidenced the potentiality of polymer molds in terms of heat accumulation and fast thermal transients. Indeed, due to the low thermal conductivity of polymer plates, the inserts were better isolated from external heat exchanges: their temperature is higher by more than 50% with respect to the configuration with steel plates (maximum insert temperature 73°C vs 42°C). The thermal conductive mass reduction on the mold promoted faster and more efficient cooling, also in consideration of the implementation of conformal cooling.

Fundings

This work was funded by the European Union under the Italian National Recovery and Resilience Plan (NRRP) of NextGenerationEU, partnership on “Next generation of sustainable and highly efficient molding processes” Italian Projects of Significant National Interest (PRIN) PNRR 2022 grant n. P2022ZE23N. This work was also supported by PNRR–M4C2INV1.5, NextGenerationEU - Avviso 3277/2021 -ECS_00000033-ECOSISTER-spk 3 and PR-FESR 2021-2027 - Priorità 1 - obiettivo specifico 1.1 - Azione 1.1.2 - Progetto “CUP E17G22001630003-SAFER”.

References

[1] H. Fu, H. Xu, et al., Overview of Injection Molding Technology for Processing Polymers and Their Composites, ES Materials & Manufacturing Volume 8 (June 2020) (2020) 3–23.

[2] G. Lucchetta, D. Masato, et. al, Optimization of mold thermal control for minimum energy consumption in injection molding of polypropylene parts, Journal of Cleaner Production 182 (2018) 217–226. https://doi.org/10.1016/j.jclepro.2018.01.258

[3] A.G. Smith, L.C. Wrobel, et. al. A computational model for the cooling phase of injection moulding, Journal of Materials Processing Technology 195 (2008) 305–313. https://doi.org/10.1016/j.jmatprotec.2007.05.018

[4] H. Mianehrow, A. Abbasian, Energy monitoring of plastic injection molding process running with hydraulic injection molding machines, Journal of Cleaner Production 148 (2017) 804–810. https://doi.org/10.1016/j.jclepro.2017.02.053

[5] K. Altaf, A. Majdi Abdul Rani, et al., Prototype production and experimental analysis for circular and profiled conformal cooling channels in aluminium filled epoxy injection mould tools, Rapid Prototyping Journal 19 (2013) 220–229. https://doi.org/10.1108/13552541311323236

[6] K.M. Au, K.M. Yu, A scaffolding architecture for conformal cooling design in rapid plastic injection moulding, Int J Adv Manuf Technol 34 (2007) 496–515. https://doi.org/10.1007/s00170-006-0628-x

[7] C. Kolbe, Strahlschmelzen - LaserCUSING® - Integration im Werkzeug- und Formenbau, RTe Journal (2010). https://rtejournal.de/rte/article/view/2010_3 (accessed March 7, 2025).

[8] G.R. Berger, D. Zorn, et al., Efficient cooling of hot spots in injection molding. A biomimetic cooling channel versus a heat-conductive mold material and a heat conductive plastics, Polymer Engineering & Science 59 (2019) E180–E188. https://doi.org/10.1002/pen.25024

[9] H.M. Silva, J.T. Noversa, et al., Design, simulation and optimization of conformal cooling channels in injection molds: a review, Int J Adv Manuf Technol 120 (2022) 4291–4305. https://doi.org/10.1007/s00170-022-08693-4

[10] S. Arman, I. Lazoglu, A comprehensive review of injection mold cooling by using conformal cooling channels and thermally enhanced molds, Int J Adv Manuf Technol 127 (2023) 2035–2106. https://doi.org/10.1007/s00170-023-11593-w

[11] V. Basile, F. Modica, et al., Micro-texturing of molds via Stereolithography for the fabrication of medical components, Procedia CIRP 110 (2022) 93–98. https://doi.org/10.1016/j.procir.2022.06.019

[12] V.F. Moritz, G.S.N. Bezerra, et al., Heat Dissipation Plays Critical Role for Longevity of Polymer-Based 3D-Printed Inserts for Plastics Injection Moulding, Journal of Manufacturing and Materials Processing 6 (2022) 117. https://doi.org/10.3390/jmmp6050117

[13] H.S. Ong, C.K. Chua, et al., Rapid Moulding Using Epoxy Tooling Resin, Int J Adv Manuf Technol 20 (2002) 368–374. https://doi.org/10.1007/s001700200165.

[14] R. Surace, V. Basile, et al., Micro Injection Molding of Thin Cavities Using Stereolithography for Mold Fabrication, Polymers 13 (2021).

[15] B. Burlaga, A. Kroma, et al., Heat Transfer Analysis of 3D Printed Wax Injection Mold Used in Investment Casting, Materials 15 (2022) 6545. https://doi.org/10.3390/ma15196545

[16] T. Lodygowski, J. Rakowski, et al., Recent Advances in Computational Mechanics, CRC Press, 2014.

[17] V. Bellantone, R. Surace, et al., Replication capability of micro injection moulding process for polymeric parts manufacturing, Int J Adv Manuf Technol 67 (2013) 1407–1421. https://doi.org/10.1007/s00170-012-4577-2

Assembly,disassembly and circular economy



Materials Research Proceedings 57 (2025) 402-409 https://doi.org/10.21741/9781644903735-47

A value-driven approach to printed circuit board inspection: Strategic use of inspection technologies to reduce waste

Stefano PUTTERO[1,a *], Elisa VERNA[1,b], Gianfranco GENTA[1,c] and Maurizio GALETTO[1,d]

[1]Politecnico di Torino, Department of Management and Production Engineering, Corso Duca degli Abruzzi 24, 10129 Torino, Italy

[a]stefano.puttero@polito.it, [b]elisa.verna@polito.it, [c]gianfranco.genta@polito.it, [d]maurizio.galetto@polito.it

Keywords: Quality, Sustainability, E-Waste

Abstract. Electronic waste is an escalating global challenge that requires innovative and sustainable strategies to mitigate its environmental impact. This paper presents a decision model designed to identify the most effective inspection processes for printed circuit boards (PCBs) to enable their reuse, recycling or remanufacturing. The goal is to maximise the recoverable value of PCBs while minimising waste. By systematically analysing inspection processes, the model provides a structured framework for determining the sequence of measurement technologies that balance cost effectiveness with the potential for value recovery. This methodology improves resource efficiency and minimises environmental impact, in addition to supporting the principles of a circular economy. Through an illustrative case study, the approach shows how targeted inspections can significantly extend the life of electronic boards, improve economic value recovery and promote environmentally friendly manufacturing practices.

Introduction

As the digital age advances, the management of electronic waste (e-waste) has become a critical environmental and economic challenge. Projections indicate that global e-waste volumes could increase from 53.6 million tonnes to 75 million tonnes by 2030, highlighting the urgent need for effective recycling and disposal methods [1]. The European Union has introduced strict measures to regulate the collection, treatment and recycling of e-waste through the Waste Electrical and Electronic Equipment (WEEE) Directive [2]. Despite these regulatory measures, the practical application of these directives is fraught with challenges, in particular the high cost of labour required to manually inspect and disassemble e-waste. This necessary but labour-intensive process of separating materials and safely disposing of toxic components is becoming economically unsustainable as the volume of e-waste increases.

The volume of discarded electronic equipment has increased dramatically as a result of accelerating technological progress and the rapid obsolescence of electronic equipment [3]. This growth in e-waste affects ecosystems and human health due to the hazardous substances it contains, and represents a significant loss of valuable materials and resources [4]. It raises critical concerns about efficient collection, treatment and recycling processes. The escalating crisis underlines the urgent need for innovative solutions and policies aimed at promoting sustainable management practices, improving recycling technologies and encouraging the development of environmentally friendly products [5].

This paper addresses the challenges of inspecting printed circuit boards (PCBs), which are essential components in many electronic devices. It proposes advanced methods to optimise PCB inspection and reuse strategies, improving inspection effectiveness to maximise the recovery of valuable components. Through a systematic analysis of inspection processes, this approach establishes a structured framework for determining the optimal sequence of measurement

Content from this work may be used under the terms of the Creative Commons Attribution 3.0 license. Any further distribution of this work must maintain attribution to the author(s) and the title of the work, journal citation and DOI. Published under license by Materials Research Forum LLC.

technologies, balancing cost effectiveness with potential value recovery. The discussion then reviews the most commonly used methods before presenting a novel methodology that improves inspection efficiency. An illustrative case study demonstrates this methodology, using numerical data to highlight its effectiveness. The paper concludes by summarising key findings, addressing limitations and suggesting future research directions.

Literature review

Traditional PCB inspection techniques are challenged by the high cost of advanced inspection tools and the inaccuracy of the more affordable alternatives. These limitations highlight the need for innovative solutions that balance cost effectiveness and accuracy while maintaining technical excellence. This section analyses the main techniques currently used to inspect PCBs and outlines their advantages and disadvantages.

Manual visual inspection is the most basic form of PCB inspection, in which trained technicians identify defects such as solder faults, component misplacement and physical damage, as shown in Fig. 1(a). While effective at detecting visible defects, this method is time-consuming, labour-intensive and prone to error. To address these limitations, neural network-based automated visual inspection systems have been developed to significantly reduce human error and labour costs, while improving inspection speed and accuracy [6].

Current over time testing is another technique for defect detection in PCBs; a qualitative output is shown in Fig. 1(b). It identifies defects by monitoring transient current spikes during device switching. This method is non-invasive, fast and capable of detecting defects early in the production process, making it ideal for both manufacturing and remanufacturing applications [7]. However, the equipment for current over time techniques costs several thousand euros, which can be a problem for small and medium-sized enterprises.

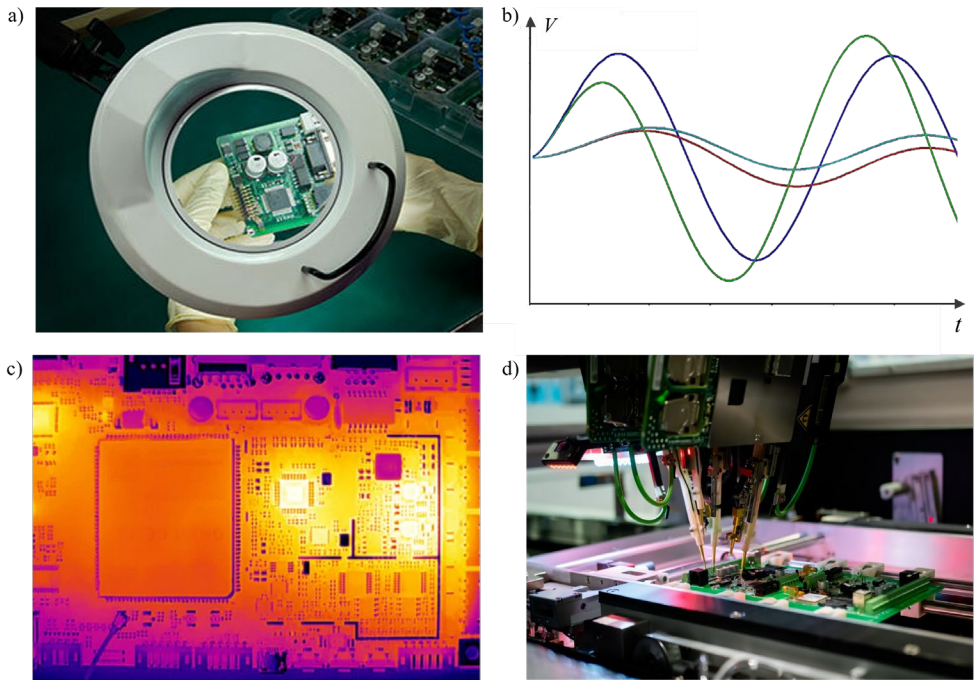


Fig. 1. *Some representative images of conventional PCB inspection methods: (a) visual inspection, (b) current over time analysis, (c) thermography and (d) flying probe test.*

Another widely used technique is thermal inspection, shown in Figure 1(c), which uses infrared thermography to detect thermal anomalies on the PCB. This technique identifies the temperature distribution of the board during operation, highlighting problems such as short circuits or inadequate heat dissipation [8]. It is particularly effective at identifying hidden defects that are

Materials Research Proceedings 57 (2025) 402-409 https://doi.org/10.21741/9781644903735-47

critical to device reliability, providing real-time, high-resolution images for rapid defect location. However, for accurate results, the PCB must reach thermal equilibrium prior to analysis [9].

The last technique worthy of mention in this paper is the flying probe test (FPT), shown in Fig. 1(d). FPT uses moving probes that contact specific points on the PCB to test interconnects without the need for custom fixtures. While FPT is slower than other tests, advances in probe technology have improved its speed and accuracy, making it a cost-effective choice for low-volume production [10]. However, FPT has limitations in terms of physical access to the board, and complex interconnects can prevent comprehensive testing of the entire board. In addition, implementing a flying probe system can be costly in terms of setup and cycle times, making it less feasible for certain applications [10].

Other widely used PCB inspection techniques, such as X-ray and bed-of-nail inspection, are not covered in this paper. X-ray inspection is effective at detecting hidden defects but it is expensive and used primarily in high-volume production [11]. In contrast, the bed-of-nails test provides accurate measurements but it requires bespoke PCB designs, resulting in higher costs [12].

Proposed methodology

The proposed approach integrates multiple inspection technologies to determine the optimal R-strategy - reuse, remanufacture or recycle - for each PCB [13]. It uses a sequential process that leverages the strengths of different inspection techniques, starting with low-cost methods such as visual inspection and progressively applying more advanced techniques such as flying probe testing to maximise resource efficiency. By consolidating data from different stages of inspection, this approach prioritises the identification of valuable components over exhaustive fault diagnosis, ensuring a cost-effective, streamlined process that balances accuracy and efficiency. Fig. 2 illustrates the basic concept of the proposed inspection methodology.

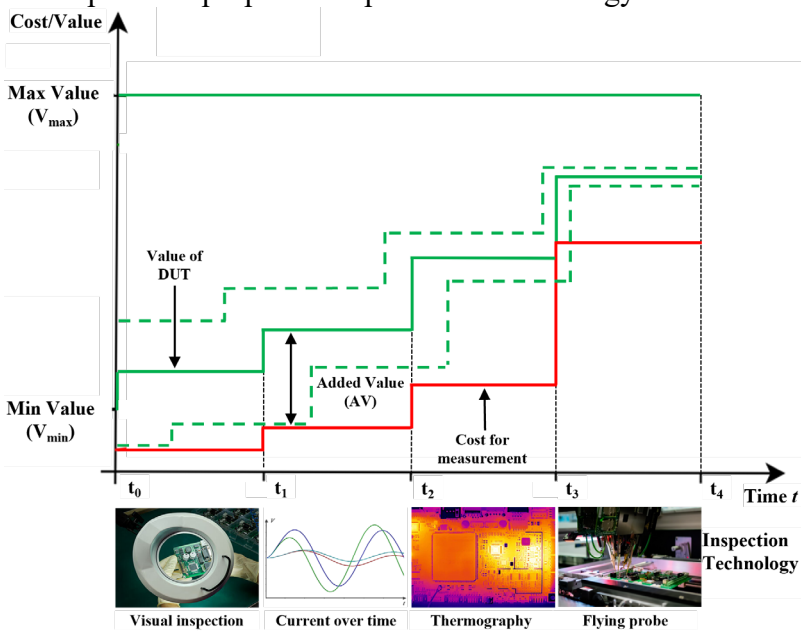


Fig. 2. *Schematic of the proposed methodology.*

The y-axis represents the value of the PCBs, while the x-axis represents the inspection techniques used and the time taken to make these measurements. For simplicity, the graph assumes equal inspection times, although in practice these times may vary for different PCBs. The value of the device under test (DUT) is represented by green lines with dashed uncertainty bands, which also include the measurement uncertainty and indicate the maximum and minimum values that can be obtained from the measurement. As more measurements are taken, these bands narrow,

Materials Research Proceedings 57 (2025) 402-409 https://doi.org/10.21741/9781644903735-47

reducing the uncertainty and ambiguity about the value of the board and emphasising the dynamic nature of the assessment process over time.

The red curve on the graph illustrates the cost of different inspection techniques, which correlates with both the value of the inspection technique and the time required to inspect a DUT. In this framework, a step function is adopted to model both cost and information gain, reflecting the fact that each inspection stage involves a fixed operational cost - such as equipment setup, test execution and data processing - and yields a discrete, measurable increase in knowledge (e.g. defect identification or pass/fail classification). Although continuous models offer mathematical tractability, they do not adequately represent the inherently staged and event-driven nature of real-world inspection workflows. As a result, the use of a step function provides a more realistic abstraction that captures the incremental structure of inspection processes [14].

Initially, PCBs are assumed to be of minimal value, with remanufacturing for raw material recovery serving as the baseline, as all components are assumed to be defective. However, as inspections progress and new technologies are introduced, data is collected to refine the understanding of the condition of each PCB. This iterative learning process improves the extraction of valuable information and optimises the value-added (AV) by balancing value and cost. With each inspection step, the uncertainty about the device under test (DUT) decreases, visually narrowing the green dashed corridor. If the process is stopped prematurely, only the minimum known value is retained, as the condition of untested components remains uncertain. However, as more data is collected, the uncertainty decreases at a faster rate, accelerating knowledge acquisition and improving the efficiency of the overall test sequence. The decision to proceed with subsequent inspection steps is guided by predefined cost-benefit analysis. After each inspection phase, the cumulative inspection costs are compared with the estimated value added. The process continues only if the expected recoverable value exceeds the incremental inspection cost by a pre-determined margin, thus ensuring cost-effective operations.

The inspection sequence begins with a visual inspection to identify evident defects and assess the overall condition of the board. Following the preliminary and subsequent data analysis, a cost-benefit evaluation of the components is carried out. If the collected data is sufficient, the board is removed from the test sequence. This process is repeated at the end of each inspection. The gathered information plays a critical role in determining the most appropriate R-strategy for the DUT. For example, if only a few components are defective, it may make more sense to replace them and reuse the entire board. Conversely, if a significant number of components are faulty, it may be preferable to salvage only the functional parts.

It is important to note that as the system analyses more boards, the methodology learns to identify the optimal R-strategy for each board type. Consequently, as the number of boards analysed increases, the value derived from each board also increases due to this learning effect [14]. In this context, Fig. 3 provides an example of this process through the logistic regression curve, which effectively illustrates the learning process across different inspection stages.

This learning effect can be expressed using the logistic regression in Eq. (1) [14]:

$$V = \frac{L}{1+e^{-k(n-n_0)}} + \varepsilon \tag{1}$$

where L is the maximum achievable value of V, indicating the saturation limit of the response. The parameter k controls the steepness of the curve and determines how quickly V approaches this maximum as n, i.e. the number of boards, changes. The inflection point n_0 is where V is equal to half of L plus a variability error, marking a critical threshold in the response. The term ε is an error included to capture the variability of the data, including measurement inaccuracies and external disturbances, which enhances the realism and applicability of the model to empirical data. These parameters can be adapted to specific industrial contexts. The integration in the model of learning

Materials Research Proceedings 57 (2025) 402-409 https://doi.org/10.21741/9781644903735-47

effect allows the model to estimate the probability of a successful inspection outcome as a function of the number of boards n. Importantly, this model can be adapted to different inspection scenarios by adding the subscript i for each parameter to reflect the specific inspection type analysed [14].

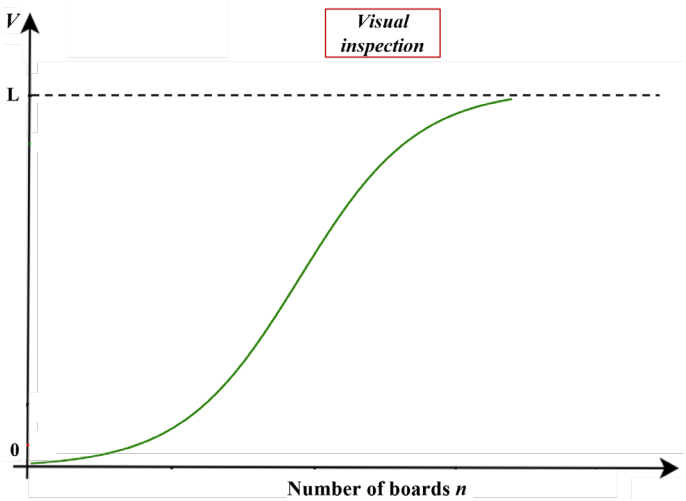


Fig. 3. *Logistic regression trend learning for examined inspection technologies (visual inspection example).*

Applying the logistic learning effect model to the scenario shown in Fig. 2 produces the revised model shown in Fig. 4, which incorporates learning effects across different inspection methods.

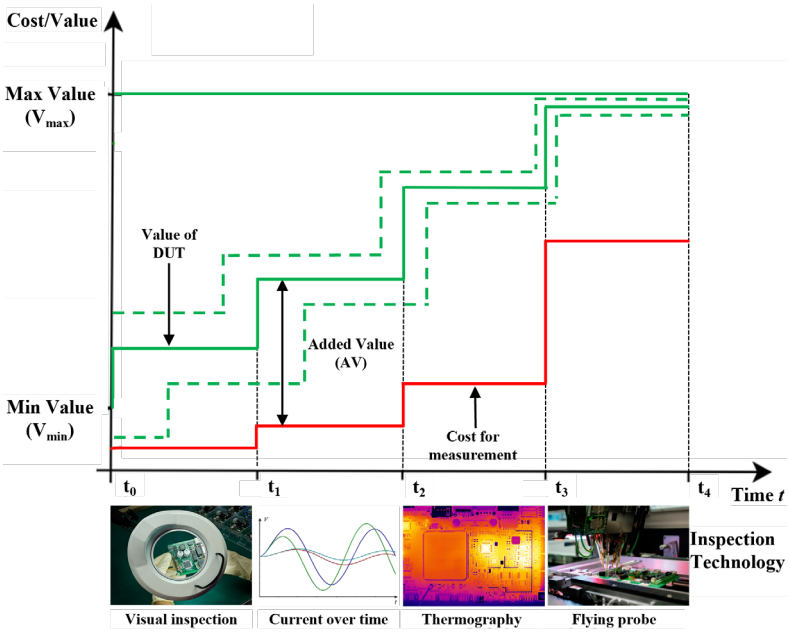


Fig. 4. *Learning effect on the proposed methodology.*

This change is evident in the graph, as the AV in Fig. 4 is significantly higher than in the previous model, reflecting the improved recoverable value from each PCB due to accumulated historical data on similar PCB types. In addition, the uncertainty associated with the recoverable value from each PCB is reduced, as indicated by the lower variability in the dashed lines of Fig. 4. This reduction in uncertainty results from the systematic integration of historical data, which increases the accuracy and effectiveness of the model in predicting the recoverable value of each PCB. Consequently, this improvement strengthens decision making in resource recovery strategies.

Materials Research Proceedings 57 (2025) 402-409 https://doi.org/10.21741/9781644903735-47

An illustrative case study

The proposed model takes a structured approach to PCB inspection, sequentially integrating multiple inspection techniques to determine the most effective recovery strategy. The aim is to optimise cost, efficiency and value recovery by applying increasingly detailed inspections only when necessary. Initial experimental testing on a simple RLC circuit, commonly used in communications system control, together with cost analysis, provided the basis for the values reported in the illustrative example below (see Fig. 5). Although simplified for illustrative purposes, these values reflect realistic scenarios and can be refined through detailed cost analysis and further market data collection.

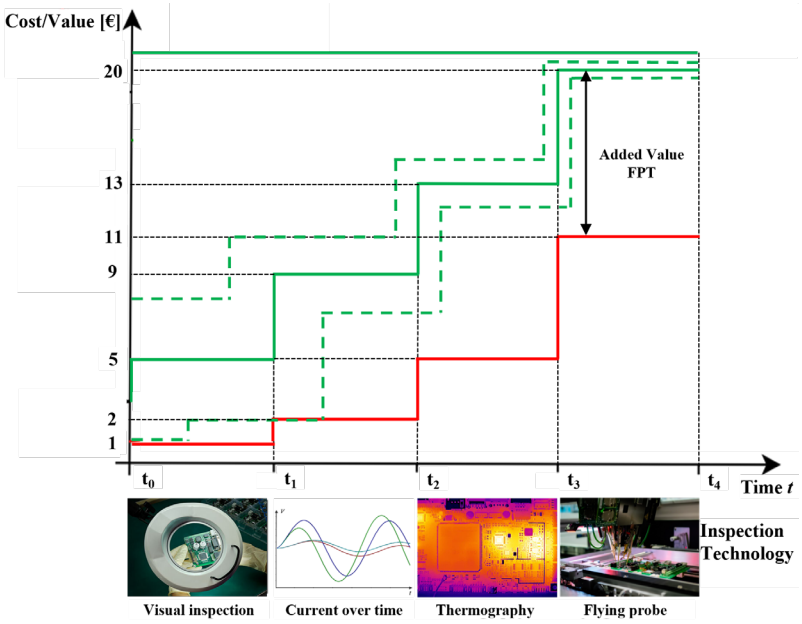


Fig. 5. *Application of the proposed methodology to real-world data.*

An initial visual inspection of a discarded board identifies evident damage such as burns or missing and broken components. The visual inspection costs approximately 1 € per board and can add approximately 5 € in recoverable value, with an uncertainty of ±3 € reflecting the variability in assessing the visible condition of the board. This first step is crucial as it sets the baseline for determining subsequent inspections and potential R-strategies.

Following the visual inspection, the board is subjected to a current over time test, which assesses the electrical integrity of the circuits and detects non-visible defects. The current over time test costs approximately 2 € per board and adds an estimated recoverable value of 9 €, with an uncertainty of ±2 €. This reflects the variability in the detection of minor electrical faults that may not immediately affect the functionality of the board but could lead to future failures.

If electrical discrepancies are not found, the board is subjected to thermography to identify problems such as localised overheating or hidden faulty connections. Such problems may be indicative of deeper electrical problems that cannot be detected by simple visual inspections or current tests. The thermography test costs on average 5 € per board and adds 13 € in recoverable value, with an uncertainty of ±1 €. This step is essential to ensure that boards with internal defects not visible to the naked eye are correctly diagnosed and directed to the appropriate action.

Boards that still show problems after thermography are then subjected to a flying probe test, a more advanced diagnostic method. This test costs approximately 11 € per board and can add 20 € in recoverable value, with an uncertainty of ±0.5 €, as it enables precise fault detection that may have been missed by earlier tests. This last step is critical as it ensures the highest level of defect

detection and assessment, providing valuable data for the final decision on the board's destination. It also contributes to the value added as shown in Fig. 5 (Added Value FPT).

At the end of the inspection process, the choice of the most appropriate R-strategy depends on a detailed analysis of the test results and the recoverable value added at each stage. This decision-making process carefully balances inspection costs against potential recoverable value to maximise the economic return for each board inspected. In addition, by analysing a larger number of boards, the learning effect can be observed, improving the efficiency of the inspection process over time. This continuous learning refines the understanding of common defects in specific board types, leading to more informed decisions about the most effective R-strategy.

Conclusions

The increasing volume of electronic waste requires innovative strategies for efficient resource recovery. This study presents a decision model that optimises PCB inspection processes to determine the most appropriate R-strategy through a cost-effective, sequential evaluation approach. By integrating multiple inspection technologies, the methodology improves resource efficiency, minimises costs and maximises recoverable value.

The proposed approach starts with low-cost visual inspections to identify major defects, followed by advanced techniques such as current over time, thermography and flying probe testing. This structured, step-by-step strategy enables effective decision-making while reducing unnecessary testing costs. The model also incorporates a learning effect where accumulated inspection data improves predictive accuracy, leading to better repair outcomes over time.

A key finding is that a sequential inspection approach optimises the trade-off between cost and information gain. By progressively reducing uncertainty about PCB condition, the methodology enables early identification of functional components while minimising resource waste on non-recoverable boards. The logistic regression model further explains the learning effect, demonstrating that as more boards are analysed, the framework becomes increasingly efficient in identifying high-value recovery opportunities.

Systematic data transfer between inspection stages refines the PCB classification and informs future inspections, strengthening the decision-making process. This adaptive learning mechanism enhances the model's ability to determine the most appropriate recovery strategy, ensuring cost efficiency and environmental sustainability. As more boards are inspected, the methodology uses historical inspection data to improve its predictive accuracy, resulting in a more refined, effective and sustainable assessment framework for e-waste management.

This research has significant implications for sustainable electronics management, supporting regulatory compliance and improving the feasibility of e-waste recovery. The proposed decision model provides a scalable, adaptable solution that balances economic viability with environmental responsibility. Future research will focus on the extensive application of the proposed inspection methodology to real and more complex industrial case studies. This will allow detailed validation of the approach through quantitative data analysis, providing practical insights into its effectiveness, scalability and economic feasibility in real-world manufacturing environments.

References

[1] O.S. Shittu, I.D. Williams, P.J. Shaw, Global E-waste management: Can WEEE make a difference? A review of e-waste trends, legislation, contemporary issues and future challenges, Waste Manag. 120 (2021) 549–563. https://doi.org/10.1016/j.wasman.2020.10.016

[2] K. Mishra, S.S. Siwal, V.K. Thakur, E-waste recycling and utilization: A review of current technologies and future perspectives, Curr. Opin. Green Sustain. Chem. 47 (2024) 100900. https://doi.org/10.1016/j.cogsc.2024.100900

[3] X.V. Wang, L. Wang, Digital twin-based WEEE recycling, recovery and remanufacturing in the background of Industry 4.0, Int. J. Prod. Res. 57 (2019) 3892–3902. https://doi.org/10.1080/00207543.2018.1497819

[4] X. Pan, C.W.Y. Wong, C. Li, Circular economy practices in the waste electrical and electronic equipment (WEEE) industry: A systematic review and future research agendas, J. Clean. Prod. 365 (2022) 132671. https://doi.org/10.1016/j.jclepro.2022.132671

[5] G. Anandh, S. PrasannaVenkatesan, M. Goh, K. Mathiyazhagan, Reuse assessment of WEEE: Systematic review of emerging themes and research directions, J. Environ. Manage. 287 (2021) 112335. https://doi.org/10.1016/j.jenvman.2021.112335

[6] V.A. Adibhatla, H.-C. Chih, C.-C. Hsu, J. Cheng, M.F. Abbod, J.-S. Shieh, Applying deep learning to defect detection in printed circuit boards via a newest model of you-only-look-once, Math. Biosci. Eng. 18 (2021) 4411–4428. https://doi.org/10.3934/mbe.2021223

[7] V.U. Sankar, G. Lakshmi, Y.S. Sankar, A Review of Various Defects in PCB, J. Electron. Test. 38 (2022) 481–491. https://doi.org/10.1007/s10836-022-06026-7

[8] M. Jeon, S. Yoo, S.-W. Kim, A Contactless PCBA Defect Detection Method: Convolutional Neural Networks With Thermographic Images, IEEE Trans. Components, Packag. Manuf. Technol. 12 (2022) 489–501. https://doi.org/10.1109/TCPMT.2022.3147319.

[9] X.P.V. Maldaque, Infrared Methodology and Technology, CRC Press, London, 2023. https://doi.org/10.1201/9781003420200

[10] R. Ionel, L. Mâțiu-Iovan, Flying probe measurement accuracy improvement by external LCR integration, Measurement. 190 (2022) 110703. https://doi.org/10.1016/j.measurement.2022.110703

[11] Y. Wang, M. Wang, Z. Zhang, Microfocus X-ray printed circuit board inspection system, Optik (Stuttg). 125 (2014) 4929–4931. https://doi.org/10.1016/j.ijleo.2014.04.027.

[12] J. Bowen, D. Bahler, A. Dholakia, An AI constraint network-based approach to bed-of-nails DFT for digital circuit design, Comput. Electr. Eng. 19 (1993) 73–85. https://doi.org/10.1016/0045-7906(93)90038-S

[13] J.D. Russell, N.Z. Nasr, Value-retained vs. impacts avoided: the differentiated contributions of remanufacturing, refurbishment, repair, and reuse within a circular economy, J. Remanufacturing. 13 (2023) 25–51. https://doi.org/10.1007/s13243-022-00119-4

[14] F. Franceschini, M. Galetto, Composition laws for learning curves of industrial manufacturing processes, Int. J. Prod. Res. 41 (2003) 1431–1447. https://doi.org/10.1080/1352816031000075035

Materials Research Proceedings 57 (2025) 410-417 https://doi.org/10.21741/9781644903735-48

Exploring multi-human multi-robot collaboration in assembly processes: Challenges and opportunities in quality and manufacturing

Matteo CAPPONI[1,a *], Aurora Sofia DI MATTEO[1,b *], Luca MASTROGIACOMO[1,c *]

[1]Politecnico di Torino, DIGEP, Corso Duca Degli Abruzzi 24, Torino, Italy

[a]matteo.capponi@polito.it, [b]aurora.dimatteo@polito.it, [c]luca.mastrogiacomo@polito.it

Keywords: Human Robot Collaboration, Safety and Well-Being, Man-Machine System, Multi-Human Multi-Robot Collaboration, Industry 5.0, Cognitive Workload

Abstract. The recent evolution of robotic systems is pushing the manufacturing sector towards continuous adaptation, incorporating novel technologies. Industry 5.0 is shifting the attention from basic human-robot interactions, typically between a single human operator and a single robot, to more complex configurations of multi-human multi-robot (MH-MR) teams. These advanced systems, in which multiple human and robot agents collaborate on shared tasks, can offer significant advantages on flexibility, adaptability and productivity, while reducing operators' workload. However, integrating these systems introduces new challenges: such as governing interactions within the team, means of communication and human behavior. Traditional models may no longer be adequate to capture the complexity of MH-MR teams. This paper aims to investigate the challenges and the open questions surrounding the adoption of MH-MR teams in manufacturing. A real case study in assembly is presented as an illustrative example to explore some of the key issues. This serves as a starting point for a broader discussion on how to effectively implement MH-MR teams in industrial contexts.

Introduction

Driven by advances in robotics, digital technologies and automation, manufacturing is undergoing a significant transformation, evolving from Industry 4.0 to Industry 5.0. Industry 5.0 aims at creating a more flexible and adaptive manufacturing environment, emphasizing efficiency, human well-being, worker support and social sustainability. Collaborative robots, i.e., robots that can work closely with humans without safety barriers, are one of the crucial technologies for this paradigm shift. Collaborative robots enable the fusion of human skills with those of robots, leading to the concept of human-robot collaboration ("HRC"). This shift, known as "human-centered manufacturing", aims to develop sustainable, adaptable production systems that balance technological progress with human needs [1–3]. Traditional HRC models, typically involving a single human and a single robot working together towards common goals [3], are evolving into more complex configurations where multiple human operators work alongside multiple robots in shared workspaces. These Multi-Human Multi-Robot (MH-MR) teams enable more efficient task distribution, improved adaptability to dynamic environments and a redefinition of how humans and robots co-exist in industrial environments [4]. By leveraging the precision of robots and the adaptability of humans [5, 6], MH-MR teams can improve performance, employee well-being and operational support. However, their introduction brings new challenges that require a rethink of existing models of collaboration. As manufacturing moves towards MH-MR systems, critical questions arise: How can multiple agents interact effectively while minimizing inefficiencies? What team dynamics emerge when humans and robots work together in more complex work structures? How should tasks be allocated and how should systems react to unexpected disturbances? [4, 7]. Beyond the technical aspects, the integration of MH-MR teams also raises

Content from this work may be used under the terms of the Creative Commons Attribution 3.0 license. Any further distribution of this work must maintain attribution to the author(s) and the title of the work, journal citation and DOI. Published under license by Materials Research Forum LLC.

issues such as communication effectiveness, workload balance and trust building [8]. Neglecting these factors can lead to inefficiencies and to compromised product and process quality.

Despite their potential, MH-MR systems are still an emerging area in industrial applications and require further research. Given the increasing demand for flexible and scalable manufacturing systems, it is essential to address these research gaps [2]. In detail, this paper tries to answer the following research question: *What are the key challenges and opportunities associated with the introduction of MH-MR teams in assembly?* Specifically, through an exploratory case-study this paper tries to gain preliminary insight into the dynamics that emerge within teams, explore the benefits achieved and identify critical challenges. The article is organized as follows: Section 2 presents a literature review on MH-MR teams in manufacturing contexts; Section 3 briefly describes the exploratory case study; Section 4 reports the preliminary results and feedback from MH-MR and human teams; Section 5 discusses challenges and opportunities of MH-MR adoption, focusing also on insights and directions for future research.

Literature review

As human-robot collaboration evolves beyond simple dyads, multi-human multi-robot (MH-MR) teams have emerged as a new frontier of research. MH-MR refers to teams with at least two humans and two robots [9, 10], representing a more advanced subset of HRC that addresses the intricate dynamics of multi-agent collaboration. In manufacturing environments, introducing multiple humans and multiple robots (MH-MR) into a team can enhance system flexibility and throughput, but it also significantly increases complexity and uncertainty in several domains. For example:

- task coordination becomes more intricate because responsibilities must be dynamically allocated among many agents [11];
- communication challenges grow as multiple humans and robots require seamless information exchange [12];
- safety risks rise due to unpredictable interactions among numerous moving agents [13];
- decision-making becomes more complicated as control and autonomy are distributed across different agents [12];
- system efficiency is more difficult to optimize with many interdependent components [7]
- performance measurement becomes complex due to the quantity of agents involved [7]

Therefore, managing MH-MR team performance, including workload distribution and role allocation, represents a critical challenge. Esterwood and Robert [13] highlighted the importance of team composition, believing that determining the optimal human-to-robot ratio and allocating roles effectively are essential for team cohesion and performance. Another critical aspect is building trust among team members, especially in dynamic environments. Trust directly influences interaction fluency, which significantly impacts overall team effectiveness [14, 15]. Similarly, cohesion in human-robot teams is crucial to reach an effective collaboration with robotic teammates [10]. Ma et al. [16] argued the impact of team members characteristics and of external factors, which can affect the outcome of teaming. Human factors such as cognitive workload, emotions, and performance are inherently variable and should be carefully managed to improve team performance [8]. Moreover, the effective design of human-robot teams requires an in-depth understanding of teamwork, supported by models and metrics that consider not only internal cognitive processes and observable behaviors, but also task characteristics, operational context and the collaborative dynamic between members [16]. In this regard, Riedelbauch et al. [7] provided a description of the relevant metrics for assessing human robot teaming in industrial scenarios considering the overall benchmarking process. Ma et al. [16] described the dimensions that should be investigated in MH-MR contexts to evaluate their effectiveness and present a case study application in spaceflight operations.

Materials Research Proceedings 57 (2025) 410-417 https://doi.org/10.21741/9781644903735-48

Despite these initial contributions, research into MH-MR collaboration is still at an early stage, particularly in manufacturing contexts. Existing studies tend to focus on isolated aspects, such as task allocation or interaction dynamics, without fully addressing the challenges of integrating these systems into real-world applications [4]. This paper aims to bridge these gaps by exploring the challenges and opportunities of MH-MR teams in manufacturing.

Case-study description

This paper explores a practical implementation of multi-human multi-robot (MH-MR) teams in a product assembly task through a case study. A comparison with fully manual teams serves only as a reference to highlight the key challenges, opportunities and implications of hybrid collaboration in light of the increasing integration of cobots in manufacturing. To achieve these objectives, experimental trials were conducted to preliminarily evaluate key performance metrics and gather qualitative feedback. The study involved six participants aged 24-25 years with no previous experience with collaborative robots. They were divided into three teams, each of which participated in the task of assembling a skateboard (see Fig. 1) in two configurations: parallel configuration (C1) and sequential configuration (C2). In parallel configuration tasks were performed simultaneously by humans or human-robot pairs in parallel, while in sequential one, tasks were divided and performed sequentially by all the agents. In addition, each configuration was performed in two modalities: manual and MHMR. In manual modality, two human agents collaborated to execute all steps of the assembly process independently, without any robotic intervention. In MHMR modality, human agents partnered with two robotic agents to complete the assembly process collaboratively.



Figure 1. *The components and the assembled skateboard used as case-study product (a,b) and the workstation with participants in MHMR modality during the assembly process (c).*

The experiments were held in the Mind4Lab of Politecnico di Torino (Italy) in controlled experimental conditions. During the experiment, participants operated at the workstation, consisting of a table and two collaborative robot Universal Robot UR3, as shown in Fig.1-c.

The assembly process involved 3 macro steps to be done twice per front and rear board to ensure the proper assembly of the skateboard: assembly of the truck, assembly of the truck on the board and assembly of the wheels on the truck. Steps to be followed for each assembly macro-phase and the related task allocation between humans and robots (for both modalities and configurations) are described in Table 1.

Materials Research Proceedings 57 (2025) 410-417 https://doi.org/10.21741/9781644903735-48

Table 1. *Skateboard assembly instructions and the related task allocation between humans (H1, H2) ad robots (R1, R2)*

Assembly macro-phase	Detailed steps	Manual Modality		MHMR Modality	
		C1	C2	C1	C2
A) Assembly of the truck (x2)	1. Take the baseplate (BP) and put it in the correct orientation.	H1/H2	H1	R1/R2	R1
	2. Insert the bolt (BL1) into the baseplate (BP)	H1/H2	H1	H1/H2	H1
	3. Mount the larger metal protector (LMP) on the larger yellow grommet (LYG).	H1/H2	H2	H1/H2	H2
	4. Insert them onto the bolt (BL1) with the larger metal protector (LMP) at the bottom.	H1/H2	H1	H1/H2	H1
	5. Put the black pin cup (PC) on the hanger (HNG).	H1/H2	H2	H1/H2	H2
	6. Mount it on the baseplate (BP).	H1/H2	H1	H1/H2	H1
	7. Mount the smallest metal protector (SMP) on the smallest yellow grommet (SYG).	H1/H2	H2	H1/H2	H2
	8. Insert them onto the bolt (BL1) with the smallest metal protector (SMP) at the top.	H1/H2	H1	H1/H2	H1
	9. Screw the nut (N1) onto the bolt	H1/H2	H1	H1/H2	H1
B) Assembly of the truck on the board (x2)	1. Take the board (B) in the correct orientation.	H1	H1	R1/R2	R1
	2. Put and align the truck on the board.	H1/H2	H1	H1/H2	H1
	3. Insert the bolts (BL2) into the four holes, tighten them with the nuts (N2) to join the truck and the board.	H1/H2	H1	H1/H2	H1
C) Assembly of the wheels on the board (x2)	1. Take the first wheel (WL).	H1/H2	H2	R1/H2	R2
	2. Mount the wheel on the hanger, insert the washer (W) and tighten with a nut (N3).	H1/H2	H2	H1/H2	H2
	3. Take the second wheel (WL).	H1/H2	H2	R1/R2	R2
	4. Mount the wheel on the hanger, insert the washer (W) and tighten with a nut (N3).	H1/H2	H2	H1/H2	H2

Each team underwent two training trials followed by two “official” trials for each of the four scenarios (two configurations in two modalities). The data collected were the following:

- Questionnaires: participants completed the NASA Task Load Index (NASA-TLX) questionnaire to assess perceived workload, providing detailed insights into the human operators' experience [17]. This tool is based on the evaluation on a scale from 0 to 100 of six dimensions affecting perceived workload: Mental Demand, Physical Demand, Temporal Demand, Performance, Effort, Frustration. The total perceived workload value is obtained through a weighted average of the scores of each dimension. A low NASA-TLX score suggests that the task was perceived as relatively easy and not demanding, while a high score implies that the user experienced significant workload during task execution.
- Unstructured feedback: open-ended questionnaires were used to gather qualitative feedback about the overall experience.

Materials Research Proceedings 57 (2025) 410-417 https://doi.org/10.21741/9781644903735-48

Preliminary results

The preliminary findings of the proposed case study serve as a starting point to better understand the implications of incorporating MH-MR teams in manufacturing assembly. Table 2 shows the results of NASA-TLX (mean perceived workload by configuration) while Table 3 shows an overview of the unstructured feedback collected.

Table 2. *NASA-TLX preliminary results (where lower values are preferable, indicating lower perceived workload)*

	NASA-TLX [0-100]		
Configuration	Mean	Max	Min
C1-M	25.3	38	11.7
C1-MHMR	25.8	52.7	9
C2-M	38.5	52.7	23.7
C2-MHMR	18.8	44.7	9.7

Table 3. *Overview of the preliminary unstructured feedback (voice of participants) collected, grouped by macro-categories for the two modalities (manual and MHMR)*

Voice of participants		
Macro category	**Manual modality**	**MHMR Modality**
Operational efficiency	• Higher execution speed • Higher flexibility in adapting to change	• Stable execution • High dependency on cobots' pace with potential slowdowns due to technical limitations
Workload	• Higher physical effort due to the absence of cobots' support • Higher mental effort required to coordinate work	• Reduced physical strain due to cobot support • Effort to adapt to cobot interactions
Task Structure and Coordination	• Dynamic roles with higher individual responsibility • Need for continuous adjustment	• More predefined and rigid roles • Cobots assist rather than actively collaborating
Control and Autonomy	• Full control over work pace and task management	• Dependency on cobots' timing • Limited ability to intervene freely in the process
Team Dynamics	• Strong cohesion and greater sense of belonging within the team • Natural communication	• Lower interpersonal engagement • Cobots are perceived as tools rather than collaborative partners

The lowest mean workload was observed in C2-MHMR (18.8), suggesting that according to participants the support of cobots reduced the perceived workload. Conversely, C2-M reported a much higher workload (38.5), potentially reflecting the cognitive and emotional challenges of high-interaction in human teams. Given the exploratory nature of this study, feedback from participants were analyzed and reorganized in macro-categories, as shown in Table 3. MH-MR teams have the potential to improve ergonomic comfort and streamline workflows with cobot support. Furthermore, the unstructured feedback suggests that MH-MR teams, while requiring

some adaptation, can lead to increased efficiency and reduced physical and cognitive effort in repetitive tasks, making them a sustainable and feasible solution for future manufacturing contexts.

Discussion and conclusions

The introduction of multi-human multi-robot (MH-MR) teams in manufacturing represents a paradigm shift with the potential to redefine industrial workflows. As highlighted by participant feedback and supported by the literature, MH-MR systems offer a promising pathway to increased worker well-being. However, their integration also presents significant challenges that need to be addressed in order to fully realize their benefits. MH-MR teams unlock several opportunities that can drive the transformation of manufacturing environments:

- *Improved worker support and dynamic task allocation*: Robots relieve workers of repetitive and physically demanding tasks, allowing them to focus on high-value cognitive activities. This redistribution of workload aligns with the broader goal of improving workers' condition within Industry 5.0. The presence of multiple robots and multiple human workers enables dynamic collaboration, allowing tasks to be shared in a way that can improve efficiency without overburdening any single team member [7].
- *Flexibility and agile adaptation*: In MH-MR environments, the combination of human adaptability and robotic precision enhances workflow agility, as different team members step in to compensate for delays, reassign tasks and optimize output together [18].
- *Improved workplace ergonomics and job satisfaction*: Reduced physical strain, as reported by participants, contributes to improved ergonomics and job quality. In MH-MR environments, workers can collaborate with multiple robots simultaneously, minimizing the risk of fatigue and allowing for a more balanced distribution of physical and cognitive workload [19].
- *Trust and transparency in human-robot interaction*: Predictability and transparency in robot behavior have been identified as key enablers for seamless collaboration. In MH-MR teams, trust dynamics become more complex due to the increased number of interacting agents. Hence, effective communication strategies and trust-building mechanisms becomes mandatory to ensure productive and coordinated teamwork [20].

Alongside the opportunities, there are also challenges to be faced in efficiently and effectively integrating MH-MR teams in manufacturing:

- Unlike simpler human-robot collaborations, MH-MR teams require sophisticated coordination of tasks between multiple agents, thus adding an additional layer of complexity. Therefore, coordination strategies need to address emergent team dynamics, where workflow adjustments are required as human and robot agents interact in real time [12].
- In MH-MR teams, human operators must simultaneously manage interactions with multiple robots and coordinate with other human teammates. Unlike single human-robot collaboration, MH-MR environments require a higher level of shared situational awareness, necessitating advanced decision support systems that reduce cognitive overload while maintaining efficient collaboration among all agents [19].
- The effectiveness of MH-MR teams cannot be measured by traditional productivity metrics alone. Unlike traditional human-robot environments, MH-MR teams exhibit complex interdependencies where performance is influenced not only by the efficiency of individual agents, but also by the overall harmony of the team. Evaluating performance requires a shift towards multi-dimensional metrics that capture also inter-agent coordination, the quality of human-robot communication and role balance.

Overall, this paper contributes to an early understanding of MH-MR teamwork by outlining key challenges, considerations and potential benefits for manufacturing contexts. However, given the small sample size findings are not generalizable, but only serve as early insights into the dynamics

of these teams in manufacturing. To advance research and practice, future research should focus on:

- Long-term effects analysis of how learning curves, trust development and worker adaptation evolve over time in MH-MR settings involving larger samples of participants. The long-term sustainability of these teams depends on their ability to integrate effectively into existing workflows and to evolve with technological advances.
- Defining a multidimensional evaluation framework. It is necessary to establish standardized methodologies to assess MH-MR performance beyond efficiency, including factors such as cognitive workload, quality of collaboration, inter-agent synchronization and well-being at work.
- Developing of adaptive coordination models. Intelligent synchronization strategies that dynamically adjust robot behavior in response to human actions are needed. Future efforts should focus on using AI and machine learning to create more responsive and context-aware MH-MR systems that optimize both productivity and human experience.

The integration of MH-MR teams represents both a challenge and an opportunity for the future of industrial manufacturing. By proactively addressing these challenges, the manufacturing industry can exploit the benefits of MH-MR systems to drive productivity, innovation and sustainable working environment.

Acknowledgements
This study was carried out within the "Empathically enhanced robot for the collaboration with HUmans in MANufacturing (E.HU.MAN)" project – funded by the Ministero dell'Università e della Ricerca – within the PRIN 2022 program (D.D.104 02/02/2022). This manuscript reflects only the authors' views and opinions, and the Ministry cannot be considered responsible for them.

References

[1] Lu, Y., Zheng, H., Chand, S., Xia, W., Liu, Z., Xu, X., Wang, L., Qin, Z., Bao, J.: Outlook on human-centric manufacturing towards Industry 5.0. Journal of Manufacturing Systems. 62, 612–627 (2022). https://doi.org/10.1016/j.jmsy.2022.02.001

[2] Maddikunta, P.K.R., Pham, Q.-V., B, P., Deepa, N., Dev, K., Gadekallu, T.R., Ruby, R., Liyanage, M.: Industry 5.0: A survey on enabling technologies and potential applications. Journal of Industrial Information Integration. 26, 100257 (2022). https://doi.org/10.1016/j.jii.2021.100257

[3] Gervasi, R., Mastrogiacomo, L., Franceschini, F.: A conceptual framework to evaluate human-robot collaboration. Int J Adv Manuf Technol. 108, 841–865 (2020). https://doi.org/10.1007/s00170-020-05363-1

[4] Yuan, Z., Wang, R., Kim, T., Zhao, D., Obi, I., Min, B.-C.: Adaptive Task Allocation in Multi-Human Multi-Robot Teams under Team Heterogeneity and Dynamic Information Uncertainty, http://arxiv.org/abs/2409.13824, (2024)

[5] Mina, T., Kannan, S.S., Jo, W., Min, B.-C.: Adaptive Workload Allocation for Multi-Human Multi-Robot Teams for Independent and Homogeneous Tasks. IEEE Access. 8, 152697–152712 (2020). https://doi.org/10.1109/ACCESS.2020.3017659

[6] Capponi, M., Gervasi, R., Mastrogiacomo, L., Franceschini, F.: Assessing perceived assembly complexity in human-robot collaboration processes: a proposal based on Thurstone's law of comparative judgement. International Journal of Production Research. 62, 5315–5335 (2024). https://doi.org/10.1080/00207543.2023.2291519

[7] Riedelbauch, D., Höllerich, N., Henrich, D.: Benchmarking Teamwork of Humans and Cobots—An Overview of Metrics, Strategies, and Tasks. IEEE Access. 11, 43648–43674 (2023). https://doi.org/10.1109/ACCESS.2023.3271602

[8] Natarajan, M., Seraj, E., Altundas, B., Paleja, R., Ye, S., Chen, L., Jensen, R., Chang, K.C., Gombolay, M.: Human-Robot Teaming: Grand Challenges. Curr Robot Rep. 4, 81–100 (2023). https://doi.org/10.1007/s43154-023-00103-1

[9] Dahiya, A., Aroyo, A.M., Dautenhahn, K., Smith, S.L.: A Survey of Multi-Agent Human-Robot Interaction Systems, http://arxiv.org/abs/2212.05286, (2022)

[10] Correia, F., Melo, F.S., Paiva, A.: When a Robot Is Your Teammate. Topics in Cognitive Science. 16, 527–553 (2024). https://doi.org/10.1111/tops.12634

[11] de Visser, E.J., Peeters, M.M.M., Jung, M.F., Kohn, S., Shaw, T.H., Pak, R., Neerincx, M.A.: Towards a Theory of Longitudinal Trust Calibration in Human–Robot Teams. Int J of Soc Robotics. 12, 459–478 (2020). https://doi.org/10.1007/s12369-019-00596-x

[12] Natarajan, M., Seraj, E., Altundas, B., Paleja, R., Ye, S., Chen, L., Jensen, R., Chang, K.C., Gombolay, M.: Human-Robot Teaming: Grand Challenges. Curr Robot Rep. 4, 81–100 (2023). https://doi.org/10.1007/s43154-023-00103-1

[13] Esterwood, C., Robert, L.P.: Human Robot Team Design. In: Proceedings of the 8th International Conference on Human-Agent Interaction. pp. 251–253. ACM, Virtual Event USA (2020)

[14] De Visser, E.J., Peeters, M.M.M., Jung, M.F., Kohn, S., Shaw, T.H., Pak, R., Neerincx, M.A.: Towards a Theory of Longitudinal Trust Calibration in Human–Robot Teams. Int J of Soc Robotics. 12, 459–478 (2020). https://doi.org/10.1007/s12369-019-00596-x

[15] Hoffman, G.: Evaluating Fluency in Human–Robot Collaboration. IEEE Trans. Human-Mach. Syst. 49, 209–218 (2019). https://doi.org/10.1109/THMS.2019.2904558

[16] Ma, L.M., Ijtsma, M., Feigh, K.M., Pritchett, A.R.: Metrics for Human-Robot Team Design: A Teamwork Perspective on Evaluation of Human-Robot Teams. J. Hum.-Robot Interact. 11, 1–36 (2022). https://doi.org/10.1145/3522581

[17] Hart, S.G., Staveland, L.E.: Development of NASA-TLX (Task Load Index): Results of Empirical and Theoretical Research. In: Hancock, P.A. and Meshkati, N. (eds.) Advances in Psychology. pp. 139–183. North-Holland (1988)

[18] Riedelbauch, D., Henrich, D.: Coordinating flexible human-robot teams by local world state observation. In: 2017 26th IEEE International Symposium on Robot and Human Interactive Communication (RO-MAN). pp. 1000–1005 (2017)

[19] Mina, T., Kannan, S.S., Jo, W., Min, B.-C.: Adaptive Workload Allocation for Multi-Human Multi-Robot Teams for Independent and Homogeneous Tasks. IEEE Access. 8, 152697–152712 (2020). https://doi.org/10.1109/ACCESS.2020.3017659

[20] Maurtua, I., Ibarguren, A., Kildal, J., Susperregi, L., Sierra, B.: Human–robot collaboration in industrial applications: Safety, interaction and trust. International Journal of Advanced Robotic Systems. 14, 1729881417716010 (2017). https://doi.org/10.1177/1729881417716010

Materials Research Proceedings 57 (2025) 418-425 https://doi.org/10.21741/9781644903735-49

Reuse of 316L stainless steel towards zero-waste laser powder bed fusion

Gabriele LOCATELLI[1,a *], Sara BOCCHI[1,b], Mariangela QUARTO[1,c] and Gianluca D'URSO[1,d]

[1]Department of Management, Information and Production Engineering, University of Bergamo, Via Pasubio 7/b, 24044 Dalmine, BG, Italy

[a]gabriele.locatelli@unibg.it, [b]sara.bocchi@unibg.it, [c]mariangela.quarto@unibg.it, [d]gianluca.d-urso@unibg.it

Keywords: Sustainability, Stainless Steel, Powder Bed Fusion

Abstract. Aiming to enhance the adoption of sustainable practices in the Italian manufacturing sector, this study investigated the application of powder reuse in laser powder bed fusion (L-PBF) processes. Within the "Made in Italy-Circular and Sustainable" (MICS) Extended Partnership, backed by the European Union Next-GenerationEU, an alternative reuse strategy was studied through 316L stainless steel specimens fabricated from powder subjected to five and ten reuse cycles. Compared with virgin powder data, the characterization performed through particle size analysis, hardness, and tensile testing shows that ten reuse cycles do not affect part or powder quality significantly. The results support extended powder reuse potential, highlighting how L-PBF can facilitate zero-waste production and foster Italy's transition toward greener and circular practices, improving the competitiveness of made-in-Italy products while minimizing both resource consumption and material waste.

Introduction

The Italian manufacturing industry and made-in-Italy products stand out in global markets as design and technical quality hallmarks. In particular, the mechanical and machinery production industries achieve excellence through high production quality standards and innovation [1]. Nevertheless, the manufacturing sector in Italy faces the challenge of maintaining competitiveness as the new Industry 5.0 paradigm urges the adoption of sustainable practices [2]. While already an implicit objective of Industry 4.0, environmental impact reduction has now become one of the core guiding principles of the new industrial revolution. In this context, the MICS (Made in Italy - Circular and Sustainable) Extended Partnership, funded by the European Union Next-GenerationEU, identifies Additive Manufacturing (AM) techniques as the solution Italian manufacturing companies should adopt to optimize resource consumption and minimize waste [3].

Among metal AM technologies, Laser Powder Bed Fusion (L-PBF) is the most popular, with a 54% market share as of 2020 [4]. Despite being most appropriate for low-to-medium production volumes [5], L-PBF enables reproducing complex and lightweight components, redesigned through topology optimization techniques or lattice structures, which would otherwise be unfeasible using traditional manufacturing processes. Furthermore, L-PBF allows processing a wide variety of materials, including steel alloys, titanium alloys, aluminum alloys, and nickel-based superalloys [6]. On the other hand, just a small fraction of the powder loaded in any L-PBF machine is melted during part manufacturing. The remaining portion is left on the building plate or collected into an overflow tank. Since feedstock can account for up to 30% of the build cost [7], reusing the non-consumed material is necessary to maximize powder usage efficiency and reduce the costs associated with the process [8]. However, unmelted powders collected at the end of the process are contaminated by spatters [9], an inevitable by-product of laser-powder interaction that differs from virgin powder in morphology, porosity, and surface oxidation [10]. Powder

Content from this work may be used under the terms of the Creative Commons Attribution 3.0 license. Any further distribution of this work must maintain attribution to the author(s) and the title of the work, journal citation and DOI. Published under license by Materials Research Forum LLC.

Materials Research Proceedings 57 (2025) 418-425 https://doi.org/10.21741/9781644903735-49

degradation can thus be exacerbated following multiple reuse cycles, triggering the formation of defects and oxygen inclusions that might negatively impact the quality and performance of printed parts [11]. For this reason, different reuse strategies have been implemented in recent years to investigate how feedstocks and parts are affected by powder reuse [12]. Single-batch reuse represents the most used approach as reusing the same batch of powder in successive builds until it becomes insufficient allows to directly assess degradation. Despite offering high traceability, this method leads to accelerated powder degradation as fresh material replenishment is avoided [13]. For this reason, other studies focused their attention on refreshing strategies, mixing reused and virgin powder after a variable number of builds. Such blending results in a homogeneous feedstock that offsets degradation, ensuring powder and part quality remain consistent across multiple reuse cycles [14]. However, the recurrent addition of virgin powder only partially reduces the economic and environmental impact of L-PBF, emphasizing the need for closed-loop techniques where recyclates replace virgin materials [15]. Top-up strategies can then represent a viable solution, as reused powder is loaded back into the dispenser tank after each build. Despite offering simpler powder handling than other strategies, such approaches may result in layered powder beds and virgin powder contamination since blending is not typically performed when powders are reintroduced into the system [12].

The previous considerations underscore the necessity for reuse strategies to minimize powder degradation while also ensuring resource and cost efficiency. In this context, the present article proposes an alternative approach to establish closed-loop powder reuse within a zero-waste perspective. Since manufacturing companies often delay the adoption of sustainable practices due to financial, logistical, and informational barriers [16,17], a scenario in which all the virgin powder was first consumed is considered. The strategy was thus devised to perform the first reuse cycle according to the single batch approach while successive cycles were carried out in a top-up fashion to maximize resource efficiency and minimize waste. However, blending was also performed to homogenize the feedstock before each new print. The devised reuse method thus proposes slow down degradation and reduce costs associated with powder waste through the progressive dilution of reused powders. A preliminary assessment was conducted to evaluate the effectiveness of the proposed strategy through the reuse of 316L stainless steel powder. Specifically, the particle size distribution, hardness, and tensile strength after five and ten reuse cycles were investigated and compared with benchmarking values provided by the supplier for virgin powder.

Materials and methods

Metallic powder and reuse strategy

In this study, gas-atomized 316L stainless steel powder supplied by Carpenter Additive Ltd, USA, was used. The virgin-state feedstock was characterized by a particle size distribution of D_{10} = 19.8 μm, D_{50} = 31.2 μm, and D_{90} = 49.1 μm, and chemical composition as shown in Table 1.

Table 1. *Chemical composition of the supplied virgin SS316L powder in (wt.%).*

Fe	Cr	Ni	Mo	Mn	Si	C
Bal.	16.0 - 18.0	11.0 - 14.0	2.0 - 3.0	< 2.0	< 1.0	< 0.03

A systematic strategy was devised to start with single-batch reuse at the first iteration and then dilute the progressively reused powder by blending it manually with the remainder in the dispenser tank. At each reuse step, the excess powder collected after printing was sieved in a Retsch AS300 control vibratory sieve shaker with a 63-μm mesh size and then dried in a Nabertherm LH 60/12 furnace for 4 hours at a holding temperature of 70 °C. A schematization of the strategy and experimental activities is provided in Fig. 1, where R_i and B_i indicate the i-th reused powder and build job, respectively. The starting batch used in this work consisted of excess powder collected from previous builds manufactured with only virgin powder. Such residue was sieved to remove

Materials Research Proceedings 57 (2025) 418-425 https://doi.org/10.21741/9781644903735-49

larger spatters and agglomerations and dried to remove moisture. The batch was labelled R_1 to underline that it underwent a first reuse cycle. Since no significant degradation is typically observed in the powder after just one reuse cycle [12], R_1 powder was assumed to be equivalent to virgin powder. Following a first build job produced using exclusively R_1, the unmelted powder in the build volume and overflow tank was collected, sieved, and dried. This residue was labelled R_2 to underline that a second reuse cycle was performed and then loaded back into the dispenser tank, where it was mixed with the remaining R_1 powder. A second build job was thus produced using the resulting blend of R_1 and R_2. Consequently, the powder reclaimed after the second build and labelled R_3 after sieving and drying was blended with the powder in the dispenser to form the feedstock used in the third build. The devised strategy was iterated over 10 reuse cycles, so each successive build was manufactured using blends of powders with progressively longer reuse histories. By the 10^{th} build job, the feedstock thus consisted of a blend spanning all reuse cycles from R_1 through R_{10}. The 5^{th} and 10^{th} reuse cycles were chosen for powder and part characterization to provide a preliminary assessment of the proposed reuse strategy, since they represent the intermediate and final points of the reuse path.

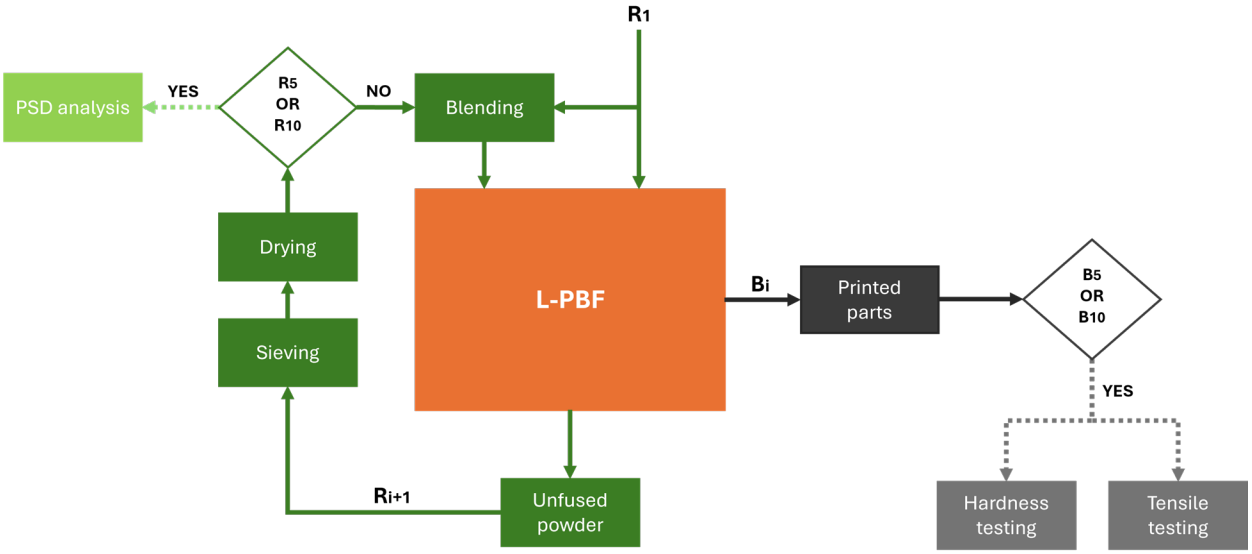


Figure 1. *Schematization of the reuse strategy proposed in this article.*

Each build was fabricated with a Print Genius 150 L-PBF machine (Prima Additive srl, Italy), mounting a 300W continuous Yb-fiber laser operating at a 1070 nm wavelength. The process was conducted in an inert argon atmosphere, keeping the oxygen level below 0.1%, as the shielding gas was constantly blown in the build chamber to remove spatter and laser plume. The following process parameters were used: 130 W laser power, 100 µm laser spot diameter, 900 mm/s scanning speed, 50 µm hatch distance, and 30 µm layer thickness. Layers were processed against gas flow using a stripe scanning strategy with 67° inter-layer rotation. The build platform was preheated and kept at 80 °C during each build. In the builds labeled B_5 and B_{10}, a 30×30×5 mm^3 prism and three horizontally built cylinders (10 mm diameter, 115 mm length) were fabricated to characterize hardness and tensile strength, respectively. The volume of these builds (27096 mm^3) occupied ~17% of the deposited powder bed. To avoid altering spatter formation and maintain powder reuse consistency, the same powder volume was consumed in the other builds to fabricate cubic and cylindrical samples destined for laboratory activities.

Materials Research Proceedings 57 (2025) 418-425 https://doi.org/10.21741/9781644903735-49

Powder and part characterization

The 5th and 10th reuse cycles were chosen for powder and part characterization to provide a preliminary assessment of the proposed reuse strategy, since they represent the intermediate and final points of the reuse path.

After sieving and drying, R_5 and R_{10} powder samples were collected for the particle size distribution (PSD) analysis performed with a Malvern 3000E laser diffraction analyzer, according to the ASTM B822-17 standard [18].

Data provided by the supplier [19] were used as benchmarks for comparison with properties achieved using only virgin powder. All specimens were removed from the build plate via Wire Electrical Discharge Machining (WEDM). After polishing, the top surface of each prism was subjected to nine Rockwell-B hardness tests according to ISO 6508-1 [20] using an Officine Galileo hardness tester. The tensile specimens (Fig. 2) machined from the printed geometry were designed and tested according to ISO 6892-1 guidelines [21]. The uniaxial tensile tests were conducted at room temperature using a Galdabini Sun 5 testing machine with a cross-head displacement rate of 0.0085 mm/s.

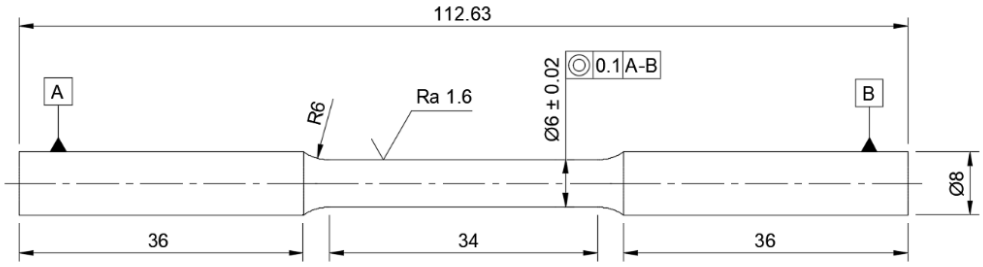
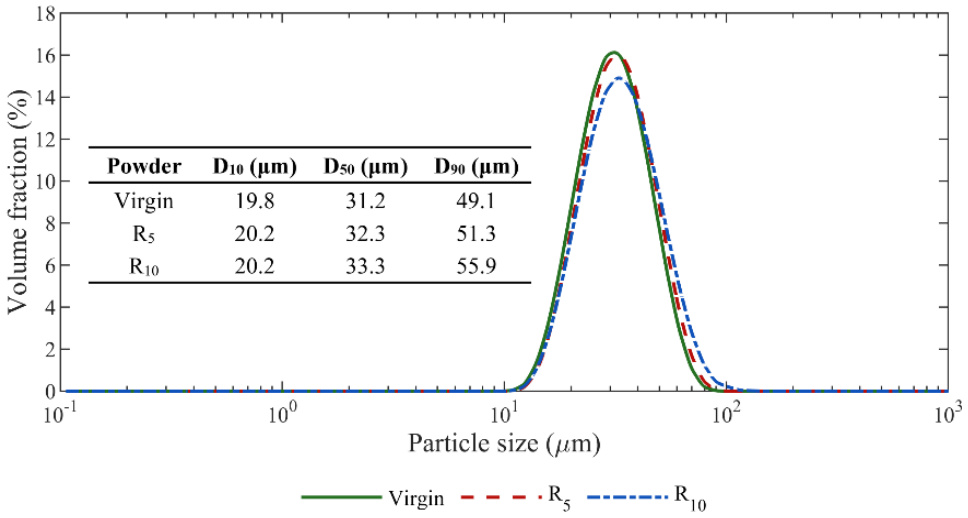


Figure 2. *Tensile specimen after machining (dimensions in mm).*

Results and discussion

The PSD analysis reported in Fig. 3 revealed a progressive coarsening of the powder over the ten reuse cycles. However, this result directly stems from the implementation of powder reuse since particles larger than layer thickness are spread past the build area in the L-PBF process, and more are collected for reuse. While D_{10} and D_{50} values remained relatively stable, the more pronounced increase exhibited by D_{90} (14 %) can be mainly attributed to increased spatter formation and agglomeration mechanisms leading to the accumulation of larger particles that survived sieving. The stable values of D_{10}, particularly between the 5th and 10th reuse cycles, suggest that the proposed dilution-based reuse strategy helps mitigate the preferential loss of fine particles typically observed in single-batch reuse [13]. By systematically mixing powders with different reuse histories, the method implemented in this study appears to be compatible with refreshing strategies, which generally have a minimal effect on PSD over ten reuse cycles [12].

Materials Research Proceedings 57 (2025) 418-425 https://doi.org/10.21741/9781644903735-49



Powder	D_{10} (µm)	D_{50} (µm)	D_{90} (µm)
Virgin	19.8	31.2	49.1
R_5	20.2	32.3	51.3
R_{10}	20.2	33.3	55.9

Figure 3. *Particle size distribution of 316L powder at virgin state, 5th reuse, and 10th reuse.*

The tensile properties and hardness results in Fig. 4 and Table 2, respectively, further reinforce the stability achieved by the proposed approach. Indeed, the increase in larger particles helps retain mechanical properties by improving flowability and packing density [22].

Fig. 4a shows that the engineering tensile stress-strain responses after five and ten reuse cycles remain consistent and comparable despite performing powder reuse multiple times in between. Furthermore, Fig. 4b demonstrates that the yield strength (YS) and ultimate tensile strength (UTS) achieved do not exhibit significant deviations from the virgin powder baselines of 552 MPa and 703 MPa, respectively. However, it is important to note that a significant reduction was instead observed in ductility compared to virgin powder. Indeed, Fig. 4b depicts a decrease in the elongation at break (A) from 57 % to 43 % and 41 % at the 5th and 10th reuse cycles. However, considering that the results achieved by both builds B_5 and B_{10} compare well with each other and reflect the same trend of stress values, the difference with the benchmark was attributed to the supplier testing the tensile properties of virgin powder builds with shorter specimen gauge length according to a different standard [19]. Overall, these findings clearly show that a reuse strategy based on reused powder dilution allows tensile performances to remain within acceptable ranges. Most importantly, the results compare favourably with findings from commonly performed reuse strategies. Indeed, in their review study, Werner et al. [12] observed that most results in the literature indicate minor or no changes in the tensile properties and ductility of stainless steels subjected to either single-batch or top-up powder reuse. Insignificant changes in YS, UTS, and A were also observed when refreshing strategies were adopted to reuse different alloys. However, further comparison with the present study cannot be drawn at the moment, as the effects of refreshing on stainless steel parts have never been investigated.

The Rockwell B hardness measurements further validate the robustness of the proposed methodology. As shown in Table 2, the measured values of 94.3 ± 1.0 HRB and 93.4 ± 1.1 HRB at the 5th and 10th reuse cycles show no significant deviation from the baseline value associated with builds fabricated using only virgin powder, again drawing a parallel with results achieved using single-batch reused 316L stainless steel powder [13].

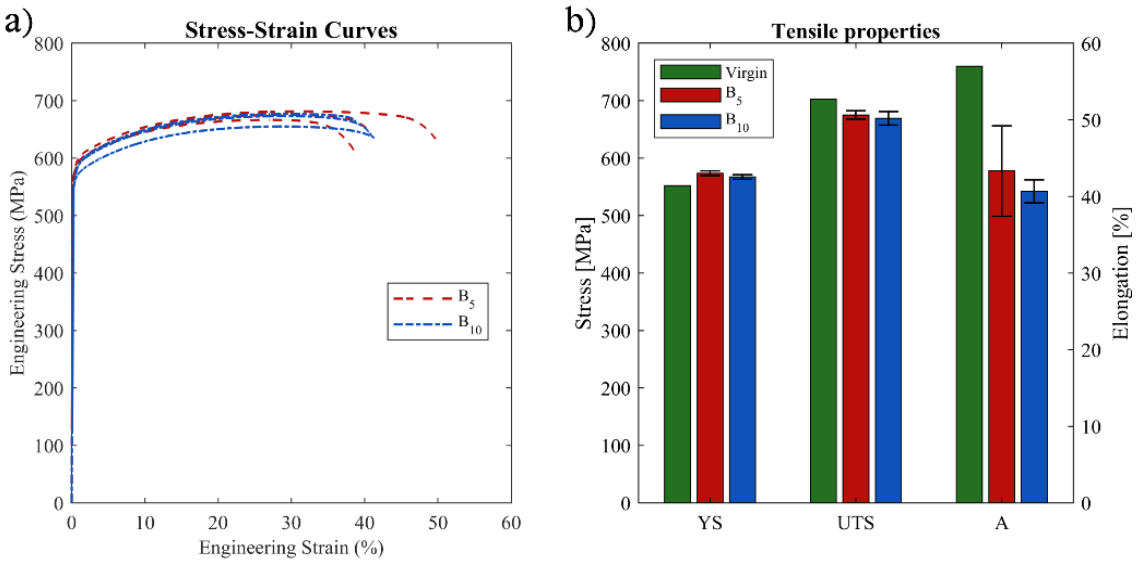


Figure 4. *Results of uniaxial tensile testing on prints B_5 and B_{10}:* ***(a)*** *engineering stress-strain curves* ***(b)*** *tensile properties comparison with powder supplier benchmark data for virgin powder.*

Table 2. *Results of Rockwell B hardness testing.*

Build	Rockwell B hardness [HRB]	
	Average	Standard deviation
Virgin	93.0	-
B_5	94.3	1.0
B_{10}	93.4	1.1

Even though limited to the 5th and 10th reuse cycles, this study shows that systematically diluting 316L stainless steel powders with different reuse histories has limited effects on particle size distribution and part properties. Comparing the devised method to commonly performed reuse strategies, where minor variations among different studies are largely attributed to differences in sieving practices and testing methodologies, it is possible to conclude that reuse does not compromise the mechanical properties of parts if powders are sieved to limit particle size below 63 µm throughout consecutive reuse cycles. Although further studies are needed to fully evaluate the influence of the proposed strategy on both powder and part properties, the preliminary results presented in this study show potential for extended powder reuse. Through careful optimization of blended proportions, dilution-based strategies may thus represent a competitive alternative to conventional reuse approaches for L-PBF powders. Even though blending powders adds to powder handling procedures and therefore represents a drawback to this technique, ensuring consistent part performance while extending the feedstock's life cycle without relying on powder rejuvenation represents a desirable advantage from environmental, economic, and quality perspectives. Dilution-based reuse would hence provide a valuable asset from an industrial perspective, as it could help manufacturers retain competitiveness on the market with reduced environmental footprints.

Conclusions

This study proposed a novel powder reuse strategy to improve the environmental and economic impact of the L-PBF technology through closed-loop reuse within a zero-waste perspective. By blending 316L stainless steel powders subjected to progressive reuse cycles, the following results were observed after five and ten iterations:

- Despite the typical coarsening of larger particles, the powder size distribution shows no significant variation, and the preferential loss of fines is halted;
- Yield strength, ultimate tensile strength, ductility, and hardness remain consistent and within a comparable range to parts manufactured using only virgin powder.

This dilution-based strategy aligns with results achieved by conventional powder reuse approaches but ensures consistent feedstock and part performance while avoiding the production of waste and the addition of fresh powder. Despite providing preliminary results for 316L stainless steel, this study poses a promising foundation for the proposed strategy to offer a valid solution to balance cost-efficiency, environmental sustainability, and part quality. Future works should thus investigate the effects of extended reuse on additional part and powder properties, as well as other L-PBF alloys, to further validate the robustness of the proposed method and foster its adoption in industrial additive manufacturing workflows. Future studies should also investigate how powder microstructure, composition, morphology, and oxygen content evolve with reuse. Such analysis would provide further insight into powder stability, thus reinforcing the findings and enhancing the completeness of the present study.

Acknowledgment
This study was carried out within the MICS (Made in Italy - Circular and Sustainable) Extended Partnership and received funding from the European Union Next-GenerationEU (PIANO NAZIONALE DI RIPRESA E RESILIENZA (PNRR) – MISSIONE 4 COMPONENTE 2, INVESTIMENTO 1.3 – D.D. 1551.11-10-2022, PE00000004). This manuscript reflects only the authors' views and opinions; neither the European Union nor the European Commission can be considered responsible for them.

References

[1] S. Rolfo, P. Rizzi, Production Specialization, Innovation and Internationalization: the case of Mechanical Engineering in Italy (2015). https://doi.org/10.1430/80603

[2] M. Breque, L. De Nul, A. Petridis, Industry 5.0: towards a sustainable, human-centric and resilient European industry (2021). https://doi.org/10.2777/308407

[3] Information on https://www.mics.tech

[4] A. Vafadar, F. Guzzomi, A. Rassau, K. Hayward, Advances in Metal Additive Manufacturing: A Review of Common Processes, Industrial Applications, and Current Challenges. Appl. Sci. 11 (2021). https://doi.org/10.3390/app11031213

[5] E. Atzeni, A. Salmi, Economics of additive manufacturing for end-usable metal parts. Int J Adv. Manuf. Technol. 62, (2012) 1147-1155. https://doi.org/10.1007/s00170-011-3878-1

[6] X. Zhao, T. Wang, Laser Powder Bed Fusion of Powder Material: A Review. 3D Print Addit. Manuf. 10 (2023) 1439-1454. https://doi.org/10.1089/3dp.2021.0297

[7] F.T. Piller, R. Poprawe, H.J. Schleifenbaum, G. Schuh, S. Barg, C. Dölle. et al. Introducing a Holistic Profitability Model for Additive Manufacturing: An Analysis of Laser-powder Bed Fusion, IEEE International Conference on Industrial Engineering and Engineering Management (2018) 1730-1735. https://doi.org/10.1109/IEEM.2018.8607729

[8] L.C. Ardila, F. Garciandia, J.B. González-Díaz, P. Álvarez, A. Echeverria, M.M. Petite, R. Deffley, J. Ochoa, Effect of IN718 recycled powder reuse on properties of parts manufactured by means of selective laser melting. Phys. Proc. 56 (2014) 99-107. https://doi.org/10.1016/j.phpro.2014.08.152

[9] E. Santecchia, S. Spigarelli, M. Cabibbo, Material Reuse in Laser Powder Bed Fusion: Side Effects of the Laser-Metal Powder Interaction. Metals 10 (2020). https://doi.org/10.3390/met10030341

[10] M.A. Oeidi, A. Mussatto, R. Groarke, R.K. Vijayaraghavan, A. Conway, D. Brabazon et al., Comprehensive assessment of spatter material generated during selective laser melting of stainless steel. Mater Today Commun 25 (2020) 101294. https://doi.org/10.1016/j.mtcomm.2020.101294

[11] M.H. Song, X. Lin, F.G. Liu, H.O. Yang, W.D. Huang, Effect of environmental oxygen content on the oxide inclusion in laser solid formed AISI 420 stainless steel. Mater. Des. 90 (2016) 459-467. https://doi.org/10.1016/j.matdes.2015.11.003

[12] J.H. Warner, S.P. Ringer, G. Proust, Strategies for metallic powder reuse in powder bed fusion: A review. J. Manuf. Process. 110 (2024) 263-290. https://doi.org/10.1016/j.jmapro.2023.12.066

[13] T. Delacroix, F. Lomello, F. Schuster, H. Maskrot, J.P. Garandet, Influence of powder recycling on 316L stainless steel feedstocks and printed parts in laser powder bed fusion. Addit. Manuf. 50 (2022) 102553. https://doi.org/10.1016/j.addma.2021.102553

[14] L. Cordova, M. Campos, T. Tinga, Revealing the Effects of Powder Reuse for Selective Laser Melting by Powder Characterization. JOM 71 (2019) 1062-1072. https://doi.org/10.1007/S11837-018-3305-2

[15] U. Lahl, B. Zeschmar-Lahl, Material Recycling of Plastics - A Challenge for Sustainability. Sustainability 16 (2024) 6630. https://doi.org/10.3390/su16156630

[16] B. Jaeger, A. Upadhyay, Understanding barriers to circular economy: cases from the manufacturing industry. J. Enterp. Inf. Manag. 33 (2020) 729-745. https://doi.org/10.1108/JEIM-02-2019-0047

[17] M.M. Bjørnbet, C. Skaar, A.M Fet, K.Ø. Schulte, Circular economy in manufacturing companies: A review of case study literature. J. Clean. Prod. 294 (2021) 126268. https://doi.org/10.1016/j.jclepro.2021.126268

[18] ASTM B822-17, Standard Test Method for Particle Size Distribution of Metal Powders and Related Compounds by Light Scattering, 2020

[19] Information on https://www.carpenteradditive.com

[20] ISO 6508-1, Metallic materials – Rockwell hardness test – Part 1: Test methods, 2023

[21] ISO 6892-1, Metallic materials – Tensile testing – Part 1: Method of test at room temperature, 2019

[22] X. Sun, M. Chen, T. Liu, K. Zhang, H. Wei, Z. Zhu, W. Liao, Characterization, preparation, and reuse of metallic powders for laser powder bed fusion: a review. International Journal of Extreme Manufacturing 6 (2023) 012003. https://doi.org/0.1088/2631-7990/acfbc3

Materials Research Proceedings 57 (2025) 426-433 https://doi.org/10.21741/9781644903735-50

Welding and wire arc additive manufacturing using FSE solid-state recycled wires: Challenges and future perspectives

Gustavo H.S.F.L. CARVALHO[1,a] *, Gianni CAMPATELLI[1,b], Gianluca BUFFA[2,c]

[1]Department of Industrial Engineering, University of Florence, Via di Santa Marta 3, 50139 Firenze, Italy

[2]Department of Engineering, University of Palermo, Via delle Scienze, 90128 Palermo, Italy

[a]gustavo.carvalho@unifi.it, [b]gianni.campatelli@unifi.it, [c]gianluca.buffa@unipa.it

Keywords: Wire Arc Additive Manufacturing (WAAM), Circular Economy, Material Extrusion

Abstract. Friction stir extrusion (FSE) is an interesting process for recycling aluminium chips. It significantly reduces waste and energy consumption by recycling materials without remelting. The possibility of producing continuous wires by FSE allows the possibility of using it as an input material in welding processes, which can significantly improve the sustainability of aluminium manufacturing. This study explores the use of FSE-recycled wires in welding and their feasibility for wire arc additive manufacturing, investigating the potential, challenges, and improvement methods for developing the process. The results show that the FSE-recycled wires can be effectively used for welding deposition. However, improving chip cleaning treatments is crucial for reducing hydrogen and oxides to further improve this application. With some improvements, potential applications and fitness for purpose can be envisioned for the process, offering an interesting circular approach in aluminum manufacturing.

Introduction

In the last few decades, environmental sustainability has become a primary concern in engineering, including manufacturing and processing. One approach to mitigating a process's environmental footprint is to employ materials with a lower environmental impact as input feedstocks, such as recycled materials in engineering and manufacturing.

The characteristics of aluminium, such as its low density (yielding a high strength-to-weight ratio), excellent thermal and electrical conductivity, and outstanding corrosion resistance [1], are leveraged in a broad spectrum of applications, from the automotive, maritime, and aerospace sectors to structural and architectural projects, storage vessels, and a variety of consumer goods [2]. Furthermore, the inherent recyclability of aluminium is essential in reducing ecological strain and preserving the Earth's natural resources. These alloys, especially those with compositions close to commercially pure alloys, experience very low or insignificant property degradation during recycling. Therefore, they maintain similar characteristics through repeated cycles and are a leading candidate for material recycling [3].

However, using recycled materials in engineering is not straightforward because virgin raw materials are usually recommended to guarantee the quality and repeatability of components with stringent requirements.

Friction Stir Extrusion (FSE) is gaining attention as a promising option for aluminium recycling, particularly for machining chips and scraps. FSE is a solid-state process that generates heat through the frictional forces between a rotating tool and workpiece. This frictional heating softens the aluminium chips within the chamber in contact with the rotating tool. The softened metal is then forced through a die to create wires, rods, and other profiles [4]. It finds a use for machining chips that are usually regarded as waste by-products of component manufacturing, and

Content from this work may be used under the terms of the Creative Commons Attribution 3.0 license. Any further distribution of this work must maintain attribution to the author(s) and the title of the work, journal citation and DOI. Published under license by Materials Research Forum LLC.

Materials Research Proceedings 57 (2025) 426-433 https://doi.org/10.21741/9781644903735-50

the process occurs in a solid state, which obviates the need for material melting for their recycling. This substantially curtails primary energy consumption compared with conventional remelting followed by wire drawing techniques, achieving energy reductions on the order of more than 70% [5].

With the capability of producing uniform and continuous products, such as wires, FSE opens up the possibility of creating materials that can be used as inputs for manufacturing components, such as welding and Wire Arc Additive Manufacturing (WAAM). Therefore, using FSE as an input for filler metal for welding and WAAM represents a remarkable possibility for reducing the environmental impact of manufacturing [6].

The possibility of using solid-state recycled wire in WAAM and welding, especially for aluminium alloys, carries several challenges that still need to be studied, defined, and overcome. For this type of application, the Gas Tungsten Arc Welding (GTAW) process is considered the most suitable because it allows the use of wires, can adapt to small variations in the wire/rod, and the feed of the filler material can be adjusted independently from electrical parameters, allowing for a more isolated evaluation of the wire [7]. Also, using alternating current (AC) is effective in mitigating the surface oxide layer issue, which has a significantly higher melting point than aluminium (approximately 2040°C compared to the 660°C of aluminium [8]).

In addition, aluminium is highly susceptible to porosity, and its high thermal conductivity leads to a more challenging deposition [8–10]. As widely reported in the literature, porosity is a prevalent defect in fusion-based welding and additive manufacturing, negatively affecting ductility, corrosion resistance, and thermal/electrical conductivity [11]. For aluminium alloys, the issue arises from the notable difference in hydrogen solubility between liquid and solid aluminium, which leads to excess dissolved hydrogen in the liquid phase being trapped during solidification [12,13].

Previous studies [7,14] have also shown that when using FSE-derived wires for welding or WAAM, multiple potential hydrogen sources exist throughout the process, making it significantly challenging to achieve components with low levels of porosity. Therefore, a comprehensive understanding of the challenges associated with using these wires, coupled with strategies for process improvement and fitness for purpose, is crucial to making the process viable and suitable for use in engineering.

This study investigates the novel application of FSE-recycled wires in GTAW-based welding and the feasibility for WAAM by comparing two conditions of solid-state recycled wires from a process perspective. Wires produced by FSE using chips directly from machining and chips that had undergone a cleaning treatment before the FSE process were tested. The depositions were evaluated from a process perspective and macroscopically characterised and analysed using high-resolution computed microtomography (micro-CT).

Materials and Methods

Several series of AC GTAW-based weld and WAAM depositions were performed using wires recycled by FSE in an automatic deposition process. The deposition system is shown in Fig. 1, it consists in a conventional GTAW welding using AC, with an independent feeding system, detailed in [14]. The deposition parameters are presented in Table 1 and were constant for all samples studied in the present work, and are a result of previous parameter optimization.

***Table 1**. GTAW welding parameters.*

Current (A)	Voltage (V)	Wire feed speed (m/min)	Travel speed (mm/min)
160	13.0	0.6	120

Materials Research Proceedings 57 (2025) 426-433 https://doi.org/10.21741/9781644903735-50

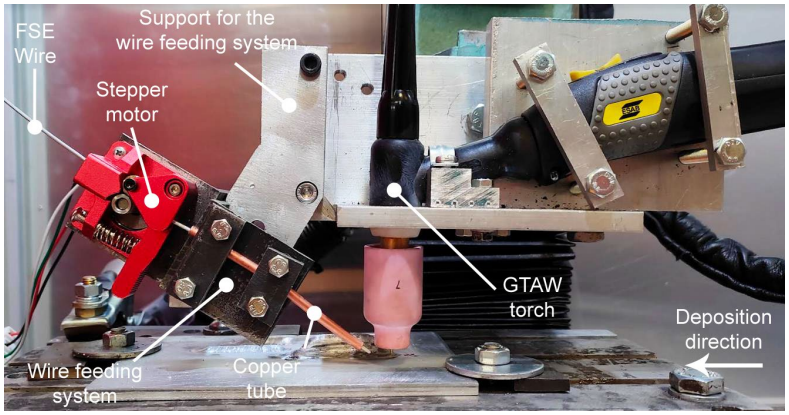


Fig. 1. *GTAW-based automatic system used for the depositions.*

The FSE filler wires were produced according to the procedure detailed by Buffa et al. [15], with process parameters of 500 RPM and 18 kN force, to produce wires of 1 mm diameter. The chips used for the FSE were collected from machining a 6082 aluminium bar under two different conditions: using chips directly from the machining to represent the worst condition scenario, and chips subjected to a cleaning process after machining before FSE processing. The chips present variable dimensions. This cleaning involved immersing the chips in acetone to remove moisture, grease, and other contaminants that are invariably present after typical machining operations. The milling operation that generated the chips was performed conventionally, mirroring standard industrial practices. AA1050 plates served as deposition substrates for all experiments and have a thickness of 5 mm. Table 2 shows the chemical compositions of the substrate and the bar that generated the chips for the manufacturing of the wires (unless otherwise specified, the values indicate the maximum allowed percentages).

Table 2. Nominal chemical composition of filler metal and substrate (% weight) [16].

	Mg	**Si**	**Mn**	**Fe**	**Cu**	**Cr**	**Ti**	**Zn**	**V**	**Al**
Substrate AA1050	0.05	0.25	0.05	0.40	0.05	-	0.03	0.05	0.05	99.5 min
AA6082 (~wires)	0.6-1.2	0.7-1.3	0.40-1.0	0.50	0.10	0.25	0.10	0.20	-	Bal

The internal porosity of the depositions was investigated using high-resolution 3D micro-computed tomography (micro-CT) employing a Skyscan 1172 high-resolution micro-CT scanner. Two-dimensional X-ray projections were acquired with a rotation increment of 0.9964° between the slices. Three-dimensional models were reconstructed and visualised using CTVox and CTVol software. Several cuts were performed using the tomography technique, such as longitudinal and transverse, to evaluate them internally.

Results

First, the wires were analysed macroscopically to determine whether there were significant differences. Fig. 2 shows the general aspect of a wire produced with chips, with and without cleaning. The main differences lie in the roughness of the external appearance. Disregarding the FSE process marks (small transverse regularly spaced lines along the wire), the wires manufactured with uncleaned chips (Fig. 2a) have a rougher surface compared to the wire manufactured with cleaned chips.. Another noteworthy feature is that the wires produced with uncleaned chips are slightly more irregular (curved) in terms of wire shape and straightness.

Materials Research Proceedings 57 (2025) 426-433 https://doi.org/10.21741/9781644903735-50

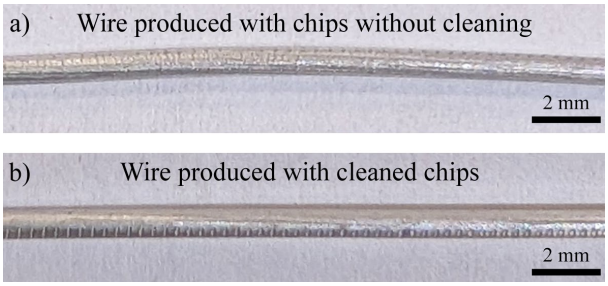


Fig. 2. *External aspects of the wires produced by FSE.*

The depositions were performed using a bead-on-plate approach to understand the effect of deposition in a simple, regular area and direction using the optimized parameters in Table 1. Therefore, the deposition was performed in the flat position (the easiest and simplest one) to discard the effects of the welding position, rectilinear and 70 mm in length.

Fig. 3 shows the top view of the two depositions performed with the two types of wires. Although the differences in the external appearance of the wires were not highly significant (Fig. 2), the depositions were entirely different. When using wires without chip cleaning (Fig. 3a), the deposition exhibited irregularities along its path, irregularities in shape, and a significant presence of oxides as dark zones. Observing the outer edge of the bead using wires produced with cleaned chips (Fig. 3b), there was a much more substantial path regularity and only small shape variations. However, the main difference observed, especially when considering the deposition of aluminium alloys, is the amount of oxides, impurities, and surface porosity observed in the deposition with wires with uncleaned chips. The amount of dark-coloured oxides was substantial, and below these oxides, there was the presence of porosity that arose on the surface. With the wire with cleaned chips, despite some oxidation, it was substantially less.

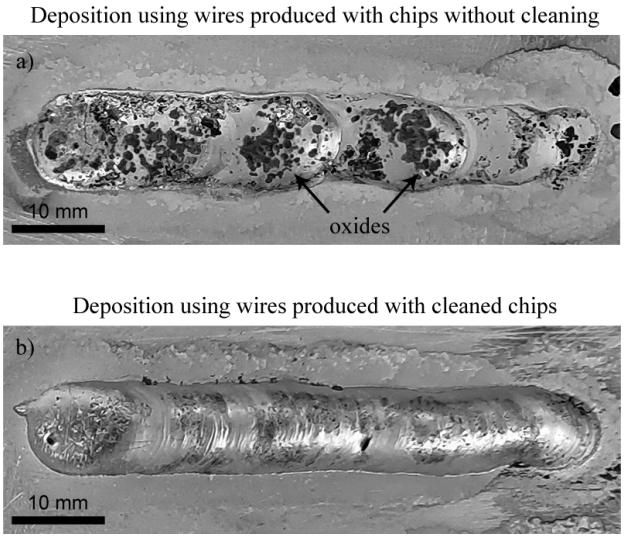


Fig. 3. *Aspects of depositions performed with the two types of wires.*

Several computed tomography tests were performed to understand the reasons for the notable difference between the depositions and to analyse the depositions internally. First, tests were conducted on the wires used in the depositions. Fig. 4 and Fig. 5 show the results of the tomography.

The wires produced with uncleaned chips (Fig. 4) have a rougher surface and some internal discontinuities (arrows). On the other hand, the wires produced with cleaned chips (Fig. 5) do not have internal defects and have a smoother external surface. For alloys such as aluminium, which

Materials Research Proceedings 57 (2025) 426-433 https://doi.org/10.21741/9781644903735-50

are very sensitive to impurities and moisture (due to hydrogen), these defects may cause significant problems during deposition because they may carry impurities and humidity from the chips to the deposition area. The deposition results in Fig. 3a indicate that many impurities and hydrogen sources were present, resulting in poor deposition. Using cleaned chips as the input material for the FSE process significantly improved the external and internal qualities of the manufactured wires.

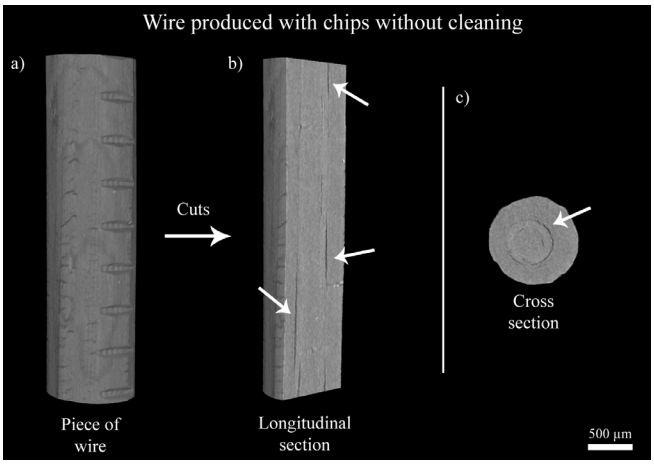


Fig. 4. *Microtomography of wires produced with chips without cleaning (from left to right: wire aspect, longitudinal cut, and wire cross section). The small arrows indicate the discontinuities found inside the wires.*

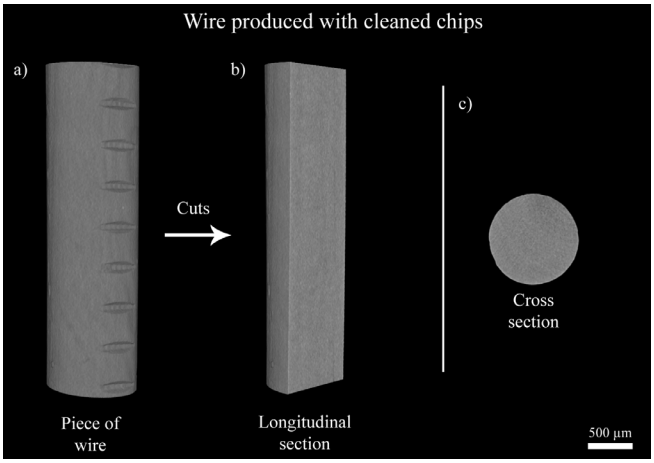


Fig. 5. *Microtomography of wires produced with cleaned chips (from left to right: wire aspect, longitudinal cut, and wire cross section).*

Fig. 6 and Fig. 7 present the microtomography analysis of the deposited beads. The aluminium metallic part is represented in white (to which a 40% transparency was applied to see the interior), while the red part represents the voids/pores. A significant presence of pores was observed in both depositions, regardless of the wire type. However, some significant differences should be noted. First, several pores appeared on the surface when using the wire with uncleaned chips (Fig. 5a), whereas the same did not occur when the wire with cleaned chips was used (Fig. 6b).

There was also a significant difference in the porosity. Fig. 7 shows the top views of the samples. The lower images show only the pores in detail, where it is possible to see that the wire produced with uncleaned chips generated a much larger number of pores. Not only is the quantity greater, but the size of the pores is much larger, and some of them are concentrated in some zones,

Materials Research Proceedings 57 (2025) 426-433 https://doi.org/10.21741/9781644903735-50

which is even more harmful to the material's properties. When using wires produced with cleaned chips, the pores were smaller and more evenly distributed.

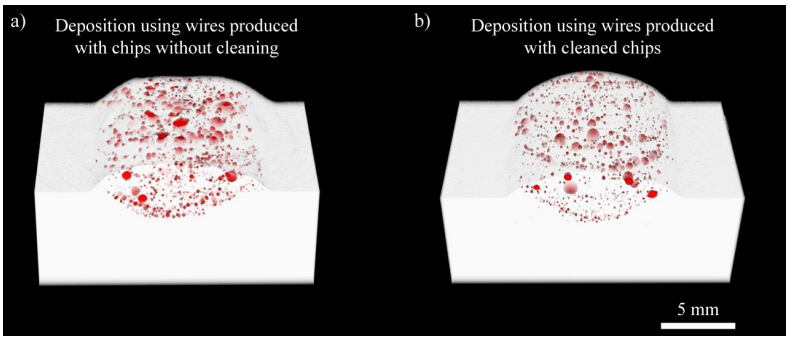


Fig. 6. *Microtomography of depositions. Aluminium is represented in white, and voids/pores are represented in red.*

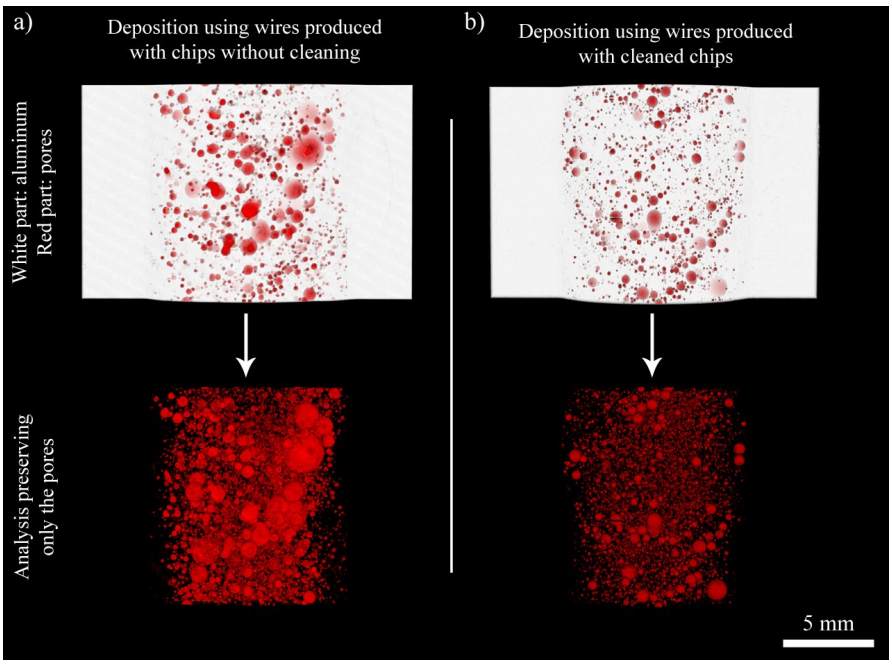


Fig. 7. *Top view of microtomography. The images at the bottom show only the porosity isolated from the materials. Aluminium is represented in white, and voids/pores are represented in red.*

The use of wires recycled by FSE for WAAM deposition is feasible and presents interesting perspectives for the manufacturing industry. The results proved that consistent beads can be formed without electric-arc instability. The rationale for utilising recycled materials in manufacturing is compelling: it offers a pathway to resource conservation, reduces reliance on virgin material extraction, and contributes to a circular economy model.

However, the porosity found suggests that the current cleaning protocols need to be improved. Therefore, further research is required to optimise and develop more effective cleaning treatments and detect the possible sources of hydrogen that could be introduced in the process. This could involve exploring different cleaning agents, cleaning durations, and temperatures or employing multiple cleaning stages. In addition to chip cleaning, the welding environment plays a crucial role in controlling porosity. The moisture in the surrounding atmosphere can contribute to the hydrogen pick-up by molten aluminium. Therefore, the overall care in the WAAM process with FSE wires should be greater than that in conventional aluminium deposition.

Conclusions

This study explored the feasibility of utilising FSE-derived recycled rods for material deposition and identified the key challenges associated with this process. The following conclusions were drawn:

- The results show that using FSE solid-state recycled wires as filler material in WAAM and welding is feasible and effective.
- Pre-FSE cleaning of machining chips is essential to minimise impurities and potential hydrogen sources in the resulting wire. Porosity was observed in depositions made with both cleaned and uncleaned chip-derived wires, but significantly improved results were obtained using wires with cleaned chips.
- Despite pre-FSE chip cleaning, some porosity persisted in the deposited material, indicating the need for further optimisation of cleaning protocols and investigation of impurity sources to enhance the overall deposition quality. Further refinement of the welding parameters and control of the welding environment may also prove beneficial.

Acknowledgments

This study was carried out within the activity of project “PERPETUAL 100% Material utilization using sOlid sTate recycling and Additive Manufacturing for productION and repairing of aluminum components (PERPETUAL MOTION)”, funded by the European Union - Next Generation EU, Mission 4 Component C2, Project: 20224H9YC9, CUP: B53D23005510006.

References

[1] R.N. Lumley, Fundamentals of Aluminium Metallurgy: Production, Processing and Applications, 1st ed., Woodhead Publishing Limited, 2011.

[2] X. Yang, R. Li, T. Yuan, L. Ke, J. Bai, K. Yang, A comprehensive overview of additive manufacturing aluminum alloys: Classifications, structures, properties and defects elimination, Mater. Sci. Eng. A. 919 (2025) 147464. https://doi.org/10.1016/j.msea.2024.147464

[3] S.N.A. Rahim, M.A. Lajis, S. Ariffin, A Review on Recycling Aluminum Chips by Hot Extrusion Process, Procedia CIRP. 26 (2015) 761–766. https://doi.org/10.1016/j.procir.2015.01.013

[4] Y.M. Altharan, S. Shamsudin, S. Al-Alimi, Y. Saif, W. Zhou, A review on solid-state recycling of aluminum machining chips and their morphology effect on recycled part quality, Heliyon. 10 (2024) e34433. https://doi.org/10.1016/j.heliyon.2024.e34433

[5] D. Baffari, A.P. Reynolds, A. Masnata, L. Fratini, G. Ingarao, Friction stir extrusion to recycle aluminum alloys scraps: Energy efficiency characterization, J. Manuf. Process. 43 (2019) 63–69. https://doi.org/10.1016/j.jmapro.2019.03.049

[6] G. Ingarao, M. Amato, A. Latif, A.D. La Rosa, R. Di Lorenzo, L. Fratini, Life Cycle Assessment of aluminum alloys chips recycling through single and multi-step Friction Stir Consolidation processes, J. Manuf. Syst. 68 (2023) 651–659. https://doi.org/10.1016/j.jmsy.2023.05.021

[7] G.H.S.F.L. Carvalho, G. Campatelli, L. Fratini, Feasibility study of using friction stir extruded recycled aluminum rods for welding and additive manufacturing, Manuf. Lett. 42 (2024) 52–55. https://doi.org/10.1016/j.mfglet.2024.10.007

[8] T. Anderson, B.E. Anderson, F.G. Armao, P. Berube, T. Burns, D.M. DePauw, J. Ginder, B.W. Hemmert, R.B. Hirsch, C. Hsu, M.S. Kadlec, S.F. McCleary, M.A. Palmer, S.E. Pollard, M.J. Russell, D.J. Spinella, M.P. Vandenberg, K.L. Williams, J. Zhang, J.H. Myers, Aluminum

and Aluminum Alloys, in: A. O'Brien (Ed.), AWS Weld. Handb. Vol. 5 - Mater. Appl. Part 2, 9th ed., American Welding Society, Miami, USA, 2015: pp. 1–135.

[9] M. Arana, E. Ukar, I. Rodriguez, A. Iturrioz, P. Alvarez, Strategies to reduce porosity in Al-Mg WAAM parts and their impact on mechanical properties, Metals (Basel). 11 (2021). https://doi.org/10.3390/met11030524

[10] R. Fu, S. Tang, J. Lu, Y. Cui, Z. Li, H. Zhang, T. Xu, Z. Chen, C. Liu, Hot-wire arc additive manufacturing of aluminum alloy with reduced porosity and high deposition rate, Mater. Des. 199 (2021) 109370. https://doi.org/10.1016/j.matdes.2020.109370

[11] S. Chandra, J. Radhakrishnan, S. Huang, S. Wei, U. Ramamurty, Solidification in metal additive manufacturing: challenges, solutions, and opportunities, Prog. Mater. Sci. 148 (2025) 101361. https://doi.org/10.1016/j.pmatsci.2024.101361

[12] N. Trometer, B. Chen, M. Moodispaw, W. Cai, T. Rinker, S. Kamat, Z. Velasco, A.A. Luo, Modeling and validation of hydrogen porosity formation in aluminum laser welding, J. Manuf. Process. 124 (2024) 877–890. https://doi.org/10.1016/j.jmapro.2024.06.052

[13] G. Mathers, The Welding of Aluminium and its Alloys, 1st ed., Woodhead Publishing Limited, Cambridge, England, 2002. https://doi.org/10.1007/s13398-014-0173-7.2

[14] G.H.S.F.L. Carvalho, G. Campatelli, B.S. Cota, D. Campanella, R. Di Lorenzo, Development of a NC-Controlled GTAW-Based Wire Arc Additive Manufacturing System for Using Friction Stir Extrusion Recycled Wires, Machines. 13 (2025) 10. https://doi.org/10.3390/machines13010010

[15] G. Buffa, D. Campanella, M. Adnan, U. La Commare, G. Ingarao, L. Fratini, Improving the Industrial Efficiency of Recycling Aluminum Alloy Chips Using Friction Stir Extrusion: Thin Wires Production Process, Int. J. Precis. Eng. Manuf. Technol. (2024). https://doi.org/10.1007/s40684-023-00573-w

[16] J.R. Davis, ASM Speciality Handbook: Aluminum and Aluminum Alloys, 4th ed., ASM International, Materials Park, Ohio, USA, 1998.

Materials Research Proceedings 57 (2025) 434-440 https://doi.org/10.21741/9781644903735-51

Optimization of manufacturing processes for PS-paper powder compounds in sustainable foodservice plates

Arif Enes KARACA[1,a*], Alessandra CAGGIANO[1,b], Massimiliano BARLETTA[1,c]

[1]Via della Vasca Navale 79, 00146 Roma, Department of Industrial, Electronics, and Mechanical Engineering, University of Roma Tre, Rome, Italy

[a]arifenes.karaca@uniroma3.it, [b]alessandra.caggiano@uniroma3.it, [c]massimiliano.barletta@uniroma3.it

Keywords: Plastic and Composite Materials Processes, Extrusion, Sustainability

Abstract. The increasing demand for sustainable foodservice packaging has prompted the exploration of alternative materials that balance performance and environmental impact. This study investigates the potential of incorporating paper powder into polystyrene (PS) to develop eco-friendly foodservice plates. PS was compounded with paper powder at varying weight fractions (10%, 15%, and 20%), alongside compatibilizers and processing aids to improve dispersion and material properties. The compounding process was optimized using a twin-screw extruder, followed by film production via minicast extrusion. The processing temperatures dropped by 18% compared to pure PS, suggesting meaningful energy savings. Various characterization tests, including density, melt flow rate (MFR), tensile properties, impact strength, tear strength, and heat deflection temperature (HDT), were performed to evaluate the compounds' mechanical performance and processability. The results showed that the addition of paper powder reduced the density (by 3.8%) and MFR of the PS compounds, indicating potential environmental benefits, such as reduced material usage and transportation costs. While the tensile strength and impact resistance decreased with increasing paper content, tear strength improved significantly, making the compounds suitable for foodservice applications. The thermal stability of the compounds remained comparable to pure PS, suggesting that paper powder incorporation does not negatively impact the material's performance under moderate temperatures. Additionally, the incorporation of paper powder led to a darker color in the films, with processing temperatures adjusted to mitigate excessive darkening. This study demonstrates that PS-paper powder compounds offer a promising alternative for sustainable foodservice packaging, combining reduced environmental impact with adequate mechanical properties for practical use in disposable tableware.

Introduction

The increasing demand for sustainable foodservice packaging has driven research into alternative materials that balance functionality and environmental impact [1]. Traditional polystyrene (PS) plates are widely used due to their lightweight and cost-effectiveness; however, their non-biodegradability poses a significant environmental challenge [2]. With growing concerns over plastic waste accumulation and pollution, the need for eco-friendly alternatives has become a priority in the packaging industry [3,4,5].

One promising approach to reducing the environmental impact of PS-based products is incorporating natural fillers such as paper powder into the polymer matrix. Paper powder, derived from recycled or processed paper, is a biodegradable material that can enhance sustainability without compromising essential performance characteristics. By partially replacing PS with paper powder, the overall plastic consumption in foodservice plates can be reduced, leading to lower carbon footprints and improved material efficiency [6,7].

Content from this work may be used under the terms of the Creative Commons Attribution 3.0 license. Any further distribution of this work must maintain attribution to the author(s) and the title of the work, journal citation and DOI. Published under license by Materials Research Forum LLC.

Materials Research Proceedings 57 (2025) 434-440 https://doi.org/10.21741/9781644903735-51

However, integrating paper powder into PS presents several challenges. Ensuring proper dispersion, preventing thermal degradation during processing, and maintaining adequate mechanical properties are crucial factors that must be addressed. Poor dispersion may lead to weak spots in the final product, while excessive heat during extrusion could degrade the paper component, affecting structural integrity and aesthetics. Therefore, optimizing the manufacturing process is essential to achieving a balance between sustainability and functionality [8].

This study focuses on optimizing the manufacturing processes for PS-paper powder compounds, particularly for potential foodservice plate applications. The compounding process involves twin-screw extrusion, where paper powder is incorporated at weight fractions of 10%, 15%, and 20%, along with compatibilizers to enhance dispersion and adhesion. Mini-cast film production is employed to evaluate the processability and material properties. Key process modifications include adjusting extrusion temperature and screw speed to improve processing efficiency while maintaining product integrity.

By valorizing post-industrial paper waste and reducing polymer use, this work targets lightweight, resource-efficient foodservice packaging without compromising performance, which represents a step toward circular economy goals. The objective of this research is to investigate the impact of paper powder incorporation on the mechanical properties, processability, and sustainability of PS-based foodservice plates. By evaluating the influence of process parameters on material performance, this study aims to provide insights into scalable and eco-friendly manufacturing solutions for disposable tableware. The findings contribute to the ongoing efforts toward sustainable packaging alternatives, aligning with global initiatives to reduce plastic waste and promote circular economy principles.

Materials and Methods

Materials

The following materials were employed to formulate the blends: PS Edistir R850E grade from Versalis S.p.A; paper powders (post processing waste) from Aristea SpA; ethylene-butyl acrylate copolymer Lotryl® 30BA02 from SK Functional Polymer; ethylene-methyl acrylate-glycidyl methacrylate terpolymer Lotader AX8900 from SK Functional Polymer; ethylene bis stearamide Evivax 140 from Eigenmann & Veronelli S.p.A; antioxidant ADK STAB A-611 from Adeka Polymer Additives Europe; and zinc stearate from Andrea Gallo di Luigi Srl. These additives served roles as compatibilizers, stabilizers, and processing aids to improve interfacial adhesion, thermal stability, and processability. The recipe of compounds is given in Table 1.

Table 1. *The Recipes of PS-Paper Powder Compounds*

Component	PS-10 (%)	PS-15 (%)	PS-20 (%)
Polystyrene (Edistir R850E)	84.10	78.10	71.10
Paper Powder	10	15	20
Lotryl® 30BA02	2	3	5
Lotader AX8900	2.5	2.5	2.5
EBS (Eviwax 140)	1	1	1
ADK STAB A-611	0.25	0.25	0.25
Zinc Stearate	0.15	0.15	0.15

Compounding

PS/Paper Powder were compounded on a COMAC EBC25HT 26D (Bergamo, Italy) with an L/D ratio of 26. PS/Paper Powder were compounded with varying processing conditions with a screw configuration with kneading, and transportation elements with varying geometry arranged along the barrel length. While PS and additives were fed together from the first feeding zone, the paper powders were fed separately from another feeding zone. The extrusion parameters (Table 2) were

selected based on the technical datasheet for PS, which recommends a melt temperature of 210-240°C for pure PS. To minimize paper degradation (linked to darkening in Fig. 1), temperatures were reduced to 180-220°C, suggesting energy savings - a critical sustainability lever in extrusion. The extruder speed (240 rpm) ensured homogeneous blending and moderate torque, balancing dispersion efficiency with shear-induced heat avoidance. Extrudate strands granulated after passing through a cooling bath were kept in oven at 90°C for 4 hours to remove excess water.

Table 2. *Compounding Parameters for PS-Paper Powder Compounds*

Melt Pressure [bar]					13.9	**Temperature Melt [°C]**					191
Throughput, [kg/h]					20	**Extruder Speed [rpm]**					240
Temperature Profile [°C]											
T1	T2	T3	T4	T5	T6	T7	T8	T9	T10	T11	T12
180	190	200	210	210	220	220	220	220	215	215	210

Preparation of test samples by injection molding

The compounds were molded at RI.P.I. 60 EUROMAP 620 H-220 to prepare test samples for various characterizations such as density, tensile, Izod, HDT, etc. The temperature profile varied between 180-190°C and melted temperature was almost 187°C. It was clearly observed that processing temperature decreased to prevent thermal degradation as paper ratio increased.

Production of film samples by minicast film

The pellets were extruded using Minicast EUR.EX.MA to produce film samples. The heating profile was adjusted to accommodate the presence of paper powder, ensuring proper forming without excessive degradation. For this reason, as the paper ratio increased in the compounds, the temperature decreased from 210°C to 180°C. The extruder speed varied between 100 and 120 rpm during production.

Characterization

The granules and prepared test samples via injection molding and minicast film were used to evaluate the properties of compounds by various characterization tests, including:

- Colour Analysis: The difference of colour between compounds was examined.
- Density (ISO 1183-1): The compounds were measured by mass per unit volume (g/cm^3) at room temperature. The tests were carried out with three replicates per sample.
- Melt Flow Rate (MFR) (ISO 1133-1): The flowability of molten compounds was evaluated in grams per 10 minutes (g/10 min) under 200°C and 5 kg. Two replicates were made per sample.
- Differential Scanning Calorimetry (DSC) (ISO 11357-1): It was performed to determine thermal transitions of the compounds such as glass transition (Tg), melting (Tm), and crystallization (Tc). The temperature range was preferred between 25°C and 280°C.
- Tensile Properties (ISO 527-2): Tensile strength (MPa), elongation at break (%), and Young's modulus (MPa) were assessed. The test speed was adjusted as 10 mm/min. The tests were performed with five replicates per sample.
- Izod Impact Strength (ISO 180): The impact resistance of test samples with a 2 mm notch in kilojoules per square meter (kJ/m^2) was evaluated. Five replicates were made per sample.
- Tear Resistance (Elmendorf) (ISO 6383-2): Tear strength of the samples in newtons (N) per mm was measured. The tests were operated five times per sample.
- Heat Deflection Temperature (HDT) (ISO 75-2): The temperature (°C) at which the compounds deform under a 0.45 MPa load was measured. The tests were performed with three replicates per sample.

Materials Research Proceedings 57 (2025) 434-440 https://doi.org/10.21741/9781644903735-51

Results and Discussion

As the paper powder content increased, the film samples exhibited a progressively darker appearance (see Fig. 1). This visual change indicates the direct influence of paper incorporation on the colour of the final compounds. The temperature during production was adjusted to prevent excessive darkening of the compounds as the paper powder content increased.

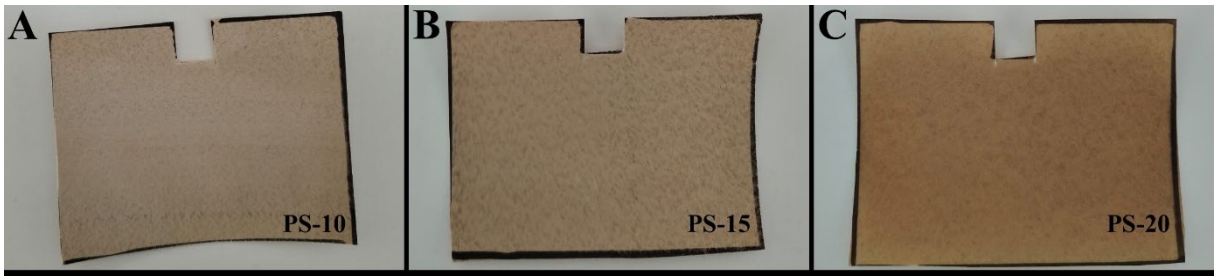


Figure 1. *Colour Analysis of (A) PS-10, (B) PS-15, (C) PS-20*

Although the density of pure PS is 1.04 g/cm3, density trends were non-linear: PS-10 achieved a 3.8% reduction (1.00 g/cm³), but PS-20 neared pure PS (1.035 g/cm³), as shown Fig. 2. This reduction in density is advantageous from a sustainability perspective, as it suggests a decrease in the overall weight of the final product. For a typical 20 g PS plate, this saves 0.76 g of virgin plastic per plate - scalable to tons annually in mass production. A lower material density can contribute to reduced raw material consumption and lower transportation costs, ultimately minimizing the environmental impact. These findings highlight the potential of compounds as a more resource-efficient alternative for food service tableware applications.

As anticipated, MFR of the compounds decreased with the addition of paper powder, as given in Fig. 2. This reduction in MFR can be attributed to the increased viscosity of the material due to the presence of paper powder, which acts as a filler. While this decrease typically suggests a slower flow of the material, it did not adversely affect the processing during film production. The film production process remained stable, indicating that the compounds retained adequate processability, likely due to the manageable increase in viscosity. This suggests that the material can be processed effectively without significant alterations to standard processing conditions, even with the incorporation of paper powder.

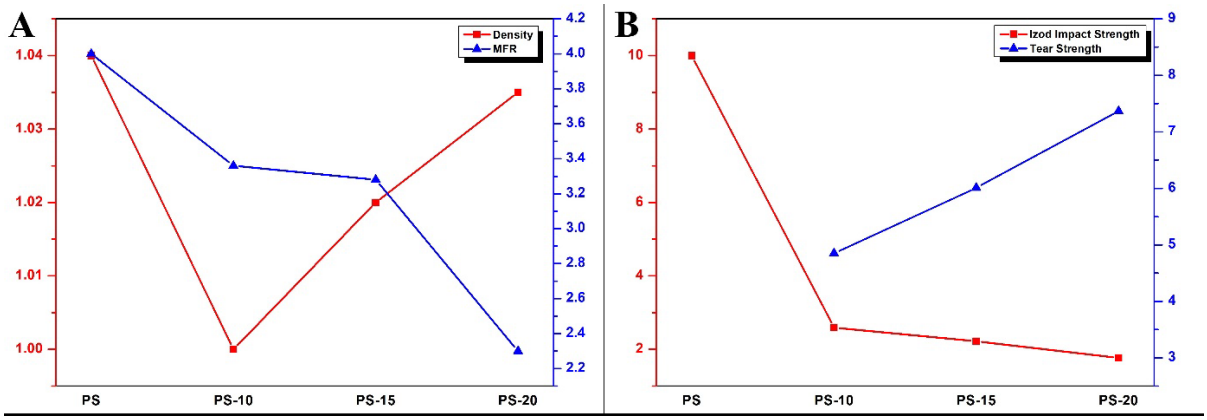


Figure 2. *(A) Density and MFR, (B) Izod Impact Strength and Tear Strength*

DSC analysis confirmed the amorphous nature of the PS-paper powder compounds, with a consistent glass transition temperature (Tg) observed between 100-120°C in both heating cycles, as observed in Fig. 3. The addition of paper powder did not significantly affect the thermal transitions of PS, indicating good dispersion without major structural modifications.

Materials Research Proceedings 57 (2025) 434-440 https://doi.org/10.21741/9781644903735-51

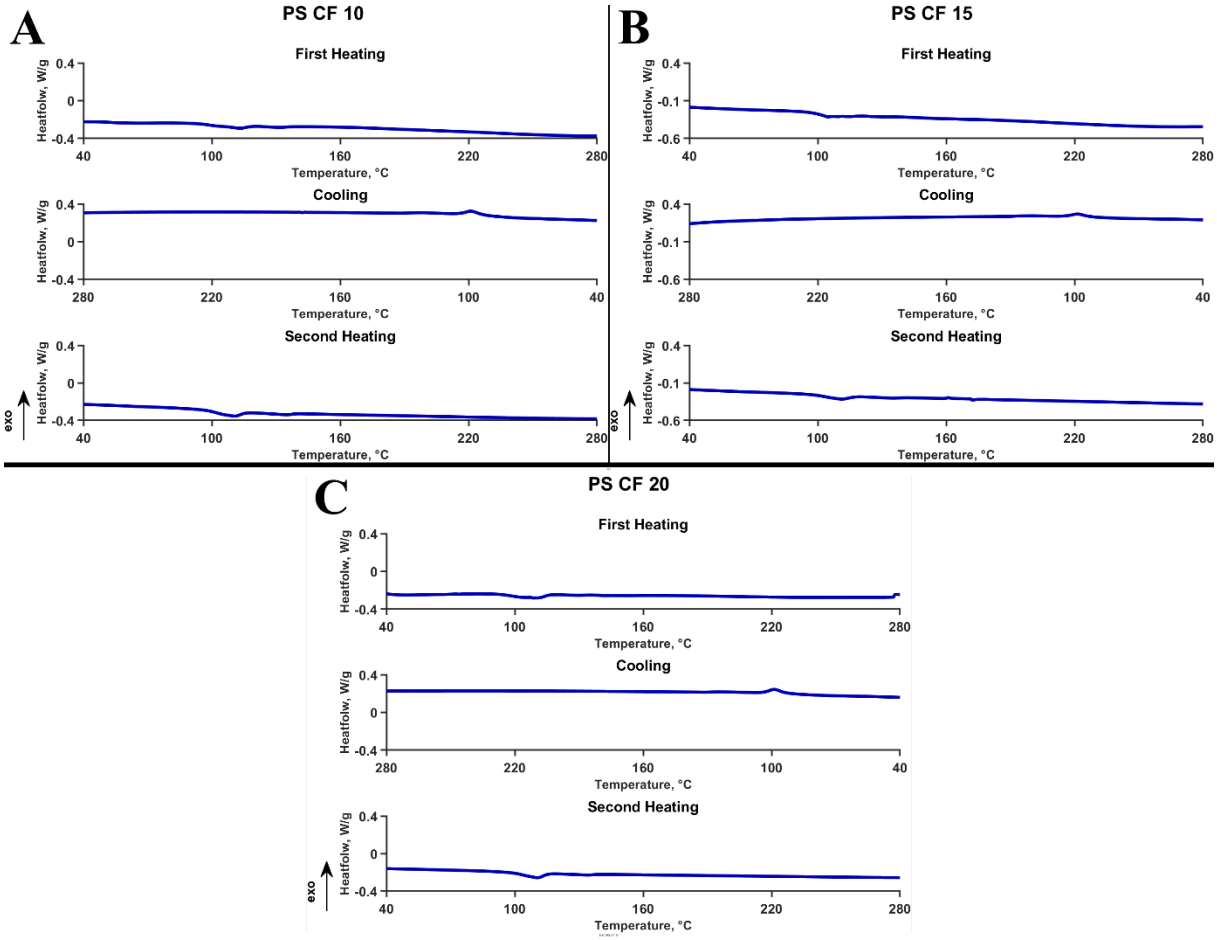


Figure 3. *DSC Graph of (A) PS-10, (B) PS-15, (C) PS-20*

The addition of paper powder to polystyrene compounds resulted in a decrease in tensile strength, elongation, and tensile modulus compared to pure PS, as shown in Table 3. The reduction in mechanical properties is characteristic of particulate-filled polymer systems, attributed to weak interfacial adhesion between hydrophilic paper powder and hydrophobic PS. To mitigate these effects, compatibilizers (Lotryl® 30BA02 and Lotader AX8900) were incorporated at higher ratios with increasing paper content (Table 1). These additives enhance polarity and interfacial bonding. For further optimization, future studies could explore surface treatments (e.g., silanization) or hybrid fillers (e.g., nanoclay-paper combinations) to balance sustainability and mechanical performance. Similar to previous studies on polymer composites, the tensile strength of PP-wood fiber compounds decreased with increasing wood fiber content [9]. As reported by Kim et al., this reduction can be attributed to the weak interfacial adhesion and low compatibility between the hydrophilic paper powder and the hydrophobic PS matrix. The decrease in tensile strength is not considered a significant drawback for the intended final applications, as the material is expected to perform well in food service tableware applications where impact resistance, tear strength, and sustainability are of greater importance than high tensile strength. The reduction in elongation is also anticipated, as the paper powder filler contributes to a more rigid structure. While this lower elongation value might limit the material flexibility, it does not pose a significant issue for thermoforming processes. Lastly, the decrease in tensile modulus from 1900 MPa to 700-750 MPa indicates a reduction in rigidity, which may actually be advantageous for applications requiring some flexibility or resilience.

Materials Research Proceedings 57 (2025) 434-440 https://doi.org/10.21741/9781644903735-51

Table 3. *Tensile Test and HDT Results*

Characterizations [10]	**PS**	**PS-10**	**PS-15**	**PS-20**
Tensile Strength [MPa]	28 ± 0.5	15.33 ± 0.7	15.6 ± 0.6	17.1 ± 0.8
Elongation [%]	70 ± 2.1	18.23 ± 1.2	8.4 ± 0.9	6.7 ± 0.5
Tensile Modulus [MPa]	1900 ± 50	708 ± 25	696 ± 30	774 ± 28
HDT [°C]	85 ± 0.3	84.8 ± 0.4	84.3 ± 0.5	84.4 ± 0.4

The Izod impact test revealed a decrease in impact resistance for the compounds compared to pure PS (Fig. 2). While pure PS showed a value of 10 kJ/m2, the compounds exhibited values of 2.59, 2.22, and 1.77 kJ/m2, respectively, depending on the paper powder content. This reduction in impact strength is consistent with the incorporation of paper powder, as the filler particles can disrupt the polymer's ability to absorb impact energy. Despite this decrease, the reduction in impact strength does not pose a significant issue for the intended food service tableware applications. Similarly, Nygård et al. observed the same effect of wood powder on impact strength of PP compounds [11]. Furthermore, they stated that the impact strength of PP compounds with addition of wood powder dramatically decreased without coupling agent. The importance of a coupling agent is to provide the uniform distribution of the stress by dispersing wood powder [12].

The addition of paper powder to polystyrene (PS) compounds resulted in a notable increase in tear strength, with values of 4.85 N/mm, 6.01 N/mm, and 7.37 N/mm for PS-10, PS-15, and PS-20, respectively (Fig. 2). This increase suggests that the paper powder acts as a reinforcing agent, improving the material's resistance to tearing. The positive trend observed in tear strength can be attributed to the improved stress distribution and interfacial interaction between the filler and the PS matrix. These results highlight the potential of paper powder-filled PS as a more tear-resistant material, suitable for applications where tear resistance is a critical performance requirement.

The HDT at 0.45 MPa for the compounds was found to be almost identical to that of pure PS, with values around 84°C for all compounds compared to 85°C for pure PS, as shown in Table 3. This suggests that the incorporation of paper powder does not negatively impact the material's thermal stability. The compounds maintain similar thermal performance to pure PS, which is a promising result, particularly for applications that involve exposure to moderate temperatures, such as in the food service industry. This outcome indicates that the addition of paper powder contributes to the sustainability of the material without sacrificing its thermal performance.

Conclusion

The incorporation of paper powder into PS compounds effectively reduces material density, providing a more sustainable and lightweight alternative for food service tableware. Additionally, the 18% reduction in processing temperatures for paper-filled compounds suggests meaningful energy savings during production, further enhancing their sustainability profile. Among the tested formulations, PS-20 exhibits the most promising performance, achieving the highest tear strength (7.37 N/mm) and maintaining thermal stability comparable to pure PS, with a heat deflection temperature (HDT) of 84.4°C. Although slight reductions in tensile strength and elongation are observed, these do not pose significant limitations for food service applications, where tear resistance and sustainability are key priorities. Additionally, increasing paper powder content leads to a darker coloration in the compounds, which may influence aesthetic considerations in product design. Overall, PS-20 emerges as an ideal candidate for food service tableware, offering a balance of durability, thermal stability, and environmental benefits. Future work should explore: (1) higher paper filler ratios (>20%) with coupling agents (e.g., silane) to enhance interfacial adhesion and mechanical properties, (2) quantification of biobased content for sustainability claims, (3) industrial-scale processing feasibility, and (4) life cycle analysis (LCA). These steps would bridge lab-scale innovation with commercial viability. Future LCAs will provide a detailed quantification

of cradle-to-gate impacts. However, the current results, including 3.8% material savings, 8% energy reduction, and waste reuse already demonstrate measurable progress over virgin PS.

References

[1] R. Meys, F. Frick, S. Westhues, A. Sternberg, J. Klankermayer, ve A. Bardow, "Towards a circular economy for plastic packaging wastes – the environmental potential of chemical recycling", Resources, Conservation and Recycling, c. 162, s. 105010, Kas. 2020. https://doi.org/10.1016/j.resconrec.2020.105010

[2] B. Chen ve J. Liu, "Properties of lightweight expanded polystyrene concrete reinforced with steel fiber", Cement and Concrete Research, c. 34, sy 7, ss. 1259-1263, Tem. 2004. https://doi.org/10.1016/j.cemconres.2003.12.014

[3] N. H. Ramli Sulong, S. A. S. Mustapa, ve M. K. Abdul Rashid, "Application of expanded polystyrene (EPS) in buildings and constructions: A review", Journal of Applied Polymer Science, c. 136, sy 20, s. 47529, May. 2019. https://doi.org/10.1002/app.47529

[4] B. Gautam, T.-H. Tsai, ve J.-T. Chen, "Towards sustainable solutions: A review of polystyrene upcycling and degradation techniques", Polymer Degradation and Stability, c. 225, s. 110779, Tem. 2024. https://doi.org/10.1016/j.polymdegradstab.2024.110779

[5] M. Mihai, M. A. Huneault, ve B. D. Favis, "Foaming of Polystyrene/ Thermoplastic Starch Blends", Journal of Cellular Plastics, c. 43, sy 3, ss. 215-236, May. 2007. https://doi.org/10.1177/0021955X07076532

[6] S. Doroudiani ve M. T. Kortschot, "Expanded Wood Fiber Polystyrene Composites: Processing–Structure–Mechanical Properties Relationships", Journal of Thermoplastic Composite Materials, c. 17, sy 1, ss. 13-30, Oca. 2004. https://doi.org/10.1177/0892705704035405

[7] K. B. Adhikary, S. Pang, ve M. P. Staiger, "Dimensional stability and mechanical behaviour of wood–plastic composites based on recycled and virgin high-density polyethylene (HDPE)", Composites Part B: Engineering, c. 39, sy 5, ss. 807-815, Tem. 2008. https://doi.org/10.1016/j.compositesb.2007.10.005

[8] M. Poletto, J. Dettenborn, M. Zeni, ve A. J. Zattera, "Characterization of composites based on expanded polystyrene wastes and wood flour", Waste Management, c. 31, sy 4, ss. 779-784, Nis. 2011. https://doi.org/10.1016/j.wasman.2010.10.027

[9] H.-S. Kim, B.-H. Lee, S.-W. Choi, S. Kim, ve H.-J. Kim, "The effect of types of maleic anhydride-grafted polypropylene (MAPP) on the interfacial adhesion properties of bio-flour-filled polypropylene composites", Composites Part A: Applied Science and Manufacturing, c. 38, sy 6, ss. 1473-1482, Haz. 2007. https://doi.org/10.1016/j.compositesa.2007.01.004

[10] Information on https://versalis.eni.com

[11] P. Nygård, B. S. Tanem, T. Karlsen, P. Brachet, ve B. Leinsvang, "Extrusion-based wood fibre–PP composites: Wood powder and pelletized wood fibres – a comparative study", Composites Science and Technology, c. 68, sy 15, ss. 3418-3424, Ara. 2008. https://doi.org/10.1016/j.compscitech.2008.09.029

[12] A. Ashori ve A. Nourbakhsh, "Bio-based composites from waste agricultural residues", Waste Management, c. 30, sy 4, ss. 680-684, Nis. 2010. https://doi.org/10.1016/j.wasman.2009.08.003

Materials Research Proceedings 57 (2025) 441-448 https://doi.org/10.21741/9781644903735-52

Towards the wire-feed friction stir extrusion-based additive manufacturing of aluminum alloys

Kirill KALASHNIKOV[1,a], Davide CAMPANELLA[1,b], Muhammad ADNAN[1,c], Rosa DI LORENZO[1,d], Giuseppe INGARAO[1,e], Gianluca BUFFA[1,f *], Livan FRATINI[1,g]

[1]Department of Engineering, University of Palermo, Viale delle Scienze 90128, Palermo, Italy

[a]kirill.kalashnikov@unipa.it, [b]davide.campanella@unipa.it, [c]muhammad.adnan06@unipa.it, [d]rosa.dilorenzo@unipa.it, [e]giuseppe.ingarao@unipa.it, [f]gianluca.buffa@unipa.it, [g]livan.fratini@unipa.it

Keywords: Additive Manufacturing, Aluminum Alloys, Sustainable Processes

Abstract. In this work, wire-feed friction stir extrusion-based additive manufacturing (FSE-AM) was studied to assess its potential for multi-layer deposition of aluminum alloys. FSE-AM is a novel technology devoted to avoiding fusion-related defect formation for large-scale additive manufacturing. Using AA1070 feedstock, features of the layer formation were observed, as well as the mechanical properties of the material were analyzed. Energy characterization was carried out to assess the energy efficiency of the proposed method.

Introduction

Additive manufacturing (AM) of aluminum alloys is one of the most significant scientific and engineering topics due to the unique properties of these materials, such as corrosion resistance, a high strength-to-weight ratio, and other advantageous characteristics, making them widely used in various industrial applications [1, 2]. At the same time, many additive technologies are based on fusion, leading to several challenges that impede their adoption [3].

Using common fusion-based technologies, such as Laser Powder Bed Fusion (LPBF), issues such as porosity and hot cracking in aluminum alloys have been observed [4]. Porosity can form due to gases trapped during melting-solidification cycles, especially in alloys containing elements such as Mg, which tend to evaporate due to their relatively low boiling temperature [5, 6]. This defect significantly affects the mechanical properties of additively manufactured materials and limits their industrial applications. Hot cracking is another significant defect caused by high thermal gradients and residual stresses during additive manufacturing. It is particularly prevalent in high-strength aluminum alloys, especially dispersion-hardened ones [7, 8].

To address these issues, alternative AM approaches have been developed, some of which are based on frictional interaction and occur in the solid state [9, 10]. The primary advantage of these methods is that they operate below the melting point of the material (approximately 0.6–0.8 of melting temperature) [11]. By avoiding melting, it is possible to eliminate defect formation, such as porosity and cracking, thereby improving the mechanical properties of aluminum alloy components [3]. These techniques are generally based on friction stir welding (FSW), a well-known method for joining various aluminum alloys [11]. A variation of this, friction stir additive manufacturing, was the first attempt to adapt FSW for AM purposes. However, this method requires layer-by-layer welding of plates, resulting in very high material costs [12].

As an alternative, friction surfacing-based deposition [13] and additive friction stir deposition [14] have been developed to utilize consumable tools and significantly reduce metal scrap. The authors of [15] demonstrated that such techniques provide high-quality deposition for aluminum alloys, although the mechanical properties are slightly lower than expected compared to the parent material. An additional issue with these methods is discontinuous deposition due to the use of

Content from this work may be used under the terms of the Creative Commons Attribution 3.0 license. Any further distribution of this work must maintain attribution to the author(s) and the title of the work, journal citation and DOI. Published under license by Materials Research Forum LLC.

Materials Research Proceedings 57 (2025) 441-448 https://doi.org/10.21741/9781644903735-52

consumable rods with a limited length. At the same time, for large-scale additive manufacturing, continuous deposition—as seen in Wire Arc Additive Manufacturing (WAAM) and similar techniques—would be more beneficial [16].

For this reason, new technologies based on friction stir extrusion are being developed to enable continuous solid-state deposition. These approaches offer high material versatility, allowing the processing of a wide range of aluminum alloys in the form of wire [17], rods [18], and powder [19]. More than that, it enables suitability for high-strength alloys, such as aluminum and titanium alloys, which suffer from solidification defects, residual stresses, and distortion in conventional AM. In [20], the authors demonstrated that this approach can be implemented with a robotic setup, broadening the possibilities and applicability of wire-based solid-state deposition techniques for large-scale manufacturing. As a near-net-shape process, friction stir extrusion-based methods can significantly reduce material waste compared to other AM techniques aligning with global sustainability goals [21]. Moreover, by combining these methods with friction stir extrusion recycling, it might be possible to significantly decrease their environmental impact [22]. However, the development of these techniques is still in its preliminary stages, necessitating urgent investigation of challenges like material and feedstock form compatibility, process scalability, and tool wear to enable widespread industrial implementation.

In this way, this study aims to investigate the feasibility of solid-state deposition of AA1070 aluminum alloy using wire-feed friction stir extrusion-based additive manufacturing, to investigate the characteristics of layer formation and the mechanical properties of the produced material, as well as to preliminary assess sustainability and material efficiency of the proposed technology.

Materials and methods

In this work, technically pure aluminum AA1070 wires (ESAB OK Tigrod 1070) with a diameter of 2.4 mm were used as a feedstock for wire-feed friction stir extrusion-based additive manufacturing.

AM process was performed on dedicated friction stir welding machine ESAB Legio 3ST. For this purpose, a special tool system was designed (Fig. 1). The system consists of two parts: rotary tool (1) and stationary shoulder (2). The first part is designed to serve as an extrusion chamber and a shoulder during deposition. At the same time, the second part is plasticizing the feedstock material fed through the channel (3) and transporting it into the deposition area, where it is stirred by pins. The following process parameters were selected by preliminary experimental campaign: rotation speed of 1400 rpm, wire feeding and tool travel speed of 600 mm/min, and pin plunge depth of 0.2 mm. The last parameter responsible for the layer thickness and the force applied by the stationary shoulder: the lower the plunge depth, the higher the gap between substrate and shoulder and, subsequently, the lower the loading force during the deposition process. As a result of the experiment, samples with one layer and two layers of deposition were produced.

During the FSE-AM process, the electrical energy used by the equipment was recorded using a power and energy quality analyzer Chauvin Arnoux C.A 8331 connected to the input of the ESAB Legio.

After the deposition, cross-section and longitudinal section of samples were cut out for metallography and microhardness measurement. Sections were mechanically grinded, polished, and then etched to reveal features of material flow. Microhardness was measured using Remet HBV-30A tester with a loading force of 0.5 kg and indentation time of 15 seconds. Metallographic analysis was performed using Olympus GX51 optical microscope.

Materials Research Proceedings 57 (2025) 441-448 https://doi.org/10.21741/9781644903735-52

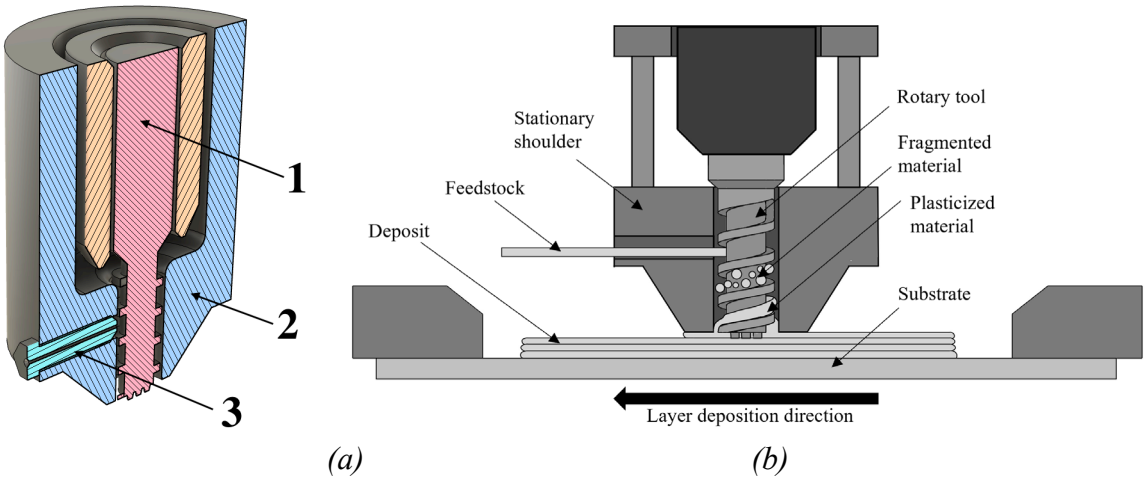


Fig. 1. (a) Cross-section of the FSE-AM tooling system CAD-model and (b) scheme of the FSE-AM process. 1 – rotary tool, 2 – stationary shoulder, 3 – wire-feeding channel

Results and discussion

During the experimental campaign preliminary process parameters selection has been carried out to achieve stable material deposition. As shown in Fig. 2, when process parameters are not correct, the deposition occurs with irregular shape and thickness (Fig. 2 (a, b, c)), while using appropriate mode, layer shape irregularities eliminate (Fig. 2 (d)). Due to a high adhesion of pure aluminum to steel, there is a detachment effect leading to unbonding of the layer in starting and ending positions. Despite that, there are no visible defects in the main body of the deposit shown in Fig. 2 (d), which was selected for detailed analysis.

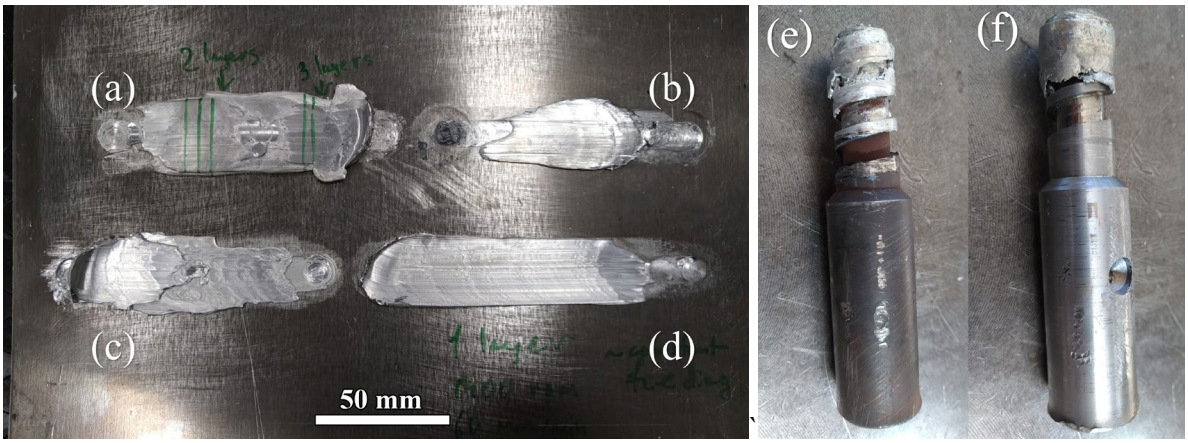


Fig. 2. Samples made by FSE-AM during preliminary parameter selection. (a – c) – defective samples, (d) – sample with acceptable deposition quality produced with rotation speed of 1400 rpm and tool travel speed of 600 mm/min, (e – f) – rotary tools after process

High aluminum adhesion also affects the rotary tool, leading to the formation of a coating on its surface. It is clear from Figure 2 that the material fills the grooves of the tool and, depending on the production mode, it can be partially (Fig. 2 (e)) or fully (Fig. 2 (f)) covered by aluminum. In fact, this coating is the material plasticized but not effectively transferred to the substrate, and to avoid this effect, some dwell time after the deposition can be suggested to empty the extrusion chamber.

Materials Research Proceedings 57 (2025) 441-448 https://doi.org/10.21741/9781644903735-52

In Fig. 3, the cross-section of a single layer discussed above is shown. It is visible from the figure that the deposited volume contains no defects such as pores, voids, and cracks. However, on both the advancing and retreating sides of the sample, there is a lack of bonding. Such defects occurred only in the stationary shoulder effect area. It must be noted that on the advancing side, such an effect is considerably low in comparison to the retreating one. Such behavior can be connected to the heat distribution in the deposition area, as it was shown for the friction surfacing method [23], but it will be studied in future research. The main body of the deposited layer is well bonded with the substrate due to the presence of pins.



Fig. 3. Cross-section of FSE-AM single layer of AA1070 alloy

Further deposition of the second layer leads to an improvement of the previously deposited layer bonding (Fig. 4 (a)), while there are still some edge defects in the interface between the layers. It is also visible that the second layer has a lower width than the first one, but at the current development stage, the difference is acceptable. The longitudinal section, in turn, shows that the defect-free structure can be observed over the whole length of the sample in the layer deposition direction.

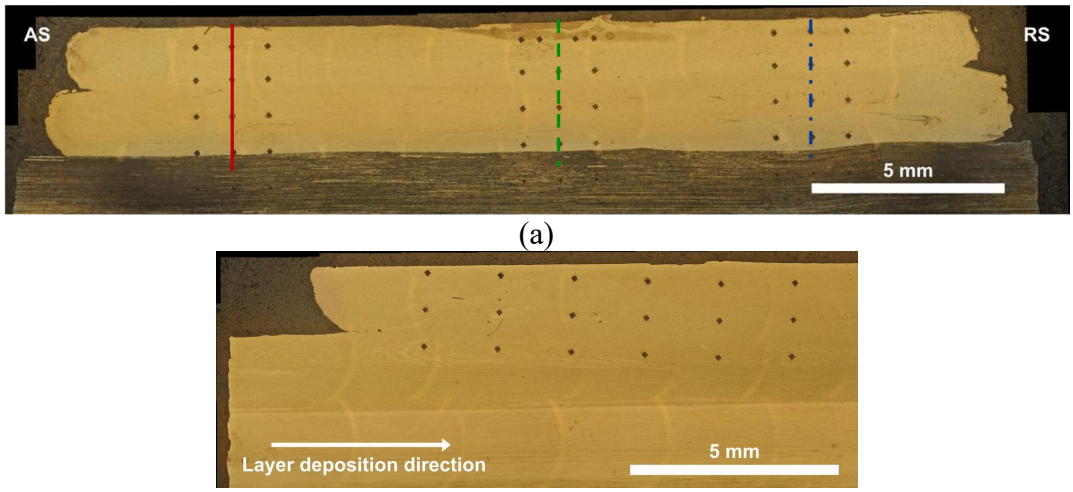
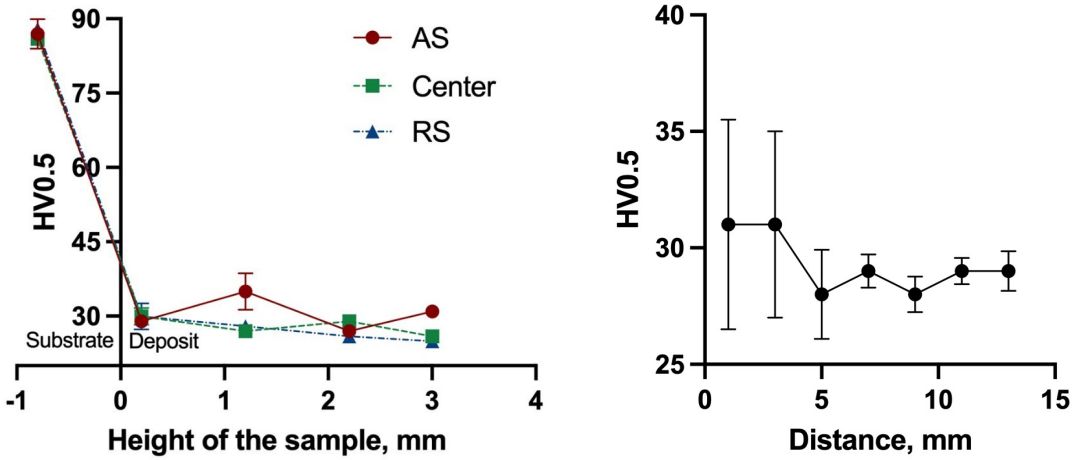


Fig. 4. (a) Cross-section and (b) longitudinal section of multi-layer FSE-AM sample of AA1070 alloy with traces of microhardness measurements. Colored lines are showing corresponding colors of hardness profiles in Fig. 5

Microhardness measurements show that there is no significant anisotropy of mechanical properties along the height of the FSE-AM AA1070 sample, while it occurs when comparing different sections of the sample. In a cross-section, Vickers value averages at about 30 MPa level, although on the edges it slightly decreases (Fig. 5 (a)). In the longitudinal section, the average value is about 29 MPa, leading to an anisotropy level of about 4 %, which is extremely low in comparison to fusion-based methods [24].

Materials Research Proceedings 57 (2025) 441-448 https://doi.org/10.21741/9781644903735-52



(a) (b)

Fig. 5. Microhardness distribution in (a) cross-section and (b) longitudinal section of multi-layer FSE-AM sample of AA1070 alloy

Obtained results show that wire-feed friction stir extrusion-based additive manufacturing is well suitable for operating with aluminum alloys. Proper parameter selection leads to a stable and efficient material deposition with no critical defects which can affect the performance of the sample. However, obtained hardness values show that the material after the deposition faces a reduction in mechanical properties. In work [25], authors show the microhardness of AA1070 alloy on a level of 35 MPa. At the same time, as-built FSE-AM material achieves a maximum of 30 MPa, which is about 15% lower than the parent material. Because of the complex thermo-mechanical action of the tool during the deposition, the material must undergo significant microstructural changes, leading to a hardness decrease effect. Similar material behavior was observed in related solid-state additive processes [15], making this a common problem of friction-based techniques. In this way, it is necessary to deeply analyze the microstructural changes, which will be the aim for future works connected to this method.

To investigate the process from the environmental point of view, electric energy was studied along with the deposition rate. The electric power trend was analyzed, demonstrating three main stages of the FSE-AM process (Fig. 6): tool plunge, during which pins penetrate the substrate; dwell-time accompanied by initiation of wire feeding; and deposition stage with the tool moved along the welding line. It is visible that maximum power is achieved only about halfway through the deposition stage. This fact is because of the filling of the extrusion chamber by plasticized material. The weight of a single layer was measured, and the deposition rate was calculated to be 0.42 g/s. To assess the energy required for the deposition process, Specific Energy Consumption was found out at a level of 5.14 kWh/kg. In this way, the proposed method is able to meet competition with other solid-state additive manufacturing. For example, the Additive Friction Stir Deposition method, which can be used for additive manufacturing with various aluminum alloys, demonstrates from 3.8 to 4.6 kWh/kg depending on the material used at a similar deposition rate [26].

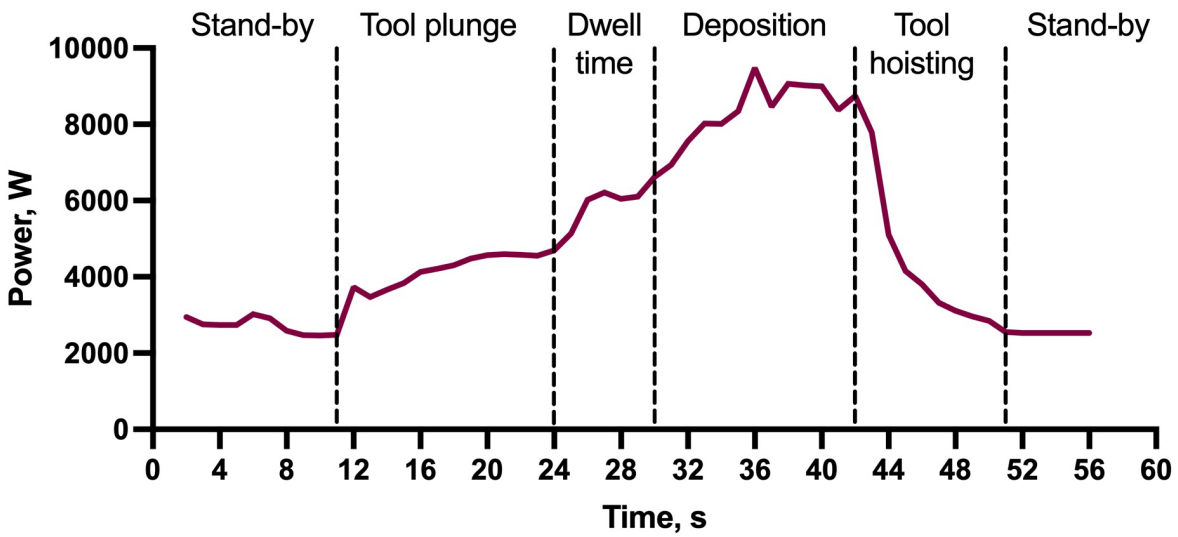


Fig. 6. Electric power trend of FSE-AM single layer deposition

In this way, the FSE-AM technology demonstrates high potential for aluminum additive manufacturing purposes, providing high quality of layer deposition with relatively low energy demand required for the deposition. Flexibility of this technology can also enable metal scrap recycling, significantly increasing its sustainability [22]. This effect can reduce the environmental impact of the method, although full life-cycle assessment analysis must be performed to get detailed data.

Conclusions

As a result of the experimental campaign on the FSE-AM of AA1070 aluminum alloy carried out, the following conclusions have been made.

- If wrong process parameters are used, geometrical irregularities during the deposition occur. After the proper mode selection, it is possible to achieve a stable deposition process.
- FSE-AM samples show well-bonded layers formed with no internal defects like voids or cracks. However, edges of the samples consist of defects known as lack of bonding. Further layer deposition, in turn, improves the quality of previous layer bonding to the substrate.
- Additive AA1070 alloy demonstrates microhardness on a level of 30 MPa, which is 15 % lower than the parent material. At the same time, the anisotropy of mechanical properties is significantly low and does not exceed 4%.
- The method demonstrates a high deposition rate on a level of 0.42 g/s and Specific Energy Consumption of 5.19 kWh/kg, which are of the order of other solid-state techniques.

Funding or Acknowledgement

This study was carried out within the research activities of project “PERPETUAL MOTION” (2022X5RPSM PRIN 2022), financed by the European Community – Next Generation EU.

References

[1] S. Lathabai, Chapter 2 - Additive Manufacturing of Aluminium-Based Alloys and Composites, In: Lumley RNBT-F of AM (ed), Woodhead Publishing Series in Metals and Surface Engineering, Woodhead Publishing, 2018, pp. 47–92.

[2] D. Herzog, V. Seyda, E. Wycisk, C. Emmelmann, Additive manufacturing of metals, Acta Mater. 117 (2016) 371–392. https://doi.org/https://doi.org/10.1016/j.actamat.2016.07.019

[3] P. Kah, R. Rajan, J. Martikainen, R. Suoranta, Investigation of weld defects in friction-stir welding and fusion welding of aluminium alloys, Int. J. Mech. Mater. Eng. 10 (2015) 26. https://doi.org/10.1186/s40712-015-0053-8

[4] M. Kumar, G.J. Gibbons, A. Das, et al, Additive manufacturing of aluminium alloy 2024 by laser powder bed fusion: microstructural evolution, defects and mechanical properties, Rapid Prototyp. J. 27 (2021) 1388–1397. https://doi.org/10.1108/RPJ-10-2020-0241

[5] V.R. Utyaganova, A.V. Filippov, N.N. Shamarin, et al, Controlling the porosity using exponential decay heat input regimes during electron beam wire-feed additive manufacturing of Al-Mg alloy, Int. J. Adv. Manuf. Technol. 108 (2020) 2823–2838. https://doi.org/10.1007/s00170-020-05539-9

[6] L. Deillon, F. Jensch, F. Palm, M. Bambach, A new high strength Al–Mg–Sc alloy for laser powder bed fusion with calcium addition to effectively prevent magnesium evaporation, J. Mater. Process. Technol. 300 (2022) 117416. https://doi.org/https://doi.org/10.1016/j.jmatprotec.2021.117416

[7] T. Klein, A. Arnoldt, R. Lahnsteiner, M. Schnall, Microstructure and mechanical properties of a structurally refined Al–Mg–Si alloy for wire-arc additive manufacturing, Mater. Sci. Eng. A. 830 (2022) 142318. https://doi.org/https://doi.org/10.1016/j.msea.2021.142318

[8] Y. Chen, D. Zhang, P. O'Toole, et al, In situ observation and reduction of hot-cracks in laser additive manufacturing, Commun. Mater. 5 (2024) 84. https://doi.org/10.1038/s43246-024-00522-3

[9] N. Tuncer, A. Bose, Solid-State Metal Additive Manufacturing: A Review, JOM. 72 (2020) 3090–3111. https://doi.org/10.1007/s11837-020-04260-y

[10] R.S. Mishra, H.Z. Yu, Friction Stir Based Solid-State Additive Manufacturing, JOM. 75 (2023) 4182–4184. https://doi.org/10.1007/s11837-023-06138-1

[11] T. Balawender, P. Myśliwiec, Experimental Analysis of FSW Process Forces, Adv. Manuf. Sci. Technol. 44 (2020) 51–56. https://doi.org/10.2478/amst-2019-0006

[12] A. Kumar Srivastava, N. Kumar, A. Rai Dixit, Friction stir additive manufacturing – An innovative tool to enhance mechanical and microstructural properties. Mater. Sci. Eng. B. 263 (2021) 114832. https://doi.org/https://doi.org/10.1016/j.mseb.2020.114832

[13] E. Seidi, S.F. Miller, B.E. Carlson, Friction Surfacing Deposition by Consumable Tools. J Manuf Sci Eng 143 (2021). https://doi.org/10.1115/1.4050924

[14] J. Shao, A. Samaei, T. Xue, et al, Additive friction stir deposition of metallic materials: Process, structure and properties, Mater. Des. 234 (2023) 112356. https://doi.org/https://doi.org/10.1016/j.matdes.2023.112356

[15] M.M.Z. Ahmed, M.M. El-Sayed Seleman, E. Elfishawy, et al, The Effect of Temper Condition and Feeding Speed on the Additive Manufacturing of AA2011 Parts Using Friction Stir Deposition, Materials (Basel). 14 (2021) 6396. https://doi.org/10.3390/ma14216396

[16] G. Campatelli, D. Campanella, A. Barcellona, et al, Microstructural, mechanical and energy demand characterization of alternative WAAM techniques for Al-alloy parts production, CIRP J. Manuf. Sci. Technol. 31 (2020) 492–499. https://doi.org/https://doi.org/10.1016/j.cirpj.2020.08.001

[17] H. Chen, X. Meng, J. Chen, et al, Wire-based friction stir additive manufacturing, Addit. Manuf. 70 (2023) 103557. https://doi.org/https://doi.org/10.1016/j.addma.2023.103557

[18] R.S. Haridas, W. Knight, J. Tiu, et al, SolidStir technology: A novel solid-state integrated manufacturing process for structural fabrication, Manuf. Lett. 40 (2024) 154–158. https://doi.org/https://doi.org/10.1016/j.mfglet.2024.05.001

[19] S. Bhowmik, P. Varshney, O.El. Atwani, et al, Investigating microstructural evolution in SolidStir^{TM} extruded oxide dispersion strengthened 14YWT alloy fuel cladding tube, J. Nucl. Mater. 584 (2023) 154580. https://doi.org/https://doi.org/10.1016/j.jnucmat.2023.154580

[20] Z. Zhang, L. Wan, X. Meng, et al, Robotic wire-based friction stir additive manufacturing. Addit. Manuf. 88 (2024) 104261. https://doi.org/https://doi.org/10.1016/j.addma.2024.104261

[21] A.A. Ahmed, M.A. Nazzal, B.M. Darras, et al, Comparative sustainability assessment of powder bed fusion and solid-state additive manufacturing processes: The case of direct metal laser sintering versus additive friction stir deposition, Sustain. Mater. Technol. 39 (2024) e00858. https://doi.org/https://doi.org/10.1016/j.susmat.2024.e00858

[22] D. Baffari, A.P. Reynolds, A. Masnata, et al, Friction stir extrusion to recycle aluminum alloys scraps: Energy efficiency characterization, J. Manuf. Process. 43 (2019) 63–69. https://doi.org/https://doi.org/10.1016/j.jmapro.2019.03.049

[23] H. Jamshidi Aval, Comprehensive thermo-mechanical simulation of friction surfacing of aluminum alloys using smoothed particle hydrodynamics method, Surf. Coatings Technol. 419 (2021) 127274. https://doi.org/https://doi.org/10.1016/j.surfcoat.2021.127274

[24] T. Vilaro, C. Colin, J.D. Bartout, As-Fabricated and Heat-Treated Microstructures of the Ti-6Al-4V Alloy Processed by Selective Laser Melting, Metall. Mater. Trans. A. 42 (2011) 3190–3199. https://doi.org/10.1007/s11661-011-0731-y

[25] W. Abdel-Aziem, A. Hamada, T. Makino, M.A. Hassan, Microstructure Evolution of AA1070 Aluminum Alloy Processed by Micro/Meso-Scale Equal Channel Angular Pressing, Met. Mater. Int. 27 (2021) 1756–1768. https://doi.org/10.1007/s12540-019-00544-4

[26] J.K. Yoder, G.D. Hahn, N. Zhao, et al, Additive friction stir deposition-enabled upcycling of automotive cast aluminum chips, Addit. Manuf. Lett. 4 (2023) 100108. https://doi.org/https://doi.org/10.1016/j.addlet.2022.100108

Materials Research Proceedings 57 (2025) 449-456 https://doi.org/10.21741/9781644903735-53

Development of low environmental impact technological solutions based on PLA, PBS, PBAT and Talc blends for multilayer food packaging manufacturing

Marzio MILO DI VILLAGRAZIA[1,a *], Alessandra CAGGIANO[1,b *], Annalisa GENOVESI[1,c] and Massimiliano BARLETTA[1,d]

[1]Università degli Studi Roma Tre, Dipartimento di Ingegneria Industriale, Elettronica e Meccanica, Via Vito Volterra 62, 00146 Roma, Italy

[a]marzio.milodivillagrazia@uniroma3.it, [b]alessandra.caggiano@uniroma3.it, [c]annalisa.genovesi@uniroma3.it, [d]massimiliano.barletta@uniroma3.it

Keywords: Plastic and Composite Material Processes, Extrusion, Environmental Impact

Abstract. This research focuses on manufacturing of innovative multilayer food packaging solutions employing PLA, PBS and PBAT to investigate the use of bio-based, biodegradable and compostable polymeric materials to replace fossil-based plastics. To meet the final product technological and functional requirements, three material formulations were investigated. Co-rotating twin-screw extrusion was used to produce the compounds for the single layers. A multilayer sheet extrusion process was then used to create a multilayer film made of an inner core and two equal outer layers with the aim to meet varying property requirements across the film thickness. Finally, thermoforming of the films was carried out to produce prototype food containers that were tested to evaluate their thermo-mechanical properties. The integration of material, process and product design allowed to develop biodegradable and compostable food packaging solutions, notably reducing the environmental footprint of these products.

1. Introduction

Food packaging plays a central role in food manufacturing, as it preserves the quality of food products for storage, transportation and end use [1]. In rigid food packaging, polyolefins are often used as they offer a good compromise among cost, ease of molding and performance [2]. For multilayer packaging, the most employed materials include low-density polyethylene (LDPE), polypropylene (PP), high-density polyethylene (HDPE) and polyethylene terephthalate (PET) [3]. The production of fossil-based plastics represents a global concern as it disrupts the global carbon cycle [4]. The end of life of these products is an issue, as they are often improperly managed. As a matter of fact, open air incineration or disposal in landfills can harm the ecosystem via contamination of air, soil and water [5]. Millions of tons of plastics are annually dumped into landfills, occupying large volumes and contributing to capacity shortage [6].

Various research efforts have been carried out to develop bio-based blends suitable for manufacturing thermoformed products. Compostable blends specifically designed for thermoforming, including those based on PLA, have been extensively explored in the literature [7]. However, bioplastics are much more expensive than traditional petroleum-based polymers.

This study aims to validate the feasibility and processability of new low cost, bio-based and biodegradable polymer compounds to manufacture multilayer sheets to be thermoformed with the aim of producing food trays with performances comparable to those of traditional fossil-based products. Three compound formulations were designed to produce three different materials. Two alternative configurations of a three-layer sheet were designed to explore the best solution providing a structural inner core layer with high impermeability properties and low material cost, and two identical outer surfaces with high flexibility. The three materials were produced by twin

Content from this work may be used under the terms of the Creative Commons Attribution 3.0 license. Any further distribution of this work must maintain attribution to the author(s) and the title of the work, journal citation and DOI. Published under license by Materials Research Forum LLC.

Materials Research Proceedings 57 (2025) 449-456 https://doi.org/10.21741/9781644903735-53

screw extrusion process while the three-layer sheets were fabricated by multilayer cast extrusion. The semifinished products were then thermoformed to manufacture a food tray prototype made of bio-based, bio-degradable and compostable polymeric materials.

2. Materials and methods

The initial material formulations are presented in Table 1. The first (INN) is intended as the core layer of the sheet while OUT_T1p and OUT_T2p are designed to serve as the outer surface layers.

Table 1. Initial formulations.

Sample ID	**INN (Inner layer)**	**OUT_T1p (Outer layer Type 1)**	**OUT_T2p (Outer layer Type 2)**
Components	***wt.%***	***wt.%***	***wt.%***
PLA Luminy L175	48%	20%	0%
PBS A200 MF	12%	80%	80%
PLA Luminy D120	2%	0%	0%
Talc CHX05L	36,9%	0%	0%
EBS EVIWAX	1%	0%	0%
Joncryl ADR 4400	0,1%	0%	0%
PBAT KB100	0%	0%	20%

PLA Luminy L175 and PLA Luminy D120 from Total Corbion PLA (TotalEnergies Corbion, Stadhuisplein, NL) were selected to produce a bio-based and compostable polymeric phase. PBS A200 MF and PBAT KB100 from Kingfa (Guangzhou, CN) were used as compostable polymeric phases. A large amount of talc (from IMI Fabi S.p.A., Milan, Italy) was used as mineral filler to reduce production costs and improve the properties of the inner layer compound, such as rigidity, strength, hardness, flexural modulus, dimensional stability and thermal conductivity; it was also used as nucleating agent [8]. EBS (Ethylene bis stearamide) waxy lubricant was used as process aid. Joncryl ADR 4400 (Basf, Ludwigshafen, Germany) was used as chain extender. Each material was chosen for its compliance with food contact regulations, as stated in the technical data sheets.

During cast extrusion, the outer layer materials in both formulations exhibited processability issues, as the film surfaces were excessively sticky on the calenders, leading to delamination of the multilayer sheet. Thus, OUT_T1p and OUT_T2p were redesigned by adding 10% of talc to both formulations. Actually, a preliminary compound can often highlight, during processing, the need for mineral fillers and rheological additives to enhance its processability [7]. A mineral additive such as talc is affordable and can be used as an anti-blocking agent, reducing moisture absorption and increasing scratch resistance [3]. OUT_T1p and OUT_T2p were then re-extruded with the optimized formulations presented in Table 2 to produce OUT_T1 and OUT_T2 surface materials.

Table 2. Optimized formulations.

Sample ID	**INN (Inner layer)**	**OUT_T1 (Outer layer Type 1)**	**OUT_T2 (Outer layer Type 2)**
Components	***wt.%***	***wt.%***	***wt.%***
PLA Luminy L175	48%	18%	0%
PBS A200 MF	12%	72%	72%
PLA Luminy D120	2%	0%	0%
Talc CHX05L	36,9%	10%	10%
EBS EVIWAX	1%	0%	0%
Joncryl ADR 4400	0,1%	0%	0%
PBAT KB100	0%	0%	18%

2.1 Compounding, cast extrusion and thermoforming.

The processes were carried out in sequential phases with different extruders for each film component. The inner layer (INN) material of the film was produced via twin screw extrusion on a Leistritz ZSE MAXX 27 I extruder (Leistritz AG, Nuremberg, Germany) with 27 mm screws

Materials Research Proceedings 57 (2025) 449-456 https://doi.org/10.21741/9781644903735-53

and length to diameter ratio of 40. Table 3 shows the process parameters and temperature profile.

A hump-back temperature profile with a maximum temperature of 180°C was set to ease the processability of PLA. The set screw speed was relatively low (250 - 270 rpm) to avoid any excessive torque or pressure increase due to the presence of talc which, when compounded with polylactic acid, tends to increase the viscosity of the melt [9]. Increasing screw speeds can enhance material mixing and plasticization; however, they also raise the risk of elevated torque and pressure. Hence, it is crucial to carefully regulate screws speed to optimize material properties while minimizing excessive mechanical stress [10].

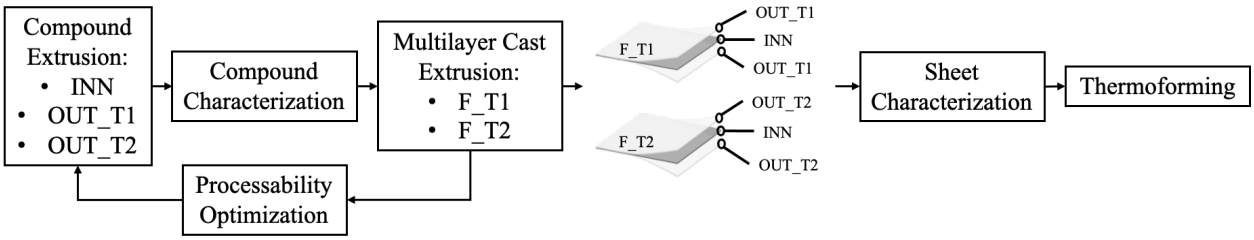


Figure 1: Overall process scheme

Table 3. Temperature profile and processing parameters for INN inner layer material extrusion.

Temperature profile [°C]									
T1	**T2**	**T3**	**T4**	**T5**	**T6**	**T7**	**T8**	**T9**	**Die**
170	172	175	177	180	180	180	175	175	173

Processing parameters							
Screws speed [rpm]	**Feeder speed [rpm]**	**Granules flow [%]**	**Powders flow [kg/h]**	**Melting temperature [°C]**	**Pressure [bar]**	**Torque [%]**	**Cutting speed [%]**
250	256	15	8,77	182	62	30	80

The mineral filler was fed into the extrusion cylinder in its 4th zone, just before reaching the maximum temperature value, to facilitate the mixing of the powder with the polymer matrix. Also, a low screw speed allows a longer stay of the melt in the extruder cylinder, giving the talc more time to mix with the other components.

The extrusion of the outer layer materials required two consecutive stages because of the above mentioned issue. They were produced with the same technology as the inner layer but using, for the first stage, a Thermo Scientific HAAKE PolyLab 24/40-MC OS machine (Thermo Fisher Scientific, Karlsruhe, Germany). The latter was selected for the outer layer materials without mineral powders because, with 24 mm-screws and a length to diameter ratio of 40, it is smaller and easier to manage when no additional powders or liquid additives are needed. Table 4 presents the process parameters and temperature profile for the outer layer material Type 1 (OUT_T1p).

Table 4. Temperature profile and processing parameters for OUT_T1p.

Temperature profile [°C]									
T1	**T2**	**T3**	**T4**	**T5**	**T6**	**T7**	**T8**	**T9**	**Die**
150	152	153	155	160	160	160	160	155	153

Processing parameters				
Screws speed [rpm]	**Granules flow [%]**	**Pressure [bar]**	**Torque [%]**	**Cutting speed [%]**
270	35	14,1	81	3,5

Also in this case, a hump-back temperature profile was chosen. The formulated blend was prepared by mixing the raw materials in a CABO Mix Space 490 planetary mixer for 10 min and the mixture was fed via volumetric feeder in the first feed zone of the extruder. For the extrusion

Materials Research Proceedings 57 (2025) 449-456 https://doi.org/10.21741/9781644903735-53

of the outer layer material Type 2 (OUT_T2p), the blend preparation process was the same, and the process parameters and temperature profile presented in Table 5 were adopted.

The process parameters for the extrusion of OUT_T1p and OUT_T2p were almost the same except for the granules flow: it was observed that, even with a lower granules feed rate, the presence of PLA instead of PBAT caused an increase of pressure and torque.

Table 5. Temperature profile and processing parameters for OUT_T2p.

Temperature profile [°C]									
T1	**T2**	**T3**	**T4**	**T5**	**T6**	**T7**	**T8**	**T9**	**Die**
150	152	153	155	160	160	160	160	155	153
Processing parameters									
Screws speed [rpm]		**Granules flow [%]**		**Pressure [bar]**		**Torque [%]**		**Cutting speed [%]**	
270		50		9,4		78		3,5	

In a first attempt, the three extruded compounds were cast extruded to produce the two multilayer sheet configurations. The films were produced using a MiniCast Coex 5 machine (Eurotech Extrusion Machinery - Eurexma, Tradate (VA), Italy), which allows to produce multilayer sheets up to five layers.

The study involves the production of two multilayer sheets with different configurations. Type 1 film F_T1 consists of an inner layer of INN material and two identical outer layers of OUT_T1p on both external sides. Type 2 sheet F_T2 has the same inner layer and two outer surfaces of OUT_T2p. The cast extrusion process parameters are the same for both F_T1 and F_T2 (Table 6).

Table 6. Temperature profile and processing parameters for cast extrusion of F_T1 and F_T2.

			Temperature profile [°C]						
	Rotational speed [m/min]	**Screw speed [rpm]**	**Zone 1**	**Zone 2**	**Zone 3**	**Central back zone**	**Central front zone**	**Left lateral zone**	**Right lateral zone**
Drive	1,1								
Calender 1	0,6								
Calender 2	0,8								
Extruder A (outer layer)		71	140	145	145				
Extruder C (inner layer)		73	200	200	200				
Extruder B (outer layer)		71	140	145	145				
Die						150	165	155	155

The screw rotational speed for the inner layer was slightly higher than the screw speed chosen for the extrusion of the outer sides of the sheet in order to reduce the thickness of the surfaces compared to the core layer. The temperature profile for the outer layers was set to slightly lower values compared to the relative twin screw extrusion profile to reach a lower flow of the melt with an already processed material. For the inner layer, it is important to at least reach the activation temperature between 190°C and 200°C for the chain extender Joncryl ADR 4400 and then reduce the temperature to decrease the melt flow through the die. The die temperature profile was chosen considering the different heat transfer of the external surfaces of the die.

For each sheet configuration, the cast extrusion process showed that the outer layers were too sticky on the calenders and the process could not be completed. The design of the surface layers was consequently modified to optimize the processability in cast extrusion. 10% of talc was added to the original design as a solid lubricant to mitigate the adhesion phenomenon on the calenders. The final design configuration is shown in Table 2. The issue was successfully solved, and the cast

Materials Research Proceedings 57 (2025) 449-456 https://doi.org/10.21741/9781644903735-53

extrusion process was completed for both configurations, producing the two multilayer sheets, F_T1 and F_T2, with the MiniCast Coex 5 and the processing parameters of Table 6.

In Figure 2 it is possible to see the cast extrusion process , in calender mode, with a focus on the die and the extruded sheet during the fabrication of the semifinished products.



Figure 2: Cast extrusion process on EUR.EX.MA MiniCast Coex 5.

The thermoforming process was performed using a Formech 450DT (Formech International Limited, Thrales End, UK), a pilot device equipped with a single cavity mold with vacuum. The final products thermoformed from F_T1 and F_T2 semifinished products are shown in Figure 3. Injection molded samples used for material characterization were produced using a manual test sample injection molding apparatus Ray-Ran (Kelsey, UK).



Figure 3: Food trays thermoformed from F_T1 sheet (left) and F_T2 sheet (right)

2.2 Characterization.

The mechanical characterization of the film was made according to ISO 527 on both dogbone injection molded samples and cast extruded sheets in Machine Direction (MD) and Transverse Direction (TD) using a Shimadzu AGS-X tensile tester (Shimadzu Corporation, Kyoto, Japan).

The cast extruded films were tested imposing a strain rate of 10 mm/min for F_T1 and F_T2 sheets for both machine direction (MD) and transversal direction (TD) specimens. The impact resistance of the film was evaluated using a IZOD XJUD series pendulum (AMSE S.r.l., Turin, Italy). The selected load was 2.75 J for the INN specimens. An increasing load, from 2.75 J to 11 J, was chosen for both the outer layers. In fact, OUT_T1 and OUT_T2 resisted to the increasing impact load till the highest one. A DSC (Differential Scanning Calorimetry Analysis) was performed on the produced pellets using a DSC3 (Mettler Toledo, Columbus, Ohio). The samples were put in aluminum crucibles and a flow of 50 ml/min of Nitrogen was used as purge gas,

Materials Research Proceedings 57 (2025) 449-456 https://doi.org/10.21741/9781644903735-53

according to ISO 11357. Three thermal ramps were applied to the samples: a first heating ramp at 10°C/min from -70°C to 250°C, a cooling ramp at -10°C/min from 250°C to -70°C and a second heating ramp at 10°C/min from -70°C to 250°C.

The Heat Deflection Temperature (HDT) was measured according to ASTM-D648 using a HDT/V-1113 tester (AMSE s.r.l., Turin, Italy). The samples were submerged in silicone oil at constant temperature for 5 min before starting the test. The oil heating rate was set at 120°C/h.

3. Results and discussion

3.1 Processability.

The processing parameters adopted for twin screw extrusion of the initial formulations are presented in Table 3, Table 4 and Table 5. The produced materials were then cast extruded to fabricate the two multilayer sheets, using processing parameters specified in Table 6. The first one, F_T1, has a total thickness of 566 ± 17 μm, the second one, F_T2, has a total thickness of 703 ± 42 μm. Both the semifinished products were suitable to thermoform a solid bio-based food tray.

3.2 Mechanical properties.

A tensile test was conducted on specimens of F_T1 and F_T2 sheets in both machine and transversal directions. The analysis was conducted with 10 mm/min strain rate using pneumatic brackets. The results are reported in *Table 7*.

Table 7: Tensile test results

Sample ID	Max Stress [N/mm^2]	Max Strain [%]	Young Module [N/mm^2]	Yield Stress [N/mm^2]
F_T1 MD	46,2 ± 2,7	13,3 ± 2,8	837,5 ± 235,4	42,2 ± 3,5
F_T2 MD	45,9 ± 2,5	35,4 ± 1,7	726,2 ± 116,9	15,2 ± 2,1
F_T1 TD	34,3 ± 1,5	4,3 ± 0,2	977,8 ± 120,5	15,7 ± 4,5
F_T2 TD	37,2 ± 1,7	20,9 ± 12,2	953,8 ± 374,7	27,1 ± 7,5

The strain values recorded for F_T1 sheet are lower than the F_T2 values for both machine and transversal direction. This is due to the use of PBAT instead of PLA in blend with PBS for the outer layers of the F_T2 sheet. In fact, PBAT can increase the material elongation and toughness when blended with other biopolymers [11, 12]. The maximum stress values are mostly alike.

The IZOD impact test was led on the specimens of each material to examine their behavior when subjected to an impact stress. The test results are indicated in Table 8.

Table 8. IZOD Test results.

Material	Load [J]	Impact energy [J]	Strength [kJ/m2]
INN	2,75	0,444 ± 0,079	11,10 ± 1,98
OUT_T1	11	Resist	Resist
OUT_T2	11	Resist	Resist

The considerable amount of mineral filler used in the core layer made it significantly brittle. Otherwise, it is necessary to reduce moisture, water vapor and oxygen transmission rate of the layer improving barrier performances [13].

3.4 Thermal properties.

A heat deflection temperature analysis was done for each material and the relative test results are shown in Table 9.

Table 9. HDT Test results.

Material	Deflection [mm]	Temperature [°C]
INN	0,34	91,5 ± 0,8
OUT_T1	0,34	64,6 ± 11,8
OUT_T2	0,34	83,2 ± 2,1

Materials Research Proceedings 57 (2025) 449-456 https://doi.org/10.21741/9781644903735-53

A differential scanning calorimetry was conducted on a pellet of each material in order to analyze its thermal properties. The relevant temperatures of the three materiales are presented in Table 10. From the inner layer DSC analysis, it was possible to notice a glass transition at -32,8°C for PBS and, at 61,8°C for PLA phase. An endothermic peak at 115,5°C could be associated to the melting point of PBS and another endothermic peak at 177,3°C is ascribable to PLA. There are two other endothermic peaks of the second heating curve for the INN material. One of them was detected at 148,2°C while the second one at 216,0°C. These two peaks can be attributed to the presence of more stable crystalline regions of PBS and PLA that melt at higher temperatures. These structures could be generated by the presence of talc, acting as nucleating agent, during the twin screw extrusion process. For the PBS – PBAT blend it is difficult to distinguish the respective peaks because of their strong similarity in thermal characteristics.

Table 10: DSC analysis for INN, OUT_T1 and OUT_T2

Material	Component	wt%	T_g [°C]	T_m [°C]
INN	**PLA**	48%	61,8	177,3
	PBS	12%	-32,8	115,5
OUT_T1	**PLA**	20%	61,7	174,0
	PBS	80%	-33,8	116,5
OUT_T2	**PBS**	80%	-31,5	114,8
	PBAT	20%	-31,5	114,8

A last empirical stress test was conducted on food trays prototypes fabricated with F_T1 and F_T2 semifinished products. For both of them, no relevant damage was observed when subjected to a typical use. In a 25°C environment, they were full filled with water at 100°C for 1h, making the fluid and the trays free to exchange heat with surrounding environment. For both the trays was noted just a slight hazing on the internal surface, in the fluid first contact zone.

4. Conclusions

This paper investigated the manufacturing of innovative multilayer food packaging using bio-based, biodegradable and compostable polymeric materials such as PLA, PBS and PBAT as alternatives to conventional fossil-based plastics. Two configurations of a three-layer sheet were designed to study the best solution providing a structural inner core layer with high impermeability and low cost, and two identical outer surfaces with high flexibility. The mechanical, thermal and rheological analyses confirmed that the designed materials exhibit properties comparable to those of traditional polymers and can be processed using established industrial technologies. The three materials were produced by twin screw extrusion process while the three-layer sheets were fabricated by multilayer cast extrusion. Proper tuning and optimization of the manufacturing processes and material formulations were required to deal with processability issues of the new materials. The cast extrusion process revealed the need to optimize the initial material formulations to improve their processability and prevent delamination of the multilayer sheets. The redesigned formulations, with the addition of 10% of talc as an anti-blocking agent, made the outer surfaces more brittle but less vulnerable to scratches and prone to moisture and water vapor transmission. The semifinished products were then thermoformed to manufacture a food tray prototype. A final thermal empirical test demonstrated that the prototypes of the final products were not prone to hot water damage. The developed solutions, based on PLA, PBS, PBAT and talc blends, enable a significant reduction in the overall environmental footprint of the products at the end of their life cycle as all the materials used for the main polymeric phases of the compounds are biodegradable and compatible with composting processes, allowing for disposal alongside organic waste. With advancements in waste management infrastructure, this product has the potential to reduce the

burden on landfills and contribute to the mitigation of environmental plastic pollution. Future developments of this research will focus on conducting a comprehensive life cycle assessment (LCA) of the final product to validate its overall environmental impact in more detail. In addition, further studies may investigate the feasibility and cost-effectiveness of industrial-scale production.

References

[1] Han, J.H.: Chapter 1 - A Review of Food Packaging Technologies and Innovations. In: Han, J.H. (ed.) Innovations in Food Packaging (Second Edition). pp. 3–12. Academic Press, San Diego (2014). https://doi.org/10.1016/B978-0-12-394601-0.00001-1.
[2] Jabarin, S.A., Kollen, W.J.: Polyolefin properties for rigid food packaging. Polymer Engineering & Science. 28, 1156–1161 (1988). https://doi.org/10.1002/pen.760281804.
[3] Dziadowiec, D., Matykiewicz, D., Szostak, M., Andrzejewski, J.: Overview of the Cast Polyolefin Film Extrusion Technology for Multi-Layer Packaging Applications. Materials. 16, 1071 (2023). https://doi.org/10.3390/ma16031071.
[4] Yao, L., Zhao, S., Tremblay, L.A., Wang, W., LeBlanc, G.A., AN, L.: Implications of plastic pollution on global carbon cycle. Carbon Res. 4, 21 (2025). https://doi.org/10.1007/s44246-024-00188-z.
[5] Abimbola, A.N., Adejumobi, V.O., Aribisala, O.C., Oyeniyi, E.O.: Influence of Plastic Waste Management on the Environment: A review. Environmental Technology and Science Journal. 14, 56–64 (2023). https://doi.org/10.4314/etsj.v14i2.8.
[6] Swift, G.: Degradable Polymers and Plastics in Landfill Sites. In: Encyclopedia of Polymer Science and Technology. pp. 1–13. John Wiley & Sons, Ltd (2015). https://doi.org/10.1002/0471440264.pst457.pub2.
[7] Genovesi, A., Koca, N., Barletta, M., Aversa, C.: Extrusion and thermoforming of poly(butylene succinate–co-butylene adipate)/poly(3–hydroxybutyrate–co–3–hydroxyhexanoate) bio-based blends for the fabrication of disposable packaging. J of Applied Polymer Sci. 141, e55464 (2024). https://doi.org/10.1002/app.55464.
[8] Świetlicki, M., Chocyk, D., Klepka, T., Prószyński, A., Kwaśniewska, A., Borc, J., Gładyszewski, G.: The Structure and Mechanical Properties of the Surface Layer of Polypropylene Polymers with Talc Additions. Materials. 13, 698 (2020). https://doi.org/10.3390/ma13030698.
[9] De Santis, F., Pantani, R.: Melt compounding of poly (Lactic Acid) and talc: assessment of material behavior during processing and resulting crystallization. J Polym Res. 22, 242 (2015). https://doi.org/10.1007/s10965-015-0885-1.
[10] Ikuse, Marina & Richter, Jana & Ganjyal, Girish. (2024). Talc and calcium carbonate inclusions in direct expanded pea starch extrudates exhibit different behavior under increasing screw speeds. Journal of Food Science. 89. 10.1111/1750-3841.16951.
[11] Qiu, T.Y., Song, M., Zhao, L.G.: Testing, characterization and modelling of mechanical behaviour of poly (lactic-acid) and poly (butylene succinate) blends. Mech Adv Mater Mod Process. 2, 7 (2016). https://doi.org/10.1186/s40759-016-0014-9.
[12] De Matos Costa, A.R., Crocitti, A., Hecker De Carvalho, L., Carroccio, S.C., Cerruti, P., Santagata, G.: Properties of Biodegradable Films Based on Poly(butylene Succinate) (PBS) and Poly(butylene Adipate-co-Terephthalate) (PBAT) Blends. Polymers. 12, 2317 (2020). https://doi.org/10.3390/polym12102317.
[13] Helanto, K., Talja, R., Rojas, O.J.: Talc reinforcement of polylactide and biodegradable polyester blends via injection-molding and pilot-scale film extrusion. Journal of Applied Polymer Science. 138, 51225 (2021). https://doi.org/10.1002/app.51225.

Materials Research Proceedings 57 (2025) 457-465 https://doi.org/10.21741/9781644903735-54

Reciprocal human–machine learning flow modelling for assisted assembly systems

Yuchen FAN[1,a *], Alessandro SIMEONE[1,b *] and Dario ANTONELLI[1,c *]

[1]Department of Management and Production Engineering, Politecnico di Torino, Turin, Italy

[a]yuchen.fan@polito.it, [b]alessandro.simeone@polito.it, [c]dario.antonalli@polito.it

Keywords: Human-Robot Collaboration, Real-Time Object Detection, Multi-Modal Instruction Interfaces, Assisted Assembly Systems, Generative AI

Abstract. Industry 5.0 emphasizes human-centric manufacturing by integrating advanced assistive technologies for inclusive production environments. Large Language Models (LLMs) offer new possibilities for assembly error detection and correction. This study introduces a reciprocal human–machine learning framework utilizing LLMs vision capabilities to improve assembly accuracy through real-time image comparison and corrective instruction generation. Human and machine-in-the-loop mechanisms enable continuous refinement, minimizing labeled datasets while enhancing responsiveness. Experimental validation demonstrates the system's ability to detect errors, diagnose causes, and provide corrective actions. Findings show LLM-driven reciprocal learning improves efficiency, supports diverse operator needs, and enables adaptive error detection in manufacturing.

Introduction

The manufacturing sector is undergoing a significant transformation under the Industry 5.0 paradigm, which seeks to integrate advanced technologies with human expertise to create inclusive, adaptive, and efficient production environments [1]. Central to this transformation is the development of human–machine collaboration systems supporting improved productivity while addressing the diverse needs of modern operators [2]. Advancements in generative artificial intelligence have led to novel assisted assembly systems capable of real-time object detection, natural language processing, and multimodal instructional content [3]. This research introduces a reciprocal human–machine learning framework that integrates these AI capabilities with operator feedback to enhance error detection in dynamic assembly environments while ensuring regulatory and ethical compliance [4]. Traditional assembly monitoring relies on pre-trained models with extensive task-specific datasets, limiting adaptability and responsiveness in dynamic manufacturing environments [5]. This research proposes an LLM-based system integrating vision processing and operator feedback for error detection. Rather than advancing real-time vision algorithms, the approach leverages built-in vision capabilities of LLMs to preserve adaptability across diverse manufacturing contexts.

Unlike CNNs requiring extensive training, this system uses prompt-based inference for adaptive assessment without large labeled datasets [6]. Deviations from reference images are detected dynamically, enabling immediate corrective guidance. The proposed system operates within an assisted assembly framework that provides real-time, multimodal feedback through auditory, visual, and robotic interventions.

Literature review

Generative AI and LLMs have revolutionized object recognition and industrial assembly through multimodal learning, visual reasoning, and automated decision-making [7]. Recent advances in multimodal LLMs have enabled the seamless integration of language processing with visual and other sensory modalities. Their impact spans across object detection, recognition, and human-robot

Content from this work may be used under the terms of the Creative Commons Attribution 3.0 license. Any further distribution of this work must maintain attribution to the author(s) and the title of the work, journal citation and DOI. Published under license by Materials Research Forum LLC.

collaboration, enabling new levels of adaptability and efficiency in manufacturing and robotics [8].

Multimodal LLMs enhance object recognition by integrating vision with language processing. Frameworks like ContextDET [9] and open-vocabulary detection systems [10] improve recognition beyond fixed training sets. LLMs in object detection enhance interpretability through richer feature representations, benefiting medical imaging, industrial inspection, and transportation [11]. New attention mechanisms optimize detection in low-data settings by balancing localization and classification [12].

In industrial applications, LLMs enhance human-robot collaboration through digital twin communication [13], natural language command execution [14], and contingency handling with hierarchical task networks [15]. Challenges include computational efficiency, robustness, and hallucination in vision-language models [16], along with addressing bias for better generalization across diverse scenarios [17]. Future developments will focus on optimizing model architectures, improving domain adaptation, and incorporating retrieval-augmented generation to enhance LLM performance in real-world applications.

A critical gap in current research lies in the application of generative AI for assembly error detection. While LLMs have demonstrated potential in recognizing objects and guiding robotic tasks, their role in detecting and responding to assembly errors remains underdeveloped. Recent studies highlight the challenges in designing error detection mechanisms that integrate seamlessly with multimodal AI frameworks. For example, research on linguistic error detection methods for LLMs suggests that multimodal models can be adapted for error identification by deploying contextual reasoning and external validation techniques [9]. Similarly, work on robotic assembly error correction shows that integrating structured visual reasoning with LLMs improves performance in identifying and rectifying misalignments in mechanical assembly tasks [18]. However, these approaches remain limited in scalability and adaptability across different industrial environments. While previous studies have explored LLMs for object recognition and robotic tasks, their integration into real-time assembly error detection with human/machine-in-the-loop mechanisms remains limited. This research addresses these gaps through a reciprocal learning framework combining LLM reasoning with vision-based analysis for dynamic, context-aware adaptation.

Framework

The framework, shown in Fig. 1, enables error detection in collaborative assembly by comparing real-time images against references using LLMs, generating error descriptions and corrective instructions while continuously improving through operator feedback [19]. The system monitors assembly tasks and processes three types of inputs: structured assembly instructions (detailing operations sequence, tools, and quality criteria), reference images (visual ground truth), and real-time images of the assembly progress. Reference images, showing the correct execution of the various assembly steps, including the selection of tools and components, must be acquired prior to assembly task as ground truth. Real-time images are captured continuously with industrial cameras maintaining consistent viewpoints and lighting to enable accurate comparisons. Prompt Management interfaces the assembly tasks with generative AI through three functions: Prompt Storage (repository of refined prompts), Input Conversion (reformatting instructions into standardized layouts), Context Specification (defining operational parameters). Such functions are incorporated into a predefined template to standardize task specifications and error detection requirements. All input data sources, activated by the prompt, are provided to the LLM Error Detection Module. This module performs three primary functions: error detection, error diagnosis with comprehensive error description, and prognosis, which consists of corrective instruction generation. The error detection function systematically compares real-time images with reference images to identify deviations during the assembly process. This approach minimizes the need for

Materials Research Proceedings 57 (2025) 457-465 https://doi.org/10.21741/9781644903735-54

extensive labeling and training because it utilizes predefined reference images along with contextual operator feedback for comparison. The method relies on structural similarities between real-time and reference data, allowing the system to detect discrepancies without relying on large annotated datasets or complex supervised learning methods. When employing LLMs, two inherent challenges must be addressed: hallucination [16]. and catastrophic forgetting [20].

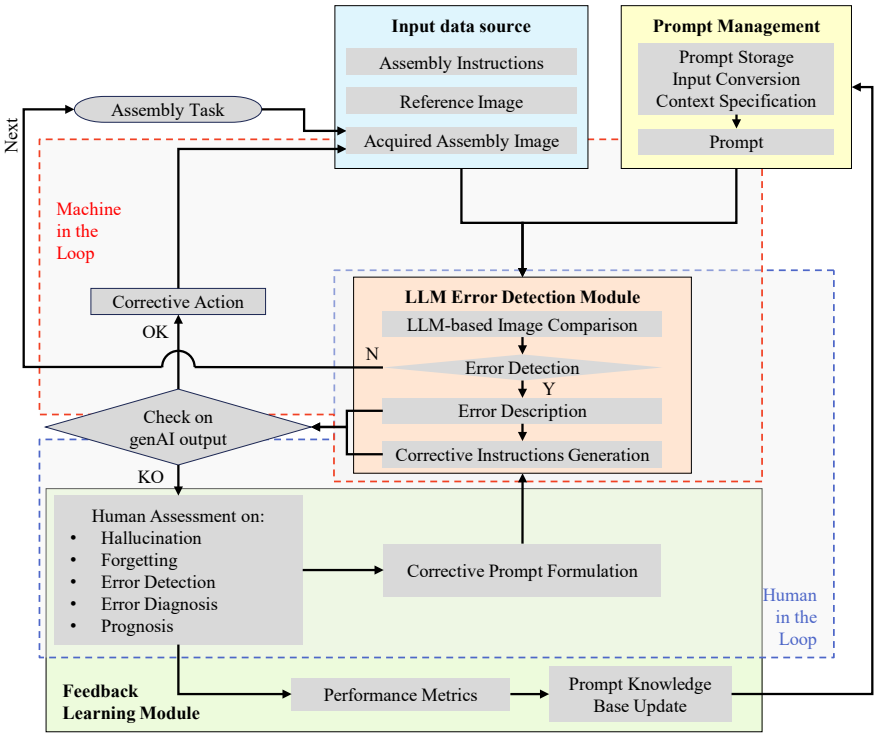


Fig. 1. *Framework flowchart diagram.*

The system mitigates hallucinations through consistency checks using confidence thresholds and feature comparisons to ensure alignment with visual evidence [16]. To address catastrophic forgetting, detection is confined to a single session, maintaining relevant memory without continuous retraining [20]. If no error is detected, the operator is notified, allowing the assembly task to proceed to the next stage. In case an error is detected, the module conducts error diagnosis and provides a detailed error description. In this phase, the system characterizes the nature, severity, and underlying causes of the detected assembly errors by merging automated feature analysis with contextual operator input [21]. Finally, the module performs prognosis, which consists of automatically generating corrective instructions aimed at reversing the error based on the diagnostic output. These instructions are then delivered to the operator, while subsequent responses are captured to continuously refine system performance and improve prognostic accuracy. The Feedback Learning Module enhances performance through human evaluation [22], deriving metrics to analyze discrepancies between detections and outcomes. Human evaluators formulate corrective prompts when needed [23], with refinements integrated into the Knowledge Base for cumulative learning without extensive retraining. The approach integrates two complementary loops (see Fig. 1): Human-in-the-Loop, where operators evaluate and refine LLM outputs through feedback on detection accuracy and corrective instructions; and Machine-in-the-Loop, where the system autonomously detects errors by comparing real-time images with references, generates corrective instructions, and iteratively improves based on learned adjustments.

Materials Research Proceedings 57 (2025) 457-465 https://doi.org/10.21741/9781644903735-54

Experimental Validation

This section reports laboratory validation using a cast iron centrifugal pump assembly. Fig. 2 shows the test bench with an industrial workspace, 1080p cameras (overhead and lateral), and diffused LED lighting for uniform illumination. Validation included 14 assembly tasks across 6 critical steps identified by industrial partners (examples in Table 1). Each task involved processing instruction spreadsheets and comparing reference images (Fig. 3a) with real-time operation images (Fig. 3b). In addition, the prompt presented in Fig. 4 conveys the request to the LLM, specifying the input data, task requirements, and error detection criteria. The tests evaluate the system's diagnostic and prognostic capabilities for error detection, description, and instruction generation. Error detection assesses the system ability to accurately identify the presence of assembly errors. Error description evaluates the clarity and relevance of the system-generated descriptions of detected errors. Corrective instruction generation measures the effectiveness of the system in producing actionable and contextually appropriate corrective instructions.

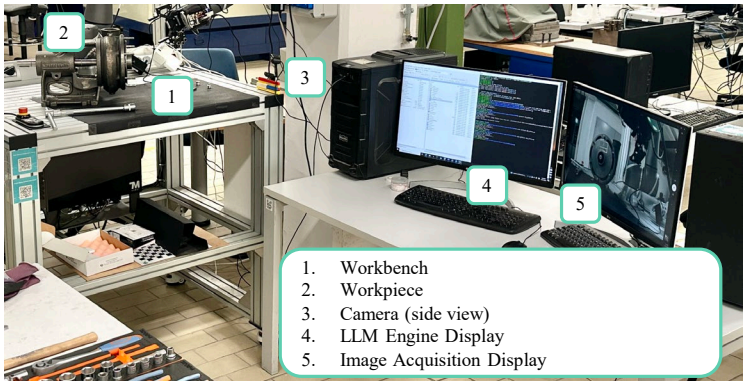


Fig. 2. *Laboratory-scale experimental setup.*

Table 1. *Assembly tasks used in the experimental tests; CS: Component Selection, AO: Assembly Operation.*

Task ID	Task Type	Work instructions
S15.1	CS	Select 1 diffuser (ID: C3) from the component table.
S15.2	AO	Position the diffuser (ID: C3) on the shaft (ID: C5) by aligning the 6 long stud bolts (ID: C22) on the pump housing (ID: C2) to the 6 holes on the diffuser.
S16.1	CS	Select 1 spacer (ID: C14) from the component table.

Materials Research Proceedings 57 (2025) 457-465 https://doi.org/10.21741/9781644903735-54



(a) (b)

***Fig.3**. (a) Reference image showing properly installed locking nut; (b) Real-time operation image showing the absence of locking nut.*

```
The type of this task is "{task_column ['task type']}". The first image shows the correct assembly reference,
and the second image shows the real-time operation result. Based on the two images and the instruction
"{task_column ['work instructions']}", please analyse whether the operator correctly completed this step.
Then, output a Detection Log, which includes: # "Error" or "Correct" # Specific error detection details #
Clear and concise correction instructions, if an error is present.
```

***Fig. 4.** Prompt #1*

The proposed framework was evaluated on two state-of-the-art LLM models: ChatGPT (GPT-4) and Claude (Claude 3). Both models were presented with the identical prompt shown in Fig. 4 and identical inputs containing (i) the assembly task instructions, in MS Excel spreadsheet format, (ii) the reference images of correctly completed assemblies and (iii) the test images of the current assembly state.

This study employed several metrics to assess the performance of the framework. Error detection was evaluated using standard classification metrics: True Positives (correctly identified error-free assemblies), True Negatives (correctly detected errors), False Positives (erroneously flagged errors), and False Negatives (missed errors).

The quality of error descriptions and corrective instructions was quantitatively evaluated using an assessment protocol based on a five-point Likert scale (ranging from 1 to 5) [24] adopting two principal metrics: Error Description Quality (EDQ) [25] and Instruction Quality (IQ) [26]. For EDQ, a score of 1 indicates that the error description is incorrect or misleading, while a score of 5 signifies a comprehensive and precise account of all relevant aspects. Similarly, IQ is rated from 1 for instructions that are vague, incomplete, or potentially harmful, to 5 for clear, actionable, and well-sequenced corrective guidance. Three independent evaluators assessed the LLM outputs using predefined criteria after a calibration session to align their interpretations. The performance is considered sufficient when the average scores for both EDQ and IQ exceed the score of 4.0.

Results and Discussion

Baseline testing without induced errors yielded 100% true positive classifications. With introduced deviations, ChatGPT showed high initial accuracy (92.9%) but limited improvement, while Claude improved from 57.1% to 71.4% after the third prompt iteration. Both maintained >90% accuracy for component/tool selection with greater variability in assembly operations (Figs. 5-6). In assembly operations, ChatGPT showed strong initial performance but minimal improvement, while Claude demonstrated better adaptability with iterative feedback.

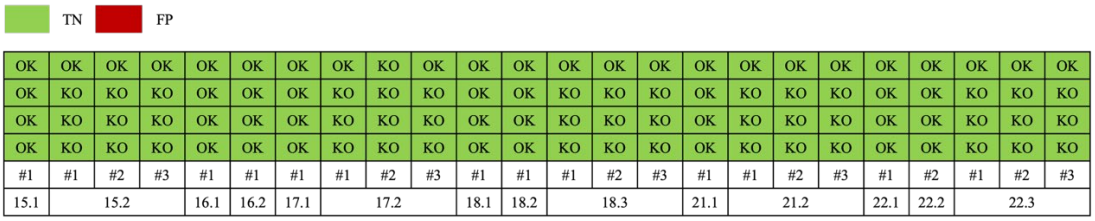


Fig. 5. *ChatGPT performance with purposedly-induced errors.*

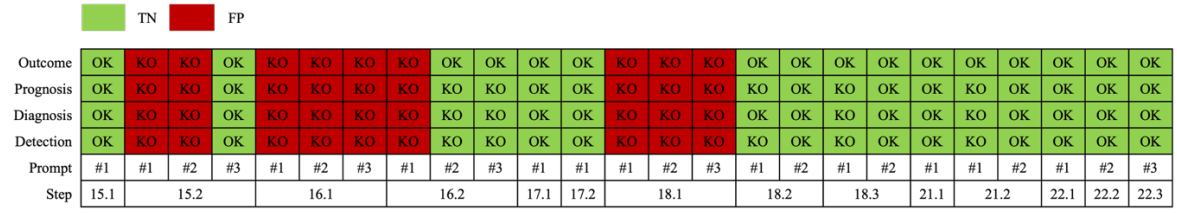


Fig. 6. *ChatGPT performance with purposedly-induced errors.*

These differing learning patterns highlight trade-offs in system design. ChatGPT offers higher initial accuracy but less adaptability, while Claude exhibits greater potential for improvement through operator feedback. The positive outcomes are enhanced adaptability of the machine assisting the operator on new tasks and improved accuracy of both human and machine in the execution of their tasks. This human-machine correction loop represents the practical implementation of the reciprocal learning framework. The system learns from operator expertise while simultaneously providing increasingly refined guidance, creating a continuous improvement cycle that enhances system adaptability over time. While machine-in-the-loop effectiveness has been extensively discussed in [2, 21, 27] in terms of reduced assembly time, error occurrence and error handling times, while human-in-the-loop, previously analyzed for traditional deep learning paradigms [2] has been developed and assessed here for LLM-based error detection, description and correction.

To comprehensively evaluate the model detection capabilities and output quality, examples of LLM-generated responses for step 18.3 were analyzed. In this instance, the operator deliberately omitted the installation of the locking nut, as illustrated in Fig. 3. Both ChatGPT and Claude responses to Prompt #1 were collected and analyzed. Both models identified errors, but with different accuracy. ChatGPT incorrectly diagnosed a "partially threaded" locking nut when it was completely missing, while Claude correctly identified the missing nut despite initial contradictions. Their correction instructions reflected these diagnoses. Following the submission and evaluation of Prompt #2 (reported in Fig. 7), Claude correctly identifies the diagnosis, whereas ChatGPT unsatisfactory performance in terms of error diagnosis and prognosis necessitated a third interaction using Prompt #3, whose content is detailed in Fig. 8.

```
Your previous response was not satisfactory in terms of ['error description and instructions generation'].
Let's refine the assessment. The type of this task is "{task_column ['task type']}". The first image shows the
correct assembly reference, and the second image shows the real-time operation result. Based on these images
and the instruction "{task_column ['work instruction']}", determine whether the correct component or tool was
selected and whether the assembly step was executed properly. Ensure that the selected item is correct,
properly positioned, oriented, aligned, and secured, and that all required components or tools, including
those from previous steps, are present. Identify any errors, such as the use of an incorrect component,
misalignment, missing elements, or improper execution of the assembly step. The Detection Log must indicate
"Error" or "Correct," provide specific details on any mistakes, and include clear and concise corrective
instructions to ensure compliance in future steps.
```

Fig. 7. *Prompt #2*

```
Your previous responses were not satisfactory in terms of ['error description and instructions generation'].
Let's refine the assessment. The type of this task is "{task_column['task type']}". Compare the first image,
which represents the correct reference, with the second image, showing the real-time operation result. Based
on "{task_column['work instruction']}", determine whether the correct component or tool was selected or if the
assembly step was executed correctly. Ensure that, when relevant, the selected item is properly positioned,
oriented, aligned, and secured. Additionally, verify that all required components or tools, including those
from previous steps, are correctly utilized and consistently present throughout the process. If a component
selection occurred in an earlier step, confirm that the same exact component is used in subsequent steps as
expected. If any errors were detected in previous steps, ensure that they have been corrected before proceeding
with this analysis. Identify any remaining errors, such as the use of an incorrect component, misalignment,
missing elements, or improper execution of the assembly step. The Detection Log must indicate "Error" or
"Correct," provide specific details on any mistakes, and include clear and concise corrective instructions to
ensure compliance in future steps.
```

Fig. 8. *Prompt #3*

Despite three increasingly detailed prompts, ChatGPT persisted in its erroneous assessment claiming that the locking nut was partially threaded rather than completely missing. This misjudgment led to errors in subsequent descriptions and corrective instructions, ultimately resulting in a KO status. This example demonstrates the difference in the visual reasoning capabilities of the two models. While both systems correctly recognized the presence of an error, ChatGPT consistently misinterpreted the visual evidence to focus on improper tightening of a non-existent part. In contrast, Claude was able to accurately identify missing parts and provide appropriate corrections after Prompt #2.

Conclusions

This research compared ChatGPT and Claude in an intelligent assisted assembly system utilizing reciprocal learning with human feedback. Results revealed ChatGPT higher initial accuracy versus Claude greater adaptability through iterative refinement, highlighting trade-offs in LLM selection for collaborative tasks and the importance of reciprocal learning. Claude demonstrated superior visual reasoning, particularly in identifying missing components. Future research should focus on extending reciprocal learning to more complex assembly scenarios, optimizing system latency for real-time use, and developing automated prompt refinement strategies. Large-scale validation in diverse industrial environments is also needed to ensure the scalability and robustness of LLM-based error detection and correction systems.

Declaration of generative AI and AI-assisted technologies in the writing process

The authors used ChatGPT and DeepL to improve syntax and grammar, then reviewed and edited the content, assuming full responsibility for the final publication.

References

[1] Leng, J., Sha, W., Wang, B., Zheng, P., Zhuang, C., Liu, Q., Wuest, T., Mourtzis, D., Wang, L.: Industry 5.0: Prospect and retrospect. J Manuf Syst. 65, 279–295 (2022). https://doi.org/10.1016/j.jmsy.2022.09.017

[2] Simeone, A., Fan, Y., Antonelli, D., Catalano, A.R., Priarone, P.C., Settineri, L.: Inclusive manufacturing: A contribution to assembly processes with human-machine reciprocal learning. CIRP Ann Manuf Technol. 73, 5–8 (2024). https://doi.org/10.1016/j.cirp.2024.03.005

[3] Konstantinou, C., Antonarakos, D., Angelakis, P., Gkournelos, C., Michalos, G., Makris, S.: Leveraging Generative AI Prompt Programming for Human-Robot Collaborative Assembly. Procedia CIRP. 128, 621–626 (2024). https://doi.org/10.1016/j.procir.2024.03.040

[4] Liu, S., Zhang, J., Wang, L., Gao, R.X.: Vision AI-based human-robot collaborative assembly driven by autonomous robots. CIRP Annals. (2024). https://doi.org/10.1016/j.cirp.2024.03.004

[5] Yurong, G., Jian, M.: Optimization analysis of assembly system based on digital twin and deep learning. In: Proceedings of the 2020 4th International Conference on Electronic Information Technology and Computer Engineering. pp. 627–631. ACM, New York, NY, USA (2020). https://doi.org/10.1145/3443467.3443825

[6] Fu, B., Hadid, A., Damer, N.: Generative AI in the context of assistive technologies: Trends, limitations and future directions. Image Vis Comput. 154, 105347 (2025). https://doi.org/10.1016/j.imavis.2024.105347

[7] Fan, H., Liu, X., Fuh, J.Y.H., Lu, W.F., Li, B.: Embodied intelligence in manufacturing: leveraging large language models for autonomous industrial robotics. J Intell Manuf. (2024). https://doi.org/10.1007/s10845-023-02294-y

[8] Shafiee, S.: Generative AI in manufacturing: a literature review of recent applications and future prospects. Procedia CIRP. 132, 1–6 (2025). https://doi.org/10.1016/j.procir.2025.01.001

[9] Zang, Y., Li, W., Han, J., Zhou, K., Loy, C.C.: Contextual Object Detection with Multimodal Large Language Models. Int J Comput Vis. 133, 825–843 (2025). https://doi.org/10.1007/s11263-024-02214-4

[10] Yu, Q., Shen, X., Chen, L.-C.: Towards Open-Ended Visual Recognition with Large Language Models. Presented at the (2025). https://doi.org/10.1007/978-3-031-72630-9_21

[11] Jiang, Y., Yan, X., Ji, G.-P., Fu, K., Sun, M., Xiong, H., Fan, D.-P., Khan, F.S.: Effectiveness assessment of recent large vision-language models. Visual Intelligence. 2, 17 (2024). https://doi.org/10.1007/s44267-024-00050-1

[12] Zhang, X., Wu, K., Ma, Q., Chen, Z.: Research on Object Detection Model Based on Feature Network Optimization. Processes. 9, 1654 (2021). https://doi.org/10.3390/pr9091654

[13] Wang, Z., Qin, H.: Intelligent industrial production process automatic regulation system based on LLM agents. In: 2024 5th International Conference on Artificial Intelligence and Electromechanical Automation (AIEA). pp. 133–137. IEEE (2024). https://doi.org/10.1109/AIEA62095.2024.10692701

[14] Lim, J., Patel, S., Evans, A., Pimley, J., Li, Y., Kovalenko, I.: Enhancing Human-Robot Collaborative Assembly in Manufacturing Systems Using Large Language Models. In: 2024 IEEE 20th International Conference on Automation Science and Engineering (CASE). pp. 2581–2587. IEEE (2024). https://doi.org/10.1109/CASE59546.2024.10711843

[15] Kang, J.H., Dhanaraj, N., Wadaskar, S., Gupta, S.K.: Using Large Language Models to Generate and Apply Contingency Handling Procedures in Collaborative Assembly Applications. In: 2024 IEEE International Conference on Robotics and Automation (ICRA). pp. 15585–15592. IEEE (2024). https://doi.org/10.1109/ICRA57147.2024.10610875

[16] Salvagno, M., Taccone, F.S., Gerli, A.G.: Artificial intelligence hallucinations. Crit Care. 27, 180 (2023). https://doi.org/10.1186/s13054-023-04473-y

[17] Ashqar, H.I., Alhadidi, T.I., Elhenawy, M., Khanfar, N.O.: Leveraging Multimodal Large Language Models (MLLMs) for Enhanced Object Detection and Scene Understanding in Thermal Images for Autonomous Driving Systems. Automation. 5, 508–526 (2024). https://doi.org/10.3390/automation5040029

[18] Wang, Z., Kiyokawa, T., Sera, I., Yamanobe, N., Wan, W., Harada, K.: Error Correction in Robotic Assembly Planning From Graphical Instruction Manuals. IEEE Access. 11, 107276–107286 (2023). https://doi.org/10.1109/ACCESS.2023.3319822

[19] Langer, M., Baum, K., Schlicker, N.: Effective Human Oversight of AI-Based Systems: A Signal Detection Perspective on the Detection of Inaccurate and Unfair Outputs. Minds Mach (Dordr). 35, 1 (2024). https://doi.org/10.1007/s11023-024-09701-0

[20] Aleixo, E.L., Colonna, J.G., Cristo, M., Fernandes, E.: Catastrophic Forgetting in Deep Learning: A Comprehensive Taxonomy. Journal of the Brazilian Computer Society. 30, (2024). https://doi.org/10.5753/jbcs.2024.3966

[21] Fan, Y., Simeone, A., Antonelli, D., Caggiano, A., Priarone, P.C., Settineri, L.: A framework for digital assembly instructions as a step towards manufacturing inclusiveness. Procedia CIRP. 132, 116–121 (2025). https://doi.org/10.1016/j.procir.2025.01.020

[22] Chen, H., Li, S., Fan, J., Duan, A., Yang, C., Navarro-Alarcon, D., Zheng, P.: Human-in-the-Loop Robot Learning for Smart Manufacturing: A Human-Centric Perspective. IEEE Transactions on Automation Science and Engineering. 1–1 (2025). https://doi.org/10.1109/TASE.2025.3528051

[23] Iyenghar, P.: Clever Hans in the Loop? A Critical Examination of ChatGPT in a Human-in-the-Loop Framework for Machinery Functional Safety Risk Analysis. Eng. 6, 31 (2025). https://doi.org/10.3390/eng6020031

[24] Hatia, A., Doldo, T., Parrini, S., Chisci, E., Cipriani, L., Montagna, L., Lagana, G., Guenza, G., Agosta, E., Vinjolli, F., Hoxha, M., D'Amelio, C., Favaretto, N., Chisci, G.: Accuracy and Completeness of ChatGPT-Generated Information on Interceptive Orthodontics: A Multicenter Collaborative Study. J Clin Med. 13, 735 (2024). https://doi.org/10.3390/jcm13030735

[25] Woo, K.C., Simon, G.W., Akindutire, O., Aphinyanaphongs, Y., Austrian, J.S., Kim, J.G., Genes, N., Goldenring, J.A., Major, V.J., Pariente, C.S., Pineda, E.G., Kang, S.K.: Evaluation of GPT-4 ability to identify and generate patient instructions for actionable incidental radiology findings. Journal of the American Medical Informatics Association. 31, 1983–1993 (2024). https://doi.org/10.1093/jamia/ocae117.

[26] Govender, R.G.: My AI students: Evaluating the proficiency of three AI chatbots in completeness and accuracy. Contemp Educ Technol. 16, ep509 (2024). https://doi.org/10.30935/cedtech/14564

[27] Fan, Y., Simeone, A., Antonelli, D., Catalano, A.R., Priarone, P.C., Settineri, L.: A logic-assisted assembly support system to promote the inclusion of neurodiverse operators in manufacturing. Procedia CIRP. (2025). Accepted for publication.

Materials Research Proceedings 57 (2025) 466-474 https://doi.org/10.21741/9781644903735-55

Environmental impact assessment of adhesive joints in basalt fibre-reinforced thermoplastic composites using LCA methodology

Luigi BENVENUTO[1,a*], Chiara MANDOLFINO[1,b], Pietro RUSSO[2,c], Matteo BENVENUTO[1,d], Marco PIZZORNI[1,e], Enrico LERTORA[1,f]

[1]Department of Mechanical Engineering, Polytechnic School of University of Genoa, Via Opera Pia 15, Genoa 16145, Italy

[2]Institute for Polymers, Composites and Biomaterials, National Research Council, Via Campi Flegrei 34, Na, Pozzuoli, 80078, Italy

[a]luigi.benvenuto@edu.unige.it, [b]chiara.mandolfino@unige.it, [c]pietro.russo@ipcb.cnr.it, [d]matteo.benvenuto@edu.unige.it, [e]marco.pizzorni@unige.it, [f]enrico.lertora@unige.it

Keywords: Composites, Adhesive Bonding, Lifecycle Assessment

Abstract. This research evaluates the environmental impact of adhesive joints in basalt fibre-reinforced thermoplastic composites. Using the Life Cycle Analysis (LCA) method, the study examines the influence of individual components and surface treatments on the environmental footprint by correlating it with the mechanical properties of the bonded joint by virtue of different surface treatments. The main results indicate that polyamide 11, used as a matrix, has a significant impact on the environment, particularly in the production stages. Surface treatments were compared, including acetone cleaning, mechanical abrasion and plasma treatment, which offered superior mechanical performance but higher environmental costs due to the electrical energy required to operate the process chamber. The study also highlights the ecological benefits and the importance of partial material reuse, which reduces environmental impact.

Introduction

The increasing demand for sustainable materials in engineering applications has led to the exploration of thermoplastic composites reinforced with basalt fibre. These materials offer recyclability and mechanical strength, making them suitable for various industrial applications. Unlike thermoset composites, which are difficult to recycle, thermoplastic composites can be remelted and remoulded, allowing for total component recovery at the end of life [1]. This characteristic makes them particularly attractive for industries aiming to enhance environmental and economic sustainability [2].

Adhesive bonding in thermoplastic composites provides even stress distribution, maintaining structural integrity and reducing delamination risks. This is crucial for lightweight design in transport and renewable energy applications [3]. Optimising adhesive bonded joints is essential to improve structural integrity, efficiency and sustainability. This involves balancing technical, economic and environmental factors, with surface preparation playing a key role [4].

Surface preparation methods for adhesive bonding include mechanical abrasion and chemical and plasma treatments. Mechanical abrasion, such as sanding or grit blasting, increases surface roughness and promotes mechanical interlocking of the adhesive [5]. Chemical treatments, including acid etching and anodisation, modify the surface chemistry to enhance adhesion [6]. Plasma treatments, particularly low-pressure plasma, are increasingly used due to their ability to clean and activate surfaces without the use of hazardous chemicals [7]. Low-pressure plasma treatment involves the ionisation of gas in a vacuum chamber, creating a reactive plasma that interacts with the substrate surface, improving wettability and adhesion properties.

Content from this work may be used under the terms of the Creative Commons Attribution 3.0 license. Any further distribution of this work must maintain attribution to the author(s) and the title of the work, journal citation and DOI. Published under license by Materials Research Forum LLC.

Comparative studies have shown that low-pressure plasma treatment can significantly enhance the adhesion performance of polymeric substrates, often outperforming traditional methods like mechanical abrasion or chemical treatments. For instance, Mandolfino et al. demonstrated that low-pressure plasma treatment of polypropylene substrates resulted in higher surface energy and improved adhesive bonding compared to untreated and mechanically abraded samples. Similarly, plasma-treated polyethylene surfaces exhibited superior shear strength in adhesive joints compared to those treated with conventional primers [8]. However, this method of surface preparation requires the use of electricity and possibly a gas other than air, which can lead to a higher environmental impact than the use of solvents required for degreasing alone.

The Life Cycle Assessment (LCA) methodology is a comprehensive tool used precisely to evaluate the environmental impacts associated with all stages of a product's life, from raw material extraction through processing, manufacture, distribution, use, repair and maintenance and disposal or recycling[9], [10].

This study therefore set out to analyse the mechanical characteristics of bonded joints using thermoplastic polymer substrates reinforced with continuous basalt fibres, combining the test results with the assessment of the environmental impact by means of LCA, focusing on the influence of individual components and surface treatments. In this way, it is possible to evaluate the different bonded joints not only through technical but also environmental criteria, leaving the designer to decide whether to favour performance or sustainability.

Materials and Methods

The general approach was divided into four phases: (i) thermoplastic composite substrates were prepared with two different surface treatments; (ii) adhesive-bonded joints were prepared; (iii) bonded joints were tested to assess Tensile Shear Strength (TSS); (iv) the life cycle of the different scenarios was assessed.

Composite substrates. The study focused on thermoplastic composites with a polyamide 11 (PA11) matrix reinforced with basalt fibre. The PA11 used was commercially known as Rilsan® MB3000, produced by Arkema Inc. (Colombes, France). It exhibited a high degree of crystallinity, resulting in a highly ordered structure that provided good mechanical performance. The basalt fibre reinforcement consisted of a plain weave fabric, commercially known as BasFiberPro® supplied by Kamenny Vek (Dubna, Moscow, Russian Federation), with a mass per unit area of 210 ± 20 g/m². PA11 was chosen for its mechanical properties and recyclability as it is often of biological origin, derived from renewable sources such as castor oil as opposed to the better-known polyamides 6 and 6.6 which are generally of petrochemical origin. The basalt fibre was selected for its thermal stability and strength.

The manufacturing process was conducted by the CNR of Naples using the film stacking method. Twelve layers of basalt fibre fabric were placed between two sheets of PA11. The resulting ‘sandwich’ was heated within a mould to 225 °C (melting phase) to ensure the temperature was uniformly reached throughout the PA11 sheets, thereby achieving complete fusion at every point. Subsequently, while maintaining the temperature, an increasing pressure was applied (impregnation phase) to facilitate the impregnation of the reinforcement. Once the maximum pressure of approximately 40 bar was reached, the cooling phase commenced, during which the pressure was kept constant until the piece hardened.

This process produced two panels with dimensions 350 x 350 mm and a thickness of 2 mm, from which the substrates for bonding were obtained with dimensions 100 x 25 mm with a tolerance of 0.25 mm as per technical standard EN 1465 [11].

Before undergoing the different surface treatments, to ensure the same initial conditions, the substrates were subjected to a drying cycle in a climatic chamber for a period of 12 hours at a temperature of 23 °C and 50% relative humidity.

Surface preparations and adhesive bonding. All cut substrates were inspected, and those exhibiting defects due to proximity to the edge of the starting sheet or surface irregularities were discarded. Subsequently, the selected substrates were divided to ensure three repetitions (N=3) for each configuration and were treated separately. The first batch was cleaned and degreased using 99% pure acetone (chemical formula C_3H_6O). The second batch was treated using low-pressure plasma, also known as cold plasma. The plasma treatment was conducted using the Tucano Multi-Purpose Plasma System, produced by Gambetti Kenologia Srl (Binasco, Milan, Italy). It should be noted that acetone cleaning was not employed in this case, as the ionised gas particles during the treatment impacted the surface, breaking polymer chains and creating functional groups, while also removing contaminants, thus making degreasing unnecessary. The process parameters set were a power P=150 W and a treatment duration t=150 s, while the process gas used was air [12].

The latter method provided a uniform treatment across the entire surface of the substrates, ensuring consistent adhesion properties. However, time, energy consumption and careful control of plasma parameters were required to achieve optimal results. This implied that, from an environmental perspective, it might be more impactful, despite not necessarily involving the use of hazardous chemicals such as acetone.

The bonding was performed using Loctite HY 4070 adhesive, produced by Henkel Italia S.r.l. (Milan, Italy). This hybrid adhesive, combining cyanoacrylate and acrylic components, had a mixing ratio of 10:1, enabling rapid fixation at room temperature. It is characterised by good adhesion on various substrates, primarily plastics, rubbers and metals. Following the procedures indicated in the product's technical data sheet and adhering to the specified gelation time, six joints were obtained, with three repetitions per sample, in a single overlap configuration with tabs at the ends, as shown in Fig. 1a. The bonding area conformed to the EN 1465 standard [11] and is also depicted in Fig. 1a. Fig. 1b shows the joints after complete cross-linking. The environmental conditions were monitored throughout the procedure.

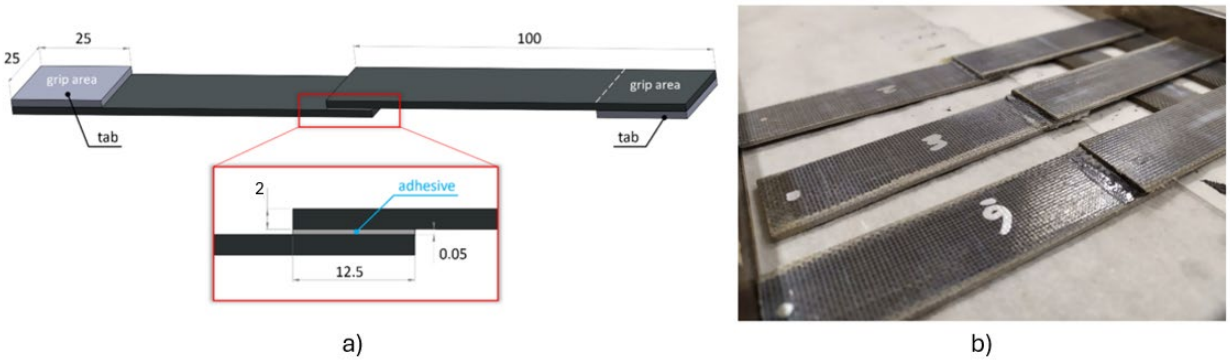


Fig. 1 - a) Joint configuration and dimensions; b) Cured joints

Table 1 summarises the characteristics of the two samples.

Table 1 - Samples tested

Sample	Treatment	Parameters
I	Degreasing (acetone)	-
II	Cold Plasma (air)	P=150 W; t=150 s

Mechanical test. Lap shear tests were conducted according to the EN 1465 standard [11] to evaluate the mechanical performance of the bonded joints under controlled environmental conditions of T=23 ± 2 °C and RH=50 ± 5%, utilising an Instron 8802 servo hydraulic testing

machine (Instron, Norwood, MA, USA) equipped with a 50 kN load cell and hydraulically actuated grips to minimise any play during movement. A crosshead displacement rate of 1.3mm/min was employed throughout the testing procedure. For each set of joints, three replicates (N=3) were tested to determine the mean ultimate load at failure (F), along with the corresponding standard deviation. The TSS was subsequently calculated as the ratio of F to the initial overlap area (A_0), which varied depending on the specific configuration.

Life Cycle Assessment (LCA). LCA methodology was used to compare the environmental impact of the two samples. The analysis followed the international standards ISO 14040 [13] and ISO 14044 [14], using SimaPro 9.4.0 software and its database, Ecoinvent3.

It is important to highlight that some of the data included in the Life Cycle Inventory (LCI) were obtained through direct measurements, while others were sourced from the literature, technical and safety data sheets of the products, or extracted from the software database.

In addition to the contribution of the adhesive and its constituents, the environmental impact of the surface treatment was assessed. During the plasma treatment, energy consumption was recorded using a power meter (KTEM02, Ketotec, PRC). The energy value considered in the impact assessment encompasses the entire plasma process, including both the initial vacuum generation phase in the treatment chamber and the actual exposure time. For the analysis, it was assumed that the energy required for joint production was supplied by the European electricity grid mix, reflecting the location where the tests were conducted.

The functional unit identified to compare the two scenarios (I and II) was then formulated as 'the set of three bonded joints'.

In this study, the Life Cycle Impact Assessment (LCIA) was conducted using the ReCiPe2016 EndPoint method [15], [16].

Results and Discussion

Tensile Testing. Fig. 2 illustrates the load-displacement curves for the two sets of specimens: one set degreased with acetone (I) and the other treated with low-pressure plasma (II).

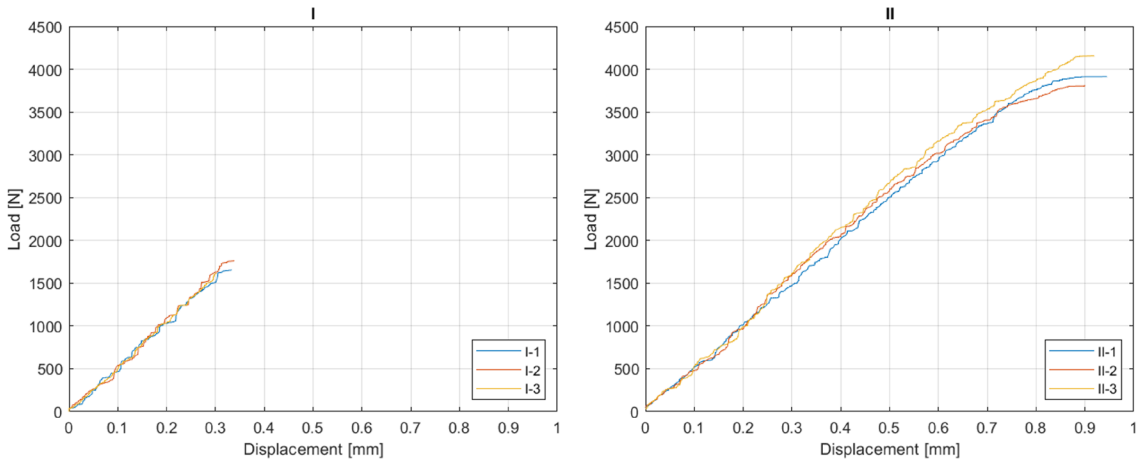


Fig. 2 - Load-Displacement curves for sample I (a) and sample II (b)

The graphs show similar trends for all samples but with variations in maximum load and elongation at break higher in the second case, demonstrating the influence of the type of surface treatment on joint performance.

As mentioned in the previous section, by dividing the breaking load by the overlap area of the individual specimen, the TSS can be calculated. Specifically, the mean values and relative standard sample deviations of the calculated quantities were 5.97 ± 0.32 MPa and 13.90 ± 0.93 MPa for

Materials Research Proceedings 57 (2025) 466-474 https://doi.org/10.21741/9781644903735-55

sample I and sample II, respectively. Plasma treatment performed with the specified parameters resulted in a 133% increase in TSS compared to the joint subjected solely to the acetone cleaning phase.

Regarding the types of failure, as can be seen in Fig. 3, a cohesive failure mode was observed in all joints. However, in the joints that did not undergo plasma treatment, a 'leopard spot' cohesive failure was detected, indicative of non-uniform adhesion. Conversely, in the plasma-treated joints, a more homogeneous distribution of the adhesive was found on both substrates.

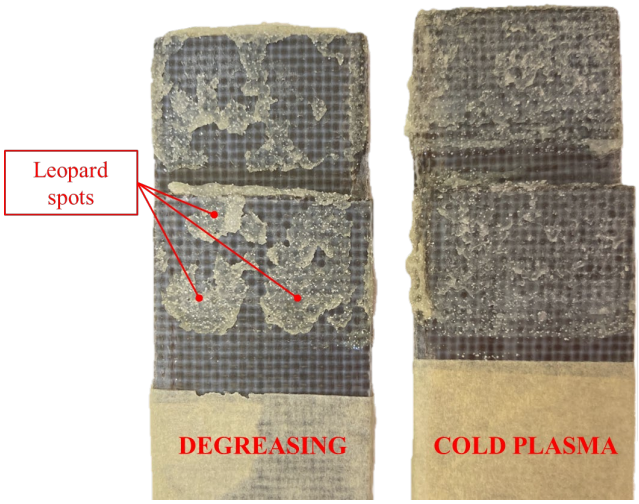


Fig. 3 - Bonded joint failure for the two tested samples

LCA results. To examine sample I, the life cycle 'from cradle to gate' was analysed, considering the entire production process from raw material extraction to the creation of the joint. Each block was represented as a process, while material and energy flows were graphically depicted using arrows whose thickness was proportional to the amount of impact, expressed as a percentage of the overall life cycle score of the joint, which constituted 100%. From the diagram in Fig. 4, it is observed that the greatest contribution is made by polyamide, which forms the matrix of the composite substrate, followed by the processes for composite assembly and the energy consumption of the climate chamber.

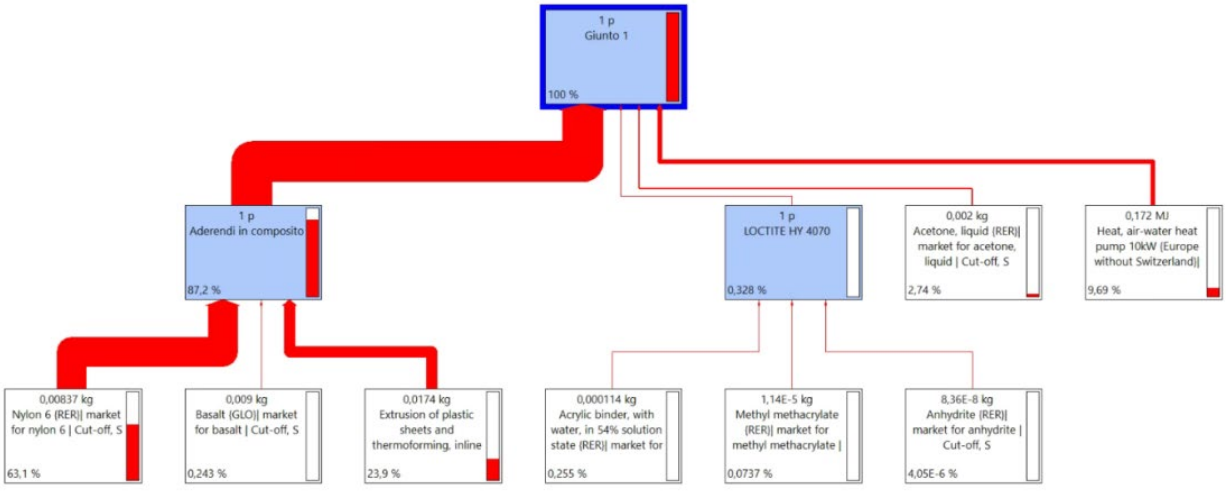


Fig. 4 - Tree diagram: LCA 'from cradle to gate' of joint I

Materials Research Proceedings 57 (2025) 466-474 https://doi.org/10.21741/9781644903735-55

In the LCIA phase, the environmental impact of the data obtained from the LCI is quantified and assigned to an impact category (*midpoint*) using calculation models. The ReCiPe 2016 method provides the characterisation of 17 impact categories based on the extent to which the substances, or elementary flows, involved contribute to various environmental issues. However, it is not feasible to perform a simple summation of substances within the same impact category, as each contributes differently to the environmental problem. To obtain an equivalent result that can subsequently be summed to yield the total value of each midpoint, each elementary flow is assigned to a 'characterisation factor' (CF) that weighs the effect of the individual substance against the contribution of the specific midpoint.

Each impact category can subsequently be traced to one or more protection areas (*endpoints*) defined as Human Health, Ecosystem Quality and Resource Scarcity. For example, global warming is an intermediate category (midpoint) which, through scientifically proven pathways, impacts human health and ecosystems (endpoints).

Since the characterisation results are not easily interpretable, the normalisation step is performed using worldwide reference values for the year 2010, as included in the ReCiPe 2016 method [15]. Although these values are dated, they constitute the most up-to-date reference currently available.

In Fig. 5, the impact of the processes involved on the three macro-categories is shown.

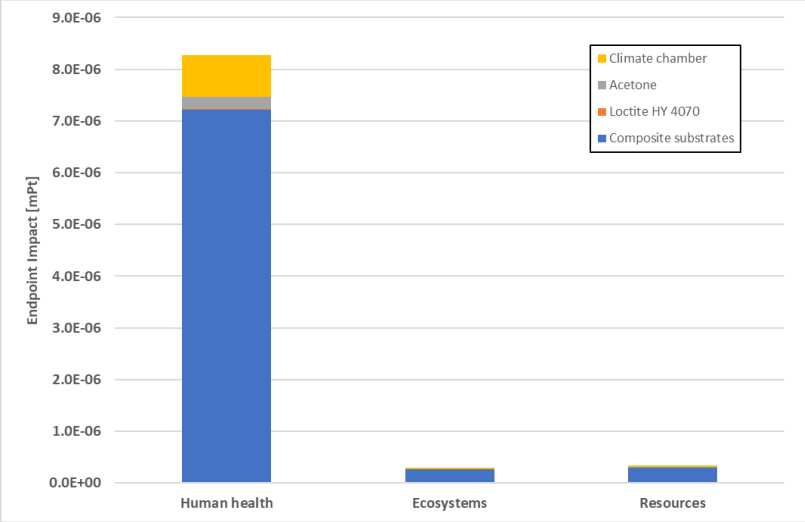


Fig. 5 - Endpoint impact assessment of joint production I

However, by expanding the investigation and including a virtuous disposal scenario, i.e., conducting a life cycle 'from cradle to grave', the network diagram presented in Fig. 6 was obtained, where green arrows correspond to a positive effect, namely a reduction in impact.

Materials Research Proceedings 57 (2025) 466-474 https://doi.org/10.21741/9781644903735-55

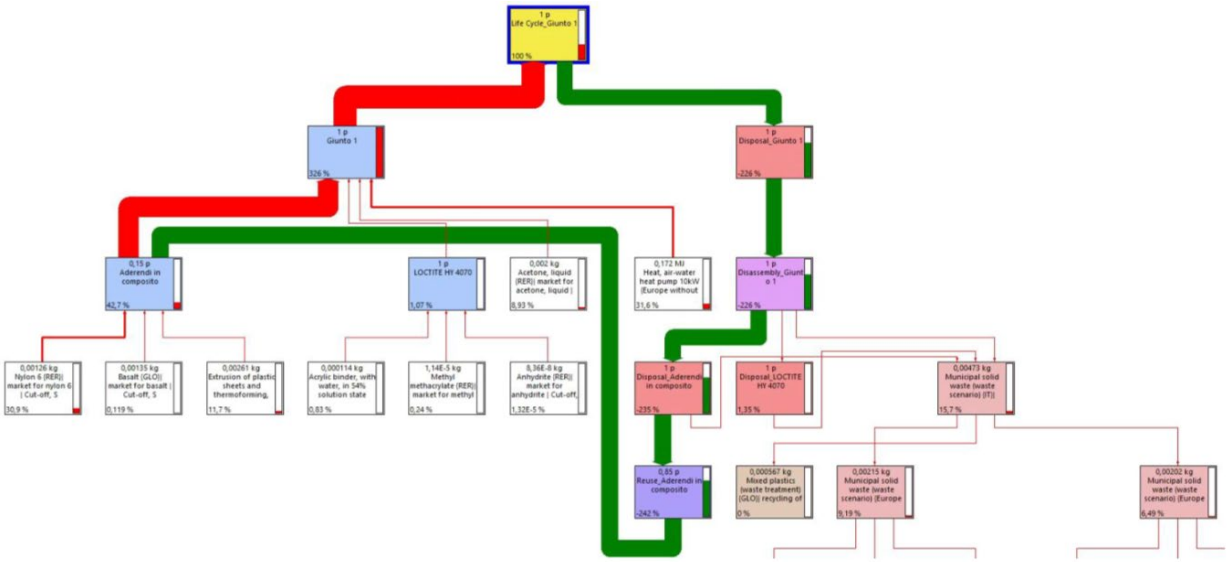


Fig. 6 - Tree diagram: LCA 'from cradle to grave' of joint I

It was observed that, thanks to partial reuse, the impact of the composite was significantly mitigated. It was hypothesised that the material, having a thermoplastic matrix, could be reused. However, the reuse was not total, as the adhesive was not designed for debonding, necessitating the removal of the adhering substrate portion by trimming (approximately 15% of the total, considering both the overlapped part and the potential meniscus). The removed substrate and adhesive would be entrusted to national waste management.

In this manner, by conducting a new endpoint comparison presented in Table 2, it can be observed how advantageous reuse is, reducing the effects in each category by 69%, 73% and 76%, respectively.

Table 2 - Endpoint assessment values of joint I without disposal scenario and with

Type of scenario	Human health [mPt]	Ecosystems [mPt]	Resources [mPt]
From cradle to gate	$8.3 \cdot 10^{-6}$	$3.0 \cdot 10^{-7}$	$3.4 \cdot 10^{-7}$
From cradle to grave	$2.6 \cdot 10^{-6}$	$8.2 \cdot 10^{-8}$	$8.4 \cdot 10^{-8}$

By performing the same type of analysis, including a disposal scenario for sample II and comparing it with the 'from cradle to grave' analysis of joint I, the result shown in Table 3 was obtained, in which sample II was found to be more impactful across all macro-categories (from 36% to 55%) despite the absence of acetone usage.

Table 3 – Impact on the 'from cradle to grave' cycle of sample I and II compared to endpoints

Sample	Human health [mPt]	Ecosystems [mPt]	Resources [mPt]
I	$2.6 \cdot 10^{-6}$	$8.2 \cdot 10^{-8}$	$8.4 \cdot 10^{-8}$
II	$3.5 \cdot 10^{-6}$	$1.2 \cdot 10^{-7}$	$1.3 \cdot 10^{-7}$

Figure 7 presents the seven most significant midpoints, each exceeding a 1% contribution. Although sample II does not involve the use of chemical substances such as acetone, which is typically employed for degreasing, it results in a higher overall environmental impact than sample I across all the categories considered. This outcome is primarily attributable to the greater

consumption of electricity, which, in the reference scenario, is generated from a mix of renewable and non-renewable sources, based on the European average.

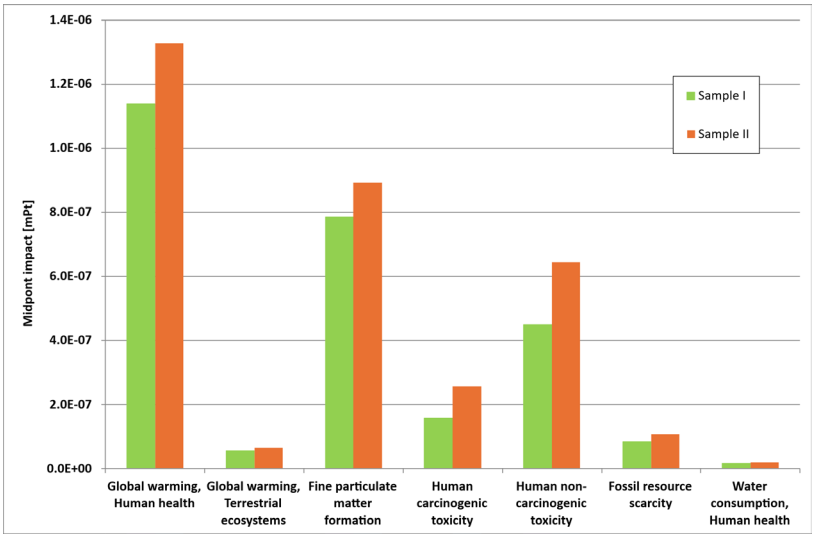


Fig. 7 - Midpoint impact assessment of two samples compared

Conclusions

From the comparison of different treatments, it emerged that plasma offered significantly superior mechanical performance (+133%), but presented greater environmental disadvantages compared to simple acetone degreasing, primarily due to the non-modularity typical of this technique. The implementation of larger capacity machinery, especially from an industrial perspective, could significantly reduce its impact.

The LCA analysis revealed that the critical point in the creation of the joint primarily resided in the polyamide and the processes required for substrate creation and drying. The impact of the adhesive, due to the small quantities involved, was almost negligible. The partial reuse of the adherend proved to be particularly beneficial, as it significantly contributed to reducing the negative effects of the polymer. Additionally, the implementation of debonding techniques could allow for the recovery of 15% of the adherend currently discarded, thereby enhancing the overall efficiency of the process.

In conclusion, future research should focus on experimenting with new methodologies to improve the efficiency and sustainability of the process. However, considering that the matrix is the most critical element, it is advisable to explore innovative solutions in the context of raw materials and their end-of-life reuse.

References

[1] C. Mandolfino, L. Cassettari, M. Pizzorni, L. Benvenuto, and E. Lertora, 'A comprehensive techno-economic and environmental comparison of plasma-treated adhesive-bonded thermoplastic composites', *Journal of Advanced Joining Processes*, vol. 10, p. 100268, Nov. 2024. https://doi.org/10.1016/J.JAJP.2024.100268

[2] C. Mandolfino, L. Cassettari, E. Lertora, and M. Pizzorni, 'Adhesive bonding of glass-fibre thermoplastic composite: process optimisation and sustainability analysis using LCA methodology', *International Journal of Advanced Manufacturing Technology*, vol. 130, no. 11–12, pp. 5709–5726, Feb. 2024. https://doi.org/10.1007/s00170-024-13022-y

[3] F. C. Campbell, *Structural Composite Materials*. 2010. [Online]. Available: www.asminternational.org

[4] V. Lunetto, M. Galati, L. Settineri, and L. Iuliano, 'Sustainability in the manufacturing of composite materials: A literature review and directions for future research', Jan. 06, 2023, *Elsevier Ltd*. https://doi.org/10.1016/j.jmapro.2022.12.020

[5] S. Hao, L. He, J. Liu, Y. Liu, C. Rudd, and X. Liu, 'Recovery of carbon fibre from waste prepreg via microwave pyrolysis', *Polymers (Basel)*, vol. 13, no. 8, Apr. 2021. https://doi.org/10.3390/polym13081231

[6] C. Mandolfino, E. Lertora, C. Gambaro, and M. Bruno, 'Improving adhesion performance of polyethylene surfaces by cold plasma treatment', *Meccanica*, vol. 49, no. 10, pp. 2299–2306, 2014. https://doi.org/10.1007/s11012-014-9993-y

[7] C. Mandolfino, L. Cassettari, M. Pizzorni, S. Saccaro, and E. Lertora, 'A design-of-experiments approach to estimate the effect of plasma-treatment parameters on the mechanical resistance of adhesive-bonded joints', *J Manuf Process*, vol. 67, pp. 177–194, Jul. 2021. https://doi.org/10.1016/J.JMAPRO.2021.04.054

[8] C. Mandolfino, 'Polypropylene surface modification by low pressure plasma to increase adhesive bonding: Effect of process parameters', *Surf Coat Technol*, vol. 366, pp. 331–337, May 2019. https://doi.org/10.1016/J.SURFCOAT.2019.03.047

[9] G. Finnveden *et al.*, 'Recent developments in Life Cycle Assessment', *J Environ Manage*, vol. 91, no. 1, pp. 1–21, Oct. 2009. https://doi.org/10.1016/J.JENVMAN.2009.06.018

[10] H. Alhazmi, F. H. Almansour, and Z. Aldhafeeri, 'Plastic Waste Management: A Review of Existing Life Cycle Assessment Studies', *Sustainability*, vol. 13, no. 10, p. 5340, May 2021. https://doi.org/10.3390/su13105340

[11] European Standard, 'EN 1465. Adhesives - Determination of tensile lap-shear strength of bonded assemblies', 2009.

[12] M. Pizzorni, E. Lertora, C. Gambaro, C. Mandolfino, M. Salerno, and M. Prato, 'Low-pressure plasma treatment of CFRP substrates for epoxy-adhesive bonding: an investigation of the effect of various process gases', *International Journal of Advanced Manufacturing Technology*, vol. 102, no. 9–12, pp. 3021–3035, Jun. 2019. https://doi.org/10.1007/s00170-019-03350-9

[13] International Standard, 'ISO 14040+A1. Environmental management: Life cycle assessment: principles and framework', 2020, *BSI Standards Limited*.

[14] International Standard, 'ISO 14044+A2. Environmental management. Life cycle assessment. Requirements and guidelines', 2021, *British Standards Institution*.

[15] M. A. J. Huijbregts *et al.*, 'ReCiPe2016: a harmonised life cycle impact assessment method at midpoint and endpoint level', *International Journal of Life Cycle Assessment*, vol. 22, no. 2, pp. 138–147, Feb. 2017. https://doi.org/10.1007/s11367-016-1246-y

[16] D. Hunkeler, 'Life Cycle Assessment (LCA): A Guide to Best Practice', *Int J Life Cycle Assess*, vol. 21, no. 7, pp. 1063–1066, Jul. 2016. https://doi.org/10.1007/s11367-016-1083-z

Materials Research Proceedings 57 (2025) 475-483 https://doi.org/10.21741/9781644903735-56

A decisional framework for second-life applications of textile waste: A data-driven and generative AI approach

Giovanni DE MARTINO[1,2,a *], Rosa LEONE[1,3,b], Marica BUCCI[1,3,c], Michele DASSISTI[1,d]

[1]Department of Mechanical, Mathematics and Management (DMMM), Polytechnical University of Bari, Bari, Italy

[2]Department of Science, Technologies and Society, University School for Advanced Studies Pavia – IUSS Pavia, Italy, 27100 Pavia, Italy

[3]Department of Agricultural, Environmental and Land Sciences, University of Bari, Bari, Italy

[a]giovanni.demartino@poliba.it, [b]r.leone59@phd.uniba.it, [c]m.bucci40@phd.uniba.it, [d]michele.dassisti@poliba.it

Keywords: Sustainable Processes, Machine Learning, Textile Demanufacturing

Abstract. The textile sector generates significant waste materials demonstrating potential for innovative repurposing applications. This study presents a decision-making framework utilizing physical-qualitative criteria including composition strength and weight of textile waste to identify reuse opportunities across new sectors. The methodology integrates laboratory analyses with generative artificial intelligence-supported decision models examining data patterns and proposing innovative reuse scenarios. Generative AI analyzes collected data to explore creative applications incorporating technical economic and sustainability parameters ensuring optimal resource utilization. The framework's objective focuses on identifying novel applications while maximizing value creation and minimizing environmental impact through systematic evaluation of material properties based on quantifiable metrics. Findings indicate that textile waste can be effectively repurposed into high-value applications across multiple industries, demonstrating the necessity of standardized evaluation criteria, cross-sector collaboration and traceability mechanisms to enhance scalability and sustainability within circular economy frameworks.

Introduction

Industrial symbiosis (IS) has emerged as a transformative strategy to foster transitions toward a circular economy by facilitating cross-sectoral resource exchanges, though its implementation remains uneven across industrial domains. Grounded in collaborative frameworks, IS integrates traditionally disconnected production systems, transforming waste into valuable inputs—a concept epitomized by the Kalundborg Symbiosis in Denmark, where energy, water and by-products are shared among a power plant, refinery and pharmaceutical facilities [1], [2]. While sectors such as steelmaking and chemicals have advanced IS practices—for instance, slag reuse in construction [3] or CO_2 recovery for synthetic fuels [4]—others, like textiles, lag behind due to systemic fragmentation and technological barriers. In the textile industry, IS applications include synergies for wastewater management [5]. Recent advancements in digital platforms (e.g., blockchain for material tracking) and policy drivers, such as the EU Circular Economy Action Plan, signal potential accelerators for IS adoption [6]. To fully realize the benefits of IS, critical priorities remain interdisciplinary collaboration, standardized protocols and incentives for cross-sectoral partnerships.

Among industries requiring urgent circular solutions, the textile and fashion sector emerges as a critical case. With annual fiber production exceeding 110 million tons [7], it combines economic significance with substantial environmental impacts. It accounts for 10% of global CO_2 emissions

Content from this work may be used under the terms of the Creative Commons Attribution 3.0 license. Any further distribution of this work must maintain attribution to the author(s) and the title of the work, journal citation and DOI. Published under license by Materials Research Forum LLC.

and 20% of industrial water pollution, consuming 79 billion cubic meters of water annually [8], [9]. However, the dominant linear model generates over 92 million tons of textile waste each year, with only 1% undergoing closed-loop recycling into new garments, while 85% is disposed of in landfills or incineration facilities [7], [10]. Fast fashion has exacerbated this crisis by reducing the average garment lifecycle by 36% since 2005, accelerating consumption patterns and waste accumulation [8], [9]. Synthetic fibers, particularly polyester, dominate the market with a 62% share, while cotton accounts for 24% [8]. Although economically and technically advantageous, petroleum-based synthetics pose significant environmental challenges: their non-biodegradability could contribute 22 million tons of oceanic microplastic pollution by 2050, while their production is highly energy-intensive and generates substantial CO_2 emissions [7], [9]. Furthermore, the increasing prevalence of blended fabrics (over 30% of the market) further complicates recycling, as material heterogeneity hinders efficient recovery, relegating most waste to downcycling processes [8], [10]. With textile waste projected to reach 148 million tons by 2030 [10], scalable and technologically advanced solutions are needed to unlock the latent value of discarded materials.

This research presents a replicable decision-making framework for the systematic valorization of textile waste, aligned with global sustainability objectives and fostering cross-sectoral collaborative networks, exploring the potential of different textile materials for effective integration into circular processes.

Methodology

A framework for industrial symbiosis provides guidelines and tools to optimize resources in the circular economy. Despite sustainability efforts in the automotive sector, a unified framework for energy and material flows is lacking, hindering a fully integrated circular model [11]. Frameworks facilitate secondary raw material use, reduce resource consumption and integrate traceability to preserve material value [12][13]. Their effectiveness is evident in prefabricated construction, enhancing reusability and recyclability [14].

Circular economy implementation varies by sector and depends on specific frameworks. In the automotive industry, comprehensive frameworks for managing material and energy flows are still under development [11]. Construction has more established tools like the Circular Construction Evaluation Framework (CCEF) and the EU Level(s) initiative, which assess sustainability through indicators such as recycled material use and waste management [13], [15]. The textile sector focuses on waste recovery and recycling technologies, emphasizing traceability [16].

Reference frameworks guide circular strategies. The ReSOLVE framework defines six key strategies—reduce, reuse, repair, renew, recycle and recover—also applied in construction [13].

The Framework for Circular Buildings, developed by the Dutch Green Building Council and Metabolic, enhances sustainable design [17]. Tools like Material Flow Analysis (MFA) optimize material flows, exemplified by the Detailed Wheel of Fibre in the paper sector [18]. Decision-making models further refine textile waste recovery pathways, adapting to material types and recovery technologies [19].

Framework description This framework provides a structured methodology for identifying innovative applications for existing materials by leveraging their intrinsic properties. Through a sequential process of material analysis, functional mapping, application ideation and validation, it enables the discovery of novel industrial, technological and design uses while fostering sustainability and high-value reuse strategies.

The framework consists of four phases. The first phase involves a comprehensive material characterization, examining physical, chemical, mechanical, thermal, optical, acoustic and sensory properties. This step establishes a foundation for functional mapping by systematically cataloging key attributes through literature reviews, experimental data and contextual analyses.

Materials Research Proceedings 57 (2025) 475-483 https://doi.org/10.21741/9781644903735-56

The second phase translates these characteristics into functional capabilities, linking material properties to specific operational roles such as absorption, protection, or insulation. Generative AI models, including ChatGPT-4o and DeepSeek R1, assist in systematically mapping these functions across various industries, ensuring a broad exploration of potential applications.

The third phase focuses on application ideation, where identified functions are systematically associated with industry challenges and opportunities. Techniques such as analogy, reverse engineering and combinatorial thinking are employed to generate a range of conventional and novel applications. AI-driven tools further refine these ideas, assessing their feasibility, sustainability and potential impact.

The fourth and final phase involves structured validation through expert assessment. Applications are evaluated based on technical feasibility, innovation level, environmental impact and economic viability. A scoring matrix facilitates prioritization, ensuring that only the most promising solutions proceed to development. High-scoring applications undergo in-depth analysis to identify regulatory, technological, or economic constraints, while lower-scoring applications are refined or integrated with other ideas to enhance viability.

By systematically transforming raw material data into actionable innovation pathways, this framework proposes a rigorous yet adaptable approach to optimizing material reuse.

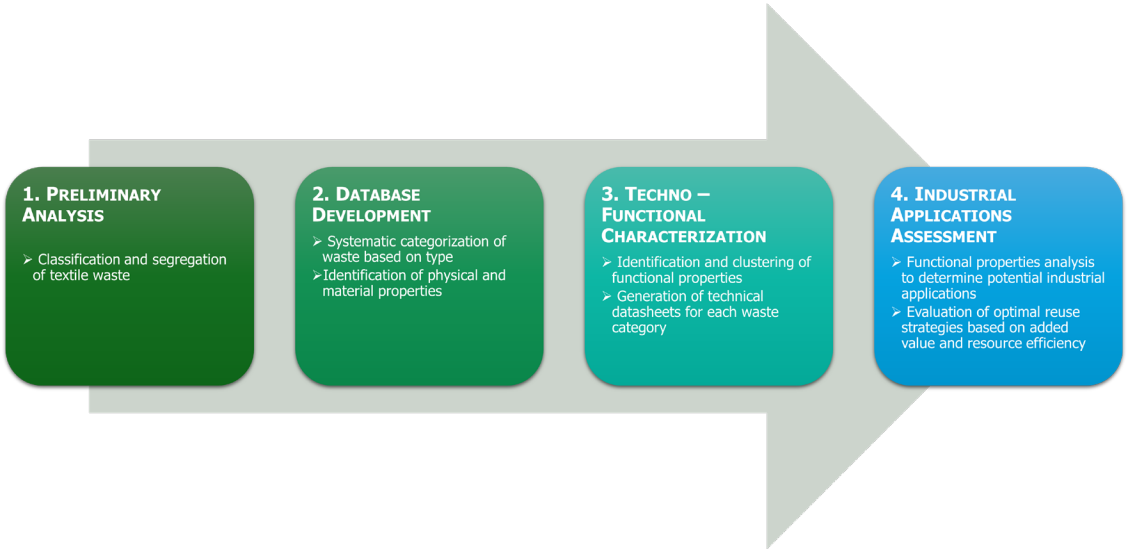


Figure 1 - Framework scheme

Case study

Phase 1: Material characterization and property analysis. The initial phase of systematic characterization of textile waste—fundamental for defining effective industrial symbiosis pathways—involves selecting key material properties to generate a comprehensive profile.

To validate the efficacy of the proposed decision-making framework, a systematic selection process identified a representative denim fabric with specific compositional and structural attributes. The experimental data utilized in this investigation were derived from extant literature documenting comparative performance analyses of denim fabrics manufactured from both rigid and stretch cotton/polyester blended yarns. The investigation examined warp yarns of Ne14/1 (42 tex) comprising 100% cotton and weft yarns of Ne18/1 (33 tex) consisting of cotton-polyester blends in varying proportions, as documented in the aforementioned study [20].

Among the various yarn configurations analyzed, this study specifically focused on rigid yarn with a 75% cotton - 25% polyester blend to evaluate the methodological framework using a

Materials Research Proceedings 57 (2025) 475-483 https://doi.org/10.21741/9781644903735-56

representative blended textile configuration. To ensure methodological validity and consistency, the specimen underwent standardized finishing treatments.

To comprehensively assess the performance characteristics of the selected fabric and evaluate the decision-making framework's capacity to generate targeted recommendations, fifteen critical parameters were systematically characterized (Table 1), encompassing physical, mechanical and comfort-related properties, including dimensional stability, mechanical strength, stiffness and permeability.

Table 1 - Characterization of 75%CO / 25%PES Fabric Blend

PARAMETER	VALUE
Strength (cN/tex)	15,7
Elongation (%)	7,1
Uneveness (%)	10,1
Hairness (H)	6,9
Dry fabric weight (gsm)	248
Washed fabric weight (gsm)	238,6
Warp dimensional changes (%)	-1,2
Weft dimensional changes (%)	3
Warp tensile strenght (Kgf)	58,6
Weft tensile strenght (Kgf)	35,6
Warp tearing strenght (grf)	4827,7
Weft tearing strenght (grf)	4162,3
Stiffness (kg)	0,562
Air permeability (mm/s)	127,4
Water vapor permeability (g/m²/24h)	83,31

The comprehensive analysis conducted on this specific fabric configuration provides the empirical foundation for the subsequent phase, in which the material characteristics will be translated into functional attributes.

Phase 2: Translation of Characteristics into Functions. The transformation of material characteristics into functional attributes is a critical phase in the industrial symbiosis framework, which aims to repurpose textile waste into valuable resources. This framework follows a structured methodology that systematically analyzes material properties through industrial databases and decision-making tools, ensuring a data-driven approach to identifying reuse applications. The process differentiates between primary applications, directly linked to intrinsic properties and secondary applications, emerging from the interaction of multiple characteristics. Furthermore, multifunctionality is considered to identify hybrid applications where materials serve dual roles, such as structural reinforcement combined with energy dissipation.

This framework leverages AI models such as ChatGPT-4o and DeepSeek R1 to enhance the identification and classification of functional attributes. ChatGPT employs a categorical approach, organizing material properties into five primary functional roles: mechanical resistance, thermal comfort, dimensional stability, durability and versatility. In contrast, DeepSeek adopts an application-driven perspective, focusing on industry-specific use cases in technical textiles, sportswear and industrial sectors.

A comparative analysis of these AI models highlights methodological differences within the framework: ChatGPT provides a systematic classification of material properties, enabling structured decision-making, whereas DeepSeek prioritizes practical applications and sector-specific implementations.

Materials Research Proceedings 57 (2025) 475-483 https://doi.org/10.21741/9781644903735-56

Table 2 - Phase 2 output

	ChatGPT 4o		Deepseek R1
Fabric Property	**Primary Function**	**Secondary Function(s)**	**Functions**
Tensile Strength (cN/tex)	Mechanical Resistance	Durability	Mechanical resistance, durability under stress
Tear Strength (grf)	Mechanical Resistance	Stability	Tear resistance, enhanced durability
Elongation (%)	Dimensional Stability	Comfort	Moderate elasticity, adaptability
Unevenness (%)	Durability	Quality Control	Texture variation, aesthetic and functional effects
Hairiness (H)	Durability	Comfort	Surface roughness, friction modulation
Dry Weight (gsm)	Durability	Mechanical Resistance	Moisture absorption, weight consistency control
Wet Weight (gsm)	Moisture Management	Stability	
Shrinkage (%)	Dimensional Stability	Durability	Dimensional stability, resilience to shrinkage
Air Permeability (mm/s)	Thermal Comfort	Breathability	Breathability, air circulation
Vapor Permeability ($g/m^2/24h$)	Thermal Comfort	Moisture Regulation	Moisture management, comfort regulation
Fabric Rigidity (kg)	Mechanical Resistance	Stability	Structural support, reduced flexibility

Phase 3: Identification of Applications for Industrial Symbiosis. This step ensures that waste materials are not only recognized for their functional potential but also aligned with industrial requirements, facilitating their integration into existing production cycles. A structured approach is employed, analyzing potential sectors, evaluating material compatibility and identifying innovation-driven opportunities in industries such as construction, automotive, packaging and filtration.

To optimize application mapping, advanced AI-powered tools, specifically Large Language Models (LLMs) like ChatGPT-4o and DeepSeek R1, play a pivotal role. These models extract industry trends, compare existing solutions and generate insights into emerging application areas. Applications are classified based on feasibility, sustainability and economic viability, employing multi-criteria decision-making techniques to prioritize the most impactful solutions.

The comparative analysis between ChatGPT and DeepSeek revealed differing methodologies. DeepSeek employed a broad, problem-solving strategy, utilizing analogical reasoning and combinatorial approaches to identify cross-sectoral applications in sustainable construction, medical textiles and wearable technology. In contrast, ChatGPT adopted a sector-specific approach, systematically linking material functions to established and emerging applications. While DeepSeek emphasized hybrid applications that integrate multiple material functions, ChatGPT provided direct industry mappings, focusing on traditional and novel product applications.

The insights gained from this phase lay the groundwork for Phase 4, where applications are further evaluated refining their potential for industrial scalability.

Materials Research Proceedings 57 (2025) 475-483 https://doi.org/10.21741/9781644903735-56

Table 3 - Phase 3 output

	ChatGPT 4o		Deepseek R1
Function	**Associated Applications**	**Innovative Applications**	**Associated Applications**
Mechanical Resistance	Durable work uniforms, automotive seat coverings	Technical textiles for trekking footwear	Reinforcements for trekking backpacks, Protective covers for conveyor belts, Padding for bumpers in electric vehicles
Thermal Comfort	Breathable workwear, climate-adaptive bedding	Plastic-free sweat-resistant sportswear	ND
Dimensional Stability	High-quality tailoring fabrics	Sustainable interior linings for electric vehicles	Substrates for digital printing on advertising banners, Reusable tarps for fresh product transport, Outdoor cushions for marine seating
Durability	Resilient outdoor gear	Washable textile filters for ventilation systems	ND
Versatility of Use	Composite textiles for innovative construction materials	Breathable greenhouse covers for agricultural optimization	ND
Breathability	ND	ND	Post-operative breathable suits, Breathable covers for bioclimatic greenhouses, Moisture-resistant cases for musical instruments
Comfort vs Resistance	ND	ND	Children's pants with invisible knee reinforcements, Foldable ergonomic shopping bags, Durable seat coverings for urban transport
Surface Non-Adherence	ND	ND	Anti-static coatings for laboratory floors, Non-slip linings for toolboxes, Separation sheets for 3D printing platforms
Dynamic Adaptation	ND	ND	Soft robotics sensorized gloves, Erosion control nets for agricultural slopes, Thermoregulating textiles for smart clothing

Phase 4: Evaluation. The fourth phase of the framework focuses on validating the proposed applications by assessing their feasibility, innovation potential and alignment with technical, economic and environmental criteria. This stage ensures that the selected applications are viable, novel and suitable for industrial implementation, enhancing their likelihood of market adoption.

The evaluation process begins with the establishment of clear assessment criteria, considering four key aspects: technical feasibility (compatibility with existing technologies), innovation (differentiation from current solutions), environmental impact (waste reduction and sustainability) and economic viability (financial feasibility and scalability). A structured evaluation matrix is then applied, where applications are scored based on these parameters through a collaborative review process. This approach enables a thorough and objective prioritization of the most promising applications.

Following this assessment, high-scoring applications undergo a deeper analysis to identify potential barriers, including technological, regulatory, or economic constraints. Applications with lower scores are reassessed for potential improvements, such as refining their design, integrating additional functionalities, or adapting them for alternative markets. The final selection consolidates the strongest applications into a strategic development plan, outlining key market opportunities and implementation pathways.

Materials Research Proceedings 57 (2025) 475-483 https://doi.org/10.21741/9781644903735-56

Table 6 presents the ten applications that achieved the highest evaluation scores. Additional applications were subjected to identical assessment protocols but received lower numerical ratings across the established criteria. Despite their lower overall performance metrics, several of these secondary applications demonstrate distinctive functionalities or exhibit substantial development potential for specific industrial implementation contexts.

Table 4 - Evaluation of individual applications

Applications	Feasibility	Innovativeness	Environmental Impact	Economic Impact	Total
Sustainable padding and interior linings for electric vehicles	4	4	5	3	16
Children's pants with invisible knee reinforcements	5	2	4	4	15
Composite textiles for innovative construction materials	3	4	5	3	15
Technical textiles for trekking footwear	4	4	4	3	15
Washable textile filters for ventilation systems	4	4	4	3	15
Anti-static coatings for laboratory floors	4	3	3	4	14
Climate-adaptive bedding	4	3	4	3	14
Moisture-resistant cases for musical instruments	4	3	4	3	14
Reinforcements for trekking backpacks	4	3	4	3	14
Reusable tarps for fresh product transport	4	2	4	4	14

Results and Conclusions

This study introduces a four stage framework on a sample of denim (75 % cotton, 25 % polyester), characterizing fifteen material parameters *(see Table 1)*. In Stage 2, these parameters were mapped to six key performance functions—mechanical strength, tear resistance, elasticity, breathability, dimensional stability, and moisture management, using ChatGPT 4o and DeepSeek R1, yielding over 90 % concordance with expert assessments. During Stage 3, twenty-five candidate second life applications were generated and subsequently filtered across fourteen distinct industrial scenarios. In Stage 4, a multi criteria evaluation matrix *(Table 6)* scored each option on technical feasibility, innovation potential, environmental impact, and economic viability, ultimately identifying ten applications with a score of 15 or higher out of 20. The most promising outcome—sustainable interior linings for electric vehicles—achieved 16/20, driven by optimal tensile strength (15.7 cN/tex) and tear resistance (4827.7 grf) compliant with automotive standards. Childrenswear trousers with concealed knee reinforcements scored 15/20, demonstrating durability and comfort over more than 100 standard wash cycles. Similarly, washable textile filters and composite construction materials each secured a 15/20 rating, indicating strong scalability prospects. Beyond pinpointing high value reuse pathways, our approach quantifies associated environmental benefits, laying the groundwork for industrial scale implementation.

Next steps include pilot trials of the top three applications in partnership with industry stakeholders, augmented by blockchain enabled traceability systems and life cycle assessments to ensure process transparency and continuous optimization.

References

[1] J. Ehrenfeld, N. Gertler, and T. Business, "The Evolution of Interdependence at Kalundborg," 1997.

[2] M. R. Chertow, "Industrial symbiosis: Literature and taxonomy," *Annual Review of Energy and the Environment*, vol. 25, pp. 313–337, 2000. https://doi.org/10.1146/annurev.energy.25.1.313

[3] Y. Geng, J. Fu, J. Sarkis, and B. Xue, "Towards a national circular economy indicator system in China: An evaluation and critical analysis," *J Clean Prod*, vol. 23, no. 1, pp. 216–224, Mar. 2012. https://doi.org/10.1016/j.jclepro.2011.07.005

[4] J. Zhu and M. Ruth, "Exploring the resilience of industrial ecosystems," *J Environ Manage*, vol. 122, pp. 65–75, Jun. 2013. https://doi.org/10.1016/j.jenvman.2013.02.052

[5] M. A. Franco, "Circular economy at the micro level: A dynamic view of incumbents' struggles and challenges in the textile industry," *J Clean Prod*, vol. 168, pp. 833–845, Dec. 2017. https://doi.org/10.1016/j.jclepro.2017.09.056

[6] A. Urbinati, D. Chiaroni, V. Chiesa, and F. Frattini, "The role of digital technologies in open innovation processes: an exploratory multiple case study analysis," in *R and D Management*, Blackwell Publishing Ltd, Jan. 2020, pp. 136–160. https://doi.org/10.1111/radm.12313

[7] B. Ütebay, P. Çelik, and A. Çay, "Textile Wastes: Status and Perspectives," in *Waste in Textile and Leather Sectors*, IntechOpen, 2020. https://doi.org/10.5772/intechopen.92234

[8] Deckers J., Manshoven S., and Fogh Mortensen L., "The role of bio-based textile fibres in a circular and sustainable textiles system," May 2023. [Online]. Available: https://www.eionet.europa.eu/etcs/etc-ce

[9] K. Niinimäki, G. Peters, H. Dahlbo, P. Perry, T. Rissanen, and A. Gwilt, "The environmental price of fast fashion," Apr. 01, 2020, *Springer Nature*. https://doi.org/10.1038/s43017-020-0039-9

[10] M. D. Stanescu, "State of the art of post-consumer textile waste upcycling to reach the zero waste milestone," *Environmental Science and Pollution Research*, vol. 28, pp. 14253–14270, 2021. https://doi.org/10.1007/s11356-021-12416-9/Published

[11] L. C. Aguilar Esteva, A. Kasliwal, M. S. Kinzler, H. C. Kim, and G. A. Keoleian, "Circular economy framework for automobiles: Closing energy and material loops," *J Ind Ecol*, vol. 25, no. 4, pp. 877–889, Aug. 2021. https://doi.org/10.1111/jiec.13088

[12] A. Almusaed, I. Yitmen, J. A. Myhren, and A. Almssad, "Assessing the Impact of Recycled Building Materials on Environmental Sustainability and Energy Efficiency: A Comprehensive Framework for Reducing Greenhouse Gas Emissions," *Buildings*, vol. 14, no. 6, Jun. 2024. https://doi.org/10.3390/buildings14061566

[13] Bragança L. *et al.*, *Circular Economy Design and Management in the Built Environment*. in Springer Tracts in Civil Engineering. Cham: Springer Nature Switzerland, 2025. https://doi.org/10.1007/978-3-031-73490-8

[14] R. Minunno, T. O'Grady, G. M. Morrison, R. L. Gruner, and M. Colling, "Strategies for applying the circular economy to prefabricated buildings," *Buildings*, vol. 8, no. 9, 2018. https://doi.org/10.3390/buildings8090125

[15] E. M. Medina, F. Fu, and F. Fu, "A new circular economy framework for construction projects," *Proceedings of the Institution of Civil Engineers: Engineering Sustainability*, vol. 174, no. 6, pp. 304–315, Apr. 2021. https://doi.org/10.1680/jensu.20.00067

[16] L. G. L. M. Edirisinghe, A. A. P. de Alwis, and M. Wijayasundara, "Sustainable circular practices in the textile product life cycle: A comprehensive approach to environmental impact mitigation," *Environmental Challenges*, vol. 16, Aug. 2024. https://doi.org/10.1016/j.envc.2024.100985

[17] G. Finch, G. Marriage, A. Pelosi, and M. Gjerde, "Building envelope systems for the circular economy; Evaluation parameters, current performance and key challenges," *Sustain Cities Soc*, vol. 64, Jan. 2021. https://doi.org/10.1016/j.scs.2020.102561

[18] I. Ervasti, R. Miranda, and I. Kauranen, "Paper recycling framework, the 'Wheel of Fiber,'" *J Environ Manage*, vol. 174, pp. 35–44, Jun. 2016. https://doi.org/10.1016/j.jenvman.2016.03.004

[19] L. G. L. M. Edirisinghe, A. A. P. de Alwis, S. Prakash, and M. Wijayasundara, "Optimizing material circularity pathways in industrial waste streams: A decision-making model," *MethodsX*, vol. 13, Dec. 2024. https://doi.org/10.1016/j.mex.2024.102813

[20] M. A. Shahid, N. Okyay, and O. Babaarslan, "A Comparative Analysis of Denim Fabric Performances from Cotton/Polyester Blended Rigid and Stretched Yarns," *Fibers*, vol. 12, no. 10, Oct. 2024. https://doi.org/10.3390/fib12100086

Materials Research Proceedings 57 (2025) 484-492 https://doi.org/10.21741/9781644903735-57

Thermal and Joule effect debonding techniques: Evaluation of mechanical strength and LCA analysis of bonded joints

Matteo Benvenuto[1,a *], Enrico Lertora[1,b], Marco Pizzorni[1,c], Luigi Benvenuto[1,d], Alessia Lusiani[2,e], Chiara Mandolfino[1,f]

[1]Department of Mechanical Engineering, Polytechnic School of University of Genoa, Via opera pia 15, 16145, Genoa, Italy

[2]University of Genoa, Via Balbi 5, 16126 Genoa, Italy

[a]matteo.benvenuto@edu.unige.it, [b]enrico.lertora@unige.it, [c]marco.pizzorni@unige.it, [d]luigi.benvenuto@edu.unige.it, [e]alessia.lusiani@gmail.com, [f]chiara.mandolfino@unige.it

Keywords: Demanufacturing Processes, Debonding, Lifecycle Assessment

Abstract. Bonded joints play a crucial role in various engineering applications, particularly in aerospace, automotive, and structural industries, where they provide lightweight and high-strength connections. However, their permanent nature poses challenges when disassembly is required for maintenance, repair, or recycling. Efficient debonding techniques are essential to enable disassembly while minimizing damage to the substrates, preserving material integrity, and reducing environmental impact. Among the available methods, thermal debonding and Joule heating represent promising approaches, as they allow for localized heating, weakening the adhesive without excessive degradation of the substrate. These techniques leverage controlled temperature increases to reduce the adhesive's strength, facilitating joint separation. The effectiveness of these methods depends on several factors, including adhesive type, substrate material, and process parameters such as temperature, heating rate, and exposure duration. A comprehensive evaluation of these debonding strategies is essential to identify those that ensure structural integrity, ease of disassembly, and sustainability. This study focuses on thermal and Joule heating debonding techniques applied to aluminium substrates. The selected methods demonstrated a reduction of at least 75% in tensile shear stress at failure, enabling easy hand disassembly. Furthermore, the environmental sustainability of these solutions was assessed through a Life Cycle Assessment (LCA) to identify the techniques with the lowest environmental impact.

Introduction

The responsible use of natural resources and environmental protection have become imperative across the Western world. In particular, the European Union has placed environmental sustainability at the core of its policies through the 2019 "Green Deal," which addresses various aspects such as climate change, resource management, pollution, and circular economy principles [1], [2]. The EU's environmental policy is based on four fundamental principles: precaution (avoiding potentially harmful actions in the absence of scientific certainty), prevention (anticipating and mitigating environmental damage), pollution control at the source (direct intervention on the problem), and the "polluter pays" principle (assigning remediation costs to those responsible) [3]. Consequently, the recycling and reuse of materials, particularly those that are poor in nature, have become a priority for many nations, especially those lacking significant raw material reserves or recognizing that recycling generally leads to both economic savings and a reduction in environmental pollution [4].

This philosophy is also applicable to adhesive bonding, where research efforts continue to focus on recyclability [5], [6]. Although adhesive bonding provides an effective solution for joining

Content from this work may be used under the terms of the Creative Commons Attribution 3.0 license. Any further distribution of this work must maintain attribution to the author(s) and the title of the work, journal citation and DOI. Published under license by Materials Research Forum LLC.

Materials Research Proceedings 57 (2025) 484-492 https://doi.org/10.21741/9781644903735-57

materials, it presents challenges when disassembly is required during a product's lifecycle. As the industrial sector shifts away from the extractive model of "take, make, dispose" -which results in a continuous loss of valuable materials due to the abundance and low cost of natural resources- toward embracing circular economy principles, it becomes crucial to integrate debonding techniques at the design stage. These techniques enable the transformation of waste generated in one phase of a product's lifecycle into resources for another, thus promoting sustainability. To enhance the product lifecycle, greater attention must be given to debonding technologies, tools, and techniques during the design phase. The primary goal of debonding is to recover as many components as possible from an assembly without causing damage to the parts, the environment, or personnel, while minimizing or eliminating adhesive residues from surfaces and avoiding the use of excessively expensive tools or technologies [7].

Debonding techniques are classified based on the applied energy and the detachment mechanism. One of the most employed methods is mechanical separation, which exploits critical stresses such as peel stress and cleavage. However, this approach is generally ineffective for structural adhesives, as it tends to damage the substrates and leaves adhesive residues [8]. Conversely, thermal debonding utilizes temperature increases to reduce adhesive strength, with subsequent removal of residues through mechanical abrasion [9]. A hybrid variant is thermo-mechanical debonding, which combines heat and applied load and requires an understanding of the mechanical properties of materials as a function of temperature. An example of this is thermal-peel debonding, where the adhesive is heated beyond its glass transition temperature, making it more ductile and facilitating its removal [10].

This paper focuses on two specific debonding techniques, thermal debonding and Joule-effect debonding, to assess the recyclability potential of bonded joints. The evaluations were conducted through lap shear strength tests and Life Cycle Assessment (LCA) analyses to determine the environmental sustainability of the proposed debonding solutions.

Experimental details

The debonding analysis was conducted by evaluating disassembly techniques that could be easily applied in a short time, that required low energy consumption and that could be operated manually without the use of tools or instruments, preserving the integrity of the substrate. The essential condition was that the strength of the joint created with the selected adhesive remained unchanged or varied only slightly from a standard joint, even with design modifications to facilitate subsequent disassembly. The debonding techniques investigated in this study are summarised in Figure 1 and were performed on single-lap joints with a bonding area of 25 x 12.5 mm, following the guidelines of ASTM D1002 [11]. All substrates were made of 6061 T6 aluminium alloy with a thickness of 1.6 mm. Additionally, to perform Joule heating-based disassembly, it was necessary to introduce an electrically and thermally conductive element at the adhesive layer during the bonding process. Specifically, two materials were employed in this experimental campaign: a 304 stainless steel mesh consisting of 0.05 mm diameter wires with a 0.1 mm mesh opening and a carbon fibre tape with a thickness of 0.1 mm, cut to match the width of the overlap area. Their selection was also motivated by the ease with which they can be incorporated into the bonded joint during the bonding process. The adhesive selected for this study was 3M™ DP490, a two-component thixotropic structural epoxy resin prepared with a 2:1 mixing ratio.

Materials Research Proceedings 57 (2025) 484-492 https://doi.org/10.21741/9781644903735-57

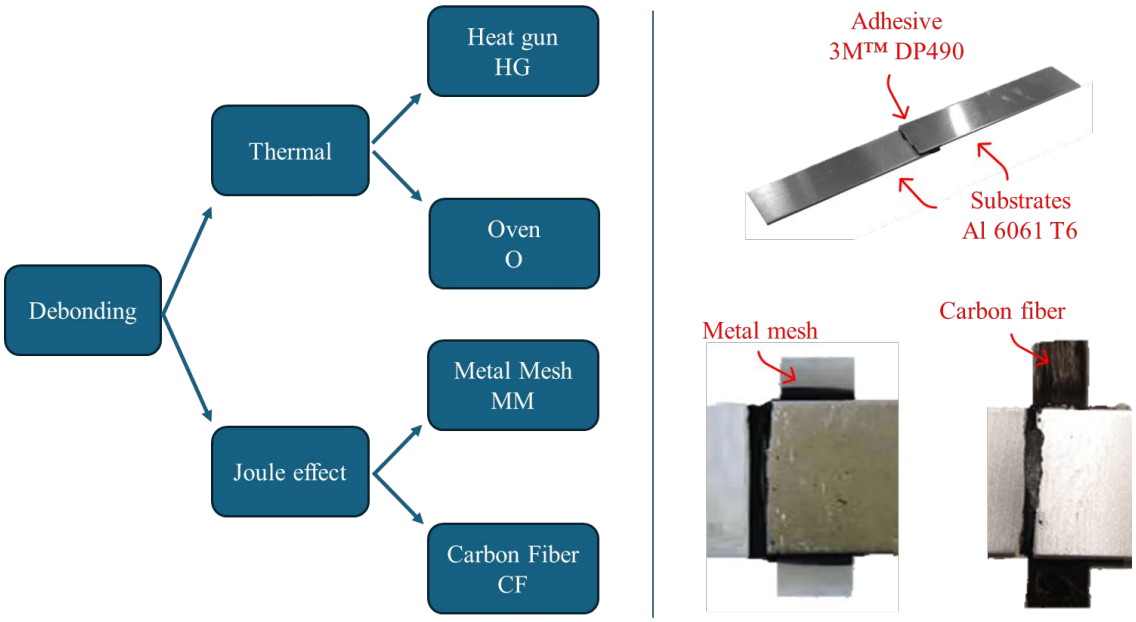


Figure 1 - The debonding techniques analysed in this study: summary diagram and joint structure.

Adhesive bonding. Prior to bonding, all substrates were degreased using acetone-soaked absorbent paper, followed by manual abrasion with 3M™ Scotch Brite™ MX-SR to increase surface roughness and promote mechanical interlocking with the resin. After a second acetone cleaning to remove any surface residues, the overlap area of the joint was delineated using masking tape to ensure precise area identification and proper adhesive application. Additionally, all elements to be incorporated into the bonding area (metal mesh and carbon fibre tape) were cleaned with acetone.

The two adhesives were then overlapped after inserting carbon fibre tape or wire mesh where necessary, and pressure was applied to eject the excess adhesive. The latter was subsequently removed to shape the fillet, thereby preventing stress concentrations at the extremities of the bonded area. Immediately after, the joint was loaded with appropriately sized weights to maintain correct alignment between the parts and apply the necessary pressure to assist curing. To achieve complete hardening, the joints were left at room temperature for 24 hours, followed by a post-curing treatment in an oven at 80°C for 1 hour.

Debonding. Two strategies were adopted for debonding: the first involved thermal detachment using hot air (via an AEG HG 600V heat gun or a Memmert UF260plus oven), while the second relied on Joule heating by using a metal mesh strip or a carbon fibre tape as conductors.

For detachment using the heat gun, the device was held above the overlap area of the joint at 10-20 cm. Throughout the heating process, the joint temperature was continuously monitored via a thermocouple to ensure it remained within the 130-200°C range. For the oven tests, the temperature was set to 180°C for 20 minutes to ensure that the joint reached a temperature consistent with the range used for the heat gun application. Joule heating-based debonding tests were conducted by connecting a DC power supply (IPSXP™ KPS1203D) to the metal mesh or carbon fibre tape, while the temperature was monitored using a thermocouple.

Table 1 lists the main parameters employed in the four different test cases, which were derived from preliminary experiments conducted in advance.

Materials Research Proceedings 57 (2025) 484-492 https://doi.org/10.21741/9781644903735-57

Table 1 - Parameters set for the debonding processes performed

Joint type	***t [min]***	***T [°C]***	***V [V]***	***I [A]***
Heat gun	5	< 200	-	-
Oven	20	180	-	-
Metal mesh	10	130	3.3-4.0	10.3
Carbon fibre	0.5	< 200	16	8.38

Mechanical testing. The reduction in mechanical resistance was quantified through lap-shear strength tests. To evaluate the impact of the adopted debonding solutions, tests were performed on two batches of specimens: one tested immediately after bonding and the other after undergoing the debonding process.

To ensure uniform initial conditions of the samples before mechanical testing, all joints were conditioned for 24 hours in a WEISS WK3 340 climatic chamber at a temperature of 23°C and a relative humidity of 50%. Subsequently, tensile tests were performed under standard laboratory conditions (T = 23 ± 2°C, RH = 40 ± 5%) using an Instron 8802 servo-hydraulic testing machine equipped with a 50 kN load cell.

To prevent specimen slippage during crosshead movement and, if necessary, ensure proper load alignment, each specimen was equipped with gripping tabs (25 mm × 25 mm). The specimens were then secured in the hydraulic grips of the testing machine, and the test was conducted at a crosshead displacement rate of 1.3 mm/min until joint failure, following ASTM D1002 guidelines [11]. Data acquisition was managed via Bluehill® software. The mean values of the maximum failure load, F, and the corresponding standard deviation were determined by testing three replicates for each joint series (N = 3).

Life Cycle Assessment. Environmental sustainability was assessed through a Life Cycle Assessment (LCA) conducted using SimaPro 9.6.0 (Analyst), in accordance with EN ISO 14040 and 14044 standards [12], [13]. The functional unit was defined as ten single-lap adhesive joints, each exhibiting a stress reduction of at least 75%. This number was selected to maximize the operational efficiency of the debonding equipment.

The system boundaries included the production and end-of-life phases, while the use, maintenance, and transport stages were excluded, assuming they were identical across all joint configurations. A cradle-to-cradle approach was applied to all scenarios involving material recovery after debonding, encompassing both production and reuse phases. An exception was made for the no-debonding (ND) scenario, modelled with a cradle-to-grave perspective. In this case, the system covered extraction, manufacturing and final disposal at waste collection facilities with no recycling stage. Including this scenario enabled direct comparison with debonding-enabled configurations, highlighting the environmental advantages of reuse.

The Life Cycle Inventory (LCI) was developed through a comprehensive input-output analysis of all processes within the defined system boundaries. Wherever possible, primary data measured in the laboratory were employed. When unavailable, secondary data were sourced from literature or from SimaPro's internal databases, with priority given to the Ecoinvent 3.9.1 database (allocation, cut-off by classification) [14]. Material and consumable masses (including aluminium substrates, DP490 adhesive, stainless steel mesh, carbon fiber tape, acetone, blotting paper, and abrasives) were measured using laboratory precision scales. Energy consumption during disassembly was recorded with a power meter Ketotek KTEM02. Since the adhesive was not available in Ecoinvent, a custom inventory was created based on its material safety data sheet [15], considering only substances exceeding 2% by mass. Similarly, carbon fibre tape was modelled

Materials Research Proceedings 57 (2025) 484-492 https://doi.org/10.21741/9781644903735-57

following a literature-based process, including PAN (polyacrylonitrile) precursor synthesis from acrylonitrile, followed by stabilization and carbonization steps [16].

All pre-bonding surface preparation steps were also accounted for in the LCI. These included degreasing with acetone-soaked paper, manual abrasion using 3M™ Scotch-Brite™ MX-SR pads, second acetone cleaning, masking of the bonding area, and acetone cleaning of the inserts. Quantitative data were collected for all materials used in these operations.

At the end-of-life stage, the aluminium substrate was assumed to be 99% reusable, while the DP490 adhesive and carbon fibre were treated as non-recyclable waste. The stainless-steel mesh was considered 80% reusable. Energy consumption for the debonding process varied by technique, ranging from 1.412 kWh (thermal oven) to 0.001 kWh (Joule-effect debonding with carbon fibre inserts).

Environmental impact assessment was carried out using the ReCiPe 2016 Endpoint H method, considering all midpoints as defined by the methodology. Results were expressed in millipoints [mPt] and are directly comparable with values reported in the scientific literature [17].

Result and discussion

Mechanical results: Table 2 and Figure 2 present the shear strength values of the joints before and after debonding, following the previously described methods. The effectiveness of the process was assessed by determining the percentage reduction in strength.

Table 2 – Comparison of the mechanical shear strengths of bonded joints before and after the debonding operation.

DEBONDING TYPE	***SHEAR STRENGTH [MPA]***		***DECREASE***
	Predebonding	***Postdebonding***	***[%]***
HEAT GUN	24.3 ± 2.80	4.93 ± 1.64	-79.7%
OVEN	24.3 ± 2.80	5.93 ± 1.92	-75.5%
METAL MESH	25.5 ± 2.58	6.11 ± 2.11	-76.0%
CARBON FIBRE	19.0 ± 0.73	3.96 ± 0.87	-79.2%

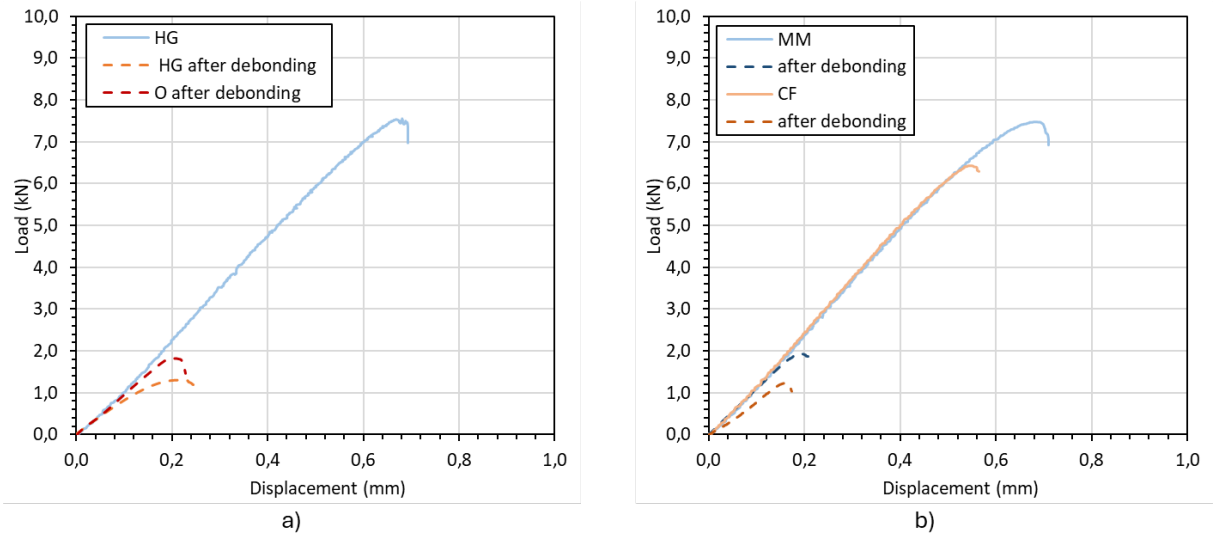


Figure 2 - Mechanical characteristic decreasing before and after debonding operation in cases of thermal (a) and Joule effect debonding (b).

For the thermally debonded joints, the batch that did not undergo any debonding process showed an average shear strength of 24.3 MPa. In contrast, the joints modified with a metal mesh showed

Materials Research Proceedings 57 (2025) 484-492 https://doi.org/10.21741/9781644903735-57

an increase in strength to 25.5 MPa, suggesting that the mesh helped to improve the anchorage of the adhesive through a mechanical interlocking effect (Fig. 3a). In particular, the adhesive penetrated the openings of the mesh, improving load distribution and reducing the tendency of the fracture to deadhesion phenomena. In contrast, joints containing carbon fibre showed a reduction in strength at 19.0 MPa, indicating that the addition of the carbon fibre tape hindered proper adhesion between the adhesive and the substrates. The analysis of the fracture surface revealed a distinct behaviour compared to the other two cases: the insufficient resin impregnation of the carbon fibres led to a premature detachment of the adhesive, resulting in a predominantly deadhesive failure mode (Fig. 3b). In addition, the transverse orientation of the fibres with respect to the loading direction negatively affected the performance of the joint, reducing the effectiveness of the adhesive bond.

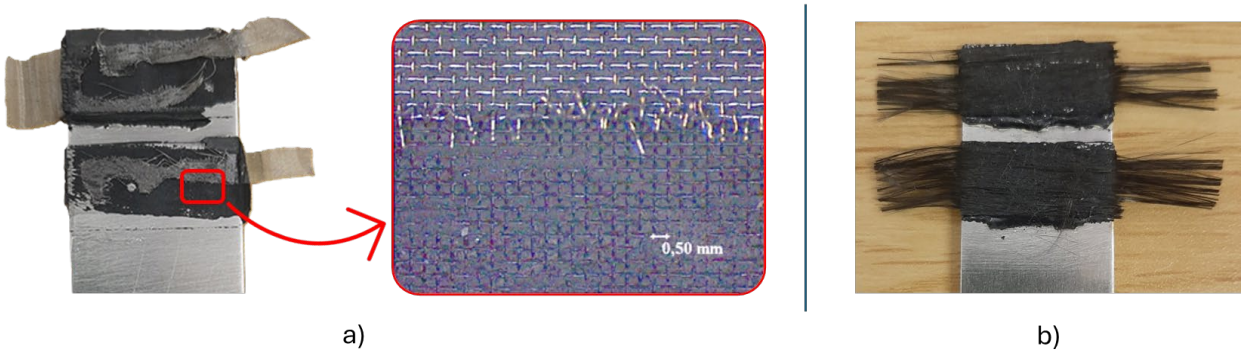


Figure 3 - Fracture surfaces typically manifested with Joule effect debonding: Metal Mesh MM (a) and Carbon Fibre CF (b)

The debonding tests confirmed that all the applied techniques led to a significant reduction in shear strength, with decreases exceeding 75%. The paint remover, applied under the previously described conditions, resulted in the greatest reduction, with a 75.5% decrease in strength. Similarly, heat treatment in an oven at 180°C for 20 minutes proved highly effective, achieving a comparable 75.5% reduction in just 5 minutes. For the joints with metal mesh and carbon fibre, debonding was particularly effective, with strength reductions of 76.0% and 79.2%, respectively. It was also observed that in cases where manual disassembly was performed, bending or cleavage forces were often applied, altering the joint's behaviour compared to standard loading conditions. These findings suggest that the incorporation of a metal mesh not only enhances the mechanical strength of the joint but also facilitates controlled debonding. In contrast, while carbon fibre provides a reasonable level of strength, it proves less effective both in terms of adhesion and controlled removal.

LCA results. Concerning the environmental sustainability analysis, Table 3 presents the main midpoints values for all analysed cases, together with the final score, obtained from the sum of all contributions. Data show that the scenario without debonding (ND) is the most impactful, with the highest overall score, since, in this mode, no reuse of the joint takes place. As expected, in the cases where debonding was performed, the millipoint scores were significantly lower, with the lowest values recorded in the Joule effect debonding scenarios: precisely 7.93 for metal mesh and 7.28 for carbon fibre.

Materials Research Proceedings 57 (2025) 484-492 https://doi.org/10.21741/9781644903735-57

Table 3 – Distribution of the main midpoints for the five cases analysed: joints with no debonding (NG), with debonding by hot gun (HG) and oven (O) and with debonding by Joule effect through metal mesh (MM) and carbon fibre (CF).

Characterization factors	***ND***	***HG***	***O***	***MM***	***CF***
GWP, HH	30.12	6.84	11.21	3.25	3.02
PMFP	41.64	4.30	7.20	1.93	1.75
HTPc	21.73	1.04	1.62	0.57	0.53
HTPnc	11.45	2.49	3.61	1.57	1.49
FFP	0.73	0.38	0.57	0.21	0.21
Others	2.94	0.71	1.19	0.40	0.28
Total	108.59	15.76	25.40	7.93	7.28

Regarding the global warming potential and impact on human health (GWP-HH), the case without debonding (ND) showed the highest value (30.12), while the configurations with debonding showed a significant reduction, with the lowest value of 3.02 for the carbon fibre debonding. A similar trend was also observed in the PMFP, where the ND case reached a value of 41.64, significantly higher than the other scenarios, confirming a higher environmental impact.

The HTPc and HTPnc, which quantify carcinogenic and non-carcinogenic human toxicity respectively, show a marked difference between the ND case and the other scenarios. For the HTPc, the ND value (21.73) is about 20 times higher than for the Joule effect debonding cases, while for the HTPnc, although the difference is smaller, it is still significant (11.45 for ND versus values between 2.49 and 1.49 in the other scenarios). Fossil fuel consumption (FFP) follows a similar trend: the ND case has the highest value (0.73), while a significant reduction is observed in the other scenarios, with values close to zero.

Taken as a whole, the analysis shows that the scenarios in which electricity was applied in the joint are the most sustainable, with the lowest overall environmental impact. These results suggest that the strategies adopted in these cases can contribute significantly to the reduction of emissions and associated negative effects. On the contrary, cases where hot gun or oven was used scored less favourably, negatively influenced by the GWP-HH category due to higher electricity consumption. However, it is important to emphasise that, even in these scenarios, the scores in the various categories were always lower than in the case without debonding (ND).

Table 4 presents the values assumed by the different endpoint categories for the five analysed cases.

Table 4 – Endpoints for joints with no debonding (NG), with debonding by hot gun (HG) and oven (O) and with debonding by Joule effect through metal mesh (MM) and carbon fibre (CF).

Endpoint	***ND***	***HG***	***O***	***MM***	***CF***
Human health	105.33	14.86	23.98	7.46	6.84
Ecosystems	2.50	0.52	0.84	0.26	0.23
Resources	0.76	0.38	0.58	0.21	0.21
Total	108.59	15.76	25.40	7.93	7.28

As observed, regardless of the specific debonding scenario examined, the most influential endpoint is human health. This result is primarily due to the significant electricity consumption required by all the considered methods, as well as the substrate cleaning procedures during the bonding phase.

When analysing the behaviour of the different joint configurations, the control series (ND) exhibits the highest impact across all evaluated endpoints. Notably, its effect on human health is significantly greater than that of the other series. Additionally, in terms of ecosystem and resource

impacts, this joint type shows higher values, although the difference is less pronounced compared to the human health category.

The series in which an oven or a hot gun was used show an intermediate influence, with a relevant impact but significantly lower than the ND joint, especially regarding human health. The most favourable results were obtained in both Joule-heating-based debonding cases, which recorded the lowest values across all impact categories analysed.

Conclusion

This study investigated the efficiency and environmental sustainability of thermal and Joule-effect debonding techniques applied to bonded aluminium joints. The results demonstrated that all tested debonding methods significantly reduced the shear strength of the joints by at least 75%, allowing for efficient manual disassembly without compromising substrate integrity.

From a mechanical perspective, the introduction of a metal mesh within the bonded joint not only facilitated Joule heating but also improved initial shear strength due to mechanical interlocking. Conversely, the inclusion of a carbon fibre tape slightly reduced the initial bond strength, likely due to inadequate adhesion between the adhesive and carbon fibres. Nevertheless, both conductive materials enabled effective Joule heating-based debonding, confirming their suitability for sustainable disassembly.

The Life Cycle Assessment results revealed that the most environmentally sustainable debonding methods were those utilizing Joule heating, particularly with carbon fibre and metal mesh conductors. These techniques exhibited the lowest overall environmental impact, as indicated by significantly reduced values in global warming potential, human health impact, and fossil fuel consumption. Traditional thermal methods, such as heat gun and oven heating, while effective, were associated with higher energy consumption and environmental burdens. However, it is important to note that the environmental impact values associated with oven heating are higher than those of other debonding techniques. This can be attributed, at least in part, to the limited number of samples (10) considered in the analysis for this method. A larger sample size would likely provide a more representative evaluation, potentially influencing the midpoint and endpoint impact on values.

Overall, the findings support the adoption of Joule heating-based debonding as a viable, sustainable alternative to traditional thermal debonding techniques. Implementing such approaches in industrial applications could enhance material recyclability, reduce environmental impact, and facilitate the transition toward a circular economy. Future research should explore the scalability of these methods in different adhesive-substrate combinations and assess their applicability in real-world manufacturing and recycling scenarios. Moreover, further investigation should focus on the topic of rebonding, particularly identifying the most effective resin removal methodologies after disassembly and evaluating the performance of re-bonded joints.

References

[1] E. Trincado, A. Sánchez-Bayón, and J. M. Vindel, “The European union green deal: Clean energy wellbeing opportunities and the risk of the Jevons paradox,” Energies (Basel), vol. 14, no. 14, 2021. https://doi.org/10.3390/en14144148

[2] E. Eckert and O. Kovalevska, “Sustainability in the European Union: Analyzing the Discourse of the European Green Deal,” Journal of Risk and Financial Management, vol. 14, no. 2, 2021. https://doi.org/10.3390/jrfm14020080

[3] Christian Kurrer and Alyssia Petit, “Environment policy: general principles and basic framework.” Accessed: Feb. 09, 2025. [Online]. Available: https://www.europarl.europa.eu /factsheets/en/sheet/71/environment-policy-general-principles-and-basic-framework

[4] I. Anastopoulos, E. Bontempi, M. Coccia, M. Quina, and M. Shaaban, “Sustainable strategic materials recovery, what’s next?,” Next Sustainability, vol. 1, 2023. https://doi.org/10.1016/j.nxsust.2023.100006

[5] N. Boix Rodríguez, F. Moroni, A. H. A. Lutey, and C. Favi, “Sustainable design and life cycle engineering of adhesive joints for polymeric products: assessment of surface activation technologies,” International Journal of Advanced Manufacturing Technology, vol. 130, no. 3–4, 2024. https://doi.org/10.1007/s00170-023-12717-y

[6] K. R. Mulcahy, A. F. R. Kilpatrick, G. D. J. Harper, A. Walton, and A. P. Abbott, “Debondable adhesives and their use in recycling,” 2022. https://doi.org/10.1039/d1gc03306a

[7] O. Battaïa, A. Dolgui, S. S. Heragu, S. M. Meerkov, and M. K. Tiwari, “Design for manufacturing and assembly/disassembly: joint design of products and production systems,” 2018. https://doi.org/10.1080/00207543.2018.1549795

[8] A. C. Marques et al., “Review on adhesives and surface treatments for structural applications: Recent developments on sustainability and implementation for metal and composite substrates,” 2020. https://doi.org/10.3390/ma13245590

[9] O. Kachouri, J. Bardon, D. Ruch, and A. Laachachi, “Use of intumescent flame-retardant systems in epoxy adhesives for debonding purpose,” Heliyon, vol. 10, no. 3, 2024. https://doi.org/10.1016/j.heliyon.2024.e25240

[10] D. Vadugappatty Srinivasan and S. Idapalapati, “Thermo-mechanical debonding map for repairing composite–metal adhesive joints,” J Adhes Sci Technol, vol. 35, no. 1, 2021. https://doi.org/10.1080/01694243.2020.1785991

[11] “Test Method for Apparent Shear Strength of Single-Lap-Joint Adhesively Bonded Metal Specimens by Tension Loading (Metal-to-Metal),” Apr. 01, 2019, ASTM International, West Conshohocken, PA. https://doi.org/10.1520/D1002-10R19

[12] Environmental management -- Life cycle assessment -- Principles and framework. BSI Standards Limited, 2020.

[13] Environmental management. Life cycle assessment. Requirements and guidelines. British Standards Institution, 2021.

[14] Ecoinvent, “System Models.” [Online]. Available: https://support.ecoinvent.org/system-models

[15] “3MTM Scotch-WeldTM DP-490 Safety Data Sheet.” [Online]. Available: https://multimedia.3m.com/mws/mediawebserver?mwsId=SSSSSuUn_zu8lAGU4Y_xM8teMv70k17zHvu9lxtD7SSSSSS--

[16] A. Forcellese, M. Marconi, M. Simoncini, and A. Vita, “Life cycle impact assessment of different manufacturing technologies for automotive CFRP components,” J Clean Prod, vol. 271, 2020. https://doi.org/10.1016/j.jclepro.2020.122677

[17] M. A. J. Huijbregts et al., “ReCiPe2016: a harmonised life cycle impact assessment method at midpoint and endpoint level,” International Journal of Life Cycle Assessment, vol. 22, no. 2, pp. 138–147, Feb. 2017. https://doi.org/10.1007/s11367-016-1246-y

Materials Research Proceedings 57 (2025) 493-501 https://doi.org/10.21741/9781644903735-58

Fostering sustainability-oriented product innovation: A comprehensive framework to support product development for a circular economy

Luigi PANZA[1,a *], Giulia BRUNO[1,b] and Paolo CHIABERT[1,c]

[1]Department of Management and Production Engineering, Politecnico di Torino, 10129, Turin, Italy

[a]luigi.panza@polito.it, [b]giulia.bruno@polito.it, [c]paolo.chiabert@polito.it

Keywords: Product Development, Product Design, Product Lifecycle, Product Lifecycle Management, Circular Economy

Abstract. Although the Circular Economy (CE) is widely recognized as a fundamental strategy for addressing environmental challenges, its adoption remains limited. A key barrier to its implementation is the lack of effective tools to support product development aligned with CE principles. This study presents a comprehensive framework to support the product development process for a CE. Specifically, a decision tree is employed to quantitatively define product requirements necessary to achieve targeted economic and environmental performance. Design guidelines are then collected through a literature review and allocated to the corresponding phases of product development, enabling practitioners to meet the defined product requirements. By integrating quantitative product requirements with actionable design recommendations, this framework provides a practical tool to align product development with the CE paradigm and drive sustainability-oriented product innovation.

Introduction

Circular Economy (CE) is widely recognized to be a potential solution to address climate change and its associated environmental challenges [1]: unlike the traditional linear economy (LE) where resources are extracted, used, and then discarded as waste, CE focuses on preserving products, components, and materials in the value chains as long as possible, enabling to decouple economic growth from resource consumption [2]. Indeed, a circularity adoption of 17% is reported to align the temperature increase with the targets set by the Paris Agreement, thus contributing significantly to climate change mitigation [3]. Nevertheless, the CE adoption is far from that target and it is even experiencing a decreasing trend, with the global circularity adoption level that has shrunk from 9.1% in 2018, to 8.6% 2020 and 7.2% in 2023 [4].

One of the main reasons behind this low CE adoption has been reported to be the lack of suitable tools to support a product development process functional for CE practices. Many authors, in fact, have written about its relevance for CE adoption [1], [5]–[9].

According to [10], the product development process of a discrete product starts with the definition of its requirements, which represent the targets to achieve during the design process. Then, three main activities can be identified: (i) *concept design*, where product ideas are created and assessed, (ii) *system-level design*, where the product architecture is defined by decomposing the product into subsystems and components, (iii) *detail design*, where the specifications for the geometry, materials, and tolerances of the product's components to be manufactured are defined.

The scientific literature has tried to support the product development process by conceiving both qualitative tools (e.g. the creation of design guidelines and frameworks) and quantitative tools (e.g. mathematical models used to optimize product lifecycle phases, such as disassembly processes, and selection of CE options). However, the current literature lacks a comprehensive

Content from this work may be used under the terms of the Creative Commons Attribution 3.0 license. Any further distribution of this work must maintain attribution to the author(s) and the title of the work, journal citation and DOI. Published under license by Materials Research Forum LLC.

Materials Research Proceedings 57 (2025) 493-501 https://doi.org/10.21741/9781644903735-58

framework that links the quantitative definition of CE-based product requirements—specifying "what" must be achieved—to the design guidelines that guide the product development process, outlining "how" to meet these requirements. Such a framework could provide valuable support in the transition from LE to CE fostering sustainability-oriented product innovation.

Recent research by the authors [11] has identified product disassembly cost, product disposal cost, and product quality as the most critical factors at the product level in the transition to a CE. Building on this finding, this study aims to support the fulfillment of CE-based product requirements. More specifically, through a systematic literature review, this work aims to gather the most frequently recurring design guidelines that can empower the design team, i.e., the group of professionals within a manufacturing organization responsible for conceiving, planning, and developing the design aspects of a product, in meeting the product requirements for a CE.

Methodology

This work builds upon the findings of [9] and [11] which quantitatively define the "what" necessary to develop a product suitable for a circular economy, referred to here as CE-based product requirements. The authors' recent research highlights key product-level factors influencing the transition from an LE to a CE paradigm [10] and [12]. These factors are visually represented through a decision tree, a decision-making tool that identifies when a CE business model outperforms an LE model based on economic and environmental criteria. Specifically, the economic criterion is defined by the costs associated with different product lifecycle phases, while the environmental criterion is measured by the corresponding CO_2-equivalent emissions. To integrate both aspects into a single metric, called total cost, the environmental impact is monetized using a carbon tax. The decision tree serves as an intuitive graphical tool for establishing the product requirements necessary to achieve a CE. By applying a few key decision rules to the most impactful parameters, it effectively identifies the optimal choice between LE and CE. The decision tree, detailed in [9] and [11] but omitted from this paper for brevity, offers a structured approach for assessing the viability of transitioning to a CE paradigm.

Starting from this, the present study aims to support the fulfillment of these CE-based product requirements, outlining "how" to meet such requirements, by gathering design guidelines from existing literature, as detailed in the following. To address the purpose of this work, a systematic literature review has been employed to gather the design guidelines that can empower the design team in meeting the CE-based product requirements.

This was performed following the approach of [12] and adopting Scopus database. The selection of this database was based on its broad coverage while maintaining a high level of rigor in indexing [12]. In fact, according to [13], the utilization of the Scopus database is recommended for conducting a thorough content quality review, given its superior citation counts. The following keyword combinations were used in the search for the sample of articles applied to the Article Title, Abstract, and Keywords: “circular economy” AND "design" AND "guidelines". The rationale behind this keyword selection was to keep include a broader set of articles and subsequently refine them. Specifically, the results of this initial search were refined as follows: (i) Scopus database filters: The search included all document types and subject areas, with a filter applied for English language only; (ii) Title screening and exclusions: Articles unrelated to product design for CE or lacking full-text access were excluded; (iii) Abstract and full-text reading: Each article was reviewed to extract design guidelines related to disassembly cost and product quality, which were added to the original set; (iv) Guidelines selection: Only the most frequently recurring guidelines were selected to ensure brevity and relevance.

These selected guidelines extracted from the articles were grouped according to the product development process introduced in Section 1, which involves the concept, system-level, and detail design phases [10]. The rationale behind this choice is to support the design team with structured assistance and guidance throughout the entire product development process. Moreover, for each

Materials Research Proceedings 57 (2025) 493-501 https://doi.org/10.21741/9781644903735-58

product requirement and within each design phase, the guidelines were further clustered according to specific tasks that the design team need to accomplish. The corresponding results can be found in the following Sections.

Design guidelines for product disassembly

The most frequently recurring design guidelines collected through the systematic literature review have been structured according to the design process introduced in section 1, which involves the concept, system-level, and detail design phases [10].

Concept design

During the phase of concept design, the primary focus lies in the creation and assessment of various product concepts. A concept in this context is a comprehensive portrayal of a product's structure, functionality, and attributes, accompanied by a corresponding set of requirements that the design team aims to achieve [10]. In this phase, the main task of the design team is the generation of ideas that simplify the product architecture and, thus, the disassembly process. The collected guidelines are reported in Table 1.

Table 1. *Most frequently recurring guidelines for the disassembly process during the concept design phase.*

Task	Design guidelines
Generation of ideas that simplify the product architecture	Integrate functions to minimize the overall number of materials and components (dematerialization) and to reduce the number of disassembly operations [14], [15], [16], [17], [18], [19], [20], [21], [22], [23], [24], [25], [26], [27], [28], [29], [30], [31].
	Prioritize the disassembly of components that can be subjected to technical, technological, aesthetic obsolescence and of toxic and dangerous components or materials [19], [22], [20].
	Minimise hierarchically dependent connections among components to allow a sequence independent disassembly [14], [19], [27].
	Prefer reversible connections rather than permanent connections [18], [19], [17], [32], [28], [29].

By referring to such guidelines, the design team can generate product concepts suitable for a cost-effective disassembly process.

System-level design

The system-level design phase encompasses the definition of the product architecture, a preliminary design of key components, and formulating initial plans for the production system and final assembly [10]. In this phase, the design team need to focus on defining a modular architecture with increased identifiability and accessibility to components. The most frequently recurring guidelines are reported in Table 2, clustered in two different groups according with the main task the design team aims to achieve.

Materials Research Proceedings 57 (2025) 493-501 https://doi.org/10.21741/9781644903735-58

Table 2. *Most frequently recurring guidelines for the disassembly process during the system-level design phase.*

Task	Design guidelines
Define a modular product architecture.	Use modular structure so that obsolescence occurs with components rather than with entire product [14], [19], [26], [28], [31]. Do not combine components that have different physical life [14], [17], [27].
Define the product architecture with increased identifiability and accessibility to components.	Arrange components for ease of disassembly by facilitating navigation through the product's construction. [14], [16], [19], [17], [21], [33], [34] [28]. Facilitate the identification of components, for example mark parts which must be removed first [14], [19], [18], [20], [21], [28].

y referring to such guidelines, the design team can define a modular product architecture with increased identifiability and accessibility to components for a cost-effective disassembly process.

Detail design

The system-level design phase encompasses the definition of the product architecture, a preliminary design of key components, and formulating initial plans for the production system and final assembly [10]. In this phase, the design team need to focus on defining a modular architecture with increased identifiability and accessibility to components. The most cited guidelines are reported in Table 3, clustered in two different groups according with the main task the design team aims to achieve.

Table 3. *Most frequently recurring guidelines for the disassembly process during the detail design phase.*

Task	Design guidelines
Define the final shape and size of components.	Utilize light materials to facilitate disassembly and extraction of parts [28], [35], [29]. Size components to suit the proposed means of handling and avoid difficult-to-handle components [19], [17], [30], [35]. Provide adequate tolerances for assembly and disassembly [27], [30], [29].
Maximize the standardization and compatibility of components, connections, and tools.	Standardize components to ensure their compatibility and exchangeability across other products, e.g. same type and size of screws [14], [17], [20], [21], [33], [26], [28], [30], [29]. Standardize connections to ensure compatibility and exchangeability of components across other products [14], [17], [32], [21], [26], [35], [30]. Use standardize tools to ensure compatibility and adaptability across other products, e.g., same type and size of screwdriver [17], [20], [22], [33], [27], [35].
Reversible connections.	Do not use fasteners that are not compatible with the connecting components. Fasteners are recycled together with the host component; therefore choose plastic fasteners for plastic and metal fasteners for metal to avoid polluting other material streams or end up in the waste fraction [14], [19], [22].
Define the final connections among components.	Engage easy detachable connections [18], [17], [23], [33] [27], [31].

Materials Research Proceedings 57 (2025) 493-501 https://doi.org/10.21741/9781644903735-58

	Minimize the number and types of fasteners used, and standardize the fasteners used [14], [16], [18], [19], [17], [17], [22], [34], [27], [28], [31]. Fasteners must be easily identified, accessible, and removable or destroyable [14], [18], [22], [34], [27].
Define the disassembly procedure.	Limit the number of tools needed and tool changes [14], [27], [28], [35]. Consider part order and number of reorientations [18], [19], [35]. Avoid multiple directions and complex movements for disassembly [17], [18], [19], [22], [33].

Such guidelines can provide a useful support in achieving the product requirements (in terms of disassembly cost) set by the development team.

Design guidelines for product quality

As done for the product disassembly, also the most frequently recurring design guidelines for product quality collected through the systematic literature review have been structured according to the different phases of the design process.

Concept design

In this phase, the main task of the design team is to focus on product concepts that provide desirability to the user, with high usability, and with the possibility to adapt and upgrade them. The collected guidelines are reported in Table 4.

Table 4. *Most frequently recurring guidelines for the product quality during the concept design phase.*

Task	Design guidelines
Provide desirability.	Provide emotional attachment based on user desire [14], [20], [26].

By implementing such guidelines, the design team can develop product concepts desirable and easy-to-use for the users that, in turn, reflect in a better product quality.

System-level design

Few guidelines have been identified from the literature that can support the system-level design for the product quality. Such guidelines mainly relate to the maintainability of the product and, thus, with a simplified product architecture. These guidelines are reported in Table 5.

Table 5. *Most frequently recurring guidelines for the product quality during the system-level design phase.*

Task	Design guidelines
Define the product architecture accounting for maintainability.	Ensure that all parts to be cleaned are easily accessible [14], [19], [20], [33].

By implementing such guidelines, the design team can account for product maintainability when defining the product architecture.

Materials Research Proceedings 57 (2025) 493-501 https://doi.org/10.21741/9781644903735-58

Detail design

The quality of a product largely depends on the quality of its components. During this phase, the design team need to ensure physical durability and reliability, and maintainability. The collected guidelines clustered according to such features are presented in Table 6.

Table 6. *Most frequently recurring guidelines for the product quality during the detail design phase.*

Task	Design guidelines
Provide physical durability and reliability.	Choose durable, corrosion-resistant, and robust components and materials with a long lifespan. Avoid materials that might lose strength, get brittle or get discoloured [14], [20], [21], [24], [33], [31], [29].
	Design joints and surfaces between joints using materials with high mechanical and chemical durability to face multiple disassembly and re-assembly cycles [33], [28], [29].
	Over dimension critical (easily damaged and expendable) components [14], [17], [19], [32], [28].
	Protect fasteners, components, and subassembly from corrosion and dirt and from contamination caused by wear [14], [18], [17], [22], [24], [29], [31].
	Avoid sharp edges and corners, and reduce, if possible, stress concentrators [18], [28], [31].
Provide maintainability.	Use material that would survive cleaning process e.g. ensure that material melting point is higher than clean process temperature [14], [17], [23]
	Provide user-friendly documentation on how to use, repair, upgrade, etc. with signs on how to open the product and exchange components [19], [20], [21], [33], [27], [28].

These guidelines can provide useful support to the design team in developing high quality products according to the requirements set by the development team.

Conclusions

This study introduces a comprehensive framework that incorporates CE-based product requirements into the product development process, addressing a critical need in the ongoing transition to a CE. This work builds upon an existing decision tree from the literature, which quantitatively defines the product requirements necessary to achieve a CE based on the life cycle economic cost and the life cycle monetized carbon footprint. Notably, despite considering multiple factors, only three—product disassembly cost, product disposal cost, and product quality—significantly impact the feasibility of CE adoption. The cost of product disassembly and product quality are primarily determined by decisions made throughout the product development process. In contrast, the cost of product disposal, while influenced by design choices, is largely determined by external factors such as landfill taxes and carbon taxes. Therefore, only disassembly cost and product quality are considered as key factors influencing the CE adoption. This insight simplifies the prioritization of design efforts.

In this work, design guidelines were systematically gathered from the literature and organized according to the key phases of product development: concept design, system-level design, and detail design. In this way, the proposed framework provides a structured and practical approach to aligning product development with CE principles, enabling design team to make informed decisions that enhance product circularity by providing clear guidance for sustainability-oriented

product innovation. It is worth noting that, for brevity reasons, in this work only the guidelines that appear most frequently in the literature were considered.

While this study offers valuable insights to foster product development for a CE, some limitations must be acknowledged. The framework is based on the most frequently recurring guidelines in the literature, excluding less common ones that may still be important. Therefore, alternative criteria for selecting design guidelines and prioritizing design efforts could be explored. For example, future research could employ a Delphi study to gather expert opinions on a broader set of guidelines, assessing their impact and the practical applicability of the framework.

Despite these limitations, this research provides a solid foundation for supporting CE-driven product development, offering both theoretical insights and practical tools for fostering sustainability-oriented product innovation in manufacturing and design. Future research could also focus on applying the proposed framework to a real case study to demonstrate its effectiveness in supporting the transition to a circular economy.

References

[1] M. P. Ciano, M. Peron, L. Panza, and R. Pozzi, "Industry 4.0 technologies in support of circular Economy: A 10R-based integration framework," *Comput. Ind. Eng.*, no. January, p. 110867, 2025. https://doi.org/10.1016/j.cie.2025.110867

[2] Y. Ren, K. J. Wu, M. K. Lim, and M. L. Tseng, "Technology transfer adoption to achieve a circular economy model under resource-based view: A high-tech firm," *Int. J. Prod. Econ.*, vol. 264, no. July, p. 108983, 2023. https://doi.org/10.1016/j.ijpe.2023.108983

[3] CIRCLE Economy, "The Circularity Gap Report 2021," 2021. https://www.circularity-gap.world/2021

[4] CIRCLE Economy, "THE CIRCULARITY GAP REPORT 2023," 2023, [Online]. Available: https://www.circularity-gap.world/2023#download

[5] D. Pigosso and T. McAloone, "How can design science contribute to a circular economy? / ICED23: Design in a complex world," *Proc. 21st Int. Conf. Eng. Des. (IDED 17)*, vol. 5, no. August, pp. 299–307, 2017, [Online]. Available: https://iced.designsociety.org/publication/39752/How+can+design+science+contribute+to+a+circular+economy%3F

[6] C. Sassanelli, A. Urbinati, P. Rosa, D. Chiaroni, and S. Terzi, "Addressing circular economy through design for X approaches: A systematic literature review," *Comput. Ind.*, vol. 120, p. 103245, 2020. https://doi.org/10.1016/j.compind.2020.103245

[7] J. X. Wang, H. Burke, and A. Zhang, "Overcoming barriers to circular product design," *Int. J. Prod. Econ.*, vol. 243, no. July 2020, p. 108346, 2022. https://doi.org/10.1016/j.ijpe.2021.108346

[8] L. Panza, A. Faveto, G. Bruno, and F. Lombardi, "Open product development to support circular economy through a material lifecycle management framework," *Int. J. Prod. Lifecycle Manag.*, vol. 14, no. 2–3, pp. 255–281, 2022. https://doi.org/10.1504/ijplm.2022.125826

[9] L. Panza, "Technological Innovations for Sustainable Manufacturing: Concepts, frameworks, and supporting tools," Politecnico di Torino, 2024. [Online]. Available: https://iris.polito.it/handle/11583/2986280

[10] K. T. Ulrich and S. D. Eppinger, *Product Design and Development*. McGraw-Hill Education, 2016.

[11] L. Panza and M. Peron, "The role of carbon tax in the transition from a linear economy to a circular economy business model in manufacturing," *J. Clean. Prod.*, vol. 492, no. January, p. 144873, 2025. https://doi.org/10.1016/j.jclepro.2025.144873

[12] A. B. Lopes de Sousa Jabbour *et al.*, "Circular economy business models and operations management," *J. Clean. Prod.*, vol. 235, pp. 1525–1539, 2019. https://doi.org/10.1016/j.jclepro.2019.06.349

[13] E. M. Lasda Bergman, "Finding Citations to Social Work Literature: The Relative Benefits of Using Web of Science, Scopus, or Google Scholar," *J. Acad. Librariansh.*, vol. 38, no. 6, pp. 370–379, 2012. https://doi.org/10.1016/j.acalib.2012.08.002

[14] Van Den Berg M.R. and Bakker C.A., "A product design framework for a circular economy," in *Product Lifetimes And The Environment*, 2015, pp. 365–379.

[15] A. Teischinger, J. Kalcher, E. Salzger, G. Praxmarer, and M. Vanek, "General systematic for a design for recycling-guideline for wooden windows and wood aluminium windows," *WCTE 2016 - World Conf. Timber Eng.*, no. August, 2016.

[16] C. Favi, M. Germani, M. Mandolini, and M. Marconi, "DISASSEMBLY KNOWLEDGE CLASSIFICATION AND POTENTIAL APPLICATION: A PRELIMINARY ANALYSIS ON A WASHING MACHINE," 2016.

[17] M. D. Bovea and V. Pérez-Belis, "Identifying design guidelines to meet the circular economy principles: A case study on electric and electronic equipment," *J. Environ. Manage.*, vol. 228, no. August, pp. 483–494, 2018. https://doi.org/10.1016/j.jenvman.2018.08.014

[18] B. Pozo Arcos, A. R. Balkenende, C. A. Bakker, and E. Sundin, "Product design for a circular economy: Functional recovery on focus," *Proc. Int. Des. Conf. Des.*, vol. 6, pp. 2727–2738, 2018. https://doi.org/10.21278/idc.2018.0214

[19] C. Vezzoli, *Design for environmental sustainability: Life cycle design of products: Second edition*. 2018. doi: 10.1007/978-1-4471-7364-9

[20] S. Shahbazi and A. K. Jönbrink, "Design guidelines to develop circular products: Action research on nordic industry," *Sustain.*, vol. 12, no. 9, pp. 1–14, 2020. https://doi.org/10.3390/su12093679

[21] J. K. Albæk, S. Shahbazi, T. C. McAloone, and D. C. A. Pigosso, "Circularity evaluation of alternative concepts during early product design and development," *Sustain.*, vol. 12, no. 22, pp. 1–25, 2020. https://doi.org/10.3390/su12229353

[22] J. M. Leal, S. Pompidou, C. Charbuillet, and N. Perry, "Design for and from recycling: A circular ecodesign approach to improve the circular economy," *Sustain.*, vol. 12, no. 23, pp. 1–30, 2020. https://doi.org/10.3390/su12239861

[23] N. Boix Rodríguez, M. Marconi, C. Favi, and G. Formentini, "Eco-design actions to improve life cycle environmental performance of face masks in the pandemic era," *Proc. Des. Soc.*, vol. 1, no. AUGUST, pp. 1333–1342, 2021. https://doi.org/10.1017/pds.2021.133

[24] S. Willskytt, "Design of consumables in a resource-efficient economy—a literature review," *Sustain.*, vol. 13, no. 3, pp. 1–25, 2021. https://doi.org/10.3390/su13031036

[25] H. Desing, G. Braun, and R. Hischier, "Resource pressure – A circular design method," *Resour. Conserv. Recycl.*, vol. 164, no. September 2020, p. 105179, 2021. https://doi.org/10.1016/j.resconrec.2020.105179

[26] M. F. Aguiar and D. Jugend, "Circular product design maturity matrix: A guideline to evaluate new product development in light of the circular economy transition," *J. Clean. Prod.*, vol. 365, no. May, p. 132732, 2022. https://doi.org/10.1016/j.jclepro.2022.132732

[27] M. R. Munaro and S. F. Tavares, "Design for adaptability and disassembly: guidelines for building deconstruction," *Constr. Innov.*, 2023. https://doi.org/10.1108/CI-10-2022-0266

[28] J. A. Mesa, "Design for circularity and durability: an integrated approach from DFX guidelines," *Res. Eng. Des.*, no. iii, 2023. https://doi.org/10.1007/s00163-023-00419-1

[29] A. Kręt-Grześkowiak and M. Baborska-Narożny, "Guidelines for disassembly and adaptation in architectural design compared to circular economy goals - A literature review," *Sustain. Prod. Consum.*, vol. 39, no. April, pp. 1–12, 2023. https://doi.org/10.1016/j.spc.2023.04.020

[30] C. L. C. Roxas *et al.*, "Design for Manufacturing and Assembly (DfMA) and Design for Deconstruction (DfD) in the Construction Industry: Challenges, Trends and Developments," *Buildings*, vol. 13, no. 5, 2023. https://doi.org/10.3390/buildings13051164

[31] L. Schlesinger, J. Koller, M. Pagels, and F. Döpper, "Alignment of design rules for additive manufacturing and remanufacturing," *J. Remanufacturing*, vol. 13, no. 2, pp. 99–119, 2023. https://doi.org/10.1007/s13243-022-00122-9

[32] S. Willskytt and S. A. Brambila-Macias, "Design guidelines developed from environmental assessments: A design tool for resource-efficient products," *Sustain.*, vol. 12, no. 12, 2020. https://doi.org/10.3390/SU12124953

[33] S. Shahbazi, K. Johansen, and E. Sundin, "Product design for automated remanufacturing—a case study of electric and electronic equipment in sweden," *Sustain.*, vol. 13, no. 16, pp. 1–20, 2021. https://doi.org/10.3390/su13169039

[34] B. Pozo Arcos, S. Dangal, C. Bakker, J. Faludi, and R. Balkenende, "Faults in consumer products are difficult to diagnose, and design is to blame: A user observation study," *J. Clean. Prod.*, vol. 319, no. August, p. 128741, 2021. https://doi.org/10.1016/j.jclepro.2021.128741

[35] A. Zaman, A. M. Caceres Ruiz, S. Shooshtarian, T. Ryley, S. Caldera, and T. Maqsood, "Development of the Circular Economy Design Guidelines for the Australian Built Environment Sector," *Sustain.*, vol. 15, no. 3, 2023. https://doi.org/10.3390/su15032500

Process and system simulation, optimization and digital manufacturing



Materials Research Proceedings 57 (2025) 503-511 https://doi.org/10.21741/9781644903735-59

Implementing Job Sequencing in a CONWIP fully automated assembly line

Arianna ALFIERI[1,a], Claudio CASTIGLIONE[1,b *] and Erica PASTORE[1,c]

[1]Politecnico di Torino, Department of Management and Production Engineering, Corso Duca degli Abruzzi, 24, Torino, 10129 (TO), Italy

[a]arianna.alfieri@polito.it, [b]claudio.castiglione@polito.it, [c]erica.pastore@polito.it

Keywords: Operations Management, Sequencing, Automotive

Abstract. Electric vehicle production poses several challenges from the manufacturing point of view due to the uncertainty in the price and availability of raw materials and the frequent fluctuations of market demand. Moreover, mass customisation requires flexible and reconfigurable manufacturing systems, while the automation of the assembly lines to achieve a higher throughput rate and the complexity of job handling require conveyors and carousels. This paper investigates the implementation of job sequencing policies through conveyor loops to improve the flexibility and reconfigurability of a realistic CONWIP assembly line while avoiding upstream and downstream variability propagation. Scenario analysis evaluates how different job sequencing strategies and WIP control can impact the average and standard deviation of the shift throughput, the average job flow time, and the probability of deadlocks on an assembly line for stators of electric engines.

Introduction

Improving the manufacturing system flexibility and reconfigurability while reducing upstream and downstream variability propagation is important in all the industrial fields where there is pressure for mass customisation[1], and the raw material supplies and demand are critical[2]. Mass customisation requires flexible and reconfigurable systems to produce many product variants [3], which are subjected to frequent fluctuations in demand. Moreover, some industrial fields also have an intrinsic demand variability due to many causes, such as fast obsolescence rate, technology disruptions, highly depreciable raw materials, and product demand depending on public incentives like electric car manufacturing [4].

In electric vehicle manufacturing, raw materials supplies are unstable because of the uncertainties in the availability and prices of critical raw materials, such as neodymium and dysprosium, essential for electric motors, due to their global scarcity and the geopolitical context [5]. From the point of view of production planning, increasing flexibility and reconfigurability while reducing variability propagation means changing the system throughput (TH) based on the product currently in production, its demand fluctuations, and the congestion of the downside subsystems [6] while mitigating the impacts of the fluctuations in raw material consumption rates [7].

Discrete event simulation and scenario analysis have been exploited to investigate job sequencing strategies in a part of a realistic assembly line for electric vehicle engines using a CONstant Work-In-Progress (CONWIP) logic. CONWIP systems have a fixed number of jobs, namely the WIP (W*), allowing a new part to enter the system only when a finished one leaves. In particular, the paper studies the impacts of combining different job sequencing strategies in different system workstations on the average shift TH, its standard deviation, the flowtime (FT), i.e., the total time of a job within the line, and the occurrence of disruptive events when changing TH.

Content from this work may be used under the terms of the Creative Commons Attribution 3.0 license. Any further distribution of this work must maintain attribution to the author(s) and the title of the work, journal citation and DOI. Published under license by Materials Research Forum LLC.

Materials Research Proceedings 57 (2025) 503-511 https://doi.org/10.21741/9781644903735-59

In the remainder, the Background section provides the research context through the review of the scientific literature, while the Problem description section introduces the industrial problem, the case study, the proposed approach and the design of experiment. The Results and the Conclusion sections discuss the experimental insights and conclude the paper, respectively.

Background

In general, a CONWIP logic is unsuitable for multi-product environments and lines with non-reliable machines because the position of the jobs within the system is scarcely predictable, with the risk of unbalancing the line [8]. Moreover, the workstation layout that facilitates system flexibility and reconfigurability is the matrix, as it allows customised path for each product variant, allowing the production of smaller lots and simultaneous multi-product production [9].

However, assembly line design must also consider the material handling system that ensures the most suitable material handling and transportation from one workstation to another [10]. Conveyor systems are among the most used material handling systems because of their simplicity and effectiveness, even in fully automated lines [11]. Still, conveyors represent a rigid structure scarcely compatible with matrix workstation layout [12].

In this context, production planning approaches can be helpful in overcoming the aforementioned limitations. First, the CONWIP system should work one product at a time by exploiting production paradigms like the economic lot scheduling in which the multi-product demand is satisfied by fixing the batch sizes and scheduling the batch production order [13]. Hence, it is important to investigate the impacts of production planning approaches on the system behaviour under different TH levels. In the literature, some approaches propose using a dynamic W* to adjust the TH to the overall needs [14]; however, this approach will propagate variability upstream, negatively impacting system performance.

Moreover, CONWIP is subjected to the risk of unbalancing the assembly line due to not directly controlling the WIP in each part of the system, but only its overall value. However, controlling the number of jobs in the parts of the line close to the bottlenecks can prevent extreme congestion conditions causing deadlocks.

This paper investigates the possibility of enhancing system flexibility and reconfigurability in a system that can be critical due to the use of CONWIP logic, conveyors and carousels, and the necessity of mitigating upstream and downstream variability. Discrete event simulation has been employed to evaluate the behaviour of a realistic system when different job sequencing strategies are applied. A scenario analysis is then exploited to analyse the interactions among different sequencing strategies and operational parameters of the assembly line (e.g. the identification of the W* for the CONWIP logic).

Problem description

The effectiveness of production planning actions, such as job sequencing, on system reconfigurability and flexibility depends on the system characteristics, the material handling system, and the resources that supply the raw materials to the line and move the finished products to the next production phase. This paper focuses on the effects of job sequencing on an assembly line that exploits conveyors; therefore, the main focus is on the material handling system and the short-term production planning at the workstation level.

The problem description. A part of a realistic assembly line for electric vehicle engines has been exploited as a case study. The assembly line has six manufacturing workstations (WSs) and a further WS devoted to quality checks (WSQC). Fig. 1 shows the assembly line with the loading and the unloading bays at the two line sides (pink rectangles in the figure) and the seven WSs (from WS1 to WSQC) intertwined by a fully automated material handling system based on conveyors.

Materials Research Proceedings 57 (2025) 503-511 https://doi.org/10.21741/9781644903735-59

The assembly line follows a CONWIP logic; thus, there is always a fixed number of jobs within the system [8]. Hence, when a finished job leaves the system from the unloading bay, a new job is put within an empty pallet in the loading bay.

WS1 and WS3 work according to the blocking after service policy, that is, the processed job is unloaded from the machine only when one of the successive machines becomes idle (jobs in WS1 and WS3 are unloaded when one of the two machines in WS2 or the machine of WS4 become idle, respectively). At the same time, jobs processed by WS2 remain in the conveyor loop of WS2 until WS3 becomes idle, while jobs processed by WS4 and WS5 move within the conveyor loop until one of the machines of WS5 or WS6 becomes idle, respectively.

All the WSs except for WS1 are subject to random sampling for sending the just processed job to WSCQ for quality check. WS2 and WS5 have two identical machines, and each job must be worked twice within WS5.

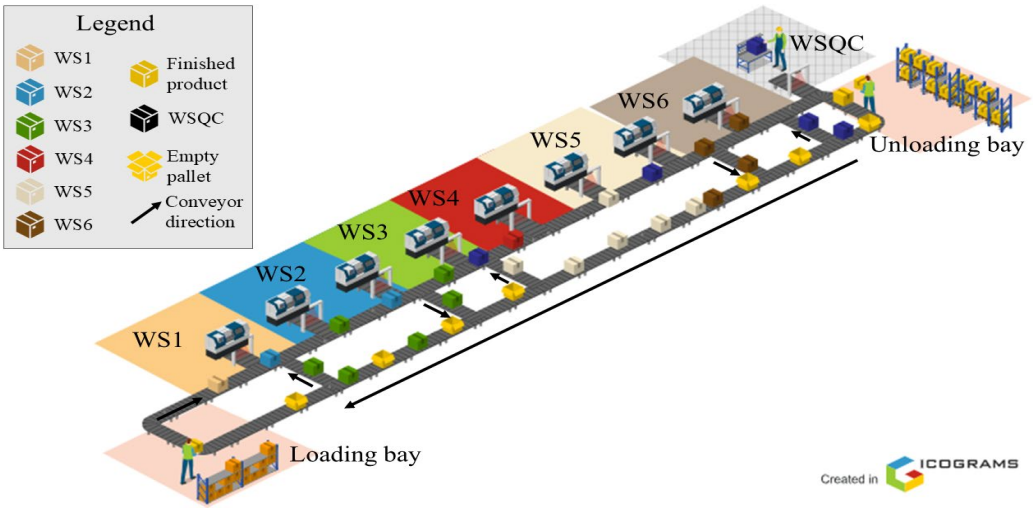


Figure 1. The assembly line has six manufacturing workstations, and the last workstation is devoted to quality checks. At the two line sides, there are the loading and unloading bays.

The proposed approach. A discrete event simulation model has been developed to simulate the system under different combinations of job sequencing rules in some WSs and different system workloads, i.e., different W*.

Some assumptions have been made to increase the experimental robustness of the results. In particular, the assembly line is balanced, i.e., all the WSs have the same processing time. WSs having two identical machines have twice the processing time of the single-machine ones; however, as WS5 has two identical machines, jobs must be processed twice, and the machine processing times are identical to the single-machine WS.

Processing times are deterministic to avoid confounding effects and focus on the variability propagation generated by the random sampling for quality check. The probability of a job being selected for quality check is 12% in each WS from 1 to 6. In the case the job is selected, it is sent to WSQC for a deterministic quality check, the duration of which is the same as the processing time of the other WSs, and then sent for rework in the origin WS.

Two job sequencing strategies have been developed: (i) a set of sequencing rules for jobs to be processed in WS5 and (ii) a set of rules for sequencing jobs waiting for the quality check in the loop of WSQC.

The two machines in WS5 follow one of the following four strategies:

- *FIFO*. First-In, First-Out strategy is the benchmark as it represents the scenario in which the jobs enter one of the two machines when they find it idle;

Materials Research Proceedings 57 (2025) 503-511 https://doi.org/10.21741/9781644903735-59

- *SymLWKR*. The two machines have symmetrical behaviours that prioritise the jobs with the least work remaining (LWKR). If, in the loop of WS5, there is a job that has already done one of the first operations required in WS5 (and, hence, has to be manufactured for the second time), it has higher priority than the jobs that have to be processed for the first time.
- *SymMWKR*. The two machines have symmetrical behaviours that prioritise the jobs with the most work remaining (MWKR). If, in the loop of WS5, there is a job that has done neither of the two processes required in WS5, it has higher priority than the jobs that have to be processed for the second time.
- *Asym.* The first of the two machines follows the LWKR rule, while the second follows the MWKR rule. Hence, there always is at least a machine dedicated to jobs that need to be worked for both the first and the second time.

Given a WS*i* (i from 1 to 6), the sequencing rules in WSQC assign priority p_i based on balancing between the number of jobs waiting to be worked in each WS (WIP_i) that have sent the jobs in the WSQC loop and their process state according to Equations (1) and (2).

$$p_i = \alpha * \frac{\sum_{i=1}^{6} WIP_i}{WIP_i} + (1-\alpha) * \frac{i}{6} \quad (1)$$

$$p_i = \alpha * \frac{\sum_{i=1}^{6} WIP_i}{WIP_i} + (1-\alpha) * \frac{1}{i} \quad (2)$$

Three values for parameter α have been used to define six job sequencing rules to assess the possible impacts of production control on inventory management:

- *FIFO*. No job sequencing is done in WSQC. It represents the benchmark;
- *Balanced incremental (B.i.*). Parameter α = 0.5 is used to give the same importance to *WIP* and *incremental* strategies by exploiting Eq. (1);
- *Balanced decremental (B.d.).*Parameter α = 0.5 is used to give the same importance to *WIP* and *decremental* strategies by exploiting Eq. (2);
- Incremental (*Inc*). Parameter α= 0 is used to apply only the *incremental* strategy Eq. (1);
- *Decremental (Dec).* Parameter α = 0 is used to apply only the *decremental* strategy, Eq (2);
- *WIP*. Parameter α = 1 is used to apply only the *WIP* strategy; Equations (1) and (2) are interchangeable.

The effectiveness of job sequencing for improving flexibility and reconfigurability is evaluated through four Key Performance Indicators (KPIs): the average shift TH, the average FT, the standard deviation of shift TH, and the occurrence of deadlocks.

The full factorial experiment has three factors: W* (ten levels), the *Scenario* indicating the sequencing strategy in WS5 (four levels), and the *WSQC Rule* indicating the sequencing strategy in WSQC (six levels). Table 1 summarises the levels of the three factors leading to 240 different scenarios.

Table 1. Experimental factors and factorial levels.

Experimental factor	Factorial levels
W*	13; 15; 17; 19; 21; 23; 25; 27; 29; 31
Scenario	*Asym*, *symLWKR*, *symMWKR*, *FIFO*
WSQC Rule	*B.d*, *B.i.*, D*ec*, *FIFO*, *Inc.*, *WIP*

Materials Research Proceedings 57 (2025) 503-511 https://doi.org/10.21741/9781644903735-59

Results

The KPIs of each one of the 240 scenarios are evaluated over 30 replications leading to 7200 experiments; each replication has a warm-up period of one year and a simulation horizon of one year. The time unit is the minute, and the daily working time is an 8-hour shift; thus, daily KPIs and shift KPIs are interchangeable.

Fig. 2 shows the impacts of the sequencing rules implemented in WS5 on the shift average TH and the average FT. Average shift TH and FT increase with W* (WIPThreshold in Fig. 2), but average shift TH increases only up to a maximum value and then decreases. In particular, Fig. 2a highlights that when implementing the *Asym* sequencing strategy, the shift average TH is slightly higher than the benchmark scenario (i.e. FIFO strategy). Conversely, the *symMWKR* sequencing strategy allows an average shift TH slightly lower than the benchmark scenario. Notably, the *symLWKR* strategy leads to a significantly lower average shift TH than the benchmark, with a TH gap from 10.86% (WIPThreshold = 13) up to 19.23% (WIPThreshold = 31).

Fig. 2b shows that only the *symLWKR* strategy is significantly different from the benchmark, increasing the flow time of a job into the system up to 19% (WIPThreshold = 31).

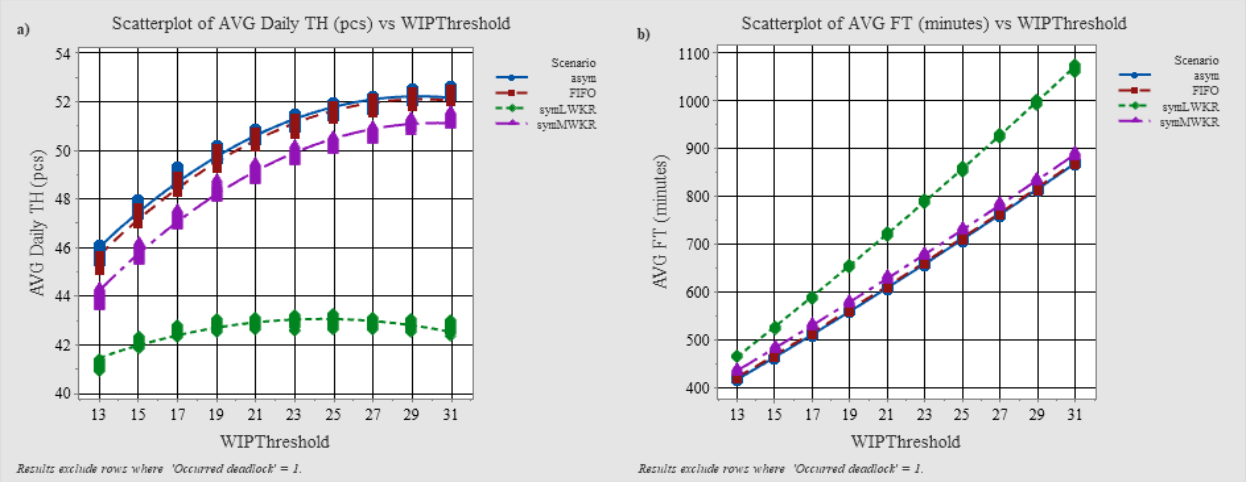


Figure 2. The impacts of the four sequencing strategies and WS5 on the average shift throughput TH (2a) and the average flowtime FT (2b) when WIPThreshold goes from 13 to 31 units.

The FT can provide insights about the reactiveness of the system by highlighting that, on average, a job stays in the system from 450 minutes (WIPThreshold = 13, almost one entire work shift) up to 900 minutes (WIPThreshold = 31, more than two working shift).

Since the job production generally spans more than one shift, the standard deviation of the average shift TH is important because highly variable average shift TH indicates scarce predictability of job completion time, upstream variability propagation to the inventory management of critical raw materials, challenges in multi-product production planning, and poor performance in reconfiguring the system for adapting to the frequent final demand fluctuations.

Fig. 3 shows the boxplots of the average shift TH standard deviation by pairwise grouping factors.

Materials Research Proceedings 57 (2025) 503-511 https://doi.org/10.21741/9781644903735-59

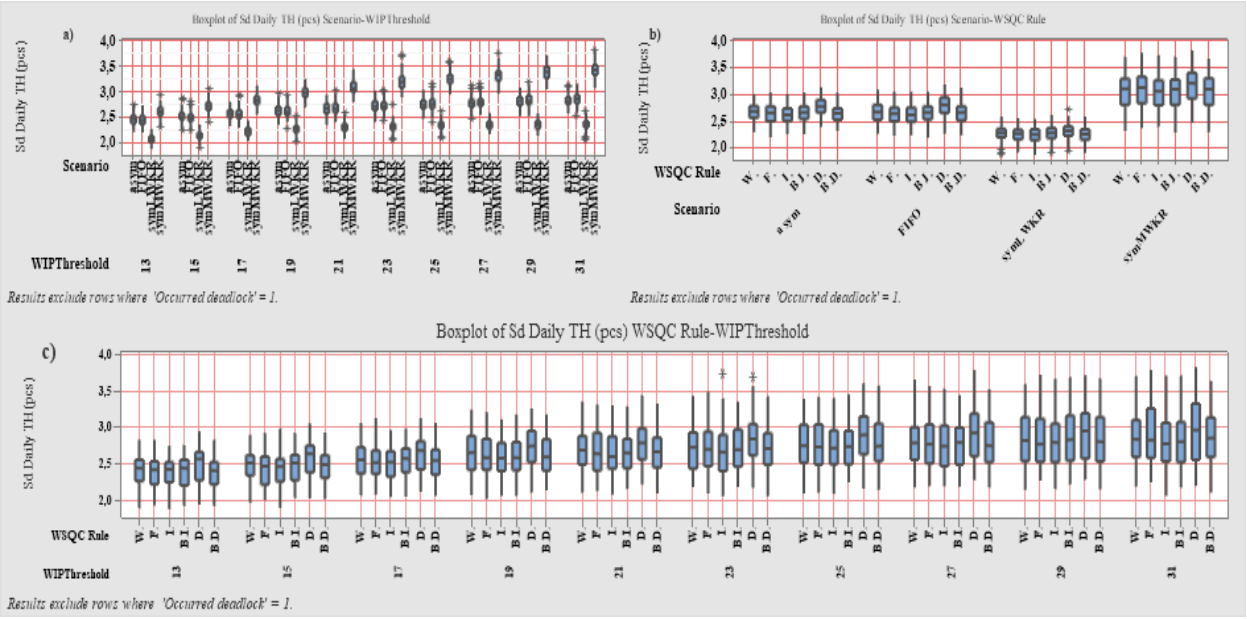


Figure 3. Boxplot of the standard deviation of average shift TH by pairwise factor grouping.

Fig. 3a highlights that the *symLKWR* strategy stabilises the variability of the average shift TH because it has a constant standard deviation that does not increase with W*. Conversely, the other sequencing strategies in WS5 have increasing standard deviation when W* increases, particularly the *symMWKR* strategy. Figures 3b and 3c show that the sequencing strategies on WSQC do not impact the standard deviation of the average shift TH (six similar boxes), but the sequencing strategies on WS5 lead to different standard deviations (Fig. 3b), which are generally increasing with W* (Fig. 3c). Note that, the analyses on standard deviations exclude all those scenarios in which a deadlock occurred (deadlock = 1) to avoid biased results. Therefore, WSQC seems marginal, but its role emerges during deadlock analysis.

The combined use of job sequencing in WS5 and WSQC is pivotal for increasing the average shift TH because the latter one increases with W*, but higher W* levels increase the deadlock probability. Fig. 4 shows the pairwise interactions of sequencing strategies on WS5, sequencing strategies on WSQC, and W* levels (*Scenario*, *WSQC Rule*, and *WIPThreshold*, respectively, in Fig. 4) impacting deadlocks that occurred over the experimentation.

Deadlocks occurred only with the WIP level equal to or greater than 27 (i.e., 27, 29, and 31). The chart in the bottom part of Fig. 4 shows that the *symLWKR* sequencing rule in WS5 is more robust to deadlock than the others, showing only one deadlock in WIPThreshold = 31 (green marker), while the benchmark (FIFO strategy) is more subjected to deadlocks than the scenarios with sequencing strategies (red line and markers are higher than the others). The two charts on the top side of Fig. 4 show that the benchmark for WSQC (*FIFO* in WSCQ) and the *Decremental* sequencing strategy prevent deadlocks (in fact, *FIFO* and *Decremental* are not in the charts of Fig. 4 because they do not have led to deadlocks). Sequencing in WSQC can reduce the probability of deadlock. Still, to minimise deadlock probability, the WSQC strategy must be selected according to the W* level and the sequencing strategy.

Materials Research Proceedings 57 (2025) 503-511 https://doi.org/10.21741/9781644903735-59

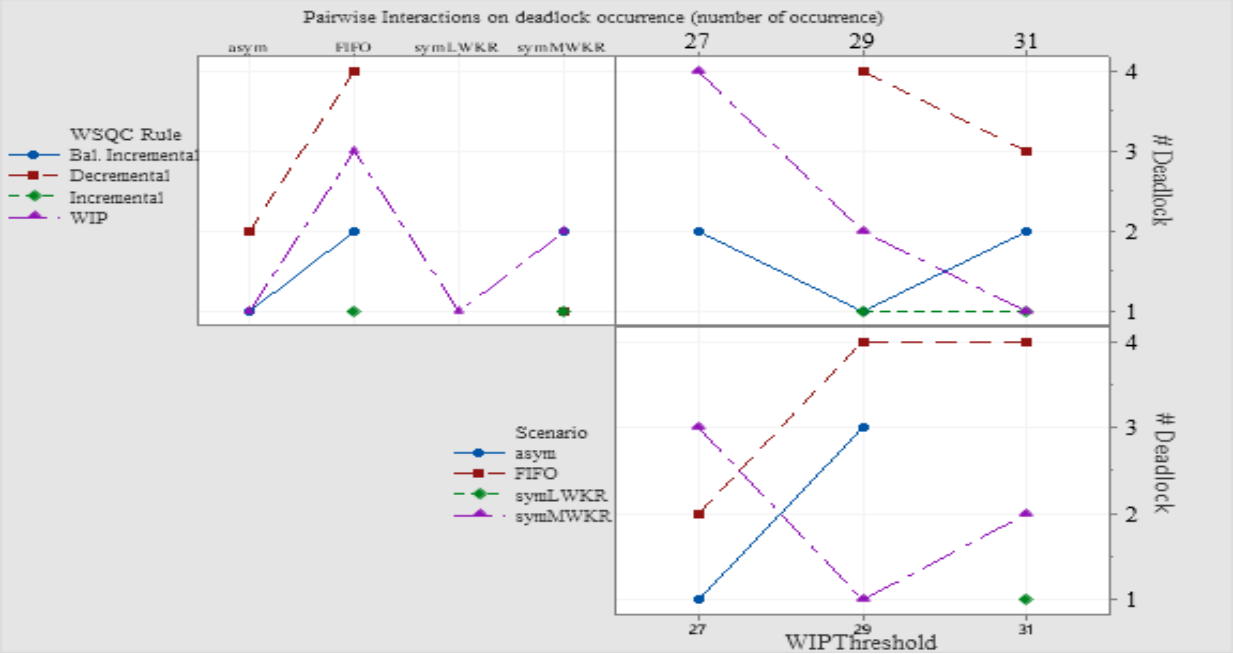


Figure 4. Pairwise interaction effects of WIPThreshold and sequencing strategies in WSQC and WS5 on the number of deadlocks that occurred during the experimentation.

Conclusion

This paper investigates the use of job sequencing in a fully automated line with workstations (WSs) connected by conveyors and controlled by a CONWIP system logic to enhance the flexibility and reconfigurability of the system. Combining sequencing rules in different WSs allows the maximisation of the average shift TH and the increase and decrease of average shift TH while reducing variability propagation. In fact, it is possible to temporarily increase or reduce the TH by combining the job sequencing rules in different manners. At the same time, it is possible to maintain a fixed consumption rate of critical raw materials by temporarily varying the critical WIP level W*.

Job sequencing WSQC can reduce the probability of deadlock, but when the sequencing rule in WS5 changes, WSQC must be adjusted. The introduction of job sequencing allows for adapting a CONWIP line, which is inherently inflexible due to the conveyor material handling system. This allows a more flexible and reconfigurable system to adjust to the product demand fluctuations, the fatigue level of the workforce, and the availability of resources moving items among the different lines or shelving while reducing the variability propagation up to the inventory management of critical raw materials.

The main limitations of this paper are that (i) the proposed approach has been investigated in a well-defined case study and (ii) the simulation approach is sensitive to the parameters used. Future research will investigate how the generalisation has to cope with the characteristics of the systems and the robustness of results. When parameters change. Moreover, the position of the WS controlling production through priority rules and the size of the conveyors and carousels are determinants for performance. Hence, future research will also investigate system design.

Finally, adaptive mechanisms will be investigated to change from one scenario to another or increase and decrease W* according to the events that impact production demand, availability and congestion of the downstream systems, and inventory management.

Acknowledgements

This study was carried out within the Motown: Smart Production Planning and Control for Manufacturing of Electric Vehicle Powertrain in Industry 4.0 Environment project – funded by

European Union – Next Generation EU, Missione 4 Componente 1 CUP E53D23007900006, within the PRIN 2022 program (D.D. 104 - 02/02/2022 Ministero dell'Università e della Ricerca). This manuscript reflects only the authors' views and opinions and the Ministry cannot be considered responsible for them.

References

[1] Brunoe, T. D., Soerensen, D. G., Nielsen, K. Modular design method for reconfigurable manufacturing systems. Procedia CIRP, 104 (2021) 1275-1279. https://doi.org/10.1016/j.procir.2021.11.214

[2] Kusiak, A. Universal manufacturing: Enablers, properties, and models. International Journal of Production Research, 60(8) (2022) 2497-2513. https://doi.org/10.1080/00207543.2021.1894370

[3] Sabioni, R. C., Daaboul, J., Le Duigou, J. An integrated approach to optimize the configuration of mass-customized products and reconfigurable manufacturing systems. The International Journal of Advanced Manufacturing Technology, 115(1) (2021) 141-163. https://doi.org/10.1007/s00170-021-06984-w

[4] Plaza, M., David, I., Shirazi, F. Management of inventory under market fluctuations the case of a Canadian high tech company. International Journal of Production Economics, 205 (2018) 215-227. https://doi.org/10.1016/j.ijpe.2018.09.007

[5] Ortego, A., Calvo, G., Valero, A., Iglesias-Embil, M., Valero, A., Villacampa, M. Assessment of strategic raw materials in the automobile sector. Resources, Conservation and Recycling, 161 (2020) 104968. https://doi.org/10.1016/j.resconrec.2020.104968

[6] Javaid, M., Haleem, A., Singh, R. P., Suman, R. Enabling flexible manufacturing system (FMS) through the applications of industry 4.0 technologies. Internet of Things and Cyber-Physical Systems, 2 (2022) 49-62. https://doi.org/10.1016/j.iotcps.2022.05.005

[7] Kombaya Touckia, J., Hamani, N., Kermad, L. Digital twin framework for reconfigurable manufacturing systems (RMSs): design and simulation. The International Journal of Advanced Manufacturing Technology, 120(7) (2022) 5431-5450. https://doi.org/10.1007/s00170-022-09118-y

[8] Dinis-Carvalho, J., Macedo, H. Challenges for Optimal Efficiency in Pull Production Within Complex Production Systems: A Literature Review. In European Lean Educator Conference (2023) pp. 327-343. Cham: Springer Nature Switzerland. https://doi.org/10.1007/978-3-031-63265-5_24

[9] Renna, P. Performance analysis of matrix-structured manufacturing systems compared to dedicated flow and reconfigurable manufacturing lines. Production Engineering, 18(3) (2024) 625-642. https://doi.org/10.1007/s11740-023-01243-1

[10] Leng, J., Wang, D., Shen, W., Li, X., Liu, Q., Chen, X. Digital twins-based smart manufacturing system design in Industry 4.0: A review. Journal of manufacturing systems, 60 (2021) 119-137. https://doi.org/10.1016/j.jmsy.2021.05.011

[11] Bortolini, M., Faccio, M., Galizia, F. G., Gamberi, M., Pilati, F. Design, engineering and testing of an innovative adaptive automation assembly system. Assembly Automation, 40(3) (2020) 531-540. https://doi.org/10.1108/AA-06-2019-0103

[12] Liu, C., Li, W., Lian, J., Yin, Y. Reconfiguration of assembly systems: From conveyor assembly line to serus. Journal of manufacturing systems, 31(3) (2012) 312-325. https://doi.org/10.1016/j.jmsy.2012.02.003

[13] Piñeyro, P., Viera, O. The economic lot-sizing problem with remanufacturing and heterogeneous returns: formulations, analysis and algorithms. International Journal of Production Research, 60(11) (2022) 3521-3533. https://doi.org/10.1080/00207543.2021.1925771

[14] Vespoli, S., Mattera, G., Marchesano, M. G., Nele, L., Guizzi, G. Adaptive manufacturing control with Deep Reinforcement Learning for dynamic WIP management in industry 4.0. Computers & Industrial Engineering (2025) 110966. https://doi.org/10.1016/j.cie.2025.110966

Materials Research Proceedings 57 (2025) 512-520 https://doi.org/10.21741/9781644903735-60

Integrating buffer "stock" and buffer loops in an assembly line with conveyors: An automotive case study

Claudio CASTIGLIONE[1,a *], Erica PASTORE[1,b] and Arianna ALFIERI[1,c]

[1]Politecnico di Torino, Department of Management and Production Engineering, Corso Duca degli Abruzzi, 24, Torino, 10129 (TO), Italy

[a]claudio.castiglione@polito.it, [b]erica.pastore@polito.it, [c]arianna.alfieri@polito.it

Keywords: System Architecture; Assembly Lines; Discrete Event Simulation

Abstract. The degree of automation in manufacturing systems, along with the characteristics of job handling and transport between workstations, and the product cycle time, determine the most suitable job handling system for each line. Conveyor systems allow for the management of re-entrant flows at the same workstations and more flexible system architecture through carousels, which also serve as a buffer loop to accommodate jobs awaiting machine availability. This paper explores the role of buffer stocks and blocking after service mechanisms, task allocation within the system, and operational characteristics to tackle the assembly line balancing problem in a fully automated assembly line interconnected by conveyors through discrete event simulation. Scenario analysis is employed to assess the impacts of constraining job flows through the conveyors on: fluctuations in throughput from shift to shift, its variability, and the critical WIP threshold for the CONWIP logic.

Introduction

The assembly line balancing problem (ALBP) cannot neglect the intersection between the choice of the material handling systems, the tasks performed along the line, and the selection of single processes to optimise production and operations management, particularly in the field of intelligent manufacturing [1]. The introduction of Industry 4.0 (I4.0) technologies impacted the reconfigurability and rebalancing of assembly systems, enabling the opportunity to remotely control workstations and material handling systems to increase or decrease line throughput according to the conditions of the external environment, such as workers' stress and fatigue levels or downstream congestion.[2].

Therefore, the human-centred manufacturing of Industry 5.0 (I5.0) [3] and I4.0 are changing the paradigm for designing manufacturing lines through sensors, automation, and digitalisation. The result is the complexity in evaluating the best configuration considering inventory, job handling systems, and transports due to the increased number of alternatives often evaluated by decentralised decision-making [4].

This paper investigates the design of a part of a real assembly line of engines for electric cars in which conveyors intertwine the workstations, machines are unreliable, and buffers and conveyor carousels must be designed to control the job flow. The assembly line exploits a Constant work-in-progress (CONWIP) logic, maintaining a fixed number of jobs (namely, critical WIP level, W*) in the system by loading a new job in the conveyor when a finished product crosses the unloading bay.

The following design issues have been investigated through discrete event simulation and scenario analysis: (i) the exploitation of the conveyor carousels rather than introducing blocking mechanisms and buffers, (ii) the identification of W* for optimising the throughput (TH) of the CONWIP system, and (iii) the choice between performing some operations one shot in slower machines or partitioning them in smaller tasks to be performed sequentially in faster machines through conveyor loops.

Content from this work may be used under the terms of the Creative Commons Attribution 3.0 license. Any further distribution of this work must maintain attribution to the author(s) and the title of the work, journal citation and DOI. Published under license by Materials Research Forum LLC.

Materials Research Proceedings 57 (2025) 512-520 https://doi.org/10.21741/9781644903735-60

In the remainder of the paper, the Background section presents the literature review, while the Problem description section introduces the characteristics of the case study system and the design alternatives. The results section presents the experimental results and the managerial insights. Finally, the Conclusion section summarises the contribution of the paper, discusses the limitations of this work, and introduces the key points for future research.

Background

Generally, the Assembly Line Balancing Problem (ALBP) aims to equally divide manufacturing tasks among workstations to obtain a smoothed and constant TH; however, combining buffer allocation and workstation processing time unbalance, under some operational characteristics, can lead to better performance [5]. Moreover, recent research [6] identified the literature gaps between assembly line balancing and real-world definition of the line: (i) the integration with the logistic activities that provide raw materials, (ii) the definition of the buffer dimensions, (iii) the transfer of semi-processed jobs from one station to another, and (iv) quality-related issues like the need for reworks, the position of quality inspections and quality control activities to minimise defectives per workstation. Moreover, lines must be rebalanced in the case of changes in the demand volume or production mix, thus leading to the need to perform the analysis again to identify a novel line setup [5].

Recent literature shows that controlling the material handling systems is important to reduce system congestion and improve system performance by identifying more efficient solutions to the ALBP [7]. Computational studies showed that the integrated decision approach can lead to more efficient design and redesign of assembly lines, enhancing the exploitation of automated transport infrastructure like AGV and AMR [8].

Also, considering the operational characteristics of the assembly line in the design phase can improve the TH while reducing design costs when buffer allocation and assembly line balancing are simultaneously addressed [9]. Short-term planning impacts on ALBP are more difficult to evaluate. On the one hand, buffer allocation and sequencing can improve line performance, depending on the production mix and operational characteristics of the problem [10]. On the other hand, the impacts of short-term production planning, like scheduling problems, increase in highly utilised manufacturing environments, while in under-utilised systems, their impact is not so significant for the objectives of ALBP [11].

In general, the assembly line design, simultaneously considering production operations, material handling system, and manufacturing technologies characteristics, is not yet comprehensively explored in the literature [11], particularly for CONWIP systems where W* must be defined.

In the literature, discrete event simulation has been widely adopted to study the ALBP. In particular, it was successfully used for system design by comparing alternatives for prototyping and alternative design solutions [12]. Moreover, in smart manufacturing system design, discrete event simulation highlights the interactions between different elements, such as buffers, their location, task allocation through the line, and operational characteristics [13]. Discrete event simulation also plays a pivotal role when integrated into digital twins, which are also used for manufacturing system design, like the Function-Structure-Behavior-Control-Intelligence-Performance (FSBCIP) framework that, after having set the production goals, supports iterative design and alternative comparison [14].

This paper exploits discrete event simulation to investigate the ALBP in a CONWIP assembly line for a part of a line producing engines for electric cars, in which conveyors interconnect machines while concurrently setting W*. The addressed problem consists of (i) determining the working conditions of a critical workstation, (ii) exploring the use of buffer stocks and blocking after service mechanisms to control the job flows through the conveyor carousels, (iii) limiting congestion into the carousels.

Materials Research Proceedings 57 (2025) 512-520 https://doi.org/10.21741/9781644903735-60

Problem description

The alternative solutions to the ALBP coupled with different W* levels impact three main Key Performance Indicators (KPIs): (i) the average shift (one daily eight-hour shift) throughput (TH), (ii) the standard deviation of the shift TH, and (iii) the carousel congestion. Critical levels of carousel congestion can cause deadlocks, that is, a system state in which the system cannot evolve into another. A deadlock example is a carousel full of recirculating jobs that prevent the workstations from unloading worked jobs and loading new ones. The intervention of resources external to the system, like operators, to manually solve the problem is the only way to overcome a deadlock state.

The alternative solutions to the ALBP combine four different working conditions of a critical workstation of a realistic assembly line (part of a line for the production of the engine of electric cars) with two buffer designs: (i) conveyor carousel, or (ii) blocking after service policies combined with standard buffers and restricted use of conveyor carousels.

Hence, this paper analyses eight line scenarios obtained by combining the two aforementioned factors. For each scenario, different W* levels are investigated.

The assembly line. Fig. 1 shows the assembly line composed of seven workstations (WSs) with one or two identical and unreliable machines. In particular, the first and the last WSs (in Fig. 1, WS1 and WSQC, respectively) are the only workstations with reliable machines. All the other workstations from WS2 to WS6 have identically unreliable machines. The sensors at the end of the machines in such workstations detect the need for a quality inspection of the just produced job with a probability δ. WS2 and WS5 consist of two identical machines, while all the other workstations are single-machine.

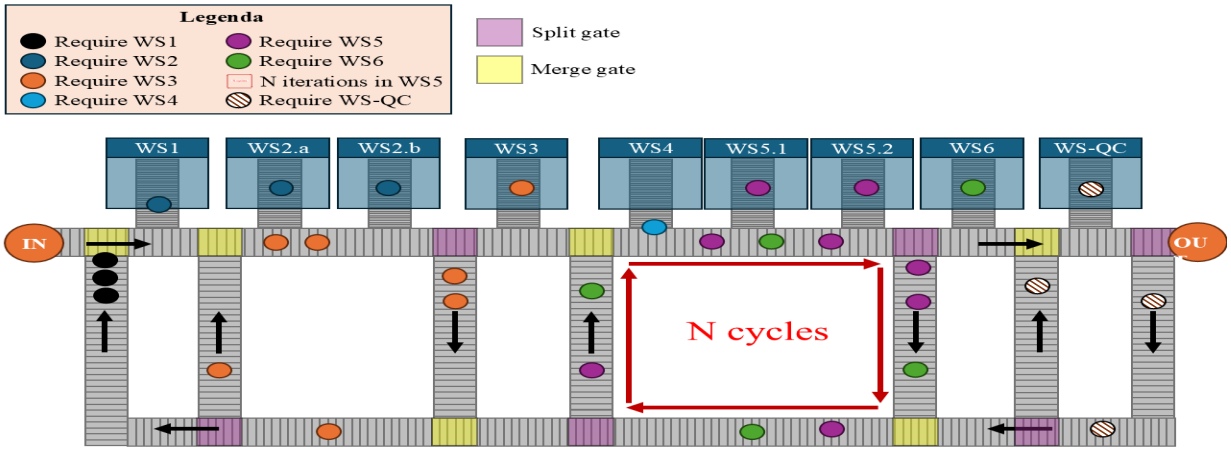


Figure 1. The assembly line has six production workstations (workstations 2 and 5 have two identical machines, namely a and b, respectively), and a final workstation is for quality inspections (WSQC).

The jobs subjected to quality inspection are sent to the quality control WS (in Fig. 1, WSQC). With probability β, they have a reparable defect that requires a rework in the station of origin; with probability γ, they were subjected to a false positive defect detection of the sensor and, hence, they are sent to the station following the one they came from, or, with probability $1 - \beta - \gamma$, they have an unrepairable defect that forces them to be discarded from the system.

The CONWIP system exploits a large number of pallets in which the jobs are put in the load bay (load and unload bays are in red in Fig. 1). The load bay controls the job entering into the system by ensuring that the number of full pallets circulating in all the carousels is always equal to W*. The pallets with the jobs just released by the load bay are stocked in a FIFO buffer close to WS1.

Materials Research Proceedings 57 (2025) 512-520 https://doi.org/10.21741/9781644903735-60

WS1 employs a blocking after service policy that allows unloading the worked job only when at least one of the two machines in WS2 is idle. The job worked in one of the two machines in WS2 recirculate in the WS2 carousel (the first conveyor carousel from the left in Fig. 1) until WS3 is idle, then the first job closer to WS3 is allowed to exit the carousel to be worked in WS3.

After WS3, jobs are processed in WS4 and WS5. WS5 is the critical workstation that can work in four alternative working conditions. WS5 consists of two identical machines, one after the other, performing an operation that can be completed in just a single iteration or up to four sequential job iterations. The processing time is proportional to the number of iterations; that is, if the entire work is performed in four different job works rather than one, the processing time will be one out of four of the processing time required to perform the work in only one iteration.

WS4 and the two machines in WS5 are in a conveyor carousel where the jobs circulate until the machine they are waiting for is idle (WS4, WS5, or WS6). Hence, the jobs that have finished the processing in WS5 circulate in the same carousel until WS6 is idle. Jobs successfully processed in WS6 are then unloaded in the unloading bay (the red box on the right side of Fig. 1) while the pallets return to the load bay.

The simulation model. The simulation model simplifies the real system to reduce the variability propagation and highlight the impact on the TH shift average and standard deviation. Specifically, the quality control performed in WSQC always sends back the jobs in the origin WS for rework due to repairable defects. The simulation model has been implemented in the commercially available software Arena Rockwell 16.0.

Due to the complexity of the system and the simulation model, an animated version of the simulation model has been used for model validation.

The WSs processing times have been fixed to ensure a balanced line; therefore, each process time is equal to 20 minutes, including WSQC, and the probability δ of requiring a quality inspection for just processed jobs is 5% in each WS except for WS1 in which it is 0%.

The design of experiment. This paper investigates the ALBP by considering both the transport and manufacturing resources. The transport resource, i.e., the conveyor, also represents a buffer between WSs because the carousels can store the jobs until the next WS becomes idle. However, blocking after service mechanisms and rules for leaving carousels can increase congestion on specific loops. Therefore, the original model is compared to a model in which the jobs can freely flow through all the conveyor loops. The original system configuration and the second one will be named *Constrained Flowing* (CF) and *Free Flowing* (FF).

WS5 can process a job in a single time or divide the process into subprocesses up to four, thus enhancing job recircles in the conveyor carousel. This could be a strategy exploited in reconfigurable systems to adjust the shift TH according to workers' performance or the entire system TH. Therefore, four scenarios are considered by assuming the two identical machines of WS5 process jobs from one single time to four times.

Finally, the overall system performance depends on the W* jobs simultaneously admitted into the system. Therefore, an experimental campaign has been done to identify the maximum number of jobs that can be allowed in the system without causing deadlocks. The experiment involves three factors: (1) the two system types, CF and FF, (2) the number of iterations performed in WS5 (from 1 to 4), and (3) W* (from 1 to 44), leading to 352 different scenarios.

Results

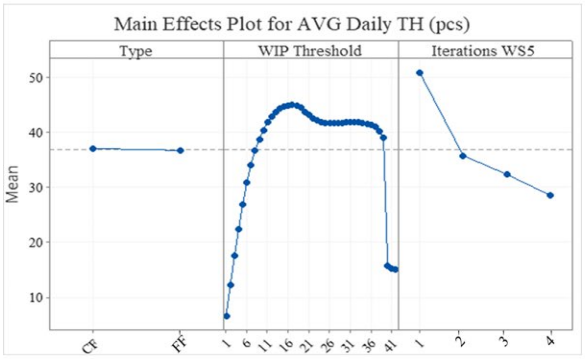
Each scenario has been simulated 30 times, and each of the 30 replications has a warm-up period of one year and a simulation horizon of another year, consisting of daily shift of 8 hours.

The average and the standard deviation of the TH in a shift are exploited to investigate (i) the number of iterations that jobs must do in WS5 and its processing time, (ii) whether the material handling system is more performant in the presence of buffer stocks and blocking mechanisms,

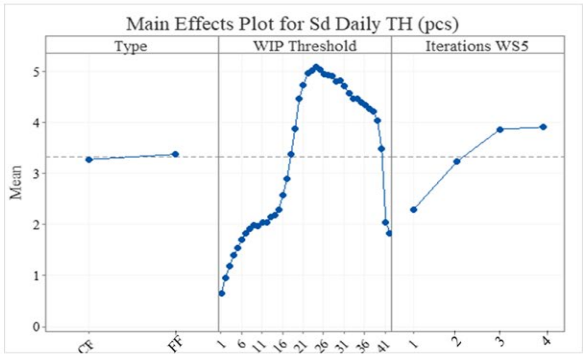
Materials Research Proceedings 57 (2025) 512-520 https://doi.org/10.21741/9781644903735-60

namely constrained flow (CF) or with jobs freely flowing through the conveyor carousels, namely freely flowing (FF), and (iii) W* for the CONWIP system.

Fig. 2 shows the main effects for each level of the experimental factors, highlighting that both for the TH average (Fig. 2a) and the TH standard deviation (Fig. 2b), the choice of the W* is critical to improve the TH and control its variability (charts in the middle in Figures 2a and 2b cover the widest area). The selection of a technology for working a job in a single iteration is preferable both for improving TH and reducing its standard deviation (chart "Iterations WS5").



a) The TH average for each level of the factors



b) The TH standard deviation for each level of the factors

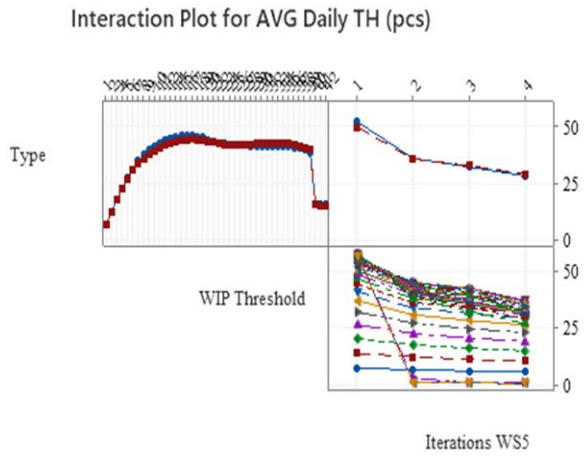
Figure 2. Average and standard deviation of the throughput (TH) for each level of the experimental factors.

The material handling system (chart "Type") seems negligible; however, a deeper investigation is necessary to exclude the presence of compensation effects that hide its impacts. To this purpose, Fig. 3 presents the interaction plots to analyse the pairwise interactions among experimental factors. The chart focused on the Type-WIP* TH average (Fig. 3a, plot on the left side) shows that for some W*, the type CF seems more efficient than FF. The same chart shows a drop in TH average with the highest value of W*. The cause of the drop is a deadlock: there are too many jobs in the system, a conveyor carousel becomes congested, the machine cannot unload processed jobs, and the system is blocked until a worker manually remove or move jobs from the line.

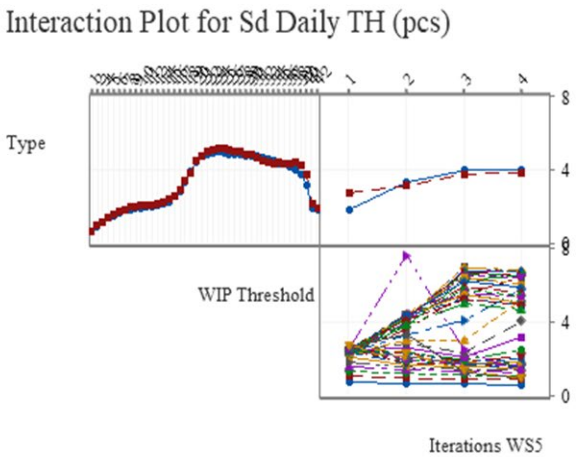
The system type is negligible as the carousel size of WS4 and WS5 is significantly larger than the others, and it also contains the critical station required by many parts, i.e., WS5. Therefore, this carousel is a sort of bottleneck that makes the blocking mechanisms and leaving rules irrelevant.

Fig. 4 deepens the TH average and standard deviation by focusing on W* and the four scenarios of technology selection for WS5. Fig. 4 presents bar charts in which the red markers indicate the average of the CF type, while the black ones are the average of the FF solution.

Materials Research Proceedings 57 (2025) 512-520 https://doi.org/10.21741/9781644903735-60



a) The experimental factor pairwise interactions for the TH average



b) The experimental factor pairwise interactions for the TH standard deviation

Figure 3. The pairwise interactions of the experimental factors for the average and standard deviation of throughput (TH)

In the case of 1 iteration in WS5, the TH average asymptotically increases with the W* while the standard deviation (the segment crossing the markers of the average) remains limited. In the other three cases, the TH average has a maximum at W*=17, then decreases again while its standard deviation increases (the whiskers are longer). The CF type is always slightly more performant at the maximum average TH, but when W* increases, FF has a higher average TH and lower standard deviation. This happens because after the maximum average TH has been reached, increasing the system WIP increases the congestion into the conveyor loops, in which jobs are more constrained due to the blocking mechanisms. In this case, jobs are randomly processed by one of the two WS5 machines. Sometimes, jobs doing their first iteration are processed before the others, also increasing the average flow time of the jobs; in other cases, only jobs at the last iteration are processed. This leads to high variability in TH and a lower TH rate. At the same time, in the case of FF, jobs can occupy several parts of the conveyor rather than being constrained in limited carousels, which mitigates the adverse effect of increasing W* over the level corresponding to the maximum average TH.

W* is a critical factor because, in CONWIP systems with unreliable machines and quality inspection workstations far from the other WSs, it can be difficult to avoid machine starvation by releasing new jobs into the system at a smooth and constant rate. However, excessively increasing W* is shown to be inefficient, particularly in the case of systems with inflexible control of buffers and carousels.

The increase in TH variability with the increase of the iteration number in WS5 and of W* is explained by the increasing number of jobs in the WS4-WS5 carousel with different remaining numbers of iterations in WS5. In fact, it can happen that for some hours, only the first and second operations of many parts have been performed, achieving TH equals 0. However, after this time, there will be a moment in which only the fourth operation is performed in WS5, having large fluctuations in TH. Also, that carousel is full of many parts with different characteristics, so the maximum achievable TH decreases from 60 (scenario 1) to 36 (scenario 4). Hence, no benefits are achieved by increasing the number of iterations.

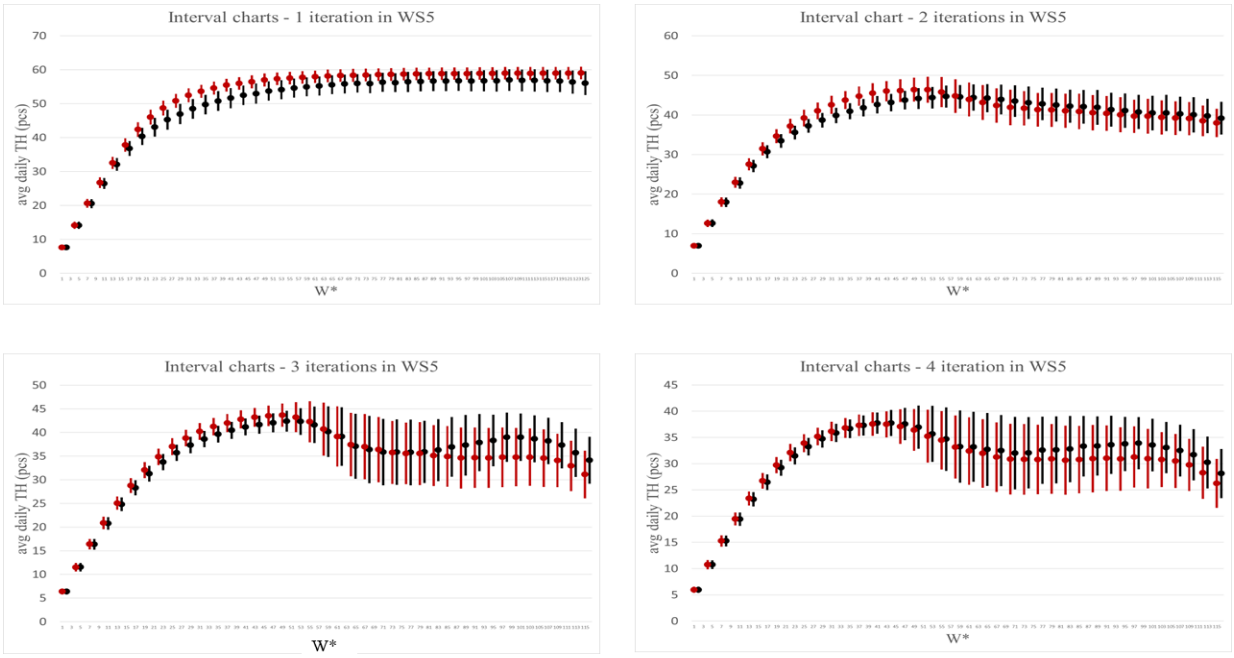


Figure 4. Interval charts showing the TH average for the two types (constrained flowing in red, free flowing in black) under the four iteration levels.

Conclusion

This paper deepens the assembly line balancing problem, taking into account material handling systems and how they are controlled, as well as the operational characteristics like the critical level of WIP in a CONWIP system and the configuration of a process that can work a job using a different number of iterations (and related processing time). Discrete event simulation has been exploited to perform scenario analyses to investigate the impacts of experimental factors and their interactions.

The results show that the control of the material handling systems, particularly the exploitation of the entire conveyor as a buffer loop or the introduction of blocking mechanisms and buffer stocks, impacts the average TH and the variability propagation in an increasing manner, proportional to W*.

This paper highlights the complexity of balancing or rebalancing lines in industrial cases in which machines can produce defective parts, and quality inspections increase variability propagation.

Moreover, advanced analyses and tools are required to exploit all the benefits of Industry 4.0 by properly configuring machines, material handling systems, and operational parameters of the lines.

This paper is tightly focused on a realistic case study, and, although the performed analyses provide insights that can affect other systems, they cannot be generalisable. An extensive design of the experiment would improve the generalisation of the results.

Future research will investigate (i) the definition of a framework for assembly line balancing problems with material handling systems and buffer allocation problems in the case of system reconfiguration; (ii) further interactions between material handling systems and production planning approaches.

Acknowledgements

This study was carried out within the Motown: Smart Production Planning and Control for Manufacturing of Electric Vehicle Powertrain in Industry 4.0 Environment project – funded by European Union – Next Generation EU, Missione 4 Componente 1 CUP E53D23007900006,

within the PRIN 2022 program (D.D. 104 - 02/02/2022 Ministero dell'Università e della Ricerca). This manuscript reflects only the authors' views and opinions and the Ministry cannot be considered responsible for them.

References

[1] Zhou, L., Jiang, Z., Geng, N., Niu, Y., Cui, F., Liu, K., & Qi, N. (2022). Production and operations management for intelligent manufacturing: A systematic literature review. International Journal of Production Research, 60(2), 808-846 https://doi.org/10.1080/00207543.2021.2017055

[2] Dolgui, A., Sgarbossa, F., & Simonetto, M. (2022). Design and management of assembly systems 4.0: systematic literature review and research agenda. International Journal of Production Research, 60(1), 184-210. https://doi.org/10.1080/00207543.2021.1990433

[3] Wang, H., Lv, L., Li, X., Li, H., Leng, J., Zhang, Y., ... & Luo, G. (2023). A safety management approach for Industry 5.0′ s human-centered manufacturing based on digital twin. Journal of Manufacturing Systems, 66, 1-12. https://doi.org/10.1016/j.jmsy.2022.11.013

[4] Cañas, H., Mula, J., Díaz-Madroñero, M., & Campuzano-Bolarín, F. (2021). Implementing industry 4.0 principles. Computers & industrial engineering, 158, 107379. https://doi.org/10.1016/j.cie.2021.107379

[5] Romero-Silva, R., & Shaaban, S. (2019). Influence of unbalanced operation time means and uneven buffer allocation on unreliable merging assembly line efficiency. International Journal of Production Research, 57(6), 1645-1666. https://doi.org/10.1080/00207543.2018.1495344

[6] Boysen, N., Schulze, P., & Scholl, A. Assembly line balancing: What happened in the last fifteen years?. European Journal of Operational Research, 301(3) (2022), 797-814. https://doi.org/10.1016/j.ejor.2021.11.043

[7] Fragapane, G., Ivanov, D., Peron, M., Sgarbossa, F., & Strandhagen, J. O. Increasing flexibility and productivity in Industry 4.0 production networks with autonomous mobile robots and smart intralogistics. Annals of operations research, 308(1) (2022), 125-143. https://doi.org/10.1007/s10479-020-03526-7

[8] Rahman, H. F., Janardhanan, M. N., & Nielsen, P. (2020). An integrated approach for line balancing and AGV scheduling towards smart assembly systems. Assembly Automation, 40(2), 219-234. https://doi.org/10.1108/AA-03-2019-0057

[9] Tiacci, L. (2015). Simultaneous balancing and buffer allocation decisions for the design of mixed-model assembly lines with parallel workstations and stochastic task times. International Journal of Production Economics, 162, 201-215. https://doi.org/10.1016/j.ijpe.2015.01.022

[10] Romero-Silva, R., Santos, J., & Hurtado-Hernández, M. (2024). A conceptual framework of the applicability of production scheduling from a contingency theory approach: addressing the theory-practice gap. Production Planning & Control, 35(3), 262-282. https://doi.org/10.1080/09537287.2022.2076627

[11] Tiacci, L. (2024). Combining balancing, sequencing and buffer allocation decisions to improve the efficiency of mixed-model asynchronous assembly lines. Computers & Industrial Engineering, 194, 110357. https://doi.org/10.1016/j.cie.2024.110357

[12] Konstantinov S, Ahmad M, Ananthanarayan K, Harrison R. The cyber-physical e-machine manufacturing system: Virtual engineering for complete lifecycle support. Procedia CIRP. 2017 Jan 1;63:119-24. https://doi.org/10.1016/j.procir.2017.02.035

[13] Santos CH, De Queiroz JA, Leal F, Montevechi JA. Use of simulation in the industry 4.0 context: Creation of a Digital Twin to optimise decision making on non-automated process. Journal of Simulation. 2022 May 4;16(3):284-97. https://doi.org/10.1080/17477778.2020.1811172

[14] Leng, J., et al. Digital twins-based smart manufacturing system design in Industry 4.0: A review. Journal of manufacturing systems. 2021, 60: 119-137. https://doi.org/10.1016/j.jmsy.2021.05.011

Materials Research Proceedings 57 (2025) 521-529 https://doi.org/10.21741/9781644903735-61

Metaheuristic approaches for solving the scheduling problem in the semiconductor diffusion work area

Roberto Rosario CORSINI[1,a*], Antonio COSTA[1,a*], Valeria FICHERA[1,a], Giuseppe ORITI[1,a] and Daniele PAGANO[2,b]

[1]University of Catania, Italy

[2]STMicroelectronics, Catania, Italy

[a]roberto.corsini@unict.it, [b]antonio.costa@unict.it, [c]valeria.fichera@phd.unict.it, [d]giuseppe.oriti@phd.unict.it, [e]daniele.pagano@st.com

Keywords: Scheduling, Semiconductor Manufacturing, Smart Manufacturing

Abstract. Motivated by a real case study of a semiconductor company, the paper addresses the scheduling problem in the diffusion area, which is recognized as one of the most critical stages in semiconductor manufacturing. This work area can be modeled as a two-stage hybrid flow shop scheduling problem with re-entrant flows. The first stage is the cleaning process, wherein impurities are removed from the wafer surface. The second one entails several tasks, such as diffusion, deposition and oxidation, to be performed into different furnaces. Based on the product recipe, wafer lots may undergo multiple operations in the second stage. The diffusion area also includes several production constraints, such as p-batching, machine eligibility and Q-time constraint, which increase the complexity of the problem. A novel metaheuristic named the Modified Harmony Search algorithm is proposed to minimize the average flow time of the system.

1. Introduction and background

Semiconductor manufacturing systems are complex, multi-stage production environments where raw silicon wafers are transformed into integrated circuits (ICs) through a large sequence of operations. The production process is divided into front-end and back-end manufacturing. The front-end phase consists of wafer fabrication, which involves hundreds of machines performing multiple operations to produce ICs, while the back-end phase encompasses final operations, such as testing and packaging, before market release. The front-end is particularly challenging due to the technological complexity and the extensive processing requirements involved. As detailed in [1], the front-end semiconductor manufacturing system is organized into different work areas, each dedicated to a specific set of operations, namely diffusion, photolithography, etching, ion implantation, and planarization. Among them, the diffusion area is widely recognized as one of the most critical stages due to long processing times and complexity of production constraints. Given its industrial significance, the scheduling problem in the diffusion work area has recently garnered growing interest from both academic researchers and practitioners (see, e.g., [2-7]).

The diffusion area is typically modeled as a two-stage flexible flow shop with re-entrant flows. Specifically, in the first stage cleaning machines are used to remove material impurities from wafer surfaces, while in the second stage furnaces execute one of three alternative operations, i.e., diffusion, deposition or oxidation. A key complexity factor is the re-entrant nature of the problem, as a wafer lot may require multiple consecutive operations executed by furnaces. Furthermore, the diffusion work area is characterized by several stringent production constraints, including: p-batching with incompatible job operations, machine eligibility, dynamic job arrivals, waiting time limits between two consecutive operations, machine-dependent batch size constraints, operation- and machine-dependent processing times and preloading operations. These scheduling constraints further increase the complexity of the scheduling problem, making it challenging to achieve

Content from this work may be used under the terms of the Creative Commons Attribution 3.0 license. Any further distribution of this work must maintain attribution to the author(s) and the title of the work, journal citation and DOI. Published under license by Materials Research Forum LLC.

Materials Research Proceedings 57 (2025) 521-529 https://doi.org/10.21741/9781644903735-61

optimal or near-optimal solutions within a reasonable computational time. To tackle the scheduling problem in the diffusion work area of semiconductor manufacturing systems, metaheuristic algorithms have been widely explored in recent literature. Among these, Simulated Annealing (SA) has been one of the most frequently proposed methods [2,3,5,9], while alternative approaches such as Variable Neighborhood Search (VNS) [4], Harmony Search (HS) [6], and Genetic Algorithms (GA) [7,8] have also been explored. Motivated by the European project named HICONNECTS, this work deals with a real-world scheduling problem in the diffusion work area of a semiconductor manufacturing facility located in the Southern Italy, with the aim of providing an efficient metaheuristic algorithm able to optimize a turnaround performance measure of the system. The main contributions of this work, with respect to the recent literature, are summarized as follows:

1. The proposed scheduling model integrates a comprehensive set of production constraints that are specific to the real-world diffusion work area under investigation. While previous studies [2–9] have commonly considered p-batching, machine eligibility, waiting time limits, and dynamic job arrivals, this work introduces additional complexities, i.e., machine-dependent minimum and maximum batch size, operation and machine-dependent processing times and preloading operations. Including these additional constraints enables a more accurate replication of the real operations within the diffusion work area, while simultaneously increasing the complexity of the scheduling problem under investigation.
2. To solve the scheduling problem at hand, a Modified Harmony Search (MHS) algorithm is proposed. The proposed MHS enhances the traditional HS approach by introducing adaptive parameter control and an embedded Local Search (LS) mechanism to improve solution quality and convergence speed. An experimental evaluation based on industrial data is conducted to assess the effectiveness of MHS compared to the standard HS algorithm [6] and the SA algorithm [2]. The flowtime performance measure has been considered as the metric for the experimental comparison

The structure of the paper is as follows. Section 2 describes the problem of the diffusion work area under study. Section 3 presents in detail the proposed MHS metaheuristic algorithm. Section 4 shows the results arising from the experimental comparison between MHS, HS and SA. Finally, Section 5 reports the concluding remarks and directions for future research.

2. Problem description

In the diffusion work area, which is illustrated in Figure 1, N wafer lots, which can be referred to as jobs ($j=1, ..., N$), are processed in a re-entrant two-stage flexible flow shop. In the first stage ($s=1$), cleaning operations are performed by M_1 cleaning machines while in the second stage, diffusion, deposition and oxidation operations are executed by M_2 furnaces. Hereinafter, the two stages are also denoted as cleaning and diffusion stages. The problem is re-entrant since, based on the wafer lot recipe φ, a wafer lot may require two consecutive diffusion operations. Furthermore, some jobs may need only a cleaning operation, while others may require only one or two furnace operations. The recipe φ also specifies the type of operation o_{js} of job j at stage s. The processing time p_{om} depends on the operation o_{js} and the selected machine m_s. The problem is subject to dynamic job arrivals, as job release times r_{js} can be greater than zero at the first stage ($r_{j1} \geq 0$), while at the second stage, they are equal to job completion times of the first stage, i.e., $r_{j2}=C_{j1}$. Each machine operates under p-batching constraint with incompatible job operations. Jobs requiring the same operation o_{js} are collected in batches b_s at each stage and processed in parallel. Batch release time r_b is the maximum job release time in the batch, i.e., $r_b=\max\{r_{js}\}$ where $j \in b_s$. Each machine m_s has a minimum $BMIN_{ms}$ and a maximum $BMAX_{ms}$ batch size constraint. Furthermore, there is the machine eligibility constraint since the o_{js} can be processed by a specific set of machines M_{os}, where $M_{os} \subseteq M_s$. Two different waiting time constraint QW are imposed in

Materials Research Proceedings 57 (2025) 521-529 https://doi.org/10.21741/9781644903735-61

the inter-operational buffer between the first and second stage to prevent job deterioration and ensure quality standards. Specifically, if the waiting time wt_j of a job coming from the cleaning stage exceeds QW_{CD}, it must be reworked and returned to the cleaning buffer. Conversely, if the waiting time wt_j of a re-entrant job from the diffusion stage exceeds QW_{DD} (i.e., waiting time constraint between two consecutive diffusion operations), then the job must be scrapped. Additionally, each diffusion furnace can preload a second batch, which is processed immediately after the first batch is completed. The preloading operation allows a batch to be inserted into the machine in advance, thereby protecting it from exposure to environmental conditions that could compromise the quality of the jobs. For this reason, the waiting time constraint for jobs in the preloaded batch is relaxed. In this study, the scheduling problem in the diffusion work area consists of selecting the batches to be loaded at each stage during an 8-hour work shift. The objective is to minimize the average flowtime of the jobs processed within the shift. The average flowtime F is calculated as follows:

$$F = \sum_{j=1}^{N}(C_{j2} - r_{j1})/N \quad (1)$$

where C_{j2} is the completion time of job j after its final operation in a furnace, r_{j1} is the job release time at cleaning stage and N is the total number of jobs processed during the shift.

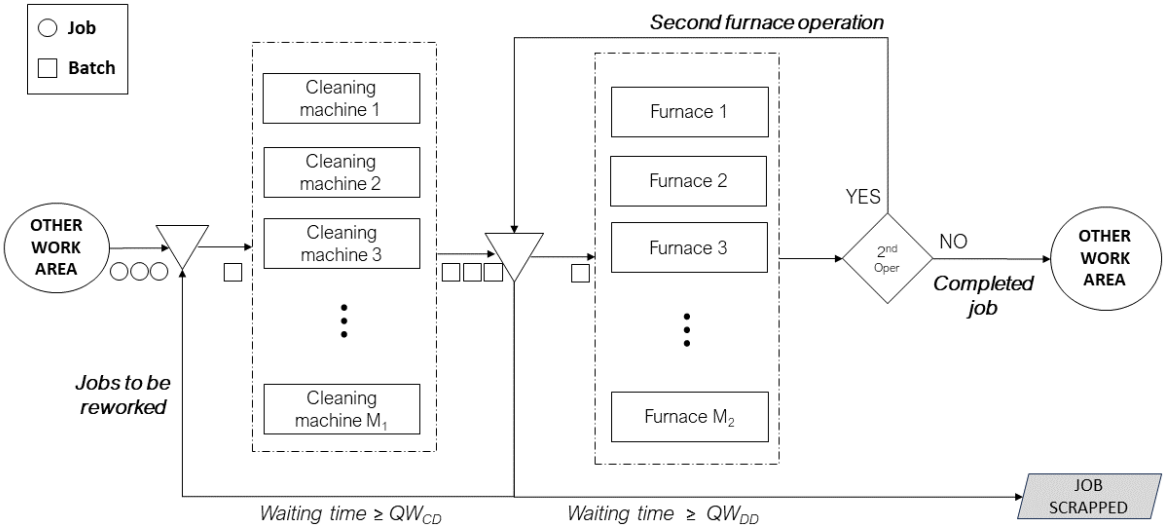


Figure 1. Schematic representation of the diffusion work area.

3. Modified Harmony Search algorithm

The HS algorithm is a well-known metaheuristic inspired by the process of musical improvisation. It is a population-based algorithm, where the population is called Harmony Memory (HM) and consists of a set of candidate solutions, referred to as harmonies:

$$HM = \{X_1, X_2, \dots, X_{HMS}\} \quad (2)$$

where X_k represents a candidate solution (harmony), and *HMS* (Harmony Memory Size) is the total number of harmonies stored in the HM. Each harmony X_k is a N-dimensional real-valued vector:

$$X_k = \{x_k(1), x_k(2), \dots, x_k(N)\} \quad (3)$$

where x_k *(j)* is a real value within the range [x_{min}, x_{max}]. Each harmony is then transformed into a sequence of wafer lots using the Smallest Position Value (SPV) rule. In this study, a MHS algorithm with two key enhancements over the traditional HS is proposed. The former consists of the integration of a LS strategy. To avoid stagnation in local optima, a probabilistic LS mechanism is applied to improve the worst solutions. Precisely, the LS process performs random swap

Materials Research Proceedings 57 (2025) 521-529 https://doi.org/10.21741/9781644903735-61

operations on the worst solution of the HMS to explore candidate solutions. The latter is the adaptive control of HS and LS parameters. Instead of using fixed values, the algorithm's parameters are dynamically adjusted during the search process based on the number of iteration (*iter*):

$$\rho(iter) = \rho^U + \frac{(iter - iter_{max}) \cdot (\rho^U - \rho^L)}{iter_{max}} \quad (4)$$

where $\rho(iter)$ varies within the range $[\rho^L, \rho^U]$ and can be applied to ρ_{cr}, ρ_{ar} and the LS parameters. The pseudo code of MHS and LS is reported in Algorithm 1 and 2, respectively.

In Step 1, HS and LS parameters are initialized. The HM is created by generating *HMS* harmonies, where each harmony represents a candidate scheduling solution. Each harmony is constructed as a real-valued vector using the following formula:

$$X = x_{min} + (x_{max} - x_{min}) \cdot rand(N) \quad (5)$$

where rand(*N*) is a *N*-dimensional vector of random values in [0,1]. To enhance the initial solution, one randomly selected harmony is replaced by the First-In-First-Out (FIFO) scheduling rule. The objective function *F(X)* of each harmony is evaluated using a simulation model coded in Python®, which emulates the diffusion work area of the semiconductor manufacturing system. The worst and best harmonies, X_{worst} and X_{best}, are identified and recorded. Step 2 consists of the Harmony Improvement (HI) phase, where new harmonies X_{new} are iteratively generated and evaluated. The number of iterations without any improvement, denoted as γ, is tracked to determine when the LS must be applied. At each iteration, the algorithm dynamically adjusts the parameters ρ_{cr} and ρ_{ar} and α as in Equation 4, so as to ensure a gradual evolution of the algorithm from the exploration to the exploitation phase. α is an adaptive parameter that defines the maximum number of iterations allowed without improvement in the algorithm. In Step 3, a new harmony X_{new} is then generated based on three possible mechanisms. First, with probability ρ_{cr}, the value of $x_{new(j)}$ is taken from an existing harmony in HM. In this case, there is an additional probability ρ_{ar} that $x_{new(j)}$ is adjusted with the real-value in position *j*, $x_{best(j)}$, of the best solution X_{best}. Otherwise, $x_{new(j)}$ is randomly generated in $[x_{min}, x_{max}]$. In Step 4, X_{new} is evaluated and if $F(X_{new})$ is lower than $F(X_{worst})$, it replaces X_{worst} in the HM and the new worst harmony is recorded. Additionally, if $F(X_{new})$ is lower than $F(X_{best})$, it becomes the new best solution and γ is set to zero. In Step 5, the LS is applied if γ is greater than α, where α is an adaptive parameter that assumes values within the range $[\alpha^L, \alpha^U]$, as in Equation 4. Further LS parameters are β and $eval_{LS}$, which controls the probability of performing a swap operation and defines the number of solutions evaluated by LS, respectively. The LS procedure is performed on X_{LS}, initially set as X_{worst}, by iteratively applying swap operations with probability β, which is also dynamically updated as in Equation 4. A total of $eval_{LS}$ number of new solutions are evaluated, and the best one, denoted as $X_{LS,best}$, is selected. If $X_{LS,best}$ improves X_{worst}, then $X_{LS,best}$ is inserted into the HM and the new X_{worst} is recorded. Furthermore, if $F(X_{LS,best})$ is lower than $F(X_{best})$, then $X_{LS,best}$ becomes the new best solution. MHS is stopped in Step 6 of Algorithm 1 when the maximum number of iterations, $iter_{max}$, is reached, returning best harmony X_{best}.

Algorithm 1. MHS

Step 1: ***Initialization***
Initialize HS and LS parameters. Generate the initial HM. Evaluate HM and store X_{worst} and X_{best}.
Step 2: ***Harmony Improvement***
for *iter* in $iter_{max}$:
$\gamma = \gamma + 1$; Calculate adaptive values for α, ρ_{cr}, ρ_{ar} (Equation 4)
Step 3: ***Generation of a new harmony***
$X_{new} = []$
for *j* in *N*:
if $rand < \rho_{cr}$ **then** $x_{new}(j) = x_a(j)$ where X_a is randomly selected from *HM*
if $rand < \rho_{ar}$ **then** $x_{new}(j) = x_{best}(j)$
else $x_{new}(j) = x_{min} + [x_{max} - x_{min}] \cdot rand$
Step 4: ***HM update***
if $F(X_{new}) < F(X_{worst})$ **then** replace X_{worst} with X_{new} in *HM* and update X_{worst}
if $F(X_{new}) < F(X_{best})$ **then** $X_{best} = X_{new}$ and $\gamma = 0$
Step 5: ***LS application***
if $\gamma > \alpha$ **then** $\gamma = 0$; apply LS (see Algorithm 2)
Stopping the algorithm
Step 6: Return X_{best} as the optimal solution

Algorithm 2. LS

Step 5.1: ***LS initialization***
Compute adaptive value for β (Equation 4)
for *i* in $eval_{LS}$:
$X_{LS} = X_{worst}$
Step 5.2: ***Performing swap operations***
for *j* in *N*:
if $rand < \beta$ **then** $x_{LS}(j)$, $x_{LS}(k) = x_{LS}(k)$, $x_{LS}(j)$ where k is a random position in [1,*N*]
Record $X_{LS,best}$
Step 5.3: ***Evaluation of the new solution***
if $F(X_{LS,best}) < F(X_{worst})$ **then** replace X_{worst} with $X_{LS,best}$ in *HM* and update X_{worst}
if $F(X_{LS,best}) < F(X_{best})$ **then** $X_{best} = X_{LS,best}$

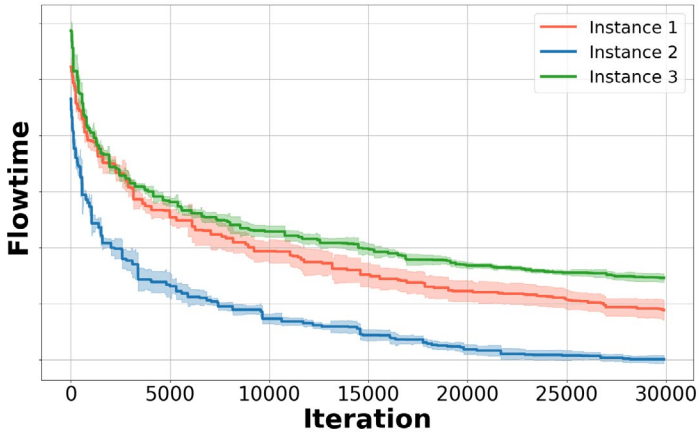
4. Experimental campaign and results

A comprehensive set of experimental analyses has been conducted to evaluate the effectiveness of the proposed MHS algorithm in addressing the scheduling problem within the diffusion work area of the semiconductor manufacturing system under investigation. The experimental scenarios have been generated using a real-world data set provided by the semiconductor company. The input parameters for the simulation model have been statistically extracted from one month of production data to ensure a realistic representation of the manufacturing environment. Due to non-disclosure agreement restrictions, input parameters (e.g., number of machines) cannot be revealed and the following information can be provided in generic terms. At each work shift, a number between 300 and 600 jobs are available for being scheduled. The number of cleaning and furnaces operations are in the range [60-90] and [150-250], respectively, while the processing times are in the range [60-120] and [240-1560] min. Batch size is in the range [1-5] jobs at the cleaning stage and [1-8] jobs at the diffusion stage. Two different versions of MHS have been tested, i.e., MHS_{AD}, which incorporates only the adaptive parameter mechanism (see Equation 4), and $MHS_{AD,LS}$, which additionally includes the LS component. The experimental evaluation is structured as follows: in section 4.1, a convergence analysis is performed to determine the computational time required for $MHS_{AD,LS}$ to reach a near-optimal solution. Then, in section 4.2, a comparative analysis is conducted, where MHS_{AD} and $MHS_{AD,LS}$ are compared with HS, SA in terms of mean flowtime. The algorithm parameters have been fine-tuned through a trial-and-error procedure, resulting in the following selected values:HMS=100; ρ_{cr}^{L}=0.9; ρ_{cr}^{U}=0.99; ρ_{ar}^{L}=0.1; ρ_{cr}^{U}=0.3; α^{L}=500; α^{U}=900; β^{L}=0.9; β^{U}=0.1; $evals_{LS}$=1500. ρ_{cr} and ρ_{ar} of HS are set equal to the mean value of [ρ_{cr}^{L}, ρ_{cr}^{U}] and [ρ_{ar}^{L}, ρ_{cr}^{U}], respectively. All algorithms have been implemented in Python®v.3.12.2 on a workstation equipped with an INTEL i9-9900 3.6 GHz 10 core CPU, 32Gb DDR4 2666 MHz RAM and Win 10 PRO OS.

Materials Research Proceedings 57 (2025) 521-529 https://doi.org/10.21741/9781644903735-61

4.1 Convergence analysis

A dedicated experimental study has been conducted to assess the convergence behavior of the proposed $MHS_{AD,LS}$ algorithm, which will later be used as the stopping criterion for all the algorithms under comparison. Specifically, three instances have been generated for this analysis. Given the stochastic nature of $MHS_{AD,LS}$, each instance has been replicated five times with different random seeds. As a result, a total of 3 × 5 = 15 runs has been performed for this convergence analysis. Figure 2 illustrates the convergence behavior in terms of flowtime as a function of the number of iterations. Due to the stochastic approach, each curve in the figure represents the median value across the five replicates for each instance, while the shaded areas indicate the standard deviation. For this analysis, a stopping criterion of 30,000 iterations has been initially considered. However, it can be observed that after 20,000 iterations, the $MHS_{AD,LS}$ does not yield any significant improvement in flowtime. Therefore, 20,000 iterations have been selected as the stopping criterion for the comparison among the metaheuristic algorithms. Figure 2 also refers to the time-to-convergence analysis, showing that approximately 13 minutes of computational time are required to reach 20,000 iterations.



Number of iterations	Average Comp. time (s)
5,000	130
10,000	340
15,000	590
20,000	810
25,000	1005
30,000	1175

Figure 2. Convergence analysis of the $MHS_{AD,LS}$ algorithm.

4.2 Results from the experimental comparison

To conduct the experimental comparison between $MHS_{AD,LS}$, $MHS_{AD,}$ HS and SA, 10 instances were generated based on the industrial data described in Section 4. Each instance was replicated 10 times using different random seeds to mitigate the influence of stochastic factors on the final results. Consequently, a total of 10 instances × 10 replicates × 4 algorithms = 400 runs were executed. The four metaheuristic algorithms were compared using the Relative Percentage Deviation (*RPD*), computed as follows:

$$RPD_{i,r,a} = \frac{F_{i,r,a} - F_{i,best}}{F_{i,best}} \% \quad (6)$$

where *i, r, a* represent the instance, replicate, and algorithm, respectively. $F_{i,r,a}$ denotes the flowtime obtained by algorithm *a* in instance *i* and replicate *r*, while $F_{i,best}$ corresponds to the lowest flowtime value among those achieved by the four metaheuristic algorithms across all replicates of instance *i*. The results of the experimental comparison are summarized in Table 1, where, for each instance, the median *RPD* (*MRPD*) value across all replicates is reported. The last row presents the average *MRPD* values for each algorithm along with the N_{best} index, which indicates the number of instances in which an algorithm achieved the best solution. The best results are highlighted in bold. The results in Table 1 highlight the effectiveness of the proposed $MHS_{AD,LS}$ algorithm for the scheduling problem in the diffusion work area under study. Specifically, $MHS_{AD,LS}$ achieves the lowest average *MRPD* value and finds the best solution in 9 out of 10

Materials Research Proceedings 57 (2025) 521-529 https://doi.org/10.21741/9781644903735-61

instances. This suggests that the combination of adaptive parameter tuning and LS mechanisms effectively enhances the search process, reducing the risk of premature convergence and improving solution quality. To further illustrate the comparative performance of the algorithms, Figure 3 presents a boxplot representation of the *RPD* values. The figure clearly demonstrates that the two proposed algorithms, MHS_{AD} and $MHS_{AD,LS}$ significantly outperform the benchmark metaheuristic algorithms from the literature (HS and SA). Notably, $MHS_{AD,LS}$ exhibits not only a lower *MRPD* but also a reduced variance compared to the other approaches, indicating a more robust and reliable performance across different problem instances. The observed results suggest that introducing adaptivity in HS parameters (MHS_{AD}) already provides a significant improvement over the standard HS, as seen in the reduction of *MRPD* values. The further enhancement achieved by $MHS_{AD,LS}$ confirms the crucial role of LS strategies in effectively navigating the solution space. Finally, non-parametric Mann-Whitney tests were conducted to compare $MHS_{AD,LS}$ metaheuristic algorithm with the three alternative algorithms. All non-parametric test provided a *p*-value of 0.00 for each comparison, indicating that the differences between $MHS_{AD,LS}$ and the other algorithms are statistically significant. The observed reduction in flowtime provided by the proposed $MHS_{AD,LS}$ a reduction of the time spent by jobs in the system. The minimization of average flowtime also implies a reduction in the overall system's work in progress (WIP) and has a significant impact on decreasing the cycle time.

Table 1. Experimental results in terms of MRPDs.

Instance	MHS_{AD}	$MHS_{AD,LS}$	HS	SA
1	6.82%	**4.39%**	10.68%	14.74%
2	2.21%	**0.80%**	6.28%	11.88%
3	4.21%	**1.83%**	8.52%	11.84%
4	2.27%	**1.40%**	5.71%	10.48%
5	3.16%	**1.48%**	6.82%	9.64%
6	3.66%	**1.31%**	8.48%	11.54%
7	**2.51%**	2.56%	7.11%	12.18%
8	2.38%	**2.19%**	6.48%	11.07%
9	2.80%	**1.06%**	6.16%	10.25%
10	5.19%	**2.97%**	8.85%	13.62%
Average (N_{best})	*3.52% (1)*	***2.00% (9)***	*7.51% (0)*	*11.73% (0)*

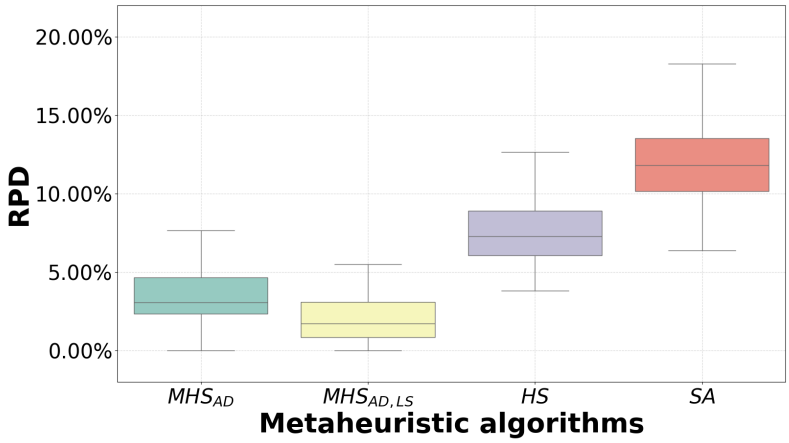


Figure 3. Boxplots to compare metaheuristic algorithms.

5. Conclusion

This paper addressed the scheduling problem in the diffusion work area of a semiconductor manufacturing system, which is modeled as a two-stage flexible flow shop with re-entrant flows and multiple complex production constraints, including machine-dependent batch sizes, operation-

and machine-dependent processing times, waiting time constraints, preloading operations and other constraints. To tackle this problem, a MHS metaheuristic algorithm was proposed, incorporating adaptive parameter control and an embedded LS procedure to enhance the effectiveness of the original algorithm for the problem at hand. Two versions of MHS were tested: MHS_{AD}, which includes only the adaptive parameter mechanism, and $MHS_{AD,LS}$, which also integrates the LS procedure. The experimental results demonstrated that the introduction of adaptive parameters improves the exploration and exploitation capabilities of the algorithm, leading to better solutions compared to the standard HS. Moreover, the inclusion of LS further refines solution quality, preventing the algorithm from getting trapped in a local optimum. From an industrial perspective, the proposed MHS may offer a valuable metaheuristic framework for semiconductor manufacturers facing the complex scheduling challenges of the diffusion work area, contributing to a reduction in terms of average wafer flowtime of the system.

One limitation of the proposed approach lies on its computational time. In a real-world production environment, it is crucial to make scheduling decisions rapidly at the beginning of each shift. In future works, the algorithm will be further optimized with the aim of being embedded into a digital twin architecture. Another limitation is that the current model does not explicitly account for minimizing the number of reworked or scrapped jobs per shift. Future developments will focus on considering a multi-objective function to minimize the number of jobs that do not respect the waiting time limit. As for future research, if the results from the real-world case study confirm those observed in the experimental analysis, the MHS algorithm can be tested for other work areas, such as photolithography or etching. Furthermore, alternative AI-based scheduling method, such as Deep Reinforcement Learning (DRL), can be developed and compared with MHS for the scheduling problem of the diffusion work area. Finally, the proposed MHS can be compared with new metaheuristic algorithms to maximize the system's throughput measure.

Acknowledgment

The work presented in this paper has received funding from the Chips Joint Undertaking (JU) under grant agreement No 101097296. The JU receives support from the European Union's Horizon EU research and innovation programs and Austria, Belgium, Denmark, Finland, France, Germany, Greece, Hungary, Israel, Italy, Netherlands, Romania, Sweden, Switzerland and Turkey.

References

[1] L. Mönch, J. W. Fowler, S. Dauzère-Pérès, S. J. Mason, O. Rose, A survey of problems, solution techniques, and future challenges in scheduling semiconductor manufacturing operations, J. Sched. 14 (2011) 583-599. https://doi.org/10.1007/s10951-010-0222-9

[2] C. Yugma, S. Dauzère-Pérès, C. Artigues, A. Derreumaux, O. Sibille, A batching and scheduling algorithm for the diffusion area in semiconductor manufacturing, Int. J. Prod. Res. 50(8) (2012) 2118-2132. https://doi.org/10.1080/00207543.2011.575090

[3] S. Knopp, S. Dauzère-Pérès, C. Yugma, A batch-oblivious approach for complex job-shop scheduling problems, Eur. J. Oper. Res 263(1) (2017) 50-61. https://doi.org/10.1016/j.ejor.2017.04.050

[4] Y. Tan, L. Mönch, J. W. Fowler, A hybrid scheduling approach for a two-stage flexible flow shop with batch processing machines, J. Sched. 21 (2018) 209-226. https://doi.org/10.1007/s10951-017-0530-4

[5] K. Tamssaouet, S. Dauzère-Pérès, S. Knopp, A. Bitar, C. Yugma, Multiobjective optimization for complex flexible job-shop scheduling problems, Eur. J. Oper. Res. 296(1) (2022) 87-100. https://doi.org/10.1016/j.ejor.2021.03.069

[6] H. Zhong, M. Liu, L. Bao, A job-priority based soft scheduling approach for uncertain work area scheduling in Semiconductor Manufacturing, Int. J. Prod. Res. 60(16) (2022) 5012-5028. https://doi.org/10.1080/00207543.2021.1948134

[7] K. Wu, E. Huang, M. Wang, M. Zheng, Job scheduling of diffusion furnaces in semiconductor fabrication facilities, Eur. J. Oper. Res. 301(1) (2022) 141-152. https://doi.org/10.1016/j.ejor.2021.09.044

[8] L. Chen, Y. Qiao, N. Wu, S. Zhang, J. Li, B. Liu (2023, August). Scheduling Analysis of Diffusion Area in Semiconductor Manufacturing. In 2023 IEEE 19th International Conference on Automation Science and Engineering (CASE) (pp. 1-6). IEEE. https://doi.org/10.1109/CASE56687.2023.10260420

[9] F. Da Ros, L. Di Gaspero, M. L. Lackner, N. Musliu, F. Winter (2025). Multi-neighborhood simulated annealing for the oven scheduling problem. Comput. Ind. Eng. 106999. https://doi.org/10.1016/j.cor.2025.106999

Materials Research Proceedings 57 (2025) 530-538 https://doi.org/10.21741/9781644903735-62

A mathematical modeling approach for job allocation at STMicroelectronics

EL ACHKAR Elias[1,a*], FRIGERIO Nicla[1,b], PAGANO Daniele[2,c] and MATTA Andrea[1,d]

[1]Politecnico di Milano, Dipartimento di Meccanica, via G. La Masa, 1, 20156, Milano, Italy

[2]STMicroelectronics, str. Primosole, 50, 95121, Catania, Italy

[a]elias.elachkar@polimi.it, [b]nicla.frigerio@polimi.it, [c]daniele.pagano@st.com, [d]andrea.matta@polimi.it

Keywords: Production Planning, Semiconductor, Smart Manufacturing

Abstract. The operative management of jobs in semiconductor fabrication plants (FABs) is highly challenging due to the complexity and scale of their processes. Inefficiencies in a FAB can disrupt the entire supply chain, increase production costs, and cause financial losses for downstream industries. This paper focuses on the Process Capacity Planning problem by proposing a novel approach that integrates with existing practices at ST. The method combines a Mixed Integer Linear Programming Model (MILP) with the FAB's Digital Twin (DT), enhancing the robustness and adaptability of the MILP-generated solution. Numerical validation is conducted on instances derived from the industrial case.

Introduction and Related Literature

ST's semiconductor fabrication plant (FAB) is managed hierarchically with four sequential decision levels. The *Aggregate Planning (level 1)* defines the Master Production Plan for the FAB over a 12-week horizon. At *level 2*, *Product Release* defines the list of products to be introduced into production on a weekly basis. This level also includes the *job formation,* which organizes *jobs* (each being a set of silicon wafers transported between machines by specialized carriers) accordingly to product release and carrier capacity. At each shift, *Process Capacity Planning (PCP, level 3)* allocates jobs, both newly released and already in progress, to machines configured for the specific processes required by the wafers within each job. Once allocated, multiple jobs might be assigned to the same machine, necessitating a *schedule* or *dispatching rule* to be established. The latter is addressed at *level 4* of the hierarchy.

This work focuses on the *PCP* and the operational management of *job allocation,* widely acknowledged as critical for the decision-making structure of this specific industrial case. Nonetheless, *PCP* poses a challenging problem for semiconductors in general [1, 2].

The ST FAB involves hundreds of machines and hundreds of different product types, each requiring a recipe of approximately 600 *events*. Events are defined as processing steps specific to an operation and machine-job combination to then achieve a finished product. Fabrication processes include photolithography, deposition, diffusion, etching, implantation, annealing, and others, all of which require strict control over machine qualification (the capability to perform a certain process on a specific product), machine configuration (setup), and critical queue times. These technological constraints impact *PCP* to minimize reconfiguration times and reworks, as well as to prevent quality issues. Considering all jobs simultaneously in progress, the *PCP* encompasses tens of thousands of potential events. The *PCP* aims to maximize the number of processing steps completed, driven by the fact that the lead time for a product spans several months. At level 3, decisions are supported by a Digital Twin (DT) that represents the dynamics of the FAB. Specifically, the DT is a discrete event simulation model that is automatically

Content from this work may be used under the terms of the Creative Commons Attribution 3.0 license. Any further distribution of this work must maintain attribution to the author(s) and the title of the work, journal citation and DOI. Published under license by Materials Research Forum LLC.

Materials Research Proceedings 57 (2025) 530-538 https://doi.org/10.21741/9781644903735-62

parameterized using actual production data collected from the shop floor at the beginning of the shift. This DT, encapsulating the detailed features of the semiconductor manufacturing equipment, is used to evaluate digitally any job allocation solution and ensure its feasibility. Ultimately, the *PCP* solution consists of a set of jobs to be processed during the shift, for each job, the number of executed events, and the event-to-machine allocation. The *PCP* solution is then passed on as the target for the next decisional level (i.e., level 4).

According to the related literature, the decisional level following order release (level 2 in ST) is typically addressed through either Full Factory Scheduling (FFS), which involves scheduling the entire facility, and considers all jobs in the FAB, or equipment-based scheduling [1]. MILP is utilized for the former, while heuristics and algorithms for job sequencing are applied for the latter. At ST, scheduling is managed at the equipment level (level 4), positioning PCP (level 3) as an intermediary step in the hierarchy, which differs from most literature approaches. In addition, the practical implementation of state-of-the-art FFS methods is often limited due to significant simplifications and high computational costs (requiring hours even for small-sized problems [3]), which are not compatible with the short decision horizon of *PCP*. Consequently, many articles reduce industrial-scale applications and problem complexity to manage the computational effort [3, 4, 5, 6, 7, 8]. For instance, the scheduling model in [5] addresses a permutation flow-shop but neglects reentrant flows, batching machines, and machine qualification and configuration. Different from make-span minimization, such as [3, 5, 6, 7], *PCP* aims to maximize a throughput indicator. Another scheduling approach is simulation-based, where a simulator embedded with dispatching rules evaluates multiple schedules in turn generated based on heuristics [9, 10]. The schedule with the best performance indicator is then selected. Notably, none of the available works combine a hybrid approach between simulation-based and MILP-based FFS.

In more detail, this paper aims to develop a novel approach to solve the *PCP* by combining an MILP with the DT of the FAB, enhancing the robustness and adaptability of the MILP-generated solution while leveraging the detailed dynamics of the FAB encapsulated in the DT. Mathematical programming alone can yield approximate or unfeasible solutions, due to the inherent complexities of FABs that cannot be represented in the MILP. Consequently, the DT plays a fundamental role in transforming the MILP-generated solution into feasible ones, and for this purpose, a Mapping Agent is proposed. Thus, the paper contribution is twofold: 1) the formal definition of the MILP that captures the specificities of the *PCP* problem, and 2) the development of the Mapping Agent that decodes and leverages the MILP-generated solution. Therefore, the paper contribution also includes the integration challenge, which establishes a structured connection between the MILP and the DT, and the challenge of extracting model parameters from the company database.

Identification of problem features and requirements

We assume the FAB includes the set J of n jobs, the set M of m machines that can perform one out of the set E of b events. In addition, the FAB is a highly dynamic environment whose state is mainly characterized by the Work-in-Progress (WIP). The initial state of the WIP is defined as WIP_I and is captured at the beginning of each shift for planning purposes. Throughout the shift, selected jobs are transferred from one machine to another, completing their events and advancing in their *sequence*. Each new instantiation of the *PCP* problem should start from the updated WIP_I and find the set $J_s \subseteq J$ of selected jobs, the processed events for each job, and their machine allocation. This section defines and formulates the product recipe (sequence) and selected FAB features, outlines the problem, and concludes with the final insights.

Product Recipe. Silicon wafers are the raw material for all end products, and through the product-dependent recipe, these wafers are transformed into finished goods. A *sequence* is defined as the unique set of ordered events establishing the *recipe* of a specific product type. In the modelling

phase, this sequence is encoded by a vector $\boldsymbol{\sigma_j}$ representing the sequence of events $\sigma_{jk} \mid k = 1 \dots t$ necessary to complete for job j. However, for a given WIP_I state, the remaining job sequence may vary due to the dynamic nature of the operating environment. To accurately capture this, the job's current sequence location s_j is updated in the job sequence vector $\tilde{\boldsymbol{\sigma}}_{\boldsymbol{j}}$ at the beginning of each shift. The matrix $\boldsymbol{\sigma} = [\tilde{\boldsymbol{\sigma}}_j]$ is then composed of the sequence vectors. This ensures that the initial row of the matrix correctly represents the latest job sequence positions. The algorithm for constructing the $\boldsymbol{\sigma}$ matrix is as follows:

Sequence Matrix Algorithm:

1. Extract from the WIP_I the set of jobs J and the total number of jobs n
2. Extract from the WIP_I the sequence location $s_j, \forall j \in J$ i.e. $j = 1 \dots n$
3. Extract the full sequence $\boldsymbol{\sigma_j} \mid j = 1 \dots n$
4. Remove all steps of $\boldsymbol{\sigma_j}$ before s_j to create $\tilde{\boldsymbol{\sigma}}_{\boldsymbol{j}} \mid j = 1 \dots n$
5. Define a the maximum number of steps of the remaining sequences $\tilde{\boldsymbol{\sigma}}_{\boldsymbol{j}}$
6. Add "*dummy*" events to have all sequences of the same length a to create $\boldsymbol{\sigma} = [\tilde{\boldsymbol{\sigma}}_j]$
7. Return $\boldsymbol{\sigma}$

Machine Characteristics and Processing Times. In the ST manufacturing FAB, all machines operate with distinct characteristics. These machines are defined by their processing times, number of chambers (a dedicated environment within a machine to accomplish the processing step), batching capabilities, and layout. The FAB includes parallel non-identical machines, which are individually modeled in the MILP, such as those used for cleaning and diffusion. Each job follows a unique sequence of events, each to be allocated to a qualified and configured machine. The qualification is governed by the $\boldsymbol{ESM} = [ESM_{ie}]$ matrix where $ESM_{ie} = 1$ indicates that event e can be processed on a machine i. Therefore, jobs with the same recipe can follow alternative machine paths. The complexity is further increased by processing times varying based on machine type and machine-specific attributes. For instance, machines, such as etching and vapor deposition machines, are equipped with multiple chambers, and others, such as furnaces for diffusion and oxidation, operate in batch mode with defined batch sizes. Therefore, the time necessary to perform event e on two machines i_1 and i_2, both qualified and configured may differ significantly. To accurately model parallel machine with non-identical configuration, the processing times are represented in a processing time matrix $\boldsymbol{P} = [p_{ie}]$. The calculation of p_{ie} is affected by machine attributes such as operating by jobs, single or batch wafers, and the number of available chambers with $p_{ie} = 0$ when machine i cannot process event e, i.e., $ESM_{ie} = 0$.

Machine Capacity. Machine capacity Cap_i represents the available time for each machine i at the start of a shift. As jobs are allocated, machine capacities decrease accordingly, based on the respective allocated processing times. However, since the WIP_I includes machines that are still processing from the previous shift, some machines may not be immediately available at the start of the next shift. To account for this, the capacity vector $\{Cap_i\} \mid i = 1 \dots m$ is set for a shift, removing the remaining processing time of machines still in operation, accurately reflecting real-time availability within the FAB.

Job Allocation and Subset Selection Problem. The industrial case analysis concludes that the *PCP* involves a job allocation and a subset selection in a multi-product complex job-shop with parallel and non-identical machines. *Job allocation* entails determining which events in each *job-sequence* need to be performed (i.e., *event loading*) and which machine is selected to perform each event (i.e., *event allocation*). More specifically, let us consider job j in the WIP_I being at a sequence

Materials Research Proceedings 57 (2025) 530-538 https://doi.org/10.21741/9781644903735-62

location s_j. The *PCP* scope is to identify the sequence location k_j^* after a given time horizon for all $j \in J$. Therefore, all events e in the job sequence between locations s_j and k_j^* are loaded for all $j \in J$. These events need to be allocated to a machine $i \in M$, where i is qualified and configured to perform e, i.e. $ESM_{ie} = 1$. The occurrence of specific events and the shift timing naturally prioritizes certain jobs. Jobs with higher priority (those selected for movement during a given shift) form the subset $J_s \subseteq J$, making the selection process a critical decision directly impacting efficiency and workflow optimization. Lastly, the key characteristics of the problem are: multiple product types, reentrant flows (such as possible repetition of the same event within the job sequence, e.g. cleaning multiple times), parallel non-identical machines, machine qualification and configuration, alternative machine sequencing, unique event sequence of jobs depending on FAB state, machines with several chambers and processing times based on the event-machine combination.

MILP Modeling and Decision Variables

The developed MILP model incorporates the aforementioned characteristics and is designed to make the following decisions: subset selection, i.e., identification of J_s, event loading y_{kej} and event allocation ρ_{kie}. The MILP objective is to maximize the total number of processing steps (Eq. (1)). The equations are designed to best describe the chosen characteristics, and are as follows, with their parameters and decision variables in Tab. 1

Table 1: Definition of model parameters and variables

Parameter	***Definition***
J, M, E, K	Sets of n total Jobs, m total machines, b total events, and a processing steps, respectively
σ_{jk}	Event at step $k = 1 \dots a$ of the sequence necessary for job $j = 1 \dots n$
p_{ie}	Processing time of event $e = 1 \dots b$ on machine $i = 1 \dots m$
Cap_i	Capacity of machine i (available time for each machine i per shift)
$Bmax_i$	Maximum batch size machine i
ESM_{ie}	Indicates which if event e can be processed by machine i
Variable	**Definition**
y_{kej}	$\in \{0; 1\}$ indicates with $y_{kej} = 1$ if job $j = 1 \dots n$ is loaded to event $e = 1 \dots b$ at step $k = 1 \dots a$
θ_j	$\in \{0; 1\}$ indicates with $\theta_j = 1$ if job $j \in J_s \vert j = 1 \dots n$
ρ_{kie}	$\in \{0; 1\}$ indicates with $\rho_{kie} = 1$ if machine i is selected to process event $e = 1 \dots b$ at step $k = 1 \dots a$
$Batching_k$	$\in \mathbb{Z}^+$ Number of batches of event e that machine i has to process at step k based on the batch size
$Single_{kie}$	$\in \mathbb{Z}^+$ Number of single jobs of event e that machine i has to process at step k

$$\max\left(\sum_{k}^{a}\sum_{e}^{b}\sum_{j}^{n} y_{kej}\right) \tag{1}$$

$$\theta_j \geq y_{kej} \quad \forall\, e \in E; j \in J; k \in K \tag{2}$$

Materials Research Proceedings 57 (2025) 530-538 https://doi.org/10.21741/9781644903735-62

$$\theta_j \leq \sum_{i}^{m}\sum_{k}^{m} y_{kej} \quad \forall\, j \in J \tag{3}$$

$$\begin{cases} y_{kej} \leq 1 - \dfrac{(\sigma_{jk} - e)}{Large\ Number} \\ y_{kej} \leq 1 + \dfrac{(\sigma_{jk} - e)}{Large\ Number} \end{cases} \quad \forall\, j \in J; k \in M; e \in E \tag{4}$$

$$y_{[k][\sigma_{jk}][j]} \leq y_{[k-1][\sigma_{j(k-1)}][j]} \quad \forall\, j \in J;\ k = 2, \dots, a \tag{5}$$

$$\rho_{kie} \leq ESM_{ie} \quad \forall\, k \in K, i \in M, e \in E \tag{6}$$

$$\sum_{e=1}^{b} \rho_{kie} = 1 \quad \forall\, k \in K, i \in M \tag{7}$$

$$\begin{cases} z_{kie} \leq |J| \cdot \rho_{kie} \\ z_{kie} \leq \sum_{j=1}^{n} y_{kej} \\ z_{kie} \geq \sum_{j=1}^{n} y_{kej} - |J| \cdot (1 - \rho_{kie}) \end{cases} \quad \forall\, k \in K, i \in M, e \in E \tag{8}$$

$$Bmax_i \cdot Batching_{kie} \leq z_{kie} \quad \forall\, i \in M, k \in K, e \in E \tag{9}$$

$$Single_{kie} \leq z_{kie} - Bmax_i \cdot Max_Batching_{kie} \ \forall\, i \in M, k \in K, e \in E \tag{10}$$

$$\sum_{j=1}^{n} y_{kej} = \sum_{i=1}^{m} (Bmax_i \cdot Max_{Batching_{kie}} + Single_{kie}) \quad \forall\, k \in K, e \in E \tag{11}$$

$$\sum_{e=1}^{b}\sum_{k=1}^{a} (Max_Batching_{kie} + Single_{kie}) \cdot p_{ie} \leq Cap_i \quad \forall\, i \in M \tag{12}$$

Eq. (2) ensures that a job can only be loaded if selected within the subset. Eq. (3) prevents a job from being included in the subset if it has no loaded events, ensuring that only active jobs are considered. Eq. (4) enforces sequencing rules by restricting jobs from being loaded only for certain events without following the predefined order. Eq. (5) further reinforces this by requiring that a step in the sequence can only be loaded if the previous step has already been allocated. Both Eq. (4) and Eq. (5) are required for the strict process precedents for a product recipe. Eq. (6) is related to both the configuration and qualifications of machines. It governs machine selection by ensuring that only machines qualified and configured for processing a given event, as defined by the ESM matrix, can be allocated. Eq. (7) restricts each machine to handling only one event per step to prevent conflicts in resource allocation. Eq. (8) introduces the linearization, using an auxiliary variable z_{kie}, of the multiplication of two decision variables (y_{kej} and ρ_{kie}), preserving the linear structure of the model. Eq. (9) defines the batching constraint, ensuring that batch sizes do not exceed a predefined upper limit, while Eq. (10) establishes the remaining single jobs to be processed after batching is applied. Eq. (11) creates a link between job event loading and batching decisions, preventing the model from batching more jobs than the total demand for a specific event at a particular machine. Eq. (12) enforces capacity constraints. Lastly, the number of variables is $abn + 4abm + n$, with 14 constraints.

Materials Research Proceedings 57 (2025) 530-538 https://doi.org/10.21741/9781644903735-62

Mapping Agent and DT Integration

Besides the extraction of WIP_I and the model parameters, the integration of the MILP with the DT also includes the mapping of the MILP-generated solution, the job allocation dataset hereby defined as JA, in the DT to obtain actual system performance. Additionally, since allocation of the MILP model can be susceptible to infeasibility, the DT serves as a validation environment. The methodology proposed in this paper is described in 6 steps to be operated at each shift:

Methodology Algorithm:

1. Extract the current the WIP_I state from the FAB
2. At the beginning of the shift, solve the MILP, considering the current FAB state and any additional job releases
3. Provide the JA to the DT with a one-shift time horizon
4. The DT reinterprets the MILP results based on real-time conditions
5. Assign targets and allocate resources based on the DT's adjusted plan for the current shift
6. At the beginning of the next shift, repeat from Step 1, incorporating updated WIP_I and new job releases

Steps 3 to 6 require the connection between the MILP and DT with the Mapping Agent, necessary to assign jobs to machines during the DT operation. The DT operates by calling an agent whenever a machine is available so that the agent selects a job from the list of available jobs for such a machine. Such Mapping Agent is the bridge between the MILP and the DT:

Mapping Agent:

1. Retrieve the machine i calling the agent, the active WIP dataset of the jobs in the DT, the JA
2. Identify the jobs that are not loaded on machines of the simulator
3. Filter JA to include only the non-loaded jobs that can be allocated to i
4. Extract the corresponding events for these jobs from WIP
5. Check if the events in WIP (current events of jobs) match events in JA (aligning indices between JA and WIP), and keep only jobs where the event matches
6. Sort based on an increasing order of the steps of the final valid jobs in JA
7. Retrieve the WIP dataset containing only the sorted final jobs as the list of available jobs
8. If the list of available jobs is empty:
    a. Get the list of all jobs that are not loaded that the machine can process
    b. Set this as the list of available jobs
9. Return the list of available jobs
10. Select the first job (batch of jobs) in the list of available jobs

Application to ST

The proposed approach is applied to two real instances, namely WIP_{I1} and WIP_{I2}, extracted from ST, and aims to solve the *PCP* for a shift of 480 minutes. Data related to jobs, sequences, machines, and events has been extracted from the records embedded in the company DT environment. An ad-hoc software procedure has been developed for such a purpose. Given the considerable time required to complete the full product recipe, the sequence matrix has been limited to 20 steps. This choice is supported by an analysis of the current system behavior, where 90% of jobs advance at most 15 steps in a single shift. At the full-scale factory, the number of decision variables poses significant challenges for in-memory storage and computation. Thus, the number of jobs has been limited to 150, with 230 operating machines, with a current computational time for instance creation, optimal solution, and simulator performance of 1.5 hours on an Intel(R) Xeon(R) Gold 6242R CPU @ 3.10GHz. This reduction in problem size reduces the computational effort with a balanced tradeoff between maintaining a sufficient problem representation and manageable

Materials Research Proceedings 57 (2025) 530-538 https://doi.org/10.21741/9781644903735-62

computational complexity. Note that machines not required by the selected instances are removed from the DT. Despite the MILP focusing on a single shift (8h), the DT is let run for 5 shifts (40h) to evaluate the performance over a longer time horizon.

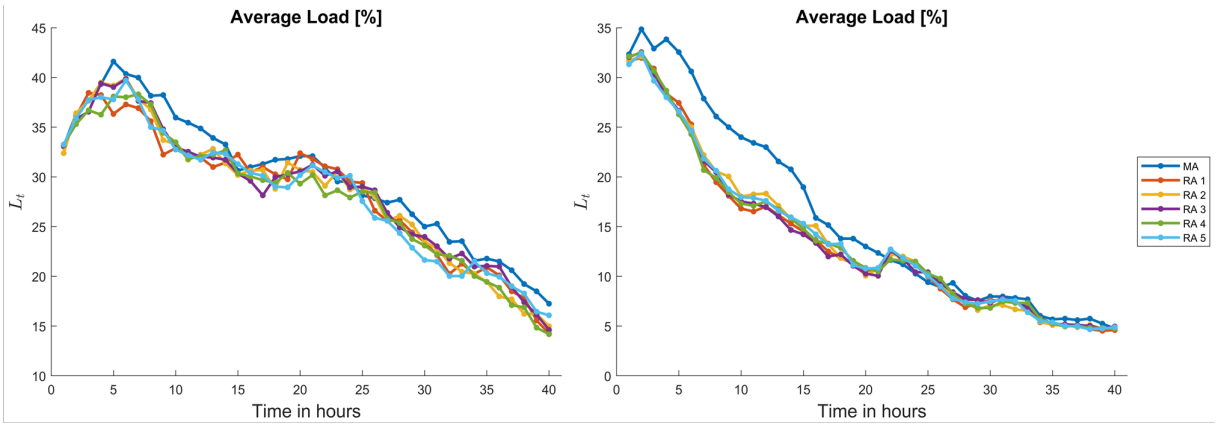
The main performance of interest are (i) the average number of steps per job $\bar{x}$, (ii) the total number of steps Π at the end of the simulation, and (iii) the average load L_t of the FAB computed at each time period ($t = 1 \dots 40$) as:

$$L_t = \frac{M_{loaded,t}}{M_{total}} \cdot 100$$

where $M_{loaded,t}$ is the number of machines processing jobs at time t and M_{total} is the total number of available machines. We compared the performance obtained with the *Mapping Agent (MA)*, integrating the MILP result in the DT, and a benchmark agent randomly selecting job j of the list of available jobs when machine i calls the agent, i.e., the *Random Agent (RA)*. Five replications are used to evaluate the mean performance of RA. The subset size selected by the MILP is 136 for WIP_{I1} and 140 for WIP_{I2}, i.e., around 91% of jobs, which is coherent with the problem-size reduction. The results of the simulation can be seen in Fig. 1 and Tab. 2.

Table 2: Performance obtained for $\boldsymbol{WIP_{I1}}$ *and* $\boldsymbol{WIP_{I2}}$ *by MA and RA (mean and half-width of the 95% CI based on 5 replications). The mean load* $\boldsymbol{\bar{L}_s}$*[%] represents the mean load obtained at 8h of each shift, s=1…5.*

$\boldsymbol{WIP_{I1}}$	$\boldsymbol{\bar{L}_1}$	$\boldsymbol{\bar{L}_2}$	$\boldsymbol{\bar{L}_3}$	$\boldsymbol{\bar{L}_4}$	$\boldsymbol{\bar{L}_5}$	$\boldsymbol{\bar{x}}$ *[step/job]*	$\boldsymbol{\Pi}$ *[step]*
MA	38.31	34.16	31.12	26.39	20.50	35.1	4769
RA	36.97 ± 0.45	32.02 ± 0.18	30.01 ± 0.61	24.74 ± 0.68	18.47 ± 0.60	33.0 ± 0.22	4493.8 ± 17.97
Δ	3.63%	6.68%	3.70%	6.66%	10.95%	6.12%	6.12%
$\boldsymbol{WIP_{I2}}$	$\boldsymbol{\bar{L}_1}$	$\boldsymbol{\bar{L}_2}$	$\boldsymbol{\bar{L}_3}$	$\boldsymbol{\bar{L}_4}$	$\boldsymbol{\bar{L}_5}$	$\boldsymbol{\bar{x}}$ *[step/job]*	$\boldsymbol{\Pi}$ *[step]*
MA	31.38	21.57	12.65	8.38	5.81	14.3	2000.0
RA	26.99 ± 0.10	16.49 ± 0.55	11.61 ± 0.23	8.01 ± 0.17	5.25 ± 0.10	12.3 ± 0.06	1721.2 ± 3.72
Δ	16.25%	30.79%	8.97%	4.64%	10.60%	16.20%	16.20%



a) WIP_{I1} b) WIP_{I2}

Figure 1: Average load ($\boldsymbol{L_t}$[%]*) over simulated time [h] for instances* $\boldsymbol{WIP_{I1}}$ *and* $\boldsymbol{WIP_{I2}}$

Fig. 1 indicates that, in both instances, the MA outperforms the RA. Therefore, the mean load $\bar{L}_s$ for each shift and the percent improvement $\Delta = \frac{\bar{L}_s^{MA} - \bar{L}_s^{RA}}{\bar{L}_s^{RA}} \cdot 100$ are reported in Tab. 2, showing that the MA improves the performance compared to the RA (p-value < 0.05).

Furthermore, the mean load $\bar{L}_s$ maintained its improvement across all shifts despite limiting the JA to 20 steps which are mostly performed in the 1st and 2nd shifts, reaching an increment up to 30.79% in WIP_{I2}. It can also be noted that the MA's use of the JA is significantly higher in WIP_{I2} than in WIP_{I1} which accounts for the relatively higher performance with of the MA compared to the RA in the second instance versus the first. Indeed, the usage of the JA for WIP_{I1} is 14.68%, while for WIP_{I2}, it averages 25.25% on average over the 5 shifts, with the expected decreasing trend in usage. As in Tab. 2, the MA achieves an average of 2 additional steps per job than the RA (e.g. $\bar{x}^{MA} = 35.1$ steps/job versus $\bar{x}^{RA} = 33.0$ steps/job in WIP_{I1}) resulting in over 275 steps increase in total (6.12% increase in WIP_{I1} and 16.12% increase in WIP_{I2}). Lastly, the observed decreasing trend of the average load throughout the simulation is attributed to the problem size reduction, leading to an undersaturation of the DT.

Conclusion

This paper addresses the operative management of semiconductor manufacturing, specifically focusing on the *PCP* problem. The proposed methodology integrates mathematical optimization with the DT of the FAB. This integration enhances decision-making and resource allocation by leveraging the strengths of both approaches. The proposed approach is validated with two problem instances derived from ST. While the current comparison is not conducted against the most advanced strategies, further analyses are required to benchmark the proposed methodology. Nonetheless, the results are promising and highlight the potential of the approach.

Future research will aim to scale up the problem to address the full FAB operations, exploring the use of metaheuristics to solve the MILP. Additionally, the MILP-generated solution can serve as a guideline for Reinforcement Learning agents, to accelerate training and as a decision-support tool during real-time execution. This approach is not limited to the full front-end but can be generalized to a broader context.

Acknowledgement

The work presented in this paper has received funding from the Chips Joint Undertaking (JU) under grant agreement No 101097296. The JU receives support from the European Union's Horizon EU research and innovation programs.

References

[1] L. Mönch, J. W. Fowler, and S. J. Mason, *Production Planning and Control for Semiconductor Wafer Fabrication Facilities*, vol. 52. New York, NY: Springer New York, 2013. https://doi.org/10.1007/978-1-4614-4472-5

[2] L. Mönch, R. Uzsoy, and J. W. Fowler, "A survey of semiconductor supply chain models part III: master planning, production planning, and demand fulfilment," 2018, *Taylor and Francis Ltd. https://doi.org/*10.1080/00207543.2017.1401234

[3] W. Y. Ku and J. C. Beck, "Mixed Integer Programming models for job shop scheduling: A computational analysis," *Comput Oper Res*, 2016. https://doi.org/10.1016/j.cor.2016.04.006

[4] I. Dimény and T. Koltai, "Comparison of MILP and CP models for balancing partially automated assembly lines," *Cent Eur J Oper Res*, 2023. https://doi.org/10.1007/s10100-023-00885-x

[5] H. Li, X. Li, and L. Gao, "An iterated greedy algorithm with acceleration of job allocation probability for distributed heterogeneous permutation flowshop scheduling problem," *Swarm Evol Comput*, 2024. https://doi.org/10.1016/j.swevo.2024.101580

[6] A. S. Manne, "On the Job-Shop Scheduling Problem," 1960. Available: https://about.jstor.org/terms

[7] E. F. Stafford, F. T. Tseng, and J. N. D. Gupta, "Comparative evaluation of MILP flowshop models," *Journal of the Operational Research Society*, 2005. https://doi.org/10.1057/palgrave.jors.2601805

[8] W. Weng, C. Chu, and P. Wu, "Resource Allocation to Minimize the Makespan with Multi-Resource Operations," *J Syst Sci Complex*, 2024. https://doi.org/10.1007/s11424-024-3284-z

[9] S. Werner, S. Horn, G. Weigert, and T. Jahnig, "Simulation Based Scheduling System in a Semiconductor Backend Facility," *Proceedings of the 2006 Winter Simulation Conference*, 2006. https://doi.org/10.1109/WSC.2006.322950

[10] G. Weigert, A. Klemmt, and S. Horn, "Design and validation of heuristic algorithms for simulation-based scheduling of a semiconductor Backend facility," in *International Journal of Production Research*, 2009. https://doi.org/10.1080/00207540902744784

Materials Research Proceedings 57 (2025) 539-547 https://doi.org/10.21741/9781644903735-63

Digitalization of broaching processes: a scalable approach to industry 4.0 in small and medium enterprises

Michele ABRUZZO[1,a*], Gino DINI[1,b], Gualtiero FANTONI[1,c], Luca ROMOLI[1,d] and Marko VUKOVIC[1,e]

[1]Università di Pisa, Dipartimento di ingegneria Civile e Industriale, Largo Lucio Lazzarino 1, Pisa, PI, Italy, 56122

[a]michele.abruzzo@ing.unipi.it, [b]gino.dini@unipi.it, [c]gualtiero.fantoni@unipi.it, [d]luca.romoli@unipi.it, [e]marko.vukovic@phd.unipi.it

Keywords: Monitoring, Performance Indicators, Predictive Maintenance

Abstract. In this work, the digitalization of a broaching process applied to polypropylene tubes for industrial use is proposed. Three different sized broaches are considered. Digital pressure sensors are used to replace analog gauges, integrating with the existing network infrastructure for real-time monitoring and cloud-based data storage for subsequent analyses. Pressure data, analyzed using polynomial regressions and hybrid techniques, enabled the creation of quantitative indices to assess process health, monitor tool wear, and establish predictive maintenance criteria. The proposed approach can be adopted to reduce downtime, improve efficiency, and minimize scrap rates due to tolerance degradation. Furthermore, it is demonstrated how scalable digital solutions can drive the transition to Industry 4.0, even in small- and medium-sized enterprises.

Introduction

Over the past two decades, the gradual (yet rapid) introduction of Industry 4.0 has revolutionized various industrial sectors. The introduction of pillars such as big data analytics, digital twins of processes, and the Industrial Internet of Things/People (IIoT/IIoP) has significantly increased the interconnection between people, machines, and sensors, fostering greater transparency in information transmission, decentralizing decision-making processes, and improving technical assistance through innovative concepts such as predictive maintenance of machines [1-3].

These advancements have brought numerous benefits, including improved production efficiency through more advanced planning and diversification of production, reduced production costs, more efficient use of resources, reduced waste, and enhanced product quality [4]. Additionally, the adoption of these technologies has strengthened the concepts of sustainability and safety, optimizing resource use and automating hazardous tasks [5].

However, the evaluation of return on investment required to digitalize decision-making and industrial processes remains one of the main obstacles to adopting Industry 4.0, particularly for small and medium-sized enterprises (SMEs). The challenges are related to financial barriers, compatibility with existing technologies, concerns about data security, lack of skilled labor, and the complexity of achieving interoperability between machines and systems [6-9]. Despite these challenges, adopting Industry 4.0 technologies in SMEs is an urgent need to ensure sustainability and agility, which are critical factors for competitiveness [10].

In this context, the proposed work explores the application of Industry 4.0 principles in a small and medium-sized enterprise in Tuscany. Specifically, it analyzes the digitalization of a broaching process for polypropylene tube processing. Following the principles of sustainable digitization, the tools were classified using an optical algorithm, and the process was sensorized with low-cost pressure sensors, connected to the company's network for real-time machine monitoring and cloud data storage. The pressure data were processed using polynomial and hybrid regression techniques to monitor the process health, tool wear, and establish predictive maintenance criteria. Finally, the

Content from this work may be used under the terms of the Creative Commons Attribution 3.0 license. Any further distribution of this work must maintain attribution to the author(s) and the title of the work, journal citation and DOI. Published under license by Materials Research Forum LLC.

Materials Research Proceedings 57 (2025) 539-547 https://doi.org/10.21741/9781644903735-63

obtained advantages and the scalability of the adopted solutions for facilitating the transition of SMEs to Industry 4.0 are discussed.

Case study

The case study focuses on the digitalization of a broaching machine used at Toscana Spazzole s.r.l., a SME based in Tuscany. The broaching process is essential for machining the inner diameter of polypropylene tubes, which serve as a fundamental component of the entire production workflow. Any issues in achieving the required inner diameter can lead to slowdowns or even a complete halt of the production line, underscoring its critical importance to the company. This makes it an ideal starting point for the implementation of Industry 4.0 principles. The polypropylene tubes, which are 2.5 m long, are connected to the broaching machine using four double V-brackets until they reach the axial stop (Fig. 1 (a)). The machine employs a special hollow broach [11], designed to mitigate issues related to chip evacuation while also reducing friction forces during cutting. This broach features 36 teeth arranged in a helical pattern along its outer cylindrical surface (Fig. 1 (b)). Depending on the required specifications, three different broach sizes can be used, with outer diameters of 102 mm, 110 mm, and 80 mm. For comparison, it is important to note that, unlike the 110 mm and 80 mm broaches, the 102 mm version is designed to maximize material removal through a two-stage cutting process. The broach is retracted inside the tube via a hydraulic system capable of delivering a maximum pressure of 15 MPa. To safeguard against potential overloads, a safety valve set at 17 MPa is also integrated into the system. The typical feed rate used in the process is 3 m/min.

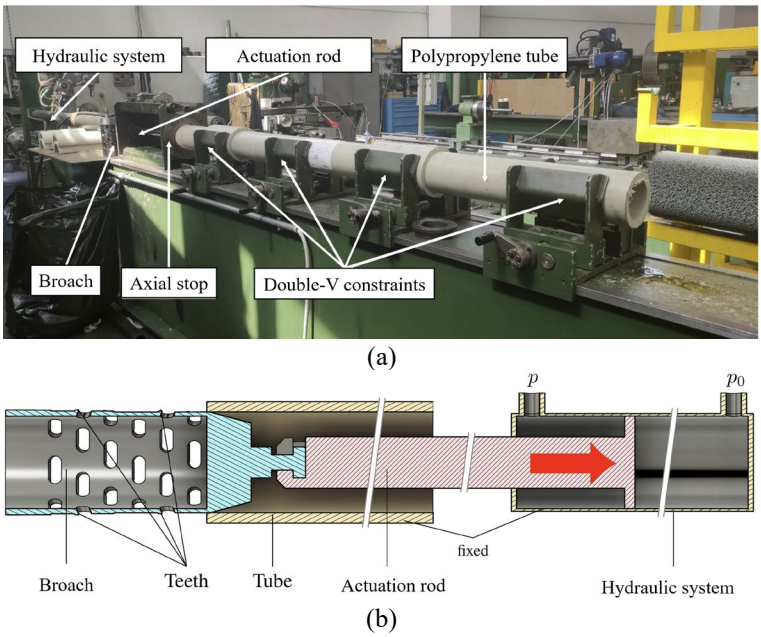


Figure 1: Non-sensorized experimental setup. (a) Broaching machine, tube constraints and hydraulic loading machine. (b) Detail of the special hollow broach and connection to the piston rod. Figures adapted from [11].

Before the digitalization initiative, the machine lacked any form of sensorization. The only available monitoring tool was an analog pressure gauge, which provided real-time pressure readings but lacked data storage capabilities, preventing effective process monitoring and analysis. Moreover, broach size was determined solely based on the maximum exerted pressure, a method influenced by tool wear and therefore unreliable for accurately identifying the tool type.

The digitalization process aims to measure the forces involved in cutting, both for individual cuts and repeated cuts over time using the same tool. This enables a qualitative comparison

between different technical solutions, helps identify potential tool wear, and supports the implementation of predictive maintenance strategies. Additionally, the extracted data could be leveraged to automate the recognition of different broaches, enhancing process automation and reducing the risk of human error.

Materials and methods

Core requirements for scalability and incremental adoption

SMEs face constraints that limit the adoption of Industry 4.0 principles [7]. Therefore, the digitalization process must balance *cost-effectiveness*, *ease of implementation*, *security*, *scalability*, and *minimal operational disruption.* Keeping investments low reduces financial risk and encourages the adoption of innovative solutions. A simpler approach allows for rapid deployment and secure data protection. The solution must be horizontally scalable (for other machines) and vertically scalable (for higher-level decision-making processes), without disrupting the existing production system. Adopting solutions that meet these criteria enables the gradual resolution of production challenges, fostering further investments and reducing decision-making inertia in SMEs.

Solutions for the broaching tool digitalization

In the digitalization of the broaching process, two measurement solutions were considered. The first involved a *direct measurement* of the total broaching force, using a dynamometer placed between the broach and piston. The second approach relied on an *indirect measurement* via a digital pressure sensor placed directly within the hydraulic system, allowing force estimation based on pressure readings [11]. While a dynamometer is more accurate, the *indirect measurement* presents challenges, such as accounting for potential pressure losses in the hydraulic system. However, integrating a dynamometer presents several practical drawbacks. Standard dynamometers do not fit within the available space between the broach and the piston, requiring custom solutions that have long production and delivery lead times, leading to extended machine downtime, which conflicts with the requirements outlined earlier. Additionally, a dynamometer costs approximately 2000 €, whereas a digital pressure sensor is available for approximately 100 € and can be easily purchased off the shelf, making the latter a far more cost-effective solution. Given the typical feed rate of 3 m/min, the required acquisition frequency is 50 Hz. Both devices can meet this requirement without the need for special configurations or additional hardware.

Considering the factors discussed, the indirect measurement using hydraulic system pressure was chosen for its immediate availability, cost-effectiveness, and ease of implementation.

The analog pressure gauge was replaced with a WIKA S-20 digital pressure sensor, capable of measuring pressures up to 25 MPa and costing approximately 200 €. A Zerynth 4ZeroBox device was installed in the machine's electrical cabinet to record the sensor's signal during the broaching operation. Data was stored on an SD card and securely transferred to Zerynth's Cloud via the existing local network infrastructure, using TLS 1.2 and 1.3 protocols for data security. The data can be visualized in real-time through the Zerynth dashboard or downloaded for further analysis.

The post-processing of the data can be performed using either a physics-driven approach or a data-driven approach, but neither would be fully exhaustive. The physics-driven approach allows for distinguishing the different phases of the cutting process, but it cannot account for the complexity arising from variables such as different tools, varying tube sizes, and external conditions (e.g., humidity or temperature). On the other hand, a purely data-driven approach provides statistical variables that may not be correlated with each other or with the process's health status. Therefore, the proposed solution uses a hybrid approach, where the statistics of the acquired data are correlated with the process physics to define an index that characterizes the system's health status, enabling its monitoring and improvement through the prototyping of different technical solutions.

Materials Research Proceedings 57 (2025) 539-547 https://doi.org/10.21741/9781644903735-63

Results and discussion

As observed in Fig. 2, the typical loading curve consists of two distinct and visually identifiable phases. The first phase corresponds to the extraction of the piston and occurs at an approximately constant pressure, except for the ramp-up and ramp-down stages. During this phase, the pressure within the hydraulic circuit remains identical in both chambers, but the piston is extracted due to the difference in the effective application area (Fig. 1(b)). Once the extraction phase is complete, the broach is installed, and the actual machining process of the polypropylene tube begins. During the broach's retraction, the applied pressure is no longer constant as in the first phase but instead exhibits a series of peaks. These variations can reasonably be attributed to irregularities in the tube's geometry, which arise from dimensional and shape tolerances. In other words, depending on different regions of the tube, the tool may need to remove more or less material compared to the nominal chip section, leading to fluctuations in cutting pressure (force).

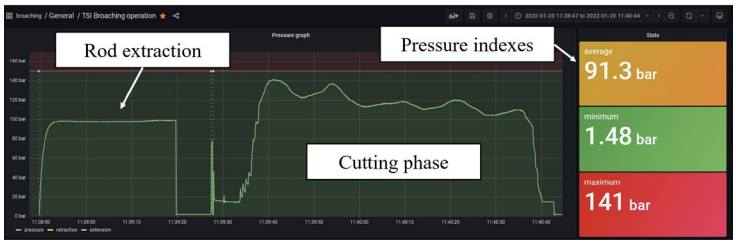


Figure 2: Example of a typical loading curve displayed on the Zerynth device dashboard, where the average, minimum, and maximum cutting pressures can be visualized.

In addition to the qualitative characteristics of the loading curve, the implemented dashboard enables the visualization of the cycle's maximum, minimum, and average pressures. This provides the operator with an immediate indicator of process health and potential anomalies. The presence of an initial pressure plateau at the beginning of each cutting operation is useful for distinguishing the actual cutting phases from the system setup phase. From a process monitoring perspective, this enables the identification of potential issues and anomalies in the hydraulic system separately from those occurring during the cutting process.

The physics-driven analysis allows for a clear distinction of the different stages of the cutting process based on the interactions between the broach and the polypropylene tube, as shown in Fig. 3. In the initial stage, when the conical surface of the broach starts interacting with the inner surface of the tube, a sudden increase in the applied pressure is observed. During this phase, no material removal occurs, and the tube undergoes elastic and plastic deformation as the broach advances. This phase corresponds to the *first engagement ramp*. Once the initial phase is completed, that is, when the cylindrical surface of the broach reaches the inner surface of the tube, the actual *tool engagement* begins. During this phase, cutting pressures increase due to the need to overcome the frictional constraint with the external cylindrical surface of the broach, until the first set of teeth is engaged. When all the teeth are engaged, a maximum pressure value is reached, after which the cutting proceeds under nearly steady-state conditions (*cutting phase*). The fluctuations visible in Fig. 3 can be attributed to dimensional and geometric tolerance variations of the tube, as well as the presence of constraints. The combined effect of these tolerances and constraints leads to variability in the volume of material removed along the tube's axis and, consequently, a variation in the cutting pressure. Once the broach passes the first clamp system, the cutting pressure tends to decrease, reaching a minimum value, and then increases again at the second clamp, just before disengaging from the tube. At the end of the process, the pressure rapidly drops to nearly zero in the *tool disengagement ramp*.

Materials Research Proceedings 57 (2025) 539-547 https://doi.org/10.21741/9781644903735-63

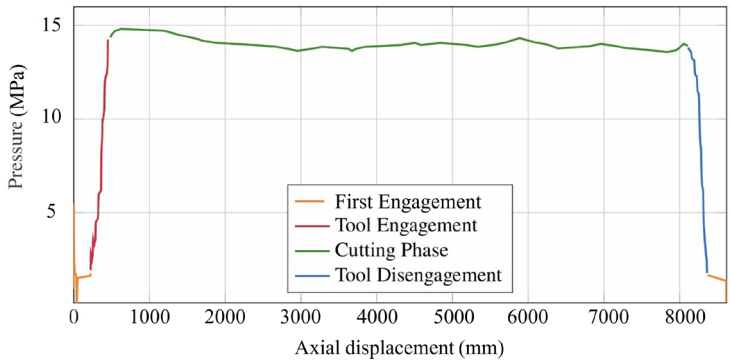


Figure 3: Example of a typical loading curve and physical-driven analysis.

Building on the previous analysis, a set of statistical parameters was defined to characterize the cutting process. *Mean, minimum, and maximum pressures* provide a quick overview of process conditions, while *variance*, *skewness*, and *kurtosis* act as variability indicators and potential wear markers. *Shannon entropy* captures signal complexity, and *moving average/variance* enable detailed analysis of specific process segments. These parameters were used to distinguish the cutting phases, especially at the entry and exit points, helping detect tooth misalignment or extraction issues. When applied to the *cutting phase*, they support real-time tool wear monitoring, tool identification, evaluation of external factors, and overall process optimization.

For the sake of brevity, the effects of individual parameters across different phases will not be discussed in detail. Instead, their application to the central cutting phase will be presented to define a wear index and a potential predictive maintenance criterion. Specifically, a wear criterion can be established by analyzing the *tool engagement ramp* and identifying peaks corresponding to the engagement of individual tooth rows (Fig. 4 (a)). By detecting these peaks through a local maximum search (Fig. 4 (b)) in the pressure derivative (with respect to time or stroke), it can be observed that they become wider and less pronounced over time. This occurs due to the dulling of the cutting edge, which increases the stroke required to initiate material removal. This trend allows for the definition of a wear index as follows:

$$I = \frac{\text{Peak Width}}{\text{Peak Heigth}} \tag{1}$$

Once the index I is defined, a predictive maintenance criterion can be established by setting a threshold beyond which product quality deteriorates to an unacceptable level. When I exceeds the threshold, the tool is deemed no longer suitable for use. The threshold value for I was not numerically determined in the present work, but is proposed as a preliminary concept for the future implementation of predictive maintenance strategies.

The threshold can be empirically established through experimental testing, by analyzing the correlation between the evolution of index I, product quality degradation (e.g., ovalization or rough surfaces), and visual inspection of the cutting edges. Moreover, the same threshold value for the wear index I can be proposed for all cutting teeth, based on the observation that wear mechanisms are consistent along the broach: although individual teeth operate independently, they experience similar cutting conditions and exhibit comparable degradation patterns. This approach allows the monitoring strategy to remain simple and effective, enabling the identification of worn or inefficient teeth without requiring replacement of the entire tool—thus significantly reducing maintenance costs and downtime.

Materials Research Proceedings 57 (2025) 539-547 https://doi.org/10.21741/9781644903735-63

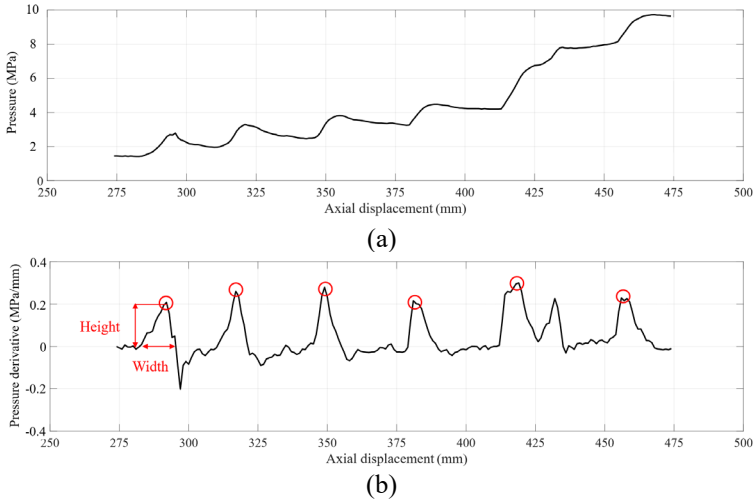


Figure 4: Determination of a wear index. (a) Tool engagement ramp pressure trend. (b) Pressure derivative as a function of the axial displacement during the tool engagement ramp (peak features are highlighted).

For any given tool, the qualitative temporal evolution of I across the six peaks corresponding to the various tooth rows shows a linear trend over time (Fig. 5), confirming the consistency of wear mechanisms along the tool. Therefore, a single threshold value can be used effectively for monitoring, ensuring simplicity and robustness in the predictive maintenance protocol.

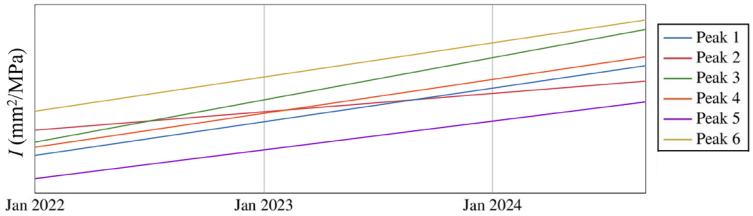


Figure 5: Qualitative evolution of the wear index as a function of time, with peaks ordered chronologically (e.g., peak one corresponds to the first cutting edge entering the tube).

At this stage, the index I is to be considered a qualitative indicator of wear progression. No numerical threshold has been calculated or validated so far. Its correlation with actual tool degradation is the subject of ongoing experimental campaigns, which also aim to establish whether energy-based or engagement-based criteria provide more reliable indicators for predictive purposes.

Additional insights into the process characteristics can be obtained by comparing the curves generated when using different tools (Fig. 6). In general, tools with increasing outer diameters exhibit progressively higher operating pressures (e.g., 80 mm and 110 mm tools), while maintaining similar trends relative to the piston stroke. The only distinct trend is observed with the intermediate-diameter tool (102 mm). In this case, the arrangement of the teeth on the outer surface of this broach is designed to maximize the material removal rate through a two-stage cutting process. As a result, the cutting pressures are significantly higher than in the other two cases—approximately twice as high as those recorded for the 110 mm broach.

Materials Research Proceedings 57 (2025) 539-547 https://doi.org/10.21741/9781644903735-63

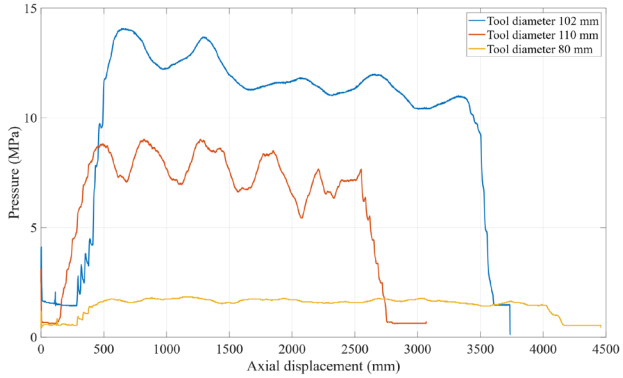


Figure 6: Contact pressure trend during the cutting phase for three different types of broach.

The results obtained highlight the strategic importance of the digitalization process implemented, demonstrating full compliance with the technical specifications outlined in the previous sections. By leveraging low-cost standard sensors, it was possible to digitalize a traditional machine within an SME environment with a total investment of just a few hundred euros, without disrupting ongoing operations during the transition. This transformation enhanced the company's competitiveness by enabling direct monitoring of a critical production process and establishing a predictive wear criterion. As a result, production efficiency increased, while material waste and downtime due to tool repair or replacement were significantly reduced.

The proposed solution also offers both horizontal and vertical scalability. Horizontally, similar digitalization strategies can be extended to other machines within the facility. Vertically, the defined indices can be integrated into higher-level decision-making processes, guiding production strategies, optimizing facility layouts, and evaluating new technical solutions with greater accuracy and reliability. For example, the collected data has already been used to refine different tube clamping solutions during machining, reducing pressure fluctuations, improving the final product quality, and extending tool lifespan (Fig. 7).

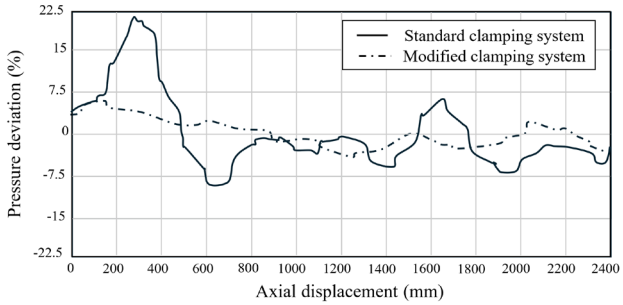


Figure 7: Pressure deviation as a function of the axial stroke with two different clamping systems.

Conclusions

This work demonstrates the feasibility and benefits of digitalizing a traditional broaching process in an SME environment, leveraging cost-effective and scalable Industry 4.0 solutions. By integrating digital pressure sensors and cloud-based data analysis, it was possible to monitor process health, establish predictive maintenance criteria, and reduce production inefficiencies. The proposed hybrid approach, combining physics-driven and data-driven analyses, enabled the identification of key process parameters, tool wear trends, and potential anomalies, enhancing process reliability and decision-making. Furthermore, while only one index has been presented in this work, multiple statistical indicators are currently under investigation to identify the most

effective parameters for real-time wear evaluation and predictive maintenance. Future work will focus on experimental validation of these indicators against measured tool wear.

The study highlights the advantages of a low-cost, non-intrusive digitalization strategy that minimizes operational disruptions while improving productivity and product quality. Furthermore, the scalability of the proposed solution—both horizontally across different machines and vertically into higher-level decision-making processes—makes it a viable model for broader Industry 4.0 adoption in SMEs.

Future developments will focus on expanding the monitoring system with additional sensors, refining predictive maintenance models, and integrating real-time adaptive control strategies to further optimize tool life and process efficiency. Additionally, extending the digitalization approach to other production stages could provide a comprehensive framework for smart manufacturing in SMEs, reinforcing their competitiveness in an increasingly data-driven industrial landscape.

References

[1] M. Hermann, T. Pentek, e B. Otto, «Design Principles for Industrie 4.0 Scenarios», in *2016 49th Hawaii International Conference on System Sciences (HICSS)*, Koloa, HI, USA: IEEE, gen. 2016, pp. 3928–3937. https://doi.org/10.1109/HICSS.2016.488

[2] P. C. Verhoef *et al.*, «Digital transformation: A multidisciplinary reflection and research agenda», *Journal of Business Research*, vol. 122, pp. 889–901, gen. 2021. https://doi.org/10.1016/j.jbusres.2019.09.022

[3] M. S. Es-haghi, C. Anitescu, e T. Rabczuk, «Methods for enabling real-time analysis in digital twins: A literature review», *Computers & Structures*, vol. 297, p. 107342, lug. 2024. https://doi.org/10.1016/j.compstruc.2024.107342

[4] E. Truant, L. Broccardo, e L.-P. Dana, «Digitalisation boosts company performance: an overview of Italian listed companies», *Technological Forecasting and Social Change*, vol. 173, p. 121173, dic. 2021. https://doi.org/10.1016/j.techfore.2021.121173

[5] R. Brozzi, D. Forti, E. Rauch, e D. T. Matt, «The Advantages of Industry 4.0 Applications for Sustainability: Results from a Sample of Manufacturing Companies», *Sustainability*, vol. 12, fasc. 9, p. 3647, mag. 2020. https://doi.org/10.3390/su12093647

[6] A. Moeuf, R. Pellerin, S. Lamouri, S. Tamayo-Giraldo, e R. Barbaray, «The industrial management of SMEs in the era of Industry 4.0», *International Journal of Production Research*, vol. 56, fasc. 3, pp. 1118–1136, feb. 2018. https://doi.org/10.1080/00207543.2017.1372647

[7] M. Ghobakhloo, M. Iranmanesh, M. Vilkas, A. Grybauskas, e A. Amran, «Drivers and barriers of Industry 4.0 technology adoption among manufacturing SMEs: a systematic review and transformation roadmap», *JMTM*, vol. 33, fasc. 6, pp. 1029–1058, set. 2022. https://doi.org/10.1108/JMTM-12-2021-0505

[8] J. Denning e K. Liyanage, «Systematic Literature Review of Industry 4.0 Implementation Frameworks Focusing on Applicability in Manufacturing SMEs», in *Advances in Transdisciplinary Engineering*, M. Shafik e K. Case, A c. di, IOS Press, 2022. https://doi.org/10.3233/ATDE220559

[9] A. Cotrino, M. A. Sebastián, e C. González-Gaya, «Industry 4.0 Roadmap: Implementation for Small and Medium-Sized Enterprises», *Applied Sciences*, vol. 10, fasc. 23, p. 8566, nov. 2020. https://doi.org/10.3390/app10238566

[10] T. Masood e P. Sonntag, «Industry 4.0: Adoption challenges and benefits for SMEs», *Computers in Industry*, vol. 121, p. 103261, ott. 2020. https://doi.org/10.1016/j.compind.2020.103261

[11] O. Jorg e G. Fantoni, «Design, development and test of a novel broach for long polypropylene tubes», *Precision Engineering*, vol. 74, pp. 224–231, mar. 2022. https://doi.org/10.1016/j.precisioneng.2021.11.012.

Materials Research Proceedings 57 (2025) 548-555 https://doi.org/10.21741/9781644903735-64

Digital twin solutions for state-aware, dynamic task allocation in flexible cyber-physical production systems

Matteo DE MARCHI[1,a *], Erwin RAUCH[1,b] and Dominik T. MATT[2,c]

[1]Industrial Engineering and Automation (IEA), Faculty of Engineering, Free University of Bolzano, Via Buozzi 1, 39100 Bolzano, Italy

[2]Research s.c.a.r.l., Via Volta 13/A, 39100 Bolzano, Italy

[a]matteo.demarchi@unibz.it, [b]erwin.rauch@unibz.it, [c]dominik.matt@unibz.it

Keywords: Industry 4.0/5.0, Smart Manufacturing, Digital Twin

Abstract. While experiencing the transition from the fourth towards the fifth industrial revolution, Cyber-Physical Production Systems are proving their potential in enhancing production effectiveness and efficiency. The core characteristics of Cyber-Physical Production Systems suggest great chances for further exploitation of this production paradigm: the generation of data and its exchange among deeply interconnected entities paves the way for the design of advanced use cases. This work aims at considering Digital Twin applications to rethink the fundamental control logic of production systems, by virtualizing and redistributing responsibilities among physical and digital entities. This foresees an integrated and bidirectional data flow that allows the physical and digital counterparts to act as one, enabling system's self-awareness and, in turn, self-optimization. Following the presentation of the technical aspects, key benefit, open challenges, and limitations are thoroughly reported.

Introduction

Context and Motivation. The manufacturing industry has undergone significant transformations over the past decades. These have been mainly marked by the change from traditional automation to the integration of advanced Cyber-Physical Systems (CPS). This process is referred to as the Fourth Industrial Revolution or Industry 4.0, emphasizes the fusion of physical production processes with digital technologies, leading to the emergence of smart factories characterized by adaptability, resource efficiency, and seamless integration across the value chain.

Prior the introduction of Industry 4.0, manufacturing processes strongly relied on centralized and hierarchical control architectures, such as Distributed Control Systems (DCS) [1]. Traditional DCS architectures often exhibit centralized decision-making procedures, especially in the fields of data processing and control logic execution. While the physical control devices are distributed, the system's logic and coordination often rely on centralized configurations and predefined rules set within supervisory levels, such as SCADA (Supervisory Control And Data Acquisition) or MES (Manufacturing Execution System) systems. These systems proved to be effective in traditional manufacturing environment, offering reliable and robust controlling tools. However, they also exhibited several major limitations. First, predefined control strategies made it challenging to adapt to changes in product design or production volume, hindering overall flexibility. Second, expanding or modifying production lines required substantial reconfiguration and downtime, limiting scalability, thus increasing costs as well as loss of earnings. Finally, traditional systems force the organization to rely on scheduled maintenance, often leading to unexpected equipment failures, resulting in increased downtime and costs, eventually affecting security too. These constraints, among others, describe the need for more flexible, scalable, adaptable, reconfigurable, and agile manufacturing systems capable of real-time adaptation to dynamic market demands and rapidly mutable production conditions. The rise of Cyber-Physical Systems and IoT has

Content from this work may be used under the terms of the Creative Commons Attribution 3.0 license. Any further distribution of this work must maintain attribution to the author(s) and the title of the work, journal citation and DOI. Published under license by Materials Research Forum LLC.

Materials Research Proceedings 57 (2025) 548-555 https://doi.org/10.21741/9781644903735-64

transformed manufacturing by enabling real-time connectivity and smart, self-optimizing environments. Among the key innovations driving this shift is the Digital Twin (DT) [2], which links physical systems to virtual replicas through continuous, bidirectional data exchange, creating a Digital Shadow [3]. DTs not only support simulation and decision-making but are evolving to take over full control of manufacturing systems. This enables real-time responsiveness, adaptability, and resource optimization, overcoming the rigidity of traditional automation. As a result, DTs enhance agility, streamline operations, and boost competitiveness in modern manufacturing.

Research Gap and Objectives. Despite the advancements in manufacturing technologies and the diffuesd adoption of CPS, traditional control architectures in production environments show significant limitations. These systems, typically hierarchical and rule-based, are often characterized by predefined decision logic, limited adaptability, and reactive rather than proactive control mechanisms. As a result, they struggle to efficiently manage dynamic production scenarios, such as fluctuating demand, process variability, or unexpected disturbances. The rigid structure of traditional control systems also leads to high reconfiguration efforts when adapting to new production requirements, reducing overall flexibility and responsiveness.

While CPS and IoT technologies have enhanced data collection and monitoring capabilities, there is a critical gap in the integration of this data into real-time, adaptive decision-making processes and self-optimization tasks. Current control methods lack the mechanisms to leverage and exploit continuous data flows for dynamically adjusting task allocations and optimizing system behavior. Moreover, decision-making remains largely centralized and static, limiting the system's ability to self-adjust based on its operational state.

In response to these challenges, this work proposes an innovative control framework based on DT technology. The key objective is to conceptualize a state-aware, dynamic task allocation approach, where control logic is virtualized within the Digital Twin, enabling real-time, bidirectional data exchange between the physical and digital layers. This framework aims to: 1) virtualize control logic by shifting decision-making processes into the Digital Twin, allowing for flexible and adaptive task allocation; 2) enable state-aware adaptability, where real-time monitoring and data analysis inform dynamic adjustments to production processes, and 3) enhance responsiveness by allowing the Digital Twin to process real-time information and autonomously propose control actions to optimize efficiency.

State of the Art

State of the Art of Manufacturing Process Control. Hierarchical structures and architectures mainly characterize traditional manufacturing process control systems. These have been mainly designed around centralized and hierarchical infrastructures, where decision-making is pre-defined, static, and typically follows a top-down approach. These architectures, may be exemplified by the ISA-95 automation pyramid. This has been designed based on the Purdue model, firstly proposed a research work by Williams [4]. The ISA-95 model defines a hierarchical structure for manufacturing systems:

The hierarchical structure of manufacturing systems spans six levels. Level 0 covers the physical production process with fast-acting sensors and actuators. Level 1 involves initial control through PLCs, operating in seconds. Level 2 uses SCADA and HMI systems for automation over minutes, while Level 3 manages production workflows via MES, functioning over hours to days. Level 4 handles enterprise planning with ERP systems, covering timeframes from days to months. Level 5, introduced with Industry 4.0, incorporates technologies like AI, cloud computing, and Big Data to enable advanced analytics and innovation, extending beyond the original ISA-95 standard.

While this structured approach has been effective in ensuring operational stability and consistency, it presents several inherent limitations, particularly in dynamic and complex manufacturing environments.

Evidence of possible evolutions on top of DCS-based models is brought to light by Dotoli et al. [5]. In their work, it is underlined how DCS frameworks may face difficulties integrating with modern, decentralized control technologies and smart sensor networks, that are among the main actors of modern, Industry 4.0 based manufacturing systems. The traditional setup can limit the integration of advanced real-time data and adaptive control mechanisms, involving CPS and IIoT-oriented entities. In the same direction goes the limitation in the field of interoperability, since traditional architectures are not always designed to easily connect with emerging technologies, such as cloud-based systems, Internet of (I)IoT devices, or Service-Oriented Architectures (SOA). Reconfiguring traditional DCS setups to accommodate new production lines or to address system faults often requires extensive manual intervention, which increases downtime and reduces operational efficiency.

Other architectures should also be considered for general knowledge, such as the RAMI4.0, the Industrial Internet Reference Architecture (IIRA), the IBM Industry 4.0 architecture, the National Institute of Standards and Technology (NIST) service-oriented smart manufacturing architecture. In this realm, the review proposed by Moghaddam et al. [6] provides deep knowledge in the comparison of currently available architectures and their limitations. In summary, they assess that: 1) the ISA-95 equipment hierarchy and object models continue to serve as a valid physical architecture for manufacturing systems. However, their relevance in the context of Industry 4.0 is enhanced through integration with the RAMI 4.0 model, which extends ISA-95 by incorporating modern digital components and technologies. 2) Although the five-layer functional hierarchy of ISA-95 remains a valid framework for categorizing manufacturing functions, it is not sufficient as a functional architecture for smart manufacturing. The increasing need for value network collaboration, digitalization, and resource sharing via IoT as micro-services suggests that SOA are more suitable for supporting the dynamic and distributed nature of Industry 4.0 environments. 3) The future of smart manufacturing architectures requires systems capable of dynamic discovery, composition, and matching of services with Industry 4.0 components. Achieving this flexibility depends on the successful design and integration of the physical and functional architectures. Emerging models, such as those proposed by IBM and NIST, aim to enhance flexibility, productivity, and balance across enterprise, plant, and edge levels (ISA-95 Levels 2-4).

Overall, it must be reported that the research of scientific works in the context of challenges and limitations of traditional industrial architectures is not flourish, this proving the need to highlight those and to subsequently propose effective improvements.

Adoption of Digital Twin Solutions to Control Manufacturing Systems. Despite the growing interest in DT technologies, their application for system control in manufacturing remains limited. Only about 10% of recent studies focus on DT-driven production control [7], with most research still theoretical or restricted to laboratory environments [8]. Existing works primarily address parameter control, motion control, and decision-making in systems with few entities [9], while the control of complex manufacturing systems is rarely explored. Moreover, nearly half of the studies rely on digital shadows rather than fully integrated DTs [7]. Key challenges to DT adoption include real-time data acquisition, processing capabilities, data security, system reliability, integration with legacy systems, and the need for specialized skills and investments. Overcoming these barriers is crucial for enabling adaptive and real-time control in modern manufacturing. Despite the rarity of works presented in this specific topic, some major contributions are mentioned hereafter.

A simulation-based Digital Twin approach utilizing the OSPS framework is presented in [10], integrating simulation models with embedded intelligence to enhance reactive control, production scheduling, and internal logistics supervision. The approach is centered around an advanced plant model, implemented in FlexSim, which orchestrates task assignments, monitors system processes, and supports optimization through interactive dashboards, API integration, and database

management [11]. The process flows use token-based triggers and custom scripts for simulation-driven optimization and control. Validation involved a small-scale setup with additive manufacturing, robotics, sensors, and a warehouse, demonstrating advanced monitoring and control—but scalability remains unproven. A software architecture integrating interoperable DT for controlling a line-less assembly system is presented in [12]. The system, structured around RAMI 4.0, includes an information system for data management and a control system for production flow and order execution. However, the integration of Digital Twins into the control system lacks detail, and the overall approach is not fully transparent for replication.

An intelligent manufacturing production line system using Digital Twin technology and a Region-based Convolutional Neural Network (R-CNN) is proposed in [13]. The system integrates virtual production components, information services, and twin data from sources like ERP, MES, local control systems, and simulation platforms. The R-CNN-based neural network supports forecasting, process diagnosis, parameter correction, and system control to enhance adaptability. The validation case study is briefly described, offering limited practical insights, and the control approach lacks detail, raising concerns about the system's maturity and methodological clarity.

Despite progress in Digital Twin-driven control systems, challenges remain in scalability, real-world validation, and clear methodologies. Current approaches are often lab-bound and struggle with real-time data, interoperability, and detailed control, highlighting the need for more practical, adaptable, and scalable solutions for industrial use.

Proposed Approach for DT-Based Task Dispatching

DT Framework for Virtualized Process Control. The Digital Twin is defined as a real-time, virtual replica of the physical production system, embodying the Digital Shadow through continuous data input from sensors and machines. Beyond reflecting the current state, it uses analytics and prediction to support intelligent decisions. Unlike previous approaches, this concept includes virtualizing high-level control, while low-level control remains on the shop floor, similar to traditional DCS systems. The proposed framework is structured into a three-layer architecture, each with distinct roles and responsibilities to enable effective virtualization and control of production processes.

Physical Layer: This layer includes the core physical elements (machines, sensors, and actuators) that perform operations and send telemetry data. Each is enhanced with a Custom Logic Component for defining high-level micro-tasks and an Interoperability Component to standardize communication across the system.

Digital Layer: The digital layer hosts the DT‘s core functions, including simulations and AI-based decision-making. It manages and adapts task execution based on real-time system monitoring, using rules and optimization to decide task allocation. This high-level control reduces the need for complex machine-specific configurations and carries out decision making tasks.

Data Layer: This communication layer enables continuous, bidirectional data flow between physical and digital layers, ensuring real-time synchronization. It shares telemetry to the DT for analysis and sends back optimized commands for execution, allowing responsive and informed control. This framework has the vision of integrating live data into adaptive, virtualized decision-making for manufacturing systems, enabling self-awareness, flexibility, and self-optimization. By embedding control logic in a Digital Twin, it simplifies management, enhances scalability, and balances centralized control with localized machine configurations.

State-Aware Task Dispatching in Digital Twin Controlled Manufacturing. In the proposed Digital Twin (DT) framework, state-aware task dispatching represents a core functionality that enables the dynamic and adaptive control of manufacturing systems. This approach ensures that tasks are assigned to the most suitable physical entities, with optimal parameters and timing, based on the real-time state of the overall system. The dispatching logic is built upon the continuous

Materials Research Proceedings 57 (2025) 548-555 https://doi.org/10.21741/9781644903735-64

interaction and data exchange between the key components of the Physical Layer, Digital Shadow Layer, and Digital Twin Layer, as represented in the detailed UML (Unified Model Language) structure of Fig. 1.

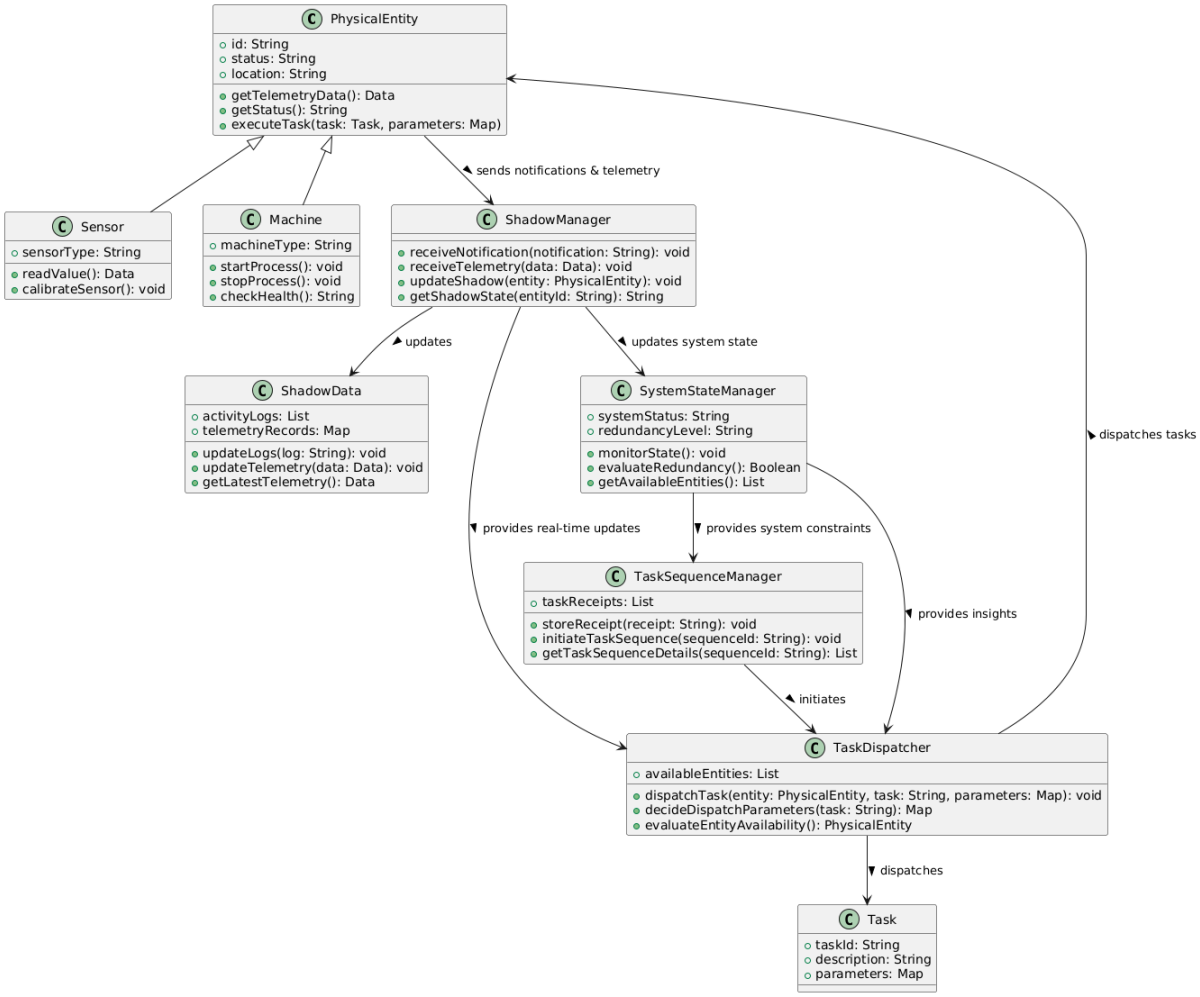


Fig. 1. *UML Class Diagram of the Digital Twin-Controlled Manufacturing System*

The Physical Layer represents the foundations of the DT framework and comprises all physical entities actively and passively engaged in the manufacturing system, including machines, sensors, and actuators. Each physical entity is characterized by attributes such as id, status, and location, enabling unique identification and state monitoring. Core functionalities include methods like *sendNotification()* to communicate the completion of tasks, *sendTelemetry()* for continuous data streaming related to operational metrics, and *executeTask()* to perform specific actions based on parameters received from the DT. Physical entities are further categorized into specialized subclasses: Sensors, which focus on environmental and operational monitoring with methods like *readValue()* and *calibrateSensor(),* and Machines, which manage production processes through functions such as *startProcess(), stopProcess(),* and *checkHealth()*. Each physical entity is also equipped with two key components to enhance its integration into the DT framework. First, the Custom Logic Component enables the definition of high-level, user-friendly functions known as micro-tasks, simplifying interaction and reducing complexity for operators. These are exposed to the DT layer, to be combined into complex and extended task sequences. The Interoperability Component, on the other hand, ensures seamless communication by translating diverse data protocols into standardized formats, allowing effective and seamless interaction within the system

Materials Research Proceedings 57 (2025) 548-555 https://doi.org/10.21741/9781644903735-64

architecture. This design allows the Physical Layer to act as a robust data source, continuously feeding the DT with real-time operational insights necessary for maintaining an accurate and responsive digital representation of the production environment.

The Digital Shadow Layer is an intermediary in the DT framework, since it ensures the continuous synchronization between the physical and digital domains. Its primary role is to maintain an accurate and real-time representation of the state of physical entities (machines, sensors, and actuators) by collecting, pre-processing, and storing data. At the core of this layer is the Shadow Manager, which actively interfaces with the Physical Layer to receive two types of data: notifications (discrete updates such as task completions) and telemetry data, representing continuous streams of operational metrics. The Shadow Manager component ensures the inner synchronization of collected data and visualizations. It has to be underlined, that the Digital Shadow is not necessarily embodied by a graphical interface. Sate awareness may also be purely data-drive, especially if the decision processes carried out in the DT layer are not assisted by human. Graphical representations are not needed by computational entities. Furthermore, the Shadow Manager provides system-wide access to updated status information through the *getShadowState()* method, supporting dynamic decision-making by higher system components. Finally, the Shadow Data component, which securely stores and organizes all operational data. It maintains detailed *activityLogs* and *telemetryRecords*, ensuring both historical traceability and real-time accessibility. This structured data management approach not only ensures system traceability but also supports predictive analysis and long-term optimization strategies in traditional systems, while represents the main source of information in DT-based applications.

The Digital Twin Layer is the characterizing part of the proposed approach, enabling state-aware and adaptive task dispatching. It virtualizes high-level control logic, managing task sequences, monitoring system status, and dynamically dispatching tasks while delegating low-level execution to physical entities. The Task Sequence Manager stores and manages predefined task sequences (receipts) and initiates them as needed. The Task Dispatcher assigns tasks to physical entities by evaluating real-time system conditions and determining optimal parameters. Also, in could be envisioned the employment of the Task Dispatcher in redundant environment, in which more than one physical entity are capable of performing the same actions and activities. The System State Manager monitors overall system status and redundancy, providing insights to support informed dispatching decisions. The Task component defines the structure and parameters of each task, ensuring clarity and traceability. Continuous interaction with the Digital Shadow Layer make sure that the dispatching of decisions reflect real-time system conditions, while feedback from the Physical Layer maintains system synchronization.

Discussion

Advantages of DT-Based Control and its Implications. Digital Twin-based control offers major advantages over traditional systems like DCS. By virtualizing high-level logic and integrating real-time data, it enhances flexibility, adaptability, and responsiveness. DTs enable state-awareness, allowing dynamic task allocation based on system conditions, which reduces manual intervention and boosts efficiency. This approach supports scalability, simplifies integration of new components, and separates high-level control from low-level execution, improving resilience and modularity. It also strengthens predictive maintenance through continuous monitoring and enhances transparency and traceability in decision-making.

To facilitate the understanding of the main differences and advantages provided by DT-based control, with respect to traditional DCS-based models, Table 1 summarizes them hereafter.

Materials Research Proceedings 57 (2025) 548-555 https://doi.org/10.21741/9781644903735-64

Table 1. *Key Differences Between Traditional and DT-Based Control Systems.*

Aspect	Traditional Control Systems	DT-Based Control Systems
Control Logic	Fixed and localized in physical controllers	Virtualized and dynamic, managed by the DT
Adaptability	Low, requires manual reconfiguration	High, with dynamic, state-aware task dispatching
Data Utilization	Limited, mainly reactive	Continuous, real-time data drives proactive decision-making
Scalability	Complex, requires manual integration of new elements	Flexible, supports modular and scalable integration
Resilience	Limited, dependent on predefined configurations	High, with dynamic reassignment in case of failures
Decision Transparency	Low, decisions are distributed and less traceable	High, with centralized orchestration and traceable logic
Maintenance Approach	Reactive, based on failures	Predictive, supported by continuous monitoring and analysis

Challenges and Future Directions. While DT-based control systems present significant potential, some major challenges and considerations should be underlined and addressed to enable their effective implementation and long-term evolution into meaningful, real-life scenarios. Although they are designed as autonomous, holistic, and generally applicable control systems, DTs are more likely to serve as supportive tools for human decision-makers for the future medium term (5–10 years). Human operators will play a crucial role in interpreting system insights, making final decisions, and managing unforeseen scenarios. The DT will function as an intelligent assistant, enhancing decision-making but not replacing human oversight, this ensures safety, transparency, and accountability. Also, the resistance towards change of personnel at any level of the organization should be taken into consideration since the adoption of DT-based control systems represents a drastic cultural change.

Considering technical aspects, main challenges include scalability and interoperability, especially in presence of legacy equipment and managing diverse data formats and communication protocols. The implementation of such complex systems requires significant customization and adaptation efforts, both in traditional systems as well as in DT-oriented ones. Additionally, the initial investment in infrastructure, technology, and specialized personnel is substantial, posing a barrier for smaller enterprises. Cybersecurity is another critical concern, as the DT framework relies on continuous, bidirectional data flow between the physical and digital environments and among the entities of the system. This introduces vulnerabilities related to unauthorized access, data breaches, and system manipulation. Robust strategies are needed to secure data transmission, protect sensitive operational data, and maintain system integrity.

Future advancements may focus on enhancing DT systems with AI agent-based analytics and autonomous reasoning, unlocking more effective and efficient dynamic task dispatching. However, these developments also introduce concerns about ethics, transparency, and explainability. Ensuring that AI-driven decisions are traceable, fair, and understandable will be critical to maintaining trust among stakeholders. Transparent algorithms, ethical data handling, and explainable AI models will be essential to ensure responsible and acceptable AI deployment.

References

[1] F.-L. Lian, J. Moyne, and D. Tilbury, 'Network design consideration for distributed control systems', IEEE transactions on control systems technology, vol. 10, no. 2, pp. 297-307, 2002. https://doi.org/10.1109/87.987076

[2] B. Wang, F. Tao, X. Fang, C. Liu, Y. Liu, and T. Freiheit, 'Smart manufacturing and intelligent manufacturing: A comparative review', Engineering, vol. 7, no. 6, pp. 738-757, 2021. https://doi.org/10.1016/j.eng.2020.07.017

[3] W. Kritzinger, M. Karner, G. Traar, J. Henjes, and W. Sihn, 'Digital Twin in manufacturing: A categorical literature review and classification', IFAC-PapersOnLine, vol. 51, no. 11, pp. 1016-1022, 2018, doi: 10.1016/j.ifacol.2018.08.474. https://doi.org/10.1016/j.ifacol.2018.08.474

[4] T. J. Williams, 'A reference model for computer integrated manufacturing from the viewpoint of industrial automation', IFAC Proceedings Volumes, vol. 23, no. 8, pp. 281-291, 1990. https://doi.org/10.1016/S1474-6670(17)51748-6

[5] M. Dotoli, A. Fay, M. Miśkowicz, and C. Seatzu, 'An overview of current technologies and emerging trends in factory automation', International Journal of Production Research, vol. 57, no. 15-16, pp. 5047-5067, 2019. https://doi.org/10.1080/00207543.2018.1510558

[6] M. Moghaddam, M. N. Cadavid, C. R. Kenley, and A. V. Deshmukh, 'Reference architectures for smart manufacturing: A critical review', Journal of manufacturing systems, vol. 49, pp. 215-225, 2018. https://doi.org/10.1016/j.jmsy.2018.10.006

[7] G. Pronost, F. Mayer, M. Camargo, and L. Dupont, 'Digital Twins along the product lifecycle: A systematic literature review of applications in manufacturing: [version 2; peer review: 2 approved, 2 approved with reservations]', Digital Twin, vol. 1, no. 2, p. 3, 2024. https://doi.org/10.12688/digitaltwin.17807.2

[8] M. Liu, S. Fang, H. Dong, and C. Xu, 'Review of digital twin about concepts, technologies, and industrial applications', Journal of manufacturing systems, vol. 58, pp. 346-361, 2021. https://doi.org/10.1016/j.jmsy.2020.06.017

[9] T. Böttjer et al., 'A review of unit level digital twin applications in the manufacturing industry', CIRP Journal of Manufacturing Science and Technology, vol. 45, pp. 162-189, 2023. https://doi.org/10.1016/j.cirpj.2023.06.011

[10] R. Santos, C. Rocha, R. Dias, and J. Quintas, 'Enhancing smart manufacturing systems: a digital twin approach employing simulation, flexible robots and additive manufacturing technologies', in EUROSIM Congress, Springer, 2023, pp. 277-291. https://doi.org/10.1007/978-3-031-68435-7_20

[11] R. Arrais et al., 'Application of the open scalable production system to machine tending of additive manufacturing operations by a mobile manipulator', in EPIA Conference on Artificial Intelligence, Springer, 2019, pp. 345-356. https://doi.org/10.1007/978-3-030-30244-3_29

[12] J. B. Mathews, J. Rachner, L. Kaven, D. Grunert, A. Göppert, and R. H. Schmitt, 'Industrial applications of a modular software architecture for line-less assembly systems based on interoperable digital twins', Frontiers in Mechanical Engineering, vol. 9, p. 1113933, 2023. https://doi.org/10.3389/fmech.2023.1113933

[13] Q. Yu-ming, D. San-peng, and others, 'Research on intelligent manufacturing flexible production line system based on digital twin', in 2020 35th Youth Academic Annual Conference of Chinese Association of Automation (YAC), IEEE, 2020, pp. 854-862. https://doi.org/10.1109/YAC51587.2020.9337500

Materials Research Proceedings 57 (2025) 556-564 https://doi.org/10.21741/9781644903735-65

Field-driven design of functionally graded TPMS-based 3D printed sandwich structures: Modeling, printing and testing

Gabriele Marabello[1,a*], Guido Di Bella[1,b]

[1]Department of Engineering, University of Messina, Contrada di Dio 1, 98166, Messina, Italy

[a]gabriele.marabello@studenti.unime.it, [b]guido.dibella@unime.it

Keywords: Material Extrusion (MEX), Design Optimization, Composites

Abstract. Sandwich structures with Triply Periodic Minimal Surface (TPMS) cores represent an innovative solution for lightweight applications requiring optimized mechanical properties and high strength-to-weight ratios. In this work, functionally graded TPMS-based sandwich structures were designed using a Field-Driven Design approach, allowing precise spatial variation of core thickness. Samples were fabricated via Material Extrusion (MEX), ensuring accurate reproduction of the designed gradient. Mechanical characterization through ASTM D790 three-point bending tests revealed that functional gradients significantly improve mechanical efficiency, particularly at higher fill percentages (≥30%), with strength increases up to 55% compared to uniform-thickness structures. However, at lower fill percentages (~20%), this advantage diminishes, highlighting a critical threshold for effective gradient application. The clear identification of this threshold constitutes a novel contribution, providing practical guidelines for the design and optimization of advanced TPMS-based sandwich structures.

Introduction

Triply Periodic Minimal Surfaces (TPMS) have gained increasing attention in recent years due to their unique structural and mechanical characteristics [1]. Characterized by continuous, smooth surfaces with zero mean curvature, TPMS-based architectures offer an optimal balance between strength and weight, making them highly desirable for lightweight structural applications. These geometries are particularly beneficial in fields such as aerospace, biomedical engineering, and mechanical design, where maximizing mechanical efficiency while minimizing material usage is a key objective. The ability of TPMS structures to provide good mechanical performance, energy absorption, and multifunctionality has driven extensive research into their applications across various engineering disciplines.

A significant advancement in the practical implementation of TPMS structures has been enabled by additive manufacturing (AM). Unlike conventional manufacturing techniques, which impose significant constraints on the fabrication of complex geometries, AM allows for the direct translation of mathematical TPMS equations into three-dimensional physical structures with high precision. This capability eliminates the need for approximations or simplifications that were previously necessary when attempting to manufacture TPMS-based components through traditional methods. The freedom provided by AM not only facilitates the realization of intricate periodic architectures but also enables the integration of functionally graded designs, unlocking new possibilities for performance optimization.

In the context of advanced lightweight structures, TPMS architectures are often employed as the core of sandwich structures. A sandwich structure consists of a lightweight core material, typically featuring cellular or lattice geometries, enclosed between two stiff outer skins. This configuration optimizes mechanical performance by leveraging the high bending stiffness of the skins and the energy absorption capacity of the core. TPMS-based sandwich structures, in particular, benefit from the inherent strength-to-weight ratio of minimal surface geometries while further enhancing load distribution and resistance to mechanical failure. This makes them ideal for

Content from this work may be used under the terms of the Creative Commons Attribution 3.0 license. Any further distribution of this work must maintain attribution to the author(s) and the title of the work, journal citation and DOI. Published under license by Materials Research Forum LLC.

applications where both strength and weight reduction are critical, such as aerospace, automotive, and biomedical implants.

One of the most promising aspects of TPMS-based sandwich structures is the ability to implement functional grading within their architecture [2]. By leveraging functionally graded design principles, the structural density, mechanical stiffness, and mass distribution of a component can be precisely controlled according to predefined criteria. This approach is particularly advantageous in applications where non-uniform loading conditions exist, as it allows for material distribution to be optimized by reinforcing regions experiencing higher mechanical stress while minimizing material usage in less critical areas. The ability to spatially vary TPMS thickness across a structure provides a powerful tool for tailoring mechanical responses, enhancing durability, and improving overall structural efficiency.

Recent advancements in the design and application of functionally graded gyroid structures have demonstrated significant improvements in mechanical performance and structural efficiency across various engineering domains. Noronha et al. [3] provided a comprehensive overview of additively manufactured functionally graded lattices, emphasizing the role of density gradients in tailoring mechanical responses. Their study highlighted how continuous and stepwise variations in lattice geometry can be employed to optimize deformation behavior and energy absorption, particularly in applications requiring lightweight yet robust structures. Junaedi et al. [4] investigated sandwich panels incorporating 3D-printed bio-inspired gyroid cores combined with carbon fiber-reinforced polymer laminate face-sheets. Their experimental results demonstrated that varying the relative density of the gyroid core significantly influences the flexural properties of the sandwich structures, with higher densities enhancing stiffness and load-bearing capacity. In a different application, Kedziora et al. [5] explored the use of functionally graded shell lattices as infill in additive manufacturing, specifically targeting lightweight design in mechanical components. Their findings indicated that implementing a graded lattice infill could achieve a substantial increase in the stiffness-to-mass ratio, suggesting potential for material and weight optimization in structural elements. Collectively, these studies underscore the versatility and effectiveness of functionally graded gyroid structures in enhancing mechanical performance and structural efficiency, paving the way for their broader adoption in advanced manufacturing and engineering applications.

In this study, Gyroid geometry is selected as the core of a TPMS sandwich structure due to its well-documented advantages in terms of mechanical performance and manufacturability. A key innovation of this work is the introduction of a thickness gradient within the TPMS core, achieved through a Field-Driven Design approach. By functionally varying the TPMS wall thickness, the material distribution is optimized to reinforce critical regions experiencing higher mechanical stress. This strategy enables a more efficient load-bearing capability while maintaining a lightweight configuration. To evaluate the mechanical response of the functionally graded TPMS-based sandwich structures, three-point bending tests are performed [6].

Materials and methods

3D Modeling

The sandwich panel structure consists of a TPMS-based core enclosed by two outer skins. The 3D CAD modeling of the specimens was performed using nTopology, a software that enables the application of field-driven methodologies to define complex geometries. The sandwich structure is composed of a Gyroid core measuring 160 mm × 40 mm × 10 mm [7], designed [8] to maximize bending resistance and manufacturability via Material Extrusion (MEX) [9]. This core is enclosed by two outer skins, each with a 1 mm thickness, resulting in overall specimen dimensions of 160 mm × 40 mm × 12 mm. These outer skins contribute to enhanced flexural stiffness and surface durability. To introduce a controlled thickness gradient within the core [10,11], a field-driven design was applied. The gradient was managed through a planar element modeled as an

Materials Research Proceedings 57 (2025) 556-564 https://doi.org/10.21741/9781644903735-65

infinitesimally thin parallelepiped (1000 mm × 1000 mm × 0.01 mm), positioned perpendicular to the specimen's length. This configuration allows for a linear transition of thickness along the XZ plane, while maintaining constant thickness in the YZ plane, as illustrated in the updated Figure 1, which now includes the core and skins' dimensions. This design optimizes material placement, reinforcing critical bending regions while minimizing weight [12].

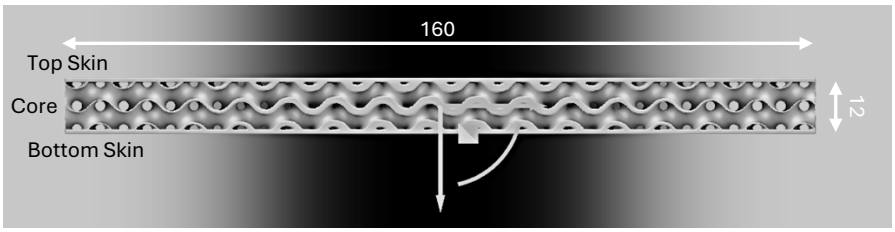


Figure 1. *Lateral view of the specimen (XZ plane) immersed in the scalar field.*

Six different configurations were designed to systematically evaluate their influence on mechanical performance, divided into two main classes: Class A (min thickness 0.5 mm): Thin peripheral regions (0.5 mm) transitioning to maximum thicknesses of 1.5 mm, 2.0 mm, and 2.5 mm (Figure 2); Class B (min thickness 1.0 mm): Increased peripheral thickness (1.0 mm) transitioning to maximum values of 1.5 mm, 2.0 mm, and 2.5 mm. The geometric characteristics, structure volume, and fill percentage of each configuration are reported in Table 1.

Table 1. *Geometric characteristics of the different specimens.*

Class	Min Thickness (mm)	Max Thickness (mm)	Structure Volume (mm³)	Fill %
A	0.5	1.5	12398.5	19.4
	0.5	2.0	15525.9	24.2
	0.5	2.5	18660.0	29.1
B	1.0	1.5	15508.4	24.2
	1.0	2.0	18632.9	29.1
	1.0	2.5	21804.7	34.1

As the maximum thickness increases, the total volume and fill percentage rise proportionally. Configurations with 0.5 mm minimum thickness exhibit lower volume and fill percentages, while those with 1.0 mm minimum thickness contain more material, contributing to enhanced mechanical properties.

Manufacturing

The specimens were fabricated using Material Extrusion (MEX) technology with a Bambu Lab X1 Carbon 3D printer. Polylactic Acid (PLA) was chosen as the printing material due to its excellent printability, dimensional stability, and compatibility with MEX technology, which allows for precise fabrication of complex geometries typical of TPMS-based sandwich structure [13]. The slicing settings on Bambu Studio software are reported in Table 2. The main modifications made to the default settings included: Reducing all line widths to 0.3 mm to ensure accurate deposition of the thinnest specimen areas, minimizing defects in the thickness gradient; Setting the full fill percentage to 100%, ensuring a fully dense TPMS core; Changing the fill pattern to "linear", a choice specifically aimed at optimizing the distribution of material in high-stress regions, promoting uniform load transfer and minimizing internal defects. These adjustments ensured a high-fidelity reproduction of the TPMS model, maintaining the precision and consistency of the gradient variation during printing.

Materials Research Proceedings 57 (2025) 556-564 https://doi.org/10.21741/9781644903735-65

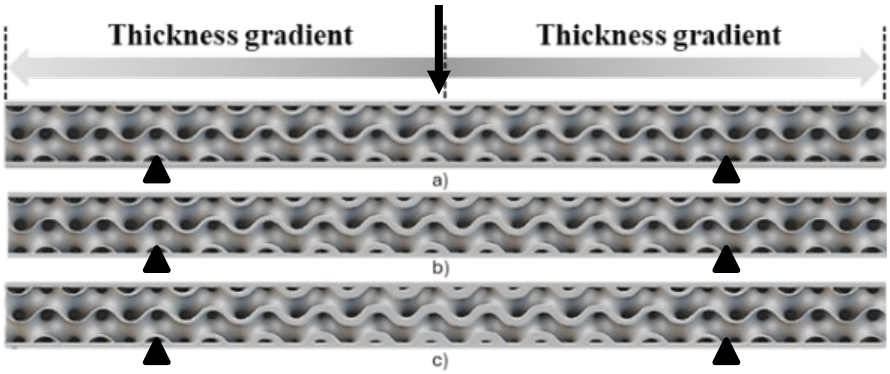


Figure 2. *Lateral view of the samples a) 0.5-1.5 mm, b) 0.5-2.0 mm, c) 0.5-2.5 mm.*

Table 2. Main printing parameters.

Parameter	Value
Layer height	0.2 mm
Line width	0.3 mm
Nozzle temperature	220°C
Bed temperature	35°C
Full filling percentage	100%
Fill pattern	Linear
First layer speed	50 mm/s
Outer wall speed	200 mm/s
Inner wall speed	300 mm/s

Mechanical Tests

To evaluate the effectiveness of thickness modulation on mechanical strength, three samples for configuration were tested in accordance with ASTM D790 standards [7], using a Zwick Roell testing machine, equipped with a 2.5 kN load cell, with a rate of 1 mm/min. To validate the mechanical differences observed, a one-way ANOVA test was performed, confirming statistically significant differences among the configurations. A Hirox Digital Microscope KH 8700 was employed to analyze the samples and assess failure modes.

Results and Discussions

Mechanical testing

Fig. 3 illustrates the experimental measurements of the weight distribution for each specimen configuration. As expected, the weight increases with the maximum thickness for both Class A (0.5 mm min.) and Class B (1.0 mm min.) samples, due to the larger amount of material deposited in the central regions. Class B specimens are consistently heavier than Class A at the same maximum thickness, reflecting the increased peripheral thickness. This difference in mass is critical for understanding mechanical performance, as it influences the load-bearing capacity and stiffness of each configuration. The lightest configuration is 0.5–1.5 mm, while the heaviest is 1.0–2.5 mm. Knowing the real weight of each specimen allows for proper stress normalization, ensuring effective mechanical comparisons.

Materials Research Proceedings 57 (2025) 556-564 https://doi.org/10.21741/9781644903735-65

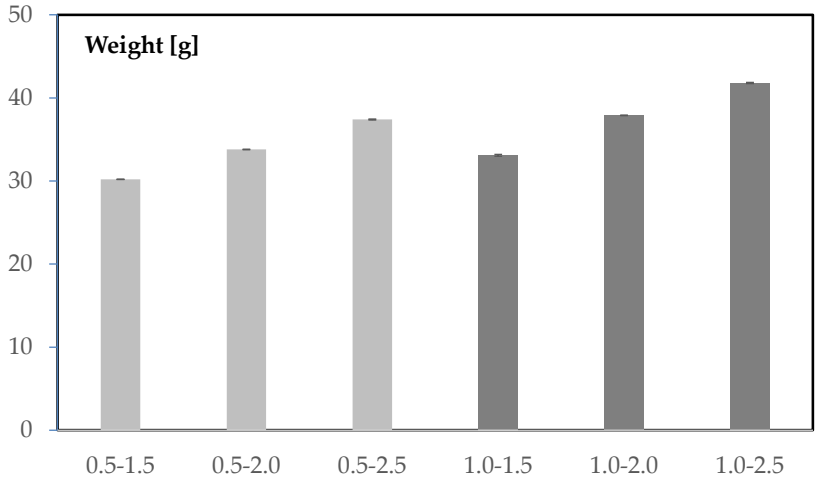


Fig. 3. *Mean weight for each configuration.*

Fig. 4 presents the average stress-strain curves for each configuration. In the initial elastic phase, all configurations behave similarly, with differences emerging as the load increases. Configurations with greater maximum thickness (0.5–2.5 mm and 1.0–2.5 mm) show higher stiffness and peak stress values, exceeding 35 MPa, indicating enhanced load-bearing capacity. Class B configurations (min. 1.0 mm) outperform Class A (min. 0.5 mm), confirming that a thicker base improves structural strength. Medium gradient configurations (0.5–2.0 mm and 1.0–2.0 mm) exhibit behavior similar to minimum gradients, with abrupt stress drops characteristic of brittle failure. In contrast, configurations with pronounced thickness gradients (0.5–2.5 mm and 1.0–2.5 mm) show more gradual stress drops, suggesting ductile failure and improved energy absorption.

Fig. 5 shows the evolution of the elastic modulus as a function of strain [14]. During the initial phase, all configurations display stable modulus values, reflecting effective load resistance. However, specimens with greater maximum thickness (0.5–2.5 mm and 1.0–2.5 mm) maintain higher modulus values, indicating better stiffness retention. Thinner configurations (0.5–1.5 mm and 1.0–1.5 mm) exhibit a more rapid decline, suggesting premature failure. This confirms that increasing both minimum and maximum thickness enhances stiffness and delays material degradation.

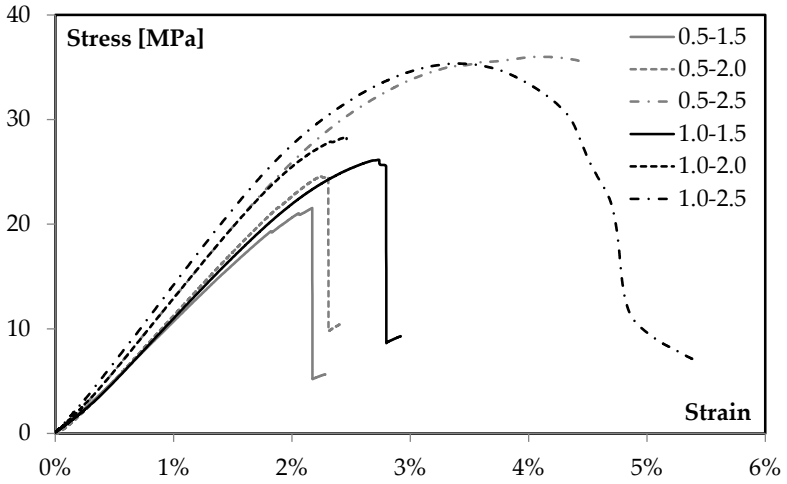


Fig. 4. *Average stress-strain curves for each configuration.*

Materials Research Proceedings 57 (2025) 556-564 https://doi.org/10.21741/9781644903735-65

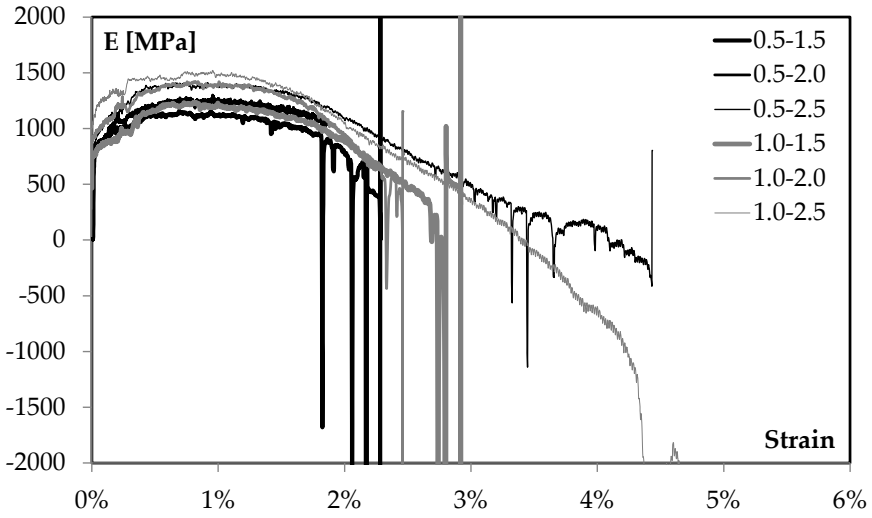


Fig. 5. *Typical flexural modulus trend for each configuration.*

Fig. 6 displays the specific maximum stress (MPa/kg), revealing the efficiency of each configuration. Among all configurations, 0.5–2.5 mm achieves the highest specific stress, nearly 1000 MPa/kg, highlighting its superior strength-to-weight ratio. Class A specimens generally outperform Class B in terms of material efficiency, with the exception of 1.0–2.5 mm, which shows comparable performance. This indicates that a steep gradient transition maximizes mechanical efficiency, concentrating material where stresses are highest while minimizing weight elsewhere.

Table 3 presents a comparative analysis between functionally graded and regular gyroid structures at equivalent infill percentages, as reported in the previous study [14]. The results show that at higher fill levels (≥30%), functionally graded structures significantly outperform their regular counterparts, with the 0.5–2.5 mm configuration achieving a +55.73% increase in maximum stress compared to the 1.55 mm gyroid. At 20% infill, however, the 0.5–1.5 mm structure is slightly less efficient than the 1.04 mm regular gyroid. This behavior suggests the existence of a threshold effect, where below a certain fill density, the thinner peripheral regions of the graded structure lack sufficient material to effectively redistribute stresses, leading to premature failure. This observation aligns with findings in the literature, indicating that the material distribution at low infill levels is critical to maintaining mechanical stability. This highlights the importance of optimizing the minimum thickness and fill percentage to avoid performance drops at low densities.

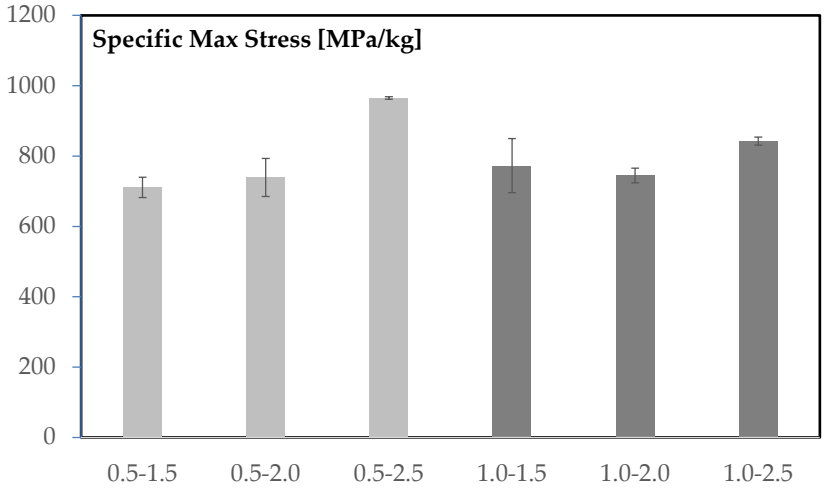


Fig. 6. *Stress-to-weight comparison.*

Materials Research Proceedings 57 (2025) 556-564 https://doi.org/10.21741/9781644903735-65

Table 3. *Comparison between functionally graded and regular structures.*

Fill %	Functionally graded		Regular		Δ
	Thickness [mm]	Stress [Mpa]	Thickness [mm]	Stress [Mpa]	[%]
20	0.5–1.5	21.5	1.04	22.6	-5.05
30	0.5–2.5	36.1	1.55	23.2	+55.73
30	1.0–2.0	28.2	1.55	23.2	+21.65

Optical Microscope Analysis

Fig. 7a illustrates the failure modes of Class A specimens. The 0.5–1.5 mm configuration shows brittle failure, with cracks initiating in the thin 0.5 mm peripheral regions, leading to abrupt fracture. The 0.5–2.0 mm configuration displays a slightly more progressive failure, with ligament bridging delaying complete collapse. For the 0.5–2.5 mm specimen, the thicker core effectively delays failure, resulting in a more gradual crack propagation and enhanced energy absorption. This configuration reached the highest recorded stress (36.1 MPa, +55.73% compared to the regular gyroid), confirming its superior load-bearing capacity and controlled damage evolution. Fig. 7b shows the typical failure modes of Class B specimens. The 1.0–1.5 mm configuration displays more uniform crack propagation compared to Class A, with gradual extension across TPMS struts, preventing sudden collapse. This results in improved structural continuity and controlled load redistribution, reflected in its moderate strength (28.2 MPa, +21.65% over the regular gyroid). The 1.0–2.0 mm specimen exhibits combined brittle and progressive failure, with cracks initiating centrally and propagating across multiple cells, indicating better stress distribution. Finally, the 1.0–2.5 mm configuration shows the most distributed failure, with gradual crack propagation and higher energy absorption, demonstrating improved load distribution and structural integrity.

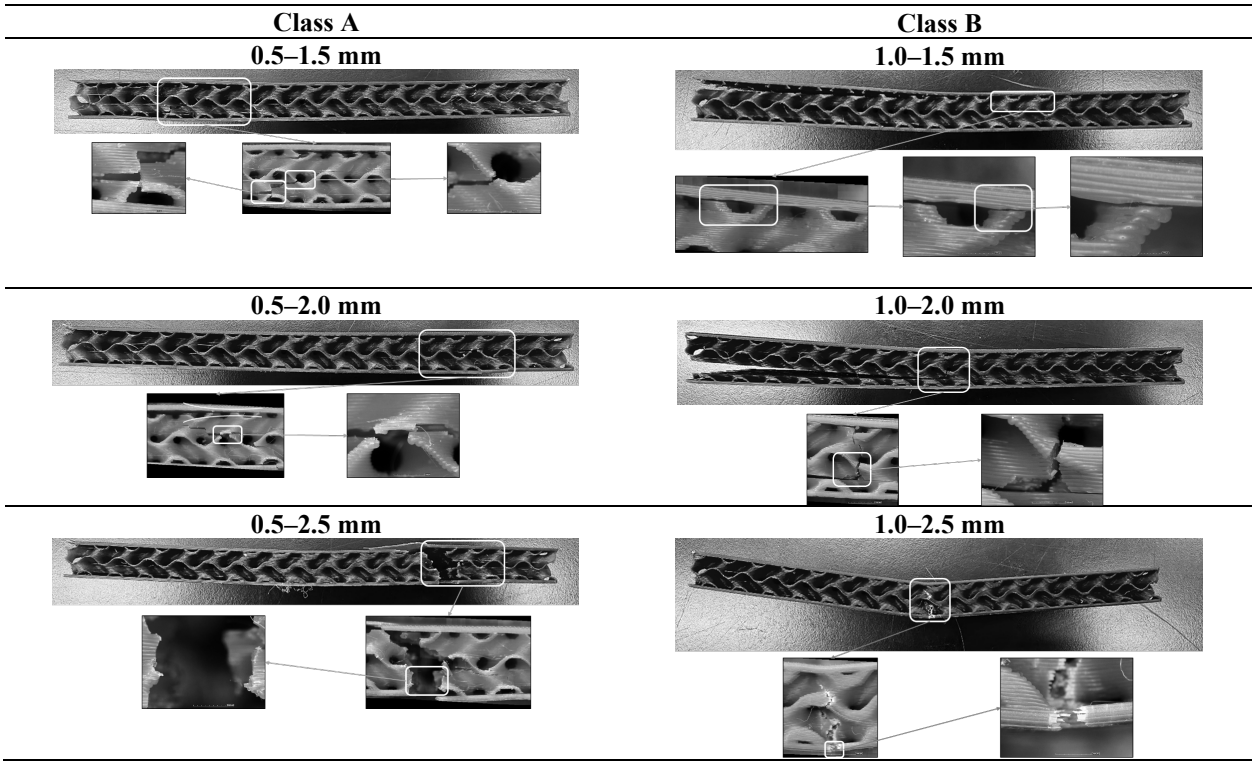


Fig. 7. *Failure modes of Class A (a) and B (b) samples.*

Conclusions

This study investigated the mechanical performance of functionally graded TPMS sandwich structures fabricated using Material Extrusion (MEX) technology. The main objective was to assess how thickness gradients within the gyroid core influence load-bearing capacity, energy absorption, and failure mechanisms under bending loads. The experimental results confirmed that steeper thickness gradients (0.5–2.5 mm and 1.0–2.5 mm) significantly enhance mechanical strength, delay failure onset, and promote more controlled damage progression. In contrast, thinner configurations (0.5–X mm) showed more brittle failure unless compensated by a thicker core, while medium gradient configurations (0.5–2.0 mm and 1.0–2.0 mm) behaved similarly to the minimum gradients, with sharp drops in stress post-peak. The analysis of the modulus evolution, stress-strain response, and fracture behavior highlighted the role of functionally graded designs in optimizing the mechanical performance of lightweight sandwich structures. These findings suggest that TPMS-based sandwich structures with controlled thickness gradients are promising candidates for applications where weight reduction and high mechanical efficiency are crucial.

References

[1] Nian Y, Wan S, Avcar M, et al (2023) 3D printing functionally graded metamaterial structure: Design, fabrication, reinforcement, optimization. Int J Mech Sci 258:108580. https://doi.org/10.1016/j.ijmecsci.2023.108580

[2] Alkunte S, Gupta M, Rajeshirke M, et al (2024) Functionally Graded Metamaterials: Fabrication Techniques, Modeling, and Applications—A Review. Processes 12:2252. https://doi.org/10.3390/pr12102252

[3] Noronha J, Dash J, et al (2023) Additively Manufactured Functionally Graded Lattices: Design, Mechanical Response, Deformation Behavior, Applications, and Insights. JOM 75:5729-5754. https://doi.org/10.1007/s11837-023-06190-x

[4] Junaedi H, Abd El-baky MA et al (2024) Mechanical Characteristics of Sandwich Structures with 3D-Printed Bio-Inspired Gyroid Structure Core and Carbon Fiber-Reinforced Polymer Laminate Face-Sheet. Polymers 16:1698. https://doi.org/10.3390/polym16121698.

[5] Kedziora S, Decker T, et al (2023) Application of Functionally Graded Shell Lattice as Infill in Additive Manufacturing. Materials 16: 4401. https://doi.org/10.3390/ma16124401.

[6] Li T, Wang L (2017) Bending behavior of sandwich composite structures with tunable 3D-printed core materials. Compos Struct 175:46–57. https://doi.org/10.1016/j.compstruct.2017.05.001

[7] (2017) Test Methods for Flexural Properties of Unreinforced and Reinforced Plastics and Electrical Insulating Materials

[8] Zhang J, Xie S, Li T, et al (2023) A study of multi-stage energy absorption characteristics of hybrid sheet TPMS lattices. Thin-Walled Structures 190:. https://doi.org/10.1016/j.tws.2023.110989

[9] Peng C, Tran P (2020) Bioinspired functionally graded gyroid sandwich panel subjected to impulsive loadings. Compos B Eng 188:. https://doi.org/10.1016/j.compositesb.2020.107773

[10] Song J, Wang M, Li D, Zhang J (2024) Deformation and Energy Absorption Performance of Functionally Graded TPMS Structures Fabricated by Selective Laser Melting. Applied Sciences (Switzerland) 14:. https://doi.org/10.3390/app14052064

[11] Wang Y, Liu F, Zhang X, et al (2021) Cell-size graded sandwich enhances additive manufacturing fidelity and energy absorption. Int J Mech Sci 211:. https://doi.org/10.1016/j.ijmecsci.2021.106798

[12] Chen D, Gao K, Yang J, Zhang L (2023) Functionally graded porous structures: Analyses, performances, and applications – A Review. Thin-Walled Structures 191

[13] Cao Y, Lai S, Wu W, et al (2023) Design and mechanical evaluation of additively-manufactured graded TPMS lattices with biodegradable polymer composites. Journal of Materials Research and Technology 23:2868–2880. https://doi.org/10.1016/j.jmrt.2023.01.221

[14] Calabrese L, Marabello G, Chairi M, Di Bella G (2025) Optimization of Deposition Temperature and Gyroid Infill to Improve Flexural Performance of PLA and PLA–Flax Fiber Composite Sandwich Structures. Journal of Manufacturing and Materials Processing 9:31. https://doi.org/10.3390/jmmp9020031

Materials Research Proceedings 57 (2025) 565-573 https://doi.org/10.21741/9781644903735-66

Deep learning-based monitoring of laser beam direct energy deposition to detect deviations in process conditions

M. Mazzarisi, M.G. Guerra, A. Angelastro, L M. Galantucci, S.L. Campanelli

Department of Mechanics, Mathematics and Management, Polytechnic University of Bari, Via Edoardo Orabona, 4, 70126 Bari, Italy

Keywords: Additive Manufacturing, Direct Energy Deposition, Deep Learning

Abstract. Laser Beam Direct Energy Deposition (DED-LB) is an additive manufacturing technique that requires precise process control to ensure defect-free parts. This study proposes an AI-driven monitoring framework utilizing deep learning techniques to evaluate process conditions and identify anomalies that may compromise the integrity of the manufactured part. During deposition, an off-axis high-resolution camera properly configured was used to acquire frames that were subsequently processed to extract brightness values and deposition head motion. To test the proposed methodology, controlled variations in key process parameters, including laser power, powder flow rate, and deposition speed, were introduced to induce anomalies. Laser shutdown and powder flow interruption produced appreciable reductions in brightness while the variation in speed had no detectable effect on laser-particle interaction. The results were statistically evaluated and compared with metallographic analysis.

Introduction

Laser Beam Directed Energy Deposition (DED-LB), sometimes referred to as Laser Metal Deposition, is an advanced Additive Manufacturing (AM) technique that utilizes a focused laser beam to melt and deposit metallic materials. This process enables the fabrication of complex geometries and the repair of existing components [1]. Despite its versatility, DED-LB presents challenges related to process stability and part quality, necessitating robust in-process monitoring and control strategies. These strategies are essential for detecting and mitigating defects caused by fluctuations in process conditions, which may result from uncontrolled variations in process parameters or environmental factors [2].

Defects commonly associated with DED-LB include porosity, cracking, distortion, and warping, all of which degrade the mechanical properties of fabricated components [3]. In-situ monitoring enables real-time assessment of critical process parameters such as temperature, powder flow, and the geometrical attributes of the deposited material. The effectiveness of in-situ monitoring depends on accurately identifying process signatures, which may be derived from different regions of interest, including the melt pool (size and temperature), an entire layer, or a partially built component, depending on the monitoring equipment employed [4–6].

In recent years, various optical techniques have been developed to assess the quality of AM components and their correlation with specific process parameters [7]. These methods primarily employ CCD/CMOS cameras, laser scanners, and structured light scanners. CCD/CMOS cameras, widely used due to their flexibility and ease of implementation, are typically integrated into the deposition head, either coaxially aligned with the laser beam [8,9] or positioned off-axis [10,11]. These imaging systems facilitate the monitoring of melt pool geometry, temperature distribution, and layer height estimation during the deposition process. Additionally, laser line and structured light systems have been successfully employed to monitor deposited layer height and partially built components [5,12].

Beyond direct monitoring of the deposited material, real-time evaluation of process parameters and the interaction between powder flow and the laser beam is crucial [13]. Variations in carrier

Content from this work may be used under the terms of the Creative Commons Attribution 3.0 license. Any further distribution of this work must maintain attribution to the author(s) and the title of the work, journal citation and DOI. Published under license by Materials Research Forum LLC.

gas flow, fluctuations in powder delivery, and other process instabilities can cause spattering and inconsistencies in the powder stream, leading to defects in the final component. Nozzle clogging, a critical anomaly, may occur due to oversized particles, impurities, or aggregated powder lumps in the feedstock or from improper evacuation of excess powder [14]. The complex interaction between the laser and the material benefits from advanced process monitoring techniques to ensure process stability and final part quality.

In this context, Artificial Intelligence (AI) methodologies, particularly machine learning (ML) and deep learning (DL), have demonstrated strong potential in enhancing real-time monitoring, process optimization, and predictive modeling [15]. Object detection algorithms, usually based on deep learning, are particularly advantageous. YOLO (You Only Look Once), a state-of-the-art object detection algorithm, enables precise identification and localization of multiple objects in an image or video in real time. The primary advantage of YOLO is its speed and accuracy, making it well-suited for real-time in-process monitoring applications.

In the literature, object detection algorithms and AI-driven methodologies have been adopted for the in-process monitoring of key process signatures. For instance, a deep learning-based multi-modality convolutional neural network (m-CNN) has been trained to process molten pool images and thermal profiles to estimate the geometric properties of the build bead in Wire Arc Additive Manufacturing (WAAM) systems [16]. A CNN-based models has been employed in a Laser Wire Directed Energy Deposition process for the detection, annotation, and segmentation of the melt pool, enabling the prediction of essential parameters such as melt pool area, height, width, center of area, and the center point of the bounding box enclosing the melt pool [17]. Another study introduces a smart monitoring system for online diagnosis of the DED-LB/M process, employing image-based monitoring and a CNN model trained to identify stability levels in material deposition [18]. This system integrates a novel process stability indicator, calculated from the model's probabilistic output distribution, offering a continuous metric that accurately reflects transitions between stable and unstable states.

This study introduces an AI-driven monitoring framework that employs deep learning techniques to assess flow area conditions, enabling the identification of process anomalies linked to defects in the final geometry. During deposition, frames were captured using an off-axis high-resolution camera and processed to extract brightness values and deposition head motion. To validate the proposed methodology, controlled variations in key process parameters, such as laser power, powder flow rate, and deposition speed, were introduced to induce anomalies. The results were statistically evaluated and compared with metallographic analysis.

Materials and Methods

The DED-LB system used in this study was a Trumpf Lasercell TLC 1005, integrating a 3 kW CO_2 laser, CNC control, and a five-axis gantry for precision. A three-way multijet nozzle and pneumatic powder delivery system facilitated clad deposition. Gas-atomized AISI 316L stainless steel powder (15–45 μm) was transported via helium carrier gas to the nozzle, directing it into the melt pool. AISI 316L substrates (25 mm thick) minimized thermal distortion during processing. Helium was used as both carrier and shielding gas. The deposition process was carried out using a laser power of 1600 W, a laser spot diameter of 2.00 mm, and a translation speed of 200 mm/min. The powder feed rate was set to 5.0 g/min, while the carrier gas and shielding gas flow rates were maintained at 5.0 l/min and 11.0 l/min, respectively.

A 7-layer sample of rectangular shape with nominal dimensions of 25 x 50 mm was fabricated using a bidirectional hatch strategy, with an interlayer rotation of 90° and an overlap of 30% between adjacent tracks was adopted. Intentional defects were introduced during the fabrication of the sample. Specifically, a laser shutdown was induced twice at layer 3, with durations of 30 seconds and 15 seconds. Powder flow was suspended twice at layer 5, each time for approximately 30 seconds. At layer 7, the deposition speed was deliberately altered, reduced to 25% of the

Materials Research Proceedings 57 (2025) 565-573 https://doi.org/10.21741/9781644903735-66

nominal value for 8 seconds, to 50% for 20 seconds, and increased to 150% for 20 seconds. These controlled variations were introduced to evaluate the capability of the proposed monitoring system in detecting and characterizing process anomalies.

The DED-LB system was equipped with a monitoring system consisting of a Canon EOS 760D DSLR camera and a 50 mm lens at the minimum focusing distance (Fig. 1a). Mounted on an adjustable height stand, it captured full HD (1920 × 1080 px) video at 25 fps, enabling the monitoring and early detection of production anomalies.

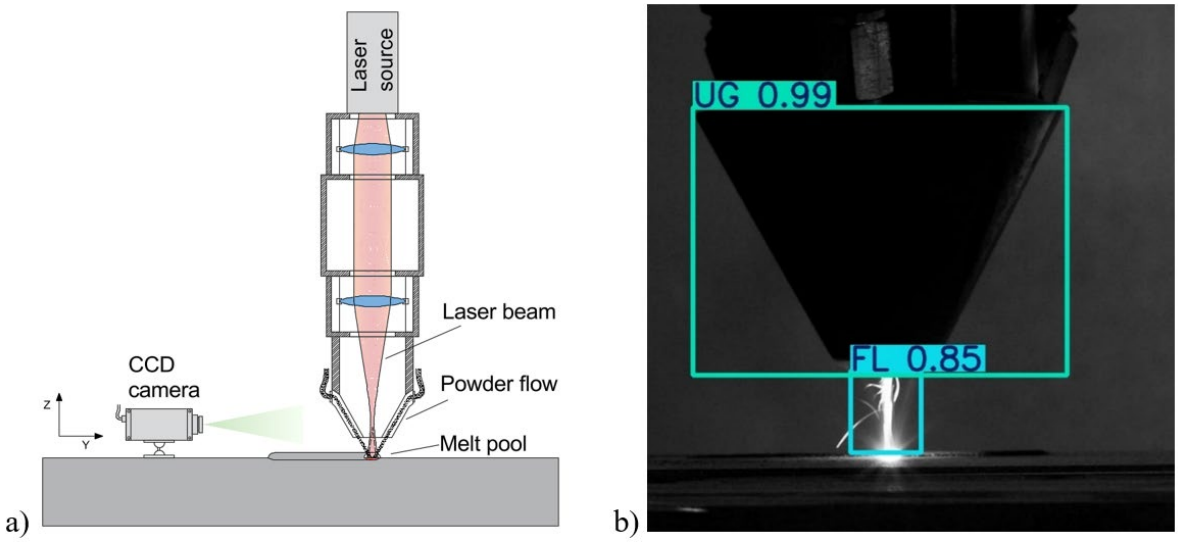


Figure 1 - a) Schematic of the monitoring system and b) algorithmic tracking of the nozzle (UG) and flow area (FL).

The training of the algorithm was conducted on a dataset consisting of images randomly selected on similar deposition process. Each image was processed in Labelme software to annotate regions of interest and label accordingly. The dataset was allocated into 70% training, 20% validation, and 10% testing. With key hyperparameters set, YOLOv11 was trained for 100 epochs, maximizing tracking accuracy (0.996 precision, 1.00 recall and 0.995 mAP50). This led to highly accurate tracking of two key features: the nozzle (UG) and the flow area (FL), as shown in the Fig. 1b.

Results and Discussion

Analysis of Brightness Values

The analysis was conducted by evaluating the average brightness within the FL region of interest. To this end, an algorithm was developed and implemented to compute the average brightness values of each pixel within the region, expressed on a scale from 0 to 255. This parameter is particularly significant as it provides a concise representation of the laser-powder interaction, which is fundamental to the deposition process. The deposition process is characterized by two primary components: the laser beam, which is focused onto the substrate, and the powder flow, which is conveyed to the deposition plane by a carrier gas. A stable and well-regulated interaction between these elements is essential to ensuring a uniform deposition process and, consequently, the production of high-quality samples. To assess the reliability of the analytical system, complete shutdown of laser power and powder flow were introduced as representative disturbances. While this initial study focused on abrupt anomalies, the approach shows promising potential for detecting more localized variations in process parameters, which will be explored in future work.

Materials Research Proceedings 57 (2025) 565-573 https://doi.org/10.21741/9781644903735-66

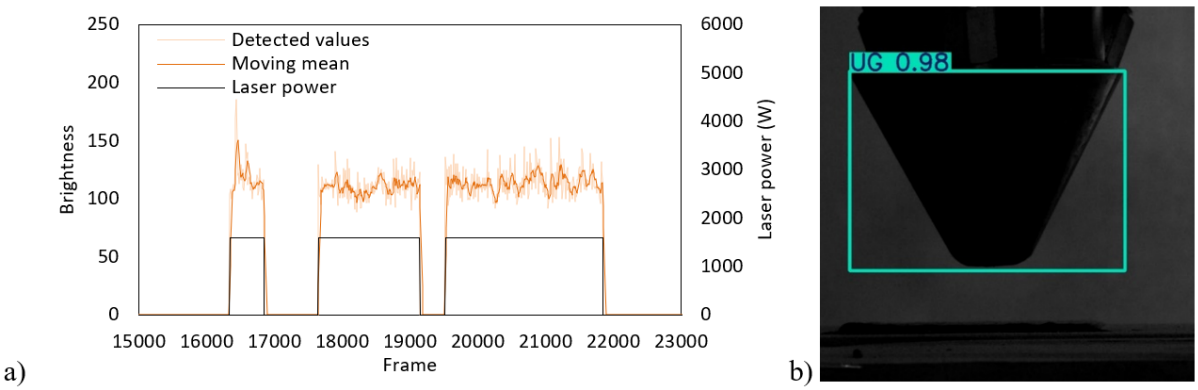


Figure 2 - (a) Average brightness of the flow area and moving-mean trend of layer 3 and (b) frame 17501 of the process.

Fig. 2a illustrates the trend of average brightness in the flow area during the deposition of the third layer. The five-point moving average trend exhibits discontinuities due to the interruption of laser power, which was applied at two distinct points in the manufacturing process. This interruption inevitably disrupts the interaction between the laser and the powder particles, preventing the formation of the melt pool on the underlying layer. Consequently, the algorithm loses critical reference points necessary for identifying the flow area, resulting in an inability to accurately locate it. Fig. 2b presents frame 17501, in which the algorithm successfully identifies the nozzle with exceptionally high reliability (0.98 out of 1). This result demonstrates the AI-based model's capability to distinguish active processing phases from idle periods by analyzing brightness levels. Additionally, the graph indicates that as soon as the laser is reactivated, the monitored brightness values realign with those recorded in previous layers, confirming the system's ability to resume monitoring under continuous operational conditions.

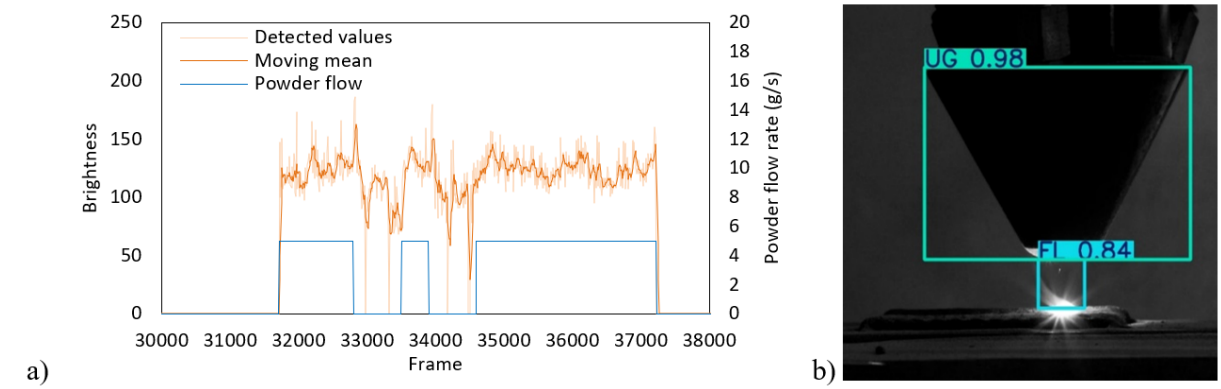


Figure 3 - (a) Average brightness of the flow area and moving-mean trend of layer 5 and (b) frame 33461 of the process.

During the fabrication of the fifth layer, the powder flow delivery was interrupted twice. As shown in Fig. 3a, this event caused significant variations in the average brightness levels. Specifically, peaks followed by abrupt drops can be observed in the brightness trend. The powder flow exhibits inherent inertia in responding to changes in its operational state. While the laser source reacts instantaneously to the interruption of energy delivery, the powder flow requires a longer response time when the carrier gas flow is shut off. This behavior can be attributed to the gradual pressure reduction within the powder feed system, which extends from the powder feeder to the deposition nozzle. As a result, a pronounced variability in the brightness of the flow area is observed, with sharp decreases when the powder flow is completely absent. In contrast, when the

Materials Research Proceedings 57 (2025) 565-573 https://doi.org/10.21741/9781644903735-66

laser remains active, the base material continues to melt, forming the melt pool. Under these conditions, the monitoring algorithm is capable of identifying the necessary references to detect the flow area (Fig. 3b). However, in rare instances, the absence of powder in the work area may lead to insufficient reference points, resulting in a loss of FL tracking.

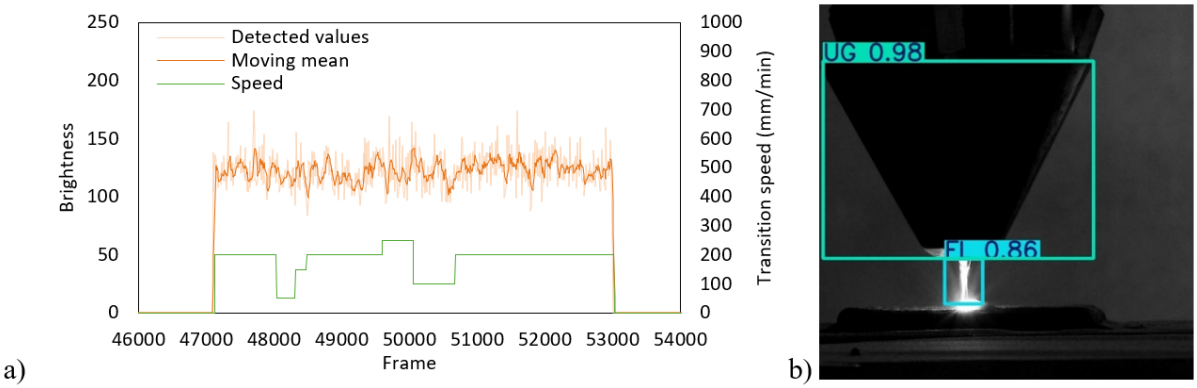


Figure 4 - (a) Average brightness of the flow area and moving-mean trend of layer 7 and (b) frame 33461 of the process.

In the seventh layer, the translation speed of the laser head was adjusted to evaluate its effects on the deposition process. As shown in Fig. 4a, reducing the laser head speed did not result in significant variations in the brightness of the flow area. However, this deceleration led to an increase in the size of the melt pool and the deposited material, locally reducing the standoff distance from the nozzle and consequently decreasing the height of the flow area (Fig. 4b). The analysis algorithm does not consider this region, instead identifying the flow area as the space extending from the terminal section of the nozzle to the upper surface of the deposited material. The laser–powder interaction remained stable during the reduction in translation speed, without showing significant brightness imbalances. A similar behavior was observed when increasing the translation speed of the laser head, where the slight variation detected fell within the expected range of analytical variability and was not clearly distinguishable from it. The brightness values were statistically analyzed to assess the impact of variations in process conditions on process stability. Evaluating the standard deviation for each layer, it was noted that this parameter stands at values between 13.5 and 15.0 for even (defect-free) layers, while for layer 5 it is 21.7 and for layer 3 as high as 47.5. In contrast, for layer 7 the value stands at 14.3, emphasizing the low impact on laser- powder interaction. These conclusions are remarked by the calculation of the coefficient of variation (standard deviation on mean), which for layer 5 gives a value of 0.18, for layer 5 of 0.53, and for layer 7 and even ones a stable value on 0.12.

Analysis of nozzle movement

The exceptional tracking capabilities of the developed algorithm are primarily demonstrated by its highly accurate tracking of the nozzle. This element serves as the principal reference point for flow area analysis and is also instrumental in determining the spatial position of the deposition process. Specifically, by tracking a reference point on the nozzle, the position of the deposition in the plane perpendicular to the camera view can be reconstructed frame by frame. Fig. 5 illustrates the evolution of the nozzle position along the x-axis during the deposition of the first and second layers. This analysis reveals the employed deposition strategy with odd layers (1, 3, 5, and 7) deposited along the x-axis, as evidenced by the characteristic sawtooth pattern resulting from the alternating forward and backward movements. Conversely, even layers (2, 4, and 6) are deposited along the y-axis, which is perpendicular to the camera's viewing plane and thus more challenging to discern by the camera. As a result, the deposition in these layers follows a more linear pattern,

Materials Research Proceedings 57 (2025) 565-573 https://doi.org/10.21741/9781644903735-66

characterized by a gradual progression along the x-axis, starting from one edge of the component and terminating at the opposite end.

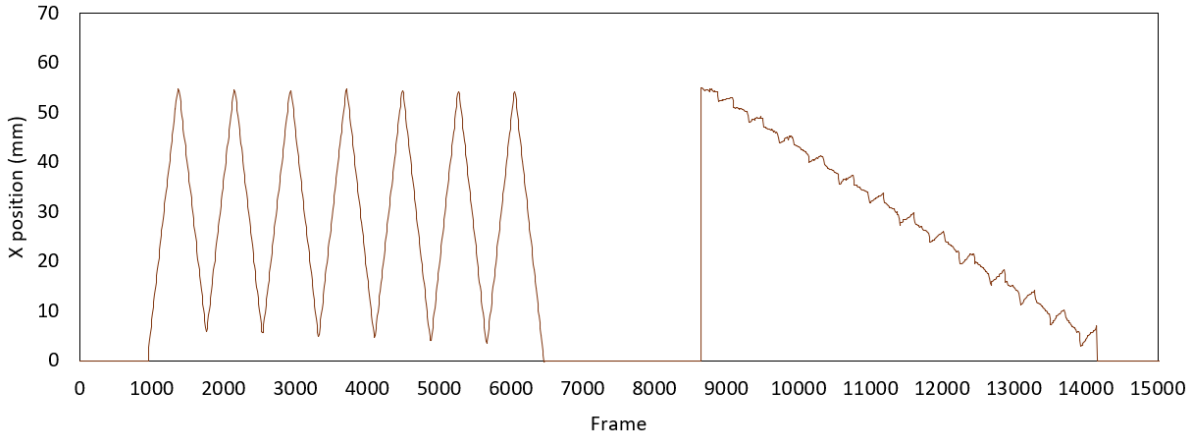
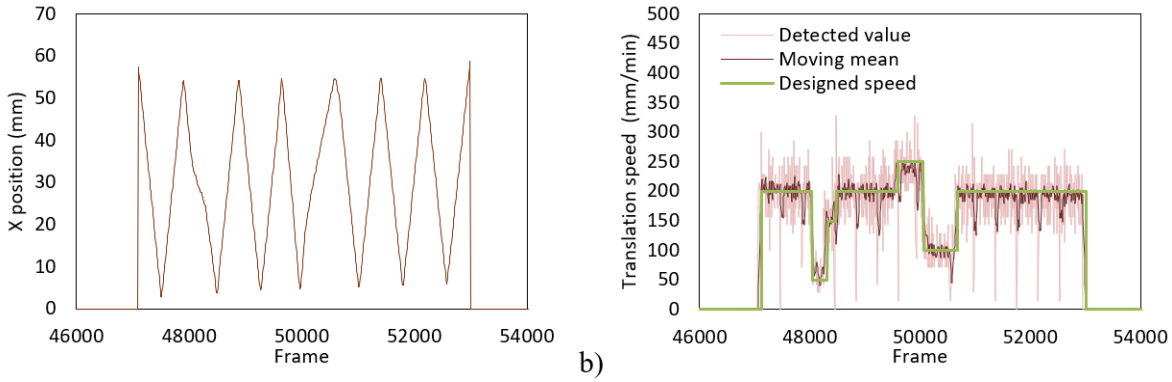


Figure 5 - Tracking of nozzle position along the x-axis in the manufacturing of the first and second layer.

Focusing on layer 7 (Fig. 6), where variations in the nozzle translation speed were deliberately introduced, noticeable irregularities emerge in the expected sawtooth pattern. Specifically, deceleration is observed at the second and fifth peaks, while acceleration occurs at the fourth peak of the trajectory. Furthermore, by analyzing the displacement data in conjunction with the camera frame rate, it is possible to compute the x-axis component of the nozzle translation speed. Fig. 6b presents a comparison between the designed speed parameter and the actual nozzle speed profile. The correspondence between the datasets is remarkably high, demonstrating the excellent tracking capability of the algorithm.



a) b)

Figure 6 – a) X-axis component of the position and b) speed of the nozzle in the production of the seventh layer.

Accurate in-plane identification of the deposition trajectory enables precise localization of anomalies in the component geometry and facilitates validation of the monitoring method through direct comparison with metallographic analysis.

Comparison with metallographic analysis

The specimen was analyzed using metallographic techniques (Fig. 7). Specifically, it was separated from the bulk substrate, which minimized thermal deformation, and sectioned along a median yz plane. Subsequently, the specimen was embedded in epoxy resin, polished using abrasive papers and cloths, and chemically etched by Glyceregia to reveal tracks and layers.

Materials Research Proceedings 57 (2025) 565-573 https://doi.org/10.21741/9781644903735-66

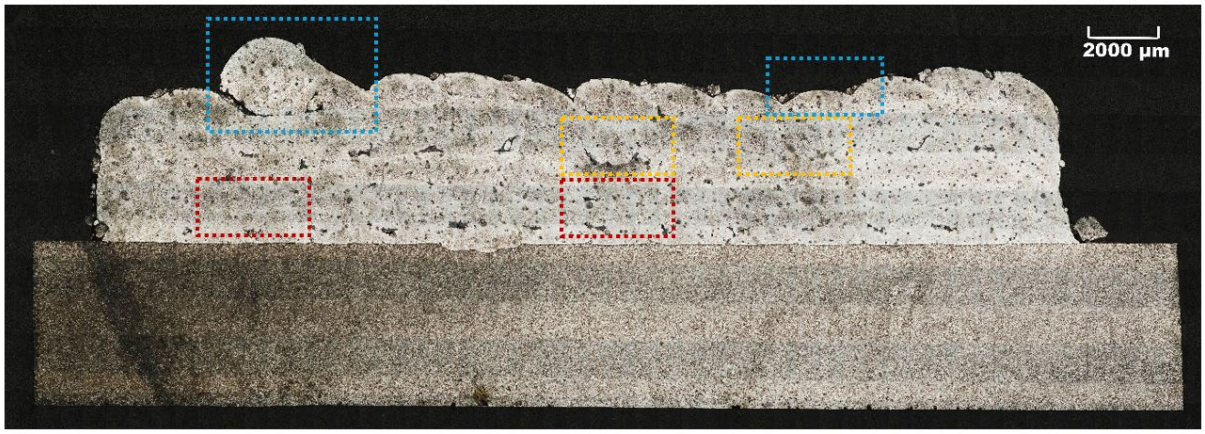


Figure 7 – Metallographic cross-section of the specimen with boxes indicating defects due to laser shutdown (red), powder interruption (yellow) and speed variation (blue).

Microscopic analysis of the polished section revealed an internal structure characterized by some deposition defects (porosity and lack of fusion) related to variations in process conditions. Fig. 8a shows the absence of a track at layer 3, attributed to the laser shutdown that completely inhibited the deposition process. Similarly, a track is missing in layer 5 due to an interruption in the powder flow. Additionally, remelting of the underlying track, caused by the passage of the laser beam, is highlighted (Fig. 8b). The lack of tracks resulted in an uneven deposition surface for the upper layers, which locally caused interlayer porosity issues. Finally, in layer 7, a significant accretion is observed, resulting from a reduction in the nozzle movement speed (Fig. 8c). This oversized track is characterized by a lack of bonding with the underlying layer. Conversely, the effects of increased speed, which led to a reduction in track dimensions, are less pronounced.



Figure 8 – Effects of perturbation of process parameters on a) layer 3, b) layer 5 and c) layer 7.

Conclusion

The AI algorithm for monitoring the Laser-Based Directed Energy Deposition (DED-LB) process has demonstrated high performance. The tracking of the nozzle (UG) and the flow area (FL), performed using YOLO v11, provides critical information on the laser-powder interaction, which is essential for evaluating the outcome of the deposition process. Specifically, the following results were obtained:

- The laser shutdown was clearly and instantaneously identified by the algorithm, which loses the reference points required for recognizing the FL region and determines the suspension of the deposition process.
- The interruption of the powder flow resulted in a significant decrease in brightness levels, attributable to the reduced interaction between the powder stream and the laser beam.
- Variations in deposition speed did not produce detectable effects in the brightness analysis of the FL area. However, nozzle tracking allowed for the reconstruction of its position and speed throughout the entire manufacturing process.

- The monitoring results were compared with data obtained from the metallographic analysis of the specimen. This comparison highlighted the impact of each defect in terms of interlayer porosity and lack of fusion on the final quality of the manufactured part.

The algorithm showed remarkable potential for DED-LB monitoring, which will be further explored on other deposition conditions and process aspects such as working distance, with the goal of achieving accurate and intelligent monitoring leading to industrial adoption.

References

[1] K. Kanishka, B. Acherjee, A systematic review of additive manufacturing-based remanufacturing techniques for component repair and restoration, Journal of Manufacturing Processes 89 (2023) 220–283. https://doi.org/10.1016/j.jmapro.2023.01.034

[2] Z. Tang, W. Liu, Y. Wang, K.M. Saleheen, Z. Liu, S. Peng, Z. Zhang, H. Zhang, A review on in situ monitoring technology for directed energy deposition of metals, Int J Adv Manuf Technol 108 (2020) 3437–3463. https://doi.org/10.1007/s00170-020-05569-3

[3] M.C. Brennan, J.S. Keist, T.A. Palmer, Defects in Metal Additive Manufacturing Processes, J. of Materi Eng and Perform 30 (2021) 4808–4818. https://doi.org/10.1007/s11665-021-05919-6

[4] M. Mazzarisi, A. Angelastro, M. Latte, T. Colucci, F. Palano, S.L. Campanelli, Thermal monitoring of laser metal deposition strategies using infrared thermography, Journal of Manufacturing Processes 85 (2023) 594–611. https://doi.org/10.1016/j.jmapro.2022.11.067

[5] M. Latte, M. Mazzarisi, M.G. Guerra, S.L. Campanelli, L.M. Galantucci, Key performance indexes for the evaluation of geometrical characteristics and subsurface defects through laser line monitoring of laser metal deposition process, Optics & Laser Technology 182 (2025) 112085. https://doi.org/10.1016/j.optlastec.2024.112085

[6] J. Whiting, A. Springer, F. Sciammarella, Real-time acoustic emission monitoring of powder mass flow rate for directed energy deposition, Additive Manufacturing 23 (2018) 312–318. https://doi.org/10.1016/j.addma.2018.08.015

[7] L. Yi, A. Shokrani, R. Bertolini, U. Mutilba, M.G. Guerra, E.G. Loukaides, P. Woizeschke, Optical sensor-based process monitoring in additive manufacturing, Procedia CIRP 115 (2022) 107–112. https://doi.org/10.1016/j.procir.2022.10.058

[8] M. Mazzarisi, A. Angelastro, S.L. Campanelli, V. Errico, P. Posa, A. Fusco, T. Colucci, A.J. Edwards, S. Corigliano, Monitoring of Directed Energy Deposition Laser Beam of Nickel-Based Superalloy via High-Speed Mid-Wave Infrared Coaxial Camera, JMMP 8 (2024) 294. https://doi.org/10.3390/jmmp8060294

[9] A. Vandone, S. Baraldo, A. Valente, F. Mazzucato, Vision-based melt pool monitoring system setup for additive manufacturing, Procedia CIRP 81 (2019) 747–752. https://doi.org/10.1016/j.procir.2019.03.188

[10] H.-W. Hsu, Y.-L. Lo, M.-H. Lee, Vision-based inspection system for cladding height measurement in Direct Energy Deposition (DED), Additive Manufacturing 27 (2019) 372–378. https://doi.org/10.1016/j.addma.2019.03.017

[11] M. Mazzarisi, M.G. Guerra, M. Latte, F. Devito, L.M. Galantucci, S.L. Campanelli, F. Lavecchia, M. Dassisti, In-Process Detection of Defects on Parts Produced by Laser Metal Deposition Using Off-Axis Optical Monitoring, in: H. Kohl, G. Seliger, F. Dietrich, S. Mur (Eds.), Sustainable Manufacturing as a Driver for Growth, Springer Nature Switzerland, Cham, 2025: pp. 755–762. https://doi.org/10.1007/978-3-031-77429-4_84

[12] E. Binega, L. Yang, H. Sohn, J.C.P. Cheng, Online geometry monitoring during directed energy deposition additive manufacturing using laser line scanning, Precision Engineering 73 (2022) 104–114. https://doi.org/10.1016/j.precisioneng.2021.09.005

[13] M. Mazzarisi, V. Errico, A. Angelastro, S.L. Campanelli, Influence of standoff distance and laser defocusing distance on direct laser metal deposition of a nickel-based superalloy, Int J Adv Manuf Technol 120 (2022) 2407–2428. https://doi.org/10.1007/s00170-022-08945-3

[14] H. Lee, W. Heogh, J. Yang, J. Yoon, J. Park, S. Ji, H. Lee, Deep learning for in-situ powder stream fault detection in directed energy deposition process, Journal of Manufacturing Systems 62 (2022) 575–587. https://doi.org/10.1016/j.jmsy.2022.01.013

[15] F. Ciccone, A. Bacciaglia, A. Ceruti, Optimization with artificial intelligence in additive manufacturing: a systematic review, J Braz. Soc. Mech. Sci. Eng. 45 (2023) 303. https://doi.org/10.1007/s40430-023-04200-2

[16] W. Li, H. Zhang, G. Wang, G. Xiong, M. Zhao, G. Li, R. Li, Deep learning based online metallic surface defect detection method for wire and arc additive manufacturing, Robotics and Computer-Integrated Manufacturing 80 (2023) 102470. https://doi.org/10.1016/j.rcim.2022.102470

[17] R. Asadi, A. Queguineur, O. Wiikinkoski, H. Mokhtarian, T. Aihkisalo, A. Revuelta, I.F. Ituarte, Process monitoring by deep neural networks in directed energy deposition: CNN-based detection, segmentation, and statistical analysis of melt pools, Robotics and Computer-Integrated Manufacturing 87 (2024) 102710. https://doi.org/10.1016/j.rcim.2023.102710

[18] J. Flores, I. Cabanes, A. Gutierrez, K.L. De Calle, O. Gonzalo, E. Portillo, An innovative smart monitoring system for DED-LB/MW process stability based on machine learning techniques, Int J Adv Manuf Technol 137 (2025) 1759–1773. https://doi.org/10.1007/s00170-025-15134-5

Miscellaneous



Materials Research Proceedings 57 (2025) 575-582 https://doi.org/10.21741/9781644903735-67

Nanoscale topographical characterization of permeability-related features in the production of polymeric films for food packaging

Giacomo MACULOTTI[1,a *], Alberto PIOVANO[1,b], Gianfranco GENTA[1,c] and Maurizio GALETTO[1,d]

[1]Department of Management and Production Engineering, Politecnico di Torino, Corso Duca degli Abruzzi 24, 10129 Turin, Italy

[a]giacomo.maculotti@polito.it, [b]alberto.piovano@polito.it, [c]gianfranco.genta@polito.it, [d]maurizio.galetto@polito.it

Keywords: Surfaces, Atomic Force Microscopy (AFM), Polymers

Abstract. Polymeric films play a vital role in food packaging, offering protective barriers that preserve the quality, safety, and shelf life of food products. Their performance depends on properties such as mechanical strength, thermal stability and permeability. Permeability is particularly important as it regulates the transfer of gases from the environment to food. Thus, permeability affects the shelf life, taste and safety of food products. The interaction between nanoscale surface features and permeability is a critical but under-explored aspect of film design. This study aims to test capability of surface topographical characterization as an alternative quality inspection tool for permeability in commercial polymer films. Advanced techniques such as Atomic Force Microscopy (AFM) are used to characterize surface features including roughness and morphology. The results will provide an alternative route for the permeability quality control in manufacturing processes of state-of-the-art commercial polymer films for food packaging.

Introduction

Food packaging represents a critical processing step in secondary agri-food industry because it severely affects food products quality, with functions that encompass product safety during transport to shelf-life extension. In fact, food products exposition in uncontrolled packaged environments might promote both biochemical and physical alterations in the good, e.g. bacterial metabolism, colour and texture variation, which depending on the case could be harmful to the consumers' health [1]. Therefore, both packaging in modified atmosphere and packaging technologies have been widely studied to extend the shelf-life by preserving organoleptic properties [1], while strict international regulations have been put in place to control requirements of packaging in direct contact with food [2]. In particular, polymeric films for food packaging represent a critical component for ensuring intermediate life-span duration of goods both for industry, distribution, and consumers. Polymeric films offer a protective barrier between food products and external environmental factors, thereby preventing contamination, dehydration, and oxidation. Gas permeation process exerts a substantial influence on the shelf life, organoleptic properties, and safety of packaged foods, emphasizing the necessity for precise control and comprehensive understanding of these properties in the development of effective packaging solutions [3]. The widespread adoption of polymeric films in food packaging applications can be attributed to their versatility, cost-effectiveness and lightweight nature. Polymeric films for food packaging are mostly manufactured by extrusion process, which allows high degree of control over the thickness and composition of the resultant film [4]. The materials most frequently employed in the production of such films include polyethylene (PE), polyvinyl chloride (PVC), polyethylene terephthalate (PET), polypropylene (PP), and polyvinylidene chloride (PVDC), and polyamide (PA) [5]. Commercially, PVC and PVDC have been more attractive than PE recently thanks to their greater barrier and capability of withstanding higher temperature, opening to wider range of

Content from this work may be used under the terms of the Creative Commons Attribution 3.0 license. Any further distribution of this work must maintain attribution to the author(s) and the title of the work, journal citation and DOI. Published under license by Materials Research Forum LLC.

Materials Research Proceedings 57 (2025) 575-582 https://doi.org/10.21741/9781644903735-67

packaging atmospheres and applications [6]. Also, more recently, extensive research on high-barrier properties material, e.g. based on multilayer structure [6], bio-based materials [7], and surface functionalized films by ceramics layers [8].

The distinct barrier properties of these materials are tailored to specific requirements for food packaging. The primary function of these films is to act as barriers to oxygen (O_2) and water vapour ($H_2O_{(v)}$), thereby preserving the integrity and freshness of food products. Usually, the barrier properties of these films are quantified using permeability (*P*) measurements, and the gas transmission rate (*TR*), typically of oxygen (*OTR*) and water vapour (*WVTR*), across the film in standard tests conditions [9]. Respectively, the *P* describes the flux per unit area and per unit partial pressure of a certain gas across a certain material; *P* is a thickness (*t*) and pressure independent parameter, it is a material intrinsic property, and is expressed in SI units in $mol \cdot m^{-1} \cdot s^{-1} \cdot Pa^{-1}$, even though in the practice several other units are used. On the other hand, *TR* is the permeability per unit thickness, i.e. $TR=P/t$, and allows catering for the contribution of the film thickness [3,9,10]. The determination of gas *P* and *TR* of polymeric films for food packaging is governed by a series of regulatory frameworks, including ISO 15105 and ISO 15106 [11,12]. Table 1 reports typical values for the most common food packaging film polymers. These frameworks delineate the methodologies for conducting such measurements. Whilst these standard permeability tests provide reliable data, they are often time-consuming, requiring long stabilization time for the baseline evaluation, which makes them less feasible for rapid quality control assessments in industrial settings. The permeability of a material depends on several factors, e.g., the polymer composition, temperature, humidity, and film morphology. In particular, a positive correlation has been shown in sparse cases between permeability and topography [13,14]. The roughness of a film's surface has been demonstrated impact gas diffusion through films, with smoother surfaces generally exhibiting lower permeability [15]. However, literature only reports root mean square height parameter Sq neglecting other surface parameters which might be suitable for describing a porous structure, e.g., the average height gradient.

Table 1 *Reference gas transmission rate value for oxygen (OTR) and water vapour (WVTR) of typical polymeric materials for films for food packaging (LD-PE is low-density PE and HD-PE is high-density PE). Unit d is day (86400 s). Values refer to 38 °C and 90% relative humidity [16,17]. Higher permeability corresponds to lower barrier. WVTR is the conventional unit as per ISO 15106 [14].*

	LD-PE	**HD-PE**	**PP**	**PET**	**PVC**	**PA**	**PVDC**
OTR / $cm^3 \cdot m^{-2} \cdot d^{-1} \cdot atm^{-1}$	6500-8500	1600-2000	2000-4500	100-150	20-100	50-75	2-4
WVTR / $g \cdot m^{-2} \cdot d^{-1}$	10-20	3-10	5-15	15-20	5-10	500-1000	0.5-1

This work aims at leveraging partial results presented in the literature to test capability of surface topographical characterization as an alternative quality inspection tool for permeability. This would allow much faster and readily usable inspection and quality verification methods than current standard permeability tests, which can take as long as 1 day. To bridge this gap, this work will focus on commercially available films for food packaging to provide suitability of surface topography measurements in assessing quality differences and typical variability of roughness values of commercial food packaging films. In particular, the work will investigate the variability of surface topography parameters for commercial polymeric film for food packaging. Furthermore, the study will investigate representativeness of different measurement length scale by characterizing film both at nano-scale by Atomic Force Microscopy (AFM) and at micro-scale by surface topography optical measuring instrument. Such investigation will provide insight representativeness of characterization, which is typically limited to AFM [15].

Materials Research Proceedings 57 (2025) 575-582 https://doi.org/10.21741/9781644903735-67

Materials and Methods

This work focuses on assessing the variability of surface topography of commercially available customer-grade polymer films for food packaging. Considering the commercial availability of the considered products, legal requirements linked to quality tolerances for permeability are considered satisfied [2].

Thickness measurements were performed replicating three measurements with a Sensofar SNeox Confocal Microscope with a 20× magnification objective (squared pixel of 0.69 μm) [18].

Topographical measurements were performed considering two length scale: micro- and nano-scale. Per each measurement length scale, three measurement replications per condition were performed to increase the degrees of freedom to estimate random errors. Measurements were performed by stretching a sample of polymeric food packaging film over a pair of silicon wafer shards with a gap in between, and measurements were performed on the free area, to eliminate any effect of the substrate. Microscale surface topography was assessed by performing measurement the surface of the film by a Sensofar SNeox Coherence Scanning Interferometer (CSI) equipped with 20× magnification Mirau objective, with 0.40 Numerical Aperture, squared pixel size of 0.69 μm, and field of view (FoV) of (845×707) μm. The instrument was calibrated as per ISO 25178-700:2023 showing a measurement noise of 0.78 nm. Scale limited (SL) surface topography was evaluated by a sequence of a F-operator (levelling by subtraction of least-square fitted plane), robust gaussian S-filter (N_{is} of 2.5 μm), and L-filter (N_{ic} of 0.25 mm) [19,20]. The N_{is} follows a 3:1 ratio with the maximum sampling distance, approximated by the pixel size, and the N_{ic} a 100:1 ratio with the N_{is}, which is the smallest choice according to the standard [19,20]. Nanoscale surface topography was assessed by measuring the surface of the film by an Anton Paar Tosca400 atomic force microscope (AFM) having a measurement noise of 11 pm. Measurements were performed in tapping mode investigating a FoV of (10×10) μm with a lateral resolution of 25 nm. To elicit the comparison of the two measured scales, only levelling was performed [21].

The considered measured and post-processed topographies were characterized in terms of height and hybrid surface topography parameters, namely the arithmetic mean height Sa, the root mean square height Sq, the maximum pit depth Sv, the maximum height Sz, the root mean square gradient Sdq, and the developed interfacial are ratio Sdr [19]. Surface characterization was performed by MountainLab v8.1.

Table 2. *Factors, Levels and nesting of the factorial design. "Manufacturer" is nested in "Material", and "Batch" is nested in "Material" and "Manufacturer".*

Material	Manufacturer (Perceived Quality)	Batch
PE	A (Low)	b-A1
		b-A2
PVC	B (Medium)	b-B1
		b-B2
	C (High)	b-C1
		b-C2

Considering the reported positive nonlinear correlation between surface roughness of films and oxygen and water vapour permeability [8,9], a factorial design was implemented to test the effect of the main features of shelf-grade polymeric food packaging film on surface topography. Specifically, the two polymeric materials, namely PE and PVC, and three manufacturers were considered. The manufacturers were selected based on the customer-perceived quality of the shelf-grade polymeric film depending on the shelf-cost. Brand and manufactured are not disclosed, for a market comparison is considered out of the limited scope of the present work. Considering commercial availability of the considered materials, the manufacturer resulted nested in the

Materials Research Proceedings 57 (2025) 575-582 https://doi.org/10.21741/9781644903735-67

material, and, consequently, the batch resulted nested in both the manufacturer and the material. Additional variability components were included in the factorial design, to gather further insights into factors possibly impacting on the permeability of the film. Specifically, manufacturing reproducibility is considered by testing one product from 2 batches per manufacturer. The resulting nested factorial design, summarized in Table 2, consisted of a 2×3×3=18 measurements per measuring instrument, and was analysed by means of Generalized Linear Model (GLM) to investigate factors-induced significant systematic effect on the evaluated surface topography parameters [22].

Results and Discussion

Fig. 1 shows pseudo-colour surface topographies measured for the three manufacturers. As it can be qualitatively appreciated, CSI measurements present a range of surface heights larger than one order of magnitude. This is due to the fact that the larger field of view of CSI inherently caters for the topography shape, here represented by residual wrinkles of the surface. Conversely, the AFM measurement shows a highly isotropic surface, which was also confirmed by the phase signal. ANOVA performed by GLM confirmed the difference induced by the measurement length scale is systematic with a p-value < 0.001 for all the considered surface topography parameters. Accordingly, to gather more insights the two measurement length scales were then further analysed separately.

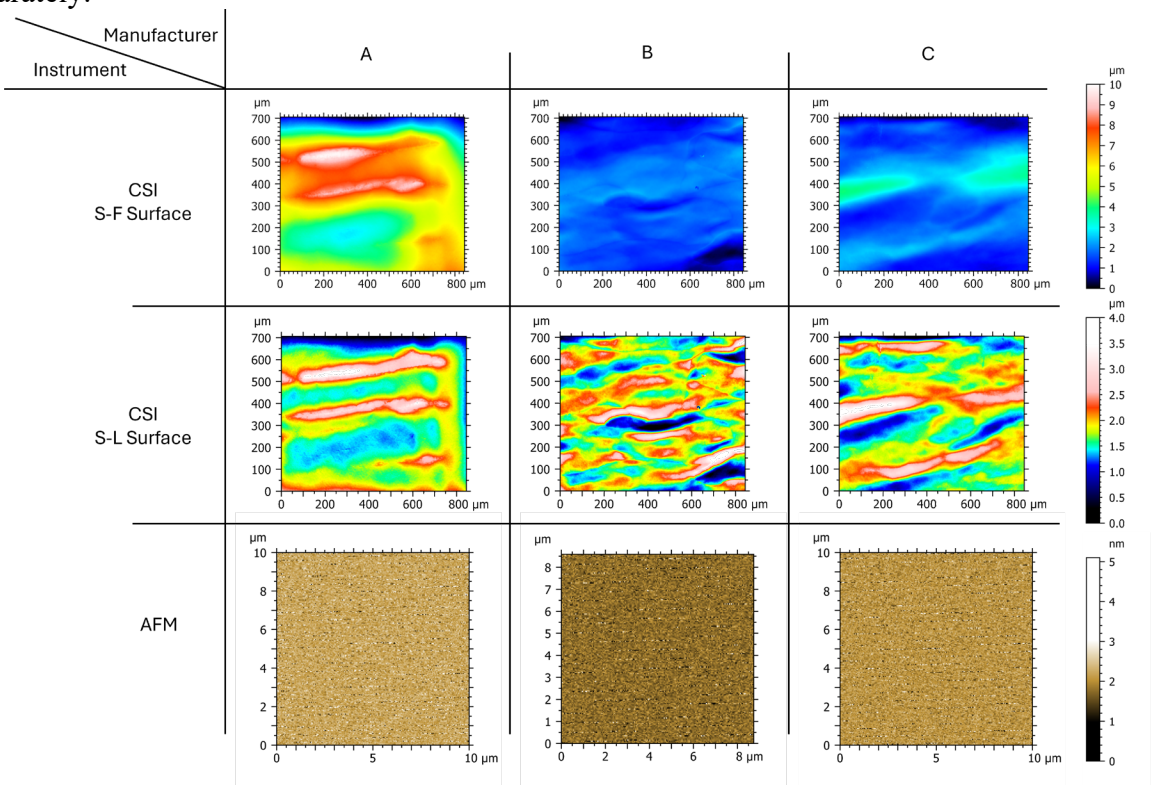


Fig. 1 *Pseudo-colour views of measured surface topography for the examined instrument-manufacturer configurations. Only one batch and one replication are shown for each configuration. CSI measurements report both S-F (nesting index 2.5 µm) and S-L surface (nesting index 0.25 mm). For AFM, levelled surface is shown.*

Considering a greater measurement area, by CSI, the material was marginally significant (e.g., requiring varying and as high as 12% risks of error) and the GLM was weakly informative, presenting a coefficient of determination R^2 lower or equal than 60% (see Table 3). The large part of not explained variability can be due to the wrinkles and remaining shape of the topography after the mounting. Conversely, as shown in Table 3, localized measurements obtained at nano-scale

Materials Research Proceedings 57 (2025) 575-582 https://doi.org/10.21741/9781644903735-67

thanks to AFM are adequately explained by the considered factors, presenting GLM R^2 of about 90%. Surface extreme height parameters (Sv and Sz) variability was not explained by the considering factors, suggesting a main contribution from the measurement noise. For other surface topography parameters, a highly significant effect introduced by the material could be appreciated. The effect of measurement length scale and greater significance of AFM highly localized and spatially resolved measurements provide a formal motivation to the AFM use for food packaging film characterization as a literature best practice [9].

Table 3 *p-values and coefficients of determination (R^2) for the considered factors effect on surface topography parameters at micro- and nano-length scale (respectively CSI and AFM). Factors in brackets indicate nesting.*

	CSI				AFM			
	Material	**Manufacturer (Material)**	**Batch (Material, Manufacturer)**	**R^2**	**Material**	**Manufacturer (Material)**	**Batch (Material, Manufacturer)**	**R^2**
Sa	0.055	0.344	0.147	0.50	<0.001	>0.99	0.028	0.89
Sq	0.069	0.423	0.112	0.50	<0.001	0.834	0.1	0.92
Sv	0.044	0.942	0.177	0.48	0.805	0.102	0.824	0.26
Sz	0.075	0.242	0.18	0.48	0.357	0.267	0.813	0.21
Sdq	0.031	0.122	0.073	0.60	<0.001	0.566	0.006	0.96
Sdr	0.116	0.252	0.197	0.45	<0.001	0.605	0.006	0.96

Fig. 2 reports main effect and interaction plots for Sq. Trends are similar for other parameters, and considering the reported correlation between the gas permeability and transmission rates and Sq, further discussion is focused – for sake of brevity – solely on the root mean square height. Both measurement scales – despite the smaller statistical difference for the micro-scale – indicate a significantly smaller surface roughness for PVC. This is well in line with the expected better barrier property, i.e., smaller P and TR, of PVC than PE, as summarized in Introduction and in Table 1. From a manufacturing perspective, the poorer permeability of PE is compensated – to respect regulatory requirements – with a thicker film. In fact, confocal microscope measurements showed that the PE thickness is 1.5 µm systematically larger than PVC films (*p*-value of 0.012 with a t-Student test).

Table 4. S*ix-sigma intervals for the considered surface topography parameters for the investigated materials.*

Material	**Sa / nm**	**Sq / nm**	**Sv / nm**	**Sz / nm**	**Sdq / -**	**Sdr / %**
PE	0.173±0.004	0.241±0.006	1.982±0.245	4.132±0.621	9e-3±7e-5	4e-3±6e-5
PVC	0.164±0.002	0.226±0.002	1.955±0.188	3.953±0.218	9e-3±7e-5	4e-3±6e-5

Although the nested design did not allow to test significance of interactions, interaction plots provide a qualitative insight into their effect on topographical parameters, and consequently on permeability. In particular, it allows appreciating the greater stability of AFM measurements, which are less sensitive to shape variation, and show that (as confirmed by the GLM ANOVA) despite the different market positioning and cost-perceived quality, no statistically significant differences could be appreciated between the PVC-based films. Interaction plot, also show a quite large, difference between the batches of the same manufacturer, which – in some cases – was also confirmed by the ANOVA in Table 3. Thus, Attenuated Total Reflectance Infrared (ATR-IR) spectroscopy was performed to investigate material homogeneity between batches. Results in Fig. 3 shows that only the lower quality PVC (B manufacturer) has a poorer control over material

Materials Research Proceedings 57 (2025) 575-582 https://doi.org/10.21741/9781644903735-67

composition, which though (see interaction plots in Fig. 2) does not affect the surface topography. Conversely, the greater between-batch variability for manufacturer C cannot be ascribed to compositional differences and shall be traced back to measurement complex reproducibility. Finally, six-sigma intervals for the considered topographical parameters is evaluated, according to GLM results, per each material class. Results are summarized in Table 4.

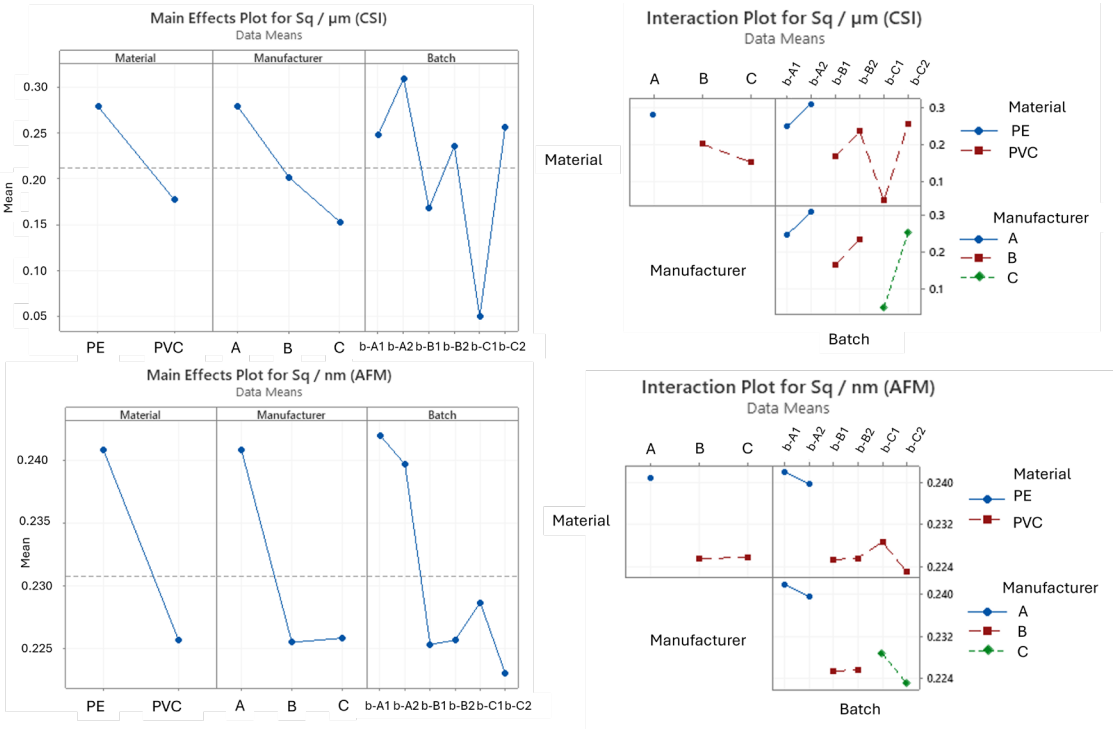


Fig. 2 *Main effects (left) and Interaction plots (right) for Sq. Top row: CSI, bottom row AFM.*

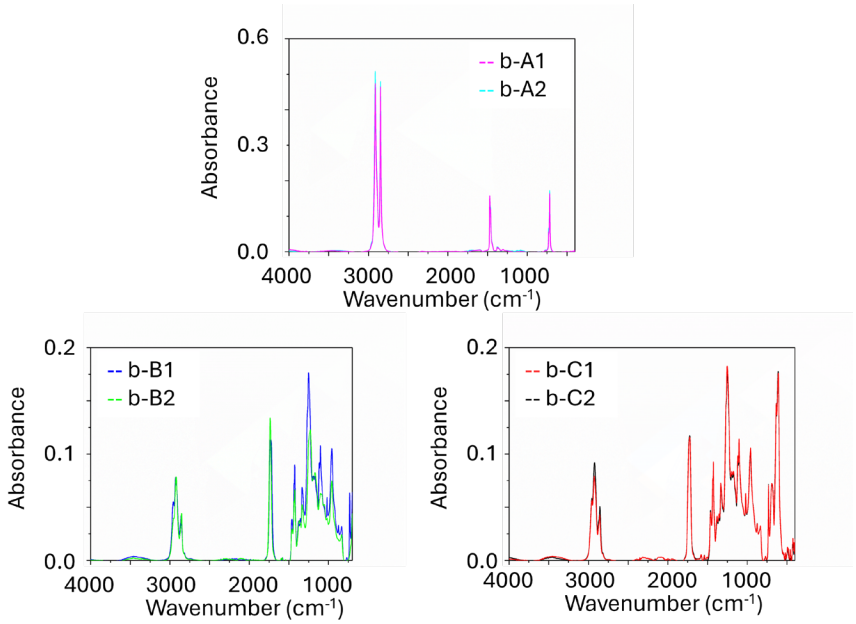


Fig. 3 *ATR-IR spectra of the six samples (two batches per three manufacturer). The lower quality PVC (manufacturer B) shows a greater variability of composition (notice the difference between b-B1 and b-B2).*

Conclusions

This work investigated methods to characterize the surface topography of polymeric films for food packaging. Surface topography is correlated to films barrier properties, which is an essential functional feature to guarantee safety and integrity of the food and extend its shelf life. This work investigated the capability of surface topography measuring instruments as an alternate indirect route for permeability quality control, representing a faster and cost-effective solution to conventional standard solutions. The results showed the relevance of the selection of the correct characterization scale. In particular, AFM provides high-resolution insights into nanoscale surface morphology providing results more robust to film topographical shape suitable for studying the interplay between topography and permeability. The investigation carried out on commercially available polymeric films showed that in some cases, the customer perceived quality – linked to similar material processed by different manufacturers - do not translate into improved functional performances. The findings of this study will contribute to the development of more efficient quality control methodologies for food packaging applications, offering manufacturers a reliable and practical means of assessing material performance. In particular, future works will calibrate the correlation between the surface topography parameters and permeability to enable faster quality control inspection procedures based on AFM measurements.

Acknowledgement

This work is a part of the project NODES which has received funding from the MUR-M4C2 1.5 of PNRR funded by the European Union – NextGenerationEU (Grant agreement no. ECS00000036)

References

[1] F. Acerbi, V. Guillard, C. Guillaume, N. Gontard, Assessment of gas permeability of the whole packaging system mimicking industrial conditions, Food Packag Shelf Life (2016) 8:81–5. https://doi.org/10.1016/j.fpsl.2016.04.003

[2] K. Wiszumirska, Legal requirements for plastic materials and articles that come into direct contact with food, Towaroznawcze Problemy Jakości (2019) 6:11–9.

[3] M. Giacinti Baschetti, M. Minelli, Test methods for the characterization of gas and vapor permeability in polymers for food packaging application: A review, Polym Test (2020) 89:106606. https://doi.org/10.1016/j.polymertesting.2020.106606

[4] A. Riley, Plastics manufacturing processes for packaging materials, Packaging Technology (2012) 310–60. https://doi.org/10.1533/9780857095701.2.310

[5] Y. Teck Kim, B. Min, K. Won Kim, General Characteristics of Packaging Materials for Food System, Innovations in Food Packaging, Elsevier (2014) 13–35. https://doi.org/10.1016/B978-0-12-394601-0.00002-3

[6] M. Fereydoon, S. Ebnesajjad, Development of High-Barrier Film for Food Packaging, Plastic Films in Food Packaging, Elsevier (2013) 71–92. https://doi.org/10.1016/B978-1-4557-3112-1.00005-3

[7] SM. Sapuan, Ilyas Rahmad, Bio-based packaging: material, environmental and economic aspects, John Wiley & Sons, Inc, 2021

[8] CF. Struller, P.J. Kelly, N.J. Copeland, Aluminum oxide barrier coatings on polymer films for food packaging applications, Surf. Coat. Technol. (2014) 241:130–7. https://doi.org/10.1016/j.surfcoat.2013.08.011

[9] G. García-Ayuso, L. Vázquez, J.M. Martínez-Duart, Atomic force microscopy (AFM) morphological surface characterization of transparent gas barrier coatings on plastic films, Surf. Coat. Technol. (1996) 80:203–6. https://doi.org/10.1016/0257-8972(95)02712-2

[10] J. Gajdoš, K. Galic, G. Galic, Z. Elimir Kurtanjek, N.C. Cikovic, Gas permeability and DSC characteristics of polymers used in food packaging, Polymer Testing (2001) 49-57. https://doi.org/10.1016/S0142-9418(99)00078-1

[11] ISO 15105:2007 - Plastics — Film and sheeting — Determination of gas-transmission rate. ISO, Genève.

[12] ISO 15106:2015 - Plastics — Film and sheeting — Determination of water vapour transmission rate. ISO, Genève.

[13] P.S.P. De Herrmann, C.M. Pedroso Yoshida, A.J. Antunes, J.A. Marcondes, Surface evaluation of whey protein films by atomic force microscopy and water vapour permeability analysis, Packaging Technology and Science (2004) 267–73. https://doi.org/10.1002/PTS.662.

[14] K. Mueller, C. Schoenweitz, H.C. Langowski, Thin Laminate Films for Barrier Packaging Application – Influence of Down Gauging and Substrate Surface Properties on the Permeation Properties, Packaging Technology and Science (2012) 25:137–48. https://doi.org/10.1002/PTS.966

[15] F. Marinello, A. La Storia, G. Mauriello, D. Passeri, Atomic Force microscopy techniques to investigate activated food packaging materials, Trends Food Sci Technol. (2019) 87:84–93. https://doi.org/10.1016/J.TIFS.2018.05.028

[16] D.S. Lee, K.L. Yam, L. Piergiovanni, Food Packaging Science and Technology, CRC Press, 2008. https://doi.org/10.1201/9781439894071

[17] M.J. Kirwan, J.W. Strawbridge, Plastics in food packaging. In: R. Coles, M.J. Kirwan, (Eds.), Food and Beverage Packaging Technology, Wiley-Blackwell, Chichester, UK, 2011, pp. 157–212. https://doi.org/ 10.1002/9781444392180

[18] Y-M. Choi, H. Yoo, D. Kang , Large-area thickness measurement of transparent multi-layer films based on laser confocal reflection sensor, Measurement (2020) 153:107390. https://doi.org/10.1016/j.measurement.2019.107390

[19] ISO 25178-2:2021 Geometrical product specifications (GPS) — Surface texture. Areal Part 2: Terms, definitions and surface texture parameters. ISO, Genève.

[20] ISO 25178-3:2012 Geometrical product specifications (GPS) — Surface texture: Areal Part 3: Specification operators. ISO, Genève.

[21] R. Leach, H. Haitjema, Bandwidth characteristics and comparisons of surface texture measuring instruments, Meas. Sci. Technol. (2010) 21. https://doi.org/10.1088/0957-0233/21/3/032001.

[23] D. Montgomery, Design and analysis of experiments, John wiley & sons, New York, 2017.

Materials Research Proceedings 57 (2025) 583-591 https://doi.org/10.21741/9781644903735-68

Design optimization and one-shot 3D printing of a bio-inspired soft robot capable of counter-flexural motion at low actuation pressures

Luca DI LEO[1,2,a*], Alessio PRICCI[1,2,b], Andrea GRAVILI[3,c], Gianluca PERCOCO[1,2,d]

[1]Intedisciplinary Additive Manufacturing (IAM) Laboratory, Polytechnic University of Bari, Taranto, Italy

[2]Department of Mechanics, Mathematics and Management (DMMM), Polytechnic University of Bari, Via E. Orabona 4, 70125 Bari, Italy

[3]Department of Engineering for Innovation, University of Salento, Lecce 73100, Italy

[a]l.dileo1@phd.poliba.it, [b]alessio.pricci@poliba.it, [c]andrea.gravili1@studenti.unisalento.it, [d]gianluca.percoco@poliba.it

Keywords: Material Extrusion, Product Design, Virtual Modeling

Abstract. This work presents the design, fabrication, and numerical analysis of a soft actuator with counter-flexural motion fabricated in thermoplastic polyurethan (TPU), aiming at mimicking the serpentine movement of snakes. Printing parameters were chosen to allow the one-shot 3D printing of the soft robot, ensuring its air tightness up to 200 [kPa]. The hyperelastic behavior of TPU was characterized by means of uniaxial tensile tests of samples produced with the abovementioned optimal printing settings. Non-linear finite element simulations were conducted to perform a design optimization of the pneumatic chambers; the purpose is to minimize the actuation pressure needed to achieve a prescribed bending. The experimentally measured deflections were compared with numerical results, showing a very good agreement. Practical relapses are in the field of medical devices where the proposed low-pressure actuated design will allow safer human-robot interactions.

Introduction

The versatility of 3D printing has enabled its application across different fields, from aerospace, mechanics and architecture to emerging sectors like soft robotics.

Soft robots represent one of the most promising innovations in contemporary robotics [1], [2]. Unlike traditional robots, which are characterized by rigid materials and a limited number of degrees of freedom, soft robots utilize flexible materials, allowing them to better adapt to the environment.

In this context, bio-inspiration is an important source of innovation for the development of innovative technologies [3], [4], and it has become beneficial for soft robotics, where innovative grippers [5], [6], octopus-like tentacles [7] and custom-made prostheses and gloves [8], [9] have been proposed.

Soft grippers consist of a series of pneumatic chambers which allow to bend when pressurized with air [10], [11], [12], [13]. More recently, different solutions have been proposed to achieve bending starting from an actuator designed for only elongational deformation; among the simplest yet efficient approaches there is the possibility to internally split the pneumatic chambers with one or more walls in a way that only the desired sections will be pressurized. This results in a bending motion in a prescribed plane [14]. This design allows even more complex movements and a wide range of bending angles without the use of mechanical valves.

Several works have shown the possibility of exploiting soft materials to achieve innovative forms of locomotion; among these, the movement of snakes is paramount because it allows to

Content from this work may be used under the terms of the Creative Commons Attribution 3.0 license. Any further distribution of this work must maintain attribution to the author(s) and the title of the work, journal citation and DOI. Published under license by Materials Research Forum LLC.

Materials Research Proceedings 57 (2025) 583-591 https://doi.org/10.21741/9781644903735-68

leverage skin frictional anisotropy to move on irregular surfaces with very low energy consumption [15], [16], [17], [18], [19].

Despite the wide number of attempts to fabricate soft snakes, the solutions available in current literature often involve i) a considerable number of manual assembly steps and ii) the use of wheels to provide frictional anisotropy [20].

In this research the first fully one-shot 3D printable soft actuator capable of achieving counter-bending in a plane, aiming at mimicking the snake locomotion, has been created. The actuator is first produced according to the material's process parameters which ensures its airtightness. Then the design has been optimized to achieve significant bending even at low actuation pressures. The motivation lies in the importance of promoting safer human-robot interaction. In fact, achieving a prescribed displacement with low actuation pressure limits the possibility for the device to leak, which can be potentially dangerous. because of the force exerted by the ejected stream.

The remainder of this work is structured as follows: first, the device printing parameters and the experimental setup have been discussed; next, the characterization of the material under the aforementioned optimal printing parameters has been presented; then, the numerical grid independence study has been conducted prior to analyzing the full design space. This has been explored to identify the effect of pneumatic chamber design parameters on the maximum actuator deflection. The optimal design has been 3D printed and compared against numerical results. Finally, conclusions and further work have been highlighted.

Materials and methods

The device consists of a bellow-type soft actuator with a total of 8 chambers (see Figure 1), each having an elliptical cross-section. The minor half-axis is fixed at 2 [mm], while the major half-axis has been chosen as a design parameter. The device has an overall length of 172.60 [mm] and a uniform chamber wall thickness of 2 [mm].

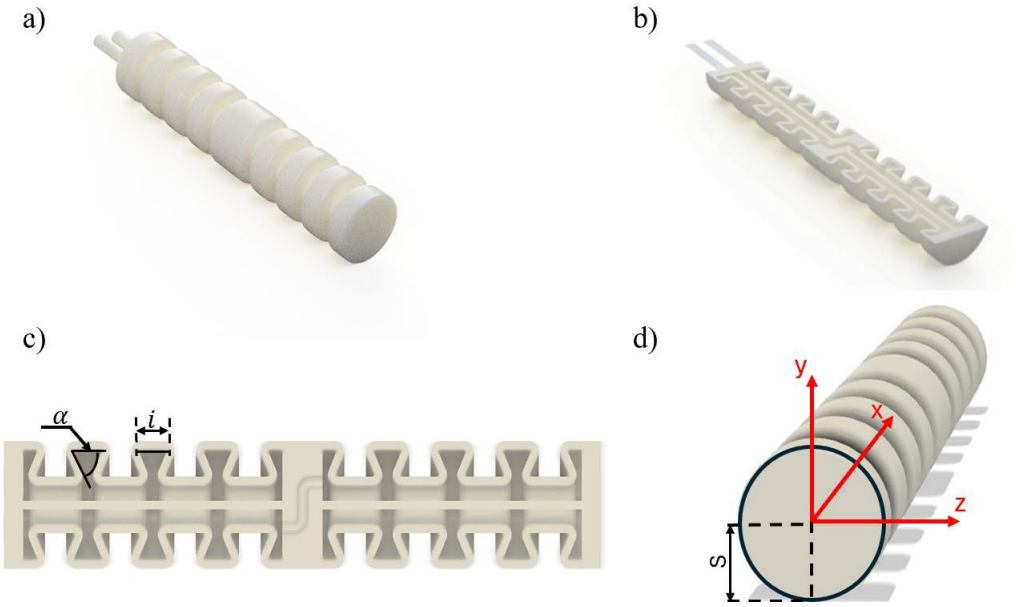


Figure 1 Perspective view of a) full device, b) inner section with details of the pneumatic chambers and air paths, and c) top view of the device cross-section and d) front view with indication of the design parameters.

The bending motion is achieved by incorporating a fluid-splitting wall into the soft actuator design, which separates the device body into two halves, similarly to the design presented in [14]. Additionally, pressurized air is forced to pass from one halve to the opposite using an intermediate block, which is fabricated alongside the actuator and positioned near the axial midpoint (see Figure

Materials Research Proceedings 57 (2025) 583-591 https://doi.org/10.21741/9781644903735-68

1 – c). The presence of this block is functional to the generation of the desired counter flexural motion.

The soft actuator was 3D printed using a TPU characterized by a Shore hardness of 85A, manufactured by BASF. The one-shot 3D printing process was performed using an Ultimaker S5 FDM 3D printer, with a 0.4 [mm] nozzle. Printing parameters were set in the Ultimaker Cura v.5.9.0 slicing software and the key extrusion settings which ensure the device airtightness have been reported in Table 1.

Table 1. Printing parameters set for the soft snake 3D printing.

Printing parameter	Value
Layer height	0.125 [mm]
Layer width	0.3 [mm]
Printing temperature	225 [°C]
Bed temperature	70 [°C]
Flow rate	140 %
Printing speed	27.5 [mm/s]

Although the device was positioned in the slicing software with its axis parallel to the build plate, the bottom part of the soft robot required support structures. These supports were made from the same structural material as the actuator. The three support features available in the Cura Ultimaker facilitated easy removal of the supports and minimized the need for post-processing.

Finite element modeling and structural parameters.

Numerical simulations were conducted using ANSYS v.19.2, which employs the finite element method to solve the structural partial differential equations. The Static Structural module was utilized for all calculations.

Due to the complex geometry of the device, an unstructured mesh was selected to discretize the soft actuator. The mesh resolution was progressively refined to identify the minimum number of finite elements that yields mesh-independent results.

Subsequently, the key design parameters of the soft actuator chambers highlighted in Figure 1 – c were varied on three levels, following a full design of experiment.

Bending bench setup.

The experimental setup consists of an industrial compressor (Metabo – basic 250-24 W) which supplies pressurized air to the 3D printed soft actuator, along with image acquisition devices to monitor deformation. The device was inserted into a custom-made fully 3D printed setup and it was fixed with a gripper to the tensile testing machine to hold the correct position during the pneumatic test.

A leakage test was conducted prior to measuring the displacement of the optimal device; the goal was to find the processing parameters which ensure airtightness at all actuation pressures. In particular, the device produced with optimized process parameters (see Table 1) has no leakages up to 3 [bar].

Additionally, a charge-coupled device (CCD) camera (Canon EOS 4000D, Tokyo, Japan) was used to capture images during experimental tests. The acquired images were subsequently post-processed using MATLAB R2021b (MathWorks Inc.) to quantify the maximum displacement of the one-shot 3D printed flexible device.

Materials Research Proceedings 57 (2025) 583-591 https://doi.org/10.21741/9781644903735-68

Results and discussion

Material characterization.

Uniaxial tensile tests have been performed to characterize the TPU hyperelastic behavior according to the optimized printing parameters declared in Table 1. Four samples have been 3D printed and tested following the ASTM D638 standard (dogbones type IV). Tensile tests have been conducted using INSTRON universal testing machine with a 5 [kN] load cell. The head speed was set to 50 [mm/s] following the standard. In Figure 2 the mean stress-strain curve with error bars has been reported.

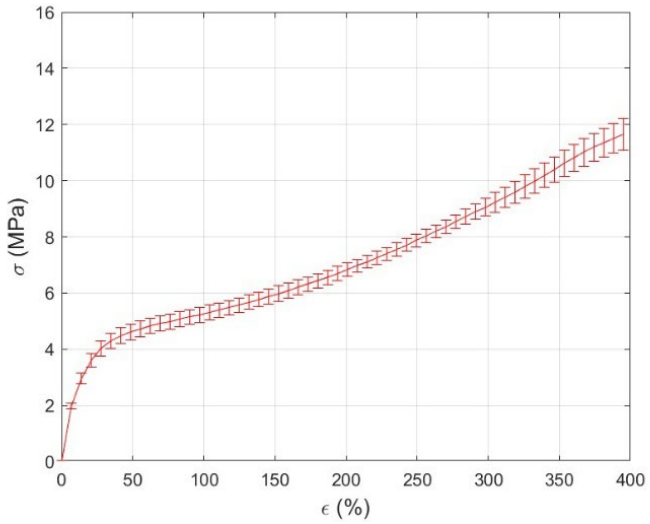


Figure 2. Mean stress-strain curve of TPU 85A.

A prominent hyperelastic behavior can be noted, especially at higher strains. The mean stress-strain curve was then imported in ANSYS Workbench to perform hyperelastic regression; the Engineering Data suite allowed to perform least square regression on experimental data. The different hyperelastic models and corresponding cumulated normalized residuals have been reported in Table 2.

Table 2. Least square fit test for different hyperelastic material models.

Hyperelastic model	Normalized residual [–]
2-parameters Mooney Rivlin	2.0592
3-parameters Mooney Rivlin	1.2197
5-parameters Mooney Rivlin	1.0058
3-terms polynomial	1.0004
2-parameters Ogden	2.7046
3-parameters Yeoh	2.6603

The 3-terms polynomial model with C_{01}=30.13 [MPa], C_{10}= – 23.48 [MPa], C_{11}= – 427.78 [MPa], C_{12}= – 48.87 [MPa], C_{02}=245.99 [MPa], C_{20}=197.55 [MPa], C_{21}= – 0.086 [MPa], C_{03}=31.50 [MPa] and C_{30}= 5.32 [kPa] leads to the lowest cumulated normalized residual with respect to experimental data. For that reason, this model was chosen for further computations.

Materials Research Proceedings 57 (2025) 583-591 https://doi.org/10.21741/9781644903735-68

Grid-independence study.
The optimized hyperelastic model and its parameters were imported in ANSYS Static Structural module to perform finite element simulations. These have been conducted on an Intel i7-10700F workstation with 32 GB DDR4 3200 MHz RAM.

The element size of the unstructured mesh was progressively refined to ensure grid-independent results. This preliminary study was carried out for an applied pressure of 50 [kPa] under the abovementioned optimized hyperelastic material model and constants.

The overall shape of the proposed actuator geometry with $\alpha = 65$ [°], $i = 8$ [mm] and $s = 3$ [mm] has been studied at increasing levels of mesh refinement (i.e., decreasing values of average element mesh size). For each grid size the maximum displacement (A_{max}) was registered.

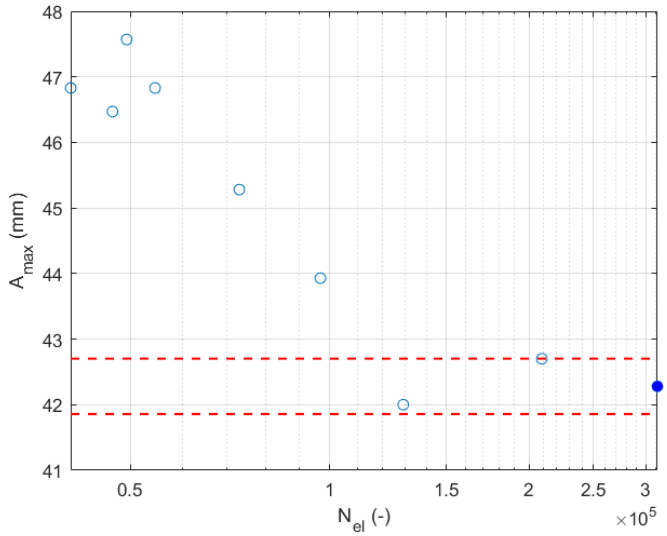


Figure 3. Results of the grid-independence study.

A 1.2 [mm] mesh size leads to minimum discrepancy and has been selected for further studies. In fact, as finer computational grids are considered (i.e., higher numbers of overall finite elements, N_{el}) computational time increases, while A_{max} stabilizes around a constant value. The dotted red lines in Figure 3 represent ±1% of the A_{max} value computed for the highest N_{el} value, corresponding to the finest computational grid (i.e., blue filled point in Figure 3).

It stems from Figure 3 that the mesh with N_{el} =129.031 yields grid-independent results for the hyperelastic simulations. The corresponding unstructured mesh resolution (i.e., element size equal to 1.2 [mm]) was selected for simulating the actuator's behavior at all remaining pressures and investigated designs.

Effect of design parameters on maximum displacement.
In order to assess the influence of the device geometry on its deformation, three geometric parameters were selected for analysis, accordingly to Figure 1:

- Chamber opening angle (α): the characteristic angle of the chamber.
- Interaxis (i): the minimum distance between contiguous chamber walls.
- Semi-axis (S): the length of the semi-axis of the device front section.

Simulations were conducted, varying the chamber opening angle and interaxis for assigned semi-axis, at pressures ranging from 50 [kPa] to 200 [kPa], to assess which configuration gives the maximum displacement.

Materials Research Proceedings 57 (2025) 583-591 https://doi.org/10.21741/9781644903735-68

A comprehensive graphical representation of the effect of the abovementioned design parameters on A_{max} has been reported in Figure 4.

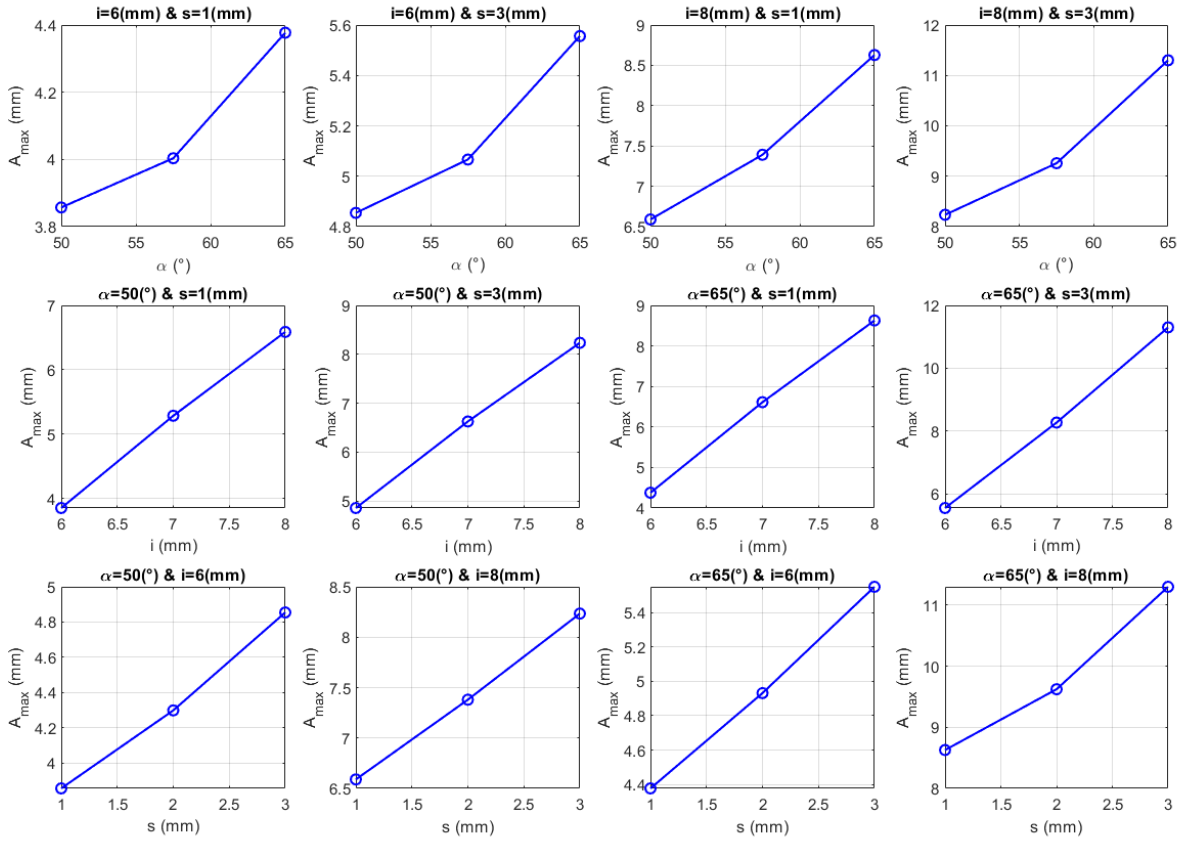


Figure 4. Effect of design process parameters on soft snake maximum displacement.

The soft snake with optimized design parameters (i.e., $\alpha = 65$ [°]; $i = 8$ [mm] and $S = 3$ [mm]) lead to the maximum overall displacement at minimum pressure (i.e., 50 [kPa]). In addition, increasing α for given values of semi-axis and interaxis produced higher bending. The same applies interestingly to the other combinations (i.e., i design parameter for given α and S, and S for given values of α and i). The optimized design has been chosen for both 3D printing and further investigations at all remaining pressures.

Comparison with experimental results.

The optimized soft snake design was 3D printed and tested with the purpose of comparing its deformation with hyperelastic results under different values of actuation pressure.

Materials Research Proceedings 57 (2025) 583-591 https://doi.org/10.21741/9781644903735-68

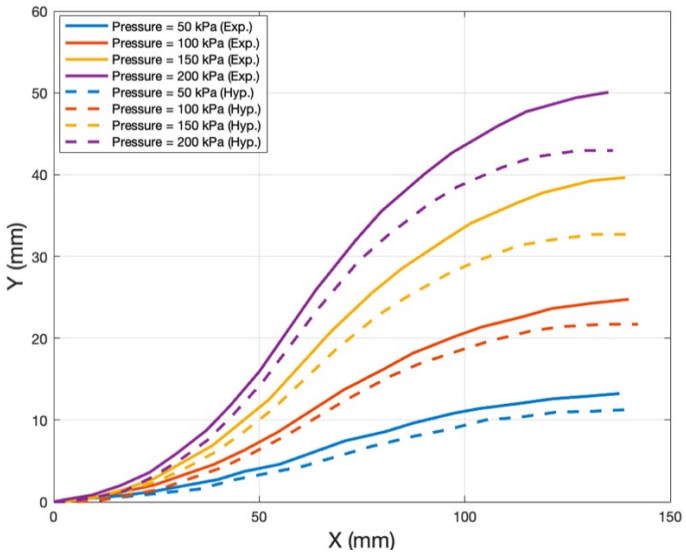


Figure 5. Comparison between experimentally observed and numerically predicted shape deformations of the 3D printed soft snake under varying actuation pressures.

A direct comparison of experimental and numerical data has been shown in Figure 6.

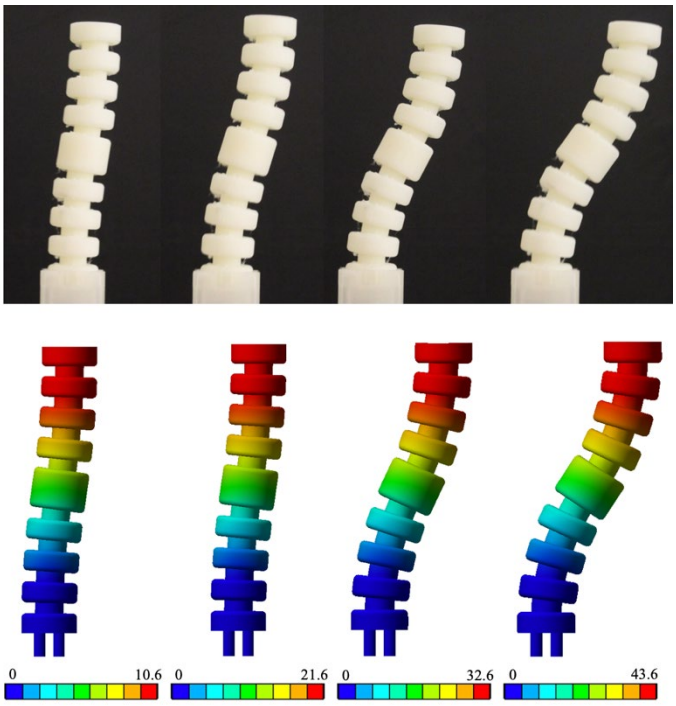


Figure 6. Experimental (top) and numerical (bottom) results under an applied pressure of 50-100-150-200 [kPa] (left to right); all dimensions are in millimeters.

Conclusions and further work

In the present work the design of an innovative soft actuator capable of achieving a counter flexural motion similar to the serpentine movement of snakes has been proposed.

Material printing parameters were optimized to ensure device airtightness up to 200 [kPa] and hyperelastic regressions pave the way for the application of finite element simulations to optimize the design. This was optimized to achieve the maximum value of displacement, A_{max}, with respect

to neutral axis at minimum actuation pressure; this is critical to provide an increasingly safe human-robot interaction.

The design optimization showed that by increasing chamber opening angle, interaxis and soft snake semiaxis the A_{max} value increases monotonically.

The optimized design was 3D printed one-shot and experimentally tested; under an applied pressure of 200 [kPa] a tip displacement of 50 [mm] was registered for the 3D printed actuator, showing a very good agreement with hyperelastic simulations, where a value of 47 [mm] was registered.

A novel design has been developed to enable the counter-bending of a pneumatic soft actuator, which is useful for simulating the typical locomotion of snakes, thus giving the possibility to explore environments characterized by uncertain conditions with ease. Additionally, it ensures the safety of these devices in medical applications. Further works will focus on equipping the device with scales to enhance surface grip and facilitate rectilinear locomotion and embed sensors to provide proprioceptive and exteroceptive features for explorative missions.

References

[1] C. Lee *et al.*, "Soft robot review," *Int J Control Autom Syst*, vol. 15, no. 1, pp. 3–15, Feb. 2017. https://doi.org/10.1007/s12555-016-0462-3

[2] C. Laschi, J. Rossiter, F. Iida, M. Cianchetti, and L. Margheri, Eds., *Soft Robotics: Trends, Applications and Challenges*, vol. 17. Cham: Springer International Publishing, 2017. https://doi.org/10.1007/978-3-319-46460-2

[3] S. Coyle, C. Majidi, P. LeDuc, and K. J. Hsia, "Bio-inspired soft robotics: Material selection, actuation, and design," *Extreme Mech Lett*, vol. 22, pp. 51–59, Jul. 2018. https://doi.org/10.1016/j.eml.2018.05.003

[4] Y. Yang, C. Ai, W. Chen, J. Zhen, X. Kong, and Y. Jiang, "Recent Advances in Sources of Bio-Inspiration and Materials for Robotics and Actuators," *Small Methods*, vol. 7, no. 9, Sep. 2023. https://doi.org/10.1002/smtd.202300338

[5] M. Manti, T. Hassan, G. Passetti, N. D'Elia, C. Laschi, and M. Cianchetti, "A Bioinspired Soft Robotic Gripper for Adaptable and Effective Grasping," *Soft Robot*, vol. 2, no. 3, pp. 107–116, Sep. 2015. https://doi.org/10.1089/soro.2015.0009

[6] B. T. Phillips *et al.*, "A Dexterous, Glove-Based Teleoperable Low-Power Soft Robotic Arm for Delicate Deep-Sea Biological Exploration," *Sci Rep*, vol. 8, no. 1, p. 14779, Oct. 2018. https://doi.org/10.1038/s41598-018-33138-y

[7] Y. Pu, S. Zheng, X. Hu, S. Tang, and N. An, "Robotic skins inspired by auxetic metamaterials for programmable bending of soft actuators," *Mater Des*, vol. 246, p. 113334, Oct. 2024. https://doi.org/10.1016/j.matdes.2024.113334

[8] P. Polygerinos, Z. Wang, K. C. Galloway, R. J. Wood, and C. J. Walsh, "Soft robotic glove for combined assistance and at-home rehabilitation," *Rob Auton Syst*, vol. 73, pp. 135–143, Nov. 2015. https://doi.org/10.1016/j.robot.2014.08.014

[9] M. Afschrift *et al.*, "Assisting walking balance using a bio-inspired exoskeleton controller," *J Neuroeng Rehabil*, vol. 20, no. 1, p. 82, Jun. 2023. https://doi.org/10.1186/s12984-023-01205-9

[10] X. Zhang *et al.*, "A Modular Soft Gripper with Combined Pneu-Net Actuators," *Actuators*, vol. 12, no. 4, p. 172, Apr. 2023. https://doi.org/10.3390/act12040172

[11] C. L. Tennakoon, A. L. Kulasekera, R. A. R. C. Gopura, and D. S. Chathuranga, "PneuNet Based Hybrid Soft Gripper for Multi-Shape Object Handling," *IEEE Access*, vol. 12, pp. 190158–190168, 2024. https://doi.org/10.1109/ACCESS.2024.3515265

[12] W. Park, S. Seo, and J. Bae, "A Hybrid Gripper With Soft Material and Rigid Structures," *IEEE Robot Autom Lett*, vol. 4, no. 1, pp. 65–72, Jan. 2019. https://doi.org/10.1109/LRA.2018.2878972

[13] M. Manns, J. Morales, and P. Frohn, "Additive manufacturing of silicon based PneuNets as soft robotic actuators," *Procedia CIRP*, vol. 72, pp. 328–333, 2018. https://doi.org/10.1016/j.procir.2018.03.186

[14] M. S. Xavier, C. D. Tawk, Y. K. Yong, and A. J. Fleming, "3D-printed omnidirectional soft pneumatic actuators: Design, modeling and characterization," *Sens Actuators A Phys*, vol. 332, p. 113199, Dec. 2021. https://doi.org/10.1016/j.sna.2021.113199

[15] X. Qi, T. Gao, and X. Tan, "Bioinspired 3D-Printed Snakeskins Enable Effective Serpentine Locomotion of a Soft Robotic Snake," *Soft Robot*, vol. 10, no. 3, pp. 568–579, Jun. 2023. https://doi.org/10.1089/soro.2022.0051

[16] Y. Dikici, H. Jiang, B. Li, K. A. Daltorio, and O. Akkus, "Piece-By-Piece Shape-Morphing: Engineering Compatible Auxetic and Non-Auxetic Lattices to Improve Soft Robot Performance in Confined Spaces," *Adv Eng Mater*, vol. 24, no. 9, Sep. 2022. https://doi.org/10.1002/adem.202101620

[17] S. Lee, I. Her, W. Jung, and Y. Hwang, "Snakeskin-Inspired 3D Printable Soft Robot Composed of Multi-Modular Vacuum-Powered Actuators," *Actuators*, vol. 12, no. 2, p. 62, Jan. 2023. https://doi.org/10.3390/act12020062

[18] A. Jusufi, D. M. Vogt, R. J. Wood, and G. V. Lauder, "Undulatory Swimming Performance and Body Stiffness Modulation in a Soft Robotic Fish-Inspired Physical Model," *Soft Robot*, vol. 4, no. 3, pp. 202–210, Sep. 2017. https://doi.org/10.1089/soro.2016.0053

[19] X. Qi, H. Shi, T. Pinto, and X. Tan, "A Novel Pneumatic Soft Snake Robot Using Traveling-Wave Locomotion in Constrained Environments," *IEEE Robot Autom Lett*, vol. 5, no. 2, pp. 1610–1617, Apr. 2020. https://doi.org/10.1109/LRA.2020.2969923

[20] C. D. Onal and D. Rus, "Autonomous undulatory serpentine locomotion utilizing body dynamics of a fluidic soft robot," *Bioinspir Biomim*, vol. 8, no. 2, p. 026003, Mar. 2013. https://doi.org/10.1088/1748-3182/8/2/026003

Materials Research Proceedings 57 (2025) 592-599 https://doi.org/10.21741/9781644903735-69

Fabrication of shape memory composites for non-explosive release mechanisms in space applications

Denise BELLISARIO[1,a *], Leandro IORIO[2,b], Dounia NOQRA[1,c], Giorgio PARTIZII[1,d], Alice PROIETTI[1,e], Fabrizio QUADRINI[1,f] and Loredana SANTO[1,g]

[1]Department of Industrial Engineering, University of Rome "Tor Vergata", Rome, Italy

[2]Faculty of Technological Sciences and Innovation, University "Mercatorum", Rome, Italy

[a]denise.bellisario@uniroma2.it, [b]leandro.iorio@unimercatorum.it, [c]dounia.noqra@uniroma2.it, [d]giorgio.patrizii@uniroma2.it, [e]alice.proietti@uniroma2.it, [f]fabrizio.quadrini@uniroma2.it, [g]loredana.santo@uniroma2.it

Keywords: Compression Moulding; Smart Materials; Space Sustainability

Abstract. Deployment of space structures, like telescopes and satellites, is performed by using pre-loaded springs and explosive charges for their release. In fact, most of the deployments are one-way, without repetition needs, and related mechanisms must be light, compact and easy to activate. Nevertheless, explosive actuators are very critical because of the excess of released energy and the risk of rebounds or damage. A new release mechanism has been prototyped by using shape memory polymer composites (SMPCs) for greater spatial sustainability. The non-explosive actuator (NEA) is made by laminating carbon fibre reinforced plies, shape memory polymer (SMP) interlayers and SMP foams. Its consolidation is achieved by one-step compression moulding. An embedded heater allows shape transition in thermo-mechanical cycling. The SMPC-NEA has been tested in memory and recovery tests at different voltages of the heater. It has been integrated into a 3D printed frame to prototype a full HDRM (hold-down release mechanism).

Introduction

A type of smart material known as shape memory polymer composite (SMPC) can change shape in response to external stimuli, primarily heat ones. The identical stimulus is used to restore the initial equilibrium form. SMPCs are composed of efficient fibers embedded in an SMP matrix. SMPCs have potential applications in important industrial domains including aerospace and aviation when combined with carbon fibers. Their potential applications include heat-shrinkable packaging materials, morphing wing systems, wrinkle-free textiles, and self-deploying sun-sails or antennae [1].

Since SMPCs can combine multiple properties into a single material, such as stiffness and actuation, they are an excellent option for producing non-explosive actuators (NEAs) for use in space. Conventional explosive actuators often use pre-loaded springs, which produces an extremely quick actuation; with the significant chance of structure damage or rebounding due to the high deployment forces [2]. According to NEAs, a pre-established electrical current to a fuse-wire system triggers the planned release of the deployable satellite or payload by breaking the wire under stress and triggering a mechanical bolt that has been pre-loaded [3]. The NEAs are electrically triggered Hold-Down Release Mechanism (HDRM) that has the capacity to carry a high tensile preload until produced to disengage, with the further benefit of very low output shock. In this context, SMPCs function as soft actuators with regulated form development and low speed during deployment. Research is being done on SMPC applications such as deployable hinges or soft actuator for space claims. The SMPCs' micro-buckling improved the space deployable structures' storage ratio, offering alternatives for big structure packaging and transit. [4] A hinge

Content from this work may be used under the terms of the Creative Commons Attribution 3.0 license. Any further distribution of this work must maintain attribution to the author(s) and the title of the work, journal citation and DOI. Published under license by Materials Research Forum LLC.

Materials Research Proceedings 57 (2025) 592-599 https://doi.org/10.21741/9781644903735-69

which can electrothermally deploy was developed by Composite Technology Development, Inc. (CTD) and optimized to generate a higher driving force. [5] Using a hinge based on SMPCs, Lan et al. completed their study for controlling a solar array. [6] Chen et al. used composite spring bands and SMPCs to build a space-deployable mechanism (SDM). [7] The incorporated hinge system, which was supposed to be utilized in space grab and multi-angle imaging equipment, was developed by Liu et al. without the need for intricate mechanical connections. [8]. A lenticular collapsible composite tube (LCCT) for an adaptable solar array was created by Liu et al. Robinson et al. created a deployable structure with shape memory carbon fibre composites interleaved with layers of polystyrene [9]. Xin et al. studied two types of SMPCs self-driven hinges utilizing epoxy-based SMPs and fabricated by vacuum-assisted resin transfer moulding. [10]

In the current study, a commercial epoxy SMP interlayer between CFR plies was used but fabricated by co-curing the CFR layers and the SMP interlayers in a single manufacturing step. This, together with the use of commercial materials already tested in the space applications, are the innovations adopted. In fact, co-curing SMP resins with commercial prepregs has increased process consistency and facilitated the diffusion of technology to industries. In previously published research, the same authors explored the usage of prepregs for aerospace parts together with an SMP epoxy resin [11]. Solid-state foaming was used to create SMP epoxy foams [12], which were then tested in space and in microgravity simulators on the BION-M1 experimental unit and the International Space Station. These foams were additionally used as the cores of SMPC sandwiches and showed remarkable SM behaviour and self-repairing properties.

This study examines the recovery behaviour of a SM polymer composite release device with a sandwich construction. To provide the required heating for the shape memory transition a flexible heating element inserted in the neutral plane of the sandwich. The SMP resin interlayers keep the flexible heating element isolated from the CFR skins. Furthermore, to improve the actuator's deformability, two thin SMP foams have also been incorporated. A good SMPC structure for a release device for NEA actuators needs to have adequate recovery loads. For a single instrumented thermo-mechanical cycle, these performance characteristics have been measured [11,13]. This study evaluates the SMPC-NEA in constrained-recovery tests at different voltages of the heater to define the actuation loads as function of the applied voltage and heating temperature reached by the SMPC actuator. Finally, the device has been integrated into a 3D printed frame to prototype a full HDRM (hold-down release mechanism). Providing an interesting application to SMPCs as non-explosive HDRM systems reducing weights compared to bolts and metal parts and ensuring the necessary mechanical resistance.

Experimental

The SMPC device consists of four CFR plies, two SM epoxy foam layers, and two SM epoxy interlayers in the form of uncured powder (Fig. 1) and measures 20 x 45 mm². A flat micro-heater is positioned in the neutral plane, and the two SM epoxy interlayers avoid direct contact with the CFR ply. This structure is the result of numerous prior experiments with various configurations and stacking sequences, and it allows for high deformability of the sandwich structure due to the mechanism of cell collapsing, which is typical for foams. The thin heater was positioned adjacent to the internal CFR layers to provide heat transmission symmetry and to limit the heater deformation. SMP interlayer has also been utilized to ensure the flat heater's adherence to CFR layers. Constrained recovery tests were carried out applying various voltages varying from 20 V to 24 V to the heating unit. Moreover, the SMPC unit was integrated into a full HDRM system through the support of a specially designed frame made using FDM (fused deposition modelling).

Materials Research Proceedings 57 (2025) 592-599 https://doi.org/10.21741/9781644903735-69

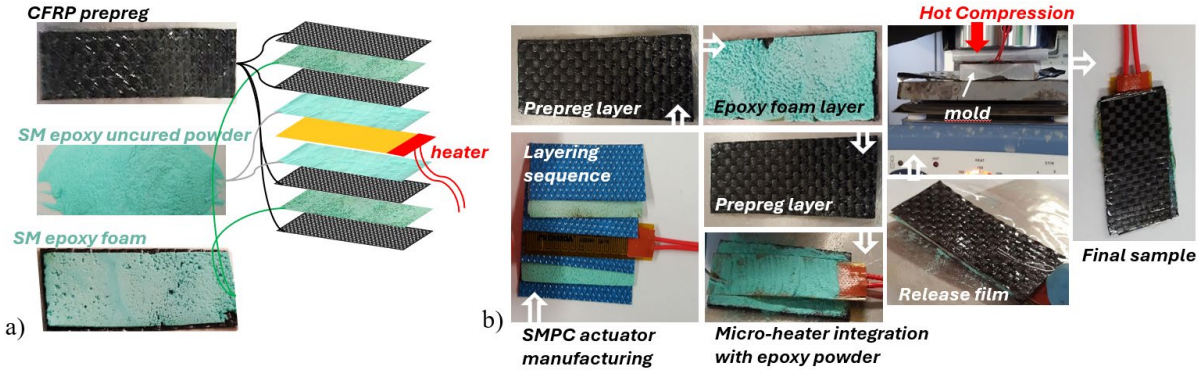


Figure 1. a) Architecture of the SMPC actuator and b) SMPC actuator manufacturing process sequence.

Materials. The SMPC device is made by compression moulding of commercially available raw materials. Hexcel's Hex-Ply/M49/42%/CHS-3K CFR prepregs were plain woven, with a nominal epoxy resin content of 42 w%, a nominal areal density of 200 g/m^2, and a thickness of around 350 µm. Aeronautics uses this high-performance 0/90 woven cloth prepreg. The SMP interlayer was a one-part, heat curable, thermosetting epoxy coating made of uncured epoxy resin (Scotchkote 206N, 3M), which came in green powder form. The density of this material is 1.44 g/cm³. It has been applied to the flexible micro-heater (KHLVA-0502/10 by OMEGA) for insulating protection. This thin heater (surface size of 20×50 mm² and thickness of 50.8 µm) has a resistance of 80 Ω and can be powered at a maximum input voltage of 28 V. Because of its flexibility and low thickness, the heating element can be put into the SMPC unit during lamination. Finally, commercial thermoplastic filaments (diameter 1.75 mm) were used to create the FDM frame: a gray TPU (Flexfill TPU 98A) and a metallic gray PLA (Prusament PLA Galaxy Silver).

SMP foam. Solid-state foaming was used to create SMP foams from precursor tablets (2.1 g, 20 mm diameter and 5 mm height) created by cold pressing the uncured epoxy powder. This compression step is essential for increasing density and thermal diffusivity of the powder. A universal material testing machine (MTS Alliance RT 50) was used to compress the tablets at a pressure of 130 MPa and a holding time of 2 min. After, the tablets were foamed for eight minutes at 320 °C in an open aluminium mold [11]. In solid-state foaming, contemporaneous polymerization freezes the bubbles that are created by the resin overheating. Foams were machined to produce thin plates with a density of 0.5 g/cm^3 and a thickness of 1 mm at the end of the process.

SMPC actuator manufacturing. The process shown in Fig. 1b was used to create the SMPC actuator. The prepregs were trimmed to 20 x 50 mm³. An uncured CFR prepreg ply was put on a release film to begin the lamination process. The prepreg was then covered with a thin foam core and a second CFR prepreg ply. SMP interlayer was then created by pouring uncured epoxy resin. The 13 x 50 mm^2 flexible heater was now put in place, and a second coat of SM epoxy powder was applied. The heater's top was ultimately laminated using the same process as the bottom. The SMP interlayer was made with a nominal thickness of 100 µm by using 0.15 g of mass on both sides of the microheater. The SMP resin powder was used as both an adhesive and a functional interlayer between the CFR plies and the heater. On a heater plate, the laminated device was cured for 90 min at 180 °C and 70 kPa of holding pressure. To prevent damage during manufacture, the datasheet established the cure temperature based on the heater's maximum working temperature. During the lamination process, two CFR plies and one SMP foam core were added to make the symmetric structure.

Actuation load measurements. A three-point bending fixture and an instrumented thermo-mechanical cycle on the universal testing machine (MTS Insight 5) were used to determine the actuation load of the SMPC device, as illustrated in Fig. 2a. Since the heating of actuators is

Materials Research Proceedings 57 (2025) 592-599 https://doi.org/10.21741/9781644903735-69

controlled by current, temperature calibration was necessary. So, the device temperature was monitored by thermocouple for 5 min applying different voltages ranging from 20 to 24 V (by step of 1 V) to the heater. The SMPC was programmed using a 1 mm downward deformation and a 45 mm span in a single cycle, conducted in hot deformation mode at 24 V. After deformation and cooling in the constrained shape, constrained-recovery tests were performed. During testing, a small preload (1 N) was applied to the deformed actuator to prevent premature recovery beneath the flexing clamps of the apparatus. The testing configuration parameters were selected based on prior experimental setups reported in previous studies [12]. The force exerted by the SMPC actuator on the plunger during heating was also measured. This setup allowed for monitoring of load variations over time as the sample was heated. Fig. 2b shows the typical profile of a constrained-recovery test: in the first phase, the load increases to a plateau—known as the recovery or actuation load (La)—which remains constant throughout the heating period. After 5 minutes of heating, the heater is turned off, and the load drops to a second plateau, corresponding to the secondary residual elastic load (Ls).

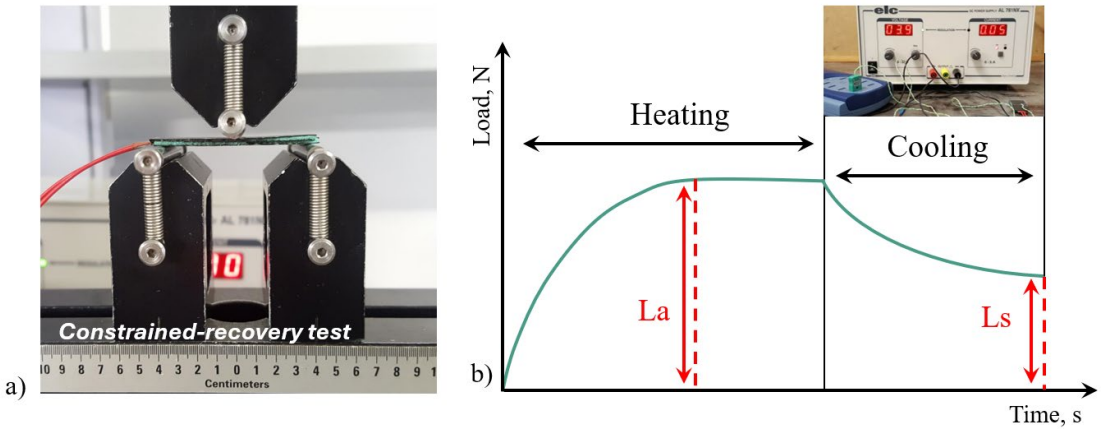


Figure 2. a) Constrained-recovery test on MTS Insight 5 machine with three-point bending fixture and b) a schematic of a constrained-recovery Load-Time curve evolution.

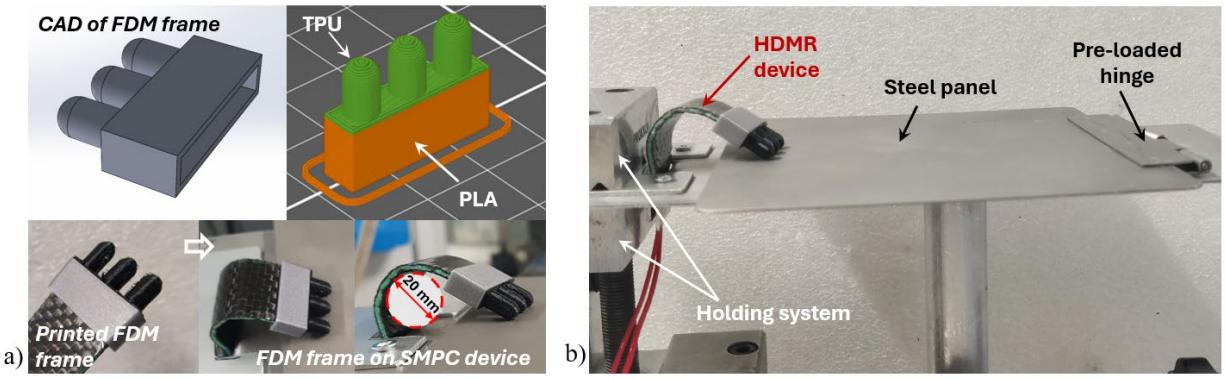


Figure 3. a) FDM frame design, printing and implementation on SMPC actuator and b) prototype HDRM testing system.

SMPC prototype for HDRM system. The SMPC was used in its deformed configuration as HDRM system in a prototype testing system. The SMPC was memorized heating at 24 V for 3 min imposing a curvature radius of 10 mm in the middle (Fig. 3a). The memorized SMPC was inserted into frame made by FDM and used as a release mechanism. The FDM frame was created to simulate a soft and dampening contact between the rigid SMPC and the part to be released. To this end, three pins have been made of TPU to realize a soft contact, and a PLA frame has been made to fit the SMPC actuator. The entire FDM-printed frame was made in a single operation with

Materials Research Proceedings 57 (2025) 592-599 https://doi.org/10.21741/9781644903735-69

filament change on an Original Prusa i3 MK3 (Fig.5a). The overall prototype system has been designed so that a steel panel operated by a pre-loaded hinge remained locked thanks to the HDRM system namely the SMPC device. The system configuration is shown in Fig 5b. A camera (240 fps) and thermo-camera (Testo 883-1) recorded the releasing phase of the HDRM prototype system.

Results and Discussion

After moulding the SMPC actuator was tested to monitor the temperature of the device during time with different applied voltages to the embedded heater. The temperature-time curves are reported in Fig.4a. The effect of the increase of the applied voltages is marked. After 5 min the SMPC temperature is increased by 22% more in the 24V applied test than in the 20V applied one. The expected effect is thus monitored and the effect it has on the force-time curves during constrained-recovery tests is evident (Fig.4b). It is noted that the curves lower as the voltage increases and the point at which the first plateau is reached is anticipated.

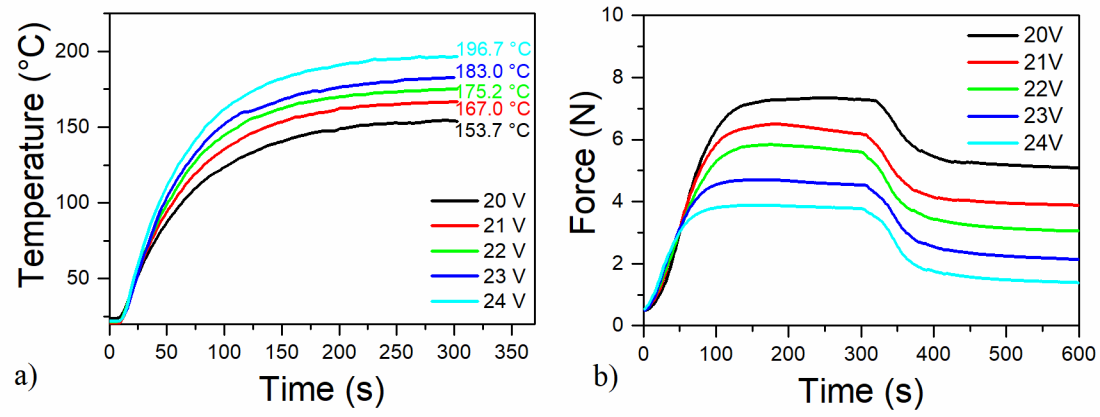


Figure 4. a) SMPC device temperature vs time at different voltages and b) force vs time during constrained-recovery tests at different applied voltages.

To evaluate the voltage effects on the recovery force (*La*), on the activation time and on the temperature reached at activation time, these quantities were extracted from the curves in Fig.4. Specifically, the recovery force (*La*) was extracted as the average load for the first plateau, the activation time as the slope change of the load-time curve, and the temperature was extracted from the temperature curves for that specific activation time. The trends of the extracted values are shown in Fig.5. In general terms, the effect of the voltage on the SM properties is close to expectations. By increasing the voltage, the SMPC device temperature increases, and recovery forces are expected to reduce because of the reduction of the elastic modulus. In fact, it is evident that as the volts applied to the device increase, both the activation times and the recovery force *La*, exerted during the first plateau in hot recovery, decrease. The activation times decreased from 130 ±12s to 69 ± 8 s respectively for 20 V and 24 V. This means that the time to exert the recovery force *La* is reduced by 47% by activating the SMPC device with a current of 24V. The temperature reached at the activation time slightly increased at the increase of the current applied in constrained-recovery tests. This underlines how the different times to reach the recovery temperature affects the activation time, i.e. shorter for higher voltages, but also the temperature reached. The faster the heating takes place, the slightly higher the temperature reached to exert La. Thus, the recovery force decreases from 7±0.6 to 3.77±0.1 N passing from 20 V to 24 V. Faster heating has an adverse effect on the forces exerted during recovery, as higher temperatures are reached more quickly, especially in the areas adjacent to the microheater and spread faster in the structure. This effect dampens the maximum forces reached and exerted during the recovery phase

Materials Research Proceedings 57 (2025) 592-599 https://doi.org/10.21741/9781644903735-69

of the SMPC actuator. Anyway, for the purposes of an HDRM, the activation time (69 s for 24V) and the stiffness (144.4 ±6.3 N/mm^2) to weight (1.32 g/cm^3) ratio are crucial parameters. Consequently, for the HDRM prototype system a microheater supply current of 24 V was chosen to maximize the recovery speed of the release device.

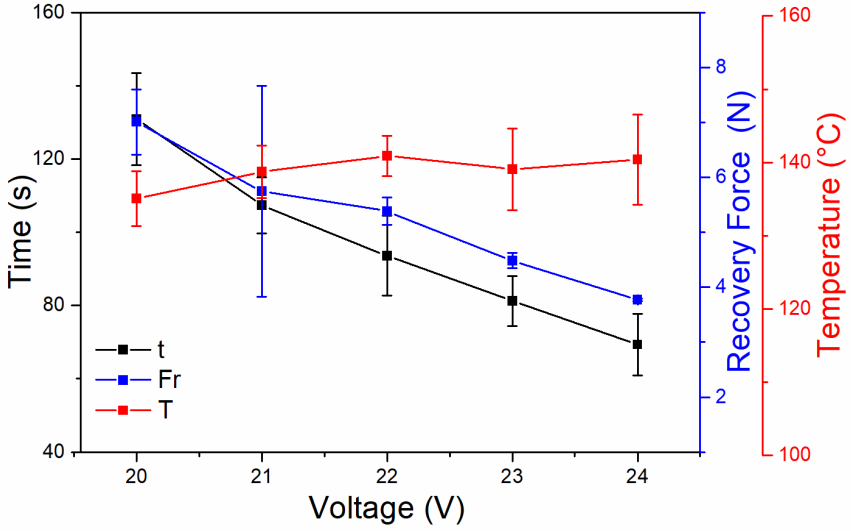


Figure 5. Recovery force, activation time and reached temperature vs applied voltages.

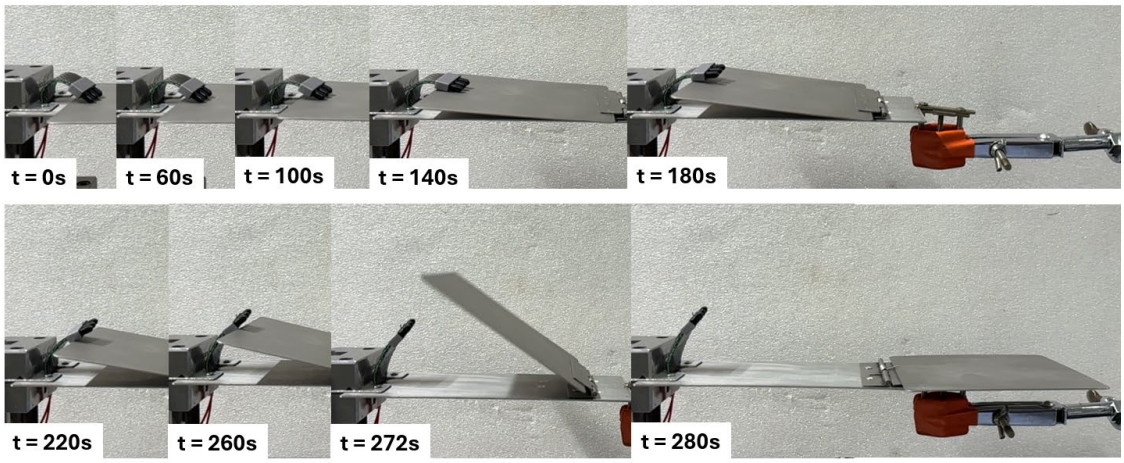


Figure 6. Sequence of images of the SMPC release system activation (extracted from video).

The HDRM prototype, which consists of the SMPC actuator with the 3D printed frame at the end that must keep the panel of the prototype system closed, weights 4.68 g (Fig. 3a). This is low weight also considering the micro and light duty HDRM systems currently available (~9g). To evaluate the system, the HDRM prototype was tested, and the images of the recovery-releasing phases were taken and summarized in Fig.6. The heater was switched on at t= 0s with 24V, and after 280 s the release was completed and the heater switched off. The final SMPC configuration showed a residual deformation which endured because of residual stress after the manufacturing step. This test, even if susceptible to further optimization for the final configuration, demonstrated the good operation of the HDRM system. In addition, the images taken by the thermo-camera before, during and after recovery are shown in Fig.7. The heating and cooling phases—after microheater activation and deactivation—were monitored. Surface temperature values align with those in Fig. 4a, with a slight delay in peak temperature after switch-off due to external

measurement. Rapid heating triggers the release mechanism, followed by quick cooling of the SMPC.

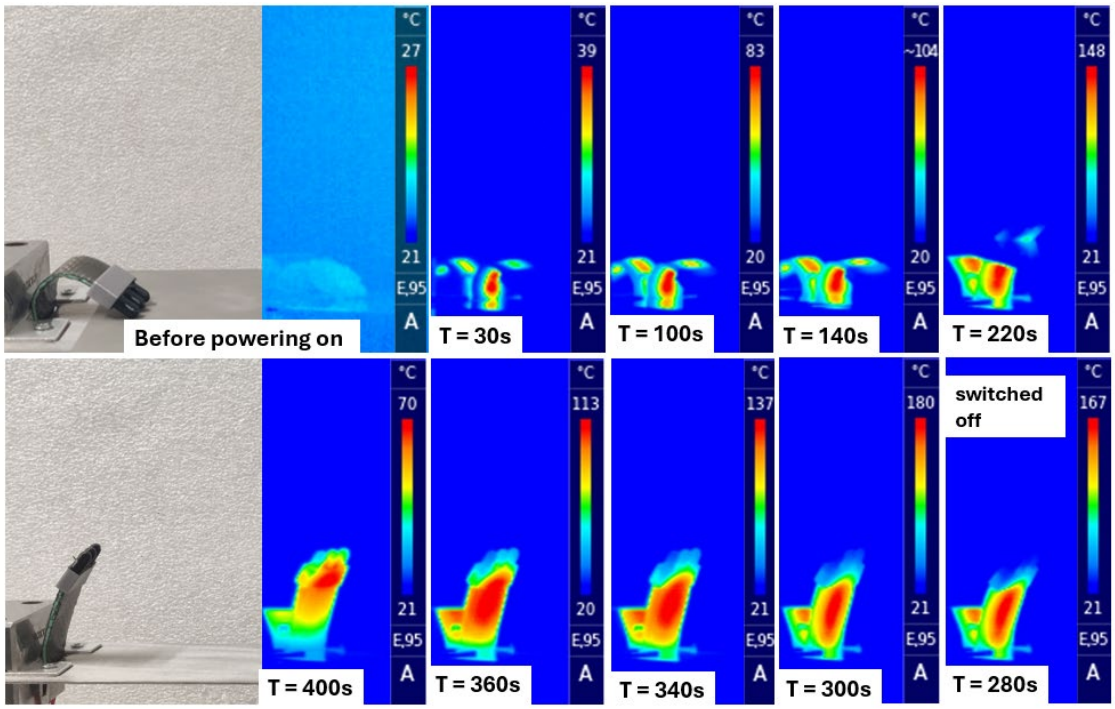


Figure 7. Thermal images before, during, and after the release phase of the HDRM prototype

Summary

In this study, compression moulding has been used at a lab-scale level to produce SMPC laminate with commercial materials. These SMPCs have been proposed for different aerospace applications like solar sails and grabbing systems operating in open space but in the current study, for the first time, an SMPC has been tested as HDRM system. By changing the supply voltage of the recovery step, it is possible to tune the recovery loads from 3.7 N to 7 N, and the activation times from 130 s to 69 s. By increasing the voltage, due to the increase of the device temperature, loads and stiffness of the device reduce. This fact was expected and to find the best behaviour of the SMPC-NEA in the experimented range of test voltages, a good compromise is at the supply voltage of 24 V to maximize the release time of the HDRM system. The SMPC-HDRM prototype was designed including an FDM frame that improves the hold down device. The final system showed good behaviour in the release test and a complete release was successfully finalized in about 280 s. SMPC-based HDRM systems offer a significant weight reduction (47%), even compared to commercially available lightweight models (~9 g). These findings underline that the proposed HDRM system, even with further optimization, can be successfully used for releasing devices in the aerospace field.

Acknowledgements

This study was carried out within the Space It Up project funded by the Italian Space Agency, ASI, and the Ministry of University and Research, MUR, under contract n. 2024-5E.0 – CUP n. I53D24000060005.

References

[1] L. Luo, F. Zhang, L. Wang, Y. Liu, J. Leng, Recent Advances in Shape Memory Polymers: Multifunctional Materials, Multiscale Structures, and Applications. Adv. Funct. Mater. 34 (2024), 2312036. https://doi.org/10.1002/adfm.202312036

[2] H. Yue, Y. Yang, Y. Lu, F. Yang, J. Wu, Q. Ruan, Z. Deng, Research progress of space non-pyrotechnic low-shock connection and separation technology (SNLT): A review, Chinese Journal of Aeronautics, 35 (2022), 11, 113-154, https://doi.org/10.1016/j.cja.2021.07.001.

[3] K Zając, C.R. Raum, M. Oswald, A. Glaswerk, Development and testing of a pinpuller for hold down and release mechanism, Deutscher Luft- und Raumfahrtkongress (2020). 490037 https://doi.org/10.25967/490037. urn:nbn:de:101:1-202001171211451851402 7

[4] X. Lan, Y. Liu, H. Lv, X. Wang, J. Leng, S. Du, Fiber reinforced shape-memory polymer composite and its application in a deployable hinge, (2009) Smart Mate. Struct. 18, (2009) 2 https://doi.org/10.1088/0964-1726/18/2/024002

[5] W Francis, M. Lake, K. Mallick, G. Freebury, A. Maji Development and testing of a hinge/actuator using elastic memory composites. In 44th AIAA/ASME/ASCE/AHS/ASC structures, structural dynamics, and materials conference (2003) pp.1496.

[6] Q. Chen, Z. Yao, Y. Hou, H. Fang, Design and testing of a space deployable mechanism. In 4th AIAA spacecraft structures conference (2017) pp. 0176.

[7] T. Liu, L. Liu, M. Yu, Q. Li, C. Zeng, X. Lan, J. Leng, Integrative hinge based on shape memory polymer composites: Material, design, properties and application. Composite Structures, 206 (2018). https://doi.org/164-176. 10.1016/j.compstruct.2018.08.041

[8] P. Robinson, A. Bismarck, B. Zhang, H. A. Maples Deployable, shape memory carbon fibre composites without shape memory constituents. Compos. Sci. Technol 145 (2017) 96–104. https://doi.org/10.1016/j.compscitech.2017.02.024

[9] X. Xin, C. Lin, B. Li, C. Zeng, L. Liu, Y. Liu, J. Leng, Self-driven intelligent curved hinge based on shape-morphing composites, Compos. Struct, 345 (2024), 118329, https://doi.org/10.1016/j.compstruct.2024.118329

[10] F. Quadrini, L. Iorio, D. Bellisario, L. Santo Shape memory polymer composites unit with embedded heater, Smart Mater. Struct. 30 (2021):075009. https://doi.org/10.1088/1361-665X/ac00cb

[11] E. A. Squeo, F. Quadrini Shape memory epoxy foams by solid-state foaming Smart Mater. Struct. 19 (2010) 105002 https://doi.org/10.1088/0964-1726/19/10/105002

[12] L. Iorio, D. Bellisario, F. Quadrini, Manufacturing and Testing of Shape Memory Polymer Composite Actuators, Lect. Notes Mech. Eng, F1351 (2024) 141 – 1572024 https://doi.org/10.1007/978-3-031-41163-2_9

Materials Research Proceedings 57 (2025) 600-607 https://doi.org/10.21741/9781644903735-70

Towards efficient defect detection in injection molding with transformer models

Andrea PIERESSA[1,a *], Marco SORGATO[1,b] and Giovanni LUCCHETTA[1,c]

[1]Department of Industrial Engineering, University of Padova, via Venezia 1, 35131, Padova, Italy

[a]andrea.pieressa@phd.unipd.it, [b]marco.sorgato@unipd.it, [c]giovanni.lucchetta@unipd.it

Keywords: Object Recognition, Zero Defect, Injection Molding

Abstract. The startup process in injection molding, traditionally reliant on expert personnel, has become critical due to small-batch production and a shortage of skilled workers. This shift requires efficient quality monitoring, especially for visually demanding plastic products. This study evaluates transformer-based computer vision models like RT-DETR for detecting defects characterized by domain-specific patterns and high intra- and inter-class variability. The research compares general models with specialized models trained for specific component-defect combinations, focusing on key computer vision metrics and computational demands. Injection molding features such as representative dimensions and aspect ratio are analyzed to assess knowledge transferability from pre-trained models to new scenarios. The findings could enhance defect detection accuracy, reduce reliance on experts, and boost production efficiency in small-batch, visually critical manufacturing.

Introduction

High-quality injection-molded components are vital for visually critical products, where surface defects can cause economic losses through rejections, rework, and reduced customer trust [1]. Industries like automotive and consumer electronics require flawless finishes, making defect detection essential. Traditionally, skilled personnel manually inspect parts, but this is resource-intensive and impractical due to small-batch production and a shortage of experienced operators [2].

Injection molding's complexity, driven by variables like mold temperature, injection speed, and material properties, leads to diverse defects such as flow marks and sink marks [3,4,5]. Nonlinear correlations between parameters and defects make manual inspection and trial-and-error optimization inefficient, especially with rapid mold changes and mass customization [6]. AI and machine learning, particularly CNN-based deep learning models, offer automated defect detection [7,8,9,10]. However, CNNs require large labeled datasets, which are scarce, and struggle with high defect variability, limiting generalization across products [11]. To address these limitations, transformer-based computer vision models have emerged as a promising alternative [12,13,14]. Transformers, originally developed for natural language processing, have demonstrated superior performance in various vision tasks due to their ability to capture long-range dependencies and contextual information in images [15]. In this study, we evaluated the effectiveness of the Real-Time DEtection TRansformer (RT-DETR) model for defect detection in injection molding [16]. RT-DETR was selected over other transformer-based models (e.g., ViT or DETR) due to its real-time processing capabilities, anchor-free detection mechanism, and efficiency in handling small datasets, which align with the short cycle times and data scarcity in injection molding. We compared general models trained on diverse datasets with specialized models fine-tuned for specific component-defect combinations. Furthermore, we analyzed the impact of injection molding features, such as representative dimensions (the primary or most critical dimension of a

Content from this work may be used under the terms of the Creative Commons Attribution 3.0 license. Any further distribution of this work must maintain attribution to the author(s) and the title of the work, journal citation and DOI. Published under license by Materials Research Forum LLC.

Materials Research Proceedings 57 (2025) 600-607 https://doi.org/10.21741/9781644903735-70

component that significantly influences its design and functionality) and aspect ratio, on the transferability of knowledge from pre-trained models to new manufacturing scenarios.

The main contributions of this study are as follows:

- Investigation of whether it is more effective to train specific models tailored to defect/component combinations or to develop a generalized model that can be shared across multiple components, reducing computational costs and training time.
- Analysis of model transferability in the injection molding domain, exploring whether a model trained on a specific component can effectively detect defects in different components that share similar geometric characteristics such as aspect ratio and representative dimensions. Additionally, we examine how these features influence transfer learning and whether the model maintains consistent defect pattern recognition across varying conditions.

Material and Methods

Theoretical Background–RT-DETR. RT-DETR is a transformer-based object detection model designed for high-speed performance without the need for anchor boxes. It employs a query-based attention mechanism to efficiently capture complex spatial relationships and long-range dependencies, making it highly effective in detecting objects with varying shapes, sizes, and textures [16]. Unlike traditional CNN-based approaches, which often struggle with generalization and require extensive labeled data, RT-DETR leverages the strengths of transformers to enhance detection accuracy and robustness.

Defects in molded components often exhibit high intra- and inter-class variability due to the influence of process parameters such as mold temperature, injection speed, and material flow dynamics [10]. RT-DETR's ability to focus on contextual information and adapt to diverse defect patterns makes it a promising tool for automated inspection.

Material and Setup. The components used in this study were injection-molded power socket parts, all manufactured using polycarbonate. These components were selected due to their critical importance to the company providing the samples, particularly in terms of aesthetic quality. Their opaque surface presents a challenge for defect detection, as surface imperfections become visible only from specific viewing angles or under appropriate lighting conditions. Fig. 1 illustrates the components analyzed in this study, highlighting the defects observed after the molding process.

The company uses Netstal SynErgy 800.230 hydraulic presses with a clamping force of 80 tons and a 40mm screw diameter to manufacture these parts and similar ones.

Table 1 summarizes the injection-molded components analyzed in this study, including their material, identification codes used throughout the paper, aspect ratio (A/R), representative dimensions, types of defects encountered, and the number of frames used for training and testing. It also reports the ratio of defective to non-defective parts in the dataset. Data were collected using an experimental setup consisting of an industrial illuminator and a Triton TRI050S-C (5.0 MP) industrial camera equipped with a Fujinon HF16XA-5M lens. All videos were recorded at a resolution of 1224×1024 pixels, and frames were randomly sampled to generate the training datasets. A conveyor belt, typically used for handling injection-molded parts, was employed during data collection.

The training datasets included both defective and non-defective components. Bounding boxes—rectangular regions that spatially enclose objects of interest—were used to annotate each component. For defective samples, bounding boxes were additionally labeled with specific defect types (e.g., weld line, sink mark), enabling RT-DETR to perform both component classification and precise defect localization.

Materials Research Proceedings 57 (2025) 600-607 https://doi.org/10.21741/9781644903735-70

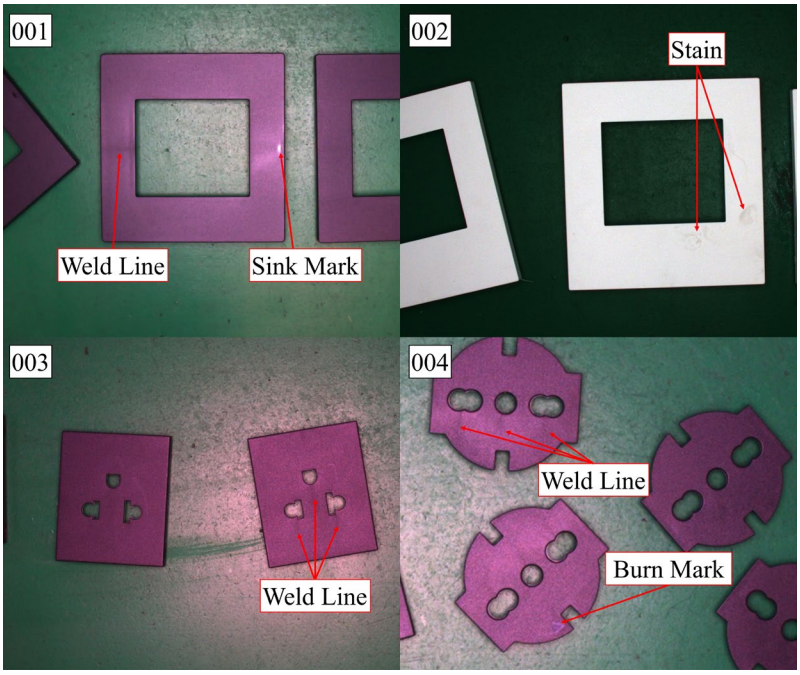


Fig. 1 Geometries of the analyzed components and observed defects.

Additionally, to evaluate whether training a model on a broad dataset yields better performance compared to multiple models specialized in specific defect-component combinations, we introduce the 000-type dataset. This dataset consists of images randomly selected from the individual component datasets to facilitate the assessment of model generalization across diverse conditions.

Among the available pre-trained RT-DETR scales, the smallest one (RTDETR-L) was selected to achieve reduced inference times, aligning with the short cycle times of the injection molding process. Both generalized and specialized models used the same RTDETR-L architecture, differing only in their training datasets.

Table 1 Summary of Molded Components, Material Properties, Defects, and Dataset Composition.

ID Code	*Material*	**Representative dimension *[mm]***	*A/R (h/w)*	*Training Set Size*	*Validation Set Size*	*Defective/Non-Defective Ratio [%]*	*Type of Defects*
000	PC	/	/	100	25	69.86	Weld Line, Sink Mark, Burn Mark, Stain
001	PC	53.5	0.98	100	25	67.22	Weld Line, Sink Mark, Stain
002	PC	52.1	1.01	100	25	74.12	Stain
003	PC	5.4	1.18	100	25	70.3	Weld Line, Burn Mark
004	PC	5.5	0.92	0	25	63.66	Weld Line, Sink Mark, Burn Mark

To determine whether it is more effective to train multiple specialized models tailored to specific defect/component combinations or a single generalized model capable of handling all possible defects across different components, we conducted a comparative analysis. The use of a generalized model could offer significant cost savings for companies by eliminating the need to

Materials Research Proceedings 57 (2025) 600-607 https://doi.org/10.21741/9781644903735-70

train multiple models, thereby reducing computational resource consumption. This could also facilitate the spread of digital twins in injection molding companies, enabling more efficient process monitoring and optimization.

For this evaluation, we trained a model on the 000-type dataset, which was constructed by randomly selecting 100 images from the specialized datasets. This generalized model was then compared against the specialized models, each of which was trained on a specific defect/component. The models were assessed using three key performance metrics commonly employed in object detection:

- Precision: measures the proportion of correctly identified defects out of all instances predicted as defects, indicating how reliable the model's detections are.

$$Precision = \frac{True\ Positives\ (TP)}{True\ Positives\ (TP) + False\ Positives\ (FP)} \quad (1)$$

- Recall: evaluates the model's ability to detect all actual defects, representing its sensitivity to identifying defects present in the dataset.

$$Recall = \frac{True\ Positives\ (TP)}{True\ Positives\ (TP) + False\ Negatives\ (F)} \quad (2)$$

- F1-score: provides a balanced measure of precision and recall, offering a single performance metric that accounts for both false positives and false negatives.

$$F1\ score = \frac{2 * Precision * Recall}{Precision + Recall} \quad (3)$$

Since specialized models are inherently limited to detecting only the defects present in their respective training datasets, their performance metrics were averaged to enable a fair comparison with the generalized model. This approach allowed us to assess whether a single, broadly trained model could achieve competitive or superior performance while significantly reducing training and deployment costs in an industrial setting.

To assess the transfer learning capabilities of models trained on different source domains, we conducted inference using each trained model on all available validation datasets. This approach allowed us to evaluate the extent to which knowledge acquired from one dataset could be effectively applied to different component-defect combinations. Notably, as indicated in Table 1, no model was specifically trained on the 004 dataset. Instead, this dataset was reserved solely for inference testing, as the components belonging to 004 represent a distinct class within the company's product line. By evaluating model performance on 004, we aimed to assess the generalization ability of models when applied to an entirely different class of components, providing insights into their adaptability beyond the originally trained domain.

Results and Discussion

Comparative Analysis of Specialized vs. Generalized Models for IM Defect Detection. The boxplots in Fig. 2 illustrate the performance of the generalized model (000) and the specialized models (Others) across different defect types using precision, recall, and F1-score as evaluation metrics. Overall, the results suggest that both model types are capable of detecting defects, though their effectiveness varies depending on the defect category.

Materials Research Proceedings 57 (2025) 600-607 https://doi.org/10.21741/9781644903735-70

For defects such as weld lines, both models exhibit relatively high precision, recall, and F1-score, indicating strong detection performance. This suggests that weld line features are well captured regardless of the training approach. Burn marks, on the other hand, show greater variability, particularly in recall and F1-score, implying that they may be more challenging to detect consistently. The specialized models appear to struggle more in terms of recall, which indicate a higher rate of missed detections. The patterns learned by the 000 model, trained on a broader range of images, appear to have enabled it to better capture burn marks, suggesting that its higher performance in this case stems from a more comprehensive understanding of the defect. This implies that the generalized model benefits from the diverse defect patterns present in the dataset, potentially leveraging features extracted from other defect types to enhance its recognition of burn marks. In contrast, the specialized models, restricted to specific defect-component combinations, lack access to this broader feature set, which may limit their ability to generalize across variations of burn marks.

For sink marks, both model types exhibit comparable performance, suggesting that this defect type is adequately learned in both generalized and specialized training approaches. However, stains seem to present a more noticeable gap between the two model types, with the generalized model (000) displaying a wider range of values in precision and F1-score. This could indicate that stains are more dependent on component-specific characteristics, making them harder for a generalized model to recognize reliably. Specialized models may excel at detecting subtle or component-specific defects, but generalized models offer broader applicability with comparable or superior performance due to their exposure to diverse patterns. Training a generalized model is preferable, as it maintains high performance, reduces deployment costs, and eliminates the need for multiple specialized models.

Transfer Learning Performance Across Source and Target Datasets. Fig. 3 provides insights into the effectiveness of transfer learning across different dataset pairs. Inference was performed using models trained on the source dataset and tested on the target datasets. Therefore, the diagonal values in the heatmaps represent the predictions of each model on its own validation set, while off-diagonal values indicate transfer learning scenarios. The 004 dataset does not appear as a source dataset, as introduced in Section 2. The performance metrics considered are precision, recall, and F1-score.

For each batch of predictions on the available validation images of the target dataset, the mean and standard deviation of the metrics were computed. This approach provides a more comprehensive evaluation by not only assessing the average model performance but also capturing the variability and stability of predictions. The cells with a value of 0 indicate that the model trained on the i-th source dataset is unable to identify defects in the j-th target dataset, meaning the two datasets do not share common injection molding defects.

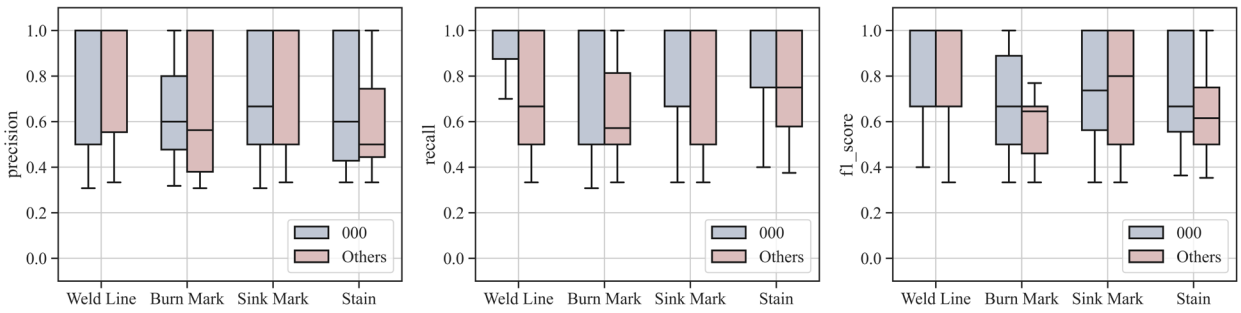


Fig. 2 Comparison of precision, recall, and F1-score for defect detection using the generalized model (000) and specialized models (Others).

Materials Research Proceedings 57 (2025) 600-607 https://doi.org/10.21741/9781644903735-70

For each graph, the row corresponding to the source dataset 000 represents the predictions of the model trained on the dataset containing all components and all types of analyzed injection molding defects. As expected, it maintains good performance across all target datasets, with high mean values and low standard deviations. This suggests that, despite having access to the same volume of data as other models, exposure to a broader range of defects and components allows the model to develop a more generalized understanding of injection molding defect patterns. Notably, the model trained on data from component 003 exhibits significantly high performance when making inferences on the target dataset 004. This can be attributed to the two components having similar values in terms of aspect ratio and representative feature dimensions, indicating that the knowledge learned by a model from images of a single component can be transferred for the detection of injection molding defects based on similar geometric features.

The inference of the model trained on the source dataset 003 on the target dataset 001 shows high precision but low recall and F1-score. This could be due to the model being highly confident in the defects it identifies, leading to a low false positive rate. However, the low recall suggests that it fails to detect a significant portion of actual defects, possibly because certain defect types present in the target dataset are underrepresented in the source dataset. This mismatch in defect distribution or feature representation could limit the model's ability to generalize effectively.

The 000 dataset model achieves high performance (though lower than the 003 dataset model) when inferring on the target dataset 004, which consists of components belonging to a different class for the company. This further supports the idea that the geometric features of components play a significant role in knowledge transfer, as only a random subset of type 003 components is present in the 000 dataset. In the same context, the 001 dataset model shows lower performance metrics, likely due to a more limited representation of relevant features necessary for effective defect detection on dataset 004.

In general, the standard deviation values are comparable across different scenarios, with the 000 dataset model performing slightly better than the others. This could be attributed to its exposure to a more diverse set of defects and components, leading to more stable predictions. Conversely, the inference of the 001 dataset model on the target dataset 004 shows slightly higher standard deviation values, likely due to a weaker feature alignment between the two datasets, resulting in less consistent predictions.

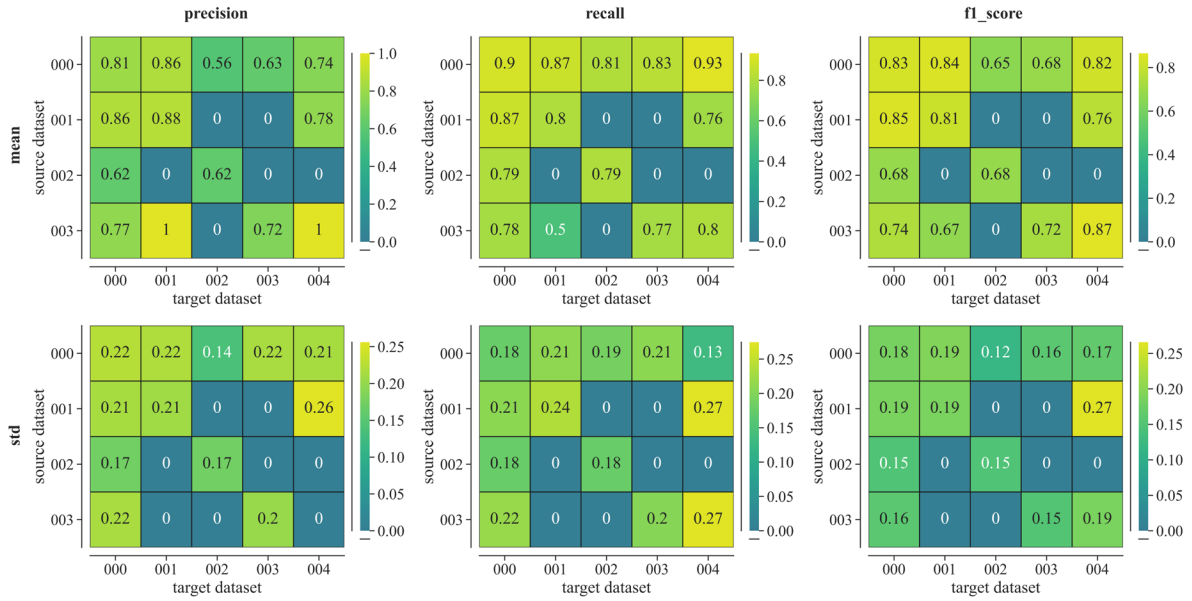


Fig. 3 Comparison of transfer learning effectiveness for models trained on source datasets and evaluated on target datasets. Precision, recall, and F1-score are analysed, highlighting their mean and standard deviation. The 004 dataset was used exclusively for inference testing.

Conclusion

The complexity of injection molding, small-batch production, and a shortage of skilled personnel render manual defect detection inefficient. Deep learning models show promise for automated defect detection but often need large labeled datasets and struggle with generalization. This study evaluated the RT-DETR transformer model, comparing generalized and specialized models for injection molding defect detection. Generalized models, trained on diverse defect-component combinations, matched or outperformed specialized models, reducing computational costs. They excelled at recognizing complex defects like burn marks. Transfer learning across component datasets showed that similar geometric features, such as dimensions and aspect ratios, improved model transferability, minimizing retraining needs. These findings support AI-driven, generalized defect detection systems to enhance quality control and reduce manual inspection reliance.

Effective deployment of such systems requires integration with existing conveyor systems and robust hardware to ensure real-time, scalable quality control in industrial settings. Future studies should focus on integrating these systems with process parameter data, particularly during startup phases, to move beyond merely storing defect information and develop predictive models that proactively prevent defects, thereby enhancing the overall capabilities of injection molding quality control.

References

[1] J.-B. E. M. Steenkamp, «Conceptual model of the quality perception process», *Journal of Business Research*, vol. 21, fasc. 4, pp. 309–333, dic. 1990. https://doi.org/10.1016/0148-2963(90)90019-A

[2] Z. Chen e L. Turng, «A review of current developments in process and quality control for injection molding», *Adv Polym Technol*, vol. 24, fasc. 3, pp. 165–182, set. 2005. https://doi.org/10.1002/adv.20046

[3] K.-M. Tsai, C.-Y. Hsieh, e W.-C. Lo, «A study of the effects of process parameters for injection molding on surface quality of optical lenses», *Journal of Materials Processing*

Technology, vol. 209, fasc. 7, pp. 3469–3477, apr. 2009. https://doi.org/10.1016/j.jmatprotec.2008.08.006

[4] J. Gim e L.-S. Turng, «A review of current advancements in high surface quality injection molding: Measurement, influencing factors, prediction, and control», *Polymer Testing*, vol. 115, p. 107718, nov. 2022. https://doi.org/10.1016/j.polymertesting.2022.107718

[5] C.-C. An e R.-H. Chen, «The experimental study on the defects occurrence of SL mold in injection molding», *Journal of Materials Processing Technology*, vol. 201, fasc. 1–3, pp. 706–709, mag. 2008. https://doi.org/10.1016/j.jmatprotec.2007.11.179

[6] R. Kerkstra e S. Brammer, *Injection Molding Advanced Troubleshooting Guide*. München: Carl Hanser Verlag GmbH & Co. KG, 2018. https://doi.org/10.3139/9781569906460

[7] G. Baruffa, A. Pieressa, M. Sorgato, e G. Lucchetta, «Transfer Learning-Based Artificial Neural Network for Predicting Weld Line Occurrence through Process Simulations and Molding Trials», *JMMP*, vol. 8, fasc. 3, p. 98, mag. 2024. https://doi.org/10.3390/jmmp8030098

[8] R. Zhang, Y. Li, e Z. Guan, «Research on injection molded parts defect detection algorithm based on multiplicative feature fusion and improved attention mechanism», *Sci Rep*, vol. 14, fasc. 1, p. 30864, dic. 2024. https://doi.org/10.1038/s41598-024-81430-x

[9] J. Gim, H. Yang, e L.-S. Turng, «Transfer learning of machine learning models for multi-objective process optimization of a transferred mold to ensure efficient and robust injection molding of high surface quality parts», *Journal of Manufacturing Processes*, vol. 87, pp. 11–24, feb. 2023. https://doi.org/10.1016/j.jmapro.2022.12.055

[10] J. Liu, F. Guo, H. Gao, M. Li, Y. Zhang, e H. Zhou, «Defect detection of injection molding products on small datasets using transfer learning», *Journal of Manufacturing Processes*, vol. 70, pp. 400–413, ott. 2021. https://doi.org/10.1016/j.jmapro.2021.08.034

[11] A. Pieressa, G. Baruffa, M. Sorgato, e G. Lucchetta, «Enhancing weld line visibility prediction in injection molding using physics-informed neural networks», *J Intell Manuf*, lug. 2024. https://doi.org/10.1007/s10845-024-02460-w

[12] G. A. Pereira e M. Hussain, «A Review of Transformer-Based Models for Computer Vision Tasks: Capturing Global Context and Spatial Relationships», 27 agosto 2024, *arXiv*: arXiv:2408.15178. https://doi.org/10.48550/arXiv.2408.15178

[13] A. Dosovitskiy *et al.*, «An Image is Worth 16x16 Words: Transformers for Image Recognition at Scale», 3 giugno 2021 *arXiv*: arXiv:2010.11929. https://doi.org/10.48550/arXiv.2010.11929.

[14] S. Khan, M. Naseer, M. Hayat, S. W. Zamir, F. S. Khan, e M. Shah, «Transformers in Vision: A Survey», *ACM Comput. Surv.*, vol. 54, fasc. 10s, set. 2022. https://doi.org/10.1145/3505244

[15] N. Carion, F. Massa, G. Synnaeve, N. Usunier, A. Kirillov, e S. Zagoruyko, «End-to-End Object Detection with Transformers», 28 maggio 2020, *arXiv*: arXiv:2005.12872. https://doi.org/10.48550/arXiv.2005.12872

[16] Y. Zhao *et al.*, «DETRs Beat YOLOs on Real-time Object Detection», 3 aprile 2024, *arXiv*: arXiv:2304.08069. https://doi.org/10.48550/arXiv.2304.08069

Materials Research Proceedings 57 (2025) 608-616 https://doi.org/10.21741/9781644903735-71

Supervised autoencoder for fault detection and diagnosis in predictive maintenance of bearing ring grinding machine

Pietro Andrea MICIACCIA[1,a], Giovanni PASCOSCHI[1,b], Antonio DECATALDO[1,c], Domenico MONOPOLI[1,d], Concetta SEMERARO[3,e] and Michele DASSISTI[1,f]

[1]Department of Mechanical, Mathematics, and Management (DMMM), Polytechnic University of Bari, Bari, Italy

[2]SKF Industry Spa, Bari, Italy

[3]Department of Industrial and Management Engineering, University of Sharjah, 27272 Sharjah, United Arab Emirates

[a]pietroandrea.miciaccia@poliba.it, [b]giovanni.pascoschi@poliba.it, [c]a.decataldo2@studenti.poliba.it, [d]d.monopoli2@phd.poliba.it, [e]csemeraro@sharjah.ac.ae, [f]michele.dassisti@poliba.it

Keywords: Grinding, Artificial Intelligence, Zero Defect

Abstract. Modern manufacturing industry requires advanced maintenance strategies to ensure process reliability and efficiency. This study develops a deep learning-based algorithm using an autoencoder for fault detection and diagnosis in a bearing ring grinding machine. The proposed methodology follows a two-step classification framework: a binary classifier detects the presence of faults, while a multi-class classifier identifies the specific failure type. The dataset, sourced from the Swedish National Data Service, is analyzed using deep learning techniques to optimize predictive maintenance. Experimental results demonstrate high classification accuracy, enabling real-time monitoring and early identification of machine degradation. This approach enhances maintenance planning, reduces unexpected failures, and improves overall operational performance. Future research will focus on refining the estimation of Remaining Useful Life (RUL) to further optimize maintenance strategies.

Introduction

Grinding, a term used to describe machining processes that use hard abrasive particles as a cutting medium, is likely the oldest known manufacturing process and remains an essential final step in various manufacturing operations. A workpiece that undergoes grinding has usually already passed through most stages of the process chain, carrying the highest added value. As a result, scrap generated during grinding is the most expensive and should be minimized as much as possible [1], [2]. In recent years, the growing demand for high-quality grinding and the increasing complexity of manufacturing systems have led to significant progress in the development and integration of industrial equipment [3]. On one hand, this makes unexpected failures more costly, causing financial losses and production delays. On the other hand, it emphasizes the importance of early fault detection and prediction, which help prevent failures from turning into more serious problems by allowing maintenance actions to be planned [4]. In the industrial sector, maintenance is essential to keeping processes running efficiently over time [5]. Maintenance strategies have evolved, becoming more advanced and structured (Fig. 1). Today, they can be divided into five main types: corrective maintenance (CM), preventive maintenance (PM), condition-based maintenance (CBM), predictive maintenance (PdM), and prescriptive maintenance (PsM). Corrective maintenance (CM) is the oldest approach and consists of replacing or repairing equipment components only when they fail and can no longer function. For this reason, it is often called the "run-to-failure" strategy. According to [6], this method leads to high costs due to unexpected

Content from this work may be used under the terms of the Creative Commons Attribution 3.0 license. Any further distribution of this work must maintain attribution to the author(s) and the title of the work, journal citation and DOI. Published under license by Materials Research Forum LLC.

Materials Research Proceedings 57 (2025) 608-616 https://doi.org/10.21741/9781644903735-71

production stoppages, and repair times are difficult to estimate. Today, corrective maintenance is mainly used in processes where sudden failures do not severely impact production. Over time, CM has been replaced by a more proactive approach known as preventive maintenance (PM). This strategy involves inspecting and, if necessary, replacing components at scheduled intervals or after a certain number of operating cycles. These tasks are carried out by specialized maintenance teams to reduce the risk of system failures. Unlike CM, PM is performed outside production hours to minimize the need for emergency repairs [7]. However, a key drawback of this method is the risk of replacing components too early or too late, leading to unnecessary costs or unexpected failures. With the rise of Industry 4.0 and technologies such as the Internet of Things (IoT) and Industrial Analytics (IA) [8], condition-based maintenance (CBM) has become more common. In this approach, maintenance is carried out based on real-time monitoring of physical parameters (such as acoustic signals, vibrations, temperature etc.) collected from sensors and monitoring devices installed on machines. An even more advanced approach is predictive maintenance (PdM), which combines Industry 4.0 technologies with automation, IoT, and data analysis. PdM allows for accurate failure predictions and estimates the system's remaining useful life (RUL), making maintenance more efficient and reducing downtime. The latest and most advanced strategy is prescriptive maintenance (PsM), which not only predicts failures but also provides recommendations on how to optimize maintenance activities and extend the system's RUL [9]. According to [10], PdM consists of six key stages (see Fig. 1), which include data acquisition, data processing, feature extraction, anomaly detection, fault diagnosis, and decision-making. These steps form the foundation of an effective PdM system, enabling early identification of potential failures and optimizing maintenance strategies. Building upon this framework, this paper aims to develop an autoencoder-based algorithm capable of detecting anomalies through binary classification (fault/no-fault) and performing fault diagnosis using multi-class classification. By leveraging machine learning techniques, the proposed approach seeks to enhance reliability and efficiency in industrial maintenance.

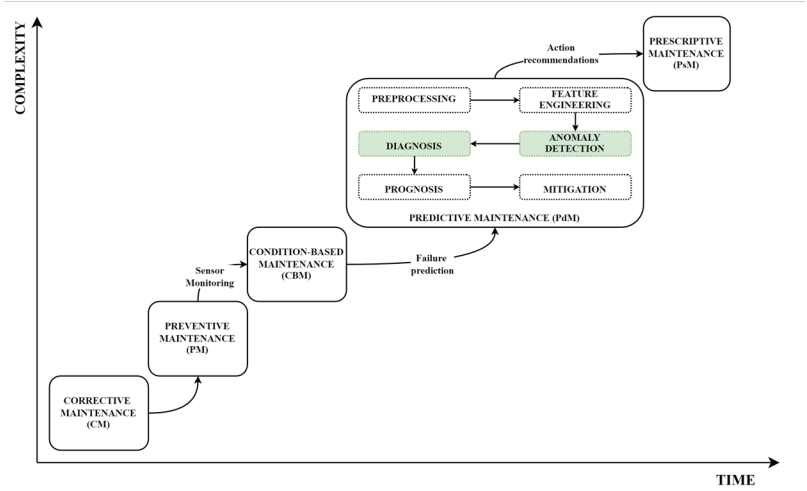


Figure 1. Evolution of Maintenance approach over the time.

Related Work

Predictive Maintenance (PdM) has become increasingly critical in modern manufacturing to ensure process reliability and reduce unexpected downtimes. Fault Detection and Diagnosis (FDD) techniques within PdM are typically developed using supervised or unsupervised learning approaches, each with distinct strengths and limitations [11]. Supervised learning methods such as Convolutional Neural Networks (CNNs), Random Forests, and hybrid models, have shown high accuracy in classifying known fault types [12], [13]. For example, [12] used a deep autoencoder-based CNN for fault classification in induction motors, achieving high performance, while [13]

proposed a hybrid CNN-LSTM model with transfer learning to enhance adaptability. However, these methods rely on large, labeled datasets—often costly and difficult to obtain in industrial settings. Unsupervised and semi-supervised approaches have emerged as promising alternatives for scenarios with limited labeled data. Autoencoders, clustering algorithms, and novelty detection techniques can identify anomalies and unknown failure patterns without requiring prior labels [14], [15]. While effective in some contexts, these models often suffer from interpretability challenges and limited specificity in fault localization. In the context of grinding processes, fault detection is particularly complex due to the interplay of multiple physical variables and nonlinear wear mechanisms [16]. Recent studies have explored various approaches: [17] applied a Random Forest model on a bearing ring grinding machine, achieving 99% accuracy while minimizing sensor costs. Others combined Support Vector Machines (SVM) with Genetic Algorithms to improve fault detection during abrasive belt grinding [18]. However, such methods still require significant feature engineering and domain-specific tuning [16]. Furthermore, grinding operations are rarely addressed in the mainstream PdM literature, which predominantly focuses on rotating machinery, CNC tools, or motor systems [19]. A recent review by [1] highlights the lack of tailored solutions for high-precision processes like grinding, where data availability, noise, and process complexity pose major obstacles.

This paper aims to fill this gap by applying a Supervised Autoencoder (SAE) architecture for real-time fault detection and diagnosis on a bearing ring grinding machine. By combining anomaly detection (binary classification) and fault diagnosis (multi-class classification) within a single deep learning framework, the proposed approach offers both precision and scalability. To the best of our knowledge, this is one of the first studies to successfully implement SAE-based PdM on grinding processes using real-world experimental data.

Material and Method

The data used in this research are stored on the Swedish National Data Service website and were collected during the research conducted by Dr. Muhammad Ahmer at SKF Manufacturing Development (MD) in Göteborg, Sweden [20].

Specifically, the ring grinder utilized in this study is an external plunge grinder manufactured by Lidköping Machine Tools (SGB-55). This grinding machine is designed to perform raceways and shoulder grinding on the inner ring of a Deep Groove Ball Bearing (DGBB). In this research, tests were conducted on the SKF-6210 bearing ring.

The machine consists of three main spindle units: the grinding spindle unit, the dressing spindle unit, and the workhead spindle unit. The grinding and workhead spindles operate on hydrostatic bearings, while the dressing spindle is supported by conventional bearings. These spindles are driven by electric motors through a system of belts and pulleys. The same three primary subsystems are the focus of the research's work and are equipped with vibration, acoustic emission, and force sensors (see Figure 2 and Table 1). All data collected from the sensors described in Table 1 were systematically employed for the purposes of this research.

Materials Research Proceedings 57 (2025) 608-616 https://doi.org/10.21741/9781644903735-71

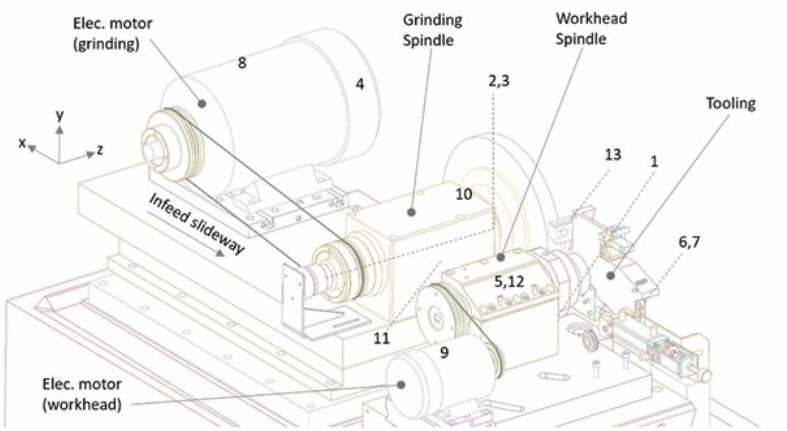


Figure 2. Location of the sensors installed in the grinding machine SGB-55 [21].

Table 1. List of sensors installed in SGB 55B grinding machine.

ID	Measured quantity	Sensor	Target subsystem
1	Force	Kistler 9105C	Workhead
2	Acoustic emission	Dittel m6000	Grinding spindle
3	Balancing Unit	Marposs P7	Grinding spindle
4	Power	Montronix PS100	Elec.motor (grinding)
5	Strain	Kistler 9238B	Workhead
6	Acoustic emission	Parker 247 Ultraspan	Tooling
7	Vibration	PCB triax A45	Tooling
8	Vibration	SKF CMSS2200	Elec.motor (grinding)
9	Vibration	SKF CMSS2200	Elec.motor (workhead)
10	Vibration	IMI601A01	Grinding spindle
11	Temperature	NTCALUG02A103F	Grinding spindle
12	Temperature	NTCALUG02A103F	Workhead spindle
13	Temperature	NTCALUG02A103F	Tooling

Failure modes were identified based on the maintenance history of similar machines and technician interviews. Specifically, five different failure modes have been identified, namely:

- Workhead drive belt damage.
- Workhead spindle unbalance
- Material wear/failure of drive plate.
- Set up errore of workhead tooling
- Material failure/crash of workhead tooling support.

The proposed architecture is a supervised autoencoder designed for multiclass classification tasks while preserving the ability to reconstruct the input data. The model consists of three main components: an encoder, a decoder, and a classifier, all implemented within the PyTorch framework. The encoder maps the input vector $x \in \mathbb{R}^d$ into a lower-dimensional latent space $z \in \mathbb{R}^l$, where d is the input dimensionality and l = 2 is the latent dimensionality. The encoder comprises a sequence of fully connected layers defined by a list of hidden $[h_1, h_2, \ldots, h_n]$. Each layer applies a linear transformation followed by a ReLU activation and dropout regularization with a specified dropout rate p = 0.2. The final output of the encoder is a linear projection into the latent space. The decoder performs the inverse mapping, reconstructing the input from the latent representation. It mirrors the encoder's architecture in reverse, using the same hidden dimensions

Materials Research Proceedings 57 (2025) 608-616 https://doi.org/10.21741/9781644903735-71

in reversed order. Each layer again consists of a linear transformation, ReLU activation, and dropout. The final layer of the decoder projects the latent vector back to the original input dimension d, with no activation function applied, as the reconstruction loss is computed using the Mean Squared Error (MSE) loss function.

In parallel to the decoder, a classifier is trained on top of the latent space. It consists of a single fully connected layer mapping the latent vector z to a vector of class logits $y \in \mathbb{R}^C$, where C is the number of output classes. The classification loss is computed using the Cross-Entropy Loss. The training objective is the joint minimization of the reconstruction and classification losses. The total loss function L is defined as $L = L_{recon} + L_{class} = MSE(x, \hat{x}) + CrossEntropy(\hat{y}, y)$ where xˆis the reconstructed input and yˆis the predicted class logits.

Training was conducted using the Adam optimizer with early stopping based on the validation loss; training was halted if no improvement occurred over 10 consecutive epochs. The dataset was evenly split, with 50% used for training and 50% for testing, and 20% of the training set further allocated for validation. Data, collected from experimental test runs on individual rings, required minimal preprocessing due to its structured format and high-frequency sampling, which ensures accurate representation of process dynamics. The acquired data was segmented into shorter time intervals corresponding to different phases of the grinding process to enable fine-grained analysis and phase-specific pattern recognition. Segmentation was based on acoustic emission signals from the working head—the only sensor suitable for this task. The derivative of the signal was used to identify three key transition points (see Figure 3), with oversampling reduced by selecting one point every 5000 samples to avoid sensitivity to minor fluctuations. The force build-up phase (S2) was excluded due to transient effects caused by the initial tool-workpiece contact, which is highly dependent on the quality of the incoming ring. The remaining three segments—initial (S1), grinding (S3), and final (S4)—were retained, and features were extracted from each to construct a labeled dataset for training machine learning models.

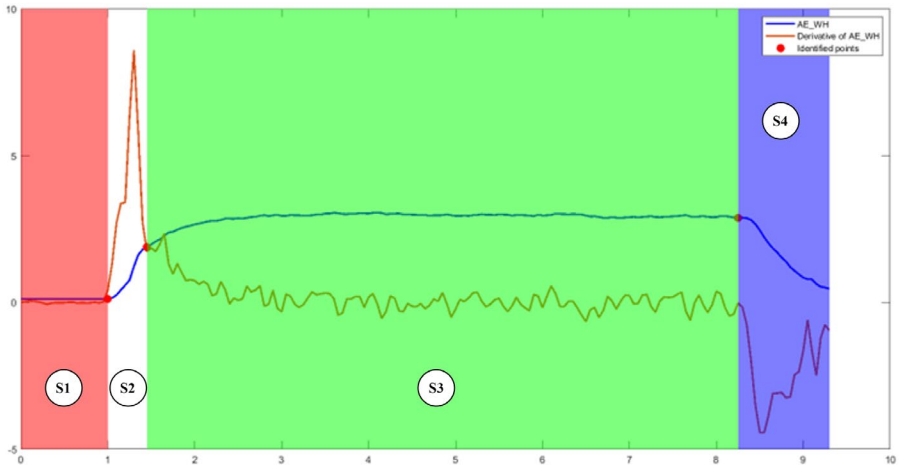


Figure 3. Segmentation of the grinding cycle used in the research work.

As introduced in the Introduction and shown in Figure 1, the PdM strategy begins with anomaly detection—distinguishing normal operating conditions from machine failures—and proceeds to fault diagnosis. A two-step classification framework is proposed, involving separate classifiers. The first, a binary classifier, detects the presence of a failure mode in the grinding machine. The second, a multi-class classifier, identifies the specific failure type. This hierarchical structure leverages the natural decomposition of the problem, improving efficiency and scalability by first addressing a simpler binary task. After feature extraction, the dataset is labeled to indicate both failure presence and type for each ring. The multi-class classification test set is then used to

validate the diagnostic framework. For evaluation, the dataset is evenly split into training and testing sets.

Result and Discussion

The following Figure 4 illustrate the performance of the binary classifier in the latent space. The left plot (A) shows the actual labels, while the right (B) plot presents the autoencoder's predictions on test data. A confusion matrix 4 is also included to quantify classification accuracy. The results of the binary classification confirm that the two classes are clearly separable. Additionally, Figure 5 (C) and (D) (left and right, respectively) also illustrate the classification based on the different failure modes used to train the Supervised AutoEncoder (SAE). The results show a clear distinction between the various failure classes, enabling both real-time and early identification of the specific machine component undergoing degradation.

Conclusion and Future Works

In this study, we applied a supervised autoencoder-based algorithm (SAE) to perform both binary and multiclass classification of fault conditions in a grinding process. The results obtained are highly promising, demonstrating excellent accuracy in fault detection and diagnosis. These findings highlight the potential of autoencoder-based approaches for enhancing PdM in grinding operations. This capability allows for timely maintenance planning, ensuring proactive intervention before critical failures occur. The model achieves an accuracy of 95.09%, precision of 85.84%, recall of 100%, and an F1-score of 92.38%. The data projected into the latent space show a much clearer separation, which is crucial to achieve PdM. One major advantage of the trained Supervised AutoEncoder (SAE) model is its capability for real-time machine monitoring. When the machine is operating normally, the model classifies the output within the "Normal" cluster. As wear and degradation occur, the output gradually shifts toward the "Fault" cluster. The speed of this transition can serve as an early indicator of machine deterioration, helping determine the optimal timing for maintenance actions and reducing unexpected failures. Additionally, this approach enables the identification of specific failure types by incorporating a multi-class classifier. Each fault scenario is assigned a corresponding class label, and the same autoencoder-classifier method is applied to accurately classify different failure modes. Based on this study, which has already demonstrated high effectiveness in identifying failure types using the Supervised AutoEncoder (SAE) and detecting weak signals of component degradation in a grinding machine, future research should focus on refining the estimation of the Remaining Useful Life (RUL) of system components. Accurate RUL estimation would allow for more strategic maintenance planning, optimizing both the type of intervention and the timing to maximize system efficiency and reliability. Additionally, integrating advanced machine learning techniques and real-time monitoring systems could further enhance predictive maintenance capabilities, reducing unexpected failures and improving overall operational performance. Moreover, potential research direction involves identifying general fault conditions in machines that have not been pre-classified, allowing for a more effective implementation of predictive maintenance through an unsupervised learning approach. Although the results achieved in this study are highly promising, further experimental validation is required to ensure their robustness. Specifically, comparative analyses with alternative methodologies and the use of larger and more diverse datasets are necessary to enhance the generalizability and reliability of the proposed approach. In particular, future validation efforts should involve data collected over a longer time span, in order to assess the methodology's performance under varying operational conditions and to support its broader generalizability. Finally, we aim to establish a correlation between potential fault conditions and production quality parameters. This will help identify not only the degradation of machine components but also potential impacts on the quality of the final products, ensuring a more comprehensive and proactive maintenance strategy.

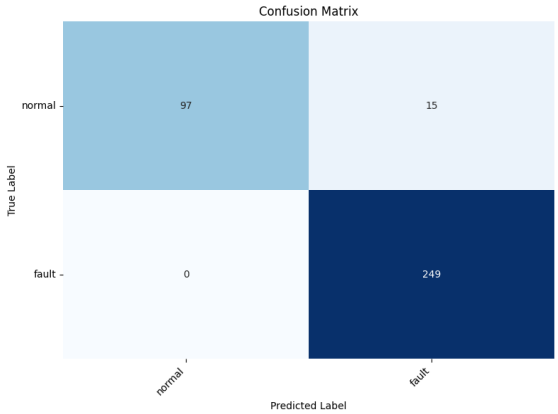


Figure 4. The confusion matrix for binary classification.

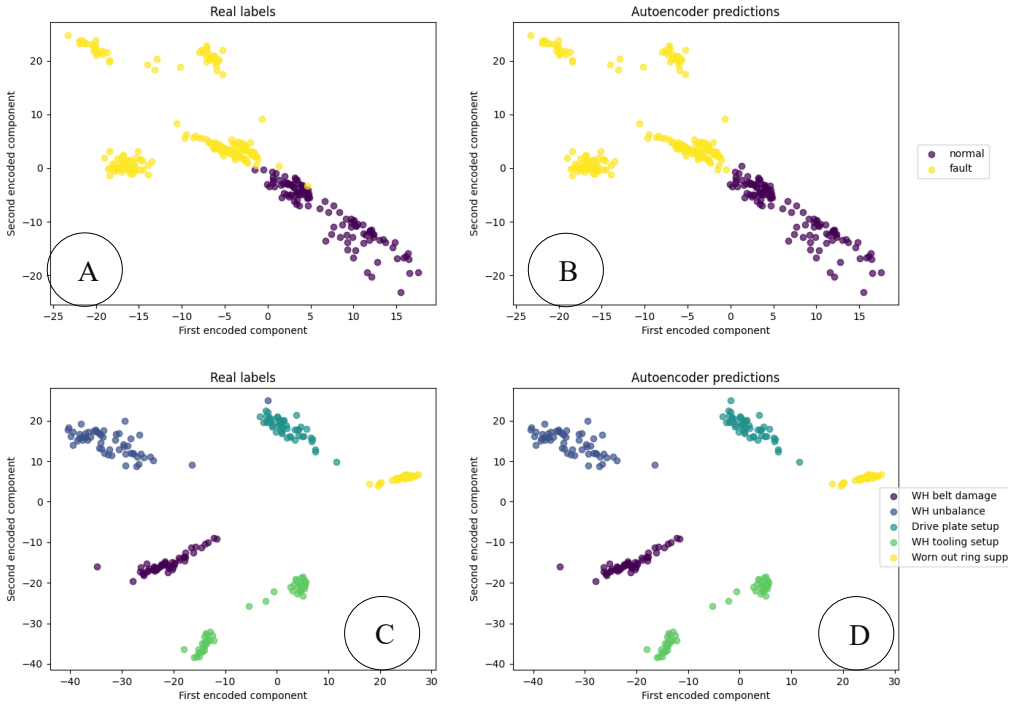


Figure 5. Binary classifier. (A) for Real Label and (B) for SAE prediction. Multi-class classifier. (C) for Real Label and (D) for SAE prediction.

References

[1] K. Wegener, F. Bleicher, P. Krajnik, H.-W. Hoffmeister, and C. Brecher, "Recent developments in grinding machines," *CIRP Annals*, vol. 66, no. 2, pp. 779–802, 2017. https://doi.org/10.1016/j.cirp.2017.05.006.

[2] S. and G. C. Malkin, *Grinding Technology: Theory and Application of Machining with Abrasives*. 2008.

[3] Z. Li, Y. Wang, and K.-S. Wang, "Intelligent predictive maintenance for fault diagnosis and prognosis in machine centers: Industry 4.0 scenario," *Adv Manuf*, vol. 5, no. 4, pp. 377–387, Dec. 2017. https://doi.org/10.1007/s40436-017-0203-8.

[4] C. Zhao, "Fault subspace selection and analysis of relative changes based reconstruction modeling for multi-fault diagnosis," in *The 26th Chinese Control and Decision Conference (2014 CCDC)*, IEEE, May 2014, pp. 235–240. https://doi.org/10.1109/CCDC.2014.6852151.

[5] D. Galar, M. Palo, A. Van Horenbeek, and L. Pintelon, "Integration of disparate data sources to perform maintenance prognosis and optimal decision making," *Insight - Non-Destructive Testing and Condition Monitoring*, vol. 54, no. 8, pp. 440–445, Aug. 2012. https://doi.org/10.1784/insi.2012.54.8.440.

[6] P. Nunes, J. Santos, and E. Rocha, "Challenges in predictive maintenance – A review," *CIRP J Manuf Sci Technol*, vol. 40, pp. 53–67, Feb. 2023. https://doi.org/10.1016/j.cirpj.2022.11.004.

[7] A. Jimenez-Cortadi, I. Irigoien, F. Boto, B. Sierra, and G. Rodriguez, "Predictive Maintenance on the Machining Process and Machine Tool," *Applied Sciences*, vol. 10, no. 1, p. 224, Dec. 2019. https://doi.org/10.3390/app10010224.

[8] M. Ahmer, F. Sandin, P. Marklund, M. Gustafsson, and K. Berglund, "Failure mode classification for condition-based maintenance in a bearing ring grinding machine," *The International Journal of Advanced Manufacturing Technology*, vol. 122, no. 3–4, pp. 1479–1495, Sep. 2022. https://doi.org/10.1007/s00170-022-09930-6.

[9] H. Fox, A. C. Pillai, D. Friedrich, M. Collu, T. Dawood, and L. Johanning, "A Review of Predictive and Prescriptive Offshore Wind Farm Operation and Maintenance," *Energies (Basel)*, vol. 15, no. 2, p. 504, Jan. 2022. https://doi.org/10.3390/en15020504.

[10] O. Serradilla, E. Zugasti, J. Rodriguez, and U. Zurutuza, "Deep learning models for predictive maintenance: a survey, comparison, challenges and prospects," *Applied Intelligence*, vol. 52, no. 10, pp. 10934–10964, Aug. 2022. https://doi.org/10.1007/s10489-021-03004-y.

[11] O. Serradilla, E. Zugasti, J. Rodriguez, and U. Zurutuza, "Deep learning models for predictive maintenance: a survey, comparison, challenges and prospects," *Applied Intelligence*, vol. 52, no. 10, pp. 10934–10964, Aug. 2022. https://doi.org/10.1007/s10489-021-03004-y.

[12] R. N. Toma, F. Piltan, and J. M. Kim, "A deep autoencoder-based convolution neural network framework for bearing fault classification in induction motors," *Sensors*, vol. 21, no. 24, Dec. 2021. https://doi.org/10.3390/s21248453.

[13] Y. Liang, Y. Wang, W. Li, D. T. Pham, and J. Lu, "Adaptive fault diagnosis of machining processes enabled by hybrid deep learning and incremental transfer learning," *Comput Ind*, vol. 167, May 2025. https://doi.org/10.1016/j.compind.2025.104262.

[14] X. Wu, Y. Zhang, C. Cheng, and Z. Peng, "A hybrid classification autoencoder for semi-supervised fault diagnosis in rotating machinery," *Mech Syst Signal Process*, vol. 149, Feb. 2021. https://doi.org/10.1016/j.ymssp.2020.107327.

[15] T. McLeay, M. S. Turner, and K. Worden, "A novel approach to machining process fault detection using unsupervised learning," *Proc Inst Mech Eng B J Eng Manuf*, vol. 235, no. 10, pp. 1533–1542, Aug. 2021. https://doi.org/10.1177/0954405420937556.

[16] M. Ahmer, F. Sandin, P. Marklund, M. Gustafsson, and K. Berglund, "Using Multivariate Quality Statistic for Maintenance Decision Support in a Bearing Ring Grinder," *Machines*, vol. 10, no. 9, Sep. 2022. https://doi.org/10.3390/machines10090794.

[17] M. Ahmer, F. Sandin, P. Marklund, M. Gustafsson, and K. Berglund, "Failure mode classification for condition-based maintenance in a bearing ring grinding machine," *International*

Journal of Advanced Manufacturing Technology, vol. 122, no. 3–4, pp. 1479–1495, Sep. 2022. https://doi.org/10.1007/s00170-022-09930-6.

[18] V. Pandiyan, W. Caesarendra, T. Tjahjowidodo, and H. H. Tan, "In-process tool condition monitoring in compliant abrasive belt grinding process using support vector machine and genetic algorithm," *J Manuf Process*, vol. 31, pp. 199–213, Jan. 2018. https://doi.org/10.1016/j.jmapro.2017.11.014.

[19] P. M. Mbilong, Z. Aarab, F. Z. Belouadha, and M. I. Kabbaj, "Enhancing Fault Detection in CNC Machinery: A Deep Learning and Genetic Algorithm Approach," *Ingenierie des Systemes d'Information*, vol. 28, no. 5, pp. 1361–1375, 2023. https://doi.org/10.18280/isi.280525.

[20] M. Ahmer, *Dataset Concerning the Process Monitoring and Condition Monitoring Data of a Bearing Ring Grinder*. 2023.

[21] M. Ahmer, F. Sandin, P. Marklund, M. Gustafsson, and K. Berglund, "Using Multivariate Quality Statistic for Maintenance Decision Support in a Bearing Ring Grinder," *Machines*, vol. 10, no. 9, p. 794, Sep. 2022. https://doi.org/10.3390/machines10090794.

Materials Research Proceedings 57 (2025) 617-624 https://doi.org/10.21741/9781644903735-72

An experimental approach exploiting high-voltage fragmentation as a selective comminution technology for the recovery of key metals

Marco DIANI[1,a] *, Shravan TORVI[1,b] and Marcello COLLEDANI[1,c]

[1]Politecnico di Milano, Mechanical Department, via La Masa 1, Milan, 20156, Italy

[a]marco.diani@polimi.it, [b]shravan.torvi@polimi.it, [c]marcello.colledani@polimi.it

Keywords: Circular Economy, Mechanical Separation, Demanufacturing, Recycling, High-Voltage Fragmentation

Abstract. The recycling of common-use waste has been of paramount importance for several years, leading to different directives as the WEEE 2012/19/EU, which sets optimistic thresholds for recovery as high as 85%, or the ELV directive with a recovery rate of 95% for EoL vehicles. Among them, some particularly interesting products, due to the presence of key metals and rare earths, are Printed Circuit Boards, photovoltaic panels, and sparkplugs, which showed relevant continuously increasing waste volumes. Typically, they are treated through mechanical pretreatment, leading to mixed, non-well-liberated flows. This article shows a novel alternative to them, with High-Voltage Fragmentation as a selective comminution technique for the separation of these key metals from non-target materials. The process works on the principle of electrodynamic fragmentation by creating a plasma channel to delaminate the structure of these products at the material phase boundaries, leading to highly liberated fractions.

Introduction

This work discusses the potentiality of recycling commonly used products with an innovative recycling technique called High-Voltage Fragmentation (HVF) to enable and enhance the urban mining concept. In particular, three products have been considered from three different sectors: spark plugs, photovoltaic panels and Printed Circuit Boards. Photovoltaic (PV) panels and Printed Circuit Boards (PCBs) together with Waste from Electric and Electronic Equipment (WEEE) are subjected to very ambitious recycling rates as high as 85% as part of the EU waste directive 2012/19/EU, that regulates e-waste collection, treatment and recycling. The growth in the PV panels installations in Europe is one of the fastest growing forms of non-conventional energy resources with PV installations increasing 2500-fold since the beginning of the year 2000. The installed capacity of PV panels in EU27 reached 269GW at the end of 2023, with a growth rate that is expected to remain in double digits between 2024 and 2028 [1]. Owing to these huge numbers of PV installations in the past decades and with solar energy generation reaching 42,5% of Europe's energy mix by 2030, the amount of PV waste is predicted to be in the order of a few million tons with an estimation of 5,6 million tons at the end of the year 2025 [2]. As PV panels contain key and precious metals such as Ag, Si, Au, Al and sometimes Pt and Pd that makes their recycling not only environmentally sustainable but also economically interesting, the first European recycling plant, set up in France in the year 2018 is expected to recycle 10000 tons worth of PV panels in the year 2025 [3].

Similarly, with the increased use of electronics over the past decades and a continued growth in the global PCB market at a CAGR of 5.6% for the next five years, recycling PCBs represents one of the most compelling examples of urban mining. Precious metals such as Au, Ag, Cu, Ni, Pd and Pt are found in high concentrations in e-waste. As an example, gold has a staggeringly higher concentration in e-waste (between 100 and 1300g/ton) than in the naturally occurring ore form (1,4-8,3g/ton) [4]. However, of the record 62 billion kilograms of e-waste generated during 2022, only 23% was recycled and, while the market of recycling of e-waste is expected to grow,

Content from this work may be used under the terms of the Creative Commons Attribution 3.0 license. Any further distribution of this work must maintain attribution to the author(s) and the title of the work, journal citation and DOI. Published under license by Materials Research Forum LLC.

Materials Research Proceedings 57 (2025) 617-624 https://doi.org/10.21741/9781644903735-72

the recycling rates themselves are not reaching values where they will start to make a difference [5]. The total e-waste is, however, expected to rise to approximately 82 million tons by the year 2030.

While sparkplugs are not a part of the WEEE waste category and are dealt with under the ELV directive with a target recycling rate of 95%, they do contain precious metals such as Pt, Ir (for the counter electrode tips) along with metal oxides of Cu and Al.

The presence of these key metals makes WEEE waste and spark plugs very promising for urban mining opportunities. Urban mining is the process of obtaining these precious metals by collecting, treating, recycling and extracting precious elements from post-use components. Urban mining enables circular economy by not only recovering key elements which are otherwise lost due to wasteful treatment pathways such as incineration and landfilling but it helps reduce the primary mining, that puts strong pressure on earth's biosphere due to deforestation, drilling and polluting the crust. In addition, urban mining is a very important lever to strength and localize the supply chain of these key metals since their deposits are often found in sensitive geolocations.

Despite these undeniable advantages, nowadays the most common industry principle of recovery and recycling for WEEE waste is mechanical shredding followed by separation techniques or thermal treatments to obtain precious metals. The complex structure of these components compounded by mechanical recycling makes separation challenging, while increasing the cost in case of high temperature solutions, leading to an economically unreliable process.

This work discusses the application of an innovative technology called High-Voltage Fragmentation working on the electrodynamic fragmentation principle to liberate target components/materials from these complex structures with the help of a plasma channel between two electrodes acting at the material boundaries. The concept is to exploit this technique to enrich pretreated flows, allowing maximum recovery and a better separation of key metals from non-target materials such as polymers in PCBs, glass and plastics in PV panels and ceramics for spark plugs.

Literature review

The process of High-Voltage Fragmentation was discovered during the 1960s primary as a technique to separate minerals from their ores due to its unique working principle [6]. HVF works on the electrodynamic fragmentation which exploits different relative electric permittivity of varying materials to create cracks that propagate from the physical grain boundaries eventually separating materials (more details in "Materials & Methods"). Considering its working principle, during the late 1990s it was studied as an effective technique in recycling, starting from incinerator bottom ashes from Municipal Solid Waste. The idea was to separate metal fractions from the ashes that can then be reused into concrete as a reinforcement [6]. High-Voltage fragmentation has been then experimented to recycle fiber reinforced plastics waste, where door hinges of an aircraft made from PEEK resin with reinforced carbon fiber were recycled using HVF in a cradle-to-cradle approach [7]. The recycled materials were reintroduced in door hinges with no loss of performance observed. HVF was used to recycle GFRP waste, and the results were compared to traditional mechanical recycling. The results obtained pointed out that, while energy consumption was higher compared to shredding techniques, the glass fibers obtained from HVF were cleaner and had a wider-length distribution, opening the potential upcycling of the obtained material [8][9][10].

Electrohydraulic fragmentation in which the shockwaves are produced in water and not in the solid samples as in the case of HVF has been briefly studied to recycle sparkplugs as seen in with the objective of separating ceramic from metals with promising results [11]. HVF fragmentation has also been studied to recycle PV panels [12]. More than 95% of copper and 96% of gold were in size fractions smaller than 1 mm, and 85% of aluminum was found between 0.25 mm and 2 mm. The energy consumption was lower in this specific application compared to mechanical recycling at 0,056kWh/kg [12]. Bi-facial solar panels were treated using HVF by and complete

separation was observed at 300 pulses and 160kV with the added advantage of no cross-contamination [13].

HVF was also investigated to recycle PCBs in where the technique was used as a crushing technique and compared to mechanical shredding. It was found that HVF had a greater degree of metal liberation from the polymer components in the size fraction around 1mm, where 96% liberation was observed. In comparison, the metal liberation observed for mechanical crushing was around 90% around the same size fraction. However, the paper found that energy consumption was significantly high, 3000 kWH/t for HVF compared to 100 kWh/t for mechanical crushing [14]. Other areas where HVF has been investigated as a recycling technique is in recycling of ultra high-performance fiber reinforced concrete, mainly due to their high compressive strengths that cause high wear of traditional crushing equipment. About 30% recovery of steel fibers was observed at 5kWh/t that increased to 60% at 13,4kWh/t [15].

Materials & methods

Equipment

The experiments were conducted using a High-Voltage Fragmentation machine from SelFrag AG (laboratory-scale model). This machine operates on the principle of selective breakdown of materials through high-voltage electrical pulses. An electrode is positioned at the top of the working vessel, containing the sample in a liquid medium, typically deionized water, while a counter-electrode is placed at the bottom. The machine generates high-voltage electric discharges between the two electrodes within a nitrogen atmosphere. During this process, an electrical discharge with high energy creates a plasma channel that reaches temperatures exceeding 10^4 K and pressures around 10^9-10^{10} Pa. This energy concentrates at the interface between materials with different electric permittivity, generating stress that surpasses the strength of solid materials. When the electrical pulses rise time decreases to as low as 500 ns, ionization ceases, and the plasma breakdown path concludes. These effects produce localized shock waves, similar to lightning strikes, leading to fractures at the phase boundaries of the solid material. After multiple discharges, these fractures expand, ultimately causing fragmentation. As electrons are situated at the material boundaries, fragmentation energy is concentrated along the material interface. This results in high liberation and selective fragmentation of the product.

The process vessel can be either open or closed. In the open type, a sieve inlay (grid) can be utilized to allow material that has reached the desired size to fall into a rubber container. In the closed-type vessel, the material remains inside until the processing is complete.

The controllable parameters of this process include voltage (ranging from 90-200 KV), the distance between electrodes (10-40 mm), pulse repetition rate (1-5 Hz), and number of electric pulses.

The primary aim of the initial experimental campaign was to examine the effectiveness of High-Voltage Fragmentation as a mechanical pretreatment for spark plugs, photovoltaic panels, and PCBs in urban mining. The following three subsections provide a concise overview of these products and their relevance in material recovery, stressing the different materials' composition.

Spark plugs

A spark plug consists of several parts made from different materials that allow it to ignite the air-fuel mixture in an internal combustion engine. The central electrode, composed of nickel alloy, platinum or iridium, ensures electric and thermal conduction while providing heat resistance. A threaded metal sheath, made of steel, secures the spark plug and helps heat dissipation. Around the electrode, an aluminum oxide ceramic insulator protects it from thermal and mechanical stress, while the ignition terminal, connected to the ignition system, is made from steel or brass. When the ground electrode (made by nickel alloy, platinum, or iridium) receives an electric current, a

high voltage spark is generated, which ionizes and combusts the air-fuel mixture, powering the engine.

Photovoltaic panels

The efficiency and longevity of monocrystalline silicon photovoltaic panels is grounded on their key materials. Solar cells hail from high-purity monocrystalline silicon, the most electrically conductive form of silicon, as it has a uniform crystal structure. Incoming light is allowed to pass through tempered glass as it is shielded by the protective layer. The encapsulation layers composed of ethylene vinyl acetate (EVA) safeguard the cells from both mechanical stress and moisture. Polymer materials (e.g. PET) are used for the back sheet to provide both protection from weather elements as well as electrical insulation. An anodized aluminum frame offers structural support and mounting. Electric conduction from solar cells to external circuitry is done efficiently through wiring contacts that have a copper core and are covered by silver. Highly conductive grid lines are created when silver paste is screen-printed onto the surface of the silicon cells. These grid lines then collect and transport the generated electric current.

Printed Circuit Boards

Material recovery processes are more efficient when electronic components are first separated from the PCB, resulting in fewer contaminations. In this way, gold, silver, palladium, tantalum, and other precious metals can be recovered with a high purity level. Removing the components from the board can also favor safe disposal of hazardous materials containing lead and flame retardants. In this way, it is easier to apply industrial recycling methods targeted to specific materials with greater accuracy, increasing metals and rare earths recovery, and reducing damage to the entire ecosystem. Contaminations included in PCBs, such as glass fibers or resins, are more difficult to remove if they are processed together with all the other materials. In turn, specialized melting and dissolution techniques that use water can be used more efficiently on the separated components, allowing a robust and high-level grade recovery of materials, also lowering the emission to the environment.

Results & discussion

The preliminary work was a feasibility analysis to understand the potentiality to use HVF in urban mining. Most promising results will be highlighted in the following three subsections. Then a preliminary extended campaign has been conducted to better understand the influence of the different parameters on the final result. The last part of each subsection reports these outcomes. In particular, the initial focus has been posed on the voltage (considering 120, 150 and 180 kV), the number of discharges (100, 250, and 500) and the presence or not of the grid.

Spark plugs

The results on spark plugs indicate that HVF technology may be applicable to these products. As shown in the picture below, High-Voltage Fragmentation disassembled the spark plug into its fundamental components, often maintaining their original shapes. The plasma channel appears to concentrate on the central electrode (made of iridium in this case), which is conductive, directing the shockwaves along it. This results in the detachment of the aluminum oxide ceramic insulator, revealing a clean iridium electrode. This outcome was achieved through a short process involving only 100 pulses at a frequency of 5Hz, taking approximately 20 seconds.

With respect to literature, HVF seems to work in a different way than electrohydraulic fragmentation. In this case the spark plugs is created directly inside the spark plug exploiting the conductivity of the central part. The work towards optimization showed that it is possible to use the process at low kV, but enough to obtain dielectric breakdown effect in the spark plug. This happens already with a voltage higher than 120 kV, but with more pulses needed. Further analysis

Materials Research Proceedings 57 (2025) 617-624 https://doi.org/10.21741/9781644903735-72

has to focus on finding the threshold between voltage and number of discharges based mainly on energy consumption.



Fig. 1: Spark plugs before (left) and after (right) the HVF treatment.

Photovoltaic panels

The results for photovoltaic panels appear promising, although further investigation is required. Considering the literature that highlights the concentration of metals in the smallest fractions, this study aimed to explore the potential of inserting a grid to discharge material upon reaching a specific dimension. As illustrated in the accompanying image, the detachment of metals from the plastic sheet appears effective, although some material remained attached. A noteworthy issue is that the glass was also reduced to a dimension smaller than the grid size. Despite being a partially favorable outcome, several significant observations have been made.

Firstly, it was decided to sieve the obtained material. The sieving process revealed that metallic materials concentrated in the lower sieve, specifically at dimensions less than 710 microns, while the upper sieves primarily contained glass. Consequently, the material was analyzed using SEM and EDS technology, which confirmed these findings. Additionally, SEM images indicated that the process successfully detached not only metals but also metal paste, such as silver. This suggested that further experiments should be conducted, particularly exploring the influence of the grid size, which appears to be the most crucial and impactful parameter for these products. In particular, the use of a grid size with a dimension of 1 mm seems to be the optimal solution. In this way, it was possible to obtain a presorted recycled material composed mainly by metal, with most of the glass remaining in the upper region of the vessel. Regrettably, no grids with smaller dimensions were available. However, the subsequent steps will concentrate on utilizing cut pieces rather than crushed material, which is expected to improve the separation process.

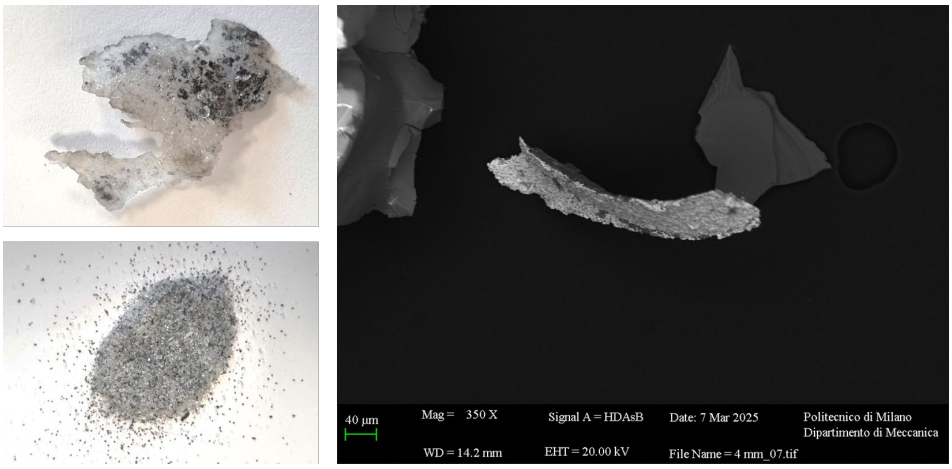


Fig. 2: Results obtained after the treatment of PV panels: plastic foil with some metal residues (up left), mixed material under the grid (bottom left), SEM image of a silver particle (right).

Printed Circuit Boards

The treatment of PCBs through HVF resulted in effective disassembly of components from the board. This process was conducted on whole End-of-Life PCBs with different levels of components presence.

In all treated samples, both if they resulted as shredded or intact, components were disassembled from the PCB with minimal or no damage. As an example, Fig. 3 shows two obtained outcomes. The left image displays the treatment of a PCB with few components (the green one). After the process, it results as shredded ones, while most of its components remain undamaged and disassembled from the board. The right image shows a PCB with numerous components (the blue one), highlighting a nearly perfect disassembly from the board, which remains intact. Various components, such as capacitors, microchips, and connectors, can be identified. This indicates that, after optimizing the process, HVF could serve as an efficient disassembly technology to concentrate materials for subsequent recycling stages, results that improve the use of HVF as simple crusher, overcoming the high energy consumption reported in literature. In this case, the preliminary experimental campaign towards optimization was held on a specific model (the same of the one on the right in Fig. 3), showing that in this case the result is not influenced by a single factor, but by a combination in particular of voltage and number of discharges. Low number of pulses and high voltage seems to be the best combination, but an extension of the work to different kinds of PCBs is needed, in particular based on the number of components, to generalize the results.

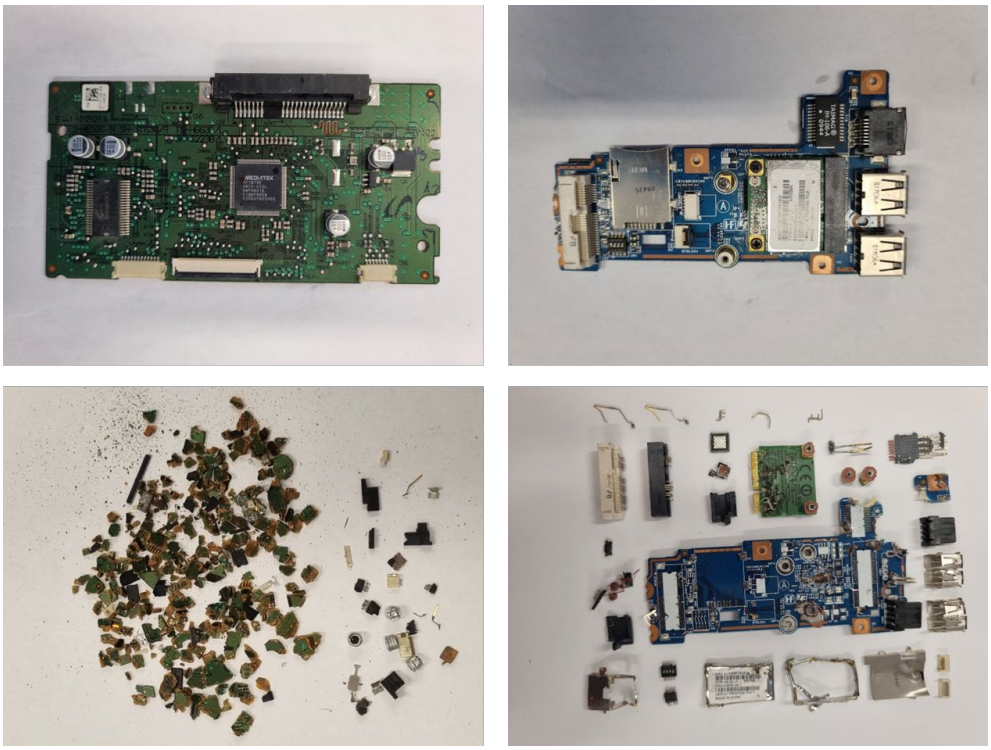


Fig. 3: Two different PCBs before (top) and after (bottom) the HVF treatment.

Conclusions

This study presented the results of a preliminary experimental approach aimed at recovering key metals and rare earths from commonly used products and components, thereby facilitating the implementation of the urban mining concept. Specifically, three products were selected for analysis: spark plugs, photovoltaic panels, and Printed Circuit Boards. Each product showed promising results, indicating that further in-depth research is not only warranted but also essential to develop robust circular solutions.

For spark plugs, the High-Voltage Fragmentation technique successfully separated the aluminum oxide ceramic insulator from the iridium electrode, yielding clean and pure liberated components suitable for direct recycling. Photovoltaic panels demonstrated effective detachment of metals from the plastic sheet, mainly influenced by the grid size, to achieve effective preconcentration of metals relative to glass particles. Lastly, PCBs treated with HVF resulted in efficient disassembly of components from the board with minimal or no damage, suggesting its potential as a viable disassembly technology for subsequent recycling stages. An in-depth study is necessary to achieve perfect disassembly without causing damage to either the components or the board on the base of the number of components.

For sure, next steps have to focus on the influence also on other process factors not considered in this work (as the distance between the electrodes and the dimension of the grid and not only its presence) and on the energy consumption of the process, which has been only partially considered.

References

[1] Information on https://www.solarpowereurope.org/insights/interactive-data/total-eu-27-solar-pv-capacity-a-growth-story

[2] Nain, P., & Anctil, A. (2024). End-of-life solar photovoltaic waste management: A comparison as per European Union and United States regulatory approaches. Resources, Conservation & Recycling Advances, 21, 200212.

[3] Information on https://www.eea.europa.eu/en/european-zero-pollution-dashboards/indicators/recycling-from-green-technology

[4] Szałatkiewicz, J. (2014). Metals content in printed circuit board waste. Pol. J. Environ. Stud, 23(6), 2365-2369.

[5] Information on https://earth.org/e-waste-recycling-rates-remain-dangerously-low-as-demand-for-electronic-devices-booms-un-report-reveals/

[6] Bluhm, H., Frey, W., Giese, H., Hoppe, P., Schultheiss, C., & Strassner, R. (2000). Application of pulsed HV discharges to material fragmentation and recycling. IEEE Transactions on Dielectrics and Electrical Insulation, 7(5), 625-636. https://doi.org/10.1109/94.879358

[7] Roux, M., Eguemann, N., Giger, L., & Dransfeld, C. (2013, March). High performance thermoplastic composite processing and recycling: from cradle to cradle. In Proceedings of the SAMPE 34th International Technical Conference, Paris, France (pp. 11-12).

[8] Rouholamin, D., Shyng, Y. T., Savage, L., & Ghita, O. (2014, June). A comparative study into mechanical performance of glass fibres recovered through mechanical grinding and high voltage pulse power fragmentation. In Proceedings of the ECCM16-16th European Conference on Composite Materials, Seville, Spain (pp. 22-26). 7

[9] Mativenga, P. T., Shuaib, N. A., Howarth, J., Pestalozzi, F., & Woidasky, J. (2016). High voltage fragmentation and mechanical recycling of glass fibre thermoset composite. CIRP annals, 65(1), 45-48. https://doi.org/10.1016/j.cirp.2016.04.107

[10] Diani, M., Torvi, S., & Colledani, M. (2024). Exploiting High Voltage Fragmentation to Enable Demand-Driven Recycling of End-of-Life Wind Blades. Procedia CIRP, 122, 837-842.

[11] Herdegen, J., Benner, W., Bokelmann, K., Hartfeil, T., & Gellermann, C. (2016). Separationsmethoden zur Aufarbeitung von metallhaltigen Verbundwerkstoffen.

[12] Song, B. P., Zhang, M. Y., Fan, Y., Jiang, L., Kang, J., Gou, T. T., ... & Zhou, X. (2020). Recycling experimental investigation on end of life photovoltaic panels by application of high

voltage fragmentation. Waste Management, 101, 180-187. https://doi.org/10.1016/j.wasman.2019.10.015

[13] Song, B. P., Zhang, M. Y., Fan, Y., Jiang, L., Kang, J., Gou, T. T., ... & Zhou, X. (2020). End-of-life management of bifacial solar panels using high-voltage fragmentation as pretreatment approach. Journal of Cleaner Production, 276, 124212. https://doi.org/10.1016/j.jclepro.2020.124212

[14] Zherlitsyn, A. A., Alexeenko, V. M., Kumpyak, E. V., & Kondratiev, S. S. (2022). Fragmentation of printed circuit boards by sub-microsecond and microsecond high-voltage pulses. Minerals Engineering, 176, 107340. https://doi.org/10.1016/j.mineng.2021.107340

[15] Ménard, Y., Bru, K., Touzé, S., Lemoign, A., Poirier, J. E., Ruffie, G., ... & von Der Weid, F. (2013). Innovative process routes for a high-quality concrete recycling. Waste management, 33(6), 1561-1565. https://doi.org/10.1016/j.wasman.2013.02.006

Work in progress and laboratories



Materials Research Proceedings 57 (2025) 626-630 https://doi.org/10.21741/9781644903735-73

An automatic system of handling and heating samples during dynamic hot compression tests

G. Soardi[1,a], C. Guerra[1,b], M. Seiti[1,c], A. Abeni[1,d*], A. Attanasio[1,e], E. Ceretti[1,f]

[1]Department of Mechanical and Industrial Engineering, Università degli Studi di Brescia, Via Branze 38, Brescia, 25123, Italy

[a]giuseppe.soardi@unibs.it, [b]costantino.guerra@unibs.it, [c]miriam.seiti@unibs.it, [d]andrea.abeni@unibs.it, [e]aldo.attanasio@unibs.it, [f]elisabetta.ceretti@unibs.it

Keywords: Mechanical Testing Equipment, Constitutive Models, Hot Compression Test

Abstract. The study describes an innovative system to minimize the effect of thermal gradient in hot compression tests for alloy characterization. The mechanism separates the sample from the tool by using a pneumatic handle with refractory terminals and heats the samples through induction. Once a uniform temperature distribution is achieved, the samples are positioned on the lower punch, and the compressions are performed. Tests on stainless steel validated the efficacy, enabling calibration of Hansel-Spittel constitutive model using Particle Swarm Optimization. Results demonstrate that the innovative system and the data elaboration algorithm improves the precision of flow stress, under several temperatures and strain rates up to 20 s^{-1}. This method can be employed to achieve material calibration, useful for the virtual simulation of the processes with Finite Element Method. This approach offers a robust, cost-effective alternative for material testing in hot plastic deformation processes.

Introduction

The Finite Element Method (FEM) is widely employed to simulate metal hot-forming operations, including rolling, forging, and extrusion. The accuracy of numerical simulations is significantly influenced by input factors such as friction conditions, contact modelling, and material characterization [1]. Flow stress models are crucial for precisely characterising material behaviour under different strain, temperature, and strain rate [2,3].

Experimental methods, such as isothermal hot compression tests, are commonly employed to build constitutive models. These models can be obtained with three methodologies: i) physically-based, which consider metallurgical mechanisms and require extensive calibration settings; ii) artificial neural networks (ANNs), which exploits machine learning algorithm for predictions without predefined equations; iii) phenomenological models, such as Hansel-Spittel, Johnson-Cook, and Arrhenius, which offer a balance between computational efficiency and accuracy, making them widely used in high-temperature forming simulations [4,5].

Independent from the methodology selected, the material behaviour at increased temperatures and high strain rates is significantly influenced by dynamic strain hardening. According to the strain rate specifications, different experimental systems can be selected. Servo-hydraulic presses are often employed for strain rates up to 10 s^{-1}, while strain rates higher than 1000 s^{-1} usually require Split Hopkinson Pressure Bar (SHPB) [6]. Although successful, compression tests frequently encounter temperature gradients due to heat transfer and friction, which compromise the precision of flows stress characterization [7].

Therefore, this study introduces a novel, automated, controlled method for sample handling and heating, aimed at ensuring constant temperature distribution during hot compression experiments. The technology is validated through experiments on AISI 304 stainless steel, chosen due to the challenges of electromagnetic induction heating, which causes thermal gradients at the contact surface. Experimental data are used to calibrate Hansel-Spittel model through Particle Swarm

Content from this work may be used under the terms of the Creative Commons Attribution 3.0 license. Any further distribution of this work must maintain attribution to the author(s) and the title of the work, journal citation and DOI. Published under license by Materials Research Forum LLC.

Materials Research Proceedings 57 (2025) 626-630 https://doi.org/10.21741/9781644903735-73

Optimisation. Once the model is calibrated on the experimental data, it can be easily implemented in commercial FEM software to simulate hot plastic deformation processes involving the material.

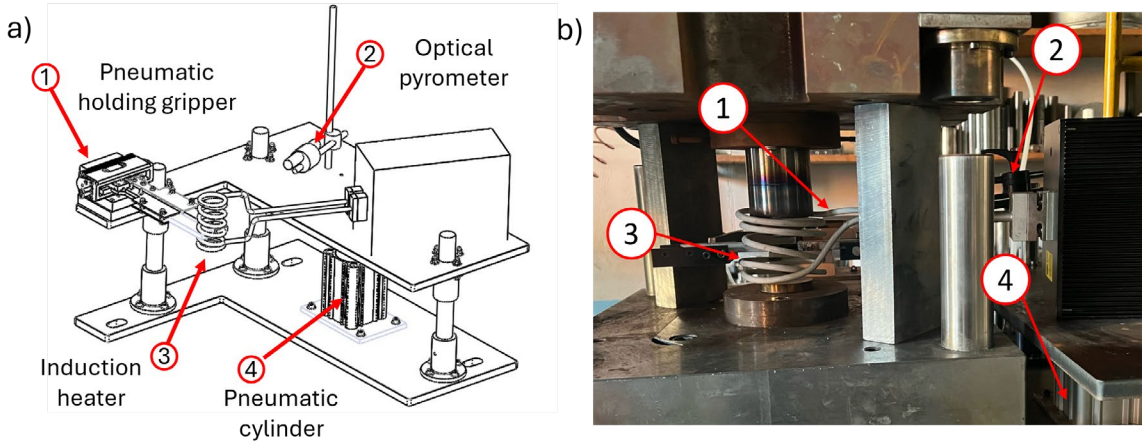


***Fig. 1**. Representative (a) technical drawing and (b) figure of the developed system.*

Materials and Methods

This section describes the methodology used to characterize AISI 304 through the proposed high-speed hot compression test system. The samples were prepared by cutting a Ø10 mm bar, achieving cylinders with the same diameter and a height equal to 30 mm. A 100-ton hydraulic press was employed, equipped with four loadcells (Gefran CM K30M) and a linear potentiometer to measure the upper die displacement. A data acquisition system recorded signals with a sampling rate of 2 kHz. An induction heater with a feedback-controlled optical pyrometer was used to ensure rapid and contact-free sample heating. To minimize thermal gradients, an automated sample-handling system was then developed. This innovative system, visible in Fig. 1, featuring a pneumatic gripper and lifting mechanism, prevents heat conduction between the specimen and the lower plate, ensuring homogeneous heating. The functioning can be summarized as follows:

1. The cold sample is positioned on the lower punch, the holding gripper is open, and the pneumatic cylinder is lowered
2. The holding gripper is closed, and the sample is grabbed with the terminals built in a cement-based material with low conductivity and invisible to the magnetic field.
3. The pneumatic cylinder lifts the plate with the gripper, the induction heater and the pyrometer, raising the sample from the lower punch (no contact).
4. The induction system heats the sample to the target temperature with the feedback control of the pyrometer.
5. Once the temperature is achieved, the pneumatic cylinder lowers the plate, and the sample returns in contact with the lower punch.
6. Immediately after, the holding gripper is open with a distance higher than the upper punch diameter, which descends, and the compression occurs.

A full factorial 3^2 experimental plan was performed by testing three temperatures (900, 1050, and 1200 °C) and three compression speeds which were selected in order to obtain the following average strain rates of: 2.4, 7.2 and 15.8 s^{-1}. The selected temperatures and strain rates represent typical values employed in hot plastic deformation processing of AISI 304, especially in forging and hot rolling. Each test was repeated three times to statistically validate the procedure for a total amount of 27 compression tests.

The Hansel-Spittel constitutive model (as depicted in Eq. 1) was calibrated by using the Particle Swarm Optimization (PSO) stochastic algorithm. A population of 100 particles and 2000 iterations

Materials Research Proceedings 57 (2025) 626-630 https://doi.org/10.21741/9781644903735-73

was employed to find the optimized set of Hansel-Spittel constants. The lower limits of the model coefficients were set to -1, while the upper limits of coefficient A was set to 10000 while the coefficients m_1, m_2, m_3, m_4 were set to 1.

$$\sigma(\varepsilon, \dot{\varepsilon}, T) = Ae^{m_1 T} \varepsilon^{m_2} \dot{\varepsilon}^{m_3} e^{\frac{m_4}{\varepsilon}} \quad \text{Eq. (1)}$$

Results

Fig. 2 shows a morphological comparison between a sample heated in contact with the lower plate and a sample heated with the proposed system. In Fig. 2(a) is visible as the thermal gradient affected material deformation, while in Fig. 2(b) the shape of the compressed sample is uniform as a consequence of a constant temperature distribution. The experimental stress-strain values were fitted in the Hansel-Spittel model, and the optimized coefficients determined with PSO algorithm are visible in Table 1.

Table 1. *Optimized coefficients of the Hansel-Spittel model.*

A	m_1	m_2	m_3	m_4
10838	-0.00409	-0.257	0.161	-0.107



(a) (b)

Fig. 2. *Samples compressed, without using the manipulation system (a) and with the system (b).*

Fig. 3 offers an example of the computed stress versus strain for T = 900°C. Analogue charts were obtained for the other temperatures. The complete dataset was subsequently used to fit the Hansel-Spittel model.

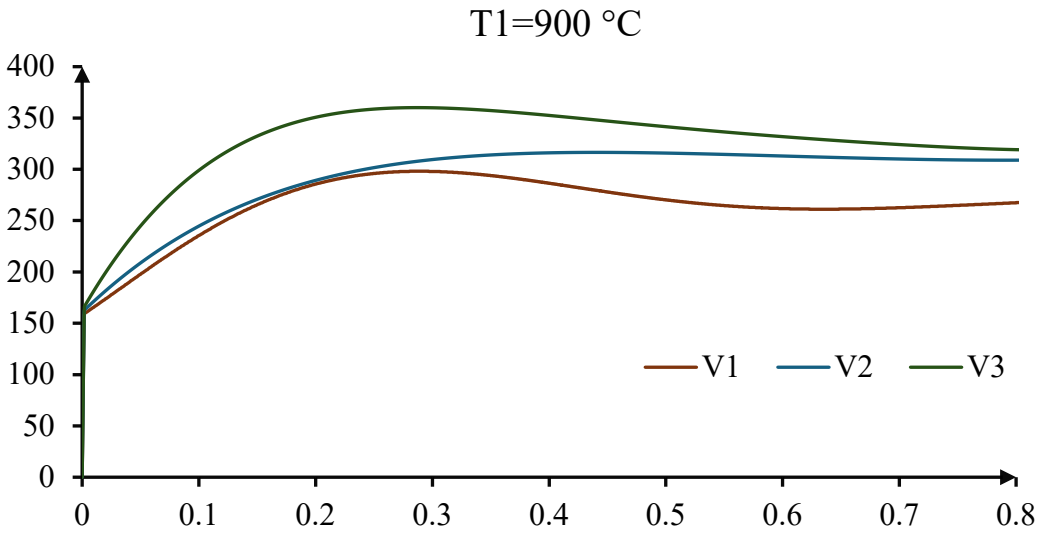


Fig. 3. *Flow stress data for T = 900°C with three different compression speeds.*

Materials Research Proceedings 57 (2025) 626-630 https://doi.org/10.21741/9781644903735-73

Fig. 4 shows the calibrated Hansel-Spittel model, which demonstrates accurate predictions for maximum stress. The flow stress increases up to a plastic strain of 0.3 and subsequently it slightly decreases. The strain rate influence decreases at higher temperatures. Particularly high temperatures significantly soften the material, whereas strain rate variations have a limited effect.

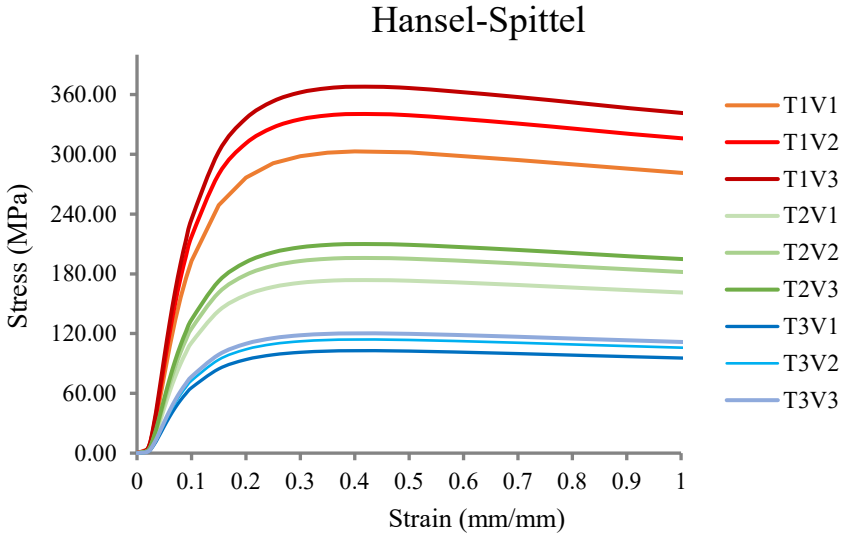


Fig. 4. *Calibrated flow stress model at T=900 °C, T=1050 °C and T=1200°C, by changing the strain rates.*

Preliminary Conclusion

This work presents the development of an innovative pneumatic handling system designed to enhance the reliability of high-speed hot compression tests, particularly for metallic alloys such as AISI 304 stainless steel. The system addresses the issue of thermal gradients induced by the contact between the sample and the dies during the heating phase. By avoiding contact during the heating phase until the target temperature is reached, the proposed solution ensures improved thermal homogeneity, increasing the accuracy of the mechanical characterization. Hansel-Spittel constitutive model was calibrated employing a Particle Swarm Optimization algorithm, achieving findings which confirm that the proposed model effectively captures the material response under varying thermal and strain rate conditions. The resulting model can be added to commercial Finite Element software to simulate thermo-mechanical processes considering the actual properties of the workpiece material. Despite being a work in progress, the proposed methodology aims to develop a cost-effective alternative to commercial testing machines, as it can be integrated with existing industrial hydraulic or mechanical presses.

Acknowledgments

The authors of this paper gratefully acknowledge Metal Work S.p.A. for providing the pneumatic components.

Funding

The authors acknowledge the MICS (Made in Italy – Circular and Sustainable) Extended Partnership (Next Generation EU (Italian PNRR – M4 C2, 1.3–D.D.1551.11-10-2022, PE00000004 CUP D73C22001250001).

References

[1] Y. Wang, J. Peng, L. Zhong, F. Pan, Modeling and application of constitutive model considering the compensation of strain during hot deformation, Journal of Alloys and Compounds 681 (2016) 455-470. https://doi.org/10.1016/j.jallcom.2016.04.153

[2] Y. C. Lin, M.S. Chen, J. Zhang, Modeling of flow stress of 42CrMo steel under hot compression, Materials Science and Engineering A 499 (1-2) (2009), 88-92. https://doi.org/10.1016/j.msea.2007.11.119

[3] A. Chamanfar, M.T. Alamoudi, N.E. Nanninga, W.Z. Misiolek, Analysis of flow stress and microstructure during hot compression of 6099 aluminum alloy (AA6099), Materials Science and Engineering: A 743 (2019) 684-696. https://doi.org/10.1016/j.msea.2018.11.076

[4] X. Chen, Y. Du, K. Du, T. Lian, B. Liu, Z. Li, X. Zhou, Identification of the Constitutive Model Parameters by Inverse Optimization Method and Characterization of Hot Deformation Behavior for Ultra-Supercritical Rotor Steel, Materials 14 (8)(2021) 1958. https://doi.org/10.3390/ma14081958

[5] P. Cheng, D. Wang, J. Zhou, S. Zuo, P. Zhang, Comparison of the Warm Deformation Constitutive Model of GH4169 Alloy Based on Neural Network and the Arrhenius Model, Metals 12 (9) (2022) 1429. https://doi.org/10.3390/met12091429

[6] J.H. Guo, Y.J. Sun, Q. Liu, S. Ma, J.W. Yang, X.D. Zhang, The study on plastic flow behavior and constitutive model of h96 brass alloy under compression, Journal of Physics: Conference Series 1721 (2021) 012049. https://doi.org/10.1088/1742-6596/1721/1/012049

[7] B. Song, B.R. Antoun, W. Chen, Dynamic High-temperature Compressive Response of A 304L Steel, SEM Annual Conference, Springfield, MA, June 3-6, 2007.

Materials Research Proceedings 57 (2025) 631-638 https://doi.org/10.21741/9781644903735-74

A technological analysis and prototype design for efficient and flexible stacking processes

Sen BAI[1,a*], Nicla FRIGERIO[1,b], Daniela FONTANA[2,c] and Andrea MATTA[1,d]

[1]Politecnico di Milano, Dipartimento di Meccanica, via G. la Masa, 1, 20156 Milano, Italy

[2]COMAU spa, via Rivalta, 30, 10095, Grugliasco (TO), Italy

[a]sen.bai@polimi.it, [b]nicla.frigerio@polimi.it, [c]daniela.fontana@comau.com, [d]andrea.matta@polimi.it

Keywords: Machine Tools & Automation, Process Planning & Control, Battery Cell Stacking Process

Abstract. The stacking process is a critical bottleneck in EV battery manufacturing with requirements for throughput, quality, and flexibility, especially with the increase of e-mobility and transition to solid-state batteries. This paper presents the analysis of the stacking process from a technological perspective to address industrial challenges and to support the development of more efficient and adaptable manufacturing solutions. Grounded on a solid literature review, the first outcome of the project is the design of a stacking prototype, developed in alignment with industrial targets. The prototype not only serves as a basis for improving current stacking process performance but also provides a platform for future research into key aspects. Central to this work is the investigation for the relationships between key parameters and stacking performances under sub-processes such as gripper speed, suction force, and motion trajectory etc. to enable fast, continuous stacking operations.

Introduction

With the development of electrical mobility, the demand for batteries keeps expanding and has reached 160 GWh of cell energy production in 2018 and is expected to exceed 1000 GWh by 2030 [1]. To develop high-performance batteries with less production cost becomes the main challenge in this field [2]. The transition from traditional Lithium-ion (Li-ion) to Solid-State Batteries (SSBs) is key to further improve energy density while more efficient manufacturing processes is fundamental for cost reduction. This paper targets more efficient manufacturing processes, to produce a battery cell composed by a stack of anodes and cathodes intermitted by a separator. Multiple cells are assembled into battery modules, then being connected together into a battery pack [3]. Focusing on the production of a battery cell, the process is divided into three main stages: electrode manufacturing, cell assembly, and cell finishing [4]. Electrode manufacturing creates coils of anode and cathode, later assembled into a stack or a jelly roll, packed and finished with activation and aging. For Li-ion battery manufacturing, the cell assembly stage takes around 20% of costs and the stacking process requires 54% of cell assembly costs [4] and it is expected to grow in the transition toward solid-state batteries. Key manufacturing processes in the cell assembly stage are *electrode cutting*, where laser application are breakthrough technologies, and electrode stacking, known as a critical bottleneck in EV battery manufacturing [5]. Further, stacking precision affect battery capacity since any misalignment in the stack may lead to discharge capacity reduction [6].

This paper presents the analysis of the *stacking process* from a technological perspective to address raising industrial challenges and to support the development of more efficient and adaptable manufacturing solutions. A battery stacking prototype is designed in alignment with industrial targets and to provide a platform for future research into key aspects of the process.

Content from this work may be used under the terms of the Creative Commons Attribution 3.0 license. Any further distribution of this work must maintain attribution to the author(s) and the title of the work, journal citation and DOI. Published under license by Materials Research Forum LLC.

Materials Research Proceedings 57 (2025) 631-638 https://doi.org/10.21741/9781644903735-74

In the literature, there are three main methods to assemble the stack or jelly roll, each with different features: *winding*, *z-folding*, and *single sheet stacking*. Winding, the fastest and most developed and standardized method in industry [7], is a continuous method used for cylindrical and small prismatic cells that combine the anode, cathode and separator into an electrode roll. Z-folding is a semi-continuous stacking method used for prismatic and pouch cells that insert anode and cathode alternately into a z-shaped continuous separator.

Recent literature focuses on process parameter optimization. For example, the particle emission during electrode gripping are evaluated in [8] to suggest the most appropriate gripper principle. Material-specific boundaries for bending stress during winding and z-folding is studied in [9]. The design of alternative feeding processes to supply electrode for the stacking process is discussed in [10,11]. While focusing on parameter optimization, the overall view of the process is not the focus of those papers. Further, literature rarely presents both digital and physical counterparts of the production system, thus showing a lack of physical validation in many cases. For example, the model-based design approach for stacking optimization in [12], the simulation from coating to stacking in [13], and the study on Z-folding speed effect on the web tension of electrodes in [14] are not validated with physical experiments.

Single sheet stacking assembles single sheets of anode, cathode and separator (Fig. 1). Despite it is currently underdeveloped and slower with respect to the other stacking methods, single sheet stacking has the highest flexibility in terms of electrode materials and shapes, and is considered the most promising method for SSB and it is spreading as prototypal method both in academia and industry. Z-folding and winding could still be applied in SSB manufacturing, but only with flexible materials (e.g. polymeric electrolytes). Most of the research on SSB stacking focuses on material and cell development. Also, the presence of the separator may not be necessary for SSBs, since the solid electrolyte, acting also as a separator, can be deposited directly on the electrode surface. Nonetheless, new studies on SSB single-sheet stacking are available in recent literature. For example, a material-flexible single sheet handling system is developed and validated with a physical prototype in [15] and a cell assembly prototype for SSB stacking is developed in [16].

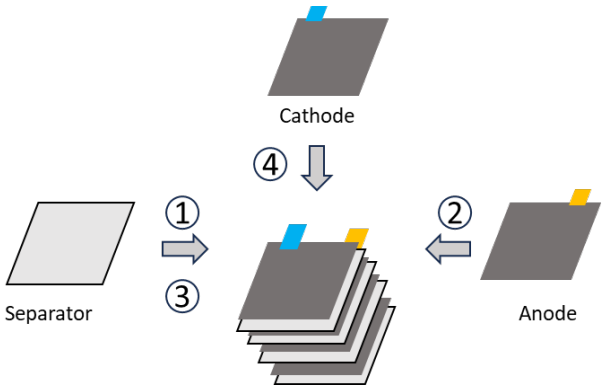


Figure 1 The mechanisms of single sheet stacking with numbered order of the layers.

Analysis and decomposition of the stacking process

The stacking process can be decomposed into several sub-processes that are electrode feeding, electrode handling (i.e. picking and transferring), visual inspection, electrode placing and electrode fixing. The last two sub-processes may be considered as the actual stacking phase. Each sub-process has different objectives, requirements and challenges due to the effects they may have on the final cell. First of all, damages of the electrode coating may reduce battery capacity and, similarly, electrode deformation may reduce effective contact areas or may cause coating-anode detachment. In addition, as electrodes are stacked together, any misalignment between electrode

layers may reduce battery charge/discharge capacity. As worst case, severe misalignment may cause contact between anode and cathode which will lead to shortcut. In details:

- *Electrode feeding* is to feed the electrode flat and tight to the picking location after single sheet of anode and cathode are notched and cut. This sub-process can be operated by continuous conveyors or by creating pre-set electrode magazines. The accuracy of the electrode location may affect the picking process and, to further enhance the challenge, the coordination between the feeding and the electrode picking shall be executed at high speed.
- *Electrode handling* is to pick the electrode from the picking base by a gripper and to transfer it to the stack location. A gentle picking is necessary to maintain electrode integrity avoiding coating damages and electrode deformation. A firm picking avoid electrode slitting and flapping during complex motion and allows a higher velocity. Electrode picking, as feeding, may affect electrode integrity and it is strongly related to stacking cycle time.
- *Visual inspection* occurs during the electrode transferring and serves to assess the misalignment of electrode on the gripper in terms of translation and rotation with respect to the target location so that it is possible to adjust the position. The challenges of the sub-process are to design the visual detection system to have an accurate image of the electrode while in motion, to quickly elaborate the image, and to control and actuate the proper adjustment. Visual inspection may affect the stacking cycle time and the stack misalignment.
- *Electrode stacking* is to release the electrode onto the stacking base and to fix the new layer over the stack while maintaining the position of the previous layers. This sub-process requires the coordination between the handling system and the stack base. The coordination between the placing motion and the finger motion shall be executed gently, without bending the electrodes and avoiding collisions and electrode edge damages.

As described, the stacking accuracy is influenced by many factors, e.g. feeding accuracy, gripping accuracy, slide during motion, placing accuracy, electrode deformation etc.

Prototype design and modularity

The prototype, schematized in Fig. 2 includes a modular structure where each module is designed at support of dedicated research questions and experimental activities. The six modules are: (1) the electrode picking base, (2) the linear handling system, (3) the visual inspection system, (4) the stacking base, (5) the rotating handling system and (6) the secondary stack area. In addition, a camera at the top of the stacking base, not represented in the figure, will enable the evaluation of position accuracy. The latter camera and lighting are designed to measure electrode position with the precision required by the product on an area of around 200 mm x 100 mm.

In the electrode picking base (module 1), the electrode feed is operated by pre-set electrode magazines, one for each material. Furthermore, the modular structure of the prototype allows the integration of new modules. The handling system is composed by a vacuum gripper and a linear rail that enables the transferring of electrode from module 1 to module 4. Vacuum grippers are considered the best choice for electrode handling in battery manufacturing for their low-contact gripping force and gentle handling of thin and fragile materials [8]. Custom grippers and flexible grippers shall be evaluated to understand which solution is the best for a certain material and application. An example of flexible gripper with vacuum cups is in Fig. 3. The visual inspection system (module 3) is equipped with high-speed camera and a suitable vision lighting. The stacking base is equipped with a set of fingers to maintain the stack in place and the fingers have adjustable stroke to evaluate different configurations while placing the electrodes. In the rotating handling system (module 5), the vacuum gripper is mounted on a rotating axis to evaluate more complex handling trajectories from module 1 to the secondary placing area (module 6). The secondary placing area does not include fixing devices.

Materials Research Proceedings 57 (2025) 631-638 https://doi.org/10.21741/9781644903735-74

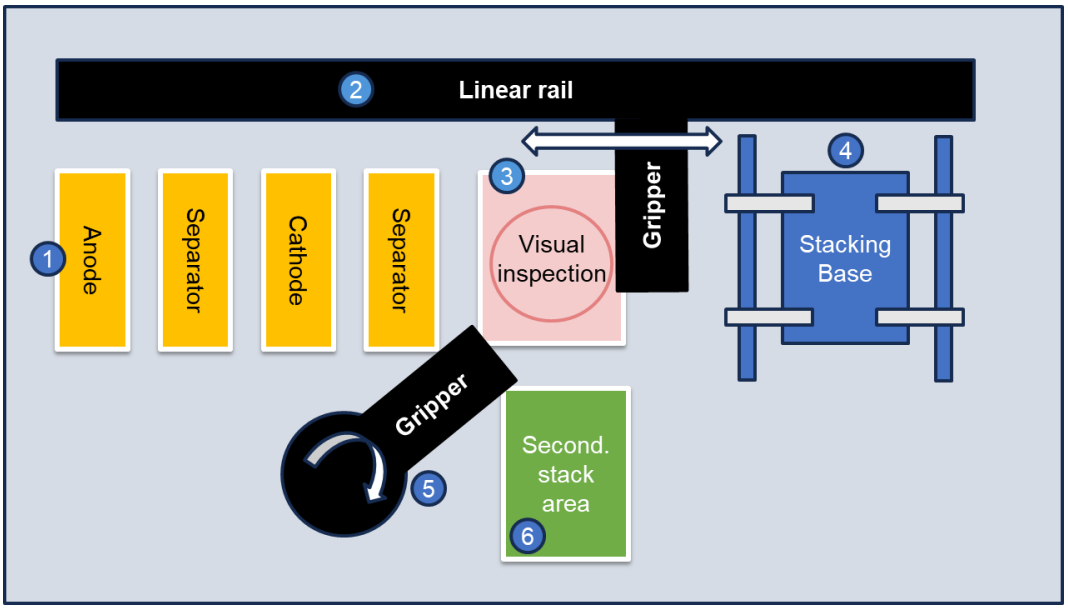


Figure 2 Prototype layout and modular structure (Modules 1 to 5 described in text)

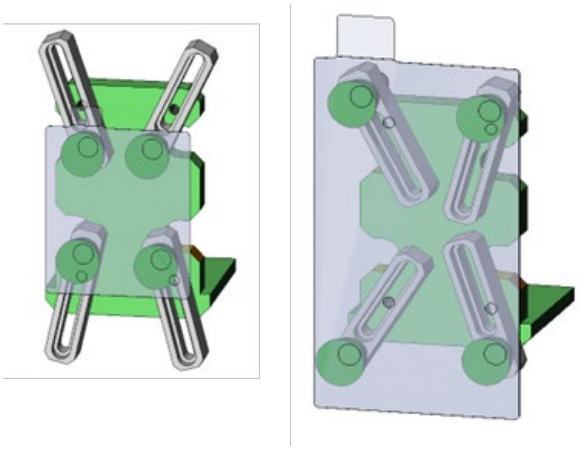


Figure 3 Example of flexible vacuum gripper handling different electrode sizes

The described modules have been selected and designed as validation environment for several stacking solutions, according to specific research and industrial challenges related to the stacking process. In Table 1, each module is linked with demonstration activities and relevance focusing on the critical aspects of the battery stacking process, such as process optimization, quality inspection, accuracy and flexibility.

Grasping Subprocess Evaluation. Combining the first two modules (modules 1 and 2) it is possible to assess the grasping process with static feeding conditions. Further, to study the interaction between the gripper and the electrode serves at understanding stress and deformation on the electrode. As an example, several grippers are evaluated in [8] and the air-flow effect on the electrode and gripper is the focus of [17].

Linear and Rotating Handling Movements. The two handling modules, both equipped with vacuum grippers, ensure the pick-and-place of electrodes, evaluating how electrodes are transported through linear (module 2) and rotational (module 5) movements. Handling motions face technological challenges and trade-offs between speed and forces, thus affecting the overall cycle time of the stacking significantly.

Flexible Stacking and Electrode Damage Prevention. Excessive forces and friction during stacking can damage the surface and can cause deformation [18]. The capacity of managing materials with different properties and responses to variable stress condition is key to design and evaluate flexible stacking solution. Flexibility is increasing importance with SSB.

Layer Placement and Accuracy Assessment. The stacking (modules 2 and 4) must assure a proper alignment and positioning of electrodes. Indeed, stacking accuracy may significantly affect the electro-chemical properties of batteries [6]. By the use of the vision (module 3), a proper adjustment of handling motions ensures accurate electrode placement [19].

Table 1 Module relevance and demonstration activity

Modules	Activity	Relevance
1 + 2	Evaluate grasping subprocess under static feeding.	Ensure the grasping of layers before handling and stacking. Ensure the electrode placing base can position the electrode into a specific pose (manual positioning).
2 5	Evaluate the linear and rotating handling movements.	Ensure Pick and Place of electrodes.
2 + 4	Evaluate stacking. Avoid/Reduce electrode bending/damage during fixing.	Achieve the declared flexibility of prototype.
2 + 4 5 + 6	Evaluate placement of layers.	Achieve the declared flexibility of prototype in the proposal and evaluate accuracy.
4	Adjust finger position and optimize finger trajectory.	Achieve the declared flexibility of prototype.

In Table 2 a similar approach is followed for sensors and devices. The primary focus is on control, electrode integrity, and quality assessment by the use of high-speed cameras, and ad-hoc measurement systems. First, a high-speed camera (module 3) enables control of handling and placing alignment. The controllable vacuum generator regulates the grasping force during handling. To detect layer detaching phenomena serves for process optimization and improvement of gripping reliability. Layer position assessment evaluates the quality and accuracy of stacked layers to optimize, verify and validate layer alignment and stacking quality, which are used for the overall performance of the battery cell. An external measurement system can be used to evaluate surface damages caused by grippers and fingers.

Table 2 Required devices and relevance

Module	Required Device	Activity	Relevance
3	High-speed camera	Evaluate position to control handling and placement	Development of the control adjustment
2+5	Controllable vacuum generator	Enable the control of the grasping force (suction force)	Analysis of gripper/electrode interaction under different forces.
2	Action camera	Identification of possible detaching phenomena between layer and gripper during handling	Layer detaching phenomena from gripper in movement
--	*External measurement systems*	Evaluate surface damages on single electrode due to grippers and fingers	Electrode surface quality evaluation
4	Measuring system at stacking base	Evaluate quality of the layers	Layer/Stack position accuracy and quality evaluation

A model-based approach for stacking process.

The long-term objective of this project is to develop a model-based approach for analyzing the battery cell stacking process, focusing on how different sub-processes influence key performance indicators (KPIs). For example, to model the motion during electrode placement over the stack and to model the gripper-electrode interaction can support the evaluation of electrode damages due to stress conditions. Such evaluation can be executing in static or dynamic simulation SW. Results from analytical models and simulation models can be integrated with experimental results to create surrogate models tailored to each use case. Discrete Event Simulation models may help in understanding how the stacking process may affect the performance of the overall cell assembly stage. This approach enables the evaluation of battery quality (i.e. the main KPI) as related to electrode integrity (e.g., surface damage, contamination, edge damage) and stacking accuracy (e.g., slide during motion, misalignments). Furthermore, process simulators and digital twins can assess how each sub-process contributes to overall process duration providing insights for line balancing and operative management of the manufacturing line. Indeed, a model-based approach enables predictive analysis, where different input parameters, e.g. electrode material properties and geometry, gripping force, handling speed, stack properties etc.) can be modified before the actual physical validation. This approach will help in identifying optimal process parameters for improved processes and predicting the impact of design modifications before implementation in a real production setting. This approach will provide a modular evaluation where different sub-process models can be validated independently and then integrated into a larger multi-phase digital twin.

With this idea in mind, we defined a series of possible Proof-Of-Concept activities and experiments as aligned with the description in Table 1 and Table 2. After the first testing of the prototype, ensuring that the overall stacking process is valid, the evaluation of layer position accuracy and stack accuracy is of high relevance. The evaluation of process parameter effects will support process improvement and optimization activities. A key challenge will be the position adjustment, for example applying a closed-loop control logic for the adjustment to reduce the misalignment.

As for the investigation of quality (as electrode surface integrity), the response of interest is divided into deformation and surface damage and, on both of them, the effect of gripper, motion, placement and fingers may have will be investigated. How process parameters may affect the quality is part of these activities, for example, how different handling speeds require different gripping forces, thus stress on the electrode.

Beside quality, process speed is one of the most important industrial requirements. However, high speed can cause electrode detachment from the gripper and gives less time to control layer accuracy.

Further, flexibility is an important factor of competitiveness in single-sheet stacking. Our target is to investigate the flexible, fast process with damage-free stacking. The prototype has been designed to support a series of activities to evaluate the stacking flexibility by adjusting the size and materials of electrodes.

Work-In-Progress and Future Directions

In this paper, the objective of the research project related to EV battery manufacturing, specifically on cell stacking, is presented and motivated. The first outcome of the activities is the development of a single-sheet stacking prototype designed based on key parameters influencing the stacking and designed for modular experimental validation. A series of possible demonstration activities aimed at evaluating stacking accuracy, electrode integrity, and process flexibility is described. Further, the key research questions underlined in the project are as listed in the following:

- What is the significance and the influence of stacking parameters on battery quality? To model and estimate the relationship between processing parameters, stacking process

alternatives on accuracy, electrode integrity, and process flexibility will be necessary in future research.

- What are the trade-offs between experimental validation and simulation-based modeling in battery stacking research? To assess the cost-effectiveness, accuracy, and scalability of physical experiments versus computational modeling builds the foundation of DT usage in this field.
- How different requirements, such as different materials, electrode and stack sizes, and configurations of the stacking process would influence the cell assembly performance in mass production? To accurately estimate the performance at system level increases responsiveness to industrial demand changes.

These activities and research questions form the foundation for the development of Digital Twins (DTs) and models for different sub-processes of the stacking process, including the impact of electrode materials and their mechanical characteristics. This modelling approach is aimed to provide estimates on how different process parameters may influence cell quality and assembly performance, allowing for predictive analysis and optimization. The research line aims to bridge the gap between research and industrial applications, improving process efficiency and reducing industrialization effort in the transition toward SSB.

Developed solution will be tested and validated through the Proof-of-Concept prototype described in this paper, laying the groundwork for integrating this technology into an industrial mass production dedicated to next-generation cells. As part of the research line, new solutions for electrode stacking will be developed and tested to meet the productivity and quality requirements of mass production. Future research should focus on exploring the relationship between stacking parameters and stacking quality. Our planned experiments will be guided by the critical factors identified in our analysis. Once the prototype is fully operational, multiple parameters, such as electrode materials, gripper properties, stacking speed, and control logic, can be evaluated.

Acknowledgement
The authors would like to express their sincere gratitude to COMAU S.p.A. for the valuable support and collaboration in this research. The activities are partially included in Project “CELl Laser cutting & Assembly: flexible lithium-ion battery cell production” of CUP H29J24000000008 e COR 17182154 from MADE Competence Center 4.0 co-funded by Next Generation Eu.

References

[1] C. Pillot, “Impact of the xEV Market growth on Lithium-Ion Batteries and Raw Materials Supply 2019-2030.” Avicenne Energy, 2020.

[2] B. G. Pollet, I. Staffell, and J. L. Shang, “Current status of hybrid, battery and fuel cell electric vehicles: From electrochemistry to market prospects,” *Electrochimica Acta*, vol. 84, pp. 235–249, 2012, doi: https://doi.org/10.1016/j.electacta.2012.03.172

[3] A. Kampker, H. H. Heimes, C. Offermanns, J. Vienenkötter, and T. Robben, “Framework and Classification of Battery System Architectures,” *World Electr. Veh. J.*, vol. 14, no. 4, 2023, doi: https://doi.org/10.3390/wevj14040088

[4] D. Küpper, K. Kuhlmann, S. Wolf, C. Pieper, G. Xu, and J. Ahmad, “The future of battery production for electric vehicles,” Boston Consulting Group: Boston, MA, USA, 2018.

[5] S. Michaelis *et al.*, *Roadmap Battery Production Equipment 2030 - Update 2023*. 2023.

[6] R. Leithoff, A. Fröhlich, and K. Dröder, “Investigation of the influence of deposition accuracy of electrodes on the electrochemical properties of lithium-ion batteries,” *Energy Technol.*, vol. 8, no. 2, p. 1900129, 2020, doi: https://doi.org/10.1002/ente.201900129

[7] I. Markets, “The guideline for battery show.” 2023. [Online]. Available: https://www.imeeventscalendar.com/en/home.html

[8] A. Fröhlich, R. Leithoff, C. von Boeselager, K. Dröder, and F. Dietrich, “Investigation of particulate emissions during handling of electrodes in lithium-ion battery assembly,” *Procedia CIRP*, vol. 78, pp. 341–346, 2018, doi: https://doi.org/10.1016/j.procir.2018.08.322

[9] A. Schilling, J. Schmitt, F. Dietrich, and K. Dröder, “Analyzing Bending Stresses on Lithium-Ion Battery Cathodes induced by the Assembly Process,” *Energy Technol.*, vol. 4, no. 12, pp. 1502–1508, 2016, doi: https://doi.org/10.1002/ente.201600131

[10] M. Baumeister and J. Fleischer, “Integrated cut and place module for high productive manufacturing of lithium-ion cells,” *CIRP Ann.*, vol. 63, no. 1, pp. 5–8, 2014, doi: https://doi.org/10.1016/j.cirp.2014.03.063

[11] M. Aydemir, A. Glodde, R. Mooy, and G. Bach, “Increasing productivity in assembling z-folded electrode-separator-composites for lithium-ion batteries,” *CIRP Ann.*, vol. 66, no. 1, pp. 25–28, 2017, doi: https://doi.org/10.1016/j.cirp.2017.04.096

[12] C. von Boeselager *et al.*, “Model-Based Design and Experimental Evaluation of a High-Throughput Electrode Feeding and Stacking Process,” *Energy Technol.*, vol. 11, no. 5, p. 2200687, 2023, doi: https://doi.org/10.1002/ente.202200687

[13] G. Reinhart *et al.*, “Research and demonstration center for the production of large-area lithium-ion cells,” in *Future Trends in Production Engineering: Proceedings of the First Conference of the German Academic Society for Production Engineering (WGP), Berlin, Germany, 8th-9th June 2011*, Springer, 2013, pp. 3–12

[14] K. Husseini, L. Boschert, S. Schabel, and J. Fleischer, “Modeling machine-side influences on the Z-Folding process of battery cells,” *Prod. Eng.*, vol. 18, no. 3, pp. 615–623, 2024.

[15] A. Fröhlich, D. Gresens, B. Vervoort, and K. Dröder, “Design and Evaluation of a Material-adapted Handling System for All-Solid-State Lithium-Ion Battery Production,” *Procedia CIRP*, vol. 93, pp. 143–148, 2020.

[16] A. Fröhlich, S. Masuch, and K. Dröder, “Design of an Automated Assembly Station for Process Development of All-Solid-State Battery Cell Assembly,” *Ann. Sci. Soc. Assem. Handl. Ind. Robot. 2021*, p. 51, 2022, doi: https://doi.org/10.1007/978-3-030-74032-0_5

[17] R. Schimanek, M. Aydemir, A. Müller, and F. Dietrich, “Flow Modeling for Vacuum Pressure-Based Handling of Porous Electrodes of Lithium-Ion Batteries,” in *MHI Colloquium*, Springer International Publishing Cham, 2022, pp. 305–315.

[18] W. Zaman and K. B. Hatzell, “Processing and manufacturing of next generation lithium-based all solid-state batteries,” *Curr. Opin. Solid State Mater. Sci.*, vol. 26, no. 4, p. 101003, 2022, doi: https://doi.org/10.1016/j.cossms.2022.101003

[19] C. von Boeselagera, S. Vogta, C. Wackera, and K. Drödera, “Enhanced Deposition Accuracy for Battery Electrodes in a Novel High-Speed Stacking Process,” *Procedia CIRP*, vol. 127, pp. 86–91, 2024.

Materials Research Proceedings 57 (2025) 639-646 https://doi.org/10.21741/9781644903735-75

Development of a repair strategy for a thin aerospace component with dot-by-dot deposition approach

Gianni CAMPATELLI[1,a *], Gustavo H.S.F.L. CARVALHO[1,b] and Paolo C. PRIARONE[2,c]

[1]Department of Industrial Engineering, University of Florence, Via di Santa Marta 3, 50139 Firenze, Italy

[2]Department of Management and Production Engineering, Politecnico di Torino, Corso Duca degli Abruzzi 24, 10129 Torino, Italy

[a]gianni.campatelli@unifi.it, [b]gustavo.carvalho@unifi.it, [c]paoloclaudio.priarone@polito.it

Keywords: Wire Arc Additive Manufacturing (WAAM), Repair, Environmental Impact

Abstract. This study presents a repair strategy for an aerospace component manufactured from a 2000-series aluminium alloy. Wire Arc Additive Manufacturing (WAAM) with a dot-by-dot deposition approach was applied to mitigate the heat input and minimise distortion, enabling the reconstruction of thin-walled features with satisfactory surface finish and accuracy. The four-step process comprises the removal of damaged material, the reference geometry definition, the new material deposition, and the finish machining. First, the research focused on determining the most effective surface preparation methods and on optimising deposition parameters and strategies to minimise the occurrence of porosity, excessive melting, and humping during the repair of thin ribs, which have been identified as geometrically-critical features. Second, a preliminary environmental assessment was conducted to evaluate the carbon footprint associated with the proposed repair solution.

Introduction

The transition to more environmentally friendly production methods is essential for the sustainable growth of the global economy. The European Union has established a comprehensive framework for sustainable development, resulting in the European Commission circular economy action plan (CEAP). In a circular economy, resources are used for as long as possible, maximising their value before products and materials are recovered and regenerated at the end of their life cycle. From a practical standpoint, retaining a product within the value chain largely depends on approaches such as reuse, repair, and remanufacturing. Repair involves mending or restoring damaged or worn products to extend their useful life, thereby preventing waste, reducing the demand for new items, and conserving resources and energy. The distinction between repair and remanufacturing lies in the extent of restoration: repair focuses on restoring the functionality of a product or component after a fault or wear, without necessarily returning it to a like-new condition, which is an objective that characterises remanufacturing [1]. Repairing metal components is particularly advantageous due to their substantial production costs in terms of materials and energy consumption. Unlike plastic parts, metal components can often be restored to their original quality without any loss in performance [2]. Moreover, the repair of high-value metal parts has proven to be economically viable [3], particularly in sectors such as aerospace, oil and gas [4, 5], as well as in the production of moulds and dies [6]. The restoration of metal components requires a technique capable of reconstructing their damaged or worn geometrical features, a task made feasible by advances in the field of Additive Manufacturing (AM). Nevertheless, the use of AM for repair is not straightforward, and its application in this domain is restricted by various limitations. A primary constraint is the need to apply new material to existing worn surfaces, which proves challenging

Content from this work may be used under the terms of the Creative Commons Attribution 3.0 license. Any further distribution of this work must maintain attribution to the author(s) and the title of the work, journal citation and DOI. Published under license by Materials Research Forum LLC.

Materials Research Proceedings 57 (2025) 639-646 https://doi.org/10.21741/9781644903735-75

with Powder Bed Fusion (PBF) technologies owing to the frequent non-planarity of such surfaces. By contrast, Directed Energy Deposition (DED) processes show promise for the repair of metal components. These employ a high-density energy source (such as a laser, plasma, electron beam, or electrical arc) to melt a metallic medium (such as powder or wire), and deposit the liquefied material onto an existing surface. By synchronising the material feed and the energy source, DED technologies build geometrical features layer by layer, thereby enabling the formation of new material beads [7].

The DED approach selected for this study is Wire Arc Additive Manufacturing (WAAM), a process that exploits an electric arc as the heat source to fuse wire feedstock into layers, creating near-net-shape components, which is often used for repair applications [8, 9]. One of the key features of WAAM is the high deposition rate, coupled with low equipment and operational costs. Additionally, using wire instead of powder results in a safer working environment for operators and lower material costs [10]. Due to the thermal cycles that components experience during the WAAM process, several studies have examined the mechanical properties of WAAM-fabricated components to determine deposition setups capable of ensuring the quality of the repaired material, and particularly the relationship between heat input and microstructure, which can affect both product lifespan and deposition direction. Research has shown that the geometry, microstructure, and wettability of aluminium alloys depend on the WAAM transfer mode, identifying viable solutions for these materials [11]. Moreover, WAAM has been recognised as a sustainable solution for repairing large-scale metal components, with the potential to reduce environmental impact by using less energy and resources than other manufacturing routes [12, 13]. The control of heat input is crucial, especially when thin structures, such as those in the aerospace sector, need to be repaired. Hence, the goal of this study is to optimise the process parameters and, consequently, the heat input of the deposition process to repair such geometries by adopting a strategy for fine-tuning the transferred heat through the deposition of single dots of material.

Repair cycle definition

The selected case study is a ribbed thin shell with a large diameter, used for space application. Its ribs have variable thicknesses depending on the location of the cylinder, ranging from 2 to 5 mm. The component is made from precipitation-hardened 2000-series aluminium, starting with the forging of a hollow cylinder, followed by material removal through machining to create the internal structure. Due to the size of the part and the associated machining time, the lead time of this component is long, making the repair process a critical step to avoid huge costs and mission delays when some problems occur during the production phase.

In most cases, manufacturing defects that require repair arise during the machining phase, with the most common being the unintended removal of part of a rib. Repairing such defects appears to be an interesting strategy to avoid discarding a component that is still in the processing stage, thereby preventing significant economic losses and the long lead time required to produce a replacement part. To carry out the repair, an aluminium alloy 2319 was selected. Although not identical to the base material, it is very similar to the substrate (differing only slightly in its zirconium and titanium content) and is chemically compatible. In addition, the alloy offers good weldability and is available in the diameter required for Gas Metal Arc Welding (GMAW). The wire used, produced by Safra, had a diameter of 1.2 mm. The chemical compositions of both the wire and the substrate are listed in Table 1.

Materials Research Proceedings 57 (2025) 639-646 https://doi.org/10.21741/9781644903735-75

Table 1. *Chemical composition of wire and substrate*

	Al	Zr	Si	Fe	Cu	Mn	Mg	Zn	Ti	Be	V
Wire	Bal.	0.10 - 0.25	<0.20	<0.30	5.8 - 6.8	0.20 - 0.40	<0.02	<0.10	0.10 - 0.20	<0.0003	0.05 - 0.15
Sub.	Bal.	0.05 - 0.15	<0.20	<0.30	5.8 - 6.8	0.20 - 0.40	<0.02	<0.10	0.02 - 0.10	-	0.05 - 0.15

Aluminium is widely used in manufacturing due to its corrosion resistance, low weight, and visually appealing qualities, making it suitable for a broad range of applications. However, its high thermal conductivity and low melting point result in a narrower processing window compared to other metals. Welding aluminium presents several challenges, such as the formation of a thin oxide film that melts at a higher temperature than the base metal, requiring elevated heat levels. However, excessive heat can lead to over-melting, potentially causing holes in the substrate. This risk is particularly critical when working with thin substrates, as is common in aerospace applications. Given the small thickness of such substrates, the phenomenon of part heating during deposition is quite relevant and may lead to a noticeable change in the bead geometry even under low heat input. This effect is shown in Figure 1 for a 3-mm substrate.

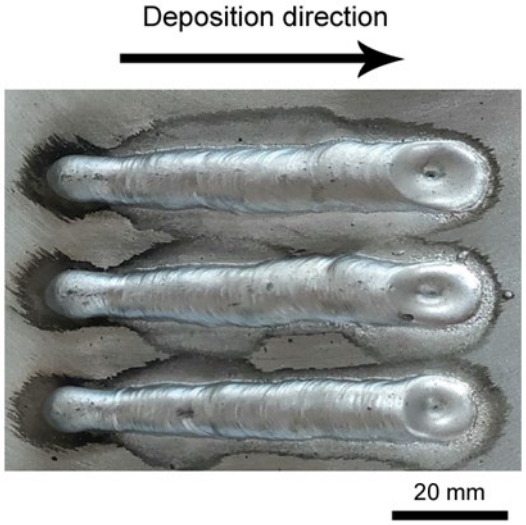


Figure 1. *Continuous deposition of aluminium alloy*

One solution to mitigate this issue is the use of Cycle Step Cold Metal Transfer (CS-CMT), a deposition technique that is a variant of the CMT technology patented by Fronius®. It combines the traditional pulsed modes of the most common GMAW sources with a micro-movement of the wire to control the detachment of a single small drop of material. The CS-CMT is characterised by a highly controlled and low heat input, as it can accurately define the number of drops produced by a CMT cycle and use a waiting time between the successive depositions. This makes it possible to locally reach the heat required for an appropriate melting of the substrate and define a time for cooling down the melt pool before starting a new deposition cycle. By correctly tuning the CS-CMT parameters, it is possible to find a stable thermal equilibrium that allows for good repeatability of the bead dimensions, avoiding the 'thermal runaway' which typically characterizes the deposition of aluminium on a thin substrate (see Figure 1).

The deposition process consists of alternating phases of material melting and waiting time; hence, it is discontinuous and results in a dot-by-dot bead morphology. It is worth noting that this approach is unnecessary for bulkier geometries, where well-established methods based on continuous beads, allowing for higher deposition rates, can be adopted instead. The most

Materials Research Proceedings 57 (2025) 639-646 https://doi.org/10.21741/9781644903735-75

influential parameters to be set are (*i*) the number of CMT cycles, which is directly related to the volume of material deposited in a single drop, and (*ii*) the waiting time, which must be adjusted to provide sufficient time for the substrate to cool down between drops. This allows to control the heat input quite accurately and to determine of the optimal processing value within the narrow window characteristic of aluminium.

The welding unit used for the experiments was a Fronius TPS320i GMAW-CMT source with synergic curves for Al-Cu alloys, mounted on a 3-axis cartesian machine retrofitted for WAAM applications. The initial tests aimed to define the optimal parameters for creating a rib starting from a thin section of material. Various thicknesses (e.g., 3, 4, and 5 mm) were tested. As an example, the parameters used for a 3-mm substrate are shown in Table 2. The results of the initial tests were used to identify the process parameters that ensured good penetration with no over-melting phenomena, and to determine the dot size for toolpath planning during deposition. The best outcome for the 3-mm case was obtained in Test #2, which employed two sequences of 20 cycles each, with a 1-second pause between them.

Table 2. *Experimental tests with a 3-mm substrate*

Test ID	CMT Cycle	Idle time [s]	N. of repetitions	WFS [m/min]	Width [mm]	Height [mm]
1	20	1	2	10	Over-melting	
2	20	1	2	10	6.5	2
3	20	1	2	10	6	2.5
4	10	1	3	10	Over-melting	
5	10	1	3	10	7	2.3
6	10	1	3	8	4.7	2.9
7	10	1	3	9	5.5	2.9

Transitioning from single-dot to a semi-continuous (dot-by-dot) deposition introduced additional complexity, as the substrate temperature gradually increased, potentially altering both penetration and dot geometry. Establishing a stable equilibrium condition thus required fine-tuning the heat flux to the part. This was achieved by adjusting the interval between successive drops. Figure 2 presents the results for waiting times of 10, 20, and 30 seconds between drops on a 4 mm rib, using a step-over between the drops of 60% of their dimension. A 30-second idle time resulted in under-heated deposition, as the lack of adhesion between dots compromised the machining allowance. The optimal configuration for these tests was achieved with a 20-second waiting time.



Figure 2. *Semi-continuous dot-by-dot tests*

To perform the repair, the deposition surface must first be prepared by creating a reference geometry for material deposition. This preparation must also consider torch accessibility and the ability of individual dots to form a continuous layer, as some configurations may lead to unwanted arcs to nearby areas of the component. A trapezoidal cavity was chosen as the simplest and most practical geometry for rib repair, with the size of the removal area tailored to fully encompass the defect. An alternating toolpath strategy (Figure 3*a*), regarded as the most effective method for building thin walls [14], was adopted.

Materials Research Proceedings 57 (2025) 639-646 https://doi.org/10.21741/9781644903735-75

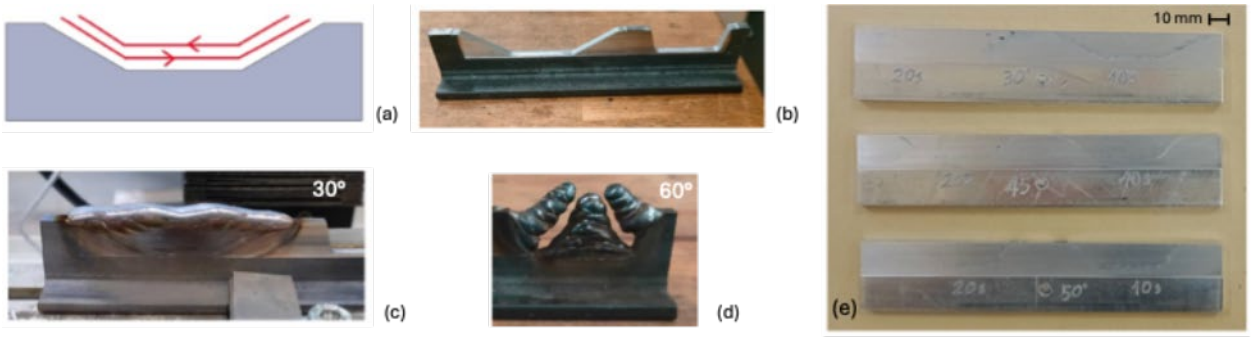


Figure 3. *Tests on sample ribs showing the deposition strategy (a), the surface preparation (b), the results at 30° (c) and 60° (d), the part after milling (e)*

Several tests were conducted to define the optimal angle of the trapezoid (Figure 3*b*). A larger angle (measured with respect to the horizontal plane) would require less material removal, thus reducing the machining waste. However, this could pose challenges in accessing the welding torch. Conversely, a smaller angle necessitates more space to create the trapezoidal cavity but ensures better access to the torch, even with a smaller contact tip-to-work-distance (CTWD). Some results are shown in Figure 3*c-d*, where excessively high angles caused the formation of a 'horned' shape, due to the sparking of the arc on the surface closer to the torch rather than on the previously deposited layer. This phenomenon is self-regenerative and leads to process defects. The minimum safe angle for this geometry was approximately 45°, which was used for the repair tests. Figure 3*e* shows the results of some tests with the suggested parameters on a thin 4-mm plate. All configurations yielded satisfactory results, with no lack of fusion observed after milling. After defining the process parameters, the developed repair strategy was applied to a small part of the selected test case, starting from the removal of material to simulate a manufacturing error. The steps of the approach and the results are illustrated in Figure 4.

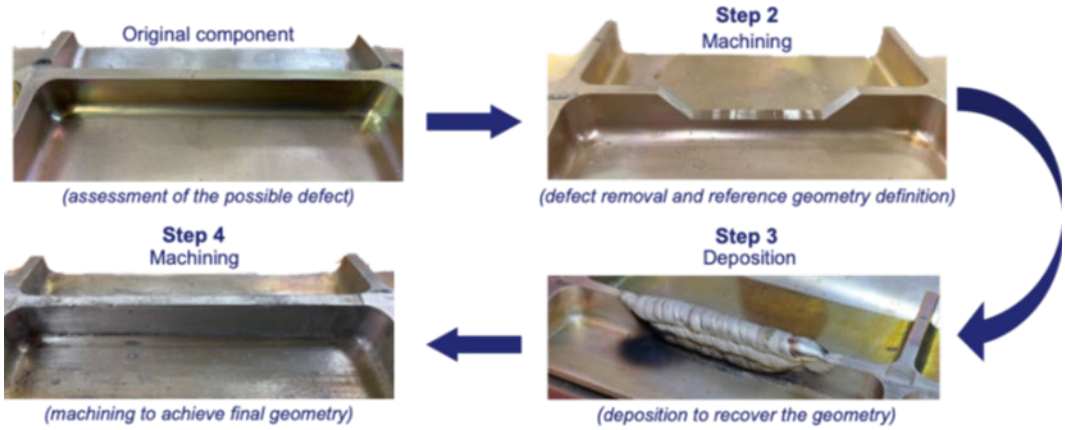


Figure 4. *Repair step for the test case*

At this stage of the ongoing research, only superficial and geometrical analyses have been carried out, while the analysis of the mechanical properties and micrographic analysis are planned.

Carbon footprint of the repair operation

The groove volume measured 1376 mm³, whereas the deposited material required to fill it amounted to 4130 mm³. Consequently, 2754 mm³ of material was removed to achieve the final surface finish after the deposition. The deposition phase required 46 dots and took approximately 410 seconds, with the majority of this time attributed to process idle, whereas only 41.5 seconds

Materials Research Proceedings 57 (2025) 639-646 https://doi.org/10.21741/9781644903735-75

were effectively spent on the actual material deposition. To conduct a preliminary assessment of the carbon footprint associated with the repair process, a Life Cycle Assessment (LCA) was performed using CO_2-equivalent emissions as the environmental stress metric. This analysis accounted for the contributions of material consumption, energy usage, and resource expenditure throughout the various phases of the repair process. In addition, the impact associated with the production of the metal wire consumed during the active deposition phase was considered, as shown in Figure 5*a*. The carbon footprint of a unit mass of wire was estimated to be 14.6 ±7% $kgCO_2/kg$, based on modelling the unit processes from raw material production through the subsequent hot shape rolling and wire drawing stages, which have yield factors of 0.95 and 0.88, respectively. The carbon footprint of raw material production was evaluated at 8.4 ±8% $kgCO_2/kg$, considering a recycled content of 43% ±5% in the current material supply, and assuming primary and secondary production emissions from the data in the CES Selector database v.17.2.0. Moreover, according to the same database, the carbon footprint contributions of hot shape rolling and wire drawing were estimated to be 0.5 ±5% $kgCO_2/kg$ and 3.5 ±5% $kgCO_2/kg$, respectively.

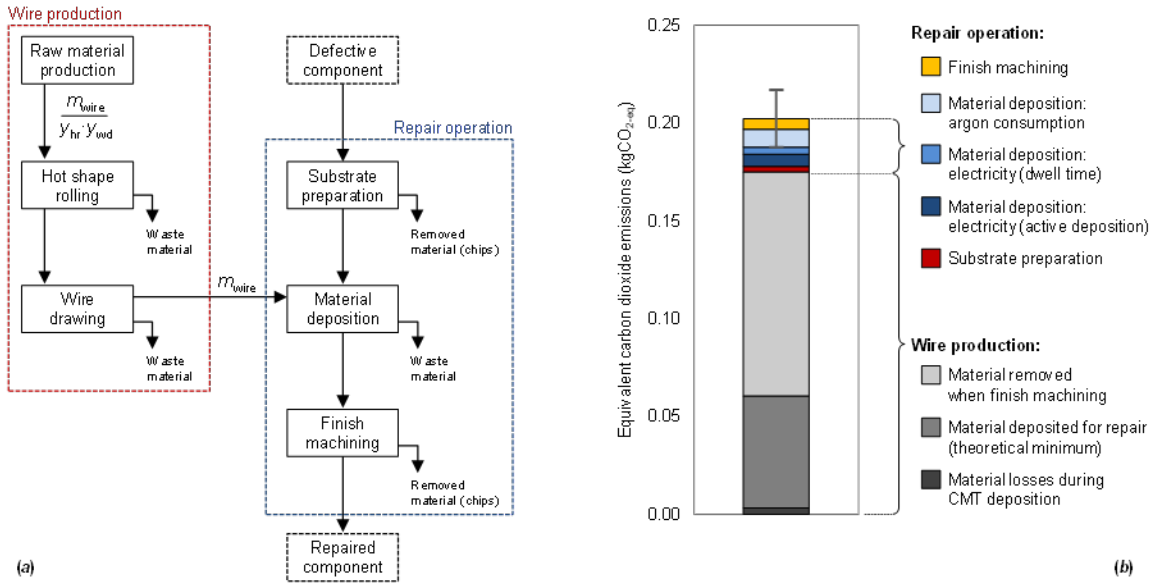


Figure 5. *Preliminary carbon footprint assessment: system boundaries (a) and main results (b)*

For the repair operation, the specific deposition energy (which accounts for the energy demand for material deposition only, as outlined in [15]) was experimentally measured at 2.5 kWh/kg, while the total energy consumption for the CMT repair operation (including contributions from idle states during both deposition and dwell time) was 4.0 kWh/kg. The specific deposition energy (SDE) values appear to be higher than those reported in the literature [15], as expected, since the dot-by-dot repair process is more time- and energy-intensive than a continuous deposition process. In contrast, comparing the specific energy consumption (SEC) with other studies should be done with caution, as idle times and idle power (which, in this case, is modest at below 0.2 kW) vary depending on the geometry of the part, the deposition path, and the specific equipment used. During the active deposition phase, which accounts for a yield factor of 0.98 to incorporate permanent material losses due to vaporization and sparking, the consumption of argon (grade 5) was quantified at 4.3 kg/kg of deposited material.

The carbon footprint of electricity was assumed to be 0.21 ± 10% $kgCO_2/kWh$, while that of argon was 0.18 ± 10% $kgCO_2/kg$ [16]. For all the machining operations, a carbon footprint of 0.70 ± 5% $kgCO_2/kg$ of material removed was considered (CES Selector v.17.2.0). Based on these

considerations and the assumptions underlying the calculation model, the results presented in Figure 5*b* were obtained. The largest share of CO_2 emissions is attributable to the aluminium wire production, while the contributions from the various process phases account for only a minor fraction, less than 15% of the total. Although these results are preliminary, specific to the case study considered, and based on both primary data measured in the laboratory and impact factors derived from secondary sources such as literature and databases, they provide insights for potential process optimization. Most of the impact associated with wire consumption is linked to the material that is first deposited and subsequently removed as chips during finishing operations. Therefore, improving material usage efficiency could yield environmental benefits, as there appears to be significant room for optimization. If the carbon footprint is theoretically limited to only the material required to fill the groove volume, the imbalance between process-related and material-related emissions would be reduced. In any case, the repair operation – especially for small repairs on large components, such as those considered in this study – is expected to be more advantageous than replacing the damaged component with a brand new one, in line with findings from previous studies (see [6] and references therein).

Conclusions

In this study, a dot-by-dot repair methodology for thin aluminium components was developed to increase the control of the heat input. The repair procedure comprised four sequential stages: removal of damaged material, establishment of a reference geometry, additive deposition of replacement material, and machining to remove the excess. Process parameters were selected to achieve a high quality restoration with proper penetration and no overmelting. Moreover, the environmental analysis of the repair process highlighted that the largest share of CO_2 emissions was due to the production of the aluminium wire, whereas process-related contributions accounted for less than 15% of the total. Therefore, in a context where repair operations are deemed more favourable than the replacement of damaged components with newly manufactured ones, improving material utilisation efficiency could offer further environmental benefits.

Acknowledgements

This study was carried out within the MICS (Made in Italy Circular and Sustainable) Extended Partnership and received funding from the European Union Next-GenerationEU (PIANO NAZIONALE DI RIPRESA E RESILIENZA (PNRR) MISSIONE 4 COMPONENTE 2, INVESTIMENTO 1.3 D.D. 1551.11-10-2022, PE00000004). This manuscript reflects only the authors views and opinions; neither the European Union nor the European Commission can be considered responsible for them.

References

[1] N. Sandeep and R. Suresh, A Study of the Circular Manufacturing System: Issues and Prospects, Journal of Systems Science and Information 12 (2024) 790–803. https://doi.org/10.21078/JSSI-2024-0088

[2] N. A. Aziz, N. A. A. Adnan, D. A. Wahab, and A. H. Azman, Component design optimisation based on artificial intelligence in support of additive manufacturing repair and restoration: Current status and future outlook for remanufacturing, J. Clean. Prod. 296 (2021) 126401. https://doi.org/10.1016/j.jclepro. 2021.126401

[3] H. Liao, C. Li, Y. Nie, J. Tan, and K. Liu, Environmental efficiency assessment for remanufacture of end of life machine and multi-objective optimization under carbon trading mechanism, J. Clean. Prod. 308 (2021) 127168. https://doi.org/10.1016/j.jclepro.2021.127168

[4] M. Sharma, S. Joshi, M. Prasad, and S. Bartwal, Overcoming barriers to circular economy implementation in the oil & gas industry: Environmental and social implications, J. Clean. Prod. 391 (2023) 136133. https://doi.org/10.1016/j.jclepro.2023.136133

[5] M. Liu, Y. Cai, C. Duan, and G. Li, Key techniques in parts repair and remanufacturing based on laser cladding: A review, J. Manuf. Process. 132 (2024) 994–1014. https://doi.org/10.1016/j.jmapro. 2024.11.039

[6] P. C. Priarone, G. Campatelli, A. R. Catalano, and F. Baffa, Life-cycle energy and carbon saving potential of Wire Arc Additive Manufacturing for the repair of mold inserts, CIRP J. Manuf. Sci. Technol. 35 (2021) 943–958. https://doi.org/10.1016/j.cirpj.2021.10.007

[7] M. Leino, J. Pekkarinen, and R. Soukka, The role of laser additive manufacturing methods of metals in repair, refurbishment and remanufacturing - Enabling circular economy, Phys. Procedia 83 (2016) 752–760. https://doi.org/10.1016/j.phpro.2016.08.077

[8] M. Vishnukumar, R. Pramod, and A. Rajesh Kannan, Wire arc additive manufacturing for repairing aluminium structures in marine applications, Mater. Lett. 299 (2021) 130112. https://doi.org/10.1016/j.matlet. 2021.130112

[9] X. Li, Q. Han, and G. Zhang, Large-size sprocket repairing based on robotic GMAW additive manufacturing, Welding in the World 65 (2021) 793–805. https://doi.org/10.1007/s40194-021-01080-9

[10] J. Obiko et al., A brief review on industrial remanufacturing of structural and functional components: Wire-Arc Additive Manufacturing Technique, Engineering Solid Mechanics 12 (2024) 363–386. https://doi.org/10.5267/j.esm.2024.5.004

[11] S. Ren et al., Comparative study of additive manufacturing thin-walled component with Al–Mg-Sc-Zr alloy using different arc modes, J. Mater. Res. Technol. 35 (2025) 5665–5674. https://doi.org/10.1016/ j.jmrt. 2025.02.053

[12] R. C. Reis, S. Kokare, J. P. Oliveira, J. C. O. Matias, and R. Godina, Life cycle assessment of metal products: A comparison between wire arc additive manufacturing and CNC milling, Advances in Industrial and Manufacturing Engineering 6 (2023) 100117. https://doi.org/10.1016/j.aime.2023.100117

[13] J. Wurst, T. Steinhoff, I. Mozgova, T. Hassel, and R. Lachmayer, Aspects of a Sustainability Focused Comparison of the Wire Arc Additive Manufacturing (WAAM) and the Laser Powder Bed Fusion (LPBF) Process, In: Smart Innovation, Systems and Technologies 338 (2023). https://doi.org/10.1007/978-981-19-9205-6_9

[14] M. Rauch, J.-Y. Hascoet, and V. Querard, A multiaxis tool path generation approach for thin wall structures made with WAAM, J. Manuf. Mater. Process. 5 (2021) 128. https://doi.org/10.3390/jmmp5040128

[15] A. R. Catalano, V. Tebaldo, P. C. Priarone, L. Settineri, and M. G. Faga, CMT deposition of stainless steel: effects of process parameters on energy demand and microstructure, Progress in Additive Manufacturing (2025). https://doi.org/10.1007/s40964-025-01022-7

[16] F. S. Gobber, P. C. Priarone, A. Pennacchio, and M. Actis Grande, Effect of inert gas pressure on the properties and carbon footprint of UNS S32760 powders made from waste materials by gas atomization, J. Mater. Res. Technol. 33 (2024) 8814–8828. https://doi.org/10.1016/j.jmrt.2024.11.195

Materials Research Proceedings 57 (2025) 647-654 https://doi.org/10.21741/9781644903735-76

Manufacturing quotation platform for turned parts: The PLAT4M project

Antonio SCIPPA[1,a *], Niccolò GROSSI[1,b]

[1]Department of Industrial Engineering, University of Florence, Via di Santa Marta 3, 50139, Firenze, Italy

[a]antonio.scippa@unifi.it, [b]niccolo.grossi@unifi.it

Keywords: Manufacturing Platforms, Machine Learning, Turning

Abstract. The increasing digitalization in the manufacturing industry, the development of digital models (Digital Twins) representing products, processes, resources, and systems, as well as the adoption of AI to support classification and automatic reasoning approaches, are paving the way for the raise of platform-based business approaches for manufacturing very shortly. The PLAT4M project aims at defining a general modelling framework, and supporting methodologies, enabling a platform-based quotation approach for mechanical components. Within this framework, customers will be able to submit technical specifications of the requested products and receive a quotation in terms of costs and delivery date. In this work the ongoing activities related to the developing of the AI-based approach for generating process plans and characterizing process steps for turned parts is presented.

Introduction

AI-based approaches for manufacturing cost estimation have become increasingly popular due to their ability to handle large amounts of data, detect patterns, and make predictions with higher accuracy. These methods can automate the estimation process, improve decision-making, and optimize resource allocation. Predicting cost is a common task among procurement professionals working to raise margins and profitability. Historically, cost modeling has been done using statistics or algorithms to produce a final estimate, that is typically based on samples of past data. In the last years online manufacturing platforms, able to provide a service of manufacturing and shipping after customers upload their computer-aided design (CAD) models to a website [1] are increased, and it is expected that this trend will be clearer in the next future. In this contest, manufacturing costs for on-demand service needs to be entirely estimated based on CAD drawings and predicted in real time to provide prompt feedback to the customer.

In literature many manufacturing costs estimating studies may be found, mainly based on analogical methodology (based on historical product data) and regression analysis or artificial neural networks (ANNs), applied in different manufacturing fields [2,3]. The mail lack of these approaches is that they cannot explain the reasons for determining manufacturing cost. Therefore, in the last years, more attention has been devoted to explainable artificial intelligence (XAI), that is able to explain the rationale of AI judgment [4]. Most of them are based on automatic or semiautomatic feature recognition approaches [5], even if there are some examples of feature-free approaches explicitly devoted to computer aided process planning [6]. Despite the differences, all the methods available in literature do not consider the process physics, that may affect manufacturing costs. Among the others key factors, limiting the focus on machining processes, both static and dynamic stiffness of the tool and the workpiece represents a critical aspect, since they dramatically affect the quality of the product [7], and then the manufacturing costs: for slender components, a reliable manufacturing costs estimation is not always possible without taking advantage of virtual models of the machining processes.

Content from this work may be used under the terms of the Creative Commons Attribution 3.0 license. Any further distribution of this work must maintain attribution to the author(s) and the title of the work, journal citation and DOI. Published under license by Materials Research Forum LLC.

Materials Research Proceedings 57 (2025) 647-654 https://doi.org/10.21741/9781644903735-76

In the last decades, several predictive methods have been proposed: the simplified models [8,9] are efficient and easy-to-use but not always effective, while the most complete and accurate approaches [10] require several inputs and computational resources, that are not compatible with the real time requirement of the manufacturing platforms. Moreover, AI models have been successfully applied in the field of machining stability [11] and machinability [12].

In this context, the present work gives a brief overview of the activities currently on going to develop a manufacturing cost estimation approach, able to consider the physics of the turning process, with a view to provide realistic manufacturing costs of difficult to machine components.

Description of the PLAT4M project

The PLAT4M project address the manufacturing of mechanical components, with the aim at focusing on a reduced set of technological processes (turning and milling) and a simplified business and logistic structure where a single supplier can provide the full set of services needed for a product. To address this area in a feasible way, two families of products are considered: a) drive shafts and flanges, that mostly require turning operations, plus a small possible set of milling/drilling operations; and b) simple prismatic parts, whose processing grounds on 2.5-dimension milling/drilling operations. The proposed structure of the platform is presented in Fig. 1, in which are highlighted in red the tools related to the turning process, that are the objective of the presented work.

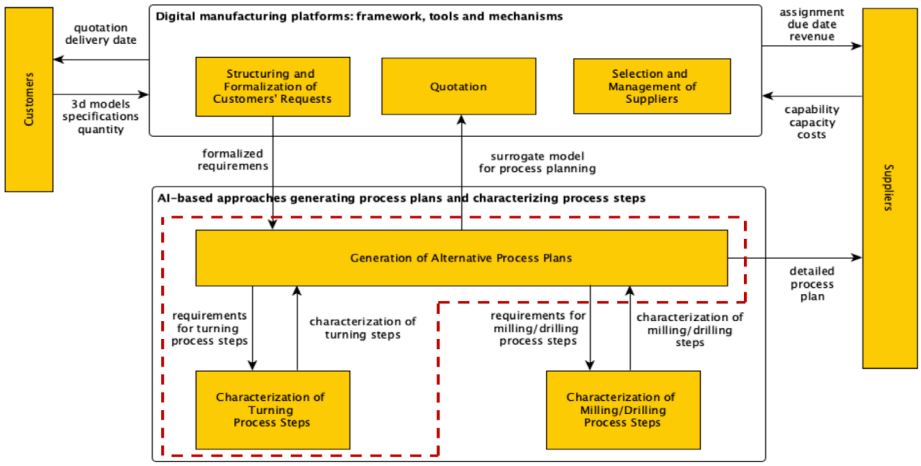


Fig. 1 Structure of the platform and related tools.

The main innovative aspects in the development of these classes of approaches is the generation of a general model based on AI, exploiting neural networks. The rapid progress of these technologies is opening the field to a wide range of possible applications in taking complex decisions. Nevertheless, the current adoption of AI approaches in manufacturing must handle with significant barriers: a) massive training data sets, necessary to guarantee their effectiveness; b) completeness of datasets, considering also extreme or specific conditions (e.g., rare, or dangerous situations), which allow to cope with a wide range of situation; and c) explainability, required in particular for large and complex AI models.

The use of synthetic data, i.e., data generated by digital models, may overcome these limitations, enabling an easy and fast generation of large sets of data covering all the scenarios and aspects to cope. This approach can be sketched according to the general workflow structured according to the following steps: a) definition of a Digital Model (DM) of the products and processes, used to generate a large amount of data to support the supervised learning of the AI approaches; b) AI training on the synthetic data generated (e.g., simulated data for process characterization, feasible/unfeasible process plans, etc.); c) transfer learning of AI approaches on

Materials Research Proceedings 57 (2025) 647-654 https://doi.org/10.21741/9781644903735-76

real data to fine-tune or further improve the AI models and enable their use in the real world; d) validation of AI approaches.

In the following chapters the implementation of the above-mentioned steps for the turning processes is briefly described.

Description of the platform approach for Turning

In the framework of the project, this specific tool aims at characterizing the turning process in terms of process times, capability, feasible process parameters and quality-related aspects.

According to the structure of the proposed platform described in Fig. 1, the general approach for turning can be organized as showed in Fig. 2, based on a common AI based "cost related parameters" evaluation module, tailored on the manufacturing capability of the suppliers joining the platform.

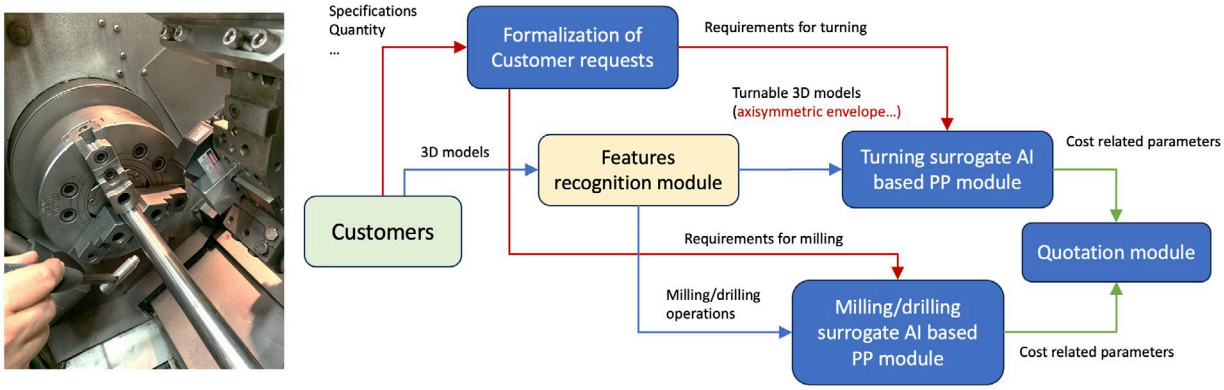


Fig. 2 General overview of the PLAT4M turning solution.

Indeed, a realistic estimation of the manufacturing process costs should consider even key aspects, specific of the workshop in which the part could be machined: some of those may be treated at higher level (e.g. the current machine tools availability, the overall productivity of the workshop, etc.), some instead should be considered in the process plan definition and simulation, as they can affect the definition of the cutting parameters to fit the required tolerance, avoiding machining errors that could occurs (due for example to chatter vibration). For these reasons the AI model should be trained with synthetic data that consider the specificity of the machine tools and cutting tools used, in case that proper information provided by the manufacturer are available.

From the abovementioned consideration clearly appears that a tailored AI module should be implemented for each supplier afferent to the platform. This approach, in addition to producing a more realistic cost estimate, has also the advantage to manage different manufacturing costs for the same part, allowing a prescreening of the possible suppliers to which require to refine the quotation, which probably represent the best approach for difficult to machining parts: the platform produce in real time a preliminary gross cost estimation, that is refined by the selected suppliers in few working days, after the acceptance of the customer, to proceed with the final quotation.

Proposed approach for the Process Step Characterization Tool

The proposed digital solution for the turning module is schematized in Fig. 3, in which are described the different technical/research challenges to be entailed in order to develop an efficient and accurate process simulation.

Materials Research Proceedings 57 (2025) 647-654 https://doi.org/10.21741/9781644903735-76

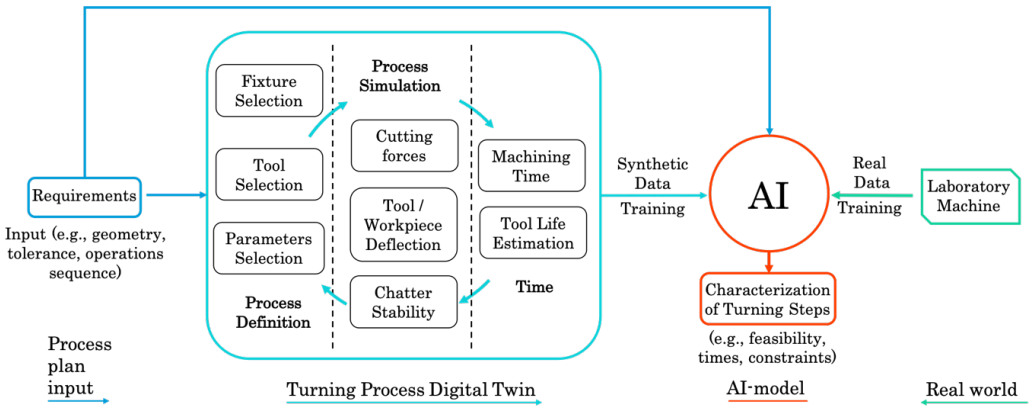


Fig. 3 General overview of the turning module.

At the background level, the proposed digital twin solution includes a toolpath generation model that is interfaced with a simplified FEM based environment able to estimate the workpiece behavior during the machining process, that represents the main cost driver for difficult to machining components.

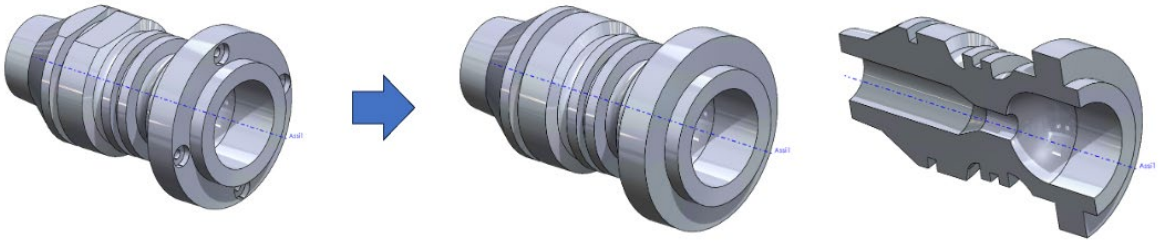
The system is composed by three modules: a) Process planning module, necessary to produce concrete manufacturing processes to be executed; b) workpiece FE modelling, c) turning process simulation. The modules are configured as an integrated solution: only the stock geometry and material, toolpath and tool geometry will be needed. The innovative idea underpinning the PLAT4M solution is to integrate the process planning module with a realistic machining simulation, considering workpiece compliance changing during the turning process, due to the complex interaction between clamping configuration, material removal, and the instantaneous cutting conditions, and which represents a critical issue for slender components.

This approach, in addition to the usual cost related parameters (e.g. machining time, tool wear, required power, etc.), allows even an estimation of possible out of tolerance, that have a great impact on the real manufacturing cost.

Pre-processing of 3D CAD model.

At platform level manufacturing costs should be evaluated based mainly on the CAD model provided by the customer, together with few additional info, which needs to be elaborated to be used in the AI framework. Among others, such elaboration entails the definition of features of the component to be machined and the identification of the pre-machined stock. A proper approach should use feature recognition algorithms to identify the machining features (i.e. pockets, slots, holes, etc…), which cannot be obtained with a turning process, and feature free approaches, like the one proposed by Behandish et al. [6], to verify turnability of the component and identify the "turnable" closure of the part, as showed in Fig. 4. Such implementation would enable a more general mill-turn Computer Aided Process Plan (CAPP), providing the required interconnection between the two machining characterization modules of the PLAT4M framework, interconnection needed to deal with complex to machining industrial parts. These aspects are however out of the scope of the project and, without loosen in generality, has not been taken into account in the project, assuming as input directly the turnable envelope of the part (i.e. only exactly axisymmetric components are considered).

Materials Research Proceedings 57 (2025) 647-654 https://doi.org/10.21741/9781644903735-76

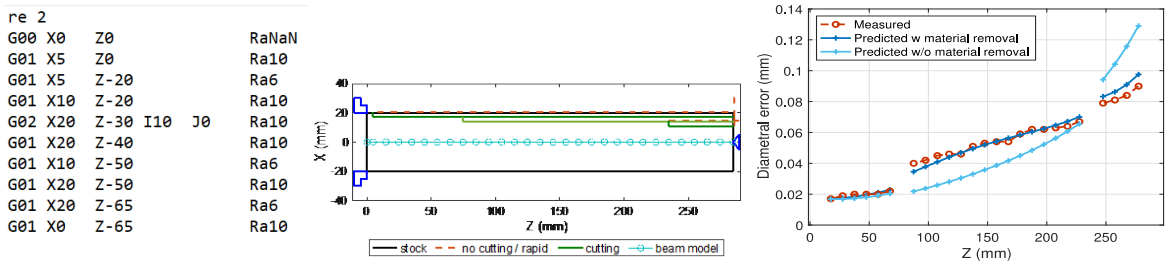


a) b) c)

Fig. 4 Procedure to convert a given 3D part (a) in its turnable closure (b), by revolute the proper section around the turning axis (dash-dot red line).

This assumption allows to simplify the description of the input geometry that can be completely described by its revolution section. To make the storage of data more efficient a G-code like approach has been used: geometry of the finished part is described using the hypothetic toolpath able to generate it (see Fig. 5), considering linear (G01) and circular interpolations (G02, G03). Quality related information (e.g. roughness, geometrical tolerances, etc.) can be easily stored for each machined surface introducing additional values at the corresponded row in the G-code. Geometrical tolerances were not considered, so as not to complicate matters further, but may be added in future by adding other columns expressing geometrical relationships between the corresponding surfaces.

The choice to use this approach also allows to quickly generate and update the FE model of the workpiece during machining: 1D Timoshenko beam elements [13] are used. This approach has been demonstrated to be sufficiently accurate to correctly predict the final shape of the finished part [14], when proper info provided by the supplier are available.



(a) (b) (c)

Fig. 5 G-code like description of the workpiece geometry (a), DT graphical representation (b) comparison between experimental and simulated diametral errors (c).

Process plan estimation.

At platform level, manufacturing costs represent normally just a preliminary evaluation, which should be as much as possible realistic, quite close to the effective manufacturing cost, but, in any case, it should represent just a first rough estimation of the real quotation. That means that a proper process plan approach shall not have to be developed to find the optimal solution, but to provide a wide spread of possible toolpaths. Such toolpaths should be analyzed in order to also evaluate the incidence of out of tolerance (i.e., scraps or rework) in relationship to the chosen machining parameters, that represents an important aspect to be taken into account for the estimation of the proper manufacturing quotation.

Materials Research Proceedings 57 (2025) 647-654 https://doi.org/10.21741/9781644903735-76

From this perspective the process plan module has been developed according to the following steps, which allow to generate several toolpaths, simply changing the number of passes for the rough machining and/or changing the sequence of the operations:

- finishing feed per revolution is evaluated by the required roughness using a kinematic approach (see Fig. 6), considering cutting tool data (i.e. corner radius, suggested depth of cut range, etc.) provided by the supplier afferent to the platform.
- fixture of the part is defined from the mean slenderness of the component, simply consider the part fixed on the spindle chuck, with the additional use of tailstock in case of slender components (a simple approach based on the mean slenderness, L/D_{mean}, or a more sophisticated approach based on a preliminary FE analysis can be used).
- maximum finishing allowance is evaluated from the diametral tolerances, considering a simple FE analysis based on the chosen fixture and the estimated cutting forces.
- roughing toolpath is evaluated considering the simple approach normally used by means of canned cycles (e.g. G68).

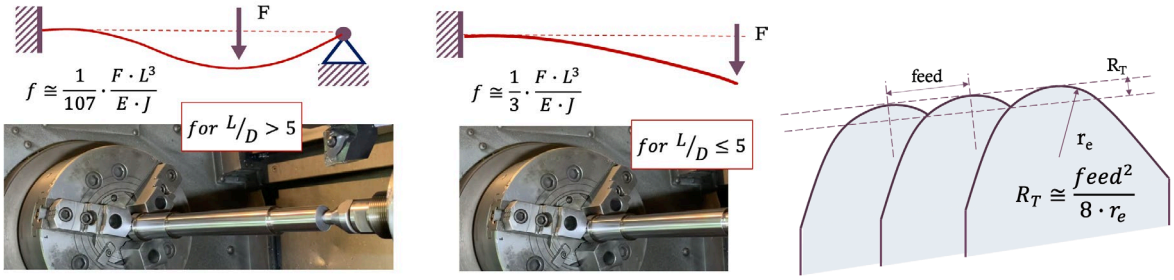


Fig. 6 Definition of part fixturing, the maximum permissible allowance and feed per revolution for the finishing phase.

An important aspect of toolpath generation is the choice of the proper shape of the cutting tools, that must be defined considering the variation of the working cutting edge angle along the toolpath. The procedure implemented is based on the following steps (see Fig. 7):

- For each segment describing the current geometry of the workpiece, the minimum cutting-edge angle is evaluated, simply considering the orientation of the current segment, and the previous and following ones in case of concave surfaces, to avoid overcutting and/or collisions. Comparing this "nominal" shape of the cutting edges with the ISO designation of the inserts stored in the supplier's database, it is possible to find, for each segment, the correct insert.
- Combining the segments at which is associated the same insert, it is possible to obtain all the operations that can be performed by the single insert. These operations can be linked with one another to achieve different operation sequences, and then different toolpaths can be obtained just changing the cutting parameters.

Each toolpath is then evaluated by means of the proposed digital twin in order to estimate the manufacturing costs related parameters (e.g. machining time, shape and number of cutting tools, tool life, percentage of out of tolerance manufacturing parts, etc.). This approach, despite computationally time consuming, allows to obtain the spread of the possible variability of the single quantity of interest, representing an interesting information for the preliminary estimation of the manufacturing costs, that could be eventually scaled according to the accuracy of the

Materials Research Proceedings 57 (2025) 647-654 https://doi.org/10.21741/9781644903735-76

workshop related information (e.g. reliability of cutting force estimation, stiffness of the spindle chuck, etc.).

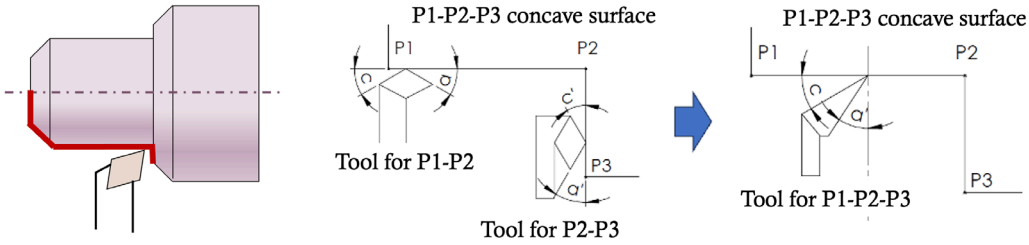


Fig. 7 definition of the tool shape.

Data obtained by the aforementioned simulations will be then used to train the AI based module that will be implemented at platform level to provide reliable manufacturing cost related parameters (e.g. machining time), given the required inputs specified by the customer (i.e. CAD model of the finished part, batch production size, dimensional tolerances, surface roughness, etc.), to provide in real time a reliable quotation.

Conclusion

The structure of the turning module for the PLAT4M project has been briefly presented highlighting the mains modules currently under developing. The basic idea underpinning the proposed implementation is to generate, for each part, many different process plans, not necessary all feasible, discarding just those that are obviously unfeasible (i.e. improper tool choice, requested machining power greater than the available one, etc.).

This approach has two different beneficial effects: a) it allows to reduce the complexity of the turning process plan definition, that has been always the main bottleneck for the developing of reliable turning CAPP; b) it makes the decision process similar to the human approach, which is mainly based on the experience of the past successes/failures in the manufacturing of similar components (company knowhow).

Moreover, the integration of the proposed process planning implementation with a realistic machining simulation, based on simplified FE analysis of the manufacturing process, allows to generate useful information related to the spread of the possible variability of each cost related parameter, representing an interesting measurement of the robustness of the preliminary estimation of the manufacturing costs.

It is meaningful to underline that the same digital approach used to train the AI based tool implemented at platform level for the “real time” preliminary estimation of the manufacturing costs, can be also used, after the acceptance of the customer, to evaluate the best two or three process plans, which can be deeply analyzed by the supplier to provide in a very short time frame the final quotation, and quickly start-up the production, being already known machine tools, cutting tools and toolpaths needed for the manufacturing of the part.

Acknowledgements

This research was developed within the PLAT4M project, funded within the PRIN22 program. The authors wish to thank all the project partners. The support of Lorenzo Sallese and Marco Ceccarelli of Meccanica Ceccarelli & Rossi s.r.l. is gratefully acknowledged.

References

[1] D. Wu, D. W. Rosen, L. Wang, D. Schaefer, Cloud-based design and manufacturing: A new paradigm in digital manufacturing and design innovation, CAD 59 (2015) 1-14. https://doi.org/10.1016/j.cad.2014.07.006

[2] A. Niazi, J. S. Dai, S. Balabani, L. Seneviratne, Product cost estimation: Technique classification and methodology review. J. of Manuf. Sci. E. 128(2) (2006) 563-575. https://doi.org/10.1115/1.2137750

[3] O. Duran, J. Maciel, N. Rodriguez, Comparisons between two types of neural networks for manufacturing cost estimation of piping elements, Expert Syst. Appl. 39(9) (2012) 7788-7795. https://doi.org/10.1016/j.eswa.2012.01.095

[4] F. Ning, Y. Shi, M. Cai, W. Xu, X. Zhang, Manufacturing cost estimation based on a deep-learning method. J. Manuf. Syst., 54 (2020), 186-195. https://doi.org/10.1016/j.jmsy.2019.12.005

[5] Y. Soyoung, K. Namwoo, Explainable artificial intelligence for manufacturing cost estimation and machining feature visualization, Expert Syst. Appl, 183 (2021). https://doi.org/10.1016/j.eswa.2021.115430

[6] M. Behandish, S. Nelaturi, C. S. Verma, M. Allard, Automated process planning for turning: a feature-free approach, Prod. Manuf. Res. 7,1 (2019) 415-432. https://doi.org/10.1080/21693277.2019.1634650

[7] Y. Altintas, Manufacturing Automation: Metal Cutting Mechanics, Machine Tool Vibrations, and CNC Design, second ed., Cambridge University Press, 2012. https://doi.org/10.1017/CBO9780511843723

[8] T.L. Schmitz, B.P. Mann, Closed-form solutions for surface location error in milling, Int. J. Mach. Tools Manuf. 46 (2006), 1369–1377. https://doi.org/10.1016/j.ijmachtools.2005.10.007

[9] E. Budak, Y. Altintas, Analytical Prediction of Chatter Stability in Milling - Part II: Application of the General Formulation to Common Milling Systems, J. Dyn. Sys. Meas. Control, 120-1 (1998), 31-36. https://doi.org/10.1115/1.2801318

[10] G. Totis, P. Albertelli, M. Torta, M. Sortino, M. Monno, Upgraded stability analysis of milling operations by means of advanced modeling of tooling system bending. Int. J. Mach. Tools Manuf. 113 (2017) 19–34. https://doi.org/10.1016/j.ijmachtools.2016.11.005

[11] H. Cherukuri, E. Perez-Bernabeu, M. Selles, T. Schmitz, Machining Chatter Prediction Using a Data Learning Model, J. Manuf. Mater. Process. 3 (2019), 3, 45. https://doi.org/10.3390/jmmp3020045

[12] B. Lutz, D. Kisskalt, D. Regulin, J. Franke, AI-based Approach for Predicting the Machinability under Consideration of Material Batch Deviations in Turning Processes, Procedia CIRP, 93 (2020), 1382-1387. https://doi.org/10.1016/j.procir.2020.04.100

[13] A. Ertürk, H.N. Özgüven, and E. Budak, Analytical modeling of spindle–tool dynamics on machine tools using Timoshenko beam model and receptance coupling for the prediction of tool point FRF, Int. J. Mach. Tools Manuf., 46 (2006), 1901–1912. http://dx.doi.org/10.1016/j.ijmachtools.2006.01.032

[14] N. Grossi, A. Scippa A, G. Campatelli, Diametral error correction in turning slender workpieces: an integrated approach. Int. J. Adv. Manuf. Technol., 130 (3-4) (2024), 1393-1404. http://dx.doi.org/10.1007/s00170-023-12825-9.

Materials Research Proceedings 57 (2025) 655-664 https://doi.org/10.21741/9781644903735-77

Preliminary numerical and experimental investigation of clamping effects on one-up drilling of stacked aluminium aerospace components

Martina Panico[1,a *], Massimo Durante[1,b], Antonio Langella[1,c] and Luca Boccarusso[1,d]

[1]Dept. of Chemical, Materials and Production Engineering, University of Naples "Federico II", P.le Tecchio 80, 80125, Naples, Italy

[a]martina.panico@unina.it, [b]mdurante@unina.it, [c]antgella@unina.it, [d]luca.boccarusso@unina.it

Keywords: Drilling, Virtual Modelling, Aeronautical & Aerospace

Abstract. The emerging challenge in the aerospace industry of integrating thin structural units (thickness < 1.0 mm) into new assemblies, coupled with the necessity of drilling their stacked components, presents new investigative opportunities in manufacturing, including the study of new phenomena that arise during the drilling process. To address these challenges, this study offers a preliminary investigation into the drilling process carried out on samples representing thin fuselage and stringer assembly. Both experimental tests and finite element (FE) analyses were conducted. The FE model was developed to predict and estimate the elastic deformation and interlayer gap arising during the drilling process. The study considers multiple clamping configurations using temporary fasteners, aiming to assess their influence on system stiffness. This ongoing research provides initial insights into optimizing drilling processes for lightweight aerospace structures by addressing the mechanical interactions within stacked configurations. The findings of this study highlight the necessity of further investigating the phenomenon and investing in new FEM approaches. This is essential for accurately predicting clamping conditions when drilling large-scale structures such as fuselages.

Introduction

The demand for fuel efficiency and energy optimization in aerospace engineering has led to the pursuit of structurally lightweight solutions. This goal is achieved by integrating advanced structural design with the development of high-performance materials that minimize weight while maintaining mechanical integrity [1,2]. Among these materials, aluminum alloys and fiber-reinforced composites have become essential due to their superior strength-to-weight ratios and adaptability to aerospace manufacturing [3]. Aluminum alloys, in particular, play a crucial role in aerospace structures due to their excellent machinability, corrosion resistance, and cost-effectiveness [4]. Among the most commonly used aluminum alloys in aerospace applications are AA2024, AA7075, and AA6061. These alloys are employed in critical structural components such as fuselage skins, wing panels, and reinforcement elements like stringers and frames [5,6]. Their superior mechanical properties enable the design and manufacturing of thin-walled structural elements that maintain high performance while minimizing weight. However, their reduced thickness and flexibility introduce challenges in mechanical joining, particularly in the drilling process required for fastener installation.

The drilling process of thin structural units in aerospace applications presents significant challenges due to their inherent low stiffness and susceptibility to deformation [7,8]. As the industry moves toward increasingly lightweight designs, the integration of thin-walled components, such as fuselage skins and stringers, into new assemblies necessitates precise and reliable drilling processes to ensure structural integrity and assembly efficiency. However,

Content from this work may be used under the terms of the Creative Commons Attribution 3.0 license. Any further distribution of this work must maintain attribution to the author(s) and the title of the work, journal citation and DOI. Published under license by Materials Research Forum LLC.

conventional small-scale studies of the drilling process often fail to capture the complexities introduced by structural boundary conditions, leading to discrepancies when transitioning from laboratory experiments to full-scale production.

One of the critical aspects of drilling thin aerospace structures is the emergence of elastic deformations and interlayer gaps, which significantly affect hole quality. When stacked thin sheets are drilled, the lack of sufficient stiffness and support results in global elastic deflection of the structure and localized deformation in the drilling area. This phenomenon simultaneously alters the planarity of the drilling surface, leading to hole ovalization [9,10], and increases plastic deformation, particularly at the exit section of the stack, where the material's resistance is minimal, resulting in a highly pronounced burr defect. The interlayer gap is particularly exacerbated in thin structures, further compromising hole quality [11,12]. Temporary fasteners, while partially suppressing the interlayer gap by locally pinning the stacked components at multiple junction points, do not contribute to increasing the flexural stiffness of the structure, as demonstrated by Panico et al. in [13].

The limitation of small-scale laboratory investigations become particularly evident when considering the scale-dependent effects of structural deformations. In a controlled environment, experiments often focus on the direct influence of machining parameters, such as cutting speed, feed rate, and tool geometry, on the drilling process [14–16], while overlooking the broader mechanical interactions within the stacked configuration. However, in an industrial setting, boundary conditions such as fixture compliance, fastener placement, and the flexural stiffness of the assembly substantially influence the overall behaviour of the stack. Consequently, the simplifications inherent in small-scale studies may lead to misleading conclusions regarding hole quality, dimensional accuracy, and surface integrity.

To bridge the gap between laboratory-scale studies and industrial production, a more comprehensive approach is required, incorporating both experimental testing and predictive Finite element (FE) simulations to offer a powerful tool to estimate elastic deformations, interlayer gaps, and stress distribution during drilling. Implementing laboratory-defined conditions in a numerical model allows for an initial evaluation of process strategies, reducing costs associated with experimental validations, it becomes possible to assess the interply between drilling parameters and structural constraints, leading to optimized process strategies tailored for thin aerospace assemblies.

This study aims to provide an initial macroscopic investigation into the drilling process of thin fuselage and stringer structures. Focusing on estimating the flexural effects induced by the applied force system. The numerical model was developed in three progressive stages:

- First level (*Baseline Model: Single Stringer Configuration*): Basic configuration with a skin coupled to a central stringer. A single hole was drilled at mid-span under maximum deformation conditions.
- Second level (*Extended Model: Multi-Stringer and Clamping Configuration Implementation*): Expansion to a structural unit with the same skin but including three evenly distributed stringers. Three different clamping configurations with temporary fasteners were tested to evaluate their impact on system stiffness.
- Ongoing development (*Advanced Simulation: Elastic Springback Prediction*): Aims to predict elastic springback effects for a refined estimation of interlayer gap evolution using an improved numerical methodology and advanced simulation tools.

The numerical model outputs interlayer gap predictions, which were experimentally validated using high-speed camera and Digital Image Correlation techniques. This structured approach improves the macroscopic understanding of the drilling process of stacked configurations and supports the development of more effective drilling strategies for thin-walled aerospace structures.

Materials Research Proceedings 57 (2025) 655-664 https://doi.org/10.21741/9781644903735-77

Materials and Methods

Experimental Setup. The experimental setup was designed to investigate the formation of the interlayer gap and the effects of clamping conditions on thin structures during the drilling process. The study involved two distinct configurations, corresponding to the first and second levels of analysis, each progressively increasing in complexity to better approximate real assembly conditions.

The first-level experimental setup focused on a simplified configuration, previously studied by Panico et al. in [17], to establish a baseline understanding of the interlayer gap phenomenon. In this configuration, the skin was pre-drilled prior to assembly, meaning that only the stringer was directly subjected to the drilling process. This assumption was made based on the hypothesis that the interlayer gap is entirely attributed to the elastic deformation of the stringer when the pre-drilled skin returns to its undeformed configuration, and the thrust force causes the stringer to flex. The structure consisted of a thin AA2024-T4 skin (1000 mm x 300 mm x 1 mm) coupled with an L-shaped stringer (16 mm x 26 mm x 1.6 mm), as shown in Figure 1a. This assembly was positioned on two lateral supports spaced 1000 mm apart, forming a simply supported beam configuration to allow for global elastic deformation under drilling forces. The drilling process was conducted using a CNC machine (C.B. Ferrari) equipped with an HSS drill bit (diameter, ϕ = 6.364 mm, point angle = 140°), operating at a spindle speed of 5000 rpm and a feed rate of 0.10 mm/rev. To capture the dynamic behavior of the interlayer gap, a high-speed camera (Olympus i-SPEED 3) was employed, while a KISTLER 9257A force sensor recorded the thrust force exerted by the drill bit. The experimental setup is depicted in Figure 1b.

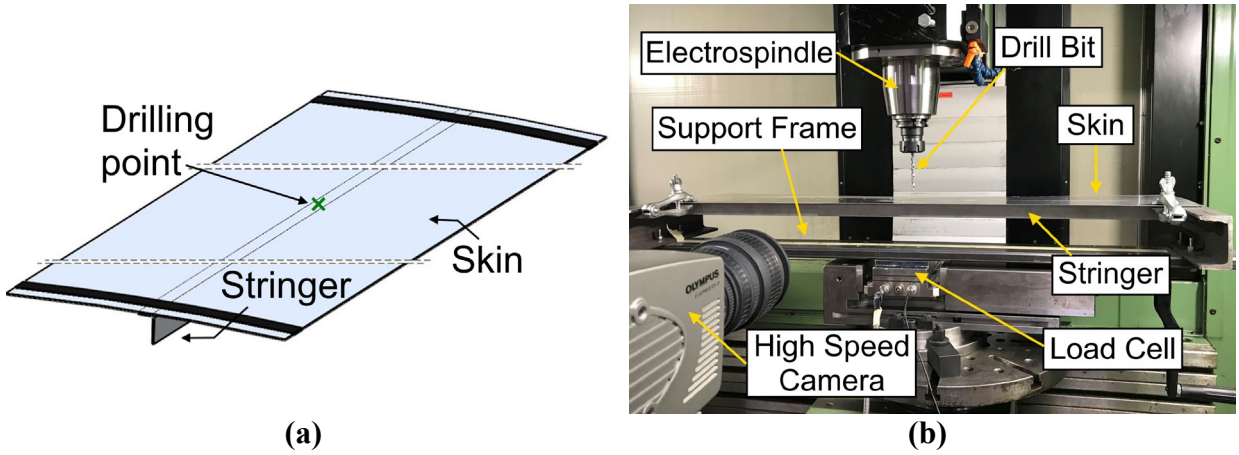


Figure 1 (a) Case study (Baseline Model: Single Stringer Configuration); (b) Experimental setup.

Building upon the findings of the first level, the second-level experimental setup introduced an enhanced structural configuration to evaluate the influence of clamping conditions on interlayer gap formation. Unlike the first level, in this configuration, the drilling process was performed on the entire skin-stringer assembly, allowing for a more comprehensive assessment of the structural response of each component during drilling. The test article retained the same AA2024-T3 skin but incorporated three evenly distributed stringers to better replicate real aerospace structures. Additionally, three different clamping configurations were implemented using Cleco fasteners, positioned at 40 mm (Section A), 300 mm (maximum flexibility condition, Section B), and 80 mm (Section C) intervals. The case study is schematised in Figure 2a. This modification allowed for the assessment of the effectiveness of localized fastening in reducing interlayer separation. The drilling operations were performed using the same CNC machine, tool, and process parameters as in the first level to maintain consistency across experiments. These conditions are summarised in

Materials Research Proceedings 57 (2025) 655-664 https://doi.org/10.21741/9781644903735-77

Table 1 and remained unchanged between the first- and second-level experimental configurations to ensure direct comparability. To enhance the accuracy of interlayer gap measurements, a Digital Image Correlation (DIC) technique was applied in conjunction with high-speed images, providing a more detailed analysis of the material deformation. The experimental setup is depicted in Figure 2b.

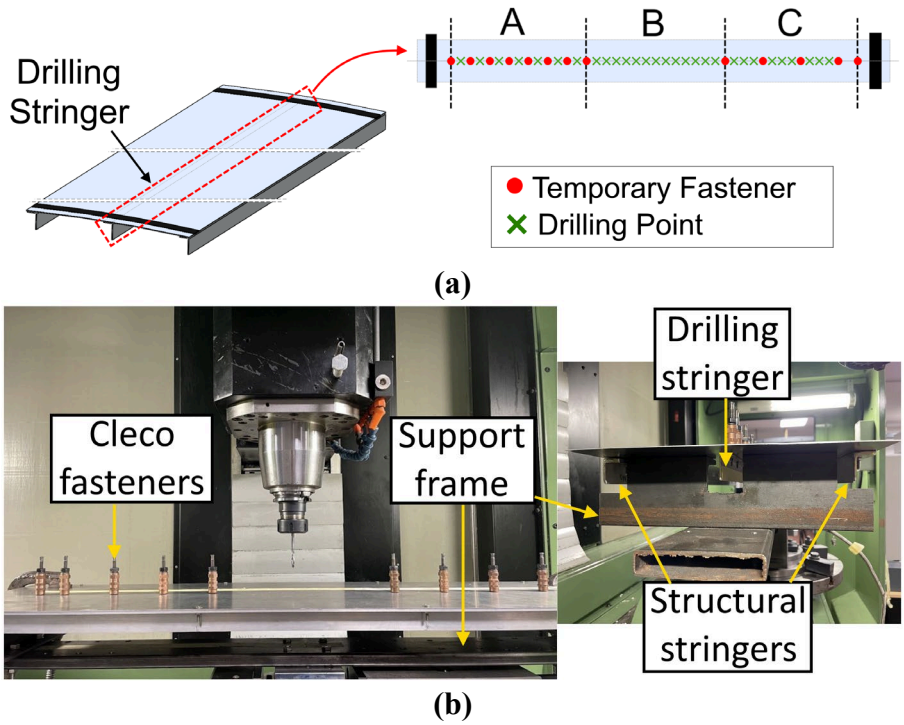


Figure 2 (a) Case study (Extended Model. Multi-Stringer and Clamping Configuration Implementation); (b) Experimental setup.

Table 1 CNC machine, tool specifications, and drilling parameters used.

Category	**Specification**
CNC Machine	C.B. Ferrari
Tool Material	HSS (High-Speed Steel)
Tool Diameter	6.346 mm
Point Angle	140°
Spindle Speed	5000 rpm
Feed Rate	0.10 mm/rev

Numerical Modelling. In the following section, a description of the numerical modelling approach used to simulate interlayer gap formation and clamping effects in thin structures is provided.

Baseline Model: Single Stringer Configuration. The three-dimensional finite element model was developed using Marc Mentat 2022.1 software. The first-level numerical model was designed to simulate the interlayer gap phenomenon in a single-stringer configuration. This model represents both skin and stringer as deformable bodies, with the skin modelled as a solid shell and the stringer as a shell along its midplane surface. Boundary conditions were imposed at the lateral edges to constrain all degree of freedom, while a time-dependent thrust force, derived from experimental measurements, was applied at the centre of the stringer's minor flange. The objective of this model was to quantify the stringer's displacement and predict the maximum interlayer gap, enabling validation with experimental results.

Materials Research Proceedings 57 (2025) 655-664 https://doi.org/10.21741/9781644903735-77

Extended Model: Multi-Stringer and Clamping Configuration Implementation. In Figure 3a, a front view of the model with the addition of two structural stringers is shown. Figure 3b illustrates an excerpt from section A, highlighting alternating drilling and pre-assembly points. At each drilling point, axial point forces are applied, equal to the maximum thrust force value extracted from the force-time curve recorded during the drilling of each point. It should be noted that n-jobs were executed, each simulating a single drilling event. For the skin-stringer joint modelling, RBE2 elements were used (details provided in Figure 3c). An RBE2 constraint links a reference node, positioned at the centre of the hole and at the skin-stringer thickness midpoint, to all nodes located on the edge of the skin and stringer hole, which are defined as tied entities.

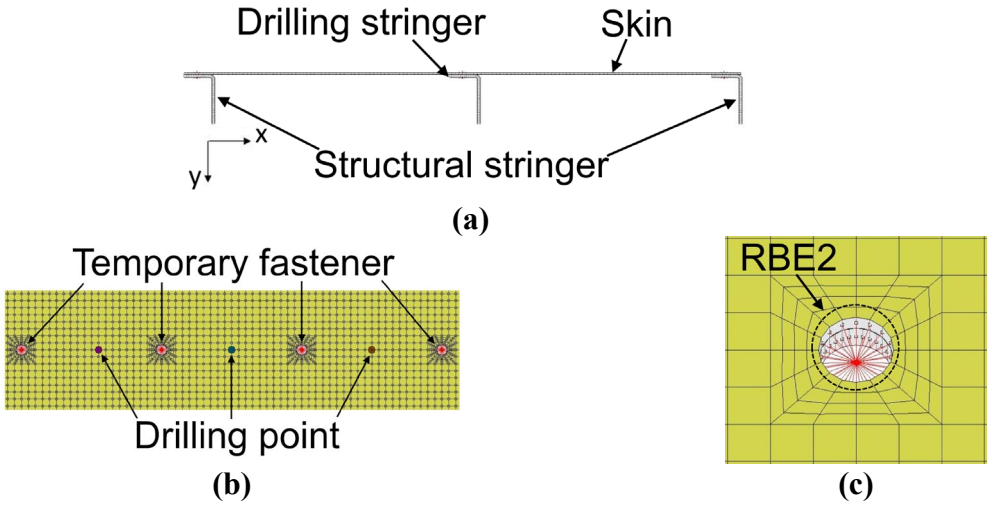


Figure 3 Details of the numerical model: (a) Finite element model overview; (b) Section A excerpt showing alternating drilling and pre-assembly points; (c) focus on modelling of temporary fasteners (RBE2 element).

It is important to note that, in both the baseline and extended models, the drilling process and material removal were not explicitly modelled. Instead, the effect of drilling was simulated by applying the experimentally measured thrust force as a boundary load to reproduce the structural deformation induced by the tool.

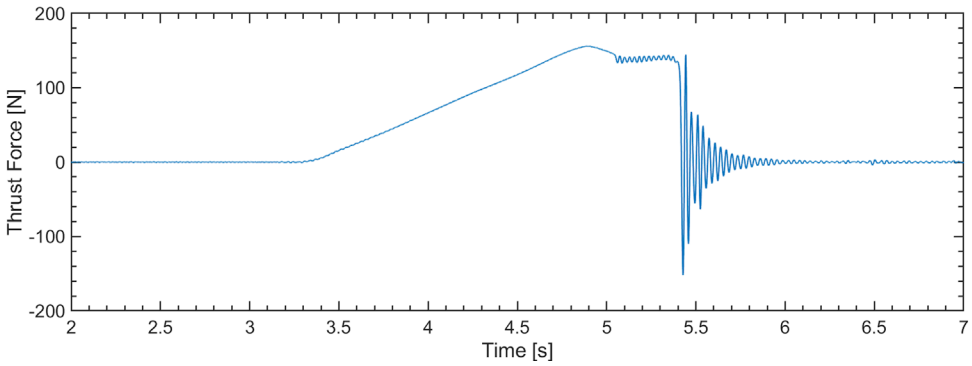
Results and Discussion

The results obtained from the numerical simulations were analysed to evaluate the accuracy and predictive capability of the developed models in estimating interlayer gap formation during the drilling process. The discussion is structured to first present the validation of the baseline numerical model before presenting and analysing the findings of the extended one. The numerical results of the baseline model underestimate the experimentally measured values by only 2.6%, indicating a strong correlation between the numerical predictions and experimental observations. This minimal discrepancy validated the reliability of the model, providing a robust foundation for further extending the numerical analysis. The high level of agreement between simulation and experimental results justified the development of a more comprehensive numerical model to explore additional structural configurations and clamping effects.

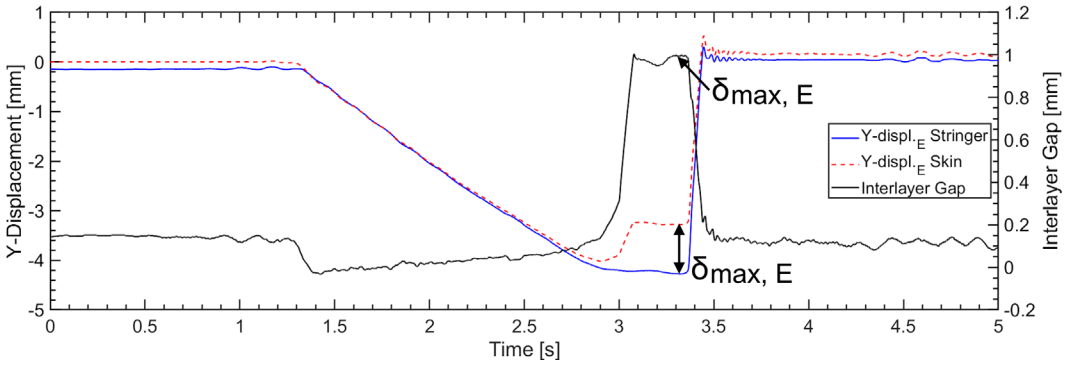
To initiate the discussion of the extended model results, the hole obtained in the section characterised by the maximum flexibility, i.e., central hole of the Section B (see Figure 2a) is considered as a representative case. Specifically, its evolution of thrust force, deflection behavior, and interlayer gap formation over time is examined. This selection provides a clear reference point for understanding the mechanical response of the assembly under drilling-induced forces.

Materials Research Proceedings 57 (2025) 655-664 https://doi.org/10.21741/9781644903735-77

Figure 4 presents the experimental acquisitions and numerical interpretation of thrust force (Figure 4a), displacement of skin and stringer and the corresponding interlayer gap (Figure 4b) of the hole under investigation. The deflection trend closely follows the thrust force curve, with maximum deflection occurring at the peak thrust force. During this phase, the skin and stringer deform cohesively, acting as a single structural unit. This behaviour is confirmed by the superimposed displacement curves for both components until the peak thrust force is reached. As the drill bit exits the skin and progressively engages with the stringer, a separation occurs between the two layers, forming a measurable interlay gap (δ_{max}), as shown in Figure 4b. Given the 1 mm thickness of the skin and the cutting edge height of the drill, the tool interacts with the stringer before fully disengaging from the skin. Consequently, the skin does not revert to its original undeformed configuration but instead exhibits a partial lift due to the tool's continued engagement with the stringer. The interlayer gap evolution is further illustrated in Figure 4c, where δ_{max} is highlighted as the absolute pointwise difference between the displacements of the skin and stringer throughout the drilling process.



(a)



(b)

Figure 4 Example case: (a) Thrust force over time; (b) y-displacement (deflection) trend for both skin and stringer over time; and (c) interlayer gap trend over time.

The following analysis continues to use the same hole as an illustrative example based on data obtained from finite element simulation. Figure 5 shows the progression of y-displacement as a function of the applied thrust force for the nodes on the skin and stringer experiencing maximum displacement.

Materials Research Proceedings 57 (2025) 655-664 https://doi.org/10.21741/9781644903735-77

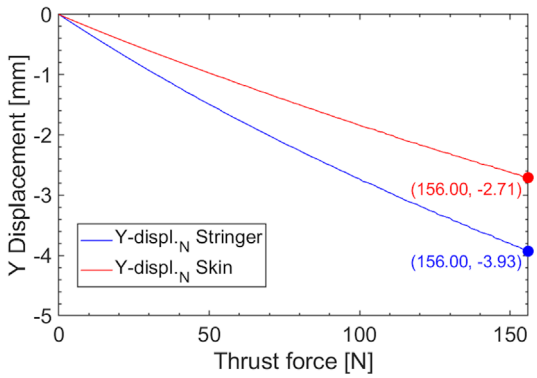
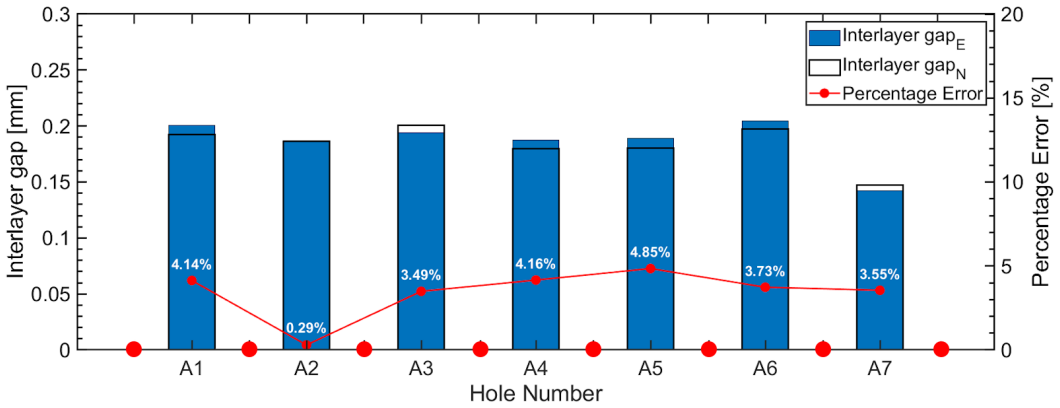


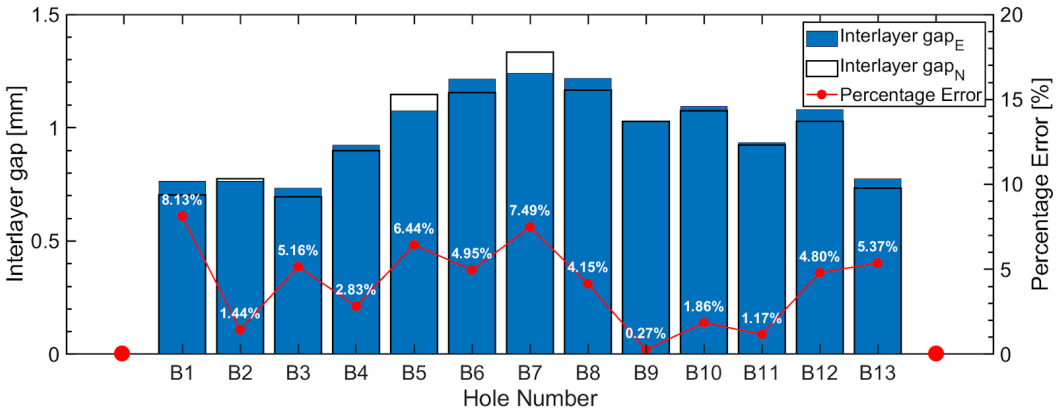
Figure 5 Example case: finite element model for hole B8. History plot of the y-displacement for the nodes where the maximum displacement is recorded.

When no thrust force (0 N) is applied, the model is in its undeformed configuration. Upon application of the maximum thrust force (156 N), the model reaches its deformed configuration. The percentage error between the experimentally obtained maximum interlayer gap (δmax, E = 1.16613 mm) and the maximum interlayer gap obtained from the numerical model (δmax, N = 1.21663 mm) is approximately 4.15%.

Figure 6 illustrates the interlayer gap values for each hole across three clamping configurations, represented in section A (Figure 6a), section B (Figure 6b), and section C (Figure 6c).

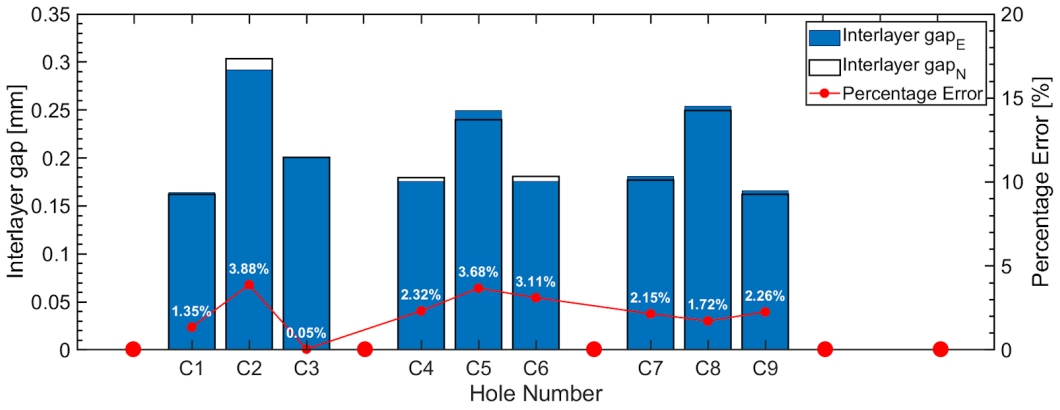


(a)



(b)

Materials Research Proceedings 57 (2025) 655-664 https://doi.org/10.21741/9781644903735-77



(c)

Figure 6 Interlayer gap values at each drilling point: (a) Section A; (b) Section B; and (c) Section C.

Each figure presents a comparison between the experimentally and numerically obtained interlayer gap values, along with the corresponding percentage error. The observed variation in percentage error across different clamping configurations can be attributed to the influence of fastener spacing (local effect) and the absolute position of the hole within the assembly (global effect). In clamping configuration B, where only two temporary fasteners are placed 300 mm apart, the highest interlayer gap values are recorded compared to the other two configurations, notably, the peak gap occurs at the midpoint between the fasteners. This phenomenon is linked to the overall increase in assembly flexibility, as this location is the farthest from the global clamping system. As a results, section B exhibits increased flexibility, leading to greater deflection under load at the drilling point in the centre of the section, thereby amplifying interlayer separation. Additionally, the highest percentage errors between experimental and numerical interlayer gap values are also observed in this configuration. This can be explained by the fact that a stiffer configuration minimizes the impact of external factors, such as vibrations and material response in terms of elastic springback, thereby improving the accuracy of numerical predictions. Conversely, increased flexibility introduces complexities that the numerical model may not fully capture, leading to higher discrepancies and percentage errors.

Advanced Simulation Approach (Ongoing Development)

The necessity to develop a more advanced simulation methodology arises from the limitations observed in the current numerical modelling approach, particularly in Section B, which exhibits the lowest flexural stiffness and is therefore more susceptible to deflection during drilling. High-speed imagining data analysed through Digital Image Correlation revealed that the elastic springback of the skin, once drilled, plays a non-negligible role in the formation of the interlayer gap.

To address this limitation, a more refined numerical strategy is under development, leveraging the NC Machining tool implemented in Marc. Unlike conventional simulations that focus on material removal and chip formation, this method does not aim to replicate the cutting mechanics but rather to isolate and analyse the elastic deformations of the individual stack components contributing to interlayer gap formation. The NC Machining tool allows for a controlled element deactivation process, ensuring that the stress distribution evolves realistically as the tool advances. The methodology relies on defining the tool geometry, particularly the point angle and cutting edge height, to guide the sequential deactivation of elements along the cutting path. This approach enables a more precise simulation of the stress redistribution within the stack as material is

progressively removed, capturing the elastic response of the skin and its influence on interlayer gap formation.

Conclusions

This study presents the work in progress research activity to develop comprehensive numerical model to predict the interlayer gap extension during the drilling of thin aerospace structures under different clamping conditions. The findings confirm that clamping configurations significantly influence interlayer gap formation, with larger fastener spans leading to increased deformation.

The first-level numerical model exhibited strong agreement with experimental results, underestimating the interlayer gap by only 2.6%. This validation justified the extension of the model to a more complex, multi-stringer configuration in the second level. The analysis revealed that sections with increased fastener spacing experienced higher interlayer gaps, particularly in Section B, where the reduced flexural stiffness amplified elastic deformations during drilling. Conversely, in Sections A and C, where clamping was more effective, the numerical predictions closely matched the experimental data, as the constraints mitigated the elastic recovery of the skin.

The discrepancies observed in Section B emphasized the necessity of refining the simulation approach to better capture the elastic recovery of the skin post-drilling. To address this, an advanced simulation methodology is being developed using the NC Machining tool in MSC Marc. Unlike conventional numerical models that focus on material removal and chip formation, this method prioritizes the precise modelling of stress redistribution by implementing controlled element deactivation along the tool path. This approach is expected to improve the predictive accuracy of numerical simulations, particularly in flexible aerospace structures where localized deflections play a crucial role in interlayer gap formation.

References

[1] Soni R, Verma R, Kumar Garg R, Sharma V. A critical review of recent advances in the aerospace materials. Mater Today Proc 2023. https://doi.org/10.1016/j.matpr.2023.08.108

[2] Sabatini R, Gardi A. Sustainable Aviation Technology and Operations. Wiley; 2023. https://doi.org/10.1002/9781118932599

[3] Jobanpreet Singh, Srivastawa K, Jana S, Dixit C, S R. Advancements in Lightweight Materials for Aerospace Structures: A Comprehensive Review. Accel Aerosp J 2024;2:173–83. https://doi.org/10.61359/11.2106-2409

[4] Li S, Yue X, Li Q, Peng H, Dong B, Liu T, et al. Development and applications of aluminum alloys for aerospace industry. J Mater Res Technol 2023;27:944–83. https://doi.org/10.1016/j.jmrt.2023.09.274

[5] Kermanidis AT. Aircraft Aluminum Alloys: Applications and Future Trends. Revolutionizing Aircraft Materials and Processes, Cham: Springer International Publishing; 2020, p. 21–55. https://doi.org/10.1007/978-3-030-35346-9_2

[6] Aglawe K, Giri S, Dhande M, Shelare S. Application of aluminum alloys in aviation industry: A review, 2023, p. 020064. https://doi.org/10.1063/5.0163002

[7] Wang Q, Hou R, Li J, Ke Y. Analytical and experimental study on deformation of thin-walled panel with non-ideal boundary conditions. Int J Mech Sci 2018;149:298–310. https://doi.org/10.1016/j.ijmecsci.2018.10.001

[8] Panico M, Durante M, Langella A, Boccarusso L. One-shot drilling process for thin CFRP/Aluminium alloys stacks. Materials and Manufacturing Processes 2024:1–16. https://doi.org/10.1080/10426914.2024.2311383

[9] Aamir M, Giasin K, Tolouei-Rad M, Vafadar A. A review: drilling performance and hole quality of aluminium alloys for aerospace applications. Journal of Materials Research and Technology 2020;9:12484–500. https://doi.org/10.1016/j.jmrt.2020.09.003

[10] Aamir M, Tolouei-Rad M, Giasin K, Vafadar A, Koklu U, Keeble W. Evaluation of the Surface Defects and Dimensional Tolerances in Multi-Hole Drilling of AA5083, AA6061, and AA2024. Applied Sciences 2021;11:4285. https://doi.org/10.3390/app11094285

[11] Pardo A, Cseke A, Heinemann R, Whiffen R. The effect of interlayer gap width on burr formation in drilling of aluminium-aluminium aerospace stacks. The International Journal of Advanced Manufacturing Technology 2019;104:3035–43. https://doi.org/10.1007/s00170-019-04202-2

[12] Liang J, He Y. Study on the evolution and suppression strategy of the interlayer gap in the drilling of CFRP/Al stacked materials. J Manuf Process 2023;92:329–37. https://doi.org/10.1016/j.jmapro.2023.02.010

[13] Panico M, D'Agostino E, De Rosa V, Durante M, Messere S, Langella A, et al. One-shot drilling of unconventional thin metal hybrid stacks for aerospace applications. Materials Research Proceedings, 2024, p. 2462–71. https://doi.org/10.21741/9781644903131-271

[14] Liang X, Wu D, Gao Y, Chen K. Investigation on the non-coaxiality in the drilling of carbon-fibre-reinforced plastic and aluminium stacks. Int J Mach Tools Manuf 2018;125:1–10. https://doi.org/10.1016/j.ijmachtools.2017.11.001

[15] Mahdi A, Turki Y, Habak M, Salem M, Bouaziz Z. Experimental study of thrust force and surface quality when drilling hybrid stacks. The International Journal of Advanced Manufacturing Technology 2020;107:3981–94. https://doi.org/10.1007/s00170-020-05252-7

[16] S S, V K. Drilling study on CFRP/Ti-6Al-4V stacks using chip breaker grooved drill. Materials and Manufacturing Processes 2022;37:1511–25. https://doi.org/10.1080/10426914.2022.2030872

[17] Panico M, Durante M, Langella A, Boccarusso L. Numerical and theoretical approach to evaluate the clamping force and the interlayer gap extent during drilling of stacked materials. Proc Inst Mech Eng B J Eng Manuf 2024. https://doi.org/10.1177/09544054241238477

Materials Research Proceedings 57 (2025) 665-672 https://doi.org/10.21741/9781644903735-78

Manufacturing of vitrimer matrix composite substrates for cold-spray coatings

Fausto TUCCI[1,a *], Barbara PALMIERI[2,b], Alessia Serena PERNA[3,c], Antonio VISCUSI[4,d], Alfonso MARTONE[2,e] and Antonello ASTARITA[3,f]

[1]Department of Industrial Engineering, University of Salerno, Italy

[2]Institute for Polymer, Composite and Biomaterials, Italian Research Council, Italy

[3]Department of Chemical, Materials and Production Engineering, University of Naples Federico II, Italy

[4]Faculty of Technology and Innovation Sciences, Universitas Mercatorum, Italy

[a]ftucci@unisa.it, [b]barbara.palmieri@ipcb.cnr.it, [c]alessiaserena.perna@unina.it, [d]antonio.viscusi@unimercatorum.it, [e]alfonso.martone@cnr.it, [f]antonello.astarita@unina.it

Keywords: Resin Infusion, Cold Spray, Vitrimer Matrix Composites

Abstract. The application of fiber-reinforced polymers in the aerospace sector is limited by their poor surface properties. However, the high specific strength and custom anisotropy push the research towards the widening of their applicability by new combinations of materials and surface coatings. This work aims at the realization of cold-spray coated composites healable, resilient, and resistant to the LEO-space environment. Vitrimer matrix was formulated to realize composites functionalized for cold-spray deposition. Vitrimers are an emerging class of epoxy-based polymers characterized by the properties of thermosets and the capability of being softened, reshaped, and remelted at high temperatures. These characteristics make the composites in high-modulus fiber-reinforced vitrimers suitable for receiving cold-spray deposition. The activities of this work investigate the formulation of vitrimers, their adoption in heat-assisted vacuum infusion, and the cold-spray coating of such substrates.

Introduction

The social need for sustainability in processes, materials, and design is pushing researchers towards the study of lightweight components topologically and structurally optimized to guarantee high performance and low environmental impact. Polymer matrix composites are a good solution for numerous ecological issues due to their high strength-to-weight ratio [1]. However, most composites are produced using thermoset matrices, which thwart recycling and reusing due to their irreversible curing reaction, making these materials impossible to remelt, and their brittleness, making these materials impossible to be reformed [2,3]. Moreover, despite their high specific mechanical properties, polymer matrix composites exhibit quite poor surface properties [4]. Surface metallization is a viable solution to improve surface properties [5]. However, coating thermoset matrix composites is extremely challenging due to their brittleness. In some cases, this issue has been overcome by adopting a thermoplastic interlayer [6]. Nevertheless, the realization of hybrid matrix composites (thermoset + thermoplastic interlayer) requires a preliminary hot compaction process and is constrained by the polymers' compatibility.

This study investigates the adoption of vitrimeric matrices for the direct infusion of a carbon fabric reinforcement. The technological properties of the vitrimer were characterized to define the manufacturing parameters and the curing cycle. The composite produced has been coated with copper powder deposited by cold spray process.

Content from this work may be used under the terms of the Creative Commons Attribution 3.0 license. Any further distribution of this work must maintain attribution to the author(s) and the title of the work, journal citation and DOI. Published under license by Materials Research Forum LLC.

Materials Research Proceedings 57 (2025) 665-672 https://doi.org/10.21741/9781644903735-78

Materials and Methods

The resin formulation in this study consists of a blend Bisphenol A diglycidyl ether (DGEBA) epoxy resin, with tetrahydro-methyl phthalic anhydride (THMPA) functioning as the hardener, and 2,4,6-tris(dimethylaminomethyl)phenol acting as the catalyst. All materials were supplied by Huntsman Corporation.

To enhance the vitrimeric properties of the epoxy system, anhydrous zinc acetyl acetonate ($Zn(Acac)_2$) was introduced as a catalyst to alter the conventional resin formulation. The formulation was prepared with a stoichiometric epoxy-to-acyl ratio of 1:1, and $Zn(Acac)_2$ was added at 10 wt.% based on the total acyl content.

The manufacturing process began with hand-mixing the epoxy resin and $Zn(Acac)_2$ powder, followed by the addition of the cross-linking anhydride. The mixture was then processed in a planetary centrifugal mixer under vacuum at room temperature. Afterward, the amine accelerator was added, and the mixture was further mixed to ensure homogeneity.

Thermogravimetric analysis (TGA) was performed using a TA Instruments Q500 to determine the thermal stability range of the polymer, following the guidelines of ASTM E1131. The measurements were carried out under an inert atmosphere by flowing nitrogen gas, with a heating rate of 10°C/min, starting from room temperature and reaching up to 800°C. At 600°C, the material's weight loss was analyzed.

The composite's thermal characteristics were further examined via differential scanning calorimetry (DSC) using a Discovery DSC instrument from TA Instruments. Specimens, each weighing approximately 10 mg, were sealed in aluminum pans before analysis. The test involved two cycles of heating and cooling between 0 and 250°C at a constant rate of 10°C/min in a nitrogen environment. Key parameters, including the glass transition temperature (Tg) and reaction enthalpy, were obtained from the resulting DSC curves in compliance with ASTM D3418.

Dynamic mechanical analysis (DMA) was performed using a TA Instruments Q800 in three Point Bending (3PB) configuration. Rectangular samples with dimensions of 60 mm in length, 10 mm in width, and roughly 4.2 mm in thickness were analyzed. The thermal behavior of polymers was assessed over a temperature range from 30°C to 180°C, applying a heating rate of 3°C/min, a strain amplitude of 30 μm, and a frequency of 1 Hz. The data were interpreted in line with ASTM D790, which outlines the flexural properties of reinforced and unreinforced plastics.

The formulated vitrimer mixture has been adopted in an infusion process to produce carbon fabric reinforced composites, by using the setup illustrated in Fig. 1.

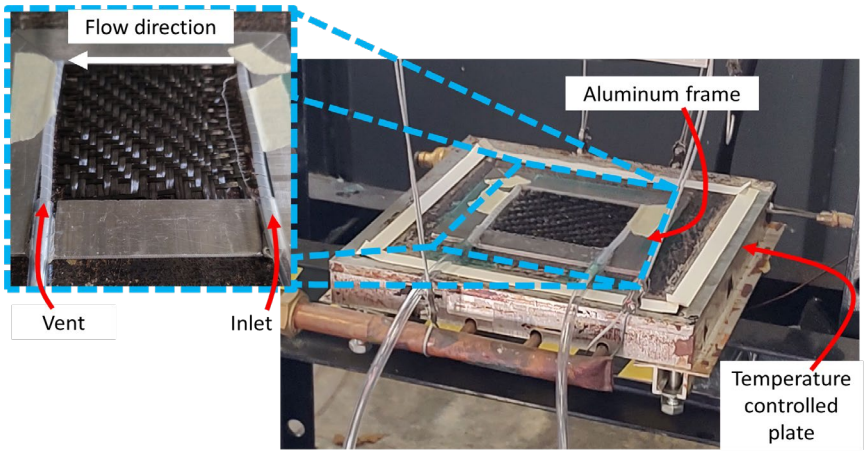


Figure 1. *Vitrimer infusion setup.*

The infusion setup has been designed to produce composite plates having thickness of 5 mm. The need for a controlled thickness and surface planarity excluded the direct usage of a vacuum

Materials Research Proceedings 57 (2025) 665-672 https://doi.org/10.21741/9781644903735-78

bag, since its flexibility does not allow to precisely set the desired shape. The carbon fabrics having an areal weight of 400 g/m^2 have been laminated on the surface of a temperature-controlled plate, previously treated with a release agent. A frame in aluminum alloy guaranteed the thickness of 5 mm. A rigid counter mold has been placed on the frame. The system described was sealed within a vacuum bag to avoid air leakages. The ingredients of the vitrimer were mixed at a temperature of 60°C to decrease the viscosity of the epoxy component. Once mixed, the vitrimeric system has been heated to 80°C and has been infused. The infusion was driven by a vacuum pump generating a relative pressure of -0.96 atm. The pressure was monitored at the pump and at the resin trap. During the infusion, the temperature of the lower mold was kept at 75°C by a PID controller governing a heating resistance embedded in the plate and monitored in feedback loop by a thermocouple. Once the infusion was completed, the inlet and vent pipes were clamped to stop the vitrimer flow and the composite system was cured for 2 hours at 120°C and successively post-cured for 2 hours at 140°C.

The cold spray deposition on vitrimeric composite panels was carried out by using copper powders provided by LPW South Group with a nominal particle diameter in the range 15-45 µm. The copper particles were selected due to their compatibility with composite materials, as demonstrated in the literature [7].

A low-pressure cold spray facility (Dymet 423) equipped with the Titomic PB-95 powder feeder was employed for spraying particles; air was used as carrier gas, and a cartesian robot controlling the spray gun and ensuring a consistent and repeatable deposition was employed for the aim. Particularly, the de-Laval nozzle with outlet diameter of 5 mm, was mounted on a three axes pantograph (High-Z S-400/T CNC-Technik) numerically controlled remotely. The cold spray deposition equipment is shown in Fig. 2.



Figure 2. *Cold spray deposition equipment.*

The gun traverse speed and the gas pressure values were kept constant throughout the experimental campaign and set to 5 mm/s and 6 bar, respectively. The powder feed rate was set in terms of density of the feeder, equal to 20 %, which corresponds to a feed rate of approximately 3.5 g/min for the powders system considered [8]. The inlet gas temperature and stand-off-distance (SoD) were chosen as variables, and two levels were selected for each of them, as reported in Tab. 1. Only one pass of the nozzle over the substrate surface was made for all the spraying conditions, resulting in a metal track measuring 50 mm in length. Note that the stand-off distance parameter plays a crucial role in ensuring effective deposition on polymeric substrates. Lower values result in increased thermal exposure and exert a pressure force due to powder collisions during additive growth [9]. Likewise, the inlet gas temperature significantly influences the heating induced on the

Materials Research Proceedings 57 (2025) 665-672 https://doi.org/10.21741/9781644903735-78

target surface, which is critical for particle adhesion [10]. The values of process parameters were defined based on the authors' knowledge and preliminary trials.

Table 1. *Experimental campaign for cold spray deposition.*

Sample identification code	Inlet Gas Temperature (°C)	SoD (mm)
CS_3_50	300	50
CS_3_70	300	70
CS_4_50	400	50
CS_4_70	400	70

Hirox microscope observations (Hirox ST-AS) were conducted to analyze the coating tracks. The results obtained were examined to deepen the understanding of how panel manufacturing strategies and cold spray process parameters influence the characteristics of the coatings.

Results and Discussion

Fig. 3 shows the TGA curves of the studied materials, for the standard and modified epoxy resin and on vitrimeric composite. The residue at 600°C increases for the Vitrimer one due to the presence of the Zinc Acetate. The thermal degradation of vitrimeric polymer, starts at a lower temperature due to the presence of zinc acetate, which degrades at around 300°C, as shown in Fig. 3. A 5% weight loss is found at 358°C for the standard epoxy system; this temperature reduces when zinc acetate is added to the vitrimeric formulation. Moreover, the actual content of CF/vitrimeric composite, reduced by the resin char, is 12.1 %.

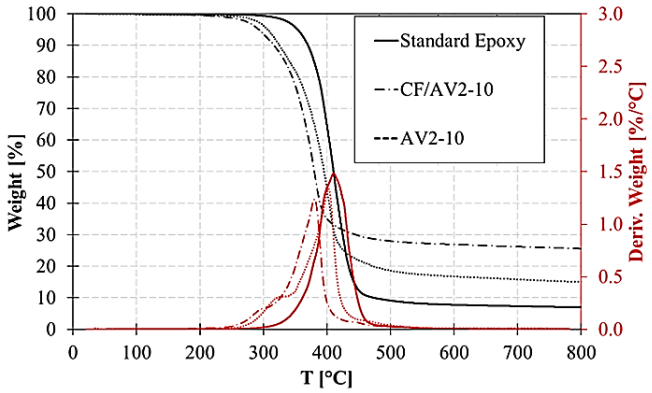


Figure 3. *Thermogravimetric analysis (TGA) curves comparing the thermal degradation of Standard Epoxy (solid black line), vitrimer (dotted line) and CF/Vitrimer (dash-dot black line). The weight percentage (left y-axis) and the derivative weight loss rate (right y-axis, red curves) are plotted against temperature (°C). The graph highlights the different thermal stability and decomposition profiles of the two materials.*

The curing behavior and glass transition temperature (Tg) of the systems are presented in Figure 4. The curing process depicted in Figure 4 for standard epoxy system and the vitrimer is based on the first scan of the DSC thermograms. Two exothermic peaks are observed: the first, around 140°C, corresponds to the curing esterification reaction, while the second, between 180°C and 230°C, is associated with the homomeric ring-opening polymerization of excess epoxy groups. Zinc acetyl acetonate plays a dual role by influencing the primary cross-linking reaction and activating a secondary reaction within the 180°C to 230°C temperature range. During the second

Materials Research Proceedings 57 (2025) 665-672 https://doi.org/10.21741/9781644903735-78

heating ramp, the absence of exothermic peaks confirms the complete conversion of the polymer. The Tg for the standard epoxy systems is measured at 111°C. However, in the vitrimeric formulation the Tg decreases due to reduced cross-linking density, while increase again in case of vitrimeric composite (CF/AV2-10). The thermal behavior of both analyzed systems, as determined by TGA and DSC experiments, is summarized in Tab. 2.

Table 2. *Results of TGA and DSC analyses*

Description	Temperature of 5% weight loss [°C]	Residue at 600°C [wt%]	$T_{g,\ DSC}$ [°C]	Reaction Enthalpy [J/g]	T_{peak} [°C]
Epoxy	358	7.8	111.2	216.6±1.2	130±5
AV2-10	305	16.8	94.3	270.3±2.0	139±2
CF/AV2-10	314.41	26.25	103.41	-	-

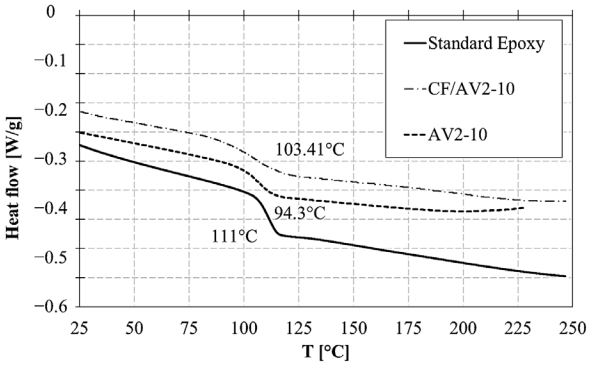


Figure 4. *Differential Scanning Calorimetry (DSC) analysis comparing Standard Epoxy, vitrimer and Vitrimer composite.*

The viscoelastic behavior of vitrimeric polymer and its composite, with temperatures up to 180°C, is presented in Fig. 5 and summarized in Table 3. DMA experiments were performed within the linear viscoelastic deformation range to verify the glass transition temperature and elastic modulus of the cross-linked samples.

For the vitrimer composite, the addition of carbon fiber reinforcement significantly influences the material's mechanical properties. The storage modulus at room temperature increases by 310%. Similarly, the dissipation capacity, represented by the loss modulus (E"), shows a substantial enhancement with the addition of carbon fiber, increasing by +272%. This results in a decrease in the loss factor (-8%) observed in the composite.

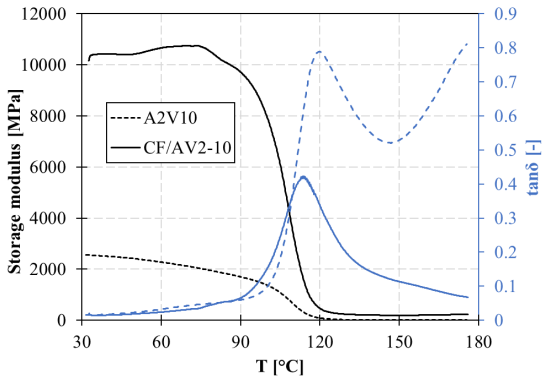


Figure 5. *DMA curves of the AV2-10 and CF/AV2-10.*

Materials Research Proceedings 57 (2025) 665-672 https://doi.org/10.21741/9781644903735-78

Table 3. *Results of DMA analysis at 35°C and 170°C.*

		@35°C			@170°C		
	$T_{g,\ DMA}$	**E'**	**E''**	**Tanδ**	**E'**	**E''**	**Tanδ**
	[°C]	**[MPa]**	**[MPa]**	**[-]**	**[MPa]**	**[MPa]**	**[-]**
AV2-10	101.0±0.7	2484±47	33.4±0.3	0.0135±0.0003	11.89±0.8	3.08±0.06	0.259±0.005
CF/AV2-10	108.16±0.9	10416±52	147.95±0.7	0.0142±0.0004	219.31±0.7	16.63±0.1	0.075±0.007

The composite plate produced exhibits good stiffness and planarity. The vitrimer matrix composite produced is presented in Fig. 6.

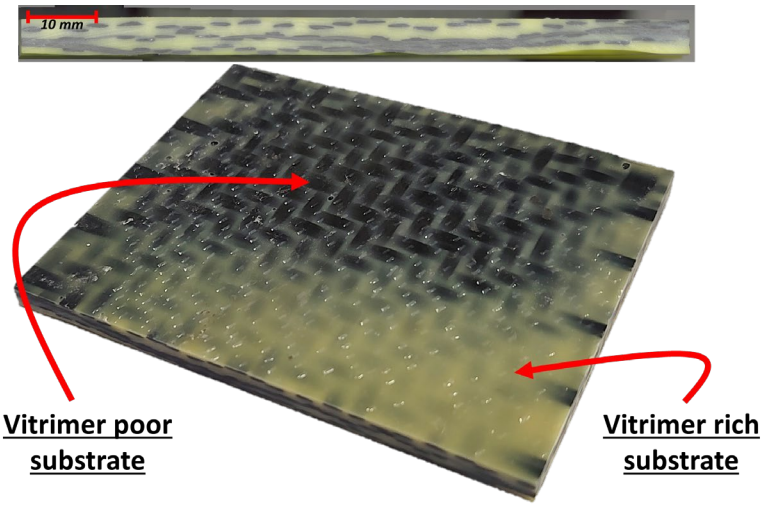


Figure 6. *Carbon-vitrimer composite produced by infusion.*

Even if sufficient planarity has been achieved, the surface of the composite produced by infusion presents inhomogeneity in the thickness of the vitrimeric substrate. Fig. 6 indicates the presence of a region exhibiting a vitrimer rich substrate and a wide region in which the vitrimer layer thickness is sensibly lower. However, the composite does not present zones with exposed reinforcement. The analysis of the cross-section evidences that during the infusion, the fabric reinforcement layers floated into the vitrimeric matrix until curing was not activated and the viscosity was still at its minimum value. This behavior explains the inhomogeneity in the vitrimeric substrate thickness.

Following the CS deposition, the coating tracks obtained on vitrimeric composite panel are presented in Fig. 7.

Materials Research Proceedings 57 (2025) 665-672 https://doi.org/10.21741/9781644903735-78

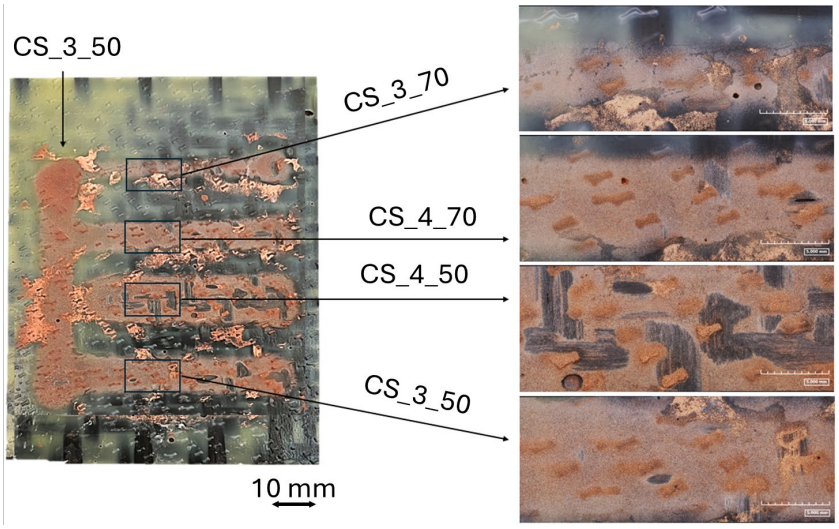


Figure 7. *Results from cold spray deposition on vitrimeric composite panel.*

Firstly, the process's feasibility was confirmed by the successful adhesion of metallic particles to the polymeric surface. This outcome suggests that an epoxy-based composite material can be effectively coated with copper particles via cold spraying when employing a specific vitrimeric formulation. However, it is essential to carefully evaluate and refine the cold spray process parameters to achieve the best coating quality.

By looking at the coating labelled CS_3_70 (T=300 °C and SoD=70 mm), it can be observed that the metallic deposition is poor as the CS process parameters are not suitable for particle adhesion. The reason is due to the reduced particle velocity and the low induced heating on the target surface promoting the adhesion mechanisms.

By increasing the inlet gas temperature at 400 °C, the particles tend to stick with the substrate due to the greater impacting velocity; however, the relatively higher induced heating on the composite surface produces erosion and damage of the exposed fibers, for both the stand-off values under examination.



Figure 8. *Hirox image of cold sprayed copper particles on epoxy-based composite material at T=300°C and SoD=50 mm.*

The best condition in terms of coating quality was found by setting the following cold spray process parameters: T=300°C, SoD=50 mm. Under these process parameters, the particle velocity as well as the induced heating on the target surface seem to be suitable to promote adhesion of copper particles on epoxy-based composite materials. The result is shown in Fig. 8.

Conclusions

This study demonstrates the feasibility of the production of vitrimer matrix composites by infusion process and of the surface metallization by cold spray process. The reactivity and the thermal behavior of the formulated vitrimeric system were characterized to define the infusion parameters and the curing route. Cold spray deposition of copper powder has been performed using different temperatures and stand-off distances, demonstrating that the effective deposition is possible, but its efficiency depends on the spray settings. Deeper testing activities will be performed to define the sensibility of the deposition efficiency to the reinforcing architectures and the deposited powder materials.

Acknowledgements

The authors acknowledge financial support under of the European Union – NextGenerationEU– Project Title “Functionally cold spRayed cOatiNgs for viTrimer composItes in lEo-space hybRid Structures – “FRONTIERS” – CUP B53D2302698000 - Grant Assignment Decree No. P2022CP94J adopted on PE8 by the Italian Ministry of University and Research (MUR).

References

[1] V. Lunetto, M. Galati, L. Settineri, L. Iuliano, Sustainability in the manufacturing of composite materials: A literature review and directions for future research, J. Manuf. Process. 85 (2023) 858–874. https://doi.org/10.1016/j.jmapro.2022.12.020

[2] A. Danish, M.A. Mosaberpanah, M.U. Salim, M. Amran, R. Fediuk, T. Ozbakkaloglu, M.F. Rashid, Utilization of recycled carbon fiber reinforced polymer in cementitious composites: A critical review, J. Build. Eng. 53 (2022) 104583. https://doi.org/10.1016/j.jobe.2022.104583

[3] M. Elen, V. Kumar, L.S. Fifield, Feasibility of Recovering and Recycling Polymer Composites from End-of-Life Marine Renewable Energy Structures: A Review, Sustain. 16 (2024). https://doi.org/10.3390/su162310515

[4] M.Z. Rong, M.Q. Zhang, W.H. Ruan, Surface modification of nanoscale fillers for improving properties of polymer nanocomposites: A review, Mater. Sci. Technol. 22 (2006) 787–796. https://doi.org/10.1179/174328406X101247

[5] H. Parmar, F. Tucci, P. Carlone, T.S. Sudarshan, Metallisation of polymers and polymer matrix composites by cold spray : state of the art and research perspectives, Int. Mater. Rev. 0 (2021) 1–25. https://doi.org/10.1080/09506608.2021.1954805

[6] H. Parmar, F. Rubino, F. Tucci, G. Rotella, P. Poza, P. Carlone, Manufacturing and cold spraying of hybrid composites — A path for metallizing thermoset matrix composites, Surf. Coatings Technol. 489 (2024). https://doi.org/10.1016/j.surfcoat.2024.131144

[7] R. Della Gatta, A.S. Perna, A. Viscusi, G. Pasquino, A. Astarita, Cold spray deposition of metallic coatings on polymers: a review, J. Mater. Sci. 57 (2022) 27–57. https://doi.org/10.1007/s10853-021-06561-2

[8] H. Parmar, F. Rubino, P. Poza, P. Carlone, Manufacturing of hybrid thermoplastic-thermoset fiber reinforced composite and metallization by cold spray technique, Mater. Res. Proc. 28 (2023) 305–312. https://doi.org/10.21741/9781644902479-33

[9] R.N. Raoelison, L. Lalu Koithara, S. Costil, Cold spray coating of PEEK surface by copper deposition: Interfacial adhesion at high deposition efficiency and bonding strength, CIRP J. Manuf. Sci. Technol. 35 (2021) 63–68. https://doi.org/10.1016/j.cirpj.2021.05.008

[10] H. Che, X. Chu, P. Vo, S. Yue, Metallization of Various Polymers by Cold Spray, J. Therm. Spray Technol. 27 (2018) 169–178. https://doi.org/10.1007/s11666-017-0663-1

Keyword Index

Additive Manufacturing 11, 99, 128, 164, 172, 190, 28, 216, 225, 441, 565
Adhesive Bonding 466
Aeronautical & Aerospace 99, 655
Aluminium Alloys 107, 327, 352, 441
Aluminum Alloy Extrusion 344
Anode-Free Batteries 286
Artificial Intelligence 608
Artificial Neural Network 344
Assembly Lines 512
Assisted Assembly Systems 457
Atomic Force Microscopy (AFM) 575
Automotive 503

Back-in-Time Repeatability 20
Battery Cell Stacking Process 631
BCC Sandwich Panels 199
Binder Jetting (BJ) 225

Casting Sand 225
Chatter 145
Circular Economy 2, 426, 493, 617
Coating 99
Cognitive Workload 410
Cold Spray 665
Composites 278, 369, 466, 556
Compression Moulding 592
Compression Test 294
Constitutive Models 626
Coordinate Metrology 64
Copper 319
Cryogenic Milling 385
Cryogenic 251

Debonding 484
Deep Learning 565
Deformation-Induced Martensitic Transformation 242
Demanufacturing Processes 484
Demanufacturing 617
Density 225
Design of Experiment 128
Design Optimization 556
Digital Twin 548
Direct Energy Deposition (DED) 99, 565
Discrete Event Simulation 512
Document-Type Classification 80
Drilling 655

Eco-Design 278
Electric Mobility 164
Energy Absorption 208
Energy Consumption 172
Energy Efficiency 393
Environmental Impact 449, 639
Ergonomics 29
E-Waste 402
Extrusion 56. 434, 449

Fiber-Reinforced Plastic 2
Filament Winding 259, 268
Finite Element Simulation 344
Foaming 311
Friction Stir Welding 327
FSE 352

Generative AI 457
Geometric Modelling 136
Geometrical Tolerances 360
Grinding 608

High Strength Steel 242
High-Entropy Alloys 99
High-Voltage Fragmentation 617

Hot Compression Test 626
Human Aspects 47
Human Robot Collaboration 29, 410, 457
Hybrid Manufacturing 234
Image Processing 64, 369
Industrial Sector 377
Industry 4.0/5.0 548
Industry 5.0 410
Injection Molding 393, 600
In-Process Measurement 369
In-Situ Monitoring 164
Inspection 20, 38
Laser Cutting 319, 335
Laser Powder Bed Fusion 199
Laser Processes 99, 128, 286, 377
Lifecycle Assessment 466, 484
Low Velocity Impact Test 172

Machine Learning 335, 369, 475, 647
Machine Tools & Automation 631
Man-Machine System 410
Manufacturing Materials 216, 352
Manufacturing Platforms 647
Manufacturing Systems 128
Material Extrusion (MEX) 116, 180, 190, 294, 426, 583, 556
Mechanical Separation 617
Mechanical Testing Equipment 626
Mechanical Testing 107, 259, 268
Metrology and Tolerancing 11
Micro Injection 303
Microstructure Prediction 344
Milling 360
Modelling 385
Mold 393
Monitoring 47, 216, 539
Multi-Human Multi-Robot Collaboration 410
Multi-Modal Instruction Interfaces 457
Multi-Physics Simulation 319

Natural Fiber Composites 172
Neural Network 369
Nitinol 91

Object Recognition 600
Operations Management 503

Performance Indicators 80, 539
Peripheral Coarse Grain 344
Plastic & Composite Material Processes 56, 434, 449
Polymers 56, 116, 154, 294, 575
Polypropylene 2
Post-Consumer Recycling 2
Powder Bed Fusion 38, 91, 107, 145, 154, 418
Predictive Maintenance 539
Predictive Model 136, 369
Press Moulding 278
Process Control 335
Process Optimization 319
Process Planning & Control 631
Product Design 493, 583
Product Development 493
Product Lifecycle Management 493
Product Lifecycle 493
Production Planning 530

Quality Control 72
Quality Engineering 29, 47
Quality Engineering 47
Quality 20, 80, 402

Radiography & Tomography 64, 268
Real-Time Object Detection 457
Recycling 617
Repair 234, 639

Residual Stresses 385
Resin Infusion 665
Resistance Welding 72
Reverse Engineering 234

Safety and Well-Being 410
Scheduling 521
Semiconductor Manufacturing 521
Semiconductor 530
Sequencing 503
Shape Memory Polymers 208
Silicone 3D Printing 180
Smart Manufacturing 521, 530, 548
Smart Materials 592
Space Sustainability 592
Stainless Steel 418
Stamping 242
Surface Functionalization 303
Surface Integrity 385
Surfaces 11, 377, 575
Sustainability 2, 259, 311, 352, 402, 418, 434
Sustainable Development 154
Sustainable Processes 441, 475
System Architecture 512

Tensile Strength 116, 327
Textile Demanufacturing 475
Texture 286
Textured Tools 251
Thermoforming 278
Thermography 38,72
Thermoplastics 278, 303, 311
Three-Point Bending Tests 199
Ti6Al4V 199
Turning 91, 251, 647

ULTEM 1010 190

Vacuum-Bag Molding 369
Vibration 145, 360
Virtual Modeling 180, 583, 655
Vitrimer Matrix Composites 665

Wire Arc Additive Manufacturing (WAAM) 136, 426, 639

Zero Defect 600, 608

d